

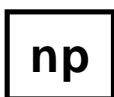
FLUIDIZATION, SOLIDS HANDLING, AND PROCESSING

Industrial Applications

Edited by

Wen-Ching Yang

Siemens Westinghouse Power Corporation
Pittsburgh, Pennsylvania



NOYES PUBLICATIONS
Westwood, New Jersey, U.S.A.

Copyright © 1998 by Noyes Publications

No part of this book may be reproduced or utilized in any form or by any means, electronic or mechanical, including photocopying, recording or by any information storage and retrieval system, without permission in writing from the Publisher.

Library of Congress Catalog Card Number: 98-18924

ISBN: 0-8155-1427-1

Printed in the United States

Published in the United States of America by

Noyes Publications

369 Fairview Avenue, Westwood, New Jersey 07675

10 9 8 7 6 5 4 3 2 1

Library of Congress Cataloging-in-Publication Data

Fluidization, solids handling, and processing : industrial applications / edited by Wen-Ching Yang.

p. cm.

Includes bibliographical references and index.

ISBN 0-8155-1427-1

1. Fluidization. 2. Bulk solids flow. I. Yang, Wen-ching, 1939-
TP156.F65F5828 1998
660'.284292--dc21

98-18924

CIP

PARTICLE TECHNOLOGY SERIES

Series Editor: Liang-Shih Fan, Ohio State University

FLUIDIZATION, SOLIDS HANDLING, AND PROCESSING: Edited by Wen-Ching Yang

INSTRUMENTATION FOR FLUID-PARTICLE FLOWS: by S. L. Soo

Contributors

John C. Chen

Department of Chemical
Engineering
Lehigh University
Bethlehem, PA

Bryan J. Ennis

E&G Associates
Nashville, TN

Liang-Shih Fan

Department of Chemical
Engineering
Ohio State University
Columbus, OH

Leon R. Glicksman

Department of Architecture,
Building Technology Program
Massachusetts Institute of
Technology
Cambridge, MA

Thomas B. Jones

Department of Electrical
Engineering
University of Rochester
Rochester, NY

S.B. Reddy Karri

Particulate Solid Research, Inc.
Chicago, IL

George E. Klinzing

Department of Chemical and
Petroleum Engineering
University of Pittsburgh
Pittsburgh, PA

Ted M. Knowlton

Particulate Solid Research, Inc.
Chicago, IL

Mooson Kwauk

Institute of Chemical Metallurgy
Adademia Sinica
Beijing, People's Republic of
China

Jack Reese

Department of Chemical
Engineering
Ohio State University
Columbus, OH

Jens Reppenhagen

Technical University Hamburg-
Harburg
Hamburg, Germany

Ellen M. Silva

Department of Chemical
Engineering
Ohio State University
Columbus, OH

Gabriel I. Tardos

Department of Chemical
Engineering
City College of City University of
New York
New York, NY

Richard Turton

Department of Chemical
Engineering
West Virginia University
Morgantown, WV

Joachim Werther

Technical University Hamburg-
Harburg
Hamburg, Germany

Peter Wypych

Department of Mechanical
Engineering
University of Wollongong
Wollongong, NSW, Australia

Shang-Tian Yang

Department of Chemical
Engineering
Ohio State University
Columbus, OH

Wen-Ching Yang

Science and Technology Center
Siemens Westinghouse Power
Corporation
Pittsburgh, PA

Frederick A. Zenz

Process Equipment Modeling &
Mfg. Co., Inc.
Cold Spring, NY

Preface

This volume, *Fluidization, Solids Handling, and Processing*, is the first of a series of volumes on “*Particle Technology*” to be published by Noyes Publications with L. S. Fan of Ohio State University as the consulting editor. Particles are important products of chemical process industries spanning the basic and specialty chemicals, agricultural products, pharmaceuticals, paints, dyestuffs and pigments, cement, ceramics, and electronic materials. *Solids handling and processing technologies* are thus essential to the operation and competitiveness of these industries. *Fluidization technology* is employed not only in chemical production, it also is applied in coal gasification and combustion for power generation, mineral processing, food processing, soil washing and other related waste treatment, environmental remediation, and resource recovery processes. The FCC (Fluid Catalytic Cracking) technology commonly employed in the modern petroleum refineries is also based on the fluidization principles.

There are already many books published on the subjects of fluidization, solids handling, and processing. On first thought, I was skeptical about the wisdom and necessity of one more book on these subjects. On closer examination, however, I found that some industrially important subjects were either not covered in those books or were skimpily rendered. It would be a good service to the profession and the engineering community to assemble all these topics in one volume. In this book, I have invited recognized experts in their respective areas to provide a detailed treatment

of those industrially important subjects. The subject areas covered in this book were selected based on two criteria: (i) the subjects are of industrial importance, and (ii) the subjects have not been covered extensively in books published to date.

The chapter on *fluidized bed scaleup* provides a stimulating approach to scale up fluidized beds. Although the scaleup issues are by no means resolved, the discussion improves the understanding of the issues and provides reassessments of current approaches. The *pressure and temperature effects and heat transfer in fluidized beds* are covered in separate chapters. They provide important information to quantify the effects of pressure and temperature. The *gas distributor and plenum design*, critical and always neglected in other books, are discussed in detail. For some applications, the conventional fluidized beds are not necessarily the best. Special design features can usually achieve the objective cheaper and be more forgiving. Two of the non-conventional fluidized beds, *recirculating fluidized beds with a draft tube* and *jetting fluidized beds*, are introduced and their design approaches discussed. *Fluidized bed coating and granulation*, applied primarily in the pharmaceutical industry, is treated from the fluidization and chemical engineering point of view. *Attrition*, which is critical in design and operation of fluidized beds and pneumatic transport lines, is discussed in detail in a separate chapter. Fluidization with no bubbles to minimize bypassing, *bubbleless fluidization*, points to potential areas of application of this technology. The industrial applications of the ever-increasingly important *three-phase fluidization systems* are included as well. The developments in *dense phase conveying* and in *long distance pneumatic transport with pipe branching* are treated separately in two chapters. The *cyclone*, the most common component employed in plants handling solids and often misunderstood, is elucidated by an experienced practitioner in the industry. The book is concluded with a discussion on electrostatics and dust explosion by an electrical engineer.

This book is not supposed to be all things to all engineers. The primary emphasis of the book is for industrial applications and the primary audience is expected to be the practitioners of the art of fluidization, solids handling, and processing. It will be particularly beneficial for engineers who operate or design plants where solids are handled, transported, and processed using fluidization technology. The book, however, can also be useful as a reference book for students, teachers, and managers who study particle technology, especially in the areas of application of fluidization technology and pneumatic transport.

I'd like to take this opportunity to thank Professor Fan who showed confidence in me to take up this task and was always supportive. I'd also like to thank the authors who contributed to this book despite their busy schedules. All of them are recognized and respected experts in the areas they wrote about. The most appreciation goes to my wife, Rae, who endured many missing weekends while I worked alone in the office.

Pittsburgh, Pennsylvania
February, 1998

Wen-Ching Yang

NOTICE

To the best of our knowledge the information in this publication is accurate; however the Publisher does not assume any responsibility or liability for the accuracy or completeness of, or consequences arising from, such information. This book is intended for informational purposes only. Mention of trade names or commercial products does not constitute endorsement or recommendation for use by the Publisher. Final determination of the suitability of any information or product for use contemplated by any user, and the manner of that use, is the sole responsibility of the user. We recommend that anyone intending to rely on any recommendation of materials or procedures mentioned in this publication should satisfy himself as to such suitability, and that he can meet all applicable safety and health standards.

Contents

1	Fluidized Bed Scale-up	1
	<i>Leon R. Glicksman</i>	
1.0	INTRODUCTION	1
2.0	REACTOR MODELING: BED DIAMETER INFLUENCE	4
3.0	INFLUENCE OF BED DIAMETER ON HYDRODYNAMICS	10
3.1	Bubbling Beds	10
3.2	Mixing	20
3.3	Influence of Bed Diameter on Circulating Fluidized Beds	22
3.4	Flow Transition	25
4.0	EXPERIMENTAL MEANS TO ACCOUNT FOR SCALE-UP: USE OF SCALE MODELS	26
4.1	Development of Scaling Parameters	27
4.2	Governing Equations	29
4.3	Fluid-Solid Forces	35
4.4	Spouting and Slugging Beds	38
5.0	SIMPLIFIED SCALING RELATIONSHIPS	39
5.1	Low Reynolds Number	39
5.2	High Reynolds Numbers	41
5.3	Low Slip Velocity	42
5.4	General Case	43
5.5	Range of Validity of Simplified Scaling	44

6.0 FURTHER SIMPLIFICATIONS IN THE SCALING
RELATIONSHIP 51

6.1 Viscous Limit 51

6.2 Other Derivations for Circulating Fluidized Beds 54

6.3 Deterministic Chaos 55

7.0 DESIGN OF SCALE MODELS 56

7.1 Full Set of Scaling Relationships 56

7.2 Design of Scale Models Using the Simplified Set
of Scaling Relationships 61

8.0 EXPERIMENTAL VERIFICATION OF SCALING LAWS FOR
BUBBLING BEDS 65

8.1 Hydrodynamic Scaling of Bubbling Beds 65

8.2 Verification of Scaling Relationships for Bubbling
and Slugging Beds 69

8.3 Verification of Scaling Laws for Spouting Beds 75

8.4 Verification of Scaling Relationships for Pressurized
Bubbling Beds 76

9.0 APPLICATIONS OF SCALING TO COMMERCIAL BUBBLING
FLUIDIZED BED UNITS 80

10.0 HYDRODYNAMIC SCALING OF CIRCULATING BEDS 91

11.0 CONCLUSIONS 100

ACKNOWLEDGMENTS 102

NOTATIONS 103

REFERENCES 104

**2 Pressure and Temperature Effects in
Fluid-Particle Systems 111**

Ted M. Knowlton

1.0 INTRODUCTION 111

1.1 Minimum Fluidization Velocity 113

1.2 Bed Voidage and Bed Expansion 120

1.3 Bubbles in Fluidized Beds 124

1.4 Bubble Size and Frequency 125

1.5 Bed-to-Surface Heat Transfer Coefficient 129

1.6 Entrainment and Transport Disengaging Height 131

1.7 Particle Attrition at Grids 134

1.8 Particle Attrition in Cyclones 136

1.9 Jet Penetration 137

1.10 Regime Transitions 139

1.11 Cyclone Efficiency 146

NOTATIONS 147

REFERENCES 149

3 Heat Transfer in Fluidized Beds153

John C. Chen

1.0 INTRODUCTION	153
2.0 BUBBLING DENSE FLUIDIZATION	154
2.1 Hydrodynamic Characteristic	154
2.2 Heat Transfer to Submerged Surfaces	155
3.0 CIRCULATING FAST FLUIDIZATION	173
3.1 Hydrodynamic Characteristics	173
3.2 Heat Transfer	178
NOTATIONS	201
Subscripts	202
REFERENCES	202

4 Gas Distributor and Plenum Design in Fluidized Beds ...209

S.B. Reddy Karri and Ted M. Knowlton

1.0 INTRODUCTION	209
2.0 TYPES OF GRIDS	210
2.1 Perforated Plates (Upwardly-Directed Flow)	210
2.2 Bubble Cap (Laterally-Directed Flow)	210
2.3 Sparger (Laterally or Downwardly-Directed Flow)	211
2.4 Conical Grids (Laterally-Directed Flow)	211
3.0 GRID DESIGN CRITERIA	212
3.1 Jet Penetration	212
3.2 Grid Pressure-Drop Criteria	214
3.3 Design Equations	215
3.4 Additional Criteria for Sparger Grids	218
3.5 Port Shrouding or Nozzle Sizing	219
4.0 PARTICLE ATTRITION AT GRIDS	220
4.1 Attrition Correlation	222
5.0 EROSION	223
6.0 EFFECTS OF TEMPERATURE AND PRESSURE	223
7.0 PLENUM DESIGN	223
8.0 DESIGN EXAMPLES	225
8.1 FCC Grid Design	225
8.2 Polyethylene Reactor Grid Design	230
NOTATIONS	233
REFERENCES	235

5 Engineering and Applications of Recirculating and Jetting Fluidized Beds236

Wen-Ching Yang

1.0 INTRODUCTION	236
------------------------	-----

2.0	RECIRCULATING FLUIDIZED BEDS WITH A DRAFT TUBE	237
2.1	Draft Tube Operated As A Fluidized Bed	240
2.2	Draft Tube Operated As A Pneumatic Transport Tube	242
2.3	Design Example for a Recirculating Fluidized Bed with a Draft Tube	257
2.4	Industrial Applications	263
3.0	JETTING FLUIDIZED BEDS	264
3.1	Jet Penetration and Bubble Dynamics	265
3.2	Gas Mixing Around the Jetting Region	281
3.3	Solids Circulation in Jetting Fluidized Beds	295
3.4	Fines Residence Time in Jetting Fluidized Beds	315
3.5	Scale-up Considerations	317
3.6	Applications	319
	NOTATIONS	319
	Greek Letters	322
	REFERENCES	323
6	Fluidized Bed Coating and Granulation	331
	<i>Richard Turton, Gabriel I. Tardos, and Bryan J. Ennis</i>	
1.0	INTRODUCTION	331
2.0	COATING OF PARTICLES IN FLUIDIZED BEDS	333
2.1	Introduction	333
2.2	Overview of Coating Process	335
2.3	Microscopic Phenomena	339
2.4	Modelling	344
2.5	Design Criteria	355
3.0	GRANULATION OF FINE POWDERS IN FLUIDIZED BEDS	365
3.1	Introduction	365
3.2	Microscopic Phenomena	366
3.3	Granule Growth Kinetics	380
3.4	Experimental Support and Theoretical Predictions	387
3.5	Granule Consolidation, Attrition and Breakage	398
3.6	Modeling of Granulation Processes	406
3.7	Unwanted Aggregation in Fluidized Beds	418
	ACKNOWLEDGMENT	424
	NOTATIONS	424
	REFERENCES	429
7	Attrition in Fluidized Beds and Pneumatic Conveying Lines	435
	<i>Joachim Werther and Jens Reppenhagen</i>	
1.0	INTRODUCTION	435
2.0	FACTORS AFFECTING ATTRITION	437
2.1	Material Properties	438
2.2	Process Conditions	440

3.0	ASSESSMENT OF ATTRITION	444
3.1	Breakage and Selection Functions	444
3.2	Attrition Rate	445
3.3	Friability Indices	446
3.4	Grindability Indices	446
4.0	ATTRITION TESTS	447
4.1	Friability Tests	447
4.2	Experiments to Study Attrition Mechanisms	448
4.3	Test Equipment and Procedures	449
5.0	ATTRITION IN FLUIDIZED BED SYSTEMS	455
5.1	Sources of Attrition	455
5.2	Attrition in the Overall Fluidized Bed System, Continuous Processes	473
5.3	Steps to Minimize Attrition in Fluidized Beds	475
6.0	ATTRITION IN PNEUMATIC CONVEYING LINES	478
6.1	Modeling	480
6.2	Parameter Effects	480
6.3	Steps to Minimize Attrition in Pneumatic Conveying Lines	482
	NOTATIONS	484
	Subscripts	485
	Greek Symbols	486
	REFERENCES	486

8 Bubbleless Fluidization492

Mooson Kwauk

1.0	INTRODUCTION	492
2.0	FLUIDIZED LEACHING AND WASHING	492
2.1	Uniform Particles	496
2.2	Mixed Particles	500
2.3	Staged Fluidized Leaching (SFL)	502
3.0	BUBBLELESS GAS/SOLID CONTACTING	502
3.1	Bubbling Fluidization and G/S Contacting Efficiency	502
3.2	Species of Bubbleless G/S Contacting	507
4.0	DILUTE RAINING FLUIDIZATION	508
4.1	Raining Particles Heat Exchanger	508
4.2	Experimental Verification	512
4.3	Baffling and Particles Distribution	515
4.4	Pilot Plant Demonstration	519
5.0	FAST FLUIDIZATION	523
5.1	Longitudinal Voidage Distribution	525
5.2	Regimes for Vertical G/S Systems	529
5.3	Radial Voidage Distribution	533
5.4	Modeling Fast Fluid-bed Reactors	533
6.0	SHALLOW FLUID BEDS	537
6.1	Dynamics for the Distributor Zone	537
6.2	Activated Solids Shallow Fluid Bed Heat Exchanger	537

6.3	Cocurrent Multistage Shallow Fluid Bed	541
6.4	The Co-MSFB as a Chemical Reactor	545
7.0	FLUIDIZATION WITH NO NET FLUID FLOW	546
7.1	Levitation of Discrete Particles	547
7.2	Semi-Fluidization through Oscillatory Flow	551
7.3	Application to Pseudo Solid-Solid Reactions	553
8.0	PARTICLES WHICH QUALIFY FOR BUBBLELESS OPERATION	556
8.1	Powder Characterization	556
8.2	Improving Fluidization by Particle Size Adjustment	562
9.0	WHY BUBBLING AND NOT PARTICULATE FLUIDIZATION	569
9.1	The Energy-Minimized Multiscale (EMMS) Model	570
9.2	Reconciling L/S and G/S Systems	573
10.0	EPILOGUE	576
	NOTATIONS	576
	REFERENCES	578

9 Industrial Applications of Three-Phase Fluidization Systems 582

*Jack Reese, Ellen M. Silva, Shang-Tian Yang,
and Liang-Shih Fan*

1.0	INTRODUCTION	582
	Part I: Smelting Reduction, Paper Processing, and Chemical Processing	588
2.0	SMELTING REDUCTION	588
2.1	Introduction	588
2.2	Principles of Smelting Reduction	590
2.3	Post-Combustion and Heat Transfer in SRF	593
2.4	Slag Layer Behavior	599
2.5	Future of Smelting Reduction of Iron Ore	603
3.0	PAPER PROCESSING	604
3.1	Introduction	604
3.2	Chemical Pulping of Wood Chips	605
3.3	Pulp Bleaching and Flotation De-inking	609
4.0	CHEMICAL PROCESSING	614
4.1	Introduction	614
4.2	Hydrotreating/Hydrocracking Petroleum Intermediates	614
4.3	Fischer-Tropsch Synthesis	619
4.4	Methanol Synthesis	621
	Part II: Three-Phase Biofluidization	623
5.0	BIOLOGICAL APPLICATIONS OF THREE-PHASE FLUIDIZATION	623
5.1	Introduction	623
5.2	Applications	629
5.3	Bioparticles	637

5.4 Hydrodynamics	643
5.5 Phase Mixing in a Three-Phase Reactor	647
5.6 Mass Transfer	648
5.7 Modeling	651
5.8 Scale Up	653
5.9 Process Strategy	655
5.10 Novel Reactors	657
5.11 Economics	661
5.12 Summary	662
ACKNOWLEDGMENT	663
NOTATIONS	663
REFERENCES	664

10 Dense Phase Conveying683

George E. Klinzing

1.0 INTRODUCTION	683
2.0 ADVANTAGES OF DENSE PHASE CONVEYING	693
3.0 BASIC PHYSICS	695
4.0 PULSED PISTON FLOWS	698
5.0 VERTICAL FLOW SYSTEMS	706
6.0 BOOSTERS	708
NOTATIONS	709
Greek	709
Subscripts	710
REFERENCES	710

11 Design Considerations of Long-Distance Pneumatic Transport and Pipe Branching712

Peter W. Wypych

1.0 INTRODUCTION	712
2.0 LONG-DISTANCE PNEUMATIC CONVEYING	713
2.1 Product Characterization and Classification	714
2.2 Blow Tank Design	733
2.3 Conveying Characteristics	738
2.4 Pressure Drop Prediction	741
2.5 Stepped-Diameter Pipelines	747
2.6 Valves	748
2.7 Pipeline Unblocking Techniques	751
2.8 General Considerations	752
3.0 PIPE BRANCHING	753
3.1 Dust Extraction	754
3.2 Flow Splitting	760
3.3 Pressure Loss	766
NOTATIONS	767
REFERENCES	769

12 Cyclone Design 773
 Frederick A. Zenz

 1.0 INTRODUCTION 773

 2.0 REQUIRED DESIGN DATA 774

 3.0 CORRELATING FRACTIONAL COLLECTION EFFICIENCY .. 775

 4.0 EFFECT OF SOLIDS LOADING 778

 5.0 CYCLONE LENGTH 778

 6.0 CONES, DUST HOPPERS AND EROSION 780

 7.0 CYCLONE INLET AND OUTLET CONFIGURATIONS 781

 8.0 THE COUPLING EFFECT 785

 9.0 PRESSURE DROP 787

 10.0 SPECIAL CASES 788

 11.0 BED PARTICLE SIZE DISTRIBUTION
 AND CYCLONE DESIGN 791

 12.0 CENTRIFUGAL VERSUS CENTRIPETAL CUT POINT
 PARTICLE SIZE 793

 13.0 CYCLONE DESIGN EXAMPLES 794

 14.0 ALTERNATE APPROACH TO SOLVING EXAMPLE B 804

 15.0 ALTERNATE APPROACH TO SOLVING EXAMPLE C 809

 16.0 DIPLEG SIZING AND CYCLONE PRESSURE BALANCE 812

 NOTATIONS 814

 REFERENCES 815

13 Electrostatics and Dust Explosions in Powder Handling 817
 Thomas B. Jones

 1.0 INTRODUCTION 817

 2.0 CHARGING OF SOLID PARTICLES 818

 2.1 Triboelectrification 819

 2.2 Charge Relaxation 823

 2.3 Induction Charging of Particles 824

 2.4 Electrostatic Fields and Potentials 825

 3.0 FLUIDIZED BED ELECTRIFICATION 829

 3.1 Background 829

 3.2 More Recent Work 832

 3.3 Beneficial Effects of Electric Charge 836

 4.0 ESD DUST IGNITION HAZARDS 836

 4.1 Basics of Suspended Solids Ignition 837

 4.2 Types of Discharges 841

 4.3 Charge Dissipation 850

 5.0 ESD HAZARDS IN FLUIDIZED BED SYSTEMS 854

 5.1 Hazards Associated with Fluidization 855

 5.2 Hazards in Peripheral Equipment and Processes 857

 5.3 Other Nuisances and Hazards 863

 6.0 CONCLUSION 864

 ACKNOWLEDGMENT 866

 REFERENCES 867

Index 872

1

Fluidized Bed Scale-up

Leon R. Glicksman

1.0 INTRODUCTION

Although fluidized beds have been used extensively in commercial operations such as fluidized bed combustors and fluid catalytic cracking, engineers are still faced with uncertainties when developing new commercial designs. Typically, the development process involves a laboratory bench scale unit, a larger pilot plant, and a still larger demonstration unit. Many of the important operating characteristics can change between the different size units. There is a critical problem of scale-up: how to accurately account for the performance changes with plant size to insure that a full size commercial unit will achieve satisfactory performance. In addition, it would be helpful if the smaller units could be used to optimize the commercial plant or solve existing problems.

One discouraging problem is the decrease in reactor or combustor performance when a pilot plant is scaled up to a larger commercial plant. These problems can be related to poor gas flow patterns, undesirable solid mixing patterns and physical operating problems (Matsen, 1985). In the synthol CFB reactors constructed in South Africa, first scale-up from the pilot plant increased the gas throughput by a factor of 500. Shingles and McDonald (1988) describe the severe problems initially encountered and their resolution.

2 *Fluidization, Solids Handling, and Processing*

In some scaled up fluidized bed combustors, the lower combustion zone has been divided into two separate subsections, sometimes referred to as a “pant leg” design, to provide better mixing of fuel and sorbent in a smaller effective cross section and reduce the potential maldistribution problems in the scaled up plant.

Matsen (1985) pointed out a number of additional problem areas in scale-up such as consideration of particle size balances which change over time due to reaction, attrition and agglomeration. Erosion of cyclones, slide valves and other components due to abrasive particles are important design considerations for commercial units which may not be resolved in pilot plants.

If mixing rates and gas-solid contacting efficiencies are kept constant between beds of different size, then thermal characteristics and chemical reaction rates should be similar. However, in general, the bed hydrodynamics will not remain similar. In some instances, the flow regime may change between small and large beds even when using the same particles, superficial gas velocity and particle circulation rate per unit area. The issue of scale-up involves an understanding of these hydrodynamic changes and how they, in turn, influence chemical and thermal conditions by variations in gas-solid contact, residence time, solid circulation and mixing and gas distribution.

There are several avenues open to deal with scale-up. Numerical models have been developed based on fundamental principals. The models range from simple one-dimensional calculations to complex multidimensional computational fluid dynamics solutions. There is no doubt that such first principal models are a great aid in synthesizing test data and guiding the development of rational correlations. In a recent model evaluation, modelers were given the geometry and operating parameters for several different circulating beds and asked to predict the hydrodynamic characteristics without prior knowledge of the test results (Knowlton et al. 1995). None of the analytical or numerical models could reliably predict all of the test conditions. Few of the models could come close to predicting the correct vertical distribution of solid density in the riser and none could do it for all of the test cases! Although it is tempting to think that these problems can be solved with the “next generation of computers,” until there is general agreement and thorough verification of the fundamental equations used to describe the hydrodynamics, the numerical models will not stand alone as reliable scale-up tools.

On the other hand, there is a blizzard of empirical and semi-empirical correlations which exist in the fluidized bed literature to predict

fluid dynamic behavior. In addition there are probably a large number of proprietary correlations used by individual companies. The danger lies in extrapolating these relations to new geometric configurations of the riser or inlet, to flow conditions outside the range of previous data, or to beds of much different sizes. Avidan and coauthors in a 1990 review of FCC summed up the state of the art: "basic understanding of complex fluidization phenomena is almost completely lacking. While many FCC licensors and operators have a large body of in-house proprietary data and correlations, some of these are not adequate, and fail when extrapolated beyond their data base." (Avidan, et al., 1990.)

As an example, consider the influence of mean particle size. In the early work on bubbling fluidized bed combustors, attempts were made to use relations from the classic fluidization literature which had concentrated on FCC applications with much smaller particles. In many cases, it was discovered that the relationships for small particles gave erroneous results for combustors with much larger particles. For example, the two phase theory equating the excess gas velocity above minimum fluidization to the visible bubble flow was shown to be severely distorted for large particle systems. Jones and Glicksman (1985) showed that the visible bubble flow in a bubbling bed combustor was less than one fifth of $u_o - u_{mf}$. In other cases even the trends of the parametric behavior were changed. Heat transfer to immersed surfaces in fine particle bubbling beds increased strongly with a decrease in the mean particle size. For large particle beds, the heat transfer, in some instances, decreased with a decreased particle diameter.

Another approach to scale-up is the use of simplified models with key parameters or lumped coefficients found by experiments in large beds. For example, May (1959) used a large scale cold reactor model during the scale-up of the fluid hydroforming process. When using the large cold models, one must be sure that the cold model properly simulates the hydrodynamics of the real process which operates at elevated pressure and temperature.

Johnsson, Grace and Graham (1987) have shown one example of verification of a model for 2.13 m diameter industrial phthalic anhydride reactor. Several bubbling bed models gave good overall prediction of conversion and selectivity when proper reaction kinetics were used along with a good estimate of the bubble size. The results were shown to be quite sensitive to the bubble diameter. The comparison is a good check of the models but the models are incomplete without the key hydrodynamic data. In this case, the bubble size estimates were obtained from measurements of overall bed density in the reactor.

4 *Fluidization, Solids Handling, and Processing*

As Matsen expresses it, after over a half a century of scale-up activity in the chemical process industry, “such scale-up is still not an exact science but is rather a mix of physics, mathematics, witchcraft, history and common sense which we call engineering.” (Matsen, 1995.)

A complete treatment of scale-up should include the models, numerical calculation procedures and experimental data designers need to carry out successful scale-up from small size beds to commercial units. This would involve a large measure of the existing fluidized bed research and development effort; clearly, such a task is beyond the scope of a single chapter. Since changes in the bed size primarily influence scale-up through changes in the bed hydrodynamics, one focus of this chapter is on experimental results and models which deal explicitly with the influence of bed diameter on hydrodynamic performance for both bubbling and circulating fluidized beds. The changes in the bed dynamics will, in turn, impact the overall chemical conversion or combustion efficiency through changes in the particle-to-gas mass transfer and the heat transfer from the bed to immersed surfaces or the bed wall. Several examples of this influence are also reviewed.

The second focus of this chapter is on the use of small scale experimental models which permit the direct simulation of the hydrodynamics of a hot, possibly pressurized, pilot plant or commercial bed. By use of this modeling technique, beds of different diameters, as well as different geometries and operating conditions, can be simulated in the laboratory. To date, this technique has been successfully applied to fluidized bed combustors and gasifiers. Derivation of the scale modeling rules is presented for a variety of situations for gas solid fluidized beds. Verification experiments and comparisons to large scale commercial systems are shown. Rules for the use of this experimental modeling technique for FCC operations as well as for the simulation of bed-to-solid surface heat transfer are also given.

2.0 REACTOR MODELING: BED DIAMETER INFLUENCE

In this section, representative results are reviewed to provide a prospective of reactor modeling techniques which deal with bed size. There probably is additional unpublished proprietary material in this area. Early studies of fluidized reactors recognized the influence of bed diameter on conversion due to less efficient gas-solid contacting. Experimental studies were used to predict reactor performance. Frye et al. (1958) used

a substitute reaction of ozone decomposition to study hydrocarbon synthesis. The ozone decomposition can be run at low pressures and temperatures and can be rate-controlled in the same way and by the same catalyst as the reaction under development. Frye and coworkers used three beds of 2 inch, 8 inch and 30 inch diameter, respectively, to study the size influence. We should interject a caution that the use of pressures and temperatures different than the actual reaction may mean that the hydrodynamics of the substitute reaction model will differ from the actual application; this is illustrated later in the chapter. Figure 1 shows the apparent reaction rate constant for the different bed diameters at two different bed heights with the other parameters held constant. Note that the rate constant decreased by roughly a factor of three between the 2 inch and 30 inch beds.

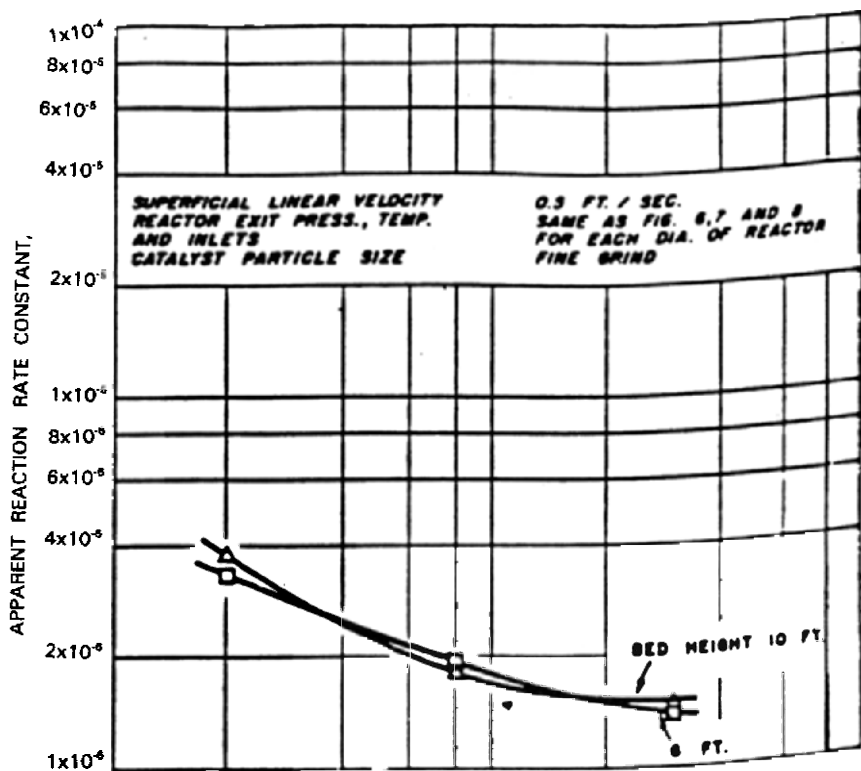


Figure 1. Apparent reaction-rate constant vs. reactor diameter and bed height. (From Frye et al., 1958.)

6 *Fluidization, Solids Handling, and Processing*

May (1959) reports results of tests done in cold models used to simulate the flow through large reactors whose performance had been found to be inferior to that of smaller pilot units. The importance of this problem can be appreciated from the scale of the equipment used. Figure 2 shows the 5 foot diameter unit used for the scale-up tests. This unit was fluidized with compressed air at 27 to 38°C (80 to 100°F) and pressures up to 689 KPa (100 psi). Gas residence time in the bed was determined by the use of tracer gas. Radioactive solid tracers were introduced into the bed to determine solid mixing. The data obtained in the larger units are much more erratic with evidence of large scale mixing patterns. Figure 3 shows the axial mixing coefficients obtained in experiments with different size beds. Mixing in the larger diameter bed is an order of magnitude larger than that in a small laboratory unit. The measured hydrodynamic behavior of the gas and solid was combined with a reaction model to predict the reactor behavior. Here again, there should be concern about the accuracy with the air experiments done at ambient temperature. Use of identical bed geometry and bed solid material does not guarantee identical hydrodynamics. The shift in gas properties from the cold model to the hot reactor may cause a marked difference in behavior. Additional scaling parameters must be maintained constant between the reactor and the cold model to insure identical hydrodynamics, and in some cases just to guarantee identical flow regimes!

Volk et al. (1962) show the effect of bed diameter on the conversion of CO in the "Hydrocol" reaction in which hydrogen and carbon dioxide are converted over an iron catalyst to hydrocarbons and oxygenated hydrocarbons in a bubbling or possibly slugging bed. Figure 4 shows the CO conversion. It is seen that the conversion rate is reduced as the reactor diameter increases. Volk used vertical tubes within the reactor to reduce the equivalent diameter of the system, equal to the hydraulic diameter, four times the free cross sectional area divided by the wetted perimeters of all surfaces in the cross section. The performance was found to be correlated by the equivalent diameter. It was also found that bed expansion was correlated with bed diameter. In their process, larger beds were built with internals which kept the equivalent diameter the same as that of smaller units. The large units with internals appeared to give comparable gas-to-solid contacting. The use of vertical internals may not be feasible for a number of reasons, such as tube erosion. The use of the equivalent diameter approach may not be universally valid.

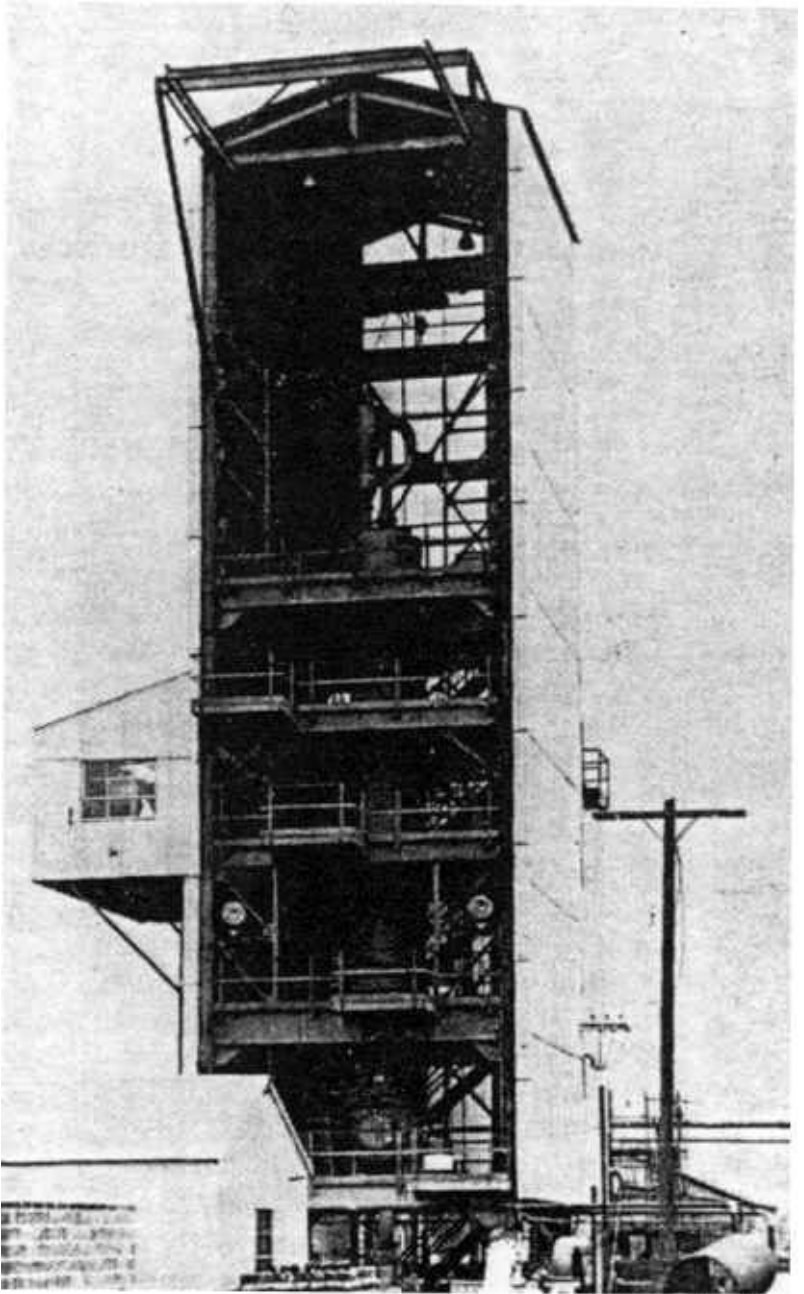


Figure 2. Very large equipment built to study scale-up problems. (*From May, 1959.*)

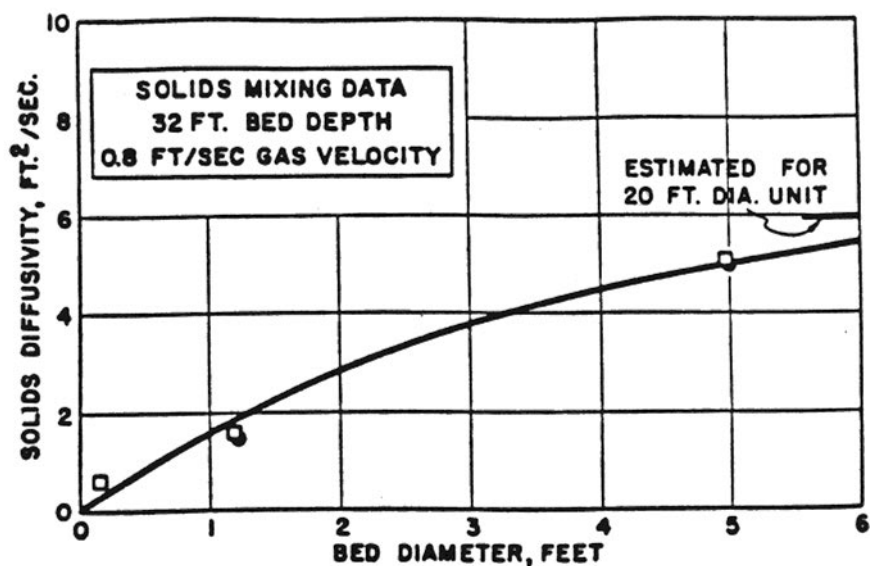


Figure 3. Solid diffusivity in axial direction for large units. (From May, 1959.)

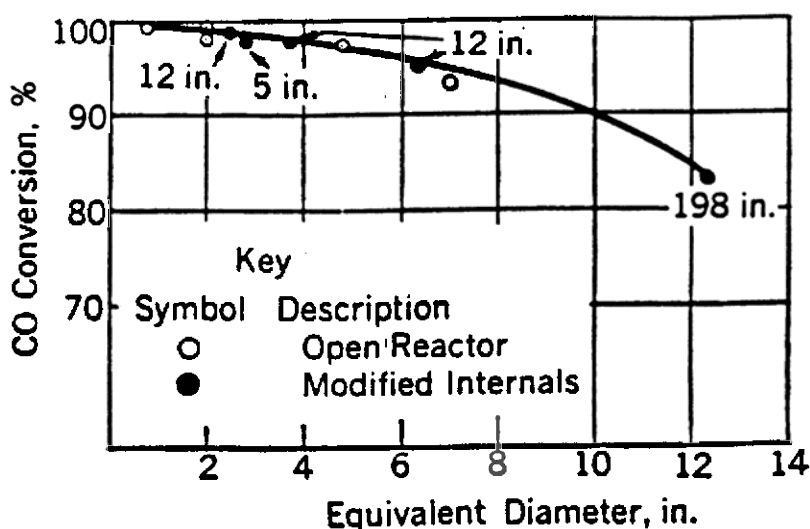


Figure 4. CO conversion in Hydrocol reaction for several reactor diameters. (From Volk et al., 1962.)

Van Swaaij and Zuiderweg (1972) used the ozone decomposition reaction to study the conversion characteristics in a bubbling bed. Studies were made with beds of 5, 10, 23, 30 and 60 cm diameter and up to 300 cm bed heights. The results were compared with predictions using a two-phase flow model with the mass transfer coefficient between the bubble and dense phase derived from residence time distribution results of gas-tracer pulse response tests. Figure 5 shows the height of the mass transfer unit H_a , which is equivalent to u/a where a is the mass transfer coefficient, as a function of the bed diameter. The results from the ozone conversion and the residence time distribution interpreted by the two phase model gave reasonably similar results. In these cases, the mass transfer between phases is the limiting resistance for the reaction. Note that for larger bed diameters the mass transfer coefficient decreases. Van Swaaij and Zuiderweg (1973) showed that the inclusion of vertical tubes in a bed gave bubble to dense phase mass transfer results which were roughly equivalent to a smaller open bed with the same hydraulic diameter while the solids axial mixing was higher than that predicted using the hydraulic diameter.

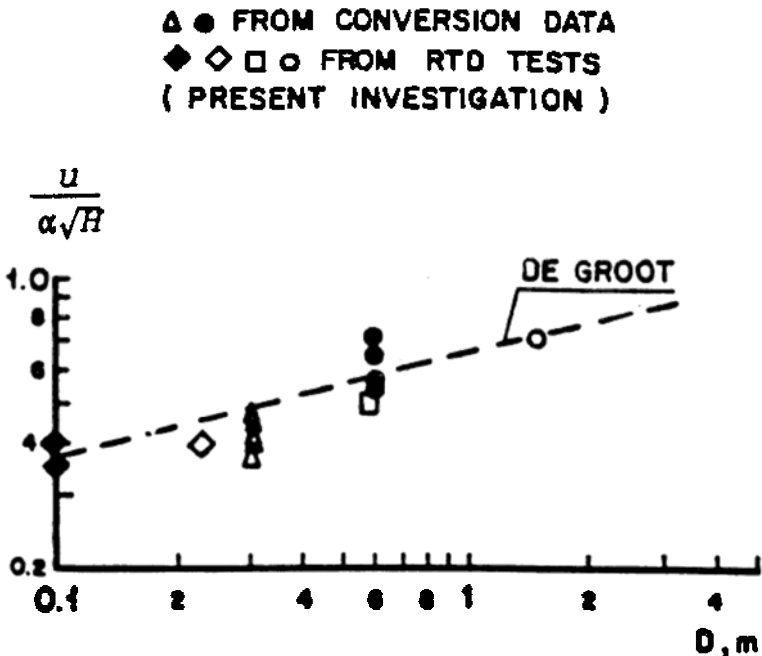


Figure 5. Mass transfer unit for ozone conversion for different bed diameters. (From Van Swaaij and Zuiderweg, 1972.)

10 Fluidization, Solids Handling, and Processing

Bauer et al. (1981) measured the influence of bed diameter on the catalytic decomposition of ozone. Figure 6 shows the decrease of the conversion with bed diameter for Bauer's data. This figure also shows the influence of distributor design on conversion. In many small scale experiments, a porous plate is used which will give better performance than the distributors used in large shallow bed commercial designs.

Avidan and Edwards (1986) successfully scaled up from bench scale to demonstration plant from 0.04 m to 0.6 m diameter while maintaining nearly 100% conversion for a fluid bed methanol to gasoline process. In this case, they ran at a superficial gas velocity which was high enough to be in the turbulent flow regime suppressing bubbles. By this technique they eliminated the losses associated with gas bypassing in bubbles.

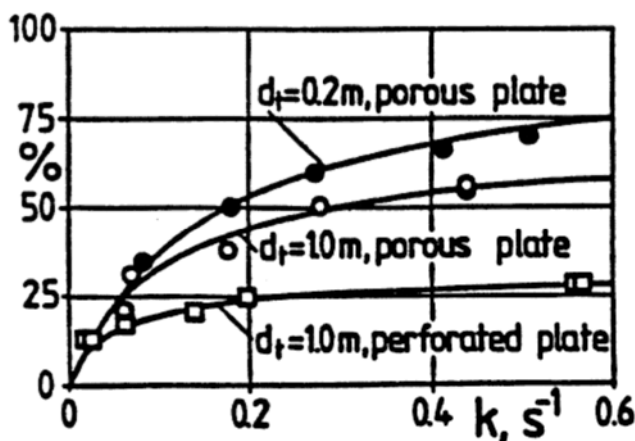


Figure 6. Conversion catalytic decomposition of ozone for different bed diameters and distributors. (From Werther, 1992.)

3.0 INFLUENCE OF BED DIAMETER ON HYDRODYNAMICS

3.1 Bubbling Beds

In the studies mentioned above, the major objective was the experimental determination of conversion as a function of overall design

parameters and particle properties. There have also been studies which have looked at the influence of bed diameter on the hydrodynamics in an effort to understand the cause of the conversion loss with bed size increase. These studies have aided in the development of physical models of reactor performance.

De Groot (1967) measured gas residence time, bed expansion and solid axial mixing in a series of beds at different diameter fluidized with air at ambient conditions. He used a narrow size range and broad size range of crushed silica with sizes below $250\text{ }\mu\text{m}$. Beds with diameters of 0.1, 0.15, 0.3, 0.6, and 1.5 m were used in the tests. There was a substantial decrease in bed expansion and bubble fraction for narrow size range particles at large bed diameters, indicating the possibility of gas bypassing in bubble channels (Fig. 7). The axial diffusivity also increased with bed diameter and was a strong function of particle size distribution (Fig. 8).

% BED EXPANSION

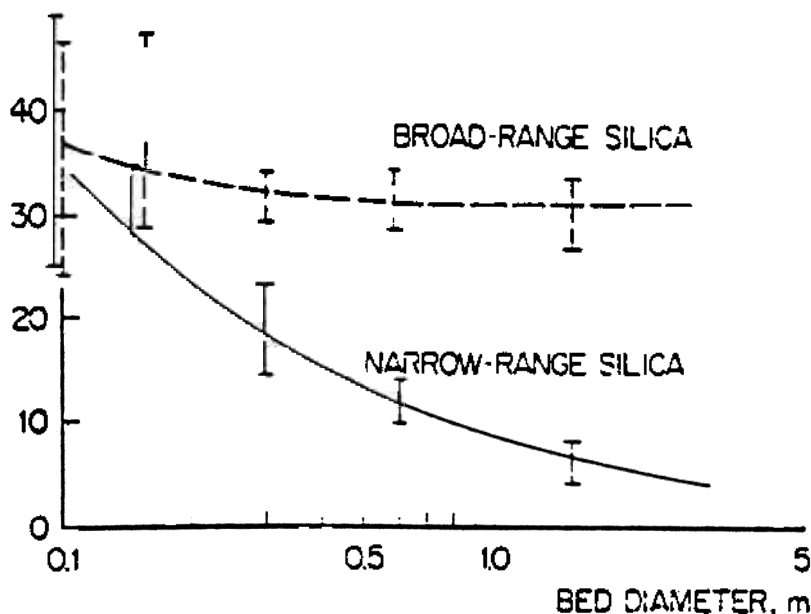


Figure 7. Bed expansion as a function of bed diameter at a fluidization velocity of $\approx 0.20\text{ m/sec}$. (From DeGroot, 1967.)

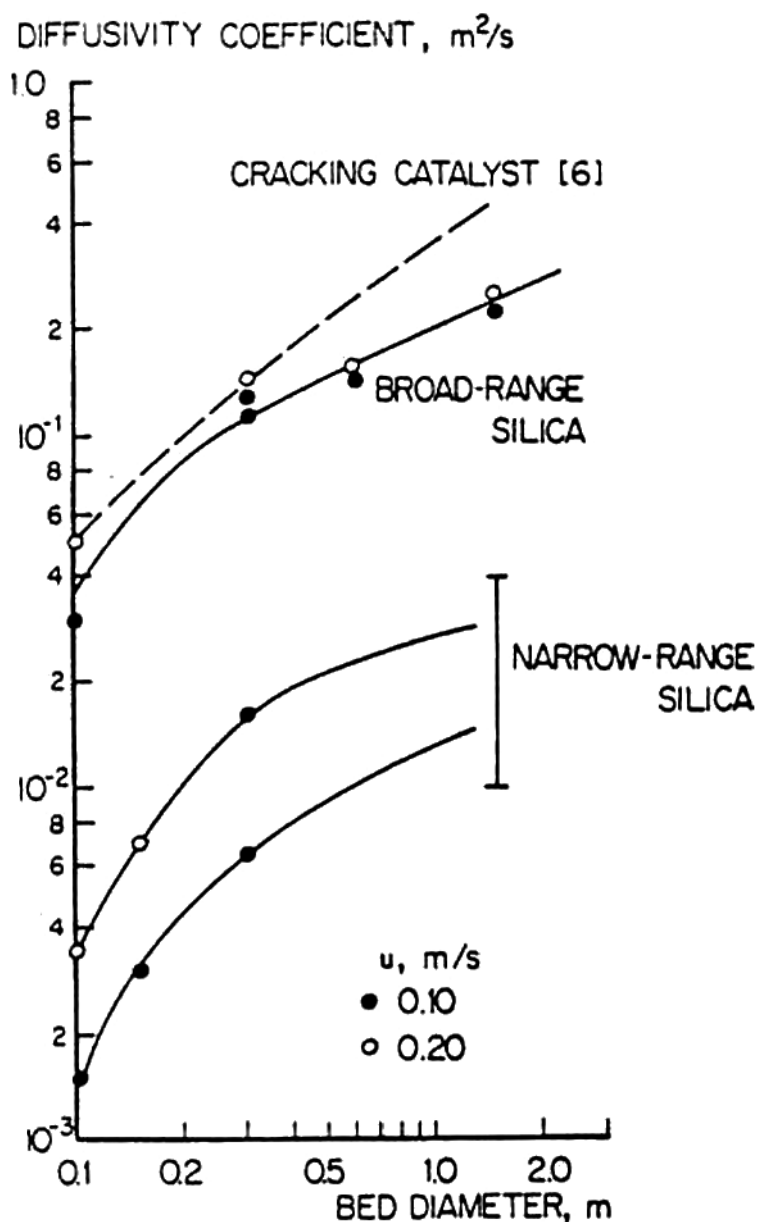


Figure 8. Effective axial diffusivity coefficients for solids mixing. (From DeGroot, 1967.)

Weather (1974) measured the bubble characteristics in cylindrical beds of diameters 100, 200, 450 and 1000 mm, respectively, for fine particles with a mean particle diameter of 83 μm . He showed that for beds 200 mm or smaller, common sizes used for laboratory experiments, the bed diameter had a strong effect on the bed hydrodynamics. There was a zone of preferred bubble flow near the bed walls at lower elevations (Fig. 9). The bubbles grew in size and moved toward the centerline, presumably by coalescence, higher up in the bed (Fig. 10). The transition to slugging occurred higher up in the larger bed at the same superficial gas velocity. The bubble velocity increased with height until slug flow was approached, after which the velocity decreases. For the only case shown, the 100 mm bed, the maximum velocity occurred when the bubble dimension was about one third of the bed diameter. In larger beds, the bubble rise velocity was higher for the same bubble volume (Fig. 11). Hovmand and Davidson (1971) reviewed data on bubble rise velocity and concluded that the bubble rise velocity is governed by the bed diameter rather than the bubble diameter when the bubble diameter exceeded 1/3 of the bed diameter. Note that Weather's results at different superficial velocity are well correlated by the drift flux form,

$$\text{Eq. (1)} \quad u_b \sim \Phi(u_o - u_{mf}) + c\sqrt{gd_v}$$

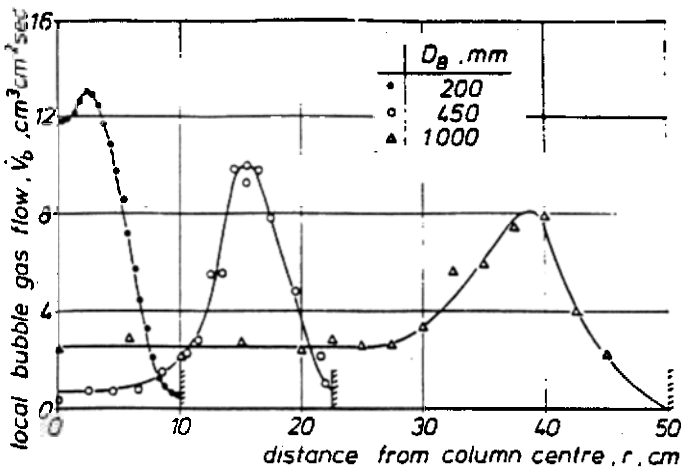


Figure 9. Bubble gas flow V_b as a function of the distance r from the vessel center line in a height of 30 cm above the distributor in beds of different diameters D_B ($u_o = 9 \text{ cm/sec}$, $H = 50 \text{ cm}$). (From Werther, 1974.)

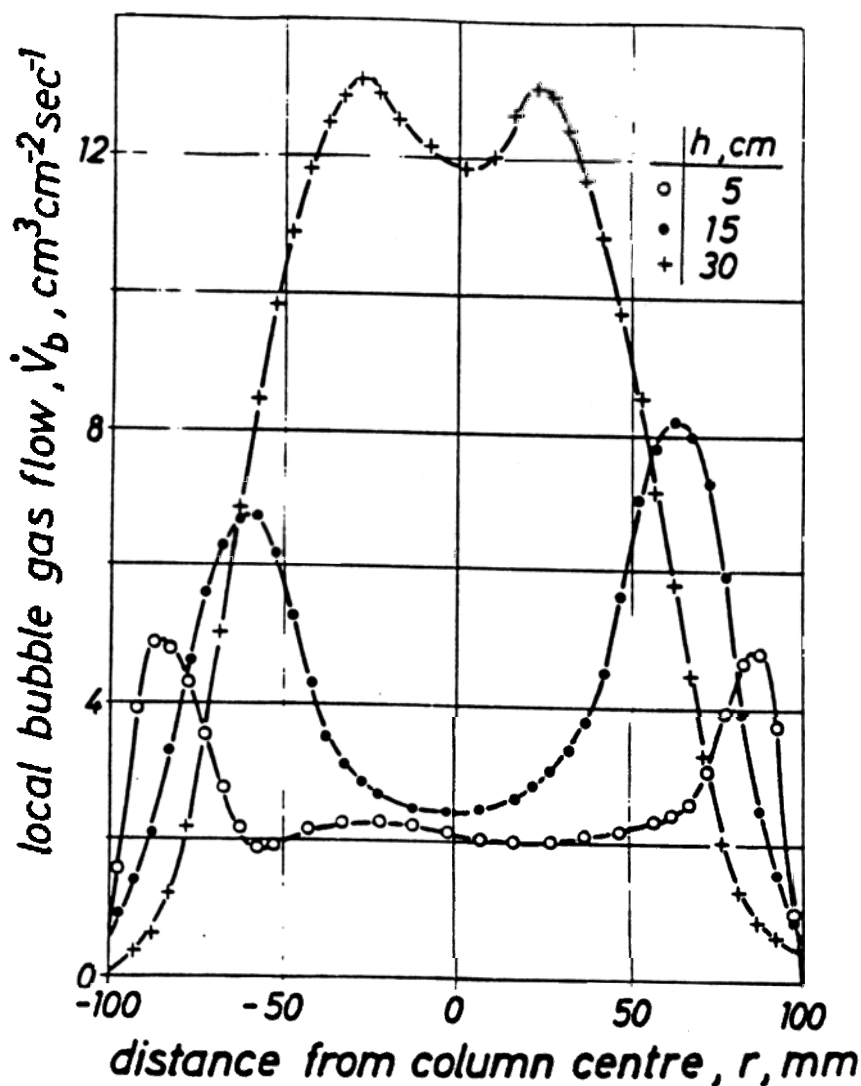


Figure 10. The flow pattern of the bubble phase in a bed of 200 mm diameter ($u_o = 9$ cm/sec, $H = 50$ cm). (From Werther, 1974.)

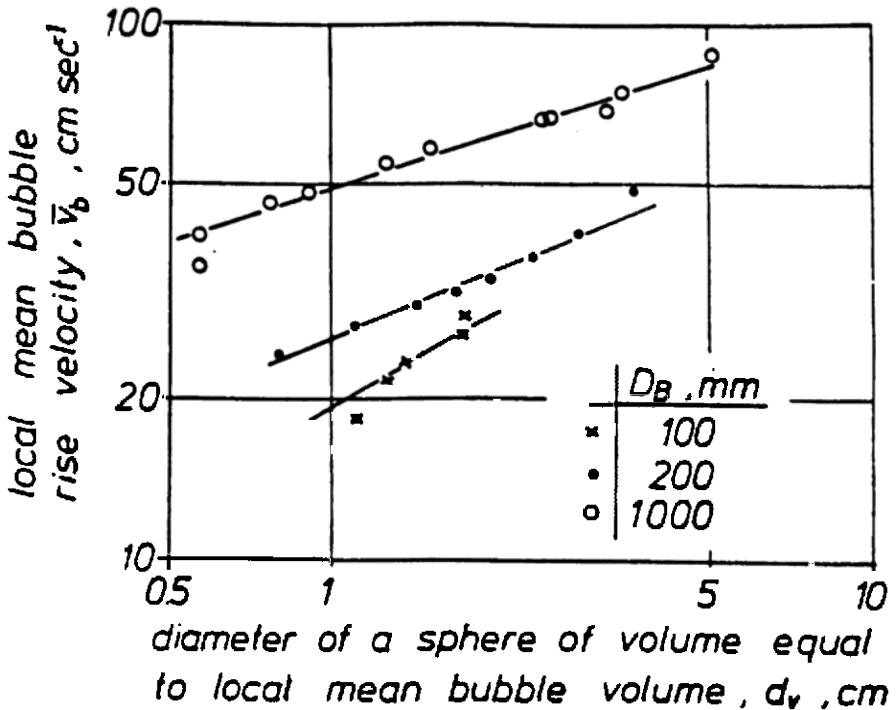


Figure 11. Relationship between local mean bubble size and local mean bubble rise velocity in beds of different diameters ($u_o = 9 \text{ cm/sec}$). (From Werther, 1974.)

It is curious that the influence of bed size appeared to hold, even when the bubble is much smaller than the bed diameter. This may be tied to the local concentration of bubbles within certain sections of the bed. The increased local bubble flow led to higher coalescence rates and higher local bubble velocities. There was a distinction in bubble velocity between Geldart group A and B powder while the ratio of visible bubble flow to $u - u_{mf}$ seems to be independent of the group. Werther also found that the visible bubble flow, the product of the number of bubbles per unit time crossing a given surface and their respective volumes was considerably less than $u - u_{mf}$ especially in the lower regions of the smaller bed and throughout large diameter beds. The residence time of bubbles was significantly higher for beds 200 mm or smaller, than it was for larger diameter beds. Werther concludes that the smallest bed diameter that appears suitable for obtaining good scale-up results is 500 mm. It should be pointed out that this criterion will probably vary with flow conditions,

16 Fluidization, Solids Handling, and Processing

bed depth and particle size. Also, Werther's experiments were carried out with air at ambient conditions. Although the trends and physical picture may be similar for beds at elevated temperature and pressure, there may be some changes in the criteria.

Whitehead (1978) found patterns of bubble tracks in a large 1.2 m square bed similar to Werther: preferred bubble tracks near the walls and corners of a shallow open bed and merging of bubbles toward the bed center at higher elevations. Nguyen, Potter, and Whitehead (1979) also found that a horizontal tube bank in the large bed caused smaller bubbles which appeared in more random locations across the upper surface of the bed. This work was carried out for fine solids at low superficial velocity, 15 cm/sec, and modest bed depths.

Geldart (1970) showed a substantial distinction between bubble sizes in two dimensional and three dimensional beds. He used 128 μ m river sand in a 30.8 cm round bed and a 68×1.27 cm rectangular cross section bed. The results, shown in Fig. 12, show that the bubbles in the three dimensional bed are larger. There were differences in the visible bubble flow rate at the same superficial velocity. Geldart ascribes the differences in bubble diameter to differences in visible bubble flow rate as well as to out-of-line coalescence in the three dimensional bed.

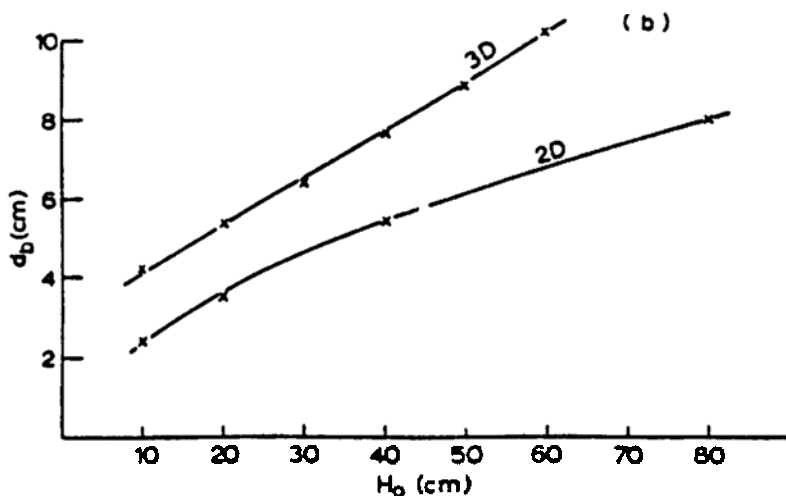


Figure 12. Variation of bubble diameter and concentration with initial bed height; $u - u_o = 6$ cm/sec for two dimensional and three dimensional beds. (From Geldart, 1970/71.)

Glicksman and McAndrews (1985) determined the effect of bed width on the hydrodynamics of large particle bubbling beds. Sand particles with a mean diameter of 1 mm were fluidized by air at ambient conditions. The bed width ranged from 7.6 cm to 122 cm while the other cross sectional dimension remained constant at 122 cm. Most experiments were carried out with an open bed. The bubble rise velocity increased with the bed width, in the representation of bubble velocity as

$$\text{Eq. (2)} \qquad u_b = u_o - u_{mf} + \phi \sqrt{gd_B}$$

the value of ϕ varied from 0.4 in a two-dimensional bed to 0.6 in the three dimensional bed (Fig. 13). The mean vertical chord length of bubbles decreased with bed width (Fig. 14). The visible bubble flow decreased dramatically with an increase of bed width at a fixed superficial velocity (Fig. 15). The gas throughflow coefficient m , used to represent the total gas flow,

$$\text{Eq. (3)} \qquad u_o = Q_b + (1 - \delta)u_{mf} + m \delta u_{mf}$$

increased from a mean value of 3.6 for the two dimensional bed to a mean value of 11.7 for the largest, 1.22×1.22 m bed cross section. The bed depths at minimum fluidization were 46 cm and 76 cm in the tests. For these rather shallow beds there were no observable preferred bubble tracks; the location of erupting bubbles was random across the bed surface. For the cases observed, with u_o/u_{mf} varying from 1.3 to 1.8, the influence of the wall was absent when the bubble diameter was roughly 1/5 the bed width or less. For deeper beds or higher gas velocity, the ratio of bubble diameter to bed width is expected to be the best criterion for determining when wall effects will be negligible. For one test series, five staggered rows of horizontal tubes with a horizontal center-to-center spacing of 15.2 cm were placed in the 1.22 m square bed. The tube bed results are shown in Figs. 13–15 with a T symbol. The behavior of bubbles in the bed with the tube bank resembled that of an open bed with smaller width.

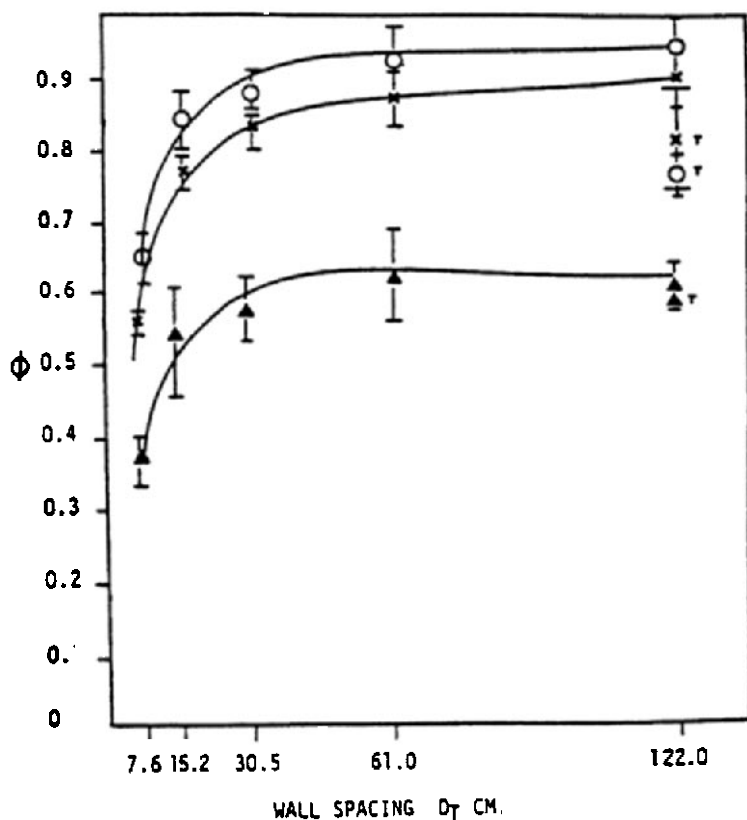


Figure 13. Variation of bubble rise velocity with wall spacing; I : standard deviation, T denotes with tubes. O : $\phi = U_b/(gD_b)^{1/2}$; x : $\phi = \bar{U}_b - Q_{bf}/(gD_b)^{1/2}$; Δ : $\phi = \bar{U}_b - (U - U_{mf})/(g\bar{D}_b)^{1/2}$. (From Glicksman and McAndrews, 1985.)

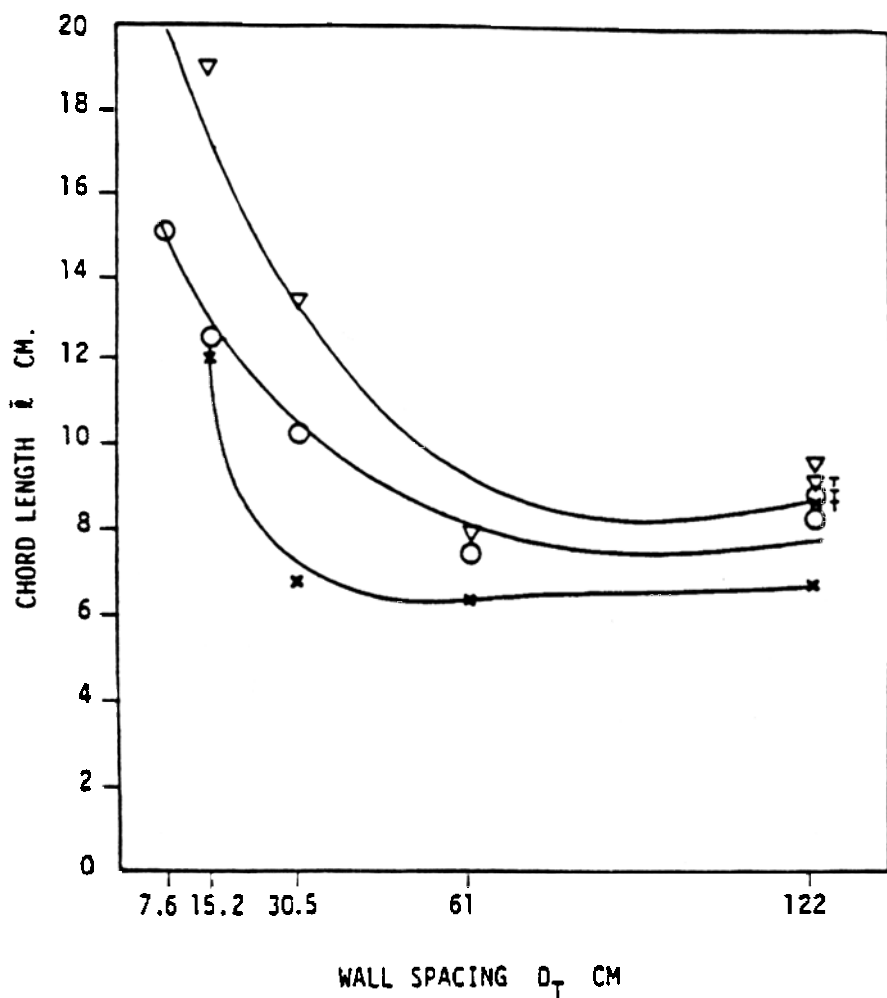


Figure 14. Variation of main chord length with wall spacing. $l_{mf} = 76$ cm, probe height = 46 cm, $\times = 1.3U_{mf}$; $O = 1.5U_{mf}$; $\nabla = 1.8U_{mf}$; T denotes with tubes. (From Glicksman and McAndrews, 1985.)

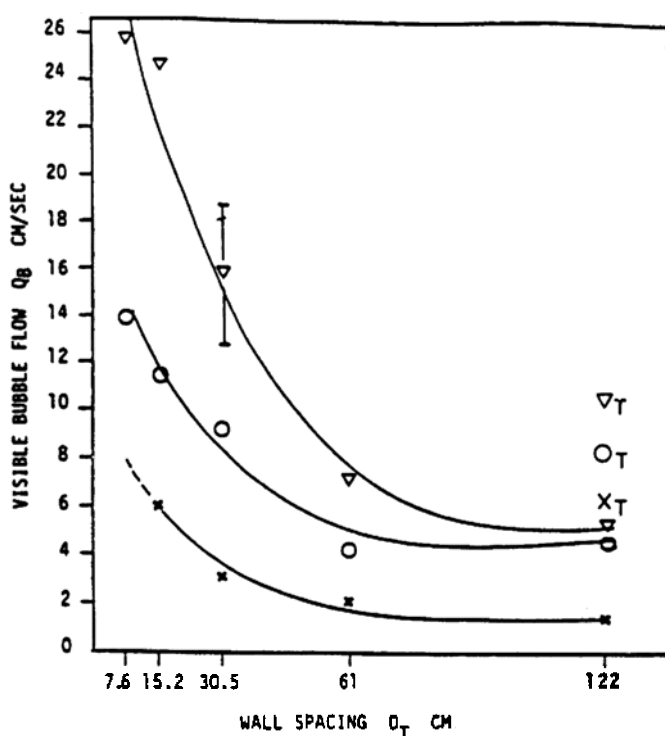


Figure 15. Visible bubble flow Q_b , $l_{mf} = 76$ cm, probe height = 46 cm. $x = 1.3 U_{mf}$; $\circ = 1.5 U_{mf}$; $\nabla = 1.8 U_{mf}$; T denotes with tubes. Experiment uncertainty = 20%. (From Glicksman and McAndrews, 1985.)

3.2 Mixing

Van Deemter (1980) surveyed data on solid mixing in fluidized beds of different diameters. Many of the experiments in large beds were considered inconclusive. The compiled data for longitudinal fluid dispersion, M_L ; gas back mixing, M_B ; and longitudinal dispersion of solids, M_S are shown in Fig. 16. Note the strong influence of bed diameter on mixing. The scatter in the data was attributed to differences in gas velocity and range of particle sizes. Large differences between small and large bed diameters may be due to flow regime transitions.

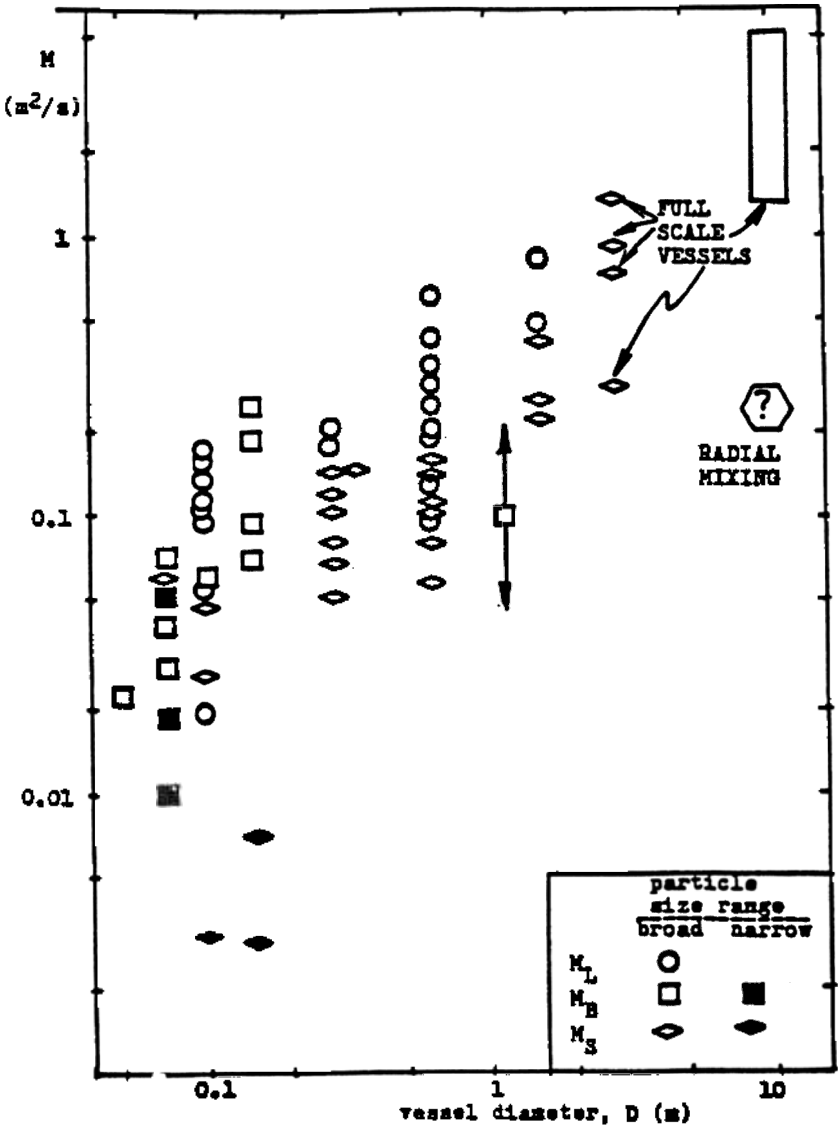


Figure 16. Mixing coefficients for different vessel diameters; M_L : longitudinal dispersion of fluid, M_B : gas backmixing, M_S : longitudinal solid dispersion. (From Van Deemter, 1980.)

The differences in behavior between small laboratory beds and larger demonstration units can, in part, be attributed to a switch from porous plate distributors in the small bed to discrete hole or bubble caps in

the larger beds. The porous plates give a better quality of fluidization, e.g., smaller bubbles, for shallow beds and beds of moderate depth (Rowe and Stapleton, 1961).

Yerushalmi and Avidan (1985) suggest that the axial dispersion coefficient of solids in slugging and turbulent flow varies approximately linearly with the bed diameter, similar to Thiel and Potter (1978). The data are shown in Fig. 17 although May's results are probably in the bubbling fluidization regime rather than turbulent flow.

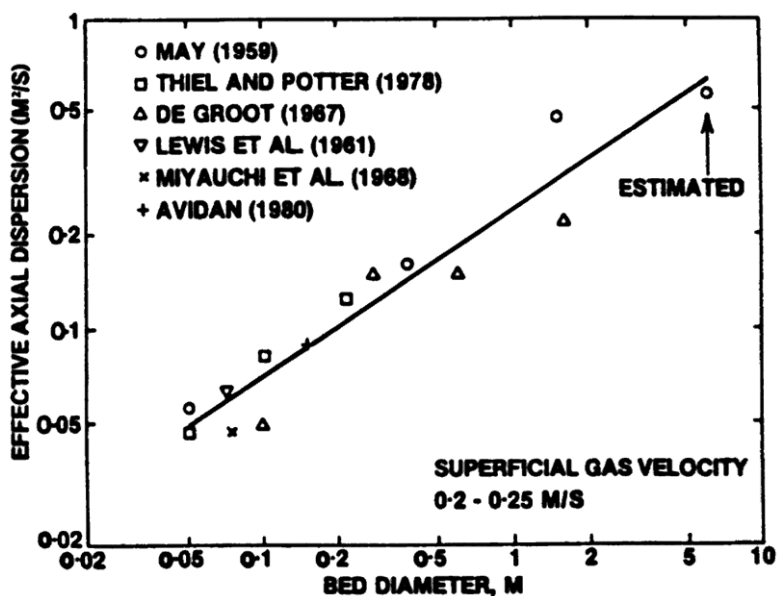


Figure 17. The effect of bed diameter on solid mixing. (*From Yerushalmi & Avidan, 1985.*)

3.3 Influence of Bed Diameter on Circulating Fluidized Beds

Arena et al. (1988) measured the hydrodynamic behavior of two circulating fluidized beds (CFB) with riser diameters of 0.041 m and 0.12 m ID, respectively, of roughly the same height. At the same superficial gas velocity and solid recirculation rate, the larger diameter column had a higher solids fraction. The average slip velocities derived from this data are also higher for the large diameter riser (see Hartge et al. 1985). Yerushalmi and Avidan (1985) found a similar trend when comparing

15.2 cm and 7.6 cm columns. Noymer et al. (1995) also compared two columns of 5.08 cm and 7.68 cm diameter of the same height which were used to simulate larger pressurized fluidized bed combustors. They found higher solids loading for the larger diameter riser at equal gas velocity and solid recirculation. In addition, the fraction of the wall covered by clusters was higher for the larger diameter column when the two beds had equal solids flow and when the two beds had equal cross section averaged solids concentration.

Rhodes et al. (1992) compared the solids flux profiles across the cross sections of a 0.152 m and 0.305 m diameter circulating bed riser. They found a region where the solid profile, given by the ratio of local flux to average flux, had a similar variation over the cross section, which was insensitive to the level of solid flux. The variation of the local solids flux over the radius was a function of the gas velocity and the riser diameter. In the larger riser, the profiles were somewhat flatter and the thickness of the downflowing region relative to the bed radius was smaller. The comparisons were not exact since the cross sections compared for the two beds were at different heights.

Zhang, Tung and Johnsson (1991) carried out investigations with three different fast bed systems with diameters of 32, 90 and 300 mm, respectively. They found that the radial voidage distribution, as a ratio of the cross sectional average, was independent of bed diameter and solids recycle rate (Fig. 18). The similarity does not hold at transition to the turbulent regime. The results are for the center of the riser excluding the entrance and exit regions. It would be interesting to determine if the similar voidage profiles hold for larger diameter risers.

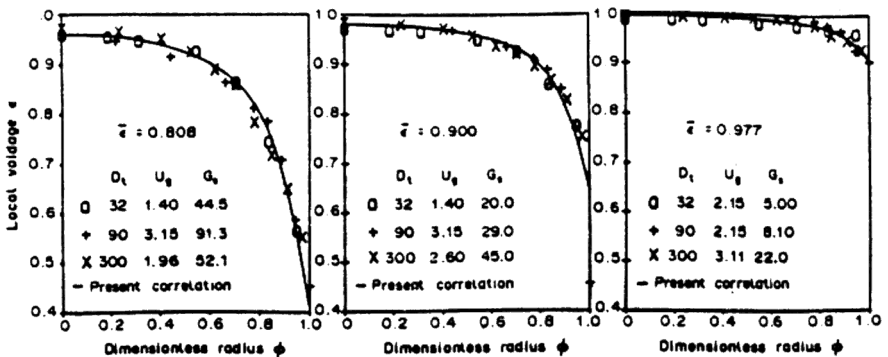


Figure 18. Comparison of radial voidage profiles calculated by correlation with experimental data in the three different beds used (FCC/air). (From Zhang et al., 1991.)

The thickness of the downflowing layers at the wall of the CFB is typically defined as the distance from the wall to the position of zero vertical solid flux. Measurements of the layer thickness were made on a 12 MW and 165 MW CFB boiler by Zhang, Johnsson and Leckner (1995). They found that the thickness increased for the larger bed. They related data from many different beds (Fig. 19), with the equivalent bed diameter, taken as the hydraulic diameter, using the following form

Eq. (4) $d = 0.05 De^{0.74}$

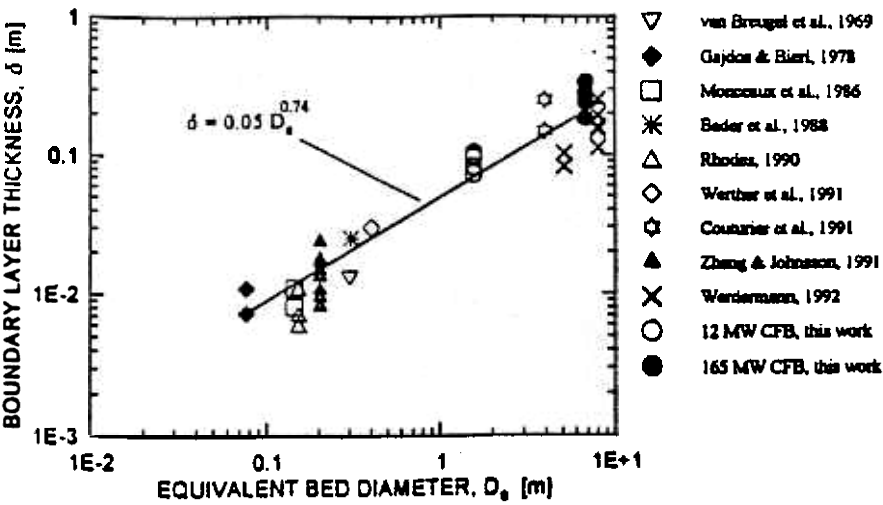


Figure 19. Empirical correlation and experimental data of thickness of downflowing layer at the wall of a CFB as a function of the equivalent bed diameter. (From Zhang et al., 1995.)

The thickness, d , was found to be insensitive to particle concentration, gas velocity and height within the furnace. That suggests that the thickness results from a balance of solids internal circulation which is generally much higher than net throughflow. If the local solids flux profile,

as a ratio of the cross sectional average, is roughly invariant over the cross section for these larger beds, the thickness of the wall layer follows from a mass balance. The upflow is proportional to the core area and the downflow to the product of perimeter and layer thickness. Thus the thickness should vary as the ratio of cross sectional area to perimeter, i.e., proportional to the hydrodynamic diameter.

Patience et al. (1992) developed a dimensionless correlation for the mean slip factor between the gas and solid by using solid suspension data from various small laboratory beds. The proposed correlation relates the slip to the Froude number based on the bed diameter. It remains to be seen if the correlation will hold at Froude numbers typical of large beds and if other dimensionless factors are important.

3.4 Flow Transition

Hovmand and Davidson (1971) review Stewart's criterion for the transition from bubbling to slug flow,

$$\text{Eq. (5)} \quad \frac{u_o - u_{mf}}{0.35(gD)^{1/2}} = 0.2$$

and show it gives good agreement with most experiments. Thus, a small diameter laboratory bed may exhibit behavior which is far different than a scaled up pilot plant. There is some data which suggests the bed depth to bed diameter may also influence the bubble to slug transition.

Thiel and Potter (1977) carried out slugging flow experiments in three different diameter beds, the largest being 0.22 m in diameter. They found that the bed aspect ratio influenced the onset of slug formation. They also found that the transition to turbulent flow occurred at much lower superficial gas velocity in the 0.22 m diameter bed than in the 0.1 m bed. With the fluid cracking catalyst, the transition velocity decreased from 20 cm/s to 2.5 cm/s. Yerushalmi and Avidan (1985) assert that in large shallow beds where slugging does not occur, transition from bubbling to turbulent flow should be independent of bed size.

4.0 **EXPERIMENTAL MEANS TO ACCOUNT FOR SCALE-UP: USE OF SCALE MODELS**

Since large pilot plants are costly, it may not be feasible to undertake an extensive scale-up program. Furthermore, large beds are difficult to instrument to observe detailed behavior. Thus, many test results from beds at elevated temperatures and pressure are confined to overall operating characteristics leaving the designers to speculate on the cause of shifts in performance with bed size. Full scale cold models are also expensive and require lengthy construction schedules. As we will see below, the full scale cold test may not correctly simulate the hydrodynamics of the actual process at elevated temperature and pressure. Indeed, a familiar occurrence in atmospheric bubbling fluidized bed combustors is the marked difference in flow behavior between a bed fluidized with cold air and the same bed run at normal operating conditions.

A technique which can assist in the scale-up of commercial plants designs is the use of scale models. A scale model is an experimental model which is smaller than the hot commercial bed but which has identical hydrodynamic behavior. Usually the scale model is fluidized with air at ambient conditions and requires particles of a different size and density than those used in the commercial bed. The scale model relies on the theory of similitude, sometimes through use of Buckingham's "pi theorem," to design a model which gives identical hydrodynamic behavior to the commercial bed. Such a method is used in the wind tunnel testing of small model aircraft or in the towing tank studies of naval vessels.

Once a technique has been established to design a model which simulates the hydrodynamics of a hot (possibly pressurized) fluidized bed, then a series of different sized models can be used to determine the influence of bed size on the performance of commercial beds, see Fig. 20. Model A' simulates the behavior of commercial bed A, model B' simulates a larger commercial bed B and so forth. Then by comparing models A', B' with C' we can determine the expected changes in operating characteristics when commercial bed A is replaced by larger beds B and C.

Designing a model fluidized bed which simulates the hydrodynamics of a commercial bed requires accounting for all of the mechanical forces in the system. In some instances, convective heat transfer can also be scaled but, at present, proper scaling relationships for chemical reactions or hydromechanical effects, such as particle attrition or the rate of tube erosion, have not been established.

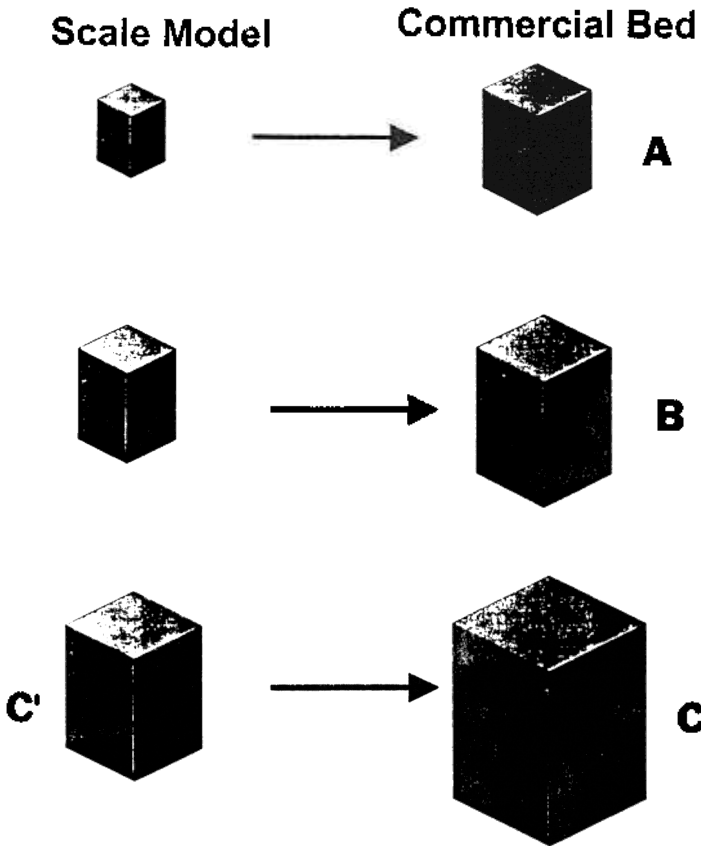


Figure 20. Use of scale models with different bed diameters to simulate the influence of diameter on the hydrodynamics of a hot commercial reactor.

4.1 Development of Scaling Parameters

There are several approaches to developing the correct scaling relationships. Probably the most straightforward is the nondimensionalization of the governing equations. If we can write the proper equations governing the fluid and particle dynamic behavior, we can develop the proper scaling relationships even if we can't solve the equations (at present we can't). In essence, if a model is designed which follows the

exact same equations and boundary conditions as the commercial bed, with the same values of the coefficients, then the model and the commercial bed should have identical behavior. The trick is to nondimensionalize all of the terms of the equations so that the model and the commercial beds have identical nondimensionalized values of the parameters. That is, if the coordinates are nondimensionalized by dividing them by the bed diameter,

$$\text{Eq. (6)} \quad x' = \frac{x}{D} ; \quad y' = \frac{y}{D}$$

and the local gas velocity in the x direction is nondimensionalized by dividing it by the superficial gas velocity $u' = u/u_o$, then at the same value of x' and y' in a commercial bed and a properly scaled model, u' will have the same value. Note, this nondimensionalization will extend to time as well. Generally the physical values of x , y , u , and t will be different in the model and the commercial bed, while the dimensionless values x' , y' , u' and t' are the same for the two beds.

It is important to include all of the relevant physical effects in the equations to be nondimensionalized. This can be difficult because there isn't always consensus about which effects are important. Moreover, there is controversy over how to properly represent these effects in equation form. For our purposes the question is: Have all of the important parameters been included in the nondimensional equations? Pragmatically, the success to date of the scaling experiments using the formulation as presented adds confidence to the use of these simplifications which will be employed. Also, a limited number of tests have verified the omission of parameters specifically related to several phenomena.

In some cases, if we are too precise and include effects of marginal significance, the resulting modeling rules may be overly restrictive, limiting the choice of models or requiring the models which are too big. These questions are most expeditiously settled by experiments since an exact theoretical answer is not presently available.

The equations of motion can either be formulated for individual particles and the surrounding fluid, or the fluid and the particulate phases can each be considered a continuum. Both approaches yield identical results, see Glicksman et al. (1994) for a complete derivation. For our purposes, we will base the derivation on the continuum model formulated by Jackson.

4.2 Governing Equations

The use of governing equations has the merit of tying specific dimensionless parameters to particular physical phenomena (Glicksman, 1984, 1988). If the proper equations can be written, even if they cannot be solved, they yield considerable insight into the process.

Early derivation of these dimensionless parameters was based on a continuum model (Scharff et al., 1978; Glicksman, 1984). Inclusion of the individual particle approach extends the results to instances where a continuum model may not be applicable.

For simplicity, the fluid will be considered incompressible although the results do not depend on this condition. The continuum equations will be developed similar to those given by Anderson and Jackson (1967). These equations are based on a continuum picture of the suspension of solids in the fluid. The solids and the fluid are considered individual phases, and variables for each phase such as velocity or voidage are average values over regions large compared to a single particle but small compared to the scale of the macroscopic bed behavior. The derivation follows that given by Jackson (1971).

For the fluid, conservation of mass is

$$\text{Eq. (7)} \quad \frac{\partial \mathbf{e}}{\partial t} + \text{div}(\mathbf{e} \bar{\mathbf{u}}) = 0$$

and for the solid phase,

$$\text{Eq. (8)} \quad \frac{\partial}{\partial t}(1 - \mathbf{e}) + \text{div}[(1 - \mathbf{e}) \bar{\mathbf{u}}] = 0$$

where $\bar{\mathbf{u}}$ and $\bar{\mathbf{u}}$ are the vectorial form of the fluid and solid phase velocities, respectively.

The equation of motion for the fluid can be written as,

$$\text{Eq. (9)} \quad \mathbf{r}_f \mathbf{e} \left(\frac{\partial \bar{\mathbf{u}}}{\partial t} + \bar{\mathbf{u}} \bullet \nabla \bar{\mathbf{u}} \right) + \bar{\mathbf{i}} \mathbf{r}_f g \mathbf{e} - \nabla \bullet \mathbf{E}_f + \bar{\mathbf{F}} = 0$$

30 *Fluidization, Solids Handling, and Processing*

while for the particle phase,

$$\text{Eq. (10)} \quad \rho_s(1-\varepsilon)\left(\frac{\partial \bar{v}}{\partial t} + \bar{v} \cdot \nabla \bar{v}\right) + \bar{i} \rho_s g(1-\varepsilon) - \bar{F} - \nabla \cdot E_p = 0$$

where \bar{i} is the unit vector in the vertical direction, and the drag force between the fluid and the particle is represented by F . The terms E_f and E_p are the local average stress tensors associated with the fluid and particle phases, respectively. The proper formulation of the stress tensors is still a subject of controversy. The fluid-to-particle force term can be represented by a drag term proportional to the relative velocity between the two phases and a virtual mass term (C_A is the added mass coefficient),

$$\text{Eq. (11)} \quad \bar{F} = \beta(\bar{u} - \bar{v}) + (1-\varepsilon)C_A \rho_f \frac{d}{dt}(\bar{u} - \bar{v}) + (1-\varepsilon)\nabla \cdot E_f$$

Note β is, in general, not a constant, rather it must be found from a general expression for the drag force.

Given the uncertainty in the form of the stress tensors, many authors have adopted a form analogous to single phase Newtonian fluid relating the stress terms to the pressure and viscosity of the fluid and particle phase, respectively.

The physical basis of the particle phase pressure and viscosity still has not been resolved in the fluidization literature. In particular, dealing with stability between minimum fluidization and minimum bubbling some investigators have considered interparticle forces as purely hydrodynamic, such as Foscolo and Gibilaro (1984) and Batchelor (1988), while others contend that the interparticle forces are due to phenomena such as electrostatic or van der Waals forces (Rietema and Piepers, 1990; Rietema et al. 1993). For very fine particles, particle to particle cohesive forces are recognized as influencing the point of bubbling for gas fluidized beds (Baeyans and Geldart, 1973).

For larger particles, the nature of interparticle forces is still unresolved. A typical operating condition for most commercial gas solid beds is well beyond the point of minimum bubbling. It might be expected that

electrostatic or van der Waals forces are not as important as they are near the point of minimum fluidization. It is likely that particle-particle collisions, dependent on the coefficient of restitution and sliding friction, come into play at much higher u_o/u_{mf} .

Litka and Glicksman (1985) carried out systematic experiments to determine the importance of particle mechanical properties on the behavior of bubbling beds. These tests helped to evaluate the importance of non-hydrodynamic forces on particle-particle interactions. Two beds were compared with particles having identical properties save one. In one test, particles with a different coefficient of restitution were tested, in a second test, particles with a different coefficient of sliding friction were compared. In these tests, both groups of particles had the same size, shape and density. In all tests, the two different particles exhibited the same bubble frequency and size as well as the same particle transit time both upward and downward. Chang and Louge (1992) found that in a circulating bed the vertical solids distribution could be changed if particles with artificially low surface friction were used. In the range of surface friction for usual commercial and test material there wasn't any influence.

Given the results of Litka and Glicksman and Change and Louge, as well as the lack of consensus concerning the nature and importance of interparticle interactions, such terms will not be considered further in this development and the particle-particle forces will be considered hydrodynamic. Foscolo et al. (1990) have shown that if the interparticle forces are hydrodynamic in nature, the dimensionless parameters obtained are identical to those obtained by neglecting interparticle interaction. The success of scaling experiments for bubbling and circulating beds, which to date has omitted parameters specifically related to nonhydrodynamic interparticle interactions, suggest that in the range of parameters investigated, such an omission is valid.

The boundary conditions for the bed at the side wall with no net flow of particles across it are at

$$\begin{aligned} \text{Eq. (12)} \quad & x = 0, D \\ & v_{normal} = 0 \end{aligned}$$

where this is the solids velocity normal to the wall.

32 *Fluidization, Solids Handling, and Processing*

At the bottom

$$\text{Eq. (13)} \quad \begin{array}{l} \text{at } y = 0 \\ v_{normal} = \frac{G_s}{\rho_s (1 - \varepsilon)} \end{array}$$

where G_s is the average solids feed rate per unit area from outside the bed through the bottom. This form holds when the solids feed is uniformly distributed over the bottom. If solids feed takes place along the side wall, an expression similar to Eq. (13) must be used in place of Eq. (12). For gas velocity at the walls,

$$\text{Eq. (14)} \quad \text{at } x = 0, D \quad \bar{u} = 0$$

while at the distributor,

$$\text{Eq. (15)} \quad \begin{array}{l} \text{at } y = 0 \\ \bar{u} = \bar{i}u_o / \Delta \quad \text{above the distributor holes} \\ \bar{u} = 0 \quad \text{elsewhere} \end{array}$$

where Δ is the voidage of the distributor plate assumed in this case to be a perforated plate and u_o is the superficial gas velocity. For bubble caps or other gas inlet devices, boundary conditions such as Eq. (15) apply over the gas inlet plane of the device. Boundary conditions, Eqs. (12) and (14), also apply to the surfaces of any internal elements in the bed, for example: heat transfer tubes.

At all x_s, y_s (internal surfaces)

$$\text{Eq. (16)} \quad \bar{u} = 0, \quad v_N = 0$$

Also at the distributor

$$\text{Eq. (17)} \quad \text{at } y = 0, \quad P = P_o$$

Nondimensionalizing the variables as,

$$\bar{v}' = \frac{\bar{v}}{u_o}, \quad \bar{u}' = \frac{\bar{u}}{u_o}$$

$$\nabla' = L\nabla,$$

$$t' = \frac{u_o}{L}t$$

Eq. (18)

$$x' = \frac{x}{L}$$

$$y' = \frac{y}{L}$$

where L is a typical bed dimension, e.g., the bed height or diameter. Note that u' , v' as well as ε are dependent variables of x' , y' , and t' which are determined by the boundary conditions and the independent dimensionless parameters of the governing equations.

Applying these definitions to the governing equations and rearranging them so the parameters form nondimensional groups, the continuity equations become

Eq. (19) $\frac{\partial \varepsilon}{\partial t'} + \text{div}(\varepsilon \bar{u}') = 0$

and

Eq. (20) $\frac{\partial}{\partial t'}(1 - \varepsilon') + \text{div}[(1 - \varepsilon')\bar{v}'] = 0$

The fluid-particle interaction force, omitting the virtual mass term and combining the pressure terms in the equation of motion becomes

34 Fluidization, Solids Handling, and Processing

$$\text{Eq. (21)} \quad \frac{L\bar{F}}{\rho_f u_o^2} = \frac{\beta L}{\rho_f u_o} (\bar{u}' - \bar{v}')$$

The equations of motion in dimensionless form are,

$$\text{Eq. (22)} \quad \varepsilon \left[\frac{\partial \bar{u}'}{\partial t'} + \bar{u}' \bullet \nabla' u' \right] + \bar{i} \frac{gL}{u_o^2} \varepsilon - \nabla' \bullet \frac{p}{\rho_f u_o^2} + \frac{L\beta}{\rho_f u_o} = 0$$

and for the particle phase, without the particle stress tensor,

$$\text{Eq. (23)} \quad (1 - \varepsilon) \left[\frac{\partial \bar{v}'}{\partial t'} + \bar{v}' \bullet \nabla' \bar{v}' \right] + \frac{\bar{i}gL}{u_o^2} (1 - \varepsilon) - \left(\frac{\rho_f}{\rho_s} \right) \left(\frac{L\beta}{\rho_f u_o} \right)$$

The dimensionless boundary conditions become,

$$\begin{aligned} &\text{at } x' = 0, D/L \\ \text{Eq. (24)} \quad &v_{normal} = 0 \end{aligned}$$

$$\begin{aligned} &\text{at } y = 0 \\ \text{Eq. (25)} \quad &v_{normal} = \frac{G_s}{\rho_s u_o} \frac{1}{1 - \varepsilon} \end{aligned}$$

$$\begin{aligned} &\text{at } x = 0, \frac{D}{L} \\ \text{Eq. (26)} \quad &\bar{u}' = 0 \end{aligned}$$

at $y = 0$

$$\begin{aligned} \text{Eq. (27)} \quad \bar{u}' &= i/\Delta \quad \text{above distribution holes} \\ \bar{u}' &= 0 \quad \text{elsewhere} \end{aligned}$$

At all internal surfaces x'_s , y'_s

$$\text{Eq. (28)} \quad \bar{u}' = 0, \quad v'_N = 0$$

Eq. (29)

The term $P_o / (\rho_f u_o^2)$ can be ignored when the fluid velocity is small compared to sonic velocity or the absolute pressure does not change enough to influence the thermodynamic properties of the fluid; it will be ignored in this development. Note that the fluid pressure level still influences the fluid density.

From the continuity and momentum equations for the fluid and solid phases along with the boundary conditions, the following groups of independent dimensionless parameters are found to control the hydrodynamics, noting our assumption that the particle-particle forces are only dependent on hydrodynamic parameters,

$$\text{Eq. (30)} \quad \frac{u_o^2}{gL}, \quad \frac{\rho_s}{\rho_f}, \quad \frac{\beta L}{\rho_s u_o}, \quad \frac{G_s}{\rho_s u_o}$$

as well as bed geometry.

The dimensionless fluid pressure is not included since it is a dependent parameter.

4.3 Fluid-Solid Forces

The drag coefficient β can be expressed in several different limiting forms depending on the flow conditions. At low voidages typical

36 *Fluidization, Solids Handling, and Processing*

of bubbling beds, the Ergun relationship or similar form can be used. In that case β can be expressed as,

Eq. (31)

$$\frac{\beta L \phi_s}{\rho_s u_o} = 150 \frac{\epsilon(1-\epsilon)^2}{\epsilon^3} \frac{\mu}{\rho_s u_o \phi d_p} \frac{L}{d_p} + 1.75 \frac{(1-\epsilon)|\bar{u}' - \bar{v}'|}{\epsilon^3} \frac{\epsilon^2}{d_p} \frac{L \rho_f}{\rho_s}$$

In the limit of very high voidage, the drag coefficient can be related to the single particle drag coefficient. For the case of spherical particles,

Eq. (32)
$$\frac{\beta L}{\rho_s u_o} = \frac{3}{4} C_D |\bar{u}' - \bar{v}'| f(\epsilon) \frac{\rho_f}{\rho_s} \frac{L}{d_p}$$

where the drag coefficient, C_D , in turn can be expressed in the form of

Eq. (33)
$$C_D = f \left[\frac{\rho_f u_o d_p}{\mu} \right]$$

In the more general case, C_D will also be a function of particle shape, sphericity, surface roughness and turbulence intensity of the fluid.

The dimensionless drag coefficient $\beta L / (\rho_s u_o)$ in Eq. (30) can be expressed in terms of other fluid parameters by the use of Eqs. (31–33). For low voidages where the Ergun-like expression holds,

Eq. (34)
$$\frac{\beta L}{\rho_s u_o} = f \left[\frac{\rho_s u_o d_p^2 \phi^2}{\mu L}, \frac{L}{d_p \phi} \frac{\rho_f}{\rho_s} \right]$$

In this expression d_p represents the mean diameter when a distribution of different size particles are in the bed.

At high voidage, using Eqs. (32) and (33),

Eq. (35)

$$\frac{\beta L}{\rho_s u_o} = f \left[\frac{\rho_f u_o d_p}{\mu}, \frac{\rho_f}{\rho_s} \frac{L}{d_p}, \phi \text{ or shape, roughness, fluid turbulence} \right]$$

Traditionally, the mean diameter is defined as the surface area averaged mean. Although this mean may be appropriate for flow resistance primarily due to surface shear forces, it is not the proper choice for drag which prevails at higher particle Reynolds numbers (nor is it the obvious choice for a mean diameter to use for bed-to-surface heat or mass transfer). It is more general to include along with the mean particle diameter, the particle size distribution, the particle size nondimensionalized with respect to the mean diameter, and the particle sphericity. To be more exact, the particle aspect ratio and surface roughness should be included at high particle Reynolds numbers. By use of isotropic material with common roughness levels, these last two parameters can be overlooked.

Using Eq. (34), the set of independent dimensionless parameters (Eq. 30) becomes,

Eq. (36)

$$\frac{u_o^2}{gL}, \frac{\rho_s}{\rho_f}, \frac{\rho_s u_o d_p^2 \phi^2}{\mu L}, \frac{\rho_f u_o L}{\mu}, \frac{G_s}{\rho_s u_o}, \frac{L}{D}, \text{ Bed geometry, } \phi, \text{ particle size distribution (PSD)}$$

These can be rearranged by combination of parameters. It must be borne in mind that such manipulation by itself does not lead to any decrease in the number of dimensionless parameters. One such modification is,

Eq. (37)

$$\frac{u_o^2}{gL}, \frac{\rho_s}{\rho_f}, \frac{\rho_s u_o d_p}{\mu}, \frac{\rho_f u_o L}{\mu}, \frac{G_s}{\rho_s u_o}, \frac{L}{D}, \text{ Bed geometry, } \phi, \text{ PSD}$$

38 *Fluidization, Solids Handling, and Processing*

In this form, u_o^2/gL , the Froude number, can be viewed as a ratio of inertial to gravity forces; ρ_s/ρ_f is a ratio of particle to fluid inertial forces; $\rho_s u_o d_p/\mu$ is the Reynolds number or ratio of particle inertial to fluid viscous forces; and $\rho_f u_o L/\mu$, a Reynolds number based on the bed dimensions and fluid density, is a ratio of fluid inertial to viscous forces.

Another common form is obtained by combining the Froude and Reynolds number to obtain the Archimedes number, which omits u_o ,

$$\text{Eq. (38)} \quad \frac{\rho_f \rho_s d_p^3 g}{\mu^2} = \left(\frac{\rho_f u_o d_p}{\mu_f} \right)^3 \frac{gL}{u_o^2} \left(\frac{\mu_f}{\rho_f u_o L} \right) \left(\frac{\rho_s}{\rho_f} \right)$$

The list of dimensionless parameters can be rewritten as,

Eq. (39)

$$\frac{\rho_f \rho_s d_p^3 g}{\mu^2}, \frac{\rho_s}{\rho_f}, \frac{u_o^2}{gL}, \frac{\rho_f u_o L}{\mu}, \frac{G_s}{\rho_s u_o}, \frac{L}{D}, \text{ Bed geometry, } \phi, \text{ PSD}$$

Note that there isn't anything more "fundamental" about one form compared to the others. Each has the same number of dimensionless groups which are made up of independent parameters which can be set by the bed design and operation and the choice of particles. However, when the number of dimensionless groups is simplified by omitting some phenomena, the reduction in number of groups could be influenced by the form chosen.

This set, Eqs. (36), (37) or (39), will be referred to as the full set of scaling relationships.

4.4 **Spouting and Slugging Beds**

He, Lim and Grace (1995) have shown that for spouting beds, cohesive factors are important and this group must be augmented by including the internal friction angle and the loose packed voidage to achieve similar scale models. Since interparticle friction can occur in slugging beds, these additional parameters should be included to properly scale slugging beds.

5.0 SIMPLIFIED SCALING RELATIONSHIPS

In later sections, the use of the scaling relationships to design small scale models will be illustrated. For scaling to hold, all of the dimensionless parameters given in Eqs. (36), (37) or (39) must be identical in the scale model and the commercial bed under study. If the small scale model is fluidized with air at ambient conditions, then the fluid density and viscosity are fixed and it will be shown there is only one unique modeling condition which will allow complete similarity. In some cases this requires a model which is too large and unwieldy to simulate a large commercial bed.

To allow more flexibility, we will explore means of simplifying the scaling relationships by reducing the number of parameters which must be maintained constant. In most situations, one would expect that not all of the parameters are of first order importance. By reducing the number of parameters which must be maintained in the model, it may be possible to model larger commercial beds with small scale models. We will look at simplifications of the interparticle drag at the extreme of small and large Reynolds numbers based on particle diameter. This will span the range from low velocity FCC bubbling beds to high velocity fast beds or pneumatic transport using large particles. If the same simplification can be shown to hold in both of these limits, it is reasonable to consider application of the simplification over the entire range of conditions.

5.1 Low Reynolds Number

At low particle Reynolds numbers for a bubbling bed, the Ergun expression can be simplified using only the first term in Eq. (31).

Thus,

$$\text{Eq. (40)} \quad \frac{bL}{r_s u_o} \rightarrow 150 \frac{(1-e)^2}{e^2} \frac{mL}{r_s u_o (f d_p)^2} \quad \text{for} \quad \frac{r_f u_o d_p}{m} \rightarrow 0$$

At the same limit, the minimum fluidization velocity can be written as,

$$\text{Eq. (41)} \quad \frac{\Delta p}{L} = (r_s - r_f) g (1 - e_{mf}) = 150 \frac{(1 - e_{mf})^2}{e_{mf}^3} \frac{m u_{mf}}{(f d_p)^2}$$

40 Fluidization, Solids Handling, and Processing

For gas fluidized beds where $\mathbf{r}_s - \mathbf{r}_f$ can be replaced by \mathbf{r}_s ,

$$\text{Eq. (42)} \quad u_{mf} = \frac{\mathbf{r}_s g (1 - \mathbf{e}_{mf})}{\left[150 \frac{(1 - \mathbf{e}_{mf})^2}{\mathbf{e}_{mf}^3} \frac{\mathbf{m}}{(\mathbf{f} d_p)^2} \right]}$$

Substituting Eq. (42) into Eq. (40),

$$\text{Eq. (43)} \quad \frac{\mathbf{b} L}{\mathbf{r}_s u_o} = \frac{g (1 - \mathbf{e})^2}{u_{mf} (1 - \mathbf{e}_{mf}) \mathbf{e}^2} \frac{\mathbf{e}_{mf}^3 L}{\mathbf{r}_s u_o}$$

and

$$\text{Eq. (44)} \quad \frac{\mathbf{b} L}{\mathbf{r}_s u_o} Fr = \frac{u_o}{u_{mf}} \frac{(1 - \mathbf{e})^2 \mathbf{e}_{mf}^3}{\mathbf{e}^2 (1 - \mathbf{e}_{mf})}$$

Thus, in the low particle Reynolds number limit, maintaining u_o/u_{mf} , \mathbf{e}_{mf} , and Fr identical between two fluidized bed guarantees that $\mathbf{b} L/\mathbf{r}_s u_o$ is also identical. Although \mathbf{f} and d_p are eliminated between Eqs. (40) and (42), in general, particle sphericity and dimensionless size distribution should be held constant in the scaling since they influence \mathbf{e}_{mf} . The use of \mathbf{f} and a mean diameter in the Ergun expression only approximates the effects of these parameters. Note if the two models display identical dynamic characteristics, then \mathbf{e} is a dependent variable whose distribution throughout the bed should be identical for both fluidized beds. In this limit, the governing parameters given in Eq. (36) can be expressed as

$$\text{Eq. (45)} \quad \frac{u_o^2}{gL}, \frac{\mathbf{r}_s}{\mathbf{r}_f}, \frac{u_o}{u_{mf}}, \frac{L_1}{L_2}, \frac{G_s}{\mathbf{r}_s u_o} \text{ bed geometry, } \mathbf{f}, \text{ PSD}$$

where \mathbf{e}_{mf} will be a function of particle sphericity and size distribution.

This will be referred to as the *simplified scaling relationship*. At low Reynolds numbers, this still includes the gas-to-particle density ratio.

5.2 High Reynolds Numbers

Consider the limit of high particle Reynolds numbers where the inertial term in the Ergun equations dominates.

In this limit,

$$\text{Eq. (46)} \quad \frac{\mathbf{b}L}{\mathbf{r}_s u_o} \rightarrow 1.75 \frac{(1 - \mathbf{e})}{\mathbf{e}} \frac{\mathbf{r}_f}{\mathbf{r}_s} \frac{L/|u' - v'|}{\mathbf{f}d_p} \text{ for } \frac{\mathbf{r}_f u_o d_p}{\mathbf{m}} \gg 1$$

where $u' = u/u_o$ and $v' = v/u_o$ and $u' - v'$ is a dimensionless slip velocity.

The minimum fluidization velocity can be expressed as,

$$\text{Eq. (47)} \quad \frac{\Delta p}{L} = (\mathbf{r}_s - \mathbf{r}_f)g(1 - \mathbf{e}_{mf}) \sim \frac{1.75(1 - \mathbf{e}_{mf})}{\mathbf{e}_{mf}^3} \mathbf{r}_f \frac{u_{mf}^2}{\mathbf{f}d_p}$$

rearranging and using \mathbf{r}_s in place of $\mathbf{r}_s - \mathbf{r}_f$,

$$\text{Eq. (48)} \quad \frac{1.75(1 - \mathbf{e}_{mf})}{\mathbf{e}_{mf}^3} \frac{\mathbf{r}_f}{\mathbf{r}_s \mathbf{f}d_p} = \frac{g(1 - \mathbf{e}_{mf})}{u_{mf}^2}$$

Substituting this into Eq. (46) and multiplying by Fr ,

Eq. (49)

$$Fr \frac{\mathbf{b}L}{\mathbf{r}_s u_o} = \frac{u_o^2}{gL} \frac{\mathbf{e}_{mf}^3 L/|u' - v'| g(1 - \mathbf{e})}{\mathbf{e} u_{mf}^2} = \frac{u_o^2}{u_{mf}^2} \frac{\mathbf{e}_{mf}^3 (1 - \mathbf{e})/|u' - v'|}{\mathbf{e}}$$

At large particle Reynolds numbers, just as at low Reynolds numbers, the dimensionless drag, $\mathbf{b}L/\mathbf{r}_s u_o$, is identical when u_o/u_{mf} , \mathbf{e}_{mf}

and Fr are identical. The variables \mathbf{e} , u' and v' are dependent dimensionless variables which are identical for two similar fluidized beds. In this limit the same set of governing dimensionless parameters applies as in the low Reynolds number limit, given by Eq. (45).

5.3 Low Slip Velocity

Finally, consider the case when the magnitude of the slip velocity between the particles and the gas is close to u_{mf}/\mathbf{e} everywhere in the fluidized bed. With the vertical pressure drop equal to the particle weight, the following holds for any value of the particle Reynolds number,

$$\text{Eq. (50)} \quad \frac{\Delta p}{L} = \mathbf{b} / u - v \approx \mathbf{b} \frac{u_{mf}}{\mathbf{e}} = \mathbf{r}_s g (1 - \mathbf{e})$$

$$\text{Eq. (51)} \quad \mathbf{b} = \mathbf{r}_s g (1 - \mathbf{e}) \frac{\mathbf{e}}{u_{mf}}$$

and

$$\text{Eq. (52)} \quad \frac{\mathbf{b}L}{\mathbf{r}_s u_o} Fr = u_o / u_{mf} (1 - \mathbf{e}) \mathbf{e} \text{ for } u' - v' \rightarrow \frac{1}{\mathbf{e}} \frac{u_{mf}}{u_o}$$

Again, when u_o/u_{mf} and Fr are identical for two beds and the slip velocity is close to u_{mf}/\mathbf{e} , the dimensionless drag coefficient is also identical for two beds.

For all three limiting cases identified above, similitude can be obtained by maintaining constant values for the dimensionless parameters,

$$\text{Eq. (53)} \quad \frac{u_o^2}{gL}, \frac{\mathbf{r}_s}{\mathbf{r}_f}, \frac{u_o}{u_{mf}}, \frac{L_1}{L_2}, \frac{G_s}{\mathbf{r}_s u_o}, \text{ bed geometry, } \mathbf{f}_s, \text{ PSD}$$

5.4 General Case

Since the same simplified set of dimensionless parameters holds exactly at both high and low Reynolds numbers, it is reasonable to expect that it will hold, at least approximately, over the entire range of conditions for which the drag coefficient can be determined by the Ergun equation or an equation of similar form.

The validity of the simplified parameters can be checked numerically for the intermediate range of values.

From Eq. (31),

Eq. (54)

$$\frac{\mathbf{b}L}{\mathbf{r}_s u_o} = \frac{150(1-\mathbf{e})^2}{\mathbf{e}^2} \frac{\mathbf{m}L}{\mathbf{r}_s u_o (\mathbf{f}d_p)^2} + \frac{1.75(1-\mathbf{e})}{\mathbf{e}} \frac{\mathbf{r}_f}{\mathbf{r}_s} \frac{L|u'-v'|}{\mathbf{f}d_p}$$

where $u' - v'$ can also be represented as u_{slip}/u_o .

Using the Ergun equation to determine u_{mf} ,

Eq. (55)

$$\frac{\Delta p}{L} = \mathbf{r}_s g(1-\mathbf{e}_{mf}) = 150 \frac{(1-\mathbf{e}_{mf})^2}{\mathbf{e}_{mf}^3} \frac{\mathbf{m}u_{mf}}{(\mathbf{f}d_p)^2} + \frac{1.75(1-\mathbf{e}_{mf})}{\mathbf{e}_{mf}^3} \frac{\mathbf{r}_f u_{mf}^2}{\mathbf{f}d_p}$$

Dividing Eq. (54) by 55, and rearranging,

$$\text{Eq. (56)} \quad \left(\frac{\mathbf{b}L}{\mathbf{r}_s u_o} \right) \frac{Fr(1-\mathbf{e}_{mf})\mathbf{e}^2}{\left(\frac{u_o}{u_{mf}} \right) (1-\mathbf{e})^2 \mathbf{e}_{mf}^3} = \left[\frac{1 + \frac{1.75}{150} \frac{\mathbf{f}_s Re}{(1-\mathbf{e})} \mathbf{e}|u'-v'|}{1 + \frac{1.75}{150} \frac{\mathbf{f}_s Re}{(1-\mathbf{e}_{mf})} \frac{u_{mf}}{u_o}} \right]$$

where $Re = \mathbf{r}_f u_o d_p / \mathbf{m}$.

It is easy to verify the three limits defined previously by use of Eq. (56).

For the more general case, Fig. 21 shows the value of \mathbf{b} given by Eq. (56) relative to \mathbf{b} at low Re over a range of conditions when u_o/u_{mf} is 10 and 3, respectively, and Fr and \mathbf{f}_s remain constant. When u_o/u_{mf} and the slip velocity are high, there is a larger variation of dimensionless drag coefficient with Reynolds number. Note that \mathbf{b} does not vary with particle Reynolds number when the Reynolds number remains above about 10^3 or below about 10. Figure 22 illustrates the results when u_o/u_{mf} is 1000, a condition approached with very fine particle bubbling beds or circulating beds. In the latter instance, the use of the Ergun relationship is questionable except for the dense lower part of the bed.

5.5 Range of Validity of Simplified Scaling

To determine the validity of the simplified scaling laws over a wide range of conditions the simplified scaling laws have been used (Eq. 53) to design hypothetical models whose linear dimensions are 1/4 and 1/16, respectively, of the linear dimensions of a model designed using the full set of scaling laws, Eq. (37). To determine the validity of the smaller, simplified models, the dimensionless drag coefficient $\mathbf{b}L/\mathbf{r}_s u_o$ will be compared between the simplified models and the model using the full set of scaling laws. Figure 23 shows a comparison of the exact model and the simplified models for a pressurized fluidized combustor. Using the full set of scaling laws, the exact model, fluidized by ambient air, is approximately the same size as the combustor. The simplified models are reduced in size by their respective assumed length scale. The other parameters of the simplified model are then calculated to match the simplified parameters. For example, when the length scale is reduced to 1/4 that of the exact model, the velocity is reduced by 1/2 to keep the Froude number constant. The particle diameter is then reduced appropriately to keep the ratio of u_o/u_{mf} constant. These calculations were carried out over a range of particle Reynolds numbers, Re_{pE} , based on the full scaling law, or exact, model. In the simplified scaling relationships, the Reynolds number is not maintained constant. The concern is how much the drag coefficient is impacted by the shift in Reynolds number. It was found that the particle Reynolds number for the 1/4 scale simplified model remained roughly equal to $0.34 Re_{pE}$ over a wide range of values for Re_{pE} , whereas the particle Reynolds number for the 1/16 scale model was roughly $0.12 Re_{pE}$.

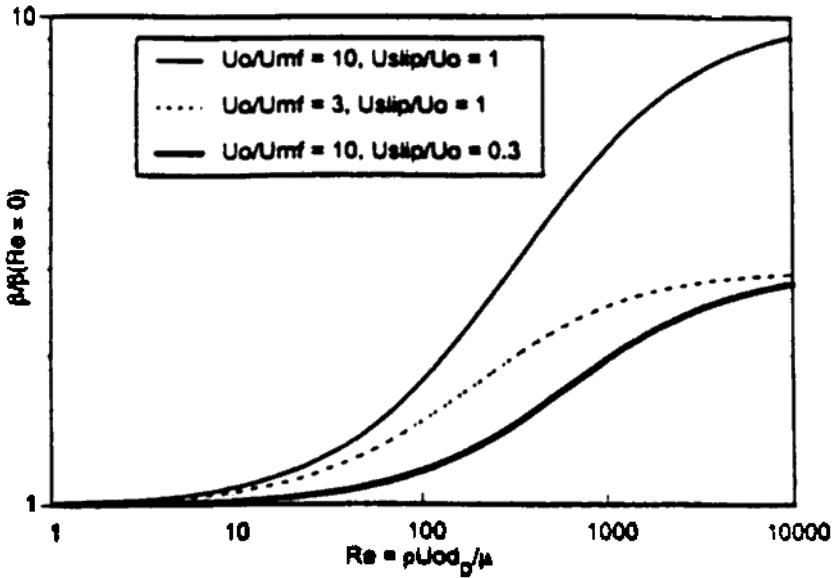


Figure 21. Ratio of drag coefficient to low Reynolds number drag coefficient, $u_o/u_{mf} = 10$ and 3. (From Glicksman et al., 1993b.)

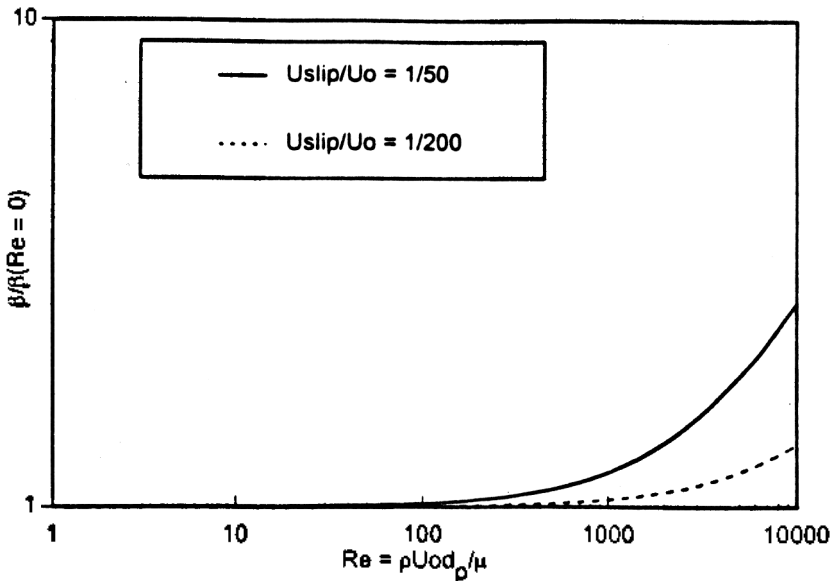


Figure 22. Ratio of drag coefficient to low Reynolds number drag coefficients, $u_o/u_{mf} = 1000$. (From Glicksman et al., 1993b.)

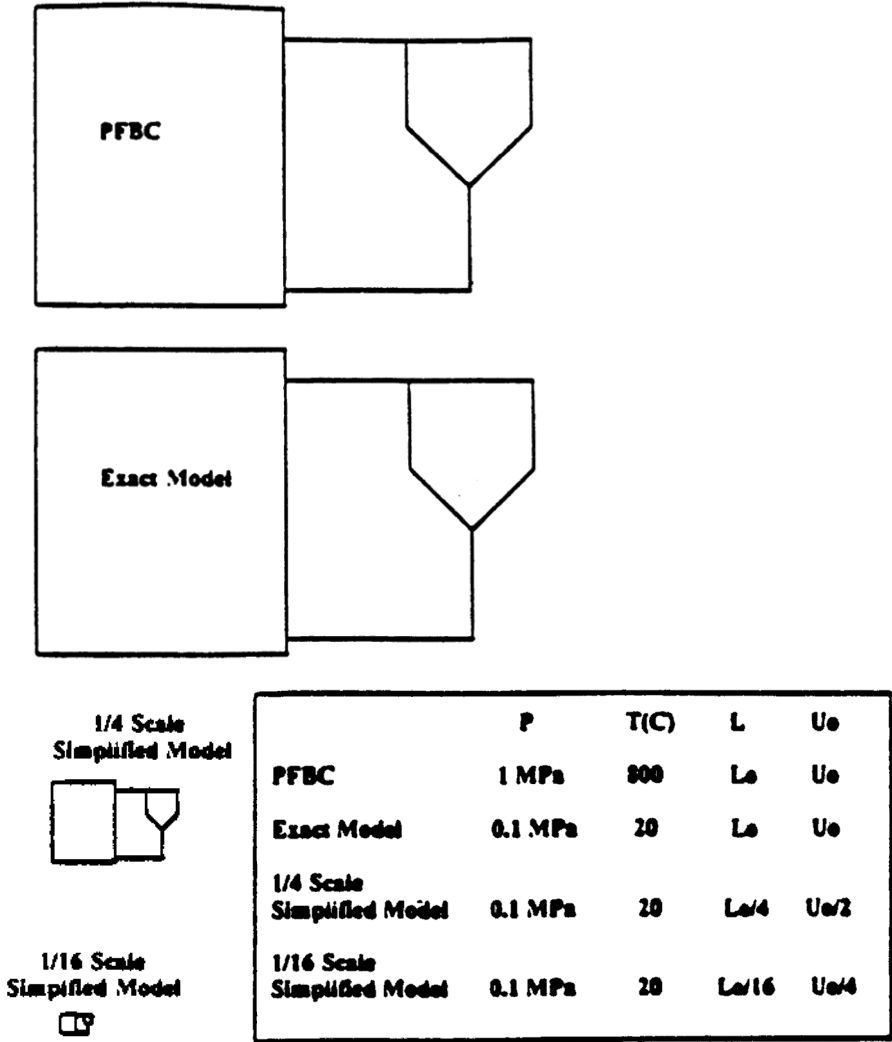


Figure 23. Exact and simplified models of a pressurized fluidized bed combustor. (From Glicksman *et al.*, 1993*b*.)

Using these Reynolds number scale factors, the errors in the dimensionless drag coefficient $bL/r_s u_o$ using the simplified scaling models are shown in Figs. 24 and 25 for u_o/u_{mf} of 10 and 1000, respectively, plotted as a function of Re_{pE} based on parameters for the exact scaled bed. For a particle Reynolds number of 1000 or less, which corresponds to

pressurized beds with particles of 1 mm or less, the error in the drag coefficient with the simplified scaling laws is twenty percent or less for a one quarter length scale model. The error is forty percent or less for a one sixteenth length scale model. At u_o/u_{mf} of 1000 and u_{slip}/u_{mf} of 1/50, the errors for the 1/16 scale model are twenty percent or less for Re_{pE} less than 10^3 . For particles of 0.2 mm or less, corresponding to a Reynolds number of 100 or less, the errors in drag coefficient are minimal. When the Ergun equation applies for the drag coefficient, a one quarter scale model based on the simplified scaling laws should be valid for any conditions. A 1/16 scale model should be valid for particle diameters of about 0.2 mm or less for a pressurized bubbling bed with u_o/u_{mf} of 10 and u_{slip}/U_o of 0.3. At u_o/u_{mf} of 1000 and u_{slip}/U_o of 1/50, the 1/16 scale model should be valid for pressurized beds with particles up to 1 mm in diameter. These conclusions apply when the particle to fluid drag term is given by the Ergun equation or similar relationships and the scaled particles are not so small that interparticle surface forces come into play.

Clusters. In the freeboard of a bubbling bed or in the upper portion of a circulating bed where particles generally are considered to act in clusters or groups, a similar examination of scaling of the gas-to-solid drag can be made. Consider all of the particles grouped into clusters with an effective diameter d_c and the clusters occupying a volume fraction e_c of the bed volume. The cluster-to-gas drag will be represented by the drag coefficient for a solid sphere of diameter d_c ,

$$\text{Eq. (57)} \quad \mathbf{b}/\bar{u} - \bar{v}/\frac{\mathbf{p} d_c^3}{6(1 - e_c)} = \frac{1}{2} \mathbf{r}_f \frac{\mathbf{p} d_c^2}{4} / \bar{u} - \bar{v}^2 C_D$$

This can be rewritten as,

$$\text{Eq. (58)} \quad \frac{\mathbf{b}L}{\mathbf{r}_s u_o} = \frac{3}{4} \left(\frac{\mathbf{r}_f}{\mathbf{r}_s} \right) / \bar{u}' - \bar{v}'^2 / C_D \frac{L}{d_c} (1 - e_c)$$

If the diameter of individual particles does not influence the drag of a cluster of particles, then when the solid-to-gas density ratio is held constant between the combustor and the model, the dimensionless drag $\mathbf{b}L/\mathbf{r}_s u_o$ is properly scaled when C_D is invariant.

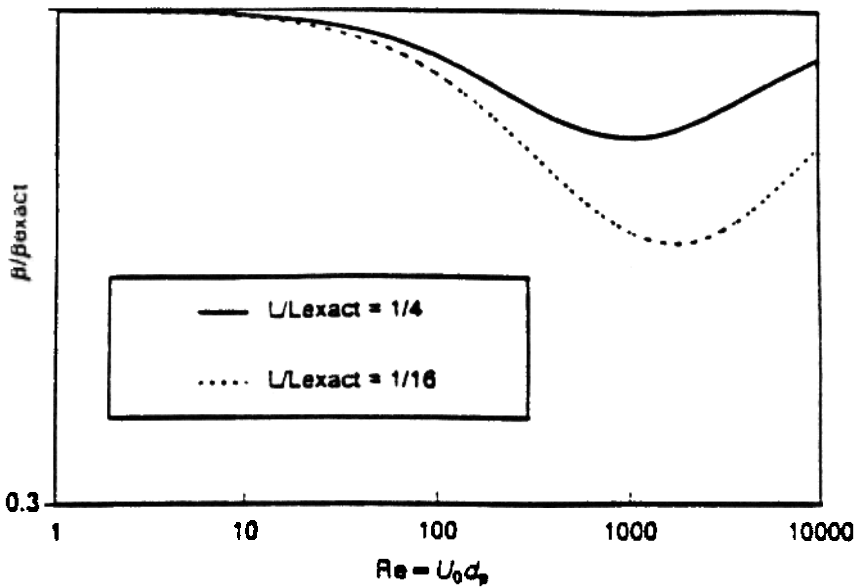


Figure 24. Error in drag coefficient for simplified scaling relationships, $u_o/u_{mf} = 10$. (From Glicksman *et al.*, 1993b.)

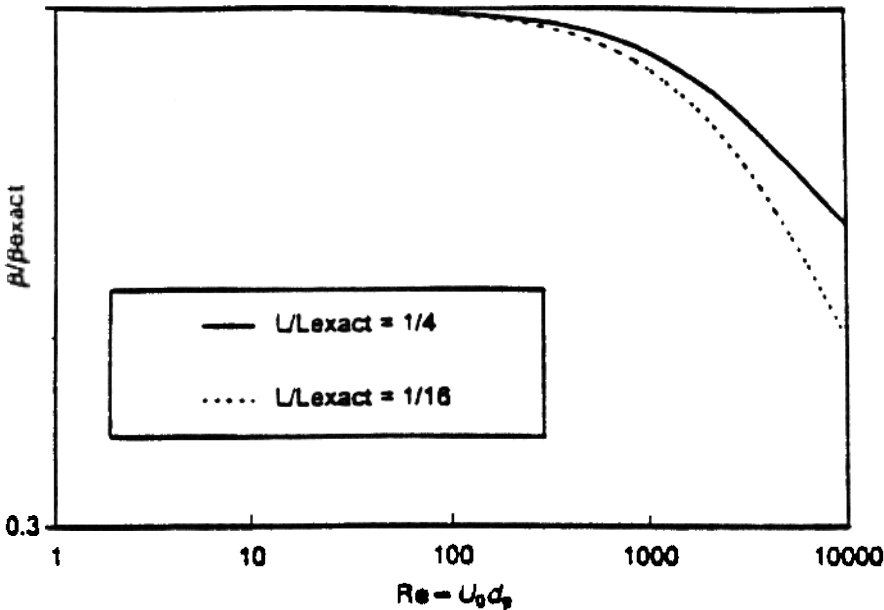


Figure 25. Error in drag coefficient for simplified scaling relationships, $u_o/u_{mf} = 1000$. (From Glicksman *et al.*, 1993b.)

If the reduced scale models faithfully reproduce the dynamics of the exact case, the cluster dimensions should scale directly with the linear dimensions of the bed. Thus, a one-quarter linear scale model which has a velocity one-half that of the exact case will have a cluster Reynolds number (Re_{dc}) one-eighth that of the exact bed. From the relationship of C_D with Re , the change of C_D with model scale at a given Reynolds number of the exact bed can be determined. Figure 26 shows the shift in C_D using the C_D relationship of White (1974) for length scales of 1/4, 1/8 and 1/16, respectively, of the exact bed length as a function of the cluster Reynolds number of the exact bed. Also shown on the figure is the typical Reynolds number of an atmospheric combustor with a 0.3 m cluster diameter, approximately 1.5×10^4 . In a bubbling bed, the cluster diameter in the freeboard should be at least equal in size to the diameter of bubbles erupting at the bed surface. For beds with horizontal tubes, the bubble diameter will be equal to or larger than the horizontal tube spacing. In a bubbling bed without tubes, the bubbles and clusters can be much larger. In an open circulating bed the cluster diameter is more difficult to determine. It is reasonable to assume its diameter is proportional to the bed diameter, equal in magnitude to the bed diameter or one order of magnitude smaller. From these considerations, the Reynolds number based on the cluster diameter should be 10^4 or larger in an atmospheric combustor with a cluster diameter of 0.2 m. The cluster Reynolds number should be 10^5 or larger in a pressurized combustor. From Fig. 26, it can be seen that a one quarter scale or an eighth scale model should have drag coefficients similar to the exact bed. For pressurized beds, the drag coefficients should be very close in magnitude.

Individual Particles. If the drag coefficient, b , is influenced by the characteristics of individual particles, the detailed particle dynamics of the simplified scale models must be examined. In this case

$$\text{Eq. (59)} \quad \frac{bL}{r_s u_o} = \frac{3}{4} \left(\frac{r_f}{r_s} \right) / \bar{u}' \cdot \bar{v}' / C_D \frac{L}{d_p} (1 - e)$$

where C_D is the drag coefficient of a single particle. This can be rewritten in terms of the single particle terminal velocity which can be found from

$$\text{Eq. (60)} \quad \frac{r_s \rho d_p^3 g}{6} = \frac{1}{2} \frac{r_f \rho d_p^2}{4} C_D u_t^2$$

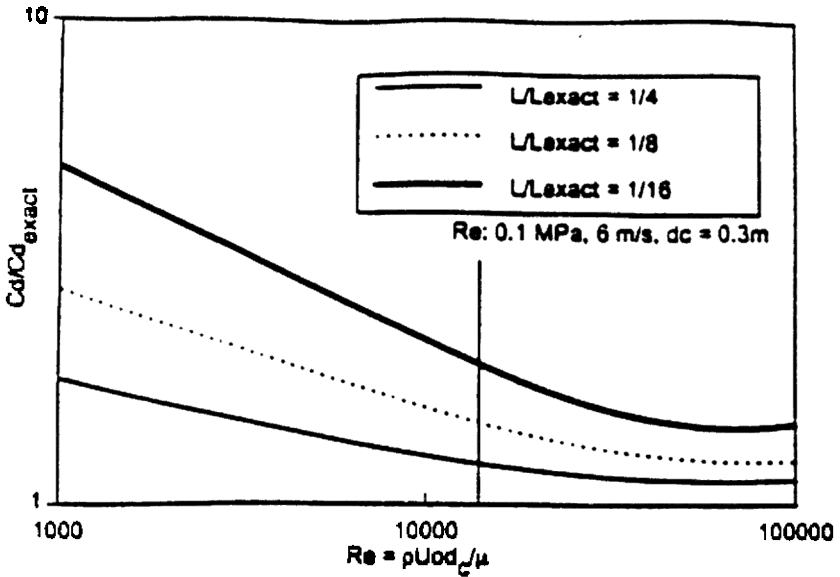


Figure 26. Error in cluster drag coefficient for fixed u_o/u_{mf} using C_d for a solid sphere. (From Glicksman et al., 1993b.)

Substituting Eq. (60) into Eq. (59) to eliminate C_D , one obtains

$$\text{Eq. (61)} \quad \frac{bL}{r_s u_o} Fr = \frac{u_o^2}{u_t^2} / \overline{u'} - \overline{v'} / (1 - e)$$

Since u_o/u_{mf} and Fr are held constant in the simplified scaling process, we will examine the ratio u_t/u_{mf} to determine if the drag coefficient $bL/r_s u_o$ remains constant.

The Ergun equation can be solved to find u_{mf}

$$\text{Eq. (62)}$$

$$r_f \frac{u_{mf} d_p}{m} = \frac{\frac{-(150)(1 - e_{mf})^2}{e_{mf}^3} + \sqrt{\left[\frac{-(150)(1 - e_{mf})^2}{e_{mf}^3} \right]^2 + \frac{7(1 - e_{mf})^2}{e_{mf}^3} f_s^3 Ar}}{3.5(1 - e_{mf}) f_s / e_{mf}^3}$$

where $Ar = r_s r_f d_p^3 g / m^2$ is the Archimedes number.

The relationship given by White (1974) for C_D written as,

$$\text{Eq. (63)} \quad Re_t^2 = \frac{\frac{4}{3} Ar}{\frac{24}{Re_t} + \frac{6}{1 + \sqrt{Re_t}} + 0.4}$$

where $Re_t = \mathbf{r}_f u_t d_p / \mathbf{m}$ can be used to relate u_t to Ar .

At small and large values of Ar , the ratio of u_t/u_{mf} which is the ratio of $Re_t / (\mathbf{r}_f u_{mf} d_p / \mathbf{m})$ approaches a constant value. In these two limits, the simplified scaling laws will yield exact agreement of u_t/u_{mf} between the combustor and the simplified models. The errors in u_t/u_{mf} are shown in Figs. 27 and 28 for simplified scale models at two different linear dimensions. Scaling a combustor with comparatively small particles, 0.2 mm or less, gives good agreement for u_t/u_{mf} even at one-sixteenth linear scale, while for large particles a linear scale of one-fourth gives fair agreement for u_t/u_{mf} . Since u_o/u_{mf} is held constant in the simplified scaling laws, close agreement of u_t/u_{mf} also results in close agreement of u_t/u_o . For a circulating bed, pneumatic transport, or other low solids volume fraction, it might be more correct to scale the model to achieve closer agreement for u_t/u_o , allowing u_o/u_{mf} to deviate between the model and full scale bed.

6.0 FURTHER SIMPLIFICATIONS IN THE SCALING RELATIONSHIP

6.1 Viscous Limit

Glicksman (1984) showed that the list of controlling dimensionless parameters could be reduced if the fluid-particle drag is primarily viscous or primarily inertial. The standard viscous and inertial limits for the drag coefficient apply. This gives approximately

$$\begin{aligned} \text{Eq. (64)} \quad & \text{Viscous: } Re_{u_{rel}, d_p} / \overline{|\mathbf{u}' - \mathbf{v}'|} < 10 \\ & \text{Inertial: } Re_{u_{rel}, d_p} / \overline{|\mathbf{u}' - \mathbf{v}'|} > 1000 \end{aligned}$$

using the Ergun equation.

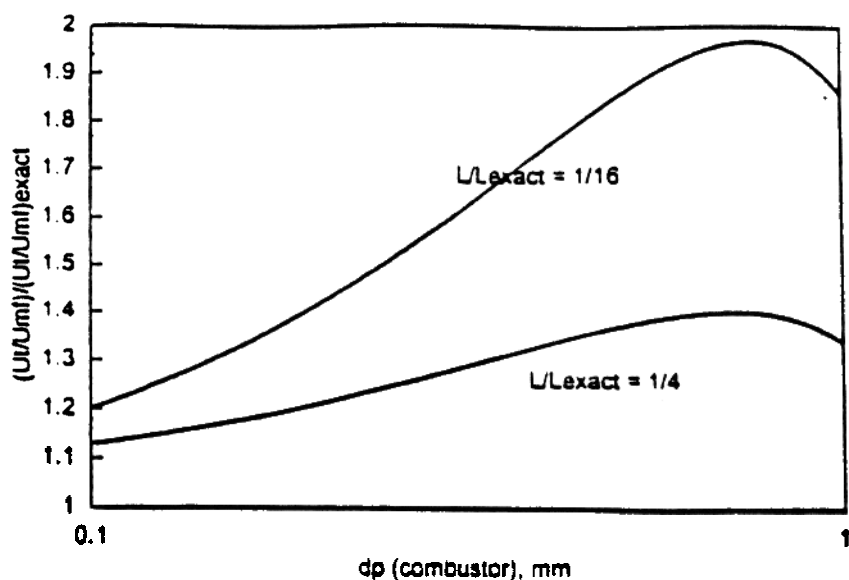


Figure 27. Error in terminal velocity using simplified scaling at 1013 kPa and 800°C. (From Glicksman et al., 1994.)

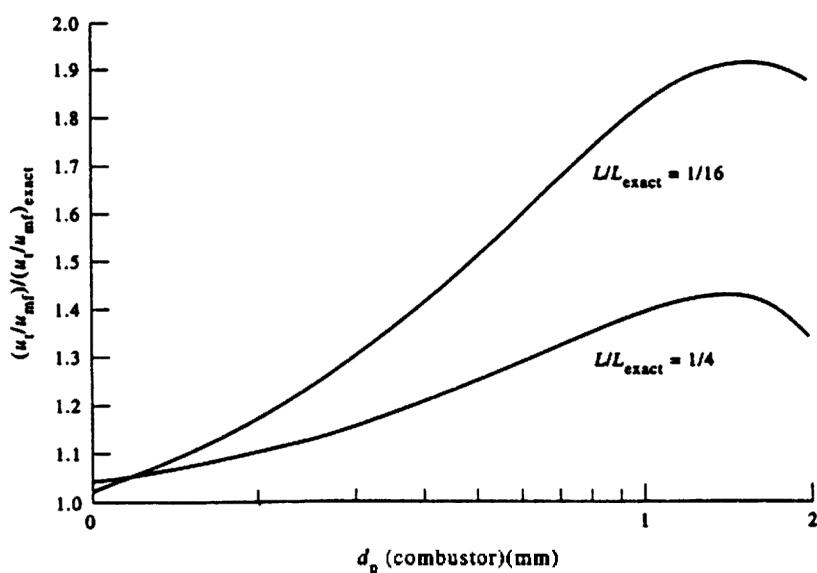


Figure 28. Error in terminal velocity using simplified scaling at 101.3 kPa and 800°C. (From Glicksman et al., 1994.)

The use of a Reynolds number based on relative velocity rather than superficial velocity in setting these limits was suggested by Horio (1990). In setting viscous or inertial limits, it is the interphase drag which is characterized as being dominated by viscous or inertial forces. The particle inertia is important even if the interphase drag is viscous dominated. This is because of the typically large solid-to-gas density ratio.

For viscous dominated flows, it can be assumed that the gas inertia and the gas gravitational forces are negligible. By dropping the gas inertia and gravity time from the gas momentum equation and simplifying the dimensionless drag coefficient to the linear viscous term, the set of dimensionless equations does not include gas-to-solid density ratio as a parameter.

The ratio between the bed and particle diameters and the Reynolds number based on bed diameter, superficial velocity, and solid density appear only in the modified drag expression, in which they are combined, see Eq. (40). These parameters form a single parameter, as discussed by Glicksman (1988) and other investigators. The set of independent parameters controlling viscous dominated flow are then

$$\text{Eq. (65)} \quad \frac{\mathbf{r}_s u_o d_p^2}{mL}, \mathbf{f}_s, \frac{gL}{u_o^2}, \frac{D}{L}, \frac{G_s}{\mathbf{r}_s u_o}, \text{ bed geometry, PSD}$$

The first term in the list multiplied by the third term has been shown by Glicksman (1988) to be equivalent to the ratio of superficial and minimum fluidization velocities in the viscous limit. The controlling parameters can therefore be written as

$$\text{Eq. (66)} \quad \frac{u_{mf}}{u_o}, \mathbf{f}_s, \frac{gL}{u_o^2}, \frac{D}{L}, \frac{G_s}{\mathbf{r}_s u_o}, \text{ bed geometry, PSD}$$

Note this is a subset of the simplified scaling laws presented above with the solid-to-gas density ratio removed. The viscous limit requirement is based on the assumptions that the gas inertial forces are negligible compared to gas-solid interaction forces and the dimensionless interphase drag can be modelled as a linear function of the particle Reynolds number. Because of clustering of particles, this may not be a valid assumption, and the requirements for neglecting gas inertia may be much more stringent than given by Eq. (64). As will be discussed in the experimental verification of simplified scaling laws, a viscous limit for interphase drag may not exist in circulating fluidized beds.

It must be borne in mind that this set is valid only when fluid inertial effects are negligible, i.e., it is a subset of the general relationships and the simplified relationship. Glicksman (1984) used the criteria for the viscous limit in a bubbling bed that the ratio of viscous forces to fluid inertial forces in the Ergun equation is ten or larger. From Table 1 of that reference, for a bed of glass or sand fluidized with air at standard conditions with u_o/u_{mf} of 3, the viscous limit occurs when particles are less than about 200 microns. In regions where particles behave individually, the viscous limit occurs for particles less than 60 microns (assuming the particle/gas relative velocity is equal to the particle terminal velocity and the single particle viscous limit criterion is $Re_{u_{rel}, d_p} < 1$). There are some data to suggest this Reynolds number limit may be too restrictive.

6.2 Other Derivations for Circulating Fluidized Beds

The most dramatic departure from the above procedure for derivation of scaling laws is that of Horio (1989). Although the procedure is different, the results are identical to the scaling laws described in the previous sections. Horio has presented a scaling law for circulating fluidized beds which is based on the Clustering Annular Flow Model (CAFM) of Ishii et al. (1989). The CAFM describes the flow in a circulating fluidized bed as particle clusters moving upward in the core and downward in an annulus at the wall. The analysis was similar to that of Nakamura and Capes (1973). Completeness of the model was achieved by assuming minimization of pressure gradient.

Horio's scaling law derivation was based on the requirement that two similar circulating fluidized beds have equal values of voidage distribution, dimensionless core radius, gas splitting to core and annulus, solid splitting to core and annulus, and cluster voidage. The CAFM equations were then examined to determine how these requirements could be met.

Questions as to the validity of the theory supporting Horio's development are based on deficiencies of the CAFM to fully describe circulating fluidized bed flow and the lack of justification for the premise that the five characteristics comprise all that is of interest in a circulating fluidized bed. In particular, the assumption of pressure drop minimization, although convenient, is not justified physically.

The scaling law proposed by Horio for circulating fluidized beds can be shown to be equivalent to the simplified set of parameters. Horio also discussed reductions to his list of scaling parameters in which the solid/gas density ratio is omitted. He claimed that this reduced scaling law

is sufficient for “macroscopic similarity” and sacrifices only cluster size similarity. This reduced law is identical to the bubbling bed scaling law developed by Horio (1986) and has been shown by Glicksman (1988) to be equivalent to the viscous limit scaling law presented in the previous section. Horio’s suggestion that the density ratio can be neglected because sacrificing cluster size does not necessarily alter the macroscopic behavior of a circulating fluidized bed is somewhat curious since his development is based on the CAFM which assumes clusters are the primary mechanism of particle transport.

From an operational standpoint, the paramount question for a designer is which scaling law must be followed. Since Horio’s reduced set is equivalent to the viscous limit, Eq. (66), it must be determined if the density ratio can be omitted in the scaling relationship, i.e., is the viscous limit an adequate set of scaling parameters or must the density ratio also be included as is done in the simplified scaling relationships, Eq. (53). As will be shown in a later section, density ratio is not a parameter which can be omitted when scaling circulating fluidized beds and the density ratio is generally required for scaling bubbling beds.

6.3 Deterministic Chaos

Recent studies have indicated that fluidized beds may be deterministic chaotic systems (Daw et al., 1990; Daw and Harlow, 1991; Schouten and van den Bleek, 1991; van den Bleek and Schouten, 1993). Such systems are characterized by a limited ability to predict their evolution with time. If fluidized beds are deterministic chaotic systems, the scaling laws should reflect the restricted predictability associated with such systems.

Van den Bleek and Schouten (1993) have suggested that if two beds are properly scaled, the rate of information change in both systems will be the same. They suggest that two scaled beds will exhibit the same Kolmogorov entropy, or information generation rate, when measured on the same time scale. Hence, they adopt an additional method for verifying dynamic similarity requiring that the information group, Kt , remain constant (where $t = d_p/u_o$ and K is the Kolmogorov entropy) along with the full set of scaling parameters we have described.

Further work is needed to determine in which regimes, if any, fluid bed behave as chaotic systems. Additional testing is needed to determine the sensitivity of important bed hydrodynamic characteristics to the Kolmogorov entropy, to quantitatively relate changes of entropy to

shifts in hydrodynamic behavior. It may be that the requirement of Kt equality may be an over-restrictive condition, that is, similarity of hydrodynamic characteristics such as solid mixing and gas-to-solid transfer may be achieved even when Kt varies considerably.

7.0 DESIGN OF SCALE MODELS

7.1 Full Set of Scaling Relationships

We will first consider the steps to design a model which is similar to another bed based on the full set of scaling parameters, Eqs. (37) or (39).

To construct a model which will give behavior similar to another bed, for example, a commercial bed, all of the dimensionless parameters listed in Eqs. (37) or (39) must have the same value for the two beds. The requirements of similar bed geometry is met by use of geometrically similar beds; the ratio of all linear bed dimensions to a reference dimension such as the bed diameter must be the same for the model and the commercial bed. This includes the dimensions of the bed internals. The dimensions of elements external to the bed such as the particle return loop do not have to be matched as long as the return loop is designed to provide the proper external solids flow rate and size distribution and solid or gas flow fluctuations in the return loop do not influence the riser behavior (Rhodes and Laussman, 1992).

Proper conditions must be chosen to design a scale model to match the dimensionless parameters of the commercial bed. To model a gas fluidized commercial bed, a scale model using air at standard conditions is most convenient, although several investigators have used other gases (Fitzgerald and Crane, 1980; Fitzgerald et al., 1984; Chang and Louge, 1992) or pressurized scale models (Almstedt and Zakkay, 1990; Di Felice et al., 1992 a,b). The gas chosen for the model, along with the gas pressure and temperature, determines the values of \mathbf{r}_f and \mathbf{m} . The particle density for the model is chosen to match the density ratio, so that

$$\text{Eq. (67)} \quad \left(\frac{\mathbf{r}_f}{\mathbf{r}_s} \right)_m = \left(\frac{\mathbf{r}_f}{\mathbf{r}_s} \right)_c$$

where the subscript m is for the model and c is for the commercial bed. For the remaining parameters, the form of Eq. (37) will be chosen for the

dimensionless parameters. Combining the Reynolds number based on bed diameter and the square root of the Froude number,

$$\text{Eq. (68)} \quad \frac{\mathbf{r}_f u_o L}{\mathbf{m}_f} \frac{\sqrt{gL}}{u_o} = \left(\frac{L^{\frac{3}{2}} \sqrt{g}}{\mathbf{n}_f} \right)_m = \left(\frac{L^{\frac{3}{2}} \sqrt{g}}{\mathbf{n}_f} \right)_c$$

Rearranging,

$$\text{Eq. (69)} \quad \left(\frac{L_m}{L_c} \right) = \left(\frac{(\mathbf{n}_f)_m}{(\mathbf{n}_f)_c} \right)^{\frac{2}{3}}$$

All of the linear dimensions of the model are scaled to the corresponding dimensions of the commercial bed by the ratio of the kinematic viscosities of the gas raised to the two-thirds power. By taking the ratio of Reynolds number based on the particle diameter to Reynolds number based on the bed diameter

$$\text{Eq. (70)} \quad \frac{\mathbf{r}_f u_o L}{\mathbf{m}_f} \cdot \frac{\mathbf{m}_f}{\mathbf{r}_f u_o d_p} = \left(\frac{L}{d_p} \right)_m = \left(\frac{L}{d_p} \right)_c$$

The particle diameters in the model scale by the same factor as the bed diameter, by the ratio of the kinematic viscosities to the two-thirds power.

Equating the Froude number and rearranging,

$$\text{Eq. (71)} \quad \frac{u_{om}}{u_{oc}} = \left(\frac{L_m}{L_c} \right)^{\frac{1}{2}}$$

Thus, the velocity scales are the square root of the linear dimension scale.

By satisfying both Eq. (69) and Eq. (71), the Reynolds number and the Froude numbers are kept identical between the model and the commercial bed.

Combining $G_s/\mathbf{r}_s u_o$ and the product of Reynolds and Froude number along with Eq. (69), it can be shown that

$$\text{Eq. (72)} \quad \frac{\left(\frac{G_s}{r_s}\right)_m}{\left(\frac{G_s}{r_s}\right)_c} = \left(\frac{n_{fm}}{n_{fc}}\right)^{\frac{1}{3}}$$

so that the ratio of solids-flow to solids-density scales as the ratio of the cube root of the kinematic viscosity.

Once the model fluid and its pressure and temperature are chosen, which sets the gas density and viscosity, there is only one unique set of parameters for the model which gives similarity when using the full set of dimensionless parameters. The dependent variables, as nondimensionalized by Eq. (18), will be the same in the respective dimensionless time and spatial coordinates of the model as the commercial bed. The spatial variables are nondimensionalized by the bed diameter so that the dimensional and spatial coordinates of the model is proportional to the two-thirds power of the kinematic viscosity, as given by Eq. (69)

$$\text{Eq. (73)} \quad \frac{x_m}{x_c} = \left(\frac{n_{fm}}{n_{fc}}\right)^{\frac{2}{3}}$$

Since the velocity scales with $v_f^{1/3}$, the ratio of time scales can be expressed as

$$\text{Eq. (74)} \quad \frac{t_m}{t_c} = \left(\frac{n_{fm}}{n_{fc}}\right)^{\frac{1}{3}}$$

Similarly, it can be shown that the frequency scales as

$$\text{Eq. (75)} \quad \frac{f_M}{f_c} = \left(\frac{n_{fc}}{n_{fm}}\right)^{\frac{1}{3}}$$

Table 1 gives the values of design and operating parameters of a scale model fluidized with air at ambient conditions which simulates the dynamics of an atmospheric fluidized bed combustor operating at 850°C. Fortunately, the linear dimensions of the model are much smaller, roughly one quarter those of the combustor. The particle density in the model must be much higher than the particle density in the combustor to maintain a constant value of the gas-to-solid density ratio. Note that the superficial velocity of the model differs from that of the combustor along with the spatial and temporal variables.

When modelling a pressurized hot bed (Table 2) the ambient temperature model fluidized with air has dimensions very close to those of the pressurized combustor. If another gas is used in the model, particularly a gas with a higher density, the model can be made much smaller than the pressurized combustor (see Table 3). Care must be taken to select a safe modelling gas and one which yields a solid density for the model which is available.

Table 1. Atmospheric Combustor Modelled by a Bed Fluidized with Air at Ambient Conditions

GIVEN:	Commercial Bed	Scale Model, full scaling laws
Temperature (°C)	850	25
Gas Viscosity (10^{-5} kg/ms)	4.45	1.81
Density (kg/m ³)	0.314	1.20
Derived from Scaling Laws:		
Solid Density	r_{sc}	$3.82r_{sc}$
Bed Diameter, Length	D_c	$0.225D_c$
Particle Diameter	d_{pc}	$0.225d_{pc}$
Superficial Velocity	u_{oc}	$0.47u_{oc}$
Volumetric Solid Flux	$(G_s/r_s)_c$	$0.47(G_s/r_s)_c$
Time	t_c	$0.47t_c$
Frequency	f_c	$2.13f_c$

Table 2. Pressurized Combustor Modelled by a Bed Fluidized with Air at Ambient Conditions

GIVEN:	Commercial Bed	Scale Model, full scaling laws
Temperature (°C)	850	20
Gas Viscosity (10 ⁻⁵ kg/ms)	4.45	1.81
Density (kg/m ³)	3.14	1.20
Pressure (bar)	10	1
Derived from Scaling Laws:		
Solid Density	ρ_{sc}	$0.382\rho_{sc}$
Bed Diameter, length	D_c	$1.05D_c$
Particle Diameter	d_{pc}	$1.05 d_{pc}$
Superficial Velocity	u_{oc}	$1.01 u_{oc}$
Volumetric Solid Flux	$(G_s/\rho_s)_c$	$1.01(G_s/\rho_s)_c$
Time	t_c	$1.01t_c$
Frequency	f_c	$0.98f_c$

Table 3. Pressurized Combustor Modelled by a Bed Fluidized with Refrigerant Vapor 134a at Ambient Conditions

GIVEN:	Commercial Bed	Scale Model, full scaling laws
Temperature (°C)	850	20
Gas Viscosity (10 ⁻⁵ kg/ms)	4.45	1.19
Density (kg/m ³)	3.14	4.34
Pressure (bar)	10	1
Derived from Scaling Laws:		
Solid Density	ρ_{sc}	$1.38\rho_{sc}$
Bed Diameter, length	D_c	$0.334D_c$
Particle Diameter	d_{pc}	$0.334 d_{pc}$
Superficial Velocity	u_{oc}	$0.58 u_{oc}$
Volumetric Solid Flux	$(G_s/\rho_s)_c$	$0.58(G_s/\rho_s)_c$
Time	t_c	$0.58t_c$
Frequency	f_c	$1.7f_c$

7.2 Design of Scale Models Using the Simplified Set of Scaling Relationships

The simplified scaling relationships, Eq. (53), offer some flexibility in the model design since fewer parameters must be matched than with the full set of scaling relationships. When the fluidizing gas, the pressure and temperature of the scale model are chosen, the gas density and viscosity for the scale model are set. The model must still be geometrically similar to the commercial bed. There is still one free parameter. Generally this will be the linear scale of the model. For the simplified scaling relationships, the gas-to-solid density ratio must be maintained constant

$$\text{Eq. (76)} \quad \left(\frac{\mathbf{r}_f}{\mathbf{r}_s} \right)_m = \left(\frac{\mathbf{r}_f}{\mathbf{r}_s} \right)_c$$

With \mathbf{r}_f of the model set by the fluidized gas and its state, the solid density in the model follows from Eq. (76). Choosing the length coordinate of the model, L_m , which is now a free parameter, the superficial velocity in the model is determined so that the Froude number remains the same,

$$\text{Eq. (77)} \quad \left(\frac{u_o^2}{gL} \right)_m = \left(\frac{u_o^2}{gL} \right)_c$$

so that

$$\text{Eq. (78)} \quad \frac{u_{om}}{u_{oc}} = \left(\frac{L_m}{L_c} \right)^{1/2}$$

Note that in simplified case, the velocity scaling is not uniquely tied to just the gas properties as it is in the full scaling relationship. With u_o and \mathbf{r}_s set, the solids recycle rate can be determined by

$$\text{Eq. (79)} \quad \left(\frac{G_s}{\mathbf{r}_s u_o} \right)_m = \left(\frac{G_s}{\mathbf{r}_s u_o} \right)_c$$

$$\text{Eq. (80)} \quad \frac{G_{sm}}{G_{sc}} = \left(\frac{\mathbf{r}_{sm}}{\mathbf{r}_{sc}} \right) \left(\frac{u_{om}}{u_{oc}} \right) = \left(\frac{\mathbf{r}_{fm}}{\mathbf{r}_{fc}} \right) \left(\frac{L_m}{L_c} \right)^{\frac{1}{2}}$$

Finally the mean particle size for the model as well as the sphericity and particle size distribution must be determined. The particle size is determined by the need for equal values of u_o/u_{mf} between the model and the commercial bed.

$$\text{Eq. (81)} \quad \left(\frac{u_o}{u_{mf}} \right)_m = \left(\frac{u_o}{u_{mf}} \right)_c$$

$$\text{Eq. (82)} \quad (u_{mf})_m = (u_{mf})_c \left(\frac{u_{om}}{u_{oc}} \right) = (u_{mf})_c \left(\frac{L_m}{L_c} \right)^{1/2}$$

In general, u_{mf} is a function of the particle diameter and gas properties, as well as \mathbf{f} and \mathbf{e}_{mf} . Once the fluidizing gas and the length of scale of the model is chosen, the proper particle diameter is that which gives the value of u_{mf} needed in Eq. (82).

If both the model and commercial bed are in the region where the respective Reynolds numbers based on particle diameter and gas density are very low, then a single algebraic relationship can be developed. In that region

$$\text{Eq. (83)} \quad u_{mf} \sim \frac{\mathbf{r}_s d_p^2}{\mathbf{m}}$$

$$\text{Eq. (84)} \quad \frac{u_{mf_m}}{u_{mf_c}} = \left(\frac{d_{pm}}{d_{pc}} \right)^2 \frac{\mathbf{r}_{sm}}{\mathbf{r}_{sc}} \frac{\mathbf{m}_c}{\mathbf{m}_m} = \frac{u_{om}}{u_{oc}} = \left(\frac{L_m}{L_c} \right)^{\frac{1}{2}}$$

$$\text{Eq. (85)} \quad \left(\frac{d_{pm}}{d_{pc}} \right)^2 = \frac{\mathbf{r}_{sc}}{\mathbf{r}_{sm}} \frac{\mathbf{m}_m}{\mathbf{m}_c} \left(\frac{L_m}{L_c} \right)^{\frac{1}{2}}$$

$$\text{Eq. (86)} \quad \left(\frac{d_{pm}}{d_{pc}} \right)^2 = \frac{\mathbf{r}_{fc}}{\mathbf{r}_{fm}} \frac{\mathbf{m}_m}{\mathbf{m}_c} \left(\frac{L_m}{L_c} \right)^{1/2}$$

when both $(Re_{dp})_m$ and $(Re_{dp})_c < 20$.

When the Reynolds number of the model and commercial bed are both very large

$$\text{Eq. (87)} \quad u_{mf}^2 \sim d_p \frac{\mathbf{r}_s}{\mathbf{r}_f}$$

Since the gas-to-solid density ratio of the model and the commercial beds must be the same to satisfy the simplified scaling relationships, Eq. (87) combined with Eqs. (81) and (78) becomes,

$$\text{Eq. (88)} \quad \frac{u_{mf_m}^2}{u_{mf_c}^2} = \frac{d_{pm}}{d_{pc}} \frac{\left(\frac{\mathbf{r}_s}{\mathbf{r}_f} \right)_m}{\left(\frac{\mathbf{r}_s}{\mathbf{r}_f} \right)_c} = \frac{u_{om}^2}{u_{oc}^2} = \frac{L_m}{L_c}$$

When both $(Re_{dp})_m$ and $(Re_{dp})_c > 1000$

$$\text{Eq. (89)} \quad \frac{d_{pm}}{d_{pc}} = \frac{L_m}{L_c}$$

Tables 4 and 5 show the values of the mean particle diameter for models of an atmospheric and pressurized commercial bed, respectively, for different selected linear scale ratios between the model and commercial bed.

By the use of the simplified scaling parameters, the linear scale factor can be changed as shown in Tables 4 and 5. Note that as the linear

scale factors are changed the particle diameters change much more slowly. The scale model of the 10-atmospheres bed has a mean particle diameter which is quite close to the mean particle diameter of the commercial bed. The model particles have a substantially lower density in this case.

It is not clear where cohesive forces will become important. The use of very dense particles (for the models of the one atmospheric bed) will cause a shift of the boundary of cohesive influence as given, for example, by Geldart’s classification. However, adequate experimental data is still lacking with such dense fine particles to definitely set the limits of cohesive influence.

Note that for completeness, the nondimensional particle size distribution, sphericity and the internal angle of friction (for slugging and spouting beds) should also be matched between the two beds.

Table 4. Scale Models of Atmospheric Commercial Hot Bed Using the Simplified Scaling Relationship

Commercial Beds		Particle Diameter of Model with Bed Linear Scale Factor	
d_p	u_{mf}	$L_m/L_c = 1/4$	$L_m/L_c = 1/9$
40 μm	$7.45 \times 10^{-4} \text{ m/s}$	10 μm	8 μm
60	1.68×10^{-3}	15	12
100	4.66×10^{-3}	24	20
200	1.86×10^{-2}	49	40
400	7.42×10^{-2}	98	80
1000	0.441	245	198

Commercial Bed: $T = 800^\circ\text{C}$, $P = 1 \text{ atm}$, $r_s = 2500 \text{ kg/m}^3$, gas:air
Model Bed: $r_s = 8960 \text{ kg/m}^3$, gas:air at STP

Table 5. Scale Model of 10 Atm Commercial Hot Bed Using the Simplified Scaling Relationships

Commercial Beds		Particle Diameter of Model with Bed Linear Scale Factor	
d_p	u_{mf}	$L_m/L_c = 1/4$	$L_m/L_c = 1/9$
40 mm	7.44×10^{-4} m/s	31 mm	25 mm
60	1.67×10^{-3}	46	38
100	4.65×10^{-3}	78	63
200	1.85×10^{-2}	155	126
400	7.18×10^{-2}	310	250
1000	0.329	610	550

Commercial Bed: $T = 800^\circ\text{C}$, $P = 10$ atm, $\mathbf{r}_s = 2500$ kg/m³, gas:air
 Model Bed: $\mathbf{r}_s = 896$ kg/m³, gas:air at STP

8.0 EXPERIMENTAL VERIFICATION OF SCALING LAWS FOR BUBBLING BEDS

8.1 Hydrodynamic Scaling of Bubbling Beds

Experiments using scaled models of bubbling beds have been carried out since 1980 using the scaling relationships presented in previous sections. The earliest work was concerned with experimental testing and verification of the scaling relationships. Hot bed behavior was compared to cold scaled models in several studies. In others, cold beds of different sizes were compared to each other. For bubbling beds, verification of the scaling relationships needs to include direct or indirect measurements of bubble characteristics. Since bubbles are the prime motive agents for both gas and solids displacement, a detailed verification should involve comparison of bubble properties throughout the large bed and the

scale model. This is preferable to comparison of overall performance parameters for a bed based solely on input and exhaust measurements.

For beds fluidized with air at ambient conditions, a number of direct techniques to measure or infer bubble properties exist including local capacitance probes, light reflection, light transmission, videos of bed walls and even computer tomographic techniques. These local methods are difficult, if not impossible to use in a high temperature reactor or combustor. Alternatively, many investigators have used pressure fluctuations to infer bubble characteristics. Lirag and Littman (1971) used statistical analysis of pressure fluctuations to estimate the average size of bubbles leaving a bubbling bed. Fan et al. (1981) concluded that bubble motion and coalescence are responsible for pressure fluctuations in fluidized beds. They also found that the amplitude of the pressure fluctuations is related to bubble size. Therefore, pressure fluctuation measurements, when properly made, have been shown to reflect bed hydrodynamics. For local bed behavior, the differential pressure measurements should be made over a modest bed level rather than using a single pressure tap in the bed with the other tap in the freeboard. Differential pressure measurements reflect local conditions. Roy and Davidson (1989) found that the maximum pressure difference between two closely spaced pressure taps is related to the bubble diameter at that level in the bed. Use of a single bed pressure point can be difficult to interpret since pressure fluctuations can be due to local effects, bubbles erupting at the bed surface, or even fluctuations in the supply system. Roy and Davidson found that pressure fluctuations measured using a single pressure point are primarily due to surface bubbles. They also concluded that the dominant frequency and amplitude measured at a single pressure point are independent of position in the bed. Due to the existence of pressure waves from many locations in a gas fluidized bed, Bi, Grace and Zhu (1995) concluded that absolute probes are not suitable for determining local bubble behavior. Although complete bubble characteristics cannot be determined from differential pressure fluctuations, if the time-resolved differential pressure signal from several locations in a large bed are identical to measurements at corresponding location in the scale model, it is likely that the local characteristics of bubbles are similar.

Table 6 presents the range of scaling parameters for tests undertaken by different investigators to verify the scaling relationships for a bubbling bed.

Table 6. Scaling Parameter Values for Bubbling Fluidized Bed Experimental Studies

Reference	Hot/Cold	$\rho\mu_b D/\mu$	u_b^2/gD	ρ_b/ρ_t	L/D	D/d_p	Φ	Scaling Laws	d_p (μm)	Other Parameters
Fitzgerald and Crane (1980)	Cold Cold	8915-11138 9259-11562	.018-.027 .018-.027	126 110	1.0 1.0	234 235	N/A	Full	2068 240	$Re_{b0} = 38.1 - 47.6$ $Re_{b0} = 39.4 - 49.2$
Fitzgerald Bushnell, Crane and Shieh (1984)	Hot Cold	28881 3200	0.33 0.31	8224 8214	3.0 3.0	915 920	N/A	Full	2000 500	$Re_{b0} = 31.6$ $Re_{b0} = 34.8$
Nicasstro and Glicksman (1984)	Hot Cold	4658 4781	0.143 0.143	7280 5920	7.21 7.21	901 897	0.80 0.80	Full	677 170	$Re_{b0} = 5.2$ $Re_{b0} = 5.3$
Horio, Nonaka, Sawa and Muehi (1986a)	Cold Cold Cold	3514 954 247	0.021 0.022 0.021	2117 2117 2117	Scaled	638 328 174	N/A	Simplified	376 305 236	$Re_{b0} = 5.5$ $u_b/u_{mf} = 2.00$ $Re_{b0} = 2.9$ $u_b/u_{mf} = 1.97$ $Re_{b0} = 1.4$ $u_b/u_{mf} = 2.00$
Horio, Takada, Ishida and Tanaka (1986b)	Cold Cold Cold Cold	4448 1520 537 105	0.0024 0.0023 0.0023 0.0024	2203 2203 2203 2203	0.325 0.327 0.333 0.340	3297 2000 1163 472	N/A	Simplified	182 150 129 106	$Re_{b0} = 1.4$ $u_b/u_{mf} = 4.4$ $Re_{b0} = 0.8$ $u_b/u_{mf} = 4.6$ $Re_{b0} = 0.5$ $u_b/u_{mf} = 5.3$ $Re_{b0} = 0.2$ $u_b/u_{mf} = 4.7$
Newby and Kearns (1986)	Cold Cold Cold	1134-2523 1134-2523 1059-2406	.00068-.0034 .00068-.0034 .00062-.0032	2091 2484 2332	1.67 1.67 1.67	1800 1800 1800	N/A	Full	200 200 100	$Re_{b0} = 0.63 - 1.40$ $u_b/u_{mf} = 1.0 - 2.2$ $Re_{b0} = 0.63 - 1.40$ $u_b/u_{mf} = 1.1 - 2.5$ $Re_{b0} = 0.99 - 1.34$ $u_b/u_{mf} = 1.1 - 2.5$
Zhang and Yang (1987)	Cold Cold Cold Cold Cold Cold	65784 12658 77147 14792 88510 16984	0.135 0.135 0.185 0.184 0.244 0.243	2208 2208 2208 2208 2208 2208	0.462 0.422 0.462 0.422 0.462 0.422	1137 529 1137 529 1137 529	Matched	Simplified	805 577 805 577 805 577	$Re_{b0} = 58$ $u_b/u_{mf} = 1.8$ $Re_{b0} = 24$ $u_b/u_{mf} = 1.8$ $Re_{b0} = 68$ $u_b/u_{mf} = 2.1$ $Re_{b0} = 28$ $u_b/u_{mf} = 2.1$ $Re_{b0} = 78$ $u_b/u_{mf} = 2.4$ $Re_{b0} = 32$ $u_b/u_{mf} = 2.4$

Table 6 (cont'd.)

Reference	Hot/Cold	$\rho_p u_p D/\mu$	u_p^2/gD	ρ_p/ρ_f	L/D	D/d_p	Φ	Scaling Laws	d_p (μm)	Other Parameters
Roy and Davidson (1989)	Hot	923	0.462	6667	N/A	225	N/A	Full/ Viscous Limit	600	$Re_{dp} = 4.1$ $u_p/u_{mf} = 5.2$ $Re_{dp} = 5.5$ $u_p/u_{mf} = 5.0$ $Re_{dp} = 33$ $u_p/u_{mf} = 1.6$ $Re_{dp} = 105$ $u_p/u_{mf} = 1.3$ $Re_{dp} = 7.4$ $u_p/u_{mf} = 6.1$ $Re_{dp} = 5$ $u_p/u_{mf} = 13.5$ $Re_{dp} = 8$ $u_p/u_{mf} = 16.0$ $Re_{dp} = 1.5$ $u_p/u_{mf} = 8.5$ $Re_{dp} = 4$ $u_p/u_{mf} = 4.6$ $Re_{dp} = 64$ $u_p/u_{mf} = 2.7$ $Re_{dp} = 12$ $u_p/u_{mf} = 2.1$
	Cold	1375	0.490	5882		250			180	
	Cold	2970	2.100	5882		90			500	
	Cold	5250	5.950	5882		50			900	
	Cold	1388	0.436	2041		188			240	
	Cold	5835	0.026	3030		1167			240	
	Cold	6664	0.026	3448		833				
	Cold	1250	0.029	2041		833			120	
	Cold	4667	0.032	2041		1167			120	
	Cold	11636	0.058	3448		182			240	
	Cold	2184	0.084	2041		182			550	
									550	
Almstedt and Zakkay (1990)	Hot	54135	0.21	913	3.13	811	0.82	Full	962	$Re_{dp} = 66.8$ $Re_{dp} = 66.4$ $Re_{dp} = 66.4$ $Re_{dp} = 131.4$
	Cold	53861	0.21	1068	3.12	811	0.75		486	
	Cold	53861	0.21	911	3.12	811	0.82		486	
	Cold	53861	0.21	911	3.12	410	0.82		962	
Di Felice, Rapagna and Foscolo (1992)	Cold	1468-8922	.009-.331	1126	N/A	322	1.0	Full	397	$Re_{dp} = 4.6-27.7$ $u_p/u_{mf} = 1.0-5.3$ $Re_{dp} = 4.4-26.3$ $u_p/u_{mf} = 1.0-5.4$ $Re_{dp} = 4.6-26.7$ $u_p/u_{mf} = 1.0-5.0$ $Re_{dp} = 3.9-28.1$ $u_p/u_{mf} = 0.4-2.7$ $Re_{dp} = 2.7-16.0$ $u_p/u_{mf} = 1.1-6.5$
	Cold	1351-8025	.010-.340	1128		305	1.0		348	
	Cold	1395-8367	.009-.333	1136		313	1.0			
	Cold	1173-7330	.007-.290	1007		304	0.6		158	
	Cold	1468-8809	.009-.323	24444		552	1.0		163	
	Cold								348	
Di Felice, Rapagna, Foscolo and Gibularo (1992)	Cold	31.3-500.4	$(.21-.53) \cdot 10^3$	769	5.5	3536	N/A	Full	14	$Re_{dp} = 0.009-0.14$ $Re_{dp} = 0.007-0.14$ $Re_{dp} = 6.8-22.7$ $Re_{dp} = 6.8-24.1$
	Cold	18.4-402.6	$(9.14-.65) \cdot 10^4$	794	4/5	2824			68	
	Cold	2078-6928	.0216-.2405	1100	2.8, 5.6*	305			348	
	Cold	2186-7765	.0192-.2420	1105	2.6, 5.2*	322			597	
* Slugging Cases	Cold	15242-33564	.346 - 1.89	2000	1.0, 2.0*	112			950	$Re_{dp} = 136.1-317.5$ $Re_{dp} = 214.9-329.5$
	Cold	24714-37895	.834 - 1.96	2036	1.1, 2.1*	115			2400	
Glucksmann and Farrell (1995)	Hot	188330	0.025	898	scaled	3995	0.82	Simplified	851	$Re_{dp} = 47.1$ $u_p/u_{mf} = 3.8$ $Re_{dp} = 16.2$ $u_p/u_{mf} = 3.8$
	Cold	22637	0.025	835		1396	0.85		609	

8.2 Verification of Scaling Relationships for Bubbling and Slugging Beds

Most early experiments devoted to verifying the scaling relationships have dealt with the full set of scaling relationships. Several more recent experiments have dealt with a reduced set of dimensionless parameters. In some experiments, additional scaling parameters were unintentionally matched.

Fitzgerald and Crane (1980) were one of the first to evaluate the full set of hydrodynamic scaling parameters. They compared the hydrodynamics of two scaled beds using pressure fluctuation measurements and movies. In one bed, cork particles were fluidized with air; the other bed used sand fluidized with pressurized refrigerant 12 vapor. Movies showed qualitative agreement between bubble growth and the solids flow in the beds. The ratio of the bed minimum fluidization velocities was within 20% of the theoretical value; the difference was attributed to the angular shape of the cork particles, ϕ_s was not matched between the beds. The fast Fourier transform of the pressure fluctuations was used to determine the average frequency of the fluctuations which should be related to the bubble frequencies. The ratio of average frequencies for the two beds was in fair agreement with the theoretical velocity-time scale factor. The pressure fluctuation data were taken with a single bed pressure tap. This may be responsible for the level of agreement in the frequency ratios. Some additional qualitative slugging comparisons were made using movies of bed behavior; the slugs appeared to have the same scaled lengths and velocities.

Fitzgerald et al. (1984) measured pressure fluctuations in an atmospheric fluidized bed combustor and a quarter-scale cold model. The full set of scaling parameters was matched between the beds. The autocorrelation function of the pressure fluctuations was similar for the two beds but not within the 95% confidence levels they had anticipated. The amplitude of the autocorrelation function for the hot combustor was significantly lower than that for the cold model. Also, the experimentally determined time-scaling factor differed from the theoretical value by 24%. They suggested that the differences could be due to electrostatic effects. Particle sphericity and size distribution were not discussed; failure to match these could also have influenced the hydrodynamic similarity of the two beds. Bed pressure fluctuations were measured using a single pressure point which, as discussed previously, may not accurately represent the local hydrodynamics within the bed. Similar results were

obtained between two two-dimensional beds: a bed of reacted limestone fluidized with helium and a half-scale bed of copper fluidized with air.

Nicastro and Glicksman (1984) experimentally verified the full set of scaling laws for bubbling fluidized beds. They compared the time-resolved differential pressure measurements from a bubbling fluidized bed combustor and a scaled cold model. Good agreement was obtained between the spectral content and the probability density distribution of the differential pressure fluctuations, indicative of the bubble size distribution, between the hot combustor and the cold model. Figure 29 presents the comparisons. They concluded that hydrodynamic similarity had been achieved between the hot combustor and the cold model. The solid-to-gas density ratio, which was not matched exactly in the comparison, differed by 23%, but the Reynolds number based on particle diameter (Re_{dp}) was approximately 5, suggesting the beds were operating in the viscous limit. At low particle Reynolds numbers, viscous forces are more important than fluid inertial forces making the density ratio a less important scaling parameter. When actual hot bed material was used in the cold model, a violation of the scaling laws, the model's behavior was very different from that of the hot bed.

Horio et al. (1986a) used three geometrically similar bubbling beds, fluidized with ambient air, to verify their proposed scaling laws. This has been shown by Glicksman (1988) to be equivalent to the viscous limit scaling laws, Eq. (66). The solid-to-gas density ratio was not varied in the experiments although it was not one of the proposed scaling parameters. By maintaining a constant density ratio, they, in essence, used the simplified set of scaling parameters, Eq. (53). Video analysis of bubble eruptions at the bed surface were used to determine the cross-sectional average bubble diameter, bubble diameter distribution, and radial distribution of superficial bubble velocity. Similarity was achieved in these hydrodynamic parameters when bed Froude number, density ratio, and the ratio of superficial to minimum fluidization velocities were matched.

Horio et al. (1986b) verified the bubbling bed scaling laws of Horio et al. (1986a) for solid mixing and segregation. Sand was used as a bed material in straight and tapered bed geometries. A bed sectioning technique was used to measure the transient radial dispersion coefficient and the distribution of float tracers. They concluded that bed mixing and the behavior of floating bodies obey the scaling laws in both straight and tapered beds. The solid-to-gas density ratio was again held constant in the tests, satisfying the simplified set of scaling laws. The particle Reynolds numbers (Re_{dp}) were approximately unity or less.

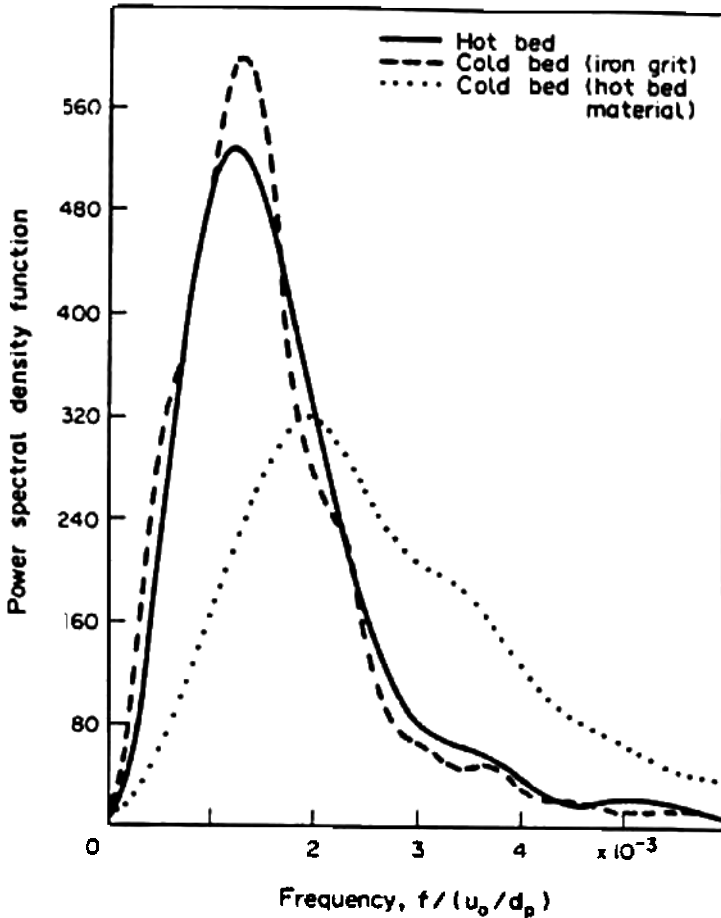


Figure 29. Comparison of dimensionless power spectra of differential pressure fluctuations. Double probe across levels 2 and 3; $x/L = 0.0$, coal burning bubbling bed combustor. Full set of scaling laws with iron grit in cold bed; hot bed material in cold bed violates scaling laws. (From Nicastro and Glicksman, 1984.)

Newby and Keairns (1986) made bubbling bed scaling comparisons between two cold models using the full set of scaling laws. One bed was fluidized with two different $200\text{ }\mu\text{m}$ glass powders using ambient air. The second bed, which was a half-scale model of the first, used pressurized air to fluidize $100\text{ }\mu\text{m}$ steel powder. High-speed movies showed good agreement between the nondimensional bubble frequencies in the two beds. Figure 30 is a plot of the nondimensional bubble frequencies as a function of bed Froude number. They also found reasonably good agreement between the nondimensional amplitudes of the pressure fluctuations in the beds.

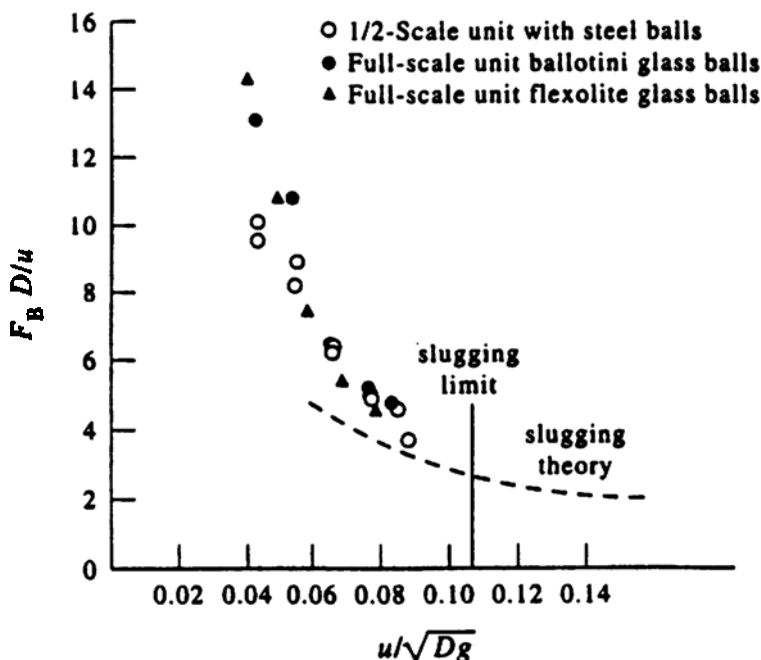


Figure 30. Comparison of non-dimensional bubble frequencies from two cold scaled models. (Newby and Kearns, 1986.)

Zhang and Yang (1987) carried out scaling comparisons between two two-dimensional beds with u_o^2/gD and u_o/u_{mf} matched between them. They also inadvertently kept the solid-to-gas density ratio constant; thus they matched the simplified scaling parameters. They found through photographs that the beds appeared qualitatively similar. The beds also had similar dimensionless freeboard entrainment rates and dimensionless bed heights over a range of u_o/u_{mf} .

Roy and Davidson (1989) considered the validity of the full and viscous limit scaling laws at elevated pressures and temperatures. The nondimensional dominant frequency and amplitude of the pressure drop fluctuations were used as the basis of the comparison. They concluded that when the full set of scaling parameters is matched, similarity is achieved. They also suggested that it is not necessary to match the density ratio ($\mathbf{r}_s/\mathbf{r}_f$) and d_p/D , the simplification for viscous limit scaling, for particle Reynolds numbers (Re_{dp}) less than 30. Although the only run with Re_{dp} near 30 which was similar to the low Reynolds number test had the same density ratio as the low Re_{dp} runs. These conclusions may be open to different interpretations. As shown in Table 6, the scaling parameters neither matched closely nor varied in a systematic manner.

Di Felice et al. (1992a) investigated the validity of the full set of scaling laws for bubbling and slugging fluidized beds. They used an experimental facility which permitted the pressurization of different diameter test sections to match the scaling parameters. Minimum fluidization measurements, video measurements of bed expansion, and pressure fluctuation data were used to compare the similarity of five different bed configurations. Three of the beds were scaled properly, the fourth had a mismatched particle sphericity, and the fifth bed was purposefully mis-scaled relative to the others (see Table 6). The voidage at minimum fluidization was found to be the same for all the beds except the one with the different particle sphericity. In the bubbling regime, good agreement in the nondimensional bed expansion measurements was obtained for all but the bed with the mis-scaled particle sphericity. The lower particle sphericity increased u_{mf} for the system which effectively shifted the bed expansion curve for this case. The pressure fluctuations for the three properly scaled beds in the bubbling regime showed good agreement while the mis-scaled beds exhibited poor agreement with the other three. Figure 31 is a plot of the dimensionless dynamic pressure variance for the five beds in the bubbling regime. The two sets of data which deviate from the other three correspond to the mis-scaled beds.

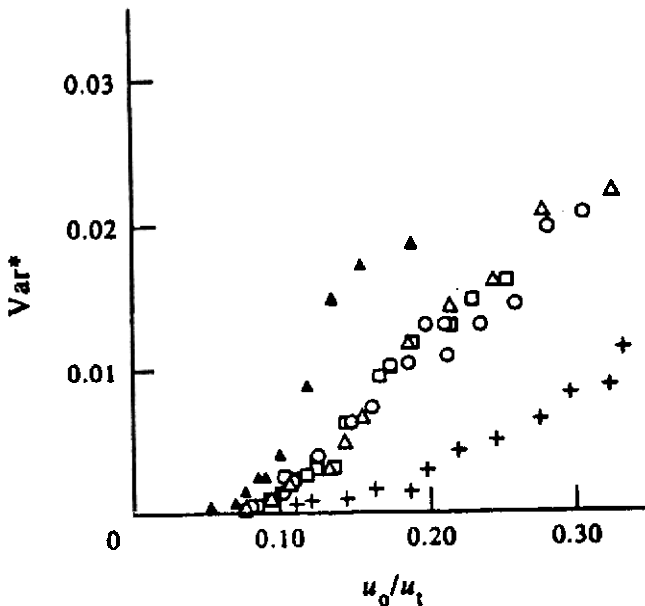


Figure 31. Comparison of dynamic pressure variance for three properly scaled beds and two mis-scaled beds in bubbling regime (DiFelice, et al., 1992a). Properly scaled: \square , laposorb; Δ , sand; \circ , bronze. Intentionally mis-scaled: $+$, iron; \square , sand.

In the slugging regime, Di Felice et al. (1992a) found that the bed expansion characteristics were similar to those in the bubbling regime, but the pressure fluctuation characteristics for all five beds were in poor agreement with each other. Figure 32 is the plot of the dimensionless dynamic pressure variance for the five beds in the slugging regime. They attributed this to the importance of particle material properties and some particle-particle interaction effects which are not accounted for in the full set of scaling laws. This is discussed further below in the light of recent results for spouting beds.

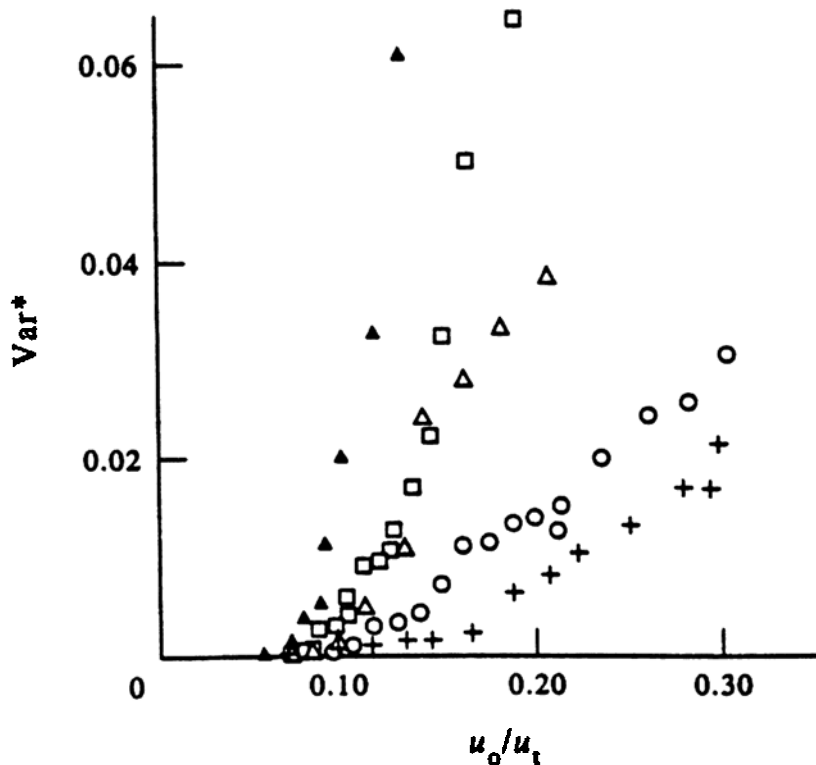


Figure 32. Comparison of dynamic pressure variance for three properly scaled beds and two mis-scaled beds in slugging regime (*DiFelice et al., 1992a*). Properly scaled: \square , laposorb; Δ , sand; \circ , bronze. Intentionally mis-scaled: +, iron; \square , sand.

Di Felice et al. (1992b) evaluated the full set of scaling laws for three different Geldart powder categories (A, B, and D) in the bubbling and slugging fluidization regimes. Pressure fluctuations were used as the basis for the scaling comparisons. In the bubbling regime, the RMS and dominant frequencies of the pressure fluctuations showed good agreement for all three powder categories. Only Geldart groups B and D were considered in the slugging regime. They exhibited fair agreement in the RMS of their pressure fluctuations, but their dominant frequencies disagreed. They found that the full set of scaling laws are valid for bubbling beds fluidizing powders in Geldart groups A, B, and D. They also concluded that the full set of scaling laws is not sufficient for slugging beds where particle-particle interactions are also thought to be important.

8.3 Verification of Scaling Laws for Spouting Beds

He et al. extended the scaling considerations to spouting beds. They showed that for spouting beds the full set of scaling relationships, Eq. 37, must be augmented with two new parameters, the internal friction angle and the loose packed voidage. By systematic tests in different sized cold beds as well as comparisons between hot and cold beds, they showed excellent agreement when the full set of scaling parameters augmented with the two spouting bed parameters were held constant. Close agreement was found for spout diameter, fountain height, longitudinal pressure profiles and dead zone boundary. Figure 33 shows a comparison of dimensionless spout diameter versus dimensionless height. Cases A and B differ in bed diameter by a factor of 2 but all of the dimensionless groups are maintained equal. In case C, the Reynolds numbers based on particle diameter and bed diameter are mismatched and in case D, the Froude number is mismatched. When the internal friction angle and sphericity were mismatched, there was a large disagreement in fountain height.

The internal friction angle is also important for slugging beds (Zenz and Othmer, 1960). DiFelice et al. (1992 a, b) did not report their values; it could be that the disagreement they found in their slugging bed tests was due to mismatches of the internal friction angle.

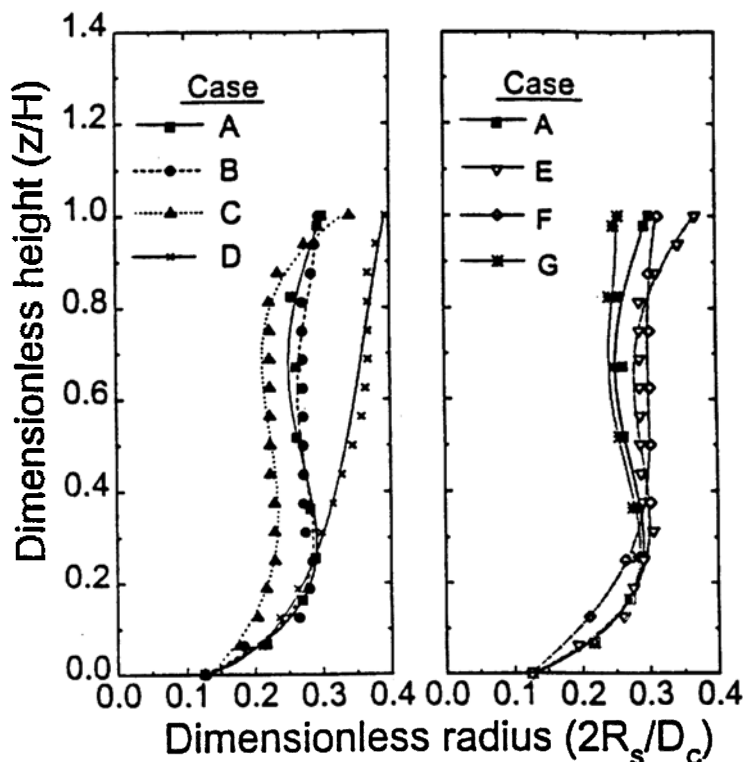


Figure 33. Dimensionless spout diameters as a function of dimensionless height for small columns. Case A: test case; Case B: all dimensionless parameters matched, bed diameter halved; Case C: particle Reynolds number mismatched; Case D: Froude number mismatched; Case E: density ratio, Reynolds number mismatched; Case F: bed Reynolds number mismatched; Case G: internal friction angle, loose packed voidage mismatched. (From He *et al.*, 1995.)

8.4 Verification of Scaling Relationships for Pressurized Bubbling Beds

Almstedt and Zakkay (1990) made scaling comparisons between a hot pressurized fluidized bed combustor with horizontal tubes and a pressurized cold scale model using the full set of scaling laws. The cold model had linear dimensions one-half those of the hot bed. A capacitance probe was used to measure the mean values of the bubble frequency, pierced length, bubble rise velocity, and bubble volume fraction. Scaling comparisons were made using the dimensionless form of these dependent

hydrodynamic parameters. Three different bed materials were used in the cold bed: Olivine sand and two different size distributions of the hot-bed material, one properly scaled and one out of scale. The solid-to-gas density ratio of the sand was 17% higher than the ratio for the combustor while the scaled down hot bed material, when used in the cold bed, has a solid-to-gas density 14% lower than the ratio for the combustor. The sand also had a lower sphericity than the hot bed material. The out-of-scale hot-bed material was also used to illustrate the sensitivity of the scaling to the D/d_p parameter. The nondimensional form of the capacitance probe measurements agreed within 25% for the sand and the properly scaled hot-bed material; the agreement was best in the upper part of the bed. The dimensionless bubble velocity disagreed by as much as 18%. The properly scaled hot-bed material showed only slightly better agreement than that for the sand, but the mismatch in the density ratio and the sphericity for the sand was small. The improperly scaled hot-bed material had a maximum deviation of 38% from the hydrodynamics of the hot-bed combustor. When the pressure or the superficial velocity of the cold bed was changed from the correct value based on the scaling parameters, the disagreement in bubble properties increased. Almstedt and Zakkay concluded that behavior which is hydrodynamically similar to that of a pressurized fluidized bed combustor can be achieved using a properly scaled cold model.

Glicksman and Farrell (1995) constructed a scale model of the Tidd 70 MW_e pressurized fluidized bed combustor. The scale model was fluidized with air at atmospheric pressure and temperature. They used the simplified set of scaling relationships to construct a one-quarter length scale model of a section of the Tidd combustor shown in Fig. 34. Based on the results of Glicksman and McAndrews (1985), the bubble characteristics within a bank of horizontal tubes should be independent of wall effects at locations at least three to five bubble diameters away from the wall. Low density polyurethane beads were used to obtain a close fit with the solid-to-gas density ratio for the combustor as well as the particle sphericity and particle size distribution (Table 6).

Differential pressure measurements were made between several vertical elevations within the bed. The probability density function of the cold model and combustor gave very close agreement (Fig. 35). The solid fraction profiles were obtained from the vertical pressure profile with a hydrostatic assumption. The cold model solid fraction profile showed very close agreement with data taken from pressure taps in two different locations within the combustor (Fig. 36). The solid fraction shows a

somewhat unexpected behavior with a lower value near the distributor, possibly due to many small low velocity bubbles at that location which coalesce and increase in velocity until the tube bank is encountered. The power spectral density of the combustor exhibited several distinct peaks at increasingly higher frequencies. All but the first peak were not seen in the cold model. The peaks could be due to tube vibrations in the hot bed, fluctuations upstream or downstream of the bed or hydromechanical interactions between the bed and the internals. The long length of the pressure leads or the in-bed location of the taps could also have contributed to the peaks. Further measurements in the combustor are needed to resolve their origin.

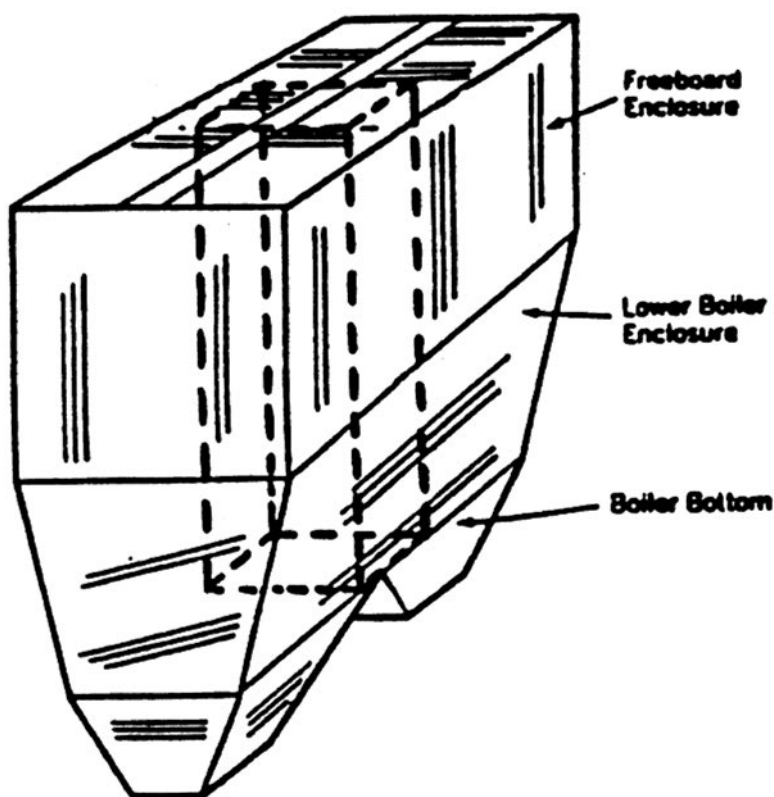


Figure 34. Tidd boiler enclosure with scaled section designated. (From Glicksman and Farrell, 1995.)

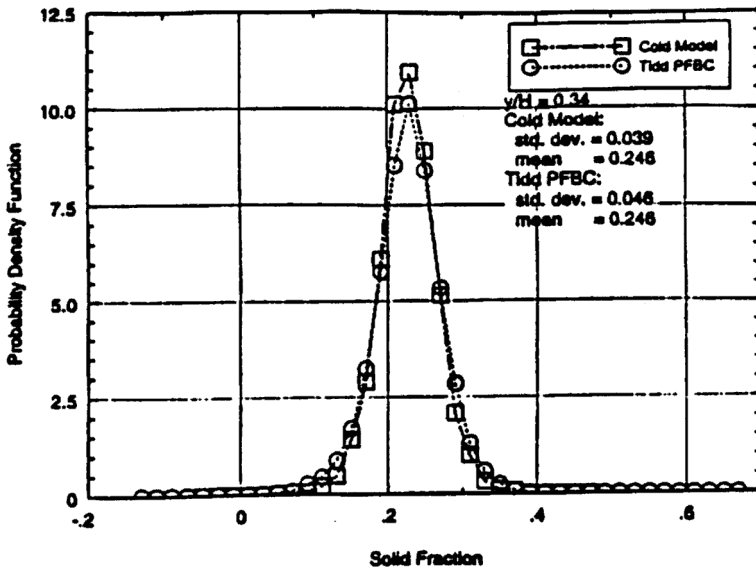


Figure 35. Comparison of the Tidd PFBC and cold model based on simplified scaling laws at $y/H = 0.34$. (From Glicksman and Farrell, 1995.)

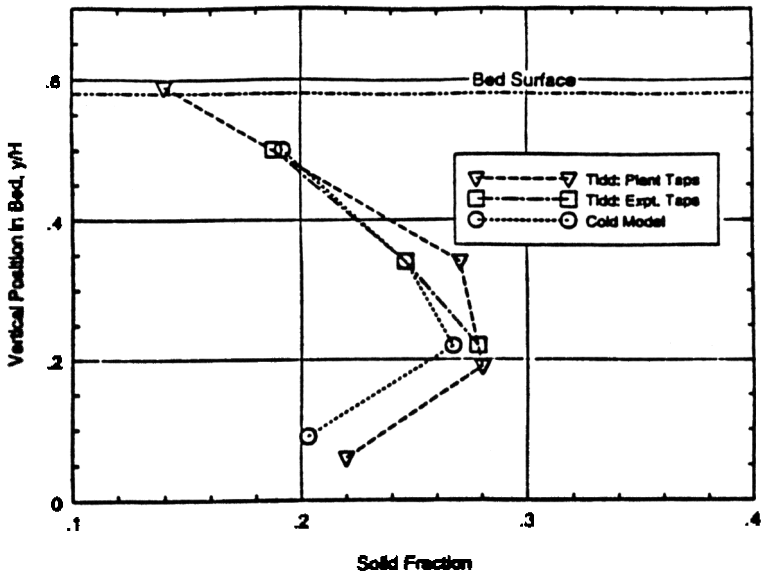


Figure 36. Solid fraction profile comparisons for Tidd PFBC and cold model based on simplified scaling laws. (From Glicksman and Farrell, 1995.)

Farrell (1996) experimentally evaluated the importance of the solid-to-gas density ratio ($\mathbf{r}_s/\mathbf{r}_f$) for scaling the hydrodynamics of bubbling and slugging fluidized beds. Two bed materials, polyethylene plastic ($\mathbf{r}_s = 918 \text{ kg/m}^3$) and a dolomite/limestone sorbent mixture ($\mathbf{r}_s = 2670 \text{ kg/m}^3$), were used to create a mismatch in the density ratio. The size of the particles was chosen such that the remaining simplified scaling parameters were matched. Measurements showed that the internal angle of friction was similar between the two materials. A 10.2 cm diameter bed with a mock tube bundle was used to make bubbling regime comparisons, while a 5.1 cm diameter bed was used to compare the behavior of the two materials in the slugging regime. In addition, the character of the bubbling-slugging transition was also explored.

Figure 37 compares the solid fraction profiles in the 10.2 cm bubbling bed for the two bed materials at $u_o/u_{mf} = 1.2$. In this particular case, the solid fraction of the sorbent material is less than the plastic in the lower regions of the bed, with good agreement in the upper section of the bed. However, for the same conditions, the dimensionless standard deviation of the time-varying pressure drop showed the best agreement in the bottom of the bed with a large discrepancy in the upper portion of the bed. The bubbling-slugging transition behavior was evaluated in the 5.1 cm diameter bed. Horio et al. (1992) proposed using the inflection points in plots of the root-mean-square of the gauge pressure versus superficial velocity (u_o) to identify flow regime boundaries. Figure 38 shows this behavior for the two bed materials. The plastic bed material has a much broader transition region between its fully bubbling and fully slugging regimes than the sorbent material and the nature of this transition is different between the two materials. Therefore the solid-to-gas density ratio influences both the hydrodynamics in the bubbling regime and the boundary at which the transition to slugging occurs. This is consistent with the conclusion of Glicksman et al. (1993b) where they found that it is essential to match the density ratio when scaling circulating fluidized bed hydrodynamics.

9.0 APPLICATIONS OF SCALING TO COMMERCIAL BUBBLING FLUIDIZED BED UNITS

A substantial number of experimental demonstrations of the validity of scaling has increased awareness of the concept and confidence in its application. Although applications to commercial designs have been undertaken, unfortunately only a modest number have been documented in the open literature.

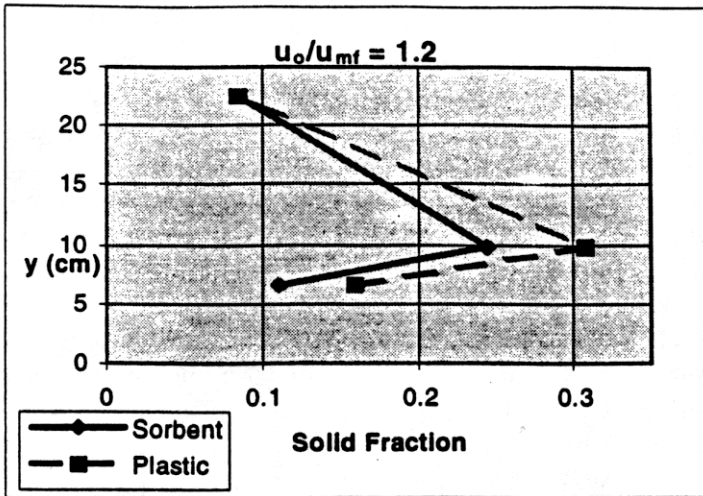


Figure 37. Bubbling bed solid fraction profile for $u_o/u_{mf} = 1.2$ for two different solid-to-gas density ratios.

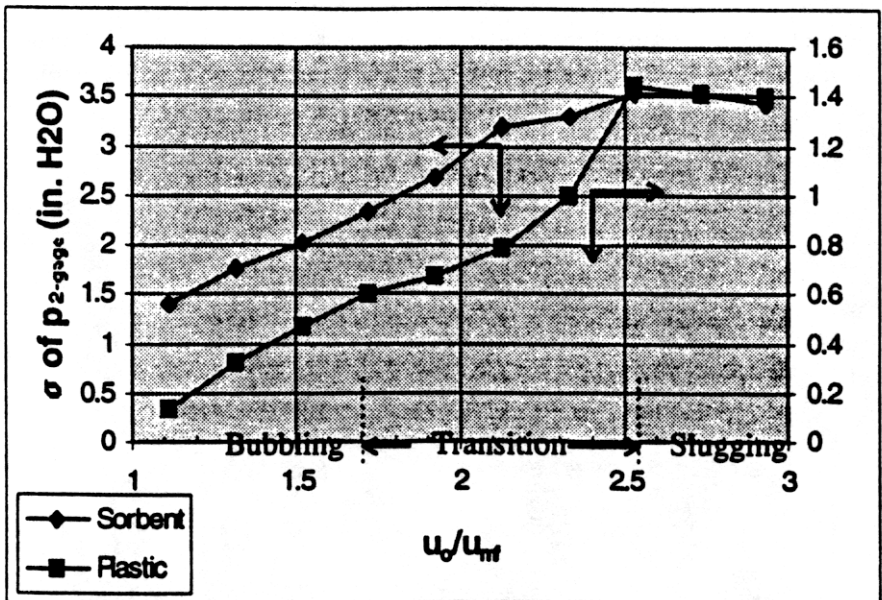


Figure 38. Bubbling-slugging transition evaluation for two different solid-to-gas density ratios.

Scaling has many useful applications. The dynamic characteristics of different bed designs can be quickly compared. The influence of bed diameter on hydrodynamic behavior can be studied by the use of several different size models. The models allow easy experimental examination of existing operating characteristics. The beds also can be used to quickly confirm the influence of proposed modifications. Since the models usually operate at ambient conditions, it is possible to instrument them to observe detailed behavior. This allows a better understanding of the fundamental physics as well as the identification of hydrodynamic factors needed for proper correlation of performance.

The earliest scaling studies were directed at atmospheric bubbling bed combustors. To date, a rich variety of questions have been addressed. Jones and Glicksman (1986) constructed a model of the 20 MW_e bubbling bed pilot plant jointly sponsored by the Tennessee Valley Authority and the Electric Power Research Institute (EPRI) at Paducah, Kentucky. Figure 39 shows a photograph of the in-bed tubes installed in the scale model. The model, which is roughly 100 by 120 cm in cross section, simulates two-thirds of the entire 20 MW pilot plant. Care was taken to carefully match the pilot plant tube bundle geometry and distributor design. Steel grit particles with the same dimensionless size distribution and sphericity as the hot bed material were used. The full set of scaling parameters was matched in the model and the combustor. The largest discrepancy was in the solid-to-gas density ratio which was 18% smaller in the model than the pilot plant.

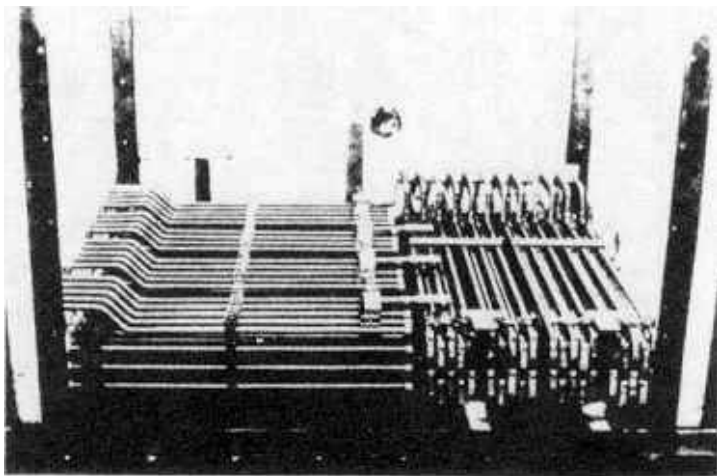


Figure 39. Model of 20 MW bubbling fluidized bed combustor showing tube arrangement. (From Jones and Glicksman, 1986.)

Optical probes were used to measure the bubble size, frequency and velocity within the dense bed. The bubble velocity for an actively bubbling bed was found to closely agree with the drift flux form proposed by Davidson and Harrison (1963). In contrast, the volumetric flow rate of the bubbles was found to be far less than that predicted by the two-phase hypothesis (Fig. 40).

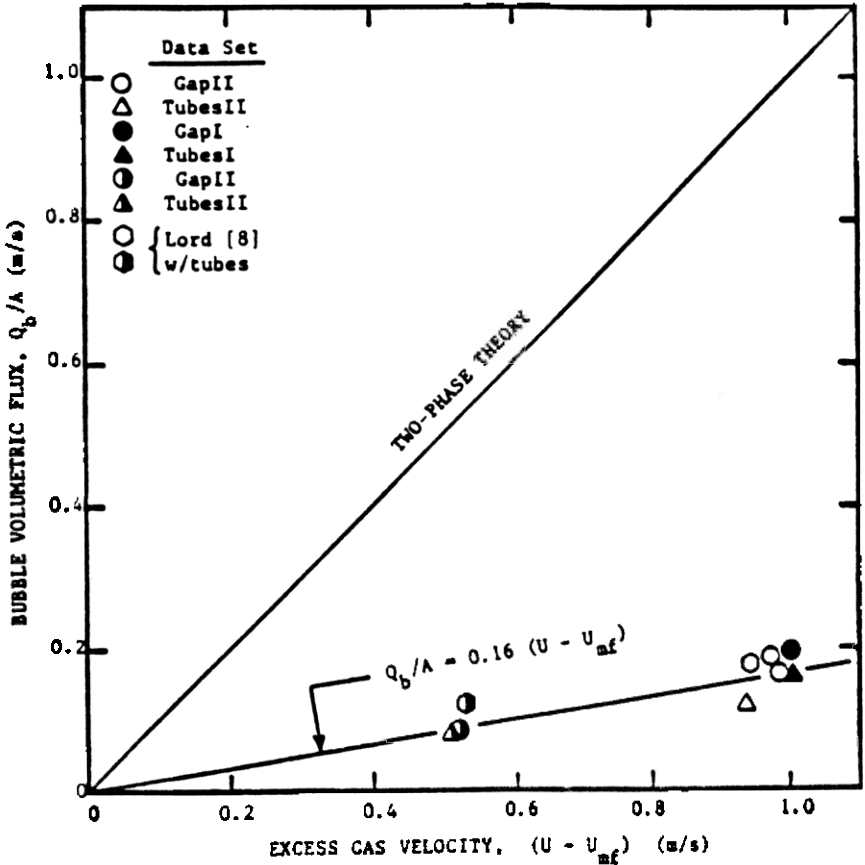


Figure 40. Deviation from two-phase theory for model of bubbling fluidized bed combustor. (From Jones and Glicksman, 1986.)

The larger particles were thrown high in the splash zone; higher than predicted by a ballistic trajectory using the bubble rise velocity as the initial velocity and neglecting any air drag. Later observations of this model showed that, when bubbles erupt at the surface, the accompanying

gas flow has a velocity much higher than the bubble rise velocity (Glicksman and Piper, 1987). This led to a mechanistic model for gas throughflow aided by the low resistance of the bubble cavity (Yule and Glicksman, 1988) and an accurate prediction of bubble volume flow rate and bed expansion (Glicksman et al. 1991b).

Commercial bubbling bed combustors must operate satisfactorily over a range of part-load conditions. While reducing the total combustion rate, it is necessary to keep bed operating temperature constant. This requires a reduction in the heat transfer to the water-filled tubes within the bed. One technique utilizes the contraction of the bed which accompanies a decrease in superficial velocity. As the bed contracts, some of the tube rows are uncovered, reducing the net heat transfer. The scale model allowed many different tube arrangements to be tested; six tube configurations were examined. Figure 41 shows three of the six different tube bank configurations which were tested. The validity of the scaling technique was confirmed by a comparison of the bed expansion measured for the pilot plant and that found in the model equipped with the same tube bank geometry (Fig. 42).

A second method to reduce load while maintaining constant bed temperature is to reduce the superficial velocity below u_{mf} to a portion of the bed. In this design, the bed does not contain vertical partitions above the distributor. The scale model was used to determine the rate of growth of the fixed bed in the defluidized zone along with the heat transfer to tubes in that region. Figure 43 shows a typical pattern of particle accumulation in a slumped zone adjacent to an actively fluidized zone. Heat transfer coefficients are also shown. Note that tubes near the upper surface of the defluidized zone, which experience a downflow of solids, have a very high heat transfer rate.

In a bubbling bed operating at high ratio of u_o/u_{mf} , there is a considerable amount of solids present in the freeboard, particularly near the bed surface in the so-called "splash zone." The high density of particles in the freeboard can cause substantial combustion and emission release in that zone as well as freeboard overheating if tubes are not present. The average density of solids was measured in the freeboard of the scale model of the 20 MW pilot plant (Glicksman and Piper, 1987). As shown in Fig. 44, the average density in the freeboard decreases exponentially with distance above the dense bed. Also shown on the figure is the predicted behavior based on a bubble eruption model (Glicksman and Yule, 1991).

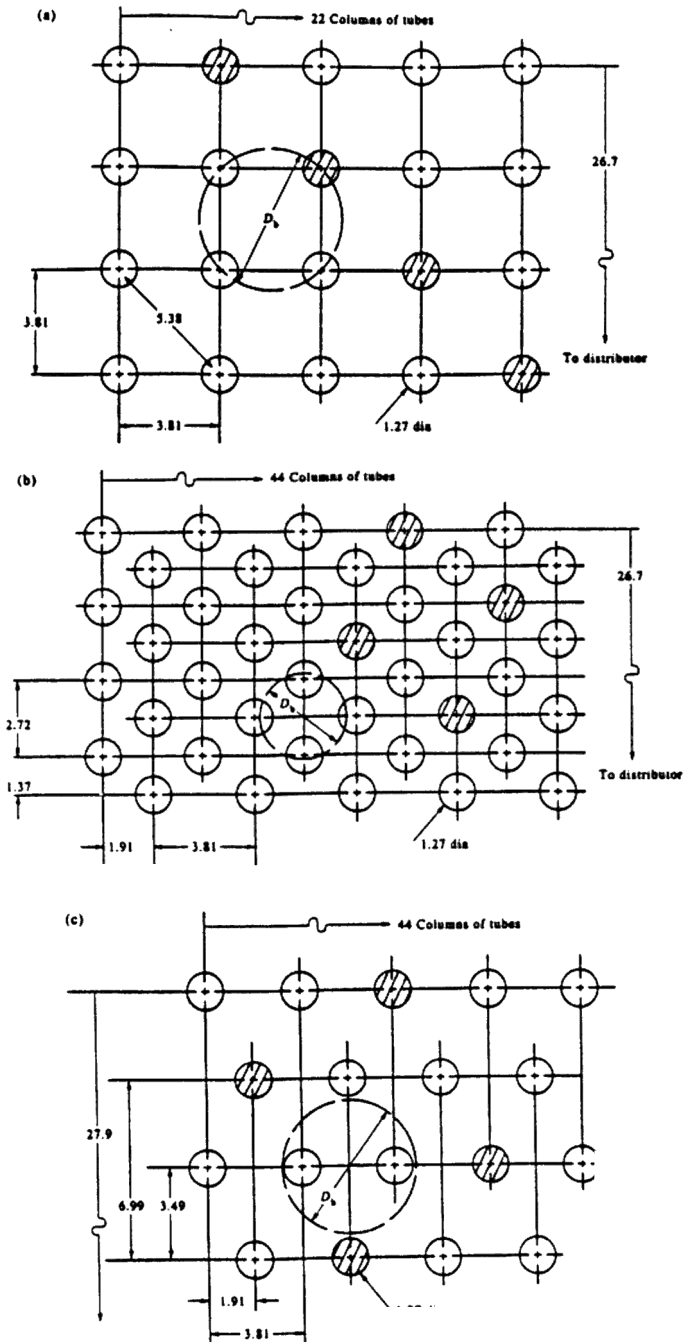


Figure 41. Tube configuration used for bed expansion studies. Note: all dimensions in cm scaled to equivalent sizes in the combustor. (From Glicksman *et al.*, 1991b.)

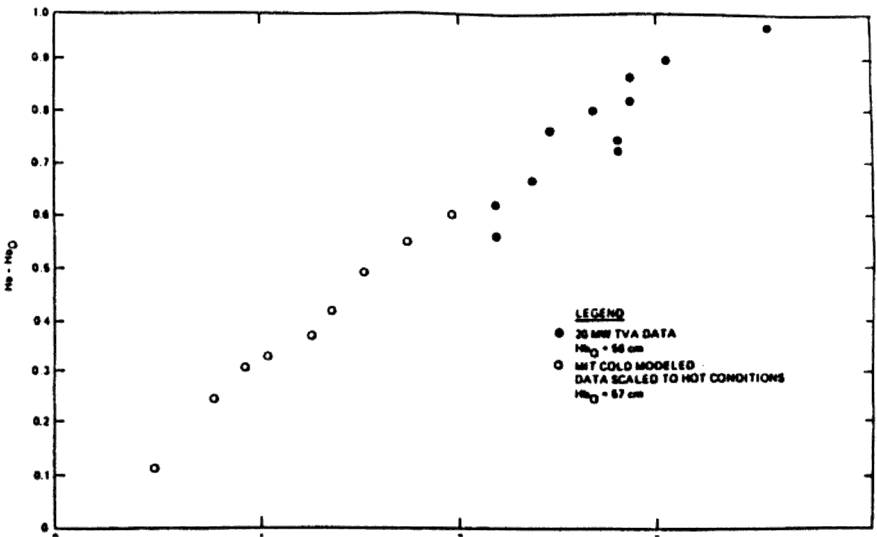


Figure 42. Bed expansion for TVA 20 MW_e FBC and for scale model, shown in Fig. 39. (From Glicksman *et al.*, 1989.)

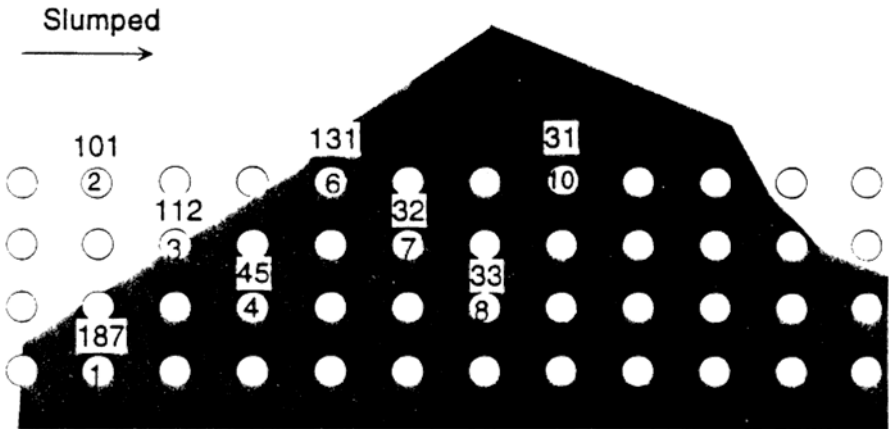


Figure 43. Particle accumulation in slumped zone adjacent to active bed: air velocity through active region = 151 cm/s; air velocity through slumped region = 7.3 cm/s; numbers above heater are heat transfer coefficient in $W/m^2 \text{ } ^\circ C$ after 15–30 min. (From Glicksman *et al.*, 1992.)

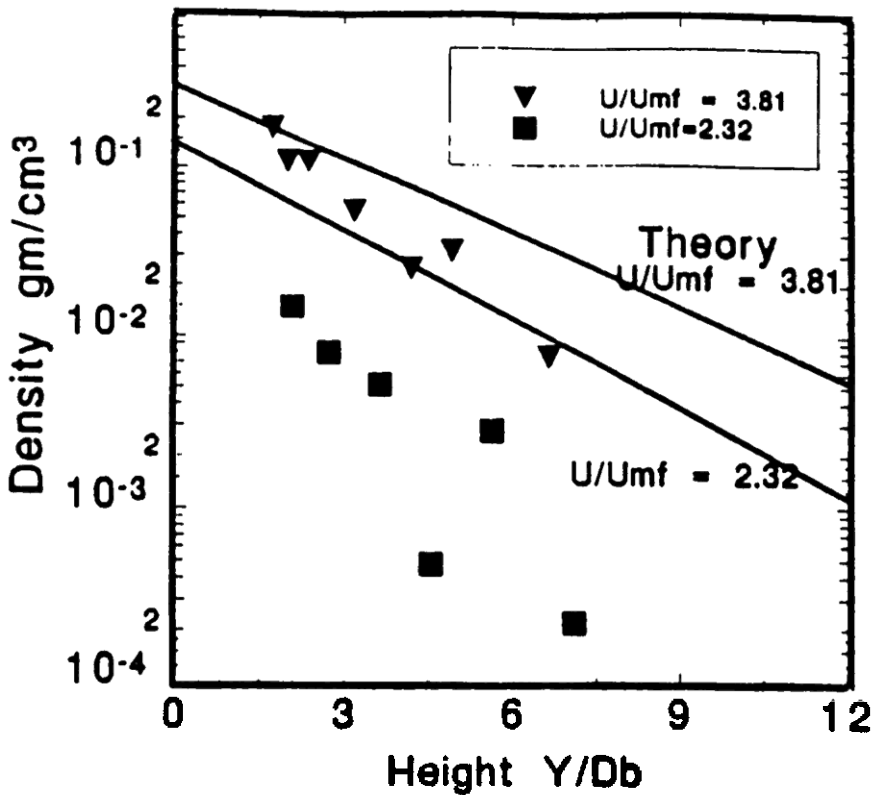


Figure 44. Density in freeboard of bubbling bed, present theory with D_b equal to horizontal tube pitch, 3.9 cm. (Data of Glicksman and Piper, 1987.)

The heat transfer from tubes in the freeboard was also measured for the 20 MW model. Figure 45 shows a comparison of the measured overall heat transfer coefficient in the 20 MW pilot plant versus that predicted from the scale model test. When the bed height is lowered, uncovering some tubes, the heat transfer is reduced because there are fewer particles contacting the tube surface. Although the scale model did not include proper scaling for convective heat transfer, the rate of change of the overall heat transfer should be a function of the hydrodynamics.

Ackeskog et al. (1993) made the first heat transfer measurements in a scale model of a pressurized bubbling bed combustor. These results shed light on the influence of particle size, density and pressure levels on the fundamental mechanism of heat transfer, e.g., the increased importance of the gas convective component with increased pressure.

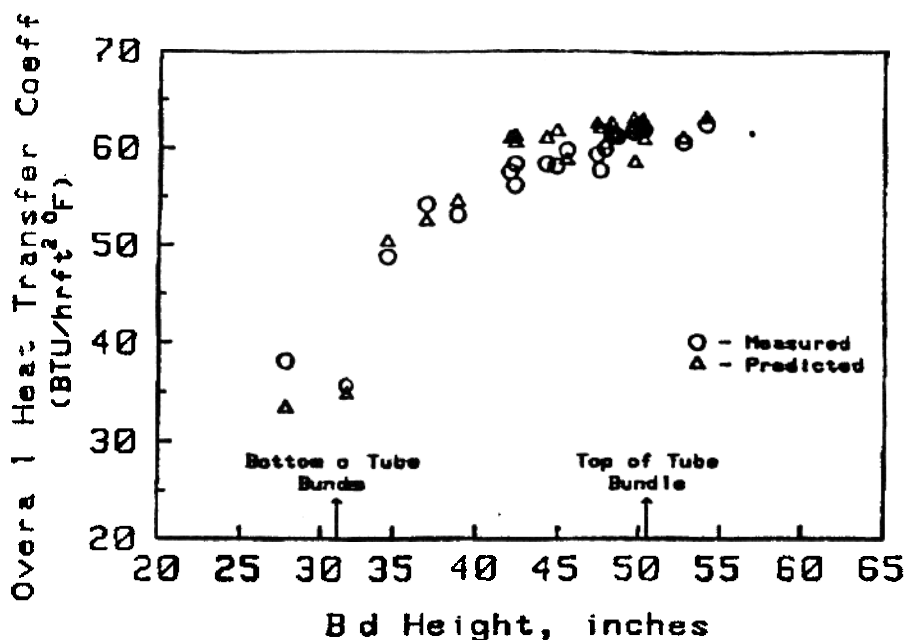


Figure 45. Comparison of heat transfer coefficient measured in 20 MW bubbling bed combustor vs prediction from MIT cold test. (From Glicksman et al., 1987)

A multisolids bed contains a mixture of large solids which are contained in a dense region at the bottom of the bed and finer particles which recirculate through the bed and external cyclone. Ake and Glicksman (1989) used a cold scale model of a multisolids combustor to determine the dense bed expansion, see Fig. 46. The measured expansion in a properly scaled quarter-scale model using steel pellets to simulate the coarse particles with the proper solid-to-gas density ratio gave good agreement with field data. It was also demonstrated that an improperly scaled cold model, using the same coarse material as the hot bed had an incorrect gas-to-particle density ratio and substantially exceeded the hot bed expansion.

Tube erosion has been observed in both atmospheric and pressurized bed combustors. The scaling analysis presented earlier can be used to construct an accurate hydrodynamic simulation of the commercial bed. This can be used to qualitatively investigate factors related to tube wear such as the location of highest wear around the circumference of an individual tube and the location within the bed of the tube experiencing the highest wear. Quantitative wear rates cannot be obtained from model tests

unless the parameters governing both the hydrodynamics and the wear phenomena are matched between the model and the commercial bed. Figure 47 shows relative tube wear for the model of the TVA-EPRI 20 MW_e bubbling bed pilot plant. Increasing the proportion of large particles causes an increase in the wear rate. The second row of tubes is shielded by the first row, closest to the distributor, reducing the incidence of strikes by large, high velocity bubbles. In the interface between actively fluidized and slumped bed, see Fig. 43, there is a flow of particles down the slumped surface which causes higher wear. The relative changes in wear rate with tube location, as well as the circumferential location with highest wear, agreed closely between the cold model and the 20 MW combustor.

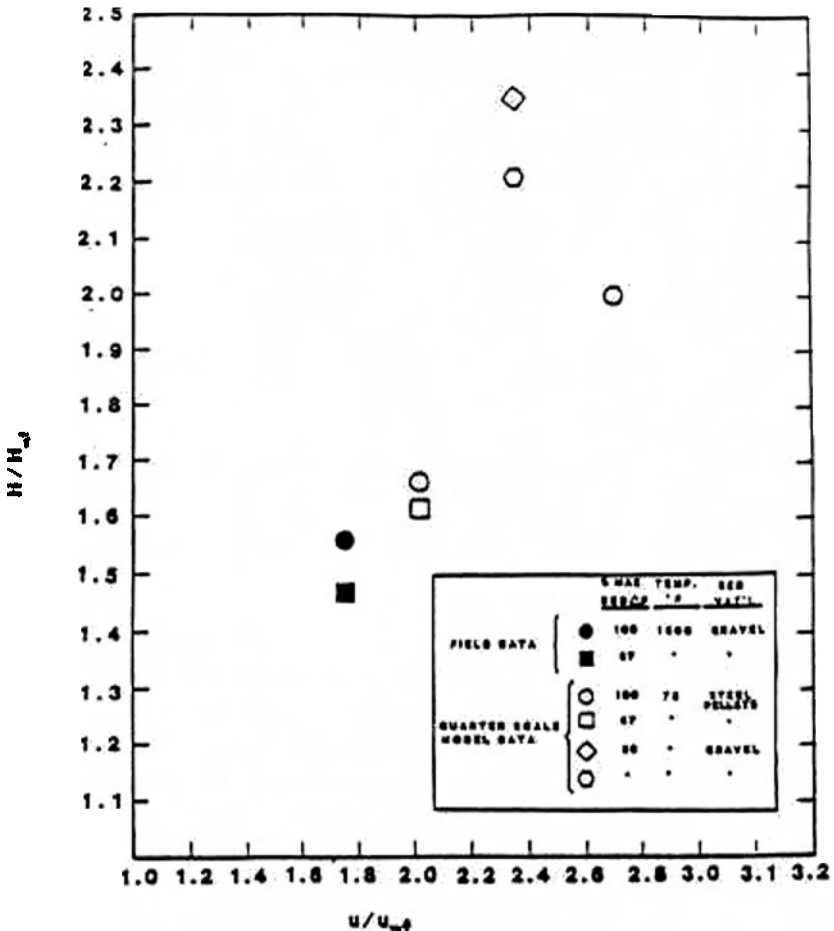


Figure 46. Expanded bed height model data compared to field data for multisolids fluidized bed for properly scaled steel pellets and mis-scaled gravel particles. (From Ake and Glicksman, 1989.)

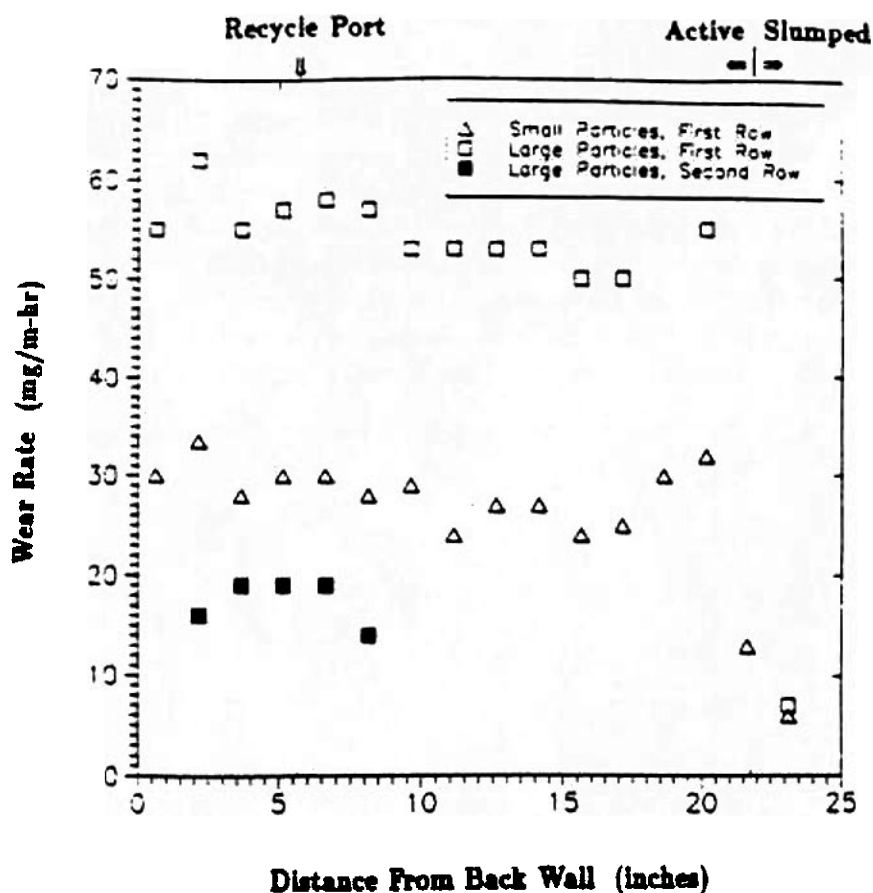


Figure 47. Wear rates for in-line tubes, simulation of 20 MW bubbling bed combustor. (From Glicksman et al., 1987b.)

Other boiler manufacturers have used scale models to aid in the design of large bubbling bed combustors and gasifiers. Yang, Newby and Keairns (1995) used atmospheric cold models of 30 cm and 3 m diameter to simulate a large jetting fluidized bed gasifier to be operated at about 12 atm. They used the full set of scaling relations which required the model to be about the same dimensions as the hot bed. A half round bed with a transparent wall was used to photograph the jet behavior. They measured and developed correlations for jet penetration, bubble frequency, vertical bubble size and jet half angle, among others. They also found considerable gas leakage from the bubbles to the emulsion phase. This data covers much larger bed sizes than had been examined before.

10.0 HYDRODYNAMIC SCALING OF CIRCULATING BEDS

Given the success in scaling bubbling beds, research has progressed to the scaling of circulating fast beds. The initial research has focused on the verification of both the full and the simplified scaling relationships for circulating beds. The verification using data from combustors was complicated by the difficulty in accurately measuring the recycle rate of solids, an important parameter. Table 7 presents the range of scaling parameters for experimental studies undertaken for circulating beds. Figure 48 shows the range in terms of the Froude number based on bed diameter and the Reynolds number based on particle diameter and the superficial gas velocity.

Horio et al. (1989) experimentally verified their proposed circulating fluidized bed scaling laws. The solid-to-gas density ratio was maintained constant in the tests, thus they effectively verified the simplified set of scaling laws. Two cold scaled CFBs, fluidized using ambient air, were used in the verification. Good agreement in the axial solid fraction profiles was obtained for most of the conditions tested. A “choking-like transition” was found to occur for cases with higher solids fluxes and lower gas superficial velocities. A discrepancy in the “choking” transition point for the two beds was attributed to differences in the geometry of the bed exit and the solids recycle lines. The transition point was found to be very sensitive to the particle size ratio. An optical probe was used to verify similarity in the annular flow structures and the cluster velocities.

Ishii and Murakami (1991) evaluated the CFB scaling relationships of Horio et al. (1989) using two cold CFB models. Solids flux, pressure drop, and optical probe measurements were used to measure a large number of hydrodynamic parameters to serve as the basis for the comparison. Fair to good similarity was obtained between the beds. Dependent hydrodynamic parameters such as the pressure drop and pressure fluctuation characteristics, cluster length and voidage, and the core diameter were compared between the two beds. The gas-to-solid density ratio was not varied between the beds. As seen in Table 7, the dimensionless solids flux decreased as the superficial velocity was increased because the solids flux was held constant.

Table 7. Scaling Parameter Values for Circulating Fluidized Bed Experimental Studies

References	Hot/ Cold	$\rho_t u_o D/\mu$	u_o^2/gD	ρ/ρ_t	L/D	D/d _p	$G/\rho_t u_o$	Φ	Scaling Laws	d _p (μ m)	Other Parameters
Horio, Ishii, Kobukai and Yamanishi (1989)	Cold	9885-16063	0.33-0.86	1508	8	2528	.0028-.0052	N/A	Simplified	79	$Re_{dp} = 3.9-6.4$ $u_o/u_{mf} \approx 229-371$
	Cold	1236-2008	0.33-0.86	1508	8	816	.0028-.0052			61	$Re_{dp} = 1.5-2.5$ $u_o/u_{mf} \approx 190-310$
Ishii and Murakami (1991)	Cold	9885-14827	.326-.734	1508	N/A	3263	.0056-.0037	N/A	Simplified	61	$Re_{dp} = 3.0-4.5$ $u_o/u_{mf} \approx 281-571$
	Cold	1236-1853	.326-.734	1508		1078	.0056-.0037			46	$Re_{dp} = 1.1-1.7$ $u_o/u_{mf} \approx 333-500$
Tsukada, Nakanishi, Takei, Ishii and Horio (1991)	Cold	1518	0.510	1534	8	1078	0.0067	N/A	Viscous limit	46	$Re_{dp} = 1.4$ $u_o/u_{mf} = 417$
	Cold	2736	0.510	852	8	1078	0.0067			46	$Re_{dp} = 2.5$ $u_o/u_{mf} = 417$
	Cold	5327	0.510	437	8	1078	0.0067			46	$Re_{dp} = 4.9$ $u_o/u_{mf} = 417$
Glicksman, Westphalen, Brereton and Grace (1991)	Hot	6984	66.94	8700	48.7	822	0.0017	N/A	Full	185	$Re_{dp} = 8.5$
	Cold	6785	66.54	6000	48.0	646	0.0016	N/A		52	$Re_{dp} = 10.5$
Chang and Louge (1992)	Cold	15630	13.84	4800	35	855	.0044	0.69	Full	234	$Fr^* = 131$, $M = 21$
	Cold	22977	9.34	4961	35	1835	.0042	1.0		109	$Ar^* \approx 45$, $R \approx 4880$
	Cold	53454	4.20	4966	35	2985	.0020	0.73		67	$Fr^* = 131$, $M = 10$
Glicksman, Hyre and Westphalen (1993a)	Hot	29170	5.26	8500	11.43	2917	0.0013	N/A	Full	240	$Re_{dp} = 10.0$
	Cold	30349	5.63	6200	11.25	2759	0.0011			58	$Re_{dp} = 11.0$

Table 7 (cont'd.)

References	Hot/Cold	$\rho u_0 D / \mu$	u_0^2 / gD	ρ_f / ρ_t	L/D	D/d _p	$G_f / \rho_t u_0$	Φ	Scaling Laws	d _p (μ m)	Other Parameters
Glicksman, Hyre and Woloshun (1993b)	Cold Cold	3211-5352	7.1-19.7	2117	14.2	412	$(4-7)10^{-3}$	1.0	Viscous Limit	79	$Re_{dp} = 7.8-13.0$ $u_0/u_{mf} = 106-176$
		3211-5352	7.1-19.7	1167	14.2	326	$(4-7)10^{-3}$.6-.8		100	$Re_{dp} = 9.9-16.5$ $u_0/u_{mf} = 176-294$
	Cold Cold	25699-45146	7.1-19.6	2117	14.1	1158	$(4-7)10^{-3}$	1.0	Simplified	112	$Re_{dp} = 22.2-39.0$ $u_0/u_{mf} = 104-174$
		3171-5286	7.2-19.9	2117	14.4	407	$(4-7)10^{-3}$	1.0		79	$Re_{dp} = 7.8-13.0$ $u_0/u_{mf} = 106-176$
	Cold Cold	24030-43020	7.1-19.6	1167	14.1	900	$(2-3)10^{-3}$.6-.8	Simplified	145	$Re_{dp} = 26.7-47.8$ $u_0/u_{mf} = 200-333$
		3188-5313	7.2-19.9	1167	14.4	322	$(2-3)10^{-3}$.6-.8		100	$Re_{dp} = 9.9-16.5$ $u_0/u_{mf} = 176-294$
	Hot Cold Cold	27975-36938	5.6-9.9	8400	12.2	2716	$(.5-1.8)^{-3}$	N/A	Full/Simplified	243	$Re_{dp} = 10.3-13.6$
		25008-31993	7.1-12.5	6200	14.1	2253	$(.5-1.8)^{-3}$.6-.8		58	$Re_{dp} = 11.1-14.2$ $u_0/u_{mf} = 214-286$
Glicksman, Hyre, Torpey and Wheeldon (1995)	Hot Cold	43430	3.66	758	40.9	1230	0.016	0.84	Simplified	165	$Re_{dp} = 35.3$ $u_0/u_{mf} = 113$
		12530	3.62	758	40.9	564	0.016	0.85		180	$Re_{dp} = 22.2$ $u_0/u_{mf} = 107$
	Hot Cold	53149	4.40	681	40.9	1230	0.016	0.84	Simplified	165	$Re_{dp} = 43.2$ $u_0/u_{mf} = 124$
		13771	4.38	758	40.9	564	0.016	0.85		180	$Re_{dp} = 24.4$ $u_0/u_{mf} = 118$
	Hot Cold	48228	4.02	718	40.9	1230	0.015	0.84	Simplified	165	$Re_{dp} = 39.2$ $u_0/u_{mf} = 118$
		13207	4.01	758	40.9	564	0.015	0.85		180	$Re_{dp} = 23.4$ $u_0/u_{mf} = 113$
	Hot Cold	49212	3.85	688	40.94	1230	0.0035	0.84	Simplified	165	$Re_{dp} = 40.0$ $u_0/u_{mf} = 116$
		12925	3.85	758	0.9	564	0.0035	0.85		180	$Re_{dp} = 22.9$ $u_0/u_{mf} = 111$

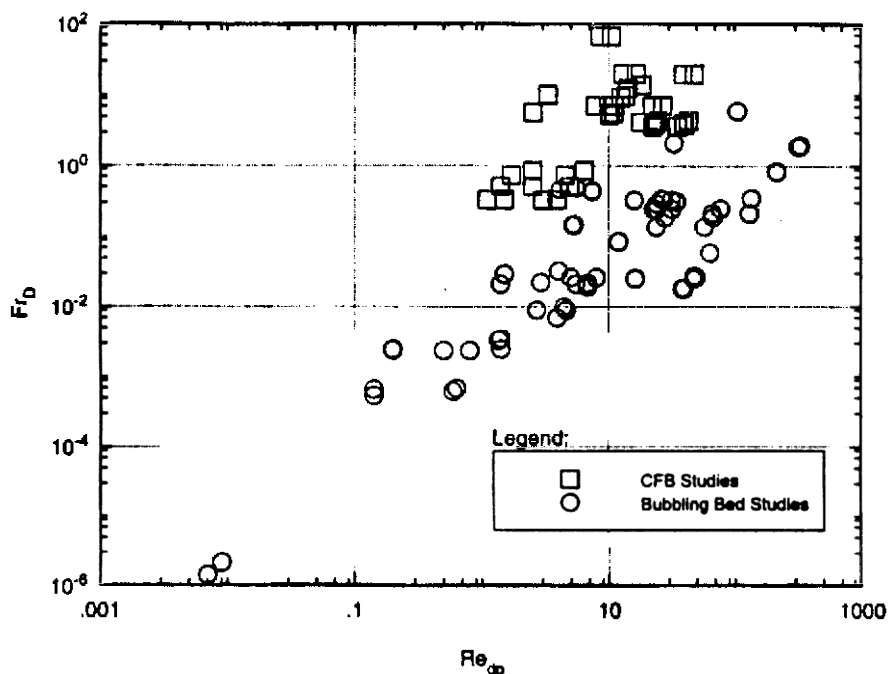


Figure 48. Range of experimental scaling studies for circulating and bubbling fluidized beds.

Tsukada et al. (1991) applied the CFB scaling laws of Horio et al. (1989) at several different elevated pressures (viscous limit scaling laws). A single bed and bed material were used in the study. A pressure vessel was used to vary the gas pressure. The bed was fluidized with ambient temperature air at three different pressures (0.1, 0.18, and 0.35 MPa). Axial solid fraction profiles and optical probe measurements were used as the basis for their similarity comparison. They found that as the pressure was increased, the axial solid fraction profile changed, indicating a change in the hydrodynamics. It was suggested that the effect on the axial solid fraction profile could be due to reaching a Reynolds number limit, e.g., the upper boundary for the viscous limit. They also suggest that it could be due to a change in gas bypassing between the riser and the downcomer. In this study, the gas-to-solid density ratio changes with pressure level. It is likely based on the recent results of Glicksman et al. (1993b) that the change in gas-to-solid density ratio led to the influence of the pressure level on the bed hydrodynamics. This points out the deficiencies of the viscous limit, the Horio et al. (1989) scaling relationship.

Glicksman et al. (1991) made scaling comparisons between an experimental circulating fluidized bed combustor and a scaled cold model based on the full set of scaling laws. The time-resolved pressure fluctuations and the time-averaged pressure drop were measured. Due to uncertainties in the hot bed solid circulation measurements, the cold bed solids flux was adjusted until the average bed solid fraction matched that of the hot bed. Differences could also be due to the mismatch in the solid-to-gas density ratio between the model and the hot bed. The vertical solid fraction profiles, the probability density function and the Fourier transform of the pressure fluctuations were compared between the hot and cold bed. Good agreement was obtained between the vertical solid fraction profiles except near the top of the beds. It was suggested that the differences in the solid fraction profiles at the top of the bed could be due to protrusions or wall roughness in the hot bed which were not modeled in the cold bed. Good agreement was also obtained in the comparison of the probability density distribution and the Fourier transform of the pressure fluctuations.

Chang and Louge (1992) carried out tests on a circulating bed in which they could vary the gas composition. By combining this with particles of different density and size, they were able to scale a series of different size hot commercial beds with diameters up to five times larger than the cold bed. Comparisons between glass and plastic particles showed identical mean vertical solids fraction profiles. The corresponding pressure fluctuations for plastic and glass are found to scale with $r_s g f d_p$; one would expect the pressure fluctuations to scale with $r_s u_o^2$. This is probably an artifice of the experimental design since Froude number based on particle diameter, $u_o^2/g f d_p$, was matched in the comparisons whereas Froude number based on bed diameter could not be matched since the experimental bed diameter was fixed in the tests. The inability to alter the bed diameter also made it impossible to match the D/d_p scaling parameter. Chang and Louge matched a modified form of the full set of scaling laws. Particle sphericity is not explicitly included as an independent parameter, rather it is included with the particle diameter based on a combination of the gas to particle drag coefficient. Their modified parameters are:

Eq. (90)

$$Fr^* = \frac{u_o^2}{g f d_p}, L^* = \frac{D}{d_p f}, M = \frac{G_s}{r_s u_o}, R = \frac{r_s}{r_f}, \text{ and } Ar^* = \frac{r_s r_g (d_p f)^3 g}{m^2}$$

The values of the parameters matched for scaling are presented in the "Other Parameters" column of Table 7. Steel and glass particles were also compared. The similarity using steel and glass was poor because the bed using the steel particles was choked while the bed with glass particles was not. Yang's (1983) correlation indicates that choking is a strong function of the Froude number based on bed diameter (Fr_D). The value of Fr_D could not be matched between the beds which caused them to choke under different conditions.

Glicksman et al. (1993a) evaluated the full set of scaling laws for circulating fluidized beds. Solid fraction data were obtained from the 2.5 MW_{th} Studsvik atmospheric CFB prototype. The full set of scaling laws were evaluated through solid fraction profile comparisons between Studsvik and a 1/4 scale cold model. Fairly good agreement was obtained; the profiles most closely matched in the top of the beds. Differences between the profiles were attributed to uncertainty in the hot bed solid flux measurements and to the mismatch in the solid-to-gas density ratio.

The viscous limit scaling laws were also evaluated by Glicksman et al. (1993b) in a series of comparison tests using circulating beds. To compare two cases based on the viscous limit while deliberately mismatching the solid-to-gas density ratio, scaling was attempted between glass/steel and glass/plastic (i.e., different density ratios) in the same bed. The average solid fraction profiles, solid fraction probability density functions, and power spectral densities were all in poor agreement. Figure 49 is a sample solid fraction profile comparison based on viscous limit scaling. It is believed the beds were operating near the point of incipient choking condition as predicted by the Yang (1983) correlation. Because this correlation indicates that choking is a strong function of the solid-to-gas density ratio, the viscous limit scaling parameters are unable to model bed hydrodynamics near the boundary between different flow regimes. Figure 50 shows a somewhat better agreement near the top of the bed at higher velocities. They concluded that since low u_o is required for the viscous limit scaling to be valid while sufficiently high u_o is required to prevent choking, the applicability of the viscous limit scaling parameters for circulating fluidized beds is limited. It was suggested that these scaling parameters may have a wider range of validity in bubbling beds.

The simplified scaling laws were used by Glicksman et al. (1993b) to compare two geometrically similar beds, one having linear dimensions four times larger than the other. In one series of tests, properly sized plastic particles were used in both beds; in another test series, glass particles were used in the two beds. The average solid fraction profiles showed excellent agreement (Figs. 51 and 52). The probability density functions and power

spectral densities also agreed well. In contrast to the viscous limit scaling results, the simplified scaling laws which include the gas-to-solid density ratio as a scaling parameter gave good agreement even for conditions where Yang's (1983) correlation predicted the bed was choked.

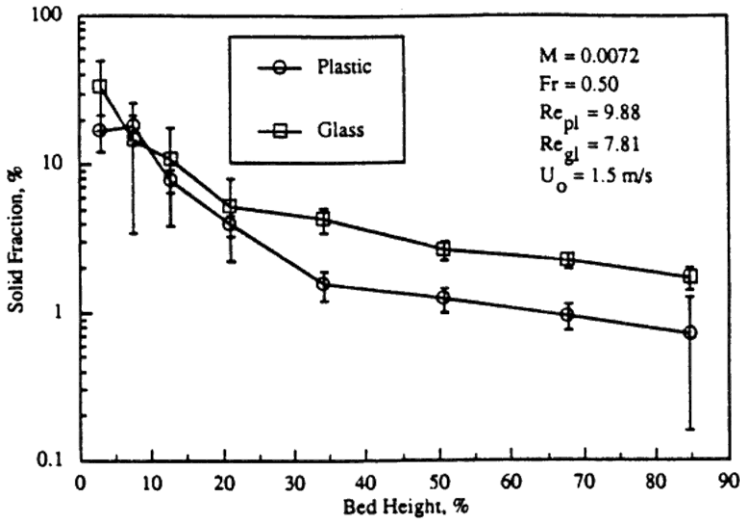


Figure 49. Solid fraction profiles, glass/plastic viscous limit scaling; density ratio mismatched, low velocity case. (From Glicksman et al., 1993a.)

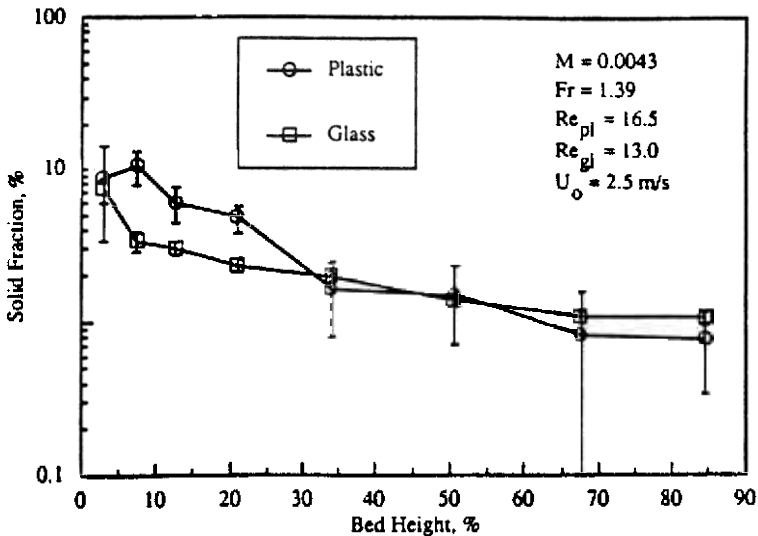


Figure 50. Solid fraction profiles, glass/plastic viscous limit scaling, high velocity case. (From Glicksman et al., 1993a.)

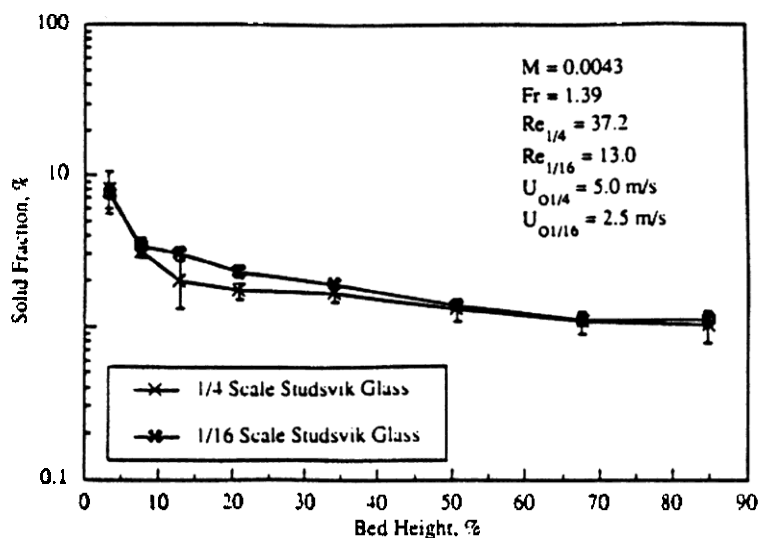


Figure 51. Solid fraction profiles, glass simplified scaling, high velocity case. (From Glicksman et al., 1993a.)

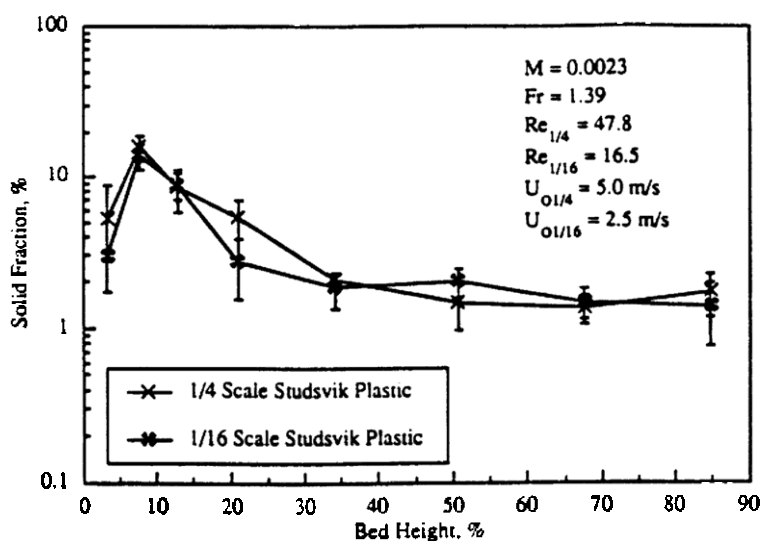


Figure 52. Solid fraction profiles, plastic simplified scaling, high velocity case. (From Glicksman et al., 1993a.)

Glicksman et al. (1993b) verified the simplified scaling laws for hot beds by comparing the solid fraction profiles for the Studsvik bed, the one-quarter scale cold model using the full scaling law, and a one-sixteenth scale cold model using the simplified scaling law. The one-sixteenth scale model had across sectional area of 16cm^2 to simulate a 2.5 MW combustor! The average solid fraction profiles were in good agreement for most of the conditions tested. The agreement was excellent between the one-quarter scale cold model, which utilized the full set of scaling laws, and the one-sixteenth scale model which utilized the simplified set of scaling laws. Thus, any disagreement between the Studsvik bed and the one-sixteenth scale model is not due to the simplifications of the full set of scaling laws. The density ratio was not matched exactly between the hot bed and the two cold beds which may have affected the agreement. Figure 53 provides a typical comparison of the solid fraction profiles in the three beds. The authors concluded that the simplified set of scaling laws, which includes the solid-to-gas density ratio, gives acceptable results over a wide range of particle densities and bed sizes, even when the length ratio is as small as one-sixteenth for an atmospheric combustor.

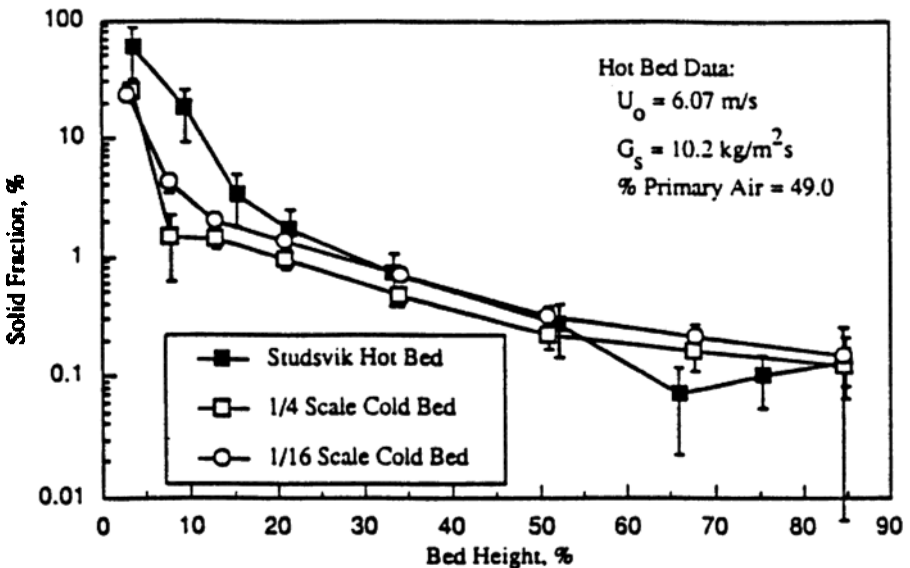


Figure 53. Solid fraction profiles, hot bed scaling with simplified scaling laws, low velocity, 49% primary air. (From Glicksman et al., 1993a.)

100 Fluidization, Solids Handling, and Processing

Glicksman et al. (1995) used the simplified scaling parameters to construct a one-half linear scale model of a Foster Wheeler circulating bed combustor pressurized to 14 bar. The combustor has a 20.3 cm inner diameter with an overall height of 8.3 m with both a primary and secondary air supply. The solids recycle rate was determined by a calorimetric balance of a fluidized bed heat exchanger in the return loop of the circulating bed. The cold model, one half scale, used polyethylene plastic particles to match the dimensionless particle size distribution as well as the gas-to-solid density ratio. The time-averaged vertical pressure difference was used to determine the solid fraction distribution in the combustor and the cold model. Figure 54 shows the close agreement between the combustor and the cold model. Three test cases had similar solid fraction versus height profiles. The fourth, operated at low gas velocity and solids recycle rate had a more abrupt decrease of solid fraction with bed height. The cold model reflected the same behavior, as shown in Fig. 55. The probability density function of one pair of time resolved differential pressure measurements is shown in Fig. 56 for the combustor and hot bed; again close agreement is observed. There was some discrepancy near the secondary air inlets. This might be due to fluctuations set up by the bubbling bed heat exchanger upstream of the secondary air inlet to the combustor. The bubbling bed was not duplicated in the cold scale model. Recent experiments have shown close agreement between a Foster Wheeler pressurized circulating bed combustor and a 1/6.5 linear scale model.

11.0 CONCLUSIONS

As fluidized beds are scaled up from bench scale to commercial plant size the hydrodynamic behavior of the bed changes, resulting, in many cases, in a loss of performance. Although there have been some studies of the influence of bed diameter on overall performance as well as detailed behavior such as solids mixing and bubble characteristics, generalized rules to guide scale-up are not available. The influence of bed diameter on performance will differ for different flow regimes of fluidization.

Small, properly scaled laboratory models operated at ambient conditions have been shown to accurately simulate the dynamics of large hot bubbling and circulating beds operating at atmospheric and elevated pressures. These models should shed light on the overall operating characteristics and the influence of hydrodynamics factors such as bubble distribution and trajectories. A series of different sized scale models can be used to simulate changes in bed behavior with bed size.

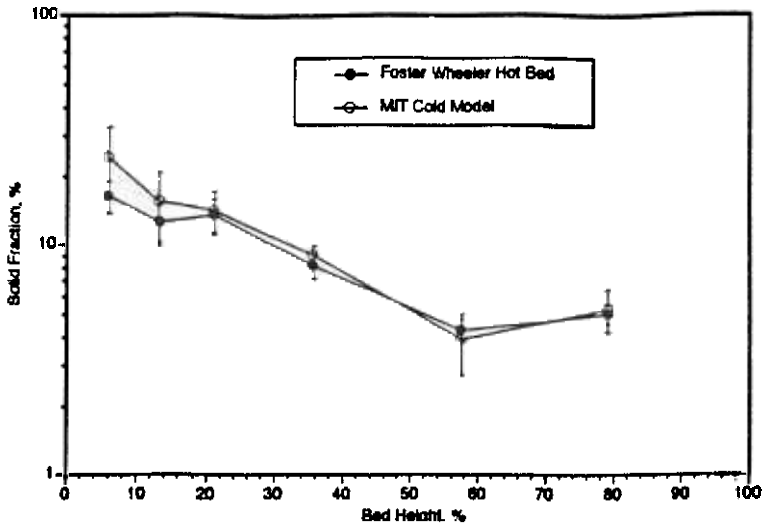


Figure 54. Solid fraction profile comparison between pressurized circulating fluidized bed combustor and one-half size scale model based on simplified scaling law. (*Glicksman et al., 1995.*)

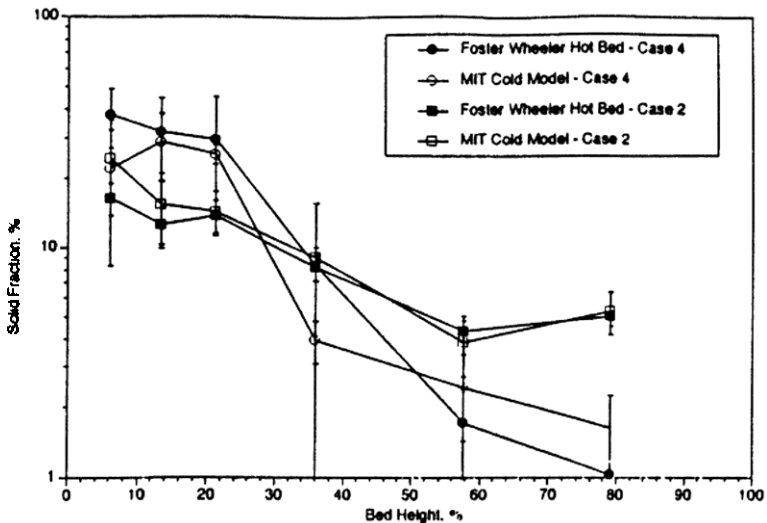


Figure 55. Solid fraction profile comparison between pressurized circulating fluidized bed combustor and one half size scale model based on simplified scaling. Two different operation conditions. (*From Glicksman et al., 1995.*)

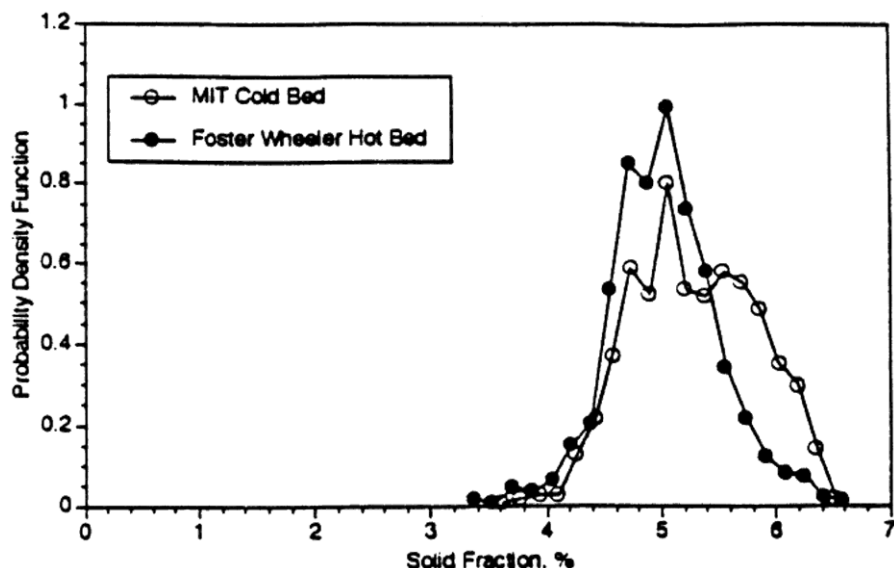


Figure 56. Histograms: test condition 2 of Fig. 55. Dimensionless distance up bed (x/H) = 0.80. (From Glicksman *et al.*, 1995.)

The scale models must be carefully designed. Failure to match the important dimensionless parameters will lead to erroneous simulation results. Modeling can be extended to particle convective heat transfer. Wear or erosion of in-bed surfaces can be qualitatively studied, although quantitative assessment requires the identification and simulation of additional wear-related parameters.

Most of the simulation effort has been applied to fluidized bed combustors which use relatively large size particles. Simulation can also be used for other fluidization processes in the petrochemical industry. Research should be undertaken to identify the proper scaling parameters for beds fluidized with smaller particles. Similar simulations may also apply to components such as cyclones.

ACKNOWLEDGMENTS

The author would like to acknowledge the contributions of many present and former M.I.T. students who carried out scaling studies of fluidized beds. Much of the M.I.T. research mentioned in this chapter has

been sponsored by the Electric Power Research Institute, the National Science Foundation, the U.S. Department of Energy, and the Tennessee Valley Authority.

NOTATIONS

C_D	drag coefficient of sphere
D	Bed diameter
d_B	Bubble diameter
d_c	Cluster diameter
d_p	Particle diameter
d_V	Equivalent bubble diameter
E	Local average stress tensor
f	Frequency
F	Drag force between fluid and particle
G_S	Solids recycle rate per unit area
g	Acceleration of gravity
L	Typical bed dimensions
m	Coefficient (Eq. 3)
p	Pressure
Q_B	Bubble volume flow rate
t	Time
u	Gas velocity
u_b	Bubble rise velocity
u_{mf}	Minimum fluidization velocity
u_o	Superficial gas velocity
u_t	Terminal velocity
v	Particle velocity
x,y	Coordinates

Dimensionless

Ar	Archimedes number
Fr	Froude number based on L
PSD	Dimensionless particle size distribution
Re	Reynolds number

Greek

b	Drag coefficient
d	Bubble volume fraction
d	Boundary layer thickness in a fast bed
D	Distributor plate voidage
e	Void fraction
e_c	Cluster void fraction
e_{mf}	Void fraction at minimum fluidization
r_f	Fluid density
r_s	Solid density
m	Fluid viscosity
u	Fluid kinematic viscosity

Subscripts

$()_c$	Commercial bed
$()_m$	Model bed

Superscripts

$()'$	Dimensionless
$()^-$	Vector

REFERENCES

- Ackeskog, H. B. R., Almstedt, A. E., and Zakkay, V., "An Investigation of Fluidized-bed Scaling: Heat Transfer Measurements in a Pressurized Fluidized-bed Combustor and a Cold Model Bed," *Chem. Eng. Sci.*, 48:1459 (1993)
- Ake, T. R., and Glicksman, L. R., "Scale Model and Full Scale Test Results of a Circulating Fluidized Bed Combustor," *Proc. 1988 Seminar on Fluidized Bed Comb. Technol. for Utility Appl.*, EPRI, 1-24-1 (1989)
- Almstedt, A. E., and Zakkay, V., "An Investigation of Fluidized-bed Scaling-capacitance Probe Measurements in a Pressurized Fluidized-bed Combustor and a Cold Model Bed," *Chem. Eng. Sci.*, 45(4):1071 (1990)
- Anderson, T. B., and Jackson, R., "A Fluid Mechanical Description of Fluidized Bed," *I & EC Fundamentals*, 6:527 (1967)
- Arena, U., Cammarota, A., Massimilla, L., and Pirozzi, D., "The Hydrodynamic Behavior of Two Circulating Fluidized Bed Units of Different Size," *Circulating Fluidized Bed Technol. II*, (P. Basu, and J. F. Large, eds.), Pergamon Press, Oxford (1988)

- Avidan, A., and Edwards, M., "Modeling and Scale Up of Mobil's Fluid Bed MTG Process," *Fluidization V*, (K. Ostergaard, and A. Sorensen, eds.), Engineering Foundation, New York (1986)
- Avidan, A., Edwards M., and Owen, H., "50 Years of Catalytic Cracking," *Oil and Gas J.*, p. 33 (1990)
- Baeyans, J., and Geldart, D., "Predictive Calculations of Flow Parameters in Gas Fluidized Bed and Fluidization Behavior of Various Powders," *Proc. Int. Symp. on Fluidization and its Appl.*, p. 263 (1973)
- Batchelor, G. K., "A New Theory for the Instability of a Fluidized Bed," *J. Fluid Mech.*, 31:657 (1988)
- Bauer, W., Werther, J., and Emig, G., "Influence of Gas Distributor Design on the Performance of Fluidized Bed Reactor," *Ger. Chem. Eng.*, 4:291 (1981)
- Bi, H. T., Grace, J. R., and Zhu, J., "Propagation of Pressure Waves and Forced Oscillations in Gas-solid Fluidized Beds and their Influence on Diagnostics of Local Hydrodynamics," *Powder Technol.*, 82:239 (1995)
- Chang, H., and Louge, M., "Fluid Dynamic Similarity of Circulating Fluidized Beds," *Powder Tech.*, 70:259 (1992)
- Davidson, J. F., and Harrison, D., *Fluidized Particles*, Cambridge University Press, Cambridge, U.K. (1963)
- Daw, C. S., and Harlow, J. S., "Characteristics of Voidage and Pressure Signals from Fluidized Beds using Deterministic Chaos Theory," *Proc. 11th Int. Conf. Fluidized Bed Comb.*, 2:777 (1991)
- Daw, C. S., Lawkins, W. F., Downing, D. J., and Clapp, N. E., "Chaotic Characteristics of a Complex Gas-solids Flow," *Phys. Rev. A*, 41:1179 (1990)
- DeGroot, J. H., "Scaling-up of Gas-fluidized Bed Reactors," *Proc. of the Int. Symp. on Fluidization*, (A. A. H. Drinkenburg, ed.), Netherlands University Press, Amsterdam (1967)
- DiFelice, R., Rapagna, S., and Foscolo, P. U., "Dynamic Similarity Rules: Validity Check for Bubbling and Slugging Fluidized Beds," *Powder Technol.*, 71:281 (1992a)
- DiFelice, R., Rapagna, S., Foscolo, P. U., and Gibilaro, L. G., "Cold Modelling Studies of Fluidised Bed Reactors," *Chem. Eng. Sci.*, 47:2233 (1992b)
- Fan, L. T., Ho, T. C., Hiraoka, S., and Walawender, W. P., "Pressure Fluctuations in a Fluidized Bed", *AIChE J.*, 27:388 (1981)
- Farrell, P. A., "Hydrodynamic Scaling and Solids Mixing in Pressurized Fluidized Bed Combustors," Ph.D. Thesis, Massachusetts Institute of Technology (1996)
- Fitzgerald, T. J., Bushnell, D., Crane, S., and Shieh, Y., "Testing of Cold Scaled Bed Modeling for Fluidized-bed Combustors," *Powder Technol.*, 38:107 (1984)

106 *Fluidization, Solids Handling, and Processing*

- Fitzgerald, T. J., and Crane, S. D., "Cold Fluidized Bed Modeling," *Proc. 6th Int. Conf. Fluidized Bed Comb. III*, p. 815 (1980)
- Foscolo, P. U., DiFelice, R., Gibilaro, L. G., Pistone, L., and Piccolo, V. "Scaling Relationships for Fluidisation: The Generalized Particle Bed Model," *Chem. Eng. Sci.*, 45:1647 (1990)
- Foscolo, P. U. & Gibilaro, L. G. "A Fully Predictive Criterion for the Transition between Particulate and Aggregate Fluidization," *Chem. Eng. Sci.*, 39:1667 (1984)
- Frye, C. G., Lake, W. C., and Eckstrom, H. C., "Gas-solid Contacting with Ozone Decomposition Reaction," *AIChE J.*, 4(4):403 (1958)
- Geldart, D., "The Size and Frequency of Bubbles in Two-and Three-Dimensional Gas-Fluidised Beds," *Powder Technol.*, 4:41 (1970)
- Glicksman, L. R., "Scaling Relationships for Fluidized Beds," *Chem. Eng. Sci.*, 39:1373 (1984)
- Glicksman, L. R., and McAndrews, G., "The Effect of Bed Width on the Hydrodynamics of Large Particle Fluidized Beds," *Powder Technol.*, 42:159 (1985)
- Glicksman, L. R., and Piper, G. A. "Particle Density Distribution in a Freeboard of a Fluidized Bed," *Powder Technol.*, 53:179 (1987)
- Glicksman, L. R. "Scaling Relationships for Fluidized Beds", *Chem. Eng. Sci.*, 43:1419 (1988)
- Glicksman, L. R., Yule, T., Dyrness, A., and Carson, R., "Scaling the Hydrodynamics of Fluidized Bed Combustors with Cold Models: Experimental Confirmation," *Proc. 9th Int. Conf. on Fld. Bed Comb.*, p. 511 (1987)
- Glicksman, L. R., Mullens, G., and Yule, T. W., "Tube Wear Tests in the MIT Scaled Fluidized Bed," *Proc. of EPRI Workshop* (1987b)
- Glicksman, L. R., Yule, T., Carson, R., and Vincent, R., "Comparison of Results from TVA 20 MW Fluidized Bed Combustor with MIT Cold Scale Model," *Proc. 1988 Seminar on Fluidized Bed Comb. Technol. for Utility Appl.*, EPRI GS-6118, 1-20-1 (1989)
- Glicksman, L. R., Westphalen, D., Brereton, C., and Grace, J., "Verification of the Scaling Laws for Circulating Fluidized Beds," *Circulating Fluidized Bed Technol. III*, (P. Basu, M. Horio, and M. Hasatani, eds.), Pergamon Press, Oxford (1991)
- Glicksman, L. R., Yule, T., and Dyrness, A., "Prediction of the Expansion of Fluidized Beds Containing Tubes," *Chem. Eng. Sci.*, 46(7):1561 (1991b)
- Glicksman, L. R., Yule, T., Arencibia A., and Pangan, A., "Heat Transfer to Horizontal Tubes in a Slumped Bed Adjacent to a Fluidized Bed," *Fluidization VII, Proc. 7th Eng. Foundation Conf. on Fluidization*, p. 813, Eng. Foundation, NY (1992)

- Glicksman, L. R., Hyre, M. R., and Westphalen, D., "Verification of Scaling Relations for Circulating Fluidized Beds," *Proc. 12th Int. Conf. on Fluidized Bed Comb.*, p. 69 (1993a)
- Glicksman, L. R., Hyre, M. R., and Woloshun, K., "Simplified Scaling Relationships for Fluidized Beds," *Powder Technol.*, 77:177 (1993b)
- Glicksman, L. R., Hyre, M. and Farrell, P. "Dynamic Similarity in Fluidization," *Int. J. of Multiphase Flow*, 20:331 (1994)
- Glicksman, L. R., and Farrell, P., "Verification of Simplified Hydrodynamic Scaling Laws for Pressurized Fluidized Beds: Part I Bubbling Fluidized Beds," *Proc. 13th Int. Conf. for Fluidized Bed Comb.*, p. 981 (1995)
- Glicksman, L. R., Hyre, M., Torpey, M., and Wheeldon, J., "Verification of Simplified Hydrodynamic Scaling Laws for Pressurized Fluidized Beds: Part II Circulating Fluidized Beds," *Proc. 13th Int. Conf. for Fluidized Bed Combustion*, p. 991 (1995)
- Hartge, E.-U., Li, Y., and Werther, J., "Flow Structures in Fast Fluidized Beds," Fluidization V, *Proc. 5th Eng. Foundation Conf. on Fluidization*, Elsinore Denmark, p. 345 (1985)
- He, Y-L, Lim, C. J., and Grace, J. R., "Scale-up Studies of Spouted Beds," *Chem. Eng. Sci.*, 52:329-339 (1997)
- Horio, M., Nonaka, A., Sawa, Y., and Muchi, I., "A New Similarity Rule for Fluidized Bed Scale-up," *AIChE J.*, 32:1466 (1986a)
- Horio, M., Takada, M., Ishida, M., and Tanaka, N., "The Similarity Rule of Fluidization and its Application to Solid Mixing and Circulating Control," in: *Fluidization V*, (K. Ostergaard and A. Sorenson, eds.), Engineering Foundation, New York (1986b)
- Horio, M., Ishii, H., Kobukai, Y., and Yamanishi, N., "A Scaling Law for Circulating Fluidized Beds," *J. Chem. Eng. Jpn.*, 22:587 (1989)
- Horio, M., "Scaling Laws of Circulating Fluidized Beds," Workshop on Materials Issues in Circulating Fluidized-Bed Combustors, EPRI Report 65-6747, (12-1)-(12-14) (1990)
- Horio, M., Ishii, H., and Nishimuro, M., "On the Nature of Turbulent and Fast Fluidized Beds," *Powder Technol.*, 70(3):229 (1992)
- Hovmand, S., and Davidson, J. F., "Slug Flow Reactors," *Fluidization*, (J. F. Davidson, and D. Harrison, eds.), Academic Press, London (1971)
- Ishii, H., Nokajima, J., and Horio, M., "The Clustering Annular Flow Model of Circulating Fluidized Beds," *J. Chem Eng. Jpn.*, 22(5):484 (1989)
- Ishii, H., and Murakami, I. "Evaluation of the Scaling Law of Circulating Fluidized Beds in Regard to Cluster Behaviors," *Circulating Fluidized Bed Technol. III*, (P. Basu, M. Horio, and M. Hasatani, eds.), Pergamon Press, Oxford (1991)

108 *Fluidization, Solids Handling, and Processing*

- Jackson, R., "Fluid Mechanical Theory," *Fluidization*, Chapt. 3, (Davidson, J. F., and Harrison, D., eds.), Academic Press, New York (1971)
- Jones, L., and Glicksman, L. R., "An experimental investigation of gas flow in a scale model of a fluidized-bed combustor," *Powder Technol.*, 45:201 (1986)
- Johnsson, J. E., Grace, J. R., and Graham, J. J., "Fluidized Bed Reactor Model Verification on a Reactor of Industrial Scale," *AIChE J.*, 33(4):619 (1987)
- Jones, L., and Glicksman, L. R., "An Experimental Investigation of Gas Flow in a Scale Model of a Fluidized-bed Combustor," *Powder Technol.*, 45:201 (1986)
- Knowlton, T. M., Geldart, D., and Matsen, J., oral presentation, *Fluidization VIII*, Inter. Symp. of the Eng. Foundation, pp. 14–19, Tours, France (1995)
- Lirag, R. C., and Littman, H., "Statistical Study of the Pressure Fluctuations in a Fluidized Bed," *AIChE Symp. Ser.*, 166(67):11 (1971)
- Litka, T., and Glicksman, L. R., "The Influence of Particle Mechanical Properties on Bubble Characteristics and Solid Mixing in Fluidized Beds," *Powder Technol.*, 42:231 (1985)
- Matsen, J. M., "Fluidized Beds," *Scaleup of Chemical Processes: Conversion from Laboratory Scale Tests to Successful Commercial Size Design*, (A. Bisio, and R. L. Kabel, eds.) p. 347, John Wiley & Sons, New York (1985)
- Matsen, J. M., "Design and Scale-up of CFB Catalytic Reactors," *Circulating Fluidized Beds*, Ch. 14, (J. R. Grace, A. A. Avidan, and T. M. Knowlton, eds.) pp: 489–503, Chapman & Hill, London (1997)
- May, W. G., "Fluidized-bed Reactor Studies," *Chem. Eng. Progress*, 55(12):49 (1959)
- Nakamura, K., and Capes, C. E., "Vertical Pneumatic Conveying: A Theoretical Study of Uniform and Annular Particle Flow Models," *Can. J. Chem. Eng.*, 51:39 (1973)
- Newby, R. A., and Keairns, D. L., "Test of the Scaling Relationships for Fluid-bed Dynamics," *Fluidization V*, (K. Ostergaard and A. Sorensen, eds.), Engineering Foundation, New York (1986)
- Nguyen, H. V., Potter, O. E., and Whitehead, A. B., "Bubble Distribution and Eruption Diameter in a Fluidized Bed with a Horizontal Tube Bundle," *Chem. Eng. Sci.*, 34:1163 (1979)
- Nicastro, M. T., and Glicksman, L. R., "Experimental Verification of Scaling Relationships for Fluidized Bed," *Chem. Eng. Sci.*, 39:1381 (1984)
- Noymer, P. D., Hyre, M. R., and Glicksman, L. R., "The Influence of Bed Diameter on Hydrodynamics and Heat Transfer in Circulating Fluidized Beds," *Fluidization and Fluid-Particle Systems*, AIChE, pp. 86–90 (1995)
- Patience, G. S., Chaouki, J., Berruti, F., and Wong, R., "Scaling Considerations for Circulating Fluidized Bed Risers," *Powder Technol.*, 72, 31 (1992)

- Rhodes, M. J., Wang, X. S., Cheng, H., Hiram, T., and Gibbs, B. M., "Similar Profiles of Solids Flux in Circulating Fluidized Bed Risers," *Chem. Eng. Sci.*, 47(7):1635 (1992)
- Rhodes, M. J., and Laussman, P., "A Study of the Pressure Balance around the Loop of a Circulating Fluidized Bed," *Can. J. Chem. Eng.*, 70:625 (1992)
- Rietema, K., and Piepers, H. W., "The Effect of Interparticle Forces on the Stability of Gas-fluidized Beds--I. Experimental Evidence," *Chem Eng. Sci.*, 45:1627 (1990)
- Rietma, K., Cottaar, E. J. A., and Piepers, H. W., "The Effect of Interparticle Forces on the Stability of Gas-fluidized Beds -- II. Theoretical Derivation of Bed Elasticity on the Basis of Van der Waals Forces between powder Particles," *Chem. Eng. Sci.*, 48:1687 (1993)
- Rowe, P. N., and Stapleton, W. M., "The Behavior of 12-inch Diameter Fast Fluidized Beds," *Trans. Instn. Chem. Engrs.*, 39:181 (1961)
- Roy, R., and Davidson, J. F., "Similarity between Gas-fluidized Beds at Elevated Temperature and Pressure," *Fluidization VI*, Engineering Foundation, New York (1989)
- Scharff, M. F., Goldman, S. R., Flanagan, T. M., Gregory, T. K., and Smott, L. D., "Project to Provide an Experimental Plan for the Merc 6' x 6' Fluidized Bed Cold Test Model," Department of Energy, Final Report J772042-FR Contract EY-77-C-21-8156 (1978)
- Schouten, J. C., and Van den Bleek, C. M., "Chaotic Behavior in the Hydrodynamic Model of a Fluidized Bed Reactor," *Proc. 11th Int. Conf. on Fluidized Bed Comb.*, 1:459 (1991)
- Shingles, T., and McDonald, A. F., "Commercial Experience with Synthol CFB Reactors," in *Circulating Fluidized Bed Technol. II*, (P. Basu, and B. P. Large, eds.), Pergamon Press, Oxford (1988)
- Thiel, W. J., and Potter, O. E., "Slugging in Fluidized Beds," *Ind. Eng. Chem. Fundam.*, 16(2):242 (1977)
- Thiel, W. J., and Potter, O. E., "The Mixing of Solids in Slugging Gas Fluidized Beds," *AIChE J.*, 24:561 (1978)
- Tsukada, M., Nakanishi, D. Takei, Y., Ishii, H., and Horio, M., "Hydrodynamic Similarity of Circulating Fluidized Bed under Different Pressure Conditions," *Proc. 11th Int. Conf. Fluidized Bed Comb.*, p. 829 (1991)
- Van den Bleek, C. M., and Schouten, J. C., "Can Deterministic Chaos Create Order in Fluidized Bed Scale-up?", *Chem. Eng. Sci.*, 48:2367 (1993)
- Van Deemter, J. J., "Mixing Patterns in Large-scale Fluidized Beds," *Fluidization*, (J. R. Grace, and J. M. Matsen, eds.), Plenum Press, New York (1980)
- Van Swaaij, W. P. M., and Zuiderweg, F. J., "Investigation of Ozone Decomposition in Fluidized Beds on the Basis of a Two-phase Model," *Chemical Reaction Eng., Proc. 5th European/2nd Int. Symp. Chem. Reaction Eng.*, Elsevier, Amsterdam/London/New York (1972)

110 *Fluidization, Solids Handling, and Processing*

- Van Swaaij, W. P. M., and Zuiderweg, F. J., "The Design of Gas-Solids Fluidized Beds - Prediction of Chemical Conversion," *Proc. Int. Symp. on Fluidization and its Appl.*, Ste Chimie Industrielle, Toulouse (1973)
- Volk, W., Johnson, C. A., and Stotler, H. H., "Effect of Reactor Internals on Quality of Fluidization," *Chem. Eng. Progress*, 58:44 (1962)
- Werther, J., "Influence of Bed Diameter On the Hydrodynamics of Gas Fluidized Beds," *AIChE Symp. Ser.*, 70 (141):53 (1974)
- Werther, J., "Scale-up of Fluidized Bed Reactors," *Ger. Chem. Eng.*, 1:243 (1978)
- Werther, J., "Scale-up Modeling for Fluidized Bed Reactors," *Chem. Eng. Sci.*, 47(9-11):2457 (1992)
- Werther, J., and Schoessler, M., "Modeling Catalytic Reactions in Bubbling Fluidized Beds of Fine Particles," *Heat and Mass Transfer*, (W. P. M. Van Swaay, and H. H. Afgan, eds.), Springer, Berlin (1986)
- White, F. M., *Viscous Fluid Flow*, McGraw-Hill, New York (1974)
- Whitehead, A. B., and Young, A. D., "Fluidisation Performance in Large Scale Equipment," *Proc. Intern. Symp. on Fluidisation*, p. 294, Eindhoven (1967)
- Yang, W. C., Newby, R. A., and Kearns, D. L., "Large-scale Fluidized Bed Physical Model: Methodology and Results," *Powder Technol.*, 82:331 (1995)
- Yang, W. C., "Criteria for Choking in Vertical Pneumatic Conveying Lines," *Powder Technol.*, 35:143 (1983)
- Yerushalmi, Y., and Avidan, A., "High Velocity Fluidization," in *Fluidization*, (J. F. Davidson, R. Clift, and D. Harrison, eds.), 2nd edition, Academic Press, New York (1985)
- Yule, T., and Glicksman, L. R., "Gas Flow through Erupting Bubbles in Fluidized Beds," *AIChE Symp. Ser. Fluidization Eng.: Fundamentals and Appl.*, 262(84):1 (1988)
- Zenz, F. A., and Othmer, D. F., *Fluidization and Fluid-Particle Systems*, Reinhold Publishing Corp., New York (1960)
- Zhang, W., Tung, Y., and Johnsson, F., "Radial Voidage Profiles in Fast Fluidized Beds of Different Diameters," *Chem. Eng. Sci.*, 46(12):3045 (1991)
- Zhang, M. C., and Yang, R. Y. K., "On the Scaling Laws for Bubbling Gas-fluidized Bed Dynamics," *Powder Technol.*, 51:159 (1987)
- Zhang, W., Johnsson, F., and Leckner, B., "Fluid Dynamic Boundary Layers in CFB Boilers," *Chem. Eng. Sci.*, 50(2):201 (1995)

Pressure and Temperature Effects in Fluid-Particle Systems

Ted M. Knowlton

1.0 INTRODUCTION

Most investigations of fluidization parameters take place at ambient temperature and pressure. Yet, nearly all processes operate at elevated temperature, and many at elevated pressure. Therefore, it is necessary to know how increasing temperature and pressure affect the operation of fluidized systems. However, the operation of fluidized test facilities at temperature and pressure is much more difficult and costly than operating them at ambient conditions. It is not surprising then that information on how temperature and pressure affect the operation of fluidized beds is not as prevalent as would be desired. However, many researchers have undertaken the difficult task of building and operating units to obtain these badly needed data. The purpose of this chapter is to present what is known about operating fluidized beds at elevated temperature and pressure.

112 *Fluidization, Solids Handling, and Processing*

From the 1940's (when the significant research on fluidized beds began) until the early 1970's, there was very little information in the literature dealing with the effects of temperature and pressure on the operation of fluidized beds. This was primarily because (i) high-pressure and/or high-temperature research rigs were (and still are) costly to build and to operate, and (ii) during this period, fluidization research was primarily directed toward improving fluidized-bed catalytic cracking, which was conducted at low pressures.

The early 1970's saw the development of many new coal-based, synthetic-fuel, fluidized-bed processes which operated at high pressures. The scientists and engineers charged with designing these processes realized that there was a severe lack of information on how pressure (and also temperature) affected the operation of fluidized beds. Therefore, several studies to determine the effect of pressure on the operation of fluidized beds were commissioned. During the same period, other researchers in Japan, Europe, and the U.S. were also starting to conduct research to determine the effects that temperature and pressure have on fluidized systems.

As a result, most of the information on how temperature and pressure affect fluidized beds has been obtained during the last twenty-five years. Much of this research has been conducted in a piecemeal fashion by several researchers. However, enough information is available to allow the construction of an overall picture of how these two parameters affect fluidized beds, and fluid-particle systems in general.

Temperature and pressure affect the operation of fluid-particle systems because they affect gas density and gas viscosity. It is the variation in these two parameters that determine the effects of temperature and pressure on fluid-particle systems. Increasing system temperature causes gas density to decrease and gas viscosity to increase. Therefore, it is not possible to determine only the effect of gas viscosity on a system by changing system temperature because gas density is also changed and the resulting information is confused. Very few research facilities have the capability to change system pressure to maintain gas density constant while the temperature is being changed to vary gas viscosity.

Changing system pressure essentially only changes gas density in a system because gas viscosity is an extremely weak function of system

pressure. For example, increasing the pressure of nitrogen gas from 1 to 70 bar increases its viscosity by less than 10%.

Most fluidized-bed processes operate within the temperature and pressure ranges of ambient to 1100°C and ambient to 70 bar, respectively. Over this temperature range, gas viscosity increases by a factor of about 3 to 4, depending upon the type of gas. If the pressure of the system remains constant while temperature is changed, the gas density decreases over this temperature range by a factor of $1373/293 = 4.7$. If system pressure is increased without changing temperature, the gas density is increased by the same factor as the pressure ratio—which would be approximately 70:1 for a change in pressure from ambient to 70 bar.

The effects of temperature and pressure on fluidized-bed systems cannot be considered independently of particle size. Whether temperature and pressure have an effect (and indeed, even the direction of that effect) on a system, depends strongly on particle size. In addition, the type of interaction between gas and solids, i.e., whether the interaction is due to momentum or drag, determines if gas viscosity has an effect upon the system. As will be shown, gas viscosity is not important in systems in which momentum is important, but is important in systems dominated by drag.

This chapter will look at the effects of pressure and temperature on various types of fluidized beds: bubbling, turbulent, and circulating. More studies at elevated temperature and pressure have been conducted in bubbling fluidized beds than higher-velocity beds. Therefore, how temperature and pressure affect bubbling fluidized beds dominate this chapter. However, recent work has been conducted on how temperature and pressure affect the transitions between the various fluidization regimes, as well as limited work in the circulating fluidized bed regime.

The chapter begins by describing how temperature and pressure affect parameters important for bubbling fluidized beds, and then discusses their effect on regime transitions, circulating fluidized beds, and cyclones.

1.1 Minimum Fluidization Velocity

One of the basic parameters to be determined when designing bubbling fluidized-bed systems is the minimum fluidization velocity, U_{mf} . The effect of temperature and pressure on U_{mf} has been investigated by many researchers (Botterill and Desai, 1972; Botterill and Teoman, 1980;

Botterill et al., 1982; Geldart and Abrahamsen, 1981; Geldart and Kapoor, 1976; Knowlton, 1977; Mii et al., 1973; Richardson, 1971; Rowe, 1984; Sakuraya et al., 1976; Sobreiro and Monteiro, 1982; Varadi and Grace, 1978; Yoshida et al., 1976). They have found that the effects of temperature and pressure on U_{mf} are strongly dependent upon particle size. As shown in Fig. 1 from Rowe et al. (1984), increasing system pressure causes U_{mf} to decrease for particle sizes greater than about 100 microns. Materials of this size are essentially Geldart Group B and D powders (Geldart, 1973). For particles smaller than 100 microns (Geldart Group A powders), pressure does not affect U_{mf} .

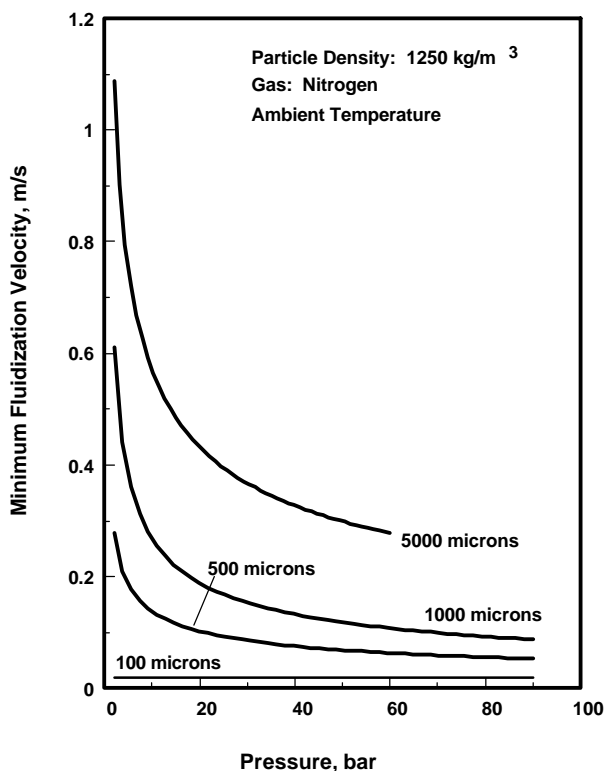


Figure 1. The effect of pressure on minimum fluidization velocity. (Rowe.)

Generally, correlations predict the effects of temperature and pressure on U_{mf} well. One of the more widely-used correlations to predict U_{mf} is the Wen and Yu Correlation (Wen and Yu, 1966). The simplified form of the Wen and Yu correlation is:

$$\text{Eq. (1)} \quad Ar = 1650 Re_{p,mf} + 24.5 (Re_{p,mf})^2$$

The first term in this equation is important if laminar, or viscous, flow predominates in a system, while the second term is important if turbulent, or inertial, flow predominates. Equation (1) can be rearranged to the form shown in Eq. (2). This form expresses U_{mf} in terms of known system parameters.

$$\text{Eq. (2)} \quad U_{mf} = \frac{\mathbf{m}}{\mathbf{r}_g d_p} \left[\frac{(33.7)^2 + 0.0408 d_p^3 \mathbf{r}_g (\mathbf{r}_p - \mathbf{r}_g) g}{\mathbf{m}^2} \right]^{0.5}$$

The effect of temperature and pressure on U_{mf} is strongly influenced by particle size. For small particles ($Re_{p,mf} < 20$), the simplified Wen and Yu Equation reduces to:

$$\text{Eq. (3)} \quad U_{mf} = \frac{d_p^2 (\mathbf{r}_p - \mathbf{r}_g) g}{1650 \mathbf{m}} \quad Re_{p,mf} < 20$$

For large particles ($Re_{p,mf} > 1000$), Eq. (1) becomes:

$$\text{Eq. (4)} \quad U_{mf}^2 = \frac{d_p (\mathbf{r}_p - \mathbf{r}_g) g}{24.5 \mathbf{r}_g} \quad Re_{p,mf} > 1000$$

Because gas viscosity does not vary significantly with pressure, the only parameter in Eq. (3) which changes with pressure is the gas density. However, because \mathbf{r}_p for most materials is so much larger than \mathbf{r}_g even at elevated pressures, the term $(\mathbf{r}_p - \mathbf{r}_g)$ essentially does not change with pressure. Therefore, for small particles, Eq. (3) predicts that U_{mf} will not change with pressure, and agrees with experimental findings.

In Eq. (4), the only term which is influenced by pressure is r_g , because $(r_p - r_g)$ does not change with pressure. For large particles, the Wen and Yu Equation predicts that U_{mf} should vary as $(1/r_g)^{0.5}$. Therefore, U_{mf} should decrease with pressure for large particles. This is also what is observed experimentally.

The variation of U_{mf} with temperature is also strongly affected by particle size. For large particles, Eq. (4) predicts that U_{mf} will vary as $(1/r_g)^{0.5}$. Because temperature causes r_g to decrease, U_{mf} should increase with temperature for large particles. For small particles, Eq. (3) shows that U_{mf} should vary as $1/m$. Therefore, U_{mf} should decrease with temperature for small particles, where viscous effects predominate. Calculated U_{mf} versus temperature curves obtained from the Wen and Yu Equation are shown in Fig. 2 for several different particle sizes. As indicated above, the Wen and Yu Equation predicts that U_{mf} increases with increasing temperature for large particles (where turbulent effects dominate), and decreases with increasing temperature for small particles (when viscous effects dominate).

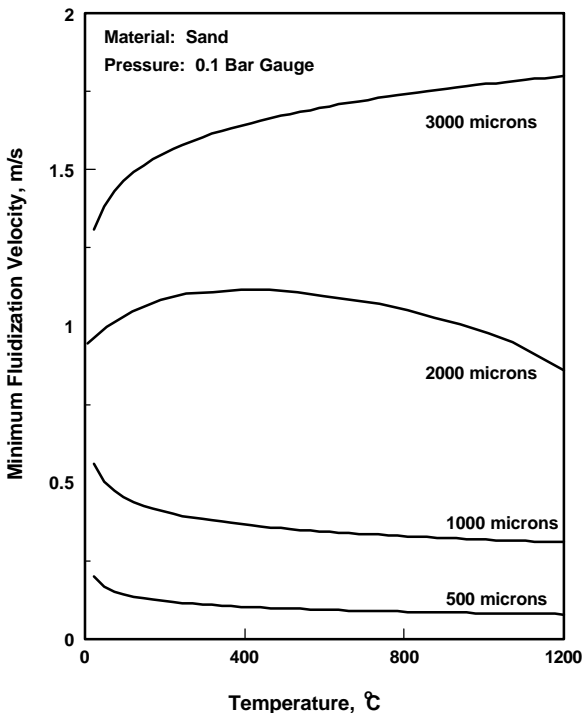


Figure 2. The effect of temperature on minimum fluidization velocity. (Wen & Yu.)

The predicted effects of temperature on U_{mf} were experimentally observed by Botterill and Teoman (1980) as shown in Fig. 3. For sand particles 462 microns in diameter, they observed that U_{mf} decreased with temperature. For larger material (2320 microns) in the “transition” region in Fig. 2 (where U_{mf} changes from increasing with temperature to decreasing with temperature), they observed an initial increase in U_{mf} with temperature at low temperatures, which was followed by a decrease in U_{mf} as increasing temperature caused viscous effects to become dominant.

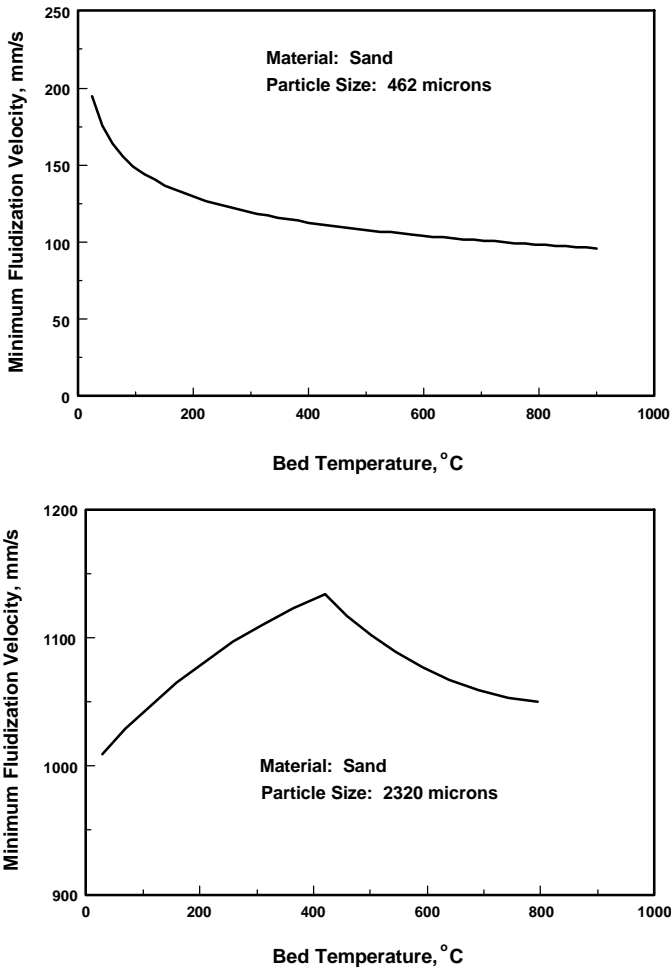


Figure 3. The effect of temperature on the minimum fluidization velocity. (*Botterill and Teoman.*)

118 Fluidization, Solids Handling, and Processing

Temperature can also affect fluidized beds if it causes the particles to sinter or become sticky. Siegel (1984) has shown that above a certain critical temperature, the fluidizing gas velocity must be increased above the minimum fluidization velocity in order to maintain fluidization in the bed. Siegel reported that the increase in velocity required to maintain fluidization was linearly proportional to the temperature increase. Increasing bed L/D , and smaller particle sizes, increased the tendency to agglomerate.

Compo (1987) also investigated the effect of temperature on the velocity required to prevent defluidization for (i) materials which agglomerated rapidly after their sintering temperature (T_s) was reached (coal, plastics, etc.), and (ii) materials which agglomerated slowly after reaching T_s (calcium chloride, etc.) For the rapidly agglomerating materials, the gas velocity had to be increased rapidly to prevent defluidization after T_s was reached. For the weakly agglomerating materials, a much smaller increase in gas velocity was required to prevent defluidization after T_s was reached.

Although the trends of varying temperature and pressure can be predicted by minimum fluidization velocity correlations, sometimes the absolute values of the predictions are significantly in error. Frequently, the primary cause of uncertainty is in determining a representative value for the average particle size to use in the U_{mf} correlation. One technique which can be used to improve upon the accuracy of the prediction of U_{mf} is to first determine U_{mf} experimentally at ambient conditions. Then, using this experimentally-obtained value for U_{mf} , back-calculate an effective particle size from the correlation. Using this effective particle size, then calculate U_{mf} at actual conditions. This technique can predict U_{mf} more accurately than by using a correlation alone. It substitutes an effective value for the shape factor and the average particle size. However, it does not account for changes in voidage which might occur with changes in temperature and pressure.

Yang et al. (1985) proposed another method of determining U_{mf} at elevated temperature and pressure. As with the procedure described above, U_{mf} is first determined experimentally at ambient conditions. This data point is then located on a curve of constant e_{mf} on a plot of

$$\left[(Re)_e^2 (C_D)_e \right]_{mf}^{1/3} \text{ vs. } \left[(Re)_e / (C_D)_e \right]_{mf}^{1/3}$$

where Re_e and CD_e are Reynolds number and drag coefficients, respectively, modified by Barnea and Mizrahi (1973) to apply to multiparticle systems. This technique produced estimates of U_{mf} which agreed extremely well with experimental U_{mf} data taken at pressures up to 6300 kPa. It also predicted the experimental data of Yoshida et al., (1976) and Mii et al., (1973) obtained at temperatures up to 850°C (Fig. 4). Shrivastava et al. (1986) applied this technique to the data of Saxena and Vogel (1977) also with excellent results.

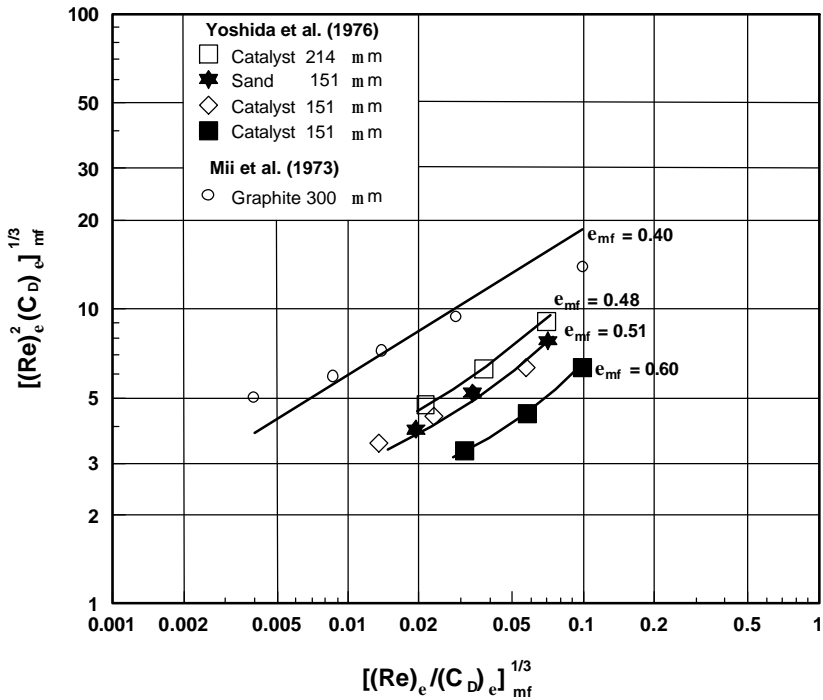


Figure 4. Comparison of data and Yang et al. procedure for U_{mf} determination.

This success of this procedure implies that e_{mf} does not change significantly with temperature and pressure. However, other researchers (see below) have reported that e_{mf} can change substantially with temperature and pressure for Geldart Group A powders. Therefore, the authors caution that this technique may not be accurate for Geldart Group A particles.

Abrahamsen and Geldart (1980) defined Group A powders as those in which $U_{mb}/U_{mf} > 1$, and Group B powders as those where $U_{mb}/U_{mf} = 1$. They developed the following equation to predict U_{mb}/U_{mf} :

$$\text{Eq. (5)} \quad \frac{U_{mb}}{U_{mf}} = \frac{2300 \mathbf{r}_g^{0.126} \mathbf{m}^{0.523} \text{Exp}(0.716F)}{d_p^{0.8} g^{0.934} (\mathbf{r}_p - \mathbf{r}_g)^{0.934}}$$

where F is a weight fraction of 0 to 44 micron particles in the distribution

Equation (5) implies that materials may shift from one Geldart Group to another as a consequence of changing system parameters. For example, if a material is in Group B near the Group B/A boundary and either the gas density and/or the gas viscosity is increased, U_{mb}/U_{mf} will increase and the material can “cross” the boundary into Group A. That this can occur has been demonstrated by experiments performed by Varadi and Grace (1978). They found that U_{mb}/U_{mf} increased from a value of 1 to a value much greater than 1 as system pressure was increased over the range of 1 to 22 atmospheres as shown in Fig. 5. Thus, the material moved from Group B to Group A as a consequence of changing system pressure. Equation (5) predicts that U_{mb}/U_{mf} is more sensitive to gas viscosity than gas density. The data of de Vries et al. (1972) agree with this prediction.

1.2 Bed Voidage and Bed Expansion

Voidage in a bubbling fluidized bed is also affected by temperature and pressure. Botterill et al. (1982) reported for Group B materials, that the Wen and Yu Equation generally over-predicts the reduction of U_{mf} with temperature. They found that the overprediction was due to the increase in voidage at minimum fluidization (\mathbf{e}_{mf}) with increasing temperature. For Geldart Group D materials, they found that \mathbf{e}_{mf} was insensitive to changes in temperature.

Pressure has been found to cause the dense-phase voidage (\mathbf{e}_d) to increase for Group A materials. The effect diminishes with increasing particle size, and for large Geldart Group B and Group D materials, \mathbf{e}_d is insensitive to pressure. Weimer and Quarderer (1983) in their high-pressure experiments, found that over a pressure range of 8 to 69 bar, \mathbf{e}_d for

66 and 108-micron activated carbon increased by 40 and 16%, respectively, as shown in Fig. 6. They reported essentially no effect of pressure on ϵ_d for larger 171-micron material. Weimer and Quaderer also reported that the correlation for dense-phase voidage developed by Kmiec (1982) matched their results well. The Kmiec correlation for dense-phase voidage is:

$$\text{Eq. (6)} \quad \epsilon_d = \frac{(18Re_p + 2.7Re_p^{1.687})^{0.209}}{Ga^{0.209}}$$

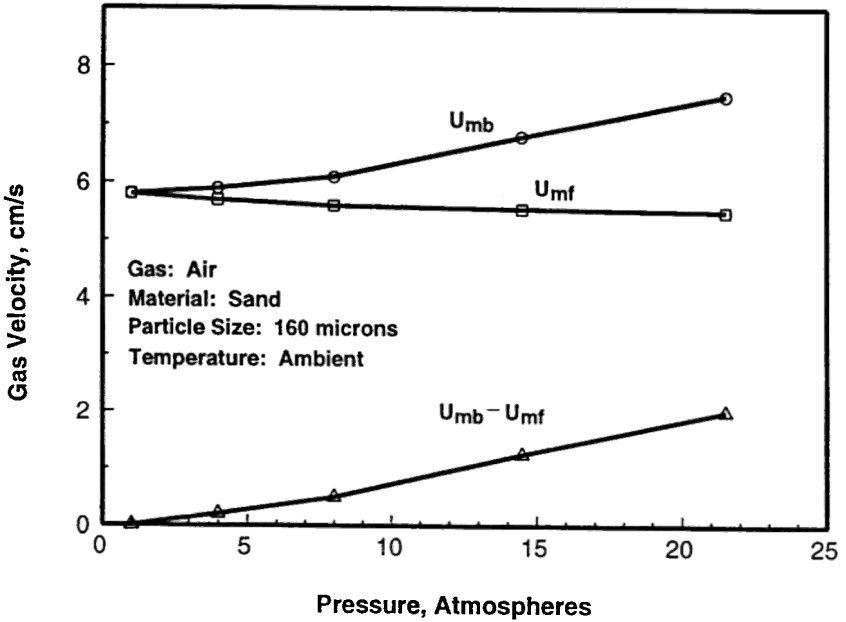


Figure 5. The effect of pressure on $U_{mb} - U_{mf}$ (Varadi & Grace).

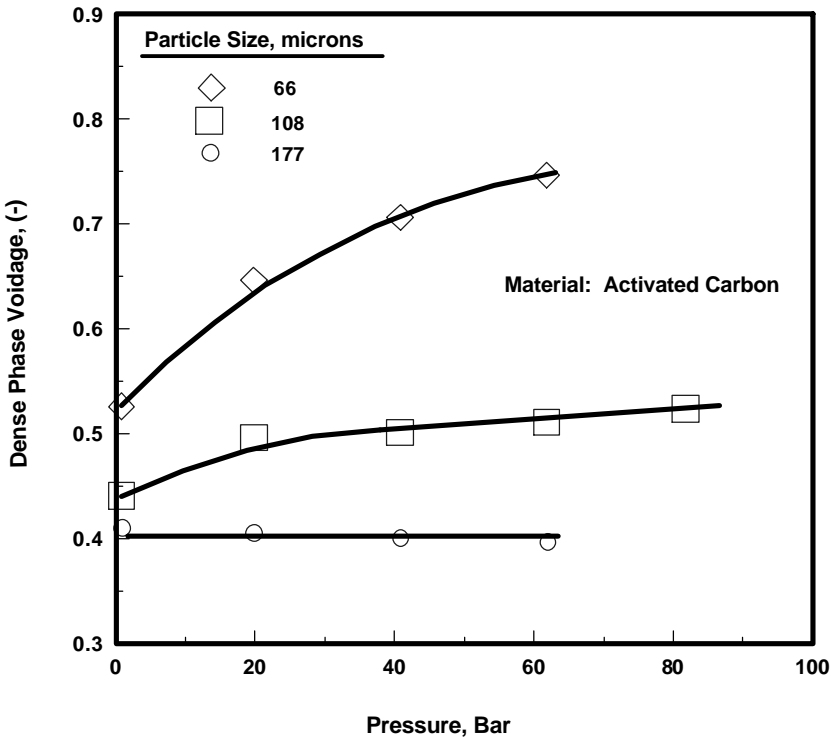


Figure 6. The effect of pressure on dense phase voidage. (Weimer & Quarderer.)

Subzwari et al. (1978) also reported that bed voidage and bed expansion increased with pressure for FCC catalyst (a Group A material). However, Knowlton (1977) reported little change in either bed density or bed expansion at U_{cf} with increasing pressure over the range of 1 to 70 atmospheres for large, -2000/+74 micron material.

The fluidized-bed voidage at minimum bubbling conditions (e_{mb}) also has been shown to increase with increasing temperature (Fig. 7) and increasing pressure (Fig. 8).

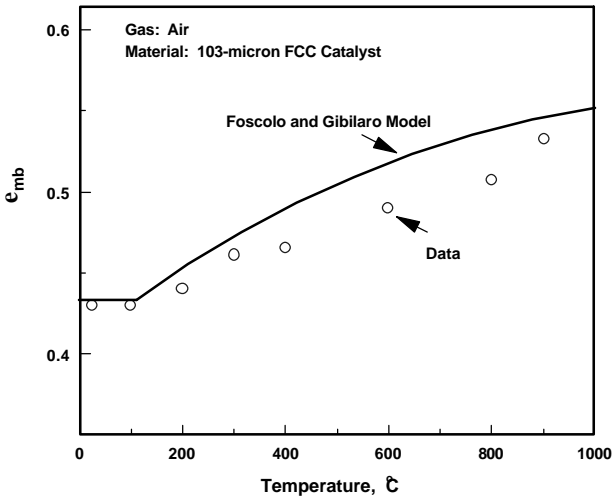


Figure 7. The effect of temperature on e_{mb} . (Rapagna et al., 1994; Yates, 1995.)

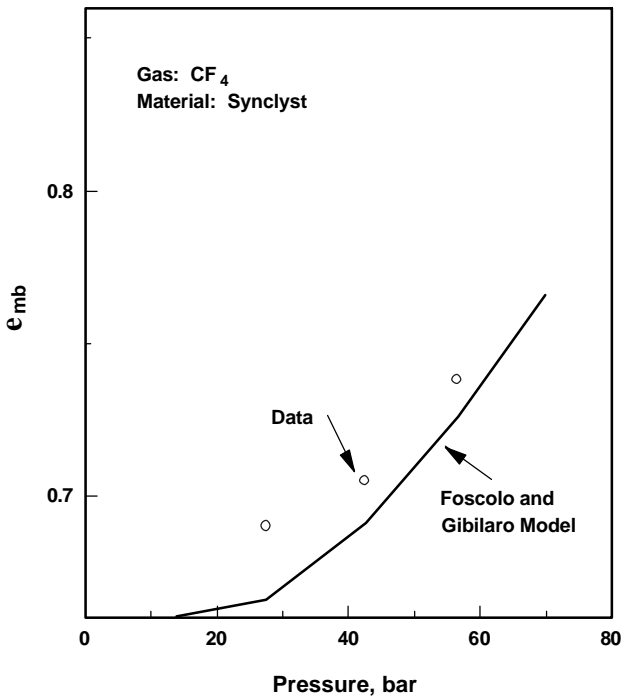


Figure 8. The effect of pressure on e_{mb} . (Crowther & Whitehead, Fluidization, Davidson and Keairns, eds., 65–70, 1978.)

1.3 Bubbles in Fluidized Beds

Hydrodynamically, fluidized beds are considered to be stable when they are not bubbling and unstable when they are bubbling. Several researchers (Knowlton, 1977; Hoffman and Yates, 1986; Guedes de Carvalho et al., 1978) have reported that fluidized beds become “smoother” at elevated pressures (i.e., have smaller bubbles) and, therefore, are more stable at high pressures. There are generally two approaches as to what causes instability in fluidized beds. Rietema and co-workers (Rietema et al. 1993) forwarded the theory that the stability of the bed depends on the level of interparticle forces in the bed. However, Foscolo and Gibilaro (1984) have proposed that hydrodynamics determines whether a fluidized bed is stable.

With the Interparticle Force Theory, interparticle forces (van der Waals, etc.) are what cause the bed to be “elastic.” Bed elasticity is characterized by an Elasticity Modulus, M_p . The criterion which determines when the fluidized bed starts to bubble is determined by the relative magnitudes of the two sides of Eq. (7).

$$\text{Eq. (7)} \quad \frac{r_p^3 d_p^4 g^2}{m^2 M_{mb}} = \left[\frac{150(1 - e_{mb})}{e_{mb}^2 (2 - 2e_{mb})} \right]^2$$

If the LHS of Eq. (7) is < the RHS: The bed is STABLE

If the LHS of Eq. (7) is > the RHS: The bed will BUBBLE

In this theory, increasing pressure causes gas to be absorbed onto the surface of the particles. This results in an increase in M_p , and, by Eq. (7), an increase in the stability of the fluidized bed.

The Hydrodynamic Theory of fluidized bed stability was proposed by Foscolo and Gibilaro who adapted the stability principle of Wallis. They postulated that a fluidized bed is composed of two interpenetrating fluids. One fluid is the gas phase, and the solids phase is also considered as a continuous fluid phase. In this theory, voidage disturbances in the bed propagate as dynamic and kinetic waves. The stability of the fluidized bed depends upon the relative velocities of these two waves. The velocities of the kinetic wave (u_e) and the dynamic wave (u_d) are:

$$\text{Eq. (8)} \quad u_e = nu_t(1-e)e^{n-1}$$

$$\text{Eq. (9)} \quad u_e = \sqrt{[3.2gd_p(1-e)(r_p - r_g)]/r_p}$$

where n is the Richardson and Zaki exponent.

If $u_e > u_e$, the bed is STABLE

If $u_e > u_e$, the bed will BUBBLE

Equating u_e and u_e and manipulating the resulting expression leads to the following stability criterion:

$$\begin{array}{cc} \text{Term 1 (T1)} & \text{Term 2 (T2)} \\ \text{Eq. (10)} & \left[\frac{gd_p(r_p - r_g)}{u_t^2 r_p} \right]^{0.5} - 0.56n(1-e_{mb})^{0.5}e_{mb}^{n-1} = C \end{array}$$

If $C > 0$ (if Term 1 is $>$ Term 2), the bed is STABLE

If $C < 0$ (If Term 1 is $<$ Term 2), the bed BUBBLES

The Hydrodynamic Theory of Foscolo and Gibilaro has been shown to predict the increase in e_{mb} with temperature and pressure very well. This is shown in Figs. 7 and 8, respectively, for the data of Rapagna (1994) and Crowther et al., (1978). Jacob and Weimer (1987) also reported that the Foscolo and Gibilaro theory successfully predicted the increase in e_{mb} with increasing pressure.

1.4 Bubble Size and Frequency

Temperature and pressure also interact with particle size to affect bubble size and frequency in fluidized beds. Information on the effect of temperature on bubble size in the literature is somewhat inconsistent. However, the information that does exist suggests that bubble size decreases slightly with temperature for Group A materials (Geldart and

Kapoor, 1976; Kai and Furusaki, 1985; Yoshida et al., 1976). Although less information exists for larger particle sizes, bubble size appears to not change with temperature for Group B materials (Sishtla et al., 1986; Wittman et al., 1981), and to increase with temperature for Group D materials (Sittiphong et al. 1981).

Workers generally report that bubble frequency increases with temperature (Mii et al., 1973; Otake et al., 1975; Yoshida et al., 1974). There is an initial rapid increase in frequency with temperature near ambient, which then tapers off at higher temperatures.

As reported above, investigators have reported that fluidization appears smoother when beds are operated at high pressure. They also report that there is a “slow motion” quality about the bed. This behavior has been attributed to a decrease in the bubble size with pressure. Indeed, there is ample experimental evidence (Barreto et al., 1984; Chan et al., 1987; Rowe et al., 1984; Weimer and Quarderer, 1983) which shows that increasing pressure causes bubble size to decrease in Group A materials. The same evidence shows that the pressure effect on bubble size decreases as the particle size increases, and that pressure does not affect bubble size significantly for large Group B, and Group D materials. The effect of pressure on bubble size for 66 micron and 171 micron material is shown in Fig. 9 from Weimer and Quarderer. As can be seen from the figure, pressure has a significant effect only for the smaller particles.

Although there is some disagreement among researchers in this area, it is generally believed that bubbles divide by splitting from the roof due to Taylor instabilities (Clift and Grace, 1972), and that the smaller bubbles observed in high-pressure beds of Group A solids are a result of the increased expansion of the dense phase with pressure. This results in an effective decrease in the viscosity of the dense phase. Taylor instability (an instability in the roof of the bubble/dense-phase interface) increases with a decrease in the viscosity of the dense phase. This results in a collapse of the bubble roof more frequently at high pressures. King and Harrison (1980) used x-rays to obtain images of bubble breakup and found that bubble breakup occurred because of “fingers” of material penetrating the bubble from the roof. This is schematically depicted in Fig. 10.

Experimental observations show that the dense-phase viscosity for small Group A particles decreases significantly with pressure (King and Harrison et al., 1980; May and Russell, 1953) as shown in Fig. 11. However, the dense-phase viscosity of Group B and Group D particles

does not change with pressure. This supports the theory that bubbles are smaller in high-pressure beds because of Taylor instability, and fits the experimental evidence that bubbles do not change significantly with pressure in beds of Group B and Group D particles. Rowe et al. (1984) also showed that at extremely high pressures, bubbles become so small that they cannot be distinguished from the dense phase.

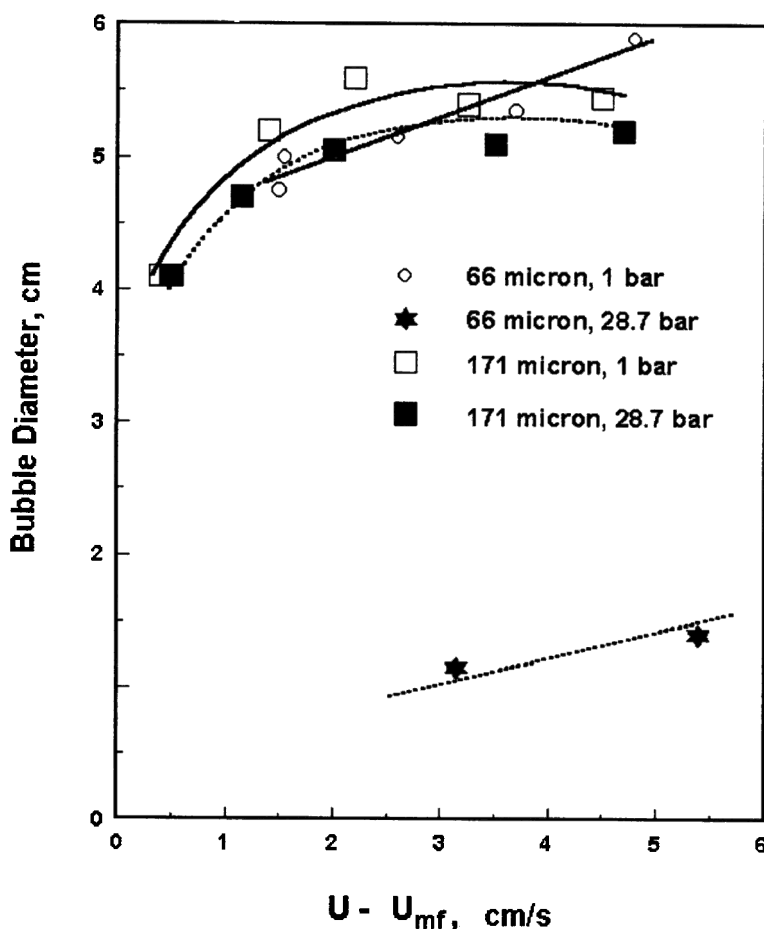
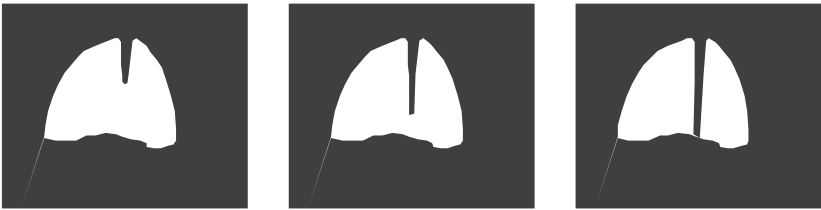


Figure 9. The effect of pressure and particle size on bubble diameter. (Weimer and Quarderer.)



- Particles Penetrate Into Bubble Roof Due to Taylor Instability
- When Penetration Completely Pierces Bubble - Bubble Splits

Figure 10. Schematic drawing of bubbles splitting from the roof.

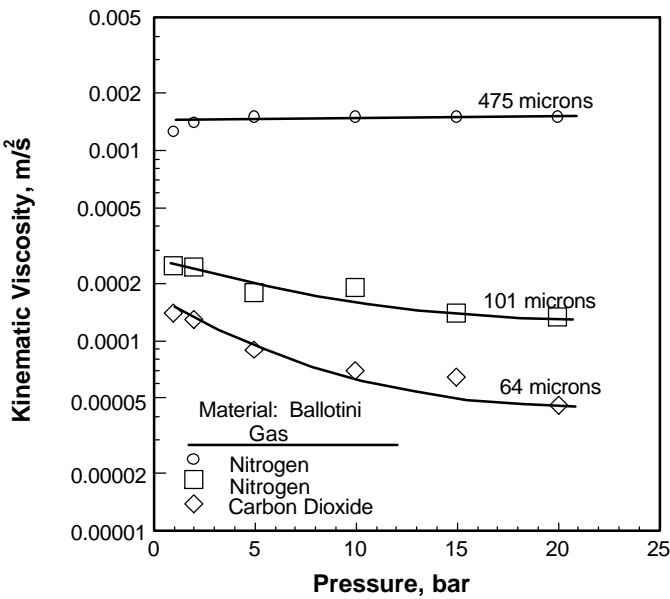


Figure 11. Kinematic viscosity versus pressure. (King & Harrison.)

Pressure also appears to cause bubble frequency to increase. This has been reported by both Rowe et al., (1984) and Chan et al., (1987). Rowe et al., (1984) also reported that bubbles were flatter at elevated pressures.

1.5 Bed-to-Surface Heat Transfer Coefficient

In general, gas-to-particle or particle-to-gas heat transfer is not limiting in fluidized beds (Botterill, 1986). Therefore, bed-to-surface heat transfer coefficients are generally limiting, and are of most interest. The overall heat transfer coefficient (h) can be viewed as the sum of the particle convective heat transfer coefficient (h_{pc}), the gas convective heat transfer coefficient (h_{gc}), and the radiant heat transfer coefficient (h_r).

$$\text{Eq. (11)} \quad h = h_{pc} + h_{gc} + h_r$$

The radiant heat transfer coefficient becomes important above about 600°C, but is difficult to predict. Baskakov et al. (1973) report that depending on particle size, h_r increases from approximately 8% to 12% of the overall heat transfer coefficient at 600°C, to 20 to 33% of h at 800°C.

Therefore, for beds operating below 600°C

$$\text{Eq. (12)} \quad h = h_{pc} + h_{gc}$$

Botterill et al. (1982) measured the overall heat transfer coefficient as a function of particle size for sand at three different conditions: 20°C and ambient pressure, 20°C and 6 atmospheres, and 600°C and ambient pressure. They found that there was a significant increase in h with pressure for Group D particles, but the pressure effect decreased as particle size decreased. At the boundary between Groups A and B, the increase of h with pressure was very small.

The effect of pressure on the heat transfer coefficient is influenced primarily by h_{gc} (Botterill and Desai, 1972; Xavier et al., 1980). This component of h transfers heat from the interstitial gas flow in the dense phase of the fluidized bed to the heat transfer surface. For Group A and small Group B particles, the interstitial gas flow in the dense phase can be assumed to be approximately equal to U_{mf}/e_d . U_{mf} is extremely small for

these relatively small materials, and, therefore, so is h_{gc} . For these materials, the dominant heat transfer component is h_{pc} . The gas convective heat transfer, h_{gc} , only becomes significant for large Group B or for Group D materials where the gas interstitial flow becomes significant. For these materials, increasing system pressure causes h_{gc} to increase because of the increased heat transfer from the gas to a surface due to higher gas densities. The effect of pressure on the overall heat transfer coefficient for Group B particles is shown in Fig. 12.

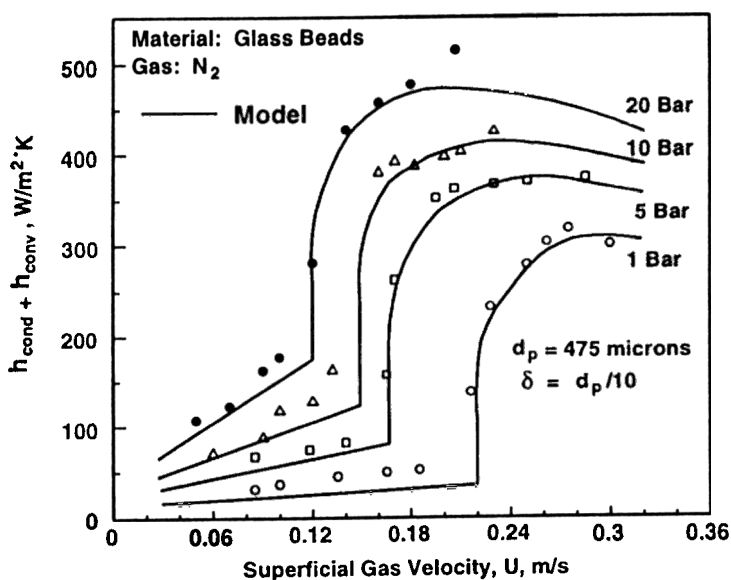


Figure 12. The effect of pressure on the overall heat transfer coefficient for group B powders. (Xavier & Davidson.)

Increasing system temperature causes h_{gc} to decrease slightly because increasing temperature causes gas density to decrease. The thermal conductivity of the gas also increases with temperature. This causes h_{pc} to increase because the solids are more effective in transferring heat to a surface. Because h_{gc} dominates for large particles, the overall heat transfer coefficient decreases with increasing temperature. For small particles where h_{nc} dominates, h increases with increasing temperature.

Increasing temperature has a large effect on h for small particles near and below the Group A/B boundary. Increasing temperature causes h to increase for these particles. The effect of temperature is less pronounced for Group B particles, and h decreases with temperature for Group D materials.

The primary effect of temperature on h is due to the particle convective component of the overall heat transfer coefficient. The particle convective heat transfer coefficient, h_{pc} , depends upon heat transfer from particle "packets" to the surface. It is influenced by factors which affect the solids circulation rate. The greatest resistance to heat transfer for particle convection is when heat has to flow between particles through the gas, which has a relatively low thermal conductivity. Heat transfer is especially low for Group A and B particles, for which the flow of interstitial gas is laminar. Therefore, because increasing the temperature of the gas increases its thermal conductivity, increasing temperature increases h_{pc} . Increasing system pressure has little effect upon h_{pc} except for Group A particles where pressure causes an increased expansion of the dense phase, and greater heat transfer because of the increased area available to transfer heat (Botterill, 1986).

1.6 Entrainment and Transport Disengaging Height

Entrainment from fluidized beds is also affected by temperature and pressure. Increasing system pressure increases the amount of solids carried over with the exit gas because the drag force on the particles increases at higher gas densities. May and Russell (1953) and Chan and Knowlton (1984) both found that pressure increased the entrainment rate from bubbling fluidized beds significantly. The data of Chan and Knowlton are shown in Fig. 13.

Increasing gas viscosity also increases the entrainment rate from fluidized beds because the drag force on the particles increases with increasing gas viscosity. Findlay and Knowlton (1985) varied gas viscosity in their experimental system (by changing system temperature) while maintaining gas density constant (by adjusting system pressure) in order to determine the effect of gas viscosity on the entrainment rate from a fluidized bed of char and limestone. They found that increasing gas viscosity significantly increased the entrainment rate from fluidized beds as shown in Fig. 14.

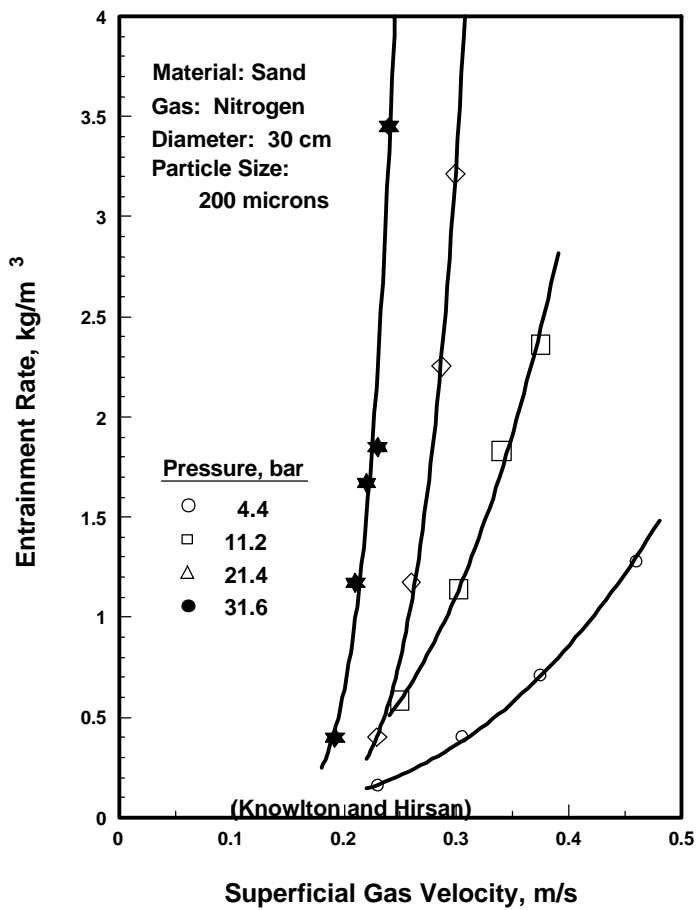


Figure 13. The effect of system pressure on entrainment. (Knowlton & Hirsan.)

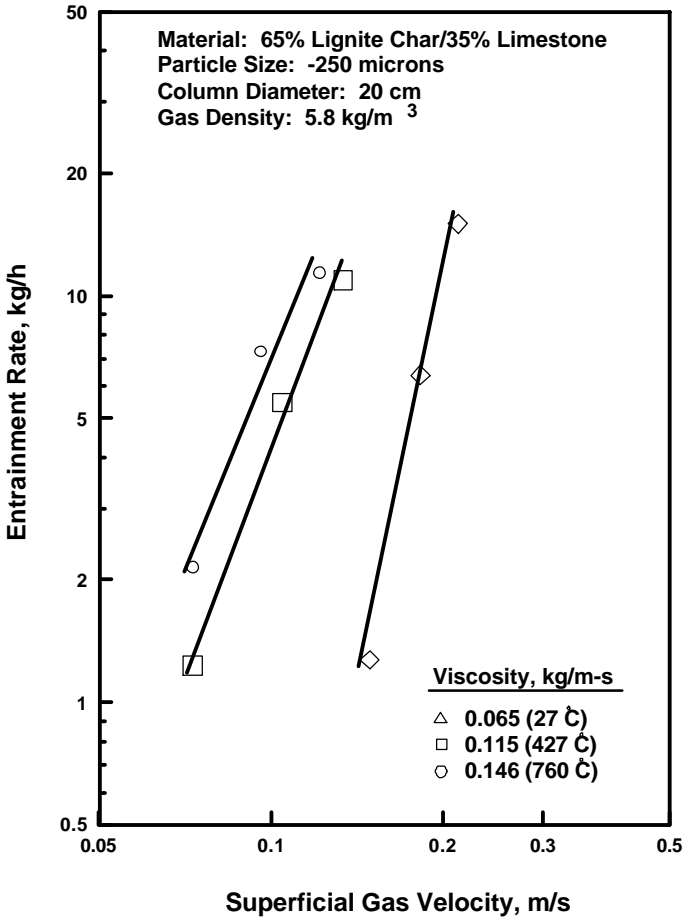


Figure 14. The effect of gas viscosity on entrainment. (*Findlay & Knowlton.*)

Chan and Knowlton (1984) also investigated the effect of system pressure on the transport disengaging height (TDH) over a pressure range of 1 to 30 bar. They found that TDH increased linearly with pressure over this range (Fig. 15). The effect of gas viscosity on TDH has not been determined experimentally by anyone thus far.

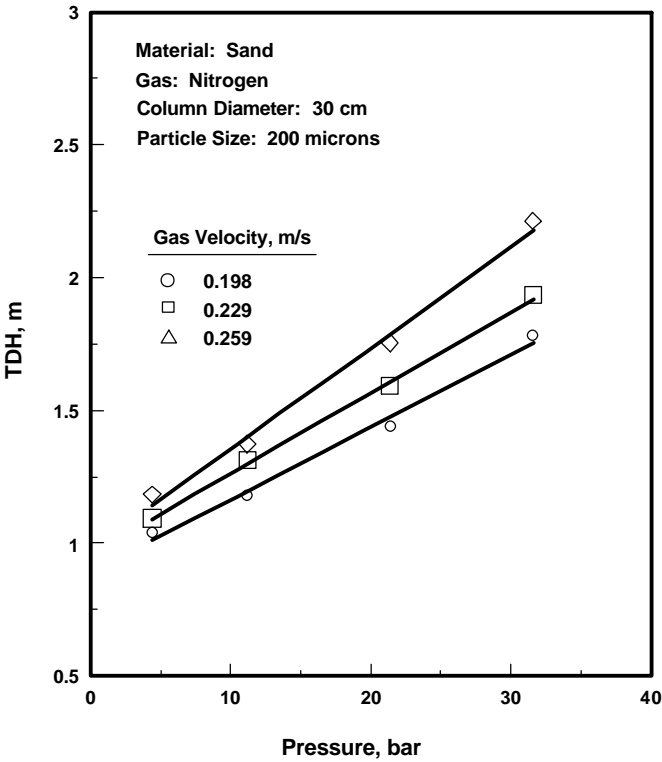


Figure 15. The effect of pressure on TDH. (*Knowlton & Hirsan.*)

1.7 Particle Attrition at Grids

Particle attrition not due to thermal or chemical reaction effects (i.e., mechanical attrition) occurs much more rapidly in the grid region of fluidized beds than in the bulk of the bed. This is due to high-velocity gas

jets at the grid which accelerate the particles and cause them to collide with others at a very high velocity.

Sishtla et al. (1989) reported that the particle attrition rate at the grid is proportional to the kinetic energy of the gas jets ($\mathbf{r}_g U_j^2$) issuing from the grid. They varied both system pressure and temperature while maintaining gas velocity constant, and found that increasing system pressure resulted in an increase in the attrition rate (Fig. 16), while increasing system temperature decreased the rate of particle attrition (Fig. 17). They attributed this behavior to the change in gas density produced by changes in temperature and pressure. Kono (1981) also observed the same effects of temperature and pressure on mechanical attrition.

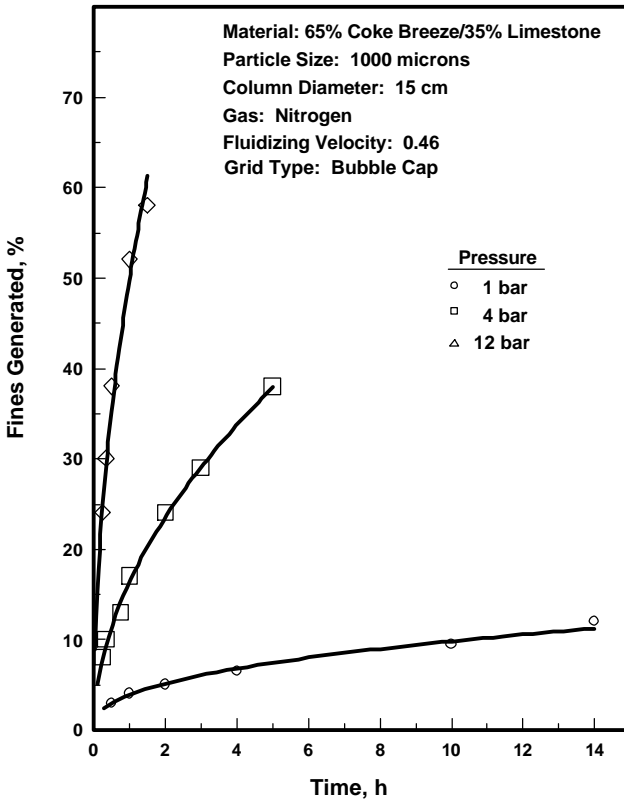


Figure 16. The effect of system pressure on attrition at the grid. (*Sishtla, et al.*)

1.8 Particle Attrition in Cyclones

There can also be substantial particle attrition in cyclones in fluidized-bed systems because particles are accelerated at the inlet of the cyclone and impacted against the cyclone wall. Although there is little information on particle attrition in cyclones in the literature, it has been reported (Sishtla) that increasing system pressure decreases the attrition rate in cyclones operating with coal char. The mechanism by which this occurred was not determined.

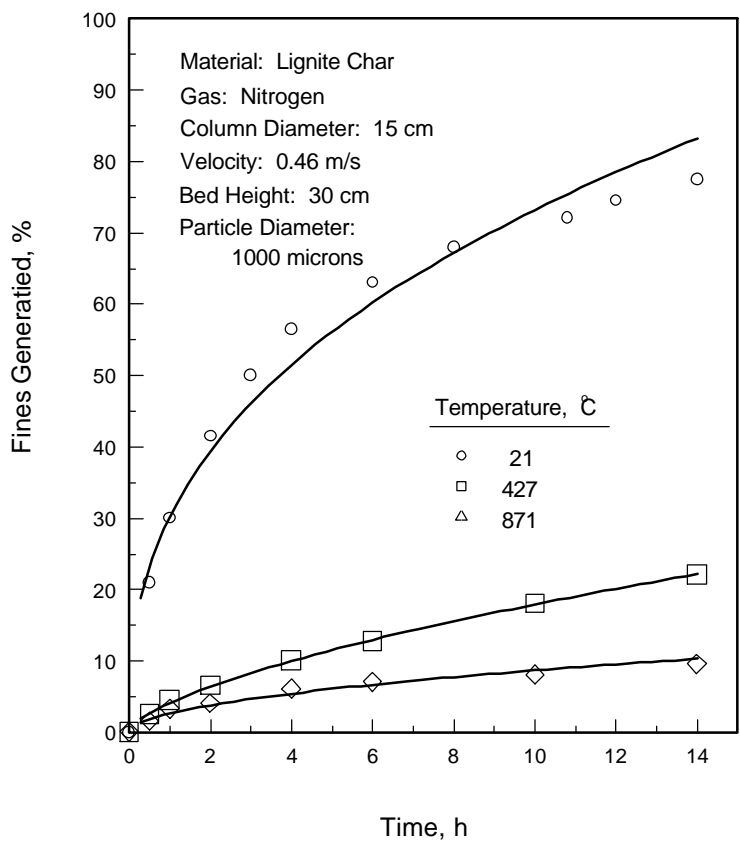


Figure 17. The effect of temperature on attrition at the grid. (*Sishtla et al.*)

1.9 Jet Penetration

Vertical jet penetration in fluidized beds increases significantly with system pressure as shown in Fig. 18. Vertical jets fluctuate in the vertical direction between a minimum and a maximum value. Most jet penetration correlations are given in terms of the maximum jet penetration length which is designated L_{max} (Hirsan et al. 1980). Over a pressure range of 1 to 50 bar with jet nozzles up to 3.8 cm in diameter, Hirsan et al. (1980) developed the following empirical correlation for the maximum jet penetration.

$$\text{Eq. (13)} \quad \frac{L_{\max}}{d_o} = 19.3 \left[\frac{\mathbf{r}_g U_o}{\mathbf{r}_p \sqrt{g d_p}} \right]^{0.83} \left[\frac{U_{cf}}{U} \right]^{0.54}$$

This correlation predicts that the maximum vertical jet penetration into a fluidized bed varies with gas density to the 0.67 power, and decreases with increasing fluidizing gas velocity and increasing particle diameter.

Yang (1981) incorporated the high-pressure data of Hirsan et al. (1980) to produce the following correlation for L_{max}

$$\text{Eq. (14)} \quad \frac{L_{\max}}{d_o} = 7.65 \left[\left(\frac{1}{R_{cf}} \right) \left(\frac{\mathbf{r}_g}{\mathbf{r}_p - \mathbf{r}_g} \right) \left(\frac{U_o^2}{g d_o} \right) \right]^{0.472}$$

where R_{cf} is defined as:

$$\text{Eq. (15)} \quad R_{cf} = \frac{(U_{cf})_{\text{pressure}}}{(U_{cf})_{\text{ambient}}}$$

Yates et al. (1986) varied system pressure up to 20 bar with jet nozzles of 2 and 4 mm diameter, and also found that the maximum jet penetration varied significantly with pressure. They then developed the following correlation for the maximum jet penetration:

Eq. (16)
$$\frac{L_{\max}}{d_o} = 9.77 \left[\left(\frac{1}{R_{cf}} \right) \left(\frac{r_g}{r_p - r_g} \right) \left(\frac{U_o^2}{g d_o} \right) \right]^{0.38}$$

which is similar in form to the correlation of Yang. Yates and Cheesman also incorporated high-temperature jet penetration data (obtained at temperatures up to 800°C) into this correlation.

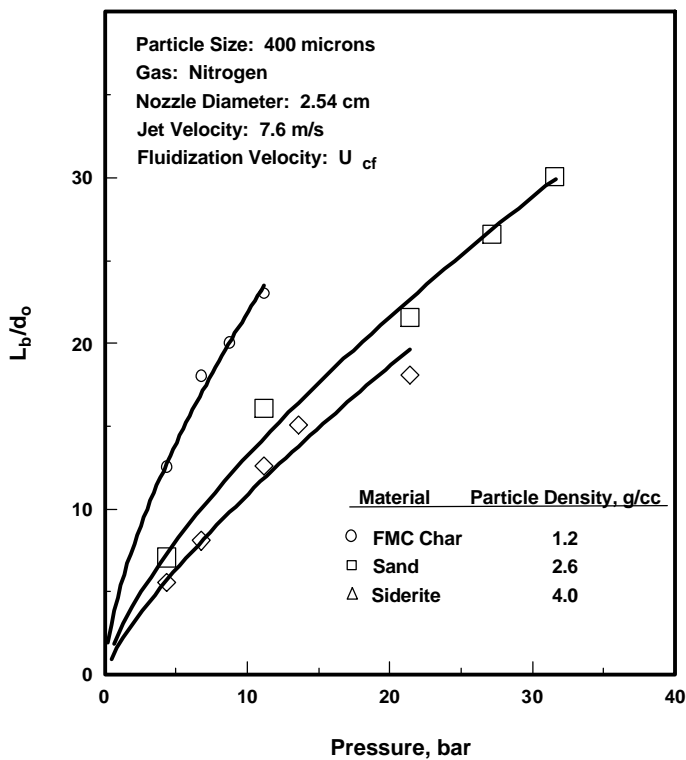


Figure 18. The effect of pressure on jet penetration. (*Knowlton and Hirsan.*)

Findlay and Knowlton (1985) investigated the effect of gas viscosity on jet penetration by varying system temperature while maintaining gas density constant. This was accomplished by adjusting system pressure at

each temperature studied. They concluded that viscosity had a negligible effect on jet penetration, and that temperature only affects jet penetration through its effect on gas density.

1.10 Regime Transitions

The transition boundaries between various fluidization regimes (i.e., bubbling/slugging to turbulent, and turbulent to fast fluidization) are also affected by gas properties. Because the minimum fluidization velocity changes with pressure for large particles, it would be expected that the transition velocities where the bed changes from the bubbling to the turbulent regime, and where the turbulent regime changes to the fast fluidization regime, would also be affected by system pressure. Indeed this is the case.

If the superficial gas velocity of a fluidized bed operating in a bubbling/slugging mode is increased, the bed is gradually transformed into a turbulent fluidized bed. The transition to turbulence occurs over a velocity range which is bounded by two unique gas velocities: U_c , the velocity at which the bed starts the transition from bubbling/slugging to turbulent, and U_k , the velocity at which the bed is fully at turbulent fluidization. U_c is often taken to be where the amplitude of the differential-pressure fluctuations in the bed are highest, and U_k is taken to be the velocity at which the amplitude of the differential-pressure fluctuations level off as indicated in Fig. 19. Recently, Marzocchella and Salatino (1996) reported that U_c and U_k can also be determined by plotting the variance of the pressure drop across the bed versus the superficial gas velocity through the bed. They conducted their tests with 175-micron glass beads fluidized by CO_2 at 40 and 60 bar pressures. They found that U_c occurred at the maximum value of the variance of the pressure drop across the bed versus superficial gas velocity curve, while U_k was determined where the variance of the pressure drop across the bed levels off (Fig. 20). This figure shows that U_c and U_k both decrease with increasing pressure. Marzocchella and Salatino also showed that power spectral densities of signals from a hot-wire anemometer inserted into the fluidized bed also can also be used to determine the packed-bed, particulate, bubbling, and turbulent regions in the fluidized bed.

Several other researchers have investigated the effects of pressure as well as temperature on the transition from bubbling/slugging to turbulent fluidization (Cai et al., 1989; Canada and McLaughlin, 1978; Yang and Chitester, 1988). Cai et al. (1989) varied system pressure over a range of 1 to 6 atmospheres for solids with different average particle sizes. They found that U_c decreased with system pressure. Yang and Chitester (1988) varied system pressure up to 64 atmospheres and also reported that increasing pressure caused a decrease in the velocity at which the transition from bubbling to turbulent fluidization occurred.

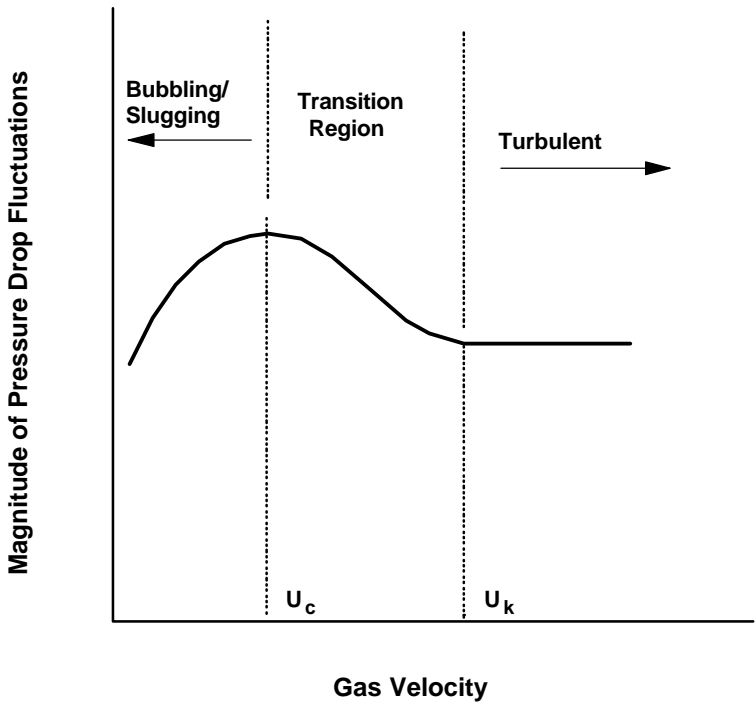


Figure 19. Bubbling-to-turbulent transition.

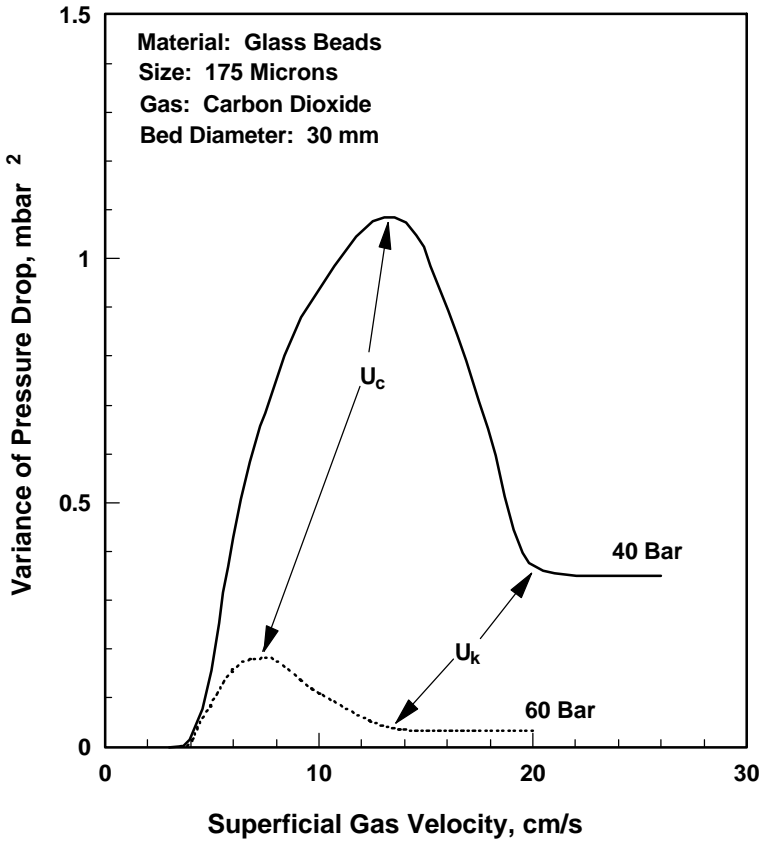


Figure 20. The variance of bed pressure drop versus superficial gas velocity. (Marzocchella & Salatino.)

Canada and McLaughlin (1978), working with 650-micron and 2600-micron particles over a pressure range of 1 to 10 atmospheres, found that U_k decreased significantly with pressure for both particle sizes (Fig. 21). They also reported that the ratio (U_k/U_c) remained relatively constant over this pressure range for both materials.

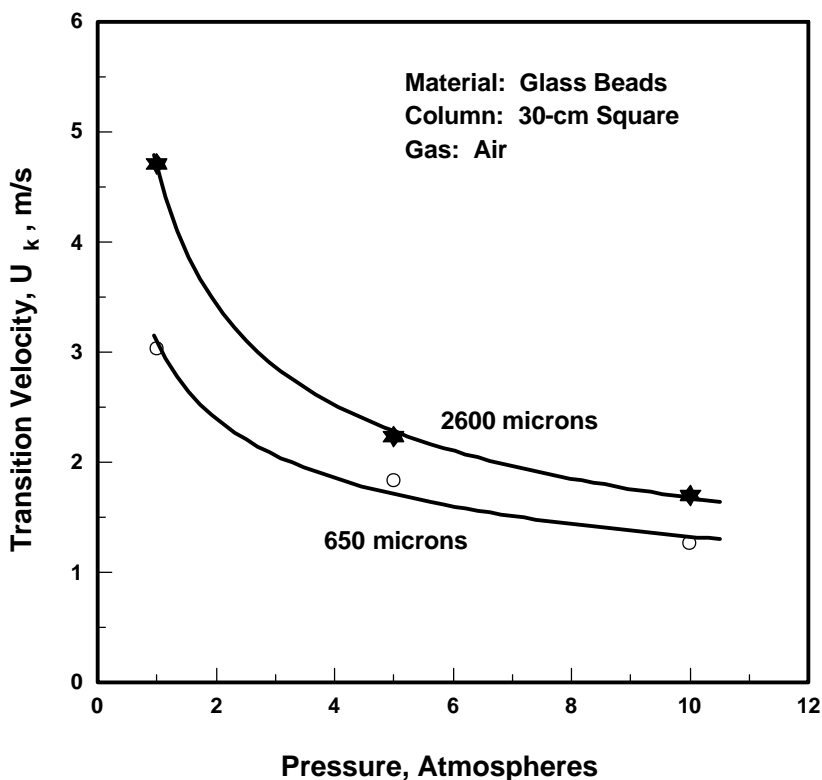


Figure 21. Effect of system pressure on U_k . (Canada & McLaughlin.)

Cai et al. (1989) also determined U_c as a function of temperature over the range 50° to 450°C. They found that U_c increased with temperature for materials belonging to Groups A, B, and D. It appears that the decrease in gas density with increasing temperature caused U_c to increase.

The boundary between the turbulent and the fast fluidization regimes has been of some dispute in the fluidization field. However, the choking velocity (U_{ch}) appears to be a practical lower-velocity boundary for this regime (Karri and Knowlton, 1991; Takeuchi et al., 1986).

Knowlton (1975), and Karri and Knowlton (1996), have also shown that the choking velocity for Group B solids decreases significantly with pressure. This is illustrated in Fig. 22 for 400-micron sand. As system pressure was increased from 1 to 31 bar, the choking velocity decreased from approximately 2.2 to 6.7 m/s for a mass flux of 210 kg/s-m². This occurs because the carrying capacity of a gas increases as the density of the gas increases due to increased drag on the particles. This results in the pressure-drop-per-unit-length-vs.-velocity curves to be shifted to the left on the phase diagram for vertical pneumatic conveying as shown in Fig. 23.

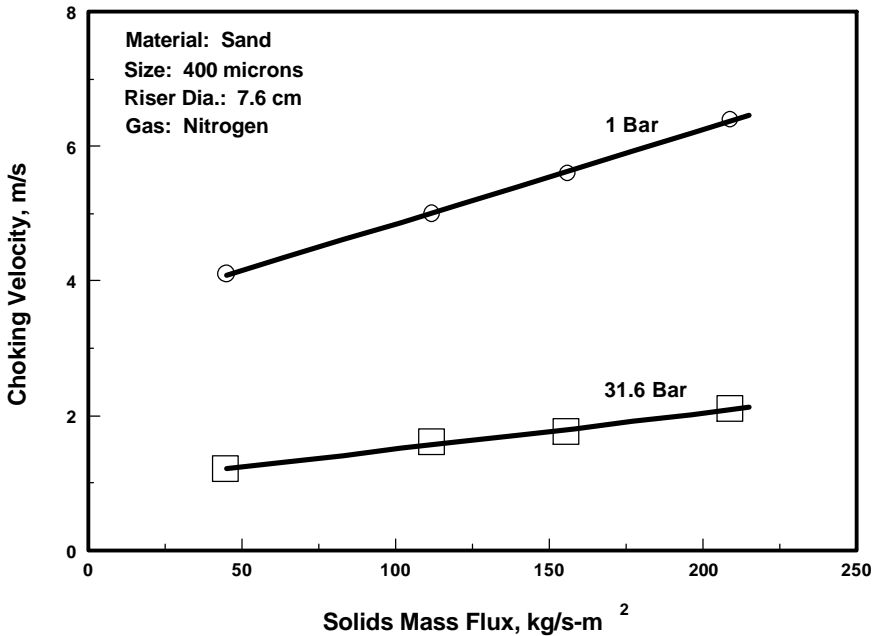


Figure 22. The variation of choking velocity with pressure. (*Knowlton.*)

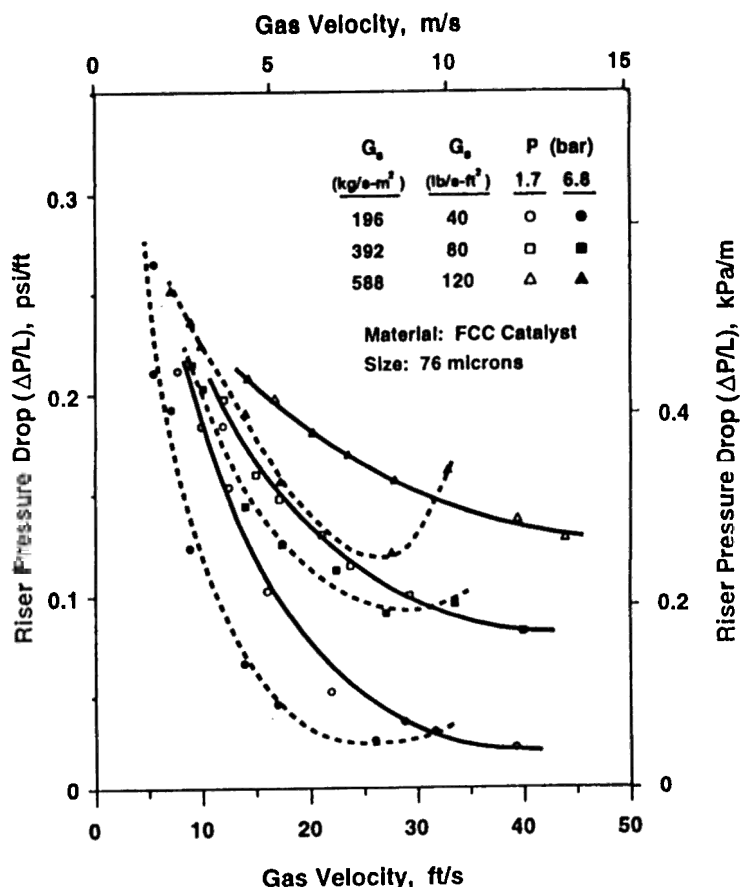


Figure 23. The effect of pressure on riser $\Delta P/L$. (Karri & Knowlton.)

As has been determined by several workers (Bader et al., 1988; Hartge et al., 1988; Horio et al., 1988; Rhodes et al., 1988; Weinstein et al., 1986), a circulating fluidized bed operates in “core-annulus” flow, in which a high-velocity, dilute core is surrounded by a denser, slower-moving annulus. At low circulating mass fluxes (as found in circulating fluidized bed combustors), the solids in the annulus are flowing downward at the wall of the riser. At high circulating mass fluxes, the solids in the annulus flow

up along the wall. Employing the circulating fluidized model of Yang (1988), which assumes that the core region is at choking conditions, and the choking-velocity correlation of Punwani et al. (1976), the annulus thickness in a circulating fluidized bed of catalyst was calculated as a function of pressure. The results showed that the annulus thickness should decrease as system pressure was increased (Fig. 24). Karri and Knowlton (1996) measured riser density as a function of radial position at two different pressures and showed that the annulus thickness does decrease as pressure increases (Fig. 25).

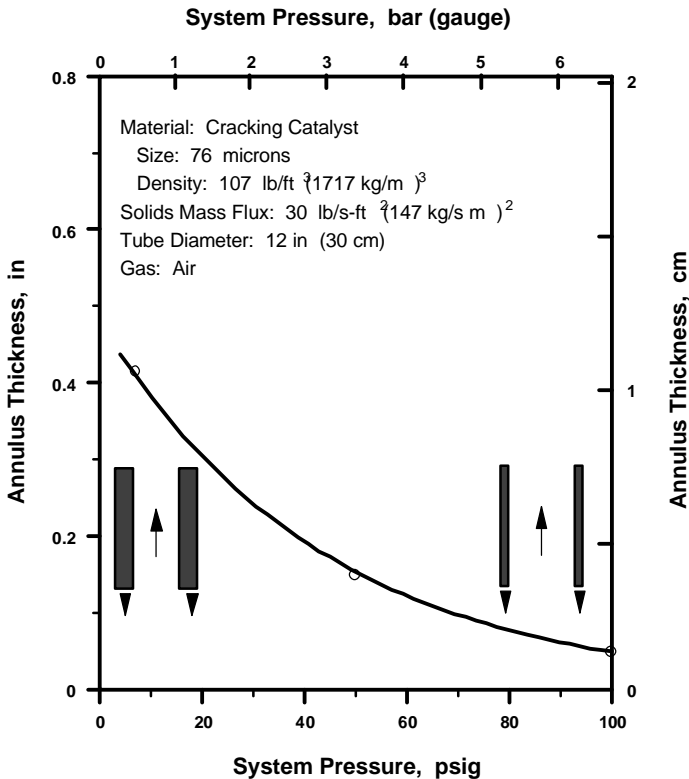


Figure 24. Annulus thickness vs system pressure. (*Calculated from model of Yang.*)

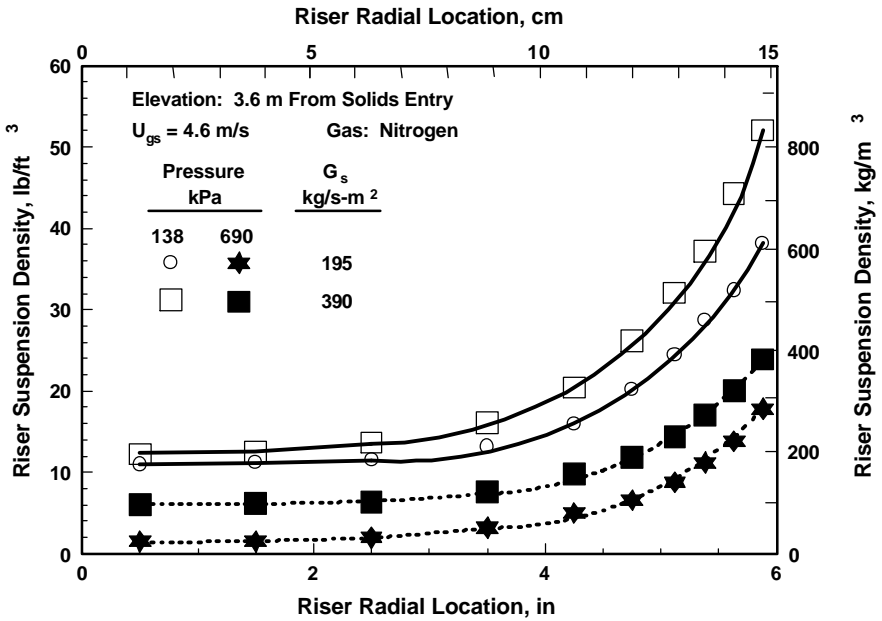


Figure 25. The effect of pressure on radial density distribution in a riser.

1.11 Cyclone Efficiency

Rosin et al. (1932) derived a simple expression for cyclone efficiency for a fixed cyclone diameter based on a force balance on the particle at the cyclone inlet, i.e.,

Eq. (17)
$$E \propto \sqrt{\frac{p N_s U_i (\mathbf{r}_p - \mathbf{r}_g)}{9 m L_w}}$$

This expression indicates that cyclone efficiency should not change with gas density because $(\mathbf{r}_p - \mathbf{r}_g)$ is insensitive to changes in pressure. However, cyclone efficiency should decrease with gas viscosity because it is harder for a particle to travel to the cyclone wall in a more viscous fluid.

There have been relatively few literature articles reporting on the observed effects of temperature and pressure on cyclone efficiency.

Parker et al. (1981) conducted tests with a 5 cm diameter cyclone at temperatures up to 700°C with 20 micron fly ash. They found that cyclone efficiencies decreased with temperature as expected. Patterson and Munz (1989) investigated the effect of temperature on cyclone efficiency up to 1700°C in a 10-cm-diameter cyclone, and also found that cyclone efficiency decreased with temperature. However, this effect was only seen at very small particle sizes (below about 12 microns) where cyclones become relatively inefficient.

According to Eq. (17), pressure should have a negligible effect on cyclone efficiency. However, Parker et al. (1981) reported that gas density caused cyclone efficiency to increase over the pressure range of 2 to 13 atmospheres. Knowlton and Bachovchin (1978) varied system pressure up to 50 atmospheres and found that, at low loadings for a conventional cyclone, the efficiency increased with increasing pressure. At higher loadings, the opposite effect was noticed. As with the studies investigating the effect of temperature, the effect of pressure in both studies was only seen at particle sizes less than about 12 microns. Therefore, for particles greater than about 10 to 15 microns, cyclone efficiency seems to be insensitive to gas properties.

NOTATIONS

Ar = Archimedes number, $g d_p^3 r_g (r_p - r_g)/\mu^2$

C_D = Drag Coefficient

$(C_D)_e$ = Modified drag coefficient:

$$(C_D)_e = C_D \frac{\epsilon^3}{1 + (1 - \epsilon)^{1/3}}$$

D = Tube diameter

d_o = Jet nozzle diameter

d_p = Average particle size

E = Cyclone efficiency

F = Weight fraction of 0–44 micron particles in mixture

148 *Fluidization, Solids Handling, and Processing*

Fr	=	Froude number, U^2/gd_p
Ga	=	Galileo number
g	=	Gravitational constant
h	=	Overall bed-to-surface heat transfer coefficient
h_{gc}	=	Gas convective heat transfer coefficient
h_{pc}	=	Particle convective heat transfer coefficient
h_r	=	Radiant heat transfer coefficient
L	=	Jet penetration length
L_w	=	Width of cyclone inlet
N_s	=	Number of spirals in cyclone
M_i	=	Elasticity modulus for a fluidized bed
M_{mb}	=	Elasticity modulus at minimum bubbling
n	=	Richardson-Zaki exponent
Re_{mf}	=	Reynolds number at minimum fluidization, $d_p U_{mf} \mathbf{r}_g / \mathbf{m}$
Re_p	=	Particle Reynolds number, $d_p U \mathbf{r}_g / \mathbf{m}$
$(Re)_\varepsilon$	=	Modified Reynolds number:

$$(Re)_\varepsilon = Re \left[\frac{1}{\varepsilon \exp\{5(1 - \varepsilon) / 3\varepsilon\}} \right]$$

T_s	=	Sintering temperature
U	=	Superficial gas velocity
U_i	=	Gas inlet velocity to cyclone
U_j	=	Gas velocity through jet or grid port
U_c	=	Superficial gas velocity where the transition from bubbling/slugging to turbulent fluidization begins
U_{ch}	=	Choking velocity
U_k	=	Superficial gas velocity where transition region from bubbling/slugging to turbulent fluidization ends
U_{mb}	=	Minimum bubbling velocity

U_{mf}	=	Minimum fluidization velocity
U_t	=	Terminal velocity
e	=	Voidage
e_d	=	Dense-phase voidage
e_{mb}	=	Dense-phase voidage at minimum bubbling
m	=	Gas viscosity
r_g	=	Gas density
r_p	=	Particle density

REFERENCES

- Abrahamsen, A., and Geldart, D., *Powder Technol.*, 26:35 (1980)
- Barnea, E. and Mizrahi, J., *Chem. Eng. J.*, 5:171 (1973)
- Bader, R., Findlay, J. G., and Knowlton, T. M., *Circulating Fluidized Bed Technol. II*, (Basu, and Large, eds.), p. 123, Pergamon Press (1988)
- Barreto, G. F., Yates, J. G., and Rowe, P. N., *Chem. Eng. Sci.*, 48(12):1935 (1984)
- Baskakov, A. P., Berg, B. V., Virr, O. K., Phillippovsky, N. F., Kirakosyan, V. A., Goldobin, J. M., and Suprun, V. M., *Powder Technol.*, 8:273 (1973)
- Botterill, J. S. M., *Gas Fluidization Technol.*, (Geldart, ed.), p. 220, J. Wiley & Sons (1986)
- Botterill, J. S. M., and Desai, M. *Powder Technol.* 6:231 (1972)
- Botterill, J. S. M., and Teoman, Y. *Fluidization*, (Grace and Matsen, eds.), pp. 93–100, Plenum Press, New York (1980)
- Botterill, J. S. M., Teoman, Y., and Yuregir, K. R., *Powder Technol.*, 31:101 (1982)
- Cai, P., Shen, S. P., Jin, Y., Yu, Z. Q., and Wang, Z. W., *AIChE Symp. Series*, 270(85):37–43 (1989)
- Canada, G. S., and McLaughlin, M. H., *AIChE Symp. Series*, 176(74) (1978)
- Chan, I., and Knowlton, T. M., *Fluidization*, (Kunii and Toei, eds.) (1984)
- Chan, I., and Knowlton, T. M., Presented at 76th AIChE Annual Meeting, San Francisco (1984)
- Chan, I., Sishla, C., and Knowlton, T. M., *Powder Technol.*, 53:217 (1987)
- Clift, R., and Grace, J. R., *Chem. Eng. Sci.*, 29:935 (1972)
- Compo, P., Pfeffer, R., and Tardos, G., *Powder Technol.*, 51:85–101 (1987)

150 *Fluidization, Solids Handling, and Processing*

- Crowther, M. E., and Whitehead, J. C., *Fluidization*, (J. F. Davidson and D. L. Keairns, eds.), pp. 65–70, Cambridge University Press (1978)
- deVries, R. J., Van Swaaij, W. P. M., Mantovani, C., and Heijkoop, A., *Proc. Conf. Chem. Reaction Eng.*, B9–59, Amsterdam (1972)
- Foscolo, P. U., and Gibilaro, L. G., Findlay, J. G., and Knowlton, T. M., Final Report for U.S. Dept. of Energy, Project, DE-AC21-83MC20314 (1985)
- Geldart, D., *Powder Technol.*, 1:285 (1973)
- Geldart, D., and Abrahamsen, A. R., *Powder Technol.*, 19:133–136 (1978)
- Geldart, D., and Abrahamsen, A. R., *Chem. Eng. Prog. Symp. Ser.*, 77(205):160 (1981)
- Geldart, D., and Kapoor, D. S., *Chem. Eng. Sci.*, 31:842–843 (1976)
- Guedes de Carvalho, J. R. F., King, D. F., and Harrison, D., *Fluidization*, (J. F. Davidson, and D. L. Keairns, eds.), pp. 59–64, Cambridge University Press (1978)
- Hartge, E.-U., Rensner, D., and Werther, J., *Circulating Fluidized Bed Technol. II*, (Basu, and Large, eds.), p 165, Pergamon Press (1988)
- Hirsan, I., Sishtla, C., and Knowlton, T. M., Presented at 73rd AIChE Annual Meeting, Chicago (1980)
- Hoffman, A. C., and Yates, J. G., *Chem. Eng. Commun.*, 41:133–149 (1986)
- Horio, M., Morishita, K., Tachibana, O., and Murata, N., *Circulating Fluidized Bed Technol. II*, (Basu and Large, eds.), p. 147, Pergamon Press (1988)
- Institute of Gas Technol. Report No. DOE/MC/19301-10 (1985)
- Jacob, K., and Weimer, A., *AIChE J.*, 33:1698–1706, (1987)
- Kai, T., and Furusaki, S., *J. Chem. Eng. Jpn.*, 18(2) (1985)
- Karri, S. B. R., and Knowlton, T. M., *Circulating Fluidized Bed Technol. III*, (Basu, Horio, and Hasatani, eds.), p. 67 (1991)
- Karri, S. B. R., and Knowlton, T. M., in: *Proc. of Fifth Int'l Conf. on Circulating Fluidized Beds*, paper DB15, Beijing (1996)
- King, D. F., and Harrison, D., *Fluidization*, (Grace and Matsen, eds.), p. 101, Plenum Press, New York (1980)
- Kmiec, A., *Chem. Eng. J.*, 23:133 (1982)
- Knowlton, T. M., Final Report for USDOE Contract No. DE-AC21-82MC19301 (1985)
- Knowlton, T. M., and Bachovchin, D. M., *Fluidization Technol.*, (Keairns, ed.), p. 253, Hemisphere Publishing Corp. (1976)
- Knowlton, T. M., and Bachovchin, D., *Coal Processing Technol.*, 4:122–127 (1978)
- Knowlton, T. M., *AIChE Symp. Series*, 161(73):22–28 (1977)

- Kono, H., *AIChE Symp. Series*, 205 (77):96 (1981)
- Marzocchella, A., and Salatino, P., *AIChE Symp. Series*, (D. King, ed.), 92:25–30 (1996)
- May, W. G., and Russell, F. R., Paper presented at New Jersey Section of A.C.S. Meeting-in-Miniature (1953)
- Mii, T., Yoshida, K., and Kunii, D., *J. Chem. Eng.*, 6:100–102, Japan. (1973)
- Otake, T., Tone, S., Kawashima, M., and Shibata, T., *J. Chem. Eng. Jpn.*, 8(5) (1975)
- Parker, R., Jain, R., Calvert, S., Drehmel, D., and Abbott, J., *Environmental Sci. Technol.*, 15(4):451 (1981)
- Patterson, P., and Munz, R., *Can. J. Chem. Eng.*, 67:321 (1989)
- Punwani, D., Modi, M., and Tarman, P., *Proc. Int'l. Powder and Bulk Solids Handling and Processing Conf.* (1976)
- Rhodes, M., Laussmann, P., Villain, F., and Geldart, D., *Circulating Fluidized Bed Technol. II*, (Basu and Large, eds.), p. 155, Pergamon Press (1988)
- Richardson, S. F., *Fluidization*, (Davidson and Harrison, eds.), Academic Press, London (1971)
- Rietema, K., Cottar, E. J. E., and Piepers, H. W., *Chem. Eng. Sci.*, 48:1687–1697 (1993)
- Rosin, P., Rammler, E., and Intelmann, W., *Zeitschrift Verein Deutscher Ingenieure*, 76:433 (1932)
- Rowe, P. N., *Chem. Eng. Sci.*, 39(1):173 (1984)
- Rowe, P. N., Foscolo, P. U., Hoffman, A. C., and Yates, J. G., *Fluidization*, (Kunii and Toei, eds.), p. 53 (1984)
- Saxena, S., and Vogel, G., *Trans. Inst. Chem. Engrs.*, 55:184 (1977)
- Sakuraya, K., Morinaka, I., Kamiya, K., and Tanaka, M., *Tetsu-to -Hagame*, 65:176 (1976)
- Shrivastava, S., Mathur, S., and Saxena, S., *AIChE J.*, 32(7):1227 (1986)
- Siegell, J. H., *Powder Technol.*, 38:13 (1984)
- Sishtla, C., Personal Communication
- Sishtla, C., Chan, I., Findlay, J., and Knowlton, T. M., *AIChE Symp. Series* 270, 85:83 (1989)
- Sishtla, C., Chan, I., and Knowlton, T. M., *Fluidization V*, (Ostergaard, and Sorenson, eds.), p. 127, Engineering Foundation (1986)
- Sittiphong, N., George, A. H., and Bushnell, D., *Chem. Eng. Sci.*, 36:1260–1263 (1981)
- Sobreiro, L. E. L., and Monteiro, J. L. F., *Powder Technol.*, 33:95 (1982)
- Subzwari, M. P., Clift, R., and Pyle, D. L., *Fluidization*, (Davidson and Keairns, eds.), Cambridge, England (1978)

152 Fluidization, Solids Handling, and Processing

- Takeuchi, H., Hirama, T., Chiba, T., Biswas, J., and Leung, L. S., *Powder Tech.*, 47(2):195–199 (1986)
- Varadi, T., and Grace, J. R., *Fluidization*, (Davidson and Keairns, eds.), Cambridge University Press (1978)
- Weimer, A. W., and Quaderer, G. J., Paper 11e, presented at the 1983 Annual AIChE Meeting, Washington, D.C. (1983)
- Weinstein, H., Shao, M., and Schnitzlein, M., *Circulating Fluidized Bed Technol.*, (Basu, ed.), p. 201, Pergamon Press (1986)
- Wen, C. Y., and Yu, Y. H., *AIChE J.*, 12:610 (1966)
- Wittman, K., Helmrich, H., and Schugerl, K., *Chem. Eng. Sci.*, 36(10):1673 (1981)
- Wu, S. Y., and Baeyens, J., *Powder Technol.*, 67:217–220 (1991)
- Xavier, A. M., King, D. F., Davidson, J. F., and Harrison D., *Fluidization*, (Grace and Matsen, eds.), p. 201, Plenum Press (1980)
- Yang, W.-C., *I & E C Fundamentals*, 20:297 (1981)
- Yang, W.-C., *AIChE J.*, 31(7):1086 (1985)
- Yang, W.-C., *Circulating Fluidized Bed Technol. II*, (Basu and Large, eds.), p. 181, Pergamon Press (1988)
- Yang, W. C., and Chitester, D. C., *AIChE Symp. Series*, 262(84):10–21 (1988)
- Yates, J. G., Bejcek, V., and Cheesman, D. J., *Fluidization V*, (Ostergaard, and Sorenson, eds.), Engineering Foundation, New York (1986)
- Yates, J. G., and Cheesman, *Chem. Eng. Sci.* (1995)
- Yoshida, K. Ueno, T., and Kunii, D., *Chem. Eng. Sci.* 29:77–82 (1974)
- Yoshida, K., Fujii, S., and Kunii, D., *Fluidization Technol.*, (Keairns, ed.), 43–48 (1976)

3

Heat Transfer in Fluidized Beds

John C. Chen

1.0 INTRODUCTION

Fluidized beds are widely used to achieve either chemical reactions or physical processing that require interfacial contact between gas and particles. Heat transfer is important in many of these applications, either to obtain energy transfer between the solid and gas phases or to obtain energy transfer between the two-phase mixture and a heating/cooling medium. The latter case is particularly important for fluidized bed reactors which require heat addition or extraction in order to achieve thermal control with heats of reaction.

Heat transfer between gas and particle phases tend to be efficient due to the large volumetric concentration of interface surface. Hence this topic is rarely of significant concern and will not be dealt with in this chapter. Most of the chapter concerns heat transfer between the two-phase medium and submerged surfaces. This is the most pertinent engineering problem since heat addition or extraction from the fluidized or conveyed mixture is commonly achieved by use of heat exchangers integral to the vessel wall or submerged in the particle/gas medium.

As discussed in other chapters of this book, two-phase flows of gas and particles occur with different flow regimes. The mechanisms for heat transfer and the resulting heat transfer coefficients are strongly affected by the different flow characteristics, resulting in different design correlations and predictive models for each flow regime. This chapter will deal with the two most often encountered flow regimes:

- Bubbling dense fluidization
- Circulating fast fluidization

2.0 BUBBLING DENSE FLUIDIZATION

2.1 Hydrodynamic Characteristic

The key characteristic of fluidized beds is the levitation of solid particles against gravity by shear-drag of the flowing gas. The resulting two-phase mixture of gas and particles behaves as a “fluid” in its response to pressure gradients. Upward flow of gas past solid particles can be classified into several fluidization regimes. At low flow rates, the gas percolates through the void spaces between stationary particles; this is termed *flow through packed beds*. With increasing gas velocity, a point is reached when the drag force between particles and fluid counterbalances the gravitational force on the particles resulting in suspension of particles by the upward flowing gas. This is the point of minimum fluidization, marking the transition from packed to fluidized beds. Particles of Geldart (1973) classification A or B (diameters in range of 50 to 500 μm and densities in range of 0.3 to 3 gm/cm^3) can be smoothly fluidized. For such particles, gas velocities above the minimum fluidization value result in bubbling fluidization wherein some fraction of the gas flows as discrete bubbles through the mobile mixture of suspended particles. The upper limit of gas velocity for bubbling dense fluidization occurs when interfacial drag becomes sufficient to entrain the particles and transport them upward through the vessel. Thus bubbling fluidization is bounded between gas velocities for minimum fluidization and terminal transport.

Using the Ergun (1952) equation for the interfacial friction factor, Wen and Yu (1966) derived the following general equation to estimate the minimum fluidization superficial velocity U_{mf} for spherical particles:

$$\text{Eq. (1)} \quad Re_{mf} = \left[(33.7)^2 + 0.0408 Ar \right]^{1/2} - 33.7$$

where

Re_{mf} = particle Reynolds number at

$$U_{mf} = \frac{u_{mf} d_p \mathbf{r}_g}{m_g}$$

$$Ar \text{ (Archimedes number)} = \frac{d_p^3 \mathbf{r}_g (\mathbf{r}_s - \mathbf{r}_g) g}{m_g^2}$$

By definition, the terminal velocity of a particle (u_t) is the superficial gas velocity which suspends an isolated particle without translational motion—i.e., the terminal free fall velocity for that particle. From force balance on the particle, the terminal velocity for an approximately spherical particle can be shown to be

$$\text{Eq. (2)} \quad u_t = \frac{4gd_p (\mathbf{r}_s - \mathbf{r}_g)^{1/2}}{3\mathbf{r}_g C_D}$$

where C_D is the drag coefficient for that particle. The magnitude of C_D depends on the particle Reynolds number at the terminal velocity, as given by Fox and McDonald (1992) or other fluid dynamic texts.

2.2 Heat Transfer to Submerged Surfaces

General Characteristics. Tubes carrying cooling or heating fluids are often submerged in bubbling fluidized beds to extract or add thermal energy. The effective heat transfer coefficient at the surface of such tubes are of engineering interest and has been the objective of numerous experimental studies. Figure 1 shows representative data measured by Chandran, Chen and Staub (1980) for a horizontal tube submerged in bubbling fluidized bed of spherical glass particles. The heat transfer coefficient is plotted as a function of the gas velocity in excess of the minimum fluidization velocity ($u_g - u_{mf}$). Typical characteristics are noted as:

- Heat transfer coefficient increases steeply as gas velocity exceeds minimum fluidization velocity
- A maximum value of the heat transfer coefficient is attained at some specific velocity which depends on the particle size.
- Beyond the maximum point, the heat transfer coefficient is almost constant, declining slightly as excess velocity increases.
- The absolute magnitude of the heat transfer coefficient is several folds greater than single-phase gas convection at the same superficial velocity.
- The heat transfer coefficient increases with decreasing particle size.

Similar behavior has been reported by other researchers for both vertical and horizontal tubes, though the magnitude of the heat transfer coefficients change with operating conditions, (Mickley and Trilling, 1949; Vreedenberg, 1960; Botterill and Desai, 1972; Ozkaynak and Chen, 1980).

One extra complication for horizontally submerged heat-transfer tubes is the lack of circumferential symmetry, as found in vertically placed tubes. The data in Fig. 1 represents averaged heat transfer coefficients around the entire circumference of the horizontal tube. The experiments of Chandran, Staub and Chen (1980) showed that the local heat transfer coefficients can actually vary significantly at different circumferential positions. The polar plot reproduced in Fig. 2 shows some results for a horizontal tube in a bubbling bed of glass spheres, for three different particle sizes. It is seen that there is substantial variation of the local heat transfer coefficient around the tube circumference. For small particles, the maximum heat transfer coefficient is found at the bottom and sides of the horizontal tube. The heat transfer coefficient at the top of the tube is noticeably smaller, implying the existence of a stagnant cap of solid particles which tends to insulate the heat transfer surface. An increase in particle size caused a decrease in heat transfer coefficients at the side and bottom segments while increasing the heat transfer coefficient at the top of the tube. For the largest particle size, a fairly uniform heat transfer coefficient is obtained, albeit with smaller magnitude when compared to the heat transfer coefficient for smaller particles. Similar observations have been made by Berg and Baskakov (1974), Gelperin et al., (1968, 1971) and Saxena et al. (1978). Evidently the nature of particle-surface contact and the subsequent heat transfer mechanism is different for different circumferential positions around the horizontal tube, and varies with gas flow rate.

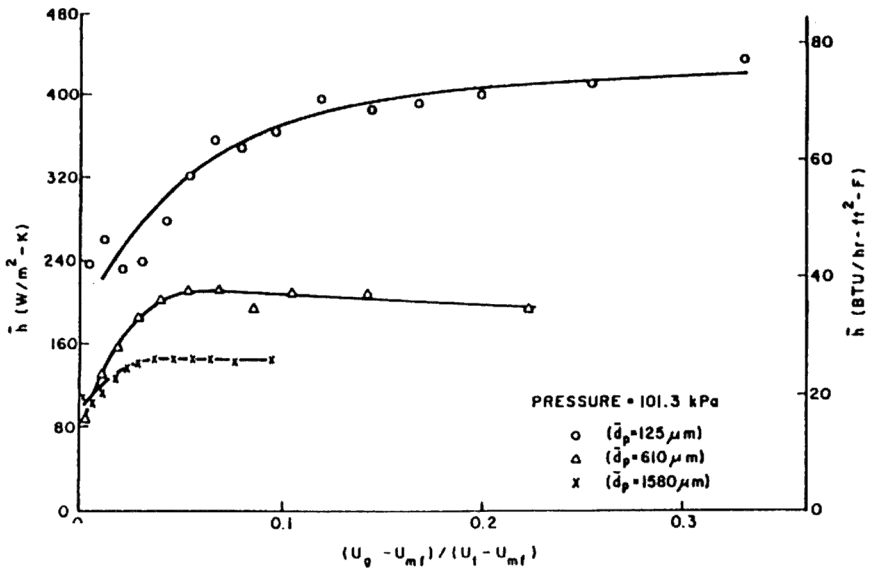


Figure 1. Average heat transfer coefficients at surface of horizontal tube in bubbling fluidized bed. (From Chandran, Chen and Staub, 1980.)

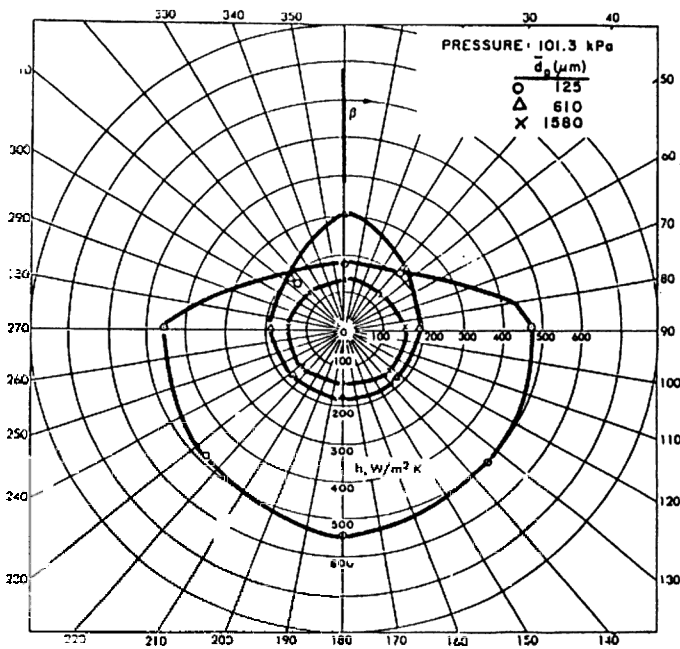


Figure 2. Local heat transfer coefficients around circumference of a horizontal tube in bubbling fluidized bed. $(U_g - U_{mf}) / (U_t - U_{mf}) \sim 0.1$. (From Chandran, Chen and Staub, 1980.)

Most practical cases involve multi-rows of tubes, which can affect bed side heat transfer coefficient by altering the dynamic behavior of the fluidized medium. Wood et al. (1978) showed that presence of a horizontal tube bank can suppress slugging by breaking up the bubbles. The bed becomes more uniform as compared to a similar bed without a tube bank. As a consequence, heat transfer coefficients may decrease up to 20% at gas velocities that correspond to slugging regime. At higher gas flow rates, this effect is reduced due to uniform nature of bubbling with or without tube banks. Tests made at atmospheric pressure further showed that heat transfer coefficients were independent of location (i.e., row or column number in the tube bank). Tamarin et al. (1976) also observed stabilizing effect of horizontal tube banks on bed side heat transfer coefficients. For vertically placed tube banks, however, Noë and Knudsen (1968) did not observe any change in measured heat transfer coefficients of single or multi tubes.

Parametric Effects. The heat transfer coefficient at submerged surfaces in bubbling fluidized beds is affected by a number of operating parameters. Two of these parametric effects are illustrated by the data of Jacob and Osberg (1957). As seen from Fig. 3, the maximum value of the heat transfer coefficient is significantly affected by the particle size as well as by the thermal conductivity of the fluidizing gas. With a constant gas conductivity, diminishing the particle diameter by an order of magnitude caused 150% increase in the heat transfer coefficient. For a relatively small particle ($d_p = 0.062$ mm), increasing the gas conductivity from 0.05 to 0.2 w/m•k caused an increase of 100% in the maximum heat transfer coefficient.

Since the heat transfer coefficient is known to vary with particle size for fluidized beds of uniformly sized particles, there is a question of how mixtures of different size particles might affect the heat transfer. Biyikli and Chen (1982) measured local and circumferentially-averaged heat transfer coefficients for horizontal tubes immersed in bubbling beds with mixtures of different-sized glass beads. Figure 4a shows the particle size distribution used in their experiments; the weight-mean averaged diameter is given in the legend for each mixture. Figure 4b shows the results, indicating the circumferentially averaged heat transfer coefficient as a function of superficial gas velocity for each mixture. It is seen that the heat transfer coefficient increased continuously as the mean particle size of the mixture decreased. For all mixtures, the qualitative variation of the average

heat transfer coefficient with superficial gas velocity is consistent, showing a slow decline in the value of the coefficient with increasing gas velocity—similar to behavior found for beds of uniformly sized particles. These authors further reported that the mean particle diameter could be used in correlations to calculate the average heat transfer coefficient with reasonably success (deviation band of $\pm 25\%$).

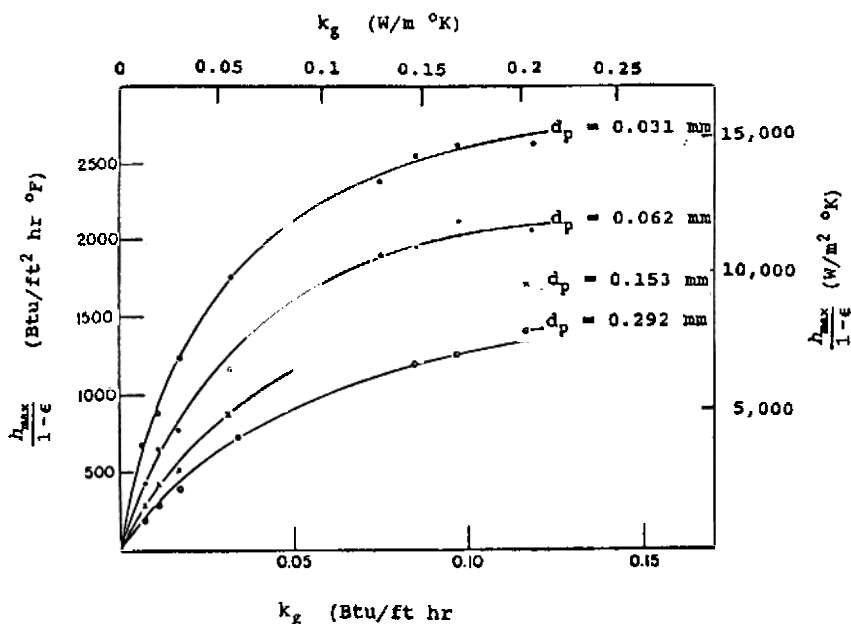


Figure 3. Parametric effects of particle size and gas conductivity. (Data of Jacob and Osberg, 1957).

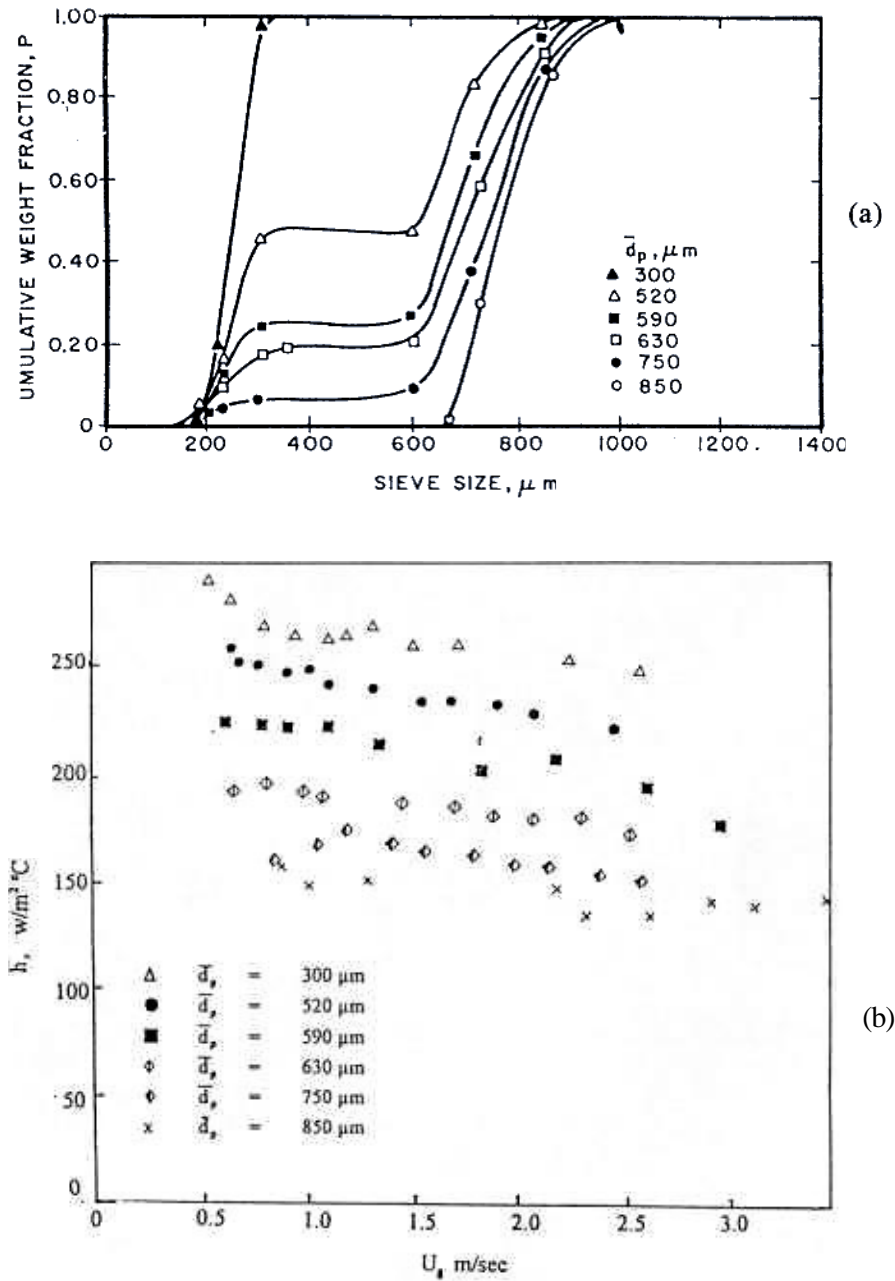


Figure 4. Effect of mixed particle sizes. (a) Particle size distribution. (b) Circumferential-average heat transfer coefficients. (Data of Biyikli and Chen, 1982).

In as much as system pressure affects thermodynamic and transport properties of the fluidizing gas, one would expect that the heat transfer coefficients would also be affected by pressure. Of particular importance is the reduction in both minimum fluidization velocity (u_{mf}) and terminal velocity (u_t) with increasing gas pressure, due to changes in gas density and viscosity. One finds that the plot of heat transfer coefficient versus superficial gas velocity shifts, with higher heat transfer coefficients occurring at lower velocities as pressure increases. This effect is illustrated by the data of Bock and Schweinzer (1986), as adapted by Kunii and Levenspiel (1991). As seen in Fig. 5, for bubbling bed of fairly large particles ($d_p = 970 \mu\text{m}$), increasing gas pressure from 1 to 25 atmospheres caused the heat transfer coefficient to increase by as much as 400%.

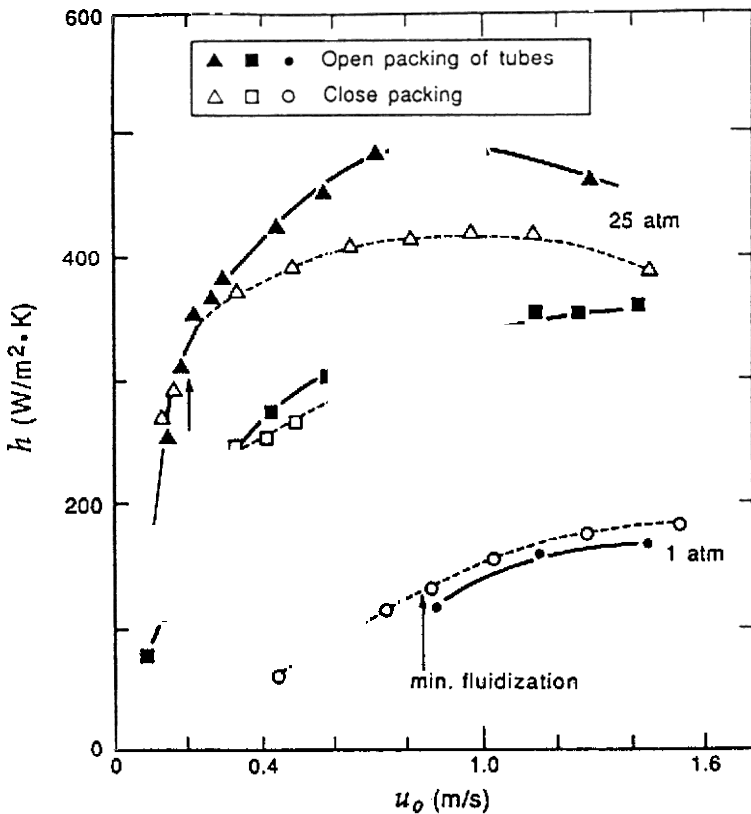


Figure 5. Effect of system pressure on heat transfer in bubbling fluidized bed. (Data of Bock and Schweinzer, 1986, as adapted by Kunii and Levenspiel, 1991.)

In contrast to the strong effect of gas properties, it has been found that the thermal properties of the solid particles have relatively small effect on the heat transfer coefficient in bubbling fluidized beds. This appears to be counter-intuitive since much of the thermal transport process at the submerged heat transfer surface is presumed to be associated with contact between solid particles and the heat transfer surface. Nevertheless, experimental measurements such as those of Ziegler et al. (1964) indicate that the heat transfer coefficient was essentially independent of particle thermal conductivity and varied only mildly with particle heat capacity. These investigators measured heat transfer coefficients in bubbling fluidized beds of different metallic particles which had essentially the same solid density but varied in thermal conductivity by a factor of nine and in heat capacity by a factor of two.

Temperature of the fluidized bed is another parameter that could influence the heat transfer coefficient. Increasing bed temperature affects not only the physical properties of the gas and solid phases, but also increases radiative heat transfer. Yoshida et al. (1974) obtained measurements up to 1100°C for bubbling beds of aluminum oxide particles with 180 μm diameter. Their results, shown in Fig. 6, indicate an increase of over 100% in the heat transfer coefficient as the bed temperature increased from 500 to 1000°C. Very similar results were reported by Ozkaynak et al. (1983) who obtained measurements for bubbling beds of sand particles ($d_p = 1030 \mu\text{m}$) at temperatures up to 800°C.

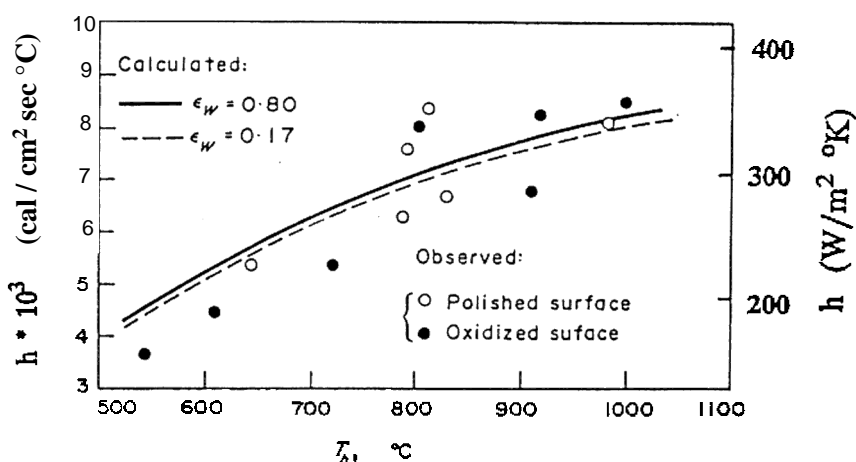


Figure 6. Effect of bed temperature on heat transfer coefficient for bubbling bed of ceramic particles. (Data of Yoshida, Ueno and Kunii, 1974.)

For relatively shallow fluidized beds (bed depths of less than 0.1 m) it appears that the bed height itself is a parameter that affects the heat transfer coefficient at submerged surfaces. Experiments carried out by Liu et al. (1986) in shallow fluidized beds of 175 μm diameter sand particles showed that the maximum heat transfer coefficient, at optimal gas velocity and tube elevation, increased steeply with bed height, reaching a maximum at a height of approximately 30 mm before declining gradually with further increases in bed height. This parametric effect is significant only for shallow beds and would be of little consequence in most commercial applications which have bed heights greater than 0.5 m.

Models and Correlations. For bubbling dense beds, it is recognized that mechanisms contributing to heat transfer at submerged surfaces include gaseous convection during times of bubble contact, particle conduction/convection during times of solid contact, and radiation in the case of high temperature operation. The effective heat transfer coefficient is often represented as the sum of the coefficients for various contributing mechanisms,

$$\text{Eq. (3)} \qquad h = f_\ell h_\ell + (1 - f_\ell) h_d + h_r$$

- where h = total effective heat transfer coefficient
- h_ℓ = heat transfer coefficient for “lean” gas phase contact
- h_d = heat transfer coefficient for “dense” (particle) phase contact
- h_r = heat transfer coefficient for radiation
- f_ℓ = time fraction of contact by lean phase

This additive representation is itself an assumption—that the various mechanisms can be superimposed, weighted by the time fraction of lean gas contact or dense particle contact at the heat transfer surface. Most researchers concur that for bubbling fluidized beds, the lean/gas convection is relatively unimportant and can often be ignored (Kunii and Levenspiel, 1991; Ozkaynak and Chen, 1980). Most modeling efforts have been focused on the dense/particle phase contribution, $(1 - f_\ell) h_d$, or on the total convective contribution $[f_\ell h_\ell + (1 - f_\ell) h_d] = h_c$. Examination of the literature reveals that the modeling approaches fall into four groups, each

emphasizing a particular mechanism for heat transport: (i) transient conduction during short contacts by particle packets, (ii) particle disruption of convective boundary layer, (iii) gaseous convection through interstitial spaces between particles packed at the heat transfer surface, and (iv) energy transport due to random motion of the particles. Each of these approaches are briefly reviewed below.

The first type of model considers the heat transfer surface to be contacted alternately by gas bubbles and packets of closely packed particles. This leads to a surface renewal process whereby heat transfer occurs primarily by transient conduction between the heat transfer surface and the particle packets during their time of residence at the surface. Mickley and Fairbanks (1955) provided the first analysis of this renewal mechanism. Treating the particle packet as a pseudo-homogeneous medium with solid volume fraction, $\epsilon_{s,pa}$, and thermal conductivity (k_{pa}), they solved the transient conduction equation to obtain the following expression for the average heat transfer coefficient due to particle packets,

$$\text{Eq. (4)} \quad h_{pa} = 2 \left[\frac{k_{pa} \mathbf{r}_s C_{ps} \epsilon_{s,pa}}{\rho \mathbf{t}_{pa}} \right]^{1/2}$$

where \mathbf{t}_{pa} is the root-square average residence time for packets on the heat transfer surface, summed over all packets,

$$\text{Eq. (5)} \quad \mathbf{t}_{pa} = \left[\frac{\sum \mathbf{t}}{\sum (\mathbf{t})^{1/2}} \right]^2$$

Assuming that this packet renewal mechanism accounts for all the heat transfer associated with the particle phase, h_{pa} can be equated to h_d in Eq. (3).

This packet renewal model has been widely accepted and in the years since 1955 many researchers have proposed various modifications in attempts to improve the Mickley-Fairbanks representation. Several of these modifications dealt with the details of the thermal transport process between the heat transfer surface and the particle packet. The original Mickley-Fairbanks model treated the packet as a pseudo-homogeneous medium with a constant "effective thermal conductivity," suggesting that

some correlation such as that of Yagi and Kunii (1957) be used to estimate the value k_{pa} . In an alternate treatment, Botterill and Williams (1963) numerically solved the transient conduction problem for a single layer of closely packed spheres in a stagnant fluid at the heat transfer surface. They reported that for particles with diameters less than 200 μm , the solid temperature in the particles approached the temperature of the heat transfer surface in as little as 10 ms. This approach was later extended by Botterill et al. (1967) to multiple layers of particles close packed on the surface in a triangular lattice geometry. While such numerical analysis can represent the transient thermal process, it requires individual solutions for different particle material, particle size, and type of fluid. To alleviate this difficulty, a number of authors recognized that particles packed at a flat surface tend to have only point contacts so that an equivalent gas film separates the packed particles from the surface. Investigators who used this concept of a film resistance to modify the packet theory include Baskakov (1964), and Xavier and Davidson (1978). Gabor (1970) further extended this approach and modeled packets as alternating slabs of gas and solid. He reported that empirical agreement between model and experiment could be obtained by choosing a gas gap of $0.015 d_p$ between particles and $0.0075 d_p$ between the wall and the first particle layer. Kubie and Broughton (1975) suggested that this film resistance can be represented more realistically by Kunii and Smith's relationship for effective thermal conductivity (1960) if the local void fraction is allowed to vary as a function of distance away from the heat transfer surface. For spherical particles, the local voidage varies with distance from the wall as a damped oscillation curve with minimum voidage at approximately one particle radius from the surface. This approach results in an effective thermal conductivity that varies with position, requiring a numerical solution of the transient conduction equation for packet heat transfer. Ozkaynak and Chen (1980) suggested a pragmatic simplification of Kubie and Broughton's approach which removed the need for numerical computations. They suggested that the packet has an effective void fraction equivalent to that of a packed bed at a distance half of the thermal penetration depth from the wall. The penetration depth was defined as the distance where the packet attains 90% of the temperature difference between wall and bulk bed during its time of residence. For long contact times or small particles, where the penetration depth is more than two particle diameters, the average packet void fraction is taken to be that of a bulk packed bed. For large particles or

short residence times, where the penetration depth is less than two particle diameters, the effective void fraction is taken to be

Eq. (6)
$$e_{g,pa} = e_{g,pa}^\infty - 3.04 \log \left(\frac{y}{d_p} \right) \text{ for } \frac{y}{d_p} < 1$$

where $e_{g,pa}^\infty$ = void fraction of bulk packing. Using this effective void fraction, these authors were able to calculate packet conductivities using some model such as that of Kunii and Smith (1960) or Yagi and Kunii (1957), and to directly apply the packet model of Mickley and Fairbanks (Eq. 4). This modified packet theory was found to give good agreement with experimental measurements as shown in Fig. 7.

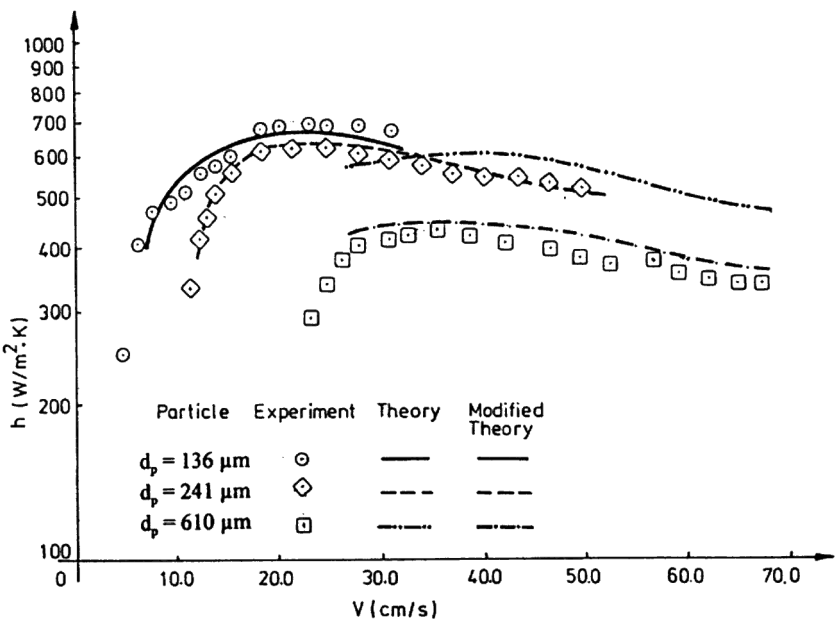


Figure 7. Comparison of data with packet theory, as modified by Ozkaynak and Chen (1980).

The second approach assigns thermal resistance to a gaseous boundary layer at the heat transfer surface. The enhancement of heat transfer found in fluidized beds is then attributed to the scouring action of solid particles on the gas film, decreasing the “effective film thickness.” The early works of Leva et al. (1949), Dow and Jacob (1951), and Levenspiel and Walton (1954) utilized this approach. Models following this approach generally attempt to correlate a heat transfer Nusselt number in terms of the fluid Prandtl number and a modified Reynolds number with either the particle diameter or the tube diameter as the characteristic length scale. Examples are:

Leva correlation for vertical surfaces, for larger particles (1952),

Eq. (7)
$$Nu = \frac{h_c d_p}{k_g} = 0.525 (Re_p)^{0.75}$$

where
$$Re_p = \frac{d_p \rho_g u}{\mu_g}$$

Vreedenberg correlation for horizontal tubes (1958),

Eq. (8)
$$Nu = \frac{h_c D_t}{k_g} = 420 \left(\frac{r_s}{r_g} Re_t \right)^{0.3} \left(\frac{m_g^2}{g r_s^2 d_p^3} \right)^{0.3} (Pr_g)^{0.3}$$

$$\text{for } \left(\frac{\rho_s}{\rho_g} Re_t \right) > 2250$$

where
$$Re_t = \frac{D_t \rho_g u}{\mu_g}$$

It should be noted that in this approach, only the convective contribution to heat transfer is considered. Chen (1976) tested five different correlations, (Vreedenberg, 1958; Wender et al., 1958; Miller et al., 1951), for vertical tubes against a uniform set of experimental data obtained by Ozkaynak (1974). Figure 8 shows a comparison of the correlations and the experimental data, for a fluidized bed of 240 μm diameter glass spheres at room temperature. It is seen that there is very little agreement between the various correlations or between correlation and data. The uncertainty is of the order of 100%.

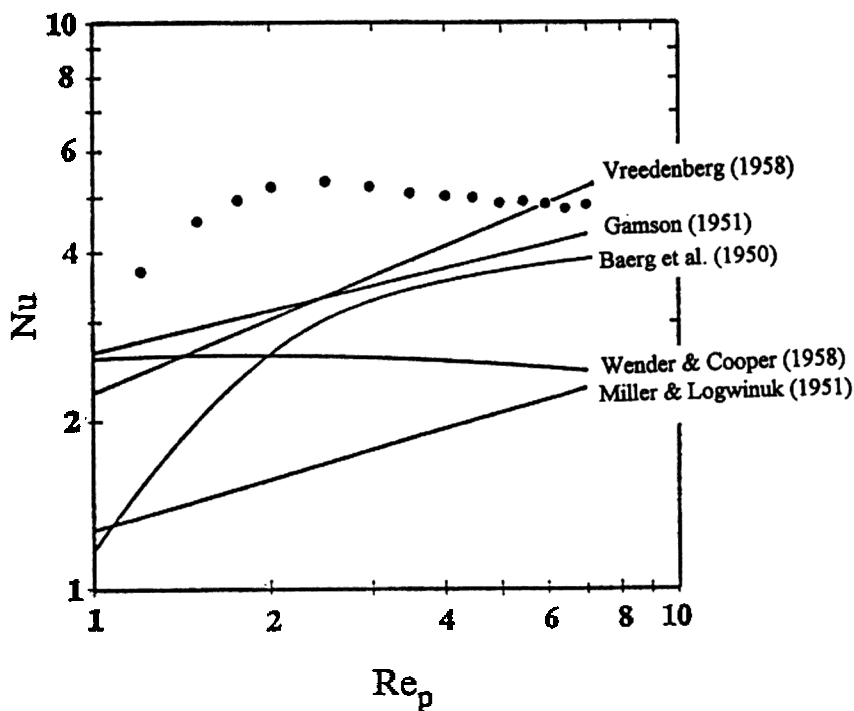


Figure 8. Comparison of data with convective correlations for vertical tube in bubbling bed of 240 μm particles. (From Chen, 1974.)

Recently, Borodulya et al. (1989, 1991) described the gas film in terms of an effective conductivity divided by an effective conduction path length. Correlation of their model with experimental data gave the following equation,

$$\text{Eq. (9)} \quad Nu = 0.74 \, Ar^{0.1} \left(\frac{r_s}{r_g} \right)^{0.14} \left(\frac{C_s}{C_g} \right)^{0.24} e_s^{2/3} + 0.46 RePr \frac{e_s^{2/3}}{e_g}$$

where the first term represents particle convection and the second term represents gas convection. Equation (9) is claimed to be good for the following ranges of parameters:

$$0.1 \leq d_p \leq 4.0 \text{ mm}$$

$$0.1 \leq p \leq 10.00 \text{ MPa}$$

$$140 \leq Ar \leq 1.1 \times 10^7$$

The correlation was tested against nine experimental sets of data with a mean-square error of 22%. Visser and Valk (1993) subsequently modified the particle convection term of the model of Borodulya et al. for low gas velocities. Their results indicated improved agreement for low velocity ranges.

In 1989 Molerus and Schweinzer (1989) presented an interesting variation of this approach. These investigators reasoned that the combined convective component of heat transfer is dominated by gas convection through the matrix of particles in the vicinity of the heat transfer surface, for beds of large particles and/or at increased system pressures. Noting that this same concept would hold for packed (fixed) beds, they then developed a nondimensional correlation which is valid for fixed beds as well as for fluidized beds of Geldart's group D particles. The convective heat transfer Nusselt number was correlated to a nondimensional group which represents the pressure drop in the bed. In fixed bed regime, the Nusselt number varies as a function of Reynolds and Euler numbers. When the gas velocity exceeds that at minimum fluidization, the bed pressure drop and the convective Nusselt number becomes constant for a given type of particles, independent of gas velocity. In the fluidized regime, the correlation of

Molerus and Schweinzer is given by the following equation for spherical (or nearly spherical) particles.

$$\text{Eq. (10)} \quad Nu = 0.0247 (Ar)^{0.4304} (Pr)^{0.33}$$

where
$$Nu = \frac{h_c d_p}{k_g}$$

$$Ar = \frac{g d_p^3 (r_s - r_g)}{r_g \nu^2}$$

$$Pr = \left(\frac{C_p \mu}{k} \right)_g$$

Figure 9 shows comparison of this model with experimental data obtained at three different pressures. The solid curve represents the relationship for fixed beds, while the dashed lines represent the behavior for fluidized beds (i.e., Eq. 10) upon exceeding minimum fluidization.

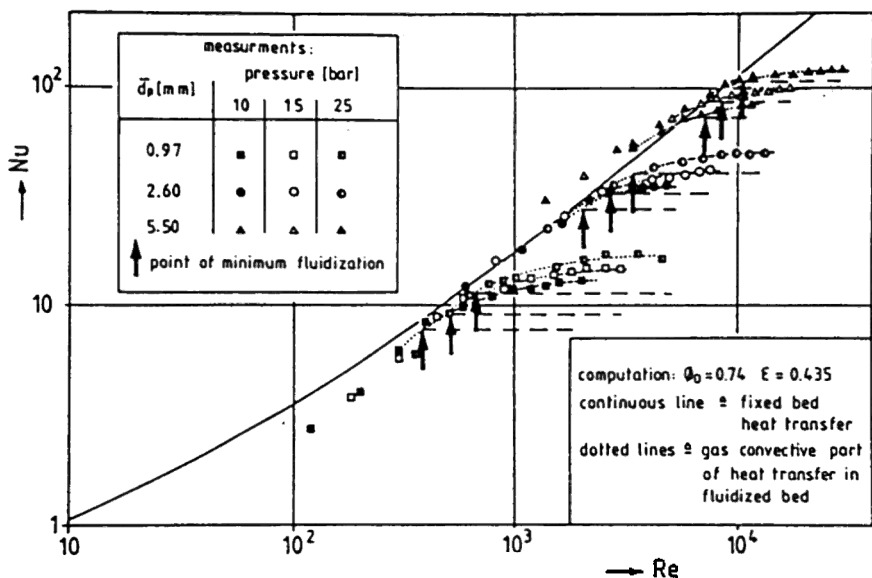


Figure 9. Comparison of data with correlation of Molerus and Schweinzer (1989).

The analyses reviewed above were concerned with the contribution due to dense-particle phase conduction/convection. As noted earlier, experimental measurements do indicate that the total heat transfer coefficient increases with increasing temperature. Some significant portion of this increase may be attributed to changes in the physical properties of the gas and solid phases with temperature, resulting in altered hydrodynamics and increasing the dense phase heat transfer coefficient (h_d). There are contradictory opinions regarding the significance of radiative heat transfer. Ozkaynak et al. (1983) summarized the results from eight different investigations and found significant disagreement regarding the importance of radiative heat transfer. For fluidized beds of approximately the same size particles at a common bed temperature of 1,000°C, the radiative contribution to total heat transfer reported by three different investigations varied from 2% to 21%. Ozkaynak's experiments showed that at bed temperatures below 500°C, the radiant contribution to total heat transfer is less than 15%. Radiant contribution increases linearly with bed temperature, becoming greater than 35% when bed temperature exceeds 800°C. The fact that this increase was not more rapid, i.e., proportional to fourth power of absolute temperature, may be attributed to the fact that convective/conductive heat transfer also increased with temperature due to changes in physical properties of the gas.

The models proposed to represent radiation transport process can be grouped into two classes. The first and simpler approach is to use some form of the Stefan-Boltzmann equation for radiant exchange between opaque gray bodies,

$$\text{Eq. (11)} \quad q_r = \frac{s (T_b^4 - T_w^4)}{\frac{A_w}{A_b} \left(\frac{1 - e_b}{e_b} \right) + \frac{1}{F} + \left(\frac{1 - e_w}{e_w} \right)}$$

where F is the view factor from wall to bed

The investigation of Ozkaynak et al. (1983), with direct experimental measurements of radiant heat flux, provides indications of the magnitude and temperature dependence of the effective bed emissivity. Taking e_w and F both to be unity, these investigators calculated that the effective bed emissivity for particles like sand is in the range of 0.8 to 1.0 at bed temperatures where radiation might be significant (greater than 700°C) and is fairly insensitive to the superficial gas velocity. Thus, a very simple, approximate model for radiant heat transfer in bubbling fluidized beds would be Eq. (11), with $A_b = A_w$, $F = 1$, $e_w = 1$, and e_w approximately equal to 0.9.

The second type of model takes a more physical representation of the radiant transport process. Generally, these models recognize that radiant photons are emitted, absorbed, and scattered by the solid particles in the fluidized bed. Bhattacharya and Harrison (1976) utilized this approach to modify the alternating layer model of Vedomurthy and Sastri (1974) by permitting radiation exchange from one layer of particles with 25 neighboring layers. The emulsion particles were treated as an absorbing and emitting medium so that radiation was attenuated exponentially with distance. A more rigorous model was presented by Chen and Chen (1981) whereby the Mickley-Fairbanks packet model was modified to include simultaneous radiative and conductive heat transfer during alternating contact of the heat transfer surface with gas bubbles and particle packets. The gas phase was taken to be transparent to thermal radiation while the particle packet was treated as a radiatively participative medium with absorption and scattering. During bubble contact, radiation was directly exchanged between parallel surfaces representing the heat transfer wall and the boundary of the bubble. During packet contact, Hamaker's two-flux formulation of radiant transport was used to describe the absorption, scattering, and emission process within the packet

$$\frac{dI}{dy} = -(A + S)I + SJ + AS T^4$$

Eq. (12)
$$\frac{dJ}{dy} = (A + S)J - SI - AS T^4$$

where I, J = forward and backward radiant fluxes, respectively
 A = volumetric absorption coefficient
 S = volumetric scattering coefficient

The one dimensional transient energy equation completed the system of equations.

Eq. (13)
$$k_{pa} \frac{\partial^2 T}{\partial y^2} + A(I + J) - 2AS T^4 = r_s C_{ps} (1 - e_{s,pa}) \frac{\partial T}{\partial t}$$

These authors numerically solved the system of equations with appropriate boundary conditions to derive the time-averaged radiant and conductive heat fluxes between the fluidized bed and the heat transfer surface. Using

approximate estimates for the radiant absorption and scattering coefficients, as well as for the packet residence times, this model was shown to agree with the experimental data of Baskakov et al. (1973) Brewster and Tien (1982) made a significant contribution to the solution of this problem by showing that particles act as independent point scatters as long as the interparticle clearance is greater than 1/3 wave lengths. The implication is that almost all packed or fluidized beds can be approximated as media of independent scatterers, thereby permitting direct estimation of the volumetric scattering coefficient from properties of individual particles. Cimini and Chen (1987) used a modulated flux technique to measure radiant transmission through both packed and fluidized beds of different size glass spheres. Their data showed that the independent scattering approximation gave a reasonable, though slightly low, prediction of the radiation transmission.

3.0 CIRCULATING FAST FLUIDIZATION

3.1 Hydrodynamic Characteristics

As noted earlier, increasing gas velocity for any given fluidized bed beyond the terminal velocity of bed particles leads to upward entrainment of particles out of the bed. To maintain solid concentration in the fluidized bed, an equal flux of solid particles must be injected at the bottom of the bed as makeup. Operation in this regime, with balanced injection of particles into the bed and entrainment of particles out of the bed, may be termed "fast fluidization," FFB. Figure 10 presents an approximate map of this fast fluidization regime, in terms of a dimensionless gas velocity and dimensionless particle diameter.

$$u^* = u \left[\frac{\mathbf{r}_g^2}{\mathbf{m}_g \left(\frac{\mathbf{r}_s - \mathbf{r}_g}{g} \right)} \right]^{1/3}$$

Eq. (14)

$$d_p^* = d_p \left[\frac{\mathbf{r}_g (\mathbf{r}_s - \mathbf{r}_g) g}{\mathbf{m}_g^2} \right]^{1/3} = Ar^{1/3}$$

It is seen that for Geldart types A and B particles, fast fluidization requires superficial gas velocities approximately an order of magnitude greater than that for bubbling dense beds. In many applications of fast fluidization, the particles exiting top of the bed are captured by cyclones and recirculated for makeup injection at the bottom of the bed, hence this regime is also denoted as “circulating fluidization,” CFB.

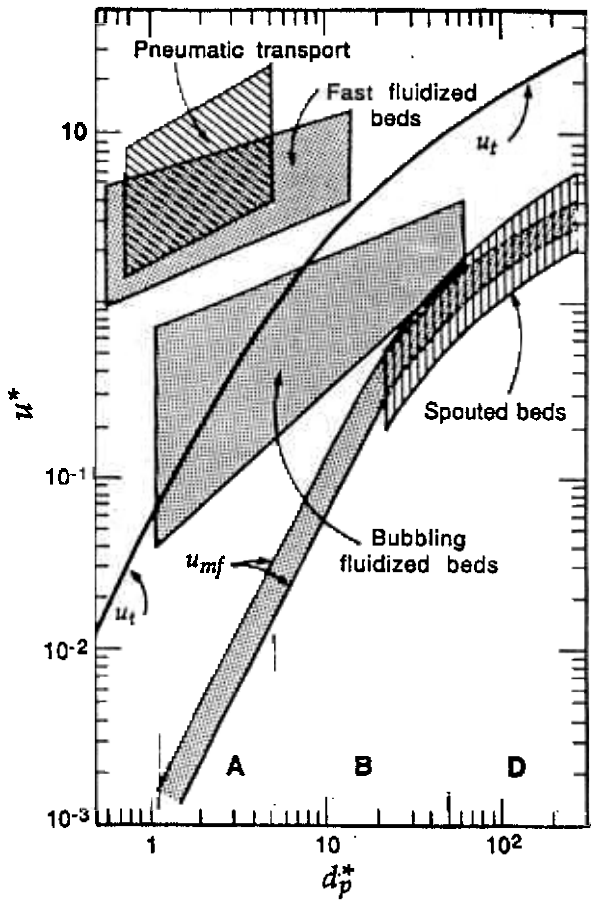


Figure 10. Fluidization regimes, adapted from Grace (1986) by Kunii and Levenspiel (1991); particles labeled by Geldart Classifications A, B, D.

In fast fluidized beds, the particles enter the bottom of the bed with little or no vertical velocity, gaining velocity by momentum transfer from the high speed gas as they pass upward through the bed. Since particle velocity increases with elevation in the bed, mass balance requires that the average solid volumetric concentration decrease with elevation along the length of the vertical bed. Figure 11 shows representative data obtained by Herb et al. (1989). For the operating conditions represented in this figure, it is seen that the axial height required to approach fully-developed flow conditions (i.e., constant solid concentration) can be many meters, increasing with increasing particle size. The data of Hartige, Li and Verther (1986), as shown in Fig. 12 indicate that the exact rate of axial development of solid concentration varies also with solid mass flux and with bed diameter. The figures also illustrate that in the fast fluidized regime, cross-sectional-averaged solid concentrations are typically less than 5%, in contrast to solid concentrations in a range of 30–40% for bubbling dense fluidization.

The hydrodynamic characteristic of fast fluidized beds is complicated by the existence of significant radial (horizontal) variations in solid concentration and velocity. Radial profiles of solid volume fraction, measured by Beaude and Louge (1995) are shown in Fig. 13. It is seen that for the same Froude number, there is increasing nonuniformity of solid concentration with increasing solid mass flux. At the higher mass fluxes shown in this figure, local solid volume fractions adjacent to the bed wall approach magnitude of 30%, in contrast to solid fractions of 1–3% near the bed centerline. Herb, Tuzla and Chen (1989) and Werther (1993) noted that such radial distributions can be normalized as a general similarity profile for various operating conditions by utilizing dimensionless ratio of local solid concentration to cross-sectional-averaged solid concentration.

Solid flow mass flux and velocity also vary in magnitude across the radius of fast fluidized beds. Experimental measurements obtained by Herb, Dou, Tuzla and Chen (1992) are plotted in Fig. 14. It is seen that while local solid fluxes are positive upward in the core of the bed, they can become negative downward in the region near the bed wall. The difference between core and bed regions becomes increasingly greater as total solid mass flux increases. This downward net flow of solid in the region near the bed wall has important significance for heat transfer at the wall.

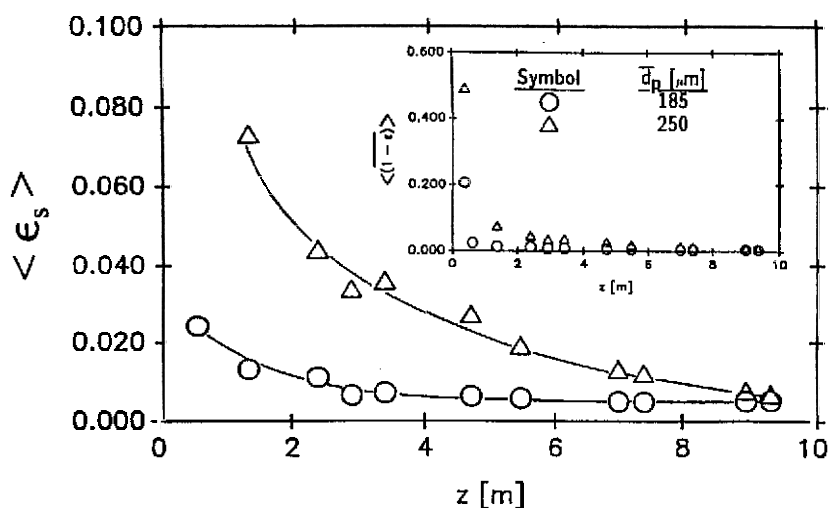


Figure 11. Axial variation of solid concentration for fast fluidized bed of sand particles, at $U = 5$ m/s and $G_s = 30$ kg/m²·s. (From Herb, Dou, Tuzla and Chen, 1989.)

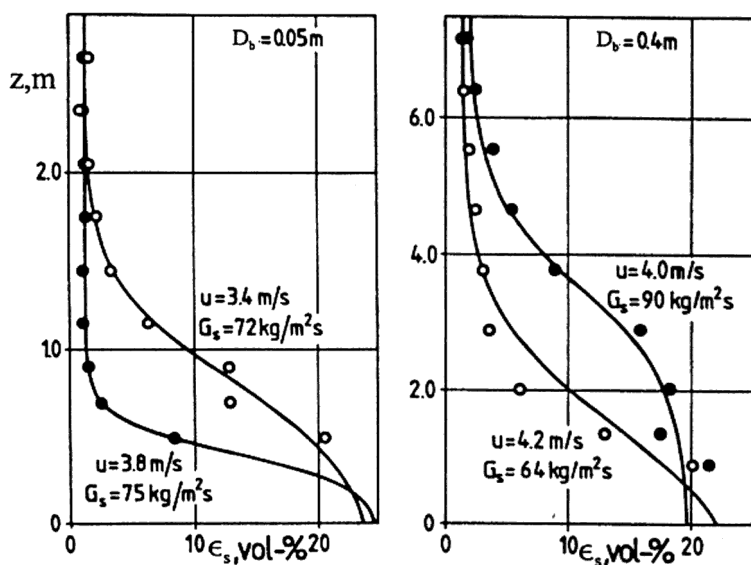


Figure 12. Effect of mass flux and bed diameter on solid concentration. (From Hartge, Li and Wether, 1986.)

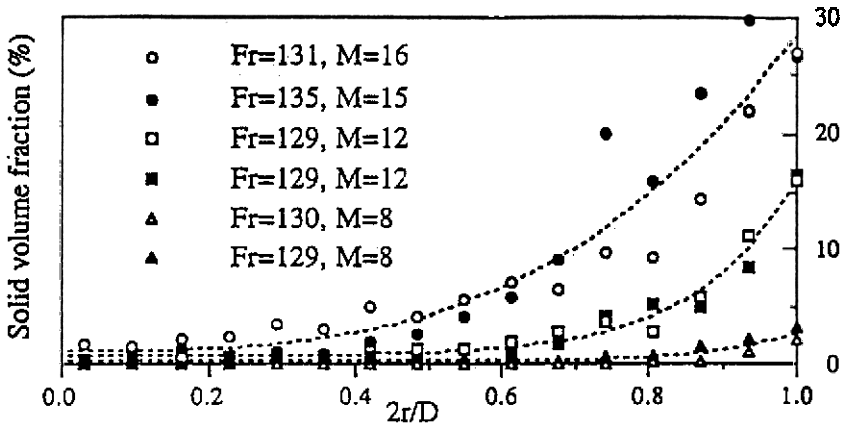


Figure 13. Radial profiles of solid volume fraction in fast fluidized bed. $Fr = U_g / \sqrt{g d_p}$, $M = G_s / (\rho_g U_g)$. (From Beaudé and Louge, 1995.)

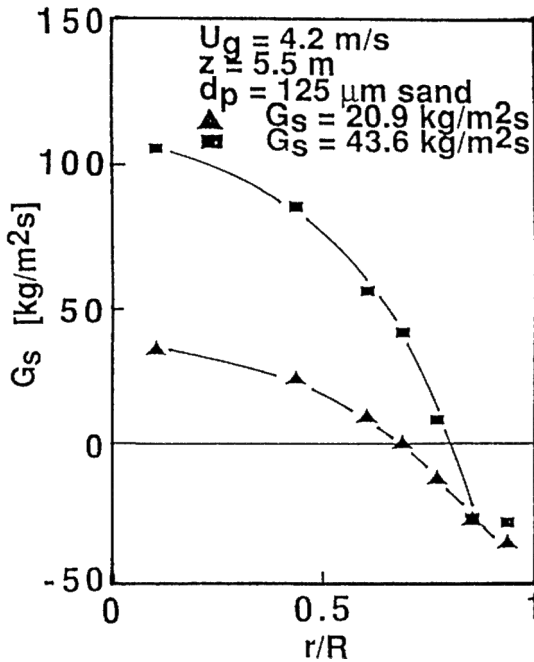


Figure 14. Radial profiles of solid mass flux in fast fluidized bed. (From Herb, Dou, Tuzla and Chen, 1992.)

Another hydrodynamic complication found in fast fluidized beds is the tendency for particles to flow as aggregate clusters rather than as individual particles, Chen (1996) and Horio et al. (1988). The solid volume concentrations in such clusters also vary with radial position and operating conditions, increasing with increasing radial position and with increasing total solid flux—as indicated by the data of Soong, Tuzla and Chen (1993) shown in Fig. 15. In general, the solid concentration in clusters can be many times greater than the overall bed-averaged concentration, with significant implications for the heat transfer mechanisms.

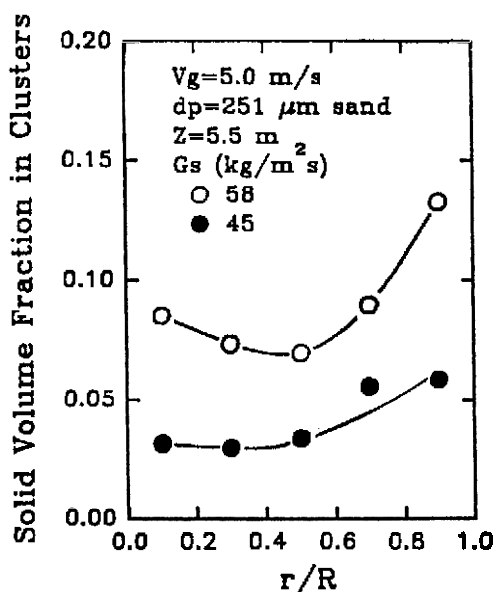


Figure 15. Concentration of solid in clusters in fast fluidized bed. (From Soong, Tuzla and Chen, 1993.)

3.2 Heat Transfer

General Characteristics. Energy addition or extraction from fast fluidized beds are commonly accomplished through vertical heat transfer surfaces in the form of membrane walls or submerged vertical tubes. Horizontal tubes or tube bundles are almost never used due to concern with

erosion in the fast-flowing two-phase flow. Thus the designer is concerned with effective heat transfer coefficients on vertical surfaces which are exposed to the fast-fluidized media. Operational parameters that are known to affect the magnitude of the heat transfer coefficient include: gas velocity, solids flow rate (mass flux), mean particle diameter, axial location of the heat transfer surface along height of the fluidized bed, radial location of the heat transfer surface across the bed, and physical dimension of the heat transfer surface. Some of the generic characteristics were indicated by the early data of Kiang et al. (1976), as shown in Fig. 16. General characteristics may be noted as:

- Magnitude of the heat transfer coefficient generally decreases with elevation along the bed.
- At low elevations the heat transfer coefficient generally decreases with increasing gas velocity.
- At higher elevations the heat transfer coefficient increases with increasing gas velocity.
- Magnitude of the heat transfer coefficient is higher than that for equivalent air convection, but lower than that found in dense bubbling beds.

These characteristics point to a correlation of the heat transfer coefficient with local solid concentration. As indicated in Fig. 11, solid concentrations tend to be higher in the bottom region of fast fluidized beds; hence the higher heat transfer coefficients in that region. Increasing gas velocity increases the upward acceleration of solid particles, causing a decrease of solid concentration at the bottom and increasing concentrations of solid at the top regions—with corresponding changes in the local heat transfer coefficients. Grace (1985) illustrates this correlation characteristic by plotting heat transfer coefficient versus the suspension density of the solid-gas mixture, using data of Fraley et al. (1983). As shown in Fig. 17, such a plot graphically illustrates the increasing heat transfer coefficient with increasing solid concentration. The various lines in Fig. 17 are correlations that attempt to capture this dependence, generally of the form,

$$\text{Eq. (15)} \quad h = a \bullet (r_{\text{susp}})^b$$

where a = empirical function of physical properties
 b = empirical exponent

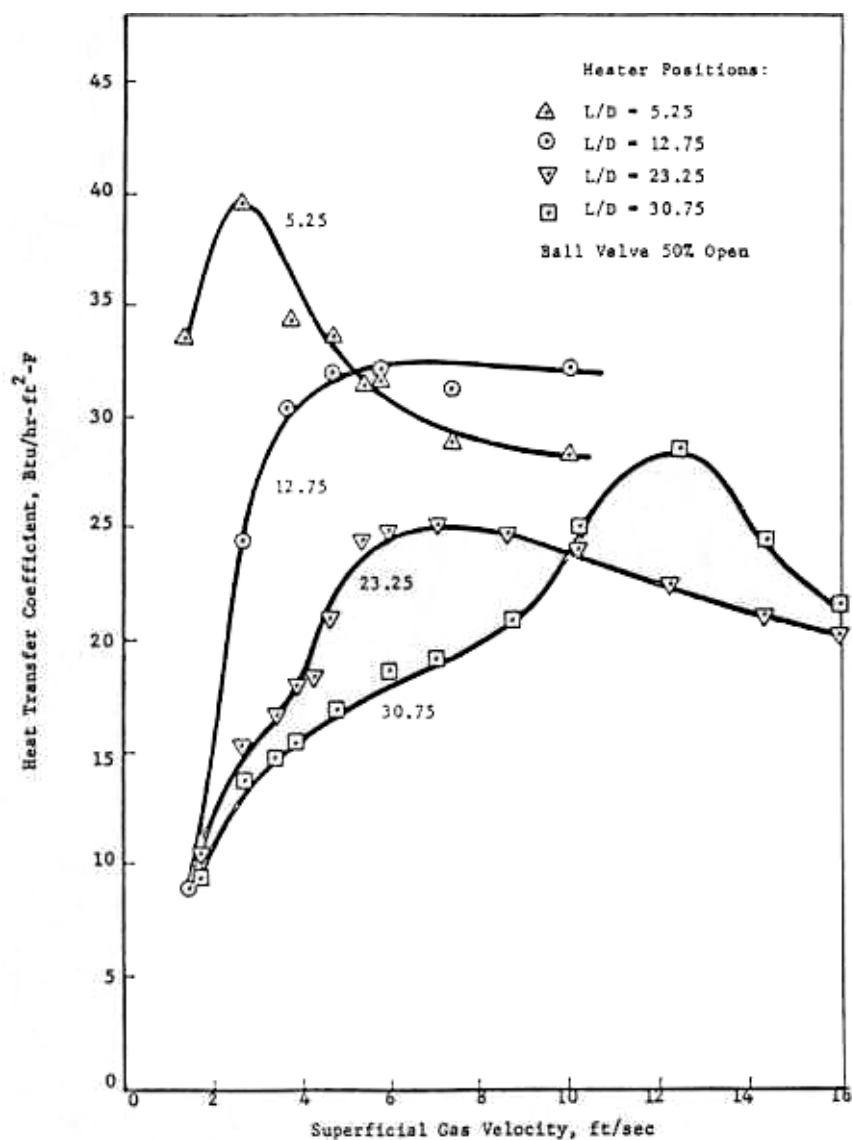


Figure 16. General heat transfer characteristics of fast fluidized bed. (From Kiang et al., 1976.)

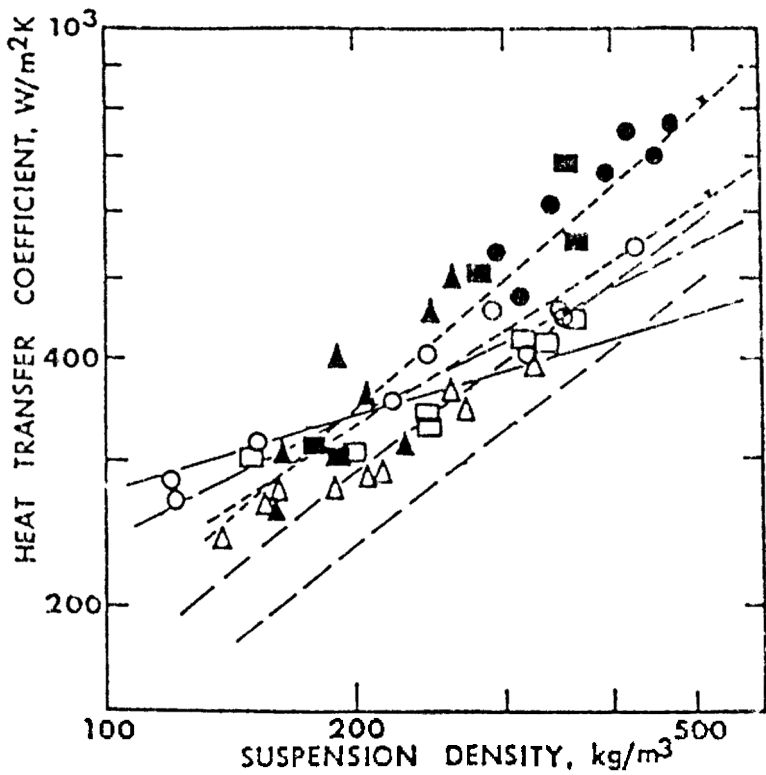


Figure 17. Dependence of heat transfer coefficient on solid concentration. (Data of Fraley et al., 1983, from Grace, 1985).

Parametric Effects. As indicated above, a number of parameters including properties of the gas and particles, flow rates of each phase, geometric location within the fluidized bed, operational parameters such as pressure and temperature, and the geometry of the heat transfer surface all are known to affect the magnitude of the heat transfer coefficient in fast fluidized beds. Experimental data collected at various research institutions and universities provide information on these parametric effects. Two of the parametric effects have already been touched upon above, as illustrated in Fig. 16. Examination of that figure shows that at axial positions greater than 10 diameters above the bottom of the bed, heat transfer coefficients generally increase with increasing gas velocity. It appears that for a given axial position, the coefficient would increase to a maximum value before

reaching a plateau or decreasing slowly with further increases in gas velocity. The data of Fig. 16 also illustrates a second parametric effect — that for a given gas velocity, the heat transfer coefficient generally decreases with axial elevation, the effect being strongest at relatively low superficial gas velocities.

Furchi et al. (1988) measured heat transfer coefficients at the wall of a 7.2 cm diameter fast fluidized bed, operating with glass particles of various diameters. Their results, shown in Fig. 18 indicates significant parametric effects of solid mass flux and of particle diameter. For a given size of particles, it is seen that there is a marked increase in the heat transfer coefficient as the solid mass flux (G_s/G_g) increases. This trend is most obvious for the smaller size particles (d_p of 109 μm), becoming less obvious with particle diameters greater than 200 μm . For a given gas velocity and solid mass flux, the data in Fig. 18 indicate significant increases in heat transfer coefficients as diameter of the fluidized particles are reduced; at a G_s/G_g of 10, the effective heat transfer coefficient is increased by approximately 300% as the particle diameter decreased from 269 to 109 μm .

The interaction of parametric effects of solid mass flux and axial location is illustrated by the data of Dou et al. (1991), shown in Fig. 19. These authors measured the heat transfer coefficient on the surface of a vertical tube suspended within the fast fluidized bed at different elevations. The data of Fig. 19 show that for a given size particle, at a given superficial gas velocity, the heat transfer coefficient consistently decreases with elevation along the bed for any given solid mass flux G_s . At a given elevation position, the heat transfer coefficient consistently increases with increasing solid mass flux; at the highest elevation of 6.5 m, where hydrodynamic conditions are most likely to be fully developed, it is seen that the heat transfer coefficient increases by approximately 50% as G_s increased from 30 to 50 $\text{kg/m}^2\text{s}$.

The experiments of Dou et al. (1991) also indicate that the heat transfer coefficient varied with radial position across the bed, even for a given cross-sectional-averaged suspension density. Their data, as shown in Fig. 20, clearly indicate that the heat transfer coefficient at the bed wall is significantly higher than that for vertical surfaces at the centerline of the bed, over the entire range of suspension densities tested. Almost certainly, this parametric effect can be attributed to radial variations in local solid concentration which tends to be high at the bed wall and low at the bed centerline.

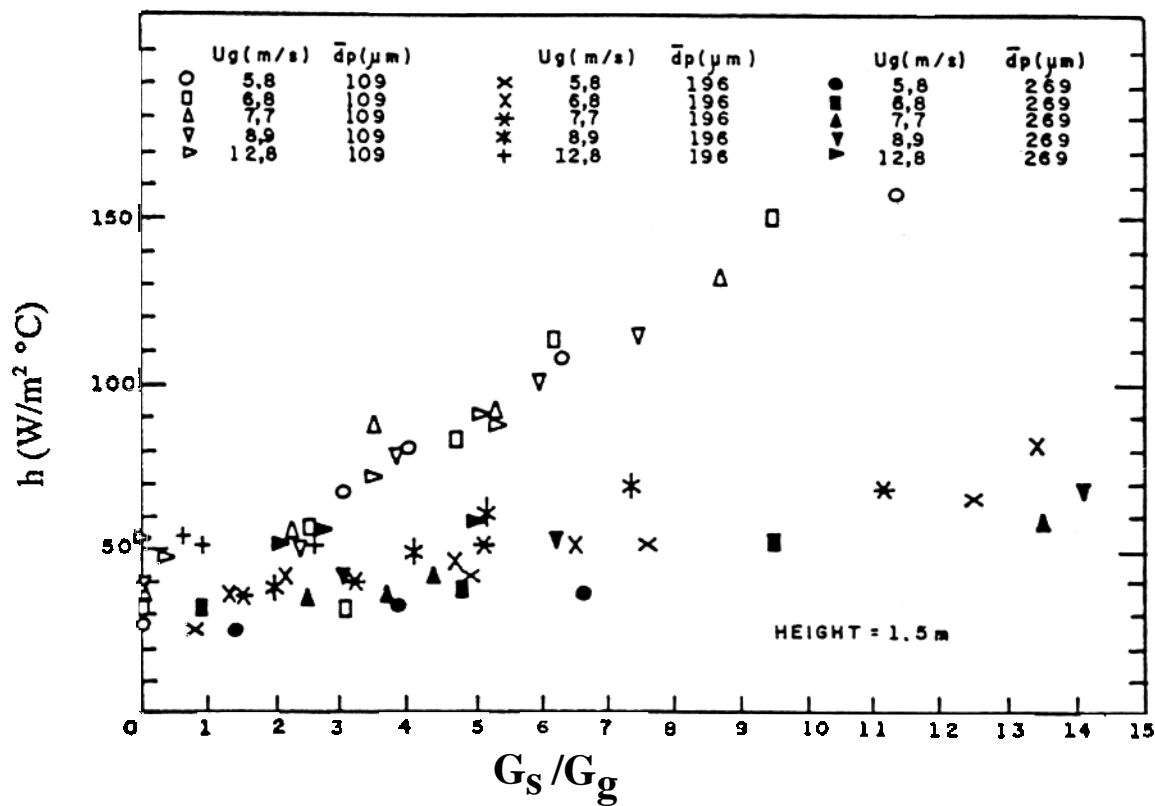


Figure 18. Parametric effects of solid flux and particle diameter on heat transfer in fast fluidized beds. (From Furchi et al., 1988).

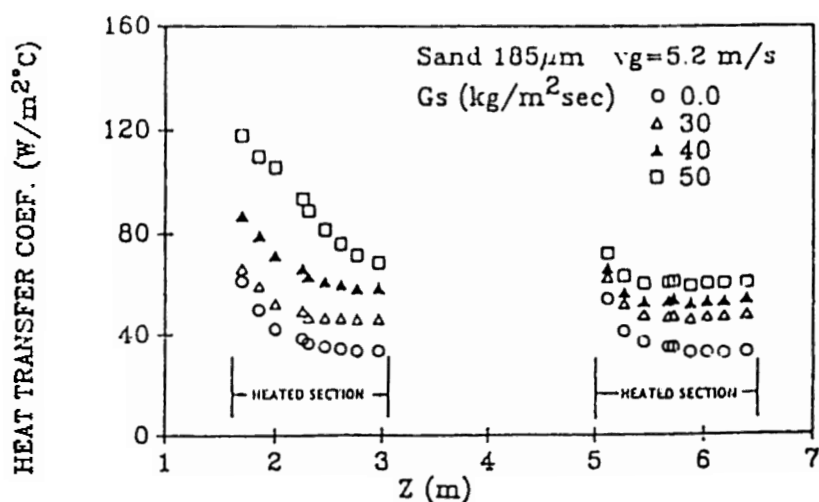


Figure 19. Interactive effects of solid flux and axial location on heat transfer in fast fluidized bed. (From Dou, Herb, Tuzla and Chen, 1991.)

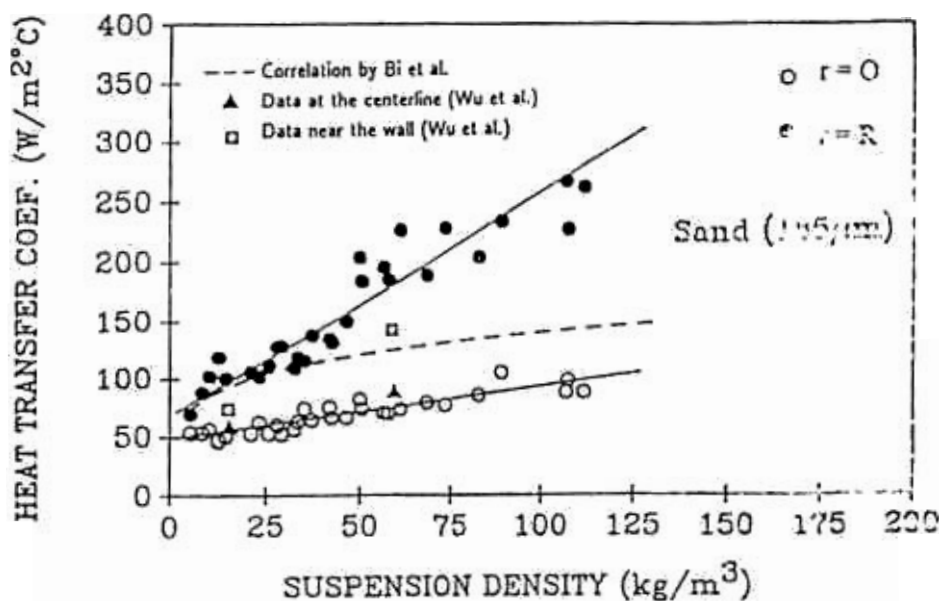


Figure 20. Variation of heat transfer coefficient with radial position across fast fluidized bed. (From Dou, Herb, Tuzla and Chen, 1991.)

The data of Fig. 20 also illustrates one of the most significant parametric effects, that of the solid concentration in the particle/gas suspension. Many of the parametric effects mentioned above (e.g., due to elevation, gas velocity, solid mass flux) can be attributed to their individual impact on solid concentration in the fast fluidized bed. Thus increasing gas velocity in order to increase particle entrainment to upper regions of the bed, or increasing solid mass flux to increase solid holdup within the bed, lead to higher solid concentrations and greater suspension densities—which correlates with higher heat transfer coefficients. This is illustrated by the data of Dou et al. in Fig. 20, which shows that for a given radial position (centerline or wall) the heat transfer coefficient correlates with cross-sectional-averaged suspension density. The increase of heat transfer coefficient with increasing average density is seen to be much more pronounced at the vessel wall than at the surface of a tube submerged at the bed centerline. It should be noted that these results include data obtained over a range of axial elevations, indicating that this latter parameter is secondary, influencing the heat transfer coefficient only through the effect of axial variations in suspension density.

The data of Fig. 20 also point out an interesting phenomenon—while the heat transfer coefficients at bed wall and bed centerline both correlate with suspension density, their correlations are quantitatively different. This strongly suggests that the cross-sectional solid concentration is an important, but not primary parameter. Dou et al. speculated that the difference may be attributed to variations in the local solid concentration across the diameter of the fast fluidized bed. They show that when the cross-sectional averaged density is modified by an empirical radial distribution to obtain local suspension densities, the heat transfer coefficient indeed then correlates as a single function with local suspension density. This is shown in Fig. 21 where the two sets of data for different radial positions now correlate as a single function with local mixture density. The conclusion is that the convective heat transfer coefficient for surfaces in a fast fluidized bed is determined primarily by the local two-phase mixture density (solid concentration) at the location of that surface, for any given type of particle. The early observed parametric effects of elevation, gas velocity, solid mass flux, and radial position are all secondary to this primary functional dependence.

The parametric effect of system pressure on the heat transfer coefficient was studied by Wirth (1995). They obtained experimental measurements of the heat transfer Nusselt number for fast fluidized beds

of various solid particles over a pressure range of 1 to 5 bars. Some of their results are shown in Fig. 22, which plots the Nusselt number as a function of Archimedes number, with solid concentration as a parameter, where the Nusselt number is defined on the basis of particle diameter and gas thermal conductivity. Wirth concluded from these observations that the effect of pressure is evident only through its influence on the hydrodynamics that result in the solid concentration in the fluidized bed. For a given gas-solid system characterized by the Archimedes number, the heat transfer Nusselt number is a function of the cross-sectional averaged solids concentration.

The parametric effect of bed temperature is expected to be reflected through higher thermal conductivity of gas and higher thermal radiation fluxes at higher temperatures. Basu and Nag (1996) show the combined effect (Fig. 23) which plots heat transfer coefficients as a function of bed temperature for data from four different sources. It is seen that for particles of approximately the same diameter, at a constant suspension density (solid concentration), the heat transfer coefficient increases by almost 300% as the bed temperatures increase from 600°C to 900°C.

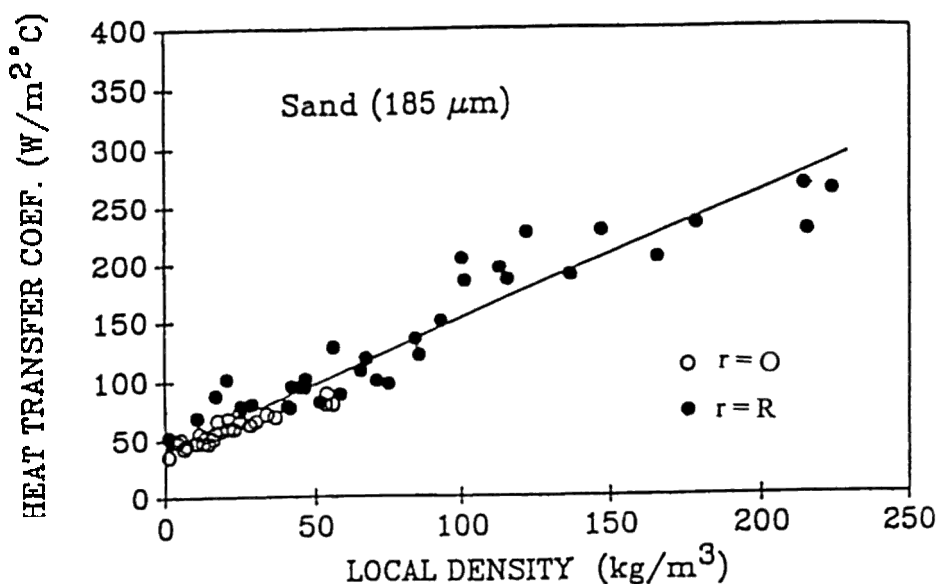


Figure 21. Significance of local suspension density for heat transfer in fast fluidized beds. (Data of Dou, Herb, Tuzla and Chen, 1991.)

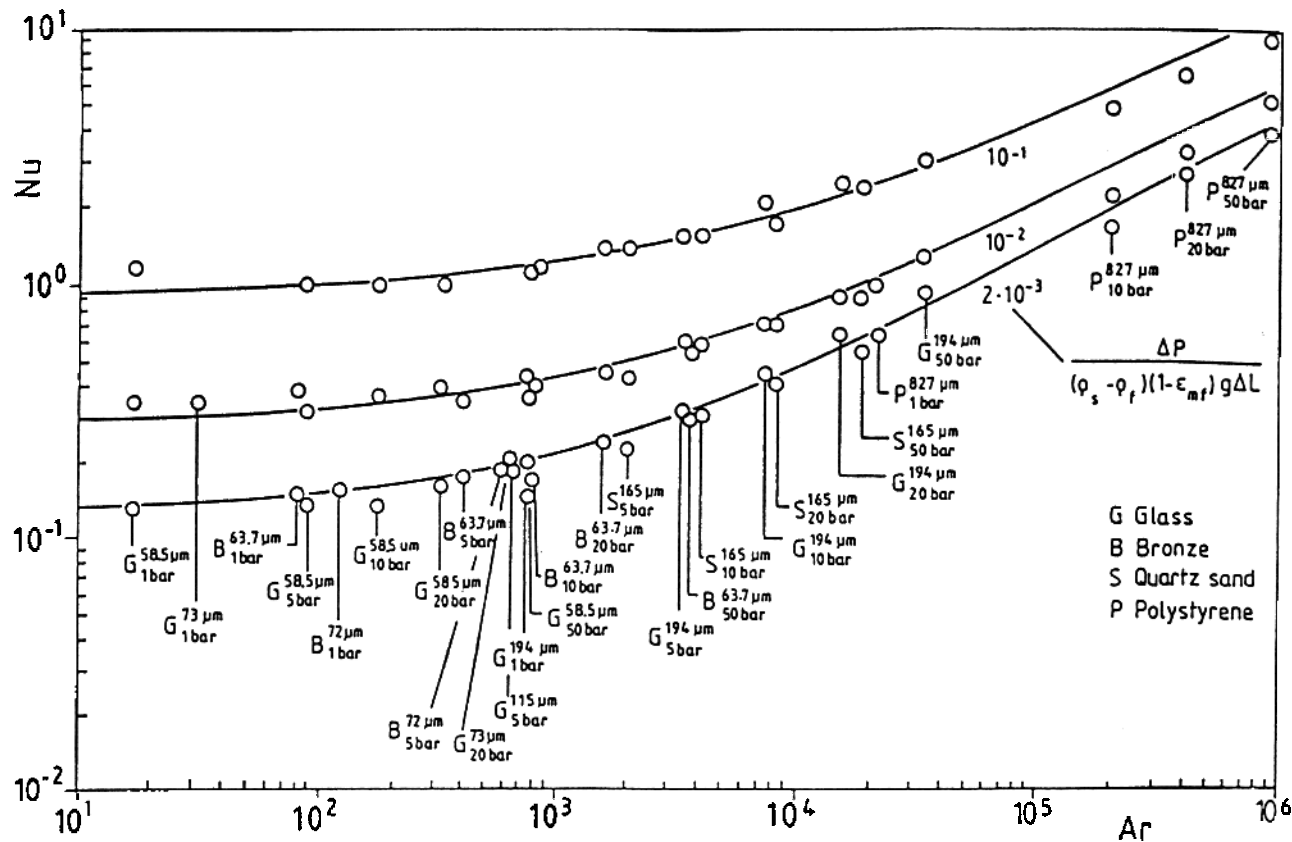


Figure 22. Heat transfer coefficients for fast fluidized beds at various pressures. (Data of Wirth, 1995.)

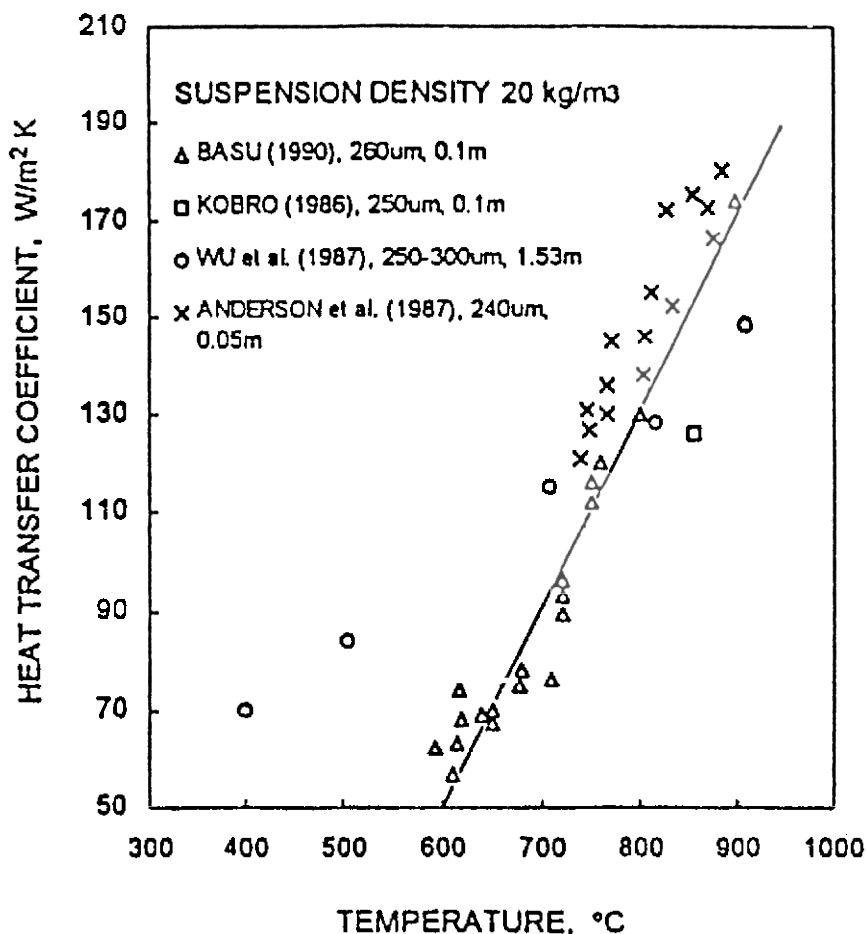


Figure 23. Effect of bed temperature on heat transfer coefficient. (From Basu and Nag, 1996.)

Another parametric effect is the apparent dependence of the heat transfer coefficient on the physical size of the heat transfer surface. Figure 24, from Burki et al. (1993), graphically illustrates this parametric effect by showing that the effective heat transfer coefficient can vary by several hundred percent with different vertical lengths of the heat transfer surface, for circulating fluidized beds of approximately the same particle diameter and suspension density. This size effect significantly contributed to confusion in the technical community since experimental measurements by inves-

tigators with different size heat transfer surfaces gave apparently contradictory results. Burki et al showed in Fig. 24 that data obtained with small heat transfer probes (of centimeter dimensions) can be fourfold greater than the coefficients measured with larger heat transfer surfaces (of order of 1–2 m). This phenomenon is likely associated with a vertical thermal development length so that small probes reflect higher heat transfer coefficients representative of not-fully-developed conditions.

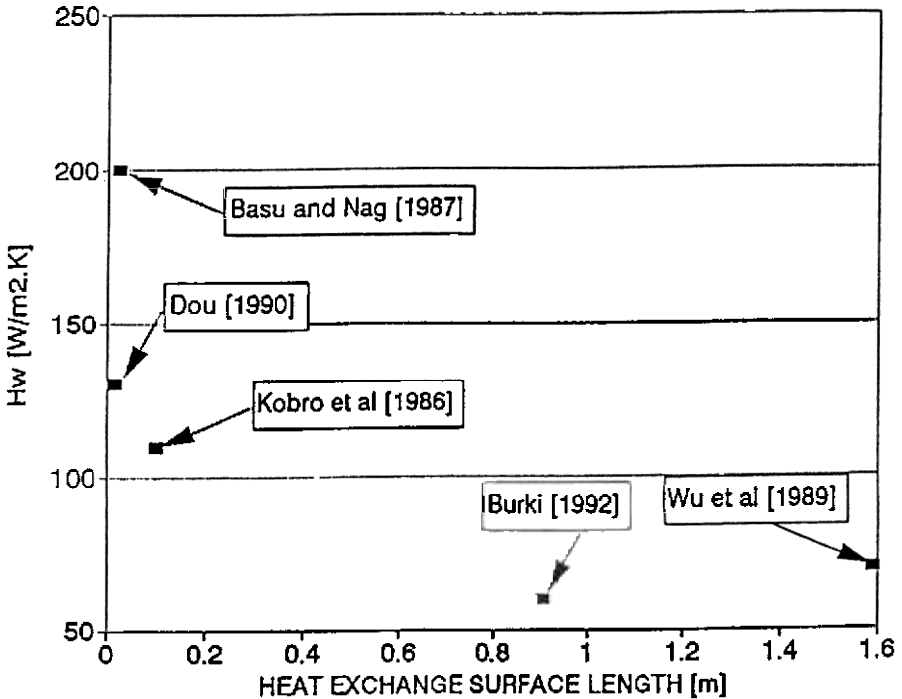


Figure 24. Dependence of heat transfer coefficient on size of heat transfer surfaces. $D_p \varnothing 245 \mu\text{m}$; Suspension Density $\varnothing 50 \text{ kg/m}^3$. (From Burki, Hirschberg, Tuzla and Chen, 1993.)

Models and Correlations. A multitude of different models and correlations have been proposed for prediction of the heat transfer coefficient at vertical surfaces in fast fluidized beds. To organize the various models in some context, it is helpful to consider the total heat transfer coefficient as comprised of convective contributions from the lean-gas

190 Fluidization, Solids Handling, and Processing

phase and the dense-particle phase plus thermal radiation, as expressed by Eq. (3). Many of the models combine individual phase convection contributions into a single convective coefficient which we can define as,

$$\text{Eq. (16)} \quad h_c = f_\ell h_\ell + (1 - f_\ell) h_d$$

All correlations based on ambient temperature data where thermal radiation is negligible should be considered to represent only the convective heat transfer coefficient h_c .

The simplest correlations are of the form shown by Eq. (15), in attempts to recognize the strong influence of solid concentration (i.e., suspension density) on the convective heat transfer coefficient. Some examples of this type of correlation, for heat transfer at vertical wall of fast fluidized beds are:

Wen and Miller (1961):

$$\text{Eq. (17)} \quad \frac{h_c d_p}{k_g} = \left(\frac{C_{ps}}{C_{pg}} \right) \left(\frac{\mathbf{r}_{susp}}{\mathbf{r}_s} \right)^{0.3} \left(\frac{u_t^2}{g d_p} \right)^{0.21} Pr_g$$

where u_t = terminal velocity of particle.

Kiang et al. (1976):

$$\text{Eq. (18)} \quad \frac{h_c d_p}{k_g} = \mathbf{e}_s^a \left(\frac{C_{ps}}{C_{pg}} \right)^b \left(\frac{\mathbf{r}_{susp}}{\mathbf{r}_s} \right)^c \left(\frac{D_b \mathbf{r}_g u_g}{\mathbf{m}_g} \right)^d Pr_g^e$$

where a, b, c, d, e are empirical constants.

Fraley et al. (1983):

$$\text{Eq. (19)} \quad h_c = 2.87 (\mathbf{r}_{susp})^{0.90}, \text{ SI Units}$$

Divilio and Boyd (1993):

$$\text{Eq. (20)} \quad h_c = 23.2 (\mathbf{r}_{susp})^{0.55}, \text{ SI Units}$$

Werdmann and Werther (1993):

$$\text{Eq. (21)} \quad \frac{h_c d_p}{k_g} = 7.46 \times 10^{-4} \left(\frac{D_b \mathbf{r}_g u_g}{\mathbf{r}_g} \right)^{0.757} (\mathbf{r}_{susp})^{0.562}$$

It should be noted that the suspension density (\mathbf{r}_{susp}) used in above correlations represent the cross-sectional-averaged value. Since Dou et al. (1991) have shown that heat transfer coefficient is primarily dependent on local solid concentration in the vicinity of the surface (rather than cross-sectional-averaged concentration), the above correlations for convective coefficient at the wall of FFBs can be justified only if there is a generic similarity profile in solid concentration relating \mathbf{e}_s at the wall to cross-sectional-averaged \mathbf{e}_s . Further study of Eqs. (17–18) indicate that there are significant uncertainties with regard to the fundamental nature of appropriate heat transfer correlations. For example, such parameters as particle size (d_p), bed diameter (D_b), particle terminal velocity (u_t), heat capacity of solid (C_{ps}), and gas thermal properties (\mathbf{r}_g , k_g , \mathbf{m}_g , C_{pg}) are incorporated in some correlations and not in others. Obviously, each of these empirical correlations is useful only for the range of parameters covered by the correlation's experimental data base.

In contrast to the purely empirical correlations, various authors have attempted to develop mechanistically based models for each of the contributions from particle convection, gas convection and thermal radiation reflected in Eq. (3). Of these, it is generally acknowledged that the dense phase convection (represented by h_d) is the dominant contributor. The lean phase gas convection (represented by h_l) is often thought to be small or negligible. The radiative contribution (represented by h_r) is acknowledged to be significant for high temperature fluidized beds, at temperatures greater than 500°C. Various models proposed for each of these contributing mechanisms are briefly summarized below.

The lean/gas phase convection contribution has received the least attention in the literature. Many models in fact assume it to be negligible in comparison to dense phase convection and set h_l to be zero. Compared to experimental data, such an approach appears to be approximately valid for fast fluidized beds where average solid concentration is above 8% by volume. Measurements obtained by Ebert, Glicksman and Lints (1993) indicate that the lean phase convection can contribute up to 20% of total

convective heat transfer when the average solid concentration becomes less than 3%, as is often found in upper regions of fast fluidized beds. A better approach is to approximate the lean phase convection by some equation for single phase gas convection, e.g., the Dittus-Boelter correlation,

$$\text{Eq. (22)} \quad \frac{h_\ell D_b}{k_g} = 0.023 \left(\frac{D_b}{m_g} \frac{\mathbf{r}_g}{u_g} \right)^{0.8} (Pr_g)^{0.33}$$

Some researchers have noted that this approach tends to underestimate the lean phase convection since solid particles dispersed in the up-flowing gas would cause enhancement of the lean phase convective heat transfer coefficient. Lints (1992) suggest that this enhancement can be partially taken into account by increasing the gas thermal conductivity by a factor of 1.1. It should also be noted that in accordance with Eq. (3), the lean phase heat transfer coefficient (h_ℓ) should only be applied to that fraction of the wall surface, or fraction of time at a given spot on the wall, which is not submerged in the dense/particle phase. This approach, therefore, requires an additional determination of the parameter f_l , to be discussed below.

The contribution of dense phase convection is acknowledged to be most important and has received the greatest attention from researchers. Models for prediction of h_d have followed two different, competing concepts. The first type of models considers the heat transfer surface to be contacted periodically by clusters or strands of closely packed particles. Similar to the packet model for dense bubbling beds, this approach leads to a surface renewal process whereby the heat transfer occurs primarily by transient conduction between the heat transfer surface and the particle clusters during their time of residence at the surface. Equation (4), from Mickley and Fairbanks (1955), can be used here to estimate the effective cluster heat transfer coefficient by treating clusters in FFBs as the equivalent of particle packets in bubbling beds. Experimental evidence supporting this concept is reported by Dou, Herb, Tuzla and Chen (1992). They obtained simultaneous measurements of the dynamic variations of solid concentration and instantaneous heat transfer coefficient at the wall of a fast fluidized bed, and found significant correlation between the two—indicating a direct dependence of the dense phase heat transfer on cluster contact. Application of this cluster type model requires information on solid concentration in the cluster ($\epsilon_{s,cl}$), average residence time of

cluster on the heat transfer surface (t_{cl}), and the effective thermal conductivity of the cluster (k_{cl}). Figure 15 shows sample measurements of solid concentration in clusters as reported by Soong, Tuzla and Chen (1993) at various locations within the fast fluidized bed. Other measurements of $e_{s,cl}$ have been reported by Wu (1989), Louge et al., (1990), and Lints (1993). Lints report that the average solids concentration in the cluster can be correlated with the cross-sectional-averaged solid concentration across the bed,

$$\text{Eq. (23)} \qquad e_{s,cl} = 1.23(e_{sb})^{0.54}$$

The average cluster residence time (t_{cl}) could be correlated directly with operating parameters (e.g., u_g , d_p , G_s , H) if sufficient experimental data on hydrodynamics were available. Alternately one can assume that the clusters of finite length, L_{cl} , fall down over the heat transfer surface with a velocity U_{cl} . For any given position on the heat transfer surface, the cluster contact time would just be the ratio L_{cl}/U_{cl} . Experimental measurements of cluster velocity and length have been reported by Hartge et al., (1986), Horio et al., (1988), Lints (1992), and Soong et al. (1995). Figure 25 shows sample data reported by Soong et al. indicating that near FFB wall, cluster velocity are in the range of 1–5 m/s downward, and cluster length are in the range 0.5–4.5 cm. While there is general agreement about the range of values for these two parameters, there are inadequate data to develop general correlations. In the absence of such correlations, Lints and Glicksman (1993) suggest that an average downward velocity of 1 m/s be assumed for the clusters, and that the vertical length of the heat transfer surface be substituted for the cluster length. Clearly this will require additional research and analysis.

Finally, to utilize this cluster concept in modeling the heat transfer, one needs to determine the fraction of time that a spot on the heat transfer surface is covered by clusters, which can be assumed to be equal to the fractional of wall coverage by clusters at any given time. Sample measurements of f_l have been obtained by Wu (1989), Rhodes et al., (1991), Louge et al., (1990), Rhodes et al., (1991), and Dou et al. (1993). Lints and Glicksman present a combined plot of some of these data, reproduced here in Fig. 26. They suggest an approximate correlation for the fractional wall coverage in terms of the cross-section-average solids concentration,

$$\text{Eq. (24)} \qquad (1 - f_\ell) = 3.5(e_{s,b})^{0.37}, \text{ at wall}$$

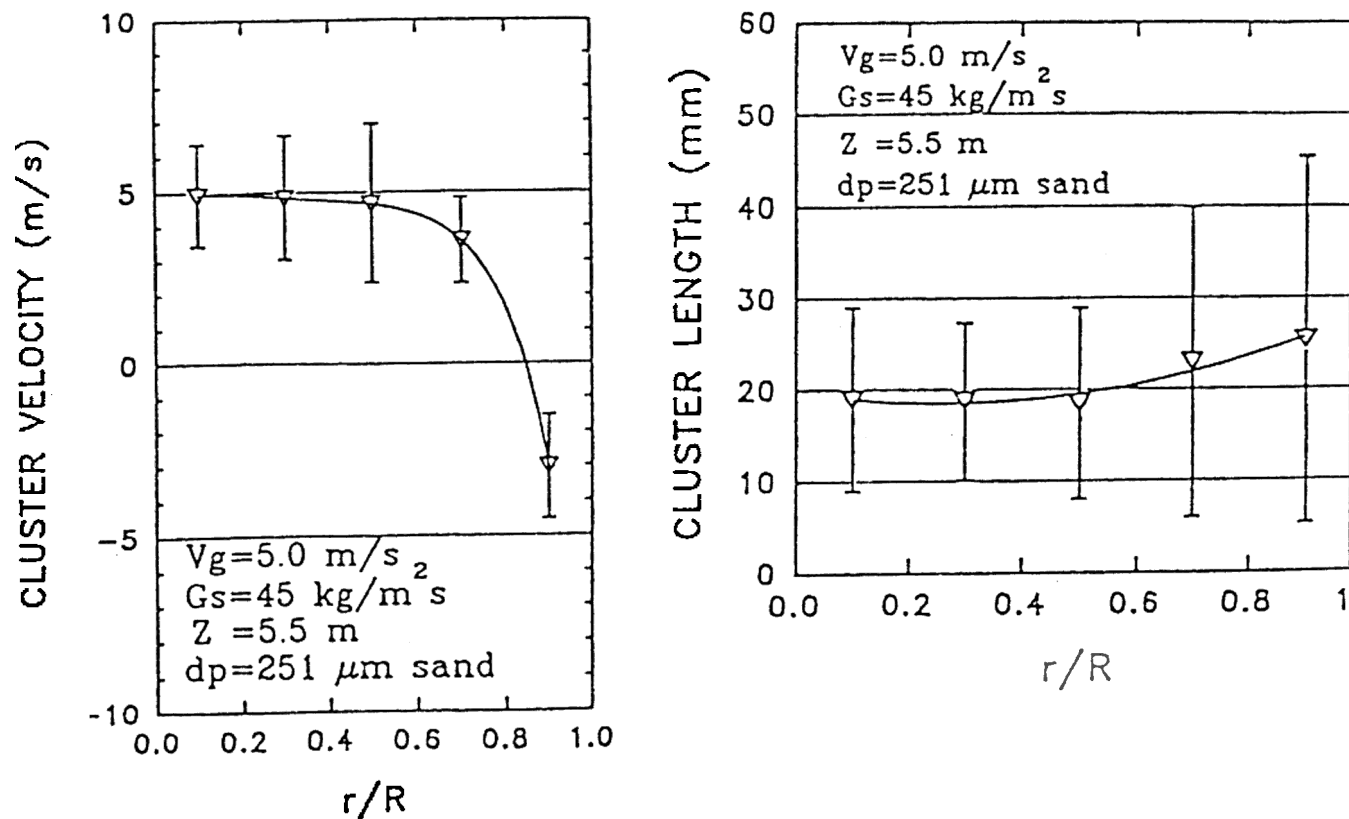


Figure 25. Sample data on cluster velocities and length. (From Soong, Tuzla and Chen, 1995.)

With the above functions and empirical correlations, it becomes possible to calculate the overall convective heat transfer coefficient h_c by Eqs. (16, 4, and 22–24). Figure 26 shows a plot presented by Lints and Glicksman which compares predictions by this method with experimental data from several different sources. Reasonably good agreement is obtained over a range of bed densities corresponding to approximately 0.5 to 3% volumetric solid concentration.

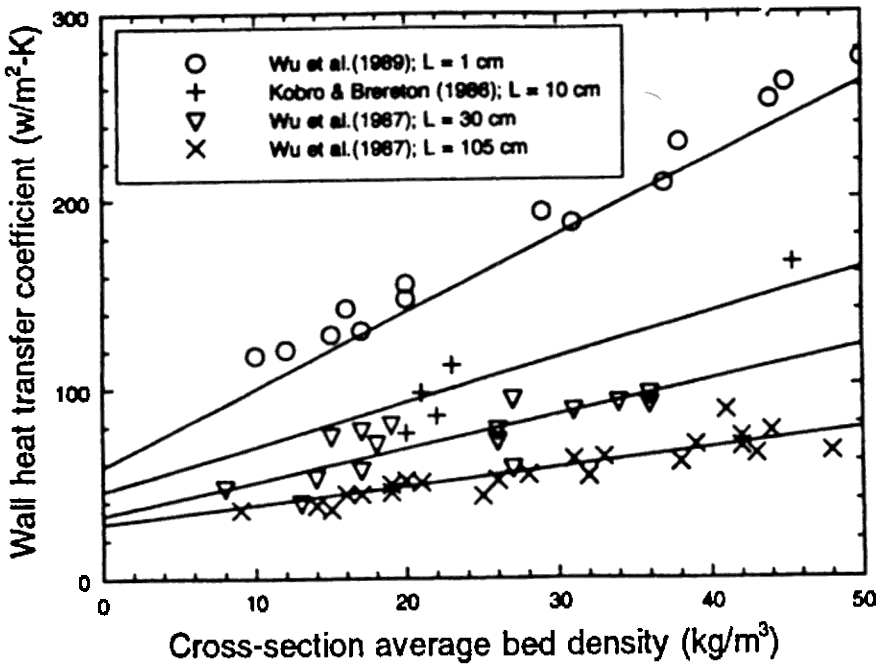


Figure 26. Comparison of predictions from cluster-based model to heat transfer data. (From Lints and Glicksman, 1993.)

An alternate to the concept of cluster renewal discussed above is the concept of two-phase convection. This second approach disregards the separate behavior of lean and dense phases, instead models the time average heat transfer process as if it were convective from a pseudo-homogeneous particle-gas medium. Thus h_g , h_{cl} , h_l , and h_d are not

calculated separately, rather a pseudo-homogeneous convective coefficient h_c is sought. Attention is thus focused on the “boundary layer” of the two-phase mixture at the heat transfer surface. Different approaches are used by various authors to represent the essence of the thermal transport process in this layer. The simplest form of this approach is to borrow from single phase convective correlations, and attempt to find general empirical relationships between an effective convective Nusselt number and some appropriate Reynolds number. Equations (17–21) represent examples of this approach, with their concurrent advantage of simplicity and disadvantage of limited applicability.

Martin (1984) suggested a more mechanistically based approach, utilizing analogy between kinetic motion of molecules in gases and particle motion in the FFB suspension. By drawing on the kinetic theory of gases, Martin developed a model to account for thermal energy transport across the boundary layer by particle motion. The resulting Nusselt number for particle-enhanced convection is obtained as

$$\text{Eq. (25)} \quad Nu_c \equiv \frac{h_c d_p}{k_g} = e_s(Z) (1 - e^{-N_{wp}/CZ})$$

where: e_s = average solid volume fraction in bed

$$Z = \frac{r_p C_{pp} d_p}{6 k_g} \bullet w_p$$

N_{wp} = Nusselt number for wall-particle heat transfer

w_p = Average velocity of random particle motion

The wall-particle N_{wp} represents the heat transfer process between the wall and a contacting particle. For gas-solid systems, where thermal resistance of the gas gap dominates,

$$\text{Eq. (26)} \quad N_{wp} \sim 4 \left[(1 + K_n) \bullet \ell_n \left(1 + \frac{1}{K_n} \right) - 1 \right]$$

198 Fluidization, Solids Handling, and Processing

correlate the convective heat transfer coefficient over wide ranges of fluid properties and operating conditions. At low Archimedes numbers, heat transfer occurs primarily by gas conduction. At higher Archimedes numbers, gaseous conduction and convection both contribute to heat transfer. The correlation suggested by Wirth (1995) simply assumes that conduction and convection are additive, resulting in the following correlation.

$$\text{Eq. (29)} \quad \frac{h_c d_p}{k_g} = 2.85 \left[\frac{\Delta P / \Delta H}{g (\mathbf{r}_s - \mathbf{r}_g)(\mathbf{e}_{s,mf})} \right]^{0.5} + 3.28 \times 10^{-3} Re_{cl} Pr_g$$

where: Re_{cl} = Reynolds number for falling cluster strands

$$= \frac{\rho_g d_p U_{cl}}{\mu_g}$$

U_{cl} = velocity of falling cluster strands

Based on some physically reasoned assumptions, Wirth (1990) obtained the following relations for estimating Reynolds number of the falling strands:

$$\text{Eq. (30)} \quad Re_{cl} = \frac{2(1-f)^2 Re_{mf} + f Re_t}{2[f + (1-f)\mathbf{e}_{gmf}]}$$

$$\left\{ \left[1 - 4(1-f)^4 Re_{mf}^2 + (1-f)^2 f Re_t Re_{mf} \right] - 189 (\mathbf{e}_{s,mf}) f^3 (1-f) Ar \right\}^{1/2}$$

$$\left\{ \left[2(1-f)^2 Re_{mf} + f Re_t \right]^{-1} + 1 \right\}$$

where:

$$\begin{aligned}
 (1 - f) &= \frac{2.3\Delta P/\Delta H}{(\mathbf{r}_s - \mathbf{r}_g)\mathbf{e}_{s,mf} g} \\
 Re_{mf} &\equiv \frac{\mathbf{r}_g u_{g,mf} d_p}{m_g} \\
 &= [1.14 \times 10^3 + 0.04 Ar]^{1/2} - 33.7 \\
 Re_t &\equiv \frac{\mathbf{r}_g u_t d_p}{m_g}
 \end{aligned}$$

Figure 27 shows a comparison of Wirth's correlation with experimental data for particles of various materials and diameter, in FFBs operating at various pressures. While the log-log plot submerges numerical differences, the agreement is generally good.

Models for estimating the radiative heat transfer contribution in fast fluidized beds parallel those proposed for dense bubbling beds, as reviewed above. The more mechanistically based approach of treating the particle-gas medium as a radiative participative medium has been attempted by only a few researchers for FFBs. Chen, Cimini and Dou (1988) used the two-flux radiative model of Eqs. (12–13) to analyze simultaneous convection and radiation in high temperature FFBs. Turbulent convection was combined with decreet radiative fluxes in the three transport equations, including a term for volumetric heat generation. Sample results for fluidized combustor conditions predicted a significant interdependence of radiative and convective heat transfer. This conclusion was verified by the experimental measurements of Han (1992) who showed that the contribution of radiative heat transfer was strongly effected by bed-averaged solid concentration, decreasing with increasing solid mass flux and decreasing gas velocity.

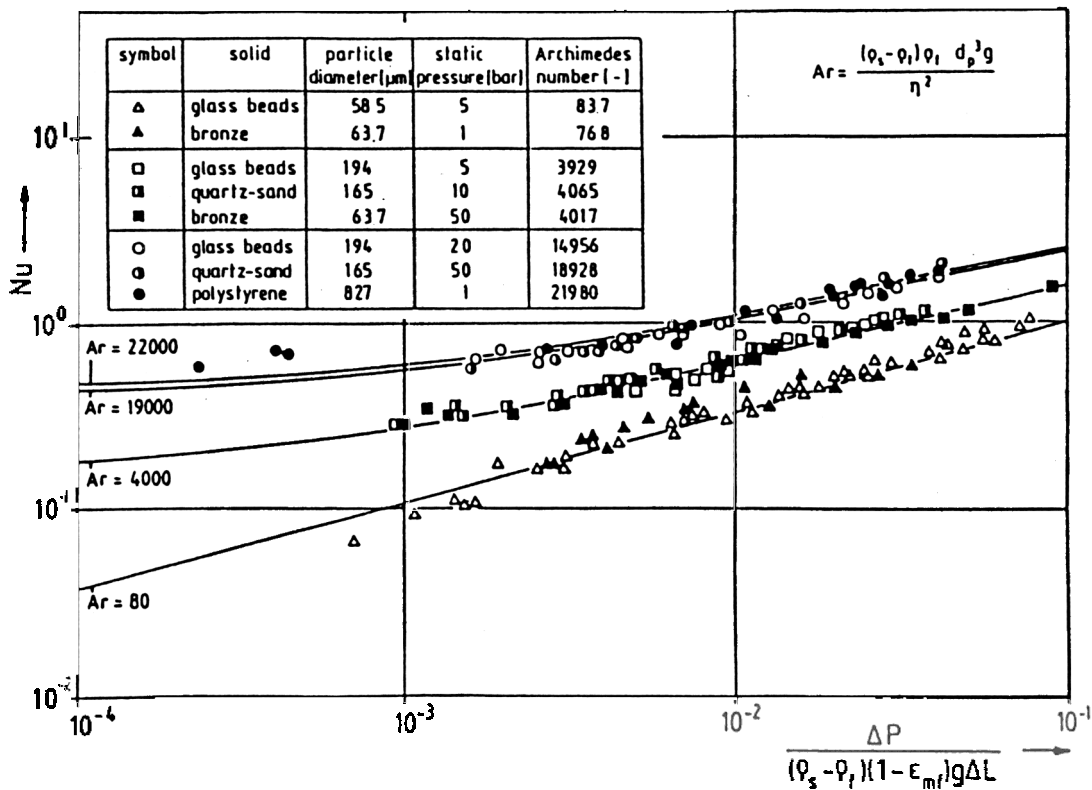


Figure 27. Comparison of model of Wirth with experimental data. (From Wirth, 1995.)

The more common approach is to treat the particle-gas suspension as an equivalent gray surface parallel to the heat transfer surface. Equation (11) would then be used with F taken as unity. Grace (1986) suggests that the emissivity of the particle-gas suspension can be approximated as,

$$\text{Eq. (31)} \quad e_b = 0.5(1 + e_s)$$

where e_s is the surface emissivity of the solid particles.

This gray body approach, or some modified version, has been the more popular approach used by various authors, including Palchonok et al., (1995), Anderson and Lechner (1993), Mahalingan and Kolar (1990).

Similar models using a multi-flux analysis of particle absorption and scattering are reported by Radauer, Glatzer and Linzer (1996).

NOTATIONS

A	Volumetric absorption coefficient of radiation
Ar	Archimedes number, Eq. (1)
C_D	Drag coefficient for single particle
C_p	Heat capacity
d, D	Diameter
D_t	Tube diameter
e	Radiative emissivity
ε	Volumetric concentration (fraction) of a phase
F	View factor for radiation
f_l	Time fraction of lean phase
G	Mass flux per unit flow area
g	Gravitational acceleration
H	Height in bed
h	effective heat transfer coefficient
I	Forward radiative flux, Eq. (12)
J	Backward radiative flux, Eq. (12)
k	Thermal conductivity
L	Length
M	Molecular weight
μ	Viscosity
Nu	Nusselt number, Eq. (7)

202 *Fluidization, Solids Handling, and Processing*

P	Pressure
Pr	Prandtl number
R	Radius of fluidized bed
r	radial distance from centerline
S	Volumetric scattering coefficient of radiation
ρ	Density
t	Residence time
T	Stefan Boltzmann constant of radiation
u	Superficial gas velocity
y	Distance from wall surface

Subscripts

b	Bed
c	Convective
cl	cluster
d	Dense phase
g	Gas
l	Lean phase
mf	Minimum fluidization
p	Particle
pa	Particle packet
r	Radiative
s	Solid
$susp$	Solid-gas suspension
t	Terminal
w	Wall

REFERENCES

- Anderson, B. A., and Lechner, B., "Local Lateral Distribution of Heat Transfer on Tube Surface of Membrane Walls in CFB Boiler," *Circ. Fluid. Bed Tech IV*, 311–318 (1993)
- Baerg, A, Klasson, J., and Gishler, P. E., "Heat Transfer in a Fluidized Solids Bed," *Can. J. of Res.*, 28(8):287 (1950)
- Baskakov, A. P., Berg, B. V., Vitt, O. K., Fillipovsky, N. F., Kirakosyn, V. A., Coldobin, J. M., and Maskaev, V. K., "Heat Transfer to Objects Immersed in Fluidized Bed," *Powder Tech.*, 8(5–6):273–282 (1973)

- Baskakov, A. P., "The Mechanism of Heat Transfer Between a Fluidized Bed and a Surface," *Int. Chem. Eng.*, 4:320 (1984)
- Basu, P., and Nag, P. K., "Heat Transfer to Walls of a Circulating Fluidized Bed Furnace," *Chem. Eng. Sci.*, 1:1-26 (1996)
- Beaude, F., and Louge, M., "Similarity of Radial Profiles of Solid Volume Fraction in a Circulating Fluidized Bed," *Fluidization VIII*, pp. 245-253 (1995)
- Berg, B. V., and Baskakov, A. P., "Investigation of Local Heat Transfer Between a Fixed Horizontal Cylinder and a Fluidized Bed," *International Chem. Eng.*, 14(3):440-443 (1974)
- Bhattacharya, and Harrison, D., "Heat Transfer in High Temperature Fluidized Beds," *Proc. Euro. Conf. In Particle Tech.*, K7 (1976)
- Biyikli, S., and Chen, J. C., "Effect of Mixed Particle Sizes on Local Heat Transfer Coefficients Around a Horizontal Tube in Fluidized Beds," *7th Int. Heat Transfer Conf.*, Munich, Germany (1982)
- Bock, H. J., and Schweinzer, J., "Heat Transfer to Horizontal Tube Banks in a Pressurized Gas/Solid Fluidized Bed," *German Chem. Eng.*, 9(1):16-23 (1986)
- Borodulya, V. A., Teplitsky, Y. S., Sorokin, A. P., Matsnev, V. V., Markevich, I. I., and Kovenskiy, V. I., "External Heat Transfer in Polydispersed Fluidized Beds at Increased Temperatures," *J. Eng. Phys.*, 56(5):767-773 (1989)
- Borodulya, V. A., Teplitsky, Y. S., Sorokin, A. P., Markevich, I. I., Hassan, A. F., and Yeryomenko, T. P., "Heat Transfer Between a Surface and a Fluidized Bed: Consideration of Pressure and Temperature Effects," *Int. J. of Heat and Mass Transfer*, 34(4):47-53 (1991)
- Botterill, J. S. M., Butt, M. H. D., Cain, G. L., and Redish, K. A., *Inter. Symp. on Fluidization*, p. 442, Univ. Press, Amsterdam, Netherlands (1967)
- Botterill, J. S. M., and Williams, J. R., "The Mechanism of Heat Transfer to Gas-Fluidized Beds," *Trans. Inst. Chem. Eng.*, 41:217-230 (1963)
- Botterill, J. S. M., and Desai, M., "Limiting Factors in Gas-Fluidized Bed Heat Transfer," *Powder Technol.*, 6(4):231-238 (1972)
- Brewster, M. O., and Tien, C. L., "Radiative Heat Transfer in Packed Fluidized Beds: Dependent Versus Independent Scattering," *J. Heat Transfer*, 104(4):574-580 (1982)
- Burki, V., Hirschberg, B., Tuzla, K., and Chen, J. C., "Thermal Development for Heat Transfer in Circulating Fluidized Beds," *ALChE Annual Meeting*, (1993)
- Chandran, R., Chen, J. C., and Staub, F. W., "Local Heat Transfer Coefficients Around Horizontal Tubes in Fluidized Beds," *J. of Heat Transfer*, 102(2):152-157 (1980)

204 *Fluidization, Solids Handling, and Processing*

- Chen, J. C., "Heat Transfer to Tube in Fluidized Beds," Invited Lecture, Paper No. 76-HT-75, National Heat Transfer Conf., St. Louis, MO., (1976)
- Chen, J. C., Chen, K. L., "Analysis of Simultaneous Radiative and Conductive Heat Transfer in Fluidized Beds," *Chem. Eng. Commun.*, 9:255–271 (1981)
- Chen, J. C., Cimini, R. J., and Dou, S. H., "A Theoretical Model for Simultaneous Convective and Radiative Heat Transfer in Circulating Fluidized Beds," *Circ. Fluid. Bed Tech. II*, 255–262 (1988)
- Chen, J. C., "Thomas Baron Plenary Lecture – Clusters," *AIChE Symp. Series*, 92(313):1–6 (1969)
- Chen, J. C., "Heat Transfer to Tubes in Fluidized Beds," Invited Lecture, Paper No. 76-HT-75, National Heat Transfer Conf., St. Louis (1976)
- Cimini, R. J., and Chen, J. C., "Experimental Measurement of Radiant Transmission Through Packed and Fluidized Media," *Experimental Heat Transfer*, 1:45–56 (1987)
- Divilio, R. J., and Boyd, T. J., "Practical Implications of the Effect of Solids Suspension Density on Heat Transfer in Large-Scale CFB Boilers," *Circ. Fluid. Bed Tech IV*, 334–339 (1993)
- Dou, S., Herb, B., Tuzla, K., and Chen, J. C., "Heat Transfer Coefficients for Tubes Submerged in Circulating Fluidized Bed," *Experimental Heat Transfer*, 4:343–353 (1991)
- Dou, S., Herb, B., Tuzla, K., and Chen, J. C., "Dynamic Variation of Solid Concentration and Heat Transfer Coefficient at Wall of Circulating Fluidized Bed," *Fluidization VII*, 793–801 (1993)
- Dow, W. M., and Jacob, M., "Heat Transfer Between a Vertical Tube and a Fluidized Air-Solid Mixture," *Chem. Eng. Progr.*, 47(12):637–648 (1951)
- Ebert, T., Glicksman, L., and Lints, M., "Determination of Particle and Gas Convective Heat Transfer Components in Circulating Fluidized Bed," *Chem. Eng. Sci.*, 48:2179–2188 (1993)
- Einshtein, V. G., and Gelperin, N. I., "Heat Transfer Between a Fluidized Bed and a Surface," *Intern. Chem. Eng.*, 6(1):67–81 (1966)
- Ergun, S., "Fluid Flow Through Packed Columns," *Chem Eng. Progress*, 48(2):89–94 (1952)
- Fox, R. W., and McDonald, A. T., *Introd. to Fluid Mechanics*, 4:444, John Wiley & Sons, New York (1992)
- Fraleigh, L. D., Lin, Y. Y., Hsiao, K. M., and Solbakken, A., ASME Paper 83-HT-92 (1983)
- Furchi, J. C. L., Goldstein, L., Jr., Lombardi, G., and Mohseni, M., "Experimental Local Heat Transfer in a Circulating Fluidized Bed," *Circ. Fluid. Bed Tech. II*, 263–270 (1988)

- Gabor, J. O., "Wall-to-Bed Heat Transfer in Fluidized and Packed beds," *AIChE Symp. Series*, 66(105):76–86 (1970)
- Gamson B. W., "Heat and Mass Transfer in a Fluid Solid System," *Chem. Eng. Progress*, 47(1):19–28 (1951)
- Geldart, D., "Types of Gas Fluidization," *Powder Technol.*, 7(5):285–292 (1973)
- Gelperin, N. I., and Einshtein, V. G., "Heat Transfer in Fluidized Beds," *Fluidization*, p. 471, London, UK (1971)
- Gelperin, N. I., Einshtein, V. G., Korotjanskaja, L. A., and Perevozchikova, J. P., *Teoreticheskie Osnovy Khimicheskoe Tech.* 2:430 (1968)
- Grace, J. R., *Can. J. Chem. Eng.* 64:353 (1986)
- Grace, J., "Heat Transfer in Circulating Fluidized Beds," *Cir. Fluid. Bed Tech.*, 63–81 (1986)
- Han, G. Y., "Experimental Study of Radiative and Particle Convective Heat Transfer in Fast Fluidized Beds," Ph.D. Dissertation, Lehigh University (1992)
- Hartige, E. U., Li, Y., and Werther, J., "Flow Structures in Fast Fluidized Beds," *Fluidization V*, 345–352 (1986)
- Herb, B. E., Dou, S., Tuzla, K., and Chen, J. C., "Axial Solid Concentration in CFBs: Experimental Measurements and Model Predictions," *AIChE Annual Meeting* (1989)
- Herb, B., Tuzla, K., and Chen, J. C., "Distribution of Solid concentrations in Circulating Fluidized Bed," *Fluidization VI*, 65–72 (1989)
- Herb, B. E., Dou, S., Tuzla, K., and Chen, J. C., "Solid Mass Fluxes in Circulating Fluidized Beds," *Powder Technol.*, 197–205 (1992)
- Horio, M., Morshita, K., Tachibana, O., and Murata, M., "Solid Distribution and Movement in Circulating Fluidized Beds," *Circ. Fluid. Bed Tech. II*, 147–154 (1988)
- Jacob, A., and Osberg, G. L., "Effect of Gas Thermal conductivity on Local Heat Transfer in a Fluidized Bed," *Canadian J. of Chem. Eng.*, 35(6):5–9 (1957)
- Jestin, L., Chaberg, C., Flamant, G., and Meyer, P., "In-situ Measurement of Particle Concentration, Temperature Distribution and Heat Flux in Vicinity of A Wall in A CFB," *Circ. Fluid. Bed Tech. IV*, 247–254 (1990)
- Kiang, K. D., Lin, K. T., Nack, H., and Oxley, J. H., "Heat Transfer in Fast Fluidized Beds," *Fluidization Technol.*, 471–483 (1976)
- Kobro, M., and Brereton, L., "Control and Fuel Flexibility of Circulation Fluidized Beds," *Circ. Fluid. Bed Tech.*, 263–272 (1986)
- Kubie, J., and Broughton, J., "A Model of Heat Transfer in Gas Fluidized Beds," *Int. J. of Heat and Mass Transfer*, 18:289–299 (1975)

206 *Fluidization, Solids Handling, and Processing*

- Kunii, K., and Smith, J. M., "Heat Transfer Characteristics of Porous Rocks," *AIChE J.* 6(1):71–78 (1960)
- Kunii, D., and Levenspiel, O., *Fluidization Eng.*, 2nd Ed., Butterworth-Heinemann, Boston (1991)
- Leva, M., Weintrub, M., and Grummer, M., "Heat Transmission Through Fluidized Beds of Fine Particles," *Chem. Eng. Progr.*, 45(9):563–572 (1949)
- Leva, M., and Grummer, M., "Correlation of Solids Turnovers in Fluidized Systems," *Chem. Eng. Progr.*, 48(6):307–313 (1952)
- Levenspiel, O., and Walton, J. S., *Chem. Eng. Progr. Symp. Series*, 50(9):1 (1954)
- Lints, M., "Particle to Wall Heat Transfer in Circulating Fluidized Beds," Ph.D. Dissertation, MIT (1992)
- Lints, M. C., and Glicksman, L. R., "Structure of Particle Clusters Near Wall of a Circulating Fluidized Bed," *AIChE Symp. Series*, 89(296):35–47 (1993)
- Lints, M. C., and Glicksman, L. R., "Parameters Governing Particle-to-Wall Heat Transfer in a Circulating Fluidized Bed," *Circ. Fluid. Bed Tech. IV*, 297–304 (19923)
- Liu, D., Liu, J., Li, T., and Kwauk, M., "Shallow Fluid Bed Tubular Heat Exchanger," *Fluidization*, pp. 401–408, 5th Eng. Foundation Conf. on Fluidization, Engineering Foundation, NY (1986)
- Louge, M., Lischer, J., and Chang, H., "Measurements of Voidage Near the wall of a Circulating Fluidized bed Riser," *Powder Tech.*, 62:269–276 (1990)
- Mahalingan, M., and Kolar, A. K., "Heat Transfer Model for Membrane Wall of a High Temperature Circulating Fluidized Bed," *Circ. Fluid. Bed Tech. III*, 239–246 (1990)
- Martin, H., "Heat Transfer Between Gas Fluidized Beds of Solid Particles and the Surface of Immersed Heat Exchanger Element," Parts I & II, *Chem. Eng. Process*, 18:157–169, 199–223 (1984)
- Mickley, H. S., and Trilling, C. A., "Heat Transfer Characteristics of Fluidized Beds," *Ind. Eng. Chem.*, 41(6):1135–1147 (1949)
- Mickley, H. S., and Fairbanks, D. F., "Mechanism of Heat Transfer to Fluidized Beds," *AIChE J.*, 1(3):374–384 (1955)
- Miller, C. O., and Logwinuk, A. K., "Fluidization Studies of Solid Particles," *Ind. & Eng. Chem.*, 43(5):1220–1226 (1951)
- Molerus, O., and Schweinzer, J., "Prediction of Gas Convective Part of the Heat Transfer to Fluidized Beds," pp. 685–693, *Fluidization IV*, Eng. Foundation, New York, USA (1989)
- Molerus, O., "Fluid Dynamics and Its Relevance for Basic Features of Heat Transfer in Circulating Fluidized Beds," *Circ. Fluid. Bed Tech. IV*, pp. 285–290 (1993)

- Noë, A. R., and Knudsen, J. G., "Local and Average Heat Transfer Coefficients in a Fluidized Bed Heat Exchanger," *Chem. Eng. Prog. Symp. Series*, 64(82):202–211 (1968)
- Ozkaynak, T. F., and Chen, J. C., "Emulsion Phase Residence time and Its Use in Heat Transfer Models in Fluidized bed," *AIChE J.*, 26(4):544–550 (1980)
- Ozkaynak, T., "Investigation of Packet Residence Time and Its Relation with the Heat Transfer Coefficient in Fluidized Beds," Ph.D.. Dissertation, Lehigh University (1974)
- Ozkaynak, T. F., Chen, J. C., and Frankenfield, T. R., "An Experimental Investigation of Radiant Heat Transfer in High Temperature Fluidized Bed," *Fluidization*, Fourth International Conf. on Fluidization, pp. 371–378, Engineering Foundation (1983)
- Palchonok, G. I., Breitholz, C., Anderson, B. A., and Lechner, B., "Heat Transfer in the Boundary Layer of a Circulating Fluidized Bed Boiler," *Fluidization VIII*, pp. 291–299 (1995)
- Radauer, H. G., Glatzer, A., and Linzer, w., "A Model Combining Convective and Radiative Heat Transfer in CFB Boilers," *Circ. Fluid. Bed Tech.* V, 9 (1996)
- Saxena, S. C., Grewal, N. S., Gabor, J. D., Zabrodsky, S. S., and Galershtein, D. M., "Heat Transfer Between a Gas Fluidized Bed and Immersed Tubes," *Adv. In Heat Transfer*, 14:145–247 (1978)
- Soong, C. H., Tuzla, K., and Chen, J. C., "Indentification of Particle Clusters in Circulating Fluidized Bed," *Circ. Fluid. Bed Tech.* IV, pp. 809–814 (1993)
- Soong, C. H., Tuzla, K., and Chen, J. C., "Experimental Determination of Cluster Size and Velocity in Circulating Fluidized Beds," *Fluidization VIII*, Engineering Foundation, pp. 219–227 (1995)
- Tamarin, A. I., Zabrodsky, S. S., and Yepanov, G., "Heat Transfer Between a Horizontal Staggered Tube Bundle and a Fluidized Bed," *Heat Transfer-Soviet Research*, 8(5):51–55 (1976)
- Vedamuthy, V. N., and Sastri, V. M. K., "An Analysis of the Conductive and Radiative Heat Transfer to Walls of Fluidized Combustors," *Intern. J. Heat Mass Transf.*, 17(1):1–9 (1074)
- Visser, G., and Valk, M., "The Porosity in a Fluidized Bed Heat Transfer Model," *Int. J. of Heat and Mass Transfer*, 36(3):627–632 (1993)
- Vreedenberg H. A., "Heat Transfer Between a Fluidized Bed and a Horizontal Tube," *Chem. Eng. Sci.*, 9(1):52–60 (1958)
- Vreedenberg H. A., "Heat Transfer Between a Fluidized Bed and a Vertical Tube," *Chem. Eng. Sci. II*, 4:274–285 (1960)
- Wen, C. Y., and Miller, E. N., *Ind. Eng. Chem.*, 53:51–53 (1966)

208 *Fluidization, Solids Handling, and Processing*

- Wen, C. Y., and Yu, Y. H., "A Generalized Method for Predicting the Minimum Fluidization Velocity, *AIChE J.*, 12(3):610–612 (1966)
- Wender, L., and Cooper, G. T., "Heat Transfer Between Fluidized-Solids Beds and Boundary Surfaces--Correlation of Data," *AIChE J.*, 4(1):15–23 (1958)
- Werdmann, C. C., and Werther, J., "Solids Flow Pattern and Heat Transfer in an Industrial Scale Fluidized Bed Heat Exchanger," *Proc. 12th Intern. Conf. on Fluid. Bed Comb.*, 2:985–990 (1993)
- Werther, J., "Fluid Mechanics of Large-Scale CFB Units," *Circ. Fluid. Bed Technol. IV*, pp. 1–14 (1993)
- Wirth, K. E., "Zirkulierende Wirbelschichten-Stromungsmechanische Grundlagen," *Anwendung in der Feuerungstechnik* (1990)
- Wirth, K. E., "Prediction of Heat Transfer in Circulating Fluidized Beds," *Circ. Fluid. Bed Tech. IV*, pp. 291–296 (1993)
- Wirth, K. E., "Heat Transfer in Circulating Fluidized Beds," *Chem. Eng. Sci.*, 50(13):2137–2151 (1995)
- Wood, R. T., Staub, F. W., Canada, G. S., and McLaughlin, M. H., "Two-Phase Flow and Heat Transfer in Fluidized Beds," Technical Report, RP 525-1, General Electric Co., Schenectady, NY (1978)
- Wu, R., Grace, J., Lim, C., and Brereton, C., "Suspension to Surface Heat Transfer in a Circulating Fluidized Bed Combustor," *AIChE J.*, 35:1685–1691 (1989)
- Wu, R. L., "Heat Transfer in Circulating Fluidized Beds," Ph.D.. Dissertation, Univ. of British Columbia (1989)
- Xavier, A. M., and Davidson, J. F., "Heat Transfer to Surfaces Immersed in Fluidized Beds, Particularly Tube Arrays," *Fluidization*, Proc. of Second Eng. Foundation Conf., pp. 333–338, Cambridge Univ. Press (1978)
- Yagi, S., and Kunii, K., "Studies on Effective Thermal Conductivities in Packed Beds," *AIChE J.*, 3:373 (1957)
- Yoshida, K., Ueno, T., and Kunii, D., "Mechanism of Bed-Wall Heat Transfer in a Fluidized Bed at High Temperature," *Chem. Eng. Sci.*, 29(1):77–82 (1974)
- Ziegler, E. N., Koppel, L. B., and Brazelton, W. T., "Effects of Solid thermal Properties on Heat Transfer to Gas Fluidized Bed," *I&EC Fundamentals*, 3(4):324–328 (1964)

Gas Distributor and Plenum Design in Fluidized Beds

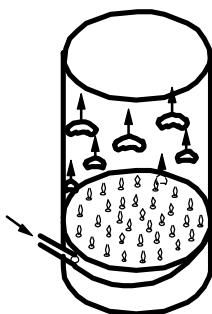
S.B. Reddy Karri and Ted M. Knowlton

1.0 INTRODUCTION

The gas distributor (also called a grid) in a fluidized bed reactor is intended to induce a uniform and stable fluidization across the entire bed cross-section, operate for long periods (years) without plugging or breaking, minimize weepage of solids into the plenum beneath the grid, minimize attrition of the bed material, and support the weight of the bed material during start-up and shut-down. In practice, grids have taken a variety of forms, a few of which are discussed in subsequent pages. Whatever the physical form, all are fundamentally classifiable in terms of the direction of gas entry: either upward, laterally, or downward. The choice depends on prevailing process conditions, mechanical feasibility, and cost. In the past, grid design has been more of an art than a science. However, more recent studies now allow grid designs based on scientific principles.

2.0 TYPES OF GRIDS

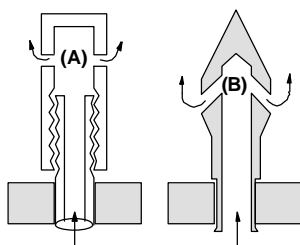
2.1 Perforated Plates (Upwardly-Directed Flow)



Main Advantages: Simple fabrication; most common; inexpensive; easy to modify hole size; easy to scale up or down; easy to clean; can be flat, concave, convex, or double dished; ports are easily shrouded.

Possible Disadvantages: Bed weepage to plenum; high pressure drop; can be subject to buckling or thermal distortion; requires peripheral seal to vessel shell; requires support over long spans.

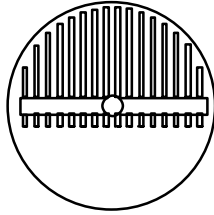
2.2 Bubble Cap (Laterally-Directed Flow)



Main Advantages: Minimizes weeping; good turndown ratio; lower pressure drop; can incorporate caps as stiffening members; can support internals.

Possible Disadvantages: Expensive; difficult to avoid stagnant regions; more subject to immediate bubble merger; difficult to clean; difficult to modify; not advisable for sticky solids; requires peripheral seal; ports not easily shrouded.

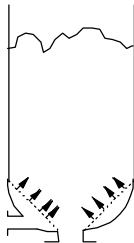
2.3 Sparger (Laterally or Downwardly-Directed Flow)



Main Advantages: Can minimize weeping; good turndown ratio; low pressure drop; can support internals; can undergo thermal expansion without damage; ports are easily shrouded; well suited to multilevel fluid injection; solids can flow from above the grid to below.

Possible Disadvantages: Defluidized solids beneath the grid; can be a less-forgiving mechanical design.

2.4 Conical Grids (Laterally-Directed Flow)



Main Advantages: Promotes solid mixing; prevents stagnant solids buildup, minimizes solids segregation.

Possible Disadvantages: Difficult to construct, requires careful design to ensure good gas distribution, requires high pressure drop for good gas distribution.

Among the foregoing advantages and limitations, the designer must select those most pertinent or critical to his process application. There are, for example, instances in which solids below the grid level are tolerable, where grid thermal expansion is significant, where bed solids are very friable, where pressure drop and, therefore, the cost of compressive

horsepower is critical, where solids are “sticky” and must be kept in motion throughout, where internal impellers or stirrers must be provided, or where grids are expected to have a short life due to corrosion.

These and many other specifics have dictated a host of design variations. It should be emphasized that each application requires thoughtful engineering consideration before final design selection.

3.0 GRID DESIGN CRITERIA

3.1 Jet Penetration

Gas flowing from the grid holes can either take the form of a series of bubbles or a permanent jet, depending on system parameters and operating conditions. However, a permanent jet prevails for most industrial conditions. Jet penetration is one of the most important design parameters since it helps in:

- (a) Determining how far to keep the bed internals, such as feed nozzles, heat exchanger tubes, etc., away from the grid to minimize erosion of internals.
- (b) Deciding on grid design parameters such as hole size and the gas jet velocity required to achieve a certain jetting region.
- (c) Minimizing or maximizing particle attrition at grids.

Knowlton and Hirsan (1980) reported that the jet penetration for upwardly-directed jets fluctuated greatly. Karri (1990) noted that jet penetration can vary as much as 30% for upwardly-directed jets. However, the jet emanating from a downwardly-directed grid hole is stable and its penetration length doesn't significantly fluctuate with time. Figure 1 indicates jet penetration configurations for jets oriented upwardly, horizontally, and downwardly. According to Karri, the jet penetrations for various orientations can be approximately related by:

$$\text{Eq. (1)} \quad L_{up} \approx 2L_{hor} \approx 3L_{down}$$

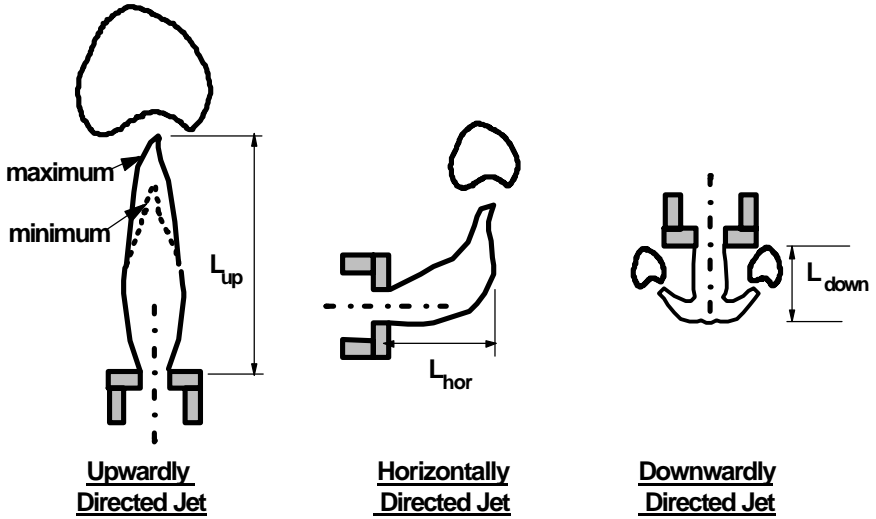


Figure 1. Jet penetrations at grid holes for different orientations.

There are numerous jet penetration correlations (Zenz, 1969; Shakhova, 1968; Merry, 1971; Yang and Keairns, 1979; Knowlton and Hirsan, 1980; Yates et al., 1986; Blake et al., 1990; Roach, 1993) in the literature. Massimilla (1985) and Karri (1990) have shown that the jet penetrations predicted by these correlations can vary by a factor of 100 or more. Among them, Merry's correlation for horizontal jets was shown (Karri; Chen and Weinstein, 1993; Roach) to give reliable predictions. Merry's correlation to calculate the penetration of horizontal jets is:

$$\text{Eq. (2)} \quad \frac{L_{hor}}{d_h} = 5.25 \left(\frac{\mathbf{r}_{g,h} U_h^2}{\mathbf{r}_p (1 - \mathbf{e}_{mf}) g d_p} \right)^{0.4} \left(\frac{\mathbf{r}_{g,b}}{\mathbf{r}_p} \right)^{0.2} \left(\frac{d_p}{d_h} \right)^{0.2}$$

The jet penetration lengths for upwardly and downwardly directed jets can be calculated from Eq. (1). These equations take into account the effects of pressure and temperature on jet penetration. Knowlton and Hirsan (1980) and Yates et al. found that the jet penetration increases significantly with system pressure. In addition, Sishtla et al. (1989) found that the jet penetration decreases with increasing system temperature. Bed

internals should not be placed in the jetting zone near the grid, otherwise the internals could be severely eroded.

3.2 Grid Pressure-Drop Criteria

For a grid, achieving equal distribution of gas flow through many parallel paths requires equal resistances and sufficient resistance to equal or exceed the maximum value of any unsteady-state pressure fluctuation. It has been determined experimentally that the “head” of solids in some fluidized beds above an upwardly-directed grid port can vary momentarily by as much as 30%. This is due to large fluctuations in the jet penetration for an upwardly-directed jet as discussed in the previous section. The equivalent variation downstream of a downwardly-directed port is less than 10%. Thus, as a rule of thumb, the criteria for good gas distribution based on the direction of gas entry are:

(a) For upwardly and laterally-directed flow:

$$\text{Eq. (3)} \quad DP_{grid} \geq 0.3 DP_{bed}$$

(b) For downwardly-directed flow:

$$\text{Eq. (4)} \quad DP_{grid} \geq 0.1 DP_{bed}$$

(c) Under no circumstances should the pressure drop across a large-scale commercial grid be less than 25 cm of water, i.e.,

$$\text{Eq. (5)} \quad DP_{grid} \geq 25 \text{ cm H}_2\text{O}$$

Several investigators (Hiby, 1964; Zuideweg, 1967; Whitehead, 1971; Siegel, 1976; and Mori and Moriyama, 1978) have found the ratio of pressure drops to be in the range of 0.015 to 0.4.

If turndown is desired, the grid pressure-drop criteria (Eqs. 3 and 4) must apply at the minimum gas flow rate. Also, if the grid is curved, i.e., concave, convex, or conical, the criterion must apply with respect to the

lowest hole on the grid. Take an example of a fluid bed with curved grid as shown in Fig. 2.

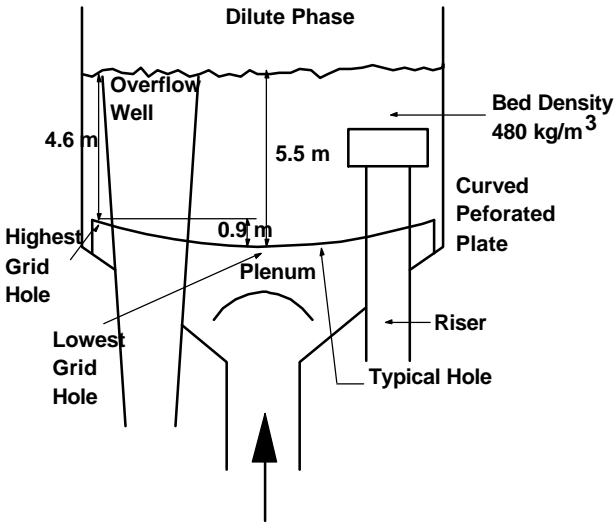


Figure 2. A typical fluid bed showing a curved perforated plate.

A pressure balance across the curved grid can be written as:

$$\text{Eq. (6)} \quad DP_h (\text{Highest Hole}) = DP_h (\text{Lowest Hole}) + r_B g (H_{high} - H_{low})$$

i.e.,

$$\begin{aligned} \text{Eq. (7)} \quad DP_h (\text{Highest Hole}) &= DP_h (\text{Lowest Hole}) + 480 \times 9.8 \times 0.9 \\ &DP_h (\text{Lowest Hole}) + 4235 \text{ Pa} \end{aligned}$$

Therefore, the lowest grid hole has the lowest pressure drop, and hence for pressure drop, the criterion must apply with respect to the lowest hole on the grid.

3.3 Design Equations

The following equations can be used to design perforated plates, spargers, and bubble-cap types of grids:

Pressure drop across the grid:

Eq. (8) $\Delta P_{grid} = Kg \, r_B L_B$

where $K = 0.3$ for upward and lateral gas entry, and 0.1 for downward gas entry.

The gas velocity through the grid hole (orifice equation):

Eq. (9) $U_h = C_d \sqrt{\frac{2\Delta P_{grid}}{r_{g,h}}}$

The orifice discharge coefficient, C_d , is typically about 0.6 for gas flowing through an orifice in a pipe (for a ratio of orifice diameter to pipe diameter in the range of 0 to 0.2). This value of the orifice coefficient is for a sharp-edged orifice. However, grids are not sharp-edged, and the orifice coefficient is greater than 0.6. A typical value of C_d for a grid hole is about 0.8. Actually, the value of C_d depends on the grid plate thickness and the hole pitch. It can be calculated from Fig. 3.

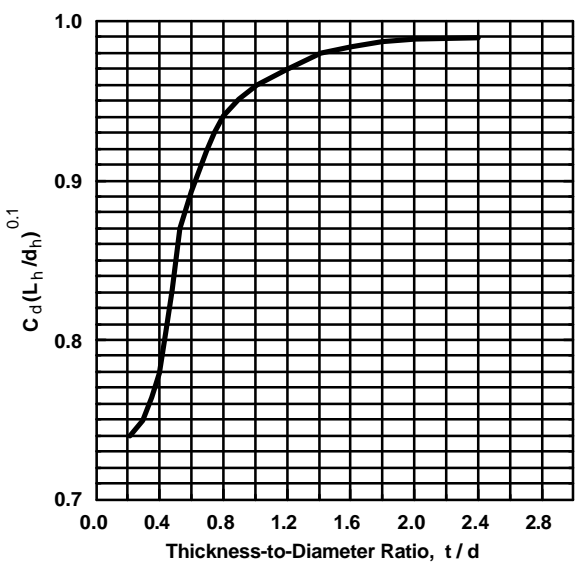


Figure 3. Grid hole discharge coefficient design chart.

Volumetric flow rate of gas:

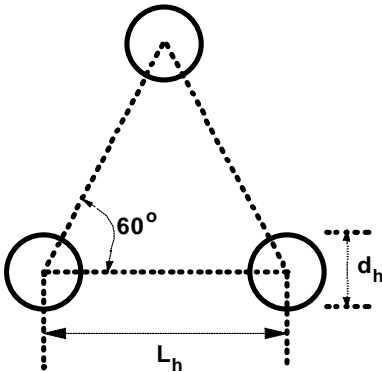
$$\text{Eq. (10)} \quad Q = N \frac{\rho d_h^2}{4} U_h$$

Hole Size. To increase the gas residence time in the bed, it is desirable to introduce the greatest number of small gas bubbles as possible into the bed. This can be achieved by maximizing N at the expense of d_h in Eq. (10) (within the limits of mechanical, cost, and scale-up constraints). To minimize stagnant zones, the number of grid holes per m^2 should be ≥ 10 . In practice, the number of grid holes per square meter is generally about 2 to 3.

Hole Layout. To increase the uniformity of fluidization, it is common to lay out the holes in triangular or square pitch as shown in Fig. 4. All the holes in a grid with triangular pitch are equidistant. This is not the case for a grid with square pitch. Triangular pitch will also result in more holes per unit area.

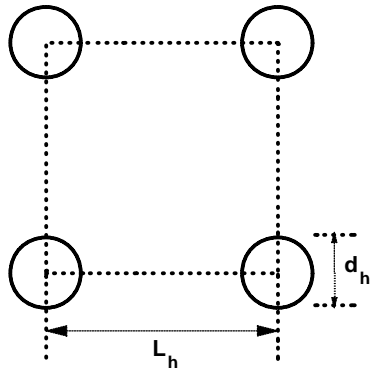
The relationship between the grid hole pitch, L_h , and the number hole density (holes per unit area of the bed), N_d , depends on whether the holes are laid out in triangular or square pitch.

• **Triangular Pitch**



$$\text{Eq. (11)} \quad L_h = \frac{1}{\sqrt{N_d \sin 60^\circ}}$$

• **Square Pitch**



$$\text{Eq. (12)} \quad L_h = \frac{1}{\sqrt{N_d}}$$

Figure 4. The relationship between hole density and grid hole pitch for triangular and square pitch.

3.4 Additional Criteria for Sparger Grids

Additional distribution criteria are used for sparger grids. To keep the pipe header pressure drop down to acceptable levels and to ensure good gas distribution, the following criteria (Karri, 1990) should be met:

- (a) The manifold should be sized based on the following equation:

Eq. (13)
$$\left(\frac{D_m^2}{N_h d_h^2} \right)^2 > 5$$

The parameters in Eq. (13) are defined in Fig. 5.

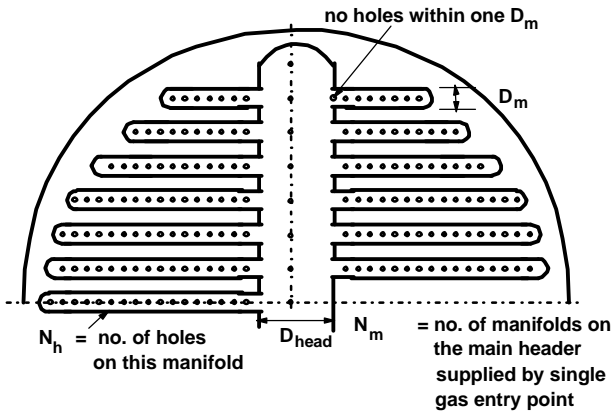


Figure 5. Manifold sparger grid showing the definitions of various parameters

Similarly, the main header pipe should be sized based on the following equation:

Eq. (14)
$$\left(\frac{D_{head}^2}{N_m D_m^2} \right)^2 > 5$$

- (b) In some instances, two to three different hole sizes are used on a given manifold to get better gas distribution.

- (c) The gas velocity in the header/manifold pipe should be <25 m/s for best distribution.
- (d) Holes should not be located closer than one D_m from any sharp bend or tee in the header/manifold to prevent solids from being sucked into the manifolds due to the vena contracta effect.

3.5 Port Shrouding or Nozzle Sizing

Shrouds are generally placed around grid holes to reduce the velocity at the gas-solids interface and reduce particle attrition. Shrouds simply consist of short pipes centered over the smaller grid holes which have been selected in size and number to operate at a hole velocity defined by Eq. (9).

To be effective, shrouds must be long enough to “contain” the expanding (11-degree included angle) gas jet leaving the grid orifice.

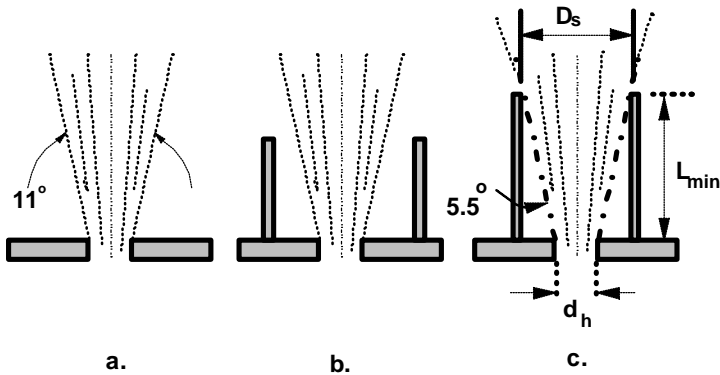


Figure 6. (a) Diverging free jet; (b) shroud too short to contain the jet; (c) minimum shroud length required to contain jet.

As can be seen from the Fig. 6, the minimum shroud length should be:

Eq. (15)
$$L_{min} = \frac{D_s - d_h}{2 \tan 5.5^\circ}$$

In practice, it is prudent to increase L_{min} by a factor of 50 to 100%. A shroud length less than L_{min} causes significantly more erosion and attrition than no shroud at all. Significant attrition can also occur if the shroud is not centered over the smaller hole.

The nozzle or shroud details inside a sparger pipe grid are illustrated in Fig. 7.

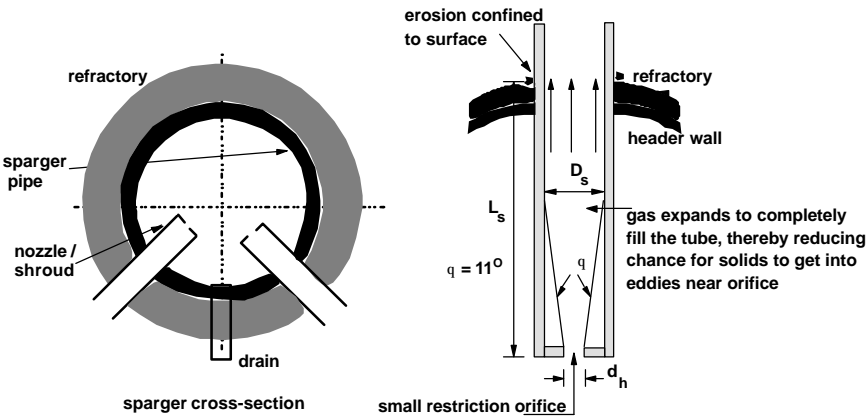


Figure 7. Shroud design for a sparger grid.

If properly sized and installed, particle attrition is reduced by a factor (Karri, 1990) calculated from:

Eq. (16)
$$\frac{\text{particle attrition without shrouds}}{\text{particle attrition with shrouds}} = \left(\frac{D_s}{d_h} \right)^{1.6}$$

4.0 PARTICLE ATTRITION AT GRIDS

Solids immediately surrounding the gas jets issuing from the grid are ingested into the jets. These particles are accelerated and collide with the particles near the tip of the jet. Figure 8 depicts how the particles are picked up and slammed into a fluidized, yielding bed for an upwardly-directed jet. However, downward-pointing jets generally issue into a non-fluidized area of particles. Therefore, particles picked up by downwardly-directed jets issuing into a non-yielding unaerated bed, results in a greater degree of particle attrition.

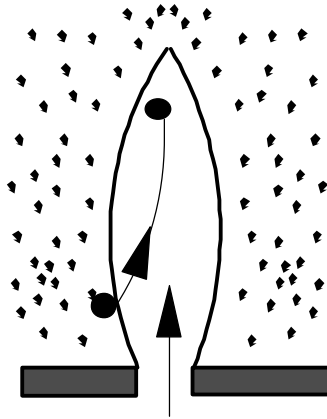


Figure 8. The mechanism of particle attrition at a submerged jet.

The attrition rate, i.e., the rate of generation of fines, $0-d_p$ microns, at the submerged jets in a fluidized bed, tends to fall off asymptotically with time to a steady-state rate as shown in Fig. 9. Initially the attrition rate is high due to the wearing off of angular corners. Typically, it takes long time, hours to days, for the particles to reach steady-state (equilibrium) where the particles tend to be more rounded. For most catalytic fluidized bed processes, the bed operates at equilibrium. That means the most significant part of the attrition rate curve is the “steady-state” rate.

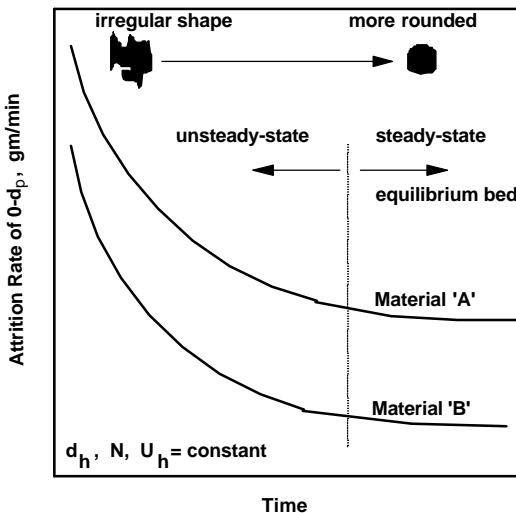


Figure 9. Typical attrition rate curve for submerged jets.

4.1 **Attrition Correlation**

There is no general correlation available to date to predict the steady state attrition rates for various materials. Zenz and Kelleher (1980) gave a simple correlation to predict steady-state attrition rates for FCC catalyst and glass beads. This is an empirical dimensional equation as given by:

Eq. (17) $\frac{f}{N} \text{ (kg/m/hole)} = K_a \left(U_h \sqrt{r_{g,h}} \right)^{2.5} \frac{\rho d_h^2}{4}$

The following table gives the attrition-rate constant (K_a) for FCC catalyst as a function of particle size range (0– d_p) for upwardly-directed jets.

Attrition to particles of	Numerical Constant, K_a
0 to d_p (μm)	in Eq. 17
0 to 2	1.11×10^{-6}
0 to 23	9.03×10^{-6}
0 to 50	2.29×10^{-5}

For glass beads, the values of K_a were found to be about $1/12$ those for FCC catalyst. For other materials, one should obtain a relative attrition index with respect to either FCC or glass beads and then obtain a value of K_a based on that index.

Karri (1990) reported that downwardly-directed jets have approximately twice the steady-state attrition rate as that of upwardly directed jets. The attrition rates for upwardly and laterally directed jets are essentially the same.

If excessive particle attrition is expected, it is a common practice to place a shroud/nozzle around a grid hole as discussed in Sec. 3.5. For properly sized nozzles, one can derive from Eq. (17), particle attrition is reduced by a factor:

Eq. (18) $\frac{\text{particle attrition without shrouds}}{\text{particle attrition with shrouds}} = \left(\frac{D_s}{d_h} \right)^3$

However, it has been determined experimentally that the exponent in Eq. (18) is more like 1.6 as shown in Eq. (16) instead of 3 as indicated in Eq. (18).

5.0 EROSION

Erosion in the grid region is primarily due to high velocity submerged jets impinging on distributor parts, bed walls, or on bed internals. Therefore, one should estimate the jet penetration heights for a given grid design and check for the following:

- (a) Bed internals should not be placed in the jetting zone near the grid, otherwise the internals could be severely eroded.
- (b) Nozzles should not be located any closer than half the jet penetration height from the bed wall.

Erosion in the nozzle or orifices is often associated with weepage of solids. This can be avoided by carefully designing a grid with the proper pressure drop criteria as presented in Sec. 3.2. Poorly designed bubble caps tend to have erosion problems due to the secondary circulation of solids. Therefore, bubble caps should be designed to minimize secondary circulation of solids.

6.0 EFFECTS OF TEMPERATURE AND PRESSURE

System temperature and pressure affect the momentum of grid jets via the gas density (see Ch. 2). The momentum of the gas jets is $\mathbf{r}_{g,h} U_h$. When the temperature is increased, the gas density decreases. For the same gas jet velocity this decreases the momentum of the jets and, therefore, decreases the jet penetration and the attrition at the grid. Similarly, when system pressure is increased, gas density increases, gas jet momentum increases and, therefore, the jet penetration and the attrition at the grid are increased.

7.0 PLENUM DESIGN

The plenum, or windbox, is the chamber immediately below the grid. If the bed-pressure-drop-to-grid-pressure-drop ratio is high enough, the plenum design will probably not be that important. However, for the case where this ratio is marginal, the plenum design may determine whether the bed will operate satisfactorily.

The typical plenum designs showing various configurations for introducing gas into the plenum, are illustrated in Fig. 10. Common sense dictates that certain plenum designs may be preferred over others. If the gas enters the plenum from the bottom, it is preferable that the plenum has a large enough distance between the outlet of the supply pipe and the grid to prevent the gas from preferentially passing through the middle of the grid. When gas enters a plenum from the side, it is preferable to route the gas to the middle of the plenum (Fig. 10 *c*) rather than have the supply pipe end at the wall of the plenum. In addition, horizontal-to-vertical down gas entry (Fig. 10 *c*) is preferable over the horizontal-to-vertical up gas entry (Fig. 10 *b*).

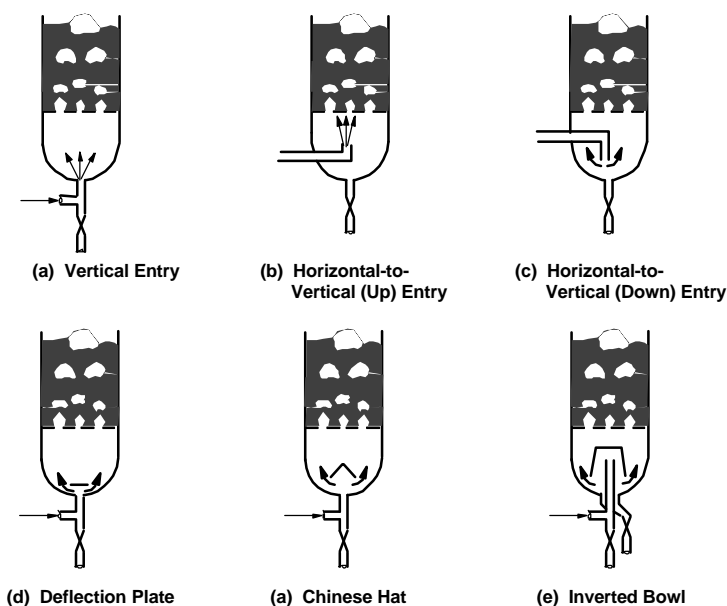


Figure 10. Different plenum configurations.

If the gas-solid or gas-liquid suspension needs to be introduced into the plenum, as for example in a polyethylene reactor and some FCC regenerators, it is preferable to introduce the suspension at the lowest point of the plenum (Fig. 10 *a, d, e*) to minimize the accumulation of solids or liquids in the regions inaccessible to reentrainment. For two-phase systems, it is preferable to have a some sort of deflection device (Fig. 10 *d, e, f*) between the outlet of the supply pipe and the grid to prevent the solids from preferentially passing through the middle of the grid due to their high

momentum. This preferential by-passing of solids causes maldistribution of gas. In addition, the configurations of Figs. 10 (e) and 10 (f) are preferable over the configurations of Figs. 10 (a) and 10 (d).

8.0 DESIGN EXAMPLES

8.1 FCC Grid Design

Example 1: A 13-m-ID bed of FCC catalyst 3 m deep, is to operate at a superficial gas velocity of 0.6 m/s. The bed density is 480 kg/m^3 . The density of the gas entering the bed is 0.64 kg/m^3 . Design the following grid types: (i) a flat perforated plate, and (ii) concentric-ring type downflow sparger. Assume a grid thickness to be 0.025 m.

Solution:

$$L_B = 3.05 \text{ m}; D = 13 \text{ m}; U_{sup} = 0.6 \text{ m/s}; r_B = 480 \text{ kg/m}^3;$$

$$r_{g,h} = 0.64 \text{ kg/m}^3; d_p = 60 \text{ } \mu\text{m}; t = 0.025 \text{ m}$$

Perforated Plate Design:

- Determine DP_{bed} and DP_{grid}

$$DP_{bed} = g r_B L_B = 9.8 \times 480 \times 3 = 14,112 \text{ Pa}$$

Choose DP_{grid} to be 30% of DP_{bed}

$$DP_{grid} = 0.3; DP_{bed} = 4,234 \text{ Pa}$$

- Determine the gas velocity through the grid holes (assume a typical value for $C_d \cong 0.77$)

$$U_h = C_d \sqrt{\frac{2\Delta P_{grid}}{r_{g,h}}} = 0.77 \sqrt{\frac{2 \times 4,234}{0.64}} = 88.6 \text{ m/s}$$

- Determine the volumetric gas flow rate at the conditions below the grid. For this example, assume the temperature of the gas below the grid is the same as in the bed. This may not be the case in an actual plant.

$$Q = U_{sup} \frac{\pi D^2}{4} = 0.6 \frac{\pi (13)^2}{4} = 79.6 \text{ m}^3/\text{s}$$

226 Fluidization, Solids Handling, and Processing

- Determine the number of grid holes required

Since
$$Q = N \frac{\underline{p} d_h^2}{4} U_h$$

$$\therefore N = \frac{Q}{U_h} \frac{1}{\frac{\underline{p} d_h^2}{4}} = \frac{79.6}{88.6} \frac{1}{\frac{\underline{p} d_h^2}{4}} = \frac{1.14}{d_h^2}$$

- The hole density is:

$$N_d = \frac{N}{\frac{\underline{p}}{4} D^2} = \frac{1.14}{d_h^2} \frac{1}{\frac{\underline{p}}{4} (13)^2} = \frac{0.0086}{d_h^2}$$

- Determine the hole pitch

$$L_h = \frac{1}{\sqrt{N_d \sin 60^\circ}} = 11.59 d_h$$

Downwardly directed gas sparger:

- Choose \underline{DP}_{grid} to be 10 % of \underline{DP}_{bed}

$$\underline{DP}_{grid} = 0.1 \underline{DP}_{bed} = 1,411 \text{ Pa} = 14.4 \text{ cm H}_2\text{O}$$

14.4 cm H₂O is less than the minimum of 25 cm H₂O \underline{DP} required for a grid. Therefore, use $\underline{DP}_{grid} = 25 \text{ cm H}_2\text{O} = 2,451 \text{ Pa}$

$$U_h = 0.77 \sqrt{\frac{2 \times 2451}{0.64}} = 67.4 \text{ m/s}$$

$$N = \frac{79.6}{67.4} \frac{1}{\frac{\underline{p} d_h^2}{4}} = \frac{1.5}{d_h^2}$$

Various combinations of N and d_h satisfy the pressure drop requirements for the two grid types as shown in the table below.

d_h	Number of holes (N)	
	perforated plate	downflow sparger
0.005	45,600	60,000
0.01	11,400	15,000
0.025	1,824	2,400
0.05	456	600

To proceed with the design, it is necessary to select a hole size (judgement call). For the purpose of this example, a hole size of 0.025 m will be chosen to compare the different grid types. This hole diameter does not result in an excessive number of holes for either type of grid.

Check the value for C_d ,

$$N_d = 13.8 \text{ holes/m}^2 \quad \text{and} \quad L_h = 0.29 \text{ m}$$

$$\frac{t}{d_h} = \frac{0.05}{0.025} = 2$$

From Fig. 3,
$$C_d \left(\frac{L_h}{d_h} \right)^{0.1} = 0.98$$

$$C_d = 0.98 \left(\frac{0.025}{0.29} \right)^{0.1} = 0.767 \text{ vs. } 0.77 \text{ (initial guess)}$$

There is a good agreement between the initial and calculated value for C_d . If not, one must repeat the calculations using the calculated C_d until both values agree.

- Therefore, for a 0.025-m hole diameter, the perforated plate has 1,824 holes arranged in a triangular pitch of 0.29 m. The hole density is 13.8 holes/m².
- For the sparger grids, it remains to determine the sparger configuration and pipe-header size. Pipe headers can be laid out in various configurations. The design calculations will depend on the configuration one chooses.

Concentric-Ring Sparger: Consider for example, a configuration of four concentric rings of 0.4-m diameter supplied by a number of gas entry points.

Sparger Grid - Concentric Ring Type

Ring No. (i)	Radius of each ring (r_i), m	Length of each ring (L_i) $2\pi r_i$, m	% of total length	Number of holes on each ring (N_i)
1	1.43	8.98	9.24	222
2	3.05	19.16	19.73	474
3	4.68	29.41	30.28	727
4	6.30	39.58	40.75	978
total=		97.13		2,400

This design results in 2,400 holes.

- Determine the hole pitch

$$L_h = \frac{97.13}{2400} = 0.04 \text{ m}$$

- To determine the header-pipe size, first determine the maximum number of holes in ring section supplied by a single effective entry of gas. If outer most ring is supplied by four gas entry points, then the number of effective gas entry points is 8, and the number of holes in each section of ring No. 4 would be $N_h = 978/8 = 122$. Then Eq. (13) gives:

$$\left(\frac{D_{head}^2}{N_h d_h^2} \right)^2 > 5; \quad \left(\frac{D_{head}^2}{122 \times 0.025^2} \right)^2 > 5$$

or $D_{head} > 0.41 \text{ m}$

- Summary: For an orifice diameter of 0.025 m, the downwardly directed concentric-ring sparger has 2,400 nozzles placed on four concentric rings. The pitch is 0.04 m. Sometimes the holes are staggered on the sparger pipe. And also, it is a common practice to place two nozzles at a given cross-section as shown in Fig. 7.

Example 2: For the conditions of Example 1 of perforated plate design, estimate the submerged jet height and particle-attrition rate in the fluidized bed.

Solution: Perforated Plate

$$U_h = 88.6 \text{ m/s}; \quad \mathbf{r}_{g,h} = 0.64 \text{ kg/m}^3; \quad \mathbf{r}_{g,b} = 0.5 \text{ kg/m}^3;$$

$$d_h = 0.025 \text{ m}; \quad N = 1,824; \quad d_p = 60 \text{ mm}; \quad \mathbf{r}_p = 1440 \text{ kg/m}^3;$$

$$e_{mf} = 0.42$$

- Attrition Rate

$$\frac{\mathbf{f}}{N} (\text{kg/m/hole}) = K_a \left(U_h \sqrt{\mathbf{r}_{g,h}} \right)^{2.5} \frac{\mathbf{p} d_h^2}{4}$$

- The attrition-rate constant for 0–50 micron FCC catalyst (from Table) is

$$K_a = 2.29 \times 10^{-5}$$

- Attrition rate per hole

$$\frac{\mathbf{f}}{N} = 2.29 \times 10^{-5} \left(88.6 \sqrt{0.64} \right)^{2.5} \frac{\mathbf{p} (0.025)^2}{4} = 4.75 \times 10^{-4} \text{ kg/min/hole}$$

- Steady-state attrition rate (generation of 0–50 micron fines)

$$\mathbf{f} = 4.75 \times 10^{-4} \times 1,824 = 0.867 \text{ kg/min}$$

or 1.25 tons/day (0.65% of bed)

- Gas jet penetration depth using Merry's correlation (Eq. 2) for horizontal jets

$$\frac{L_{hor}}{d_h} = 5.25 \left(\frac{\mathbf{r}_{g,h} U_h^2}{\mathbf{r}_p (1 - e_{mf}) g d_p} \right)^{0.4} \left(\frac{\mathbf{r}_{g,b}}{\mathbf{r}_p} \right)^{0.2} \left(\frac{d_p}{d_h} \right)^{0.2}$$

230 Fluidization, Solids Handling, and Processing

$$L_{hor} = 5.25 \left(\frac{0.64 \times 88.6^2}{1440(1 - 0.42)9.8 \times 65 \times 10^{-6}} \right)^{0.4} \left(\frac{0.5}{1440} \right)^{0.2} \left(\frac{65 \times 10^{-6}}{0.025} \right)^{0.2} \times 0.025 = 0.32 \text{ m}$$

From Eq. (1) $L_{up} \approx 2L_{hor} \approx 2 \times 0.32 \approx 0.64 \text{ m}$

Example 3: For the conditions defined in Example 1 and 2, design a shroud having an ID twice that of the grid hole, i.e., $D_s = 2d_h = 0.05 \text{ m}$.

Solution: Perforated Plate

The minimum length of the shroud should be:

$$L_{min} = \frac{0.05 - 0.025}{2 \tan 5.5^\circ} = 0.13 \text{ m}$$

- The gas jet velocity emanating from the shroud is

$$U_{h,s} = U_{h,1} \left(\frac{d_h}{D_s} \right)^2 = 88.6 \left(\frac{0.025}{0.05} \right)^2 = 22.2 \text{ m/s}$$

- Particle attrition rate will be reduced by a factor calculated from Eq. (16)

$$\frac{\text{particle attrition without shrouds}}{\text{particle attrition with shrouds}} = \left(\frac{D_s}{d_h} \right)^{1.6} = \left(\frac{0.05}{0.025} \right)^{1.6} = 3.0$$

Thus, adding a shroud to the grid reduces the attrition rate to 67% of the rate without a shroud, i.e., attrition rates with and without shrouds are 0.42 and 1.25 ton/day, respectively.

8.2 Polyethylene Reactor Grid Design

Example 4: Design a flat, perforated-plate grid for the polyethylene reactor schematically shown in Fig. 11, and calculate the gas jet penetration depth. Use a triangular pitch. System parameters are:

$$U_{sup} = 0.5 \text{ m/s}; \mathbf{r}_{g,h} = 19.2 \text{ kg/m}^3; \mathbf{r}_{g,b} = 17 \text{ kg/m}^3;$$

$$\mathbf{r}_p = 641 \text{ kg/m}^3; \mathbf{r}_B = 272 \text{ kg/m}^3; DP_{grid} = 0.4DP_{bed};$$

$$d_h = 0.01 \text{ m}; d_p = 508 \text{ mm}; e_{mf} = 0.45; t = 0.019 \text{ m}$$

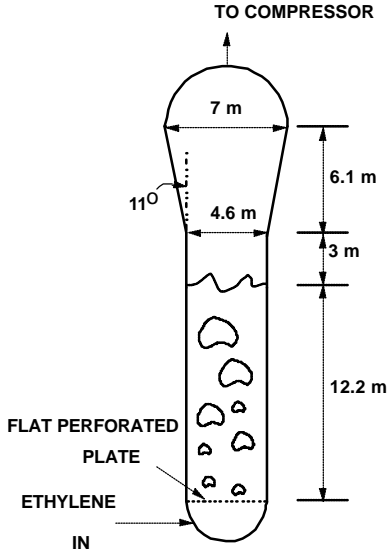


Figure 11. Schematic of polyethylene reactor

Solution:

Determine DP_{bed} and DP_{grid} ,

$$DP_{bed} = g \mathbf{r}_B L_B = 9.8 \times 272 \times 12.2 = 32,520 \text{ Pa}$$

$$DP_{grid} = 0.4DP_{bed} = 13,008 \text{ Pa}$$

Determine the gas velocity through the grid hole, (trial and error)-
assume $C_d = 0.8$

$$U_h = C_d \sqrt{\frac{2\Delta P_{grid}}{\mathbf{r}_f}} = 0.8 \sqrt{\frac{2 \times 13008}{19.2}} = 29.5 \text{ m/s}$$

232 *Fluidization, Solids Handling, and Processing*

- Determine the volumetric flow rate of gas

$$Q = U_{\text{sup}} \frac{\mathbf{p} D^2}{4} = 0.5 \frac{\mathbf{p} (4.6)^2}{4} = 8.3 \text{ m}^3/\text{s}$$

- Determine the number of grid holes required

$$N = \frac{Q}{U_h} \frac{1}{\frac{\mathbf{p} d_h^2}{4}} = \frac{8.3}{29.5} \frac{1}{\frac{\mathbf{p}}{4} (0.01)^2} = 3582$$

- hole density

$$N_d = \frac{3582}{\frac{\mathbf{p}}{4} (4.6)^2} = 215 \text{ holes/m}^2$$

- Determine the hole pitch

$$L_h = \frac{1}{\sqrt{N_d \sin 60^\circ}} = \frac{1}{\sqrt{215 \sin 60^\circ}} = 0.073 \text{ m}$$

Check the value for C_d

$$\frac{t}{d_h} = \frac{0.019}{0.01} = 1.9$$

From Fig. 3, $C_d \left(\frac{L_h}{d_h} \right)^{0.1} = 0.98$

$$\therefore C_d = 0.98 \left(\frac{0.01}{0.073} \right)^{0.1} = 0.803 \approx 0.80 \text{ (great guess)}$$

- Gas jet penetration depth using Merry's correlation (Eq. 2) for horizontal jets:

$$\frac{L_{hor}}{d_h} = 5.25 \left(\frac{\mathbf{r}_{g,h} U_h^2}{\mathbf{r}_p (1 - \mathbf{e}_{mf}) g d_p} \right)^{0.4} \left(\frac{\mathbf{r}_{g,b}}{\mathbf{r}_p} \right)^{0.2} \left(\frac{d_p}{d_h} \right)^{0.2}$$

$$L_{hor} = 5.25 \left(\frac{19.2 \times 29.5^2}{641 (1 - 0.45) 9.8 \times 508 \times 10^{-6}} \right)^{0.4} \left(\frac{17}{641} \right)^{0.2} \left(\frac{508 \times 10^{-6}}{0.01} \right)^{0.2} \times 0.01 = 0.55 \text{ m}$$

From Eq. (1) $L_{up} \approx 2L_{hor} \approx 2 \times 0.55 \approx 1.1 \text{ m}$

Coalescence factor

$$\mathbf{I} = \frac{L_h}{L_{up}/2} = \frac{0.073}{1.1/2} = 0.13 < 1$$

\ Jets coalesce.

The low value of \mathbf{I} indicates that the bed of solids is probably suspended above the coalesced jets. Therefore, the solids rarely come into contact with the grid. This type of design reduces the chances of grid pluggage due to “sticky” polyethylene solids.

- Summary: The perforated plate has 3,582 holes, each of 0.01 m diameter arranged in a triangular pitch of 0.073 m. The hole density is 215 holes/m².

NOTATIONS

C_d	=	discharge coefficient, see Fig. 1
d_h	=	grid hole diameter, m
d_p	=	sauter mean particle size, m
D	=	diameter of fluid bed, m

234 *Fluidization, Solids Handling, and Processing*

D_{head}	=	diameter of the main header pipe, m
D_m	=	diameter of the manifold pipe, m
D_s	=	shroud or nozzle diameter, m
g	=	gravitational acceleration 9.8 m/s ²
H_{high}	=	elevation of highest grid hole for curved grid, m
H_{low}	=	elevation of lowest grid hole for curved grid, m
K	=	grid pressure-drop coefficient; Eq. (6) for upward gas entry; 0.1 for lateral and downward gas entry
K_a	=	attrition-rate constant, Eq. (15)
L_B	=	operating bed depth, m
L_{down}	=	jet penetration for downwardly directed jet, m
L_h	=	grid hole pitch, cm
L_{hor}	=	jet penetration for horizontally directed jet, m
L_{min}	=	minimum shroud or nozzle length, m
L_s	=	shroud or nozzle length, m
L_{up}	=	jet penetration for upwardly directed jet, m
N	=	number of grid holes
N_d	=	number hole density (holes per unit area of the bed), holes/m ²
N_h	=	maximum number of holes per manifold pipe section supplied by gas entry
N_m	=	number of manifolds on the main header supplied by single as entry point
Q	=	total volumetric gas flow entering the grid, m ³ /s
t	=	grid thickness, m
U_h	=	velocity of gas through the grid hole, m/s
U_{sup}	=	superficial gas velocity, m/s
r_B	=	operating bed density, kg/m ³
$r_{g,b}$	=	density of gas at bed operating conditions, kg/m ³
$r_{g,h}$	=	density of gas entering the grid hole (plenum conditions), kg/m ³
r_p	=	particle density, kg/m ³
e_{mf}	=	voidage at minimum fluidizing conditions, (-)
q	=	included angle of a gas jet, degrees

DP_{bed}	=	pressure drop across the dense bed, Pa
DP_{grid}	=	pressure drop across the grid, Pa
DP_h	=	pressure drop across the grid hole, Pa
f	=	rate of formation of 0- d_p micron fines, kg/min

REFERENCES

- Blake, T. R., Webb, H., and Sunderland, P. B., *Chem. Eng. Sci.*, 45:365 (1990)
- Chen, L., and Weinstein, H., *AIChE J.*, 39(12):1901 (1993)
- Hiby, J. W., *Chem.-Ing.-Techn.*, 36:228 (1964)
- Karri, S. B. R., PSRI Research Report No. 60 (1990)
- Karri, S. B. R., Grid Design Chapter, *PSRI Design Manual* (1991)
- Knowlton, T. M., and Hirsan, I., *Fluidization*, (J. Grace, and J. Matsen, eds.), p. 315, Plenum Press (1980)
- Massimilla, L., *Fluidization*, (Davidson, et al., eds.), p. 133, Academic Press (1985)
- Merry, J. M. D., *Trans. Instn. Chem. Engrs.*, 49:189 (1971)
- Mori, S., and Moriyama, A., *Inst. Chem. Eng.*, 18:245 (1978)
- Roach, P. T., *Fluid Dyn. Res.*, 11:197 (1993)
- Shakhova, N. A., *Inzh. Fiz. Zh.*, 14(1):61 (1968)
- Siegel, R., *AIChE J.*, 22:590 (1976)
- Sishtla, C., Findlay, J., Chan, I., and Knowlton, T. M., *Fluidization VI*, (J. R. Grace, L. W. Shemilt, M. A. Bergougnou, eds.), p. 581, Engineering Foundation, p. 581 (1989)
- Whitehead, A. B., in: *Fluidization*, (J. F. Davidson, and D. Harrison, eds.), p. 781, Academic Press (1971)
- Yang W. C., and Keairns, D. L., *Ind. Eng. Chem. Fundam.*, 18:317 (1979)
- Yates, J. G., Bejcek, V., and Cheesman, D. J., *Fluidization V*, (K. Ostergaard, and A. Sorensen, eds.), p. 79, Engineering Foundation (1986)
- Zenz, F. A., and Othmer, D. F., *Fluidization and Fluid-Particle Systems*, p. 171, Reinhold Pub. Co. (1960)
- Zenz, F. A., *Inst. Chem. Eng. Symp.*, 30:136 (1968)
- Zenz, F. A., and Kelleher, E. G., *J. of Powder and Bulk Solids Tech.*, 4:13 (1980)
- Zuiderweg, *Proc. Int. Symp. On Fluidization*, (A. A. H. Drinkenburg, ed.), p. 739, Netherlands University Press (1967)

5

Engineering and Applications of Recirculating and Jetting Fluidized Beds

Wen-Ching Yang

1.0 INTRODUCTION

In a conventional fluidized bed, fluid under pressure is passed through a bed of solids via a distributor plate. At a fluid velocity beyond the minimum fluidization or minimum bubbling velocity, visible bubbles appear. The fluid thus passes through the bed in two phases, the bubble and the emulsion phases. The bubble-induced solids mixing and circulation provide the liquid-like behavior of a bed of otherwise immobile solids. The liquid-like behavior of a fluidized bed allows continuous feeding and withdrawal of bed material. The vigorous mixing of solids in the bed gives rise to a uniform bed temperature even for a highly exothermic or endothermic reaction. This leads to easier control and operation. The advantages of a fluidized bed, compared to other modes of contacting such as a packed bed, are numerous and they are described in details in standard textbooks on fluidization. The fluidized beds are widely employed in various industries for both physical and chemical operations.

The conventional fluidized beds also possess some serious deficiencies. The bubbles which are responsible for many benefits of a fluidized bed represent the fluid bypassing and reduction of fluid-solids contacting. The rapid mixing of solids in the bed leads to nonuniform solids residence time distribution in the bed. The rigorous solids mixing in the bed leads to attrition of bed material and increases the bed material loss from entrainment. Thus for many industrial applications, the conventional fluidized beds have been modified to overcome those disadvantages. Those modifications, in many ways, alter substantially the operational characteristics of the fluidized beds, and also change the design and engineering of the beds. It is the intent of this chapter to document two of the non-conventional fluidized beds in details: recirculating fluidized beds with a draft tube and the jetting fluidized beds.

2.0 RECIRCULATING FLUIDIZED BEDS WITH A DRAFT TUBE

The recirculating fluidized bed with a draft tube concept is briefly illustrated in Fig. 1. In application as a coal devolatilizer, dry coal is introduced into the devolatilizer below the bottom of the draft tube through a coal feeding tube concentric with the draft tube gas supply. The coal feed and recycled char at up to 100 times the coal feed rate are mixed inside the draft tube and carried upward pneumatically in dilute phase at velocities greater than 4.6 m/s. The solids disengage in a fluidized bed above the top of the draft tube and then descend in an annular downcomer surrounding the draft tube as a packed bed at close to minimum fluidization velocity. Gas is introduced at the base of the downcomer at a rate permitting the downward flow of the solids. The recirculating solids effectively prevent agglomeration of the caking coal as it devolatilizes and passes through the plastic stage. Many other applications have also been reported and they will be discussed in Sec. 2.4, "Industrial Applications."

This concept was first called a *recirculating fluidized bed* by Yang and Kearins (1974). Several other names have also been used to describe the same concept: the *fluid-lift solids recirculator* (Buchanan and Wilson, 1965), the *spouted fluid bed* with a draft tube (Yang and Kearins, 1983; Hadzismajlovic et al., 1992), the *internally circulating fluidized bed* (Milne et al., 1992; Lee and Kim, 1992); or simply a *circulating fluidized*

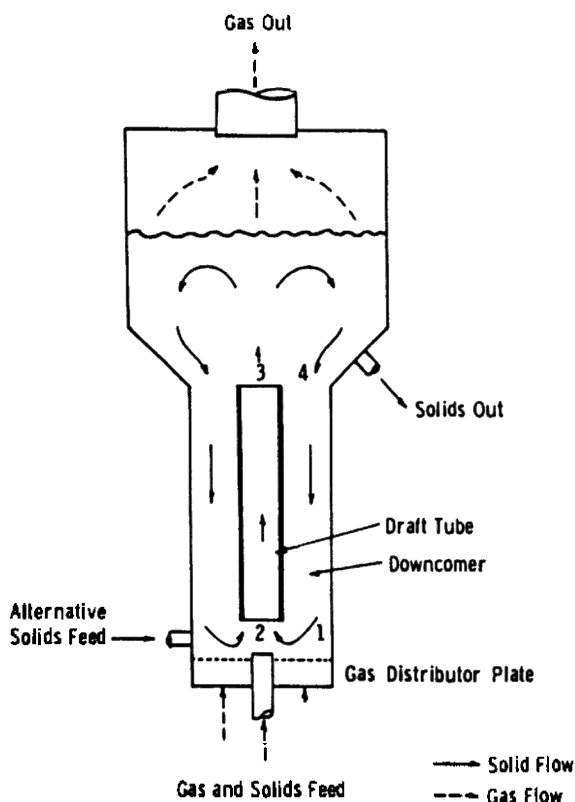


Figure 1. Recirculating fluidized bed concept—draft tube operated as a dilute phase pneumatic transport tube.

bed (LaNauze, 1976). To avoid further confusion, the recirculating fluidized bed with a draft tube will be employed here. The addition of a tubular insert, a *draft tube*, in a spouted fluid bed changes operational and design characteristics of an ordinary spouted bed. Notably, there is no limitation on the so-called maximum spoutable bed height. Theoretically, a recirculating fluidized bed with a draft tube can have any bed height desirable. The so-called minimum spouting velocity will also be less for a recirculating fluidized bed with a draft tube because the gas in the draft tube is confined and does not leak out along the spout height as in an ordinary spouted bed. There is considerably more operational and design flexibility for a recircu-

lating fluidized bed with a draft tube. The downcomer region can be separately aerated. The gas distribution between the draft tube and the downcomer can be adjusted by changing the design parameters at the draft tube inlet. Because the draft tube velocity and the downcomer aeration can be individually adjusted, the solid circulation rate in the bed can be easily controlled. The fact that the solid circulation rate depends primarily on the entrainment rate at the draft tube inlet rather than along the surface of the entire spout, allows easier manipulation through adjustment of design and operational parameters to control the residence time and cycle time distribution. Stable operation over a wide range of operating conditions, a solids circulation rate up to 100 metric tons per hour, and a solids loading of 50 (weight of solids/weight of air) in the draft tube have recently been reported by Hadzismajlovic et al. (1992) in a 95.3 cm diameter bed with a 25 cm diameter draft tube using 3.6 mm polyethylene particles.

Operating conditions for a recirculating fluidized bed can be flexible as well. The bed height can be lower than the draft tube top or just cover the draft tube top so that a spout can penetrate the bed as in a spouted bed. The bed height can also be substantially higher than the draft tube top so that a separate fluidized bed exists above the draft tube. Rather than operating the draft tube as a dilute-phase pneumatic transport tube, one can fluidize the solids inside the draft tube at lower velocities to induce the necessary recirculation of the solids. Several studies were conducted in this fashion (Ishida and Shirai, 1975; LaNauze, 1976; LaNauze and Davidson, 1976). The draft tube wall can also be solid or porous, although most of the studies in the literature employ a solid-wall draft tube. Claflin and Fane (1983) reported that a porous draft tube was suitable for applications in thermal disinfestation of wheat where control of particle movement and good gas/solid contacting could be accomplished at a modest pressure drop. The concept can also be employed as liquid-solids and liquid-gas-solids contacting devices (Oguchi and Kubo, 1973).

The important design parameters for a recirculating fluidized bed with a draft tube were identified by Yang and Keairns (1978a) as the gas bypassing characteristics of the distributor plate, the area ratio between the downcomer and the draft tube, the diameter ratio between the draft tube and the draft tube gas supply, the distance between the distributor plate and the draft tube inlet, and the area ratio of the draft tube gas supply and the concentric solids feeder. The design and operation of a recirculating fluidized bed with a draft tube are discussed below.

2.1 Draft Tube Operated As A Fluidized Bed

When the draft tube is operated as a fluidized bed rather than a dilute phase pneumatic transport tube, it can be represented by a mathematical model developed by LaNauze (1976). The driving force for solids circulation in this case was found to be the density difference between draft tube and downcomer. The energy was dissipated by particle shear at the walls. The solids circulation rate was also found to be affected only by the distance between the distributor and the draft tube and not by the draft tube length or height of bed above it. The schematic for this system is shown in Fig. 2. Because of the lower velocity in the draft tube, the draft tube diameter tends to be larger compared to draft tube operated in a dilute phase pneumatic transport mode. One disadvantage of operating the draft tube as a fluidized bed is that if the draft tube diameter is too small or the draft tube is too high, the draft tube tends to operate in a slugging bed mode. In fact, the mathematical model developed by LaNauze (1976) described below assumes that the draft tube is a slugging fluidized bed.

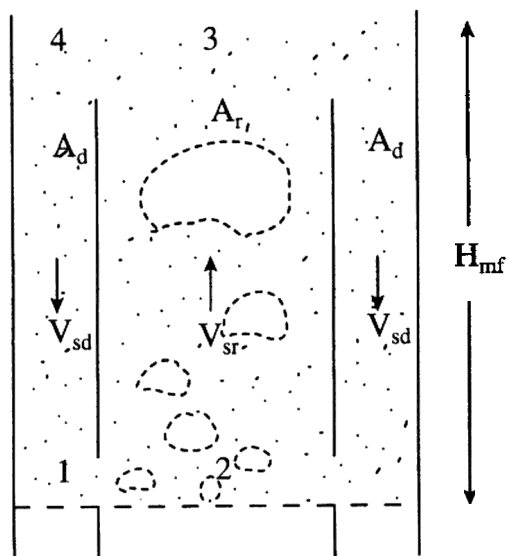


Figure 2. Recirculating fluidized bed concept—draft tube operated as a fluidized bed.

The pressure balance for the dense phase in the downcomer in the circulating fluidized system shown in Fig. 2 can be expressed as:

$$\text{Eq. (1)} \quad \Delta P_{1-4} = \mathbf{r}_b g H_{mf} (1 - \mathbf{e}_{bd}) - \frac{\mathbf{t}_d S_d}{A_d}$$

A similar expression can be written for the pressure balance in the draft tube as:

$$\text{Eq. (2)} \quad -\Delta P_{2-3} = \mathbf{r}_b g H_{mf} (1 - \mathbf{e}_{br}) + \frac{\mathbf{t}_r S_r}{A_r}$$

Combining Eqs. (1) and (2), we have

$$\text{Eq. (3)} \quad \mathbf{r}_b g H_{mf} (\mathbf{e}_{br} - \mathbf{e}_{bd}) = \frac{\mathbf{t}_d S_d}{A_d} + \frac{\mathbf{t}_r S_r}{A_r}$$

It was experimentally confirmed, using capacitance probes, that the solids flow down the downcomer at close to minimum fluidization, thus $\mathbf{e}_{bd} = 0$.

The bubble voidage in the draft tube, \mathbf{e}_{br} , was calculated on the basis of the velocity of a rising gas slug relative to its surrounding solids. The total gas superficial velocity in the draft tube, U_{fr} , can be derived to be

$$\text{Eq. (4)} \quad U_{fr} = U_{slug} \mathbf{e}_{br} + U_{mf} + \frac{V_{sr} \mathbf{e}_{mf}}{1 - \mathbf{e}_{mf}}$$

The slug velocity, U_{slug} , is defined as the rising velocity of the slug relative to the particle velocity at its nose and can be expressed as

$$\text{Eq. (5)} \quad U_{slug} = v_p + 0.35 \sqrt{gD}, \text{ and}$$

$$\text{Eq. (6)} \quad v_p = (U_{fr} - U_{mf}) + V_{sr}$$

Substituting Eq. (5) into (4), we have

$$\text{Eq. (7)} \quad \mathbf{e}_{br} = \frac{(U_{fr} - U_{mf}) - V_{sr} \mathbf{e}_{mf} / (1 - \mathbf{e}_{mf})}{(U_{fr} - U_{mf}) + V_{sr} + 0.35 \sqrt{gD}}$$

The flow rate of particles in the downcomer and the draft tube are related by a mass balance as follows:

242 *Fluidization, Solids Handling, and Processing*

$$\text{Eq. (8)} \quad V_{sr} \mathbf{r}_s A_r = V_{sd} \mathbf{r}_s A_d = W_{sd} A_d = W_{sr} A_r$$

By solving Eqs. (4) and (7) simultaneously, the mass flux can be calculated provided the wall shear stress is known as a function of particle superficial volume flow rate. Botterill and Bessant (1973) have proposed several relationships for shear stress, however, these are not general. LaNauze (1976) also proposed a method to measure this shear stress experimentally.

A similar application of the concept as a slugging lifter of solids was studied by Singh (1978) based on the two-phase theory of fluidization and the properties of slugs.

2.2 Draft Tube Operated As A Pneumatic Transport Tube

Most of the applications for the recirculating fluidized bed with a draft tube operate the draft tube as a dilute phase pneumatic transport tube. Hence we will discuss this system in more details.

Downcomer and Draft Tube Pressure Drop. Typical experimental pressure drops across the downcomer, DP_{1-4} , and the draft tube, DP_{2-3} , show that they are essentially similar. Successful design of a recirculating fluidized bed with a draft tube requires development of mathematical models for both downcomer and draft tube.

Downcomer Pressure Drop. When the downcomer is less than minimally fluidized, the pressure drop can be estimated with a modified Ergun equation substituting gas-solid slip velocities for gas velocities (Yoon and Kunii, 1970), as shown in Eq. (9).

Eq. (9)

$$\Delta P_{1-4} = \frac{L}{g_c} \left[150 \frac{\mathbf{m}(U_{gd} + U_{pd})(1 - \mathbf{e}_d)^2}{d_p^2 \mathbf{f}_s^2 \mathbf{e}_d^2} + 1.75 \frac{\mathbf{r}_f (U_{gd} + U_{pd})^2 (1 - \mathbf{e}_d)}{d_p \mathbf{f}_s \mathbf{e}_d} \right]$$

When the downcomer is fluidized, the downcomer pressure drop can be calculated as in an ordinary fluidized bed as:

$$\text{Eq. (10)} \quad \Delta P_{1-4} = L(1 - \mathbf{e}_d) \mathbf{r}_s$$

The voidage in the downcomer, e_d , can be assumed to be the same as the voidage at minimum fluidization, e_{mf} . The voidage at minimum fluidization can be determined in a separate fluidized bed. The agreement between the calculated and the experimental values is usually better than $\pm 10\%$ (Yang and Kearns, 1978a). When the downcomer is not minimally fluidized, the bed voidage depends on the amount of aeration and solid velocity. Use of the voidage at minimum fluidization is only a first approximation.

Draft Tube Pressure Drop. The pressure drop across the draft tube, DP_{2-3} , is usually similar to that across the downcomer, DP_{1-4} , in magnitude. Thus, for a practical design basis, the total pressure drop across the draft tube and across the downcomer can be assumed to be equal. In most operating conditions, the pressure drop at the bottom section of the draft tube has a steep pressure gradient due primarily to acceleration of the solid particles from essentially zero vertical velocity. The acceleration term is especially significant when the solid circulation rate is high or when the draft tube is short.

The pressure drop inside the draft tube is more complicated because it involves acceleration of solid particles from essentially zero vertical velocity. However, the model for calculating the pressure drop in vertical pneumatic conveying lines suggested by Yang (1977) can be applied. The acceleration length can be calculated from numerical integration of the following equation.

$$\text{Eq. (11)} \quad \Delta L = \int_{U_{pn}}^{U_{pr2}} \frac{U_{pr} dU_{pr}}{\frac{3}{4} C_{DS} e_r^{-4.7} \frac{\mathbf{r}_f (U_{gr} - U_{pr})^2}{(\mathbf{r}_s - \mathbf{r}_f) d_p} - (g_c + \frac{f_p U_{pr}^2}{2D})}$$

The solid friction factor, f_p , can be evaluated with the equation proposed by Yang (1978).

$$\text{Eq. (12)} \quad f_p = 0.0126 \frac{(1 - e_r)}{e_r^3} \left[(1 - e_r) \frac{(\text{Re})_t}{(\text{Re})_p} \right]^{-0.979}$$

The lower limit of integration, U_{pr1} , is derived from

$$\text{Eq. (13)} \quad W_{sr} = U_{pr} \mathbf{r}_s (1 - e_r)$$

with $e_r = 0.5$, and the upper limit, U_{pr2} , by the following equation:

$$\text{Eq. (14)} \quad U_{pr} = U_{gr} - U_t \sqrt{\left(1 + \frac{f_p U_{pr}^2}{2 g_c D}\right)} \times e_r^{4.7}$$

The total pressure drop in the acceleration region can be expressed as

$$\begin{aligned} \text{Eq. (15)} \quad \Delta P_{2-3} = & \int_0^L \mathbf{r}_s (1 - \mathbf{e}_r) dL + \int_0^L \frac{2 f_g \mathbf{r}_f U_{gr}^2}{g_c D} dL \\ & + \int_0^L \frac{f_p \mathbf{r}_s (1 - \mathbf{e}_r) U_{pr}^2}{2 g_c D} dL + \left[\frac{\mathbf{r}_s (1 - \mathbf{e}_r) U_{pr}^2}{g_c} \right]_{at-L} \end{aligned}$$

If the draft tube height is less than the acceleration length, the integration of Eq. (15) is carried out through the whole length of the draft tube. If the draft tube height is larger than the acceleration length, the integration of Eq. (15) is carried out for the total acceleration length, and the extra pressure drop for the rest of the draft tube can then be included to give the total pressure drop in the draft tube. The suggested equations have been applied to actual experimental data satisfactorily (Yang and Keairns, 1976a).

Gas Bypassing Phenomenon. Because of different design and operating parameters, the distribution of the total flow between the draft tube side and downcomer side can be very different. A summary of the design parameters that will affect the gas bypassing is presented graphically in Fig. 3 for the flat distributor plate design. Similar parameters apply for the conical distributor plate. The important design parameters that will affect gas bypassing are the area ratio between the downcomer and the draft tube, $[(D_c^2 - D^2)/D^2]$, the diameter ratio between the draft tube and the draft tube gas supply or the diameter of solid feeding tube, $(D/d_D$ and $D/d_s)$, the distance between the distributor plate and the draft tube inlet, L , the area ratio of the draft tube gas supply and the concentric solids feeder, $[(d_D^2 - d_s^2)/d_s^2]$, and the design of the downcomer gas supply nozzle. In addition to the design parameter, the operating parameters will also affect gas bypassing. The relative strength of the concentric jets of the draft tube gas supply and the solids feeder determines the half angle of the combined jet, and the jet velocity determines the jet penetration. The jet velocity of the downcomer gas supply nozzles is also important if the jets are horizontal and directed toward the draft tube.

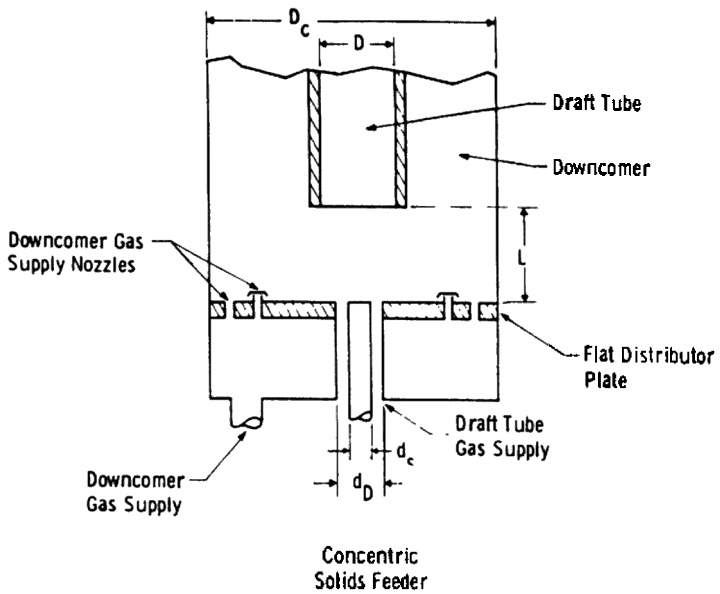


Figure 3. Important design parameters that affect gas bypassing

The gas bypassing phenomenon was studied by Stocker et al. (1989) by measuring the differential pressure drops between the draft tube and downcomer. A more rigorous investigation was conducted by Yang and Keairns (1978a) by injecting gas tracer, carbon dioxide or helium, continuously at different locations and taking gas samples from both the draft tube side and the downcomer side. A continuous gas sampling train fed gas into a Gow-Mac thermal conductivity gas analyzer and the tracer concentration was continuously recorded in a chart recorder. The actual amounts of gas passing through the draft tube and the downcomer were then obtained by solving mass conservation equations of tracer gas.

The gas bypassing results obtained from tracer gas injection studies for a flat and a conical distributor plate are shown in Fig. 4. The *flow ratio*, FR, is defined as the total gas flow supplied through the draft tube gas supply and the concentric solids feeder divided by the total gas flow supplied through the downcomer gas supply. The X and Y are the actual amounts of gas passing up the draft tube and the downcomer, respectively, determined from the tracer gas injection studies. If FR equals X/Y , there is no gas bypassing. If FR is less than X/Y , some of the flow supplied through the downcomer gas supply passes into the draft tube. If FR is larger than X/Y , the reverse is true.

Effect of Distributor Plate Design. Except for the conical plate, there is no simple gas bypassing relationship as shown in Fig. 4. The scatter of the data reflects the unstable operating characteristics of the recirculating fluidized bed using a flat distributor plate and sand as the bed material. The scatter may also be due to the sampling technique. Sampling bombs of 75 cm³ capacity were used for the test series with the flat distributor plate. Continuous gas sampling trains were implemented in the test series with the conical plate. The major reason for data scattering, however, is the change in operating conditions at each data point to be discussed in more detail later.

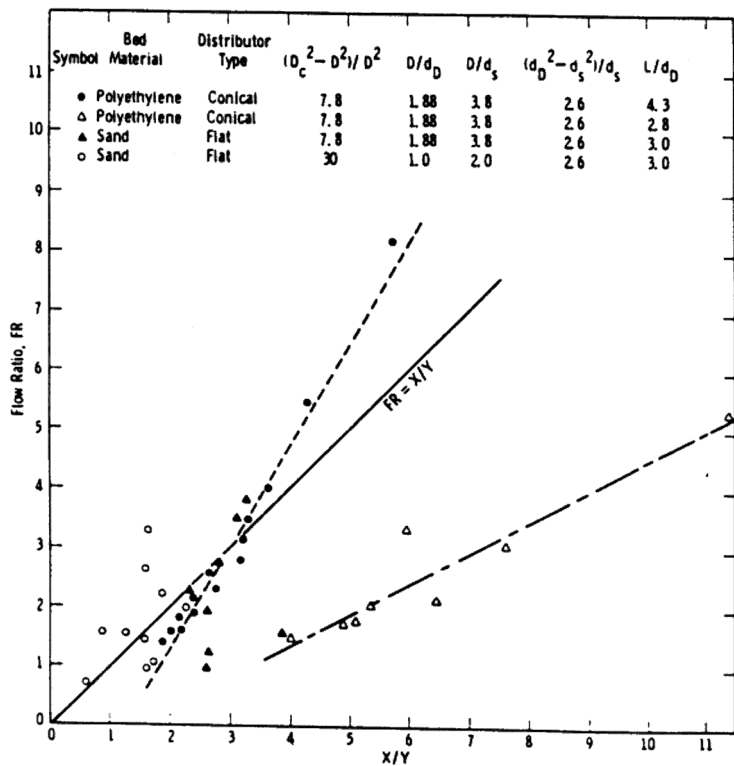


Figure 4. Summary of gas bypassing data for a conical and a flat distributor plate.

Effect of Draft Tube and Downcomer Area Ratio. When a draft tube of 9.55 cm I.D. (downcomer/draft tube area ratio = 7.8) was changed to a draft tube of 5 cm I.D. (downcomer/draft tube area ratio = 30) with other design parameters being the same, the gas bypassing reversed direction, as shown in Fig. 4. With the smaller draft tube ($D/d_D = 1$), the gas bypasses from the draft tube side into the downcomer side for most experimental conditions, except for jet velocities in excess of 76 m/s at the concentric solids feeder; with the larger draft tube ($D/d_D = 1.9$), the gas bypasses from the downcomer side into the draft tube side in most experiments.

Effect of Distance between the Distributor Plate and the Draft Tube Inlet. Figure 4 clearly indicates that the gas bypassing phenomenon depends not only on the design parameters but also on the operating conditions. For the conical plate at a distance from the draft tube inlet of $L = 21.7$ cm, gas bypasses from the draft tube side to the downcomer side at a high flow ratio and reverses the direction at a low flow ratio. When the conical plate was moved closer to the draft tube inlet at $L = 14.1$ cm, the gas bypassing direction was exclusively from the downcomer side to the draft tube side.

Gas Bypassing with a Conical Distributor Plate. Further gas bypassing results (Yang and Kearns, 1983) obtained for a conical distributor plate are shown in Figs. 5–7. The data are expressed with respect to the flow ratio (FR) as well. The flow ratio is similarly defined as the total gas flow supplied through the draft tube gas supply (No. 8 flow) and the concentric gas nozzle (No. 7 flow) divided by the total gas flow supplied through the downcomer gas supply (No. 3 flow). When the downcomer gas supply (No. 3 flow) is absent, the flow ratio FR is evaluated from the ratio of No. 7 flow and No. 8 flow. Then the total flow passing through the downcomer is calculated as $Y/(X + Y)$. The X and Y are the actual amount of gas passing up the draft tube and the downcomer, respectively, determined from the tracer gas injection studies.

When only the No. 3 and No. 7 flows are present, gas bypasses from the draft tube side to the downcomer side at a high flow ratio and reverses the direction at a low flow ratio at a distance of $L_1 = L_2 = 21.7$ cm between the conical plate and the draft tube inlet (see Fig. 5). The angle of the conical plate ($\alpha = 45^\circ$ and 60°) does not seem to affect the gas bypassing characteristics greatly. When the conical plate was moved closer to the draft tube inlet at $L_1 = L_2 = 14.1$ cm, the gas bypassing direction was exclusively from the downcomer side to the draft tube side.

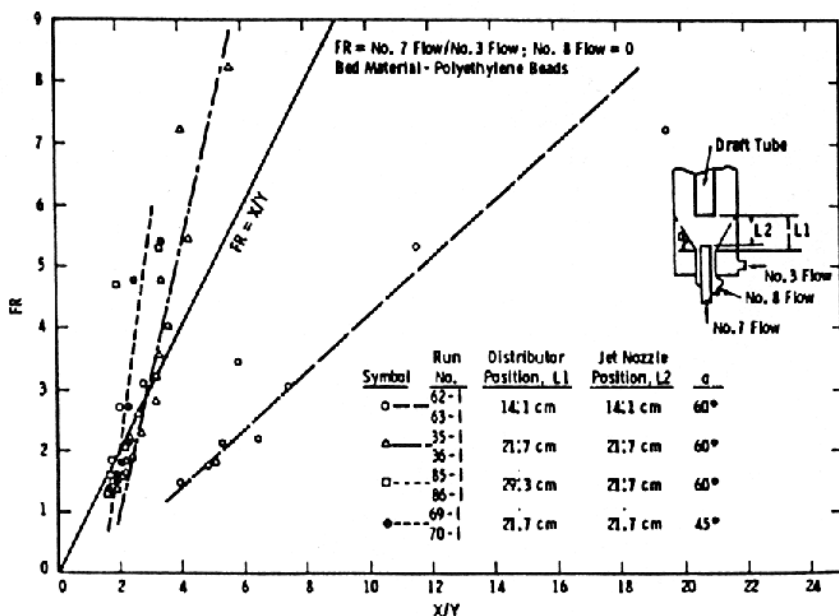


Figure 5. Gas bypassing characteristics of conical distributor plates of different design configurations (No. 3 and No. 7 flows).

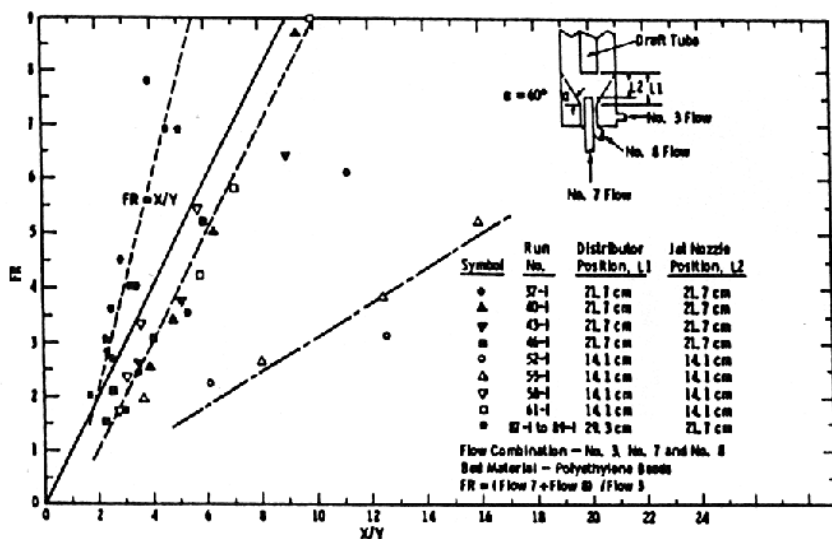


Figure 6. Gas bypassing characteristics of conical distributor plates of different design configurations (No. 3, No. 7 and No. 8 flows).

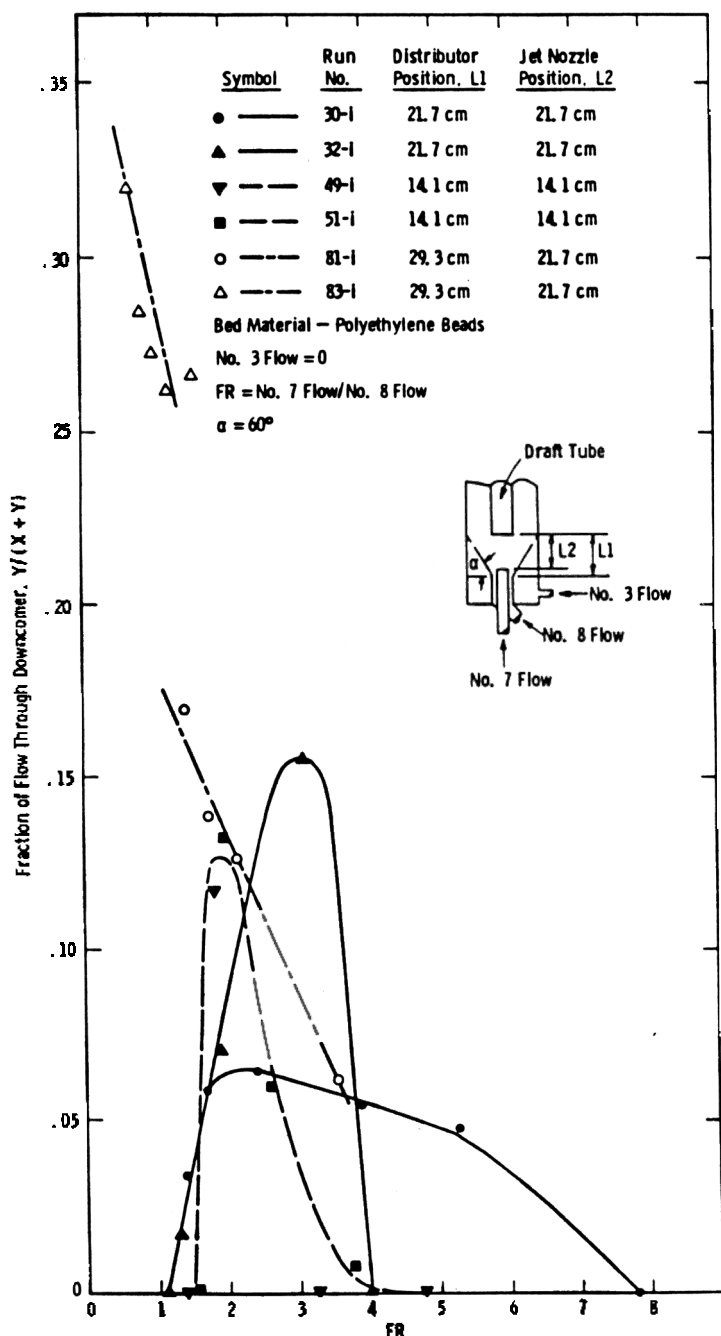


Figure 7. Gas bypassing characteristics of conical distributor plates of different design configurations (No. 7 and No. 8 flows).

250 *Fluidization, Solids Handling, and Processing*

The gas bypassing characteristics for the cases with all three flows (No. 3, No. 7, and No. 8) are presented in Fig. 6. The gas bypassing is exclusively from the downcomer side to the draft tube side when $L1 = L2$. A more favorable gas bypassing characteristics can be created even for the cases where $L1 = L2 = 14.7$ cm by holding the No. 7 flow constant and increasing the No. 8 flow as shown for Run No. 58-i and 61-i in Fig. 6. The gas bypassing characteristics in those runs are similar to that obtained when $L1 = L2 = 21.7$ cm. With $L1 = 29.3$ cm and $L2 = 21.7$ cm, the gas bypassing is exclusively from the draft tube side to the downcomer side, the most favorable gas bypassing characteristics. This accounts for the high solid circulation rates observed during the experiments to be discussed later in "Solids Circulation Rate."

There are also interesting gas bypassing phenomena observed when only No. 7 and No. 8 flows are present and the flow specifically supplied to the downcomer (No. 3 flow) is absent. When $L1 = L2$, the fraction of the total flow passing through the downcomer has a maximum as shown in Fig. 7. At very low and very high flow ratio, defined in this case as $FR = \text{No. 7 flow}/\text{No. 8 flow}$, downward gas flow in the downcomer was observed. In these cases, the solids circulation rate depends primarily on the entrainment capability of the jets. With $L1 = 29.3$ cm and $L2 = 21.7$ cm, no maximum in the flow split was observed. The fraction of the total flow passing through the downcomer is linearly and inversely proportional to the flow ratio FR . The total flow passing through the downcomer can be substantially higher. The No. 7 flow in Run No. 81-i is approximately twice that in Run No. 83-i. A stronger sink created by the No. 7 flow in Run No. 81-i tends to draw the gas toward the draft tube.

Solids Circulation Mechanisms and Solids Circulation Rate. Both solids circulation mechanisms and solids circulation rate are important aspects in designing and operating a recirculating fluidized bed with a draft tube. For commercial applications in the area of coating and encapsulation of solid particles, such as in coating of pharmaceutical tablets and in coating seeds for delayed germination and controlling the release rate of fertilizers, the particle residence time and cycle time are important considerations. The performance based on cycle time distribution analysis for coating and granulation was studied by Mann and Crosby (1973, 1975) and Mann (1983). Further discussions on this subject can be found in Ch. 6.

Solids Circulation Mechanisms. Two mechanisms for solids circulation have been observed experimentally (Yang and Keairns, 1978a).

High-speed movies (1000 to 1500 frames per second) taken at the inlet and the midsection of the draft tube with a sand bed revealed that solids transport inside the draft tube was not a conventional pneumatic transport, where uniform solid suspension prevailed, but a slugging-type transport. The high-speed movies taken at the outlet of a 23 m/s air jet showed that the air jet issuing from the jet nozzle supplying air to the draft tube was comprised of bubble rather than of a steady jet. The bubble grew from the mouth of the nozzle until its roof reached the draft tube; then the sudden suction from the draft tube punctured the roof. A continuous stream of dilute solids suspension passed through the roof into the draft tube. Simultaneously, another bubble was initiated. As this bubble grew, it pushed a slug of solids into the draft tube. The high-speed movies taken at the midsection of the draft tube exhibited alternate sections of dilute solid suspension and solids slug occupying the total cross section of the draft tube.

A steady jet without bubbling can be maintained in a sand bed between the jet nozzle and the draft tube inlet with high jet velocities of the order of 60 m/s and without downcomer aeration. Once the downcomer is aerated, the solids circulation rate increases dramatically and the steady jet becomes a bubbling jet. Apparently, the inward-flowing solids have enough momentum to shear the gas jet periodically into bubbles.

When the polyethylene beads (density = 907 kg/m^3 , average size = $2800 \text{ }\mu\text{m}$) and the hollow epoxy spheres (density = 210 kg/m^3 , average size = $2800 \text{ }\mu\text{m}$) were used as the bed material, a steady jet between the jet nozzle and the draft tube was always observed for all experiments conducted.

Solids Circulation Rate. The solids circulation rate was obtained from the particle velocity measurements at the downcomer side by following visually the tracer particles at the wall with a stop watch. The data reported here by Yang and Keairns (1983) are for polyethylene beads (907 kg/m^3 in density and $2800 \text{ }\mu\text{m}$ in average particle size) and hollow epoxy spheres (210 kg/cm^3 in density and $2800 \text{ }\mu\text{m}$ in average particle size). The experiments were carried out in a semicircular transparent Plexiglas apparatus, 28.6 cm in diameter and 610 cm in height.

The effect of downcomer aeration, of distance between the distributor plate and the draft tube inlet, and of the distributor plate design configuration on solid circulation rate is discussed below. For ease of presentation for materials of different densities, the solid particle velocity in the downcomer rather than the solid circulation rate is used.

Solids circulation rate was found to be strongly affected by the design configuration at the bottom of the draft tube and the downcomer due to changes in gas bypassing characteristics. This coupling effect indicates that an understanding of the gas bypassing characteristics is essential. Except for simple cases, the dependency of the gas bypassing characteristics on design and operating parameters are still not amenable to theoretical treatment as discussed earlier. A recent study by Alappat and Rane (1995) on the effects of various design and operational parameters on solids circulation rate essentially affirms the above conclusions.

Effect of Downcomer Aeration. When only the central gas flows (No. 7 and No. 8 flows) were employed without downcomer aeration, the solids circulation rate depended primarily on the entrainment rate of the jets. The linear relationship for both bed materials (hollow epoxy and polyethylene) in Fig. 8 shows that the volumetric concentration of the solids inside the draft tube after acceleration (or the gas voidage) is approximately constant, independent of particle density. This can be readily realized by expressing the volumetric solid loading in the draft tube as follows:

$$\text{Eq. (16)} \quad f = \frac{U_{pr} A_r (1 - e_r)}{G_r}$$

A straight line relationship between U_{pr} and G_r as shown in Fig. 8 implies that the volumetric solid loading f is approximately constant because A_r is constant and e_r can be assumed to be approximately constant when the downcomer is not fluidized. More than 85% of the gas supplied through the central No. 7 and No. 8 flows in those experiments ends up in the draft tube as can be seen from the gas bypassing data presented in Fig. 7.

Aeration of the downcomer can also be provided with a conical distributor plate (No. 3 flow) with greatly increased solids circulation rate as shown in Fig. 8. At lower downcomer aeration, the solids circulation rate is essentially similar to that without downcomer aeration at a distributor plate location of $L = 21.7$ cm. At higher downcomer aeration, however, a substantial increase in solids circulation rate is realized with the same total gas flow rate. Apparently, a minimum aeration in the downcomer is required in order to increase substantially the solids circulation rate. For polyethylene beads, this critical aeration rate is at a downcomer superficial

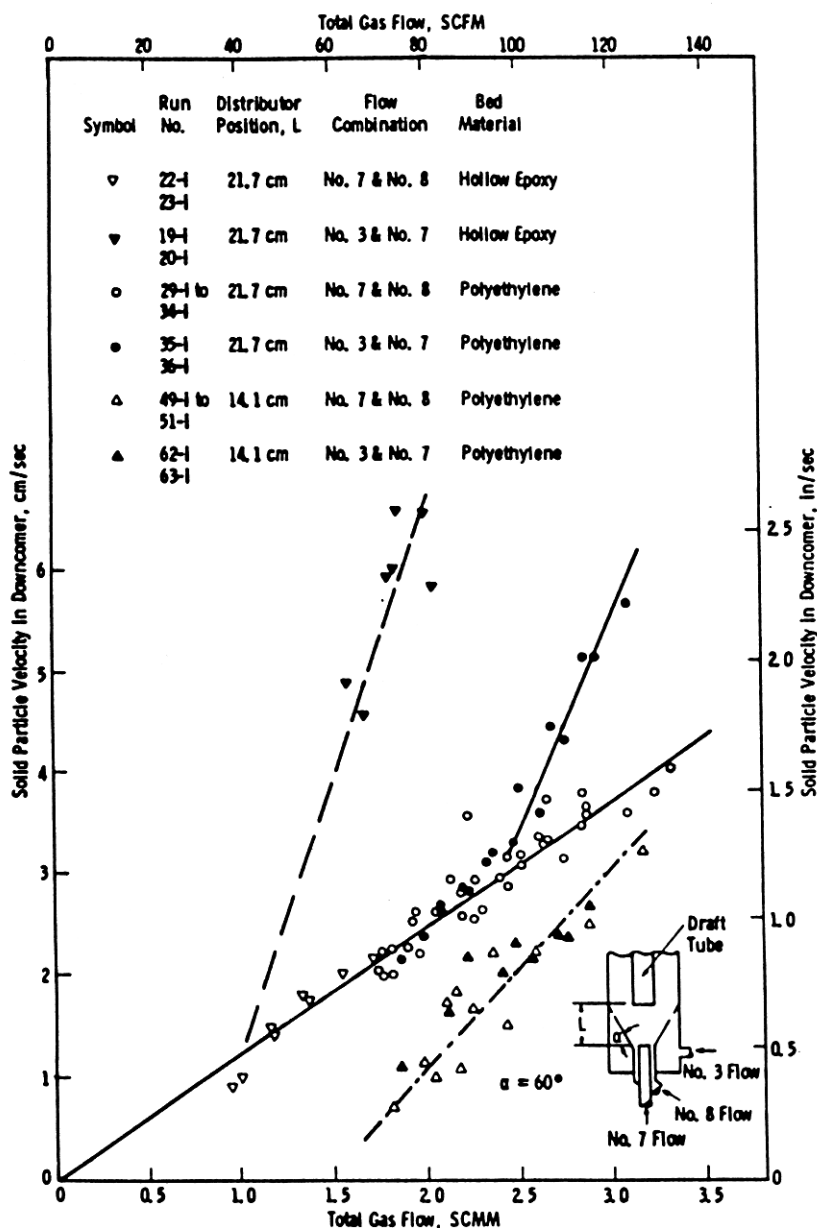


Figure 8. Effect of design and operating conditions on solid circulation rate (No. 7 and No. 8 flows or No. 3 and No. 7 flows).

gas velocity of 0.42 m/s as compared to a minimum fluidization velocity of 0.76 m/s. This critical aeration velocity in the downcomer where the solid circulation rate starts to increase substantially was obtained by tracer gas injection. Data for hollow epoxy spheres did not extend to enough gas flow rate to permit extraction of the critical aeration velocity. However, it is evident from Fig. 8 that much less gas flow is required for the hollow epoxy spheres. The minimum fluidization velocity for the hollow epoxy spheres is 0.35 m/s.

The same kind of phenomenon was not observed when distributor plate was located closer to the draft tube inlet at $L = 14.1$ cm and when only No. 7 and No. 8 or No. 7 and No. 3 flows were used. When all three flow injection locations were used, substantial improvement in solids circulation rate is possible even at $L = 14.1$ cm as shown in Fig. 9. The critical downcomer aeration velocities (superficial velocities based on downcomer area) for the data shown in Fig. 9 were determined through tracer gas injection experiments to be 0.29 m/s at $L = 21.7$ cm and 0.22 m/s at $L = 14.1$ cm.

Effect of Distributor Plate Design. Both conical distributor plates of included angles of 60° and 90° were used. They do not seem to affect the solids circulation rate as shown in Fig. 10. Proper location of the distributor plate and the gas nozzle, however, substantially increased the solids circulation rate.

When the distributor plate was located at $L1 = 29.3$ cm and the concentric jet was located at $L2 = 21.7$ cm, No. 7 and No. 8 flows alone are enough to create high solids circulation rate as though the downcomer was separately aerated by the No. 3 flow (compare Figs. 8 and 10). This design configuration changes the gas bypassing characteristics sufficiently to provide enough aeration in the downcomer. The critical aeration in the downcomer required to promote high solids circulation rate shown in Fig. 10 was determined to be 0.25 m/s (a superficial velocity based on the downcomer area) through tracer gas injection studies. This design configuration has decisive advantages in that location of the central jet at $L2 = 21.7$ cm from the draft tube inlet minimizes the start-up problem (discussed later in the section "Start-up and Shutdown Considerations), and location of the distributor plate at $L1 = 29.3$ cm eliminates the necessity of supplying separate aeration to the downcomer through an additional location such as No. 3 flow. In some industrial applications, this design feature may prove to be a critical advantage.

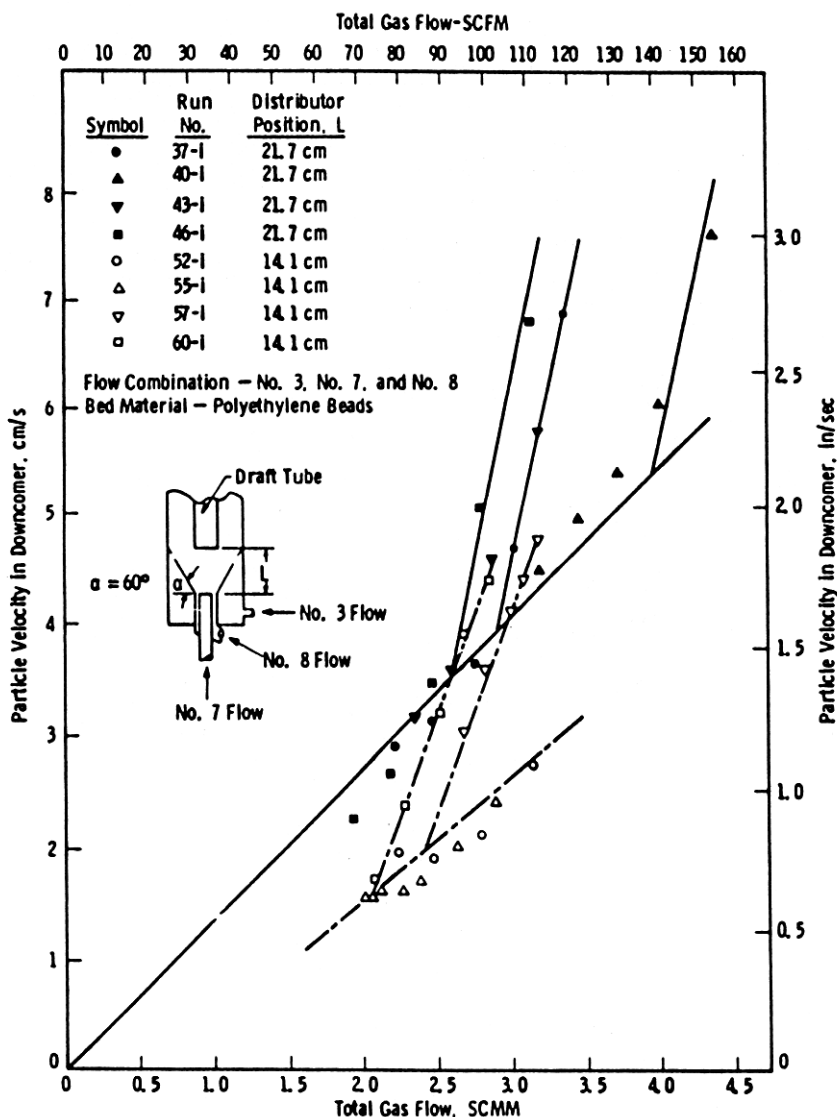


Figure 9. Effect of design and operating conditions on solid circulation rate (No. 3, No. 7 and No. 8 flows).

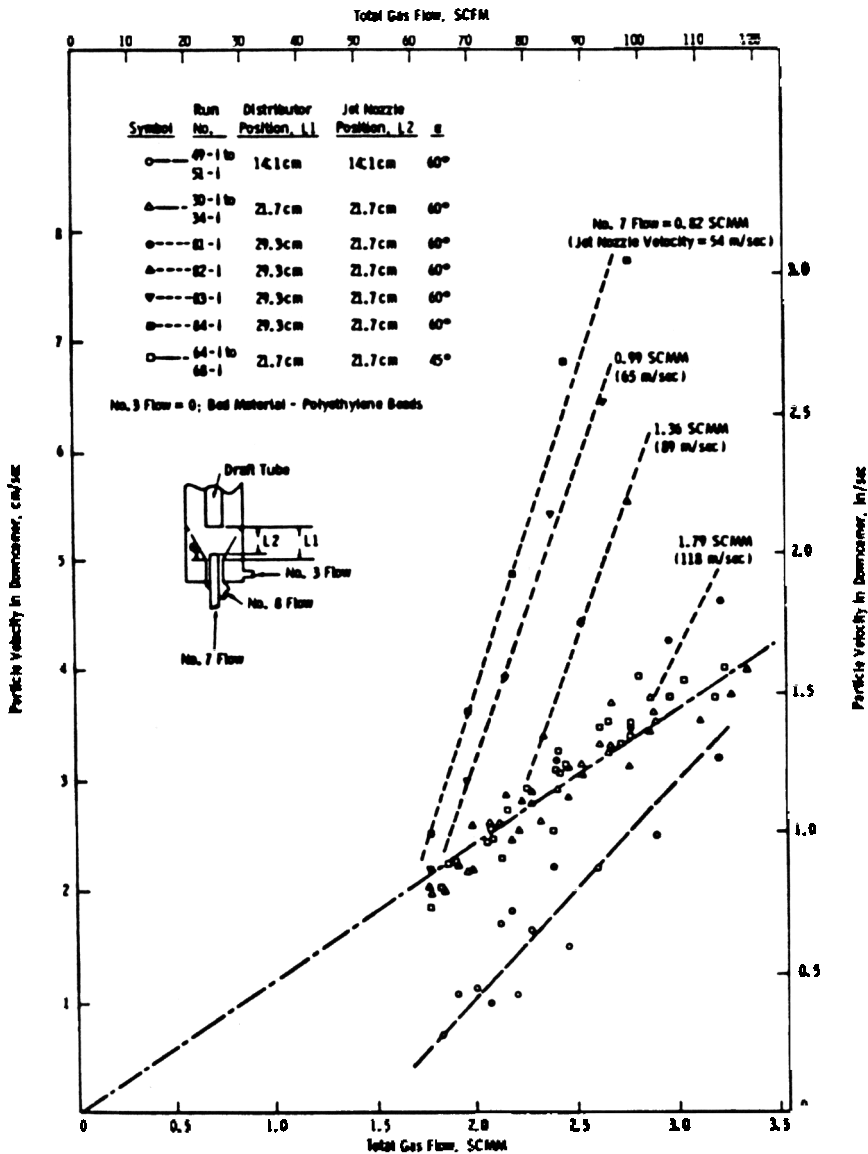


Figure 10. Comparison of solids circulation rate at different distributor plate design configurations.

Effect of Distance Between Distributor Plate and Draft Tube Inlet.

As expected, the closer the distance between the distributor plate and the draft tube inlet the lower the solids circulation rate as shown in Figs. 8 and 9. This is not only because of the physical constriction created by locating the distributor plate too close to the draft tube inlet but also because of the different gas bypassing characteristics observed at different distributor plate locations as discussed earlier. When the distance between the distributor plate and the draft tube inlet becomes large, it can create start-up problems discussed in Yang et al. (1978).

2.3 Design Example for a Recirculating Fluidized Bed with a Draft Tube

From the experimental evidence, the design of a recirculating fluidized bed with a draft tube involves the specification of a number of design parameters and an understanding of the coupling effects between the design and the operating variables. A procedure is presented here for the design of a bed to give a specified solids circulation rate. This design procedure assumes that the solids and gas characteristics, feed rates, and operating temperature and pressure are given. The design parameters to be specified include the vessel diameter, draft tube diameter, draft tube height, gas distributor, and distributor position. These parameters can be specified using the solids circulation rate model, experimental data on gas bypassing, and process requirements (e.g., selection of gas velocity in the bed above the draft tube).

Determination of the Gas Bypassing Characteristics of the Distributor Plate Experience indicates that a simple theoretical model to predict gas bypassing accurately that takes into account all the design and operating variables cannot be developed. Empirical correlations, however, can be obtained by conducting experiments with tracer gas injection for a given distributor plate design at different operating conditions and at different distances from the draft tube inlet. Distributor plate designs can be studied and an optimum design selected to provide the desired solids circulation rate.

Design for Desired Solids Circulation Rate It is assumed that the total gas flow into the bed is known. When the operating fluidizing velocity is selected for the fluidized bed above the draft tube, the diameter of the vessel is determined. The final design decisions include selection of the draft tube diameter, the distributor plate design, the separation between the draft

tube and the distributor plate, and the draft tube height. Selection of draft tube height may be determined by other considerations, such as solids residence time, though it also affects the solids recirculation rate. A gas distributor is selected to be compatible with the process and to maintain the gas velocity in the downcomer near U_{mf} . The draft tube diameter is then selected by using the solids circulation rate model to obtain the desired circulation rate.

The results of an example calculation for a recirculating fluidized bed coal devolatilizer of 0.51 m in diameter handling coal of average size 1200 μm at 870°C and 1550 kPa are presented in Fig. 11. The calculation is based on operating the fluidized bed above the draft tube at 4 times the minimum fluidization velocity. It is also based on the selection of a distributor plate to maintain the downcomer at the minimum fluidization condition. If the two-phase theory applies, this means that the slip velocity between the gas and the particles in the downcomer must equal to the interstitial minimum fluidizing velocity as shown below.

$$\text{Eq. (17)} \quad U_{fd} + U_{pd} = \frac{U_{mf}}{e_{mf}}$$

where U_{fd} and U_{mf} are positive in the upward direction and U_{pd} is positive in the downward direction. The design procedures are thus:

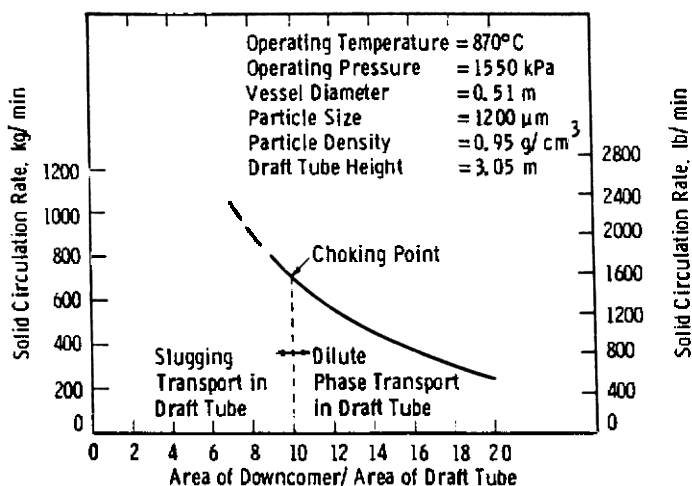


Figure 11. Projections of solid circulation rate at constant total flow and changing bed geometry—results of example calculation.

1. Assume a solid circulation rate per unit draft tube area, W_{sr} , and calculate the particle velocity in the downcomer, U_{pd} , from the following equation

$$\text{Eq. (18)} \quad W_{sr} = U_{pd}(1 - \mathbf{e}_{mf}) \mathbf{r}_s \frac{A_d}{A_r}$$

2. Calculate U_{fd} from Eq. (17) and the pressure drop across the downcomer, DP_{1-4} , from Eq. (9) assuming $\mathbf{e}_d = \mathbf{e}_{mf}$.

3. Use trial and error between Eqs. (12)–(14) to evaluate U_{pr} (the equilibrium particle velocity in the draft tube after acceleration), \mathbf{e}_r (the equilibrium voidage in the draft tube after acceleration), and f_p (the solid friction factor).

4. Numerically integrate Eq. (11) to obtain the particle acceleration length and Eq. (15) to obtain the pressure drop across the draft tube, DP_{2-3} .

5. Compare the pressure drop across the downcomer, DP_{1-4} , and that across the draft tube, DP_{2-3} . If they are not equal, repeat procedures 1 through 5 until $DP_{1-4} \cong DP_{2-3}$.

The results in Fig. 11 show that the solids circulation rate increases with a decrease in downcomer/draft tube area ratio; however, the operating condition inside the draft tube will eventually approach the choking condition where a slugging-type transport prevails. In the example, this may occur at a downcomer/draft tube area ratio of about 10. Correlations for predicting the choking point in a vertical pneumatic conveying line are available (Punwani et al., 1976; Yang, 1983). At an even lower downcomer/draft tube area ratio, the solids circulation will approach the conditions of the low-velocity circulating fluidized bed described by LaNauze (1976). His model can be used for solid circulation calculations in the low draft tube velocity regime.

Start-up and Shutdown Considerations. Both cold flow experiments and actual pilot-plant experience show that, if operating conditions and design parameter are not selected carefully, start-up (initiate solid circulation) might be a problem (Yang et al., 1978). The primary design parameters that will affect the start-up are the distance between the grid and the draft tube inlet (L) and the diameter ratio between the draft tube and the draft tube gas supply nozzle and the concentric solid feeder (D/d_D and D/d_s). The maximum allowable distance, L , can be determined by applying the jet penetration equation suggested by Yang and Keairns (1978b)

$$\text{Eq. (19)} \quad \frac{L}{d_D} = 6.5 \left(\frac{\mathbf{r}_f}{\mathbf{r}_s - \mathbf{r}_f} \cdot \frac{U_j^2}{g d_D} \right)^{1/2}$$

where U_j is the gas velocity issuing from the draft tube gas supply. For high-temperature and high-pressure operations, Eq. (23) to be discussed later should be used for calculating L . Another consideration is that the jet boundary at the end of jet penetration is preferably with the physical boundary of the draft tube inlet. Merry's expression (1975) for jet half angle can be used for this purpose

$$\text{Eq. (20)} \quad \cot(\mathbf{q}) = 10.4 \left[\frac{\mathbf{r}_f d_D}{\mathbf{r}_s d_p} \right]^{0.3}$$

or

$$\text{Eq. (21)} \quad L = \frac{(D - d_D)}{2 \cdot \tan(\mathbf{q})}$$

The L selected for the design should be the smaller one of that estimated from Eqs. (19) and (21).

A start-up technique described by Hadzismajlovic et al. (1992) is worthy of consideration if the draft tube gas supply is retractable. The draft tube gas supply nozzle can be inserted into the draft tube during start-up and shutdown. This will reduce the difficulty described here during start-up. After start-up, the supply nozzle can be lower to below draft tube inlet at a predetermined height to provide the normal operation configuration. This will prevent solids to drain into the gas supply nozzle during shutdown. Of course, if the draft tube gas supply nozzle is not movable due to hostile operating conditions, the technique can not be used. The design precautions discussed above during start-up should then be followed.

Multiple Draft Tubes. Studies in the past always concentrate on beds with a single draft tube. A literature survey failed to uncover any reference on operation of multiple draft tubes. Even in the area of conventional spouted beds, the references on multiple spouted beds are rare. Foong et al. (1975) reported that the multiple spouted bed was inherently unstable due to pulsation and regression of the spouts. Similar instability was also

observed by Peterson (1966) who found that vertical baffles covering at least one half of the bed height were necessary to stabilize the operation. In an industrial environment where solids are processed in large vessels, multiple draft tubes may be both necessary and beneficial. Exploratory tests in a two-dimensional bed with three draft tubes were reported by Yang and Keairns (1989).

A schematic of the two-dimensional test apparatus with three draft tubes is shown in Fig. 12. The two-dimensional bed is constructed with transparent Plexiglas plates in the front and aluminum plates at the back with a cross-section of 50.8 cm by 2.54 cm and 244 cm high. The three draft tubes have a cross-sectional area of 2.54 cm by 2.54 cm each and 91 cm high. The three draft tubes divide the bed into four separate downcomers. The two downcomers next to the side walls have a cross-section of 5.9 cm by 2.54 cm while the remaining two downcomers have a cross-section exactly two times, i.e., 11.8 cm by 2.54 cm. If all three draft tubes operate similarly, the bed should have three identical cells, each with a single draft tube. The distance between the draft tube inlet and the air distributor plate was maintained at a constant spacing of 5.1 cm throughout the experiments.

Polyethylene beads of relatively narrow size distribution with a harmonic mean diameter of 2800 μm and a particle density of 910 kg/m^3 were used as the bed material. A static bed height of 1.4 m was employed.

Two different series of experiments were carried out. In one series, the three draft tube velocities were maintained essentially constant while the aeration to downcomers was varied. One of the three draft tube velocities was purposely increased to simulate possible unbalanced operation conditions in an actual industrial plant in the second series of experiments. Each experiment was characterized by solid particle velocity in each downcomer, the pressure drop across each draft tube, and the pressure drop across each downcomer.

When all three draft tubes were operated at similar velocities, the pressure drops across all draft tubes and downcomers were comparable. However, solid particle velocities in outside downcomers close to the walls were substantially less due to wall effect and redistribution of downcomer aeration flow. Smooth operations under these conditions were possible. The solid particle velocities in outside downcomers can be increased by enlarging the downcomer cross-section or by increasing downcomer aeration through separate plenums to minimize wall effects.

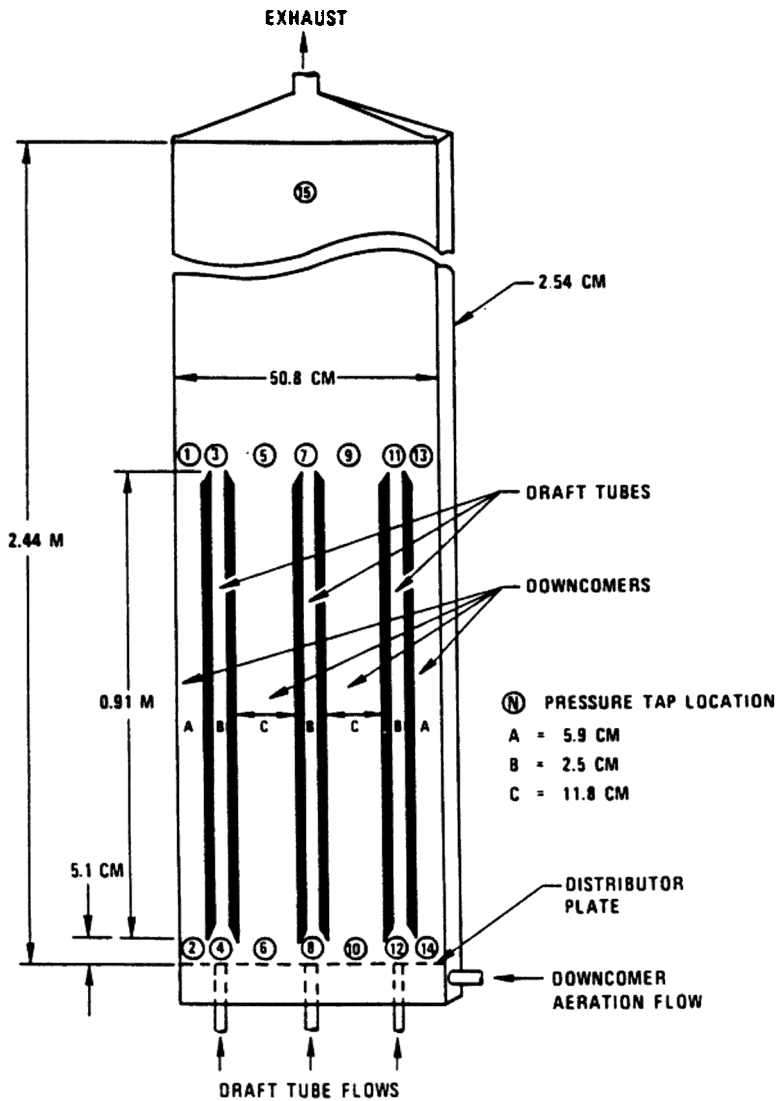


Figure 12. Schematic of a two-dimensional test apparatus with three draft tubes.

When one of the three draft tube velocities was increased to simulate upset conditions, stable operations were still possible. These upset conditions could also be detected by pressure drop differences among various draft tubes and downcomers when differences in draft tube velocities were large. For severe upset conditions, where some of the draft tubes become downcomers, pressure drop measurement alone could not distinguish the solids flow pattern inside the draft tubes.

The design methodology proposed earlier for beds with a single draft tube is still applicable here for beds with multiple draft tubes.

2.4 Industrial Applications

The application of the recirculating fluidized bed with a draft tube was probably first described by Taskaev and Kozhina (1956). They utilized the bed for low temperature carbonization of coals in a 15 cm diameter column with a 2.5 cm diameter draft tube. A "seeded coal process" was later developed by Curran et al. (1973) using the same concept to smear the "liquid" raw coal undergoing the plastic transition onto the seed char and the recirculating char during low temperature pyrolysis. Westinghouse successfully demonstrated a first stage coal devolatilizer with caking coals in a pilot scale Process Development Unit employing a similar concept where the downcomer was fluidized and the jet issuing from the draft tube was immersed in a fluidized bed above the draft tube (Westinghouse, 1977). The same concept was also proposed for extending fluidized bed combustion technology for steam and power generation (Kearns, et al., 1978). The British Gas Council has also developed the concept for oil and coal gasification (Horsler and Thompson, 1968; Horsler et al., 1969). The development eventually resulted in a large-scale recirculating fluidized bed hydrogenator gasifying heavy hydrocarbon oils (Ohoka and Conway, 1973). McMahon (1972) also described a reactor design for oil gasification using a multiplicity of draft tubes. The Dynacracking process developed by Hydrocarbon Research Inc. in the 1950's (Rakow and Calderon, 1981) for processing heavy crude oil also utilized an internal draft tube. More recently, gasification in a recirculating fluidized bed with a draft tube was described by Judd et al. (1984) and coal-water mixture combustion, by Lee and Kim (1992).

Other industrial applications of the concept include that for coating tablets in the pharmaceutical industry (Wurster et al. 1965), for drying of

dilute solutions containing solids (Hadzismajlovic, 1989), and for mixing and blending (Decamps et al. 1971/1972; Matweecha, 1973; Solt, 1972; Krambrock, 1976). Both Conair Waeschle Systems and Fuller Company supply commercial blenders based on the concept. The concept was also proposed as a controllable solids feeder to a pneumatic transport tube (Decamps et al., 1971/1972; Silva et al., 1996).

Although most of the experimental data reported here were obtained with large particles, Geldart Class B and D powders, it is believed that the concept can equally be applied for any fine aeratable and free-flowing solids, Geldart's Class A powders.

A similar concept has also been used for liquid-solids and liquid-gas-solids contacting devices (Oguchi and Kubo, 1973; Fan et al., 1984) and bioreactors (Chisti, 1989). Bubble columns fitted with draft tubes have also been employed in the chemical process industries as airlift reactors for gas-liquid contacting operations. Examples are the low-waste conversion of ethylene and chlorine to dichloroethane, biological treatment of high strength municipal and industrial effluent and bioreactors. Critical aspects of the design and operation of bubble columns with draft tubes have recently been reviewed by Chisti and Moo-Young (1993). Freedman and Davidson (1964) also carried out a fundamental analysis for gas holdup and liquid circulation in a bubble column with a draft tube. Extensive experimentation in a bubble column with a draft tube was conducted by Miyahara et al. (1986) and in-depth analysis by Siegel et al. (1986). The effects of geometrical design on performance for concentric-tube airlift reactors were studied by Merchuk et al. (1994).

3.0 JETTING FLUIDIZED BEDS

In a gas fluidized bed, the introduction of gas is usually accomplished through distributors of various designs. Any time the gas is distributed through orifices or nozzles, a jetting region appears immediately above the grid. A large fluctuation of bed density occurs in this zone, indicating extensive mixing and contacting of solids and gas. If the chemical reactions between gas and solids are fast, much of the conversion may occur in this jetting region.

Another type of fluidized bed, where the jetting phenomena is an important consideration, is the spouted fluid bed, where a large portion of

gas goes through a fairly large nozzle. Because of the dominant effect of this jetting action provided by the large nozzle, this type of fluidized bed can be more appropriately called a *jetting fluidized bed*, especially when the jet does not penetrate through the bed like that in a spouted bed. Jetting, bubbling dynamics, and solid circulation are important hydrodynamic phenomena governing the performance and operation of large-scale jetting fluidized beds. They are the focus of our discussion in this section.

3.1 Jet Penetration and Bubble Dynamics

Gas jets in fluidized beds were reviewed by Massimilla (1985). A more recent review is by Roach (1993) who also developed models to differentiate three jet flow regimes: jetting, bubbling and the transition. However, most of the data were from jets smaller than 25 mm. The discussion here will emphasize primarily large jets, up to 0.4 m in diameter, and operation at high temperatures and high pressures. The gas jets can also carry solids and are referred to as *gas-solid two-phase jets* in this discussion.

Momentum Dissipation of a Gas-Solid Two-Phase Jet. Gas velocity profiles in a gas-solid two-phase jet inside a fluidized bed were determined at five different horizontal planes perpendicular to jet direction using a pitot tube (Yang and Kearns, 1980). The velocity profiles were integrated graphically, and gas entrainment into a jet was found to occur primarily at the base of the jet.

The measured impact pressures and static pressures were converted to gas velocities using the following equation:

$$\text{Eq. (22)} \quad U_{jr} = C \sqrt{\frac{2g_c(P_i - P_o)}{r_f}}$$

The coefficient C was assumed to be 1. The typical velocity profiles are shown in Figs. 13–15 for a nominal jet velocity of 62.5 m/s and solid loadings (weight of solids/weight of gas) of 0–1.52. Note that at 1.7 cm from the jet nozzle, the velocity profile is independent of solid loadings (Fig. 13). The jet at 1.7 cm from the nozzle is still in the potential core region. At greater distances from the jet nozzle, the velocity profiles become dependent on the solid loadings (Figs. 14–15), with jets of higher solid loadings penetrating deeper into the bed, as expected.

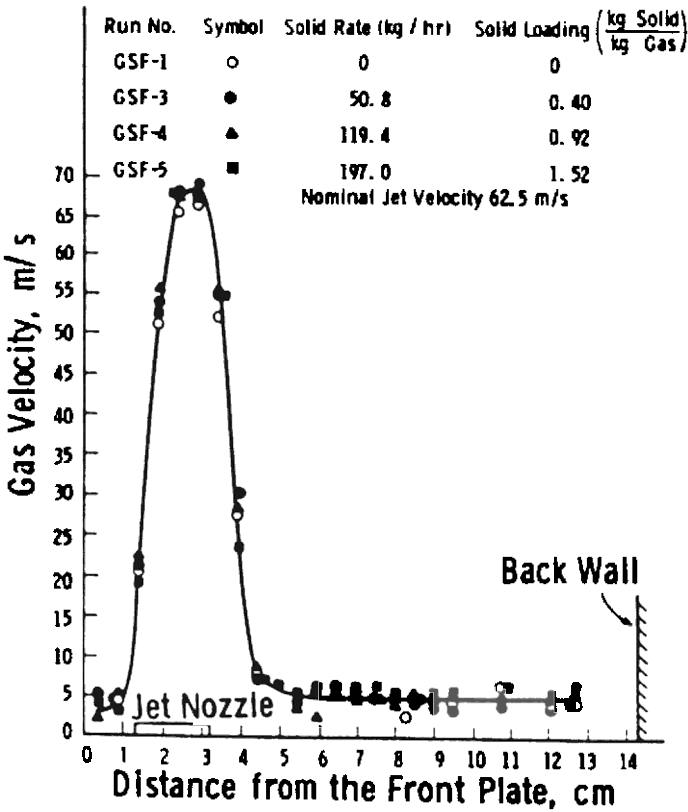


Figure 13. Jet velocity profiles at 1.7 cm from the jet nozzle.

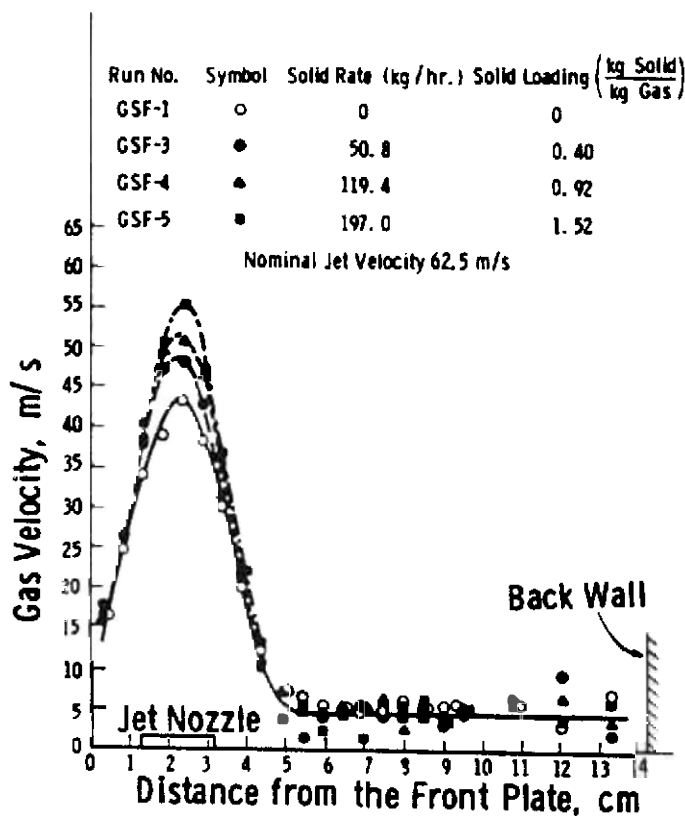


Figure 14. Jet velocity profiles at 9.3 cm from the jet nozzle.

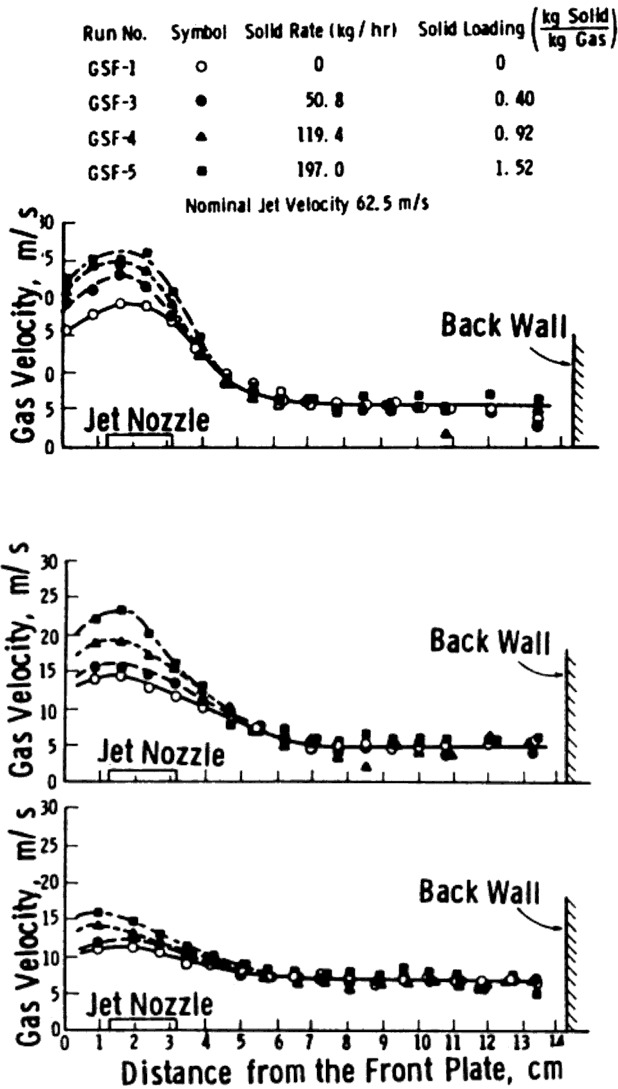


Figure 15. Jet velocity profiles at 23.6, 33.8, and 44.5 cm from the jet nozzle.

A reasonably consistent universal velocity profile is obtained by plotting $(U_{jr} - U_{jb})/(U_{jm} - U_{jb})$ vs. $r/r_{1/2}$ in Figs. 16–18, comparable with the Tollmien solution for a circular homogeneous jet in an infinite medium (Abramovich, 1963; Rajaratnam, 1976).

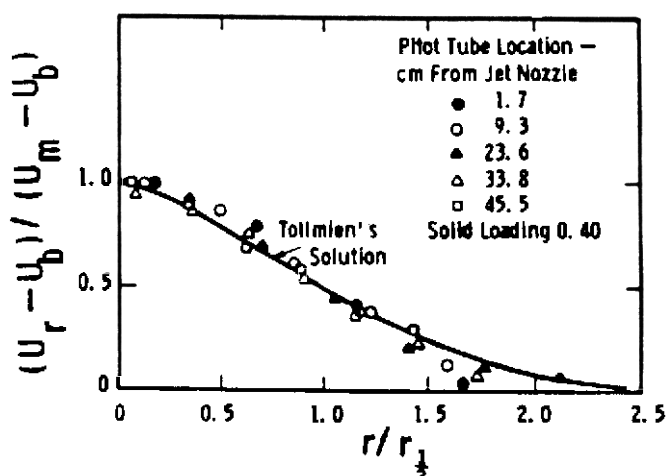


Figure 16. Universal velocity profile for Run GSF-3—comparison with Tollmien's solution.

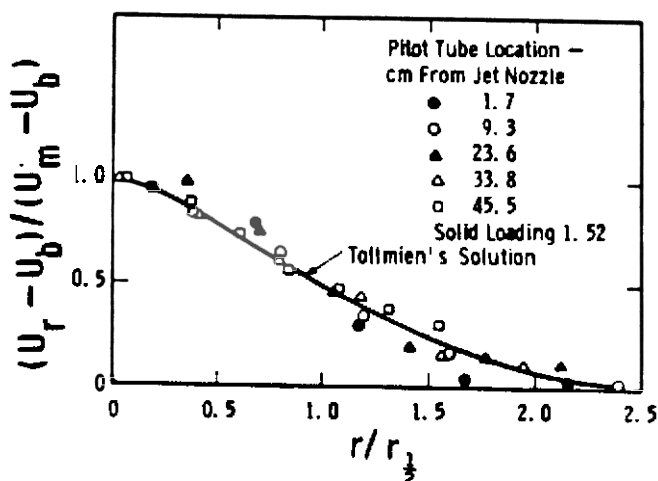


Figure 17. Universal velocity profile for Run GSF-5—comparison with Tollmien's solution.

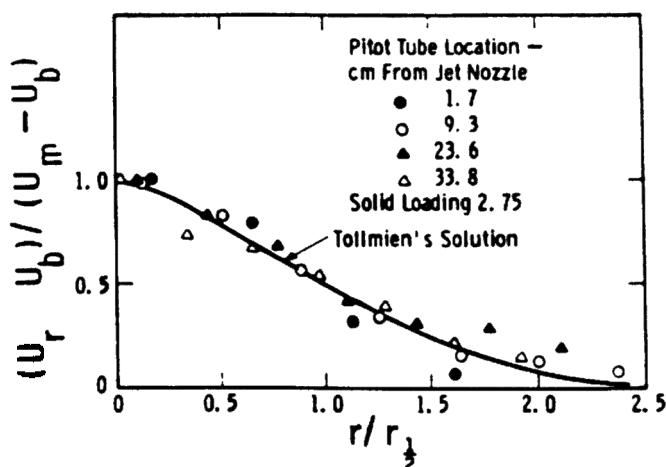


Figure 18. Universal velocity profile for Run GSF-47—comparison with Tollmien's solution.

Jet Penetration and Jet Half Angle. *Jet Penetration* Jetting phenomena were studied by Yang and Keairns (1978b) in a semicircular column 30 cm in diameter using hollow epoxy spheres ($\rho_p = 210 \text{ kg/m}^3$) as the bed material and air as the fluidizing medium to simulate the particle/gas density ratio in actual operating conditions at 1520 kPa and 1280°K. A two-phase Froude number, defined as $(\rho_f U_j^2)/(\rho_s - \rho_f)gd_o$ and derived from both the momentum balance and the dimensionless analysis, was found to correlate well with jet penetration data. The jet penetration depth was defined similarly to that by Merry (1975) and shown in Fig. 19. Other variations were found as described by Kececiloglu et al. (1984). The correlation was extended to cover the high-pressure jet penetration data of Knowlton and Hirsan (1980) at pressures up to 5300 kPa for fluidized beds of sand ($\rho_s = 2629 \text{ kg/m}^3$), FMC char ($\rho_s = 1158 \text{ kg/m}^3$), and siderite ($\rho_s = 3988 \text{ kg/m}^3$). A subsequent analysis by Yang (1981) indicated that the two-phase Froude number originally suggested could be modified slightly to account for the pressure effect. The original two-phase Froude number took into account the effect of pressure on the dynamic pressure created by the jet through the momentum flux term $\rho_f U_j^2$ but did not include a similar correction for the changes in fluidized bed properties due to pressure. The resulting correlation is shown in Eq. (23).

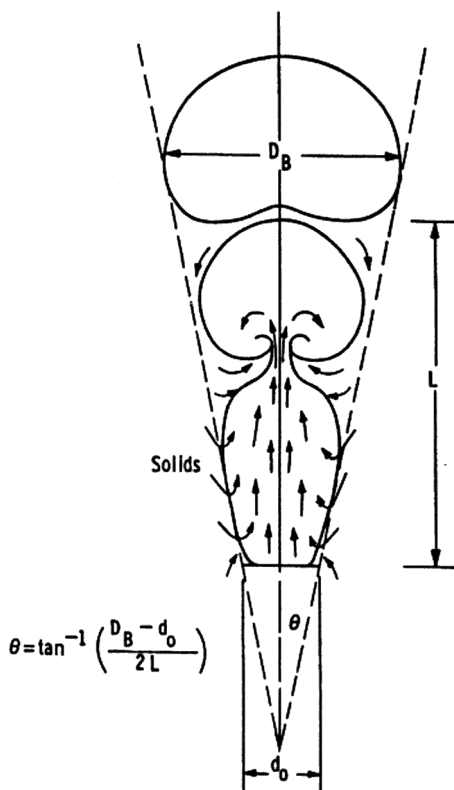


Figure 19. Definition of jet penetration depth and jet half angle.

$$\text{Eq. (23)} \quad \frac{L_j}{d_o} = 7.65 \left[\frac{1}{R_{cf}} \cdot \frac{\mathbf{r}_f}{(\mathbf{r}_s - \mathbf{r}_f)} \cdot \frac{U_j^2}{g d_o} \right]^{0.472}$$

where

$$\text{Eq. (24)} \quad R_{cf} = (U_{cf})_p / (U_{cf})_{atm}$$

In the absence of $(U_{cf})_p$ and $(U_{cf})_{atm}$, $(U_{mf})_p$ and $(U_{mf})_{atm}$ can be employed.

272 *Fluidization, Solids Handling, and Processing*

The limiting form of Eq. (24) at atmospheric pressure (101 kPa), where the correction factor $R_{cf} = 1$, approaches the correlation originally proposed for atmospheric condition, as shown in Eq. (25):

$$\text{Eq. (25)} \quad \frac{L_j}{d_o} = 6.5 \left[\frac{\mathbf{r}_f}{(\mathbf{r}_s - \mathbf{r}_f)} \cdot \frac{U_j^2}{g d_o} \right]^{0.5} = 6.5 \cdot (Fr)_j^{0.5}$$

Equation (25) now is only a special case of the general correlation expressed in Eq. (23).

For concentric jets and gas-solid two-phase jets, the jet momentum flux term $\mathbf{r}_f U_j^2$ can be evaluated as follows, as suggested by Yang et al. (1984b):

$$\text{Eq. (26)} \quad \mathbf{r}_f U_j^2 = \frac{M_o V_o + (M_g V_g + M_s V_s)}{A_o}$$

$$\text{Eq. (27)} \quad V_s = V_g - U_t$$

The solids particle velocity in the gas-solid two-phase jet can be calculated as shown in Eq. (27), assuming that the slip velocity between the gas and the solid particles equals the terminal velocity of a single particle. It should be noted that calculation of jet momentum flux by Eq. (26) for concentric jets and for gas-solid two-phase jets is only an approximation. It involves an implicit assumption that the momentum transfer between the concentric jets is very fast, essentially complete at the jet nozzle. This assumption seems to work out fine. No further refinement is necessary at this time. For a high velocity ratio between the concentric jets, some modification may be necessary.

The good agreement obtained for all data using the modified Froude number signifies the physical significance of the parameter. In fact, the dependence of jet penetration on the two-phase Froude number can be derived theoretically from the buoyancy theory following that of Turner (1973).

The momentum flux at the orifice, M , is given by

$$\text{Eq. (28)} \quad M = \frac{\rho}{4} d_o^2 U_j^2$$

The buoyancy flux at the orifice, B , can be expressed as

$$\text{Eq. (29)} \quad B = \frac{\rho}{4} d_o^2 U_j g \left(\frac{r_b}{r_f} - 1 \right)$$

The characteristic length scale, L_j , taken here to be the jet penetration depth is shown by Turner (1973) for a buoyancy jet to be

$$\text{Eq. (30)} \quad \frac{L_j}{d_o} \approx \frac{M^{3/4}}{B^{1/2} d_o} = (Fr)_j^{0.5}$$

Equation (30) is essentially similar to Eq. (25).

The experimental data included in the correlation, however, are mostly from jets of less than 6 cm in diameter. The question often asked is whether the developed correlation is applicable for scaleup to a much larger jet nozzle. The size effect will have to be verified with operational data from a jet nozzle considerably larger. Jet penetration data were obtained for a 0.4 m diameter compound jet in a 3-m diameter cold model. The experimental jet penetration data were compared with four existing correlations (Yang et al., 1995). These correlations were selected because they are all dimensionless in form and are often quoted in the literature. They were usually derived through either dimensionless analysis or semitheoretical argument. Pure empirical but dimensional correlations are not included because the dimensional empirical correlations based on small jet nozzle data base have no value for scaleup purpose. Correlations by Merry (1975), Wen et al. (1982), and Hirsan et al. (1980) predicted substantially higher jet penetration depth than that observed, probably because they included a dimensionless factor, d_o/d_p . Inclusion of this dimensionless group can exaggerate the jet penetration depth when the jet nozzle diameter, d_o , is large. Better agreement was obtained by using the correlation proposed by Yang (1981), i.e., Eq. (23).

Jet Half Angle. Determination of jet half-angle is shown also in Fig. 19. The jet half-angle can thus be calculated from the experimentally measured bubble size and jet penetration depth as follows:

$$\text{Eq. (31)} \quad q = \tan^{-1} \left(\frac{D_B - d_o}{2L_j} \right)$$

Experimentally observed jet half-angle range from 8° to 12° for the experimental data mentioned above. These compare to 10° suggested by Anagbo (1980) for a bubbling jet in liquid.

Bubble Dynamics. To adequately describe the jet, the bubble size generated by the jet needs to be studied. A substantial amount of gas leaks from the bubble, to the emulsion phase during bubble formation stage, particularly when the bed is less than minimally fluidized. A model developed on the basis of this mechanism predicted the experimental bubble diameter well when the experimental bubble frequency was used as an input. The experimentally observed bubble frequency is smaller by a factor of 3 to 5 than that calculated from the Davidson and Harrison model (1963), which assumed no net gas interchange between the bubble and the emulsion phase. This discrepancy is due primarily to the extensive bubble coalescence above the jet nozzle and the assumption that no gas leaks from the bubble phase.

High speed movies were used to document the phenomena above a 0.4 m diameter jet in a 3-meter diameter transparent semicircular jetting fluidized bed (Yang et al., 1984b). The movies were then analyzed frame by frame to extract information on bubble frequency, bubble diameter, and jet penetration depth. The process of bubble formation is very similar to that described in Kececiloglu et al. (1984), but it was much more irregular in the large 3-m bed. Because of this irregularity, it was difficult to count accurately the “bubbles” between the constrictions immediately above the jet nozzles. The initial bubble formation at the top of the jet was assumed complete when the gaseous tail with entrained solids disappeared into the gas bubbles. The largest horizontal dimension of the bubble was reported to be the bubble size; the distance between the top of the jet nozzle and the bottom of the gas bubble, the jet penetration depth.

The Davidson and Harrison (1963) model assumed there was no net exchange of gas between the bubble and the emulsion phase. The validity of this assumption was later questioned by Botterill et al. (1966), Rowe and Matsuno (1971), Nguyen and Leung (1972), and Barreto et al. (1983). The predicted bubble volume, if assumed no net gas exchange, was considerably larger than the actual bubble volume experimentally observed.

A model was developed to describe this phenomenon by assuming that the gas leaks out through the bubble boundary at a superficial velocity equivalent to the superficial minimum fluidization velocity. For a hemispherical bubble in a semicircular bed, the rate of change of bubble volume can be expressed as:

$$\text{Eq. (32)} \quad \frac{dV_B}{dt} = G_j - U_{mf} \frac{\mathbf{p} D_B^2}{2}$$

where $V_B = \mathbf{p} D_B^3/12$ for a hemispherical bubble.

Equation (32) can be reduced to show the changes of bubble diameter with respect to time in Eq. (33):

$$\text{Eq. (33)} \quad \frac{D_B^2 dD_B}{(4G_j - 2\mathbf{p} U_{mf} D_B^2)} = \frac{dt}{\mathbf{p}}$$

Integrating Eq (33) with the boundary condition that $D_B = 0$ at $t = 0$ gives:

$$\text{Eq. (34)} \quad t = \frac{1}{2U_{mf}} \left[\frac{G_j}{\sqrt{2\mathbf{p} G_j U_{mf}}} \ln \left(\frac{2G_j + D_B \sqrt{2\mathbf{p} G_j U_{mf}}}{2G_j - D_B \sqrt{2\mathbf{p} G_j U_{mf}}} \right) - D_B \right]$$

The maximum bubble size, where the total gas leakage through the bubble boundary equals the total jet flow, can be obtained from either Eq. (32) or Eq. (33):

$$\text{Eq. (35)} \quad (D_B)_{\max} = \sqrt{\frac{2G_j}{\mathbf{p} U_{mf}}}$$

The total amount of gas leakage from the bubble at a bubble size D_B is:

Eq. (36)

$$F = \frac{G_j}{2U_{mf}} \left[\frac{G_j}{\sqrt{2\mathbf{p} G_j U_{mf}}} \ln \left(\frac{2G_j + D_B \sqrt{2\mathbf{p} G_j U_{mf}}}{2G_j - D_B \sqrt{2\mathbf{p} G_j U_{mf}}} \right) - D_B \right] - \frac{\mathbf{p} D_B^3}{12}$$

Equation (34) and the experimental bubble frequency, $n = 1/t$, were used to predict the expected bubble diameter. The predicted bubble diameters are very close to those actually observed. Theoretically, Eqs. (34) and (36) can be solved to obtain both the bubble frequency and the bubble diameter if the

total gas leakage at the moment of bubble detachment, F , is known. The only correlations available now to predict F are the empirical ones shown in Fig. 20. The bubble growth equations can be similarly derived for a circular jet in a three dimensional bed. The same experimental observation and conclusions described above for a semicircular bed are expected to hold as well.

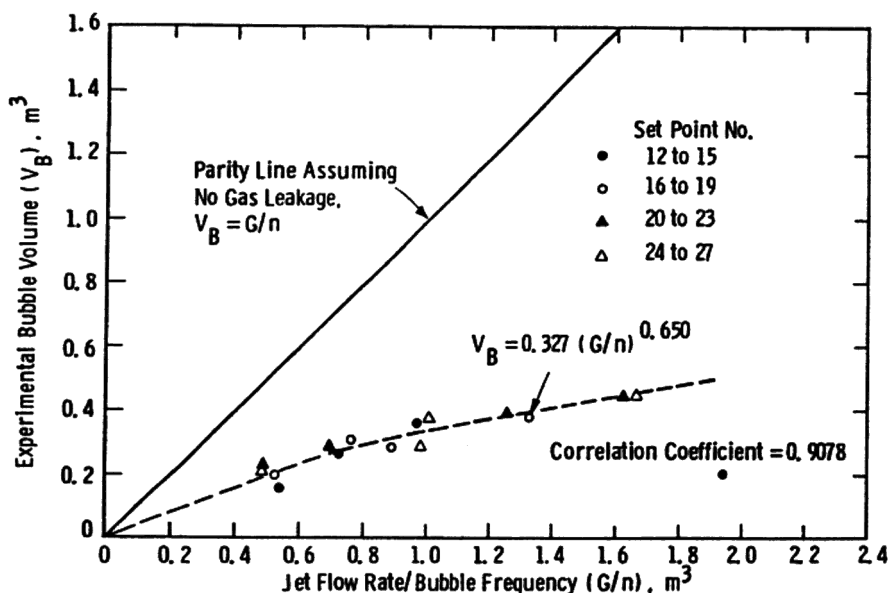


Figure 20. Comparison between the experimental bubble flow and the total flow through the jet nozzle.

Bubble frequency from the jet was also studied using a force probe in the same bed (Ettehadieh et al., 1988). The frequency characteristics of the force probe responses and their average power spectrums were calculated. Typical average power spectrum plots of the density fluctuations measured along the bed height are shown in Fig. 21. The frequencies of the more pronounced peaks in the average power spectrum plots represent the characteristic frequencies of the periodic components of the fluctuations. Due to the presence of overlapping periodic phenomena in the lower jetting sections of the bed such as jet pulsations, bubble formation and bubble coalescence, multiple major frequencies are observed in these

portions of the bed. Whereas in the middle and upper portions of the bed only a single narrow band of maximum power, or in other words, a single major frequency peak, is present. According to Broadhurst and Becker's (1976) analysis of the fluidized bed pressure fluctuations, a single maximum power peak is observed whenever a large number of random bubbles coalesce into a small number of periodic bubbles.

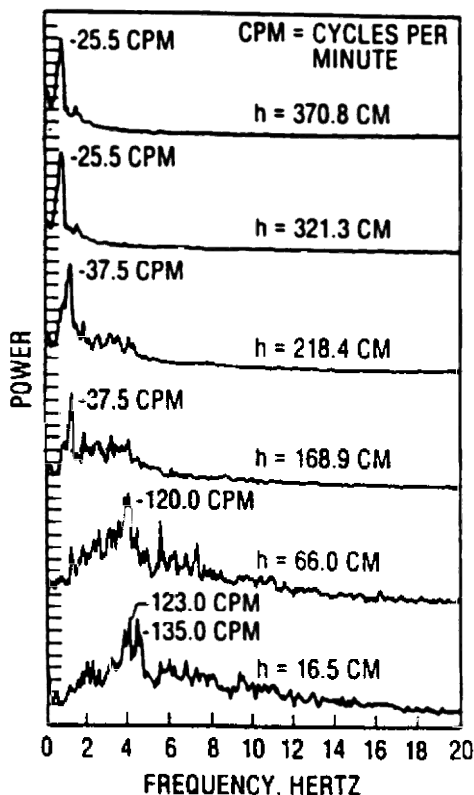


Figure 21. Typical average power spectrum plots of the bed density fluctuations measured along the bed height with the 40.6-cm jet assembly (Set Point 9).

The axial profiles of the characteristic major frequencies measured along the bed height with the 25.4-cm and the 40.6-cm jet nozzle assemblies under different jet flow rates are shown in Figs. 22 and 23. The frequency profiles reveal that increasing the jet flow rates results in an increase in the

frequency of the oscillations measured in the lower jetting and bubble coalescing portions of the bed by in effect extending the bubble coalescence region. The figures also show that regardless of the jet flow rates and the size of the two different jet diameters, the frequency profiles all level off into a narrow frequency band at approximately 2 m above the jet inlets. All visually observed jet penetration depths fall within this jet influence zone.

Bubble frequencies measured visually in the three viewing area by the frame-by-frame analysis of motion pictures are also shown in Figs. 22 and 23. Bubbling frequencies reported from the motion pictures are the frequencies of all bubbles, random or periodic, which were observed within the viewing areas. Whereas the force probe results are measured at specific bed elevations and represent the passage frequency of the most periodic single or coalesced bubbles. The slight discrepancy between the results reported by the two different sampling methods is therefore not unexpected. In the upper portions of the bed, where bubble coalescence is almost complete, the frequencies measured by the force probes are very close to the visually observed bubbling frequencies. In the lower bubble formation and coalescence portions of the bed, where bubbles form randomly and coalesce into larger bubbles, the characteristic frequencies are smaller than the overall bubbling frequencies observed visually.

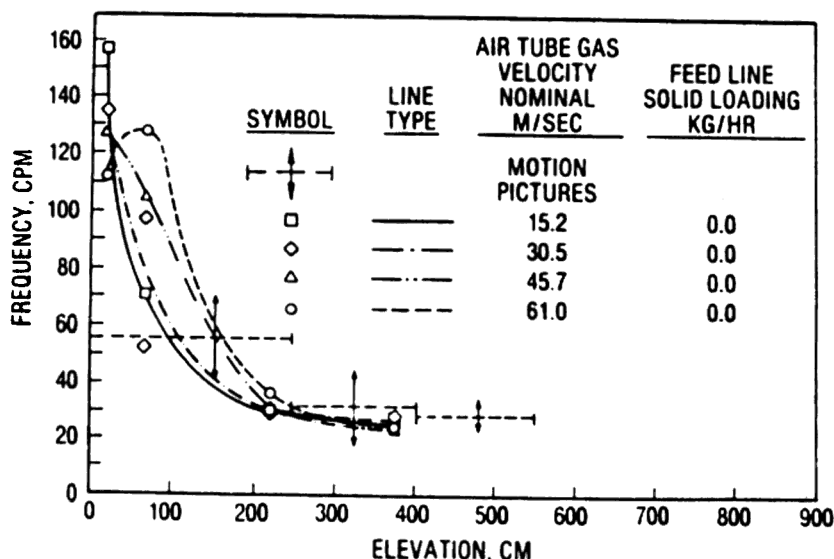


Figure 22. Profiles of the characteristic major frequencies measured along the bed height with the 25.4-cm jet assembly.

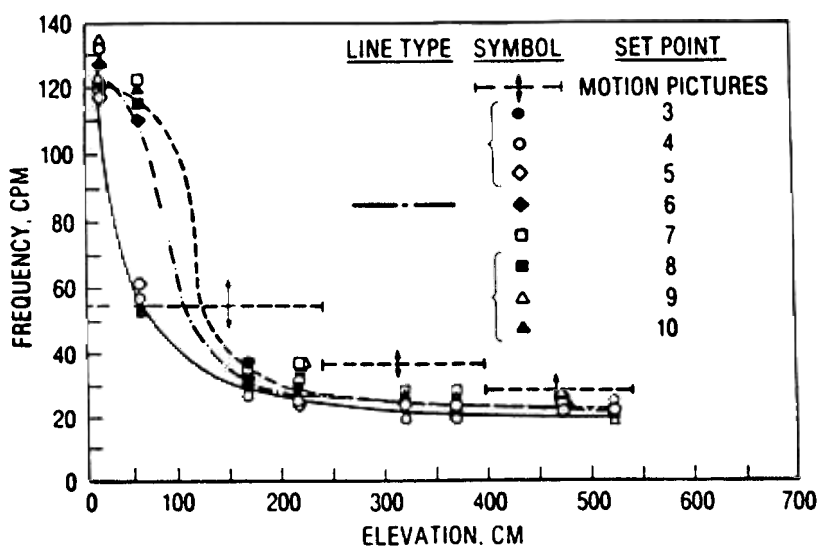


Figure 23. Profiles of the characteristic major frequencies measured along the bed height with the 40.6-cm jet assembly.

The bubbling frequencies measured in this study are much smaller than the 5–8 Hz measured by Rowe et al. (1979) and the 20 Hz measured by Hsiung and Grace (1978). The difference may be due to the dominant effect of the much larger initial bed heights and jet nozzle sizes in this study.

The size, the velocity, and the solid volume fraction of the bubbles and the solids slugs are reflected in the shape and frequency of the force probe response as shown in Fig. 24. The amplitude of the oscillations is a measure of the solid slug velocity and solid volume fraction. Inside the bubbles, the probe response is nearly flat because of the negligible solids fraction inside the bubble. The spread of the peaks and the length of the flat portions of the probe responses are measures of the size and velocity of the solid slugs and gas bubbles respectively.

The average time spent by the bubbles or solids slugs in traveling from one probe location to another was measured by calculating the average time-lag between the density fluctuations as they travel along the bed height. The average bubble rise velocities calculated from the force probe measurements with 40.6-cm jet configuration are summarized in Table 1.

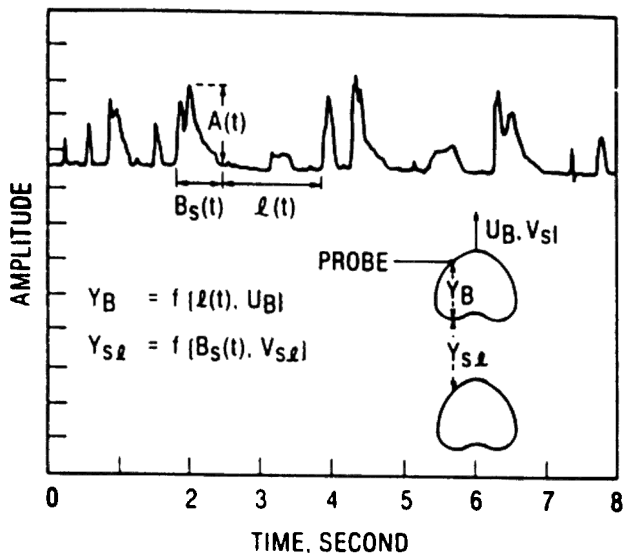


Figure 24. Typical local bed density fluctuations as measured by the force probe.

Table 1. Average Bubble Rise Velocities (m/s) Calculated from the Force Probe Measurements and Comparison with Results from the Movies; 40.6-cm Diameter Jet Assembly

Force Probe Elevation (cm)		Set Point							
Probe 1	Probe 2	3	4	5	6	7	8	9	10
321	371		3.21 (+20%) ^a	4.11 (+80%)	3.21 (+46%)	4.11 (+58%)	3.66 (+39%)	5.06 (105%)	3.3 (+39%)
321	474	2.93 (+43%)	2.71 (+1%)	3.02 (+32%)	2.87 (+30%)	3.64 (+40%)	3.15 (+20%)	3.38 (+37%)	3.71 (56%)
371	523	2.69 (+31%)			2.87 (+30%)	3.00 (+15%)	2.94 (+12%)	2.92 (+19%)	3.56 (+50%)
321	523		3.05 (+14%)	2.75 (+21%)	2.79 (+27%)		3.05 (+16%)	2.93 (+19%)	4.06 (+70%)
Movies from View	Results Overall	2.05	2.68	2.28	2.20	2.60	2.63	2.46	2.38

^a () refers to percent deviation from the results of movie analysis.

3.2 Gas Mixing Around the Jetting Region

Gas Mixing Around Single Jets. The gas exchange between the jet and the outside emulsion phase was studied by tracer gas injection and by integration of gas velocity profiles in the jet at various heights above the jet nozzle in a 28.6 cm diameter bed with a 3.5 cm jet and polyethylene beads as bed material (Yang et al., 1984a). The typical tracer concentration profiles across the bed obtained at five different elevations are shown in Figs. 25 and 26 for a nominal jet velocity of 32.6 m/s and with two different aeration flows outside the jet. The concentration profiles penetrate farther into the emulsion phase when there is less aeration flow outside the jet. The concentration profiles obtained at different elevations are also approximately similar if the local tracer concentration is normalized with the maximum tracer concentration at the axis, C/C_m , and plotted against a normalized radial distance, $r/(r_{1/2})_c$, where $(r_{1/2})_c$ is the radial position where the tracer concentration is just half the maximum tracer concentration at the axis (see Figs. 27 and 28). Thus, we experimentally determined that, in a permanent flamelike jet in a fluidized bed, not only the velocity profiles in the jet, but also the gas concentration profiles, are similar.

The gas mixing between the jetting region and the emulsion phase and the gas flow pattern around the jet were determined by solving the tracer gas conservation equation numerically along with the axial velocity profiles in the jet obtained with a pitot tube as discussed in the section, "Momentum Dissipation of a Gas-Solid Two-Phase Jet." It is concluded that the gas mixing in a jetting fluidized bed with a permanent flamelike jet is due primarily to convection and that diffusion plays a negligible role.

The resulting velocity profiles and the flow pattern inside and around the jet are shown in Figs. 29 and 30 for a jet velocity of 32.6 m/s and with two different aeration flows. The jet boundary at $V_z = 8$ m/s shown in Figs. 29 and 30 was calculated from Tollmien similarity. The boundary where the tracer gas concentration becomes zero, $C = 0$, was determined from the normalized experimental tracer gas concentration profiles shown in Figs. 27 and 28. The arrows in Figs. 29 and 30 indicate the actual axial and radial flow components, and the magnitudes are in m/s. The gas flow direction is predominantly from the emulsion phase into the jet at distances close to the jet nozzle. This flow can be from the aeration flow in the emulsion phase, as in the cases of high jet velocity or high aeration flow, or from the flow recirculated from the upper part of the jet. The

entrainment of gas into the jet occurs immediately above the jet nozzle. The extent of this region depends on both the aeration flow outside the jet and the jet velocity. Increases in aeration flow and jet velocity tend to increase the height of this region. Beyond this gas entrainment region, the gas in the jet is then expelled from the jet along the jet height. The gas expelled at the lower part of the jet is recirculated back into the jet, setting up a gas recirculation pattern at the lower part of the jet. The extent of this recirculation pattern increases with increases in jet velocity and with decreases in aeration flow outside the jet.

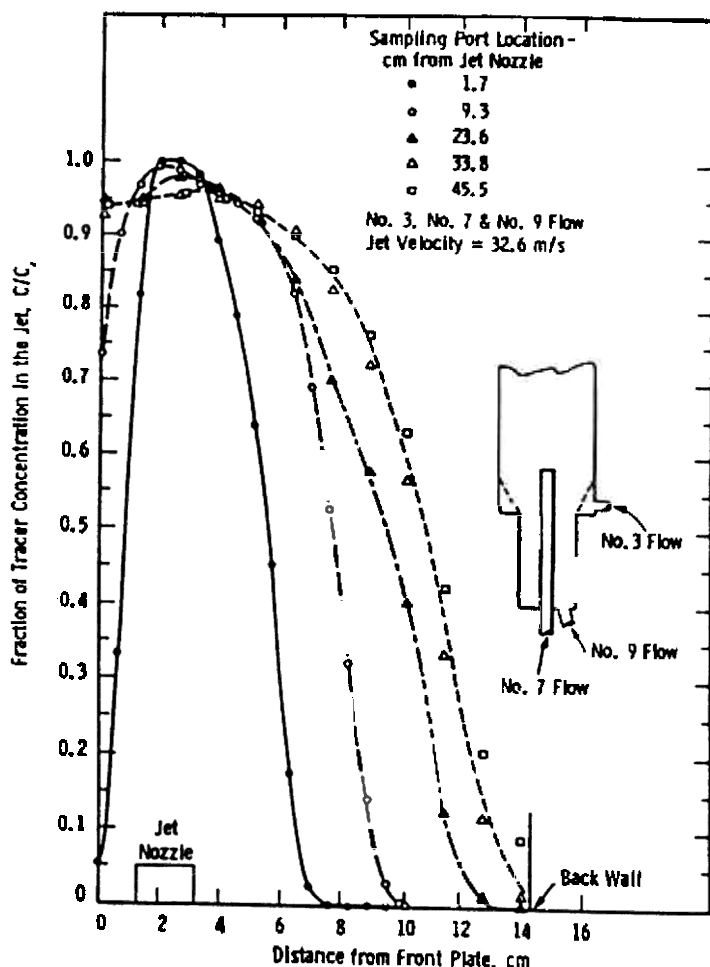


Figure 25. Experimental concentration profiles at different distances from the jet nozzle (Run GJ18).

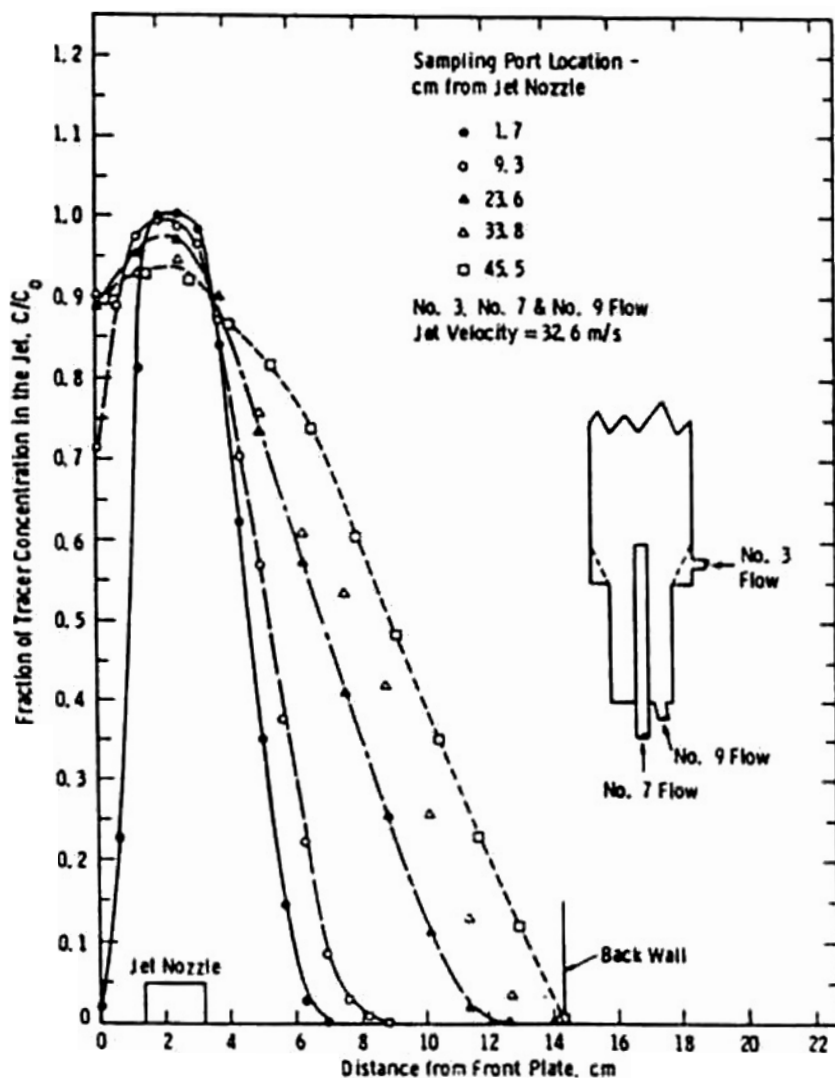


Figure 26. Experimental Concentration Profiles at Different Distances from the Jet Nozzle (Run GJ35).

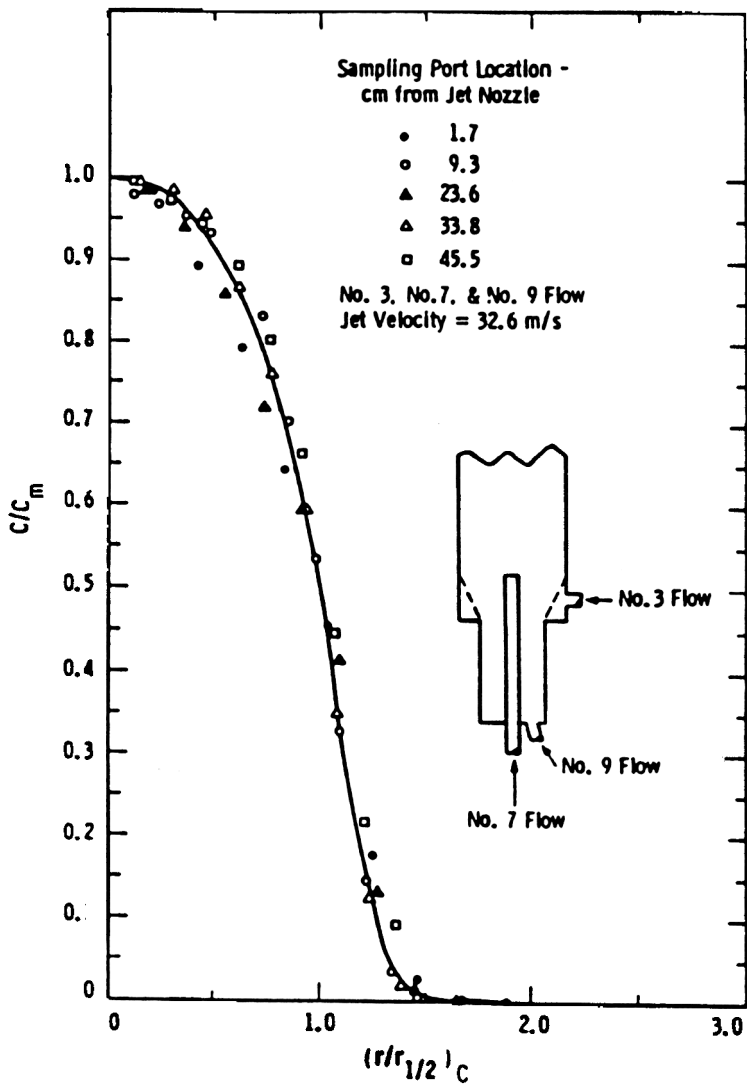


Figure 27. Normalized concentration profiles for Run GJ18.

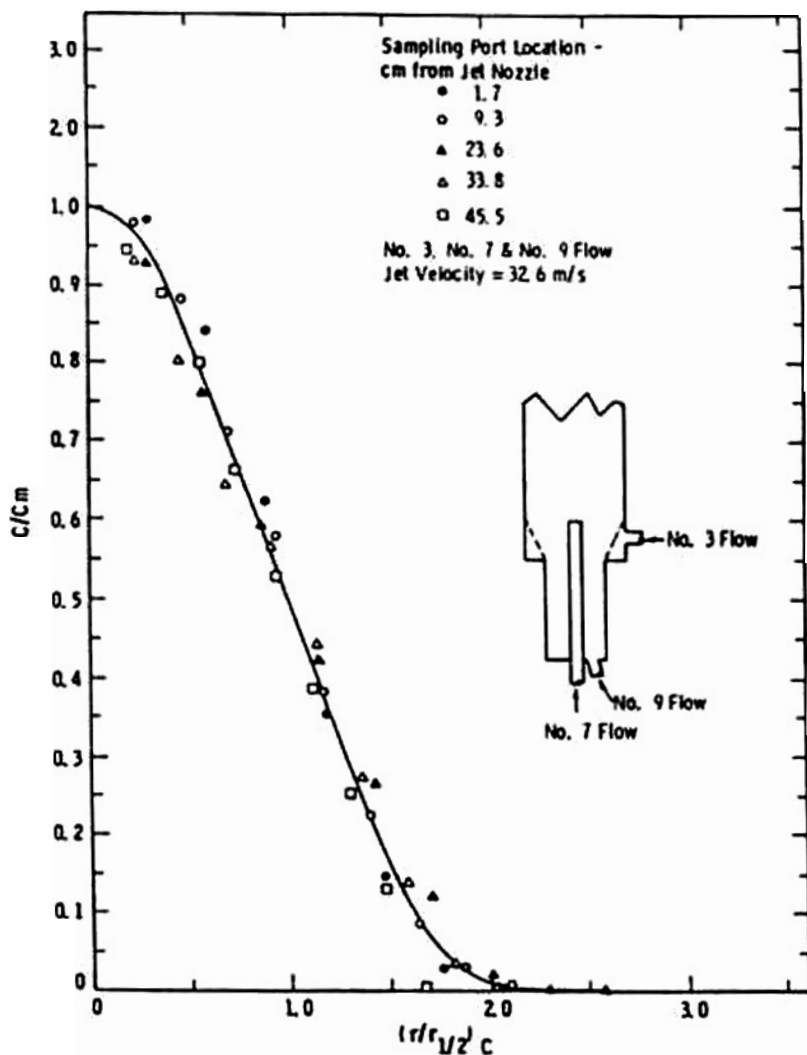


Figure 28. Normalized concentration profiles for Run GJ35.

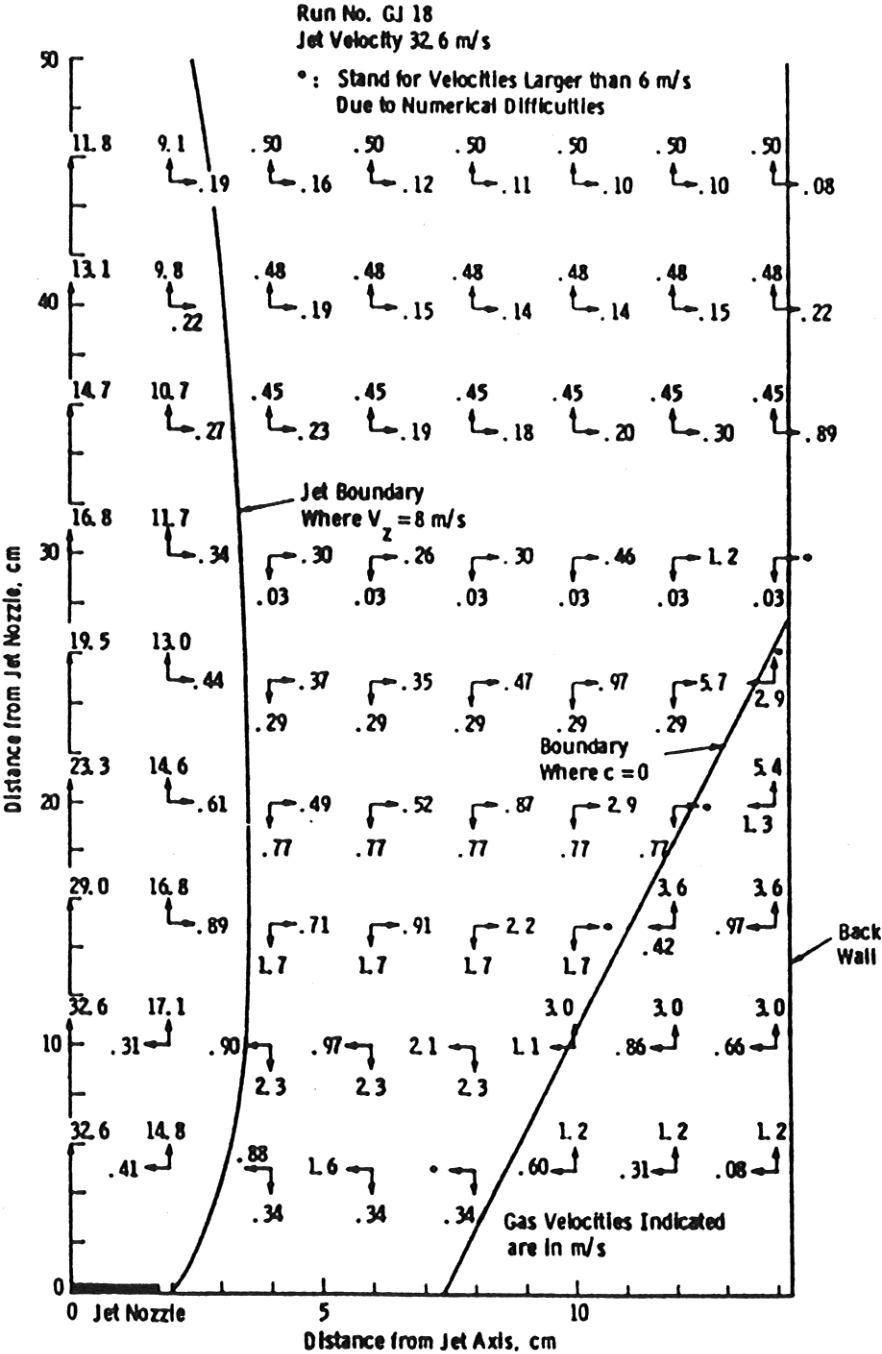


Figure 29. Calculated axial and radial gas velocity profiles for Run GJ18.

The axial velocity profiles, calculated on the basis of Tollmien similarity and experimental measurement in Yang and Keairns (1980) were integrated across the jet cross-section at different elevations to obtain the total jet flow across the respective jet cross-sections. The total jet flows at different jet cross-sections are compared with the original jet nozzle flow, as shown in Fig. 31. Up to about 50% of the original jet flow can be entrained from the emulsion phase at the lower part of the jet close to the jet nozzle. This distance can extend up to about 4 times the nozzle diameter. The gas is then expelled from the jet along the jet height.

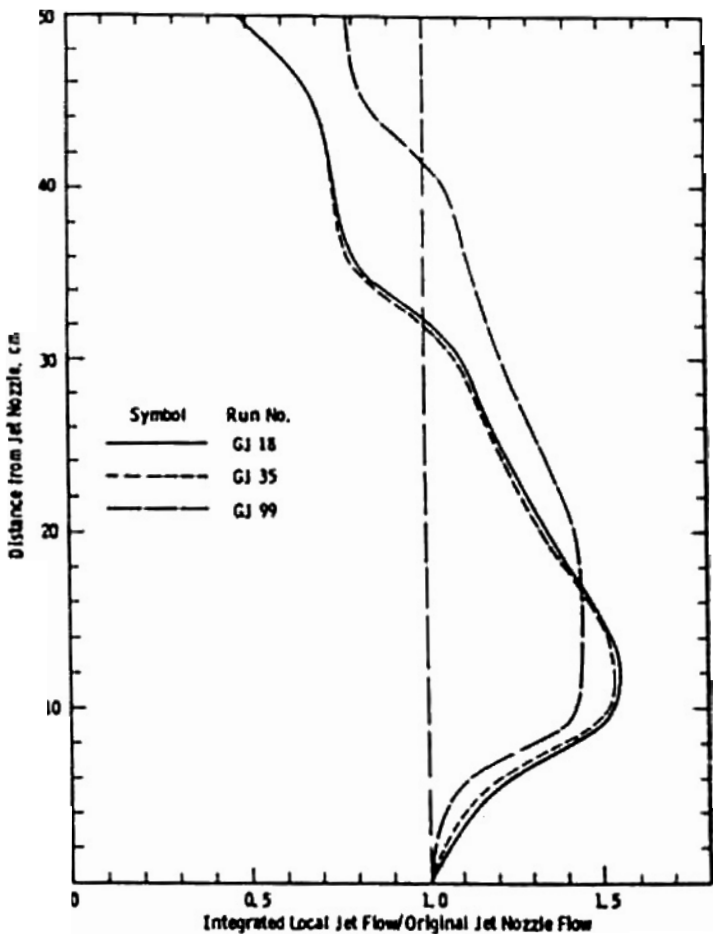


Figure 31. Calculated gas entrainment into a jet in a fluidized bed based on Tollmien's Similarity.

Gas Mixing Around Concentric Jets. Gas mixing phenomena around a concentric jet were investigated by Yang et al. (1988) in a large semicircular cold flow model, 3 meters in diameter and 10 meters high, with a triple concentric jet nozzle assembly of 25 cm in diameter. In this discussion, the outermost annulus in the triple concentric jet assembly is called the *shroud*, the innermost jet is called the *feed line*, and the middle annulus, the *air tube*. Solids were fed into the bed only through the feed line. The jet velocities employed range from 15 to 60 m/s and solid feeding rates in the concentric jets, from 0 to 3000 kg/hr. The experiments were carried out by injecting carbon dioxide as the tracer gas selectively into various flow streams and taking gas samples across different cross-sections of the bed. The bed material was -8+70 mesh crushed acrylic particles with a harmonic mean diameter of 1406 μm and a particle density of 1200 kg/m³.

A dividing gas streamline was observed experimentally which prevents the gas mixing between the jetting region and the emulsion phase until at higher bed heights. This dividing gas streamline corresponds roughly to the boundary of downflowing solids close to the walls. Similar observation was also noted in a smaller bed as discussed in the section "Gas Mixing Around Single Jets."

Typical contour profiles of equal tracer gas concentrations are shown in Figs. 32–34. In Fig. 32, the zero percent tracer concentration boundary represents the extent of the dispersion of the gas that was injected into the fluidized bed via the air tube. Increases in solids feeding rate improve the gas mixing. Similarly, the contour plots that appear in Fig. 33 show that in the initial jet expansion region, no contribution from the tracer gas that was injected through the conical grid could be detected. This means that there is no entrainment of gas from the conical section by the concentric jet flows. Partial entrainment of gas from the conical region into the core of the reactor takes place only at upper portions of the jetting region, i.e., at locations where bubbles form and coalesce. Figure 34 shows that the region of influence for the narrow shroud flow jet is limited to its immediate surrounding and that there is substantial lateral mixing of the shroud and the emulsion phase gases.

Several observations were made based on this study. Regardless of the incoming jet flow rate, the gases that are injected through the concentric jets essentially remain in the core of the reactor and do not fully mix with the gas in the dense solid downflow region of the bed. Similarly, the gas injected through the conical grid sections is not entrained by the incoming

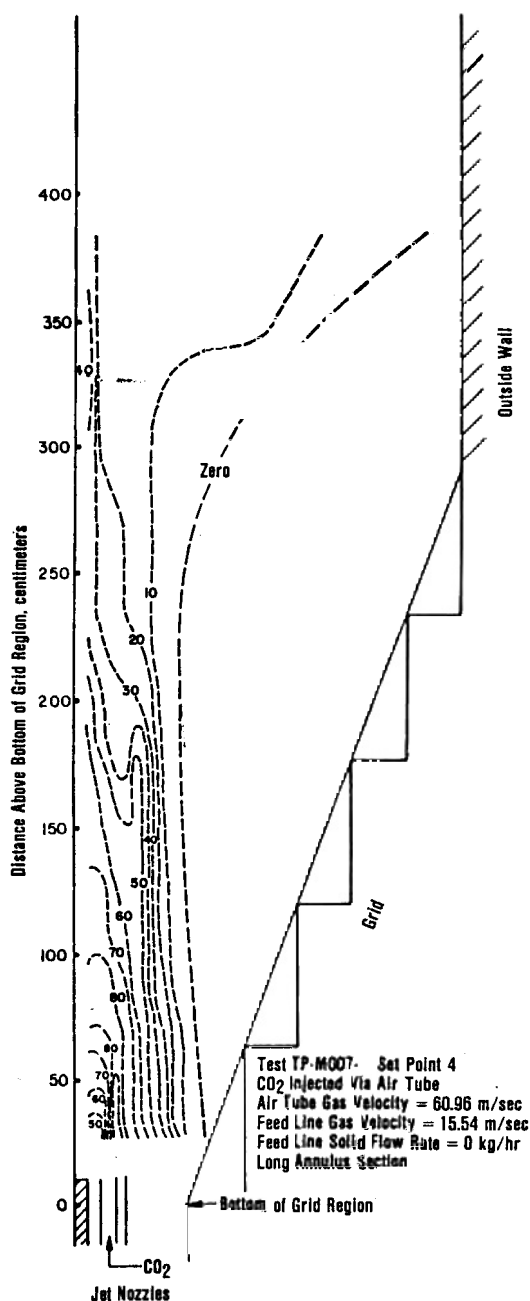


Figure 32. Tracer gas contour profiles—tracer injected via air tube.

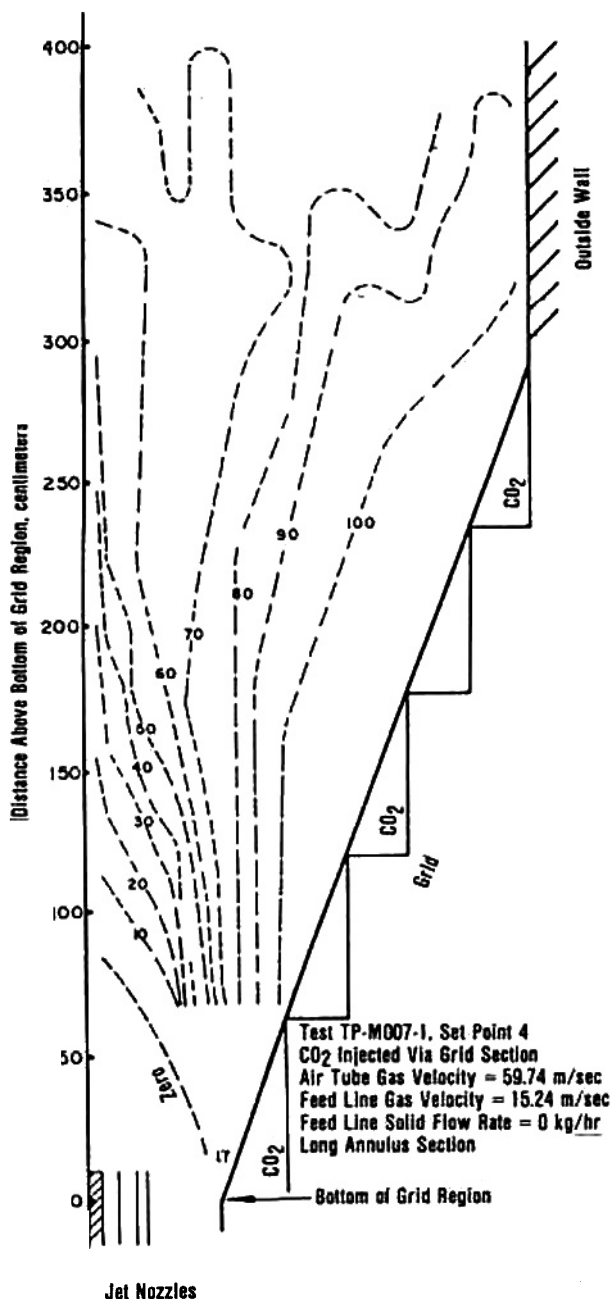


Figure 33. Tracer gas contour profiles—tracer injected via conical grid.

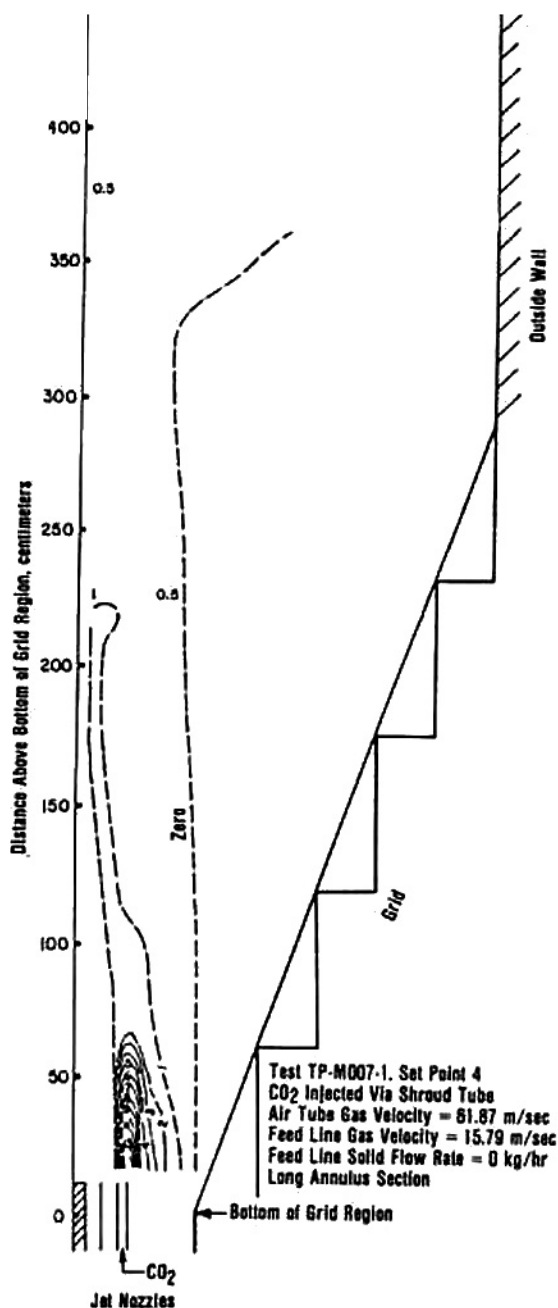


Figure 34. Tracer gas contour profiles—tracer injected via shroud.

jets. Partial entrainment and mixing of these gases occur at locations where bubble formation and bubble coalescence take place. On the contrary, the mixing among the concentric jets occurs quite fast, usually completed within the jet penetration length.

Typical axial profiles of the tracer gas concentration measured at three different radial locations above the feed line, the air tube, and the shroud are compared in Fig. 35. In this test, the carbon dioxide tracer gas was injected in the air tube flow. As expected, there is considerable mixing between the jets as they enter the fluid bed. After an initial jet mixing zone, roughly corresponding to the jet penetration depth, the three jet flows become fully mixed. Above this inner jet mixing zone, the concentration profiles continue to fall as they mix with the gas from the emulsion phase. This is the region where the bubble formation and most of the bubble coalescence take place. Above this region, the jets and the emulsion phase gases in the vicinity of the reactor core become well mixed and the concentration profiles level off. At these bed locations regular bubble passage was visually observed during bed operation.

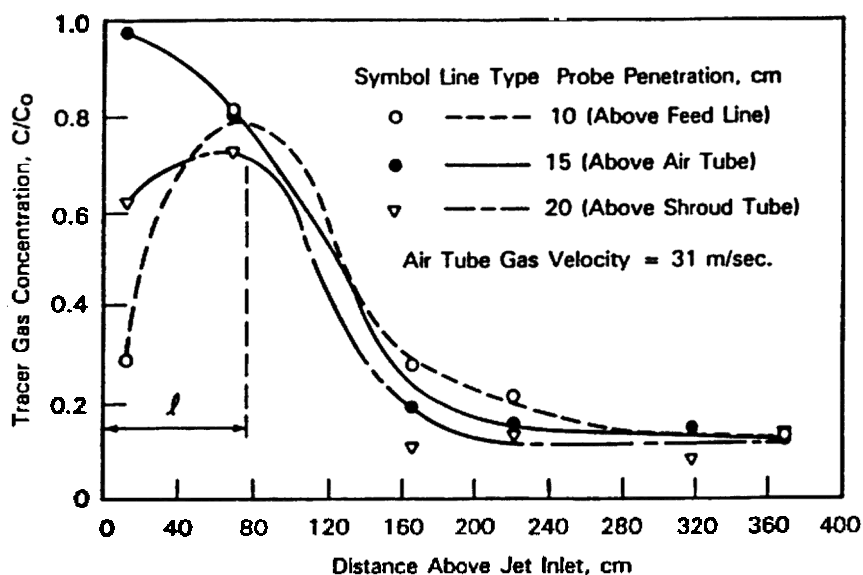


Figure 35. Typical axial tracer concentration profiles—tracer gas injected via air tube at air tube gas velocity of 31 m/s.

The dividing streamline, which prevents the gas mixing between the jets and the emulsion phase until at higher bed heights shown in Figs. 32 through 34 as the zero contour lines, corresponds roughly to the boundary of downflowing solids close to the wall. The measurement of solids flow patterns with a force probe was discussed in details by Yang et al. (1986) and will be presented in the next section.

Axial tracer concentration profiles measured with a higher air tube gas velocity are shown in Fig. 36. The mixing zone for the three concentric jets is larger due to the higher jet velocity. The effect of feed line solids loading on gas mixing of concentric jets can also be seen in Fig. 37. It clearly indicates that the mixing rate among the concentric jets increases with increasing feed line solid loading. Changes in bed height, however, have little effect on gas mixing.

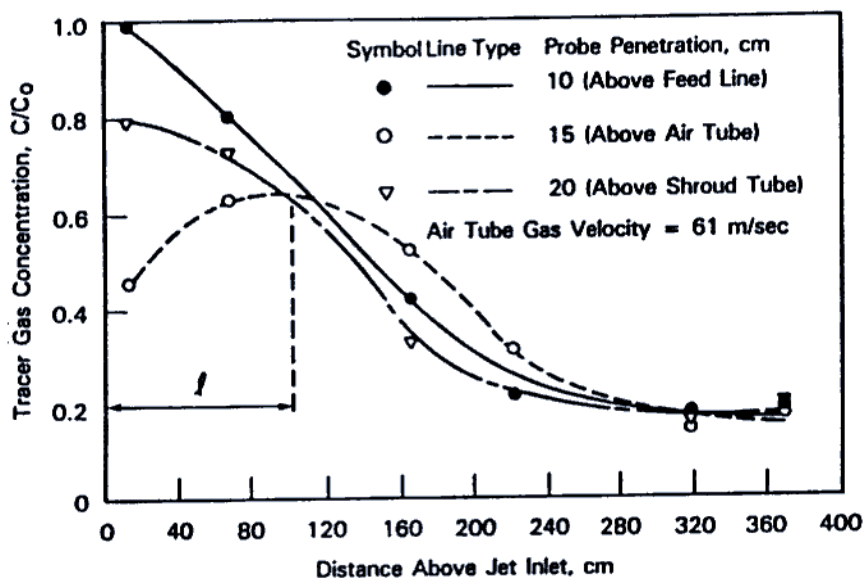


Figure 36. Typical axial tracer concentration profiles—tracer gas injected via air tube at air tube gas velocity of 61 m/s.

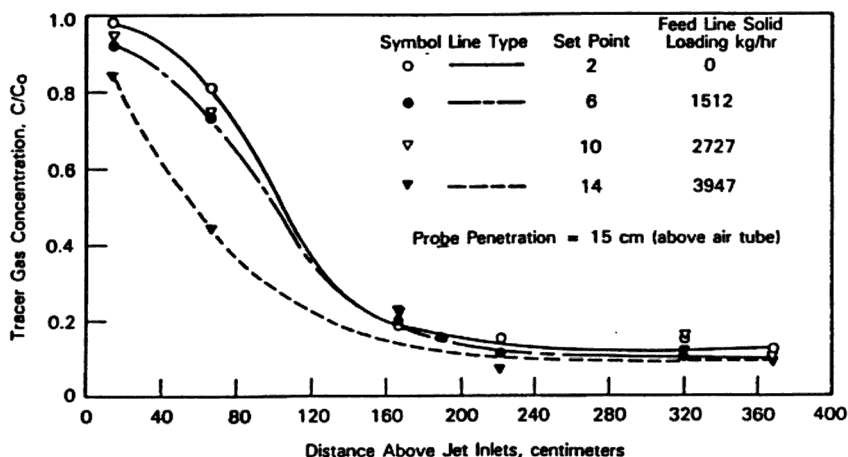


Figure 37. Effect of solids loading on gas mixing among concentric jets—tracer injected via air tube at air tube gas velocity of 31 m/s.

3.3 Solids Circulation in Jetting Fluidized Beds

The solids circulation pattern and solids circulation rate are important hydrodynamic characteristics of an operating jetting fluidized bed. They dictate directly the solids mixing and the heat and mass transfer between different regions of the bed.

In many applications, the performance of fluidized beds is frequently controlled by the hydrodynamics phenomena occurring in the beds. Applications such as the fluidized bed combustion and gasification of fossil fuels are the cases in point. In those applications, the rates of fuel devolatilization and fines combustion are of the same order of magnitude as the mixing phenomena in a fluidized bed. The mixing and contacting of the gases and solids very often are the controlling factors in the reactor performance. This is especially true in large commercial fluidized beds where only a limited number of discrete feed points for reactants is allowed due to economic considerations. Unfortunately, solids mixing in a fluidized bed has not been studied extensively, especially in large commercial fluidized beds, because of experimental difficulties.

Solids Circulation Pattern. Yang et al. (1986) have shown that, based on the traversing force probe responses, three separate axial solids flow patterns can be identified. In the central core of the bed, the solid flow direction is all upward, induced primarily by the action of the jets and the rising bubbles. In the outer regions, close to the vessel walls, the solid flow is all downward. A transition zone, in which the solids move alternately upward and downward, depending on the approach and departure of the large bubbles, was detected in between these two regions.

Solids mixing and circulation rate were studied in a fluidized bed, 3 m diameter and 10 m in height, by pulse injection of tracer particles with characteristics similar to those inside the bed but with sizes larger than those in the bed. By taking solids samples continuously at different bed locations and analyzing by sieving, the rate of particle mixing and circulation can be calculated. Experiments were conducted in two separate bed configurations. One employed a 0.25 m jet nozzle assembly, a deep-bed configuration with a bed height of 5.5 m; a 0.41 m jet nozzle assembly was used in the second configuration. Crushed acrylic particles, -6 mesh and 1,400 μm in weight-mean average size and 1,100 kg/m^3 in density, were used as the bed material.

The bed was first operated at the preselected conditions at a steady state; then about 455 kg of the coarse crushed-acrylic particles, similar to that used as the bed material but of sizes larger than 6-mesh, were injected into the bed as fast as possible to serve as the tracer particles. Solids samples were then continuously collected from five different sampling locations at 30-second intervals for the first 18 minutes and at 60-second intervals thereafter. The samples were then sieved and analyzed for coarse tracer particle concentration. Typical tracer particle concentration profiles vs. time at each sampling location are presented in Figs. 38–42 for set point 3.

Typically it took about 160 to 200 seconds to inject a pulse of about 455 kg coarse tracer particles into the bed pneumatically from the coaxial solid feed tube. It can be clearly seen from Figs. 38 to 42 that the tracer particle concentration increases from essentially zero to a final equilibrium value, depending on the location of the sampling port. The steady state was usually reached within about 5 minutes. There is considerable scatter in the data in some cases. This is to be expected because the tracer concentration to be detected is small, on the order of 4%, and absolute uniformity of mixing inside a heterogeneous fluidized bed is difficult to obtain.

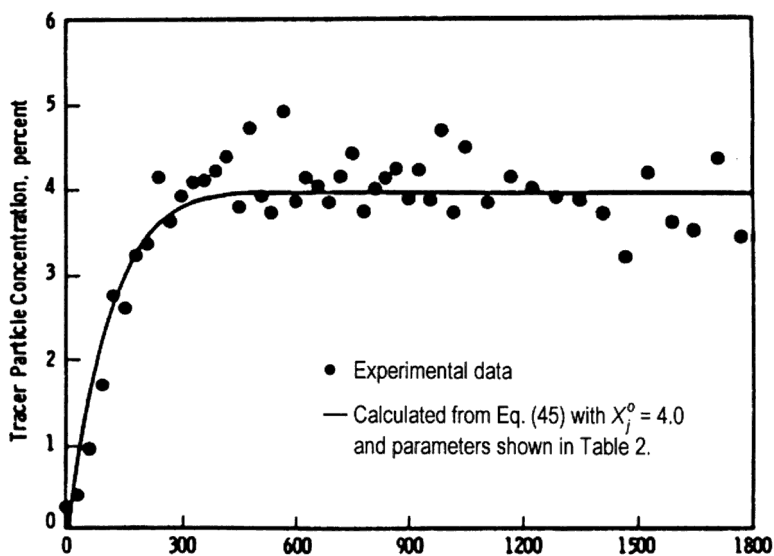


Figure 38. Experimental solids mixing data and model predictions—0.254 m jet, Set Point 3, Sampling Port A.

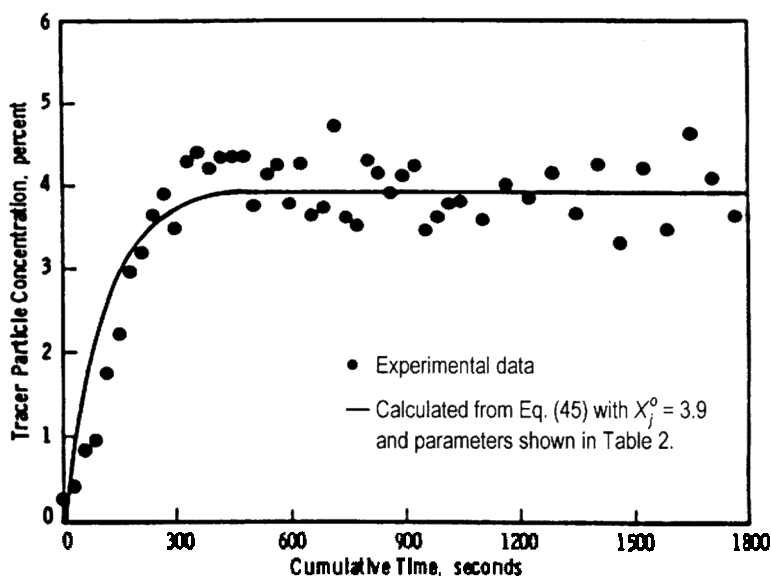


Figure 39. Experimental solids mixing data and model predictions—0.254 m jet, Set Point 3, Sampling Port B.

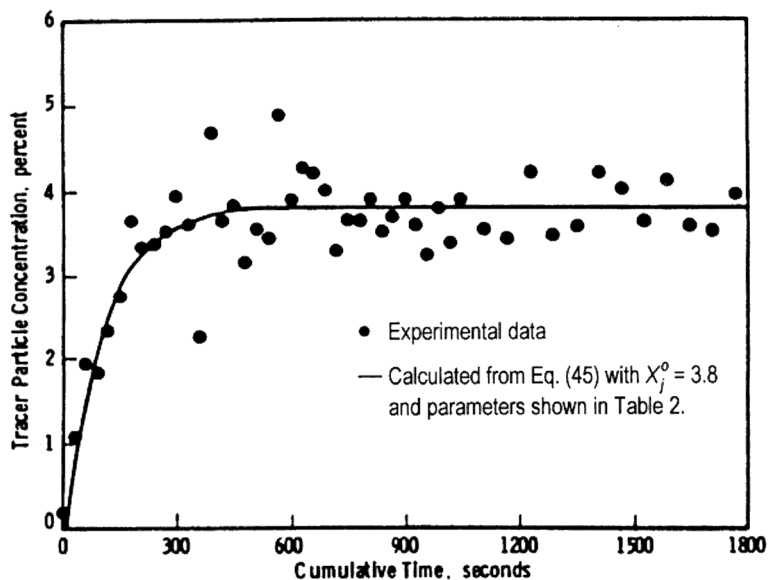


Figure 40. Experimental solids mixing data and model predictions—0.254 m jet, Set Point 3, Sampling Port C.

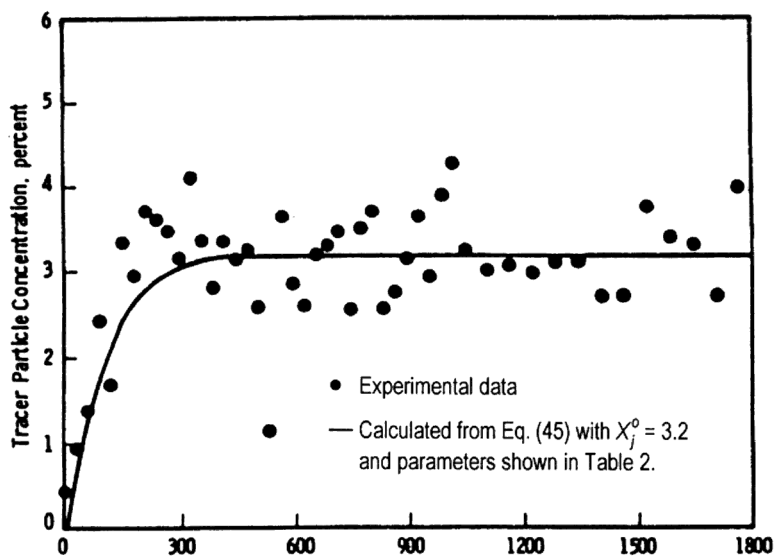


Figure 41. Experimental solids mixing data and model predictions—0.254 m jet, Set Point 3, Sampling Port D.

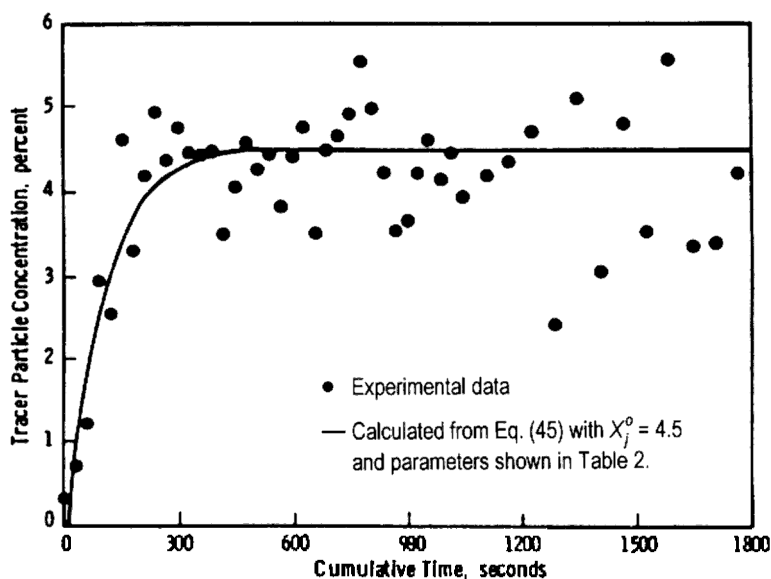


Figure 42. Experimental solids mixing data and model predictions—0.254 m jet, Set Point 3, Sampling Port E.

The solids circulation patterns were investigated with a force probe developed in-house. Typical force probe responses are presented in Figs. 43 and 44 for a probe located at 0.13 m from the jet nozzle and with different penetrations into the bed for an air tube velocity of 45.7 m/s. Since the force probe is directional, the upward solids movement will produce a positive response from the probe and vice versa, the magnitude of the response being an indication of the magnitude of solids circulation rate. The number of major peaks per unit time is closely related to the actual bubble frequency in the bed.

The force probe data allow the identification of three major solids flow regions in the 3-m model, as shown in Fig. 45. At the central portion of the bed, the solids flow is induced upward primarily by jetting action at the lower bed height and by large bubbles at the higher bed height. At the outer region next to the vessel wall, the solids flow is all downward. The region has a thickness of approximately 0.25 m. Between these two regions the solids flow is alternatively upward and downward, depending on the approach and departure of large bubbles. No stagnant region was evident

anywhere in the bed. Figure 45 was constructed on the basis of the force probe signal. At the central portion of the bed where the solids flow was upward, the probe gave a positive signal while the signal in the outer region was all negative because the solids flow was predominantly downward. The radial position where the first negative signal was observed was taken as the boundary between the central region and the intermediate region. The probe penetration where the probe signal became all negative was taken as the transition between the intermediate region and the outer region.

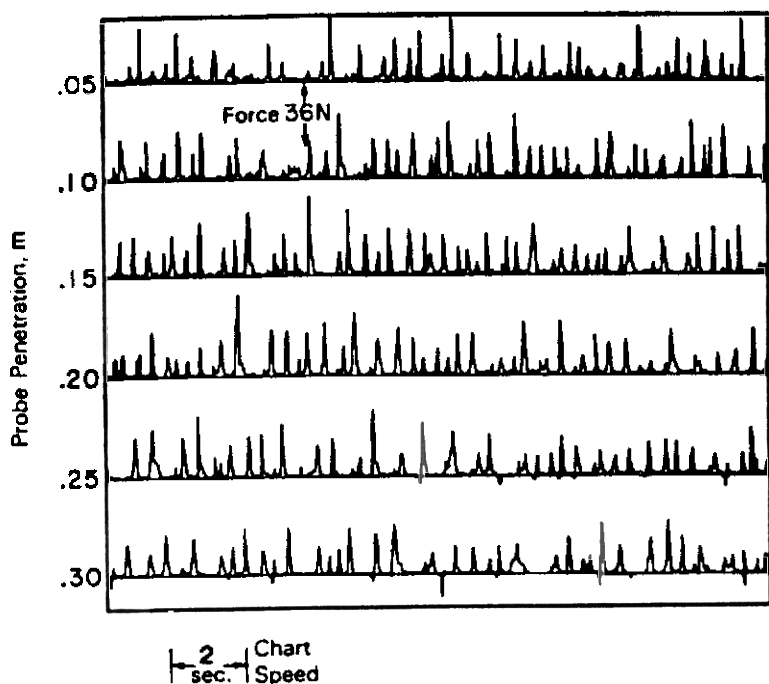


Figure 43. Force probe responses for probe penetration from 0.05 m to 0.30 m—0.13 m from jet nozzle elevation, 46 m/s jet velocity, no solid feed.

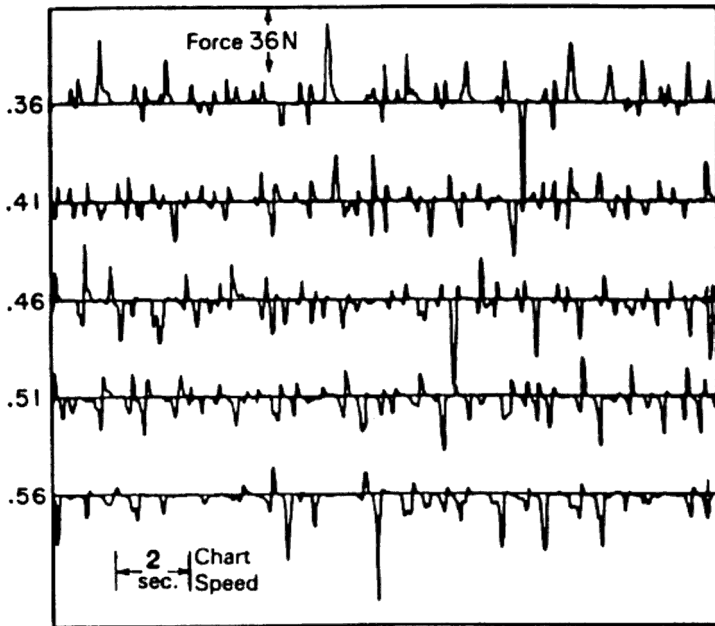


Figure 44. Force probe responses for probe penetration from 0.36 m to 0.56 m—0.13 m from jet nozzle elevation, 46 m/s jet velocity, no solid feed.

In addition to the three solids circulation regions readily identifiable, the approximate jet penetration depth and bubble size can also be obtained from Fig. 45. The jetting region can be taken to be the maximum average value of jet penetration depth. From the jet boundary at the end of the jetting region, an initial bubble diameter can be estimated. This value can be taken to be the minimum value of the initial bubble diameter. The diameter of a fully developed bubble can be obtained from the bubble boundary in the developed-bubble region, as shown in Fig. 45. The central region is thus divided further into three separate regions axially: the jetting region, the bubble-developing region, and the developed-bubble region. Bubbles were observed to coalesce in the bubble-developing region during analysis of the motion pictures taken through the transparent front plate.

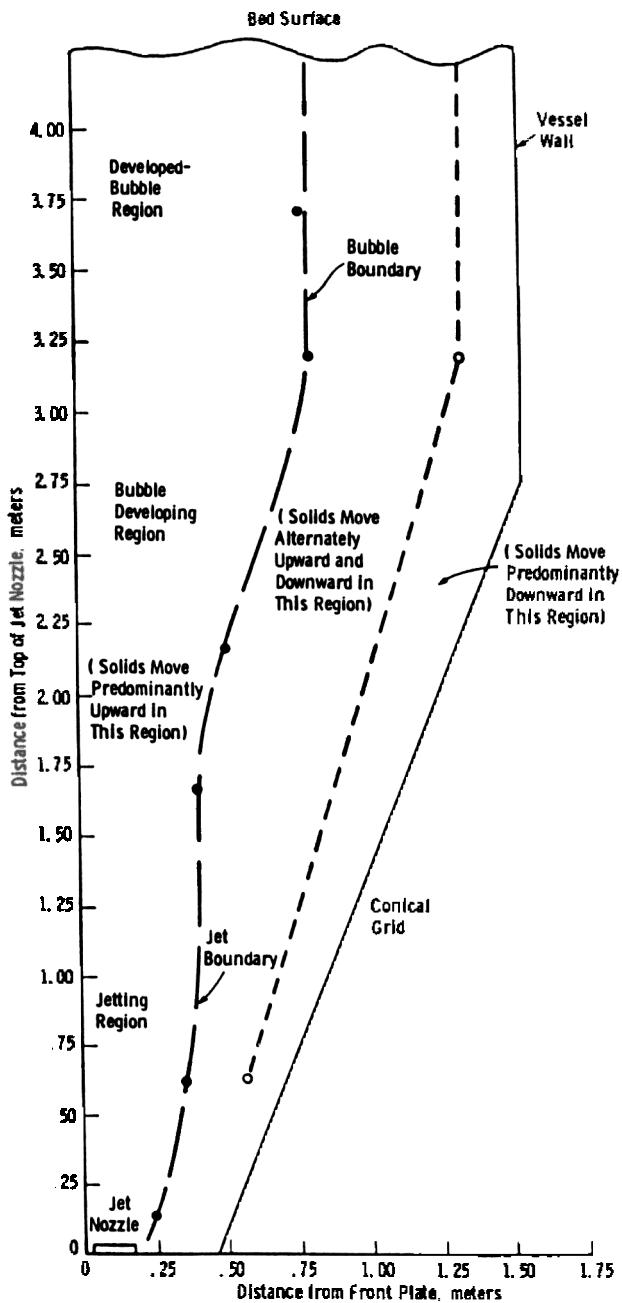


Figure 45. Three major solids flow regions in 3-m model derived from force probe signal.

Solids Circulation Rate. The results of the force probe measurement indicate that the solid circulation rates increase with increasing jet flow rates. A simple mechanistic model was developed to correlate the solids circulation data. The model assumes that the solids circulation inside the bed is induced primarily by the bubble motion. The solids circulation pattern inside the bed can be divided into two major regions radially. In the center of the bed, the particle movement is predominantly upward and the movement is induced by the bubbles disengaged from the central jet. This region has a radius similar to the radius of the average bubble size. In the outer region, the particles move primarily downward. In the meantime, the particles in both regions exchange with each other across the neighboring boundary at a constant rate of W_z g/cm²-s. This mechanistic model is shown schematically in Fig. 46. Material balance in a differential element dz as shown in Fig. 46 gives:

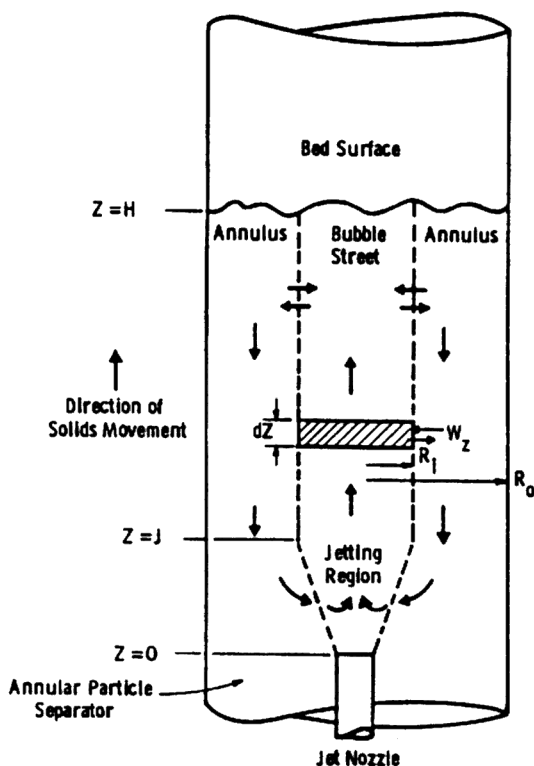


Figure 46. Mechanistic model for solids mixing.

304 Fluidization, Solids Handling, and Processing

In the bubble street region

$$\text{Eq. (37)} \quad K \frac{\mathcal{I}X_J'}{\mathcal{I}z} + \mathbf{p} R_i^2 (1 - \mathbf{e}_{mf}) \mathbf{r}_s \frac{\mathcal{I}X_J'}{\mathcal{I}t} + 2\mathbf{p} R_i W_z (X_J' - X_J) = 0$$

In the annular region

$$\text{Eq. (38)} \quad K \frac{\mathcal{I}X_J}{\mathcal{I}z} + \mathbf{p} (R_o^2 - R_i^2) (1 - \mathbf{e}_{mf}) \mathbf{r}_s \frac{\mathcal{I}X_J}{\mathcal{I}t} + 2\mathbf{p} R_i W_z (X_J - X_J') = 0$$

where

$$\text{Eq. (39)} \quad K = n V_B f_w (1 - \mathbf{e}_w) \mathbf{r}_s$$

The data do not show any clear dependence on the axial position, z . The axial dependence is thus assumed to be negligible. Equations (37) and (38) are reduced from partial differential equations to ordinary differential equations. If we consider only the annular region, Eq. (38) reduces to

$$\text{Eq. (40)} \quad \frac{dX_J}{dt} + \frac{2\mathbf{p} R_i W_z}{\mathbf{p} (R_o^2 - R_i^2) (1 - \mathbf{e}_{mf}) \mathbf{r}_s} (X_J - X_J') = 0$$

Since both X_J and X_J' are independent of z , the relationship between X_J and X_J' can be approximated by material balance of the coarse particles injected into the bed to serve as the tracer.

Solving for X_J' , we have

$$\text{Eq. (41)} \quad X_J' = \frac{W_t}{\mathbf{p} R_i^2 H (1 - \mathbf{e}_{mf}) \mathbf{r}_s} - \left[\left(\frac{R_o}{R_i} \right)^2 - 1 \right] \left(\frac{1 - \mathbf{e}_{mf}}{1 - \mathbf{e}_i} \right) X_J$$

Substituting Eq. (41) into Eq. (40), and after some mathematical manipulating, we get

$$\text{Eq. (42)} \quad \frac{dX_J}{dt} + P X_J - Q = 0$$

where

$$\text{Eq. (43)} \quad P = \frac{2R_i W_z}{(R_o^2 - R_i^2)(1 - \mathbf{e}_{mf})\mathbf{r}_s} + \frac{2W_z}{R_i(1 - \mathbf{e}_i)\mathbf{r}_s}$$

$$\text{Eq. (44)} \quad Q = \frac{2W_z W_i}{p R_i (R_o^2 - R_i^2) H (1 - \mathbf{e}_{mf}) (1 - \mathbf{e}_i) \mathbf{r}_s^2}$$

Equation (42) can be readily integrated, however, there are two limiting cases to consider.

Case I. Instantaneous Injection of Tracer Particles. If it is assumed that the tracer particles are injected instantaneously, $W_t = W_t^o = \text{a constant}$, Eq. (42) can be integrated with the boundary condition that $X_J = 0$ at $t = t_0$ to give

$$\text{Eq. (45)} \quad \frac{X_J}{X_J^o} = 1 - \exp[-P(t - t_o)]$$

Case II. Uniform Injection of Tracer Particles. Since the large amount of tracer particles usually required more than 75 seconds to inject, the other limiting case would be to assume that the injection rate was uniform over the injection period, or

$$\text{Eq. (46)} \quad W_t = \left(\frac{W_t^o}{t_w} \right) \cdot t$$

Again, Eq. (42) can be integrated with the boundary condition that $X_J = 0$ at $t = 0$ to give

$$\text{Eq. (47)} \quad \frac{X_J}{X_J^o} = \frac{1}{t_w P} \{Pt - [1 - \exp(-Pt)]\}$$

The equilibrium tracer concentration in the bed after complete mixing can be expressed as

$$\text{Eq. (48)} \quad X_J^o = \frac{W_t}{p H r_s [R_i^2(1 - \mathbf{e}_i) + (R_o^2 - R_i^2)(1 - \mathbf{e}_{mf})]}$$

306 *Fluidization, Solids Handling, and Processing*

The voidage inside the bubble street, e_i , can be calculated as follows

$$\text{Eq. (49)} \quad e_i = e_{mf} + f_B(1 - e_{mf}) = e_{mf} + \frac{nV_B}{pR_i^2U_A}(1 - e_{mf})$$

where f_B is the volumetric fraction of bubbles occupying the bubble street region at any instant; it can be evaluated from the following equation

$$\text{Eq. (50)} \quad f_B = \frac{nV_B}{pR_i^2U_A}$$

If the bubble frequency, bubble diameter, and bubble velocity are known, the solids mixing rate can be calculated.

The mechanistic model developed in the last section is applied to the data collected experimentally. Bubble diameter and bubble velocity calculations were based on the empirical equations obtained from frame-by-frame analysis of high-speed motion pictures taken under the respective operating conditions (Yang et al., 1984c). The equations used are:

For 0.254 m jet nozzle assembly

$$\text{Eq. (51)} \quad \text{Bubble diameter} \quad D_B = 12.36 \cdot G^{0.155}$$

$$\text{Eq. (52)} \quad \text{Bubble velocity} \quad U_A = 0.711\sqrt{gD_B}$$

For 0.406 m jet nozzle assembly

$$\text{Eq. (53)} \quad \text{Bubble diameter} \quad D_B = 0.0195 \cdot G^{0.620}$$

$$\text{Eq. (54)} \quad \text{Bubble velocity} \quad U_A = 0.35\sqrt{gD}$$

In correlating the data, the solid exchange rate between the two regions, W_z , was assumed to be constant. The tracer concentration data were analyzed statistically and the solids circulation rates are reported in Table 2. The positive fluxes indicate that the net solids flow is from bubble

street to annular region. The net exchange fluxes do not seem to depend on the jet velocity and the bed configuration. The solids circulation rate depends on the jet velocity, however, because higher jet velocities generate larger bubbles. The circumferential area surrounding the bubble street will then be larger and thus the solids circulation rate will be larger. The solids circulation rates derived on the basis of this model range from 47,500 to 73,400 kg/h, as shown in Table 2.

Comparison of the calculated and the experimentally observed tracer concentration profiles is good as shown in Figs. 38 through 42 for set points 3 employing the 0.254 m jet nozzle assembly.

The solids mixing study by injection of tracer particles indicated that the axial mixing of solids in the bubble street is apparently very fast. Radial mixing flux depends primarily on the bubble size, bubble velocity, and bubble frequency, which in turn depend on the size of the jet nozzle employed and the operating jet velocity.

Table 2. Statistical Analysis of Solids Mixing Data

Test No.	t_0 s	W_{z_2} kg/m ² s	$2R_i W_z (H - J)$ kg/s
0.254 m Jet Nozzle Assembly			
Set Pt. 1	8.3	1.0	13.2
Set Pt. 2	44.5	1.3	16.2
Set Pt. 3	10.2	1.3	17.7
Set Pt. 4	- 10.2	1.0	13.4
0.406 m Jet Nozzle Assembly			
Set Pt. 1	- 1.2	1.0	14.7
Set Pt. 2	- 8.6	0.84	20.4

Solid Entrainment Rate into Gas and Gas-Solid Two-Phase Jets.

A mathematical model for solid entrainment into a permanent flamelike jet in a fluidized bed was proposed by Yang and Kearns (1982). The model was supplemented by particle velocity data obtained by following movies frame by frame in a motion analyzer. The experiments were performed at three nominal jet velocities (35, 48, and 63 m/s) and with solid loadings ranging from 0 to 2.75. The particle entrainment velocity into the jet was found to increase with increases in distance from the jet nozzle, to increase with increases in jet velocity, and to decrease with increases in solid loading in the gas-solid, two-phase jet.

It is well known that jets in a fluidized bed induce high solids mixing. In one extreme, jets can be permanent and flamelike, similar to jets in spouted beds. The solids circulation in this case is created by solids entrainment into the jet along the jet height. Studies of solids circulation in spouted beds have been reviewed by Mathur and Epstein (1974). Data on solids entrainment into a permanent flamelike jet immersed in a fluidized bed, however, are meager. In another extreme, jets can be a series of rapidly coalescing bubbles, called *bubbling jets*. Solids mixing in this case is induced essentially by the solids-carrying capacity of the bubble wake and by the bubble frequency.

Another kind of jet encountered in operating fluidized beds are those created by pneumatic transport of solid particles into the fluidized beds. Here we call them *gas-solid, two-phase jets* because the incoming jet streams have already entrained solid particles at different loadings. The momentum of these solid particles is not negligible, as already shown by Yang and Kearns (1980). With high-speed movies such particles can usually be seen to penetrate right through the roof of coalescing bubbles in the bubbling jet regime.

Regular and high-speed movies were taken of the tracer particle movement around the jets at different velocities and different solid loadings. The tracer particles used are red plastic pellets of similar size and density to the bed material. The movies were then analyzed frame by frame using a motion analyzer to record the particle trajectories and the particle velocities.

Typical particle trajectories observed in the movies are shown in Fig. 47 for a jet velocity of 62.5 m/s and a solid loading of 1.52. The time elapsed between dots shown in Fig. 47 was typically 5 movie frames, while the movie speed was 24 frames/s. The colored tracer particles were followed in the vicinity of the jet until they disappeared into the jet, as

indicated by an arrow into the jet in Fig. 47. Sometimes the tracer particles disappeared into the bed before they reached the jet. In those cases, no arrow is shown in Fig. 47. If the points where the particles disappeared into the jets were connected, a jet expansion angle could be readily determined. The angle determined from Fig. 47 is approximately 15° . This gives a jet half-angle of 7.5° . Other sets of data also give a comparable jet half-angle.

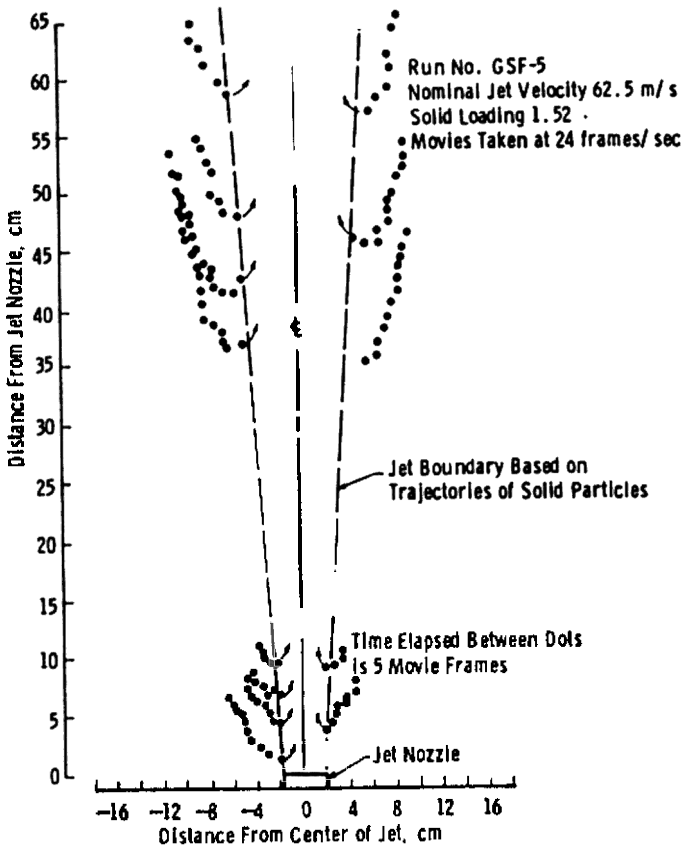


Figure 47. Particle trajectories around a jet in a fluidized bed.

The average particle velocity in each trajectory was determined by dividing the distance traveled by the particle with the total time elapsed. The particle velocity into the jet increased with the distance from the jet nozzle, decreased with increases in solid loading, and increased with increases in jet velocity. High-speed movies indicated that the entrained particles tended to bounce back to the jet boundary more readily under high solid loading conditions. This may explain why the entrainment rate decreases with increases in solid loading in a two-phase jet. A ready analogy is the relative difficulty in merging into a rush-hour traffic as compared to merging into a light traffic. The dependence of particle velocity on the distance from the jet nozzle is presented in Fig. 48 for a jet velocity of 62.5 m/s and a solid loading of 1.52. The regression analysis of this dependence at different operating conditions is summarized in Table 3.

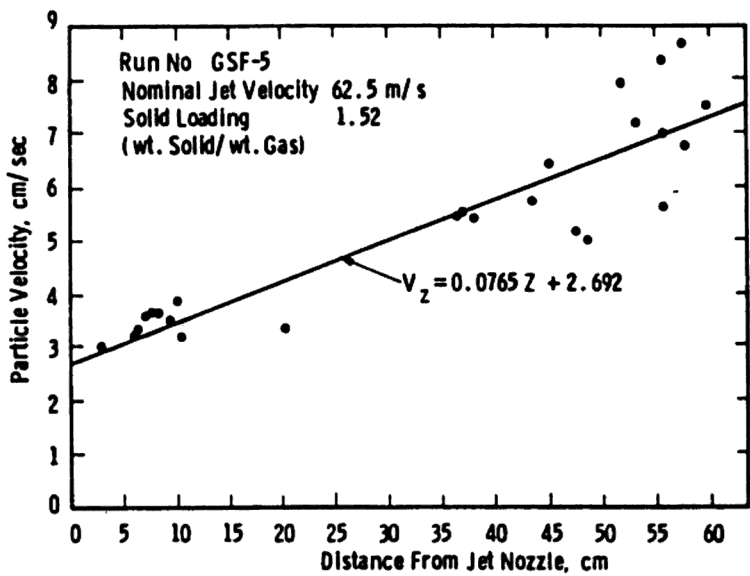


Figure 48. Experimental solid velocity into the jet.

Table 3. Summary of Experimental Solids Velocity into the Jet at Different Operating Conditions

Run No.	Nominal Jet Vel. (m/s)	Solid Loading Wt. Solid/Wt. Gas	Regression Relationship w.r.t. Dist. from Jet Nozzle (V_z = cm/s; Z = cm)	Correlation Coefficient
GSF-1	1.21	0	$V_z = 0.0788 Z + 4.707^*$	0.8158
GSF-3	1.21	0.40	$V_z = 0.0688 Z + 5.265$	0.4433
GSF-4	1.21	0.92	$V_z = 0.0842 Z + 2.979$	0.8959
GSF-5	1.21	1.52	$V_z = 0.0765 Z + 2.692$	0.9085
GSF-22	1.20	0	$V_z = 0.1811 Z + 3.119$	0.8705
GSF-23	1.20	0.51	$V_z = 0.1212 Z + 3.597$	0.8439
GSF-24	1.20	1.21	$V_z = 0.1839 Z + 2.228$	0.8953
GSF-25	1.20	1.99	$V_z = 0.1115 Z + 2.000$	0.9593
GSF-44	1.19	0	—	—
GSF-45	1.19	0.71	—	—
GSF-46	1.19	1.67	—	—
GSF-47	1.19	2.75	$V_z = 0.0967 Z + 2.576$	0.8750

* V_z = solid particle velocity, cm/s; Z = distance from jet nozzle, cm

Model for Solids Entrainment into a Permanent Flamelike Jet. A simple model for solids entrainment into a permanent flamelike jet is described here. The jet is assumed to expand at an angle $2\mathbf{q}$ as shown in Fig. 49, where \mathbf{q} is commonly known as the jet half-angle. Although the existence of a jet half-angle for the jet in a fluidized bed is not universally accepted, employment of this concept considerably simplifies the development of the model. The concept may also be applicable to a bubbling jet (Anagbo, 1980). Material balance of solid particles in a differential element inside the jet gives

$$\text{Eq. (55)} \quad W_j + dW_j - W_j = V_{jz} (2\mathbf{pr} \cdot d\mathbf{z})(1 - \mathbf{e}_z) \mathbf{r}_s$$

or

$$\text{Eq. (56)} \quad dW_j = V_{jz} \mathbf{r}_s (1 - \mathbf{e}_z) 2\mathbf{pr} \cdot d\mathbf{z}$$

where W_j = solids circulation rate, V_{jz} = horizontal component of the particle velocity into the jet at z and e_z = voidage of emulsion phase at z .

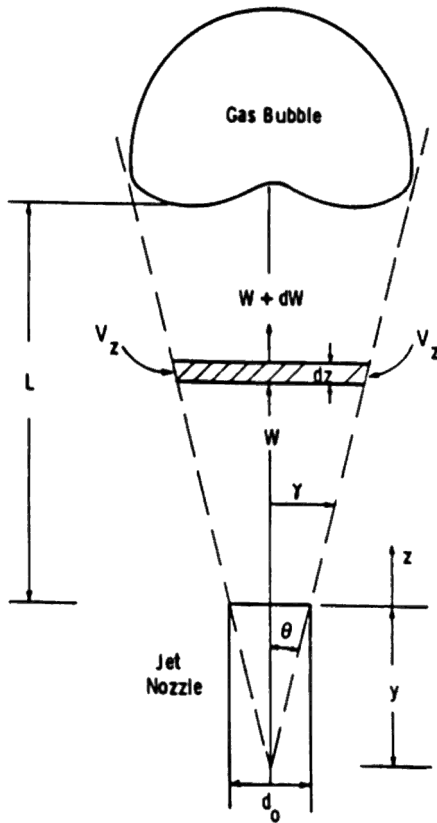


Figure 49. Schematic of jet for solids entrainment model development.

Through geometric consideration, we find that

Eq. (57)
$$r = z \cdot \tan \theta + \frac{d_o}{2}$$

where d_o is the diameter of the jet nozzle.

Substituting Eq. (57) into Eq. (56), we have

$$\text{Eq. (58)} \quad dW_j = 2pr_s(1 - e_z)V_{jz} \left(z \cdot \tan \mathbf{q} + \frac{d_o}{2} \right) dz$$

The overall entrainment rate into the jet or the rate of solid circulation induced by the jet is then

$$\text{Eq. (59)} \quad W_j = 2pr_s(1 - e_z) \int_0^{L_j} V_{jz} \left(z \cdot \tan \mathbf{q} + \frac{d_o}{2} \right) dz$$

where L_j is the jet penetration depth and e_z is assumed to be independent of jet height. We found experimentally that the particle velocity into the jet, V_{jz} , is linearly dependent on the jet height, as expressed below:

$$\text{Eq. (60)} \quad V_{jz} = C_1 z + C_2$$

where C_1 and C_2 are two empirical constants. Some of those constants at different jetting conditions were reported in Table 3. Substituting Eq. (60) into Eq. (59) and integrating, we have

Eq. (61)

$$W_j = 2pr_s(1 - e_z) \left[\frac{C_1 \tan \mathbf{q}}{3} L_j^3 + \frac{1}{2} \left(\frac{C_1 d_o}{2} + C_2 \tan \mathbf{q} \right) L_j^2 + \frac{C_2 d_o}{2} L_j \right]$$

The correlation for the jet penetration depth, L_j , was developed earlier as shown in Eq. (23).

The solids entrainment rate into a jet in a fluidized bed can be calculated from Eqs. (61) and (23) if the empirical constants C_1 and C_2 and the jet half-angle \mathbf{q} are known. The jet half-angle \mathbf{q} can be taken to be 10° as suggested by Anagbo (1980), a value very close to 7.5° obtained from solid particle trajectories reported here. The real jet half-angle will be larger than 7.5° because of the truncation of the jet by the front plate of the semicircular bed.

The particle velocity can usually be approximated as shown in Eq. (27). When the jet velocity is low or the bed particles are relatively fine or of wide size distribution, the jet tends to be a bubbling jet. A separate model

314 Fluidization, Solids Handling, and Processing

for solids circulation is required. The present model can be used as a first approximation.

The model as formulated in this section cannot be used to predict *a priori* the solids entrainment rate into the jet because of the two empirical constants in Eq. (61). Lefroy and Davidson (1969) have developed a theoretical model based on a particle collision mechanism for entrainment of solid particles into a jet. The resulting equation for particle entrainment velocity is

$$\text{Eq. (62)} \quad \frac{V_e}{V_j} = \frac{p^2 e(1+e)d_p}{16r}$$

assuming the $d_p/2r \ll 1$.

The relationship between V_e and V_{jz} can be expressed as:

$$\text{Eq. (63)} \quad V_{jz} = \frac{(1 - \mathbf{e}_j)}{(1 - \mathbf{e}_z)} \cdot \frac{(\mathbf{e}_j - \mathbf{e}_z)}{(1 - \mathbf{e}_z)} \cdot V_e$$

The first term, $(1 - \mathbf{e}_j)/(1 - \mathbf{e}_z)$, corrects for the voidage difference between that in the jet and that in the emulsion phase. The second term, $(\mathbf{e}_j - \mathbf{e}_z)/(1 - \mathbf{e}_z)$, takes into account the fact that only a fraction of the particles having the entrainment velocity V_e will be entrained, the remainder rebounding back to the jet wall due to collisions with the particles already in the jet. Substituting Eq. (63) into Eq. (62), we have

$$\text{Eq. (64)} \quad V_{jz} \cong \frac{(1 - \mathbf{e}_j)}{(1 - \mathbf{e}_z)} \cdot \frac{(\mathbf{e}_j - \mathbf{e}_z)}{(1 - \mathbf{e}_z)} \cdot \frac{p^2 e(1+e)d_p}{16r} \cdot V_j$$

Equation (64) predicts correctly the increase in solid entrainment into the jet with increases in jet velocity and the decrease with increases in solid loading in a two-phase jet. Since neither the voidage nor the particle velocity inside the jet were measured, direct verification of Eq. (64) was not performed.

The validity of extrapolating the data obtained in a semicircular model to a circular one is also of concern. Not much research was carried out in this area. Preliminary research results by Whiting and Geldart (1980) indicated that, for coarse, spoutable solids similar to the particles

used here (Geldart's Group D powders), semicircular columns could provide information very similar to that from the circular ones.

3.4 Fines Residence Time in Jetting Fluidized Beds

In operating a fluidized bed reactor such as a fluidized bed coal gasifier, fine particles tend to be elutriated from the fluidized bed. The elutriated fines, if not recovered, represent a significant carbon loss and thus a significant loss of reactor efficiency. In actual industrial practice, the fines are recycled back to the fluidized bed for further consumption. The location of the fines reinjection point into the fluidized bed reactor is important in order to maximize the consumption of fines in each pass. Otherwise, the fines will build up in the recycle loop and increase the heat load of the reactor operation. The fines reinjection location is selected to maximize the fines residence time in the bed and to provide an conducive environment for consumption, such as high temperature and an oxidizing atmosphere.

There is an abundance of literature on entrainment and elutriation of solid particles from operating fluidized beds of various sizes (see Wen and Chen, 1982; Colakyan and Levenspiel, 1984, for reviews). However, there are very few studies on fines residence time distribution in the bed and the effect of fines injection location. Geldart (1981) has measured the fines distribution in a bed of coarse particles with a bed-slumping technique and found that fines concentration increased toward the bed surface. Geldart and Pope (1983) also observed considerable interaction between the fines and the coarse particles not only in the bed but also in the freeboard as well. The only study found to be relevant to the subject under discussion here is that by Valenzuela and Glicksman (1983). They measured the residence time of fine iron powder (38–53 μm) in a two-dimensional bed of 700 μm glass beads and obtained a residence time between 5.8 and 6.5 seconds, depending on particle sizes, significantly larger than the gas residence time of 2.3 seconds. They concluded that because of the interaction between the fines and coarse particles in the bed, the fines residence time could be substantially longer than the gas residence time. Fines smaller than 10 μm usually percolate through the bed unhindered while the fines larger than 150 μm in size migrate due to the bulk movement of the coarse bed material.

Yang and Kearins (1987) describes the experiments carried out in a 30-cm diameter laboratory unit to study the fines residence time

316 *Fluidization, Solids Handling, and Processing*

distribution in the bed by injecting -170 +230 mesh crushed acrylic fine particles (average particle size = 75 μm) into the bed at two different locations, with two different bed heights, and at three different bed operating conditions. The experimental results were corrected for the transitory time required from the bed surface to the particle collecting device by solving twenty-five simultaneous equations to arrive at the true fines residence time distribution in the bed. Experiments were carried out with fines injection both radially and coaxially. In the radial injection, the fines were injected into the jetting fluidized bed below the bed surface. In the coaxial injection, fines were injected through the central jet.

Some conclusions drawn from the experimental results are:

- (i) The fines residence time in a jetting fluidized bed is of the order of 10 to 20 seconds. The transitory time of fines from the bed surface to the collecting device, the *cyclone dipleg*, dominates the characteristic particle collection time curves experimentally observed.
- (ii) The initial collection of fines increases with increasing jet velocity and overall fluidizing gas velocity. This is true for both radial and coaxial injection of fines. However, the effect of jet velocity affects the coaxial fines injection more pronouncedly.
- (iii) The rates of fines collection was the highest for the case where the fines were injected coaxially through the central jet. When the fines are injected radially into the bed, the rate of fines collection is higher for the experiments with lower bed height compared with that of higher bed height. Apparently, the elutriation mechanisms of fines are different and depend on the location of the fines injection. Substantial increase in fines collection rate for coaxial injection of fines is not surprising. The fines injected coaxially tend to concentrate in and around the jet region initially and are carried over by the eruptions of bubbles generated at the tip of the jet or by periodic penetration of the jet through the fluidized bed. The higher initial collection rate of fines for experiments carried out at lower bed height is indicative of a shorter fines residence time in the bed.

- (iv) Experiments performed during this study indicate that fines injected into the freeboard region above the bed stay in the freeboard region substantially longer than the simple transit time would indicate. This is consistent with the observation by Morooka et al. (1980) and Pemberton and Davidson (1984, 1986). Morooka et al. (1980) studied the behavior of FCC particles suspended in the freeboard region of a 12-cm I.D. fluidized bed and observed a flow pattern of internal circulation in the freeboard region. The fines traveled upward in the central region and downward closer to the wall. The holdup of circulating solids in the freeboard region was much larger than the net entrainment rate of solid particles. If this is the case, the design and configuration of the gas outlet in the freeboard region can have an important effect on the fines residence time distribution and holdup above the bed. The importance of the freeboard region for further reaction of fines merits greater emphasis in both experimental and theoretical studies.

3.5 Scale-up Considerations

The development of commercial fluidized bed processors generally requires intermediate stages of testing on physical models simulating commercial equipment. Simulation (or scale-up) criteria derived from fluidized bed momentum-conservation relations may be applied to determine the design and operating conditions for physical models discussed in Ch. 1 on Fluidized Bed Scale-up. Such criteria, while not totally established at this time, have been applied to simulate a pressurized fluidized bed gasifier having a large, vertical central jet for fuel feeding, combustion and gasification (Yang et al., 1995).

Physical models of commercial fluidized bed equipment provide an important source of design information for process development. A physical model of a commercial fluidized bed processor provides a small-scale simulation of the fluid dynamics of a commercial process. While commercial processes will typically operate at conditions making direct observation of bed fluid dynamics difficult (high temperature, high pressure, corrosive

environment), a physical model is designed to allow easy observation (room temperature and pressure, nonreactive atmosphere, transparent vessel).

Cold flow studies have several advantages. Operation at ambient temperature allows construction of the experimental units with transparent plastic material that provides full visibility of the unit during operation. In addition, the experimental unit is much easier to instrument because of operating conditions less severe than those of a hot model. The cold model can also be constructed at a lower cost in a shorter time and requires less manpower to operate. Larger experimental units, closer to commercial size, can thus be constructed at a reasonable cost and within an affordable time frame. If the simulation criteria are known, the results of cold flow model studies can then be combined with the kinetic models and the intrinsic rate equations generated from the bench-scale hot models to construct a realistic mathematical model for scale-up.

The need for physical modeling of fluidized bed processors is dictated by the state-of-the-art of fluidized bed scale-up technology. In general, no rational procedure exists for scaling up a new fluidized bed processor concept that precludes the need for physical modeling. Many empirically developed “rules-of-thumb” for fluidized bed scale-up exist in specific areas of fluidized bed application which are not generally applicable. Existing mathematical modeling approaches are themselves based heavily on empirical descriptions of fluidized bed fluid dynamics. These *bubbling bed* models can be applied only where confidence exists for the empirical bubble flow description built into the model. Fluidized bed processors operate over such a broad range of fluid dynamic regimes that this confidence rarely exists for new concepts.

Yang et al. (1995) described the application of this scale-up approach. Comprehensive testing programs were performed on two relatively large-scale simulation units for a period of several years: a 30-cm diameter (semicircular) Plexiglas cold model and a 3-m diameter (semicircular) Plexiglas cold model, both operated at atmospheric pressure.

The results are highly significant to the development of fluidized bed technology because they represent a case study of a rational fluidized bed development approach, and because the extensive data generated are unique in their equipment dimensions, pushing existing models and correlations to new extremes and offering new insights into large-scale equipment behavior. The understanding of the hydrodynamic phenomena developed from the cold flow model studies and the analytical modeling reported was

integrated with parallel studies that investigated coal gasification kinetics, ash agglomeration, char-ash separation and fines recycle to develop an integrated process design procedure.

3.6 Applications

The primary applications for large-scale jetting fluidized beds are in the area of coal gasification as described by Yang et al. (1995), Kojima et al., (1995), and Tsuji and Uemaki (1994). Smaller scale applications are for fluidized bed coating and granulation to be discussed in Chapter 6.

NOTATIONS

A_d	= cross-sectional area of the downcomer
A_o	= cross-sectional area of outer jet
A_r	= cross-sectional area of the draft tube
B	= buoyancy flux
C	= tracer gas concentration
C_{DS}	= drag coefficient of a single particle
C_m	= maximum tracer gas concentration at the jet axis
d_D	= diameter of draft tube gas supply
d_o	= diameter of jet nozzle
d_p	= mean solid particle diameter
d_s	= diameter of concentric solids feeder
D	= draft tube diameter or fluidized bed diameter
D_B	= bubble diameter
$(D_B)_{max}$	= maximum bubble diameter
D_c	= vessel diameter
e	= coefficient of restitution
F	= total amount of gas leakage during bubble formation from a jet
f_B	= volumetric fraction of bubble in bubble street
f_g	= gas friction factor

320 *Fluidization, Solids Handling, and Processing*

f_p	= solid friction factor
$(Fr)_j$	= two phase Froude number
f_w	= wake fraction of the bubble
g	= gravitational acceleration
G_j	= total gas flow rate in the jet
G_r	= total gas flow rate in the draft tube
H	= bed height of a fluidized bed
H_{mf}	= bed height at minimum fluidization
L	= height of draft tube, or height of downcomer, or distance between the distributor plate and the draft tube inlet
L_j	= jet penetration length
DL	= distance required to accelerate particle
M	= momentum flux
M_g	= mass flow rate of gas in the inner jet
M_o	= mass flow rate of gas in the outer jet
M_s	= mass flow rate of solids in the inner jet
n	= bubble frequency
P_i	= impact pressure
P_o	= local static pressure
DP_{1-2}	= pressure drop between 1 and 2 (see Fig. 1)
DP_{1-4}	= pressure drop between 1 and 4 (see Fig. 1)
DP_{2-3}	= pressure drop between 2 and 3 (see Fig. 1)
DP_{3-4}	= pressure drop between 3 and 4 (see Fig. 1)
r	= radial distance from the jet axis
$r_{1/2}$	= radial distance where gas velocity is one half the maximum gas velocity at the jet axis
$(r_{1/2})_c$	= radial distance where tracer gas concentration is one half the maximum at the jet axis
R_i	= radius of bubble street, $R_i = D_B/2$
R_o	= bed radius

- $(Re)_p$ = Reynolds number based on the slip velocity and defined as $d_p (U_{gr} - U_{pr}) \mathbf{r}_f / \mathbf{m}$
- $(Re)_t$ = Reynolds number based on the terminal velocity of the solid particles, $d_p U_t \mathbf{r}_f / \mathbf{m}$
- S_d = total wall area in the downcomer
- S_r = total wall area in the draft tube
- t = time
- t_o = time zero
- t_w = total time required to inject all tracer particles
- U_A = absolute bubble velocity
- U_B = bubble velocity
- $(U_{cf})_{atm}$ = complete fluidization velocity at atmospheric pressure
- $(U_{cf})_p$ = complete fluidization velocity at pressure P
- U_f = interstitial fluid velocity in the draft tube, U_{fr} / \mathbf{e}_r
- U_{fd} = interstitial fluid velocity in the downcomers, U_{gd} / \mathbf{e}_d
- U_{fr} = superficial fluid velocity in the draft tube
- U_{gd} = superficial gas velocity in the downcomer
- U_{gr} = superficial gas velocity in the draft tube
- U_j = superficial jet nozzle velocity
- U_{jb} = gas velocity at jet boundary
- U_{jm} = maximum gas velocity at the jet axis
- U_{jr} = gas velocity at radial distance r from the jet axis
- U_{mf} = superficial minimum fluidization velocity
- $(U_{mf})_{atm}$ = superficial minimum fluidization velocity at atmospheric pressure
- $(U_{mf})_p$ = superficial minimum fluidization velocity at pressure P
- U_{pd} = solid particle downward velocity in the downcomer
- U_{pr} = solid particle velocity in the draft tube
- U_{sl} = slip velocity between fluid and solid particle in the draft tube
- U_{slug} = rising velocity of the gas slug relative to the particle velocity at its nose
- U_t = terminal velocity of a single solid particle

322 *Fluidization, Solids Handling, and Processing*

V_B	= volume of a gas bubble
V_e	= entrainment velocity as defined in Eq. (62)
V_f	= local fluid velocity
V_j	= mean particle velocity in the jet
V_{jz}	= horizontal component of the solid particle velocity into the jet at z
V_g	= average gas velocity in the inner jet
V_o	= average gas velocity in the outer jet
V_p	= local particle velocity
V_s	= average solids velocity in the inner jet
V_{sr}	= net upward superficial volumetric flow rate of particles in the draft tube
V_z	= axial gas velocity at jet boundary
W_j	= solid circulation rate
W_{sd}	= mass flux of particles in the downcomer, $W_{sd} = V_{sd}\mathbf{r}_s$
W_{sr}	= mass flux of particles in the draft tube, $W_{sr} = V_{sr}\mathbf{r}_s$
W_{to}	= total weight of tracer particles injected
W_t	= cumulative weight of tracer particles injected after time t
W_z	= radial solids mixing flux
X_{jo}	= tracer particle weight fraction in the bed after complete mixing
X_j, X'_j	= tracer particle weight fractions in annulus and in bubble street, respectively
z	= axial coordinate

Greek Letters

e_b	= voidage of a packed bed
e_{bd}	= bubble voidage in the downcomer
e_{br}	= bubble voidage in the draft tube
e_d	= voidage in the downcomer
e_i	= voidage in bubble street
e_j	= voidage inside the jet

e_{mf}	= voidage at minimum fluidization
e_r	= voidage in the draft tube
e_w	= voidage in bubble wake
e_z	= voidage outside of jet in the emulsion phase at z
m	= viscosity of the fluid
r_b	= bed density
r_f	= density of the fluid
r_s	= solid particle density
f	= volumetric solids loading
f_s	= sphericity of the solid particle
q	= jet half angle
t_d	= particle-wall shear stress in the downcomer
t_r	= particle-wall shear stress in the draft tube
a	= angle of conical distributor plate

REFERENCES

- Abramovich, G. N., *The Theory of Turbulent Jets*, The M.I.T. Press, Cambridge, MA, (1963)
- Alappat, B. J., and Rane, V. C., "Studies on the Effects of Various Design and Operational Parameters on Solid Circulation Rate in a Recirculating Fluidized Bed," *Can. J. Chem. Eng.*, 73:248 (1995)
- Anagbo, P. E., "Derivation of Jet Cone Angle from Bubble Theory," *Chem. Eng. Sci.*, 35:1494 (1980)
- Barreto, G. F., Yates, J. G., and Rowe, P. N., "The Measurement of Emulsion Phase Voidage in Gas Fluidized Beds of Fine Powders," *Chem. Eng. Sci.*, 38:345 (1983)
- Blake, T. R., "Gas Jets in Fluidized Media, Turbulent Diffusion Flames, and Condensing Vapor Jets in Liquids," *Powder Technology* (1996)
- Botterill, J. S. M., George, J. S., and Besford, H., "Bubble Chains in Gas Fluidized Beds," *Chem. Eng. Symp. Series*, 62(62):7 (1966)
- Botterill, J. S. M., and Bessant, D. J., "The Flow Properties of Fluidized Solids," *Powder Tech.*, 8:213 (1973)

324 *Fluidization, Solids Handling, and Processing*

- Broadhurst, T. W., and Becker, H. A., "Measurement and Spectral Analysis of Pressure Fluctuations in Slugging Beds," *Fluidization Technology*, Hemisphere Publishing Corporation, New York, 1:63 (1976)
- Buchanan, R. H., and Wilson, B., "The Fluid-Lift Solids Recirculator," *Mech. Chem. Eng. Trans.* (Australia), pp. 117 (1965)
- Claflin, J. K., and Fane, A. G., "Spouting with a Porous Draft-Tube," *Can. J. Chem. Eng.*, 61:356 (1983)
- Chisti, M. Y., *Airlift Bioreactors*, Elsevier, New York, (1989)
- Chisti, M. Y., and Moo-Young, M., "Improve the Performance of Airlift Reactors," *Chem. Eng. Progr.*, pp. 38 (1993)
- Colakyan, M., and Levenspiel, O., "Elutriation from Fluidized Beds," *Powder Technol.*, 38:223 (1984)
- Curran, G. P., Pasek, B., Pell, M., and Gorin, E., "Pretreatment of Bituminous Coals for Pressure Gasification," paper presented at the Fluidized Bed Combustion Symposium, American Chemical Society Meeting, Chicago (1973)
- Davidson, J. F., and Harrison, D., *Fluidized Particles*, Cambridge University Press, England, (1963)
- Decamps, F., Dumont, G., and Goossens, W., "Vertical Pneumatic Conveyor with a Fluidized Bed as Mixing Zone," *Power Tech.*, 5:299 (1971/1972)
- Donsi, G., Massimilla, L., and Colantuoni, L., "The Dispersion of Axisymmetric Gas Jets in Fluidized Beds," *Fluidization*, (J. R. Grace, and J. M. Matsen, eds.), Plenum Press, New York, pp. 297 (1980)
- Ettehadieh, B., Yang, W. C., and Haldipur, G. B., "Motion of Solids, Jetting and Bubbling Dynamics in a Large Jetting Fluidized Bed," *Powder Tech.*, 54:243 (1988)
- Fan, L. S., Hwang, S. J., and Matsuura, A., "Some Remarks on Hydrodynamic Behavior of a Draft Tube Gas-Liquid-Solid Fluidized Bed," *AIChE Symp. Ser.*, 80(234):91 (1984)
- Foong, S. K., Barton, R. K., Ratcliffe, J. S., and Aust, F. I. E., *Mech. Chem. Eng. Trans.* (Australia), 7 (1975)
- Freedman, W., and Davidson, J. F., "Hold-Up and Liquid Circulation in Bubble Columns," *Trans. Instn. Chem. Engrs.*, 47:T251 (1964)
- Fujikawa, M., Kugo, M., and Saiga, K., "A Modification of Fluidizing Beds by Inserting Partition Walls and a Modified Distributor," *Fluidization Technology*, (D. L. Keairns, ed.), Hemisphere Publishing Corporation, Washington, II:41 (1976)
- Geldart, D., "Behavior of Fine Particles in a Fluidized Bed of Coarse Solids," *EPRI Report CS-2094*, Electric Power Research Institute, Palo Alto, CA. (1981)

- Geldart, D., and Pope, D. J., "Interaction of Fine and Coarse Particles in the Freeboard of a Fluidized Bed," *Powder Technol.*, 34:95 (1983)
- Hadzismajlovic, D. E., Povrenovic, D. S., Grbavcic, Z. B., and Vukovic, D. V., "A Spout-Fluid Bed Dryer for Dilute Solutions Containing Solids," *Fluidization VI*, (J. R. Grace, L. W. Shemilt, and M. A. Bergougnou, eds.), Engineering Foundation, New York, pp. 277 (1989)
- Hadzismajlovic, D., Grbavcic, Z., Povrenovic, D. S., Vukovic, D. V., and Garic, R. V., "The Hydrodynamic Behavior of a 0.95 m Diameter Spout-Fluid Bed with a Draft Tube," *Fluidization VII*, (O. E. Potter, and D. J. Nicklin, eds.), Engineering Foundation, New York, pp. 337 (1992)
- Hirsan, K., Sishtla, C., and Knowlton, T. M., "The Effect of Bed and Jet Parameters on Vertical Jet Penetration Length in Gas Fluidized Beds," paper presented at the 73rd Annual AIChE Meeting, Chicago (1980)
- Horsler, A. G., and Thompson, B. H., "Fluidization in the Development of Gas Making Process," *Proc. Tripartite Chem. Engr. Conf.*, pp. 51, Montreal (1968)
- Horsler, A. G., Lacey, J. A., and Thompson, B. H., "High Pressure Fluidized Beds," *Chem. Eng. Progr.*, 65:59 (1969)
- Hsiung, T. P., and Grace, J. R., "Formation of Bubbles at an Orifice in Fluidized Beds," *Fluidization*, (J. F. Davidson, and D. L. Keairns, eds.), Cambridge University Press, Cambridge, U. K., pp. 19 (1978)
- Ishida, M., and Shirai, T., "Circulation of Solid Particles within the Fluidized Bed with a Draft Tube," *J. Chem. Eng. (Japan)*, 8:477 (1975)
- Judd, M. R., Masson, H., and Meihack, W., "Solid Circulation and Gasification Experiments in a Fluidized Bed with a Draft Tube," *Fluidization*, (D. Kunii, and R. Toei, eds.), Engineering Foundation, New York, pp. 663 (1984)
- Kato, K., Shiota, Y., and Ito, U., "Screening of Particles by a Packed Fluidized Particle Classifier," in *Fluidization Technology*, (D. L. Keairns, ed.), Hemisphere Publishing Corporation, Washington, II:215. (1976)
- Keairns, D. L., Yang, W. C., Newby, R. A., Hamm, J. R., and Archer, D. H., "Circulating Bed Boiler Concepts for Steam and Power Generation," *Proc. 13th Intersociety Energy Conversion Engineering Conference*, pp. 540 (1978)
- Kececioglu, I., Yang, W. C., and Keairns, D. L., "Fate of Solids Fed Pneumatically through a Jet into a Fluidized Bed," *AIChE J.*, 30:99 (1984)
- Khoe, G. K., and Van Brakel, J., "Drying Characteristics of a Draft Tube Spouted Bed," *Can. J. Chem. Eng.*, 61:411 (1983)
- Knowlton, T. M., and Hirsan, I., "The Effect of Pressure on Jet Penetration in Semi-Cylindrical Gas-Fluidized Beds," *Fluidization*, (J. R. Grace, and J. M. Matsen, eds.), Plenum Press, New York, pp. 315 (1980)

326 *Fluidization, Solids Handling, and Processing*

- Krambrock, W., "Mixing and Homogenizing of Granular Bulk Material in a Pneumatic Mixer Unit," *Powder Technol.*, 15:199 (1976)
- Kroger, D. G., Abdelnour, G., Levy, E. K., and Chen, J. C., "Particle Distribution and Mixing in Centrifugal Fluidized Bed," *Fluidization*, (J. R. Grace, and J. M. Matsen, eds.), Plenum Press, New York, pp. 349 (1980)
- Kojima, T., and Kimura, T., "Modeling of Jetting Fluidized Bed Grid Zone for a Local Behavior of Gas and Solids," *Fluidization VII*, (O. E. Potter, and D. J. Nicklin, eds.), Engineering Foundation, New York, pp. 151 (1992)
- Kojima, T., Yoshitake, H., Kimura, T., Matsukata, M., and Uemiya, S., "Contribution of Local Reactions in the Grid Zone to the Performance of a Jetting Fluidized Bed Gasifier of Coal Char," *Energy & Fuels*, 9:379 (1995)
- LaNauze, R. D., and Davidson, J. F., "The Flow of Fluidized Solids," *Fluidization Technology*, (D. L. Keairns, ed.), Hemisphere Publishing Corporation, Washington, II:113 (1976)
- LaNauze, R. D., "A Circulating Fluidized Bed," *Powder Technol.*, 15:117 (1976)
- Lee, W. J., and Kim, S. D., "Hydrodynamics and CWM Combustion Characteristics in an Internally Circulating Fluidized Bed Combustor," *Fluidization VII*, (O. E. Potter, and D. J. Nicklin, eds.), Engineering Foundation, New York, pp. 479 (1992)
- Lefroy, G. A., and Davidson, J. F., "The Mechanics of Spouted Beds," *Trans. Inst. Chem. Engrs.*, 47:T120 (1969)
- Mann, U., and Crosby, "Cycle Time Distribution in Continuous Systems," *Chem. Eng. Sci.*, 28:623 (1973)
- Mann, U., and Crosby, E. J., "Cycle Time Distribution Measurements in Spouted Beds," *Can. J. Chem. Eng.*, 53:579 (1975)
- Mann, U., "Analysis of Spouted-Bed Coating and Granulation. 1. Batch Operation," *Ind. Eng. Chem. Process Des. Dev.*, 22:286 (1983)
- Massimilla, L., "Gas Jets in Fluidized Beds," *Fluidization*, (J. F. Davidson, R. Clift, and D. Harrison, eds.), Academic Press, London, pp. 133 (1985)
- Mathur, K. B., and Epstein, N., *Spouted Bed*, Academic Press, New York (1974)
- Matweecha, D. M., "Blending Apparatus," U.S. Patent 3,648,985 (1972); 3,729,175 (1973)
- McMahon, J. F., "Fluidized Bed Reactor," U.S. Patent 3,825,477 (1972)
- Merchuk, J. C., Ladwa, N., Cameron, A., Bulmer, M., and Pickett, A., "Concentric-Tube Airlift Reactors: Effects of Geometrical Design on Performance," *AIChE J.*, 40:1105 (1994)
- Merry, J. M. D., "Penetration of Vertical Jets into Fluidized Beds," *AIChE J.*, 21:507 (1975)

- Milne, B. J., Berruti, F., and Behie, L. A., "Solids Circulation in an Internally Circulating Fluidized Bed (ICFB) Reactor," *Fluidization VII*, (O. E. Potter, and D. J. Nicklin, eds.), Engineering Foundation, New York, pp. 235 (1992)
- Miyahara, T., Hamaguchi, M., Sukeda, Y., and Takahashi, T., "Size of Bubbles and Liquid Circulation in a Bubble Column with a Draft Tube and Sieve Plate," *Can. J. Chem. Eng.*, 64:718 (1986)
- Morooka, S., Kawazuishi, K., and Kato, Y., "Holdup and Flow Pattern of Solid Particles in Freeboard of Gas-Solid Fluidized Bed with Fine Particles," *Powder Technol.*, 26:75 (1980)
- Nguyen, X. T., and Leung, L. S., "A Note on Bubble Formation at an Orifice in a Fluidized Bed," *Chem. Eng. Sci.*, 27:1748 (1972)
- Oguchi, U., and Kubo, J., "Liquid-Solid Particles or Liquid-Gas-Solid Particle Contacting Method," U.S. Patent 3,754,993 (1973)
- Ohoka, I., and Conway, H. L., "Progress in the Gasification of Heavy Hydrocarbon Oils in a Recirculating Fluidized Bed Hydrogenator," paper presented at the 5th Synthetic Pipeline Gas Symposium, Chicago, (1973)
- Pemberton, S. T., and Davidson, J. F., "Turbulence in the Freeboard of a Gas-Fluidized Bed," *Chem. Eng. Sci.*, 39:829 (1984)
- Pemberton, S. T., and Davidson, J. F., "Elutriation from Fluidized Beds-II. Disengagement of Particles from Gas in the Freeboard," *Chem. Eng. Sci.*, 41:253 (1986)
- Peterson, W. S., "Multiple Spouted Beds," Can. Patent No. 739,660 (1966)
- Punwani, D. V., Modi, M. U., and Tarman, P. B., "A Generalized Correlation for Estimating Choking Velocity in Vertical Solids Transport," *Proc. International Powder and Bulk Solids Handling and Processing Conference*, organized by the Powder Advisory Centre and the IIT Research Institute, Chicago (1976)
- Rajaratnam, N., *Turbulent Jets*, Elsevier, New York (1976)
- Rakow, M. S., and Calderon, M., "The Dynacracking Process—An Update," *Chem. Eng. Prog.*, pp. 31 (1981)
- Rehmat, A., and Goyal, A., "Fluidization Behavior in U-Gas Ash Agglomerating Gasifier," *Fluidization*, (D. Kunii, and R. Toei, eds.), Engineering Foundation, New York, pp. 647 (1984)
- Rios, G. M., Baxerres, J. L., and Gibert, H., "Potential Improvements in the Field of Large Particle Fluidization," *Fluidization*, (J. R. Grace, and J. M. Matsen, eds.), Plenum Press, New York, pp. 529 (1980)
- Roach, P. E., "The Penetration of Jets into Fluidized Beds," *Fluid Dynamics Research*, 11:197 (1993)

328 *Fluidization, Solids Handling, and Processing*

- Rowe, P. N., and Matsuno, R., "Single Bubbles Injected into a Gas Fluidized Bed and Observed by X-rays," *Chem. Eng. Sci.*, 26:923 (1971)
- Rowe, P. N., Macgillivray, J. J., and Cheesman, D. J., "Gas Discharge from an Orifice into a Gas Fluidized Bed," *Trans. Inst. Chem. Engrs.*, 57:195 (1979)
- Siegel, M. H., Merchuk, J. C., and Schugerl, K., "Air-Lift Reactor Analysis: Interrelationships between Riser, Downcomer, and Gas-Liquid Separator Behavior, including Gas Recirculation Effects," *AIChE J.*, 32:1585 (1986)
- Silva, E. M. V., Ferreira, M. C., and Freire, J. T., "Mean Voidage Measurements and Fluid Dynamics Analysis in a Circulating Fluidized Bed with a Spouted Bed Type Solids Feeding System," *Proc. of 2nd European Thermal-Sciences and 14th UIT National Heat Transfer Conference*, Rome (1996)
- Singh, B., "Theory of Slugging Lifters," *Powder Tech.*, 21:81 (1978)
- Sitnai, O., and Whitehead, A. B., "Immersed Tubes and Other Internals," *Fluidization*, (J. F. Davidson, R. Clift, and D. Harrison, eds.), Academic Press, London, pp. 473 (1985)
- Solt, P. E., "Airlift Blending Apparatus," U.S. Patent 3,647,188 (1972)
- Stocker, R. K., Eng, J. H., Svrcek, W. Y., and Behie, L. A., "Gas Residence Time Distribution Studies in a Spouted Bed with a Draft Tube," *Fluidization VI*, (J. R. Grace, L. W. Shemilt, and M. A. Bergougnou, eds.), Engineering Foundation, New York, pp. 269 (1989)
- Taskaev, N. D., and Kozhina, M. E., "Semicoking of Kok-Yangak Coal in a Circulating Bed," *Trudy Akad. Nauk Kirgiz S.S.R.*, 7:109 (1956)
- Tsuji, T., and Uemaki, O., "Coal Gasification in a Jet-Spouted Bed," *Can. J. Chem. Eng.*, 72:504 (1994)
- Turner, J. S., *Buoyancy Effects in Fluids*, Cambridge University Press, Cambridge, England (1973)
- Valenzuela, J. A., and Glicksman, L. R., "Residence Time and Dispersion of Fine Particles in a 2-D Fluidized Bed of Large Particles," *Fluidization*, (D. Kunii, and R. Toei, eds.), Engineering Foundation, New York, pp. 161 (1983)
- Wen, C. Y., and Chen, L. H., "Fluidized Bed Freeboard Phenomena - Entrainment and Elutriation," *AIChE J.*, 28:117 (1982)
- Wen, C. Y., Deole, N. R., and Chen, L. H., "A Study of Jets in a Three-Dimensional Gas Fluidized Bed," *Powder Technol.*, 31:175 (1982)
- Westinghouse Electric Corporation, "Advanced Coal Gasification System for Electric Power Generation," Quarterly Progress Report; NTIS No. FE-1514-61 (1977)
- Whiting, K. J., and Geldart, D., "A Comparison of Cylindrical and Semi-Cylindrical Spouted Beds of Coarse Particles," *Chem. Eng. Sci.*, 35:1499 (1980)

- Wurster, D. E., Lindlof, J. A., and Battista, J. R., "Process for Preparing Agglomerates," U.S. Patent 3,207,824 (1965)
- Wurster, D. E., and Lindlof, J. A., "Particle Coating Apparatus," U.S. Patent 3,241,520 (1966)
- Yang, W. C., and Keairns, D. L., "Recirculating Fluidized Bed Reactor Data Utilizing a Two-dimensional Cold Model," *AIChE Symp. Series*, 70(141):27 (1974)
- Yang, W. C., and Keairns, D. L., "Estimating the Acceleration Pressure Drop and the Particle Acceleration Length in Vertical and Horizontal Pneumatic Transport Lines," *Pneumotransport* 3, pp. D7-89 (1976a)
- Yang, W. C., and Keairns, D. L., "Comparison of Recirculating Fluidized Bed Performance in Two-Dimensional and Three-Dimensional Beds," in *Fluidization Technology*, (D. L. Keairns, ed.), Hemisphere Publishing Corporation, Washington, IL:51. (1976b)
- Yang, W. C., "A Unified Theory on Dilute Phase Pneumatic Transport," *J. Powder Bulk Solids Tech.*, 1:89 (1977)
- Yang, W. C., Margaritis, P. J., and Keairns, D. L., "Simulation and Modeling of Startup and Shutdown in a Pilot-Scale Recirculating Fluidized Bed Coal Devolatilizer," *AIChE Symp. Ser.*, 74(176):87 (1978)
- Yang, W. C., "A Correlation for Solid Friction Factor in Vertical Pneumatic Conveying Lines," *AIChE J.*, 24:548 (1978)
- Yang, W. C., and Keairns, D. L., "Design of Recirculating Fluidized Beds for Commercial Applications," *AIChE Symp. Ser.*, 74(176):218 (1978a)
- Yang, W. C., and Keairns, D. L., "Design and Operating Parameters for a Fluidized Bed Agglomerating Combustor/Gasifier," *Fluidization*, (J. F. Davidson, and D. L. Keairns, eds.), Cambridge University Press, Cambridge, pp. 196 (1978b)
- Yang, W. C., and Keairns, D. L., "Momentum Dissipation of and Gas Entrainment into a Gas-Solid Two-Phase Jet in a Fluidized Bed," *Fluidization*, (J. R. Grace, and J. M. Matsen, eds.), Plenum Press, New York, pp. 305 (1980)
- Yang, W. C., "Jet Penetration in a Pressurized Fluidized Bed," *I&EC Fundamentals*, 20:297 (1981)
- Yang, W. C., and Keairns, D. L., "Solid Entrainment Rate into Gas and Gas-Solid, Two-Phase Jets in a Fluidized Bed," *Powder Technol.*, 33:89 (1982)
- Yang, W. C., "Criteria for Choking in Vertical Pneumatic Conveying Lines," *Powder Tech.*, 35:143 (1983)
- Yang, W. C., and Keairns, D. L., "Studies on the Solid Circulation Rate and Gas Bypassing in Spouted Fluid-Bed with a Draft Tube," *Can. J. Chem. Eng.*, 61:349 (1983)

330 *Fluidization, Solids Handling, and Processing*

- Yang, W. C., Keairns, D. L., and McLain, D. K., "Gas Mixing in a Jetting Fluidized Bed," *AIChE Symp. Series*, 80(234):32 (1984a)
- Yang, W. C., Revay, D., Anderson, R. G. Chelen, E. J., Keairns, D. L., and Cicero, D. C., "Fluidization Phenomena in a Large-Scale Cold-Flow Model," *Fluidization*, (D. Kunii, and R. Toei, eds.), Engineering Foundation, New York, p.77 (1984b)
- Yang, W. C., Ettehadieh, E., Anestis, T. C., Gizzie, R. E., and Haldipur, G. B., "Cold Flow Scaleup Facility Experimental Results and Comparison of Performance at Different Bed Configurations," KRW Energy Systems Inc. for U.S. Department of Energy, Contract No. DE-AC21-82MC19122; NTIS No. FE-19122-46 (1984c)
- Yang, W. C., Ettehadieh, B., and Haldipur, G. B., "Solids Circulation Pattern and Particles Mixing in a Large Jetting Fluidized Bed," *AIChE J.*, 32:1994 (1986)
- Yang, W. C., and Keairns, D. L., "A Study of Fine Particles Residence Time in a Jetting Fluidized Bed," *Powder Technol.*, 53:169 (1987)
- Yang, W. C., Ettehadieh, B., Anestis, T. C., Kettering, R. E., Haldipur, G. B., and Holmgren, J. D., "Gas Mixing in a Large Jetting Fluidized Bed," *Fluidization '88: Science and Technology*, (M. Kwauk, and D. Kunii, eds.), Science Press, Beijing, China, pp. 1 (1988)
- Yang, W. C., and Keairns, D. L., "Operational Characteristics of a 2-D Bed with Three Draft Tubes," in *Fluidization*, (J. R. Grace, L. W. Shemilt, and M. A. Bergougnou, eds.), Engineering Foundation, New York, pp. 285 (1989)
- Yang, W. C., Newby, R. A., and Keairns, D. L., "Large Scale Fluidized Bed Physical Model: Methodology and Results," *Powder Tech.*, 82:331 (1995)
- Yates, J. G., Rowe, P. N., and Cheesman, D. J., "Gas Entry Effects in Fluidized Bed Reactors," *AIChE J.*, 30:890 (1984)
- Yates, J. G., and Cheesman, D. J., "Dispersion of Gas from Coaxial Nozzles in a Fluidized Bed," in *Fluidization VII*, (O. E. Potter, and D. J. Nicklin, eds.), Engineering Foundation, New York, pp. 185 (1992)
- Yoon, S. M., and Kunii, D., "Gas Flow and Pressure Drop through Moving Beds," *I&EC Process Des. Develop.*, 9:559 (1970)

Fluidized Bed Coating and Granulation

*Richard Turton, Gabriel I. Tardos, and
Bryan J. Ennis*

1.0 INTRODUCTION

Over the last forty or so years, there has been an increasing interest in the use of fluidized beds in processes involving the coating and granulation of particulates. Fluidized beds, both with and without internals, offer many advantages over conventional granulation and coating equipment such as pans, drums and mixers. Fluidized beds, by virtue of the air or gas required to fluidize the solids, typically have high rates of heat and mass transfer leading to uniform temperature distribution within the bed and relatively short processing times. Moreover, the shearing forces exerted in such beds help to control the formation of agglomerates, and the movement of fluidizing gas, including bubbles, causes solids to circulate within the equipment providing a constant flow of bed particles through the spray zone, which is essential for uniform product quality.

The main goal of this chapter is to provide a technical basis or framework for analyzing fluidized bed coating and granulation operations.

When dealing with particle and powder systems, often there are many physical material parameters that are unknown. In analyzing problems in the operation or design of such equipment, it should be understood that these parameters may have to be estimated using known testing procedures or previous operating data. There also exists a large body of literature which focuses on case studies of coating and granulation processes, this literature is not cited with great frequency in this chapter since the purpose here is to generalize theories and experimental findings rather than to catalog them.

The chapter is split into two main sections. The first section (Sec. 2) covers the area of fluidized bed coating. Processes utilizing this technology are referred to as *film coating techniques*. Film coating occurs when a continuous thin film of material, often a polymer, is applied evenly over the surface of the particles comprising the bed. The film is added little by little to the particles through repeated exposure to a liquid spray in the bed. The reasons for coating the particles are varied and include: the controlled release of the active ingredient in the particle e.g., enteric or sustained release; to provide a moisture barrier; to improve the appearance of the product; to mask the taste of the product; and to control the attrition of the product. The approach presented here is to first consider some of the microscopic phenomena such as droplet formation in the atomizing nozzle and evaporation rates of the liquid drops. The modelling of the process is covered next and two approaches are considered. First, the coating process is modeled using a population balance approach then it is considered from a probabilistic or stochastic standpoint, the results from the two approaches are compared. Finally, equipment design, availability and scale-up considerations are discussed.

The second section (Sec. 3) covers the area of granulation of fine particles in fluidized beds. First, microscopic considerations such as the wetting and spreading rates of the liquid binder and the critical binder/powder ratio are considered. Next an overview of the fundamentals of the strength of the pendular liquid bridge which holds two particles together is given. By characterizing the forces holding particles together, estimates of critical parameters affecting the growth of granules can be made. The strength of granules produced from agglomeration processes is then discussed and methods to evaluate granule strength are given. The modeling of the granulation process using a population balance approach is covered next and rate expressions for nucleation, coalescence and breakage are given. Finally, the topic of unwanted agglomeration in fluidization processes is discussed.

It is the hope of the authors that this chapter will be of value to the practicing technologist and also will provide a basis for focused research in the many areas of this field which is still required.

2.0 COATING OF PARTICLES IN FLUIDIZED BEDS

2.1 Introduction

The term *fluidized bed coating* can refer to one of two fundamentally different types of processes. Figure 1 shows a general overview of fluidized bed coating. It can be seen from this figure that the objects to be coated can either be the bed material or solid objects which are immersed into a bed of coating material. The most common application of the second type of coating process is in the treatment of metal objects. For example, consider a fluidized bed comprised of fine polymer particles fluidized by an inert gas at a temperature below the melting point of the polymer. If a piece of hot metal, above the melting point of the polymer, were to be immersed into the fluidized bed, then the polymer would start to melt onto the surface of the metal. By carefully controlling the temperature, the time that the metal is immersed, and the level of fluidization in the bed, it is possible to deposit a smooth, coherent polymer film of a desired thickness onto the metal surface. This type of coating has several advantages, namely that no solvent is required in the coating process and that objects with complicated shapes can be coated easily. The coating of objects other than the particles comprising the fluidized bed, is not covered further in this chapter. Several references are provided (Ranney, 1971, Landrock, 1965 and 1967) on this subject for the reader.

The remainder of this section covers processes in which the particles comprising the fluidized bed are to be coated. The basic principle of fluidized bed particle coating and granulation operations is to inject a fine liquid spray into a bed of fluidized particles. The spray consists of a solute which acts as a coating medium, and a solvent in which the solute is dissolved or slurried. The liquid spray impinges on the fluidized particles and spreads on the surface of the bed solids. As the solvent evaporates, the solute remains on the surface of the particle. In agglomeration processes, the solute is a binder which tends to cause individual particles or groups of particles to stick together. The action of the fluidized bed causes these particle agglomerates to

move around and impinge on the walls of the vessel and on other particle agglomerates. Thus, as described in detail in Sec. 3, there exist two opposing forces on the agglomerates, one due to the binder holding the particles together and the other due to the continual movement and collision of particles causing the breakup of the agglomerates. The growth and ultimate size of the agglomerates produced is thus a function of the magnitude of these opposing forces. In coating operations, the same two basic forces are present. However, the object of coating is to produce individual particles, each with a well controlled, even coating. Clearly, in coating operations, the agglomeration of particles is undesirable, and the equipment and operating variables are tailored to maximize coating uniformity and minimize or eliminate agglomeration.

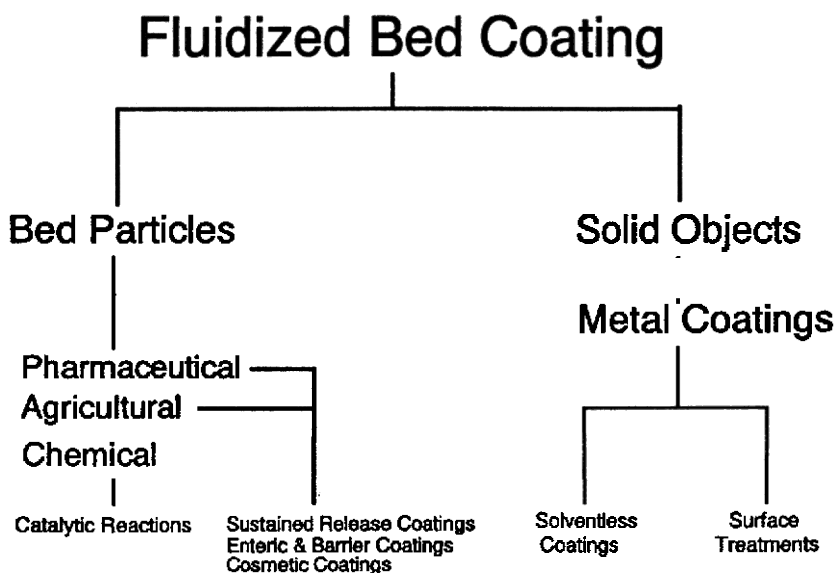


Figure 1. Overview of fluidized bed coating operations.

The use of fluidized beds to coat and agglomerate particles dates back over forty (40) years. Currently, fluidized beds are used to coat a variety of particles in the size range of $50\ \mu\text{m}$ – $1\ \text{cm}$, with a variety of functional and

nonfunctional coatings. In the pharmaceutical industry, particles with enteric and sustained release coatings, moisture barriers, and cosmetic coats are all produced in fluidized beds. In the agricultural industry, fertilizers are produced containing time release insecticides and fungicides, and seeds are coated with protective layers. In the food industry, cereals, nuts, and other food stuffs are coated with sugar coatings. In the petroleum industry, gas oil is sprayed onto the surface of hot catalyst particles in the riser of a fluidized catalytic cracking unit. In the chemical industry, catalyst is sprayed into a fluidized bed in the production of polyolefins. Although, these processes differ greatly in the products they produce, the even distribution of a liquid onto the surface of bed particles and the subsequent formation of a coating layer on the particles is common to all these processes.

2.2 Overview of Coating Process

Particle Movement in Fluid Bed Coaters. As mentioned earlier, coating can be considered to be a subset of the granulation process when the forces causing the breakup of agglomerates dominate and overwhelm the forces tending to hold particles together. With large enough particles at high superficial velocities and low spray rates, it is possible to coat particles in a dense or bubbling fluidized bed without appreciable agglomeration. However, in general, particle coating is carried out most often in some form of spouted or near-spouted bed and the solvent-solute combination should be chosen so that the liquid-to-solid transition is very fast and the resulting coating is not tacky. Two examples of spouted bed coaters are illustrated in Figs. 2(a) and 2(b). Figure 2(a) shows a conventional spouted bed coater. The liquid to be coated is introduced into the bed via a spray nozzle which can be mounted at the bottom (bottom spraying) or top (top spraying) of the bed. The fluidizing gas is fed to the conical bottom of the bed and, under the right conditions, forms a spout or central core in which solids are stripped from the dense annular bed and dragged into the upward moving central gas core. The upward movement of particles in the core, followed by their reversal in the "fountain" region, and downward movement in the dense annular bed, forms a circulation path for the solids. Figure 2(b) shows a fluidized bed with a draft tube or "Wurster Insert," as it is referred to in the pharmaceutical industry. The purpose of the draft tube is to promote the regular circulation of particles within the bed by forcing most of the fluidizing gas up through the center of the bed, thus causing the particles to

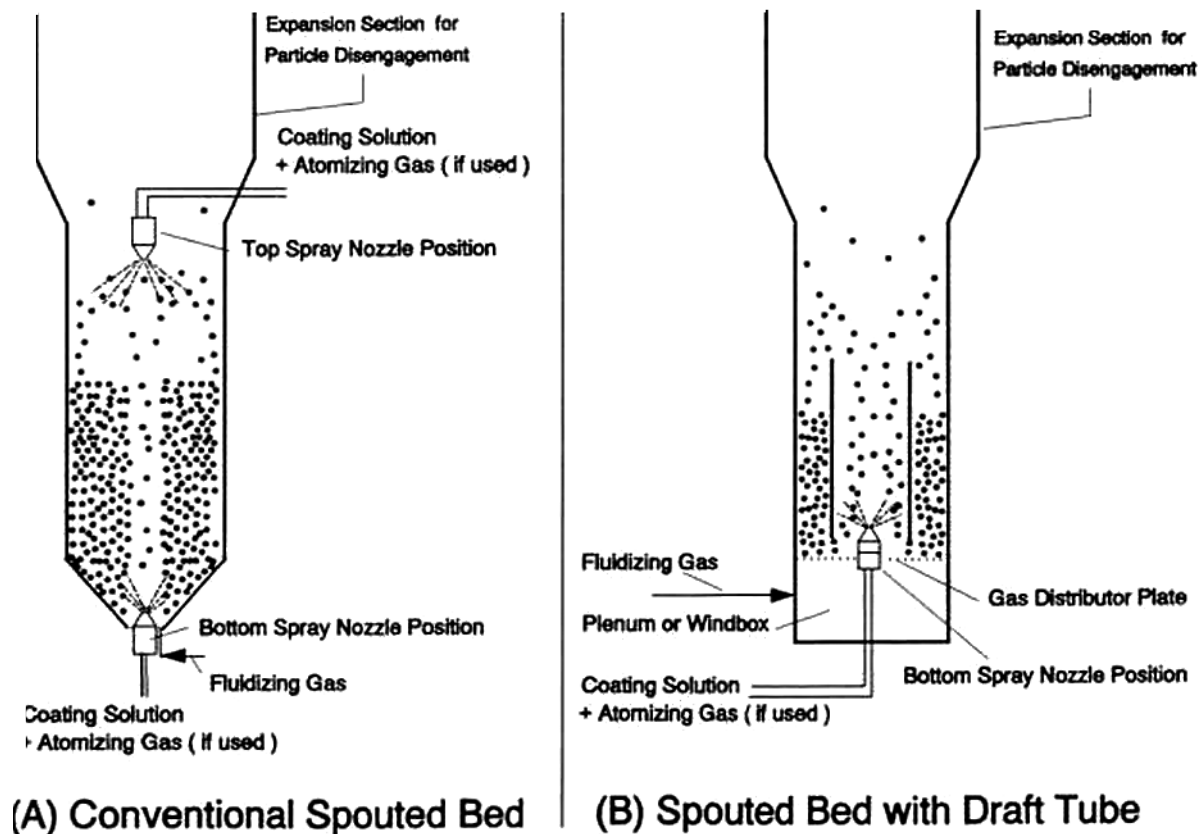


Figure 2. Spouted and fluidized beds used in coating operations.

be entrained upwards with the gas. As the gas reaches the expansion zone above the bed, the gas slows down, and the particles decelerate and fall back into the dense bed in the annular region surrounding the draft tube. The liquid is most often introduced via a nozzle located at the bottom of the bed (bottom spraying). In this type of equipment, top spraying is possible, but rarely used. The movement of solids in beds with draft tubes can be regulated by the height of the gap between the draft tube and gas distributor plate.

The Spray Zone. The movement of particles through the spray zone is illustrated in Fig. 3. From this figure, it can be seen that the liquid spray impinges on the solid bed material as it moves through the spray zone. Upon contact with the surface of the particles, the droplets of liquid will spread over the surface of the particles and will partially coat the solid surface. The repeated motion of the particles through the spray zone allows a continuous coat of material to build up, resulting in a smooth and, hopefully, uniform coat. The wetting of the particle by the liquid drops is essential for uniform coating. If the drops do not wet the surface, but instead bead up, the resulting coat may be a discontinuous layer of tiny spheres of solute rather than the desired continuous film. The use of surfactants or plasticizers may improve the spreading, film forming potential and the wetting of liquid on the surface of the particles. An example of improved wetting using surfactant is given by Weiss and Meisen (1983) who coated urea particles with molten sulfur. Their results indicated the presence of tiny pin holes in the coat of sulfur which were eliminated by the use of surface active agents capable of changing the contact angle between the urea and molten sulfur.

The wicking of liquid into a porous solid is also of importance. Excessive wicking may give rise to a coat of varying thickness. Furthermore, to produce a coat of the desired thickness, additional coating material may be required due to the loss of coating into the particle interior.

It will become evident later on, in Sec. 2.4, that the regular movement of particles through the spray zone is essential if particles are to be coated uniformly. One primary advantage of the spouted bed is that particles circulate within the bed and through the spray zone in a fairly uniform manner, which promotes uniform coating of particles. Another advantage of spouted beds is that the liquid spray is applied to particles which are in a lean or semi-lean phase. Clearly, if particle agglomeration is to be avoided, it makes sense to keep freshly wetted particles separate from each other for as long as possible. By placing the spray nozzle at the bottom of the bed,

particles are sprayed and then travel upwards in the core of the bed in a lean phase condition. During their upward passage, the particles are extensively dried by the flow of fluidizing gas and are relatively solvent free and non-sticky when they return to the dense annular bed. The details of coating equipment and ranges of operation, etc., will be discussed in Sec. 2.5.

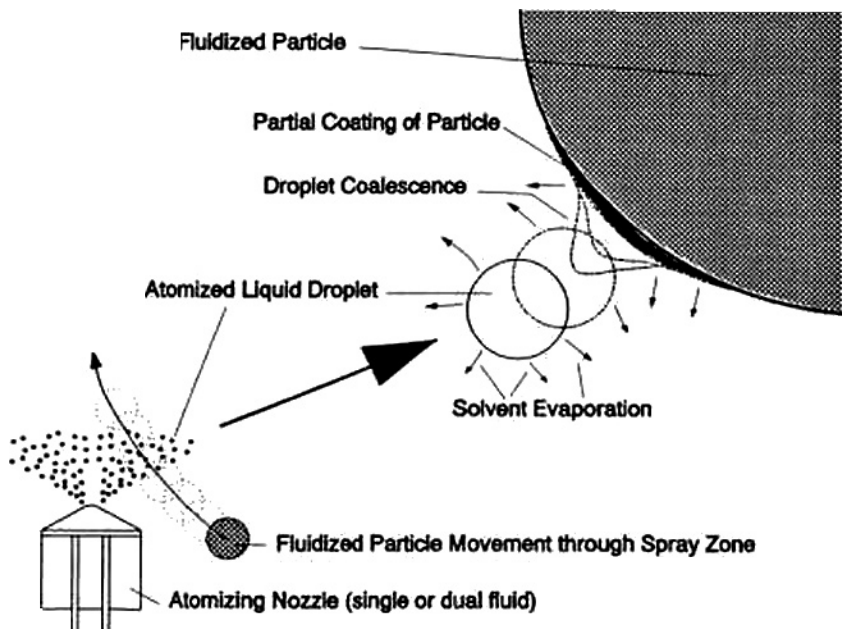


Figure 3. Interaction of particles with liquid spray.

It is worth pointing out that, although the coating process may seem relatively straightforward compared to the complex phenomena at play in the granulation process, many problems are encountered in coating particles. In addition, the quality control for coatings are very tight, especially in the pharmaceutical industry. Unlike in granulation, reprocessing of off-spec product is virtually impossible after coating has occurred. The prospect of dumping a batch of off-spec coated material, containing hundreds of thousands of dollars worth of active ingredient, highlights the importance of understanding and controlling the processes involved in fluidized bed coating.

2.3 Microscopic Phenomena

Atomization in Spray. From Sec. 2.2 above, it is apparent that the formation of a well-dispersed liquid spray is an essential prerequisite for uniform coating. The process of breaking up a liquid into a spray of fine droplets is termed *atomization*. Numerous types of atomizers are currently used, and a comprehensive description of the different nozzles available, their performance, and the atomization process in general is given by Lefebvre (1989). The most common type of atomizing nozzle used in coating operations is the dual-fluid nozzle which uses the kinetic energy of a high pressure gas (usually air or steam) to break up the liquid into a fine spray. The gas can either contact the liquid within the nozzle (internal mix) or outside the nozzle (external mix). The main advantages of dual-fluid nozzles are their good atomization, their ability to atomize high-viscosity liquids, and their resistance to blockage. However, some problems may result when using dual-fluid atomizers with highly volatile liquids due to excessive evaporation of the liquid during the atomization process. Alternatives to the use of dual-fluid nozzles are pressure or hydraulic nozzles. In these devices, the liquid used for coating is fed to the nozzle under pressure and becomes atomized by virtue of its own kinetic (pressure) energy. The hydraulic nozzle is simple to operate but generally produces a spray with a greater mean droplet size as compared to the dual-fluid nozzles. Recently, the use of ultrasonic nozzles in fluidized bed coating operations has been investigated (Olsen, 1989a,b). The liquid is atomized by an ultrasonic transducer and horn located at the tip of the nozzle. The spray produced is very fine but the throughput of such nozzles is low. The main advantage of the ultrasonic nozzle is the ability to produce a fine spray without the use of a secondary fluid, and potential applications include the ability to atomize very volatile liquids without appreciable evaporation in the nozzle.

Size Distribution of Atomized Droplets. The size distribution of droplets in a spray is a complex function of the properties of the liquid, the secondary gas (if used), and the nozzle geometry. The most reliable and often fastest way to determine this information is to experimentally measure the size distribution under the conditions of interest, and most nozzle manufacturers offer this service to their customers.

With the above statement in mind a brief summary of some important trends is given below:

Hydraulic or Pressure (Single Fluid) Spray Nozzles

- (i) Droplet size is dependent on spray rate and supply pressure, and it is difficult to adjust the spray rate independently of the droplet size (Olsen, 1989a,b).
- (ii) As the flow of liquid increases so does mean droplet size.
- (iii) Hydraulic nozzles tend to atomize effectively at liquid flow rates greater than 250 ml/min, Olsen (1989a,b).
- (iv) Typical average droplet size is on the order of 100 μm , Hall (1991).

Dual-Fluid Spray Nozzles

- (i) Flow of liquid and drop size can be controlled independently, (Olsen, 1989a,b).
- (ii) Atomizing air flow rate is not critical (Nienow and Rowe, 1985), but an increase in air pressure decreases mean droplet size.
- (iii) Typical [Air/Liquid] volumetric ratios for coating and granulation are 500–800 at an air supply pressure of 3 bar (Nienow and Rowe, 1985).
- (iv) Liquid flow rates down to 10 ml/min are possible, and droplet diameter increases with increasing liquid flow (Olsen, 1989a,b).
- (v) Typical average droplet size is 20–30 μm (Hall, 1991)

Evaporation of Atomized Droplets. The prediction of the time to totally evaporate a liquid droplet in an atomized spray is very difficult due to the complex thermal and concentration gradients present in the vicinity of the nozzle. Despite this complexity, it will be beneficial to study what happens to a single droplet of liquid when it is surrounded by a quiescent gas stream. This phenomena has been studied extensively because the time to evaporate a liquid drop has important consequences in a number of different applications; e.g., spray drying, fuel injection, and coating.

The time to evaporate a droplet of pure liquid in a stagnant gas stream was given by Marshall (1954) as:

$$\text{Eq. (1)} \quad t_v = \frac{r_l l d_{p,0}^2}{8 k_g \Delta T}$$

where ΔT is the temperature difference between the surface of the drop and the bulk temperature of the gas. The assumption of a stagnant gas stream should hold for the case of atomized droplets, since the relative velocity between the drops and the gas will be very low and is of the magnitude of the terminal velocity of the drops. The problem with Eq. (1) is that the surface temperature of the drop is generally not known. A later analysis by Kanury (1975) solves the heat and material balance equations simultaneously to yield the following equations:

$$\text{Eq. (2)} \quad t_v = \frac{r_l d_{p,0}^2}{8 r_g a_g \ln [B' + 1]}$$

and

$$\text{Eq. (3)} \quad B' \approx \frac{y_{bulk} - y_s}{y_s - y_d} \approx \frac{C_{p,g} (T_{bulk} - T_s)}{l}$$

It is further assumed that the mass fraction of solvent in the vapor phase at the surface of the droplet, y_s , is in equilibrium with the liquid at the drop's surface, thus:

$$\text{Eq. (4)} \quad y_s = \frac{1}{1 + \left[\frac{p_{tot}}{p_l^*} - 1 \right] \frac{MW_g}{MW_l}}$$

The surface temperature of the droplet, T_s , must first be solved using Eqs. (3) and (4), then the value of B' can be determined and substituted into Eq. (2). As an example, these equations were solved for a number of initial droplet sizes, liquids, and gas temperatures. The results are presented in Table 1 for the case of liquid evaporation into dry air ($y_{bulk} = 0$). The results in Table 1, along with the form of Eq. (2), indicate that the time to evaporate

a drop of pure fluid increases with an increase in initial drop size, an increase in latent heat of vaporization, a decrease in gas temperature, and a decrease in the volatility of the liquid. Other liquid and gas physical properties also play a smaller but significant role.

Table 1. Times for Liquid Drops to Completely Evaporate in Stagnant Air

$d_{p,0}$ (μm)	$T_{air}=40^{\circ}\text{C}$	$T_{air}=50^{\circ}\text{C}$	$T_{air}=60^{\circ}\text{C}$	$T_{air}=70^{\circ}\text{C}$	$T_{air}=80^{\circ}\text{C}$
10	0.047 -Water 0.010 -Ethanol 0.004 -Acetone	0.038 -Water 0.009 -Ethanol 0.004 -Acetone	0.031 0.007 0.003	0.026 0.006 0.003	0.022 0.006 0.003
20	0.189 -Water 0.041 -Ethanol 0.017 -Acetone	0.150 0.034 0.015	0.123 0.029 0.013	0.103 0.025 0.012	0.089 0.022 0.011
30	0.425 0.093 0.038	0.338 0.077 0.034	0.276 0.065 0.030	0.233 0.057 0.027	0.200 0.049 0.024
40	0.756 0.166 0.068	0.600 0.137 0.060	0.491 0.116 0.053	0.414 0.100 0.048	0.356 0.088 0.043
50	1.182 0.260 0.107	0.938 0.213 0.093	0.767 0.181 0.083	0.646 0.157 0.075	0.556 0.137 0.068
60	1.702 0.373 0.154	1.351 0.307 0.135	1.105 0.261 0.119	0.930 0.226 0.108	0.800 0.198 0.097
70	2.316 0.509 0.210	1.838 0.418 0.183	1.504 0.355 0.162	1.266 0.307 0.147	1.089 0.269 0.133
80	3.025 0.664 0.274	2.401 0.546 0.239	1.965 0.463 0.212	1.654 0.402 0.192	1.422 0.351 0.173
90	3.828 0.841 0.347	3.039 0.691 0.303	2.486 0.586 0.268	2.093 0.508 0.242	1.800 0.445 0.219
100	4.727 1.038 0.428	3.751 0.854 0.374	3.070 0.724 0.331	2.584 0.627 0.299	2.222 0.549 0.271

Evaporation times in seconds, 1st entry in a cell is for water, 2nd is for ethanol and 3rd is for acetone

Additional Factors Affecting Evaporation Times. For liquid drops containing solids, which lower the normal vapor pressure of the liquid, the net effect of the solids is to increase the time for complete evaporation, Marshall (1954). The presence of solids introduces an additional complication associated with the changing droplet surface temperature during the evaporation process. This gives rise to longer evaporation times.

For a spray of drops, two additional complications arise; namely, that there is now a distribution of drop sizes to consider and also that the heat and mass transfer to a given drop is influenced by the local phenomena occurring in the region of neighboring drops. The net result of this latter effect is that the gas no longer acts as a sink, and the gas, in the vicinity of the spray, is cooled significantly, thus, reducing the evaporation rate of drops in the spray. Local temperature profiles in the vicinity of a spray nozzle immersed in a bubbling fluidized bed were taken by Smith and Nienow (1982) who showed that significant cooling was experienced close to the nozzle.

It is evident from the discussion above that the time for complete evaporation of a drop in a spray depends on many factors in a complicated way and will be longer than that predicted by the single drop expressions given in Eqs. (1) and (2). Nevertheless, data such as that given in Table 1 and Eqs. (1) and (2) gives valuable information on the order of magnitude of the evaporation time and the role of process variables.

Consequences of Having Drops with Short and Long Evaporation Times. Combinations of small drop sizes, high bed temperatures, and volatile solvents give rise to very short evaporation times. This, in turn, gives rise to the possibility of spray drying wherein the liquid drops completely evaporate before they contact the surface of the bed material. For sprays with a large proportion of these drops, the net effect is a loss in coating efficiency, i.e., a reduction in the fraction of the liquid sprayed into the bed which ends up as coating on the solid product. Even if spray drying does not occur, the coat formed when partially evaporated drops contact the particles' surface, may be inhomogeneous due to poor wetting characteristics.

Combinations of large drop sizes, low bed temperatures, and solvents with low volatility give rise to very long evaporation times. If the evaporation time of the drop is greater than the characteristic time for the solids to circulate through the spray zone, then some fraction of the particles will still be wet just before they re-enter the spray zone. This can cause excessive moisture buildup, and local agglomeration may occur. Little work has been done in evaluating the circulation times in large industrial coating equipment.

However, for small scale equipment, Cheng (1993) and Xu (1993) measured the circulation times of a single tagged particle in a 150 mm diameter fluidized bed coater with a draft tube and found that typical circulation times were between 2–10 seconds. Robinson and Waldie (1978) made similar measurements in a 6" diameter conventional spouted bed and found mean circulation times in the range of 3–6 seconds.

Another problem arises when drop sizes are large compared to the size of the particles to be coated. For example, consider the coating of particles 1 mm and 100 μm in diameter with drops of 100 μm in diameter. For the 1 mm particles, the liquid drops would impinge and spread over the surface but for the 100 μm particles, the liquid drops would engulf the particles giving rise to a thick layer of liquid on the surface which favors particle agglomeration. The difficulty of getting a uniform small droplet size is the main reason for the difficulty in coating particles with diameters less than 100 μm . However, recently there have been reports of successful attempts to coat particles down to 50 μm in diameter with the use of supercritical fluid solutions (Tsutsumi et al., 1994). Due to the cohesive nature of very small particles, characterized as group C particles by Geldart (1973), normal fluidization is not possible, and the absolute lower limit for fluidized bed coating is for particles larger than about 30 μm in diameter.

2.4 Modelling

Before discussing modelling, it is perhaps worth focusing on the goals of the coating process and what is meant by the “quality” of a coating. The term *quality* refers to one or several properties of the finished product, e.g., loading of active ingredient, *in vitro* dissolution characteristics, and *in vivo* efficacy, crush strength, appearance and shelf life. The variation of these properties within a batch of product determines the “quality” of the product. These measures of quality and the ability to obtain repeatable product performance between different batches are the goals of any coating process. At a fundamental level, we can characterize the variation in quality to be a function of two things: *coating mass uniformity* and *coating morphology*. Coating mass uniformity refers to the variation in the amount of coating material each product particle receives during a batch coating operation. Coating morphology refers to the variation in a given property for particles containing the same amount of coating material. Thus, mass uniformity is important when an active ingredient is applied in the coating, while both mass

uniformity and morphology are important when, for example, the coating is applied for a sustained release application.

Coating Mass Uniformity and Distribution. Basically, there have been two approaches to model the accumulation of mass (coating material) on the surface of bed particles; (i) the use of population balances and (ii) the probabilistic modelling of the spray-particle interaction. We will look at each of these approaches and see how it may be possible to combine these methods to give a fuller picture of coating performance.

Population Balance Approach to Modeling Coating. The population balance approach to modelling is ideally suited to processes in which the product and starting material have a distinct distribution of particle sizes, e.g., coating a wide size distribution of solids in a fluidized bed. The presentation of the equations describing the population balance for the coating process are taken from Randolph and Larson (1988) and Liu and Litster (1993a) and are given below

$$\text{Eq. (5)} \quad \frac{\partial}{\partial t} [Nf(m)] + \frac{\partial}{\partial m} [GNf(m)] + \sum Q_k n_k = B - D$$

Equation (5) above relates the change of number of particles of a given mass (size) with the net growth rate G , the feeds and product streams into and out of the process (Q_k) and the net birth (B) and death rates (D) of the particles. A more complete formulation of Eq. (5) is given on a volume basis in Eq. (40) in Sec. 3.6, and will be used to describe granulation processes. For coating operations, we consider the situation of a batch process for illustration purposes. The development is more complicated for continuous operations, and the reader is referred to the above references for further information. For the case of batch coating processes, we have that $Q_k = 0$, since there are no feed or product streams. Furthermore, we shall assume that the birth rate (B) and the death rate (D) due to coalescence, nucleation and breakage are both negligible. With these assumptions, Eq. (5) reduces to:

$$\text{Eq. (6)} \quad \frac{\partial}{\partial t} [Nf(m)] + \frac{\partial}{\partial m} [GNf(m)] = 0$$

In order to use Eq. (6), it is necessary to know what is the initial mass (the measure of size used in Eqs. (5) and (6)) distribution of particles and the growth rate function, G .

346 *Fluidization, Solids Handling, and Processing*

In general, we may write that the growth rate is a function of the mass of the particle:

$$\text{Eq. (7)} \quad G(m) = \frac{dm_p}{dt} = km^{(2+k_1)/3}$$

The concept of growth functions is covered in more detail in Sec. 3.6. Liu and Litster (1993a) looked at two cases of Eq. (7). The first assumed that $k_1 = 0$, which is equivalent to assuming that, on average, each particle spends the same amount of time in the spray over a long period of time. Thus, G should be proportional to the projected surface area of the particle (assumed spherical) or

$$\text{Eq. (8)} \quad G(m) \propto Km^{2/3} = K'd_p^2$$

The second case assumed $k_1 = 1$. The rationale for using this form for Eq. (7) comes from the observation that in conventional spouted beds, used by Liu and Litster (1993a), the times for particles of different mass to circulate through the spray zone were not the same. In fact, Robinson and Waldie (1978) found that for a conventional spouted bed:

$$\text{Eq. (9)} \quad t_{\text{circ}} \propto \frac{1}{d_p^{0.7}}$$

Thus, larger particles circulate more often and are, therefore, more likely to receive more coating. Thus, it is justified to use a value of k_1 greater than 0 (the use of $k_1 = 1$ rather than $k_1 = 0.7$ is not significant for the accuracy of the data obtained in typical coating experiments).

Finally, we note that a mass balance on the bed particles at any time t can be written:

$$\text{Eq. (10)} \quad \int_0^\infty N f(m) G(m) dm = F_{\text{coat}} - E'$$

Liu and Litster (1993a) solved the set of equations given above and compared the number mass distribution predicted by the model with that observed experimentally. The comparison was reasonably good as shown in Fig. (4). It is worth mentioning at this point that the raw data of Liu and Litster (1993a) and Robinson and Waldie (1979) display a considerable amount of scatter, Fig. 5. The data in Fig. 5 shows that, for a particle of given mass, the amount of coating received varies considerably. For example, from Fig. 5(a) we can see that particles of original mass 4 g have an amount of coating added in the range of 0.7 g to 1.4 g. This variation in the coating amount for particles of the same initial mass cannot be predicted by the population balance approach as used by Liu and Litster (1993a), since their model is deterministic. Clearly, there appears to be a significant scatter in the data about the average value and in order to estimate the magnitude of this scatter, a stochastic or probabilistic model must be used. The level of scatter demonstrated in the experiments shown in Fig. 5 and other work can cause significant variation in the thickness of the applied coat, leading to significant variation in the functional behavior of the coat.

Probabilistic Approach to Modeling Coating. The concept that the amount of material coated onto identical particles, during a batch or continuous process, may vary significantly was first considered by Mann and Coworkers (1972, 1974, 1981 and 1983). For a batch process, Mann (1983) considered the movement of particles in a fluidized bed coater to be a renewal process. As each particle passes through the spray zone (see Fig. 3), it receives a small mass of coating, x . The total amount of coating received is the sum of all the discrete additions received over the course of the process. Thus, the total mass of coating that a single particle receives is given by:

$$\text{Eq. (11)} \quad X_{total} = x_1 + x_2 + \dots + x_n = \sum_{k=1}^{k=N} x_k$$

If we consider different particles, we can see from Eq. (11) that the variation in the total amount of material deposited on each particle is a function of the number of times the particle passes through the spray zone, N , and the amount of material that it receives in each pass, x . Since both x and N vary, we expect that X_{total} will vary between particles in the same batch. Mann (1974) has shown that for a batch coating process in which the operating time is greater than about 20 times the average circulation time,

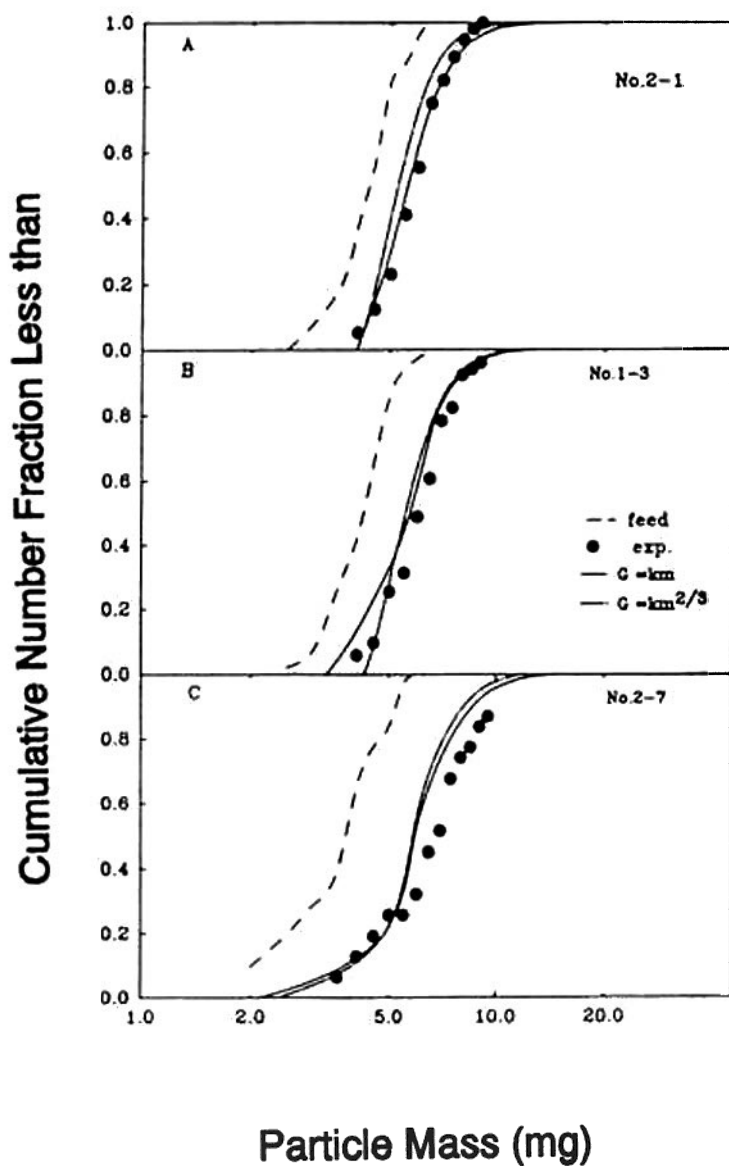
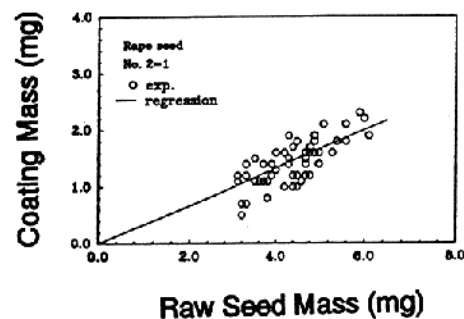
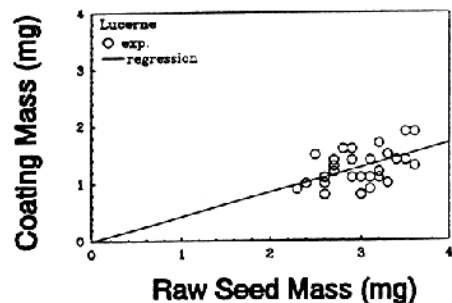
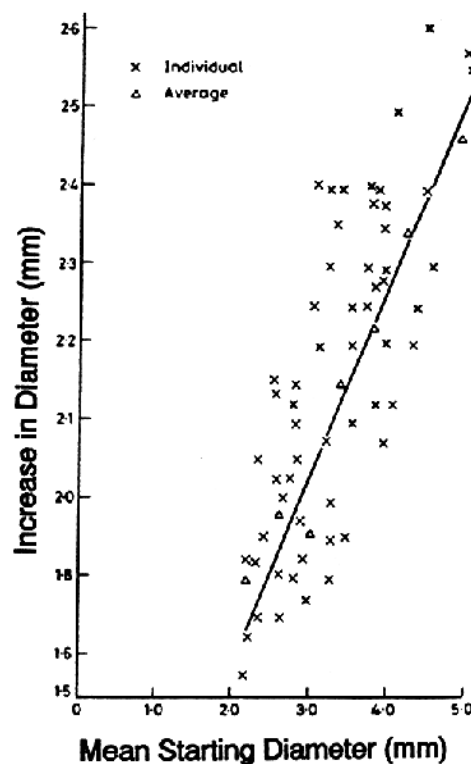


Figure 4. Number mass distribution of particles. (From Liu and Litster, *Powder Technol.*, 74:259–270, 1993, with kind permission from Elsevier Science S.A., P.O. Box 564, 1001 Lausanne, Switzerland.)



a



b

Figure 5. Results from (a) Liu and Litster, *Powder Technol.*, 74:259–270, 1993, with kind permission from Elsevier Science S.A., P.O. Box 564, 1001 Lausanne, Switzerland; and (b) Robinson and Waldie (1979) showing variability of coating mass.

then the characteristics (mean and variance) of the distribution of the number of particle passes can be determined from the distribution of cycle times, i.e., the times between successive passes. This is very useful, since the cycle time distribution can be measured experimentally while the distribution of the number of particle passes cannot be measured easily. Furthermore, Mann (1983) showed that the coefficient of variation for X_{total} , for a batch coating process in which N and x are independent, random variables, could be expressed as:

$$\text{Eq. (12)} \quad R = \frac{\sqrt{\text{Var}(X_{total})}}{[E(X_{total})]^2} = \sqrt{\frac{\text{Var}(t)}{t_{tot} E(t)} + \frac{\text{Var}(x) E(t)}{t_{tot} [E(x)]^2}}$$

where t_{tot} is the total coating time for the batch operation. Equation (12) shows that the variation in the amount of coating received per particle is the sum of two effects. The first effect concerns the variation in the number of passes a particle makes through the spray zone during the process and is given by the first term on the right hand side of Eq. (12). The second effect concerns the variation in the amount of material that a particle receives each time it passes through the spray and the average number of passes through the spray. This second effect is given by the second term on the right hand side of the equation.

Cycle Time Distribution. The variation in the number of times a particle circulates in a fluidized bed has been determined by measuring the cycle time distribution of a tagged magnetic particle in spouted beds with and without draft tubes (Mann, 1972; Cheng, 1993; and Waldie and Wilkinson, 1986). The results of Cheng (1993) showed that for beds with draft tubes, the circulation times for tagged particles of different sizes and dimensions were basically the same for the same operating conditions. Cheng (1993) and Mann (1972) also measured the variance and mean cycle times, and the results of Cheng (1993) are shown in Fig. 6. It is clear that as the mean cycle time increases, so does the variance. Typical mean circulation times varied between 2 to 10 seconds (for a 150-mm diameter bed with a 75-mm diameter draft tube). Since typical coating operations have a duration of at least one hour, it can be seen from Eq. (12) that the first term on the right hand side often contributes very little to the overall variation in coating mass uniformity. However, this may not be the case when the bed contains dead zones which lead to a very wide distribution of circulation times.

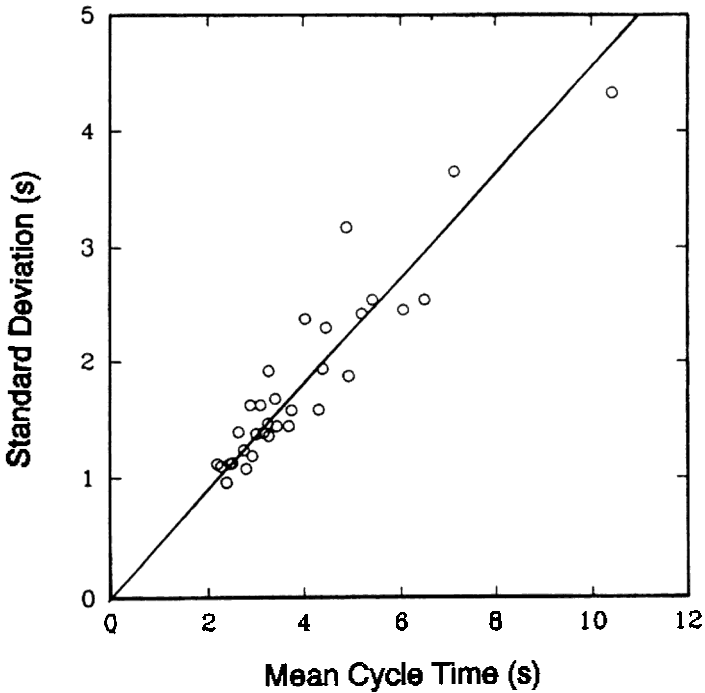


Figure 6. The relationship between mean circulation time and variance of the circulation time distribution for a 150-mm diameter fluidized bed with draft tube insert (from Cheng, 1993).

Variation of Mass Deposited per Particle Pass through the Spray Zone. We consider here the results of the work done by Cheng (1993) in a spouted bed with a draft tube. For this work, all the particles charged to the bed were essentially the same size (1.18–1.00 mm) and, thus, it can be assumed that the cycle time and mass coating distributions are unaffected by the particle size. Cheng (1993) showed that the second term on the right hand side of Eq. (12) was the dominant one and that significant variation in x could be expected, leading to significant variations in X_{total} . This variation was explained by the sheltering effect that particles close to the spray have on particles further away and is illustrated in Fig. 7. Cheng and Turton (1994) then developed an analytical expression for $\text{Var}(x)/[E(x)]^2$ based upon the voidage of particles in the spray zone and the geometry of the spray. Comparison of their expression and experimental data showed the correct order of magnitude but was oversensitive to changes in operating conditions and bed geometry.

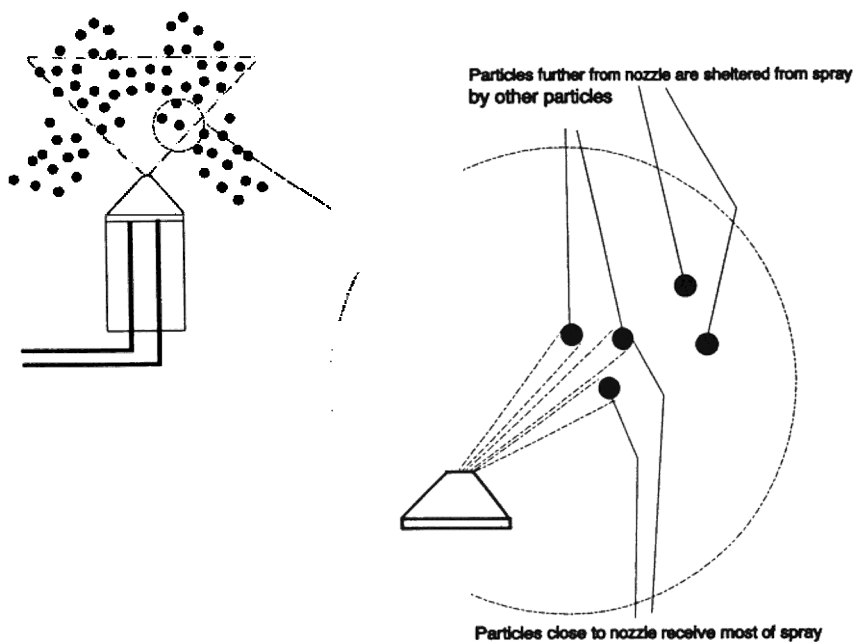


Figure 7. Sheltering effect of particles in the spray zone of a fluidized bed coater.

In summary, we can say that the variation in coating mass received by different particles during batch coating operations can be attributed to the variation in the number of particle passes through the spray (a small effect for coating operations taking longer than about thirty minutes and when the equipment does not possess any appreciable dead zones) and the variation in the amount of spray received per particle per pass through the spray (major contribution for longer spraying times).

Combining Population Balance and Probabilistic Modeling. From the discussion above, it is evident that the population balance approach is useful in predicting the average amount of coating material deposited on particles of different size. On the other hand, the probabilistic approach allows an estimation of the variation of the amount of coating on a given size of particle. The differences between these two approaches is illustrated in Fig. 8. In effect the population balance approach is useful in modeling the effects of initial size distribution and growth rates on the average product size distribution. However, the observed scatter of data about the predictions

from the population balance predictions must be modeled by a probabilistic or stochastic approach as discussed in the previous section. Although there has been no reported study to combine these two approaches, it would seem logical to do so, thus providing a complete picture of the coating process.

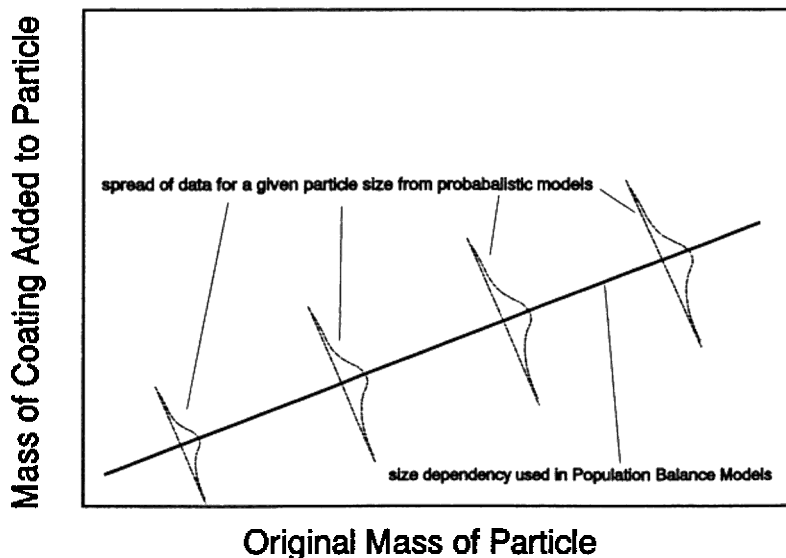


Figure 8. Illustration of information from different coating models.

In general, different sized particles may have different cycle time distributions and different mass deposition distributions in the spray zone. One approach would be to use small discrete size distribution increments and then to apply Eq. (12) to each size fraction. Inherent in this approach is the assumption that each particle size fraction acts independently. This assumption may not be valid, especially if different particles take different circulation paths within the bed. From the population balance approach, Randolph and Larson (1988) have suggested the use of an effective growth diffusivity coefficient to account for random fluctuations in growth rate. Thus Eq. (6) would be modified to give:

$$\text{Eq. (13)} \quad \frac{\partial}{\partial t} [Nf(m)] + \frac{\partial}{\partial m} [GNf(m)] = D_G \frac{\partial^2 [Nf(m)]}{\partial m^2}$$

At present, there is little information or work been performed to address the problems of coating mass uniformity. Either of the two approaches above may be useful in modeling the spread or variation in coating uniformity. However, effective diffusion coefficients, D_G , and coefficients of variation for particle coating, $[\text{Var}(x)/\{E(x)\}^2]^{1/2}$, must first be established from experiment. Therefore, without additional extensive work in this area, it will be impossible, in general, to predict *a priori*, the uniformity of coating mass for a batch of particles in a given piece of equipment at given operating conditions.

Models for Continuous Coating. From the results of coating experiments given in the section above, it is clear that considerable variation in the amount of coating per particle can occur during batch coating operations. The variation in mass uniformity between particles in a continuous coating process with feed and product withdrawal can be expected to be considerably greater due to the well mixed nature of a spouted bed. For this reason, most coating in the agricultural and pharmaceutical industries is still done in batch processes. Population balance equations and probabilistic models have been presented by Liu and Litster (1993a), Choi and Meisen (1995) and Mann (1981) for continuous systems.

Coat Morphology. It has been observed that, even for solids with a narrow distribution of coating mass, there may still be wide variations in the performance of the coated product. This is especially important when the coating provides a functional use. For example, if the product is to possess a sustained release property, then it is very important that each particle's coat provides the desired retarding action on the release of the active ingredient. If the product is intended for use in the agricultural chemicals market, a nonuniform coat might lead to premature release of an insecticide into the soil thus affecting the yield of a crop. On the other hand, if the product is for use in the pharmaceutical market, then the consequence of a nonuniform coat could be the premature release of a large quantity of drug (dose-dumping) into the patient's body rather than its gradual release over a six to twenty four hour period. The seriousness of dose-dumping leads us to a consideration of the structure or morphology of the particle coat.

In the pharmaceutical industry, when a functional coat is applied to a particle containing an active ingredient (drug), it is common to monitor the release of the active ingredient using *in vitro* dissolution. The rate at which the drug is released under a set of well-controlled conditions gives valuable information on the expected release of the drug within the body. This method is much easier to perform and less costly than *in vivo* testing using human or animal subjects. Thus, so long as a correlation between the results from *in vitro* and *in vivo* testing exists, the preferred test method for quality control is via a dissolution test. However, the fact that particles with the same amount of active ingredient and seemingly similar coats can give quite different release characteristics suggests that the morphology of the coat is an important factor in predicting the performance of a coated particle. There is an abundance of literature outlining case studies using combinations of various additives and coatings to tailor the release of an active ingredient (Mehta and Jones, 1985; Rekhi et al., 1989; Jozwiakowski et al., 1990; Wan and Lai, 1991; McGinity, 1989; and Gilligan and Po, 1991). Several studies (Weiss and Meisen, 1983; Mehta and Jones, 1985; Rekhi et al., 1989) have taken electron micrographs of cross-sections and the surface of coated particles, and qualitative differences in the morphology of the coat were discussed. However, to date there appears to be no work done in quantifying the morphology of the coat in terms of the operating parameters of the equipment used in the coating process. Some of the factors to consider regarding product quality when scaling up a process are discussed in Sec. 2.5.

2.5 Design Criteria

For a given coating application, the choice of what equipment and processing conditions to use must be based on prior experimental experience. There is no way, at present, to choose all the variables *a priori*. Experimental verification for the specific application under the specific conditions, using the desired coating formulation, must be performed for all new processes. However, there are many guidelines available to aid the engineer in making rational choices and, thus, reducing the scope of the variables to be searched. The following section attempts to catalog some of the more important design concepts to aid in the selection of equipment and conditions.

Fluidized Bed Coating Equipment. In reviewing the literature, it is evident that there are a great many variations in fluidized bed equipment used in coating applications (Olsen, 1989a and 1989b; Jones, 1985; and Mehta,

1988). Nevertheless, we may categorize all the equipment into four main groups. Each group is discussed below

Conventional Spouted Bed. The use of a conventional spouted bed (see Fig. 2a) is favored in the application of coatings to agricultural, food, and larger pharmaceutical products. A restriction in using this type of equipment is that the material to be coated must be *spoutable*. Spoutable means that the particles should be Geldart type D solids, implying that they have diameters typically 2 mm and greater (see Geldart, 1973 for a more complete definition). Gas velocities must exceed the minimum spouting velocity, and the height of the bed must not exceed the maximum spoutable height. Another important feature of the spouted bed is the angle of the air (gas) inlet cone. Correlations for these quantities are given by Liu and Litster (1991), Mathur and Epstein (1974) and Kucharski and Kmiec (1983). Since the particles are large, their velocity when leaving the top of the spout is quite high, and attrition may be excessive for friable particles or coatings. The location of the nozzle can either be at the base of the spout or in the fountain region above the bed as shown in Fig. 2a. Due to size dependent circulation rates through the spray zone (Robinson and Waldie, 1978), uniformity of coating thickness may be a problem, especially for a wide size distribution of feed material.

Fluid-Bed with Draft Tube. The use of fluidized beds with draft tube (see Fig. 2b) is the preferred method for the application of functional coatings to particles in the pharmaceutical industry. The term *functional* refers to the fact that the coating provides a delay in delivering the active ingredient contained in the fluidized solids, e.g., sustained release and enteric coatings. The application of the draft tube to particle coating is attributed to Wurster (1957 and 1966), and the draft tube is often referred to as a “Wurster Insert.” The purpose of the draft tube is to channel air (or the fluidizing gas) up through the center of the bed, thus, entraining particles with it. The circulation of solids obtained with a draft tube is well controlled, repeatable, and quite stable. This property of these beds allows the production of a batch of coated material with a relatively narrow distribution of coating thickness.

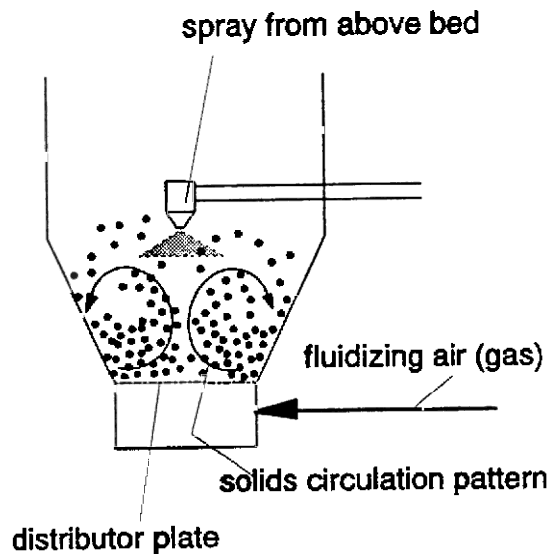
The use of a draft tube overcomes the difficulty of spouting only large particles. In fact, particles in Geldart’s A, B, and D particle categories have all been successfully coated using these devices. For smaller particles (300 μm and smaller), it has been found (Jones, 1985) that the length and angle of the expansion chamber above the bed are crucial in reducing carryover and in maximizing the circulation rate of the particles through the

spray zone. The location of the spray nozzle is almost always at the base of the draft tube (bottom spraying), and dual fluid nozzles are used most often.

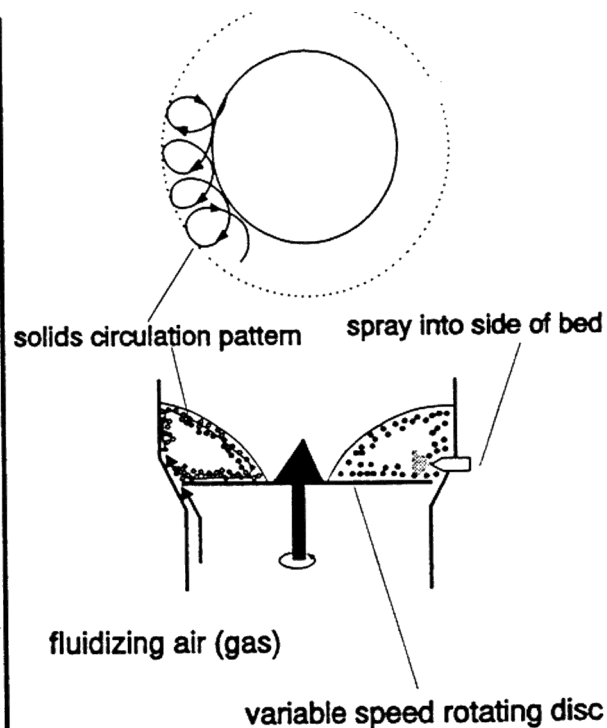
Conventional Fluid-Bed Granulator. In a conventional fluid-bed granulator, Fig. 9a, the fluidizing gas is again preferentially fed to the center of the bed. This causes particles to be dragged up in the center with the upward moving gas. The net result is that the particles circulate within the bed but in a less ordered or more chaotic manner than in conventional spouted beds with/without draft tubes. The formation of a spout is not required, therefore allowing a wide variety of particle sizes to be used. The coating liquid is nearly always sprayed downwards from the top of the bed which has the advantage that the nozzle may be removed during operation if it becomes clogged. Due to the less ordered circulation of particles, this equipment is rarely used for sustained or enteric coatings, although application of moisture barriers and cosmetic coats are common. This equipment has also been used successfully to apply hot melt (solventless) coatings.

Rotor Granulator. The last type of equipment used for powder coating is the rotor granulator, Fig. 9b. This equipment utilizes a variable speed rotating disc at the base of the bed. Fluidizing air (gas) flows between the edge of the disc and the bed wall upwards through the bed of solids. The combined action of the fluidizing gas and rotating disc causes the bed solids to circulate in the direction shown in Fig. 9b. Since the carryover of solids is small, the expansion space above the bed is small. Thus, a large volume of solids can be processed in a relatively small piece of equipment. The rotor granulator can be used in standard coating applications but its main advantage is its ability to apply a layer of powder to a solid substrate. Dry powder can be fed simultaneously with a liquid binder solution. With the correct location of feeds, the solids are first wetted by the liquid and then covered with a layer of powder. Successive cycles of wetting and powder layering allow the rapid buildup of powder on the substrate solids. This technique is particularly useful when the solute (coating powder) cannot be dissolved or slurried and when large amounts of active ingredients must be applied to a substrate solid.

Air (Gas) Handling Equipment. Both the quantity and the quality of fluidizing gas are important considerations in the design of a coating system. In general, the more fluidizing air (gas) that can be used, the greater the spraying rate and the shorter the processing time for a batch. However, other considerations, such as excessive attrition and coating mass uniformity, may well determine the maximum air flow rate and batch processing time. A



(a)



(b)

Figure 9. Coating in (a) a conventional fluid bed granulator and (b) a rotor granulator.

typical air handling system for a pharmaceutical coating process (Olsen, 1989a,b), is shown in Fig. 10. For processes in which the cleanliness of the final product is not so important, the air handling may be simplified. Nevertheless, most systems will contain one or more of the following: humidity control, filtering, and heating.

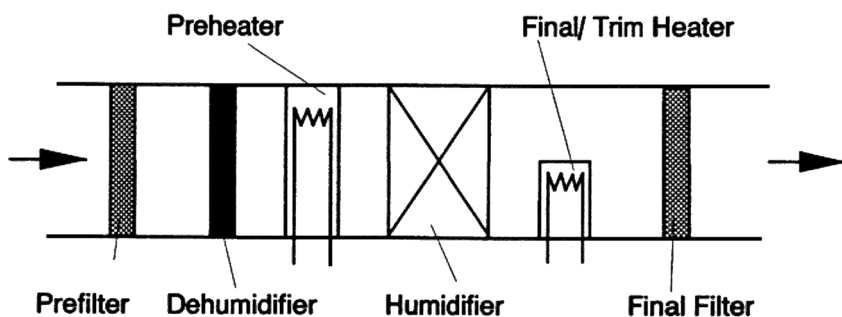


Figure 10. Elements of a typical air handling system for fluid bed coating.

Humidity Control. Humidity control is important for both aqueous and organic based solvent processes. For sprays containing aqueous solutions, the inlet air humidity directly affects the mass of water which can be absorbed by the gas. Clearly, the drier (lower dew point) the inlet air is, the greater the amount of water that is needed to saturate it and, hence, the greater the spraying rate can be. Studies by Liu and Litster (1993b) on a conventional spouted bed showed that the maximum spray rate, defined as the maximum spray rate for which the spout did not collapse, lies below the theoretical limit corresponding to saturated air leaving the bed. It was found that the limit of saturation is approached as the spouting air velocity is increased. For spouted beds with draft tubes, it is common to assume that the maximum limit for spraying corresponds to the exit air being saturated, although this rarely happens.

For organic solvent processes, the humidity of the air can also play a role in the product quality. One particular problem which can arise is that of condensation of water in the bed. In the vicinity of the nozzle, local cooling may be experienced due to solvent evaporation (Smith and Nienow, 1982), as discussed in Sec. 2.3. As a consequence of this local cooling, the temperature

may fall below the dew point of the air, and local condensation of water may occur with the result of product and coat damage. Clearly, this effect can be controlled by adjusting the humidity of the incoming air. If wide swings in humidity are expected, it may be necessary to dehumidify the air some of the time while humidifying it at other times.

Filtering. Contamination of product by foreign particulates in the fluidizing air can be minimized by the use of filtration. A trade-off may be required between air purity and increased compression costs due to higher filter pressure drops. For coating at close to ambient conditions, the cost of air handling is usually only a small percentage of the total cost, and low particulate loadings in the inlet air are easily achieved.

In addition to inlet gas filtering, it is usually necessary to use some form of filter downstream of the fluidized bed to avoid solid carryover. For fairly large particles, this is usually achieved by bag filters or screens; for very fine powders, a baghouse and cyclones may be necessary.

Heating. Along with controlling the humidity of the air, the other option for increasing the spraying rate of liquid, and hence reducing the processing time per batch, is to add heat to the system. The most common method for doing this is to heat the fluidizing air prior to feeding it to the bed. Care must be taken not to use excessively high inlet air temperatures when the active ingredients or coating material are heat sensitive; again, this is important for pharmaceutical, food, and agricultural products.

Recently, the use of microwave heating has also been applied successfully to coating processes. The use of internal heating surfaces is usually not practical since these would tend to clog and foul during the process.

Control of Fluidizing gas. For typical coating operations, a high-volume, low-head centrifugal blower is most commonly used. The location of the blower is most often at the exit of the system, thus causing the system to operate under a slight vacuum. This offers several advantages. First, fine particulate emissions to the surrounding area, through leaking seals etc., are eliminated; likewise, solvent emissions are also eliminated. In addition, the possibility of tripping explosion relief devices, through over-pressurizing the bed, are eliminated.

Distributor Plate Design vs. Split Plenum Designs. The fluidized bed with draft tube and conventional granulator designs, given earlier in this section, require the major portion of the fluidizing gas to flow through the center of the bed. There are essentially two ways to do this, as illustrated in Fig. 11. In Fig. 11a, a typical gas distributor plate for a single plenum design

is given. Clearly, the open area in the plate is much greater at the center, causing the majority of the air to enter the bed in the center. The remainder of the air is used to maintain fluidization in the rest of the bed, thus, ensuring that particles remain fluid and circulate easily. Clearly, many different designs are possible but the use of two multi-orifice plates separated by a fine screen to stop particle weeping into the plenum, is commonly used. Some new approaches for the design of distributor plates has been reviewed recently (Masters, 1992), and the use of so called “gill plates” may provide a viable alternative for fluidizing gas control.

The alternative to using a single plenum and adjusting the gas flow with the distributor plate is the use of a split plenum. Here, the gas flow is regulated separately through a central and annular plenum. The air can be supplied by a single blower but separate controls are necessary for each plenum. If independent control of the gas flow to each plenum is required, then two blowers are necessary.

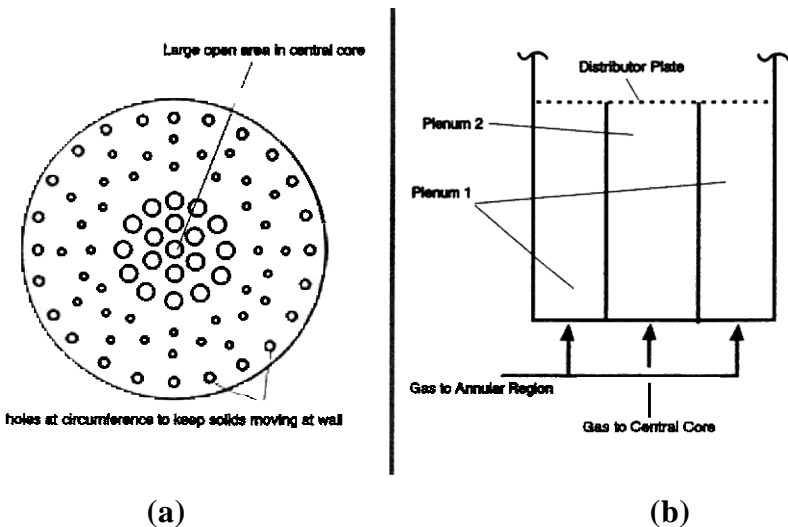


Figure 11. Alternative gas distribution systems in fluidized bed coaters, (a) single plenum and (b) split plenum.

Scale Up of Process. The scale up of fluidized bed coating processes has received little attention in the literature. Current practices in the pharmaceutical industry are reviewed by Mehta (1988). The basic approach described by Mehta (1988) is to scale the air flow and liquid spray rates based on the cross-sectional area for gas flow. This seems reasonable except for the fact that in the scaling of the equipment, the height of the bed increases with increasing batch size. For this reason, a time scale factor is also required.

Some typical fluid bed capacities used in the pharmaceutical industry are given in Table 2. From this information, it can be seen that for beds up to 450 mm (18") in diameter, one draft tube is typically used. The diameter of the draft tube is nominally one-half the bed diameter. For larger beds, the use of multiple draft tubes, 225 mm in diameter, is common. Also shown in Table 2 are the heights of the draft tubes used in each bed. Since the solids in the bed are filled close to the top of the draft tube, the capacity of the equipment is determined by the diameter of the bed, the height of the draft tube, and the density of the bed solids. An example illustrating the scale-up procedure is given below:

Test runs using a 150 mm diameter fluid bed coater indicated that a batch of 2 kg of material could be coated using a liquid spray rate of 10 ml/min for 50 minutes and a fluidizing gas rate of 40 scfm. It is desired to scale-up this process to a batch size of 200 kg of bed material. For the scaled up process, determine: the bed size; the liquid and air flow rates; and the new run time.

From Table 2: choose a 800 mm diameter bed with 3–225 mm diameter draft tubes. The air flow and liquid spray rates are scaled on draft tube diameter:

$$\text{New air flow required} = 40[3p(225)^2/4]/(p(75)^2/4) = 40(27) = 1080 \text{ scfm}$$

$$\text{New coating spray rate} = 10(27) = 270 \text{ ml/min}$$

The processing time is calculated based on the same coating mass per particle, thus:

$$\text{New coating run time} = t$$

$$\text{Coating per particle} = (270)(t)/(200) = (10)(50)/(2) \text{ ml/kg}$$

$$\text{Therefore, } t = (200)(50)(10)/(270)/(2) = 185 \text{ min (3.1 h)}$$

Table 2. Typical Capacities of Fluidized Bed Coaters with Draft Tubes used in the Pharmaceutical Industry (Mehta, 1988)

Bed Diameter (mm)	Draft Tube Diameter* (mm)	Height of Draft Tube (mm)	Number of Draft Tubes	Approximate Batch Size (kg)
150	75	225	1	0.5 - 2
225	112	300	1	7 - 10
300	150	375	1	12 - 20
450	225	600	1	35 - 55
800	225	750	3	200 - 275
1150	225	900	7	400 - 575

* Typical air flowrates are on the order of 3–5 m³/s/(m² of draft tube)

From the scale-up example given above, it is clear that the material and energy balances for the two processes have been correctly scaled. However, this scaling neither addresses nor guarantees similar product quality between the processes. From Sec. 2.4, we recall that the product quality is a strong function of the number of passes a particle makes through the spray zone and the variation in the amount of coating that a particle receives each time it passes through the spray. Both these quantities are affected greatly by the scaling process. Unfortunately, there appears to be little work published in the area of quantifying the coating mass uniformity and morphology in large equipment. Qualitative arguments are given below to describe some of the interactions which should be considered when scaling a process.

- (i) *Longer processing times.* With all other variables fixed and for particles and coatings which do not suffer appreciable attrition, the effect of longer processing times is to improve the coating uniformity. The reason for this is that as the run time increases, so does the number of particle passes through the spray. In general, it is better to add a smaller amount of coating to a particle and repeat the process many times than to do the opposite.

However, in most practical situations, both the particles and the applied coating material abrade as particles slide past each other, and a compromise between long processing times and excessive attrition must be made.

(ii) *Larger Diameter Equipment.* With all other variables unchanged, the effect of larger diameter equipment, which infers larger diameter draft tubes, is to worsen the coating uniformity. The reason for this is that as the diameter of the draft tube increases, and assuming the voidage in the draft tube does not change, then the sheltering of particles close to the center of the draft tube is more pronounced, causing $\text{Var}(x)$ to increase. This concept is discussed in more detail elsewhere (Cheng and Turton, 1994).

(iii) *Longer Draft Tube.* Even with all other variables unchanged the effect of a longer draft tube on the coating uniformity is unclear. Two opposing effects come into play when the draft tube length increases. First, as the bed height increases, the mass flow of solids into the draft tube will increase due to the increased static head in the annulus. This generally increases the particle sheltering effect (since the voidage in the draft tube falls) and increases $\text{Var}(x)$. On the other hand, the circulation time of the particles decreases, and the particles make more passes in a given time. This tends to improve the coating uniformity

Clearly, what happens when we scale up a process includes all of the above effects. Depending on the level of the scale up, it is conceivable that, in some cases, product quality might improve while, in other cases, it might worsen. In conjunction with the scale up, it may also be possible to change some of the equipment variables to compensate. For example, the circulation rate of solids is controlled by the gap between the bottom of the draft tube and the distributor plate. By adjusting this gap, it may be possible to counterbalance the effect of changing particle circulation due to scaling the process. Similarly, the use of multi-headed orifices, typically used in the larger draft tubes, may also counter the sheltering effect.

3.0 GRANULATION OF FINE POWDERS IN FLUIDIZED BEDS

3.1 Introduction

Granulation is a size enlargement operation by which a fine powder is agglomerated into larger granules in order to produce a specific size and shape, to improve flowability and appearance and to reduce dustiness. Granulation, as a unit operation, is used by a host of industries ranging from detergents, to food products, to agricultural chemicals such as pesticides and fertilizers and to pharmaceutical products such as tablets. During granulation, a liquid such as a solution (binder) or a melt is pumped, poured or atomized onto an agitated bed of different powders contained in a mixer whose main role is to provide shearing forces in the powder mass. As solvent evaporates from the binder (liquid) or the melt thickens, the powder particles stick together and, as interparticle bridges and capillary regions strengthen, larger granules of the original powder are left behind. These granules are further consolidated by the forces in the mixer and, upon final solidification of the binder or melt, strong agglomerates are formed.

Binder granulation, as it is known in industry, can be achieved in different types of mixers ranging from rotating drums and pans to high shear mixers and fluidized and spouted beds. The present review is focused on *fluidized bed granulation* which is in some ways different from other types of mixer granulation in that the gas supplied to produce powder agitation through fluidization also causes binder evaporation and cooling (or heating) of the powder. In addition, particle size increase is associated in a fluidized bed with many changes in fluidization characteristics, the most important of which are the mixing properties of the bed. These interacting phenomena make fluid bed granulation by far the most complex. At the same time it is also the most versatile, allowing drying and cooling operations to be carried out simultaneously with size increase (agglomeration).

Several excellent reviews of fluid bed granulation were published by Nienow and coworkers (Nienow, 1983, Nienow and Rowe, 1985 and Nienow, 1994) in which the operation is described in detail. Heat and mass balances on the system are presented and a granule growth model is proposed. The advantages and disadvantages of the operation are discussed. The present approach differs from the above work by looking at the microscale

processes of granule formation, growth and breakage and by studying the behavior of liquid bridges between agglomerating particles. This view is in some ways more powerful in that it generates an overall picture of binder granulation. Furthermore, specific phenomena such as particle coalescence and layering of fines or the deformation and breakage of wet granules are components which result directly from the models at the microscale.

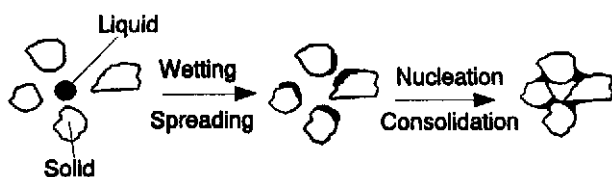
Fluid bed granulation equipment is, in general, not different from industrial fluidized bed coating devices except the spraying zone occupies a larger portion of the bed and also gas velocities used are somewhat smaller. Granulation equipment and some of their main characteristics were described in some detail in the previous section, see Figs. 2 and 9, and are not repeated here. The tendency in present industrial granulation is oriented toward the use of “combination” equipment, for example the high shear-mechanical fluidized bed type of the kind presented in Fig. 9b. These devices are very versatile and allow, in addition to very effective particle growth and coating, drying, heating and grinding operations to occur over a very short operation period.

3.2 Microscopic Phenomena

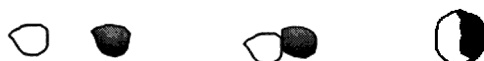
The process by which fine powder particles stick together in a shearing mass of powder to form large granules which possess, in the end, enough strength to survive in the granulator is quite complex (Ennis et al. 1990a,b, 1991; Ennis, 1990; and Tardos et al. 1991, 1993, and 1997). Figure 12 depicts some more common ways in which agglomerate growth may occur: *nucleation* is defined (Fig. 12a), as the sticking together of primary particles due to the presence of a liquid binder on the solid surface. *Coalescence*, on the other hand (Fig. 12b), is the process by which two larger agglomerates combine to form a granule. Other modes of granule growth are *layering* of a binder coated granule by small seed particles (Fig. 12c) and the capture of fines by a partially filled binder droplet (Fig. 12d).

It is instructive to simplify the above picture somewhat and consider the coalescence or sticking of two particles schematically shown in Fig. 13. One can assume that due to shear forces in the mixer, a fluidized bed in the present case, the two particles possess a relative velocity U_0 which ensures collision at some point on their trajectory and possible sticking under appropriate conditions. It is essential that some binder be present at the point of contact, as depicted in the figure. From this simplified picture, all mechanisms

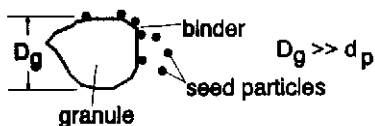
of Fig. 12 can be easily reconstructed provided that one allows for variation in size and nature (solid or liquid) of the two colliding particles. For example, if one particle is large and the other is small, layering is achieved as shown in Fig. 12c. During agglomerate growth by coalescence, depicted in Fig. 12b, pure liquid binder at the contact point is replaced by either a concentrated *slurry*, formed from the binder and the original fine powder, or by a deformable, binder “saturated” granular surface which is sufficiently malleable to allow for stickiness and subsequent deformation (Tardos, 1995; Kristensen et al, 1985a,b; Kristensen, 1988; and Schaefer et al.,1990a,b).



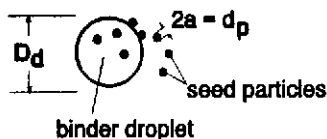
(a) Agglomerate Formation by Nucleation of Particles



(b) Agglomerate Growth by Coalescence



(c) Layering of a Binder Coated Granule



(d) Layering of a Partially Filled Binder Droplet

Figure 12. Mechanisms of granule growth, adapted from Tardos et al. (1991).

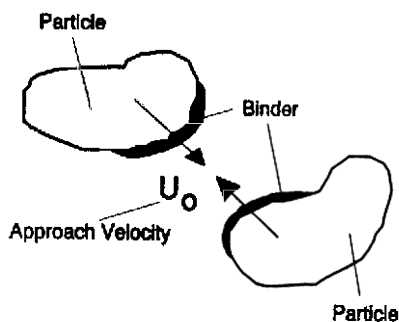


Figure 13. Coalescence of two binder-covered particles (granules).

The study of the *kinetics of granule growth* in mixer granulation using a binder can be undertaken using the above simplified picture. It essentially comes down to the conditions under which the two particles in Fig. 13 will stick together or rebound: sticking will yield growth while rebound will not. The rate of growth will then depend on the relative sizes of the individual particles and, as can easily be seen in Fig. 12, the mechanisms of coalescence (12b) and nucleation (12a) will yield higher growth rates than layering (12c and 12d) due to the larger sizes of particles involved. In order for granule growth to occur at all, however, several essential conditions have to be fulfilled *a priori*; these conditions pertain to the presence of appropriate amounts of binder on the granular surface at the points of contact.

It is intuitively obvious that a certain amount of binder is required in the powder mass before enough will be present on the surface to ensure stickiness. This critical, minimum amount of binder is an important characteristic of the system and must be determined beforehand. Equally important is the time span over which the binder either spreads on the granular surface and/or penetrates into the pores of the powder. Both, the critical binder/powder ratio and the characteristic spreading/penetration time will be discussed first before the theory of growth kinetics is presented.

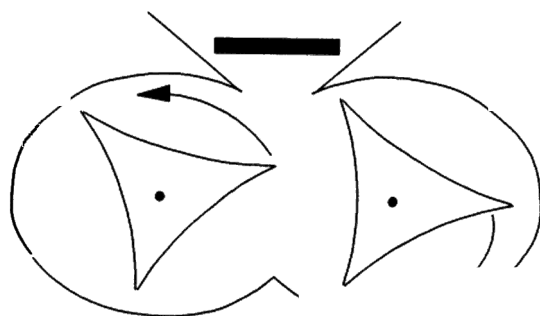
Critical Binder Liquid/Powder Ratio. When a liquid is mixed into a bulk powder made of fine particles, the liquid distributes itself first into small spaces between particles forming liquid bridges as can be seen in Fig. 12a. For very small amounts of liquid, these bridges are randomly spaced and do not influence the bulk properties of the powder. Upon introduction of larger

amounts of liquid, a situation is reached where enough of these liquid bridges are formed to create a continuous network of interconnected particles which extends throughout the bulk: this is called the *pendular state*. Many properties of the bulk powder show a significant change as this state is reached, a good example being the yield strength of the powder which shows a drastic increase. Values of the so called *saturation*, S , defined as the fraction of voids filled by the liquid to the total amount of voids in the dry solid, of the order of 20–30% are characteristic of this state.

In the other extreme, when all available voids in the bulk are filled with liquid, the so called *capillary state* is reached and under these conditions the saturation is $S = 1$. Between these limits, an intermediate, or so called *funicular state* is achieved, for which the saturation value is $0.3 < S < 1.0$. Rumpf (1975), among many others, studied the yield strength of a bulk powder as it moved from the pendular state through the funicular and finally to the capillary state by mixing into the bulk ever increasing amounts of liquid. It was found that the yield strength increases significantly at the transition between the pendular and funicular and again before the onset of the capillary state with a subsequent decrease upon formation of a wet cake or slurry. In an effort to control granulation in fluidized beds and high shear mixers, Lauenberger (1979), Schaefer (1988) and Schaefer et al. (1990a,b) introduced a shear measuring device (head) into a fluid bed granulator and also measured the torque and the power consumption of a high shear mixer while granule growth took place. These authors were able to generate curves of these quantities as a function of liquid saturation by taking samples of powder at different times during the granulation run. The increase of both the shear forces in the fluid bed as well as the torque and power consumption of the mixers as a function of saturation was found to take place at the transition between the pendular and funicular states and again between the funicular and the capillary states. This resembled, not surprisingly, the yield strength dependence of the powder on saturation, as illustrated above. This indicates that liquid bridges between particles critically influence the behavior of the bulk and the granulation characteristics of a powder-binder system and that the appropriate amount of binder can be determined by measuring one of these quantities.

The instrument and the procedure to determine the critical binder:powder ratio were developed (Tardos, 1994) based on the above observations. The instrument consists essentially of a low shear mixer, schematically represented in Fig. 14, in which the powder is slowly agitated and the binder is

continuously introduced by a metering pump (not shown in the figure). The instrument allows both the torque on the triangular paddle as well as the total electric power consumption of the mixer to be monitored continuously. An important condition to be fulfilled during this procedure is to allow adequate time during binder addition for the liquid to spread and adsorb into the interstices before new binder is introduced. In this way, one ensures that the finite spreading and adsorption rate of the liquid does not influence the results.



gear: 80 RPM

tip speed: 0.28 m/s

volume: 0.25 l

Figure 14. Schematic representation of the torque rheometer, adapted from Tardos (1994).

A typical plot of torque versus amount of liquid (di-butyl-phthalate, DBT) added is given in Fig. 15 for a very porous sodium carbonate powder mixture. The increase in measured torque at around 25% by volume DBT and again at around 65%, can easily be seen (the final decrease in torque upon the formation of the wet cake is not shown). These two points correspond to the condition under which the continuous network of bridges forms, at about 25% liquid present, and the formation of the “dry paste,” at around 65%, where enough binder is available to fill most internal voids. The amount of liquid in Fig. 15 is given as a fraction of the total volume of powder, instead

of the absolute value of the saturation, S , since this is current industrial practice. Conversion to absolute value S is easily achieved by dividing into the total void volume assumed to be approximately 68–70%, as seen in the figure. It should be noted that the high values of total porosity in this case, are a result of both internal or intra-granular as well as external or intergranular voids present in this particular powder.

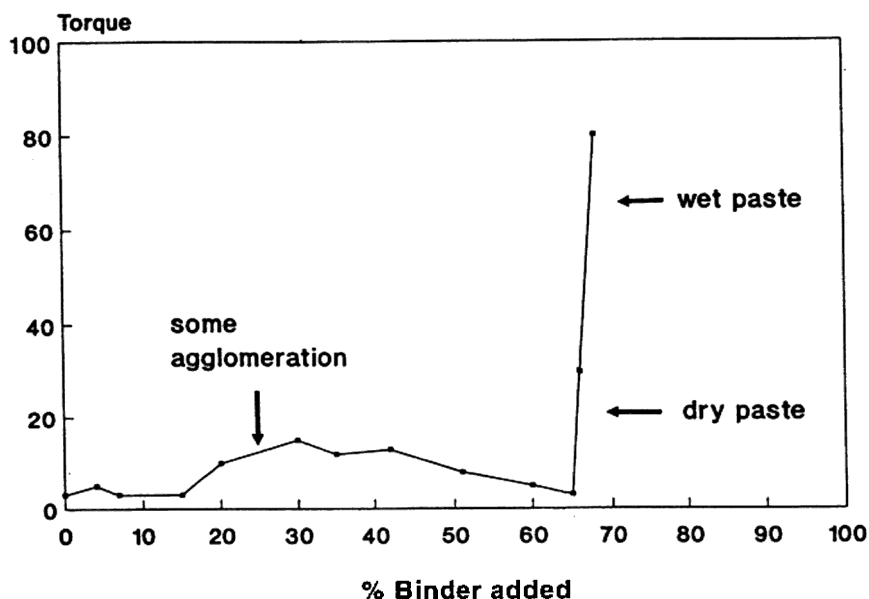


Figure 15. Experimental torque vs. binder fraction ratio for a porous sodium carbonate mixture, from Tardos (1994).

Granulation of the test powder shown in Fig. 15 can be performed either at around 30% or at about 60% by volume binder. In the first case, growth will occur mostly by nucleation with very little layering and no coalescence because of insufficient binder present while at the higher liquid content, all mechanisms of growth will occur including coalescence of larger binder filled granules as shown in Fig. 12.b. It is considered therefore that the critical binder/powder ratio in this particular case can be taken to be approximately 60–65%. One has to note that in a fluid bed granulator, due to binder evaporation during the process, some additional liquid is always necessary to compensate for the evaporated quantities.

Another important point has to be made for the case of fluid bed granulation, namely that binder introduction is usually concentrated in the so called “spray zone” and that the process of growth is not instantaneous or even rapid. Hence, agglomeration and granule growth will occur in the granulator while binder is introduced and the prevailing growth mechanisms will be locally determined by the amount of liquid present in the spray zone or in the bed. This is an essential difference as this process is compared to, for example, high shear granulation where the bed of powder is much more homogeneous.

Table 3 gives critical binder:powder ratios for a few powder-binder systems again given as percentage of dry powder. One can see that these ratios are higher for DBT than for water and also that large and porous particles such as the sodium carbonate and the agglomerated Sipernat (Sipernat is an activated silica powder produced by the Degussa Corporation) take in large amounts of liquid. Very flaky and nonporous powders such as dicalite, on the other hand, exhibit a very low critical ratio. In fact, for this powder, the transition takes place almost directly from the pendular to the capillary state and therefore, the critical ratio is quite low. Data in Table 3 is given for both water and oil (DBT); a water-based binder such as a low concentration solution will behave mostly like water while an oily surfactant binder or melt will behave like DBT. For binders used in a specific case, the above measurement has to be repeated and the actual critical ratios obtained.

Table 3. Critical Binder/Powder Ratios for Some Selected Powder-Liquid Systems

Material	Particle Size [μm]	Bulk Density [lb/ft ³]	Critical Binder Powder Ratio [%]	
			H ₂ O	DBP(oil)
Sodium Carbonate	200-400	10.0	-	60-65
Sipernat 50* 50s	50**	12.5	54	85
	8	6.2	28	41
Dicalite 436	6.5	5.0	14	26
Zeolite	3-6	25-30	24	35
Glass Powder	35-37	68.3	-	33

Characterizing Binder Wetting Properties and the Impact on Granulation. Introduction of at least the critical amount of binder into the granulator is only a first and necessary step to achieve proper granule growth. As can easily be inferred from the simplified picture of granule growth depicted in Fig. 13, the liquid binder layer present at the point of contact between two particles needs to have, at the moment of collision, a certain depth to insure sticking instead of rebound. If the layer is too thin and/or the liquid is adsorbed under the granular surface into pores, its influence will be negligible, granule growth will not occur and the binder will be lost for the process.

Figure 16 schematically depicts the process of surface wetting and liquid penetration into the pores of a particle. Under normal conditions of granulation, the binder is introduced in the bed as a spray of small droplets. These droplets impact on the solid surface and deposit on it as described in the chapter on coating: assuming that solid-liquid contact angles are such that surface spreading can take place, the binder droplet will flatten and cover an ever increasing area of the surface. At the same time however, liquid will penetrate into the surface pores of the granule and will be unavailable on the surface to ensure sticking to another granule. Both surface wetting and spreading are necessary since a non-wetting liquid will either not adhere to the surface at all or will be present on or cover a very small area, thus the number of collisions which yield growth is limited. Penetration into surface pores is also required in order to give the surface the malleable, plastic property required for large scale deformation as granules form by coalescence (Fig. 12b).

Methods of characterizing wetting include spreading of drops on powder surfaces, using a contact angle goniometer, and penetration of drops into powder beds, using the Washburn test. The first approach considers the ability of the fluid drop to spread across the powder and involves the measurement of the contact angle of a drop on a compact of the powder of interest (Aulton and Banks, 1979). The contact angle is a measure of the affinity of the fluid for the solid and it is given by the Young-Dupré equation, or

$$\text{Eq. (14)} \quad g^{sv} - g^{sl} = g^{lv} \cos q$$

where g^{sv} , g^{sl} , g^{lv} are the solid-vapor, solid-liquid and liquid-vapor interfacial energies, respectively, and q is the contact angle measured through the

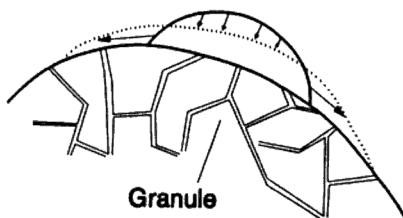
liquid as illustrated in Fig. 17. When the solid-vapor interfacial energy exceeds the solid-liquid energy, the fluid wets the solid with a contact angle less than 90° since this represents a lower energy state. In the limit of $g^{sv} - g^{sl} \geq g^{lv}$, the contact angle becomes 0° and the fluid spreads on the solid. The degree of wetting, in general, is controlled by the group $g^{lv} \cos \theta$ which is referred to as the *adhesion tension*. Sessile drop studies of contact angle can be performed on powder compacts in the same way as planar surfaces. These methods involve one or more of the following techniques:

- (i) Direct measurement of the contact angle from the air-binder interface
- (ii) Solution of the Laplace-Young equation using the contact angle as a boundary condition
- (iii) Indirect calculations of the contact angle from measurements, e.g., drop height

The compact can either be saturated with the fluid for static measurements or dynamic measurements may be made through a computer imaging goniometer which takes successive images of the drop profile.

Surface Wetting

Binder Droplet



Droplet Penetration

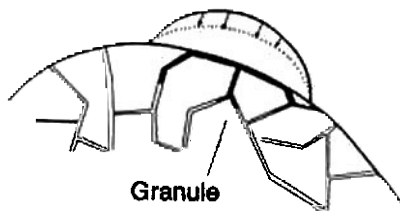


Figure 16. Schematic representation of binder droplet spreading and penetration into a porous sublayer.

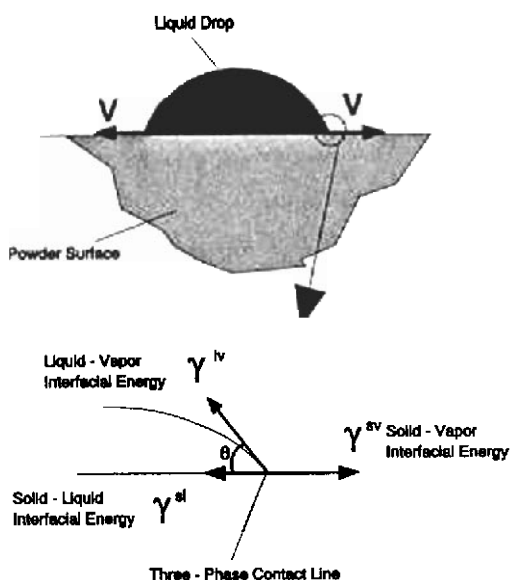


Figure 17. Contact angle on a powder surface.

As referred to earlier, wetting dynamics has a pronounced influence on the initial nuclei distribution formed from fine powder. The influence of powder contact angle on the average size of nuclei formed in fluid-bed granulation is illustrated in Fig. 18, where binder-powder contact angles were varied by changing the weight ratios of the ingredients of lactose and salicylic acid, which are hydrophilic and hydrophobic, respectively. Strictly speaking, the nuclei size should be expected to depend on adhesion tension (c.f. Eq. 14); however, the initial surface tension of the binding fluid (water) was not varied, and hence the only variable remaining was the contact angle. As seen, granule sizes increase as the wetting angle decreases, as expected.

The second approach considers the ability of the fluid to penetrate the powder bed and involves the measurement of the extent and rate of penetration into a column of powder, better known as the Washburn Test. By considering the powder to consist of capillaries of radius R , as illustrated in Fig. 19, the equilibrium height of rise, h_e , is determined by equating capillary and head pressures, or

Eq. (15)
$$h_e = \frac{2 g^{lv} \cos q}{\Delta r g R}$$

where Δr is the fluid density with respect to air, g is the acceleration due to gravity, and $g^{lv} \cos q$ is the adhesion tension. In addition to the equilibrium height of penetration, the dynamics of penetration can be of equal importance. Ignoring gravity effects, and equating viscous losses with capillary pressure, the rate of change of height (dh/dt) and the dynamic height of penetration (h) are given by

Eq. (16)
$$\frac{dh}{dt} = \left[\frac{R g^{lv} \cos q}{4 m} \right] \frac{1}{h}, \text{ or } h = \sqrt{\left[\frac{R g^{lv} \cos q}{2 m} \right] t}$$

where t is time and m is fluid viscosity. The grouping of terms in brackets involves the material properties which control the dynamics of fluid penetration, namely particle size (assumed to be related to R), adhesion tension, and binder viscosity.

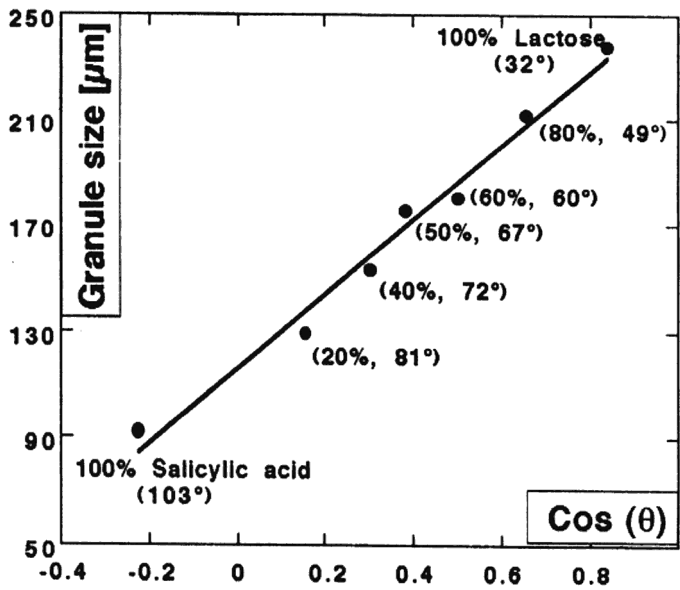


Figure 18. The influence of contact angle on fluid-bed granulation nuclei size. (From Aulton and Banks, 1979.)

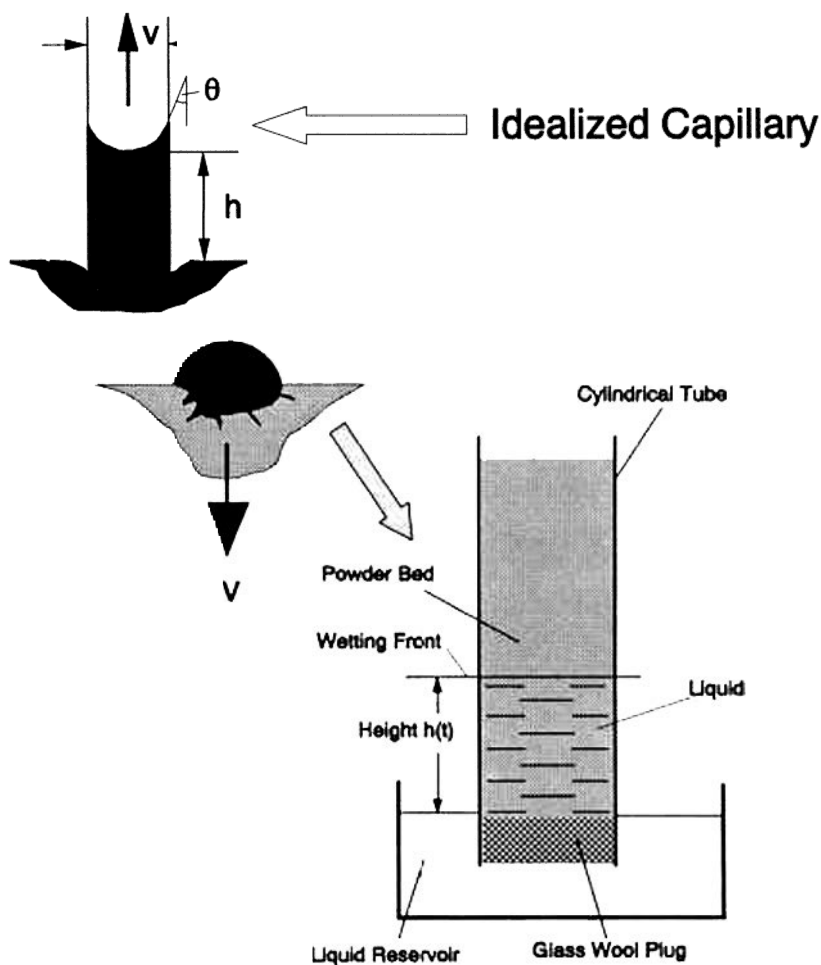


Figure 19. The Washburn Test for measuring wetting dynamics.

The effect of fluid penetration rate and the extent of penetration on granule size distribution from drum granulation experiments is illustrated in Fig. 20 (since no example for fluidized bed granulation is available). From Fig. 20, it is clear that for fluids with a similar extent of penetration, increasing the penetration rate increases the average granule size for various levels of liquid loading.

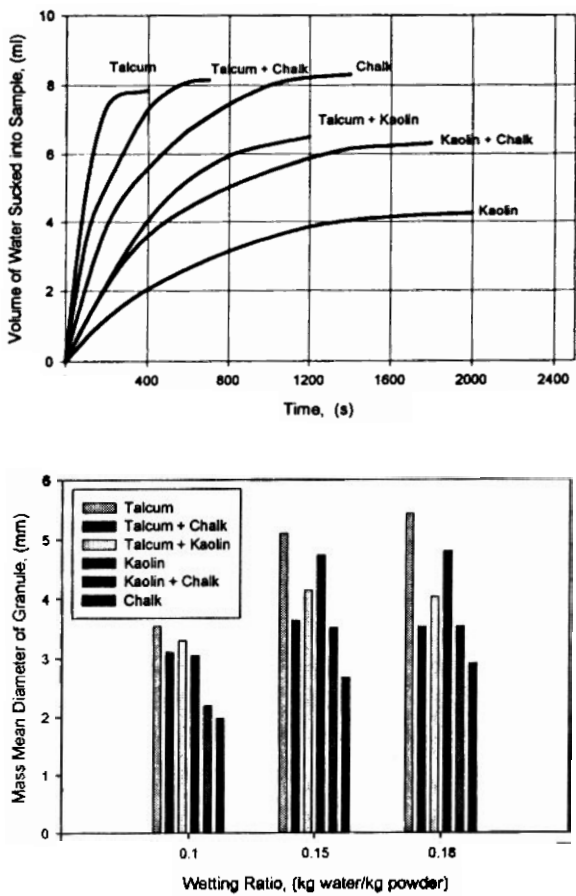


Figure 20. The influence of the extent and rate of penetration on average granule size in drum granulation for different spray rates. (From Gluba et al., 1990.)

From a processing point of view, Eqs. (15) and (16) provide the basic trends of the effects of operating variables on both wetting dynamics and wetting extent. Since drying occurs simultaneously with wetting, the effect of drying can substantially modify the expected impact of a given operating variable and this should not be overlooked. In addition, simultaneous drying often implies that the dynamics of wetting are far more important than extent. Table 4 provides a summary of the expected effects of operating variables.

Table 4. Summary of the Effects of Operating Parameters on Wetting in the Granulation Process

Formulation Properties which Enhance Wetting	Effect of Operating and Formulation Variables
Increase Adhesion Tension Maximize Surface Tension Minimize Contact Angle	Determine the critical surfactant concentration to maximize adhesion tension. Control impurity levels in particle formation
Decrease Binder Viscosity	Lower temperature since binder concentration will decrease due to drying thereby lowering viscosity. This effect generally offset due to inverse relationship between viscosity and temperature.
Increase Pore Size for Rate of Penetration Decrease Pore Size for Extent of Penetration	Alter milling, classification or formation conditions of feed, if appropriate, to modify particle size distribution.

In general, adhesion tension should be maximized from the point of view of increasing the rate and extent of both binder spreading and binder penetration. Maximizing adhesion tension is achieved by minimizing contact angle and maximizing surface tension of the binder solution. These two aspects work against each other, as surfactant is added to a binding fluid, and in general there is an optimum surfactant concentration which must be determined for each formulation. In addition, surfactant type influences adsorption and desorption kinetics at the three-phase contact line. In general, the major variable to control adhesion tension is surfactant concentration.

Decreases in binder viscosity enhance the rate of both binder spreading and binder penetration. The prime control over the viscosity of the binding solution is through binder concentration. Therefore, liquid loading and drying conditions strongly influence binder viscosity. In general, however, the dominantly observed effect is that lowering the temperature lowers the binder viscosity and enhances wetting. It is possible that the opposite takes place, since binder viscosity should decrease with increasing temperature. However, this effect is generally not observed due to the overriding effects of drying.

Changes in particle size distribution affect the pore distribution of the powder. Large pores between particles enhance the rate of binder penetration whereas they decrease the final extent. In addition, particle size distribution affects the ability of the particles to pack within the drop as well as the final degree of saturation (Waldie, 1991). In general, pore distribution will not strongly affect surface spreading outside of the competing effect of penetration. (Fine particle size may, however, impede the rate of spreading through surface roughness considerations).

As a last point, the drop distribution and spray rate have a major influence on wetting. Generally speaking, finer drops will enhance wetting as well as the distribution of binding fluid. The more important question, however, is how large may the drops be or how high a spray rate is possible. The answer depends on the wetting propensity of the feed. If the liquid loading for a given spray rate exceeds the ability of the fluid to penetrate and spread on the powder, maldistributions of binding fluid will develop in the bed. This maldistribution increases with increasing spray rate, increasing drop size, and decreasing spray area (e.g., due to bringing the nozzle closer to the bed or switching to fewer nozzles). The maldistribution will lead to large granules on the one hand and fine ungranulated powder on the other. In general, the width of the size distribution of the product will increase and the average size will generally decrease.

3.3 Granule Growth Kinetics

It will be assumed for the present considerations that sufficient binder is present in the granulator as determined by the binder/powder ratio and that the binder is appropriately spread on enough granular surfaces so as to ensure that most random collisions between particles will occur on binder-covered areas. It will also be assumed that the particles are more or less spherical having a characteristic dimension, a . The simplified system of two colliding particles is schematically shown in Fig. 21. The thickness of the liquid layer is taken to be h , while the liquid is characterized by its surface tension σ and its viscosity μ . The relative velocity U_0 is taken to be only the normal component between particles while the tangential component is neglected.

As the two particles approach each other, the first contact will be made by the outer binder layers; the liquid will subsequently be squeezed out from the space between the particles to the point where the two solid surfaces will touch. A solid rebound will occur based on the elasticity of the surface

characterized by a coefficient of restitution, e , and the particles will start to move apart. Liquid binder will now be sucked into the interparticle gap up to the point where a liquid bridge will form; upon further movement, the bridge will elongate and finally rupture as the particles separate.

The condition of coalescence, or sticking, critically hinges on the initial kinetic energy of the two particles as well as on the energy dissipated in the liquid layer (binder) and during the solid-solid collision. If the initial kinetic energy is smaller than the dissipated energy, particles will remain bonded by the liquid bridge while in the other case, total rebound will occur. However, before quantitative calculations can be made, energy dissipation in the liquid layer must be estimated and this is presented below.

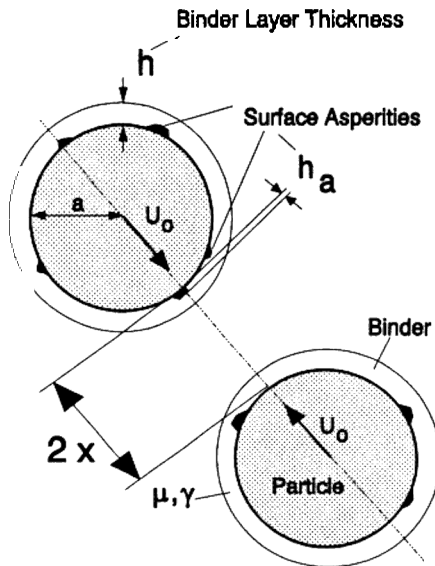


Figure 21. Two colliding binder-covered spherical particles. (From Ennis, et al., *Powder Technol.*, 65:257–272, 1991, with kind permission from Elsevier Science S.A., P.O. Box 564, 1001 Lausanne, Switzerland.)

Strength of a Pendular Bridge. The system of two particles connected by a liquid bridge is presented in Fig. 22; this is essentially the picture of the two particles in Fig. 21 after the liquid bridge is formed and liquid is being squeezed out from the intergranular space. The distance between particles is taken to be exactly $2h$, while the volume of the bridge is uniquely determined by a filling angle, f , as shown. It was demonstrated by many researchers (a summary of pertinent work in this area is given in Ennis et.al., 1990) that under fairly general conditions the total force, F , induced by the bridge can be calculated from the summation of two effects: a surface tension contribution proportional to the bridge volume or the filling angle and a viscous contribution dominated by the relative velocity. The superposition of solutions gives fairly accurate results and this can be expressed analytically by

Eq. (17)
$$\frac{F}{\rho g a} = \frac{3 Ca}{2e} + \sin^2 [f(C_o + 2)]$$

where $Ca = \mu U_o / g$ is the so called capillary number, $e = 2h/a$ is a dimensionless distance, and C_o is the Laplace-Young pressure deficiency due to the curvature of the free surface of the liquid. The first term on the right hand side is the viscous contribution which, in dimensional form, becomes

Eq. (18)
$$F_{vis} = \frac{3\mu U_o a^2}{4h}$$

while the second term is the so called capillary force

Eq. (19)
$$F_{cap} = \rho g a \sin^2 [f(C_o + 2)]$$

It is important to note that the viscous force is singular in the separation distance h and hence will predict infinite large forces at contact. Since this is physically impossible, a certain surface “roughness” has to be assigned to the granular surface as is shown in Fig. 21 where this parameter is assigned the value h_a ; this prevents particles from “touching.”

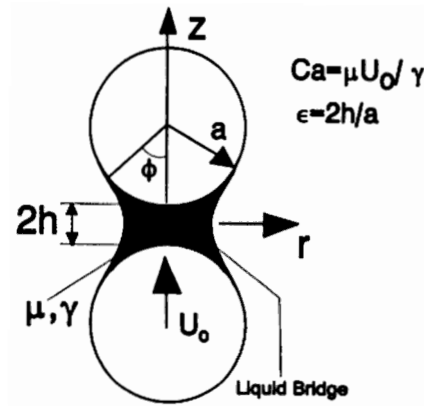


Figure 22. Pendular liquid bridge between two spherical particles. (From Ennis, et al., *Powder Technol.*, 65:257–272, 1991, with kind permission from Elsevier Science S.A., P.O. Box 564, 1001 Lausanne, Switzerland.)

Conditions of Coalescence. The outcome of the collision of two binder-covered particles is determined by the ratio of the initial kinetic energy of the system and the energy dissipated in the liquid bridge and in the particles. This can be expressed analytically by the definition of a so called Stokes number, St

$$St = (\text{initial kinetic energy})/(\text{dissipated energy})$$

$$\text{Eq. (20)} \quad St = \frac{2mU_o^2}{2F_{vis}h} = \frac{8\mathbf{r}_p U_o a}{9\mathbf{m}}$$

where \mathbf{r}_p is the particle density and m is the mass of the particle. Particle trajectory calculations show (Ennis et al., 1991) that if the Stokes number defined above is smaller than a critical value, $St < St^*$, collisions are effective and coalescence occurs while if $St > St^*$ particles rebound. One has to note that \mathbf{m} in the above equation, can be taken to be the binder viscosity or an equivalent viscosity of the granular surface as explained in the previous

section. The other observation is related to the particles size, a , which in a more general case is an equivalent size calculated from:

Eq. (21)
$$\frac{2}{a} = \frac{1}{a_1} + \frac{1}{a_2}$$

where a_1 and a_2 are the sizes of the colliding particles (granules). It is immediately apparent from this equation that during collisions between small and large particles when $a_1 \gg a_2$, the equivalent size is that of the smaller particle, $a \sim a_2$, and hence for this case, the size of the fine particle is the only relevant dimension.

The trajectory calculations mentioned above also yield analytical expressions for the critical Stokes number

Eq. (22)
$$St_{vis}^* = \left(1 + \frac{1}{e}\right) \ln\left(\frac{h}{h_a}\right)$$

where e is the restitution coefficient of the solid surface. One can see that the critical value is a direct function of the binder layer thickness, h , as expected. Consideration of the surface tension force F_{cap} instead of the viscous force F_{vis} in Eq. (19) leads to a similar set of conditions in which the critical Stokes number is given by:

Eq. (23)
$$St_{cap}^* = 2 \left(\frac{1}{e^2} - 1 \right) \left(1 - \frac{h_a}{h} \right)$$

In a real process, both binder surface tension as well as viscosity will act to dissipate energy and ensure sticking and coalescence, but no simple analytical solution exists for this case. It was also demonstrated by Ennis (Ennis et al., 1991) that conditions based on viscous dissipation are more restrictive than those based on capillary forces and hence the discussion of granulation regimes is limited, in this paper, to the former.

Regimes of Granulation. In a real granulator, a spatial distribution of particle velocities and hence of Stokes numbers almost always exists, as

depicted in Fig. 23. The value of the local Stokes number, St , must be compared with the critical value St^* to establish regions of coalescence in the bed. Direct predictions of particle size are both difficult and inaccurate from these general considerations. However, an appreciable degree of insight is gained as to the significance of the various operating and material parameters on the granulation process, by looking at limiting case scenarios of the ratio St/St^* .

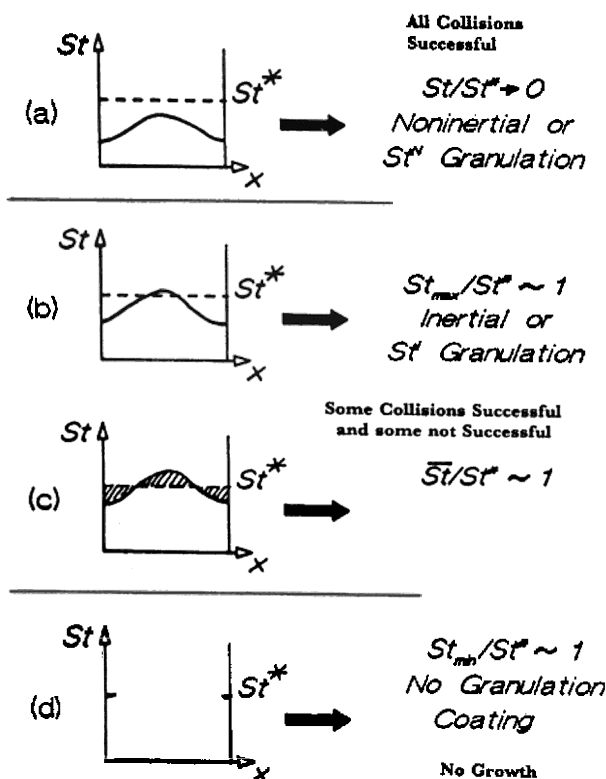


Figure 23. Regimes of granulation. (From Ennis, et al., *Powder Technol.*, 65:257–272, 1991, with kind permission from Elsevier Science S.A., P.O. Box 564, 1001 Lausanne, Switzerland.)

Let us first examine the regime where $St/St^* \rightarrow 0$ as illustrated in Fig. 23a where the entire distribution of St lies below the critical number St^* . The implication of granulation within this regime is that all collisions are successful

as long as binder is present in sufficient amounts at the point of contact. The rate of coalescence is independent of granule kinetic energy and binder viscosity and critically hinges, instead, on the distribution of binder—this regime is referred to as non-inertial or St^N granulation.

From Eq. (20) it is evident that the Stokes number, St , is proportional to (aU_0/η) . Two immediately apparent examples of this regime are the granulation of fine powders where a is smaller than say, $10\ \mu\text{m}$ and high temperature agglomeration where particle surface viscosities, due to material softening, are 10^4 – 10^6 poise are not uncommon. Another conclusion can be drawn for the case when a large granule or binder droplet is surrounded by fines as shown in Fig. 12c and 12d. As mentioned above, the equivalent size a is taken in this case to be the size of the smallest particles resulting, even for large relative velocities, in small values of the Stokes number. For these small values, all collisions between fines and the large granule take place in the non-inertial regime and, as long as binder is present on the surface, the granule will collect fines and grow preferentially. This kind of behavior is strongly supported by actual industrial practice in the operation of fluidized beds and pan granulators.

Further support for the existence of the above regime can be drawn from examining the implication of adding too much binder to the powder and hence increasing the binder thickness layer h . This results, as can be seen from Eq. (22), in a corresponding increase in the critical Stokes number, St^* ; and thus is an extension of the non-inertial regime to higher relative velocities and/or higher particle sizes; this can yield over-granulation and total defluidization of the bed if it is carried too far.

As granulation proceeds in the fluid bed and as granules grow in size, so do the granule Stokes numbers, since St is an increasing function of a . When granules have reached sufficient size such that some values of the Stokes number equals or exceeds the critical value St^* in certain regions of the granulator, coalescence will become impossible while in others, especially in regions of low bubble activity, particles will continue to coalesce and grow (see Fig. 23b). In this regime, granule kinetic energy and binder viscosity (and/or surface tension), will begin to play a role. In this “inertial” or St^I regime of granulation, increases in binder viscosity or decreases in granule kinetic energy will increase the rate of coalescence by lowering the corresponding Stokes number, as traditionally expected.

As granules grow still further, local Stokes numbers exceed the critical value St^* or $St/St^* \rightarrow \infty$ (see Fig. 23c), so that granule growth is no longer

possible and the so called *coating regime* or St^C granulation is achieved. This regime implies that a constant state of bed hydrodynamics dictated by the excess gas velocity in the fluidized bed will determine a theoretical growth limit by coalescence where only coating is possible. Only very limited growth is possible in this regime and this may be due only to layering of remaining fines in the bed and to collection of small binder droplets. The existence of this regime at high gas velocities, high granule circulation rates and non-viscous, rapidly solidifying binders is exploited in fluid bed coating as described in Sec. 2.

3.4 Experimental Support and Theoretical Predictions

Since the value of the Stokes number, St , increases with increasing granule size, the granulation of an initially fine powder should exhibit characteristics of all three granulation regimes as time progresses. This was indeed demonstrated by the author and coworkers (Ennis et al., 1991; Tardos et al., 1991) who showed that growth rates in a fluid bed granulator were independent of binder viscosity up to a critical size, where presumably granulation switched to the inertial regime. During the same experiment, the transition to the coating regime occurred for a constant excess gas velocity with larger granules generated with a binder of higher viscosity. The surprising conclusion of these and other similar experiments was the relative "shortness" of the inertial regime, i.e., the relatively rapid transition of the granulation process from the regime where all collisions were effective (non-inertial) to the final regime where no collisions were effective (coating) except the collection of fines and binder droplets by larger granules as explained above.

Prediction of Critical Sizes. In order to use the above model for actual predictions, it is necessary to assign values to the relative velocity U_o ; this is, at the present level of knowledge, an extremely difficult task since, due to bubble motion (and perhaps the presence of fixed and moving internals in a fluid bed such as, for example, draft tubes) the particle movement in a fluidized bed is extremely complex. Some crude estimates of the relative velocity between particles have been made (Ennis et al., 1991) and these were expressed as

$$\text{Eq. (24)} \quad U_{o \text{ ave}} = \frac{12U_B a}{D_B d^2} \quad \text{and} \quad U_{o \text{ max}} = \frac{12U_B a}{D_B}$$

where U_B is the bubble velocity, D_B is the bubble diameter and δ is the dimensionless bubble spacing. Using the above velocities and the conditions shown in Fig. 23, one can calculate the limiting granule sizes when the process crosses over the boundaries between different granulation regimes:

$$\text{Eq. (25)} \quad a_{N-I} = \sqrt{\frac{9m \left(1 + \frac{1}{e}\right) \ln \frac{h}{h_a}}{\frac{48 \mathbf{r}_p U_B}{D_B}}} \quad \text{and} \quad a_{I-C} = \mathbf{d} a_{N-I}$$

A schematic representation of the different regimes, their characteristics and the transition sizes are shown in Fig. 24. It can be seen that only in the inertial regime does binder viscosity, surface tension, or both have a significant effect on coalescence rates. As an illustration of the above classification and of the critical sizes calculated from Eq. (25), results from a fluid bed granulation experiment are reproduced here (Ennis et al, 1991). During this work, fine glass powder was granulated using two polymeric binder solutions which had similar surface tensions and very different viscosities: the CMC-Na(M) binder = 1.7 poise while the PVP = 0.36 poise. The results are shown in Fig. 25; three regimes of granulation are clearly observed. For the initial several hours with average granule diameters less than about 800 microns, similar rates of growth were observed for both binders, i.e., the granulation proceeded in the non-inertial regime where growth rates are independent of viscosity. In the later half of the granulation, lower binder viscosity (PVP) granule growth began to slow compared to CMC-Na, implying transition to the inertial regime (see Fig. 25). Finally PVP granule growth began to level off somewhat in excess of 900 microns indicating a transition to the coating regime. At the same time CMC-Na binder growth continued unabated, indicating non-inertial granulation throughout the run due to the higher viscosity of the binder.

Using the characteristic parameters shown in the figure, critical transition diameters were calculated. The values obtained were 570 microns for transition from non-inertial to inertial and 1140 microns from inertial to coating, and are seen to be within a factor of 1.5–2 of the experimental data which, in view of the approximate nature of these calculations, is quite remarkable. The constant rate of growth in the non-inertial regime also implies that only growth by nucleation occurred and that coalescence (see Fig. 12) was not prevalent.

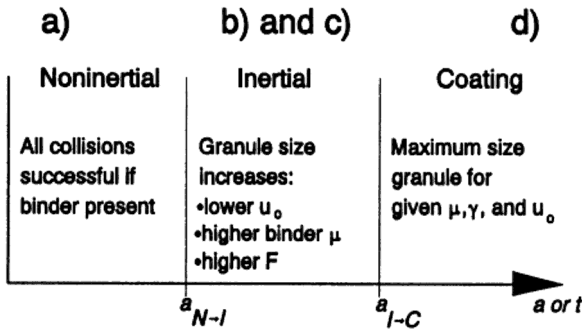
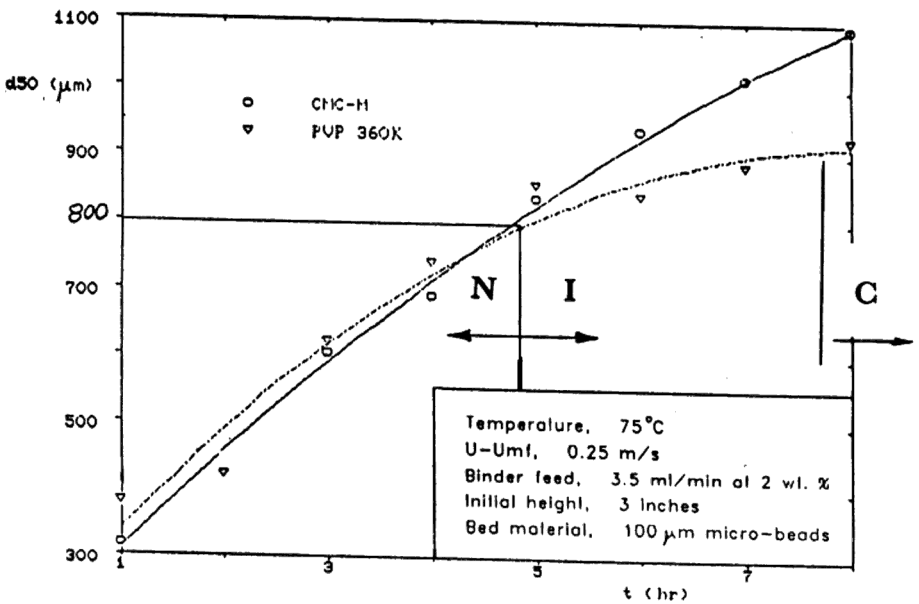


Figure 24. Schematic representation of transitions between granulation regimes.



Data : $h=10 \mu\text{m}$; $h_s=0.5 \mu\text{m}$; $e=1$
 $\mu=2 \text{ Poise}$; $U_s=50 \text{ cm/sec.}$; $D_R=2 \text{ cm}$

Figure 25. Experimental data from fluidized bed granulation. (From Ennis, et al., *Powder Technol.*, 65:257-272, 1991, with kind permission from Elsevier Science S.A., P.O. Box 564, 1001 Lausanne, Switzerland.)

To illustrate transition of growth from nucleation to coalescence, a result obtained by Ritala et al., (1986 and 1988) is shown in Fig. 26, while the characteristics of the binders used are given in the table above the figure. From the growth rate, which is seen to be independent of both viscosity and surface tension, one concludes that all granulation proceeded in the non-inertial regime. The growth rate however increased significantly as soon as the liquid saturation reached values close to 100% ($S = 1$, capillary state) implying that, under conditions of high saturation, the granule surface became soft enough to allow large granules to stick and grow by coalescence. This was not possible in the run shown in Fig. 25 because binder was added very slowly and the condition of sufficient surface softening was never reached in any particular region of the spray zone.

An important point needs to be stressed here concerning control of the final granule size in an agglomerator. In the vast majority of cases, the process is run in the non-inertial regime, i.e., in the regime where granule growth is controlled by the presence of binder and hence final granule size is determined by the total granulation time. This means that granulation is stopped or quenched somewhere at or before the point where the large increase in growth rate occurs (for $S < 1$) as seen in Figs. 15 and 26. In fluid bed granulation, this is a preventive measure to avoid de-fluidization due to excessive granule growth and has the drawback of generating a wide particle size distribution of the produced granules. Clearly, allowing the bed to reach the coating regime would yield a much more uniform distribution but, due to the relatively low shear forces in the bed, this equilibrium diameter is usually much too large to maintain homogeneous fluidization. Many different proposals to increase shear forces in the fluid bed have been put forward lately, some by introducing agitators with others using jets, in an effort to let particles reach the critical coating size, a_{LC} , and thereby improve the size distribution of the product. The recent development of high shear mixer/granulators (see, for example, Fig. 9b) which also employ fluidization are a good example of new machines which combine the advantages of both processes to ensure flexibility and uniform size.

Wet Granule Deformation and Break-Up. It would appear from the above analysis that once granules reach the critical size characteristic of the coating regime, any further increase in the Stokes number or relative velocity will maintain the size of the granules. This is certainly true for the case in which binder drying and solidification accompany growth and granule strength increases appropriately as large granules are formed. However, for this to

Binding agents and characteristics of the aqueous solutions used in the granulation experiments

Trade name	Composition	Concentration g w/w	Viscosity ¹⁾	Surface ²⁾
			mPa.s (30 °C)	tension mN.m ⁻¹ (25 °C)
Kollidon 90	PVP	3	9	68
		5	31	68
		8	109	68
Kollidon 25	PVP	3	1	68
		20	10	67
Kollidon VA64	PVP/PVA copolymer	3	1	50
		10	4	50
		20	15	47
		30	27	46
Methocel E5	HPMC	3	6	48
		6	43	48
		8	91	48
Methocel E15	HPMC	2	11	50
		3.5	59	48
		4.5	119	47

1) Viscosity determined by a Brookfield Viscometer, Type LVT.

2) Surface tension determined by drop weight method

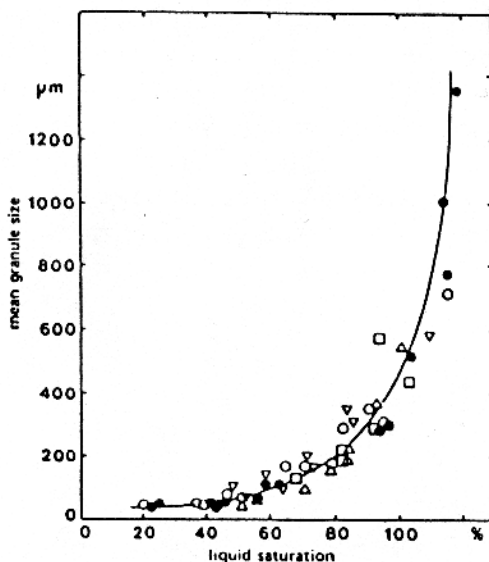


Figure 26. The effect of liquid saturation on mean granule size (Ritala et al. 1988). (Reprinted from *Drug Development and Industrial Pharmacy*, p. 1048, courtesy of Marcel Dekker, Inc.)

happen, one has to tailor both the binder characteristics and the heating (or cooling) rate in the agglomerator very carefully so as to achieve the required properties in the optimal time frame. This is both desirable and possible, and an instrument and procedure are described in the next section to achieve this.

We present, in this section, a simplified model which accounts for the behavior of “green,” i.e., non-solid granules. It is assumed that these green or “wet” agglomerates, upon formation, possess only the strength imparted to them by the liquid bridges which assured coalescence in the first place. However, they have had no opportunity to strengthen significantly, either due to lack of time or to the fact that the binder did not become more viscous (for example, an oily surfactant which does not evaporate or solidify). In such cases, granule strengthening is achieved by liquids being absorbed into inner pores of the granules or by the addition, at the end of the granulation run, of adsorbing fine powders (flow aids) to serve as adsorption sites; these processes are usually quite slow. One is then left, within the shearing powder mass, with deformable granules which can grow by layering but which can also deform and break.

An example of this kind of granulation is given here from the work of Tardos et al. (1991), where the rapid transition from the non-inertial to the coating regime is shown and the conditions of granule deformation are measured. The experiment was performed by introducing large droplets of a very viscous binder (concentrated polymer solution) in a fluidized bed of glass powder. Due to the high viscosity of the binder droplet, it was possible to ensure that it remained intact in the powder and it captured fines in a non-inertial layering mode (see Fig. 12d) until it was totally filled with powder; further growth was then achieved by layering in the coating regime. The maximum size of the granules obtained could be calculated from the equation:

$$\text{Eq. (26)} \quad a_g = a_d e^{-1/3}$$

where a_d is the droplet size and e is the powder void fraction. Equation (26) is based on the assumption that liquid fills all voids. It was found that keeping the binder concentration high enough (see Fig. 27), i.e., keeping the viscosity high and hence reducing the characteristic Stokes number, indeed yielded agglomerates of the calculated size. However, at lower concentrations (implying lower binder viscosities), only smaller granules could survive which were found to be spherical as were the larger granules. This was

assumed to mean that although the original granules were broken, a new equilibrium size was reached at the lower viscosity. Equating the Stokes number $St = St^*$ and using the definition in Eq. (20), a linear dependency of the equilibrium size on viscosity is obtained.

$$\text{Eq. (27)} \quad a_g = \frac{9 m St^*}{8 r_p U_o}$$

This dependency was also drawn onto Fig. 27 and, as can be seen, the particle sizes measured during this experiment fall more or less on the theoretical line; further lowering of the viscosity yielded no agglomerates, as expected.

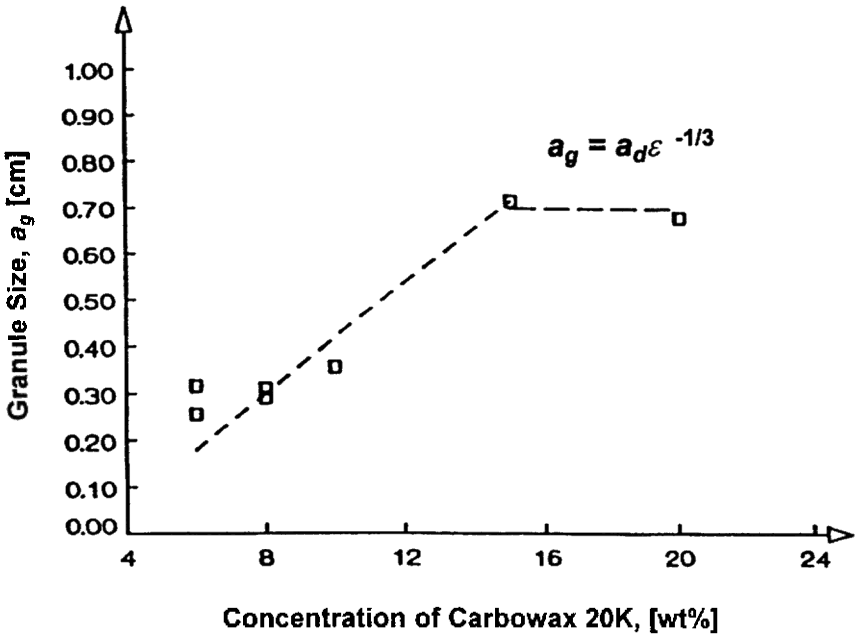


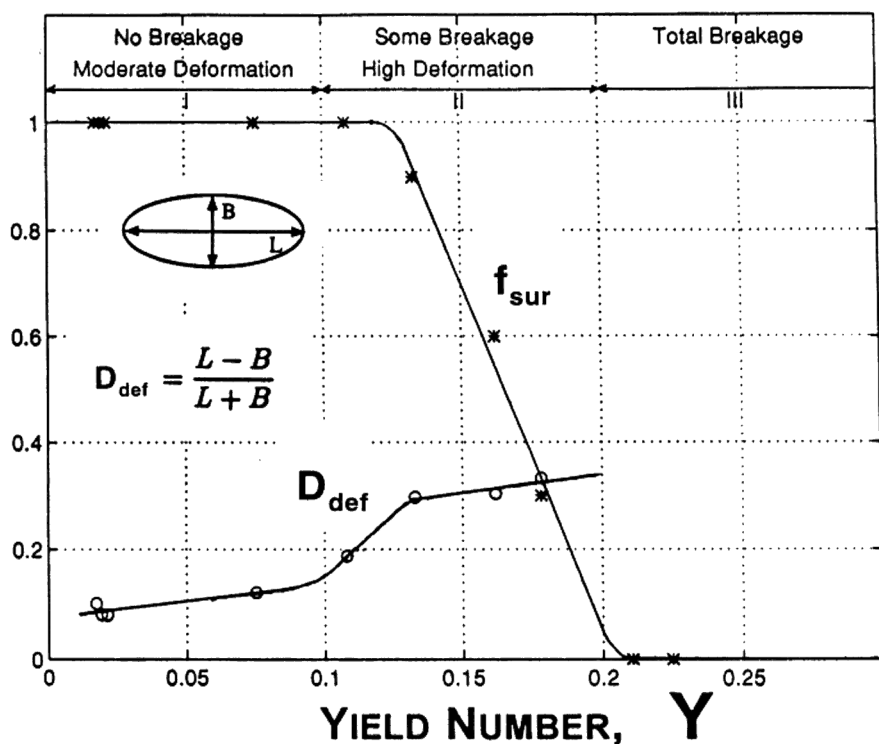
Figure 27. Granule size vs. binder concentration for drop granulation in a fluidized bed.

A somewhat more sophisticated version of the above experiment was carried out recently by Tardos and Khan (1995) and Tardos et al. (1997). To insure that the shear field in the granulator is constant and uniform, a fluidized bed Couette device was used in which a bed at minimum fluidization conditions was sheared between two concentric, rotating rough walled cylinders. Granules of glass powder using different viscosity Carbowax (PVP) solutions were formed, sheared in the device and subsequently allowed to solidify in a shear free environment. In addition to size and shape, the yield strength, t_o , of the wet or “green” granules was also measured separately. It was found that a dimensionless quantity defined as the ratio of inertial and yield forces called the Yield number

$$\text{Eq. (28)} \quad Y = \frac{r_p \Gamma^2 a^2}{t_o}$$

delimitates regions in which no deformation occurs and regions in which the granules are totally destroyed; the experimental data is given in Fig. 28. In Eq. (28) and Fig. 28, Γ , is the shear rate, the parameter f_{sur} is the fraction of surviving granules while D_{def} is the coefficient of deformation which gives $D_{def} = 0$ for a sphere. The important finding here is that beyond a Yield number of about $Y = 0.2$, no “green” agglomerates survived.

The correlation of the Yield number to the Stokes number defined earlier is not straight forward but, assuming that the shear rate is $\Gamma = U_o/a$ and that the yield strength t_o , of a green granule is a function of the binder viscosity only (the assumption is that the granule is a highly concentrated suspension of small particles), one can define an upper limit for the Stokes number from Eq. (28) beyond which no agglomerates can survive. Slightly before this critical condition is reached, elongated agglomerates form which appear to be in equilibrium at steady state. What was not found, surprisingly enough, is the existence of stable spherical agglomerates at lower binder viscosities as was the case in the fluid bed experiment described above. This seems to suggest that a fluidized bed is far from being homogeneous and the rolling motion of granules entrained by bubbles allows the formation of stable, spherical sizes from larger granules which were broken apart previously. Simple, constant shear in the Couette granulator, on the other hand, causes stable, spherical or elongated (deformed) granules to form depending on their overall yield strength and subsequent breakup if the shear rate is increased or the viscosity (yield strength) is decreased below a certain value.



$$f_{sur} = \frac{\text{Number of Surviving Granules}}{\text{Initial Number of Granules}}$$

Figure 28. Deformation and breakup of “green” granules in a constant shear device.

Critical Binder Strengthening Times. An essential condition for successful granulation is the production of final granules which gain sufficient strength that they do not fall apart once they are formed. This is achieved in fluid bed granulation by choosing an appropriate binder which generates bridges that strengthen in time due to either solvent evaporation or cooling of the melt. In both cases, strengthening is a result of increases in binder viscosity and, therefore, depends on the binder chemistry as well as on the heat and mass transfer rates in the fluid bed. Extensive research showed

that, in general, rates of heat and mass transfer in a fluid bed granulator are quite high and, hence, the choice of the appropriate binder chemistry is crucial.

In order to test binders and measure their strengthening rates, the instrument shown schematically in Fig. 29 was developed (Ennis, 1990; Ennis et al., 1990 a, b; Tardos et al., 1993; Tardos, 1994). It is essentially a force transducer and an oscillating mechanism activated by an electric motor and mounted in the view of a projection microscope. Two powder granules are mounted (glued) onto the transducer and the oscillating arm, as shown in the figure. A droplet of binder is inserted between the two particles and a pendular bridge is formed. The oscillator is put in motion and the bridge strength is recorded as a function of time. The amplitude as well as the frequency of oscillation and the bridge temperature can be changed independently.

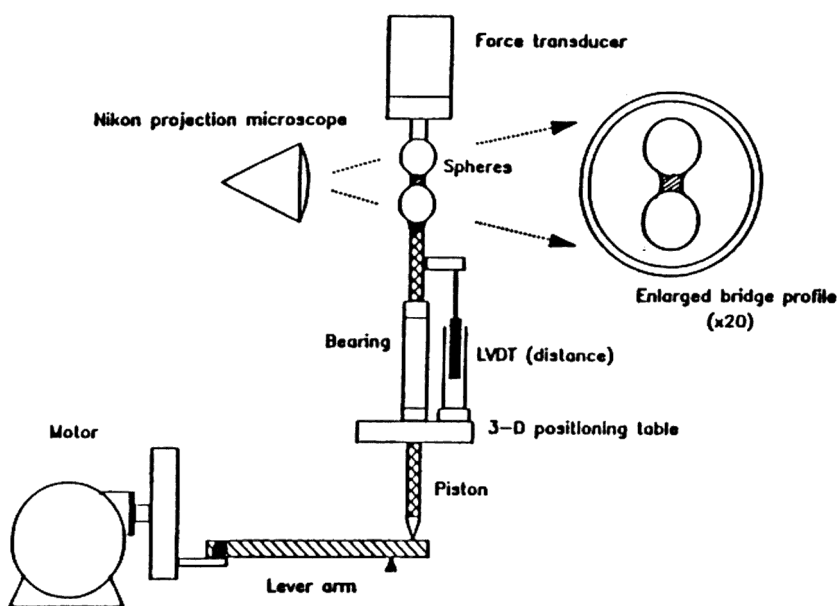


Figure 29. Schematic diagram of the pendular bridge apparatus. (From Ennis, et al., *Chem. Eng. Sci.*, 45:3071–3088, 1990, with kind permission from Elsevier Sciences Ltd., The Boulevard, Langford Lane, Kidlington OX5 1GB, UK.)

A characteristic plot of the maximum force measured by the transducer versus oscillation time is given in Fig. 30 for a CMC-Na bridge from which water is being evaporated. The corresponding concentration of the polymer solution is given on the upper abscissa. As seen, the force increases from an initial value which can be calculated from Eq. (17) to a maximum value after which the mostly solidified bridge ruptures (after 9 minutes for the case seen in Fig. 30). Both, the maximum force and the critical bridge rupture time, are important for granulation but it was found that the critical strengthening time had to be within very narrowly defined limits for the granulation to be successful.

It was shown over many granulation runs (Ennis, 1990 and Tardos, 1995) that the critical bridge rupture time, as determined above, has to be slightly less than one-half of the total granulation time in a mixer type granulator such as for example a drum or a high shear mixer. Since in a fluid bed granulator, binder is added over most of the granulation run (to compensate for evaporation, as explained in a previous section) "total granulation time" is the time necessary for the granule to grow to its final size. Since larger granules in a fluid bed fall to the bottom due to segregation, the granulation time in this case can be taken as the period spent by the particles in the spray zone.

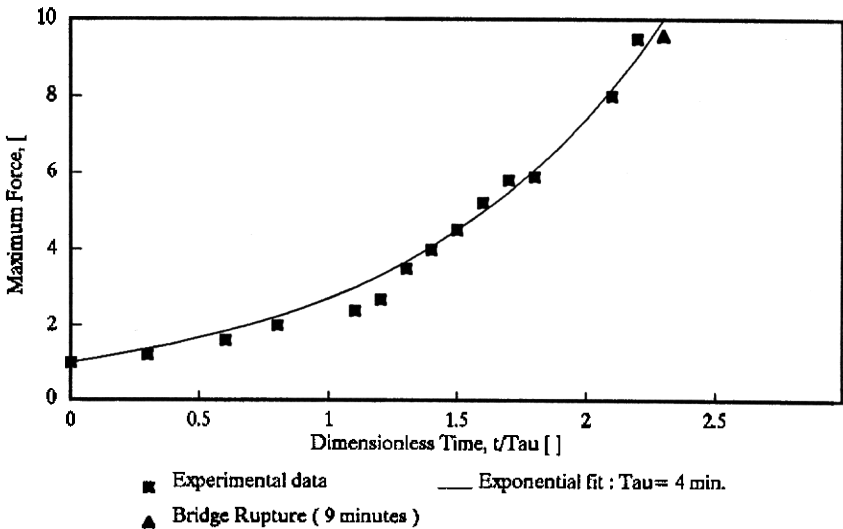


Figure 30. The time-strengthening behavior of a CMC-Na liquid bridge.

The above findings are quite significant since they indicate a clear way to design solvent evaporation in the bed when the binder is a solution or the cooling time when the binder is a melt. One has to stress, however, that the above estimates are probably not very general and may require corrections for different pairs of powders and binders. Since the experimental procedure and the instrument are quite simple and straightforward to use, such measurements should be easy to perform for each specific case.

3.5 Granule Consolidation, Attrition and Breakage

Characterizing Fracture Properties of Particulate Systems. A granule may be viewed as a nonuniform physical composite of primary particulate material, or grains. It possesses certain macroscopic mechanical properties, such as anisotropic yield stress and inherent flaw distribution. It has long been realized that materials, especially brittle ones, can fail by the propagation of cracks which act as points of stress concentration. Therefore, the failure stress of a granule may differ significantly from its true yield stress, which is more a function of inherent bond strength. Therefore, bulk attrition tests of granule strength measure both the inherent bond strength of the granule as well as its flaw distribution. In addition, the mechanism of granule breakage or attrition often is a strong function of materials properties of the granule itself, as well as the type of loading used in the mechanical testing. Thus, there is often appreciable variation in the results of different tests, which may also be different from the observed breakage in actual process handling.

The approach taken here is to employ standard materials characterization tests to measure the materials properties of the granulated product. With this information, the mechanism of attrition, i.e., breakage versus erosion, is determined. The rate of attrition can then be related, semi-empirically, to material properties of the formulation and the operating variables of the process, such as bed depth and fluidizing velocity.

It is inherently difficult to measure the “strength” of a material since this is strongly influenced by the microstructure of the material, i.e., the distribution of flaws which strongly influence the propagation of cracks. This concept is illustrated in Fig. 31, where the elastic stress distribution in an ideally elastic, brittle material is seen to become infinite as the crack tip is approached. The key properties which characterize the strength of a material are:

- (i) Fracture toughness, K_c , which is a measure of a material's ability to resist crack propagation
- (ii) The size of the process zone, r_p , which is a measure of the natural flaw size of the material
- (iii) The true yield stress of the material, s_y

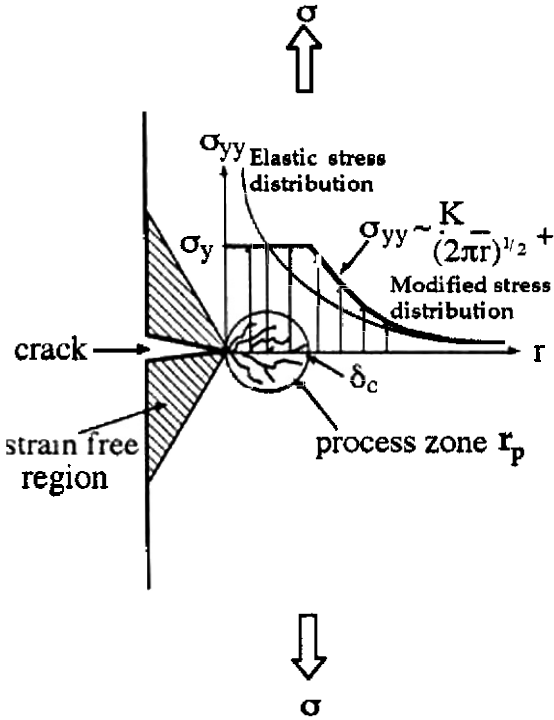


Figure 31. The stress distributions on a cracked half-plane loaded at infinity. (From Ennis and Sunshine, *Tribology Int.*, 26:319–327, 1993, with kind permission from Elsevier Sciences Ltd., The Boulevard, Langford Lane, Kidlington OX5 1GB, UK.)

In order to ascertain these properties in a reproducible manner, very specific test geometry must be used since it is necessary to know the stress distribution at predefined, induced cracks of known length. For example, the measured tensile or compressive strength of a series of glass bar

specimens each with identical geometry and material will have a wide scatter whereas the fracture toughness will not. This scatter is due to the wide variation of flaws and not the inherent strength of the material itself.

Using the picture shown in Fig. 31, the fracture toughness defines the stress distribution in the body just before fracture and is given by:

$$\text{Eq. (29)} \quad K_c = S_f \mathbf{s}_f \sqrt{\mathbf{p} \, c}$$

where \mathbf{s}_f is the applied fracture stress, c is the length of the crack in the body and S_f is a shape factor to account for the different geometries of the specimens. Since the elastic stress cannot exceed the true yield stress of the material, there is a region of local yielding at the crack tip known as the *process zone*. The characteristic size of this zone, r_p , is given by:

$$\text{Eq. (30)} \quad r_p = \lim_{\mathbf{s}_{yy} \rightarrow \mathbf{s}_y} \frac{1}{2\mathbf{p}} \left[\frac{K_c}{\mathbf{s}_{yy}} \right]^2 = \frac{1}{2\mathbf{p}} \left[\frac{K_c}{\mathbf{s}_y} \right]^2$$

The above results are derived from linear elastic fracture mechanics and are strictly valid for ideally brittle materials with the limit of the process zone size going to zero. In order to apply this simple framework of results, Irwin (1957) proposed that the process zone, r_p , be treated as an effective increase in crack length, \mathbf{d}_c . With this modification, the fracture toughness becomes

$$\text{Eq. (31)} \quad K_c = S_f \mathbf{s}_f \sqrt{\mathbf{p} (c + \mathbf{d}_c)} \quad \text{with } \mathbf{d}_c \sim r_p$$

As discussed above, because materials often fail by the propagation of cracks, particularly brittle ones, it is difficult to measure the true yield stress, \mathbf{s}_y , of a material. Instead one measures a fracture stress, \mathbf{s}_f , which is related to the size of the process zone and actual crack length by:

$$\text{Eq. (32)} \quad \frac{\mathbf{s}_f}{\mathbf{s}_y} = \sqrt{\frac{r_p}{c}}$$

Equation (32) clearly illustrates the point that as r_p becomes very small relative to c , i.e., for large cracks, the fracture stress may be orders of magnitude smaller than the true yield stress of the material.

The final fracture property of interest here is the critical strain energy release rate, G_c . This is the energy equivalent to fracture toughness. The energy analysis of fracture was the original approach to fracture mechanics first proposed by Griffith (1920). Fracture toughness and critical strain energy release rate are related by:

$$\text{Eq. (33)} \quad G_c = \frac{K_c^2}{E}$$

As stated previously, in order to determine fracture properties in a reproducible manner, very specific test geometry must be used. Two traditional methods for measuring fracture properties are the three point bend test and the indentation fracture test. In the case of the three point bend test, toughness is determined from the variance of fracture stress on induced crack length given by Eq. (31). For the indentation test, one can determine the hardness, H , from the area of the residual plastic impression, A , and the indentation load, P . The fracture toughness can be determined from the hardness and the length of cracks propagating from the indentation as a function of P . The following relationships are used for determining H and K_c from the indentation tests:

$$\text{Eq. (34)} \quad K_c = b \sqrt{\frac{E P^2}{H c^3}} \quad \text{and} \quad H \sim \frac{P}{A}$$

The Relationship Between Fracture Mechanics and Granule Attrition. Fracture properties play a very significant role in a variety of phenomena involving particles and granules. These properties control breakage and wear of particles in fluidized beds. Table 5 compares some fracture properties of some typical agglomerated materials. When comparing the values in Table 5 to those found for typical polymers and ceramics, we can make the following generalizations:

- (i) Fracture toughness is less than for typical polymers and ceramics
- (ii) Critical strain energy release rates are typical for ceramics but much less than for polymers
- (iii) The process zone sizes are large and typical for polymeric materials
- (iv) Critical displacements of 10^{-7} – 10^{-8} are typical for polymers while 10^{-9} is more typical of ceramics.

Table 5. Comparison of Fracture Properties of Agglomerated Materials

	ID in Figure 32	K_{Ic} (Mpa m ^{1/2})	G_{c} (J/m ²)	δ_{c} (μm)	E (MPa)	G_{c}/E (μm)	r_{p} (mm)	x_{c} (mm)
Bladex 60 ¹	B60	0.070	3.0	340	567	5.29	0.410	28.0
Bladex 90 ¹	B90	0.014	0.96	82.7	191	5.03	0.003	0.17
Glean ¹	G	0.035	2.9	787	261	11.1	0.083	5.50
Glean Aged ¹	GA	0.045	3.2	3510	465	6.88	0.130	8.80
CMC-Na(M) ²	CMC	0.157	117.0	641	266	440	0.260	17.0
Klucel GF ²	KGF	0.106	59.6	703	441	135	0.600	40.0
PVP 360K ²	PVP	0.585	199.0	1450	1201	166	0.510	34.0
CMC 2% 1kN ²	C2/1	0.097	16.8	1360	410	41.0	0.100	7.00
CMC 2% 5kN ²	C2/5	0.087	21.1	1260	399	52.8	0.081	5.40
CMC 5% 1kN ²	C5/1	0.068	15.9	231	317	50.2	0.170	11.0

To summarize, we can say that granulated materials should behave in a brittle manner, similar to a ceramic, in the sense of having small yield strains and small critical displacements but their behavior should also be ductile, similar to polymers, in the sense of having large process zones. The consequence of having large process zones is important since it implies that

two colliding granules are capable of absorbing elastic energy through plastic deformation thereby dissipating gross fracture. On the other hand, the energy dissipation within the process zone is expected to occur via diffuse microcracking, as would be the case for ceramic materials. The size of the process zone plays an important role in determining the mechanism of attrition. There exists a critical specimen size, x_c , for a granule which has been shown to be related to the process zone size (Ennis and Sunshine, 1993), by the following approximate relationship

$$\text{Eq. (35)} \quad x_c \sim 60 r_p$$

If a granule is smaller than x_c , then there is insufficient granule volume to concentrate enough elastic energy to propagate a gross fracture during a collision. When this is the case the most likely mechanism of attrition is one of wear or erosion. On the other hand, when the granule size is larger than x_c , gross fracture or breakage of the granule is much more likely to occur during collision. From the data presented in Table 5, it appears that the dominant mechanism for attrition should be wear or erosion for all the granules listed with the exception of Bladex 90 DF, which would appear to be susceptible to gross fracture during collision. This concept is investigated further below.

By considering wear to occur by the intersection of subsurface lateral cracks which depend on the load and material properties, Evans and Wilshaw (1976) determined the volumetric wear rate, V_{wear} , to be

$$\text{Eq. (36)} \quad V_{wear} = \frac{d^{1/2}}{A^{1/4} K_c^{3/4} H^{1/2}} P^{5/4} l$$

where d is the indenter diameter, P is the applied load, l is the wear displacement and A is the apparent area of contact of the indenter. This result implies a very specific dependence of wear rate on fracture toughness and hardness. The dependence of these two material properties, as predicted by Eq. (36), is compared in Figures 32 and 33 for bar wear rate and erosion in a fluidized bed. It is interesting to note that the wear rates of materials with radically different structures (polymer-glass vs. herbicide formulated granules) collapse onto the single line, predicted by Eq. (36).

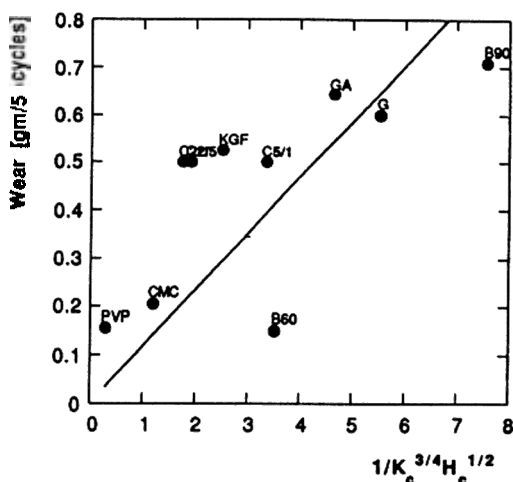


Figure 32. Bar wear rate as a function of material properties. (From Ennis and Sunshine, *Tribology Int.*, 26:319–327, 1993, with kind permission from Elsevier Sciences Ltd., The Boulevard, Langford Lane, Kidlington OX5 1GB, UK.)

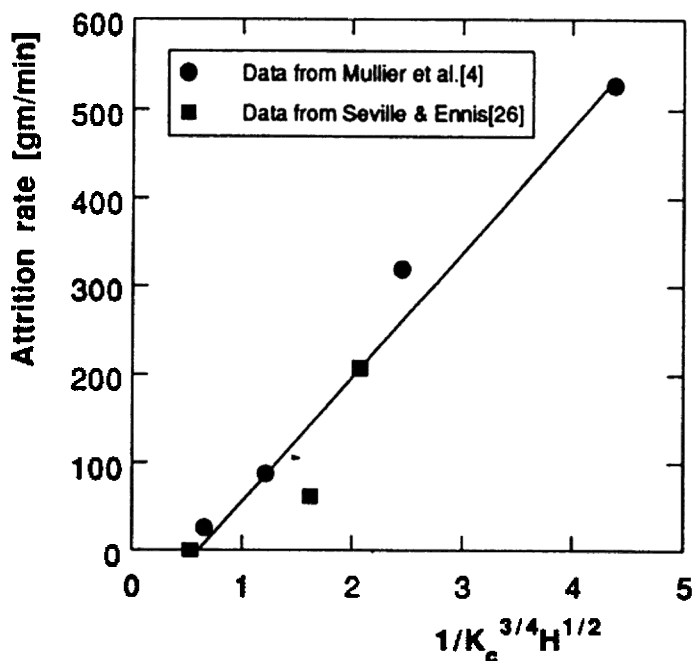


Figure 33. Fluidized bed erosion rate as a function of material properties. (From Ennis and Sunshine, *Tribology Int.*, 26:319–327, 1993, with kind permission from Elsevier Sciences Ltd., The Boulevard, Langford Lane, Kidlington OX5 1GB, UK.)

There are cases when the dominant mechanism of attrition is not granule erosion. This occurs when the process zone is small in comparison to the granule size and leads to granule fracture or breakage becoming the dominant attrition mechanism. This mechanism of attrition is observed for Bladex 90 DF. Although, this mechanism has not been studied as much as erosion, related work by Yuregir et al. (1987) on crystal attrition, has shown that the volumetric wear rate for breakage, $V_{breakage}$, is given by:

$$\text{Eq. (37)} \quad V_{breakage} = \frac{H}{K_c^2} \mathbf{r}_c U_i^2 a_c$$

where a_c is the crystal length, \mathbf{r} is the crystal density, and U_i is impact velocity. It is interesting to note that hardness plays an opposite role for breakage than it does for wear, primarily due to the fact that it concentrates stress for fracture. In addition, breakage rate is a stronger function of toughness.

Controlling Breakage in Granulation and Coating Processes. The parameters which, in general, control the attrition occurring in granulation and coating equipment are given in Table 6. From Eqs. (36) and (37), it can be shown that expressions for breakage and wear in fluidized beds are given by:

$$\text{Eq. (38)} \quad V_{wear}^{fb} \sim \frac{h_b^{5/4}}{K_c^{3/4} H^{1/2}} (U - U_{mf})$$

$$\text{Eq. (39)} \quad V_{breakage}^{fb} \sim \frac{H}{K_c^2} \mathbf{r}_p (U - U_{mf})^2$$

Both fracture toughness, K_c , and hardness, H , are strongly influenced by the compatibility of the binder with the primary particles. However, these material properties also are a very strong function of granule voidage. Therefore, both hardness and toughness increase with decreasing voidage and are strongly influenced by previous consolidation of the granules. From Eqs. (38) and (39) above, it is clear that increased fluidization velocity and bed height will increase both the wear and breakage of dried granules. However,

these same process variables may act to increase consolidation, lower the granule voidage and therefore counteract, to some extent, the breakage of the granules.

Table 6. The Effect of Operating Variables on Attrition in Granulation Processes

Properties which Minimize Attrition	Effects of Operating and Formulating Variables
Increase fracture toughness or strain energy release rate	Strongly influenced by formulation and compatibility of binder with primary particles Can be influenced in processing by modifying granule voidage
Increase hardness for wear Decrease hardness for breakage	Strongly influenced by formulation and compatibility of binder with primary particles. Can be influenced in processing by modifying granule voidage
Decrease load and contact displacement for wear Decrease impact velocity for breakage	Decrease bed height to effect load and decrease excess gas velocity to lower collision frequency and mixing and therefore contacting. Decrease excess gas velocity, also distributor plate design may be modified.

3.6 Modeling of Granulation Processes

Most process engineering problems involve mass and energy balances. However, in particulate processes, especially in cases where particle number rather than mass is of primary importance, a balance over the population of materials of a given size in the system is often necessary. This is particularly

true of granulation systems where the size distribution, in addition to granule structure and voidage, is a key property of the final product. The population balance is a statement of continuity that describes how the particle-size distribution changes with time and position. It is widely used to model particle formation and growth in a variety of processes such as crystallization (Randolph & Larson, 1988), granulation (Adetayo et al. 1995), pelletization (Sastri & Fuerstenau, 1973) and aerosol reactors (Friedlander & Wang, 1966; Landgrebe & Pratsinis, 1989). A review of the various applications of the population balance is given by Ramkrishna (1985).

The population follows the change in the granule size distribution as granules are born, die, grow, or enter or leave a control volume, as illustrated in Fig. 34. The number of particles between volume v and $v + dv$ is $n(v)dv$, where $n(v)$ is the number frequency size distribution, or the number density. The population balance for granulation is then given by

Eq. (40)

$$\frac{\partial n(v, t)}{\partial t} = \frac{v_i n_i(v)}{N} - \frac{v_e n_e(v)}{N} - \frac{\partial(G - V)n(v, t)}{\partial v} + \left[\frac{B n_B(v)}{N} \right]_{nuc} \\ + \frac{1}{2 N_t} \int_0^v \mathbf{b}(u, v - u, t) n(u, t) n(v - u, t) du - \frac{1}{N_t} \int_0^\infty \mathbf{b}(u, v, t) n(u, t) n(v, t) du$$

The left-hand side of Eq. (40) is the accumulation of particles of a given size. The terms on the right-hand side are, in turn, the bulk flow into and out of the control volume, the convective flux along the size axis due to layering and attrition, the birth of new particles due to nucleation, and birth and death of granules due to coalescence.

The granule size distribution (GSD) is a strong function of the balance between different mechanisms for size change—nucleation, layering, coalescence, attrition by erosion, and attrition by breakage (see Fig. 35). For example, Fig. 36 shows the difference in GSD for a doubling of the mean granule size due to (i) layering only, or (ii) due to coalescence only.

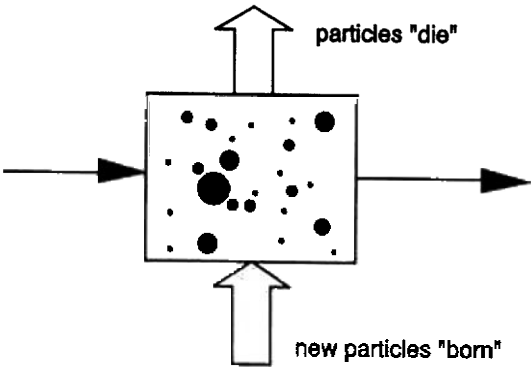


Figure 34. Control volume for performing a number balance on granules. (From Litster and Ennis, 1994.)

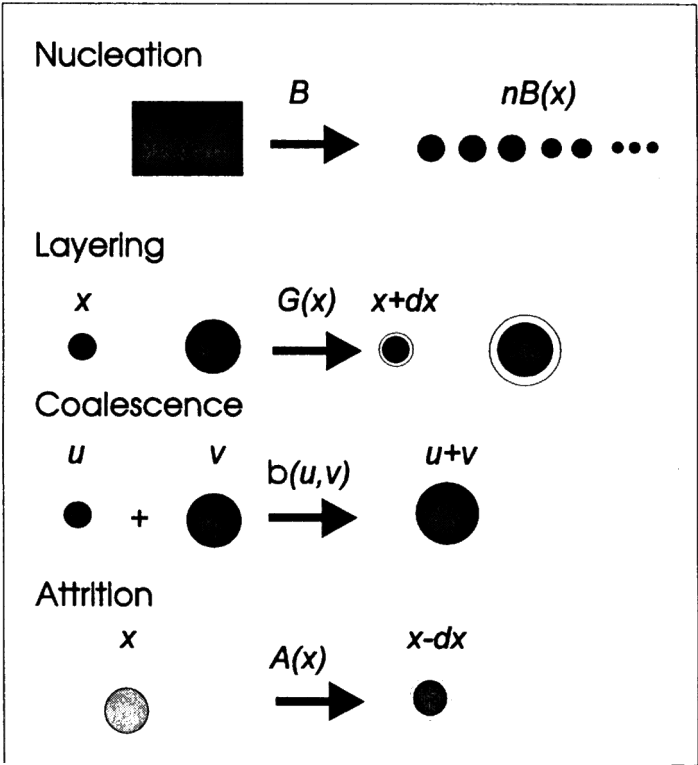


Figure 35. Granule growth mechanisms for population balance modeling. (From Litster and Ennis, 1994.)

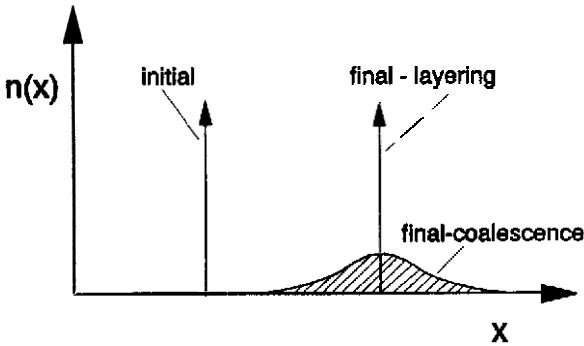


Figure 36. Contrast in granules size distribution due to layering vs. coalescence. (From Litster and Ennis, 1994.)

Modeling Individual Growth Mechanisms. Table 7 highlights the impact of the various mechanisms of size change on the granule size distribution, as well as the relevant governing equations. We discuss the mechanisms each in turn here. *Nucleation* increases both the mass and number of the granules. For true nucleation, new granules are produced by liquid feed which dries or solidifies. For ideal wetting, the size distribution and rate B of nucleation are determined by the new feed droplet size and the spray rate S , as given in Table 7. In practice, however, the nucleation process is a strong function of the wetting properties of the powder, as described above. In processes where new powder feed has a much smaller particle size than the smallest granular product, the feed powder can be considered as a “continuous phase” which can nucleate to form new granules (Sastrý, 1975). In this case, the size of the new granules is chosen arbitrarily, and the nucleation rate B must be determined empirically.

Layering is the mechanism which increases granule size by the layering of new material onto existing granules. As with nucleation, the new feed may be in liquid form (where there is simultaneous drying or cooling) or as a fine powder. Where the feed is a powder, the process is sometimes called pseudo-layering or snowballing (Sastrý, 1975). It is often reasonable to assume that the linear growth rate $G(x)$ is independent of granule size, e.g., see Fig. 37 from Capes (1967). Size independent linear growth rate implies that the volumetric growth rate $G^*(v)$ is proportional to granule surface (or projected) area, i.e., this assumption is true only if all granules receive the

same exposure to new feed. Any form of segregation will invalidate the assumption (Liu and Litster, 1991). The growth rate by layering only can be calculated directly from the mass balance, as given in Table 7, where V_{feed} is the volumetric flow rate of new feed and ϵ is the granule porosity.

Table 7. The Effect of Various Size Change Mechanisms on the Granule Size Distribution

Size Change Mechanism	Relevant Governing Equations	Reference and Comments
Nucleation	$B_{nB}(x) = S_{n_s}(x)$	Sastry (1975)
Layering	$V_{feed} = (1 - \epsilon) \int_0^\infty G(v) n(v) dv$	Sastry (1975)
Coalescence	Typical Growth Kernels: $\beta = \beta_o$	Kapur and Fuerstenau (1964) Size independent random kernel
	$\beta = \beta_o \frac{(u + v)^a}{(uv)^b}$	Kapur (1972) Size dependent preferential kernel
	$\beta = \beta_o \frac{(u^{2/3} + v^{2/3})}{(\frac{1}{u} + \frac{1}{v})}$	Sastry (1975) Balling of iron ore, limestone
	$\beta(u, v) = \begin{cases} k & , w < w^* \\ 0 & , w > w^* \end{cases}$ $w = \frac{(uv)^a}{(u + v)^b}$	Ennis and Adetayo (1994) Based on Stokes' Regime Analysis k - random rate growth constant w - harmonic average size w^* - critical cut-off volume

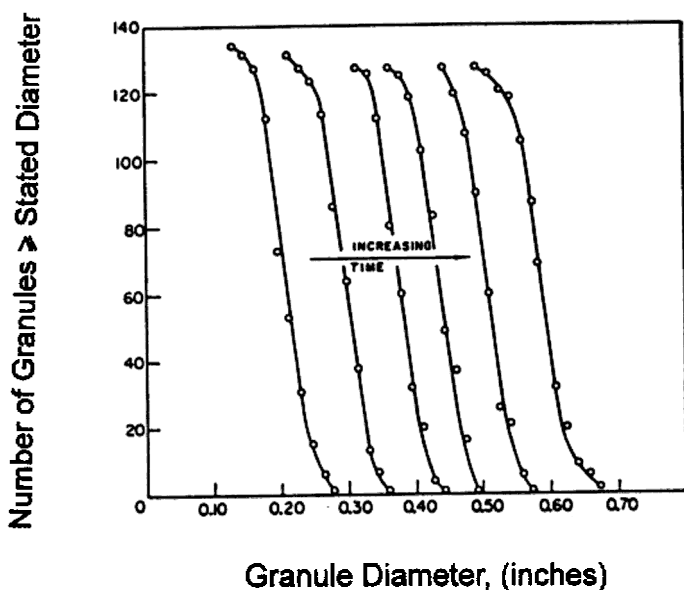


Figure 37. Size distribution of growing pellets by snowballing. (From Capes, 1967.)

Coalescence is the most difficult mechanism to model. It is easiest to write the population balance in terms of volume $n(v)$ because granule volume in a coalescence event is conserved. The key parameter is the coalescence kernel, $\mathbf{b}(u, v)$, which dictates the overall rate of coalescence, as well as the effect of granule size on coalescence rate. The order of the kernel has a major effect on the shape of the granule size distribution (Adetayo et al., 1995). No generalized kernel has yet received wide acceptance and several have been proposed and used (see Table 7). All the kernels are empirical, or semi-empirical and must be fitted to plant or laboratory data. The kernel proposed by Ennis and Adetayo (1994) is consistent with the granulation regime analysis described above and is, therefore, recommended. Note that in the non-inertial regime, where $St \ll St^*$, this kernel collapses to the simple size independent kernel, $\mathbf{b} = \mathbf{b}_o$, for which the mean granule size will increase exponentially with time. Figure 38 illustrates a comparison of the kernel of Ennis & Adetayo (1994) to a constant kernel. Note that deviation from the constant kernel occurs when the mean granule size approaches a critical value w^* , which represents the critical average granule size capable of rebound from a collision based on the Stokes' regime analysis given in Sec. 3.3 above. Figure 39 illustrates that the kernel of Ennis & Adetayo (1994) is also

capable of modeling the growth behavior of limestone (Kapur & Fuerstenau, 1964), which previously required multiple kernels to describe. Whatever the functional form, the magnitude of the kernel is a strong function of the liquid content, the unit particle size and the consolidation history of the granules (Iveson et al., 1995).

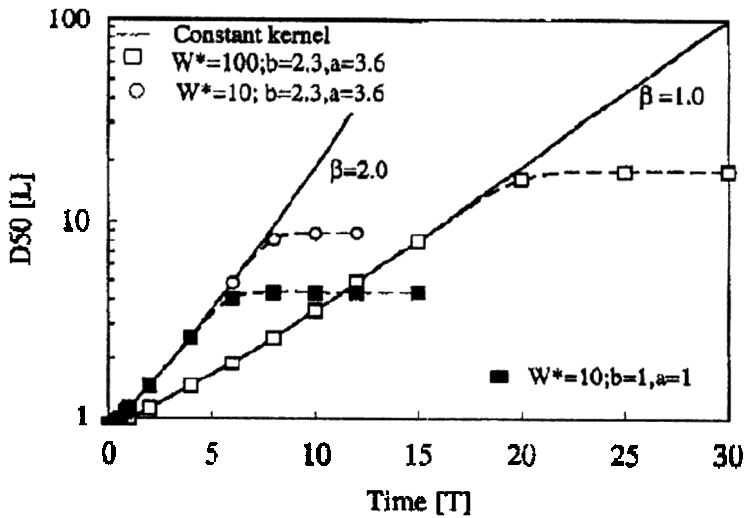


Figure 38. Comparison of cutoff kernel with random kernel. (From Adetayo and Ennis, 1996.)

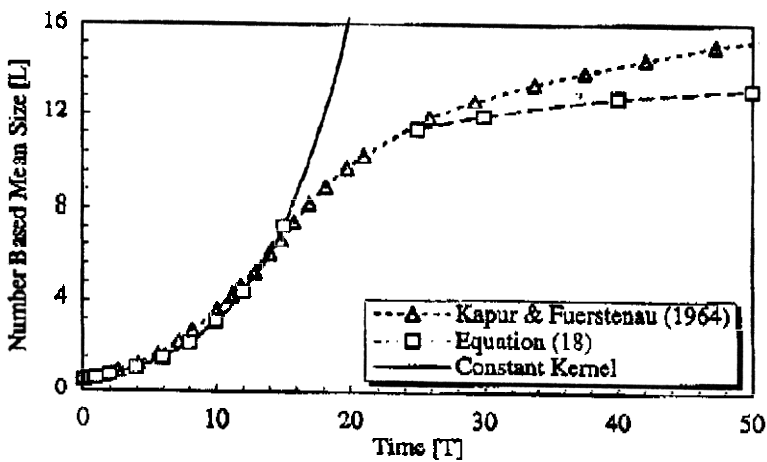


Figure 39. Modeling of the regimes of limestone granulation. (From Adetayo and Ennis, 1996.)

Attrition is the direct opposite of layering. It is a major mechanism when drying occurs simultaneously with granulation and granule velocities are high, e.g., fluidized beds and spouted beds. In a fluid bed, attrition rate is proportional to excess gas velocity and inversely proportional to granule fracture toughness, described earlier. Typical forms of attrition were given previously in Sec. 3.5.

Effect of Mixing. The degree of mixing within the granulator has an important effect on the granule size distribution. In general, the exit size distribution is broadened by good mixing in the granulator. In general, fluid-beds are modeled as well-mixed for granulation, and may either operate continuously with draw-off or batch. Some fluid-bed drying systems with simultaneous granulation may also be modeled as plug-flow. Spouted beds may be modeled as well mixed, with a two-zone model.

Solutions of the Population Balance. Solution of the population balance is not trivial. Analytical solutions are available for only a limited number of special cases. Table 8 lists analytical solutions for some special cases of practical importance. In general, analytical solutions are only available for specific initial or inlet size distributions. However, for batch coalescence, at long times the size distribution may become “self preserving.” The size distribution is self preserving if the normalized size distributions at long times are independent of mean size:

$$\text{Eq. (41)} \quad \mathbf{j} = \mathbf{j}(\mathbf{h}) \text{ only where } \mathbf{h} = \frac{v}{\bar{v}} \text{ and } \bar{v} = \int_0^{\infty} v \cdot n(v,t) dv$$

Analytical solutions of the self-preserving distribution do exist for some coalescence kernels, and such behavior is sometimes seen in practice (see Fig. 40). For most practical applications, numerical solutions to the population balance are necessary. Several numerical solution techniques have been proposed. It is usual to break the size range into discrete intervals and then solve the series of ordinary differential equations that result. A geometric discretization reduces the number of size intervals (and equations) that are required. Litster, Smit and Hounslow (1995) give a general discretized population balance for nucleation, growth and coalescence. Figure 41 illustrates the evolution of the size distribution for coalescence alone, based on the kernel of Ennis & Adetayo (1994).

Table 8. Some Analytical Solutions to the Population Balance for Granulation Processes

Mixing State	Mechanisms Considered	Initial or Inlet Size Distribution	Final or Exit Size Distribution
Batch	Layering Only $G(x) = \text{constant}$	any initial size distribution, $n_o(x)$	$n(x) = n_o(x - \Delta x)$
Batch	Size independent coalescence only $\beta(u, v) = \beta$	$n_o(x) = \frac{N_o}{v_o} \exp \left[-\frac{v}{v_o} \right]$	$n(x) = \frac{4 N_o}{v_o (\tau + 2)^2} \exp \left[-\frac{2 v}{v_o (\tau + 2)} \right]$ <p>where $\tau = N_o \beta_o t$</p>

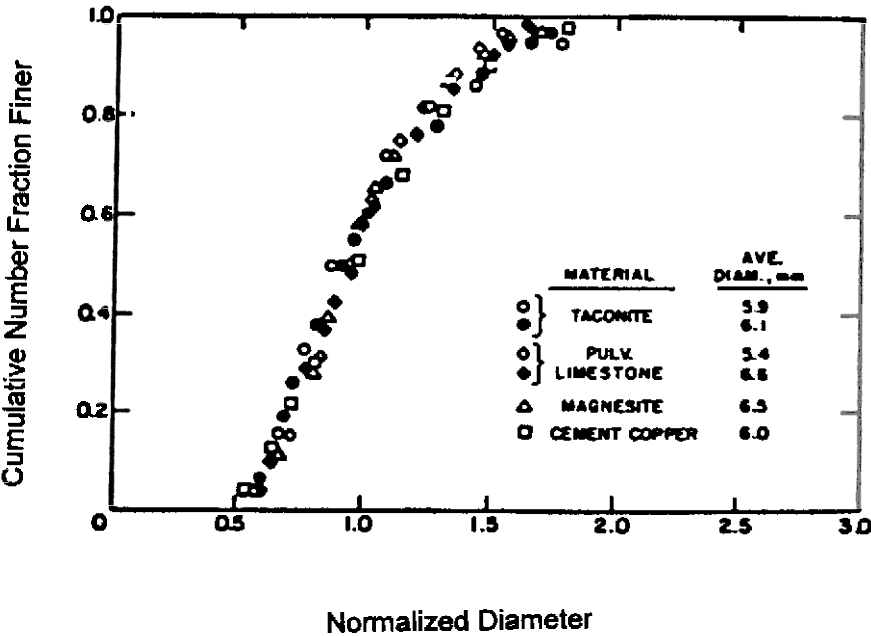


Figure 40. Self-preserving size distributions of different materials. (From Sastry, K. V. S., *Int. J. Min. Processing*, 2:187–203, 1975, with kind permission from Elsevier Science-NL, Sara Burgerhartstraat 25, 1055 KV Amsterdam, The Netherlands.)

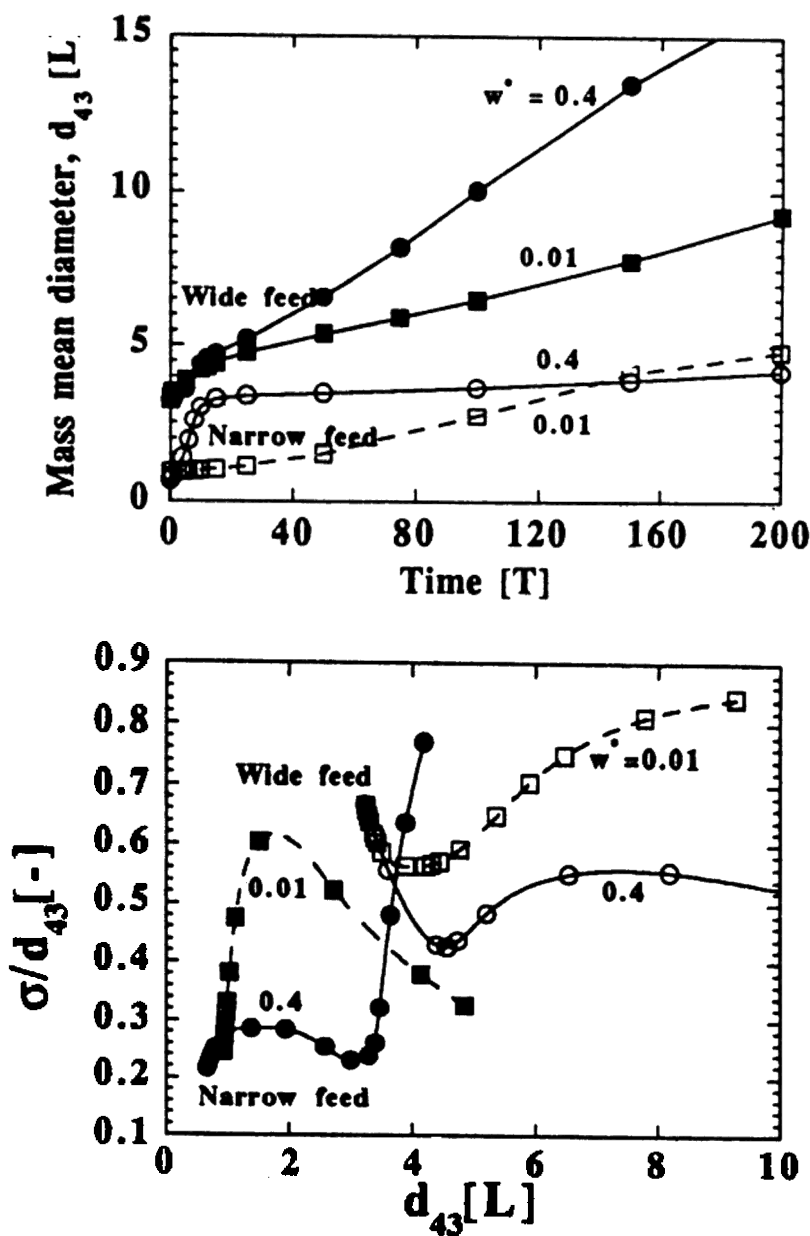


Figure 41. Evolution of variance and average size based on a cut off kernel, with $w = (wv)^2/(u + v)^3$. (From Adetayo and Ennis, 1996.)

An Example of Modeling Coalescence in Granulation Processes.

Growth by coalescence in granulation processes may be modeled by the population balance, as mentioned. It is necessary, however, to determine both the mechanism and kernels which describe growth. For fine powders within the non-inertial regime of growth where granule deformation can be neglected, all collisions result in successful coalescence provided that binder is present. Therefore, coalescence occurs via a random, or size independent kernel which is only a function of liquid loading y , or

Eq. (42)
$$b(u, v) = k = k^* \, fn(y)$$

The dependence of growth on liquid loading represented by $fn(y)$ strongly depends on wetting properties. For random growth, it may be shown that the average granule size is given by

Eq. (43)
$$a = a_o \, e^{kt}$$

where a_o is the initial nuclei size, and kt is the extent of granulation. Random growth will occur until the inertial regime of granulation is reached, at which point an additional relationship exists to determine the largest granule size possible, or

Eq. (44)
$$St = \frac{16 \, r \, U_o \, a_{\max}}{9 \, m} = St^*$$

Combining the previous two relationships allows us to estimate the extent of granulation as a function of the governing group of the Stokes number, or

Eq. (45)
$$(kt)_{\max} = 6 \ln \left[\frac{St^*}{St_o} \right] fn(y) \propto \ln \left[\frac{m}{r \, U_o \, a_o} \right]$$

Hence, the extent of non-inertial growth depends logarithmically on binder viscosity and the inverse of agitation velocity (Adetayo et al., 1995). Maximum granule size depends linearly on these variables. Also, the extent of growth has been observed to depend linearly on liquid loading y and,

therefore, maximum granule size, exponentially on liquid loading. Figure 42 illustrates the normalization of extent of growth for the drum granulation of limestone and fertilizers, using the data of Kapur (1972).

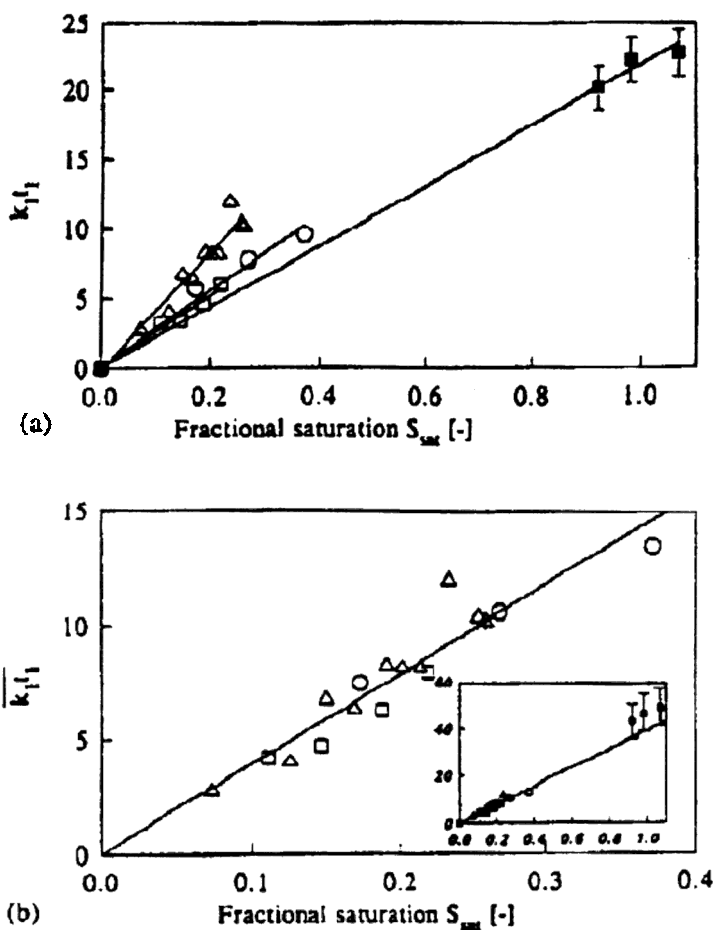


Figure 42. Extent of granulation as a function of fractional saturation. (From Adetayo, et al., *Powder Technol.*, 82:37–49, 1995, with kind permission from Elsevier Science S.A., P.O. Box 564, 1001 Lausanne, Switzerland.) (a) Extent of granulation, $k_1 t_1$, as a function of fractional saturation and (b) extent of granulation normalized for differences in St_{vo} as a function of fractional saturation. (Inset) Comparison to data of Kapur (1972): O, AS; □, MAP; Δ, DAP; ■, limestone (Kapur, 1972).

3.7 Unwanted Aggregation in Fluidized Beds

Industrial fluidized beds are operated with particles which usually contain impurities or are themselves a mixture of many components. Upon heating, some of these components soften, melt or react with each other, generating stickiness. In fluid bed reactors, the fluidizing gas as well as the solid particles can react chemically producing new components and, during this process, particle cohesion and stickiness can occur. In all these cases, the fluidization behavior of the bed changes dramatically as temperature is increased and unwanted agglomerates form. Such characteristics as the minimum fluidization and bubbling velocity, the bubble size and bubble frequency, all undergo a significant change and, in the limit, total defluidization of the bed can take place. Like in granulation, stickiness generated by surface softening or due to the presence of a sticky chemical species results in agglomerate formation and growth. However, unlike granulation, this growth is usually unintended and it proceeds in the non-inertial regime where, as long as stickiness is present, coalescence takes place and can, in some cases, become uncontrollable.

It was shown (Siegel, 1984; Compo et al., 1984; Tardos et al., 1985a,b; and Compo et al., 1987) that cohesiveness and subsequent agglomeration and sintering of fluidized particles occurs if fluid beds are operated at temperatures at or above the so-called *minimum sintering temperature* (point), T_s , of the particles. It was also shown that for pure materials fluidized in inert gases, the sintering temperature is an intrinsic property of the solid particle surface which can be estimated using constant heating rate dilatometry (Tardos et al., 1984). This temperature is usually a fraction of the melting point of the solid material and depends on structure and chemical composition; Table 9 gives a few examples for materials used by Compo et al. (1987). As can be seen from the table, the ratio of the sintering point to the melting temperature varies a great deal and can take values from approximately 0.5 to 0.95. These results show that “the rule of thumb” employed in industry for the ratio T_s/T_M to be approximately 0.8 is correct for some compounds but not for others.

Using the “dilatometer” technique, a small sample of powder (about 1–2 grams) is heated at constant rate in the apparatus depicted schematically in Fig. 43. Dilatation of the sample is measured by a linear voltage transducer (LVDT); contraction of the sample indicates particle-particle surface flattening and defines the *minimum softening point* or *sintering temperature*, T_s . In

Table 9. Dependency of Minimum Sintering Temperature on the Electronic Structure of Crystalline Material

Material	Formula	$T_m(^{\circ}\text{C})$	$T_s(^{\circ}\text{C})$	T_s/T_m (K/K)
Ionic Compounds				
Sodium Chloride	NaCl	802	400	0.63
Sodium Bromide	NaBr	755	420	0.67
Calcium Chloride	CaCl ₂	772	440	0.68
Calcium Fluoride	CaF ₂	1330	368	0.39
Magnesium Oxide	MgO	2800	1109	0.45
Covalent Network Compounds				
Polyethylene Granules		125	92	0.92
Polypropylene Beads		162	141	0.95
Polyethylene Beads		135	118	0.96
polyethylene Spheres		135	127	0.98
Aluminum Nitride	Al ₂ N ₂	2150	1108*	0.57
Zeolite Cracking Catalyst		1260	900	0.77
Metals				
Copper Shot ($d_p = 1.015$ mm)	Cu	1083	899	0.86
Copper Shot ($d_p = 0.718$ mm)	Cu	1083	844	0.83
Copper Shot ($d_p = 0.056$ mm)	Cu	1083	750	0.75
Nickel Powder	Ni	1452	434*	0.41
Molybdenum Powder	Mo	2620	814*	0.40
Covalent Compounds				
Boron Powder	B	2330	1759*	0.78
Silicon Powder	Si	1420	1335*	0.95

the same instrument, dilatation or contraction at constant temperature (isothermal dilatometry) can also be performed; this procedure yields particle surface flattening kinetics or interparticle contact deformation rates. These experiments are usually performed in an inert atmosphere such as nitrogen or helium. The results from these types of measurements can be used to predict sinter-neck growth and hence allow prediction of the rate of strengthening of formed agglomerates at constant temperature.

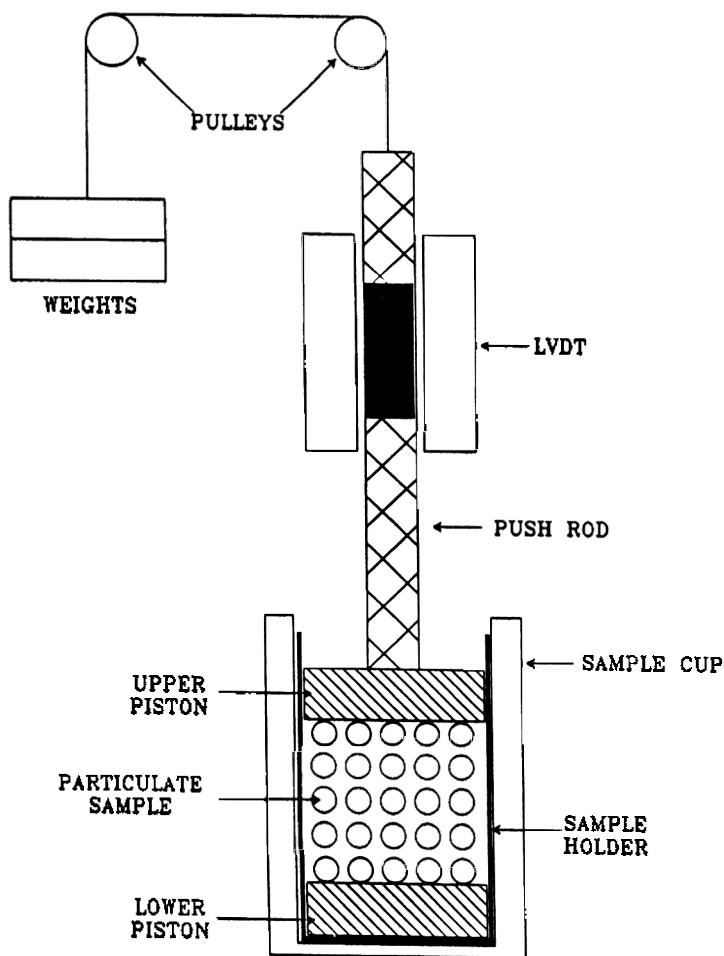


Figure 43. Schematic diagram of a dilatometer. (From Tardos and Pfeffer, *Powder Technology*, 85:29–35, 1995, with kind permission from Elsevier Science S.A., P.O. Box 564, 1001 Lausanne, Switzerland.)

A more accurate but also much more difficult and time consuming experiment to determine the sintering temperature and other fluidization properties of a given material at elevated temperatures is carried out in the three-inch diameter, temperature controlled fluidized bed depicted in Fig. 44, using 1–2 kg of fluidizable powder. Defluidization is accompanied by a large rapid change in pressure drop through the bed which can easily be detected. It was found previously that the formation of large agglomerates and bed defluidization occur at temperatures somewhat higher than the minimum sintering temperature determined in the dilatometer experiments described above. This is clearly due to the fact that in the dilatometer particles touch at fixed points while in the fluid bed some particle movement takes place and particle contacts are necessarily intermittent.

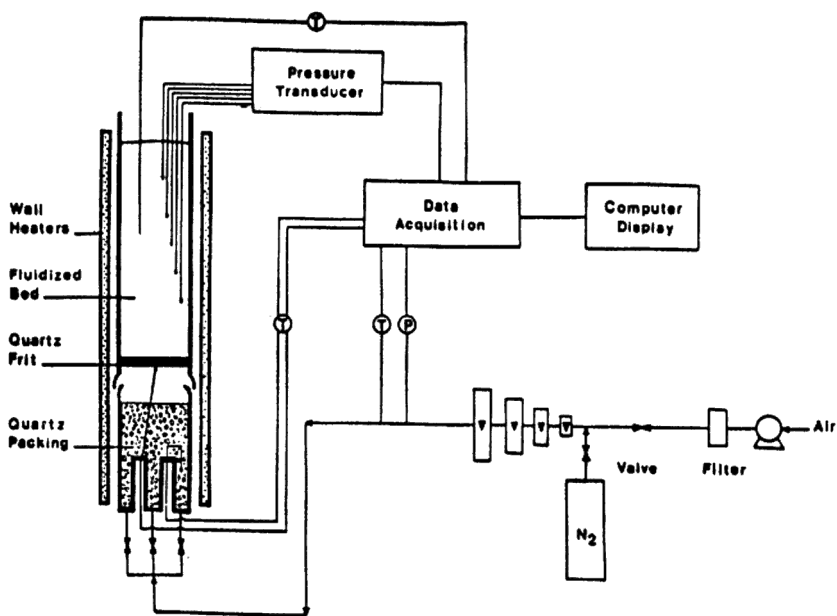


Figure 44. Schematic diagram of the high temperature fluidized bed reactor/granulator. (From Tardos and Pfeffer, *Powder Technology*, 85:29–35, 1995, with kind permission from Elsevier Science S.A., P.O. Box 564, 1001 Lausanne, Switzerland.)

It was also shown both theoretically and experimentally (Tardos et al., 1985a,b) that there is a strong correlation between the excess temperature above the minimum sintering point, $T - T_s$, and the excess gas velocity above minimum fluidization conditions (measured below the sintering point) $U - U_{mf}$, required to maintain fluidization. A general correlation was developed between the excess temperature and the excess gas velocity, which takes the form

Eq. (46)
$$\frac{U - U_{mf}}{U_{mf}} = K \frac{D_B}{d_p} \left[\frac{T - T_s}{T_s} \right]^n$$

where D_B and $d_p = 2a$ are the bed and particle diameters, and K and n are material dependent coefficients. These take different values for amorphous and crystalline materials and are given in Table 10.

Table 10. Values of Coefficients K and n

Material	K	n
Amorphous Coal Ash, Glass, Polymer	0.1	2
Crystalline Salts, Ores	0.0025	0.4–0.5

There is a significant difference in the form of Eq. (46) for amorphous and crystalline materials (Compo et al., 1987 and 1990); for the first group, a slight increase in temperature above minimum sintering results in a significant increase in excess gas velocity as can be seen in both, the value of the

constant K as well as the value of the exponent ($n = 2$, in this case). For crystalline materials, on the other hand, the correlation is weaker and the exponent is significantly smaller ($n = 0.4\text{--}0.5$).

The determination of sintering temperatures was extended to more complex materials such as coal ashes (Ladesma et al., 1987) and beneficiated ilmenite ores (Compo et al., 1987). Although these experiments were also performed in an inert atmosphere, different components within these materials reacted and sintered at different temperatures. It was again found that sintering and softening detected in the dilatometer predicted very closely the agglomeration and defluidization observed in the experimental fluid bed in accordance with the results given in Eq. (46).

During more recent work (Tardos and Pfeffer, 1995) several systems were studied where fluidizing gas actually reacted with fluidized particles and either a solid or a gaseous product was formed. The influence of product formation on fluidization was studied in both an isothermal fluidized bed and in the dilatometer. The following reactions were studied: reduction of calcium sulfate (phosphogypsum) to calcium sulfide (CaS) in hydrogen, oxidation of coke and magnesium in air and production of aluminum nitride (AlN) from a solid precursor containing aluminum and carbon by carbothermal nitridation (Nicolaescu et al., 1994).

In one case, the product was a gas (CO_2) while in others it was a solid (calcium sulfide, aluminum nitride and magnesium oxide). One of the products was a fine, extremely cohesive material (CaS) while the others were stable, free flowing materials which exhibit no cohesiveness (MgO and AlN). It was shown that in the case of the gaseous product, the bed was easily fluidizable as long as the temperature did not exceed the sintering point of the solid reactant. When the product was a noncohesive, solid powder, steady fluidization could be maintained until total conversion was achieved by keeping the temperature below the sintering point of both the reactant and the product. Production of the cohesive powder, calcium sulfide, was only possible in a fluid bed diluted with heavy inert particles (sand) which acted as fluidization media and promoted the removal of the product from the surface of the reactant powder. In the case of the aluminum nitride production, even though carbon (coke) is not readily fluidizable at temperatures above $1200\text{--}1300^\circ\text{C}$, the formation of a fluidizable product (AlN) ensured good fluidization to temperatures as high as $1500\text{--}1600^\circ\text{C}$.

ACKNOWLEDGMENT

The authors would like to acknowledge that the section dealing with population balance modeling of granulation processes is an abbreviated version of material prepared by Dr. J. D. Litster, University of Queensland, for a joint short course given by Dr. B. J. Ennis and Dr. J. D. Litster.

NOTATIONS

a	Effective radius or characteristic length of a particle	m
A	Area of indenter in indentation test	m ²
B	Birth rate of particles of a given size due to coalescence, Eq. (5) or nucleation, Eq. (40)	# particles/kg·s
B'	Dimensionless concentration, Eq. (3)	-
c	Crack length	m
Ca	Capillary number = $U_o \rho \mathbf{m}/g$	-
C_o	Laplace-Young pressure deficiency	-
D_{def}	Coefficient of deformation of a granule	
$C_{p,g}$	Specific heat capacity of gas	J/kg·°C
D	Death rate of particles by coalescence, Eqs. (5) and (40)	# particles/kg·s
D_B	Bed or bubble diameter	m
D_G	Dispersion coefficient for growth rate (growth diffusivity)	kg ² /s
d	Indenter diameter	m
d_p	Particle diameter	m
$d_{p,o}$	Initial droplet diameter	m
e	Coefficient of restitution of a solid surface	-
E	Expectation (expected or average value) or Young's Modulus	Pa
E'	Elutriation rate, Eq. (10)	kg/s
$f(m)$	Mass distribution of particles	kg ⁻¹

f_{sur}	Fraction of surviving granules	
F	Total force	N
F_{vis}	Viscous force from Eq. (18)	N
F_{cap}	Capillary force from Eq. (19)	N
F_{coat}	Feed rate of coating material (solute only)	kg/s
g	Acceleration due to gravity	m/s ²
G	Growth rate of particles due to coating	kg/s
G_c	Critical strain energy release rate	J/m ²
h	Height of wetted powder in a Washburn Test or half separation distance between two particles held in contact by a pendular liquid bridge	m
h_a	Minimum separation distance between two particles due to surface asperities	m
h_b	Height of a fluidized bed	m
h_e	Equilibrium height of rise in Eq. (15)	m
H	Hardness (from indentation test)	Pa
$k, k_p,$ K, K'	Constants in Eqs. (7, 8 and 46)	
k_g	Thermal conductivity of gas	W/m·°C
K_c	Fracture toughness of material	Pa·m ^{1/2}
l	Wear displacement	m
m	Mass	kg
MW_g	Molecular weight of gas	kg/kmol
MW_l	Molecular weight of liquid	kg/kmol
n	Coefficient in Eq. (46)	
n_k	Mass distribution of feed or product particles	kg ⁻¹
$n(v,t)$	Number frequency distribution	
N	Total number of granules or number of particle circulations	# particles
p_l^*	Vapor pressure of liquid	Pa
p_{tot}	Total pressure of system	Pa
P	Applied load in indentation test	N

426 *Fluidization, Solids Handling, and Processing*

Q_k	Rate of feed or product withdrawal	# particles/s
r_p	Characteristic length of process zone	m
R	Radius of capillary	m
S	Saturation or spray rate	-
St, St^*	Stokes number and critical Stokes number, Eq. (20)	-
S_f	Shape Factor in Eqs. (29) and (31)	-
t	Time	s
T_{bulk}	Bulk gas temperature	°C
T_s	Surface temperature of liquid droplet or minimum sintering temperature of a solid	°C
T_M	Melting point of a solid	°C
DT	$= (T_{bulk} - T_s)$	°C
t_v	Time for complete evaporation of a liquid droplet	s
t_{circ}	Time elapsed between successive passages of a particle through the spray zone	s
u	Particle size measure (volume) for coalescing particles	m ³
U	Superficial gas velocity	m/s
U_B	Rise velocity of a bubble	m/s
U_i	Impact velocity	m/s
U_{mf}	Minimum fluidizing velocity	m/s
U_o	Relative velocity of two approaching particles	m/s
v	Particle size measure (volume) for coalescing particles	m ³
V	Volumetric wear or breakage rate or volumetric flow of feed	m ³ /s
Var	Variance	
w^*	Critical average granule size capable of rebound from a collision	
X_{total}	Total mass of coating received by a particle in a batch coating operation	kg
x_c	Critical specimen size, Eq. (35)	
x_k	Amount of mass received by a particle in its kth passage through the spray zone	kg

y	Liquid loading	
y_{bulk}	Mass fraction of solvent in the bulk	-
y_d	Mass fraction of solvent in the liquid droplet	-
y_s	Mass fraction of solvent in gas at the liquid surface	-
Y	Yield number, Eq. (28)	-

Greek Letters

α	Thermal diffusivity	m^2/s
b	Constant in Eq. (34)	-
$b()$	Coalescence kernel, Eq. (40)	-
G	Shear rate	s^{-1}
g	Surface tension or interfacial energy	N/m
d	Dimensionless bubble spacing	-
d_c	Effective increase in crack length	m
e	Dimensionless separation of two particles = $2h/a$ or powder void fraction, Eq. (26)	
q	Contact angle between liquid and powder compact	
l	Latent heat of vaporization	J/kg
m	Viscosity	$\text{kg/m}\cdot\text{s}$
r	Density	kg/m^3
s_y	True yield stress of material	Pa
s_f	Applied fracture stress	Pa
t	Coating run time	s
t_o	Yield strength of wet granule	N/m^2
f	Filling angle defined in Fig. 22	
j	Probability distribution function	

Subscripts

ave	Average value
$breakage$	Breakage
c	Crystal

428 *Fluidization, Solids Handling, and Processing*

<i>circ</i>	Circulation
<i>d</i>	Droplet
<i>e</i>	Equilibrium, exit
<i>g</i>	Gas or granule
<i>i</i>	Inlet
<i>I-C</i>	Inertial to coating transition
<i>l</i>	Liquid
<i>max</i>	Maximum value
<i>N-I</i>	Non-inertial to inertial transition
<i>p</i>	Particle
<i>tot</i>	Total
<i>wear</i>	Wear
<i>yy</i>	Denotes stress value in material

Superscripts

<i>C</i>	Coating
<i>fb</i>	Fluid bed
<i>I</i>	Inertial
<i>lv</i>	Liquid-vapor
<i>N</i>	Non-inertial
<i>sv</i>	Solid vapor
<i>sl</i>	Solid-liquid
<i>*</i>	Critical value

REFERENCES

- Adetayo, A. A., and Ennis, B. J., A Unifying Approach to Modeling Coalescence Mechanisms, in Review, *AIChEJ* (1996)
- Adetayo, A. A., Litster, J. D., Pratsinis, S. E., and Ennis, B. J., "Population Balance Modelling of Drum Granulation of Materials with Wide Size Distributions," *Powder Tech.*, 82:37–49 (1995)
- Aulton, M. E., and Banks, M., *Proceedings of Powder Technology in Pharmacy Conference*, Powder Advisory Centre, Basel, Switzerland (1979)
- Capes, C. E., "A Note on Size Distributions in Granulation, Balling and Wet Pelletization," *Chem. Engineer*, 45:CE78-80 (1967)
- Cheng, X. X., "Studies of Uniformity of Particle Coating in Fluidized Beds," Ph.D. Dissertation, West Virginia University, Morgantown, WV (1993)
- Cheng, X. X., and Turton, R., "The Uniformity of Particle Coating Occurring in Fluidized Beds," *AIChE Symp. Ser.*, 301(90):142–151 (1994)
- Choi, M., and Meisen, A., "Sulfur Coating of Urea in Shallow Spouted Beds," paper presented at AIChE meeting, Miami, FL (Nov, 1995)
- Compo, P., Tardos, G. I., Mazzone, D., and Pfeffer, R., "Sintering Temperatures of Fluidizable Particles," *Particle Characterization - An International Journal*, 1:171 (1984)
- Compo, P., Pfeffer, R., and Tardos, G. I., "Minimum Sintering Temperatures and Defluidization Characteristics of Agglomerating Particles," *Powder Technology*, 51(1):87–103 (1987)
- Compo, P., Tardos, G., and Pfeffer, R., "Thermally Induced Agglomeration and Defluidization Characteristics of Fluidizable Particles," *Proceedings of the Second World Congress in Particle Technology*, Kyoto, Japan (1990)
- Ennis, B. J., "On the Mechanisms of Granulation," Ph.D. Dissertation, The City University of New York (1990)
- Ennis, B. J., Tardos, G. I., and Pfeffer, R. "A Microlevel-Based Classification of Granulation Regimes and Mechanisms," *Proceedings of the Second World Congress on Powder Technology*, p. 409, Kyoto, Japan (1990a)
- Ennis, B. J., Li, J., Tardos, G. I., and Pfeffer, R., "The Influence of Viscosity on the Strength of an Axially Strained Pendular Liquid Bridge," *Chem. Eng. Sci.*, 45:3071–3088 (1990b)
- Ennis, B. J., Tardos, G. I., and Pfeffer, R., "A Microlevel-Based Characterization of Granulation Phenomena," *Powder Technology*, 65:257–272, (1991)
- Ennis, B. J., and Sunshine, G., "On Wear as a Mechanism of Granule Attrition," *Tribology Int.*, 26:319–327 (1993)

430 *Fluidization, Solids Handling, and Processing*

- Ennis, B. J., and Adetayo, A. A., "On the Unification of Granule Coalescence Mechanisms: A New Approach," *1st Int. Part. Tech. Forum*, pp. 271–277, Denver, USA (1994)
- Evans, A. G., and Wilshaw, T. R., "Quasi-Static Solid Particle Damage in Brittle Solids - 1. Observations, Analysis and Implications," *Acta Metallurgica*, 24:939–956 (1976)
- Friedlander, S. K., and Wang, C. S., "The Self Preserving Particle Size Distribution for Coagulation by Brownian Motion," *J. Colloid Interface Sci.*, 22:126–132 (1966)
- Geldart, D., "Types of Gas Fluidization," *Powd. Technol.*, 7:285–292 (1973)
- Gilligan, C. A., and Po, A. L. W., "Factors affecting Drug Release from a Pellet System Coated with an Aqueous Colloidal Dispersion," *Int. J. Pharmaceutics*, 73:51–68 (1991)
- Gluba, T., Heim, A., and Kochanski, B., "Application of the Theory of Moments in the Estimation of Powder Granulation of Different Wettabilities," *Powder Hand. and Proc.*, 2:323–326 (1990)
- Griffith, A. A., "The Phenomena of Rupture and Flow in Solids," *Phil. Trans. Royal. Soc.*, A221:163–198 (1920)
- Hall, H. S., Coating of Granular Bioproducts, *Granulation Technology for Bioproducts*, (K. L. Kadam, ed.), Ch. 10, CRC Press, Boca Raton, FL (1991)
- Irwin, G. R., "Analysis of Stresses and Strains Near End Crack Traversing Plate," *J. Applied Mechanics*, 24:361–364 (1957)
- Iveson, S., Litster, J. D., and Ennis, B. J., "Fundamental Studies of Granule Consolidation," *21st Australasian Chem. Engng. Conf.*, CHEMECA (1994)
- Jones, D. M., "Factors to Consider in Fluid-Bed Processing," *Pharm. Tech.*, 9:50–62 (1985)
- Jozwiakowski, M. J., Jones, D. M., and Franz, R. M., "Characterization of a Hot-Melt Fluid Bed Coating Process for Fine Granules," *Pharm. Res.*, 7:1119–1126 (1990)
- Kanury, A. M., *Introduction to Combustion Phenomena*, Gordon and Breach Science Publishers, New York (1975)
- Kapur, P. C., "Kinetics of Granulation by Non-Random Coalescence Mechanism," *Chem. Eng. Sci.*, 27:1863–1869 (1972)
- Kapur, P. C., and Fuerstenau, D. W., "Kinetics of Green Pelletization," *Trans. AIME*, 229:348–355 (1964)
- Kristensen, H. G., Holm, P., and Schaefer, T., "Mechanical Properties of Moist Agglomerates in Relation to Granulation Mechanisms. Part I: Deformability of Moist Densified Agglomerates," *Powder Technology*, 44:227–237 (1985)

- Kristensen, H. G., Holm, P., and Schaefer, T., "Mechanical Properties of Moist Agglomerates in Relation to Granulation Mechanisms. Part II: Effect of Particle Size Distribution," *Powder Technology*, 44:239-247 (1985)
- Kristensen, H. G., "Agglomeration of Powders," *Acta Pharm. Soc.*, 25:187-204 (1988)
- Kucharski, J., and Kmiec, A., "Hydrodynamics, Heat and Mass Transfer During Coating of Tablets in a Spouted Bed," *Can. J. Chem. Eng.*, 61:435-439 (1983)
- Landgrebe, J. D., and Pratsinis, S. E., "Gas Phase Manufacture of Particulates: Interplay of Chemical Reaction and Aerosol Coagulation in the Free-Molecular Regime," *Ind. Eng. Chem. Res.*, 28:1474-1481 (1989)
- Ladesma, R., Compo, P., and Isaacs, L. L., "Thermal Characterization of Coal Ash Powders," *Mat. Res. Society Symp. Proc.*, 86:127 (1987)
- Landrock, A. H., *Encyclopedia of Polymer Science and Technology*, 3:808-830, Wiley, New York (1965)
- Landrock, A. H., "Fluidized Bed Coating with Plastics," *Chem. Eng. Progr.*, 63:67-74 (1967)
- Lefebvre, A. H., *Atomization and Sprays*, Hemisphere Publishing Corp., New York (1989)
- Lauenberger, H., Bier, H. P., and Sucker, H., *Pharm. Ind.*, 41:375 (1979)
- Litster, J. D., and Ennis, B. J., Granulation, Pelletisation, and Particle Coating, short course given at IChemE - Australia, Gold Beach, Australia (1994)
- Litster, J. D., Smit, D. J., and Hounslow, M. J., "Adjustable Discretized Population Balance for Growth and Aggregation," *AIChE J.*, 41:591-603 (1995)
- Liu, L. X., and Litster, J. D., "The Effect of Particle Shape on the Spouting Properties of Non-Spherical Particles," *Powd. Technol.*, 66:59-67 (1991)
- Liu, L. X., and Litster, J. D., "Coating Mass Distribution from a Spouted Bed Seed Coater: Experimental and Modelling Studies," *Powder Technol.*, 74:259-270 (1993a)
- Liu, L. X., and Litster, J. D., "Spouted Bed Seed Coating: the Effect of Process Variables on Maximum Coating Rate and Elutriation," *Powder Technol.*, 74:215-230 (1993b)
- Mann, U., Coating of Particulate Solids by Air Suspension, Ph.D. Thesis, University of Wisconsin (1972)
- Mann, U., Crosby, E. J., and Rubinovitch, M., "Number of Cycles Distribution in Circulating Systems," *Chem. Eng. Sci.*, 29, 761-765 (1974)
- Mann, U., Rubinovitch and Crosby, E. J., "Characterization and Analysis of Continuous Recycle Systems: Part II. Cascade," *AIChE J.*, 27:829-836 (1981)

432 *Fluidization, Solids Handling, and Processing*

- Mann, U., "Analysis of Spouted-Bed Coating and Granulation. 1. Batch Operation," *I.&E.C. Proc. Des. Dev.*, 22:288–292 (1983)
- Marshall, W. R., "Atomization and Spray Drying," *Chem. Eng. Prog. Monograph Series*, 50:2 (1954)
- Masters, K., "Industrial Fluid Bed Drying: Trends and Developments," *Fluidization VII*, (O. E. Potter, and D. J. Nicklin, eds.); *Proceedings of the Engineering Foundation Conference*, pp. 59–72, Brisbane, Australia (1992)
- Mathur, K. B., and Epstein, N., *Spouted Beds*, Academic Press, New York (1974)
- McGinity, J. W., *Aqueous Polymeric Coatings for Pharmaceutical Dosage Forms*, Marcel Dekker (1989)
- Mehta, A. M., and Jones, D. M., "Coated Pellets under the Microscope," *Pharm. Tech.*, 9(6):52–60 (1985)
- Mehta, A. M., "Scale-Up Considerations in the Fluid-Bed Process for Controlled Release Products," *Pharm. Tech.*, 12:46–52 (1988)
- Olsen, K. W., "Batch Fluid-Bed Processing Equipment - A Design Overview: Part I," *Pharm. Tech.*, 13(1):34–46 (1989a)
- Olsen, K. W., "Batch Fluid-Bed Processing Equipment - A Design Overview: Part II," *Pharm. Tech.*, 13(6):39–50 (1989b)
- Nicolaescu, I. V., Tardos, G. I., and Riman, R. E., "Thermogravimetric Determination of Carbon, Nitrogen and Oxygen in Aluminum Nitride," *J. Am. Ceramic Soc.*, 77(9):2265–72, (1994)
- Nienow, A. W., "Fluidized Bed Granulation," *Enlargement and Composition of Particulate Solids*, (N. G. Stanley-Wood, ed.), Butterworth and Co., London (1983)
- Nienow, A. W. and Rowe, P. M., Particle Growth and Coating in Gas-Fluidized Beds, in *Fluidization*, (J. F. Davidson, R. Clift, and D. Harrison, eds.), 2nd ed., Academic Press, London (1985)
- Nienow, A. W., "Fluidized Bed Granulation and Coating: Application to Materials, Agriculture and Biotechnology," *Proceedings of the First International Particle Technology*, Forum, Denver, CO., USA (1994).
- Ramkrishna, D., "The Status of Population Balances," *Review in Chem. Eng.*, 3(1):49–95 (1985)
- Randolph, A. D. and Larson, M. A., *Theory of Particulate Processes*, 2nd Ed., Academic Press, New York (1988)
- Ranney, M. W., *Powder Coatings and Fluidized Bed Techniques*, Noyes Data Corp., Park Ridge, NJ (1971)
- Rekhi, G. S., Mendes, R. W., Porter, S. C., and Jambhekar, S. S., "Aqueous Polymeric Dispersions for Controlled Drug Delivery - Wurster Process," *Pharm. Technol.*, 13(3):112–125 (1989)

- Ritala, M., Jungersen, O., Holm, P., Schaefer, T., and Kristensen, H. G., "A Comparison Between Binders in the Wet Phase of Granulation in a High Shear Mixer," *Drug Development and Industrial Pharmacy*, 12:(11-13), 1685-1700, Marcel Dekker, Inc. (1986)
- Ritala, M., Holm, P., Schaefer, T., and Kristensen, H. G., "Influence of Liquid Bonding Strength on Power Consumption during Granulation in a High Shear Mixer," *Drug Development and Industrial Pharmacy*, 14(8):1041-1060 (1988)
- Robinson, T., and Waldie, B., "Particle Cycle Times in a Spouted Bed of Polydisperse Particles," *Can. J. Chem. Eng.*, 56:632-635 (1978)
- Robinson, T. and Waldie, B., "Dependency of Growth on Granule Size in a Spouted Bed Granulator," *Trans. I. Chem. E.*, 57:121-127 (1979)
- Rumpf, H., *Particle Technology*, Chapman and Hall, London (1975)
- Sastry K. V. S., "Similarity Size Distribution of Agglomerates During Their Growth by Coalescence in Granulation or Green Pelletization," *Int. J. Min. Processing*, 2:187-203 (1975)
- Sastry K. V. S., and Fuersteau, D. W., "Mechanisms of Agglomerate Growth in Green Pelletization," *Powder. Tech.*, 7:97-105 (1973)
- Schaefer, T., "Equipment for Wet Granulation," *Acta Pharm. Soc.*, 25:205-228 (1988)
- Schaefer, T., Holm, P., and Kristensen, H. G., "Wet Granulation in a Laboratory Scale High Shear Mixer," *Pharm. Ind.*, 52(9):1147 (1990)
- Schaefer, T., Holm, P., and Kristensen, H. G., "Melt Granulation in a Laboratory Scale High Shear Mixer," *Drug Development and Industrial Pharmacy*, 16(8):1249-1277 (1990)
- Siegell, J. H., "High Temperature Defluidization," *Powder Technol.*, 38:13-22 (1984)
- Smith, P. G., and Nienow, A. W., "On Atomizing a Liquid into a Gas Fluidised Bed," *Chem. Eng. Sci.*, 37:950-954 (1982)
- Tardos, G. I., Mazzone, D., and Pfeffer, R., "Measurement of Surface Viscosities using a Dilatometer," *Can. J. of Chem. Eng.*, 62:884-887 (1984)
- Tardos, G. I., Mazzone, D., and Pfeffer, R., "Destabilization of Fluidized Beds Due to Agglomeration, Part I: Theoretical Analysis," *Can. J. of Chem. Eng.*, 63:377-383 (1985a)
- Tardos, G. I., Mazzone, D., and Pfeffer, R., "Destabilization of Fluidized Beds Due to Agglomeration, Part II: Experimental Verification," *Can. J. of Chem. Eng.*, 63:384-389 (1985b)
- Tardos, G. I., Pfeffer, R., and Ennis, B. J., "A Microlevel-Based Study of Granulation," *Proc. of the Powder and Bulk Solids Conf.*, pp. 221-230, Rosemont, Illinois (1991)

434 *Fluidization, Solids Handling, and Processing*

- Tardos, G. I., Garcia, J., Ahart, R., and Ratuiste, F., "How and Why Some Flow Aids Promote Bulk Powder Flow," *AIChE Symp. Series*, 296(89):18–34 (1993)
- Tardos, G. I., "Measurement of Powder and Binder Characteristics which Determine Agglomerate Growth during Granulation," *Proc. of the 25th Israel Conf. on Mech. Eng.*, Haifa, Israel (1994)
- Tardos, G. I., "A Review of High Shear Mixer Granulation," *Proc. of the First Israel Conf. for Conveying and Handling of Particulate Solids*, Herzliya, Israel (1995)
- Tardos, G. I., and Khan, M. I., "Study of Granulation in a Constant Shear Granular Flow Couette Device," Paper presented at the Annual AIChE Meeting, Miami Beach, Florida (1995)
- Tardos, G. I., and Pfeffer, R., "Chemical Reaction Induced Agglomeration and Defluidization of Fluidized Beds," *Powder Technology*, 85:29–35 (1995)
- Tardos, G. I., Klan, M. I., and Mort, P. R., "Critical Parameters and Limiting Conditions in Binder Granulation of Fine Powders," *Powder Tech.*, 94:245–258 (1997)
- Tsutsumi, A., Nakmoto, S., Mineo, T., and Yoshida, K., "A Novel Fluidized-Bed Coating of Fine Particles by Rapid Expansion of Supercritical Fluid Solutions," *Proc. 1st Int. Particle Technol. Forum*, pp. 452–455, Denver, CO (1994)
- Waldie, B., "Growth Mechanism and the Dependence of Granule Size on Drop Size in Fluidized-Bed Granulation," *Chem. Eng. Sci.*, 46:2781–2785 (1991)
- Waldie, B., and Wilkinson, D., "Measurement of Particle Movement in a Spouted Bed Using a New Microprocessor Based Technique," *Can. J. Chem. Eng.*, 64:944–949 (1986)
- Wan, L. S. C., and Lai, W. F., "Factors Affecting Drug Release from Drug-Coated Granules Prepared by Fluidized-Bed Coating," *Int. J. Pharmaceutics*, 72:163–174 (1991)
- Weiss, P. J., and Meisen, A., "Laboratory Studies on Sulphur-Coating Urea by the Spouted Bed Process," *Can. J. Chem. Eng.*, 61:440–447 (1983)
- Wurster, D., U.S. Patent 2,799,241 (1957)
- Wurster, D., U.S. Patent 3,253,944 (1966)
- Xu, M., "A Theoretical and Experimental Investigation of Spouted Beds with Draft Tubes," Ph.D. Dissertation, West Virginia University, Morgantown, WV (1993)
- Yuregir, K. R., Ghadiri, M., and Clift, R., "Impact Attrition of Sodium Chloride Crystals," *Chem. Eng. Sci.*, 42:843–853 (1987)

Attrition in Fluidized Beds and Pneumatic Conveying Lines

Joachim Werther and Jens Reppenhagen

1.0 INTRODUCTION

Attrition of particulate materials occurs wherever solids are handled and processed. In contrast to the term *comminution*, which describes the intentional particle degradation, the term *attrition* condenses all phenomena of unwanted particle degradation which may lead to a lot of different problems. The present chapter focuses on two particular process types where attrition is of special relevance, namely fluidized beds and pneumatic conveying lines. The problems caused by attrition can be divided into two broad categories. On the one hand, there is the generation of fines. In the case of fluidized bed catalytic reactors, this will lead to a loss of valuable catalyst material. Moreover, attrition may cause dust problems like explosion hazards or additional burden on the filtration systems. On the other hand, attrition causes changes in physical properties of the material such as particle size distribution or surface area. This can result in a reduction of product quality or in difficulties with operation of the plant.

Both, the mechanism and the extent of particle degradation depend not only on the process type but also on properties of the solid material, and to a large extent on the process conditions. Clift (1996) has stated that attrition is a triple-level problem, i.e., one is dealing with phenomena on three different length and time scales: the processing equipment, the individual particles, and the sub-particle phenomenon such as fracture which leads to the formation of fines. The appearance of attrition can, therefore, differ very much between the various applications. For that reason, the following section deals with the various modes of attrition and the factors affecting them.

In order to evaluate the extent of attrition and its impact on the particle size distribution, there is a need of a qualitative and quantitative characterization. This, however, is not as simple as it may seem at first. There are many different properties, parameters and effects that manifest themselves and could be measured. In addition, as will be shown, the choice of the assessment procedure is strongly connected with the definition of attrition which, on its part, depends on the degradation mechanism that is considered to be relevant to the process. Hence there are a lot of procedures and indices to characterize the process of particle attrition. Section 3 deals with those which are relevant to fluidized beds and pneumatic conveying lines.

Unfortunately, the basic physical mechanisms that control the attrition process are still poorly understood. As a consequence, particular test methods are used to evaluate the degradation tendency of the materials or to predict the rate of attrition for a given process. There are a lot of procedures using widely different devices and operations. Some of them observe the degradation of only one individual particle, whereas others treat a considerable amount of material. The particles are subjected to stress systems which range from well-defined ones like impact or compression, to those which are similar to the more or less randomized stresses occurring in natural processes. Section 4 attempts to summarize the huge variety of attrition tests in a systematic way.

Test facilities are also used to investigate specific attrition phenomena of individual processes. Up to now only a few investigations have been carried out in full-scale equipment. Most results were obtained from very special devices which makes it difficult to compare the results of various research groups and to draw general conclusions. Despite of these difficulties, the specific attrition phenomena in fluidized beds and pneumatic conveying lines will be summarized in the Secs. 5 and 6, respectively. It will

be shown that the fluidized bed systems can be divided into several regions which are characterized by completely different attrition characteristics. These regions will be discussed separately with regard to the respective influence of the operating and design parameters. Some models and correlations to predict or at least describe the extent of attrition will also be given. On the other hand, the number of papers relating to attrition in pneumatic conveying lines is so small that the results can be outlined in a qualitative manner only. At the end of both sections some general rules will be presented to reduce the attrition in a given case.

2.0 FACTORS AFFECTING ATTRITION

Before discussing the individual factors affecting attrition in detail, the distinction has to be made between two completely different modes of attrition, namely fragmentation and abrasion. The two modes and their different effects on the particle size distribution are sketched in Fig. 1. Abrasion produces a lot of very fine material removed from the surface of the initial particles that retain their identity and become only slightly smaller. Abrasion leads to a bimodal size distribution. On the other hand, fragmentation destroys the particles and produces a number of particles which are all distinctly smaller than the original ones. The resulting size distribution becomes broader and has a smaller mean diameter than the original one.

In industrial processes the two modes usually do not occur separately. They are rather combined in varying proportions. There may be, for example, an initial breakage of mother particles followed by surface abrasion of the resulting fragments. In this case a small number of intermediately sized particles and many fine particles will be produced. In general, the extent of abrasion in relation to fragmentation depends on the various factors discussed below. However, there have been several rules suggested to identify the dominant mode in a given case. They all use the change in size distribution as criterion. For instance, Dessalces et al. (1994) assessed the degradation behavior of various industrial FCC catalysts by the change in the ratio $Dd_{p3,90}/Dd_{p3,10}$, i.e., the ratio of the 90% and 10% values of the cumulative mass density distribution of the particle sizes. They got high values of this ratio (>100) if abrasion was dominant and smaller values (<10) in the case of fragmentation.

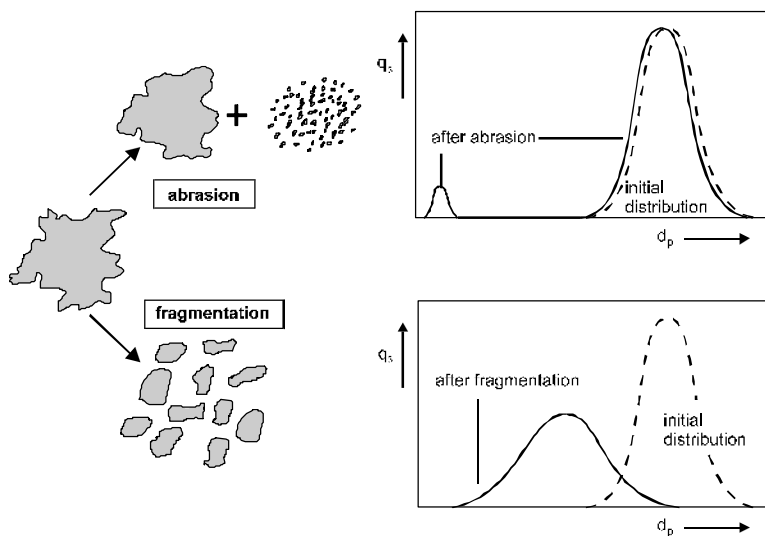


Figure 1. Attrition modes and their effects on the particle size distribution (q_3 = mass density distribution).

Often only that part of degradation which is causing problems is defined as attrition. A good example is the catalyst attrition in fluidized bed reactors where not the particle degradation in itself but the resulting material loss is mostly deemed to be the relevant problem. Consequently many researchers concentrate on the elutriated particles and define them as the only attrition product. This is usually rather fine material which results almost exclusively from abrasion. So, regardless of its extent, fragmentation is not taken into account. The fresh make-up catalyst will additionally be subjected to fragmentation upon entering into the fluidized bed.

The large amount of variables affecting attrition can be classified into two major groups, i.e., the various factors related to material properties and factors related to process conditions.

2.1 Material Properties

Particle Structure. First of all, the particle structure has a fundamental influence on the degradation propensity. The extent of degradation as well as its mode will strongly depend on whether the particle is a single crystal, has an amorphous structure or is an agglomerate. For example, spray-dried catalysts, which are often used in fluidized bed reactors, are

rather susceptible to attrition. Arena et al. (1983) and Pis et al. (1991) studied the attrition in a fluidized bed of amorphous materials such as coal or limestone and found that the size distributions of the attrited materials were independent of the initial particle size and of most operating parameters. Ray et al. (1987a) assumed that unlike crystalline materials, amorphous materials may have some kind of “natural grain size” to which the degradation finally leads.

Pretreatment and Preparation History. The unsteady-state attrition rate of a given powder sample will normally depend on the pretreatment of the solids because the higher and the longer the foregoing stress, the more the weakest points of the particles may have already been attrited. The pretreatment can even occur in the processing route of the solids. If we consider, for example, the spray-drying of catalysts, the weakest agglomerates will immediately break down. Ghadiri et al. (1991) observed that the degradation propensity of salt samples depended on their processing route. They suggested that “rough” processing conditions, as they are occurring in fluidized beds and pneumatic conveying lines, may cause microplastic deformation which in turn work-hardens the surfaces, thus increasing their propensity to degradation.

Particle Size, Shape and Surface Structure. The particle size is of primary interest with respect to particle breakage. This is because the breakage probability strongly depends on the presence of microcracks or imperfections. Smaller particles are, therefore, more difficult to break than larger ones, mainly because they tend to contain fewer faults. The mechanisms of breakage will not be further discussed in the present chapter, but a good survey is given by the British Materials Handling Board (1987). The particle shape is another relevant parameter because irregular and angular particles are inclined to have their corners knocked off in collisions and thus become rounder and naturally smaller with time. This certainly tends more to fragmentation because the debris is much bigger than the fines derived by chipping from a macroscopically smooth surface. The microscopic surface structure is also of interest. If surface asperities are broken off, very fine particles are formed which is characteristic of abrasion.

Particle Size Distribution. The particle size distribution is a significant factor with respect to attrition. Coarser particles tend more to fragmentation while smaller particles have a stronger inclination to abrasion because of their large specific surface. Since the particle degradation is composed of fragmentation as well as abrasion, both the amount and the

particle size distribution of the material that is produced by attrition will differ with the initial particle size distribution. A shift of the particle size distribution to smaller particle sizes may, for example, lead to an increased production of fines.

Moreover, the fines content can have a strong influence on the attrition propensity of the material. Forsythe et al. (1949) already observed a reduction of the degradation of FCC-catalysts in jet attrition tests due to presence of fines. They supposed some kind of cushioning effect which limits the force of collision impact leading to fragmentation of the coarse particles. The effect of fine particles is of strong interest; fines are produced by attrition, so attrition inhibits itself if the fine particles remain in the system. This is particularly valid for fluidized bed systems where the particles are for long periods subjected to the degradation forces.

Arena et al. (1983) investigated the coal attrition in a mixture with sand under hot but inert conditions. As they increased the sand particle size while keeping its mass in the bed constant, they observed an increase in the coal attrition rate. They interpreted their results by assuming that the abrasion energy is shared out on the entire material surface. On the same basis Ray et al. (1987a) developed their "attrition rate distribution model" for abrasion in a fluidized bed.

2.2 Process Conditions

The process conditions will influence the particle degradation by generating the stress on the individual particles on the one hand and by affecting the material properties and consequently the particle friability on the other.

The stress may be a mechanical one due to compression, impact or shear, a thermal one owing to evaporation of moisture or temperature shock, or a chemical one by molecular volume change or partial conversion of the solid into the gas phase. In most cases a combination of these types will occur. The effect of mechanical stress on the particle degradation was intensely investigated by several research groups, e.g., Yuregir et al. (1986, 1987), Paramanathan and Bridgwater (1983), Bridgwater (1987), Neil and Bridgwater et al. (1994), Shipway and Hutchings (1993). The respective investigations were carried out in very special test devices, some of which are described in Sec. 5.

Gas and Solid Velocity. The gas velocity is usually directly related to the particle velocity which is the most important factor affecting attrition if the particle degradation occurs as a result of mechanical stress due to interparticle collisions or collisions between the particles and a solid wall. The forces involved in the degradation process may be generated by high-speed collisions resulting preferably in breakage. Alternatively, the energy may be transmitted through a matrix of comparatively slow moving particles resulting mostly in abrasion. Particularly in the distributor region of a fluidized bed, where grid jets are issuing into the bed of particles, the impact velocities between particles can be extremely high resulting in significant particle breakage.

Solids Residence Time. The relationship between the solids residence time and the amount of material that is produced by attrition is generally non-linear. As an example, Fig. 2 shows the typical time dependence of the attrition of a fresh catalyst that is subjected to attrition in one of the test devices described in Sec. 4. The elutriated mass is defined to be the attrition product and consequently the attrition rate is defined as elutriated mass per unit time. It is clearly seen that the rate of attrition is decreasing with time. The reason is that, at the beginning, the fresh catalyst particles are very irregular and contain a lot of faults. This results in a high rate of initial particle degradation during which the particles break and their edges and asperities are knocked off. With progressing time the particles become smaller, rounder and smoother and the number of their weak points decreases. The elutriation rate, therefore, decreases continuously with time and tends to a more or less constant value which can be interpreted as some kind of a steady-state level where only abrasion takes place. The shape of the curve in Fig. 2 is typical for all particle degradation processes. However, there are some peculiarities belonging to the particular processes. With respect to pneumatic conveying, the time axis can be substituted by the pipeline length, because the particles are going only once through. With respect to fluidized beds, one has to distinguish between batch and continuous processes. In batch processes, the whole bed material is always at the same state of attrition, which changes during the operating time according to Fig. 2. On the other hand, there is a particle residence time distribution in continuous processes. The attrition rate of the entire material is, therefore, constant although the state of attrition of each particle again changes according to Fig. 2.

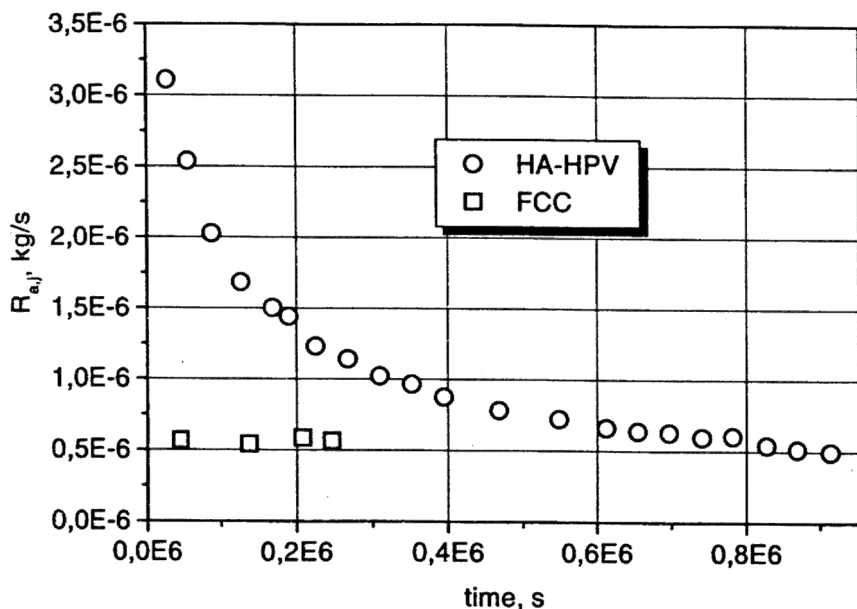


Figure 2. Time dependence of catalyst attrition in a submerged jet test ($D_t = 0.05$ m, $u_{or} = 100$ ms⁻¹, $d_{or} = 2$ mm, HA-HPV is a fresh catalyst whereas FCC is a spent cracking catalyst from a commercial unit. (From Werther and Xi, 1993.)

A lot of attempts have been made to describe the time dependence of the attrition rate in batch fluidized bed processes. Gwyn (1969) studied the degradation of catalysts in a small-scale test apparatus and defined the elutriated particles as the only attrition product. He described the increase of the elutriated mass, W_{el} , with time, t , based on the initial solid bed mass, $W_{bed,0}$, by the now widely known “Gwyn equation”

$$\text{Eq. (1)} \quad \frac{W_{el}}{W_{bed,0}} = K_a \cdot t^b$$

For several batches of the same catalyst with quite different mass median diameters, Gwyn found the exponent b to be constant, whereas the attrition constant K_a was found to decrease with mean particle size. Equation (1) is, therefore, valid for a particular size distribution only. Other

empirical correlations for the time dependence of the mass ratio $W_{el}/W_{bed,0}$ have been suggested by, for example, Pis et al. (1991) and Dessalces et al. (1994).

Temperature. There are three conceivable temperature effects that may influence the particle degradation in an either direct or indirect way, i.e., thermal shock, changes in particle properties and changes in the gas density.

The heating-up of fresh cold particles fed into a hot process can cause various phenomena that may lead to particle degradation. These are thermal stress, decrepitation, evaporation of moisture, hydrate decomposition and impurity transformation. On the other hand, particle properties such as strength, hardness and elasticity may be effected by the temperature, too. With respect to the resistance to degradation there is an optimum temperature range for any specific type of material. At lower temperatures particles become brittle and easy to break, while at higher temperatures they may soften, agglomerate or melt and lose discrete particulate properties. Consequently, it is important that the particle friability, which is the major factor for the attrition propensity of a given material, is assessed under conditions that are similar to those found in the respective process where the attrition is occurring. Moreover, the temperature can have a strong effect on the gas density, which affects the fluidization state and with it the particle motion and the stress to which the particles are subjected.

Pressure. The absolute pressure is unlikely to have a direct effect on attrition unless it affects the amount of adsorbed surface layers. But there is again an effect on the gas density that is similar to the effect of temperature mentioned above. Moreover, the rate of pressure change may have more influence.

Humidity. There are two conceivable effects of humidity. Particularly with respect to agricultural products the moisture content can influence the hardness and elasticity. For example, Segler (1951) observed that dry peas are more sensitive to breakage than wet ones. Moreover, Wyszynski and Bridgwater (1993) have reported that a lubricating layer of moisture on the particle surface can reduce the particle degradation.

Wall-Hardness. One can assume that the particle degradation increases with the hardness of the vessel wall. This effect will increase with increasing ratio of particle-to-tube diameter and will thus in practice be relevant in pneumatic conveying lines only.

Chemical Reaction. Chemical reaction of particulate material generates stresses within the particle that can lead to fracture. In the case of gas-solid reactions, the particle degradation is also desired because it accelerates the reaction by extending the reactive surface. A relevant commercial example is the particle degradation of solid fuels in combustion processes. This latter topic has been studied by Massimilla and coworkers extensively. The reader is referred for further details to a review given by Chirone et al. (1991).

3.0 ASSESSMENT OF ATTRITION

The effects of attrition on a given particulate material may be assessed in many different ways. One may base this assessment on the observation of an individual particle. Alternatively, the fate of a group of particles may be examined, or the effect of attrition on the bulk properties of a powder may be taken for this assessment. The British Materials Handling Board (1987) and Bemrose and Bridgwater (1987) have given a lot of examples for the different methods.

3.1 Breakage and Selection Functions

A description of the attrition process which is based on the individual particle can be obtained by dividing the bulk material in several size ranges to which both a respective probability of degradation and an individual size distribution of attrition products are assigned. This can be realized by a concept of two separate functions suggested by Broadbent and Calcott (1956). The first one is called *selection-for-breakage* function or probability function $S(d_p)$. It describes the degradation probability of a specific particle of size d_p in a specific time-interval. The second one is the so-called *breakage function* $B(d_{pi}, d_{pj})$ which describes the mass fraction of breakage products of size d_{pj} originating from a particle of size d_{pi} . The functions $S(d_p)$ and $B(d_{pi}, d_{pj})$ can be used as vectors and matrices, respectively, where the elements are applied to discrete particle size ranges. In detail, the vector elements s_i describe the rate of material loss of a particular size fraction of mean diameter d_{pi} and the various matrix elements b_{ij} describe the distribution of attrition products from the fraction i into the smaller fraction j . With a vector of the feed size distribution, they can be combined in a matrix

equation which yields a size distribution vector of the product (cf. British Materials Handling Board, 1987).

The use of selection and breakage functions is much more cumbersome than working with a single index number. This concept has, therefore, been used only for the description of comminution processes but not for the description of attrition.

3.2 Attrition Rate

The assessment of attrition is mainly based on the examination of the behavior of a group of particles. In fluidization technology the total or overall attrition rate $R_{a,tot}$ is commonly defined by the relative change of bed weight, W_{bed} , with time,

$$\text{Eq. (2)} \quad R_{a,tot} = - \frac{1}{W_{bed}} \frac{dW_{bed}}{dt}$$

or, alternatively by the relative change in elutriated fines, W_{el} , with time,

$$\text{Eq. (3)} \quad R_{a,tot} = \frac{1}{W_{bed}} \frac{dW_{el}}{dt}$$

Whether Eq. (2) or Eq. (3) is chosen will normally depend on the type of equipment used. When comparing different authors' works, attention should be paid to the definition of W_{bed} . For batch processes it may either be the initial bed mass or the instantaneous inventory of the bed.

In fluidized bed experiments, most authors assume that all attrition products are elutriated. Consequently, they measure either the decrease in bed mass and use Eq. (2) (e.g., Kono, 1981; Kokkoris et al., 1991, 1995) or the elutriated mass (e.g., Seville et al., 1992, Werther and Xi, 1993). It should be noted that all these authors used a certain particle size as a threshold below which all particles are assigned to be attrition products provided that all initial particles are clearly larger. Breakage events, which lead to particle sizes above the threshold level are, therefore, not considered. The choice of this threshold is very arbitrary and differs between the various research groups.

446 *Fluidization, Solids Handling, and Processing*

Special attention has to be paid to a definition of attrition rates in the case of continuous processes where fresh solid material is continuously added. This is particularly the case in heterogeneously catalyzed fluidized bed processes where fresh make-up catalyst must be added to compensate for attrition losses. The fresh catalyst may contain elutriable fines which add to the measurable elutriation rate thus leading to an apparently higher attrition rate.

Some authors (e.g., Vaux and Keairns, 1980, Sishtla et al., 1989, Pis et al., 1991) define the time integral of the attrition rate as the attrition extent $E_{a,tot}(t)$

$$\text{Eq. (4)} \quad E_{a,tot}(t) = \int_0^t R_{a,tot}(\tau) \cdot d\tau$$

although this definition includes effects of initial breakage and of initial fines content. Equation (4) will, therefore, normally not give an unambiguous assessment of the attrition process.

It should be noted here that the above definition of the attrition rate considers the bed material as a whole. More insights into the influence of elements of the fluidized bed apparatus, e.g., of the cyclone or of the gas distributor may be obtained from the observation of the change in the particle size distribution as has been demonstrated by Zenz and Kelleher (1980) and Lin et al. (1980).

3.3 Friability Indices

Data from attrition tests are usually presented as simple numbers called *friability* or *attrition indices*. Most of these indices are used as measures in quality control by subjecting the materials to a standard procedure. By comparing the test results with those of known materials, it is possible to give a relative characterization of the tested materials. Examples are given in Sec. 4.3.

3.4 Grindability Indices

There is no attrition test method that is accepted as being superior to others. However, there are two highly standardized and widely used test

methods to assess the material grindability, i.e., the Hardgrove Index and the Bond or Work Index. Both apply very large forces that cause far greater breakage than in usual fluidized bed processes, pneumatic conveying, or friability tests. Nevertheless, they may serve as a guide to the friability of some materials. For example, Sishtla et al. (1989) observed an interdependence between the Hardgrove Index and the attrition tendency of different types of char in a fluidized bed.

The Hardgrove Index is based on the quantity of new surface produced during a specific grinding process on a sample of material of a well-defined size range (595 to 1190 microns). For the practical use it is defined in ASTM D409-71. The Bond or Work Index represents the energy required in a ball mill to reduce one short ton of material from a theoretically infinitely larger particle size to a size range at which 80% of its weight is smaller than 100 μm . It is described in detail by Bond (1961).

4.0 ATTRITION TESTS

The large number of experiments that are termed attrition tests can be divided into two major fields of application, namely tests of material friability and experiments to study attrition phenomena. They will be separately discussed in the following subsections. The various test devices will be discussed afterwards.

4.1 Friability Tests

In friability tests the material's susceptibility to attrition is evaluated. But it is not as simple as it may seem at first to select the suitable test procedure. In this context Pell (1990) gave a simple thought experiment to illustrate the difficulties: If we took a batch of rubber stoppers and a batch of diamonds, and rubbed them on abrasive paper, we would conclude that the diamonds were more attrition resistant. If we instead struck the particles with a hammer we would conclude that the rubber were more attrition resistant. So, different test methods can rank materials differently with respect to their attritability. This effect was for example observed by Knight and Bridgwater (1985). They subjected spray-dried powders to a compression test, a shear test and a test in a spiral classifier. They found that each test gave a different ranking of the materials. Obviously, there is no

universal procedure for the measurement of a material's propensity to attrition. The attrition resistance is relative and depends on both the material and the stress. An ideal attrition test should, therefore, duplicate at least the controlling stress in the real process under consideration. This is the reason why, for example, fluidized bed catalysts are normally tested in especially designed fluidized bed test facilities.

Friability tests can be used for various purposes. They are widely used in quality control. Here, samples of produced material are subjected to a more or less arbitrary but well defined stress. The attrition extent is assessed by comparison with a standard value and a decision is reached whether the material meets the standard. Moreover, friability tests are often used for comparison of different materials to select the most attrition-resistant one. This is a usual procedure in the case of catalyst development. For example, Contractor et al. (1989) tested a new developed fluidized bed VPO-catalyst in a submerged-jet attrition test (described below). Furthermore, the specific attrition rate of a material in a certain process can be roughly estimated by friability tests. In this case the stress must be similar to that occurring in the process and the obtained degradation extent must be compared with those of other materials from which the process attrition rate is known.

Results that are obtained by different friability tests are usually not comparable. All these tests give only a relative attrition resistance and numerical results are only useful in connection with detailed information about the test considered.

4.2 Experiments to Study Attrition Mechanisms

Attrition cannot normally be directly investigated in the large-scale process. It is, for example, impossible to analyze the whole bulk of material and it is nearly impossible or at least very expensive to vary parameters in a running industrial process. For that reason, attrition has to be investigated in small-scale experiments. The results of these experiments require a model or at least an idea of the governing attrition mechanisms to be applied to the large-scale process. In principle, there are two different "philosophies" of attrition modeling.

The most commonly used philosophy is to design a test facility that simulates the relevant process stress. Examples of such test facilities are the various jet attrition test devices which are used in fluidization technology.

The results can either be directly extrapolated to a large-scale process or reveal relationships which may serve as guidelines in the design of this process. It should be noted that most of these tests are batch tests, but most full-scale processes are continuous. So, the transfer of the results can be difficult due to the time dependence of the degradation.

In the second attrition-modeling philosophy (e.g., Yuregir et al., 1987) it is believed that the mechanics of particle interaction in process test devices and in the large-scale processes are not sufficiently understood to maintain the necessary dynamic similarity. Instead, test devices have to be used where the material is subjected to a well-defined stress like compression, impact or shear. The chosen test should preferably apply the type of stress that is considered as the main source of attrition in the respective large-scale process. The complete process attrition can then be described by coupling of the test results with a model which describes the motion of fluid and particles and with it the frequency and extent of the stress. Ghadiri et al. (1992b, 1994, 1995) have applied this concept to jet attrition in the fluidized beds. Salman et al. (1992) used this approach to describe attrition in dilute pneumatic conveying lines.

4.3 Test Equipment and Procedures

Detailed reviews of such test procedures are given by Bemrose and Bridgwater (1987) and the British Material Handling Board (1987). The present subsection is restricted to a short discussion of those tests that are relevant for fluidized beds or pneumatic conveying lines.

Fluidized Bed Tests. These tests have direct relevance to all applications where particles are subjected to conditions of fluidization. Some authors believe that these tests can also to some extent simulate the stress of pneumatic transport. Coppinger et al. (1992) found at least a good correlation with the attrition resistance in dense-phase pneumatic conveying when they tested various powders in a slugging fluidized bed.

Most fluidized bed tests are currently carried out as so-called *submerged-jet tests*, where high-velocity gas jets submerged into a fluidized bed produce high attrition rates in a well-defined short period of time. The majority of these tests are based on the device suggested by Forsythe and Hertwig (1949). The setup consists of a 0.0254 m ID and 1.52 m long glass pipe, which bears a canvas filter at its upper end and is sealed by an orifice plate at the bottom. This latter plate contains a single 0.4 mm ID (1/64")

orifice in its center. The apparatus is operated in such a way that the jet gas velocity approaches the speed of sound in the orifice. The filter keeps all material inside the system. In order to assess the degradation extent, it is suggested to screen the material by wet sieving through -325 mesh (44 μm). The attrition rate is defined as the ratio of the increase in weight percent of -325 mesh particles and the weight percent of +325 mesh particles in the initial material. Using this test procedure, one has to take into account that the attrition-produced fines that are kept in the system might affect the material's attritability. Moreover, there are difficulties in using this test as a friability test, because the results are time integrated and have to be assessed with help of the particle size distribution. The materials which are to be compared should, therefore, have a similar initial particle size distribution and an identical pretreatment.

These difficulties are avoided in Gwyn's (1969) design (Fig. 3). Here, the attrition products are not kept inside the system but it is rather assumed that they are elutriated. In the enlarged diameter top section, gravity separation defines the limiting diameter of the elutriable particles. The attrition rate is assumed to be given by the elutriation rate. The steady-state elutriation rate can, therefore, be used as a friability index.

It should be noted here that the quantitative results obtained in a Gwyn-type attrition apparatus will in general depend not only on the cut size of the gravity separator but also on the particle size distribution of the particulate material tested. If the gas mass flow and the temperature are kept constant, then a variation in the solids density will result in a shift of the cut size and thus in the amount of material collected as "attrition product." Another point concerns the particle size distribution of the bed material. If the original solid sample is prepared by, for instance, sieving or sifting such that the smallest size is significantly larger than the cut size of the gravity separator, then one can be fairly sure that the elutriated material is indeed due to attrition. On the other hand, if the original particle size distribution contains a lot of fines, i.e., the cut size of the gravity separator is located somewhere inside the original particle size distribution, then the steady state of the attrition test will inevitably yield in the elutriated material not only attrited debris but also mother particles which have shrunk, due to attrition, to a size below the cut size. It is clear that in this latter case the attrition rate will differ from the one obtained with the previous test.

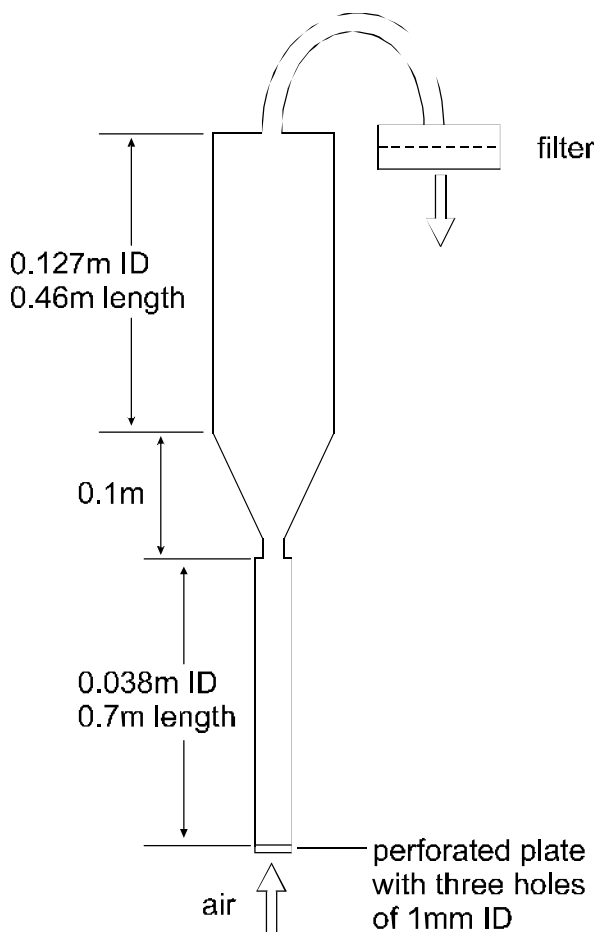


Figure 3. Schematic drawing of the fluidized bed test facility suggested by Gwyn (1969).

Both devices described above were developed in order to test the friability of fluid-cracking catalysts. Nowadays the application of these or similar tests is a common procedure in the development of fluidized bed catalysts. Contractor et al. (1989), for example, used a submerged-jet test to compare the attrition resistance of newly developed VPO catalysts. In fact, such tests can be applied to any type of fluidized bed processes. Sometimes they have to be slightly modified to adapt them to the process under consideration. The drilled plate may, for example, be substituted by

a porous plate if only attrition in the bed is of interest. Even temperature and pressure can be adapted. Vaux et al. (1981) investigated, for example, the friability of limestone sorbent that is used for fluidized bed combustion. By surrounding a “Gwyn-type” test facility with a heating system, they took thermal shock and calcination into account.

Pneumatic Conveying Tests. In contrast to fluidized bed tests, no standard equipment exists that simulates the stress on particles in pneumatic conveying lines. There is no friability test quoted in the pertinent literature that is based on a specific pneumatic conveying system.

Tests Applying Well-Defined Stress. As mentioned in Sec. 2, one can distinguish three pure and well-defined mechanical stresses on bulk solids material, namely compression, impact and shear. There are numerous tests that are based on compression and shear, e.g., Paramanathan and Bridgwater (1983), Neil and Bridgwater et al. (1994), Shipway and Hutchings (1993), but they are not further discussed in this chapter because these stresses are usually not relevant with respect to fluidized beds and pneumatic conveying lines. On the other hand, impact stress very often occurs whenever particles hit walls or other particles. Attrition caused by impacts can be observed, for instance, in grid jets, cyclones and bends or due to free fall. Consequently there is a great variety of impact tests that try to simulate these particular stresses. There are, for example, various drop shatter tests where the material falls under gravity onto a hard surface or a fixed bed. Such a test was carried out by Zenz and Kelleher (1980), who considered catalyst attrition due to free fall in a CFB downcomer. There are also standardized forms for coal and coke, respectively (ASTM D 3038). However, the probably most relevant impact tests are those where pneumatically accelerated particles are impacted onto a target. Yuregir et al. (1986, 1987) pioneered this type of test in their work on NaCl salt. Up to now such test devices have found a broad industrial application as friability tests. For example, Fig. 4 shows the set-up used by PSRI (Knowlton, 1996). It requires about 50 to 100 grams of material to conduct a test. The velocity at which the solids strike the impact plate is approximately 85 m/s. Higher velocities can be used, but the materials will completely shatter at velocities greater than a velocity called the *threshold velocity*. This is for most materials greater than 85 m/s. If velocities above the threshold velocity are used, then no relative attritability information can be obtained. The great advantage of such an impact test is that it can be used for a wide range of materials (from Geldart’s Group C to Group D).

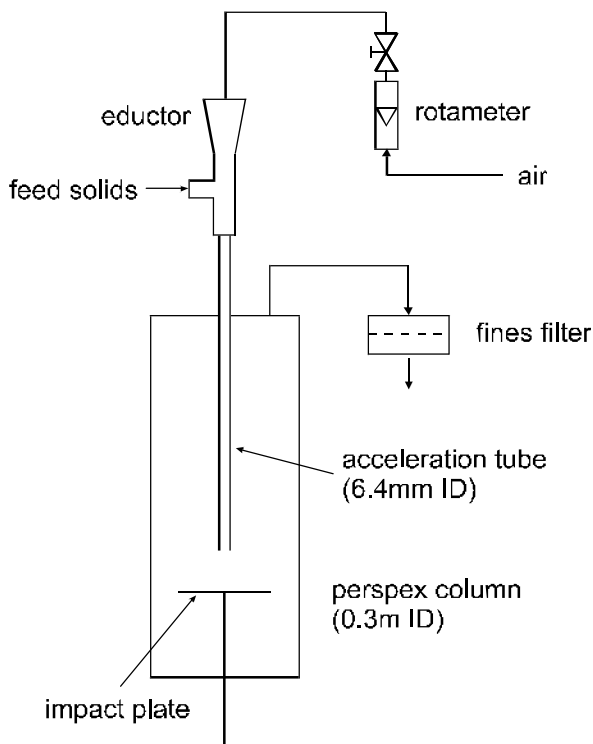


Figure 4. Schematic drawing of the impact test facility used by PSRI. (*Knowlton, 1996.*)

Other Tests. The so-called “tumbler tests” are usually used for testing material like coke, coal, iron ore pellets or tablets. They can be divided into drum tests and ball mill type tests. The latter type is used to derive both the Hardgrove Index and the Bond’s Work Index, which are often used to classify the material friability as described in Sec. 3. They are generally more suited to coarse material. The Hardgrove Grindability test requires an initial size range from 595 to 1190 microns.

The Grace-Davison jet-cup attrition test is often used to test the friability of catalysts (e.g., Weeks and Dumbill, 1990; Dessalces et al., 1994). The respective jet-cup apparatus is sketched in Fig. 5. The catalyst sample is confined to a small cup, into which air is tangentially added at a high velocity (about 150 m/s). Some authors (e.g., Dessalces et al., 1994)

assume that the stress in the jet-cup is similar to that prevailing in gas cyclones. With respect to fine catalysts, this type of test works as good as the impact test described above, but its applicability is limited to smaller sizes because larger particles tend to slug in the small cylinder. However, in the catalyst development, where at first only a little batch of catalyst is produced, this apparatus is an important friability test because it requires only a small amount of material (approximately 5 to 10 g).

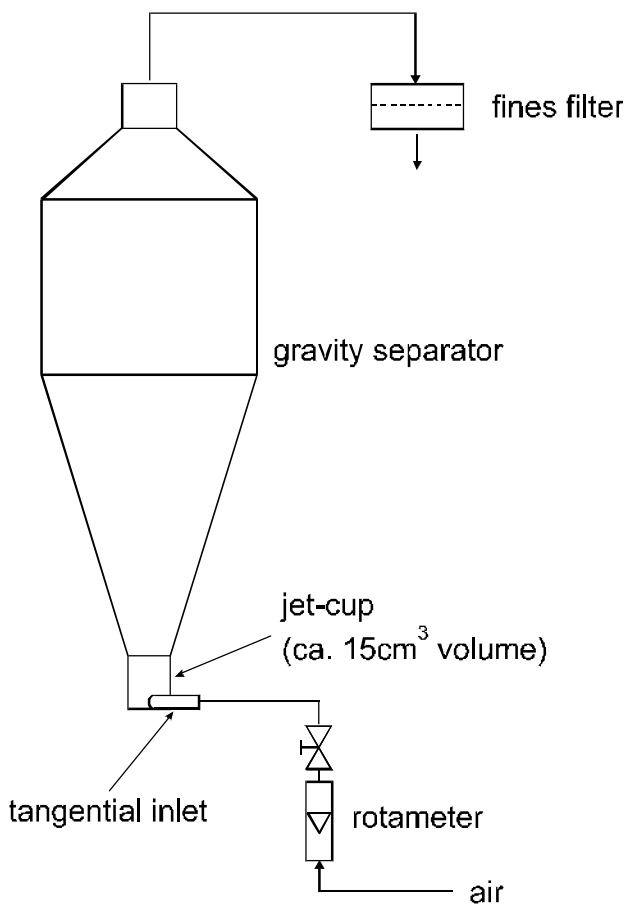


Figure 5. Schematic drawing of the Grace-Davison jet-cup attrition test. (After Weeks and Dumbill, 1990.)

5.0 ATTRITION IN FLUIDIZED BED SYSTEMS

Attrition in fluidized bed systems leads primarily to a loss of bed material since the cyclones, which are mostly used for the collection of entrained material, are not able to keep the attrition-produced debris inside the fluidized bed system. The material loss through the cyclone is, therefore, usually taken as the attrition rate. This means that among the attrition modes discussed in Sec. 2, namely fragmentation and abrasion, it is abrasion which is the attrition mode of interest for fluidized bed systems.

5.1 Sources of Attrition

There are several sources that are contributing to the attrition rate of a given fluidized bed process. Gas distributors of fluidized beds are often designed as perforated or nozzle plates. Since a minimum pressure drop is required to obtain a uniform gas distribution over the bed's cross-sectional area, the open surface area is rather small and the gas jets issuing from the distributor holes have a high velocity. Particles are entrained by these jets, accelerated to high velocities, and impacted onto the fluidized bed suspension at the end of the jets resulting in particle degradation similar to that in jet grinding processes. Above this distributor region, the motion of the bed particles is caused by the rising bubbles and their coalescence. This will result in frequent low velocity impacts between neighboring particles. Another stress situation will occur at the bed surface where bubble eruptions may lead again to high velocity impacts between the particles. Particle-wall impacts may be significant in small scale apparatus, but may probably be negligible on the industrial scale. On the other hand, impacts between bed particles and inserts like heat exchangers tube bundles or baffle plates will, in general, not be negligible. The contribution of the cyclones to the overall attrition rate in the fluidized bed system is naturally correlated to the solids loading of the gas at the cyclone inlet. Attrition will occur primarily in the inlet region where the particles impact on the wall or on other particles that are reflected and in the downward spiral path where the particles impinge onto the walls of the cyclone.

Equipment for solids transport which is usually needed in fluidized bed processes will also add to the overall attrition rate. In screw feeders or rotary valves, the particles can be crushed or sheared between the vanes and the housing. The contribution of pneumatic conveying lines is discussed in Sec. 6.

In circulating fluidized beds two main attrition sources, namely the riser and the return leg, may be distinguished. Although a lot of information is available about solids flow patterns and flow structures inside the circulating fluidized bed risers, no systematic investigations have been found in the open literature on the influence of riser geometry and flow conditions inside the riser on attrition. With respect to attrition occurring in the return leg, the work of Zenz and Kelleher (1980) on attrition due to free fall may be mentioned (cf. Sec. 4.3).

Grid Jets as a Source of Attrition. Jet attrition affects only a limited bed volume above the distributor, which is defined by the jet length. As soon as the jet is fully submerged its contribution to the particle attrition remains constant with further increasing bed height. Figure 6 shows some respective experimental results by Werther and Xi (1993). The jet penetration length can be estimated by various correlations, e.g., Zenz (1968), Merry (1975), Yates et al. (1986) or Blake et al. (1990).

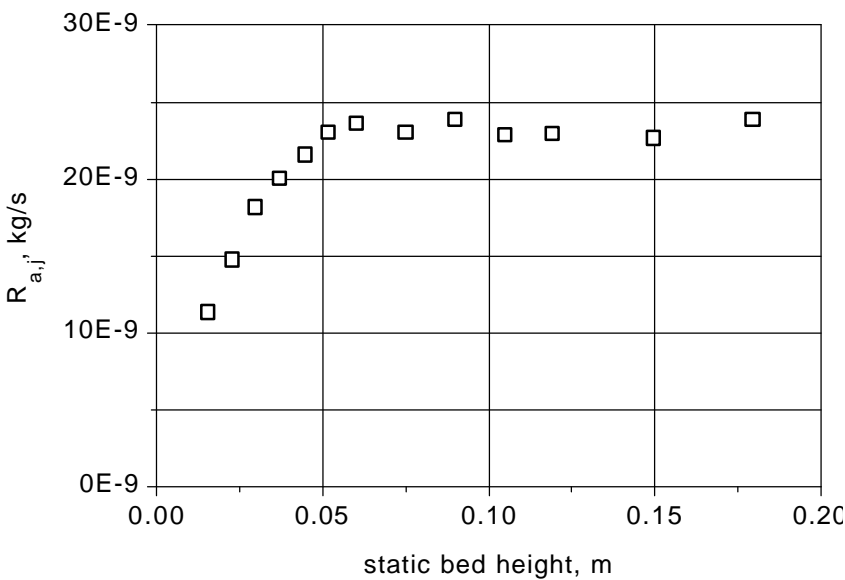


Figure 6. Influence of the static bed height on jet attrition of spent FCC catalyst in a submerged jet test facility ($D_t = 0.05$ m, $u_{or} = 100$ ms⁻¹, $d_{or} = 2$ mm. (Werther and Xi, 1993.)

In most commercial fluidized bed processes, the bed is much higher than the jet penetration length. There are several parameters that affect attrition in the jetting region, namely the design parameters of the distributor (i.e., orifice diameter, d_{or} , open surface area, A_o , number of orifices, N_{or}) and the operating parameters (i.e., gas density, \mathbf{r}_g , volumetric flow rate, v_g , superficial gas velocity, U_g , orifice velocity, u_{or}). It holds

$$\text{Eq. (5)} \quad A_o = \frac{\mathbf{p} \cdot d_{or}^2}{4} \cdot N_{or}$$

$$\text{Eq. (6)} \quad u_{or} = \frac{v_g}{A_o} = \frac{U_g \cdot A_t}{A_o}$$

Assuming there is no interaction between the individual jets, the entire attrition in the jet region can be interpreted as the sum of the contributions of the individual jets. The overall attrition rate of the distributor, $R_{a,distr}$, may thus be related to the jet attrition rate, $R_{a,j}$,

$$\text{Eq. (7)} \quad R_{a,distr} = N_{or} \cdot R_{a,j}$$

Both $R_{a,distr}$ and $R_{a,j}$ are introduced here as fines production rates with the dimension kg/s, which is in contrast to the definition of the overall attrition rate defined in Eqs. (2) and (3).

Modeling of Jet-Induced Attrition. Werther and Xi (1993) compared the jet attrition of catalysts particles under steady state conditions with a comminution process. They suggested a model which considers the efficiency of such a process by relating the surface energy created by comminution to the kinetic energy that has been spent to produce this surface area. The attrition rate, $R_{a,j}$, defined as the mass of attrited and elutriated fines per unit time produced by a single jet, is described by

$$\text{Eq. (8)} \quad R_{a,j} = K_j \cdot \mathbf{r}_g \cdot d_{or}^2 \cdot u_{or}^3$$

where K is a parameter which considers properties of the solid material, and \mathbf{r}_g is the density of the jet gas.

Ghadiri et al. (1992b, 1994, 1995) developed a more fundamental approach. They consider the particles entrained into the jet and relate the production of attrited fines to the attrition rates obtained from single particle impact tests (cf. Sec. 4.3). According to their model, it should be possible to predict jet attrition rates in fluidized beds on the basis of single particle impact tests combined with a detailed description of the jet hydrodynamics.

Experimental Techniques. Jet attrition cannot be investigated in isolation, because there is always some additional attrition of the bubbling bed. For that reason, many authors (e.g., Blinichev et al., 1968; Kutayavina et al., 1972; Arastoopour et al., 1983; Contractor et al., 1989) considered the overall attrition rate resulting from both attrition sources. In order to get direct insights into the mechanisms of jet attrition, it is necessary to separate the jet contribution from the measured overall attrition rate. This can be done in two different ways.

Seville et al. (1992) and Ghadiri et al. (1992a) measured the attrition rates at various static bed heights. As is shown in Fig. 7, they assume a linear increase of the attrition rate with bed height above the jet region. Extrapolating the measured attrition relationship to the jet length calculated from one of the available correlations yields the attrition rate $R_{a,distr}$ which is due to the jetting mechanism.

Werther and Xi (1993) used a Gwyn-type test facility with a particular distributor design where a separately fed nozzle was integrated into a porous plate (Fig. 8). At first the bed was only aerated via the porous plate. In this way the contribution of the bubbling bed attrition could be measured without any additional attrition sources. In a second step the facility was operated with a chosen jet gas velocity. In order to maintain the cut size of the gravity separator above the bed at some prescribed constant level they kept the superficial gas velocity by supplying auxiliary air through the porous plate. The resulting attrition rate measured is composed of the contributions of the jets and the bubbling bed. The jet attrition rate is now calculated by subtracting the bubble attrition rate, measured before, from the overall attrition rate. This is certainly an oversimplification since it assumes that the bubble attrition will always be the same regardless of the ratio of jet air mass flow to auxiliary mass flow. However, this method holds fairly well for low jet gas velocities, where the contribution of the jet gas flow to the total gas flow is rather small. For higher jet gas velocities the jet attrition is so large that the contribution of bubble attrition may be totally neglected.

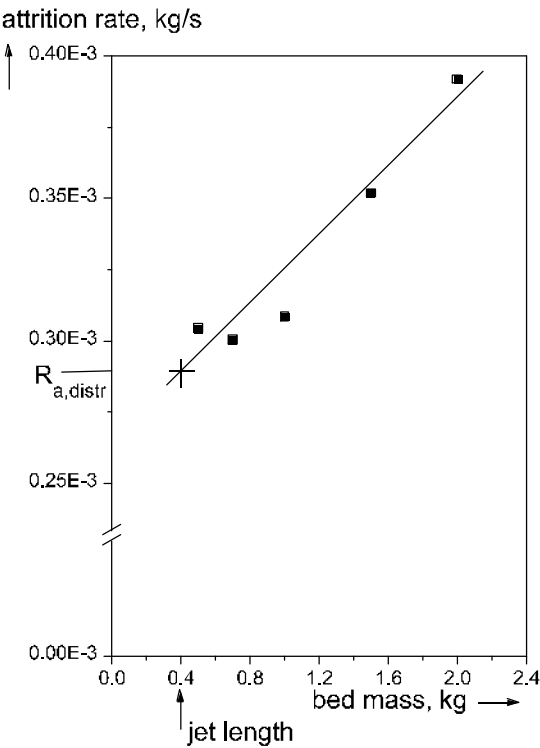


Figure 7. Evaluation procedure for the distributor attrition suggested by Seville et al. (1992).

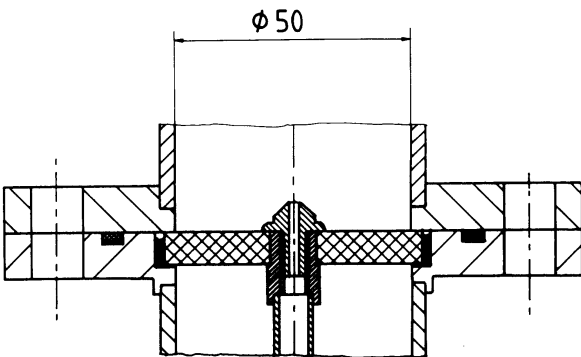


Figure 8. Distributor design suggested by Werther and Xi (1993) to separate the jet attrition and bubble-induced attrition.

Experimental Results. Orientation of the Jets. Werther and Xi (1993) have shown that the attrition effect of a horizontal jet equals that of an upward facing jet, whereas the effect of a downward issuing jet is significantly higher due to the impact of entrained particles onto the fixed bed of particles at the nose of the jet. However, up to now only upward facing jets have been investigated deeply and the following sections will, therefore, only deal with this type.

Orifice Velocity. Since the jet velocity is one of the decisive factors for jet attrition, numerous investigators have studied this subject. The attrition extent was found to be dependent on the jet gas velocity raised to a power of n , where n varied between 1 and 5.1. For example, Zenz and Kelleher (1980) found $n = 2.5$, Contractor et al. (1989): $n = 2$ to 4, Seville et al. (1992): $n = 1$, Ghadiri et al. (1992a): $n = 5.1$. Werther and Xi (1993) found $n = 3$ in accordance with Eq. (8) (see Fig. 9).

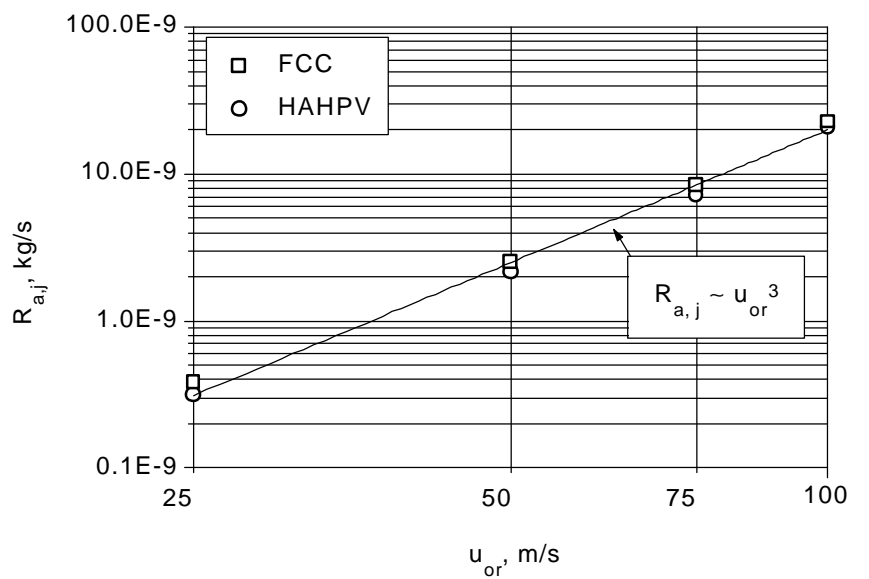


Figure 9. Influence of the jet velocity u_{or} on the jet attrition rate of catalysts ($d_{or} = 2$ mm. (Werther and Xi, 1993.)

The discrepancies between the exponents found by different authors are not astonishing considering the different methods of measurement and evaluation. For example, Ghadiri et al. (1992a) included the initial break-age in their calculation of the attrition rate, whereas Werther and Xi (1993) measured the attrition rate under steady state conditions (cf. Fig. 2).

Orifice Diameter. Werther and Xi (1993) found the attrition rate per jet to be proportional to the square of the orifice diameter, again in accordance with Eq. (8) (see Fig. 10). The same relationship was found by Zenz and Kelleher (1980) and Contractor et al. (1989) although these latter authors measured the overall attrition rate instead of the jet attrition rate.

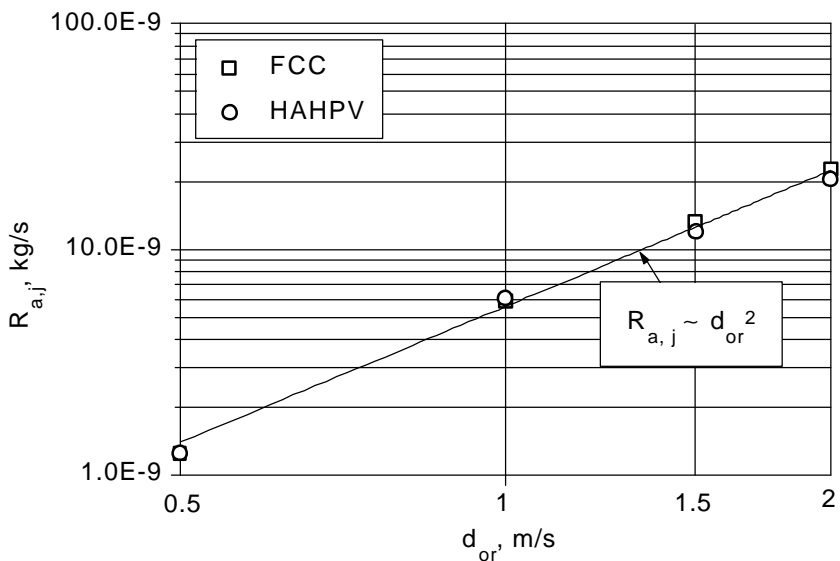


Figure 10. Influence of the orifice diameter d_{or} on the jet attrition rate of catalysts ($u_{or} = 100$ m/s. (Werther and Xi, 1993.)

Distributor Design. If in the case of a given process application, an open surface area A_o is required to create a sufficient high pressure drop for a given superficial fluidizing velocity, then the question arises whether a few large orifices or a large number of small orifices will lead to a lower distributor attrition rate, $R_{a,distr}$. It follows from Eq. (6) for a given volumetric gas flow

$$\text{Eq. (9)} \quad u_{or} \propto \frac{1}{N_{or} \cdot d_{or}^2}$$

Substitution of Eq. (9) into (8) leads to

$$\text{Eq. (10)} \quad R_{a,j} \propto \frac{1}{N_{or}^3 \cdot d_{or}^4}$$

Furthermore it follows with Eq. (7)

$$\text{Eq. (11a)} \quad R_{a,distr} \propto \frac{1}{N_{or}^2 \cdot d_{or}^4} \propto \frac{1}{A_o^2}$$

Equation (11a) reveals that the decisive quantity for the distributor attrition rate is the open surface area A_o . Obviously, with respect to attrition it is unimportant whether A_o originates from a few large or from many small orifices.

Superficial Gas Velocity. According to Eq. (6) there is a linear relationship between the superficial gas velocity U_g and the jet velocity u_{or} . With Eq. (8) it follows that the grid jet attrition rate will be proportional to the cube of the superficial gas velocity.

$$\text{Eq. (11b)} \quad R_{a,distr} \propto U_g^3$$

Bubble-Induced Attrition. Bubble-induced attrition originates from low-velocity interparticle collisions since the bubble rise velocity is of the order of 1 m/s. The energy is, therefore, generally not high enough to shatter particles into fragments. For that reason most laboratory experiments have shown the bubbles to be a minor source of attrition. However, in a deep bed with several meters of height the contribution of bubble-induced attrition may be a significant factor.

The extent of the attrition which is due to the presence of bubbles is conveniently described by the relative production rate of fines

$$\text{Eq. (12)} \quad R_{a,bub} = \frac{1}{W_{bed}} \cdot \frac{dW_{el,bub}}{dt}$$

where $dW_{el,bub}$ denotes the mass of fines which is produced by bubble-induced attrition and which is measured as elutriated material. The parameter W_{bed} is the instantaneous bed mass.

Again, as in the case of jet attrition, attention must be paid in the experimental determination of $R_{a,bub}$ to the isolation of the attrition that is due to bubbles. There are basically two ways to do this. The one is to use a porous plate distributor in order to avoid any grid jets. The other is the procedure suggested by Ghadiri et al. (1992a) which is depicted in Fig. 7: the measurement of the production rate of fines at different values of the static bed height permits to eliminate the grid jet effects.

Modeling of Bubble-Induced Attrition. Merrick and Highley (1974) have modeled bubble-induced attrition as a comminution process. According to Rittinger's law of size reduction by abrasion (cf., Perry, 1973), the rate of creation of new surface area $\Delta S/\Delta t$ is proportional to the rate of energy input $\Delta E/\Delta t$

$$\text{Eq. (13)} \quad \frac{\Delta S}{\Delta t} \propto \frac{\Delta E}{\Delta t}$$

Since the size distribution of the fines produced by abrasion is approximately constant, the rate of production of new surface can be taken to be proportional to the mass rate of production of fines,

$$\text{Eq. (14)} \quad \frac{\Delta S}{\Delta t} = R_{a,bub} \cdot W_{bed}$$

The total rate of input of energy to the fluidized bed is given by the product of the volumetric flow rate of gas ($U_g \cdot A_t$) and the pressure drop, which may be expressed as weight of the bed divided by the bed's cross sectional area, A_t . However, only part of the input energy is available for bubble formation and thus for comminution. The input energy ($U_{g,mf} \cdot W_{bed} \cdot g$) is required for keeping the particles in suspension. That part of the rate of input of energy which is remaining for bubble formation and thus for attrition is then given by $[(U_g - U_{g,mf}) \cdot W_{bed} \cdot g]$. Insertion into Eq. (14) yields

$$\text{Eq. (15)} \quad R_{a,bub} = K_{bub} \cdot (U_g - U_{g,mf})$$

where K_{bub} is an abrasion rate constant. With a similar approach Ray, et al. (1987a) arrived at the same result.

Vaux (1978), Ulerich et al. (1980) and Vaux and Schruben (1983) proposed a mechanical model of bubble-induced attrition based on the kinetic energy of particles agitated by the bubble motion. Since the bubble velocity increases with bed height due to bubble coalescence, the collision force between particles increases with bed height as well. The authors conclude that the rate of bubble-induced attrition, R_{bub} , is then proportional to the product of excess gas velocity and bed mass or bed height, respectively,

$$\text{Eq. (16)} \quad R_{a,bub} = K'_{bub} \cdot (U_g - U_{g,mf}) \cdot H_{bed}$$

Experimental Results. Gas Velocity. Merrick and Highley (1974) used a fairly large pilot-scale fluidized bed combustion plant (bed area: $0.91 \times 0.46 \text{ m}^2$, total height: 3.9 m) in their investigation of coal and limestone attrition in the fluidized bed. The bed was operated at fluidizing velocities in the range of 2 to 8 ft/s and bed heights of 2 to 4 ft. Their results confirmed the validity of Eq. (15), i.e., the bubble-induced attrition rate $R_{a,bub}$ turned out to be proportional to $(U_g - U_{g,mf})$ and was independent of the bed height.

Arena et al. (1983) and Pis et al. (1991) also found that Eq. (15) gave a good description of their experimental results. As an example, Fig. 11 shows the results of Pis et al. (1991), which were obtained in a fluidized bed column of 0.14 m in diameter. The distributor had 660 orifices of 1 mm in diameter. Unfortunately, no distinction was made between the measured attrition rate and the influence of the grid jets. However, their influence might be negligible in the present case due to the relatively small jet velocity.

Ray et al. (1987a) investigated the influence of the gas velocity in a 0.1 m diameter bed, which was equipped with a porous plate. Results of their investigation of the velocity effect on the attrition rate of narrow size fractions of limestone with particle sizes between 1.09 and 0.77 mm are plotted in Fig. 12. Similar results were obtained by Xi (1993), who investigated the attrition of fine catalyst particles with a minimum fluidization velocity $U_{g,mf}$ of 0.002 m/s (Fig. 13). As is obvious from Figs. (12) and (13), the attrition rate extrapolates to zero at a fluidizing velocity $U_{g,min}$ which is significantly larger than $U_{g,mf}$. This means that a minimum kinetic energy or a minimum extent of bubbling is necessary to cause attrition.

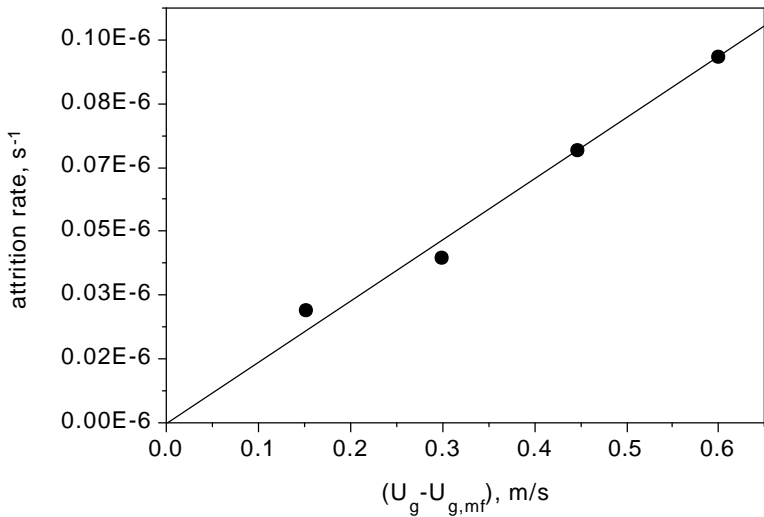


Figure 11. Variation of the steady-state attrition rate of coal ash (0.2 to 0.315 mm) with $(U_g - U_{g,mf})$. (Pis et al., 1991.)

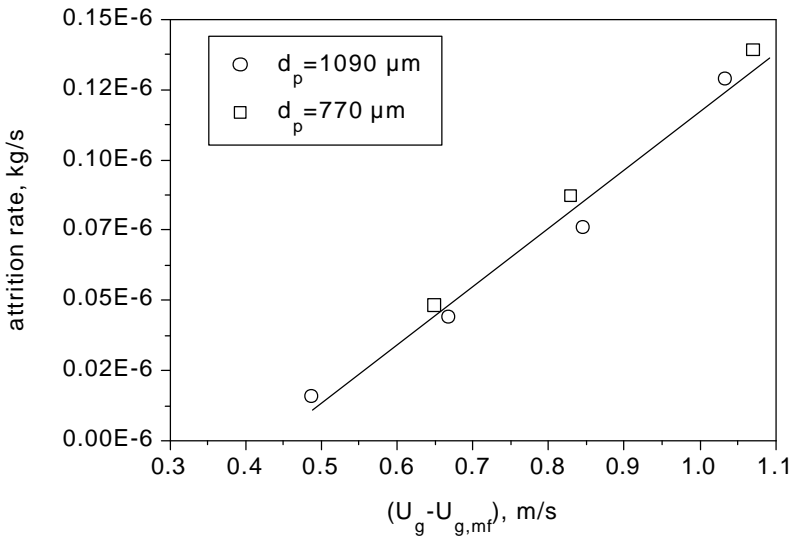


Figure 12. Variation of the steady-state attrition rate of limestone fractions with $(U_g - U_{g,mf})$. (Ray et al., 1987a.)

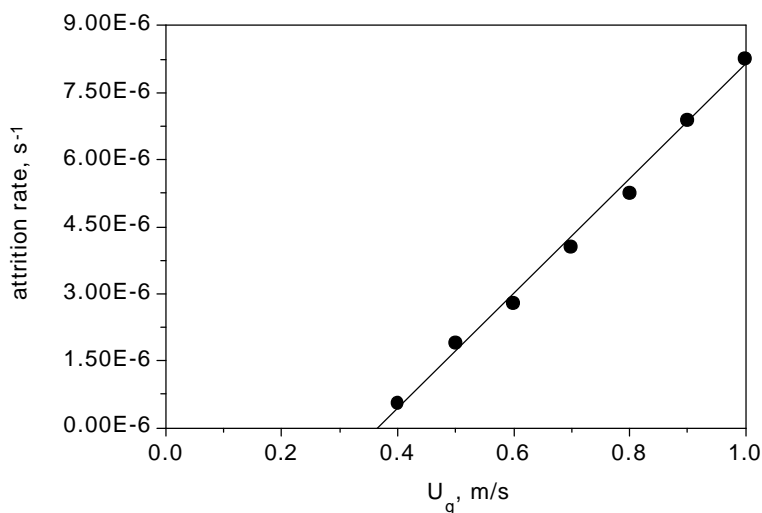


Figure 13. Variation of the steady-state attrition rate of a catalyst with superficial gas velocity (AVN 802, $U_{g,mf} = 0.002$ m/s. (Xi, 1993.)

Bed Height. The effect of the bed height or bed weight on the bubble-induced attrition rate $R_{a,bub}$ is not quite clear. Merrick and Highley (1974) and Pis et al. (1991) have found $R_{a,bub}$ to be independent of bed height in accordance with Eq. (15). Kono (1981) found the attrition rate to be proportional to the static bed height with the exponent 0.78, $R_{a,bub} \propto H_{stat}^{0.78}$. Furthermore, Ulerich et al. (1980) and Xi (1993) found $R_{a,bub}$ to be proportional to the bed height. As an example Fig. 14 shows Xi's results.

Obviously the role of bed height is not yet fully understood. Ray et al. (1987a) have explained these discrepancies by a consideration of bubble growth with height above the distributor. They argue that as long as the bubble size increases with height, the efficiency of the transformation of kinetic energy to free surface energy might increase thus leading to a bubble-induced attrition rate that increases with bed height. However, as the bed height reaches the limits of slugging in small diameter columns or maximum attainable bubble in a large diameter bed, an extra bed height will not vary the conditions of bubbling and thus will result in $R_{a,bub}$ becoming independent of bed height. However, further experiments are certainly needed in this area.

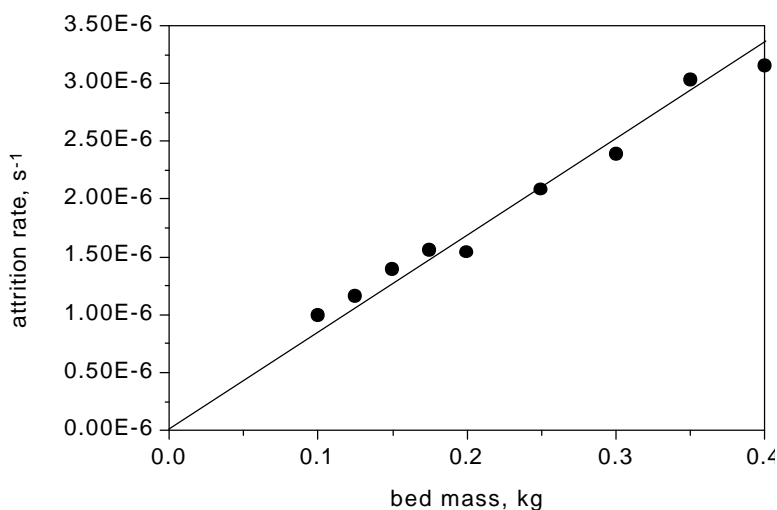


Figure 14. Variation of the steady-state attrition rate of a catalyst with bed height. (Xi, 1993.)

Internals. Commercial fluidized beds are often equipped with internals, e.g., baffle plates and heat exchanger tubes. Due to their interaction with the rising bubbles they will certainly cause particle attrition. Unfortunately, no systematic investigations are available in the open literature which could serve as practical guidelines.

Cyclones as Attrition Sources. Attrition in cyclones is a difficult field. The number of publications available in the open literature is very small. This may be due to the fact that experiences with the performance of cyclones are often considered proprietary. However, this lack of information can also be explained by strong experimental difficulties which mainly originate from the problem of making a distinction between the collection efficiency and attrition. The cyclone is a separator which is usually designed to keep as much material as possible inside the fluidized bed system. The material which cannot be kept inside the system, i.e., the loss or elutriation, is usually defined as attrition. But in fact, the elutriation rate originates from both sifted original fines entering the cyclone (i.e., from the original feed particle size distribution or produced by attrition in other parts of the fluidized bed system) and fines that are actually produced by attrition in the cyclone. Unfortunately, the attrition rates in other parts of the system and, therefore, their contribution to the elutriation rate is usually unknown.

Consequently, it is very difficult to evaluate the cyclone attrition rate from the measured elutriation rate. In order to study the cyclone attrition mechanism in detail it is necessary to study the cyclone in isolation. This can be achieved by feeding a cyclone batch-wise and directly without any additional equipment that could contribute to attrition.

Moreover, not all attrition products will be directly elutriated from the cyclone. Instead, a part will be collected by strands of the material and will be transported via the solids return line into the fluidized bed process. In subsequent passes through the cyclone, the accumulated attrition-produced fines will be elutriated due to the sifting effect of the cyclone.

For the special case of an isolated cyclone, which is fed with a mass flux $m_{c,in}$ of material sufficiently large to be sent into the catch of the cyclone, the measured mass flux in the loss of the cyclone, $m_{c,loss}$ is solely due to attrition inside the cyclone. In such a case the cyclone attrition rate $R_{a,c}$ may be defined by

$$\text{Eq. (17)} \quad R_{a,c} = \frac{m_{c,loss}}{m_{c,in}}$$

Modeling of Cyclone Attrition. A very simple model of cyclone attrition may be formulated in analogy to the models discussed with respect to jet attrition and bubble-induced attrition (Reppenhagen and Werther, 1997).

In the spiral or tangential cyclone inlet duct, the particles are accelerated to a velocity which is related to the inlet gas velocity U_e . Neglecting as a first approximation the slip between solids and gas, the kinetic energy of the solids which is transported per unit time into the cyclone is approximately given by

$$1/2 \cdot m_{c,in} \cdot U_e^2$$

The fraction h of this kinetic energy is used to create free surface energy via abrasion,

$$\text{Eq. (18)} \quad h \cdot 1/2 \cdot m_{c,in} \cdot U_e^2 = m_{c,loss} \cdot S_m \cdot g$$

where S_m is the mass specific surface area generated by abrasion and $\gamma(J/m^2)$ is the specific free surface energy of the solid material. Since abrasion produces very fine particles with a size distribution that is fairly

independent of the operating conditions, S_m may be assumed to be constant for a given material. Rearrangement of Eq. (18) yields

$$\text{Eq. (19)} \quad R_{a,c} = \frac{1}{2 \cdot g \cdot S_m} \cdot h \cdot U_e^2$$

According to Eq. (19) the cyclone attrition will be proportional to the square of the gas inlet velocity. The production rate of attrited fines, which is identical here to the mass flux in the cyclone loss, is then given by

$$\text{Eq. (20)} \quad m_{c,loss} = \frac{1}{2 \cdot g \cdot S_m} \cdot h \cdot U_e^2 \cdot m_{c,in}$$

Experimental Results. Zenz (1974) and Zenz and Kelleher (1980) considered attrition of FCC catalysts in isolated cyclones. They used different cyclones (4" to 30" ID). A suction fan was attached to the cyclone outlet. A given batch of solids was sucked through the cyclone. Afterwards the overhead and the bottom were mixed and once again sucked through the cyclone. After twenty passes through the cyclone they observed significant changes in the particle size distribution. An example is given in Fig. 15. Particles in the 70 to 100 micron size range are seen to have decreased in concentration, whereas particles in the 30 to 70 micron size range increased in number and smaller particles showed no significant change. From many experiments of this kind, Zenz and Kelleher (1980) derived design correlations for the estimation of cyclone attrition for fluidized bed systems. Unfortunately the details of these estimations remained proprietary.

More recently, Reppenhagen and Werther (1997) have conducted a comprehensive study of the attrition mechanism in a cyclone. Their experimental set-up is shown in Fig. 16. The 0.09 m ID cyclone is operated in the suction mode. The solids (spent FCC, surface mean diameter 105 microns) are introduced via a vibrating feeder into the cyclone inlet tube which allows an independent variation of cyclone inlet velocity U_e and solids loading m

$$\text{Eq. (21)} \quad m = \frac{m_{c,in}}{U_e \cdot r_g \cdot A_{c,e}}$$

where $A_{c,e}$ is the cyclone inlet cross-sectional area. After a test run, the catch of the cyclone is used as a starting material for the next run, i.e., catch and

loss are not mixed again. Figure 17 gives an example of the results. The cyclone loss rate per single pass is plotted against the number of passes for given operating conditions (U_e , m). In analogy to Fig. 2, a large initial cyclone loss rate is observed which rapidly decreases, and after 10 to 20 passes, reaches a steady-state value. The high value of the loss rate during the first couple of passes is due to the added effects of attrition and sifting, whereas the steady-state value is identical to the true cyclone attrition rate $R_{a,c}$. After thirty-four passes, the operating conditions were changed to a higher inlet velocity which, due to a constant solids feeding rate, was combined with a corresponding reduction in the solids loading. The measurements show a slow increase of the cyclone loss rate which, after another fifteen passes, leads to a steady state again. This slow transition is caused by the fact that part of the fines generated by attrition are sent into the catch of the cyclone.

According to the model described above the cyclone attrition rates $R_{a,c}$ obtained under steady-state conditions have been plotted against the square of the cyclone inlet velocity in Fig 18. Although the number of experiments is not large the general relationship between $R_{a,c}$ and U_e predicted by Eq. (19) is confirmed.

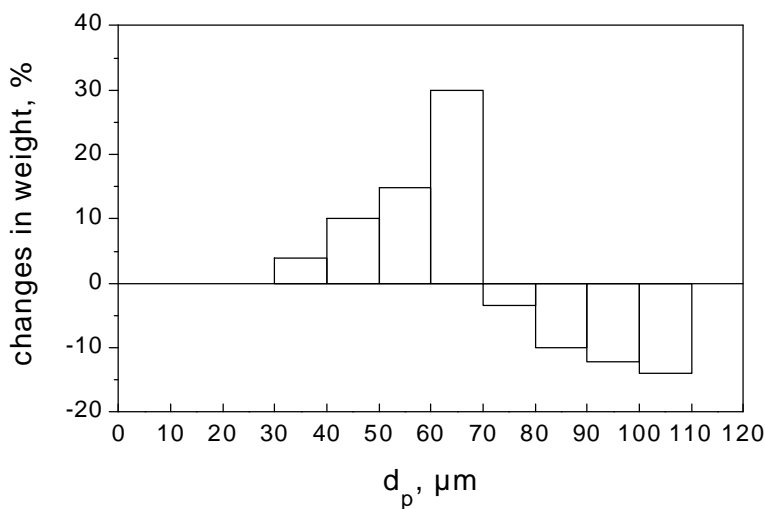


Figure 15. Changes in the size distribution of FCC catalyst due to attrition in a 5" cyclone, (inlet velocity 35ft/s). (Zenz and Kelleher, 1980.)

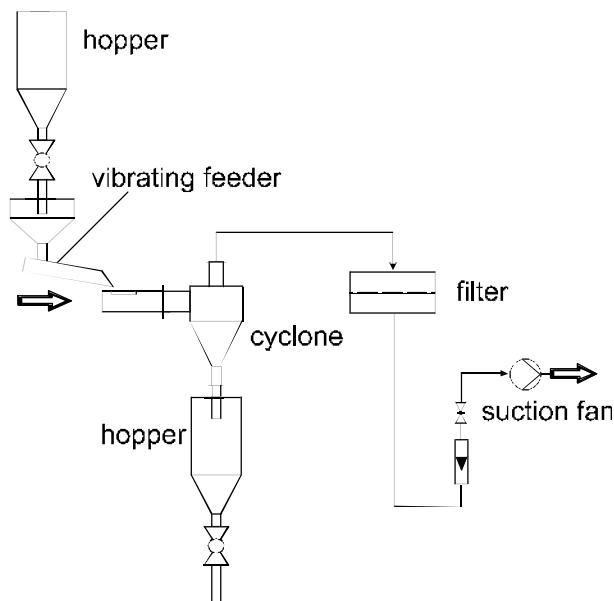


Figure 16. Experimental set-up for the isolated investigation of cyclone attrition (cyclone ID = 0.09 m). (By Reppenhagen and Werther, 1997.)

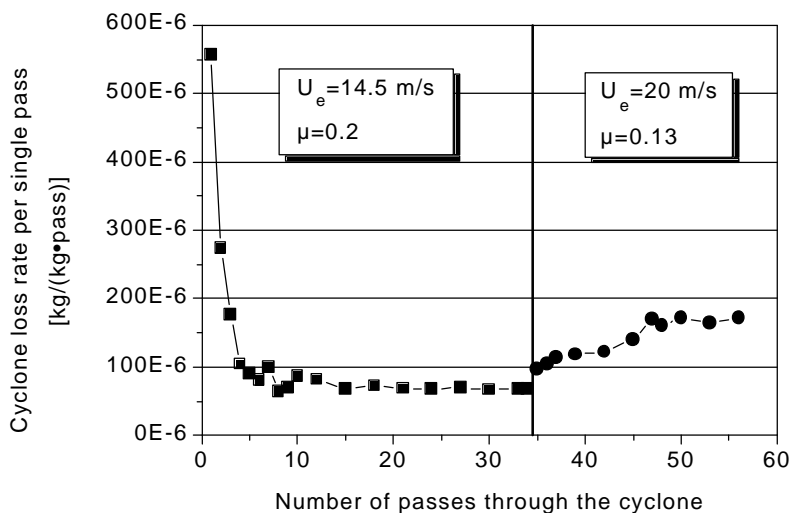


Figure 17. Cyclone loss rate of spent FCC catalyst as a function of the number of passes through the cyclone. (Reppenhagen and Werther, 1997.)

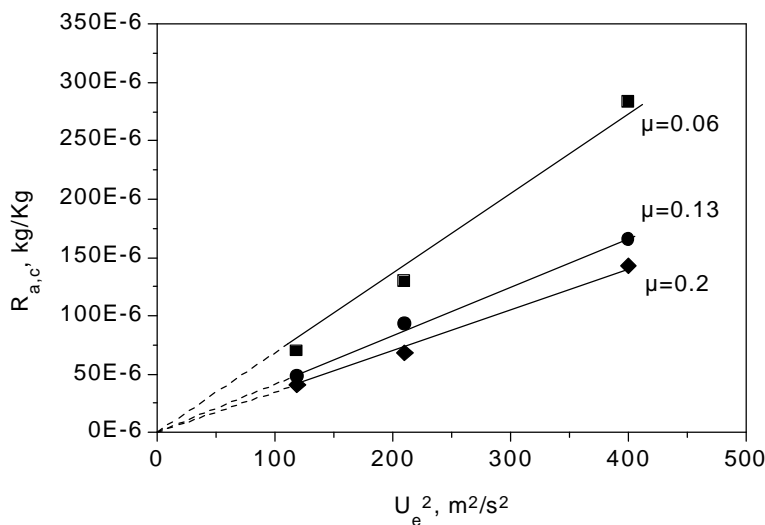


Figure 18. Influence of inlet velocity U_e and solids loading μ on the steady-state cyclone attrition rate. (Reppenhagen and Werther, 1997.)

As is seen from this latter figure, an increase of the solids loading results in a decrease in the cyclone attrition rate. This may be due to a “cushioning” effect of the increased solids concentration which is well known in comminution processes. This cushioning effect may be interpreted as a decrease in the efficiency h of the abrasion process. If we assume h to be a function of m and in its simplest form to follow an exponential function,

Eq. (22) $h \propto m^n$

it follows from Eq. (19)

Eq. (23) $R_{a,c} = K_c \cdot U_e^2 \cdot m^n$

All measurements have been plotted in Fig. 19 as $(R_{a,c}/U_e^2)$ against the solids loading on a double logarithmic grid. The measurements are seen to be well described by Eq. (23) with $n = -0.5$. It should be noted here that the range of m and U_e which has been investigated is not large enough to permit very general conclusions to be drawn. More investigations are certainly needed in this area.

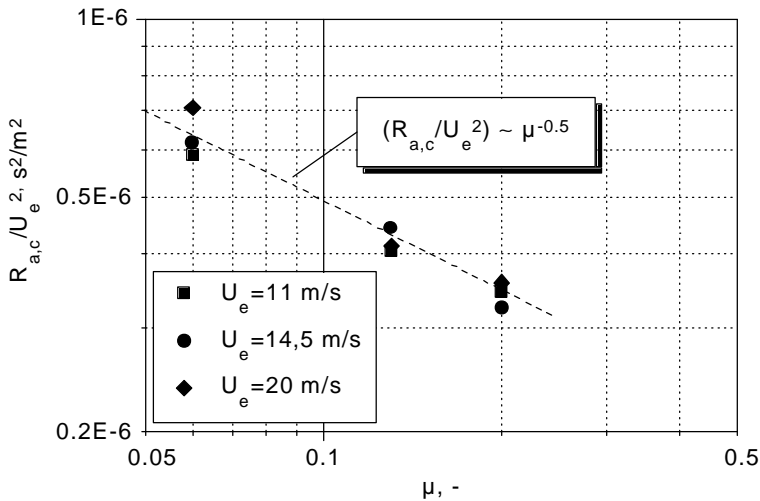


Figure 19. Influence of the solids loading μ on cyclone attrition. (Reppenhagen and Werther, 1997.)

However, the present results already allow a conclusion to be drawn with respect to the solids mass flux $m_{c,loss}$ which is lost from the cyclone as a result of attrition inside the cyclone. From Eq. (23) it follows with $n = -0.5$ and with the definition of $R_{a,c}$

Eq. (24)
$$m_{c,loss} = K_c \cdot m_{c,in} \cdot \frac{U_e^2}{m^{0.5}}$$

Eq. (25)
$$m_{c,loss} = K_c \cdot r_g^{0.5} \cdot A_{c,e}^{0.5} \cdot m_{c,in}^{0.5} \cdot U_e^{2.5}$$

The cyclone inlet velocity is thus shown to be the most significant factor influencing the solids loss due to attrition in the cyclone.

5.2 Attrition in the Overall Fluidized Bed System, Continuous Processes

As has been demonstrated above, there are several parts of the fluidized bed system with distinctly different attrition mechanisms. They all

contribute to the overall attrition rate in the fluidized bed system, $R_{a,tot}$, which is measured in the form of the cyclone loss rate by the bed mass,

$$\text{Eq. (26)} \quad R_{a,tot} = \frac{m_{c,loss}}{W_{bed}}$$

Considering the different parameter dependencies, e.g., with respect to the fluidizing velocity U_g

$$\text{Eq. (27)} \quad \text{in the distributor region: } R_{a,distr} \propto U_g^3$$

$$\text{Eq. (28)} \quad \text{in the bubbling fluidized bed: } R_{a,bub} \propto (U_g - U_{g,min})$$

$$\text{Eq. (29)} \quad \text{in the cyclone: } R_{a,c} \propto U_g^2$$

it is not surprising that experimental results from different investigations are varying widely if only overall attrition rates are compared.

Up to now attrition has been considered in batch processes only. However, most industrial fluidized bed processes are operated in a continuous mode. This means with respect to attrition in catalytic processes, that the cyclone loss is compensated for by the addition of fresh make-up catalyst. Consequently, there is an age distribution of the solids and the time dependence of attrition has to be taken into account. According to Sec. 2 there will be both high initial attrition of freshly fed material and steady state attrition of “old” particles. Zenz (1971, 1972, 1980) was among the first to suggest calculation procedures for the content of fines which is attained at equilibrium as a result of attrition and addition of new catalyst in a fluidized bed system. Levenspiel et al. (1968) and Kunii and Levenspiel (1969) suggested the consideration of particle balances in the system. Newby et al. (1983) proposed a simple mass balance for the entire system and distinguished between continuous and instantaneous attrition which was connected to the feed rate. Vaux and Schruben (1983, 1985) extrapolated their time-dependent bubble attrition model to a continuous process. Fuertes et al. (1991) coupled a description of time dependence derived from batch processes with the residence time distribution function of a continuous stirred tank reactor. More recently, Ray et al. (1987b) and Werner et al. (1995) presented population balance models to describe process attrition. In

all these models, however, the attrition mechanism is treated in a rather superficial way without making a distinction of the different mechanisms prevailing in the different parts of the system.

5.3 Steps to Minimize Attrition in Fluidized Beds

In general there are two ways to minimize attrition. First of all the solid particles should be chosen, treated or produced in such a way that they are as attrition-resistant as possible. On the other hand, the fluidized bed system should be designed in such a way that the effects of the various attrition sources are kept as small as possible.

The Bed Material. Only catalytic processes are relevant with respect to modifying the attrition resistance of the bed material. In other processes, e.g., drying, the bed material is the product and cannot be changed. In the combustion of solid fuels, the particle degradation due to attrition enlarges the reacting surface and thus increases the reactivity of the fuel. On the other hand, the lack of attrition resistance is often a major obstacle that hinders the commercialization of fluidized bed catalytic processes.

Catalysts for fluidized bed reactors are preferably prepared by spray-drying to form readily fluidizable spherical particles. A commonly used approach for imparting attrition resistance is to add 30 to 50 wt% of colloidal silica to the catalyst precursor before spray drying. By this procedure the active catalyst is embedded in a continuous, hard skeleton. But the large amount of silica may affect both the catalyst's activity and selectivity. Contractor et al. (1989) observed a significant selectivity loss for vanadium phosphate catalysts with the selective oxidation of butane to maleic anhydride. As a solution they suggested a new technology that encapsulates the active catalyst in a porous silica shell. The pore openings are large enough for the reacting species to diffuse into and out of the inner region of the particle without any effect on the selectivity. Patience and Mills (1994) reported that this new catalyst type can even be used in a circulating fluidized bed riser.

Kokkoris et al. (1991, 1995) suggested another method to impair catalyst attrition. In a small scale slugging bed they reduced the attrition rate of zeolites by addition of only very small quantities of various fine solid "lubricants." In the case of graphite the reduction was up to 30%. The fines were assumed to reduce attrition by forming a protective coating that

facilitates the sliding of the particles against each other. Similar effects were also observed by Wyszynski and Bridgwater (1993) with respect to degradation of granular salt in a powder blender. Even the attrition-produced fines can reduce attrition (Sec. 2). However, in order to apply these effects to industrial processes, it must be ensured that the fine particles have a sufficiently long residence time in the system. This might be possible, because Kato et al. (1994) and Nakagawa et al. (1995) found that fine particles remain much longer in fluidized beds than theoretically expected.

If the bed material is a mixture of different particle types, abrasion of one component can be reduced by the decrease of its surface in relation to the entire material surface in the bed (cf. Sec. 2). A potential field of application is the coal combustion process with the three components coal, ash and limestone.

Design Procedures. Gas Distributor. Perforated plates are often used as gas distributors. Although several investigations (e.g., Seville et al. (1992)) have shown the porous plate to produce the least attrition such distributors cannot be used in technical processes because of their tendency to clog. Bubble-cap distributors are more often used in commercial processes, but up to now there are only a few investigations with respect to their contribution to attrition. In comparison to drilled plates, Blinichev et al. (1968) found a smaller attrition rate of bubble-cap distributors, although Kutuyavina et al. (1972) found the attrition to be significant higher.

With respect to grid jet attrition, it is known from Sec. 5.1 that attrition is inversely proportional to the square of the free cross section A_o , which can be achieved by either a lot of small orifices or a few larger ones. A certain distributor pressure drop is generally needed to guarantee uniform gas distribution. This distributor pressure drop immediately implies a certain value of the orifice velocity, u_{or} . According to Eq. (8) the jet attrition rate is proportional to u_{or}^3 . A means to reduce the grid attrition is now to avoid direct submersion of the gas jet into the bed. This could be done either by the use of bubble caps or by retracting the jet below the distributor plate level as it is shown in the design suggested by Parker et al. (1976) and Parker and Gwyn (1977) (Fig. 20). The covering pipe surrounding the jet should be sufficiently long such that the gas jet has reached the tube wall and the average velocity in the jet has reduced with the ratio of orifice area to tube area. Caution should be exercised with this design since, if the jet is not completely filling the tube, then the bed will penetrate into the tube and the

gas jet might then act as a quite efficient jet mill. Van Swaaij et al. (1972) mentioned another fluidized bed reactor where the detailed design of a tuyere type was crucial for the interaction between bed and distributor gas jets and thus for the attrition of the catalyst particles.

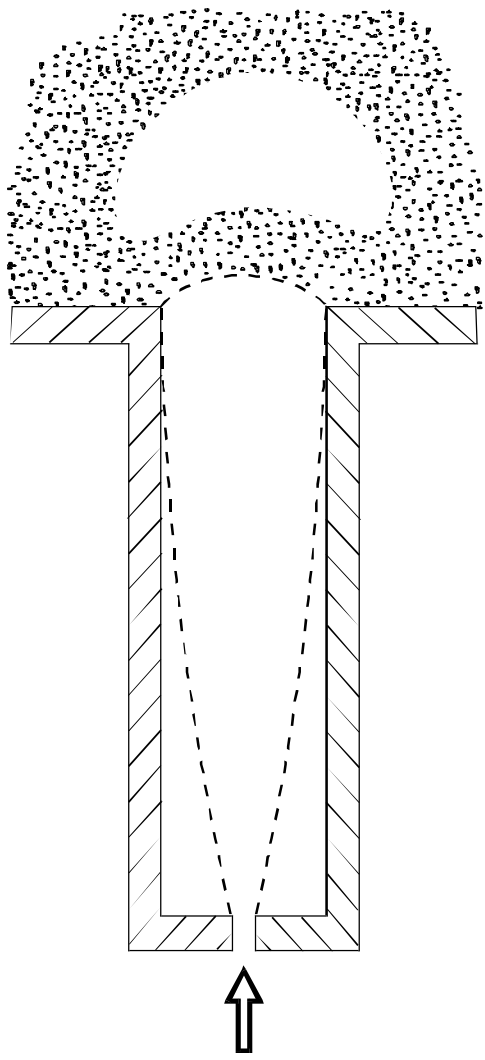


Figure 20. Schematic drawing of the attrition-minimizing distributor design suggested by Parker and Gwyn (1976, 1977).

Bubbling Bed. The parameters affecting the fines production rate due to bubble-induced attrition are gas velocity and bed height. Both parameters are normally fixed by the process. It has been mentioned in Sec. 5.1 that internals in the bed might also act as a source of attrition. In this respect it should be mentioned that internals, e.g., tube bundles, should be located in a sufficiently large distance from the distributor to avoid the grid jets impinging on them. The same is valid if for some reason additional gas is injected into the bed region. High jet velocities should be avoided and caution should be exercised with respect to neighboring internals.

Cyclones. According to the model presented above, Eq. (24), a minimum loss rate due to cyclone attrition requires to avoid both high inlet velocities U_e and high solids mass fluxes $m_{c,in}$ at the cyclone inlet. The latter requirement can be fulfilled by locating the cyclone inlet above the transport disengaging height (TDH) (Kunii and Levenspiel, 1991). In addition, an enlargement of the freeboard section will reduce the amount of particles that are entrained and thus the mass flux, $m_{c,in}$.

For the special case of circulating fluidized bed systems, which are characterized by high solids loadings μ at the primary cyclone inlet, Molerus and Glückler (1996) have recently suggested a new cyclone separator with an inlet design, which is claimed to reduce the solids attrition. As is shown in Fig. 21, the gas-solid suspension is fed vertically downward with an angle of 30° to the main axis of the cone. The inlet device is shaped in such a way that the feed is accelerated without any direct collision with the cone wall. This cyclone design was tested in a circulating fluidized bed of foamed porous glass beads under rough conditions (gas velocity $U_g = 8$ m/s, solids loading $m = 6$ kg/kg). The assessment of attrition was based on the mass fraction of particles smaller than $100\ \mu\text{m}$. The respective attrition rate in the new design was found to be significantly smaller than in a conventional cyclone.

6.0 ATTRITION IN PNEUMATIC CONVEYING LINES

Pneumatic conveying systems and in particular dilute phase conveying systems are known to create a high stress on particulate solids leading to significant attrition. In contrast to fluidized beds, it is not the material loss which is the main problem. Depending on the application, problems may rather occur in a number of different areas. Attrition may, for example,

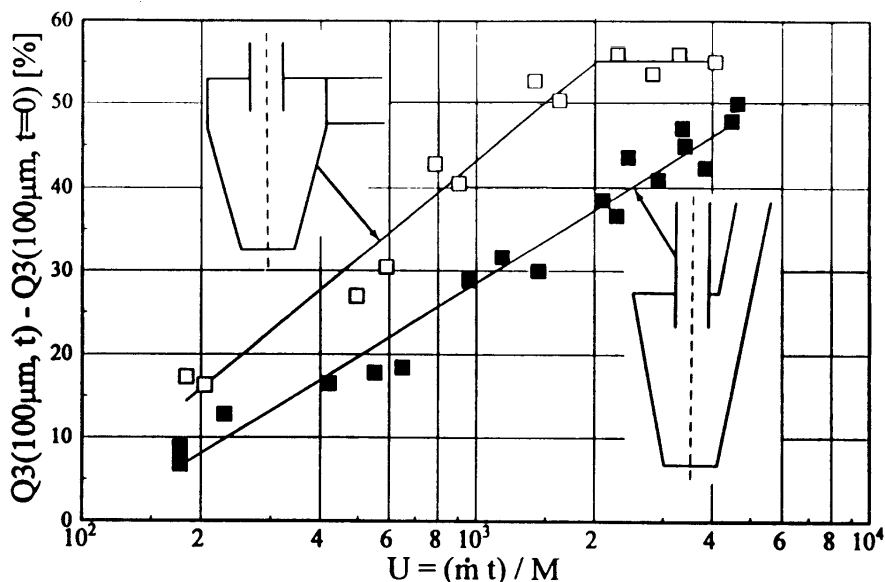


Figure 21. Attrition extent caused by a conventional cyclone and by the new cyclone design suggested by Molerus and Glückler (1996).

affect the product quality. In the case of pharmaceutical products, breakage and attrition of tablets must be avoided (Molerus et al., 1989). With respect to agricultural seeds, attrition may cause germination damage (Segler, 1951). A major consequence of attrition is the generation of dust, which may cause problems with handling of the particulate material after conveying and which furthermore requires costly cleaning systems for the conveying gas.

Despite these potential problems, remarkably little work has been published on particle degradation in pneumatic conveying systems. That may be explained by experimental problems that are even much more serious than with fluidized beds. According to the different problems mentioned above, there are more individual measurement techniques and assessment procedures required than with fluidized bed attrition. Usually, the assessment is restricted to the comparison of the particle size distribution before and after conveying. Moreover, there is no steady-state attrition that could be measured. It is only possible to measure an integrated value, which

includes initial breakage in the acceleration zone and all breakage events that have occurred along the entire length of the pneumatic conveying system. Furthermore, the main parameter, i.e., the gas velocity, is changing with pipeline length due to expansion effects. Moreover, the design of pneumatic conveying lines is very individual and a comparison of results obtained in different conveying systems is almost impossible. Even the wall material plays an important role and has to be considered as a parameter.

6.1 Modeling

Despite the little experimental data, there are two models available in the literature. Adams et al. (1992) considered dense phase conveying. They tried to predict the amount of attrition as a function of conveying distance by coupling a Monte Carlo simulation of the pneumatic conveying process with data from single-particle abrasion tests. Salman et al. (1992) focused on dilute phase conveying. They coupled a theoretical model that predicts the particle trajectory with single particle impact tests (cf. Mills, 1992).

6.2 Parameter Effects

Segler (1951) has investigated the damage of grains and peas in pneumatic conveying lines in great detail. “Damage” was considered to be breakage of the grains, germination damage, or the removal of the husk. Most experiments were carried out with peas because they are much more sensitive to mechanical damage than the grains.

Segler (1951) found the incidence of grain damage to rise approximately with the cube of the air velocity (cf. Fig. 22). Furthermore, at constant air velocity the damage was found to increase with decreasing solids loading which may be explained by the “cushioning” effect mentioned in connection with attrition in cyclones in Sec. 5.1. Both effects have been confirmed by two other groups, namely by McKee et al. (1995), who studied particle attrition of sea salt in a large-scale dilute pneumatic conveying line (Fig. 23) and by Adams et al. (1992), who investigated the degradation of some unspecified granular material in a dense phase pneumatic conveying loop. Segler (1951) also investigated the effect of the pipe diameter and found a much smaller damage in a 270 mm bore pipeline than in a smaller pipeline with 46 mm diameter.

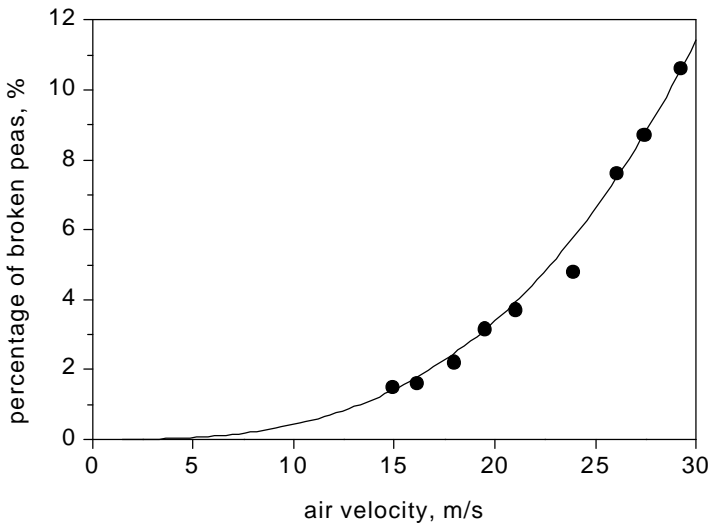


Figure 22. Influence of the air velocity on the breakage of peas. (Segler, 1951.)

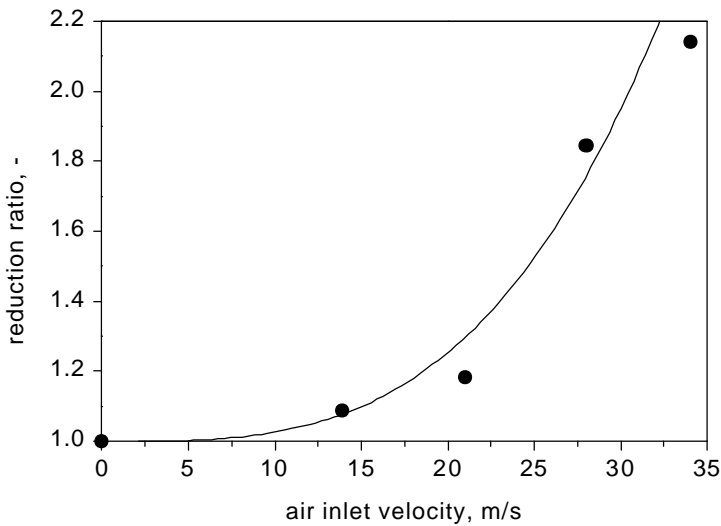


Figure 23. Influence of the conveying velocity on the reduction ratio of sea salt (the reduction ratio is defined as the ratio of the surface mean diameter before and after conveying. (McKee *et al.*, 1995.)

6.3 Steps to Minimize Attrition in Pneumatic Conveying Lines

Both Reed and Bradley (1991) and Wypych and Arnold (1993) have given surveys of techniques to minimize the particle degradation.

Reduction of the Conveying Velocity. From the experimental results presented above it is obvious that the most decisive factor affecting attrition in pneumatic conveying is the gas velocity. If a given material is known to be friable it may be necessary to change from a dilute phase conveying system, which is normally characterized by gas velocities in excess of 15 m/s to dense phase conveying systems, which can be operated at gas velocities between roughly 2 and 6 m/s. Molerus et al. (1989) have suggested a vibration-assisted pneumatic conveying system, which permits a further lowering of the conveying velocity. This latter system is, therefore, particularly suited for sensitive products, e.g., spray granules and coffee beans. Figure 24 illustrates the application of this technique for the conveying of spray granules. As is shown a conventional dense-phase, conveying without vibration causes a significant change in the particle size distribution, whereas in the case of the vibration-assisted pneumatic conveying, no significant change in the particle size distribution was detected.

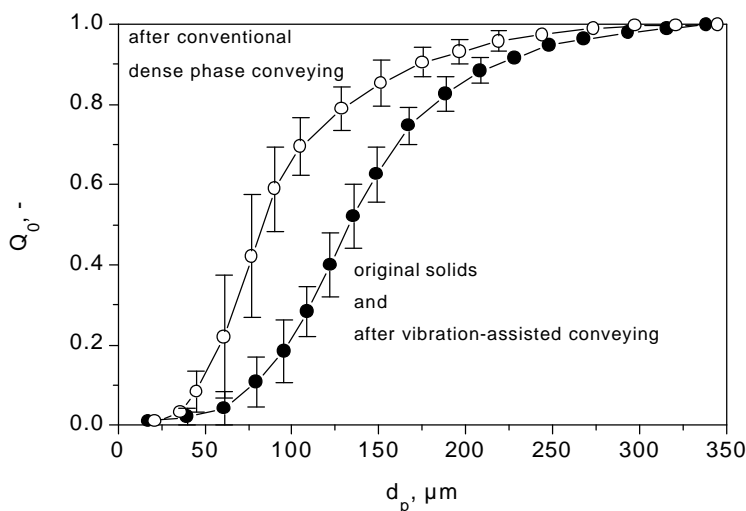


Figure 24. Effects of conventional dense phase conveying and vibration assisted conveying on the particle size distribution of spray granules (the vertical bars indicate the confidence intervals. (Molerus et al., 1989.)

Villareal and Klinzing (1994) suggested increasing the gas density in order to reduce the minimum conveying velocity by increasing either the gas pressure or the molecular weight of the gas.

If the conveying velocity is a critical parameter, then the designer of a pneumatic conveying system should also consider the expansion effect caused by the pressure drop along the conveying line. The resulting increase of the gas velocity can be accounted for by increasing the pipe diameter.

Pipeline Routing and Bend Design. Direction changes should be kept to an absolute minimum in order to keep the number of bends that are considered to be the major attrition sources as low as possible. This helps also to reduce the conveying line pressure drop and with it the gas expansion effect.

The bend type is known to have a significant effect on the particle degradation. For example, blinded-tee bends are used by many companies to prevent impact on the outer radial surface. Instead, the primary impact will, in this case, occur on the particulate product itself. This certainly leads to a reduction of bend wear, but the particle-particle impacts will probably cause higher attrition. This has been confirmed by experiments performed at PSRI (Fig. 25). To generate this plot, limestone with an average particle size of 940 microns was passed several times through a pneumatic conveying line consisting of several bends of the same type. All material less than 210 microns was assumed to be fines. The data were plotted as $(W_c^{-1} - W_{ci}^{-1})$ vs. $N^{0.5}$, where W_c is the weight percent of particles > 210 microns. The parameter W_{ci} is the weight percent of particles in the initial material > 210 microns and N is the number of passes through a bend. The blinded-tee is seen to result in a significantly higher attrition rate than the elbow-bends. The short radius elbow is not unexpectedly seen to result in a higher extent of attrition than the long radius version. This latter finding is in agreement with results of Salman (1988), who found damage of 50% of seeds that were conveyed through a bend with $r/D = 5$. As this ratio was increased to 60 only 1.5% of the seeds were found to be damaged.

Sometimes rubber bends have been successfully used to adsorb some of the impact energy in order to reduce particle attrition (Reed and Bradley, 1991.)

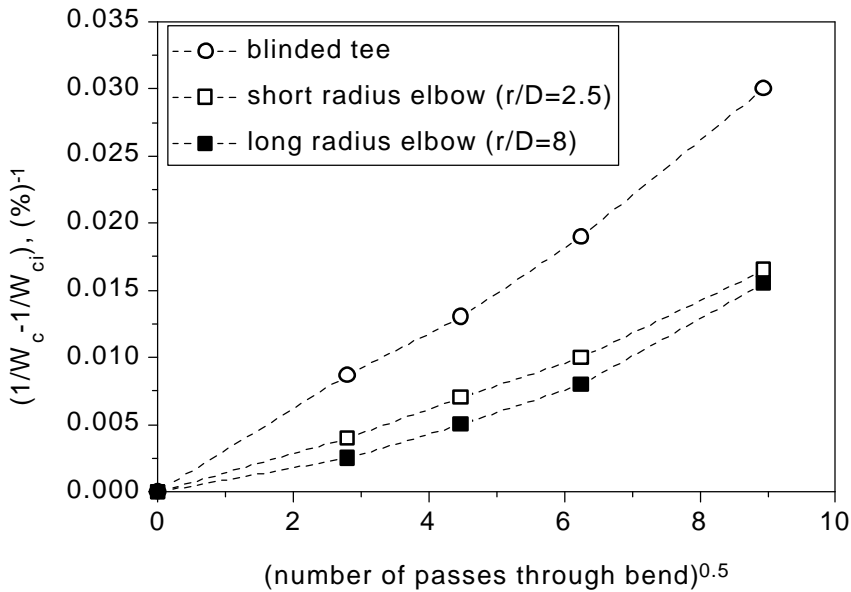


Figure 25. The effect of bend type on particle attrition (experiments by the PSRI) (Knowlton, 1996.)

NOTATIONS

$A_{c,e}$	Cross-sectional area of the cyclone inlet	m^2
A_o	Open surface area of a perforated plate distributor	m^2
A_t	Cross-sectional area of a fluidized bed	m^2
b	Exponent in the Gwyn equation, Eq. (1)	-
d	Diameter	m
d_{or}	Orifice diameter	m
d_p	Particle diameter	m
$E_{a,tot}$	Attrition extent, def. by Eq. (4)	-
g	Acceleration due to gravity	$m\,s^{-2}$
H_{bed}	Bed height	m
H_{stat}	Static bed height	m
K_a	Attrition rate constant in the Gwyn equation, Eq. (1)	s^{-b}
K_{bub}	Bubble-induced attrition rate constant, def. by Eq. (15)	m^{-1}

K'_{bub}	Bubble-induced attrition rate constant, def. by Eq. (16)	m^{-2}
K_c	Cyclone attrition rate constant, def. by Eq. (23)	$s^2 m^{-2}$
K_j	Jet attrition rate constant, def. by Eq. (8)	$s^2 m^{-2}$
$m_{c,in}$	Mass flux into the cyclone	kg/s
$m_{c,loss}$	Mass flux in the cyclone loss	kg/s
N_{or}	Number of orifices	-
p	Pressure	Pa
r	Radius	m
$R_{a,bub}$	Bubble-induced attrition rate, def. by Eq. (12)	s^{-1}
$R_{a,c}$	Cyclone attrition rate, def. by Eq. (17)	-
$R_{a,distr}$	Distributor attrition rate, def. by Eq. (7)	kg/s
$R_{a,j}$	Attrition rate per single jet, def. by Eq. (7)	kg/s
$R_{a,tot}$	Overall attrition rate, def. by Eq. (2), measured according equ.(26)	s^{-1}
S	Surface area	$4m^2$
S_m	Mass specific surface area of bulk material	m^2/kg
t	Time	s
u_{or}	Orifice velocity	m/s
U_e	Cyclone inlet velocity	m/s
U_g	Gas velocity	m/s
$U_{g,min}$	Minimum fluidizing velocity to cause bubble-induced attrition	m/s
$U_{g,mf}$	Superficial gas velocity at minimum fluidization conditions	m/s
v	Volumetric flow rate	m^3/s
W	Mass	kg

Subscripts

bed	Bed
c	Cyclone
el	Elutriation
g	Gas
or	Orifice
p	Particle
s	Solid

Greek Symbols

γ	Specific free surface energy	J/m^2
η	Efficiency of the cyclone abrasion process, def. by Eq. (18)	-
μ	Solids loading	-
ρ	Density	kg/m^3
τ	Time	s

REFERENCES

- Adams, M. J., Bellamy, G., and Briscoe, B. J., "The Wear of Particles in Pneumatic Conveying," *Wear Particles*, (Downson, et al., eds.), Elsevier Science Publishers B.V. (1992)
- Arastoopour, H., and Chen-Ya Chen, "Attrition of Char Agglomerates," *Powder Tech.*, 36:99 (1983)
- Arena, U., D'Amore, M., and Massimilla, L., "Carbon Attrition during the Fluidized Combustion of Coal," *AIChE J.*, 29:40 (1983)
- Bemrose, C. R., and Bridgwater, J., "A Review of Attrition and Attrition Test Methods," *Powder Tech.*, 49:97 (1987)
- Blake T. R., Webb H., and Sunderland P. B., "The Nondimensionalization of Equations Describing Fluidization with Application to the Correlation of Jet Penetration Height," *Chem. Eng. Sci.*, 45:365 (1990)
- Blinichev, V. N., Strel'tsov, V. V., and Lebedeva, E. S., "An Investigation of the Size Reduction of Granular Materials during their Processing in Fluidized Beds," *Int. Chem. Eng.*, 8:615 (1968)
- Bond, F. C., "Crushing & Grinding Calculations, Part I," *Brit. Chem. Eng.*, 6:378 (1961)
- Broadbent, S. R., and Calcott, T. G., *J. Inst. of Fuel*, 29:524 (1956)
- Bridgwater, J., "Attrition of High-Density Polyethylenes," *Powder Tech.*, 50:243 (1987)
- British Materials Handling Board, "Particle Attrition," *Trans Tech Publications Series on Bulk Mat. Handling*, p. 5 (1987)
- Chirone, R., Massimilla, L., and Salatino, P., "Comminution of Carbons in Fluidized Bed Combustion," *Progress in Energy and Comb. Sci.*, 17:297 (1991)
- Cleaver, J. A. S., and Ghadiri, M., "Impact Attrition of Sodium Carbonate Monohydrate Crystals," *Powder Tech.*, 76:15 (1993)

- Clift, R., "Powder Technology and Particle Science," *Powder Tech.*, 88:335 (1996)
- Contractor, R. M., Bergna, H. E., Chowdhry, U., and Sleight, A. W., "Attrition Resistant Catalysts for Fluidized Bed-Systems," *Fluidization VI*, (J. R. Grace, L. W. Shemilt, and M. A. Bergougnou, eds.), Banff, Alberta, Canada (1989)
- Coppinger, E., Discepolo, L., Tardos, G. I., and Bellamy, G., "The Influence of Granule Morphology on Attrition during Fluidization and Pneumatic Transport," *Advanced Powder Tech.*, 3:201 (1992)
- Dessalces, G., Kolenda, F., and Reymond, J. P., "Attrition Evaluation for Catalysts used in Fluidized or Circulating Fluidized Bed Reactors," *AIChE: Preprints of the First Int. Particle Technol. Forum*, II:190, Denver, Colorado (1994)
- Forsythe, W. L., and Hertwig, W. R., "Attrition Characteristics of Fluid Cracking Catalysts," *Indust. and Eng. Chem.*, 41:1200 (1949)
- Fuertes, A. B., Pis, J. J., Garcia, J. C., Rubiera, F., and Artos, V., "Prediction of Attrition in a Continuous Fluid-Bed System," *Powder Tech.*, 67:291 (1991)
- Ghadiri, M., Yuregir, K. R., Pollock, H. M., and Ross, J. D. J., "Influence of Processing Conditions on Attrition of NaCl Crystals," *Powder Tech.*, 65:311 (1991)
- Ghadiri, M., Cleaver, J. A. S., and Yuregir, K. R., "Attrition of Sodium Chloride Crystals in a Fluidized Bed," *Proc. Fluidization VII*, (O. E. Potter, and D. J. Nicklin, eds.), p. 604, Brisbane, Australia (1992a)
- Ghadiri, M., Cleaver, J. A. S., and Tuponogov, V. G., "Modelling Attrition Rates in the Jetting Region of a Fluidized Bed," *Preprint Symposium Attrition and Wear*, Utrecht (1992b)
- Ghadiri, M., Cleaver, J. A. S., Tuponogov, V. G., and Werther, J., "Attrition of FCC Powder in the Jetting Region of a Fluidized Bed," *Powder Tech.*, 80:175 (1994)
- Ghadiri, M., Cleaver, J. A. S., and Tuponogov, V. G., "Influence of Distributor Orifice Size on Attrition in the Jetting Region of Fluidized Beds," *Preprint Fluidization VIII*, 2:799 (1995)
- Gwyn, J. E., "On the Particle Size Distribution Function and the Attrition of Cracking Catalysts," *AIChE J.*, 15:35 (1969)
- Kato, K., Takaradu, T., Matsuo, N., and Suto, T., "Residence-Time Distribution of Fine Particles in a Powder-Particle Fluidized Bed," *Int. Chem. Eng.*, 34:605 (1994)
- Knight, P. C., and Bridgwater, J., "Comparison of Methods for Assessing Powder Attrition," *Powder Tech.*, 44:99 (1985)
- Knowlton, T. M., private communication (1996)

- Kokkoris, A., and Turton, R., "The Reduction of Attrition in Fluidized Beds by the Addition of Solid Lubricants," *AIChE Symp. Ser.*, 281(87):20 (1991)
- Kokkoris, A., and Turton, R., "A Phenomenological Model Predicting the Attrition and the Reduction of Attrition due to the Addition of Solid Lubricants in Slugging Beds," *Powder Tech.*, 84:39 (1995)
- Kono, H., "Attrition Rates of Relatively Coarse Solid Particles in Various Types of Fluidized Beds," *AIChE Symp. Ser.*, 205(77):96 (1981)
- Kunii, D., and Levenspiel, O., *Fluidization Eng.*, (E. Robert, ed.), Krieger Publishing Company, Huntington, NY (1969)
- Kunii, D., and Levenspiel, O., *Fluidization Eng.*, 2nd Ed., Butterworth-Heinemann, Boston (1991)
- Kutyavina, T. A., and Baskakov, A. P., "Grinding of Fine Granular Material with Fluidization," *Chem. a. Techn. of Fuels and Oils*, 8:210 (1972)
- Levenspiel, O., Kunii, D., and Fitzgerald, T., "The Processing of Solids of Changing Size in Bubbling Fluidized Beds," *Powder Tech.*, 2:87 (1968)
- Lin L., Sears J. T., and Wen, C. Y., "Elutriation and Attrition of Char from a Large FB," *Powder Tech.*, 27:105 (1980)
- McKee, S. L., Dyakowski, T., Williams, R. A., and Bell, A., "Solids Flow Imaging and Attrition Studies in a Pneumatic Conveyor," *Powder Tech.*, 82:105 (1995)
- Merrick, D., and Highley, J., "Particle Size Reduction and Elutriation in a Fluidized Bed Process," *AIChE Symp. Ser.*, 137(70):367 (1974)
- Merry, J. M. D., "Penetration of Vertical Jets into Fluidized Beds," *AIChE J.*, 21:507 (1975)
- Mills, D., "Particle Degradation in Pneumatic Conveying," *7th Int. Symp. on Freight Pipelines*, Wollongong, NSW, Australia (1992)
- Molerus, O., Siebenhaar, W., and Gericke, W., "Entwicklung eines pneumatische Förderverfahrens zum schonenden Transport bruchempfindlicher Güter," *Chem. Ing. Tech.*, 61:752 (1989)
- Molerus, O., and Glückler, M., "Development of a Cyclone Separator with New Design," *Powder Tech.*, 86:37 (1996)
- Nakagawa, N., Li, Z., Bai, D., and Kato, K., "Fundamental Study of Fine Particle Residence in a Powder-Particle Fluidized Bed / Effect of Fine Powder Concentration," *Preprint Fluidization VIII*, 1:287 (1995)
- Neil, A. U., and Bridgwater, J., "Attrition of Particulate Solids under Shear," *Powder Tech.*, 80:207 (1994)
- Newby, R. A., Vaux, W. G., and Keairns, D. L., "Particle Attrition in Fluidized-Bed Systems," *Proc. Fluidization IV*, (D. Kunii, and R. Toei, eds.), Kashikojima, Japan (1983)

- Paramanathan, B. K., and Bridgwater, J., "Attrition of Solids-I", *Chem. Eng. Sci.*, 38:197 (1983)
- Paramanathan, B. K., and Bridgwater J., "Attrition of Solids-II," *Chem. Eng. Sci.*, 38:207 (1983)
- Parker, W. A., Gwyn, J. E., and McCullogh, G. R., US Patent 3 974 091 (1976)
- Parker, W. A., and Gwyn, J. E., US Patent 4 032 300 (1977)
- Patience, G. S., and Mills, P. L., "Modelling of Propylene Oxidation in a Circulating Fluidized-Bed Reactor," *New Developments in Selective Oxidation II*, p. 1 (1994)
- Pell, M., *Gas Fluidization*, Chapt. 12: "Attrition in Fluidized Beds," *Handbook of Powder Tech.*, 1(8):97, Elsevier, Amsterdam (1990)
- Perry, R. H., and Chilton, C. H., *Chemical Engineers Handbook*, 5:8–10, McGraw-Hill, Kogakusha, Tokyo (1973)
- Pis, J. J., Fuertes, A. B., Artos, V., Suarez, A., and Rubiera, F., "Attrition of Coal and Ash Particles in a Fluidized Bed," *Powder Tech.*, 66:41 (1991)
- Ray, Y.-C., Jiang, T.-S., and Wen, C.Y., "Particle Attrition Phenomena in a Fluidized Bed," *Powder Tech.*, 49:193 (1987a)
- Ray, Y. C., Jiang, T. S., and Jiang T. L., "Particle Population Model for a Fluidized Bed with Attrition," *Powder Tech.*, 52:35 (1987b)
- Reed, A. R., and Bradley, M. S., "Techniques for Minimising Particle Degradation in Pneumatic Conveying Systems," *Powder Handling & Processing*, 3:49 (1991)
- Reppenhagen, J., Werther, J., to be published (1997)
- Salman, A. S., Verba, A., and Mills, D., "Particle Degradation in Dilute Phase Pneumatic Conveying Systems," *Proc. of the 1992 Powder & Bulk Solids Conf. and Exhibition*, Rosemont, USA (1992)
- Salman, A. S., Ph.D. Thesis on Product Degradation: Budapest Technical University, (1988)
- Schruben, J. S., and Vaux, W. G., "Attrition in the Bubbling Zone of a Steady-State Fluidized Bed," *Chem. Eng. Commun.*, 33:337 (1985)
- Segler, G., "Pneumatic Grain Conveying," 55, Braunschweig, Germany (1951)
- Seville, J. P. K, Mullier, M. A., and Adams, M. J., "Attrition of Agglomerates in Fluidized Beds," *Proc. of the 7th Eng. Found. Conf. on Fluidization*, Brisbane, Australia (1992)
- Shipway, P. H., and Hutchings, I. M., "Attrition of Brittle Spheres by Fracture under Compression and Impact Loading," *Powder Tech.*, 76:23 (1993)

- Sishtla, C., Findlay, J., Chan, I., and Knowlton, T. M., "The Effect of Temperature and Gas Velocity on Fines Generation in Non-Reactive Fluidized Beds of Coal Char," *Fluidization VI*, (J. R. Grace, L. W. Shemilt, and M. A. Bergougnou, eds.), Banff, Alberta, Canada (1989)
- Ulerich, N. H., Vaux, W. G., Newby R. A., and Keairns, L., Experimental/Engineering Support for EPA's FBC Program: Final report, Vol. 1, Sulfur Oxide Control, EPA-600/7-80-015a (1980)
- Van Swaaij, W. P. M., de Vries, R. J., Mantovani, C., and Heijkoop, A., "Design Criteria and Performance of the Commercial Reactor for the Shell Chlorine Process," *V. Europ. Symp. on Chem. React. Eng.*, Amsterdam (1972)
- Vaux, W. G., "Attrition of Particles in the Bubbling Zone of a Fluidized Bed," *Proceed. of the Am. Power Conf.*, 40:793 (1978)
- Vaux, W. G., and Keairns, D. L., "Particle Attrition in Fluid-Bed Processes," *Proc. Fluidization III*, (J. R. Grace, and J. M. Matsen, eds.), p. 437, Henniker, USA (1980)
- Vaux, W. G., and Fellers, A. W., "Measurement of Attrition Tendency in Fluidization," *AIChE Symp. Ser.*, 205(77):107 (1981)
- Vaux, W. G., and Schruben, J. S., "Kinetics of Attrition in the Bubbling Zone of a Fluidized Bed," *AIChE Symp. Ser.*, 222(79):97 (1983)
- Villareal, J. A., and Klinzing, G. E., "Pickup Velocities under Higher Pressure Conditions," *Powder Tech.*, 80:179 (1994)
- Weeks, S. A., and Dumbill, P., "Method Speeds FCC Catalyst Attrition Resistance Determinations," *Oil & Gas J.*, 88:38 (1990)
- Werther, J., and Xi, W., "Jet Attrition of Catalyst Particles in Gas Fluidized Beds," *Powder Tech.*, 76:15 (1993)
- Werner, A., Haider, M., and Linzer, W., "Modelling of Particle Population in Fluidized Beds of Particles Differing in Size and Physico-chemical Behaviour," *Preprint Fluidization VIII*, 1:557 (1995)
- Wypych, P. W., and Arnold, P. C., "Minimising Wear and Particle Damage in Pneumatic Conveying," *Powder Handling & Processing*, 5:129 (1993)
- Wyszynski, M. L., and Bridgwater, J., "The Effect of Solid Lubricants on the Powder Attrition and Breakage", *Tribology Int.*, 26:311 (1993)
- Xi, W., Ph.D. Thesis: "Katalysatorabrieb in Wirbelschichtreaktoren": Technical University Hamburg-Harburg (1993)
- Yates, J. G., Bejcek, V., and Cheesman, D. J. "Jet Penetration into Fluidized Beds at Elevated pressures," *Proc. Fluidization V*, (K. Ostergaard, and Sorensen, A., eds.), p. 79, Elsinore, Denmark (1986)
- Yuregir, K. R., Ghadiri, M., and Clift, R., "Observation of Impact Attrition of Granular Solids," *Powder Tech.*, 49:53 (1986)

- Yuregir, K. R., Ghadiri, M., and Clift, R., "Impact Attrition of Sodium Chloride Crystals," *Chem. Eng. Sci.*, 42:843 (1987)
- Zenz, F. A., "Bubble Formation and Grid Design," *Int. Chem. E. Symp. Ser.*, 30:136 (1968)
- Zenz, F. A., "Fluid Attrition in Fluid Beds," *Hydrocarbon Processing*, p. 103 (1971)
- Zenz, F. A., and Smith, R., "When are Fines at Equilibrium?" *Hydrocarbon Processing*, p. 104 (1972)
- Zenz, F. A., "Help from Project E-A-R-L," *Hydrocarbon Processing*, p. 119 (1974)
- Zenz, F. A., and Kelleher, E. G., "Studies of Attrition Rates in Fluid-Particle Systems via Free Fall, Grid Jets, and Cyclone Impact," *J. of Powder & Bulk Technol.*, 4:13 (1980)

8

Bubbleless Fluidization

Mooson Kwauk

1.0 INTRODUCTION

Most processes employing fluidization technology are concerned with gas/solid systems. We are so accustomed to the bubbling phenomenon of such systems that we often lose sight of other less common yet nonbubbling systems or fail to assess the consequences of the suppression of bubbles in gas/solid systems (Kwauk, 1992).

2.0 FLUIDIZED LEACHING AND WASHING

A representative nonbubbling system is fluidized leaching or washing which carries out, in a single columnar vessel, what is accomplished through repeated dispersal and settling of solids, and transfer of liquid and solids between stages for the normal countercurrent decantation technique (Kwauk, 1973, 1979a; Kwauk and Wang, 1981). In fluidized leaching or washing, bubbling is hardly apparent, and the relative simple fluid/particle dynamics makes possible quantitative analysis.

Figure 1a illustrates a typical fluidized leacher/washer. A slurry containing the solid particles to be leached and/or washed is fed at the top through a hydraulic distributor into an enlarged settling head where preliminary removal of excess liquor is accomplished. Solid particles then fall countercurrently against a rising stream of liquor into the fluidized leaching/washing section, in which there is normally a dilute-phase region surmounting a dense-phase region. Both regions are fluidized, with a more or less well-defined interface between the two. Fresh leaching/washing liquor enters through special spargers located at the bottom of the dense-phase region. Below the dense-phase region, the solid slurry enters a compression zone in which as much liquor as possible is removed in order to discharge a highly concentrated underflow.

By comparing this simple diagram with the conventional continuous countercurrent decantation circuit, shown in Fig. 1b (Coulson and Richardson, 1968, 1978; Treybal, 1955, 1968, 1980) for carrying out the same duty, it is easy to deduce the following characteristics for fluidized leaching and washing:

- * Complete hydraulic operation without any mechanical parts
- * Continuous countercurrent operation in a single vertical column where longitudinal concentration gradient could be established
- * Adaptability to extremely low flowing liquid-to-solid ratios, so that it is possible to obtain a relatively concentrated solution from a relatively lean solid parent material
- * Low space requirement
- * Ease of automation

Conceivably any granular solid containing a soluble component disseminated in an inert matrix could be leached rather efficiently in the fluidized state, and the leached pulp, or slurry, could again be washed in the fluidized state for removal of the remaining solution. Numerous solid particles of industrial significance are amenable to fluidized leaching and washing. In extractive metallurgy, for instance, certain low-grade copper ores could be leached with acid or ammoniacal solution advantageously in the fluidized state; cupriferous iron ores, after sulfatizing roasting, could

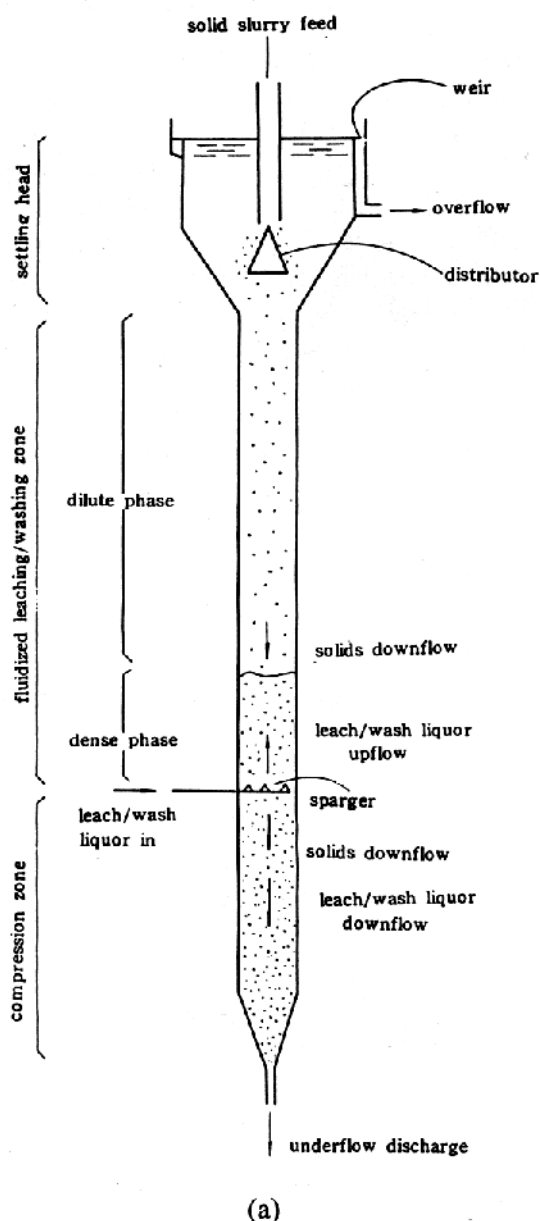
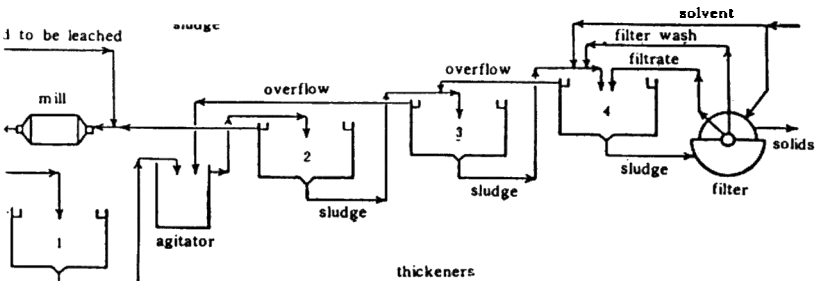
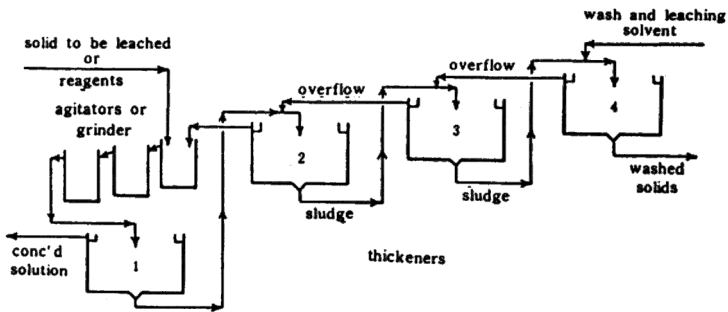
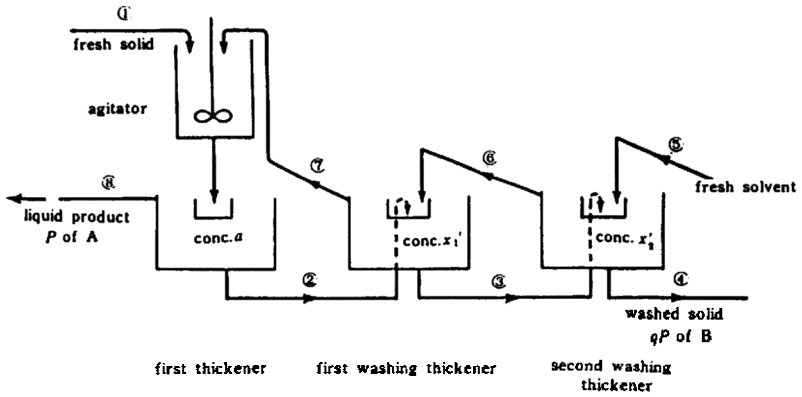


Figure 1. (a) A typical fluidized leacher/washer. (Kwauk, 1973, 1979; Kwauk and Wang, 1981.) (b) Typical CCD circuits for comparison. (Coulson and Richardson, 1968, 1978; Treybal, 1955, 1968, 1980.)



(b)

Figure 1. (Cont'd)

have their copper values recovered selectively by leaching with a very dilute acid; calcined bauxite has been leached in fluidized columns with strong alkali solutions; pyrite cinders containing nonferrous elements have been leached in the fluidized state after chloridizing roasting; in proposed processes for the hydrometallurgical winning of iron from its ores, hydrochloric acid leaching could also be carried out in fluidized columns. Certain brown coals rich in wax content could be leached in the fluidized state with a proper hydrocarbon solvent; in the production of active carbon, crude char could be treated in the fluidized state with acid and then washed with water; oil-bearing seeds as well as medicinal herbs, after proper size preparation, could be leached in fluidized apparatus for the recovery of their valuable ingredients.

2.1 Uniform Particles

Fluidized leaching and washing is a countercurrent operation with downflow of solids, called *counter-down*. The following equation for generalized fluidization

$$\text{Eq. (1)} \quad \mathbf{e}^n = u'_o - u'_d \mathbf{e} / (1 - \mathbf{e})$$

can be rewritten in terms more adapted to the practitioner, that is, solids and fluid at their respective weight rates, S and L , added to a fluidized leacher/washer having a cross-sectional area of A

$$\text{Eq. (2)} \quad \frac{L}{r_f A} + \frac{S \mathbf{e}}{r_s A (1 - \mathbf{e})} = \mathbf{e}^n u_t$$

Denote the superficial liquid-solids velocity ratio $(L/r_f A)/(S/r_s A)$ by N , and let $(S/r_s u_t) = A_t$, which is the minimal cross-sectional area if the solids were to flow at their terminal velocity, u_t , in the absence of fluid flow, and can, therefore, be called terminal cross-sectional area. Then Eq. (2) can be reduced to a dimensionless form in terms of a reduced area, A' , defined as follows

$$\text{Eq. (3)} \quad A' = \frac{A}{A_t} = \frac{A}{S / r_s u_t} = \frac{N(1 - \mathbf{e}) + \mathbf{e}}{\mathbf{e}^n (1 - \mathbf{e})} = \frac{1}{u'_d}$$

Equation (3) is plotted in the upper diagram of Fig. 2 as A' versus e with N as a parameter. It shows that corresponding to any value of N , there exists a minimum value of A' at which the fluidized leacher/washer possesses the least cross-sectional area or the maximum throughput. This minimum A' corresponds to the *flooding point* characteristic of all counter-down systems and can be calculated by setting the derivative $dA'/de = 0$, thus yielding

$$\text{Eq. (4a)} \quad e_{\min} \text{ from } N(1-e) + e = e/n(1-e)$$

$$\text{Eq. (4b)} \quad N_{\min} = \frac{e[1-n(1-e)]}{n(1-e)^2}$$

$$\text{Eq. (4c)} \quad A'_{\min} = \frac{1}{n(1-e)^2 e^{n-1}}$$

These three parameters at maximum throughput are shown in Fig. 3 as functions of the liquid/solids ratio N .

If the leaching or washing of the solids needs an average residence time q , the required height Z of the fluidized solids bed can be calculated:

$$\text{Eq. (5)} \quad q = \frac{ZA(1-e)r_s}{S}$$

Substitution of Eq. (2) for A and defining terminal height $Z_t = qu_t$ give the reduced fluidized bed height

$$\text{Eq. (6)} \quad Z' = \frac{Z}{Z_t} = \frac{Z}{qu_t} = \frac{e^n}{N(1-e) + e} = \frac{u'_d}{1-e}$$

This equation is plotted in the middle set of curves in Fig. 2 as Z' versus e with N as a parameter. It should be noted from these curves that Z' is always less than unity, signifying the fact that the congregation of particles in fluidization reduces the rate of fall of the particles, thus prolonging their residence time. This same set of curves could, therefore, be interpreted to

mean that to reduce the bed height, the only recourse lies in operation with lower voidages.

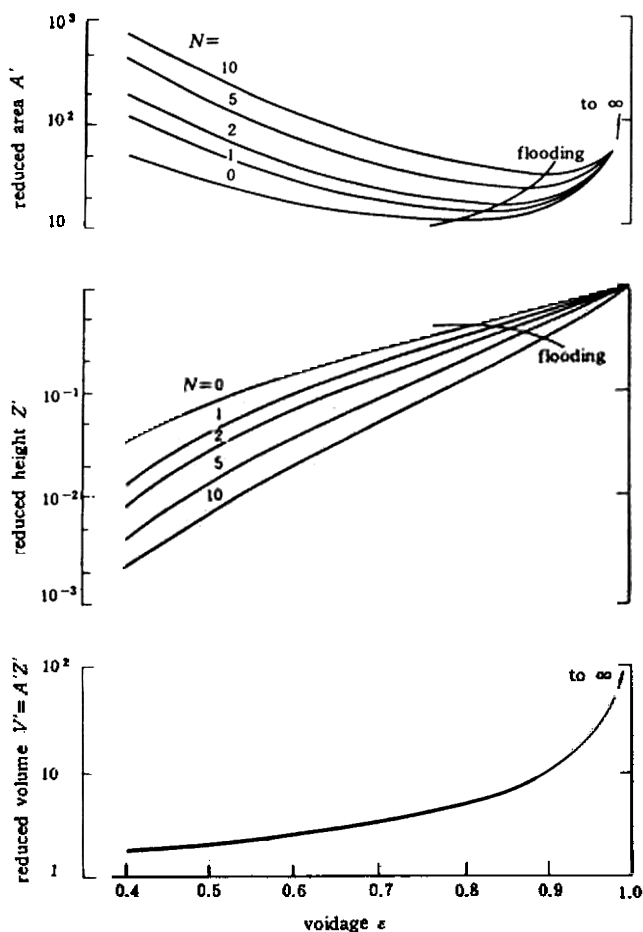


Figure 2. Fluidized leaching or washing of uniform particles—reduced vessel parameters: A' , Z' and V' . (Kwauk, 1973, 1979; Kwauk and Wang, 1981.)

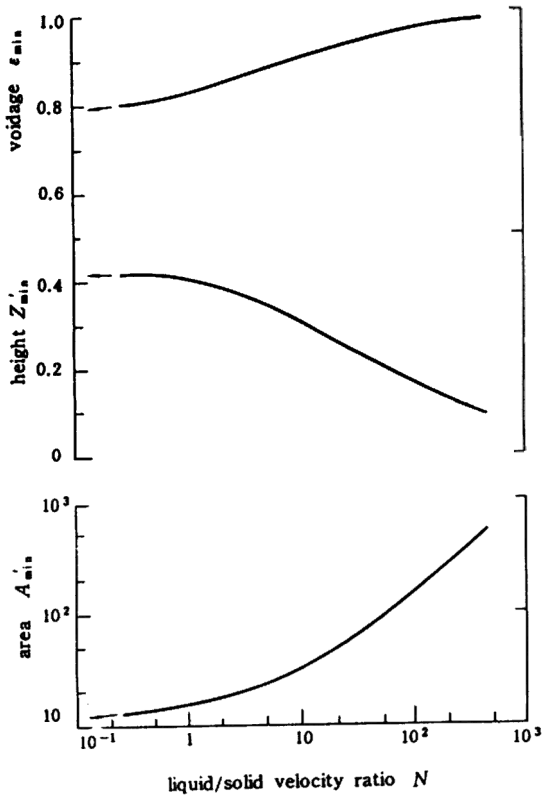


Figure 3. Fluidized leaching or washing of uniform particles—parameters of maximum throughput: e_{min} , Z'_{min} , A'_{min} .

Comparison of Eqs. (6) and (3) shows clearly that Z' and A' are not independent. Therefore, at the point for minimum cross-sectional area A'_{min} , the corresponding bed height is

$$\text{Eq. (7)} \quad Z'_{min} = n(1 - e)e^{n-1}$$

Also, combination of Eqs. (6) and (3) defines a reduced volume for the fluidized solids

$$\text{Eq. (8)} \quad V' = A'Z' = 1/(1 - e)$$

This is shown as the lowest curve in Fig. 2, from which it is evident that V' is a function of voidage only and independent of the parameter N . This curve shows further that the smallest volume can be realized only at the lowest possible voidage.

2.2 Mixed Particles

If the particles treated are not of the same size, some kind of an average particle diameter \bar{d}_p could be adopted, so that the procedure outlined for uniform particles might be followed.

For narrow particle size cuts, a more rational approach is recommended which consists of calculating the required cross-sectional area on the basis of the smallest particles having diameter d_{p2} , and computing the necessary height to insure the required residence time for the largest particles with diameter d_{p1} . Thus, one can be sure that the smallest particles will not be carried out by the liquid on the one hand, and that the largest particles will not suffer incomplete leaching or washing on the other.

According to this so-called "two- d_p method," it can be shown that the following expressions for cross-sectional area, height and volume ensue:

$$\text{Eq. (9)} \quad A' = \frac{A}{S / \mathbf{r}_s u_{t1}} = \left[\frac{N(1-\mathbf{e}) + \mathbf{e}}{\mathbf{e}^{n1}(1-\mathbf{e})} \right] \left\{ \frac{1}{M\mathbf{e}^{\Delta n}} \right\}$$

$$\text{Eq. (10)} \quad Z' = \frac{Z}{qu_{t1}} = \left[\frac{\mathbf{e}^{n1}}{N(1-\mathbf{e}) + \mathbf{e}} \right] \left\{ 1 + N \left(\frac{1-\mathbf{e}}{\mathbf{e}} \right) (1 - M\mathbf{e}^{\Delta n}) \right\}$$

$$\text{Eq. (11)} \quad V' = A'Z' = \left(\frac{1}{1-\mathbf{e}} \right) \left\{ \frac{1}{M\mathbf{e}^{\Delta n}} \left[1 + N \left(\frac{1-\mathbf{e}}{\mathbf{e}} \right) (1 - M\mathbf{e}^{\Delta n}) \right] \right\}$$

Comparison of the above three equations with their corresponding parent equations for uniform particles, reveals that A' , Z' and V' calculated from the larger particles of d_{p1} need to be corrected, due to the presence of the smaller particles, by factors shown in the large braces of these equations, all involving the factor $M\mathbf{e}^{\Delta n}$ in which $M = u_{t2}/u_{t1}$ and $\Delta n = n_2 - n_1$. Variation

of the correction factors in the large braces with Me^{Dn} are shown in Fig. 4. It is evident from these curves that the presence of the smaller particles tends to increase the cross-sectional area as well as the height, and, therefore, the volume of the fluidized leacher/washer.

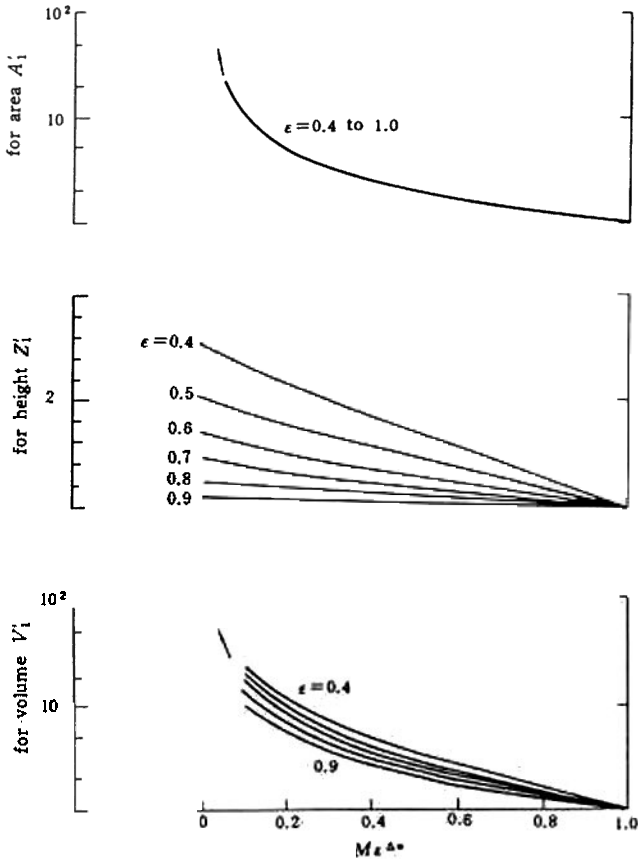


Figure 4. Fluidized leaching or washing of mixed particles—values of correction factors. (Kwauk, 1973, 1979; Kwauk and Wang, 1981.)

2.3 Staged Fluidized Leaching (SFL)

If the particle size distribution is sufficiently wide, as it often occurs for crushed ores or other disintegrated material products, it should be realized that the volumetric utilization of the leaching/washing apparatus would be rather poor, especially when the value of Me^{Dn} is down to below 0.2. For this reason, leaching or washing could be carried out in parallel columns operating at successively reduced fluid velocities. This principle of the so-called “staged fluidized leaching” (SFL) is illustrated in Fig. 5. Each leaching or washing column, or stage, together with its entrance region at the top, serves also as a hydraulic classifier. With this provision, the largest particles are treated in the first column, or stage, having the highest fluid velocity so that they may descend slowly in a rather concentrated state, and the required high residence time for these large particles may thus be guaranteed without the need of inappropriate height. The smallest particles are leached or washed in the last column, or stage, of the series operating with the lowest fluid velocity so that they may descend through the fluid at their characteristically low velocity without being carried over. Since this fraction of the smallest particles usually constitutes only a small portion of the solid feed material, the cross-sectional area devoted to their use would be far less than when all the fractions were treated en masse in a single vessel. Computations have indicated that division of the leaching or washing duty into several stages often resulted in a saving of apparatus volume by a factor amounting to as much as two orders of magnitude.

A method for designing SFL has been developed (Kwauk, 1979a), but it will not be discussed in this short presentation.

3.0 BUBBLELESS GAS/SOLID CONTACTING

3.1 Bubbling Fluidization and G/S Contacting Efficiency

Figure 6 shows that the gas entering a bubbling fluid bed splits into two paths, one through the dense-phase solids with good gas/solid (G/S) contacting and the other in the form of bubbles which essentially bypass the majority of the solid particles with limited G/S contacting. As the total flow through the fluid bed increases, the relative amount of bubble flow increases, and the overall G/S contacting efficiency suffers even greater impair-

ment. Any attempt at improving G/S contacting for the bubbles by increasing the solids bed height inevitably leads to greater pressure drop for the flowing gas stream, thus calling for greater processing energy.

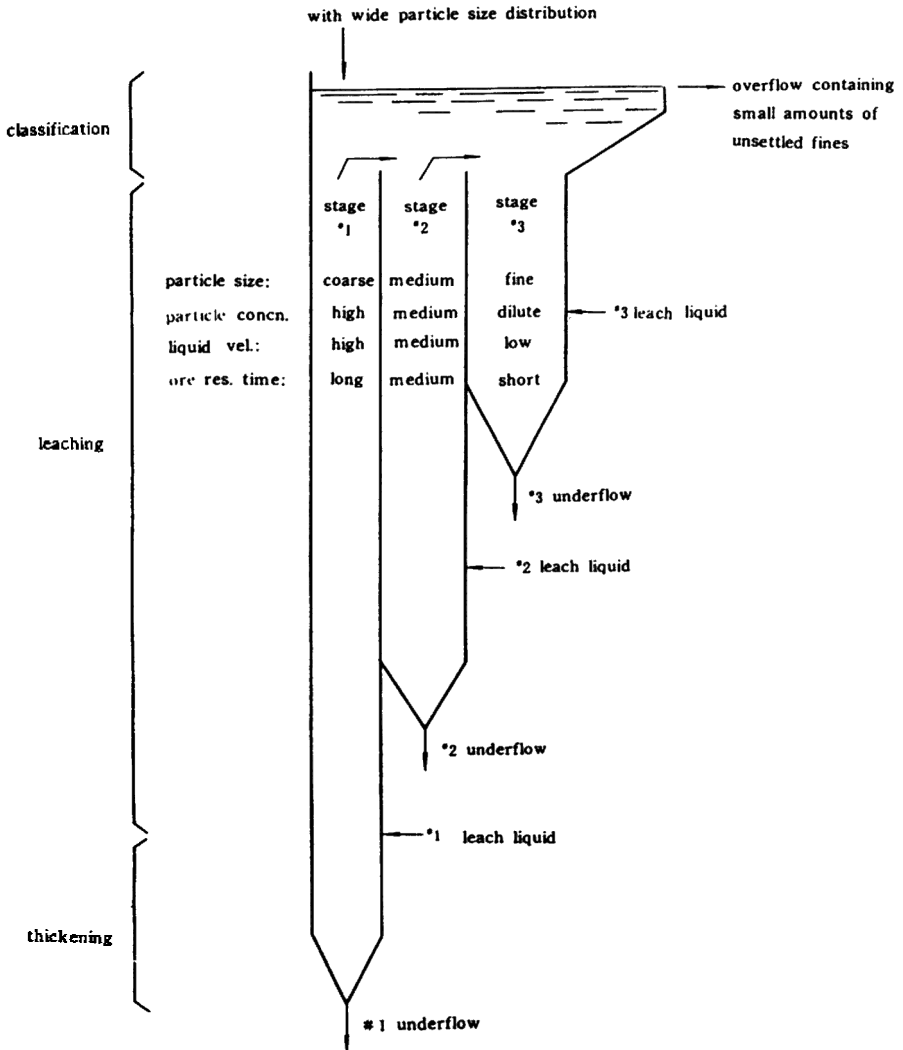


Figure 5. Staged fluidized leaching or washing. (Kwauk, 1973.)

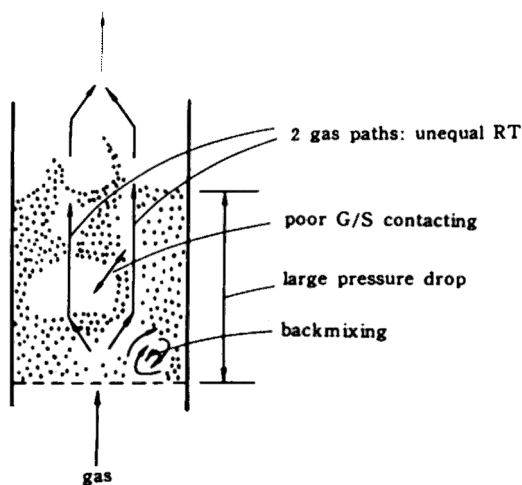


Figure 6. Split gas flow for a bubbling fluid bubbling bed.

The phenomenon of bubbling has attracted much attention from fluidization technologists to theorize on the origin and mechanics of bubbles and to elaborate on their mathematical modeling, but it has not been sufficiently recognized as indicative of the need for devising better modes of G/S contacting in which bubbles are suppressed or even totally eliminated.

Figure 7 plots the transfer coefficient $NuPr^{-1/3}$ or $ShSc^{-1/3}$ to Re for single particles, fixed bed and fluidized solids (Kwauk and Tai, 1964). The sudden drop of the transfer coefficient as soon as fluidization sets in, that is, when bubbling starts, is obvious.

In the case of heat transfer, cooling or heating of a solid particle takes place through convection across the gas film surrounding the particle and conduction inside the particles. Whether or not the overall cooling or heating process could be materially augmented by better G/S contacting depends on the relative resistance to heat transfer through these two mechanisms. Figure 8 presents the solution of the differential equations describing these two processes in series, as the relative resistance to heat flow inside/outside the particle, as a function of the Biot number defined as $Bi = hD_p/k_s$. This plot shows that when Bi is small, say 1, small particles and/or high values for k_s , the fractional resistance to heat flow by conduction inside the particle drops to < 0.1 , signifying that the overall heat transfer process can be accelerated by improved G/S contacting.

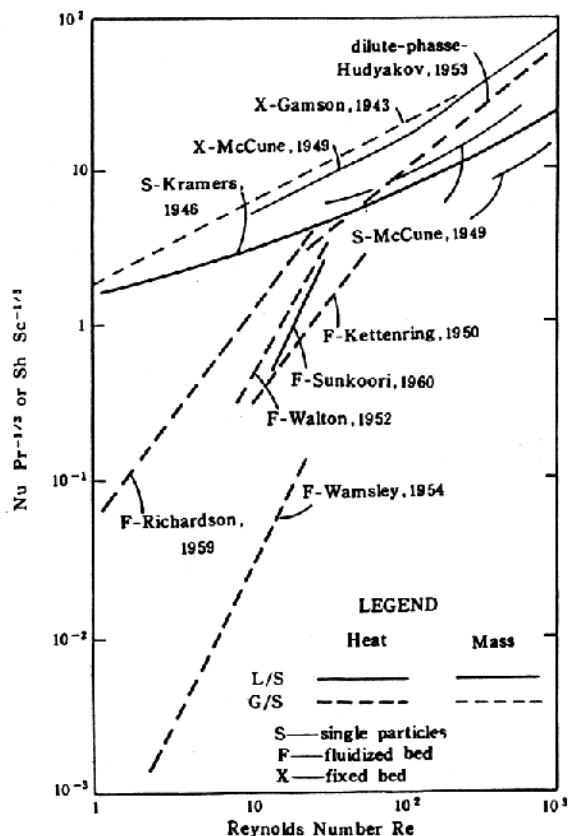


Figure 7. Comparison of transfer factors for different particle-fluid systems. (Kwauk and Tai, 1964.)

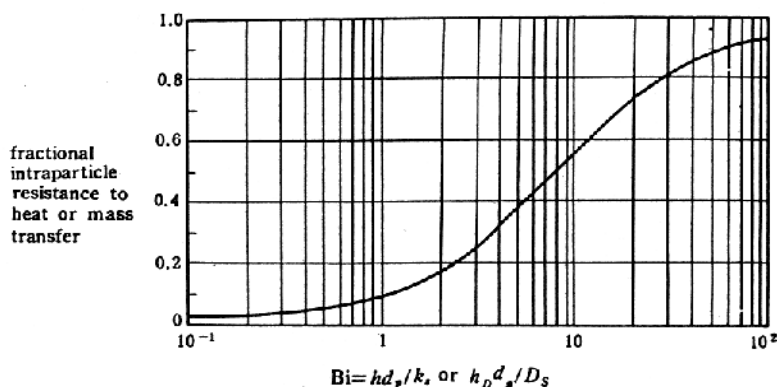


Figure 8. Relative resistance to heat and mass transfer as a function of Biot number or $h_D d_p / D_s$.

506 *Fluidization, Solids Handling, and Processing*

For G/S particle systems, enhancement in convective heat transfer is achieved at the expense of increased pressure drop in moving the gas at higher velocities. A measure of the relative benefit of enhanced heat transfer to added expenditure for fluid movement can be approximated by an effectiveness factor, E , defined as the ratio of the heat transfer coefficient to some kind of a pressure drop factor. For G/S systems in which particles are buoyed by the flowing gas stream, this pressure drop factor is expressed by the Archimedes number Ar , and E can be written

$$E = Nu Pr^{1/3}/Ar$$

By definition

$$Ar = f Re^2 ; \quad j = Nu Pr^{1/3}/Re$$

and for fixed bed operation, it is well known that $j \propto f$. Therefore,

$$E = 1/Re$$

showing that E drops in inverse proportion to increased flow. This is shown schematically by the downwardly directed curve on the left-hand side of Fig. 9. For liquid/solid (L/S) fluidization, experimental mass transfer data indicated that the transfer factor $Sh Sc^{-1/3}$ remained essentially constant as liquid velocity varied all the way from incipient fluidization to free fall. For G/S fluidization, however, as soon as the particles start to fluidize, gas bypassing through the formation of bubbles induces a sudden drop in the transfer factor. Recovery in the efficiency of G/S contacting starts somewhere in the vicinity of the transition to turbulent fluidization, and continues into the regime of pneumatic transport or free fall, where the transfer factor could even exceed that for the single particles due to the turbulence caused by the proximity of neighboring particles.

These considerations of contact efficiency and pressure drop in relation to bubbles in fluidization points to an area of endeavor where bubbles are absent.

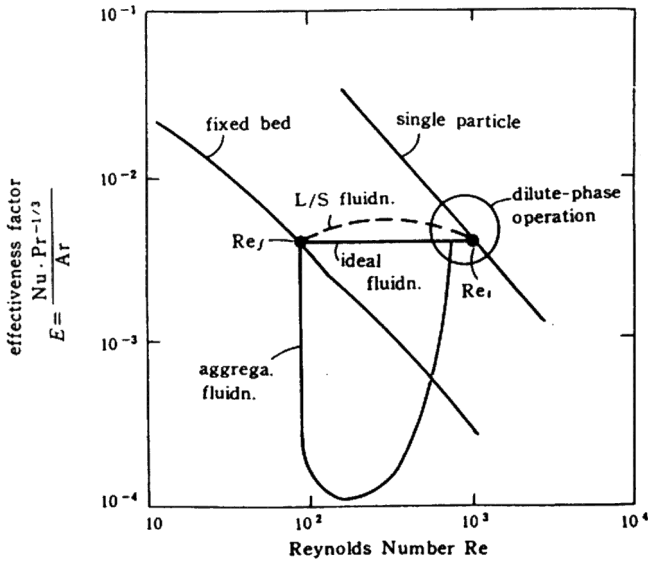


Figure 9. Effectiveness factor for particle-fluid systems. (*Kwauk and Tai, 1964.*)

3.2 Species of Bubbleless G/S Contacting

The following four species of bubbleless G/S contacting will be dealt with in this chapter:

- (i) Dilute-phase fluidization:
 - countercurrent G/S flow with cogravity fall of particles
 - cocurrent, or transport, irrespective of direction of flow
- (ii) Fast fluidization:
 - cocurrent, countergravity transport, with continual replenishment of solids at bottom by recycle from top
- (iii) Shallow fluid bed:
 - the region immediately above a distributor where bubbles have not yet taken shape
- (iv) Fluidization with no net fluid flow:
 - periodic fluidization through jiggling
 - levitation by fluid oscillation

4.0 DILUTE RAINING FLUIDIZATION

One method of improving G/S contacting consists of showering solids in dilute suspension from the top into an upflowing gas stream. Experiments verified that gas/solid heat transfer coefficient for such a system is essentially the same as for the discrete particles, and that pressure drop for gas flow is extremely low.

4.1 Raining Particles Heat Exchanger

Figure 10 shows the differential heat exchange between a gas and a solids stream flowing countercurrently and cocurrently. The efficiency of the heat transfer equipment is to be represented by the number of heat transfer stages

$$\text{Eq. (12)} \quad N_H = \frac{1}{t} \int_{T_o}^T \frac{dT_s}{T_g - T_s}$$

where $t = GC_p/SC_s$ is the relative flowing heat capacity between the gas and the solids. Integration gives

$$\text{Eq. (13)} \quad N_H = \frac{1}{1-t} \ln \frac{T'_{t+1} - T}{T_i - T_o}$$

Thus a single stage, $N_H = 1$, corresponds to a solids temperature rise (or drop) equal to the average gas-solids temperature difference, as shown in the lower left-hand side of Fig. 10. On this basis, it is convenient to define equipment efficiency in terms of a unitary heat transfer stage:

- Unitary heat transfer time, θ/N_H
- Unitary heat transfer distance, z/N_H
- Unitary heat transfer pressure drop, $\Delta P/N_H$

For good equipment performance, it is, therefore, desirable to look for a low height z/N_H and low pressure drop $\Delta P/N_H$.

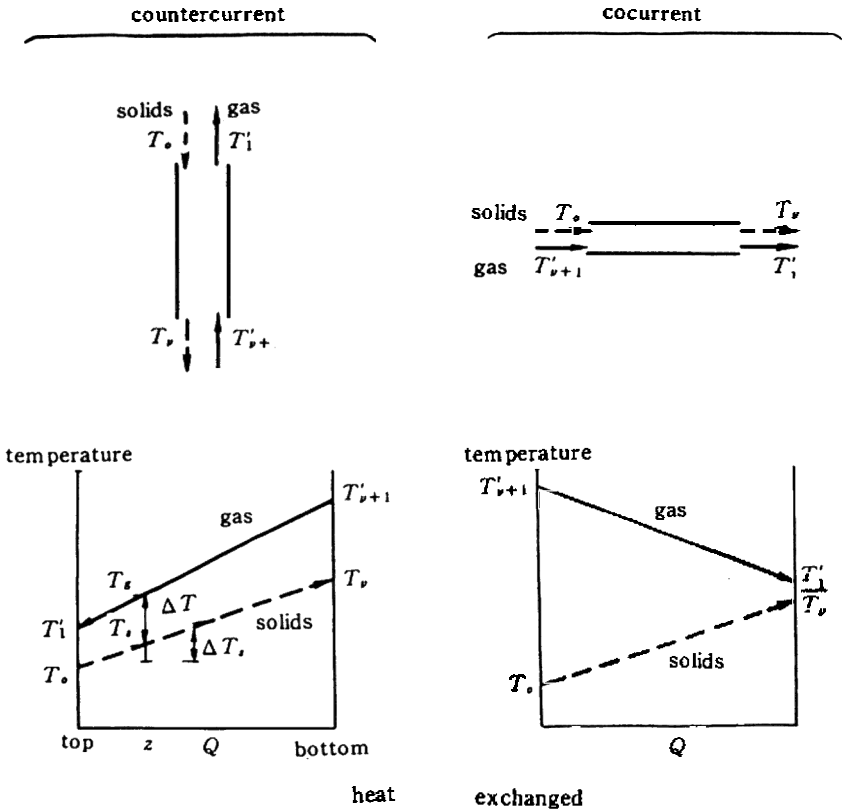


Figure 10. Continuous particle-gas heat exchange. (Kwauk and Tai, 1964.)

The fractional heat recovery h is defined as the ratio of the actual temperature rise of the gas (or of the solids) to that for complete heat transfer between the gas and the solids, that is, according to Fig. 10

$$\text{Eq. (14)} \quad h = \frac{T'_{t+1} - T'_i}{T'_{t+1} - T_o}$$

510 Fluidization, Solids Handling, and Processing

Comparison with the integrated form for N_H given yields the following expressions for G/S heat exchange

$$\text{countercurrent } h = \frac{1 - e^{-N_H(1-t)}}{1 - te^{-N_H(1-t)}}$$

$$\text{cocurrent } h = \frac{1 - e^{-N_H(1-t)}}{1 + t}$$

The particles, while exchanging heat with the flowing gas stream, are in accelerative motion in accordance with the equation

$$m \frac{du}{d\mathbf{q}} = mg \left(\frac{\Delta p}{\mathbf{r}_s} \right) - \frac{2}{3} f A_x \mathbf{r}_f u^2$$

where, for uniform spherical particles having a diameter of d_p

$$m = (\rho d_r^3 / 6) \mathbf{r}_s \quad \text{mass of particle}$$

$$A_x = \rho d_p^2 / 4 \quad \text{frontal area of particle}$$

$$u = Re (\mu / d_p \mathbf{r}_p) \quad \text{velocity of particle}$$

Integration of the above equation can be represented by three dimensionless numbers

$$\text{dimensionless time} \quad \mathbf{q}_1 = \frac{m\mathbf{q}}{d_p^2 \mathbf{r}_s} = \int_0^{Re} \frac{dRe}{Ar_{\Delta r} - f (Re_0 - Re)^2}$$

$$= \int_{Re_0}^{Re_0 + Re} \frac{dRe_s}{Ar_{\Delta r} - f Re_s^2}$$

$$\begin{aligned} \text{dimensionless distance } Z_1 &= \frac{\mathbf{r}_f^z}{d_p \mathbf{r}_s} = \int_0^{Re} \frac{Re \, dRe}{Ar_{\Delta r} - f(Re_0 - Re)^2} \\ &= \int_{Re_0}^{Re_0 + Re} \frac{Re_s \, dRe_s}{Ar_{\Delta r} - f Re_s^2} - Re_0 \mathbf{q}_1 \end{aligned}$$

dimensionless pressure drop

$$-\Phi = -\frac{\Delta p}{z \Delta \mathbf{r}} = \frac{1}{Z_1} \left(\frac{Re_d}{Re_f^m} \right) \int_{Re_0}^{Re_0 + Re} \frac{Re_s^m dRe_s}{Ar_{\Delta r} - f Re_s^2}$$

in which Re_0 is the Reynolds number for gas flowing at velocity u_o , Re_s is the slip velocity between the particles and the fluid, and m is the exponent with which pressure drop varies with velocity: $\mathbf{DP} \propto u^m$.

These three dimensionless numbers all involve what can be called the acceleration integral

$$\int F(x) = \int \frac{Re_s^x dRe_s}{Ar_{\Delta r} - f Re_s^2}$$

While the particle is experiencing the accelerating motion as described above, heat is being transferred between it and the surrounding gas stream also in an unsteady state:

$$(\mathbf{p} d_p^3 / 6) \mathbf{r}_s C_s dT_s = (\mathbf{p} d_p^2) h (T_g - T_s) d\mathbf{q}$$

Integration of this equation can be expressed in terms of the dimensionless numbers used already

$$N_H = \int_0^{q_1} Nu \, d\mathbf{q}_1$$

512 *Fluidization, Solids Handling, and Processing*

where

$$K = (6/Pr) (C_p/MC_s)$$

and the Nusselt number Nu can be correlated to the Reynolds number by the Kramers (1946; also known as the Ranz-Marshall) relation

$$Nu = a + b Re^q$$

Thus the number of heat transfer stages can be expressed in terms of the acceleration integral

$$N_H = (K/t) [a \int F(0) + b \int F(q)]$$

For G/S heat exchange, altogether eight cases may be differentiated, according to whether the operation is countercurrent or cocurrent, whether the solids are being heated or cooled, and whether the value of t is less or greater than unity.

The three unitary heat transfer parameters descriptive of equipment efficiency can now be redefined in terms of the above dimensionless integrals:

$$\text{Unitary heat transfer time: } q/N_H = (d_p^2 r_s/m) (q_1/N_H)$$

$$\text{Unitary heat transfer distance: } z/N_H = (d_p r_s/r_f) (Z_1/N_H)$$

$$\text{Unitary heat transfer pressure drop: } \Delta P/N_H = z(\Phi/N_H)$$

A method has also been developed for treating polydisperse particles (Kwauk, 1964c).

4.2 **Experimental Verification**

Experiments for verifying the efficiency of heat transfer in the dilute phase were carried out in the equipment shown in Fig. 11 (Kwauk and Tai, 1964). It consisted of two vertical heat transfer columns, i.d. = 300 mm for

solids heating and i.d. = 250 mm for solids cooling, both measuring 7.2 m in effective height, with solids circulating between the two by pneumatic transport.

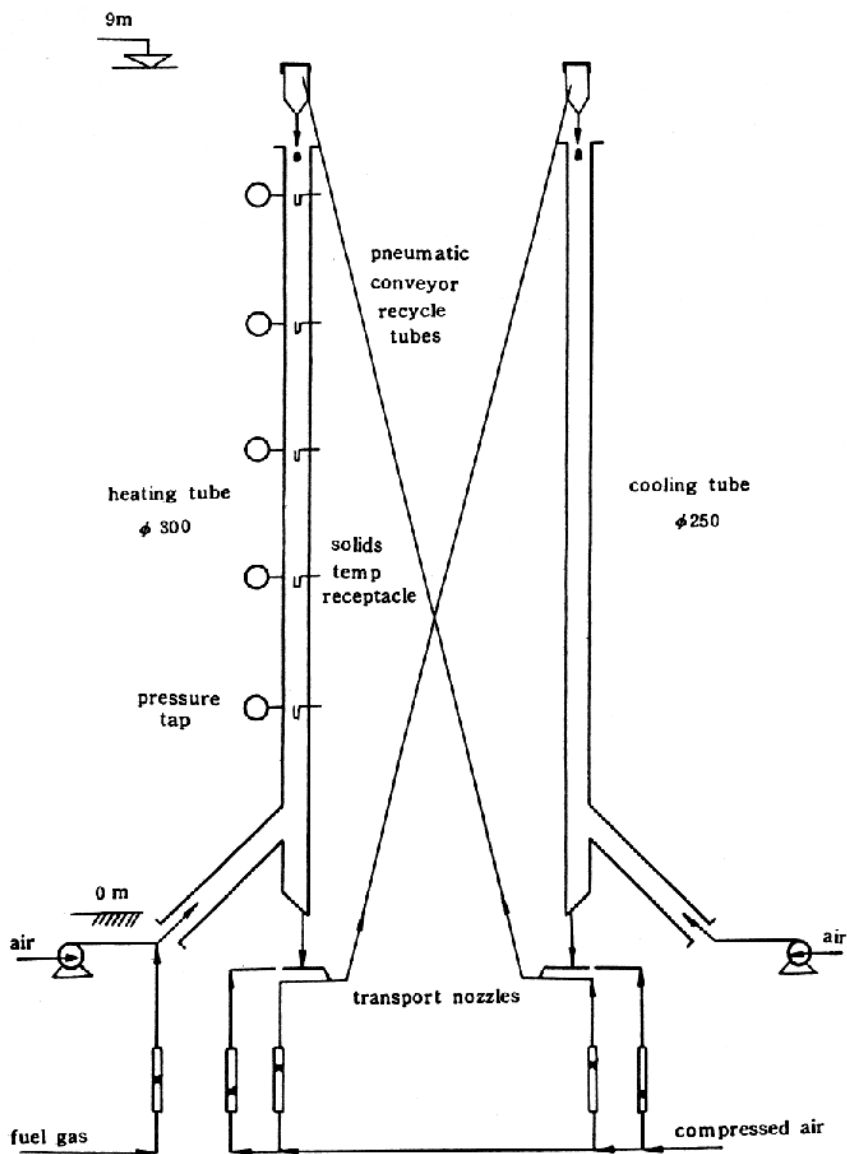


Figure 11. Experimental Setup for dilute-phase heat transfer. (Kwauk and Tai, 1964.)

Solids temperature was measured at various heights by intercepting receptacles, each of which contains a bare thermocouple which follows the solids temperature when turned upright to collect the solids, and measures the gas temperature when the solids are dumped by simply turning the receptacles 180°.

Experimental results for particles in the millimeter range are shown in Fig. 12 in terms of unitary heat transfer height z/N_H for different average particle diameters for both empty columns and columns with internal baffles. The various data give a range of N_H values between 2 and 7 for the 7.2-m experimental apparatus, corresponding to particle-to-gas heat transfer coefficients between 300 and 1,000 kcal/m²·hr·°C. The measured pressure drops for the two columns were of the order of 10 mm water gage.

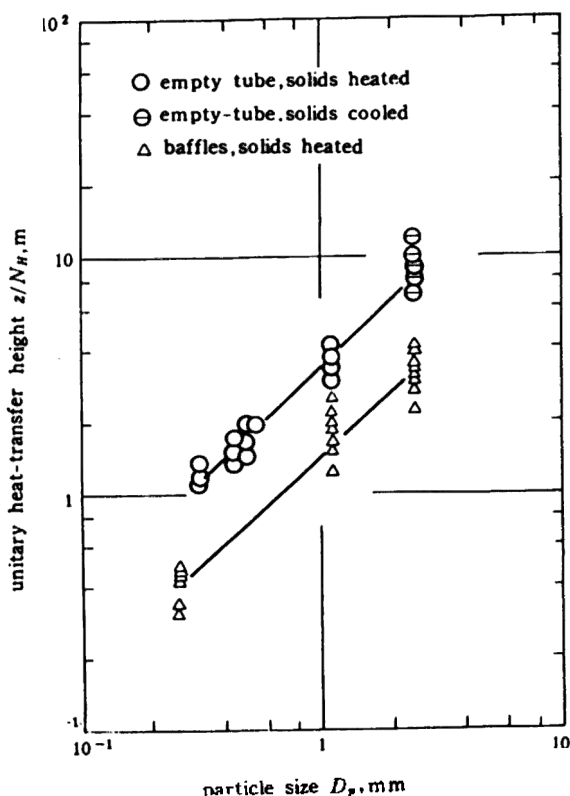


Figure 12. Experimental values for unitary heat-transfer height. (*Kwauk and Tai, 1964.*)

4.3 Baffling and Particles Distribution

To accommodate efficient heating of coarse solids, it would be desirable to break the fall of these particles during their descent by means of baffles in order to prolong their residence time, as shown schematically in Fig. 13 (Kwauk, 1979b). In this respect, a good baffle needs to cover up to 100% of the cross-sectional area traversed by vertical flow, and yet permit oblique passage as near to 100% as possible. Also, baffles should distribute solids laterally in order to give uniform solids population in the heat transfer apparatus. Thus, conceptually, an ideal baffle plate should consist of a cellular array, structurally robust, of deflectors made of infinitesimally thin sheet materials.

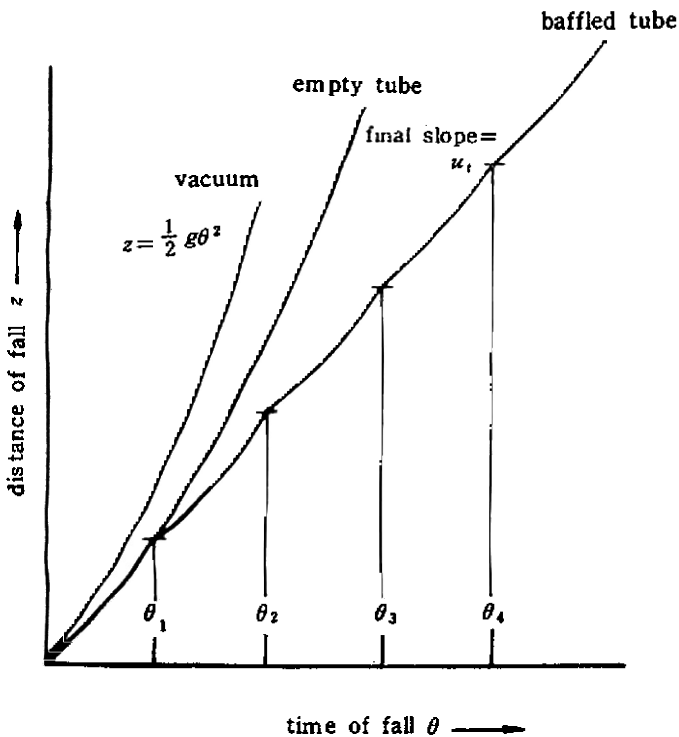


Figure 13. Longitudinal action of baffles in prolonging particle residence time (Kwauk, 1979).

516 *Fluidization, Solids Handling, and Processing*

Of prime importance is the initial distribution of solids at the top of the apparatus. Figure 14 shows the bullet-head solids distributor designed for this purpose. Solids fed from a nearly point source falls on a bullet-shaped target from which they bounce off to land at some distance below, on a fall-breaker baffle which either straightens the particles into essentially vertical paths or simply redistributes them.

Figure 15 illustrates the derivation of a criterion for assessing the lateral distribution of solids by baffles. Solid particles fed at a point source are required to be distributed as uniformly as possible throughout the circular area of radius R . The amount of solids fed is designated M , which, when uniformly distributed will give an average population density of

$$\bar{w} = M/pR^2$$

For any circular band of width dr and located at distance r from the center O , the actual density would be w , which differs from the average density \bar{w} . Thus the difference in the amount of solids collected in this band as compared to the average density \bar{w} is

$$dm = 2pr \, dr |w - \bar{w}|$$

The overall difference from uniform distribution for the entire circle R is, therefore, the integrated value of dm

$$\Delta M = \int dm = 2p \int_0^R |w - \bar{w}| r \, dr$$

When normalized against the total solids added M , this gives a nonuniformity index defined as

$$H = \frac{\Delta M}{M} = \frac{2p}{M} \int_0^R |\bar{w} - w| r \, dr$$

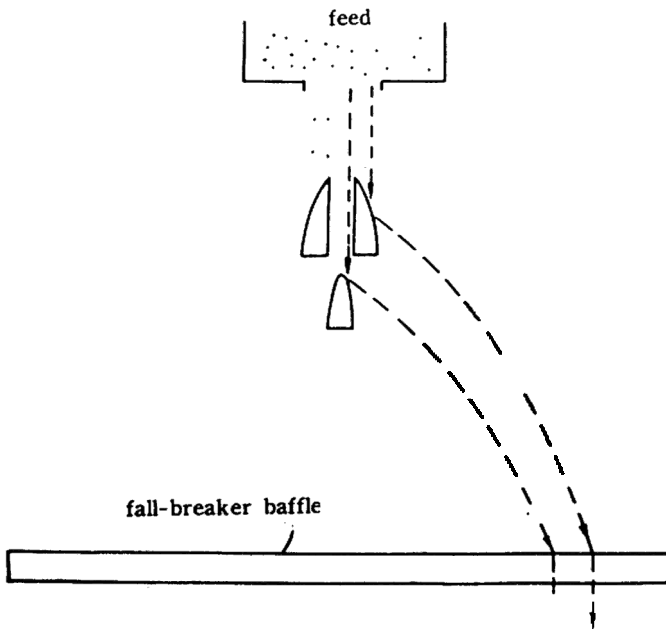


Figure 14. The bullet-head solids distributor.

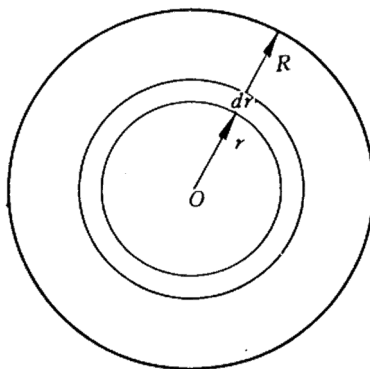


Figure 15. Assessing lateral solids distribution by baffles.

518 Fluidization, Solids Handling, and Processing

Figure 16 shows two cases for lateral solids distribution, a fairly uniform distribution illustrated on the left-hand side, and a relatively concentrated distribution near the center source, shown on the right-hand side. It is clear that for both cases, area a_1 represents the excess of solids over the average for \bar{w} near the central feed, at the expense of deficit for area a_2 near the peripheral region. Graphically the nonuniformity index is thus

$$H = \frac{a_1 + a_2}{a_3 + a_2}$$

Since the actual excess balances the peripheral deficit, that is $a_1 = a_2$,

$$H = \frac{2a_2}{a_3 + a_2}$$

It is evident from the figure that for uniform distribution, $a_2 \rightarrow 0$, and therefore, $H \rightarrow 0$, and for solids concentrated at the feed point, $a_3 \rightarrow 0$ and $H \rightarrow 2$. Thus, the limits for H are

$$\underbrace{0 < H < 2}_{\substack{\text{perfectly uniform} \\ \text{solids distribution}}} \quad \text{H} \quad \underbrace{0 < H < 2}_{\substack{\text{Solids concentrated} \\ \text{at feed point}}}$$

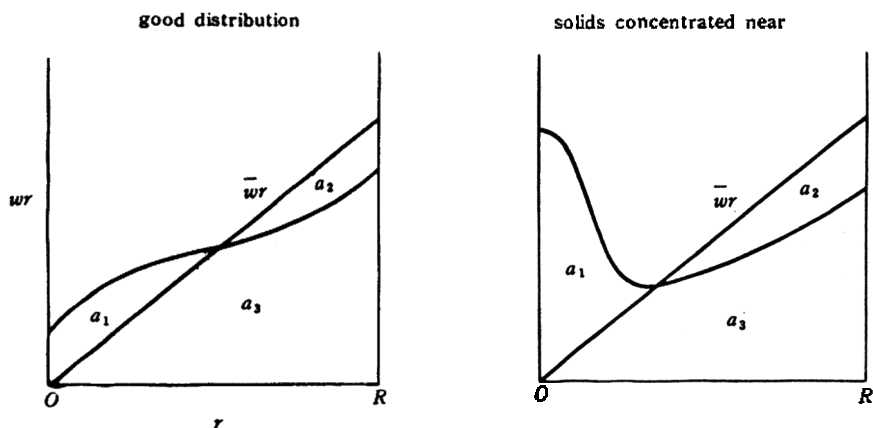


Figure 16. Nonuniform lateral solids distribution.

4.4 Pilot Plant Demonstration

A few examples will be given on the countercurrent dilute-phase G/S heat exchanger.

Ore Preheating. Figure 17 (Kwauk and Tai, 1964) shows the inside contour of a brick-lined 15-tpd pilot plant sulfatizing roaster for cupriferous iron ore. It consists of an upper section, i.d. 850 mm, heated by combustion of producer gas and provided with baffles, in which the cupriferous ore, crushed to 0–2 mm, was heated in dilute-phase through a fall of 12 meters, to the reaction temperature of 500–550°C. The preheated ore was fed pneumatically via an angle-of-repose valve into a lower section where it was sulfatized in a dense-phase fluid bed, i.d. 500 mm, with a gas containing 6–7% SO₂ produced by roasting pyrite concentrate in a separate auxiliary roaster at higher temperatures. About 60% of the copper and cobalt in the ore was rendered soluble in 0.3% sulfuric acid, while sulfatization of iron could be held below 1%. By ore preheating, the pyrite consumption was as low as 67 kg/t of the cupriferous ore, while for autogenous roasting by admixture with the cold cupriferous ore, it would have been as high as 330 kg/t.

An alternative process for winning copper from cupriferous iron ore was segregation roasting, in which the hot ore was mixed with small amounts of NaCl and powdered coal, in order to transport the copper content of the ore via the gaseous copper chlorides which were, thereby, reduced to metallic copper on the surface of the coal particles, followed by ore dressing for concentrating the metal thus formed. Figure 18 shows a segregation pilot plant, in which cupriferous iron ore was preheated in a dense fluid bed by direct injection of powdered coal, and the sensible heat of the hot flue gas was recovered by the incoming ore falling in dilute phase. Ore was introduced at the top of the roaster by a rotary feeder to a number of radially positioned bullet-head distributors located above two tiers of fall-breaker baffles. With a final ore preheat temperature of 850°C, it was possible to keep the coal consumption to about 65 kg/t of ore, at a roaster top temperature of around 250°C for the exit gas.

Semi-Conveying Magnetizing Roasting. Figure 19 shows diagrammatically the “two-phase magnetizing roaster” for low-grade iron ores—dilute-phase ore preheating in an upper section with an i.d. of 1,050 mm and dense-phase reduction with producer gas in a lower section of i.d. 825 mm. The roasting consisted of a mild reduction to convert the iron values to

magnetite followed by low-intensity magnetic ore dressing to yield an iron ore concentrate. At the junction of the two sections, approximately one-third way from the bottom, air was injected to burn most of the reducing gas issuing from the dense bed for heating the ore particles falling down from above.

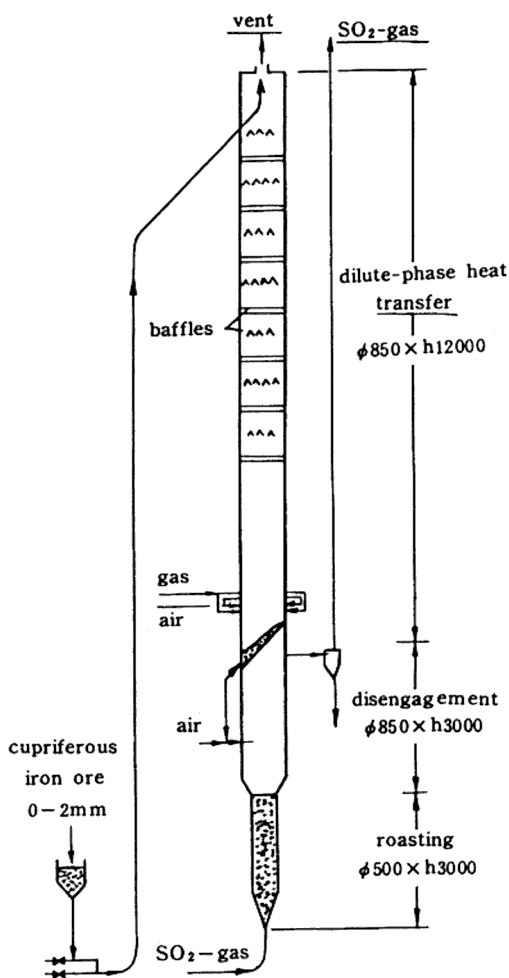


Figure 17. 15-TPD Sulfatizing pilot plant roaster. (Kwauk and Tai, 1964.)

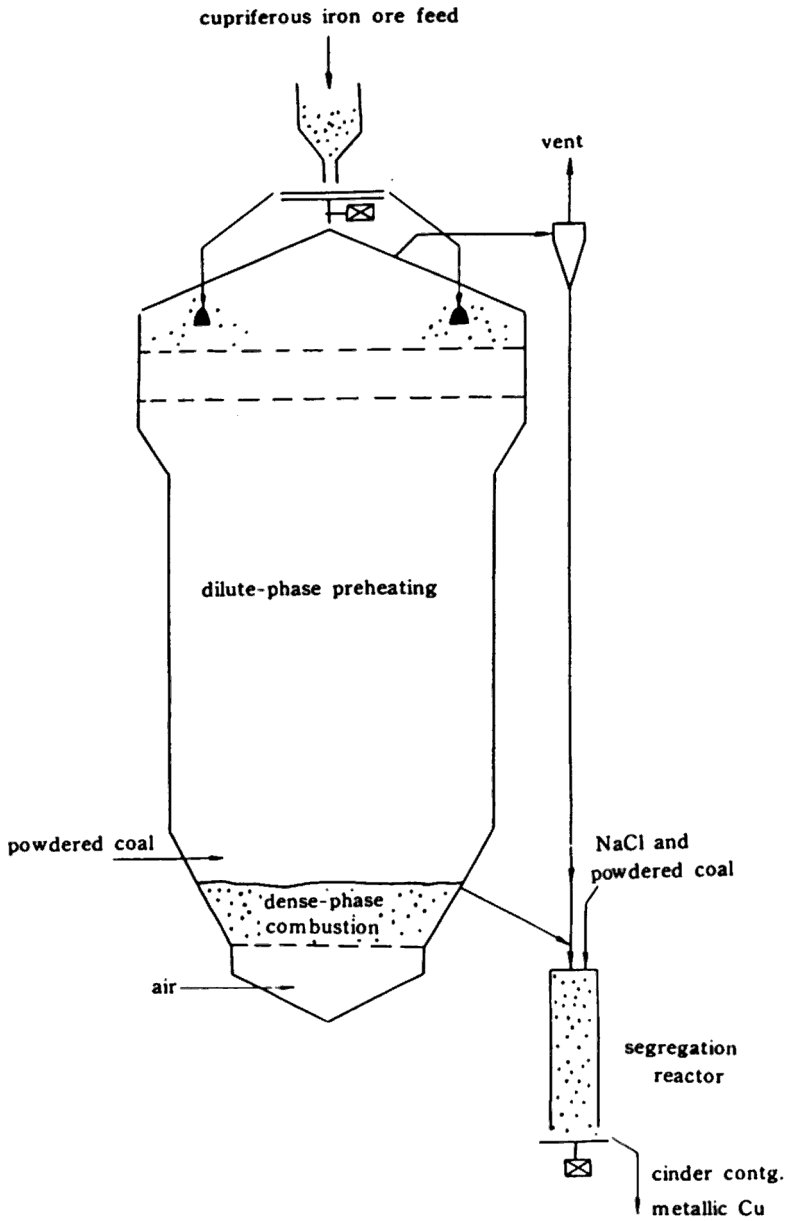


Figure 18. 250-TPD Segregation pilot roaster.

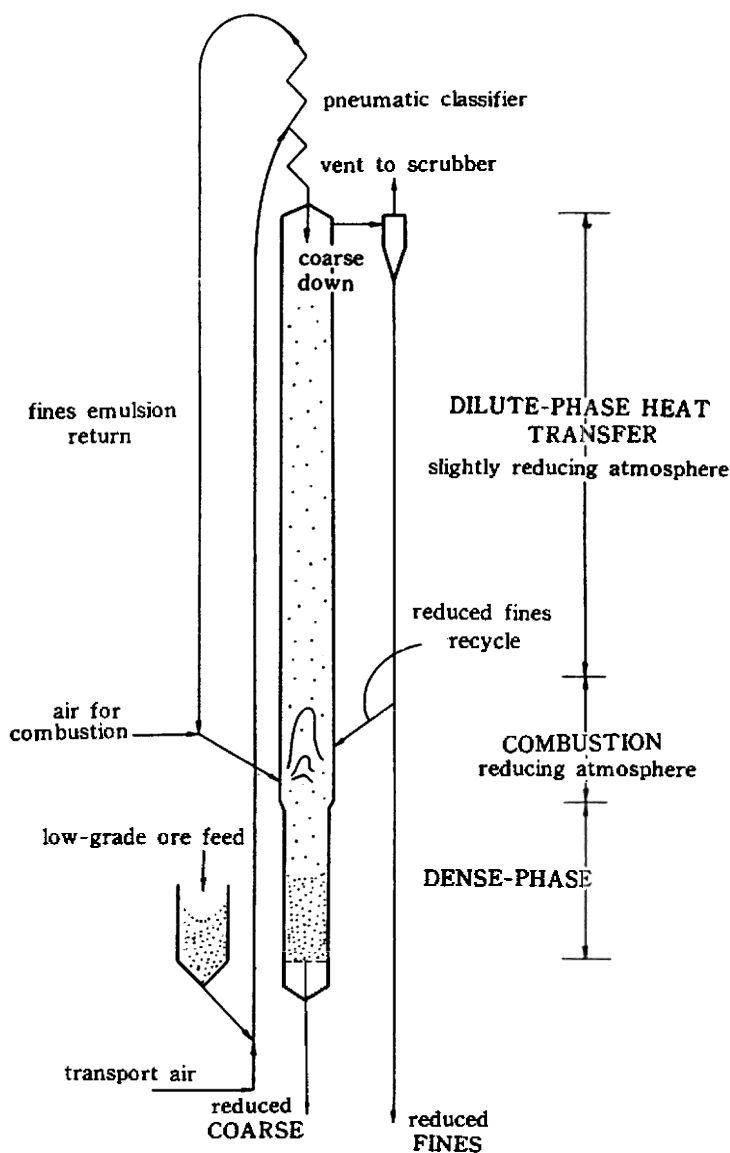


Figure 19. Semi-conveying two-phase fluid-bed magnetizing roaster.

To guard against incomplete reduction of ore fines which would be elutriated prematurely during preheating, the midsection combustion was adjusted to produce a mildly reducing flame containing approximately 4%

($H_2 + CO$). The major portion of the fines present in the ore feed was removed by pneumatic classification in a zigzag tube at the top of the vertical pneumatic transport feed pipe, whereby the remaining coarse portion was fed, as usual, by gravity at the top of the dilute-phase preheating section while the fines were carried by the same transport air downwardly again to the combustion zone, where the high temperature reducing flame converted these minute particles almost instantly to the required magnetite state. The upflowing dilute emulsion of fines travelled to the top of the roaster, delivering its heat to the falling particles of larger diameters, and the fines, now already reduced, were finally collected in an external cyclone. Thus, part of the ore, that is, the fines, was reduced during upward conveying. Inasmuch as the upflowing heat capacity was augmented by the presence of these fines, the amount of excess combustion air could be reduced, thus increasing the roaster capacity.

Heat Recovery from Both Hot Calcine and Hot Flue Gas. Figure 20 shows a roaster with two sections for dilute-phase heat recovery from both the hot calcine at the bottom and the hot flue gas at the top. With this design, low-grade cinnabar ore containing as little as 0.06% Hg and crushed to particle sizes as big as 0–12 mm, has been successfully roasted at around 800°C for mercury extraction with a coal ratio of 90 kg/t of ore. This design has recently been tested on a pilot plant scale to roast low-grade pyrite, containing 13% sulfur on the average, and therefore, hardly autogenous, to produce a gas containing over 10% SO_2 for use in sulfuric acid manufacture.

5.0 FAST FLUIDIZATION

One disadvantage of dilute raining particles is its very diluteness, signifying low volumetric utilization of equipment. Particle population may be concentrated by recycling solids to the bottom of a fluidized system. Such system can operate at relatively high gas velocities, and is, therefore, known as “fast fluidization” (Reh, 1970, 1971, 1972, 1985; Squires, 1975a, 1975b, 1975c, 1985; Kwauk, 1994). Solids suited for fast fluidization aggregate into strands (also called clusters, swarms, etc.) which form and disband in rapid succession, thus ensuring good gas/solid contact. The design of fast fluid bed reactors calls for a physical model totally different from that for bubbling fluidization.

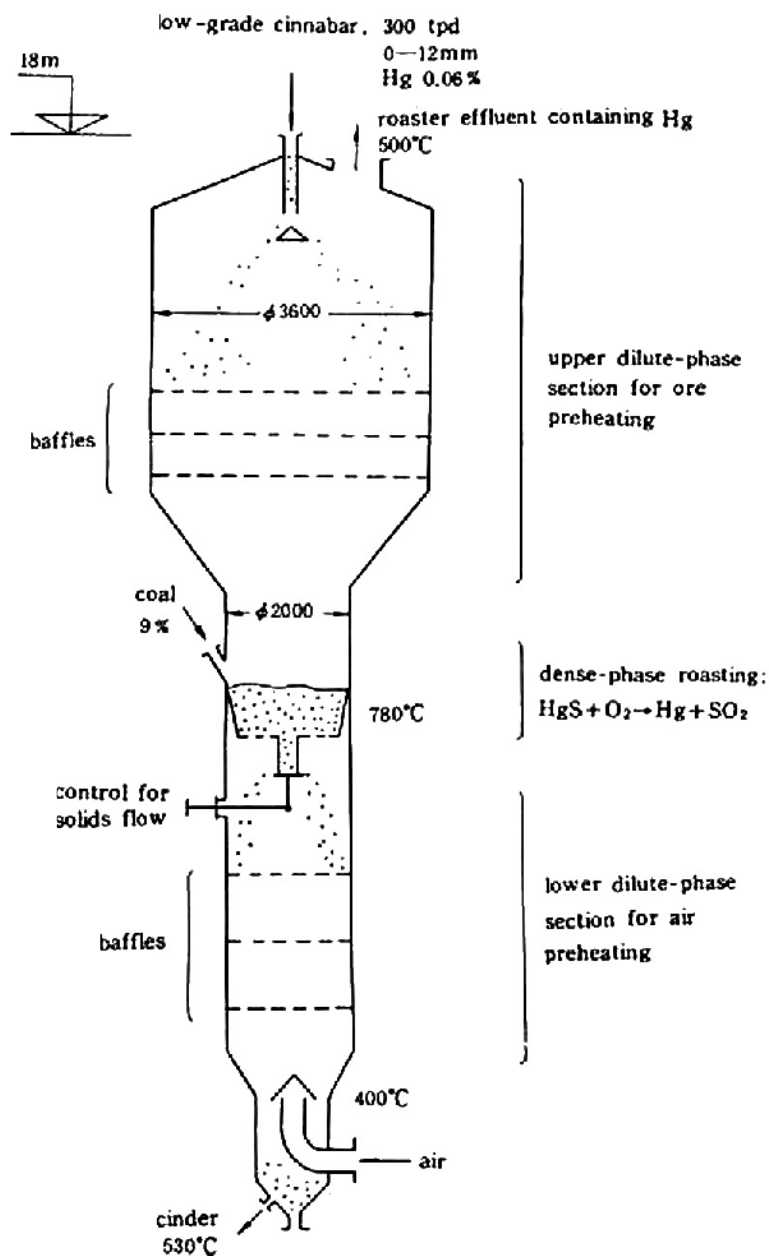


Figure 20. Double-section two-phase cinnabar roaster.

5.1 Longitudinal Voidage Distribution

Characteristically in fast fluidization, there always exists a denser region at the bottom, much more extended than would be accounted for by a one-dimensional analysis based on accelerative motion for particulate fluidization. Figure 22 (Li and Kwauk, 1980) gives four sets of representative voidage distribution curves along the bed height, taken in an i.d.-90 x h-8,000 mm experimental column shown schematically in Fig. 21 (Wang, Li Zheng and Kwauk, 1985).

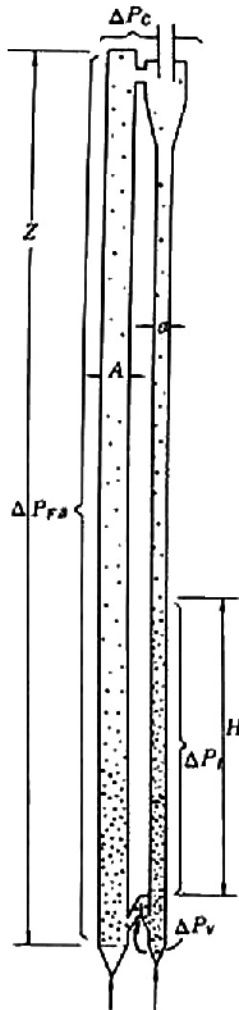


Figure 21. Fast fluidization circuit. (Wang, Li, Zheng and Kwauk, 1985.)

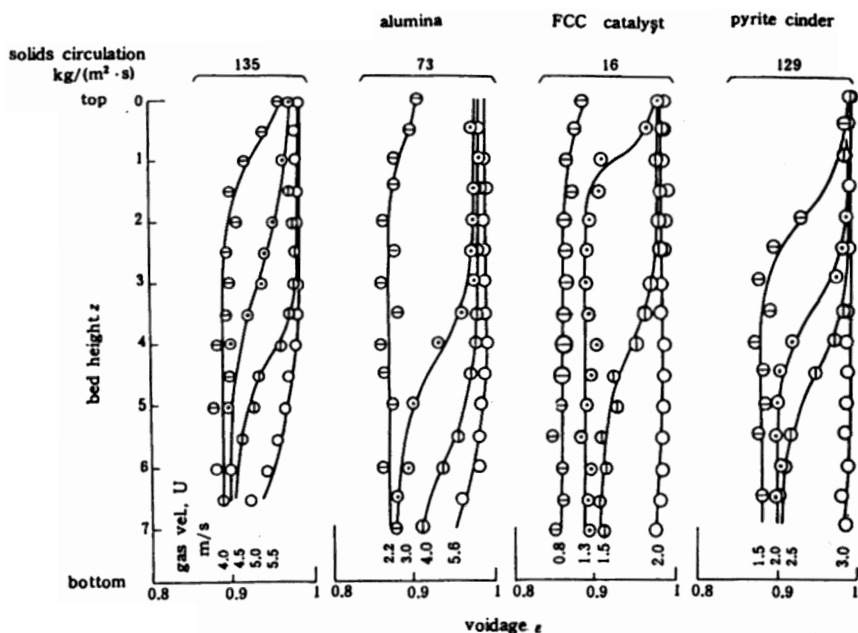


Figure 22. Vertical voidage distribution in fast fluidization. (*Li and Kwauk, 1980.*)

These characteristic voidage distribution curves, combined with the strand-cluster structure noted above for the solids bed, led to the physical model of Fig. 23 (*Li and Kwauk, 1980*). At any height, for instance z as shown in Fig. 23, the clusters are supposed to move upward through a diffusive mechanism from a region of relatively high population at the lower section, and then, when they arrive at a region above z where the average bed density is lower, they tend to fall back to the lower region of their origin by virtue of buoyancy. Dynamic equilibrium calls for equality of the diffusion and buoyancy fluxes, thus leading to a rather compact voidage distribution relation

$$\ln[(e - e_a)/(e^* - e_a)] = -(z - z_i)/Z_o$$

where Z_o has the dimension of length and will be called the *characteristic length*. This equation yields an S-shaped e -versus- z curve, approaching an asymptotic value of e^* at the top as $z \rightarrow -\infty$, and e_a at the bottom as $z \rightarrow \infty$. The value of Z_o governs the rapidity with which the dense region at the

bottom transforms into the dilute region at the top—the larger the value of Z_0 , the more gradual is this transformation; and for $Z_0 = 0$, the above equation predicts a sharp interface. Point z_i stands for the inflection in the S-shaped curve, dividing it into a dilute region at the top and a dense region at the bottom.

The curves in Fig. 22 were calculated by means of the above equation, the points being experimental values. Figure 24 (Kwauk, Wang, Li, Chen and Shen, 1985) shows empirical correlations for the constants e^* and e_a for FCC catalyst, fine and coarse alumina, pyrite cinder and iron ore concentrate.

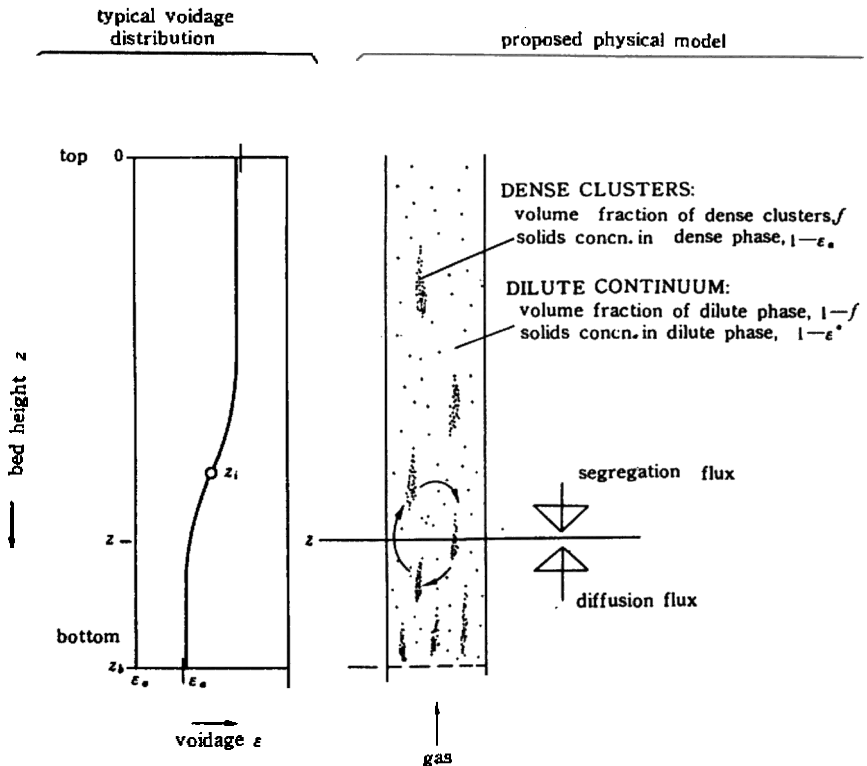


Figure 23. Modeling of fast fluidization. (Li and Kwauk, 1980.)

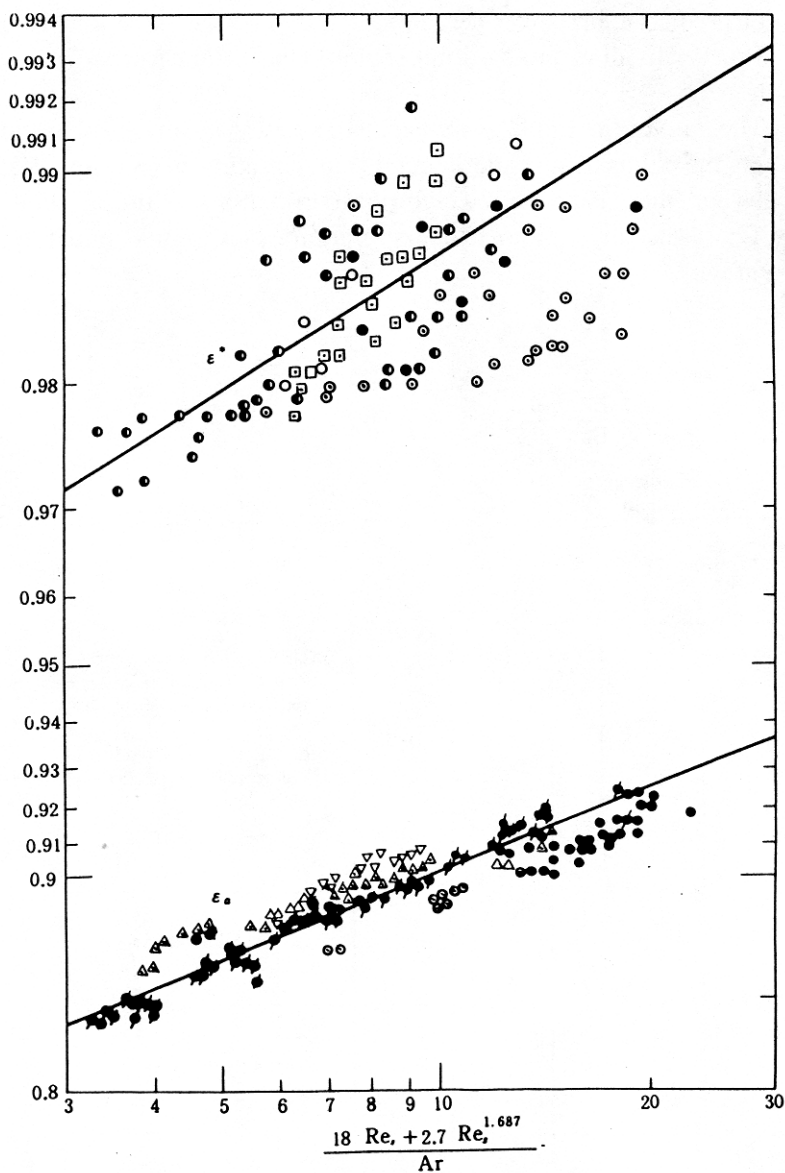


Figure 24. Empirical correlations for voidages ϵ^* and ϵ_g (Kwauk, Wang, Li, Chen and Shen, 1985.)

5.2 Regimes for Vertical G/S Systems

The voidage distribution model permits the derivation of analytical expressions for the integrated average voidage taken through the whole height, defined as

$$\bar{e} = (1/z) \int_0^z e \, dz$$

Thus, for the entire bed

$$\frac{\bar{e} - e_a}{e^* - e_a} = \frac{1}{z_i / Z_o} \ln \left[\frac{1 + \exp(z_i / Z_o)}{1 + \exp(z_i - z) / Z_o} \right]$$

for the dilute phase (phase B) above the point of inflection z_i

$$\frac{e_B - e_a}{e^* - e_a} = \frac{1}{z_i / Z_o} \ln \left[\frac{1 + \exp(z_i / Z_o)}{2} \right]$$

for the dense phase (phase A) below the point of inflection z_i

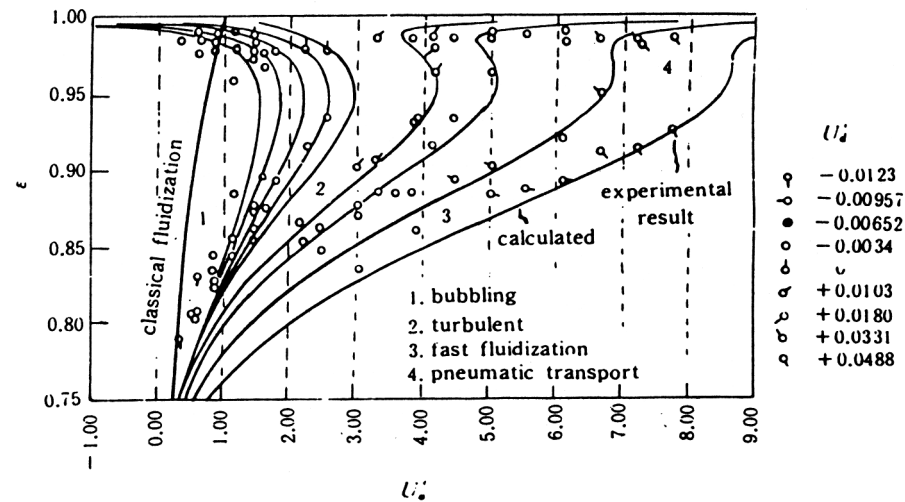
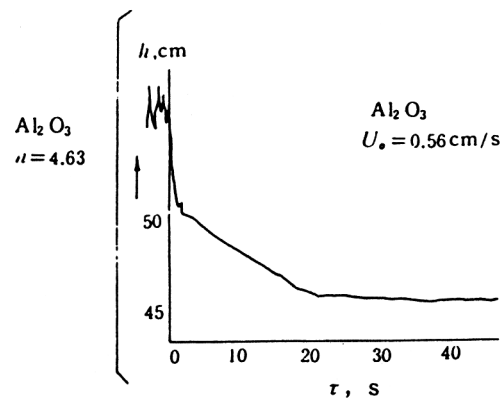
$$\frac{e_A - e_a}{e^* - e_a} = \frac{1}{(z_i - z) / Z_o} \ln \left[\frac{2}{1 + \exp(z_i - z) / Z_o} \right]$$

The A- and B-phases are shown plotted in Fig. 25 (Chen and Kwauk, 1985), whenever an inflection point exists, for FCC catalyst, Al_2O_3 and iron ore.

For a fine powder having good fluidizing characteristics and conforming to the requirements for Group A according to Geldart's classification, fluidization traverses the following regimes in succession as gas velocity increases, as demonstrated in Fig. 25:

BUBBLING — TURBULENT — FAST — TRANSPORT

As the fluidizing quality of the powder deteriorates from Group A to Group B, however, the range for fast fluidization dwindles, until, for sandy materials, TURBULENT often jumps to TRANSPORT without the intermediate FAST stage. This is shown in Fig. 25 for a titanomagnetite concentrate, which is heavy and comparatively coarse.



(Cont'd on subsequent page.)

Figure 25. (Cont'd)

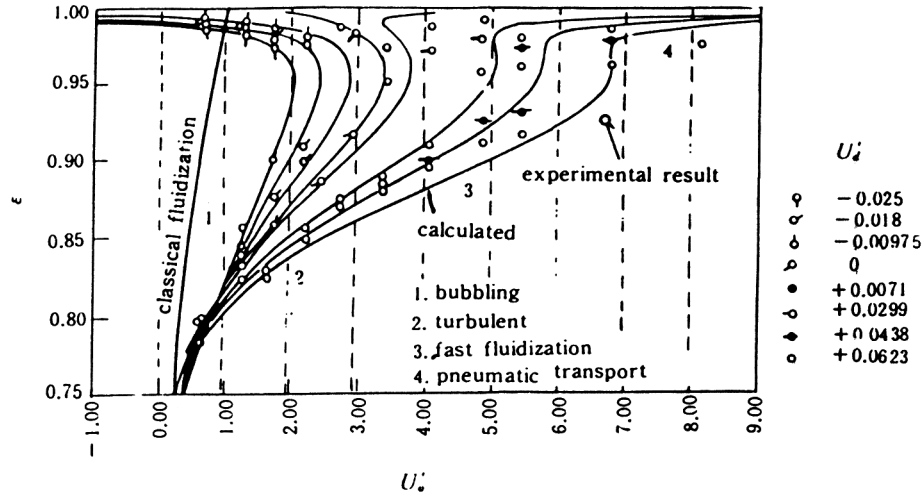
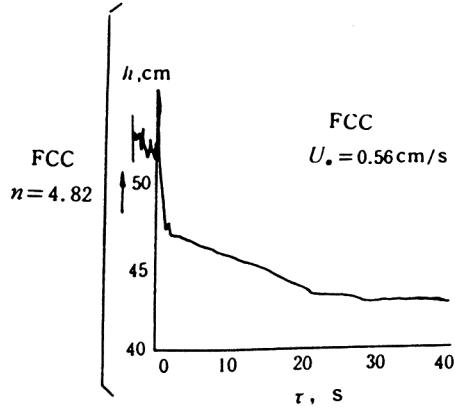


Figure 25. (Cont'd)

5.3 Radial Voidage Distribution

All the preceding sections were concerned with one-dimensional voidage distribution in the vertical direction. However, maldistribution of solids in the radial direction, generally dilute in the center and dense next to the wall, often causes unfavorable residence time distributions for both the solids and the fluidizing gas, thus resulting in undesirable product distribution. Although it has long been known that in vertical flow of G/S systems solids are preferentially scattered toward the wall, accurate measurement has not been easy.

Optical fiber measurement of local solids concentrations of FCC catalyst fluidized in a 9-cm-i.d. column gave the results shown typically in Fig. 26. Analysis of these data showed that the radial voidage profile could be described solely by the cross-section-average voidage \bar{e} , calculated as shown in Sec. 5.1, and the reduced radial coordinate r/R :

$$r/R < 0.75 \quad e = \bar{e}^{(r/R)^2} + 0.191$$

$$r/R < 0.75 \quad e = \bar{e}^{3.62(r/R)^{6.47}} + 0.191$$

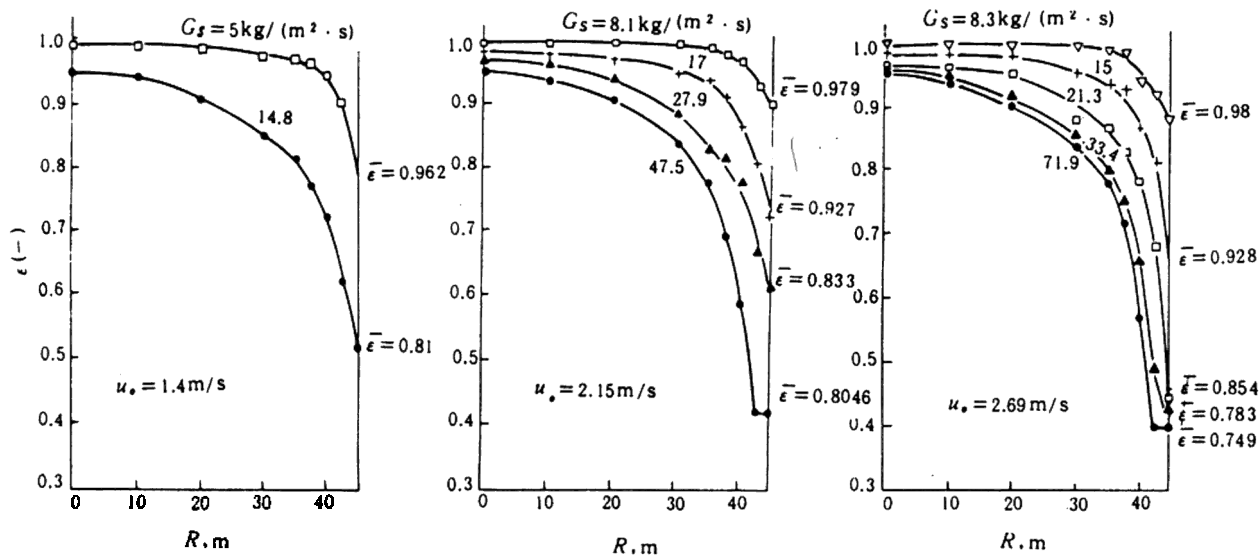
These two equations thus demarcate the radial voidage profile at a radial position of $r/R = 0.75$ into an annular region of steep voidage distribution and a core region of flat distribution. Figure 27 (Tung, Li, Zhang and Kwauk, 1987; Tung, Li and Kwauk, 1988) shows curves computed by using these two equations, which seem to check closely experimental data.

Thus, the three-dimensional voidage distribution in a fast fluidized bed can be determined, semi-empirically as our understanding stands at the present, from the physical properties of the solids and the gas and the operating variables.

From a practical point of view, for improved solids distribution, the indications are for innovative design of obstructing structures next to the wall to break the falling sheet of solids in order to equalize their flow pattern across the column through repeated redistribution.

5.4 Modeling Fast Fluid-bed Reactors

The three-dimensional voidage distribution provides the basic correlation for building a reactor model for fast fluidization, given data on particle-fluid transfer coefficients and intrinsic particle reaction kinetics.



(Cont'd on subsequent page.)

Figure 26. Radial voidage distribution for FCC catalyst in a 90 mm i.d. column, 2.25 m above the gas distributor.

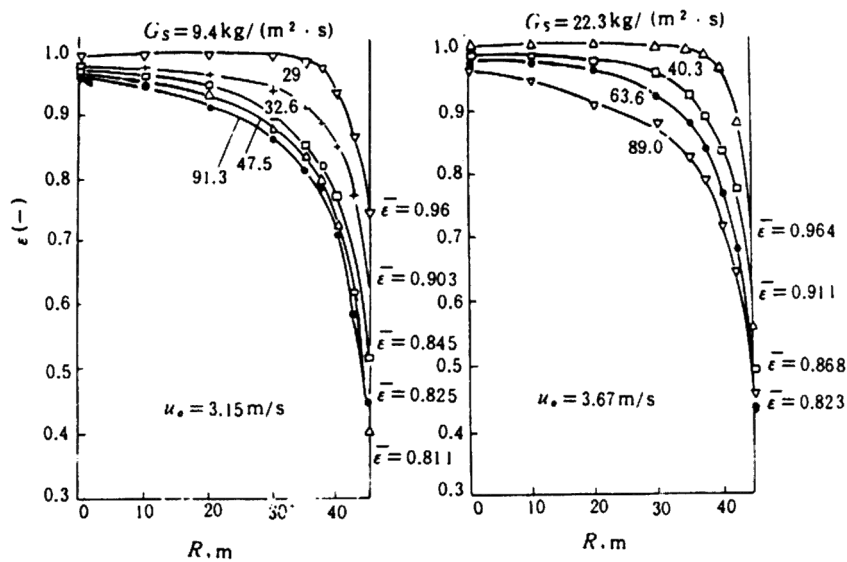


Figure 26. (Cont'd)

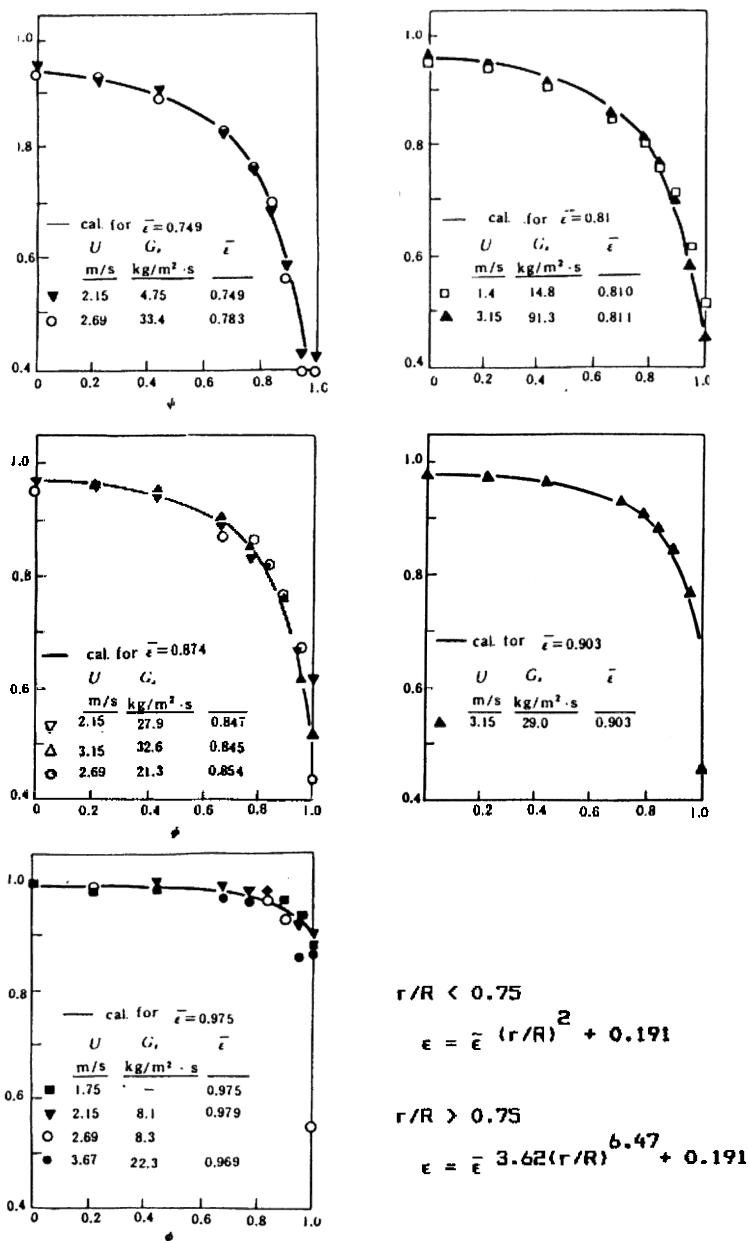


Figure 27. Radial Voidage Distribution for FCC Catalyst in a 90 mm i.d. column, 2.25 m above gas distributor (curves computed, points experimental) (Tung, Li and Kwauk, 1988).

6.0 SHALLOW FLUID BEDS

Another mode of bubbleless gas/solid contacting originated from the identification of a shallow region above the fluid bed distributor, before bubbles take shape. By far the major portion of gas/solid transfer takes place in this narrow region, and the contribution of the overlying solids is often only nominal. A critical factor in designing shallow beds is an understanding of the functioning of the fluid bed distributor to insure even gas distribution and minimal pressure drop.

6.1 Dynamics for the Distributor Zone

Figure 28 (Yan, Yao and Liu, 1982) presents the results of turbulence measurement above a distributor plate by means of a hot-wire anemometer, indicating that turbulence intensity increases sharply near the distributor, especially for the perforated plates and the cap plate, and then diminishes beyond a certain distance (40 mm in the present case) to some nearly constant low values.

Figure 29 (Qin and Liu, 1982) shows the behavior of individual particles above the distributor recorded by video camera of small clusters of particles, coated with a fluorescent material and spot-illuminated by a pulse of ultra violet light from an optical fiber. The sequential images, of which Fig. 29 just represents exposures after stated time intervals, were reconstructed to form the track of motion of the particle cluster shown in Fig. 30. Neither this track nor visual observation of the shallow bed while fluidized, reveal any vestige of bubbles. Instead, the particles are thrown up by the high velocity jets issuing from the distributor orifices to several times their static bed height.

6.2 Activated Solids Shallow Fluid Bed Heat Exchanger

Figure 31 (Liu, Liu, Li and Kwauk, 1986) shows a cylindrically shaped shallow fluid bed tubular heat exchanger. Solid particles are fluidized with a small stream of activating gas G_a , so as to insure maximal heat transfer between the particles and the exchanger tube wall. The waste gas G_w , from which heat is to be extracted, passes through the solid

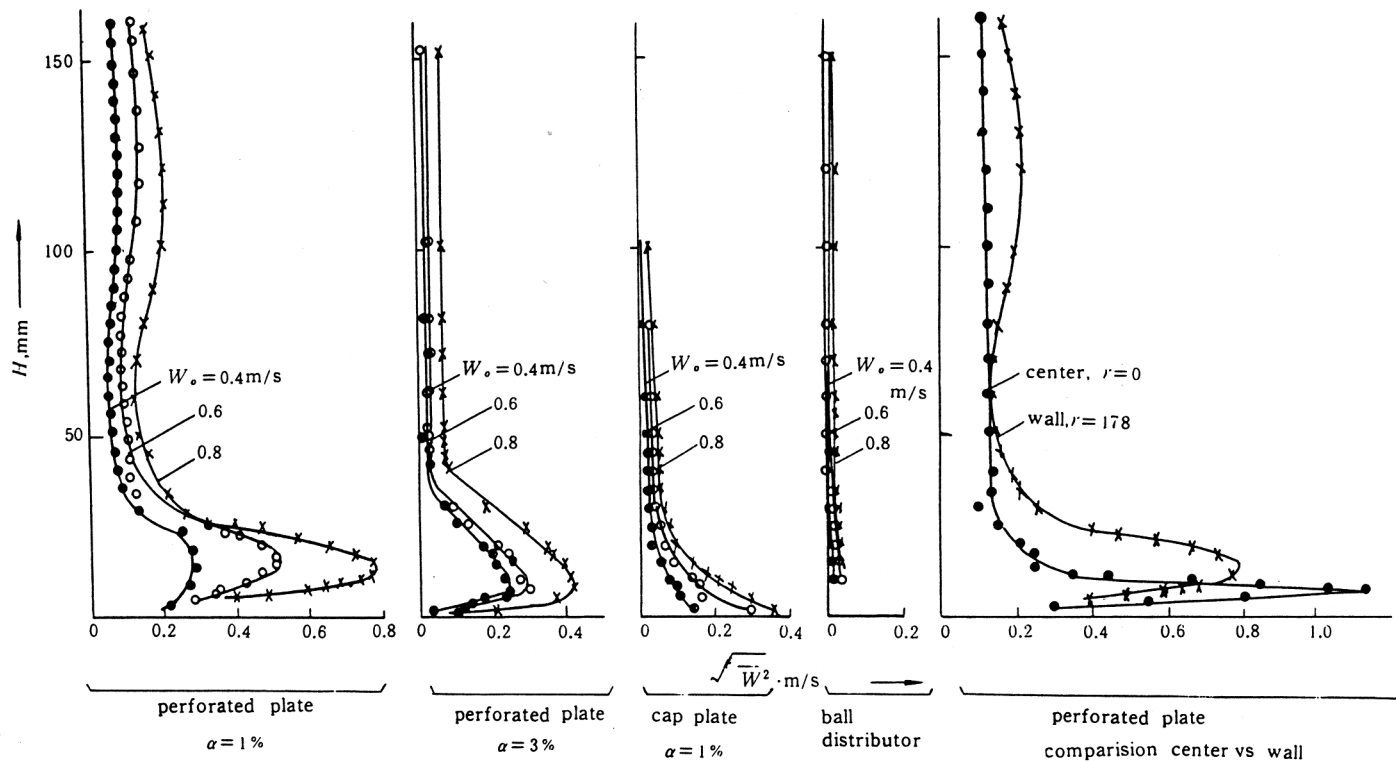


Figure 28. Turbulence intensity at center of a 180 mm dia. distributor in absence of solid particles. (Yan, Yao, and Liu, 1982.)

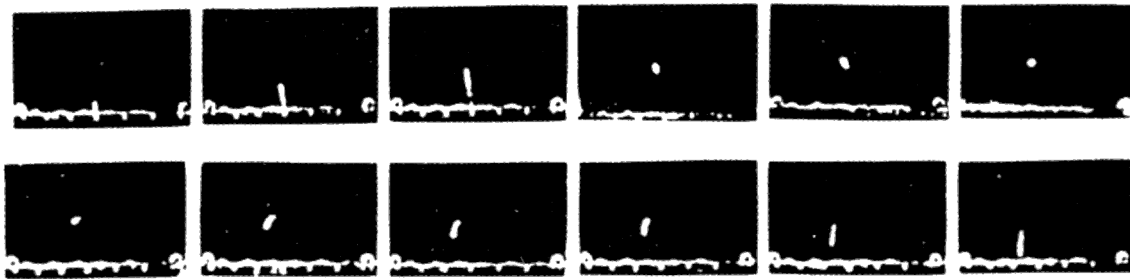


Figure 29. Motion of luminescent particles in shallow fluidized bed. (*Qin, and Liu, 1982.*)

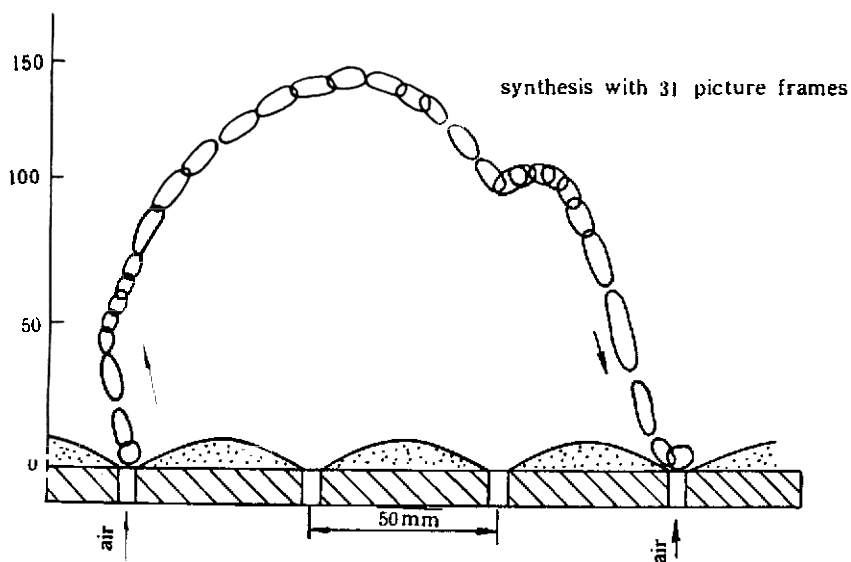


Figure 30. Track of particle motion in shallow fluidized bed. (*Qin, and Liu, 1982.*)

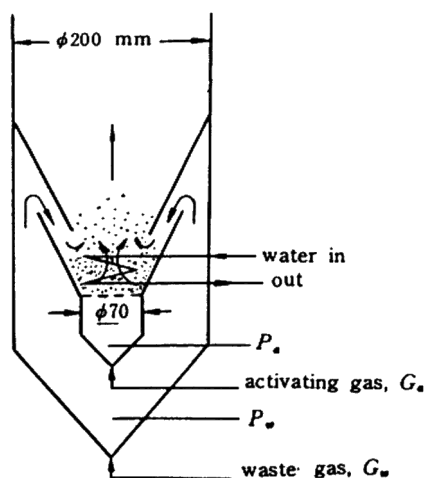


Figure 31. Activated Solids Shallow fluid-bed heat exchanger. (*Liu, Liu, Li, and Kwauk, 1986.*)

particles already suspended by the activating gas, thus heating the solid particles. In merely percolating through the suspended particles, the waste gas experiences minimal pressure drop. The waste gas does not pass through the gas distributor, and therefore, cannot possibly clog the distributor holes for the carbonaceous materials the hot gas may contain. Figure 32 shows the variation of pressure of both gas streams, G_a and G_w , with their flow ratio. Obviously the pressure of G_w is much less than that of G_a , even at a flow ratio $N = G_w/G_a$ of as high as 10.

6.3 Cocurrent Multistage Shallow Fluid Bed

For slow reactions, the shallow fluid beds have been organized into a cocurrent multistage fluid bed (MSFB) reactor as shown in Fig. 33 (Yan, Yao, Wang, Liu and Kwauk, 1983). In this reactor, solids are carried up by the flowing gas stream, and once they reach the top, they are collected through a funnel and recirculated to the bottom by means of a pneumatically controlled downcomer.

Rather unexpected flow behavior was discovered while the shallow fluid beds were connected in series for cocurrent solids flow with the gas, as shown in Fig. 34. When a shallow dense bed is present at any stage, there is a positive increase of bed height to any increase in solids flow rate, at any given gas velocity. However, if the solids rate is reduced to some critical value, the dense bed slumps to practically nil height. If the solids rate is restored gradually, the dense bed does not build up until another (upper) critical value is reached. Then the dense bed reappears all of a sudden. Between these two critical solids flow rates, there exists a hysteretic region in which there are two stable bed heights corresponding to any solids rate: a dense bed and a dilute bed. This hysteresis suggests two different mechanisms of solids transport from a lower stage to an upper stage: elutriation in the dense phase, and "jetting" in the dilute phase. Above the upper critical solids flow rate, only dense bed exists, and below the lower critical rate, only dilute bed exists, both these extreme regions being monotonic in the relation between bed height and solids flow rate.

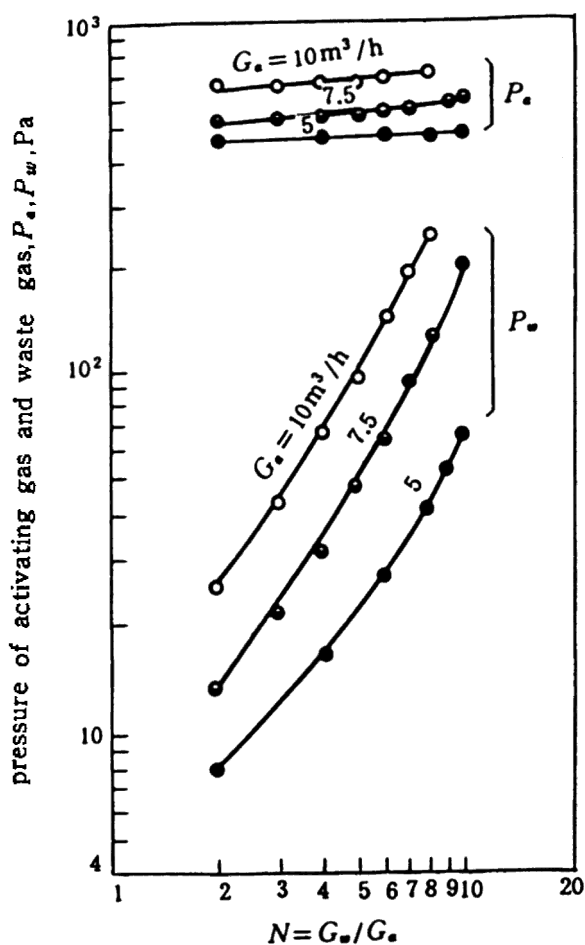


Figure 32. Variation of pressure of activating gas and waste gas with their flow ratio. (Liu, Liu, Li, and Kwauk, 1986.)

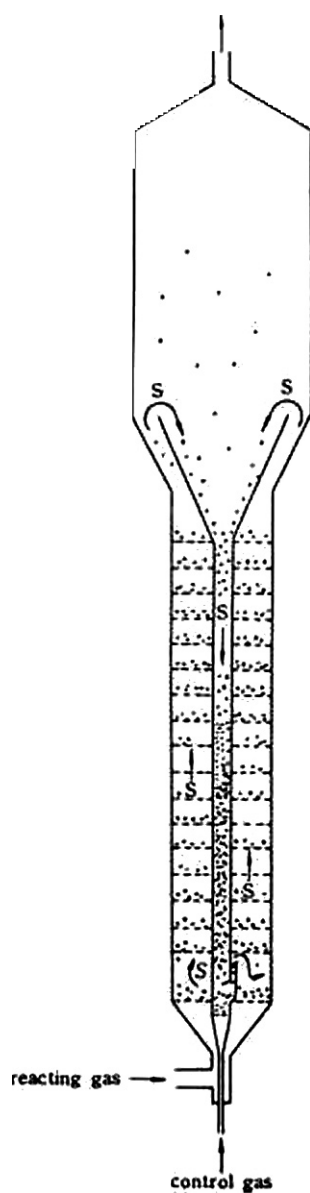


Figure 33. The cocurrent multistage (co-MSFB) fluid-bed reactor. (Yan, Yao, Wang, Liu, and Kwauk, 1983.)

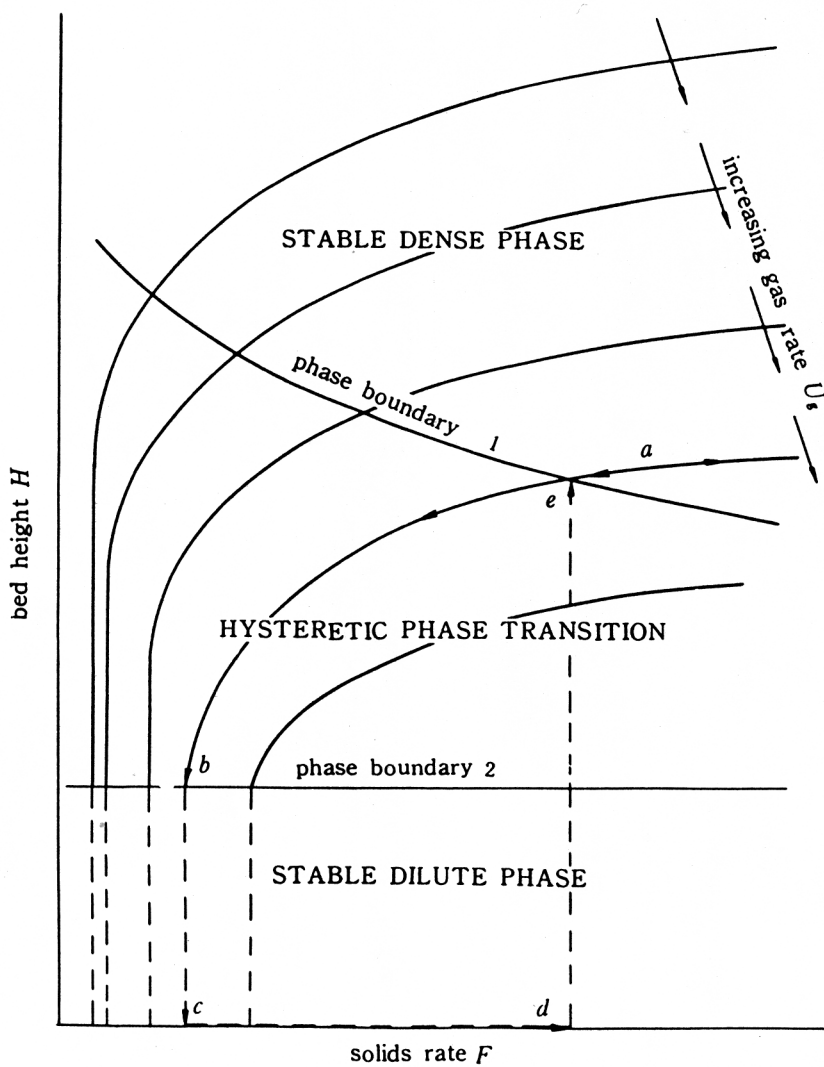


Figure 34. Phase transition for co-MSFB. (Yan, Yao, Wang, Liu, and Kwauk, 1983.)

6.4 The Co-MSFB as a Chemical Reactor

The viability of the co-MSFB as a chemical reactor for slow reactions has been examined for the gaseous reduction of iron ores. The experimental setup is shown in Fig. 35 (Yan, Yao, Wang, Liu and Kwauk, 1983), the heart of which is a 70-mm i.d. reactor, either fitted with a 13-stage co-MSFB internal, or empty. Comparative reduction tests for equal inventories of iron ore revealed that the reduction time required for any stated degree of metallization could be reduced considerably by the use of the co-MSFB internals, as shown in the set of curves of Fig. 36. Whether the advantage of the staging accrues from better G/S contacting, or from the suppression of back flow of the gas stream from stage to stage, remains yet to be corroborated from mass-transfer studies between the solids and the flowing gas.

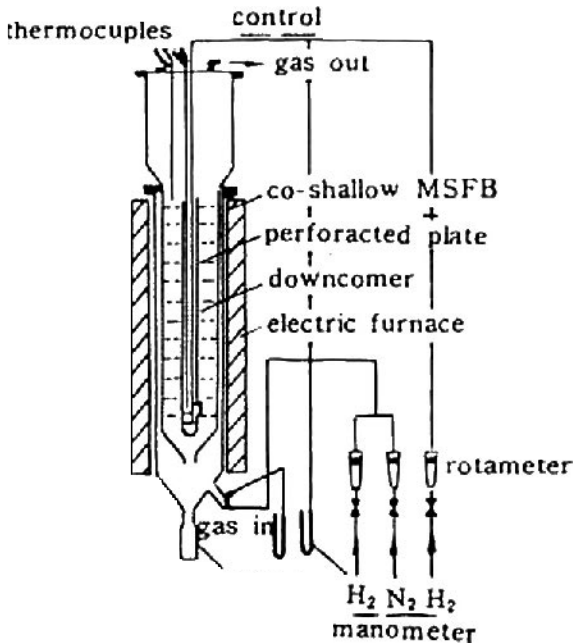


Figure 35. Experimental co-MSFB reactor for iron oxide reduction. (Yan, Yao, Wang, Liu, and Kwauk, 1983.)

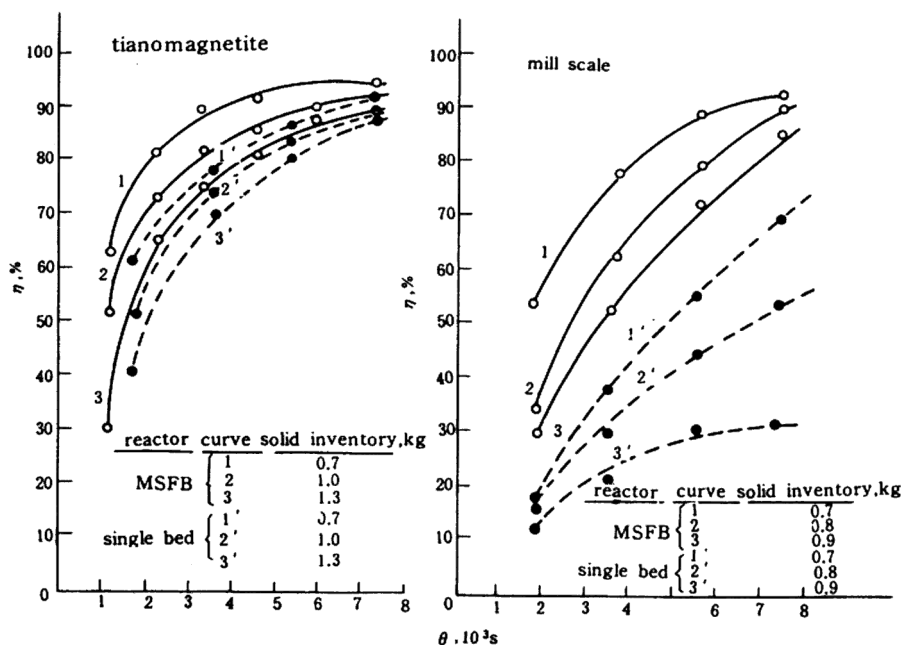


Figure 36. Comparison of rate of reduction of iron oxide with and without co-MSFB (Yan, Yao, Wang, Liu, and Kwauk, 1983).

7.0 FLUIDIZATION WITH NO NET FLUID FLOW

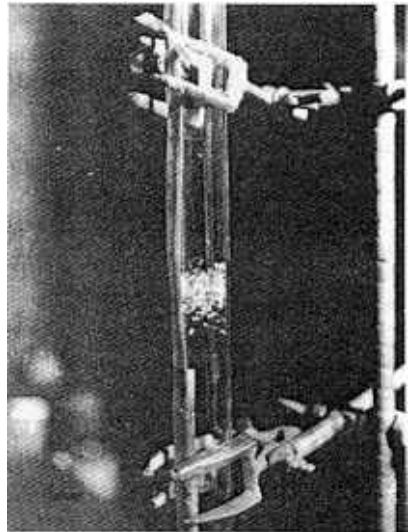
Certain reactions between solids go through intermediate steps in the gas phase. For instance, the segregating roasting of oxidic copper ores with addition of salt and coal, and the reduction of metal oxides with solid carbon. These reactions, known as pseudo-solid-solid reactions, may sometimes be carried out advantageously in the fluidized state. Solid fluidization would enhance transport of the gaseous intermediates, and would facilitate the addition and withdrawal of a circulating thermal carrier in the case of an endothermic reaction. Inasmuch as no gaseous reactant needs to be introduced, it would be logical to seek means of achieving fluidization, even on a periodic basis, with no net fluid flow.

7.1 Levitation of Discrete Particles

Levitation is a stable condition in which a particle responds to the oscillating fluid in such a way that the influence of finite buoyancy, or gravity, forces is completely neutralized so that the particle oscillates about a fixed position (Houghton, 1963, 1964, 1966, 1968; Krantz, Carley and Al-taweel, 1973; Tunstall and Houghton, 1968; Van Oeveren and Houghton, 1971). Figure 37 (Liu, 1983) shows the levitation of solid particles in air under oscillation caused by a sonic generator located at the bottom of the column.



(a)



(b)

Figure 37. Levitation of solid particles in vertically oscillating air. (a) Dilute suspension of solids. (b) Solids concentration at node. (Liu, Keling, 1983.)

A simplified analysis (Deng and Kwauk, 1990) of solids levitation led to the following ordinary differential equation involving three parameters, u_x , du_x/dx , and d^2u_x/d^2x , to be determined from experiments:

$$\begin{aligned} \frac{\rho}{6} d_p^3 \mathbf{r}_p \frac{du_p}{dt} = & -C_D \frac{\rho}{8} d_p^2 \mathbf{r}_f \left| u_p - u_f \right| (u_p - u_f) + \\ & + \frac{\rho}{6} d_p^3 \mathbf{r}_f \left\{ \left(\frac{du_f}{dt} - \frac{du_p}{dt} \right) u_x + \frac{du_p}{dr} + \right. \\ & + \left[(u_f - u_p) u_x + u_p \right] (u_f - u_p) \frac{du_x}{dx} - \\ & \left. - v(u_f - u_p) \frac{d^2 u_x}{dx^2} \right\} - \frac{\rho}{6} d_p^3 (\mathbf{r}_p - \mathbf{r}_f) g \end{aligned}$$

in which u_p is the velocity of the particles, u_f is the velocity of the piston creating oscillation, and u_x is the function of x in the variable-separated form of the fluid velocity $u(t, x)$.

Experiments for verifying the above equation were carried out in a U-shaped plexiglas tube, shown in Fig. 38a (Deng and Kwauk, 1990), one leg of which is filled with particles for oscillation tests and voids itself into a large-diameter tank at the top which both serves as a hydraulic seal for the system and also dissipates the kinetic energy of the oscillating fluid. Fluid oscillation was generated by a mechanical device, shown in Fig. 38b. Ion-exchange resin particles, 0.29 to 0.44 mm in diameter, were tested in water, and 0.44 mm glass beads in glycerol-water mixtures.

Figure 39 shows the visual appearance of resin particles in oscillating water at different frequencies. Figure 39a shows that at low frequency the particles merely jump up and then fall back to the supporting wire net. Figure 39b shows that as frequency increases, the particles may remain in the liquid for some time before falling down. Figure 39c shows that at some still higher frequency, the particles remain levitated, executing vertically oscillating motion. At even higher frequencies the particles will rise against gravity (not shown in Fig. 39).

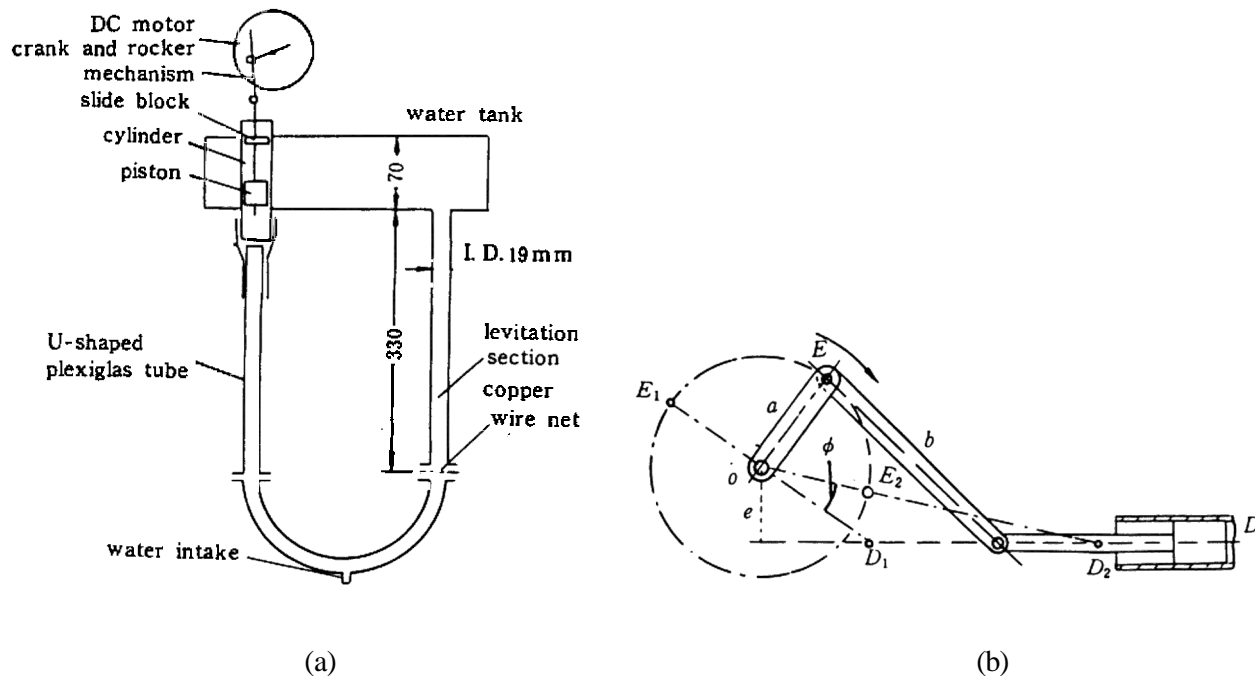


Figure 38. Liquid/solid levitation apparatus. (a) U-Shaped fluid oscillation tube. (b) Mechanical oscillation generator. (Deng and Kwauk, 1990.)

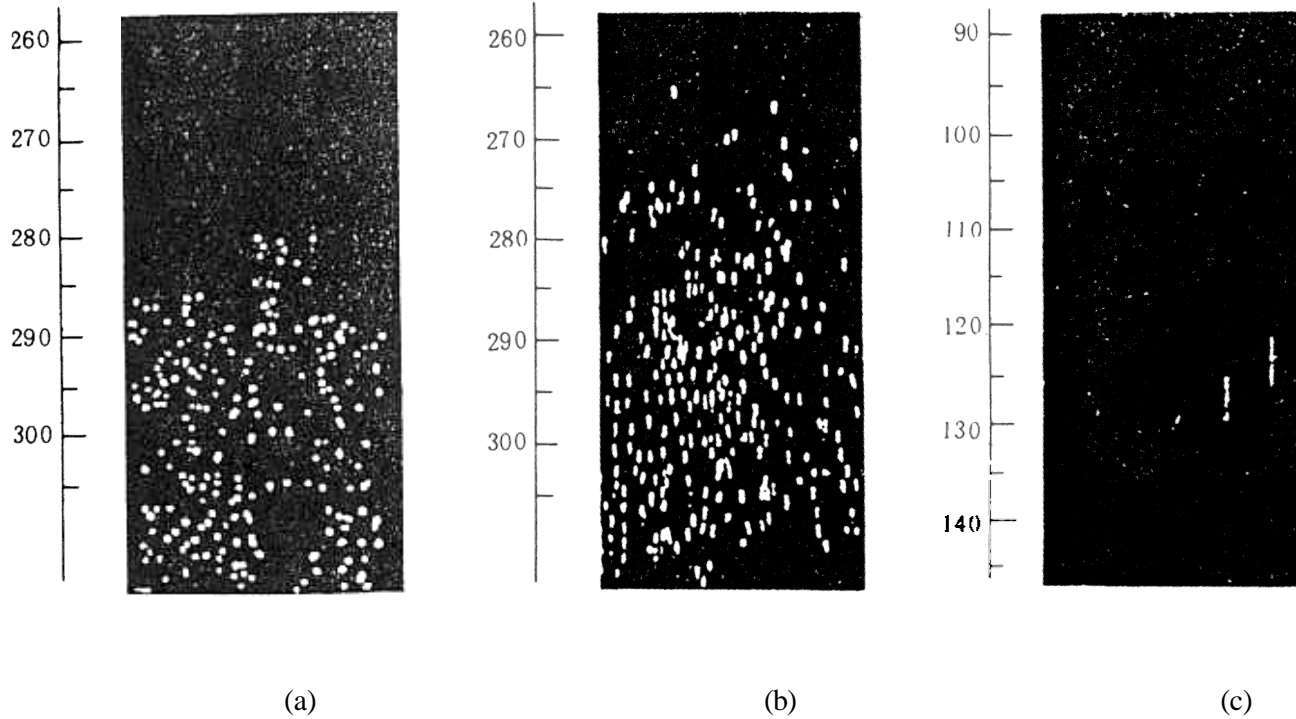


Figure 39. Ion-Exchange resin in vertically oscillating water (particle diameter 0.435 mm, amplitude 2 cm, asymmetric factor 1.2). (a) Frequency $f = 3.08$ Hz; (b) $f = 4.82$ Hz; (c) $f = 5.40$ Hz. (Deng, and Kwauk, 1990.)

The frequency of fluid oscillation at which levitation takes place is plotted in Fig. 40 against the corresponding amplitude A of oscillation, the asymmetry factor k_o or ratio of the duration of the downstroke to that of the upstroke, and the resin particle diameter d_p . From these experimental data, the three parameters of the equation were correlated to the particle diameter:

$$u_x = 11.1d_p + 0.536$$

$$\frac{du_x}{dx} = -39.5d_p + 2.20$$

$$\frac{d^2u_x}{dx^2} = -1.15 \times 10^6 d_p + 7.25 \times 10^4$$

Curves computed from the equation using these empirically correlated parameters are also shown in Fig. 40, indicating acceptable agreement.

Trajectories of a single resin particle computed from the equation are shown in Fig. 41, indicating that at $f = 4.5$ Hz the particle sinks, while at $f = 7.5$ Hz rising levitation takes place.

7.2 Semi-Fluidization through Oscillatory Flow

Both Fig. 37 and Fig. 39 show solid particles highly dispersed as a dilute phase in the oscillating fluid, either gas or liquid, without evidence of any bubbles. When a packed bed of solid particles was subjected to the action of an oscillating liquid, however, only the upstroke portion of the periodic fluid motion was capable of dispersing the solid particles against the action of gravity, while during downstroke they fell back onto the distributor plate.

The dynamics of such a mode of semi-fluidization is similar to that of jiggling in ore dressing, which is a common operation in coal or ore dressing, though little used in the design of chemical reactors. Thus, at least on a periodic basis, jiggling yields the same advantages as other modes of fluidization with no net fluid flow.

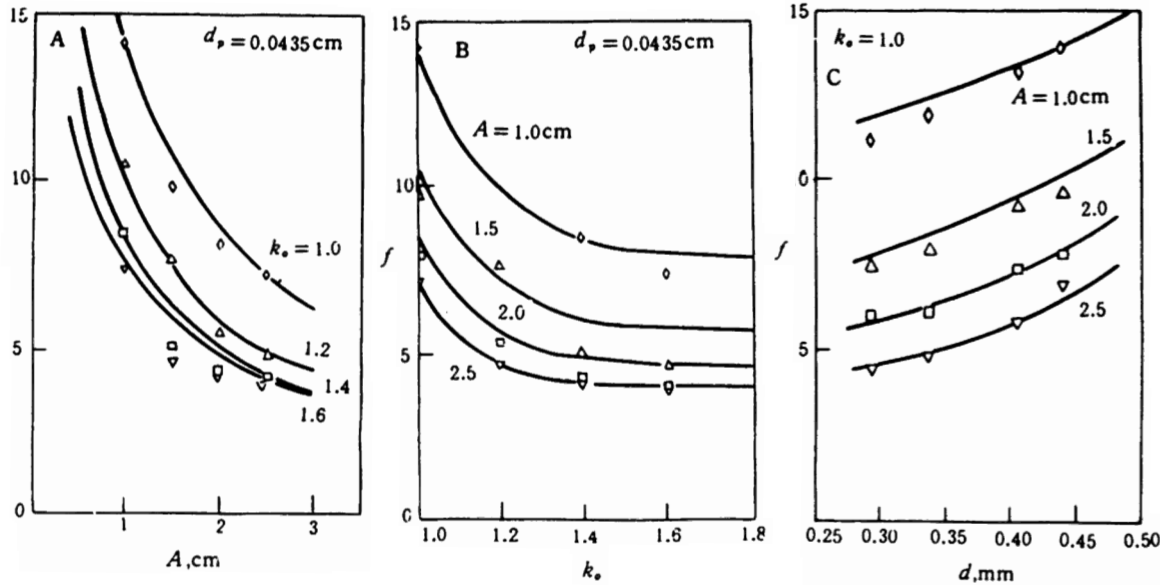


Figure 40. Comparison of computation from the equation on p. 548 with experimental data for resin-water system. (Deng, and Kwauk, 1990.)

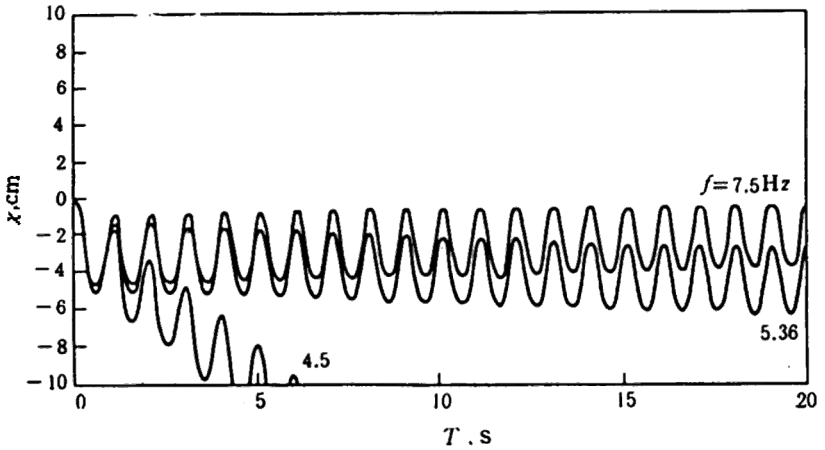
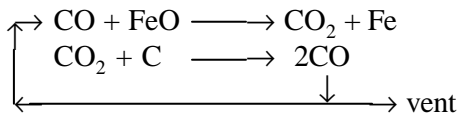


Figure 41. Trajectories of single resin particle in water computed from the equation on p. 548 (particle diameter 0.435 mm, amplitude 2 cm, asymmetric factor 1.2). (Deng, and Kwauk, 1990.)

7.3 Application to Pseudo Solid-Solid Reactions

The pseudo solid-solid reduction of oxidic iron ores with solid carbon is known to proceed through the gaseous intermediates, CO and CO₂, according to the following mechanism:



At low temperatures the overall rate is controlled by the chemical reaction $\text{CO}_2 + \text{C} \rightarrow 2\text{CO}$, but at sufficiently high temperatures the controlling steps would be taken over by mass transfer, which could be materially accelerated by oscillatory gas flow.

This pseudo solid-solid reduction of oxidic iron ores with solid carbon could be carried out in a conceptualized jiggred reducer shown in Fig. 42 (Kwauk, 1979, 1981, 1983). Ore and coke are fed as a mixture at a single

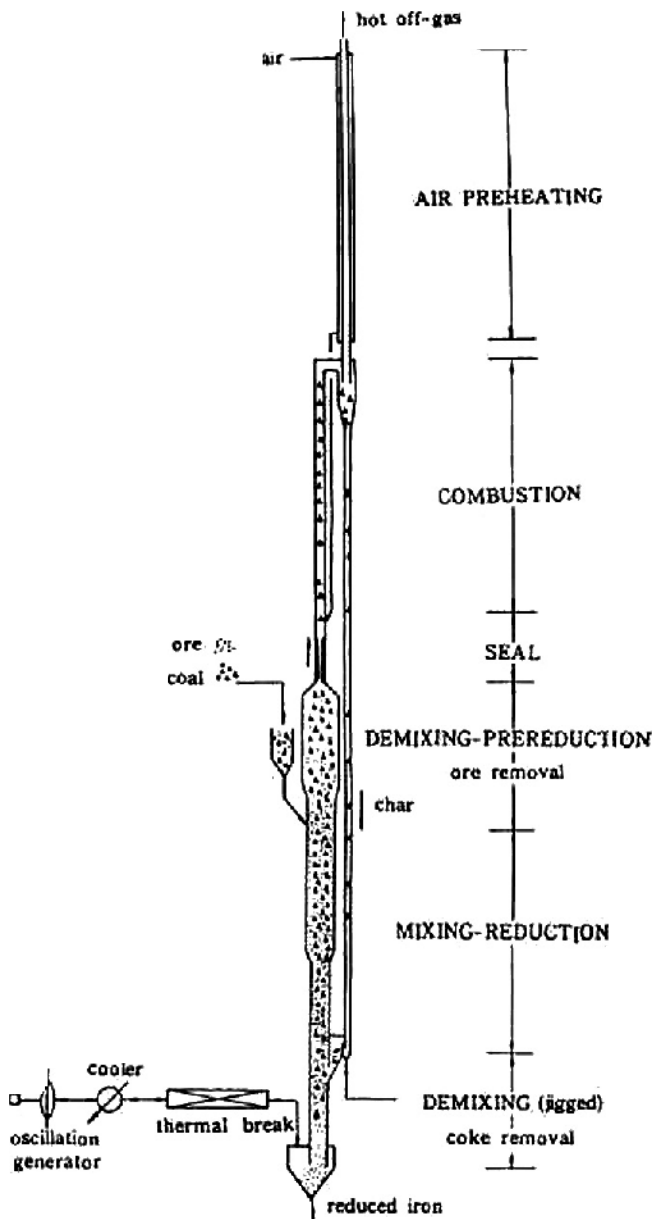


Figure 42. Conceptual design of a jiggered iron ore reducer (*Kwauk, 1979*).

point to the middle section of a three-section reducer. A considerable amount of CO is generated between reaction of C and FeO, which fluidizes the two top sections by continuous flow. Division into the two fluidized sections helps the establishment of a solids concentration gradient (dilute in the top section, and dense in the lower section) which tends to suppress longitudinal mixing. Only the lowest of the three-section reducer is semi-fluidized through jiggling, in which only the last traces of CO are evolved.

All the CO resulting from the pseudo solid-solid reaction is conducted, together with entrained char, from the top fluidized section through a constriction, in which the high-velocity gas flow prevents backflow, to a transport combustor, where the CO is burned to CO₂ with preheated air, along with as much of the char as is called for by heat balance to maintain the endothermic FeO-C reaction. The heated recycled char is separated from the off gas at the top of this transport combustor in a hot cyclone and is returned as a thermal carrier to the lower part of the lowest jiggled section, while the hot flue gas from the transport combustor is used to preheat the incoming air in a recuperator.

In the top fluidized section, where the first portion of FeO reduction, that is, prereduction, takes place, the lighter coke particles are elutriated from the heavier ore particles. The lower fluidized section is sized for adequate FeO-C mixing in order to maximize contacting of the reacting solids. Then, in the lowest section, where vestigial amounts of CO are evolved, solids are semi-fluidized through jiggling to effect an additional stage of coke upflow in order to denude the powdered metallic iron product of its accompanying char.

Jiggling is produced by a gas oscillation generator, which could be either mechanical or electromagnetic, separated from the bottom of the jiggled section first by a solids knockout hopper and then by a thermal break, which is essentially a packed-bed heat regenerator. To protect further the gas oscillation generator from hot gases, a cooler is interposed between it and the thermal break.

The process proposed in Fig. 42 uses powdered iron ore directly without prior treatment such as sintering or pelletization as called for in the case of the blast furnace, and powdered coke or coal without prior gasification. Jiggling through gas oscillation replaces expensive gas recycling which calls for first cooling and then reheating, often accompanied by unavoidable carbon deposition through the Bouduord reaction.

8.0 PARTICLES WHICH QUALIFY FOR BUBBLELESS OPERATION

Whether or not a solid powder qualifies for bubbleless gas/solid contacting depends greatly on its fluidizing characteristics, which may be determined in a bed collapsing apparatus which automatically tracks the subsiding bed surface of the collapsing bed by means of an optical-fiber probe (Qin and Liu, 1985). Modeling of the collapsing process (Tung and Kwauk, 1982; Yang, Tung and Kwauk, 1985; Tung, Yang, Xia, Zheng, Yang and Kwauk, 1989) resulted in a dimensionless number to quantify the fluidizing characteristics of powders. Certain binary and ternary solid mixtures have been shown to demonstrate synergistic actions in improving the fluidization characteristics of the component particles, implying the significance of particle size design.

8.1 Powder Characterization

Broadly speaking, for G/S systems, three modes of particle-fluid contacting may be recognized to take place simultaneously as shown in Fig. 43: bubbles containing sparsely disseminated particles, emulsion of densely suspended particles, and defluidized (transient as well as persistent) particles not fully suspended hydrodynamically by the flowing gas. For all intents and purposes, it is desirable to suppress bubbles and to prevent defluidization.

When the gas, which is fluidizing a powder exhibiting all these modes of contacting, is turned off abruptly, the fluidized bed will collapse and subside in three consecutive stages, as shown in Fig. 44 (Yang, Tung and Kwauk, 1985):

- (i) A rapid initial stage for bubble escape
- (ii) An intermediate stage of hindered sedimentation with constant velocity of the dense emulsion of mobile particles, and
- (iii) A final decelerating stage of solids consolidation for the incompletely suspended particles.

Thus, the random spatial distribution of the three modes of particle-fluid contacting is transformed into the ordered, temporal sequence of the three stages of the sedigraph.

Figure 45 shows the instrument used for automatic tracking of the surface of the collapsing bed, inclusive of a computer for data acquisition and on-line analysis. The fluidized bed, 5 cm in diameter and 120 cm high, is provided with a high pressure-drop gas distributor to insure uniform gas flow. Below the distributor is a specially designed knife valve operated by a solenoid for quick gas shutoff. An optical-fiber probe, consisting of two separate sets of projector and receiver fibers, respectively, for illumination and for reception of reflected light, is used for rapid tracking and recording of the subsiding bed surface.

Figure 46 shows a typical bed collapsing curve traced by the instrument described above.

The entire determination, from gas shutoff to printout from the computer, rarely exceeds 3 to 4 minutes for normal solids. And since all measurements are taken by the instrument, they are not subject to personal error of observation. The size of solids test sample is of the order of a kilogram or less.

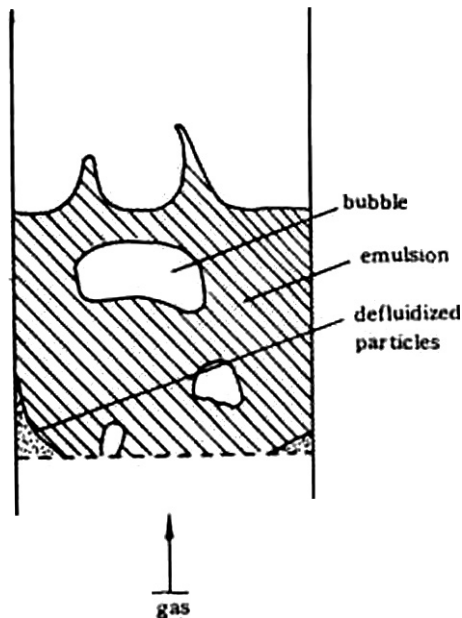


Figure 43. The three modes of particle-fluid contacting in G/S fluidization.

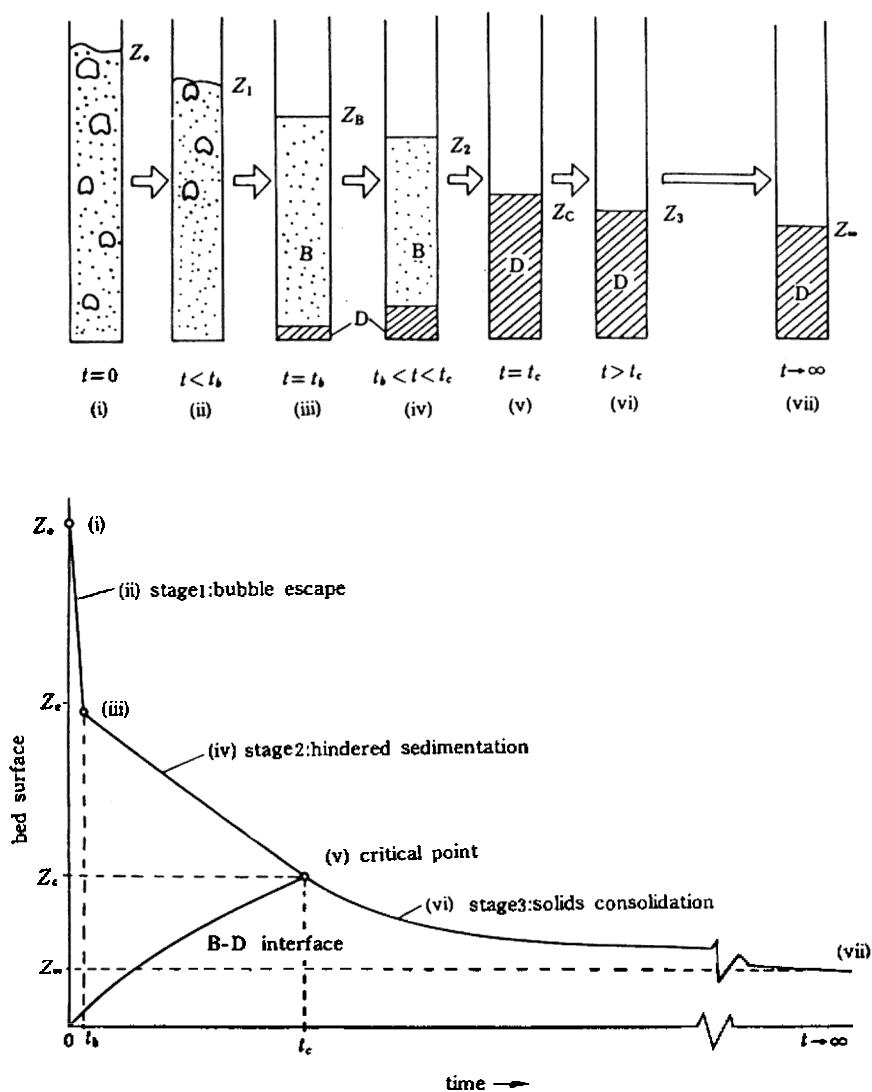


Figure 44. Modelling the three-stage bed collapsing process. (Yang, Tung, and Kwauk, 1985.)

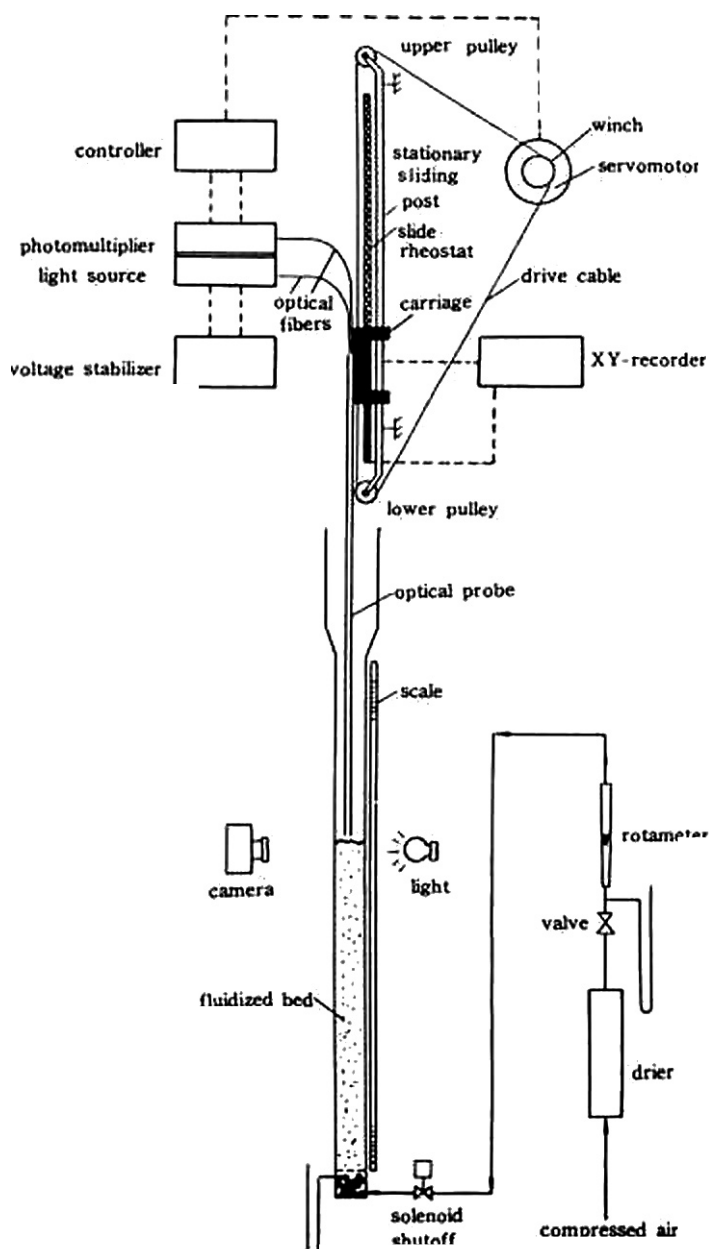


Figure 45. Instrument for automatic surface tracking and data processing. (Yang, Tung, and Kwauk, 1985.)

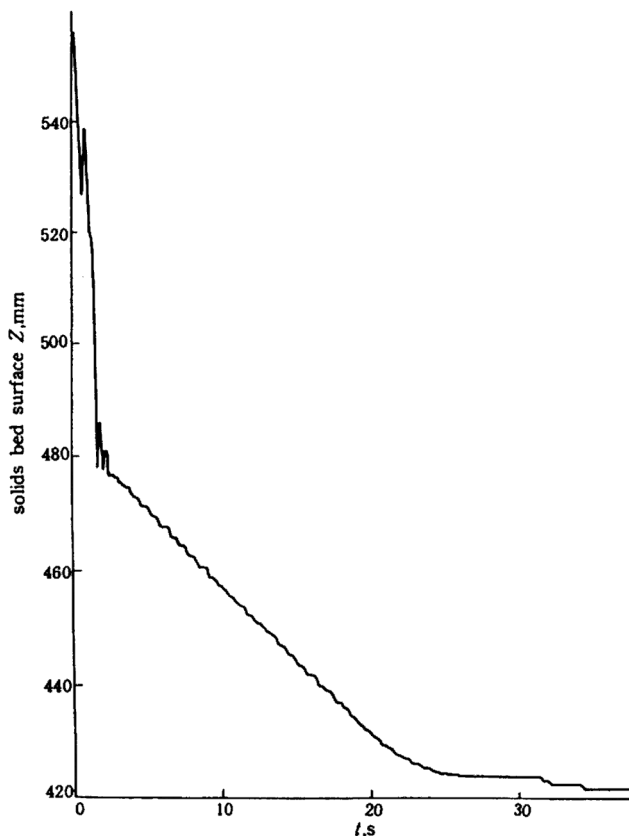


Figure 46. Typical bed collapse curve traced by optical-fiber probe tracking instrument (solids:alumina A66, 140–280 microns). (*Yang, Tung, and Kwauk, 1985.*)

Not all powders exhibit all the three stages described above, as shown in Fig. 47. Depending on the presence or absence of the above stages, a three-digit qualitative designation has been formulated:

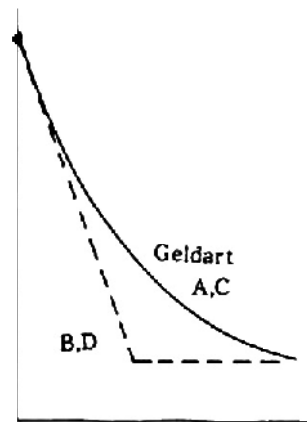
- 100 Bubble-escape stage only
- 123 Three stages: bubble escape, hindered sedimentation and solids consolidation
- 020 Hindered sedimentation only
- 023 Hindered sedimentation plus solids consolidation

SYSTEM

FLUIDIZATION
PARTICLES

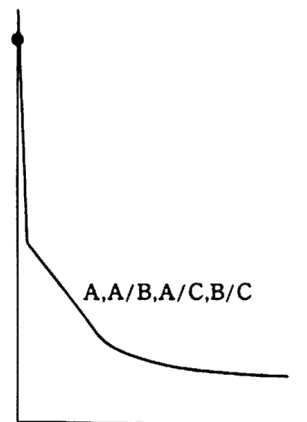
L/S

particulate
any



G/S

particulate/
aggregative
fine



aggregative
coarse

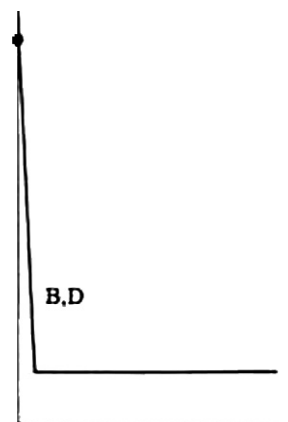


Figure 47. Essential types of bed collapsing curves.

562 *Fluidization, Solids Handling, and Processing*

Mathematical modeling of the three-stage bed collapsing process led to a more quantitative characterization of powders, in the form of a dimensionless number called the *dimensionless subsidence time*:

$$\Theta = \frac{d_p g}{u_i u_2} \left(\frac{Z_e - Z_c}{Z_\infty} \right)$$

To test the viability of Θ in quantifying fluidizing characteristics, it is plotted against the ratio of incipient bubbling velocity to incipient fluidization velocity, u_{mb}/u_{mf} , the latter being calculated after Geldart (1972). Figure 48 shows that a linear relation exists between $\ln(u_{mb}/u_{mf})$ and $\Theta^{1/4}$ as represented by the following empirical relation

$$\ln(u_{mb}/u_{mf}) = 4 \Theta^{1/4}$$

The straight line starts from $\Theta = 0$ and $u_{mb}/u_{mf} = 1$, and extends without limit towards the upper right-hand corner. The value of $u_{mb}/u_{mf} = 1$ obviously signifies bubbling. The corresponding value of Θ is zero, for which stages 1 and 2 of the bed collapsing process take place almost instantaneously. As the fluidizing characteristics improve, the value of u_{mb}/u_{mf} becomes progressively greater than unity, signifying particulate expansion. The corresponding value of Θ also increases, showing a slower bed collapsing process. As the curve tends toward even larger values of Θ , the characteristics of particulate fluidization becomes more predominant.

8.2 Improving Fluidization by Particle Size Adjustment

Catalyst powders with carefully specified particle size distribution have been known to possess good fluidization characteristics. Generally, addition of fine particles to coarse particles tends to improve the latter's fluidization characteristics. Experiments were thus conducted on binary particle mixtures, each consisting of a fairly close particle size distribution.

Figure 49 shows a set of bed collapsing curves for a Geldart Group A-A (for Geldart's classification of solid particles, see Geldart, 1972, 1973) binary solids mixture, two closely sized alumina powders, of average particle diameter 104 and 66 microns, respectively. The curve on the extreme left with 0% fines represents the pure coarse component, which is

barely Group A in fluidizing characteristics, as can be seen from its very brief stage 2. The curve on the extreme right, representing the 100% fine component, demonstrates pronounced Group A, or “123,” fluidizing characteristics with a long stage 2. Curves with intermediate compositions are shown in their ordered locations between the purely coarse and purely fine components.

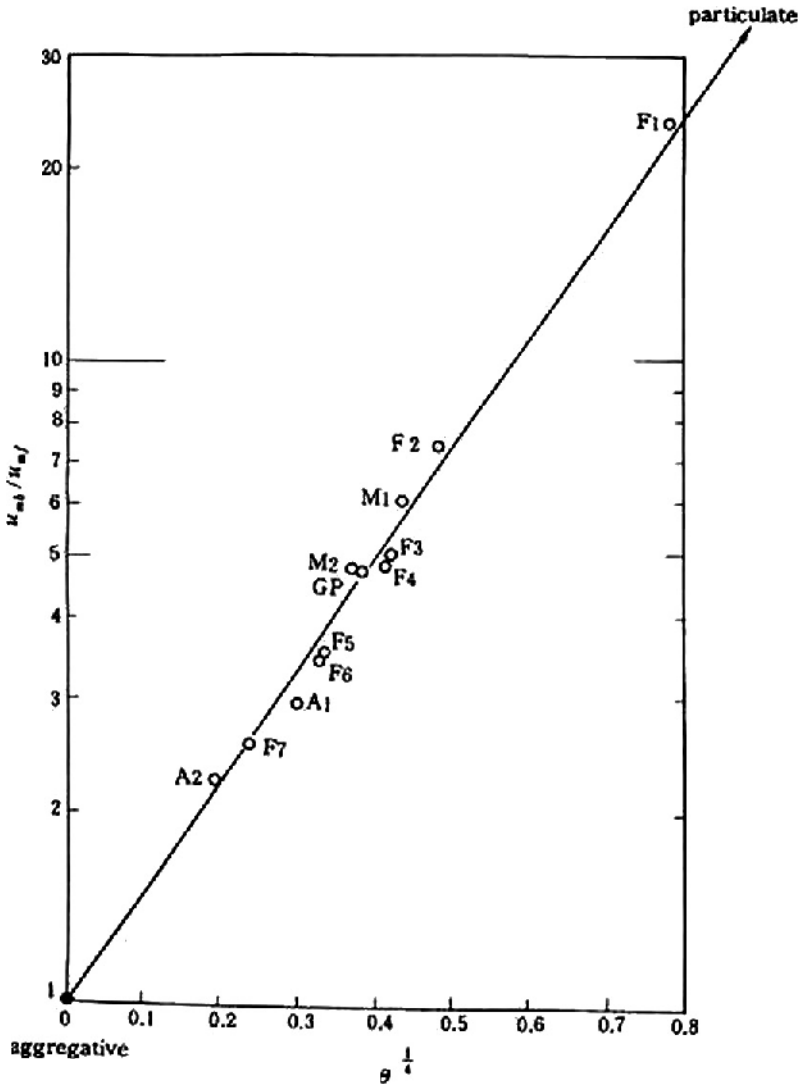


Figure 48. Plot: u_{mb}/u_{mf} versus $\Theta^{1/4}$. (Yang, Tung, and Kwauk, 1985.)

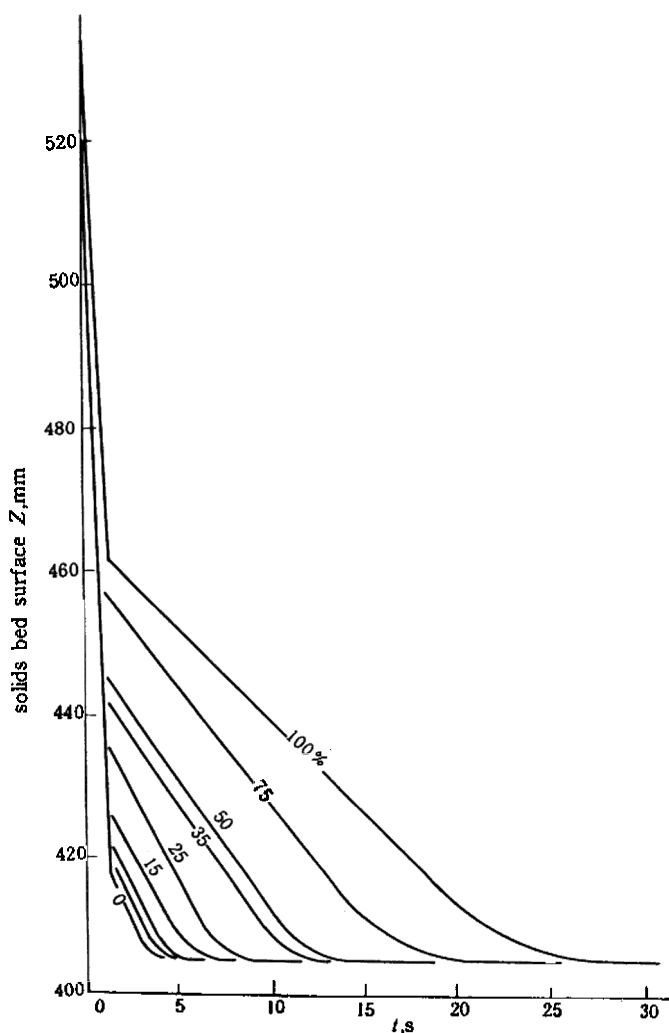


Figure 49. Bed collapse curves for a group A-A Solid Pair: Solids A104/A66 (Yang, Tung, and Kwauk, 1985).

Figure 50 illustrates the fluidizing characteristics of a set of Group B-A mixtures of relatively coarse (212 microns) polyethylene spheres mixed with a relatively fine (27 microns) FCC catalyst. As the fine FCC catalyst is added, there is a progressive predominance of the Group A fluidizing characteristics of the finer component.

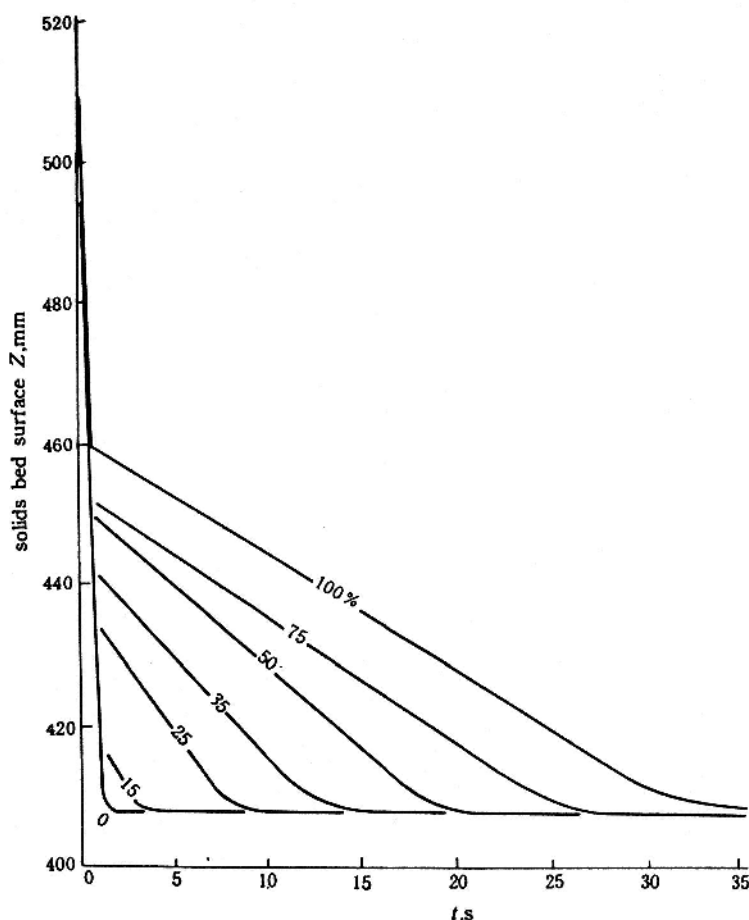


Figure 50. Bed collapse curves for a Group B-A solid pair: solids PE201/F27. (Yang, Tung, and Kwauk, 1985.)

Figure 51 shows the effect of adding talc (7 microns), Group C, to a coarse sea sand (165 microns), Group B. The beneficial effect of the fines on the fluidizing characteristics is shown to increase to a fines composition of around 25%, and then it diminishes with further fines addition.

Figure 52 plots the dimensionless subsidence time Θ for the six sets of Group A-A and Group B-A binary mixtures for different fractions of fines, x_f , showing that the improvement of fluidizing characteristics by addition of fine particles increases monotonically with increasing percentage of the fines.

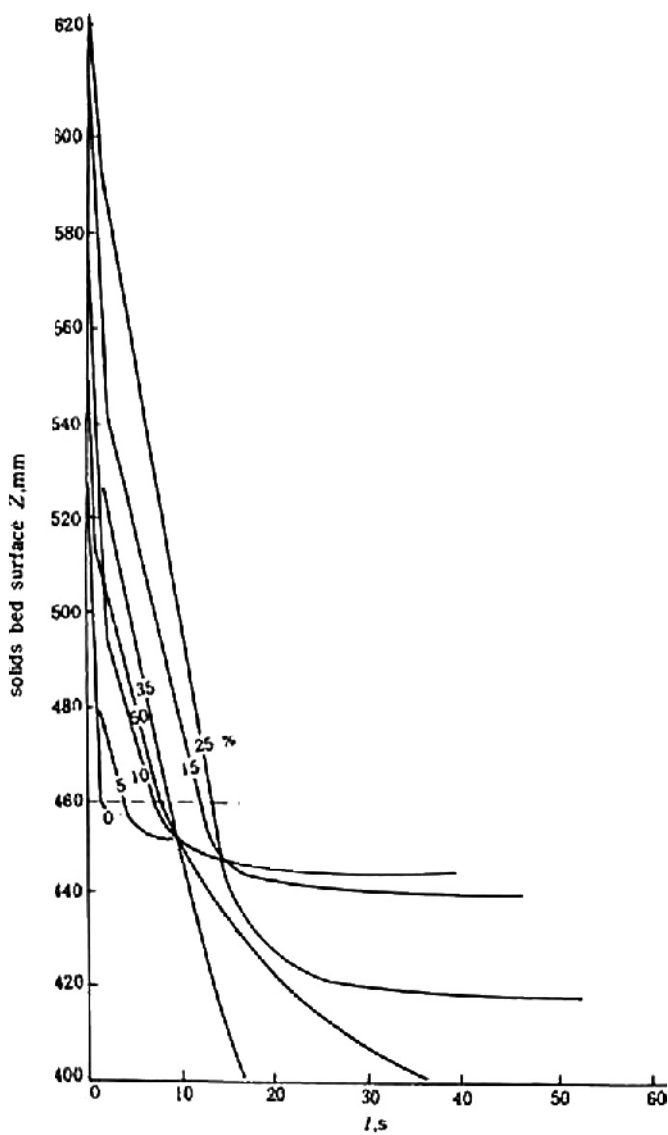


Figure 51. Bed collapse curves for a Group A-C solid pair: solids SA165/T7. (Yang, Tung, and Kwauk, 1985.)

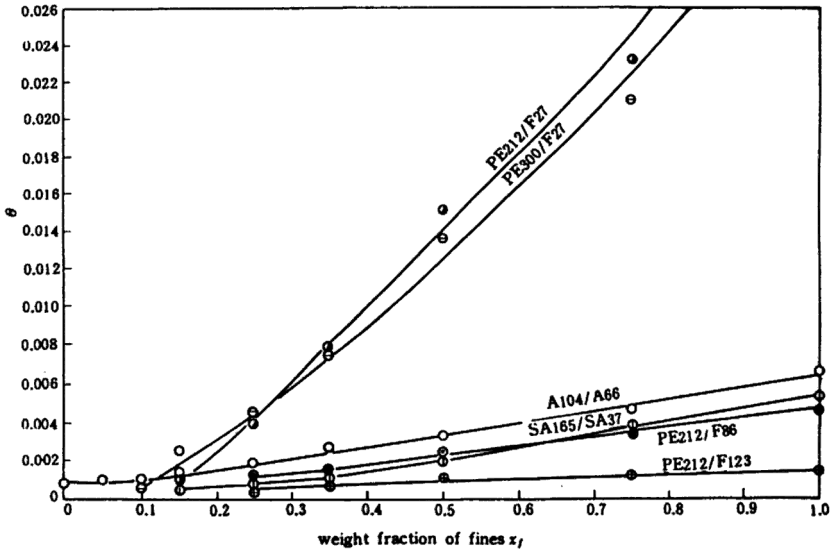


Figure 52. Improving fluidizing characteristics by fines addition, solid groups: A-A and B-A. (Yang, Tung, and Kwauk, 1985.)

Figure 53 is a similar plot, but for the ten sets of Group B-C mixtures. Most curves show that the value of Θ for Group B-C binaries give maxima at certain intermediate compositions. The presence of these maxima suggests that not only fine particles belonging to Group C may improve the fluidizing characteristics of such coarse solids as Group B, but the coarse particles may also improve the fluidizing characteristics of the fine particles, which are known to possess the notorious tendency towards channeling before fluidization sets in.

This synergism of Group B-C mixtures testifies to the significance of particle size selection and particle size distribution design, in order to tailor a solid particulate material to certain desired fluidizing characteristics.

A mathematical model has been proposed to account for the mutual synergistic action of either particle component on the other in increasing the value of the dimensionless time Θ as shown in Fig. 53, in terms of the mass fraction x_2 of fines, and two empirical parameters n_1 and n_2 :

$$\Theta = \Theta_1 (1 - x_2) (1 + x_2^{n_1}) + \Theta_2 x_2 [1 + (1 - x_2)^{n_2}]$$

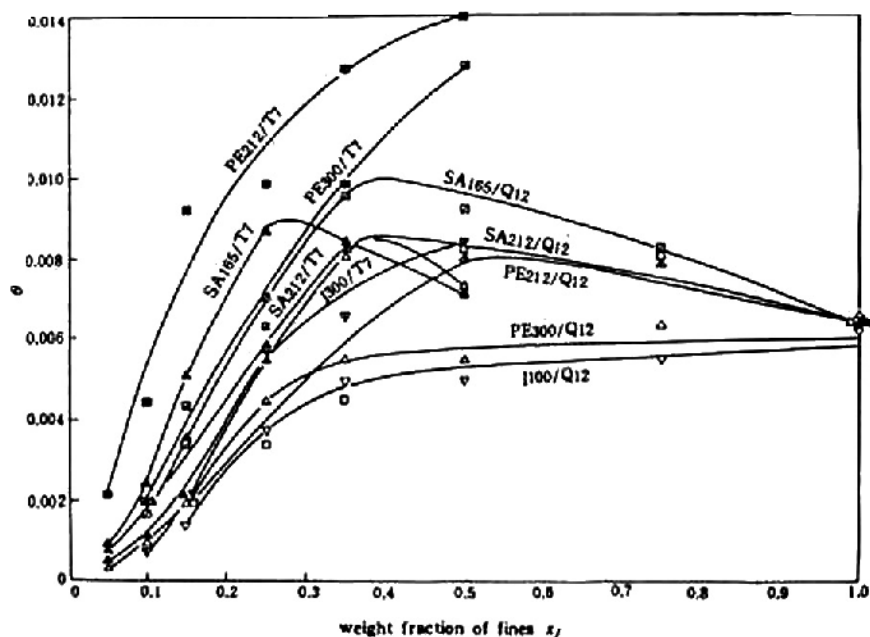


Figure 53. Improving fluidizing characteristics by fines addition, solid group: B-C. (Yang, Tung, and Kwauk, 1985.)

Mutual synergism of binary mixtures containing fine particles can be quantified in terms of the departure of the Θ - x_2 curve from a linear tie line, which signifies absence of synergism, joining Θ_1 and Θ_2 for the respective components, as shown in Fig. 54. A convenient measure of this departure is the shaded area lying between the Θ - x_2 -curve and the linear tie line. This can be derived analytically in terms of what will be called the *Synergism number* Sy , normalized with respect to $\Theta_1 + \Theta_2$ of both the coarse and the fine particles:

$$\begin{aligned}
 Sy &= \frac{1}{\Theta_1 + \Theta_2} \left[\int_0^1 \Theta dx - \frac{1}{2} (\Theta_1 + \Theta_2) \right] \\
 &= \frac{1}{(n_1 + 1)(n_1 + 2)} + \frac{\Theta_2 / \Theta_1}{(n_2 + 1)(n_2 + 2)}
 \end{aligned}$$

The larger is the value of S_y , the stronger is the mutual synergistic interaction between the coarse and fine particles. Also, an effective fine particle additive to improve the fluidizing characteristics of coarse particles calls for a large value of Θ_m produced with minimal amount of the fine material, that is, a small value of x_2 .

Such modeling has been computerized (Qian and Kwauk, 1986) for on-line data acquisition and analysis for graphing $\Theta - x_f$ curves directly from the automatic bed-collapsing instrument shown in Fig. 45.

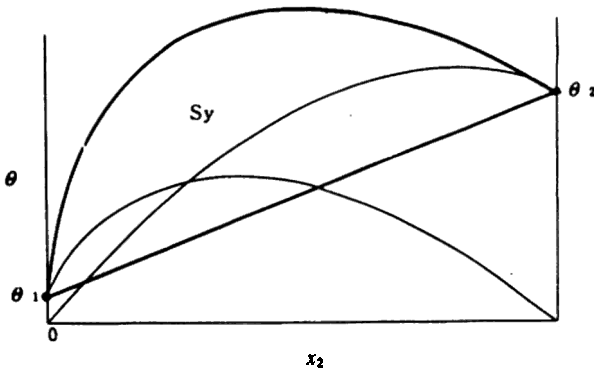


Figure 54. Measure of synergism for binary particle mixtures. (Kwauk, 1984, 1986.)

9.0 WHY BUBBLING AND NOT PARTICULATE FLUIDIZATION

A significant objective of bubbleless gas/solid contacting is to make the aggregative G/S system approach the particulate L/S system for which solid-fluid contacting is far better. Ever since the adoption of fluidization, however, there has been rather inadequate explanation of the vast difference between the bubbling G/S system and the particulate L/S system. The proposition of the so-called “energy-minimized multiscale model” generalizes all particle-fluid systems (Li, Tung and Kwauk, 1988; Li and Kwauk, 1994).

9.1 The Energy-Minimized Multiscale (EMMS) Model

With respect to the highly disparate nature of G/S and L/S fluidization, even at an early stage, the aggregative tendency of L/S fluidization was already discovered when large and/or heavy solid particles were used, and, moreover, clustering of these particles was also reported (Wilhelm and Kwauk, 1948). The particulate phenomenon present in certain G/S systems was noted, however, much later in connection with certain Geldart A-type solids, e.g., the graded, spheroidal FCC catalyst. Aggregative tendency of the normally particulate L/S fluidization on the one hand, and particulate tendency of the normally aggregative G/S fluidization on the other, led to the concept of interpolating these opposite tendencies toward an intermediate regime of transition.

Physically the EMMS model consists of a dense phase of clusters dispersed in a dilute phase composed of more or less discrete suspended particles, as shown in Fig. 55 (Li, Tung and Kwauk, 1988). The total fluid flow U_g to the system is divided into two streams, one through the dense-phase clusters U_c and one through the surrounding dilute phase U_f . Clusters are suspended by the fluid flowing inside them as well as outside them, while the discrete particles in the dilute phase are being entrained by their surrounding fluid. The dense clusters occupy a volume fraction f of the bed volume, the remaining $(1 - f)$ fraction belonging to the dilute phase. Figure 55 also tabulates the symbols for velocity U , for voidage ϵ and for drag coefficient C_D referring to the dense and the dilute phases.

There are thus three scales of interaction between the fluid and the particles:

- a. Microscale of particle size—drag on particle for both the dense and dilute phases
- b. Mesoscale of cluster size—interaction between dilute-phase fluid and clusters
- c. Macroscale for the overall two-phase flow system, involving its interaction with its boundaries, such as walls and internals.

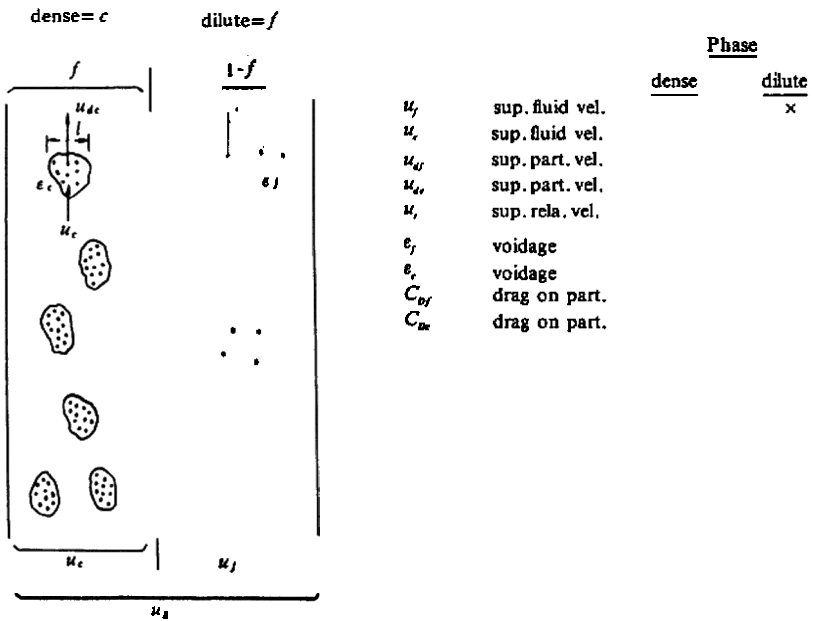


Figure 55. Physical model for multiscale modelling of particle-fluid system.

According to the above physical model, the following equations have been derived:

- (i) Force balance for clusters in unit bed volume
- (ii) Equal pressure drop. As shown in Fig. 55, the dilute-phase fluid flow has to support its discrete particles as well as, in part, the clusters in suspension, to yield a pressure drop equal to that of the parallel dense-phase fluid flow
- (iii) Particle suspension for dilute phase
- (iv) Continuity for fluid
- (v) Continuity for particles
- (vi) Cluster diameter

The above six equations for continuity and force balance do not, however, afford a complete description of a heterogeneous particle-fluid system in which a dense phase and a dilute phase coexist. An additional constraint needs to be identified to account for the stability of the system.

This constraint is to be provided through the concept of minimal energy. According to this concept, particles in a vertical flow system tend toward certain dynamic array which results in minimal energy.

The total energy associated with a flowing particle-fluid system is thus considered to consist of the sum of two portions, one used in suspending and transporting the particles, and one consumed in energy dissipated in particle collision and circulation. Alternately, in terms of the power per unit weight of solids, the total power N is composed of the suspension and transporting portion N_{ST} and the energy dissipation portion N_{ED} . The former can be split into that for particles suspension N_S and transport N_T , and in accordance with the multiscale model, also into portions for the dense cluster phase, the surrounding dilute phase and interaction between the two, that is

$$N \left\{ \begin{array}{l} N_{ST}=N_S+N_T \\ N_{ED} \end{array} \right. \left\{ \begin{array}{l} N_{dense} \\ N_{dilute} \\ N_{inter} \end{array} \right.$$

Consequently, modeling of a two-phase flow system is subject to both the constraints of the hydrodynamic equations and the constraint of minimizing N . Such modeling is a nonlinear optimization problem. Numerical solution on a computer of this mathematical system yields the eight parameters:

$$\mathbf{e}_p \ \mathbf{e}_c, f, U_p \ U_c \ l, U_{dp} \ U_{dc}$$

plus the various constituent power terms.

9.2 Reconciling L/S and G/S Systems

Figure 56 compares the computed results for the FCC/air system against those for the glass/water system, to illustrate the disparate behaviors of G/S and L/S fluidization.

The first three insets on the left-hand side show the change of voidages, e_p , e_c and e , cluster phase fraction f , and slip velocity U_s , for the FCC/air system. In the corresponding insets for the L/S system, however, the three voidages e_p , e_c and e are identical, and the cluster phase fraction f is zero, indicating the absence of clusters throughout the velocity range of U_g , that is, fluidization is homogeneous. Also, the slip velocity U_s between solid particles and the surrounding liquid is always less than the terminal velocity U_t of the particles, which remains the asymptotic value for the increasing slip velocity U_s as the entering liquid velocity U_g increases.

The lowest two insets of Fig. 56 compares the power for suspending and transporting the solid particles N_{ST} for the G/S and L/S systems. For the FCC/air system, N_{ST} is always less than the total energy N , until it jumps to the latter value at the point of sudden change, while for glass/water, N_{ST} is always the same as N in view of its homogeneous nature.

Figure 57 shows the gradual transition of the homogeneous glass/water fluidization to the highly heterogeneous or aggregative glass/air fluidization, as the particle/fluid density ratio $\mathbf{r}_p/\mathbf{r}_f$ increases from water through ethyl ether, and carbon dioxide under different stages of decreasing pressure from its critical condition, to atmospheric air. The appearance and gradual growth of the two-phase structure is evident in the order of the fluids listed. For instance, the curves in the top left inset show that at $\mathbf{r}_p/\mathbf{r}_f = 2.55$ for glass/water, $f = 0$ throughout the range of gas velocity U_g , indicating a homogeneous particle-fluid system. When the ratio $\mathbf{r}_p/\mathbf{r}_f$ has increased to 3.19 for glass/ethylether, however, the two-phase structure appears for gas velocities U_g up to 0.4 m/s. This velocity range broadens through carbon dioxide under decreasing pressures from its critical point, until at $\mathbf{r}_p/\mathbf{r}_f = 2,162$ for glass/air, this two-phase structure has extended beyond $U_g = 2$ m/s.

While Fig. 56 demonstrates, from modeling, the disparate nature between G/S and L/S fluidization, Fig. 57 shows continuity in particle-fluid behavior through properly selected intermediate systems, thus reconciling through theory the phenomenological discrimination between aggregative and particulate fluidization.

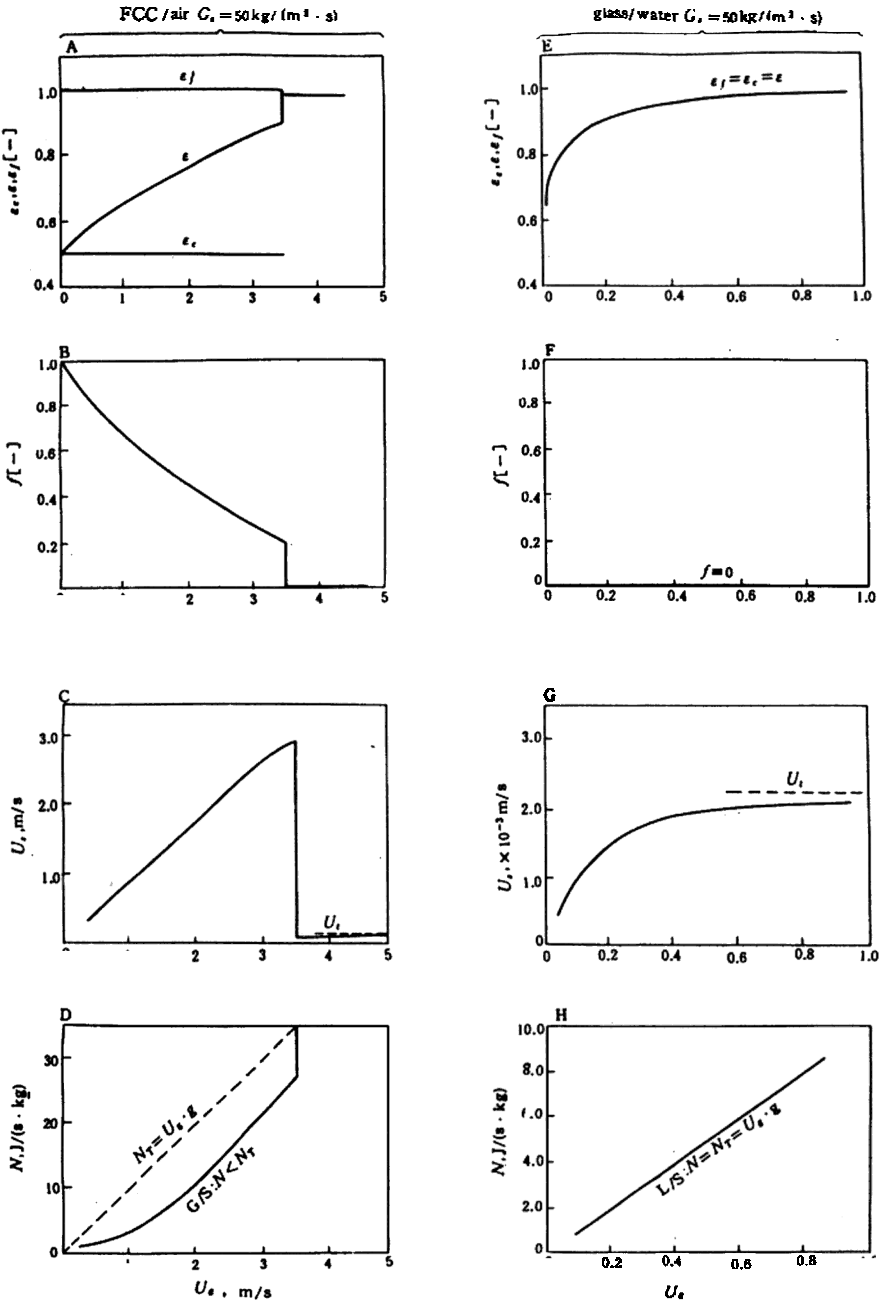


Figure 56. Comparison between G/S and L/S Systems. (Li, 1987.)

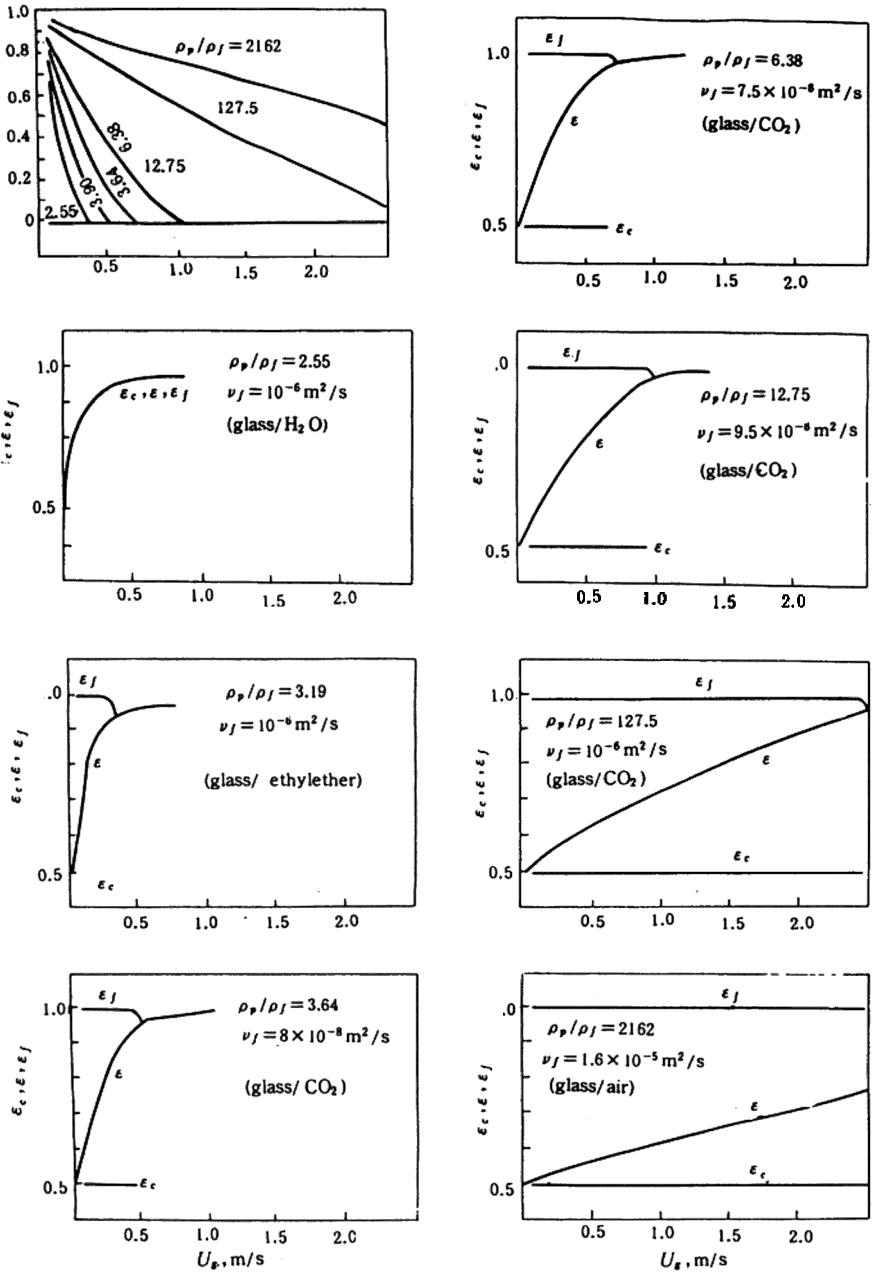


Figure 57. Computation results showing gradual transition from particulate fluidization to aggregative fluidization. (Li, 1987.)

10.0 EPILOGUE

Bubbling is the usual phenomenon in most accepted processes of fluidization. It has been demonstrated that species of fluidization with better G/S contacting are available by avoidance of bubbling. This chapter has offered certain tools for discriminating the homogeneous L/S fluidization on the one hand from the bubbling G/S fluidization on the other, in the form of the EMMS model, but this is by no means the only possible method. It has also revealed the significance of particle size choice or design in order to improve the fluidizing characteristics of a given species of fluidization through using the bed collapsing apparatus, but this, too, is by no means the only possible technique.

The message of significance is how to “particulate” a G/S system which is otherwise aggregative.

NOTATIONS

A	Area; cross-sectional area, cm^2
A_x	Frontal area of particle, cm^2
Ar	$= d_p^3 \mathbf{r}_f g \Delta p / \mu^2$, Archimedes number, dimensionless
A_t	Cross-sectional area based on particle terminal velocity, cm^2
A'	$= A/A_p$, reduced area, dimensionless
Bi	$= h d_p / k_s$, Biot number, dimensionless
C_p	Heat capacity of gas, $\text{cal/mol} \cdot ^\circ\text{C}$
C_s	Heat capacity of solids, $\text{cal/gm} \cdot ^\circ\text{C}$
d_p	Particle diameter, cm
D	Diffusivity, cm^2/sec
E	$= Nu Pr^{-1/3}/Ar$ or $Sh Sc^{-1/3}/Ar$, effectiveness factor, dimensionless
f	Friction factor, dimensionless
g	$= 980 \text{ cm/sec}^2$, acceleration of gravity
G	Mass flow rate of gas, $\text{mol/cm}^2 \cdot \text{sec}$
h	Heat transfer coefficient between particle and fluid, $\text{cal/sec} \cdot \text{cm}^2 \cdot ^\circ\text{C}$
H	Nonuniformity index, dimensionless
j	$= Nu Pr^{-1/3}/Re$ or $Sh Sc^{-1/3}/Re$, j -factor, dimensionless
k_g	Thermal conductivity of gas, $\text{cal/cm} \cdot \text{sec} \cdot ^\circ\text{C}$
k_s	Thermal conductivity of solid, $\text{cal/cm} \cdot \text{sec} \cdot ^\circ\text{C}$
L	Mass velocity of liquid, $\text{gm/cm}^2 \cdot \text{sec}$

m	Fixed bed pressure drop exponent, dimensionless
n	Fluidized bed expansion exponent, dimensionless
N	$= (L/r_f A)(S/r_s A)$, liquid-solids velocity ratio, dimensionless
N_H	Number of heat-transfer stages, dimensionless
Nu	$= hd_p/k_g$, Nusselt number, dimensionless
ΔP	Pressure drop, gm-wt/cm ²
Pr	$= C_p \mu / k_g$, Prandtl number, dimensionless
Re	$= d_p u r_f / \mu$, Reynolds number, dimensionless
S	Mass velocity of solids, gm/cm ² ·sec
Sc	$= \mu / r_f D_p$, Schmidt number, dimensionless
Sh	$= h_D d_p / D_f$, Sherwood number, dimensionless
Sy	Synergism number, dimensionless
T	Temperature, °C
u	Velocity, cm/sec
u_o	Superficial fluid velocity, cm/sec
u_d	Superficial solids velocity, cm/sec
u_{mb}	Superficial fluid velocity at incipient bubbling, cm/sec
$u_p u_{mf}$	Superficial fluid velocity at incipient fluidization, cm/sec
u_p	Actual velocity of particle, cm/sec
u_s	Relative velocity between particle and fluid, cm/sec
u_t	Terminal particle velocity, cm/sec
u'	$= u/u_p$, reduced velocity, dimensionless
V'	$= A/Z'$, reduced volume, dimensionless
w	Particle population density, gm/cm ²
x_f	Weight fraction of fines in binary particle mixture, dimensionless
z	Distance, cm
z_1	Location of point of inflection for fast fluidization, cm
Z	Height of fluidized bed, cm
Z_o	Dimensionless distance in accelerative motion of particle; characteristic length for fast fluidization voidage profile, cm
Z_t	Height based on particle terminal velocity, cm
Z_l	Dimensionless distance in heat transfer
z'	$= z/Z$, reduced distance, dimensionless
t	$= GC_p/SC_s$, flowing heat capacity ratio, dimensionless
e	Voidage or void fraction, dimensionless
e_{mf}	Voidage at incipient fluidization, dimensionless

e_o	Voidage of fixed bed, dimensionless
v	Fractional heat recovery, dimensionless
q	Time, sec
Θ	Dimensionless time in particle-fluid heat transfer; dimensionless subsidence time in bed collapsing test
μ	Viscosity, gm/cm-sec
r_s	Density of solid, gm/cm ³
r_f	Density of fluid, gm/cm ³
Δr	$= r_s - r_f$ effective density
Φ_o	Dimensionless pressure drop in accelerative particle motion

REFERENCES

- Chen, B., and Kwauk, M., Generalized Fluidization of Non-Ideal Systems, *Proc. First Intern. Conf. Circulating Fluidized Bed*, 127-132, Halifax, Canada (1985)
- Coulson, J. M., and Richardson, J. F., "Sedimentation," Vol. 2, *Chemical Engineering*, McGraw-Hill, 2nd Ed. (1968); 3rd Ed. (1978)
- Deng, Y., and Kwauk, M., "Levitation of Discrete Particles in Oscillating Liquids," *Chem. Eng. Sci.*, 45(2):483-490 (1990)
- Geldart, D., "The Effect of Particle Size and Size Distribution on the Behavior of Gas-Fluidized Beds," *Powder Technol.*, 6:201-205 (1972)
- Geldart, D., "Types of Fluidization," *Powder Technol.*, 7:285-290 (1973)
- Houghton, G., "The Behavior of Particles in a Sinusoidal Velocity Field," *Proc. Roy. Soc.*, A272:33-43 (1963)
- Houghton, G., "Digital Computer Simulation of Fluttering Lift in the Desert Locust," *Nature* 201, pp. 568-570; "Effect of Variation in Lift Coefficient, Phase Angle and Waveform on Fluttering Lift in the Desert Locust," *Nature* 202, pp. 870-872; "Simulation of Fluttering Lift in a Bird, Locust, Moth, Fly and Bee," *Nature* 202, pp. 1183-1185; "Fluttering Flight Mechanisms in Insects and Birds," *Nature* 204, pp. 447-449; "Generalized Hovering-Flight Correlation for Insects," *Nature* 204, pp. 666-668 (1964)
- Houghton, G., "Particle Trajectories and Terminal Velocities in Vertically Oscillating Fluids," *Can. J. Chem. Eng.*, 44:90-95 (1966)
- Houghton, G., "Velocity Retardation of Particles in Oscillating Fluids," *Chem. Eng. Sci.*, 23:287-288 (1968)
- Kramers, H., "Heat Transfer from Spheres to Flowing Media," *Physica*, 12:61 (1946)

- Krantz, W. B., Carley, J. F., and Al-taweel, A. M., "Levitation of Solid Spheres in Pulsating Liquids," *Ind. Eng. Chem. Fund.*, 12:391-396 (1973)
- Kwauk, M., "Fluidized Calcination of Aluminum Ore for Pre-Desilication," (unpubl.), *Inst. Chem. Metall.*, 1964-11-6 (1964c)
- Kwauk, M., and Tai, D. -W., "Transport Processes in Dilute-Phase Fluidization as Applied to Chemical Metallurgy," (I). Transport Coefficient and System Pressure Drop as Criteria for Selecting Dilute-Phase Operations; (II). Application of Dilute-Phase Technique to Heat Transfer, (in Chinese, with Eng. abs.), *Acta Metallurgica Sinica*, 7:264-280; 391-408 (1964)
- Kwauk, M., "Particulate Fluidization in Chemical Metallurgy," *Scientia Sinica*, 16:407 (1973)
- Kwauk, M., "Fluidized Leaching and Washing," (in Chinese), *Science Press*, Beijing (1979a)
- Kwauk, M., "Fluidized Roasting of Oxidic Chinese Iron Ores," *Scientia Sinica*, 22:1265 (1979b); repr. *Intern. Chem. Eng.*, 21:95-115 (1981)
- Kwauk, M., "The Jigged Reducer," (unpubl.); (i) 1979; (ii) 1981; (iii) 1983; *Inst. Chem. Metall.*
- Kwauk, M., and Wang, Y., Fluidized Leaching and Washing, *Chem. E. Symp.*, Ser. No. 63, paper D4/BB/1-21 (1981)
- Kwauk, M., Wang, N., Li, Y. Chen, B., and Shen, Z., "Fast Fluidization at ICM," *Proc. First Intern. Conf. Circulating Fluidized Bed*, p. 33-62, Halifax, Canada (1985)
- Kwauk, M., *Fluidization—Idealized and Bubbleless, with Applications*, Science Press, Beijing, and Ellis Horwood, U. K. (1992)
- Kwauk, M., "Fast Fluidization," *Advances in Chemical Engineering*, (M. Kwauk, ed.), Vol. 20, Academic Press, U.S.A. (1994)
- Li, J., Tung, Y., and Kwauk, M., "Fast Fluidization at ICM," (i) Method of Energy Minimization in Multi-Scale Modeling of Two-Phase Flow; (ii) Energy Transport and Regime Transition in Particle-Fluid Two-Phase Flow; (iii) Axial Voidage Profiles of Fast Fluidized Beds in Different Operating Regions, *Second International Conference on Circulating Fluidized Beds*, p. 75, 89, 193, Compiegne, France (1988)
- Li, J., and Kwauk, M., "Particle-Fluid Two-Phase Flow, The Energy-Minimization Multi-Scale Method," *Metallurgical Industry Press*, Beijing (1994)
- Li, Y., and Kwauk, M., "The Dynamics of Fast Fluidization," *Third Intern. Conf. Fluidization*, p. 537-544, Henniker, U.S.A. (1980)
- Liu, D., Liu, J., Li, T., and Kwauk, M., "Shallow-Fluid-Bed Tubular Heat Exchanger," *Fifth Int. Fluidization Conf.*, p. 401-408, Elsinore, Denmark (1986)

580 *Fluidization, Solids Handling, and Processing*

- Liu, K., "Particle Motion in Standing Waves in Gaseous Medium," (in Chinese, unpubl.), *Inst. Chem. Metall.* (1981)
- Qian, Z., and Kwauk, M., "Computer Application in Characterizing Fluidization by the Bed Collapsing Method," *Tenth Intern. CODATA Conf.*, Ottawa (1986)
- Qin, S., and Liu, G., "Application of Optical Fibers to Measurement and Display of Fluidized Systems," *Proc. China-Jpn. Fluidization Symp.*, p. 258–266, Hangzhou, China (1982)
- Qin, S., and Liu, G., "Automatic Surface Tracking for Collapsing Fluidized Bed," *Sec. China-Japan Fluidization Symp.*, Kunming, Elsevier, p. 468 (1985)
- Reh, L., "Calcination von Aluminumhydroxid in einer zirkulierenden Wirbelschicht," *Chem. Eng.-Tech.*, 42:447–451 (1970)
- Reh, L., "Fluidized Bed Processing," *Chem. Eng. Prog.* 67:58–63 (1971)
- Reh, L., "Calcining Aluminum Trihydrate in a Circulating Fluid Bed, a New Technique of High Thermal Efficiency, Metallurges," *Rev. Activ.*, 1972(15):58–60 (1972)
- Reh, L., "The Circulating Fluid Bed Reactor—A Key to Efficient Gas-Solid Processing," *Proc. First Intern. Conf. Circulating Fluidized Bed*, p. 105–118, Halifax, Canada (1985)
- Squires, A. M., "Applications of Fluidized Beds in Coal Technology," lecture, Intern. School on Heat and Mass Transfer Problems in Future Energy Production, Dubrovnik, Yugoslavia (1975a)
- Squires, A. M., "Gasification of Coal in High-Velocity Fluidized Beds," loc. cit. (1975b)
- Squires, A. M., "The City College Clean Fuels Institute:" Programs for (i) Gasification of Coal in High-Velocity Fluidized Beds; (ii) Hot Gas Cleaning, *Symp. Clean Fuels from Coal*, I.G.T., Chicago (1975c)
- Squires, A. M., The Story of Fluid Catalytic Cracking: "The First Circulating Fluid Bed," *Proc. First Intern. Conf. Circulating Fluidized Bed*, p. 1–19 (1985)
- Treybal, R. E., *Mass Transfer Operations*, McGraw-Hill, 1st Ed. (1955); 2nd Ed. (1968); 3rd Ed. (1980)
- Tung, Y., and Kwauk, M., Dynamics of Collapsing Fluidized Beds, *China-Jpn. Fluidization Symp.*, Hangzhou, China (1982), Science Press, Beijing, and Gordon Breach, New York, p. 155–166
- Tung, Y., Li, J., Zhang, J., and Kwauk, M., "Preliminary Experiments on Radial Voidage Distribution in Fast Fluidization," *Fourth Nat. Conf. Fluidization*, Lanzhou, China (1987)

- Tung, Y., Li, J., and Kwauk, M., "Radial Voidage Profiles in a Fast Fluidized Bed," *Proc. of Third China-Jpn. Symp. on Fluidization*, p. 139, Beijing, China (1988)
- Tung, Y., Yang, Z., Xia, Y., Zheng, W., Yang, Y., and Kwauk, M., "Assessing Fluidizing Characteristics of Powders," *Sixth Int. Fluidization Conf.*, Banff, Canada (1989)
- Tunstall, E. B., and Houghton, G., "Retardation of Falling Spheres by Hydrodynamic Oscillation," *Chem. Eng. Sci.*, 23:1067–1081 (1968)
- Van Oeveren, R. M., and Houghton, G., "Levitation and Countergravity Motion of Spheres by Nonuniform Hydrodynamic Oscillation," *Chem. Eng. Sci.*, 26:1958–1961 (1971)
- Wang, N., Li, Y., Zheng, X., and Kwauk, M., "Voidage Profiling for Fast Fluidization," *First Intern. Conf. Circulating Fluidized Beds*, Halifax, Canada (1985)
- Wilhelm, R. H., and Kwauk, M., "Fluidization of Solid Particles," *Chem. Eng. Prog.*, 44:201–218 (1948)
- Yan, Z., Yao, J., and Liu, S., "Turbulence in Grid Zone of Fluidized Reactor," *Proc. China-Jpn. Fluidization Symp.*, Hangzhou, China, p. 100–111 (1982)
- Yan, Z., Yao, J. Z., Wang, W. L., Liu, S. J., and Kwauk, M., "Cocurrent Shallow Multistage Fluid-Bed Reactor," *Third Intern. Conf. Fluidization*, Kashikojima, Japan, p. 607–614 (1983)
- Yang, Z., Tung, Y., and Kwauk, M., "Characterizing Fluidization by the Bed Collapsing Method," *Chem. Eng. Commun.*, 39:217–232 (1985)

Industrial Applications of Three-Phase Fluidization Systems

*Jack Reese, Ellen M. Silva, Shang-Tian Yang,
and Liang-Shih Fan*

1.0 INTRODUCTION

Three-phase fluidization systems offer the flexibility of a wide range of operation conditions and contacting modes and are finding increased industrial applications in reacting and physical processing schemes. This is primarily due to the increased use of three-phase fluidization systems in the rapidly growing biotechnology field, but application in other areas abound as well. Successful application of three-phase fluidization systems lies in the comprehensive understanding of the complex transport phenomena mechanisms and associated reaction parameters. For the past 30 years, large research efforts have been put forth to characterize and predict the complex behavior of three-phase systems; however, a complete understanding and the ability to reliably scale up three-phase fluidization systems have yet to be achieved.

The term *three-phase fluidization*, in this chapter, is taken as a system consisting of a gas, liquid, and solid phase, wherein the solid phase is in a non-stationary state, and includes three-phase slurry bubble columns, three-phase fluidized beds, and three-phase flotation columns, but excludes three-phase fixed bed systems. The individual phases in three-phase fluidization systems can be reactants, products, catalysts, or inert. For example, in the hydrotreating of light gas oils, the solid phase is catalyst, and the liquid and gas phases are either reactants or products; in the bleaching of paper pulp, the solid phase is both reactant and product, and the gas phase is a reactant while the liquid phase is inert; in anaerobic fermentation, the gas phase results from the biological activity, the liquid phase is product, and the solid is either a biological carrier or the microorganism itself.

The important inherent differences in the operating characteristics between fixed bed systems and fluidization systems as given by Fan (1989) are summarized here. Fixed bed systems produce high reactant conversions for reaction kinetics favoring plug flow patterns because of the small axial dispersion of phases and low macromixing present in such reactors. Fixed bed systems offer the advantage of high controllability over product selectivity for complex reactions and low solids attrition and consumption, permitting the use of precious metals as catalysts. In fluidization systems, high macromixing with large axial dispersion is prevalent which produces high reactant conversions for reaction kinetics favoring completely mixed flow patterns. The high mixing in fluidization systems also yields uniformity in the temperature throughout the system and ease in temperature control. The non-stationary nature of the particles in a fluidization system allow for ease in continuous catalyst replacement and, hence, minimum flow maldistribution.

Fan (1989) provided a detailed historical development of three-phase fluidization systems in reactor applications. Only a brief review of the significant accomplishments and the economic factors affecting the development of three-phase reactors will be provided here. Table 1 provides the important contributions in the application of three-phase fluidization systems for the past several decades. The direct liquefaction of coal to produce liquid fuels was the first commercial reactor application of three-phase fluidization systems, with development having occurred from the mid-1920's throughout the 1940's. A large effort was put forth at this time in Europe for the production of liquid fuels from coal as a direct

result of the need for such fuels during World War I and II. The commercial production of liquid fuels from direct coal liquefaction peaked at an average annual production of 4.2 million tons of primarily aviation fuel (Donath, 1963). At the end of the war, the direct production of liquid fuels from coal was phased out. Another important process which was developed during and prior to the 1940's is the application of a three-phase reactor for the reactions known as Fischer-Tropsch (F-T) synthesis. These reactions produce liquid fuels via indirect coal liquefaction involving hydrogen and synthesis gas derived from coal gasification, in the presence of a catalyst. The peak production for the liquid phase F-T synthesis occurred in the early 1950's at a daily production rate of 11.5 tons of liquid fuels (Kolbel and Ralek, 1980). Fischer-Tropsch synthesis ceased in the mid-1960's because of the availability of relatively cheap crude oil. However, renewed interest in F-T synthesis in the early 1970's, caused by the oil shortages of the time, lead to further studies in the commercial scale production of liquid fuels via F-T synthesis in slurry bubble column reactors. This development has continued throughout the 1980's and into the 1990's.

Table 1. Industrial Development and Application of Three-Phase Fluidization Systems

Decade	Application
1940's	Coal liquefaction, Fischer-Tropsch synthesis
1950's	Catalytic synthesis of chemicals
1960's	Hydrotreatment of petroleum resids
1970's	Environmental applications
1980's	Biotechnology application
1990's	Biotechnology / Chemical synthesis

The development of three-phase industrial-scale reactors in the 1950's primarily occurred in the chemical process industry through the use of slurry bubble column reactors. In the 1950's, slurry bubble column reactors were successfully utilized in the chemical process industry for the catalytic synthesis of organic chemicals and polyolefins. The slurry bubble column reactors used for catalytic reactor applications emerged in various designs and were operated under a wide range of flow conditions. Examples of reactor applications in commercial production (Germain et al., 1979) included hydrogenation of glucose to sorbitol, benzene to cyclohexane, butynediol to butenediol, esters to fatty alcohols, aluminum and ethylene to Ziegler alcohol (ALFOL process), and ethylene polymerization (Solvay process).

In the 1960's, following research and development beginning in the late 1950's, the three-phase fluidized bed reactor was first used commercially for hydrotreating petroleum resids. The technologies developed at this time are known as the *H-Oil process* and the *LC-Fining process* and are still currently in commercial operation. The three-phase fluidized bed reactors used in the hydrotreating/hydrocracking operations are commonly referred to as an *ebullated bed*. The term *ebullated bed* was first defined by P. W. Garbo in the patent of Johanson (1961) to describe a gas-liquid contacting process in contrast to the common industrial term *fluidized bed* where particles are in fluidization induced by the gas phase alone. Recent developments in the use of ebullated beds for hydrotreating/hydrocracking include the Texaco T-STAR process, introduced in the early 1990's (see Sec. 4.2).

The development of three-phase reactor technologies in the 1970's saw renewed interest in the synthetic fuel area due to the energy crisis of 1973. Several processes were developed for direct coal liquefaction using both slurry bubble column reactors (Exxon Donor Solvent process and Solvent Refined Coal process) and three-phase fluidized bed reactors (H-Coal process). These processes were again shelved in the early 1980's due to the low price of petroleum crudes.

The 1970's also brought about increased use of three-phase systems in environmental applications. A three-phase fluidized bed system, known as the *Turbulent Bed Contactor*, was commercially used in the 1970's to remove sulfur dioxide and particulates from flue gas generated by coal combustion processes. This wet scrubbing process experienced several

operational difficulties including excessive pressure drop, and its use was discontinued in the early 1980's. Today, however, wet scrubbing systems are still in use for flue gas desulfurization, although the operational mode of these systems is mainly as slurry spray columns rather than as fluidized beds. A second important environmental application of three-phase systems to come out of the 1970's is the area of biological wastewater treatment. This area of three-phase research has grown rapidly since the 1970's and continues to grow in the 1990's with increasing environmental pressures placed on the chemical process industry. Accounts of the historical development of fluidized bed bioreactor application in wastewater treatment can be found in Fan (1989), and Heijnen et al. (1989).

The 1980's and the early 1990's have seen the blossoming development of the biotechnology field. Three-phase fluidized bed bioreactors have become an essential element in the commercialization of processes to yield products and treat wastewater via biological mechanisms. Fluidized bed bioreactors have been applied in the areas of wastewater treatment, discussed previously, fermentation, and cell culture. The large scale application of three-phase fluidized bed or slurry bubble column fermentors are represented by ethanol production in a 10,000 liter fermentor (Samejima et al., 1984), penicillin production in a 200 liter fermentor (Endo et al., 1986), and the production of monoclonal antibodies in a 1,000 liter slurry bubble column bioreactor (Birch et al., 1985). Fan (1989) provides a complete review of biological applications of three-phase fluidized beds up to 1989. Part II of this chapter covers the recent developments in three-phase fluidized bed bioreactor technology.

The design and scale-up of three-phase fluidization systems is a challenging endeavor requiring a sound knowledge of all facets of reactor engineering and the underlying chemical engineering technologies (Tarmy and Coualoglou, 1992). Research efforts in the 1990's, using state-of-the-art imaging techniques, have begun to look inside small scale three-phase systems to better understand the fluid mechanics and phase interactions occurring in the system which can lead to better predictive tools for the design of three-phase reactor systems. While these studies provide insight into the hydrodynamics of the system, an important area in the industrial application of three-phase reactor systems which requires further study is the coupling of the hydrodynamics and the reaction kinetics. The complex reaction mechanisms occurring at all scales in three-phase

reacting systems need to be studied in relation to the hydrodynamic behavior transpiring at the various scales. These areas of study require improvements in experimental techniques and instrumentation to provide the necessary data required in the verification of any predictive models.

New applications and novel reactor configurations or operational modes for three-phase systems are continually being reported. These include the operation of a three-phase fluidized bed in a circulatory mode (Liang et al., 1995), similar to the commonly applied gas-solid circulating fluidized bed; the application of a three-phase fluidized bed electrode that can be used as a fuel cell (Tanaka et al., 1990); magnetically stabilized three-phase fluidized beds; centrifugal three-phase reactors; and airlift reactors.

This chapter provides an overview of recent and nontraditional industrial applications of three-phase fluidization systems. Fan (1989) has provided comprehensive tables on examples of three-phase fluidization applications as well as several chapters on common industrial applications, and readers are referred there for further information. Shah (1979) and Deckwer (1992) also provided industrial examples of three-phase fluidization systems as well as details on reactor engineering and transport phenomena of these systems. The current chapter is divided into two parts, the first focusing on chemical process applications, and the second considering the biological applications of three-phase fluidization systems. In Part I, two nontraditional industrial applications of three-phase systems are highlighted; these are smelting operations and operations in the processing of pulp and paper, including cooking of wood chips to produce pulp and flotation for recycling paper. An overview of recent developments in several classic applications of three-phase fluidization systems in the chemical process industries, including hydrotreating/hydrocracking using ebullated bed technology and hydrocarbon synthesis using slurry bubble column, are also presented in Part I. Part II of this chapter delineates the recent progress in the application of three-phase fluidization systems to the rapidly expanding biotechnology area. The current status of three-phase bioreactor research, the important differences between three-phase chemical and biological fluidized systems, and design considerations for three-phase bioreactors are covered.

Part I: Smelting Reduction, Paper Processing, and Chemical Processing

2.0 SMELTING REDUCTION

2.1 Introduction

Smelting reduction of iron ore is an intensive area of research for the replacement of the classical ironmaking process (coke ovens, agglomeration, blast furnaces). *Smelting reduction* has been defined in several ways; however, the most common definition of these processes in the recent literature is the production of hot metal from iron ore without the use of metallurgical coke (Fine et al., 1989; Oeters et al., 1994). Smelting reduction offers several advantages over blast furnace operation, which are listed in Table 2, but the process may still require another five to ten years before making a significant impact on the worldwide production of iron, primarily because the economics of the smelting reduction process are still uncertain. The key characteristics of smelting reduction as an alternative to the older blast furnace process is the ability to directly use iron ore and coal, which eliminates the need for preprocessing the iron ore and is significant for countries such as the United States that have large reservoirs of coal and the ability to handle an increased load of scrap metal, which is consistent with the worldwide environmental trend of reuse, reduce, and recycle. The development of various smelting reduction processes is occurring simultaneously worldwide. Table 3 summarizes the smelting reduction processes under development and in production around the world.

Smelting reduction processes can be classified into melter-gasifiers and iron-bath reactors (Oeters et al., 1994). In the melter-gasifier process, the coal is combusted to carbon monoxide (CO) and hydrogen (H₂) to provide the heat to melt iron pellets previously reduced from iron oxide pellets. The iron oxide pellets are reduced via direct reduction using the off-gas from the combusted coal. The most fully developed smelting reduction process is a melter-gasifier known as the *Corex process*, which is in operation in South Africa (Flickenschild, 1991). The iron-bath

reactors, however, seem to be the smelting reduction process of choice for current and future applications. Iron-bath reactors consist of three layers or zones—at the bottom of the reactor is the liquid metal bath, which contains the reduced iron product; on top of the liquid metal is the slag layer, which contains all of the solid material in the reactor, including the iron ore and coal, and is where the combustion of the coal and reduction of the iron ore occurs; the upper portion of the reactor is primarily a gaseous region where secondary or post-combustion of the gases, produced during the initial combustion of the coal in the slag layer, occurs. In iron-bath reactors, final reduction of the iron ore and post-combustion of coal occur simultaneously, while the off-gas from the post-combustion is used for the pre-reduction of iron ore in a separate reactor, generally a gas-solid fluidized bed or circulating fluidized bed. The focus of this section will be on iron-bath reactors, which are unique three-phase systems consisting of molten metal as the liquid phase and iron ore, coal, and slag particles as the solid phase. The gas phase consists of bottom injected oxygen, air or nitrogen, used for agitation of the molten metal bath, and top injected oxygen for post-combustion.

Table 2. Advantages of Smelting Reduction over Coke Oven and Blast Furnace

- | |
|-------------------------------------------------------------------------------------------------------------------------------------------------------------------------------------------------------------------------------------------------------------------------------------------------------------------------------------------------------------------------------------------------------------------------------------------------------------------------------------------------------------------------------------------------------------------|
| <ul style="list-style-type: none">· Elimination of coke oven by direct use of coal· Direct use of fine ores, do not require agglomeration plant· Lower investment cost as a result of above factors· Lower operating costs due to cheaper raw materials and lack of preparation plants· Lower level of emissions· Higher specific productivity· Increased flexibility in production and operation· Improved controllability· Possibility for direct alloying of steel melts |
|-------------------------------------------------------------------------------------------------------------------------------------------------------------------------------------------------------------------------------------------------------------------------------------------------------------------------------------------------------------------------------------------------------------------------------------------------------------------------------------------------------------------------------------------------------------------|

Table 3. Smelting Reduction Processes Under Development Throughout the World

Country	Smelting reduction process
Japan	DIOS (Direct iron ore smelting)
Australia	HIsmelt (High intensity smelting)
USA	AISI (Direct steelmaking program)
Germany	Corex
France and Germany	Jupiter
Great Britain, Holland, Italy	CCF (Cyclone converter furnace)
Canada	LB (Lu-Bryk process)
Russia	ROMELT (Rossia Melt)

2.2 Principles of Smelting Reduction

Smelting reduction in iron-bath reactors consists of two major steps, pre-reduction of the iron ore in a fluidized bed reactor or pre-reduction reactor (PRR) and smelting reduction in a smelting reduction furnace (SRF), see Fig. 1. A brief summary of the components and chemical reactions in the SRF are given in Fig. 2. The coarse coal particles are charged directly into the furnace, while lump and fine iron ore are injected into the iron-carbon slag layer or simply added to the top of the vessel at an approximate temperature of 800°C after pre-reduction by the off-gas. The iron ore is reduced at temperatures between 1400–1600°C. The gaseous products from the combustion of coal and reduction of iron oxide contain large amounts of carbon monoxide and hydrogen. A layer of slag on the liquid iron bath protects the liquid iron product from reoxidation. The predominant components of the slag layer are lime, silica, and iron oxide. On the surface of the slag and in the upper portion of the furnace, the burning of the carbon monoxide and hydrogen with oxygen and/or air injected through a top penetrating lance is called *post-combustion*. The

heat generated by post-combustion, if efficiently transferred back to the iron bath, significantly reduces coal consumption. In the SRF, the iron bath is also agitated by bottom injection of nitrogen, oxygen, carbon dioxide, or air to improve heat transfer and increase slag circulation. The hot metal is continuously removed from the bottom of the SRF at temperatures around 1500°C.

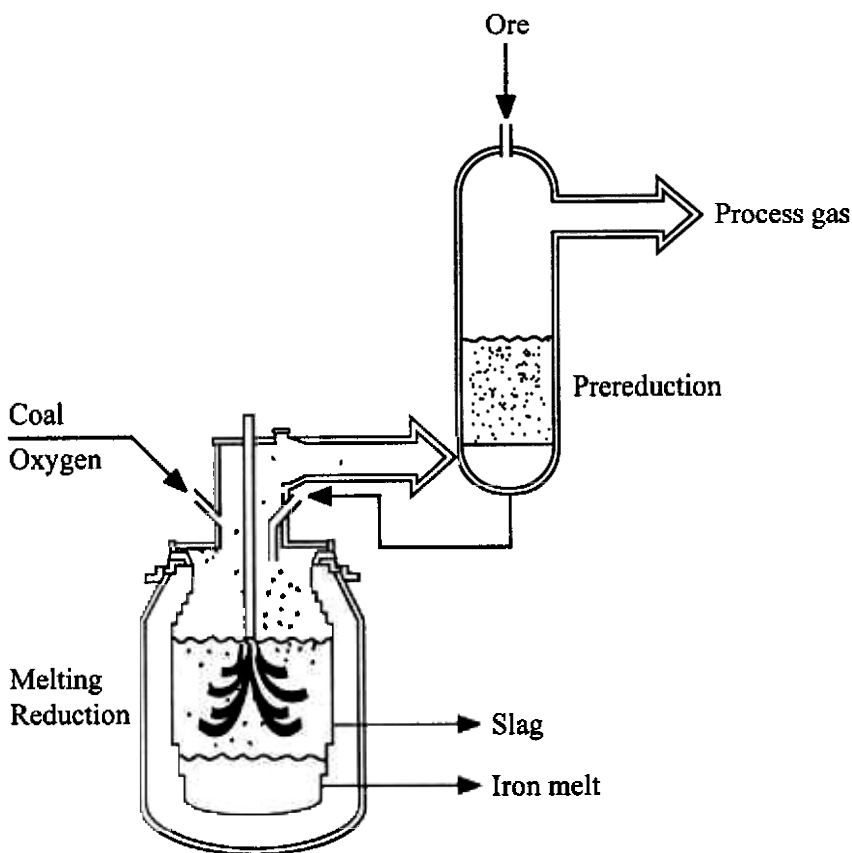


Figure 1. Two-stage smelting reduction process using an iron-bath reactor. (*From Japan Metal Bull., 1988.*)

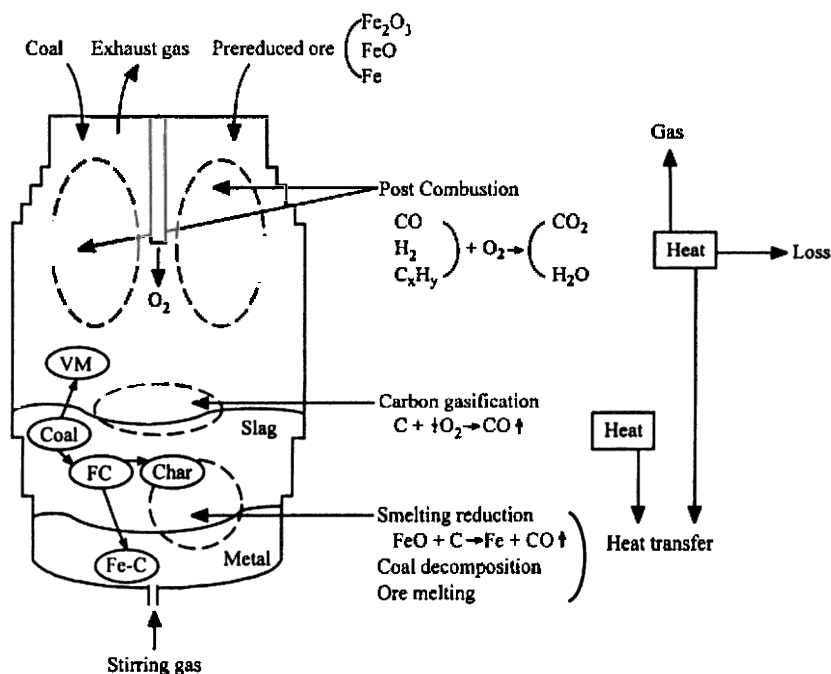


Figure 2. Components and chemical reactions of an iron-bath smelting reduction¹ furnace. (From Shinotake and Takamoto, 1993.)

In a two-stage smelting reduction process, several primary factors influence the operation, including the degree of pre-reduction, degree of post-combustion, slag behavior, heat transfer efficiency, and bath agitation. During the pre-reduction of the iron ore using the off-gas, the carbon monoxide requirement for pre-reduction and the evolution of carbon monoxide in the smelting reduction process can be harmonized (Oeters et al., 1994). The two-stage smelting reduction process can be optimized at a certain degree of pre-reduction depending on the CO requirement for pre-reduction and the evolution of CO in smelting reduction. A reasonably high degree of post combustion associated with a high heat transfer efficiency is also essential for the efficient operation of a smelting reduction process. The complex behavior of the multiphase slag layer plays an integral role in the performance of the furnace because of the layer's importance in heat transfer, mass transfer, and chemical reaction. The following sections review current research and factors affecting post-combustion and slag behavior.

2.3 Post-Combustion and Heat Transfer in SRF

The energy required in smelting reduction in iron-bath reactors for heating the bath, for melting scrap material, for reducing iron oxide, and for gasifying coal is supplied primarily by the combustion of carbon or coal to carbon monoxide (Zhang and Oeters, 1991a). The total energy available in the coal is not entirely utilized because of incomplete combustion of the coal. Therefore, to improve the energy efficiency in the furnace, carbon monoxide and hydrogen produced from the combustion of coal in the slag layer undergo further combustion to carbon dioxide and steam in the upper portion of the furnace providing additional heat that can be transferred back into the slag layer and iron-bath. A measure of the post-combustion is the *post-combustion ratio* (PCR), which is one of the important process parameters in smelting reduction processes, defined by:

$$\text{Eq. (1)} \quad \text{PCR} = \frac{\% \text{CO}_2 + \% \text{H}_2\text{O}}{\% \text{CO} + \% \text{CO}_2 + \% \text{H}_2 + \% \text{H}_2\text{O}}$$

Higher post-combustion ratios imply that more heat is generated which can be utilized in carrying out the smelting operations. Typical post-combustion ratios are in the range of 40–60% (Brotzmann, 1989; Ibaraki et al., 1990; Romenets, 1990; Takahashi et al., 1992; Katayama et al., 1993b). As in any process, however, not all the heat generated by the post-combustion reactions is transferred back to the bath; thus a second parameter known as the *heat transfer efficiency* (HTE) is defined as the portion of the heat generated by post-combustion transferred to the bath.

$$\text{Eq. (2)} \quad \text{HTE} = \left(1 - \frac{\text{Excess heat in the off-gas}}{\text{Heat generated by post-combustion}} \right) \times 100$$

With this definition, a heat transfer efficiency of 100% implies that the temperature of the off-gas will be the same as the temperature of the bath. The HTE reported in the literature are in the 80–90% range (Ibaraki et al., 1990; Takahashi et al., 1992; Katayama et al., 1993b). Several authors (i.e., Gou et al., 1993, and Gudenau et al., 1993) have indicated that this definition has limitations because the heat losses to the furnace walls

(refractories) and the top penetrating gas lance are not taken into account. The losses are accounted for in the HTE definition proposed by Gudenau et al. (1993) given in Eq. (3).

$$\text{Eq. (3)} \quad \text{HTE} = \left(1 - \frac{\text{heat loss of the off-gas} + \text{other losses in furnace}}{\text{total heat generated by post-combustion}} \right)$$

Several studies have investigated the relationship between PCR and HTE with the results, in general, demonstrating an inverse relationship (Zhang and Oeters, 1991b; Farrand et al., 1992; Hirata et al., 1992; Katayama et al., 1992; Gudenau et al., 1993). Ideally, high levels of PCR coupled with high levels of HTE are desirable; however, to achieve high levels of PCR, the amount of oxygen fed to the reactor must increase. This can lead to reoxidation of the iron droplets in the slag layer and may increase the off-gas temperatures to the point of damaging the refractory material of the furnace. The increase in the off-gas temperature can be minimized with an increase in the heat transfer to the slag layer; however, the mechanisms of heat transfer may limit the degree of post-combustion. The factors affecting the relationship between PCR and HTE are numerous and complicated (including amount and contents of coal); further studies in theoretical analysis and experimental evaluation are required.

The main aspects of heat transfer in a SRF are the heat transfer from the post-combustion gas to the slag layer and from the slag layer to the iron bath. In the mixing process of the slag layer, slag and iron particles are ejected into the gas space where they acquire heat from the post-combustion gas. The particles, after a short time in the gas space, fall back into the slag layer with the iron contained in the particles melting due to a rise in the temperature of the particles, and accumulating in the molten iron bath. The heat is transferred in this way from the post-combustion gases in the upper portion of the reactor to the liquid iron bath at the lower portion of the reactor. Heat transfer from the gas phase to particulate phase consists of convective and radiative transfer. Oeters et al. (1994) stated that, for conditions where the post-combustion took place by the top blown gas penetrating the slag layer, the main resistance to heat transfer was between the gas phase and slag, and that the radiative transfer between the gas and slag was the most important heat transfer mechanism. Katayama et al. (1992) reported that under actual operating conditions, 30% of the heat

transfer could be explained by radiation and convection, while the rest was attributed to circulation of superheated carbonaceous materials within the slag. Ibaraki (1994) considered the heat transfer to be caused by two mechanisms; (i) radiation heat transfer from the gasses in the upper portion of the reactor to the slag layer and (ii) heat transfer from the flame of the oxygen jet through the surface of the slag cavity created by the oxygen jet. For the first mechanism, the radiation increased the temperature of the slag surface, and the slag motion made the temperature homogeneous throughout the slag layer. Ibaraki (1994) concluded, based on his prediction, that the radiation heat transfer is not significant, accounting for 20% of the heat transfer. Based on another calculation using a flame temperature of 2600 K and an estimation of the cavity surface area, Ibaraki (1994) stated that the second mechanism accounted for only 20% of the heat transfer. Since these two mechanisms accounted for only 40% of the total heat transfer, Ibaraki (1994) proposed a third mechanism for heat transfer that accounted for the final 60% of the heat transfer. The third heat transfer mechanism is the transfer of heat from the combustion process in the slag to the reduction sites. The oxygen from the jet is not completely reacted upon reaching the slag layer, therefore, a portion of the oxygen reacted with gas, iron droplets, and char in the slag.

In order to provide further insight into the post-combustion ratio and the heat transfer efficiency, the factors that affect the PCR and HTE will be delineated. The factors that affect the PCR and HTE will be discussed separately with the understanding that a complex relationship may exist between the two parameters. The factors that affect the PCR are shown in Table 4, and Fig. 3 demonstrates the primary conditions for post-combustion. The PCR should be kept relatively high, since the fuel consumption decreases with an increase in the PCR at the same HTE (Aukrust, 1993). However, as mentioned, high PCR may lead to problems due to increases in:

- Off-gas temperature, with detrimental effects on the refractories and gas handling systems (Fruehan et al., 1989)
- Oxidation potential of the off-gas (Brotzmann, 1989)
- Volume of the off-gas, which may cause difficulties with the gas and dust handling (Hoffman, 1991)

Since a detailed discussion of the factors listed in Table 4 is beyond the scope of this review, the reader is referred to the listed references for further information. Several of the factors affecting the PCR also affect the slag layer and these are discussed in more detail in Sec. 2.4.

The heat transfer efficiency is significantly affected by the slag layer properties and behavior; therefore, those factors other than slag phenomena that affect HTE are presented in Table 5. As for the PCR, it is desirable to keep the HTE as high as possible. An increase in HTE at the same PCR decreases fuel consumption (Fruehan et al., 1989; Keogh et al., 1991) and the off-gas temperature (Fruehan et al., 1989; Takahashi et al., 1992).

Table 4. Factors That Affect the PCR

Factor	References
· Carbonaceous material - volatile matter, coal feed rate, location of coal injection	Keogh et al. (1991); Hardie et al. (1993); Ibaraki (1994)
· Ore feed rate	Shinotake and Takamoto (1993)
· Iron droplet behavior - mixing, reoxidation	Ibaraki et al. (1990); Zhang and Oeters (1991b); Ibaraki et al. (1995a)
· Slag layer foaming	Tsujino et al. (1985); Hirai et al. (1987); Farrand et al. (1992); Ibaraki et al. (1995a)
· Temperature and depth of the metal bath	Keogh et al. (1991); Hardie et al. (1993)
· Agitation of metal bath	Ibaraki et al. (1990); Hirata et al. (1991); Katayama et al. (1992)
· Type of agitation gas and location of injection	Ibaraki et al. (1990); Hirata et al. (1991); Hardie et al. (1993)
· Lance design - height, number of holes	Takashiba et al. (1989); Ibaraki et al. (1990); Farrand et al. (1992); Takahashi et al. (1992);
· Type of top-blown injector gas - oxygen, air	Keogh et al. (1991); Zhang and Oeters (1993a,b)
· Furnace pressure	Takahashi et al. (1992)

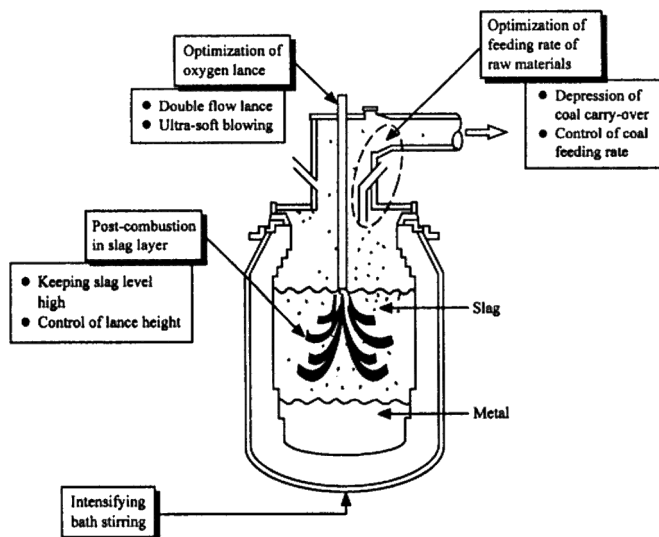


Figure 3. Key factors to achieve efficient post-combustion in an iron-bath smelting reduction furnace. (From Takahashi et al., 1992.)

Table 5. Factors Other Than Slag Phenomena That Affect the HTE

Factor	References
· Volatility and feed rate of coal	Ibaraki et al. (1990); Takahashi et al. (1992)
· Ore feed rate	Takahashi et al. (1992)
· Reoxidation of metal droplets above the bath	Ibaraki et al. (1990); Hirata et al. (1991); Keogh et al. (1991);
· Metal bath agitation	Tanabe et al. (1989); Ibaraki et al. (1990); Hirata et al. (1991); Katayama et al. (1992)
· Lance height	Tanabe et al. (1989); Gou et al. (1993); Takahashi et al. (1992)
· Type of top blown injector gas - oxygen, air	Gudenau et al. (1993)
· Furnace pressure	Takahashi et al. (1992)
· Heat losses due to dust generation and furnace geometry	Gou et al. (1993); Ibaraki et al. (1995b)

Several authors have attempted theoretical modeling of post-combustion (Fruehan et al., 1989; Zhang and Oeters, 1991a, 1991b, 1993a, 1993b; Hardie et al., 1992; Gou et al., 1993; Gudenau et al., 1993). The models consider the convective and radiative nature of the heat transfer under steady-state conditions for various gas types including oxygen and air. The model equations consist of heat and mass balances of the various components in the furnace (i.e., iron and carbon dioxide) and, in some cases, momentum balances for the flow behavior. Gou et al. (1993) provided one of the more comprehensive models for heat transfer. The model, by incorporating the momentum balances, allowed not only for the calculation of the composition and temperatures but also the steady-state gaseous flow patterns. The model determined the location, shape, and temperature of the combustion flame front and coupled equations for the turbulent convective transfer to those for the radiative transfer. They use the DeMarco-Lockwood flux model to calculate the radiation transfer for a turbulent, high-temperature reacting flow system. In the DeMarco-Lockwood flux model, the radiation fluxes for axisymmetric flow are expressed in the following form:

$$\text{Eq. (4)} \quad \frac{\partial}{\partial z} \frac{1}{k_a} \frac{\partial F_z}{\partial z} = \frac{4}{3} k_a (2 F_z - F_r - \mathbf{S} T^4)$$

$$\text{Eq. (5)} \quad \frac{1}{r} \frac{\partial}{\partial z} \frac{r}{k_a} \frac{\partial F_r}{\partial r} = \frac{4}{3} k_a (2 F_z - F_z - \mathbf{S} T^4)$$

where F_z and F_r are the radiation heat fluxes in the z and r directions, respectively. The radiation heat fluxes are coupled to the convective heat transfer via a source term in the transport equation for the stagnation enthalpy of the form:

$$\text{Eq. (6)} \quad S_H = \frac{16}{9} k_a (F_z + F_r - 2 \mathbf{S} T^4)$$

where S_H is the source term from the enthalpy equation.

Future requirements for the modeling of smelting furnaces will be for a detailed account of the heat transfer mechanisms as developed by Zhang and Oeters (1991a, 1991b, 1993a, 1993b) and a consideration of the fluid dynamics of the system such as that described above by Gou et al. (1993) while considering the effects of the raw materials to maintain model flexibility. The slag layer has tremendous effects on the overall behavior of the furnace, but the complex multiphase nature of the system is still in the early development stages of modeling. Another important factor that needs to be researched further and included in models is the reduction kinetics of iron oxide from liquid slags (Fine et al., 1989; Oeters, 1989; Oeters and Xie, 1995).

2.4 Slag Layer Behavior

The slag layer is composed of molten slag, solid materials such as carbonaceous materials and undissolved ore, gas bubbles, and metal droplets. The operational characteristics, including post-combustion, heat efficiency, dust generation, and carbon content of the bath, of a SRF are highly influenced by the behavior of the slag layer (Katayama et al., 1993a). The slag added to a SRF consists primarily of lime (CaO) and silica (SiO_2) with significant amounts of iron oxide (FeO) becoming present when the smelting reduction process commences. Small amounts of additives, such as P_2O_5 , S, MgO , or CaF_2 , may also be present in the slag layer. The slag layer is present primarily to serve as a heat flux between the combustion space and the metal bath and to protect the metal bath from the oxidizing atmosphere above the slag. The two most researched topics concerning the slag layer behavior are the optimal height of the slag layer and the mechanisms and control of foaming of the slag layer. Smelting reduction processes are conducted with both a relatively thin slag layer, as in the HIs melt process developed in Australia (Hardie et al., 1992), and with a thick slag layer, as in the DIOS process developed in Japan (Inatani, 1991).

The main reactions in smelting reduction processes are the gasification of coal and iron oxide reduction in the slag. These reactions produce large quantities of gaseous carbon monoxide and hydrogen on the slag/iron or slag/carbon surface. The slag foam is created by the gas bubbles formed as a result of these reactions becoming entrained in the slag, and in not being able to readily coalesce, forming a system of tightly packed bubbles separated by one another by thin films of liquid slag (Gaskell,

1989). In studies conducted on the foaming behavior of metallurgical slags, it is generally agreed that the principle factors in controlling the foaming behavior are surface tension, viscosity, viscoelastic characteristics of the liquid films, basicity, solid particles, and bubble size. There is, however, considerable disagreement in the relative importance of each factor (Gaskell, 1989; Utigard and Zamalloa, 1993). Obviously, in a complicated three-phase system, it becomes extremely difficult to ascertain the individual effects of the stated factors, which is why many studies on the foaming behavior are conducted in non-reacting systems. The stabilization and intensification of foams are favored for low surface tension and high viscosity of the slag (Fine et al., 1989). Gaskell (1989) provided an example of how the presence of a surface active solute, in this case SiO_2 , in a nominally-basic slag led to stabilization of the foam. The surface active solute decreased the surface tension of the slag by preferential segregation of SiO_2 to the slag surface and increased the viscosity as a result of the surface being more siliceous than the bulk melt (i.e., the viscosity of the surface is higher than that of the bulk melt). Aukrust and Dowling (1991) reported that a foaming slag was stable when the basicity was between 1.2 and 1.5. Good summaries of the more fundamental behavior of slag properties can be found in Gaskell (1989), Gudenau et al. (1992), Hara and Ogino (1992), Ogawa et al. (1993), Utigard and Zamalloa (1993), and Gou et al. (1994).

Other factors that are more engineering or design oriented are also found to affect the foaming behavior of the slag layer. Gudenau et al. (1992) reported that the top oxygen blowing parameters, such as lance penetration distance, gas velocity, and expansion angle of the gas stream, affected the foam generation and proper selection of these parameters can assist in controlling excess foaming. They also found that the foaming decreased with increased pre-reduction degree. Ibaraki et al. (1990) found that weak bath agitation and a low bath temperature promoted foaming. They also reported that bath agitation affected the iron droplet mixing in the slag and the slag circulation. An increase in bath agitation lifted more iron droplets into the slag resulting in lower PCR and increased the ferrous dust in the off-gas. They suggested a bath agitation of 2 to 4 kW/ton of metal. Ogawa et al. (1992) reported that an increase in iron ore feed rate promoted foaming.

Foaming of the slag layer is inevitably going to occur during the smelting reduction process, therefore, ways of controlling the foaming to prevent overflow of the system have been studied. The most widely reported and possibly easiest way to control foaming is the addition of carbonaceous material to the slag. The DIOS smelting reduction furnace, under development in Japan, is chosen to demonstrate the control of the slag layer foaming because the process has been described in the literature in more detail than other processes and it operates with a thick layer of slag. The thick layer of slag is required to shield the stirred metal bath from the top blown oxygen jet. The thick slag layer consists of molten slag, carbonaceous materials, and gas bubbles. The carbonaceous material, consisting of char or coke, is suspended in the slag to control foaming. Ogawa et al. (1992) reported that the carbonaceous material promoted the coalescence of small bubbles into larger bubbles that are able to rise through the slag layer. With the use of x-ray fluoroscopic observation of the slag layer in a 1-ton furnace, Ogawa et al. (1992) concluded that the carbonaceous material controlled the slag foaming by increasing the coalescence of small bubbles on the surface of the carbonaceous material because the carbonaceous material was not easily wettable with slag and, therefore, the CO gas was likely to spread along its surface. The amount of carbonaceous material required for stable operation is between 10–20% of the slag's weight (Ibaraki et al., 1990; Ogawa et al., 1992). Katayama et al. (1993a) measured the slag height and by assuming that all the carbonaceous materials were entrapped in the slag layer, calculated the volume proportions of the slag layer to be as follows: molten slag: 22–28 vol%, carbonaceous materials: 22–28 vol%, and gas bubbles: 44–55 vol%. Lump carbonaceous material is preferred over fine material, because the turbulence created by the larger particles lead to more frequent contact with the small bubbles, and the fine material is only sparsely scattered when charged into the furnace (Ogawa et al., 1992).

The slag layer plays important roles in heat transfer and the reduction of iron oxide. The role of the slag layer in heat transfer was described in Sec. 2.3. Katayama et al. (1992) proposed that the reduction of iron oxide occurred at the following three locations

- (i) Interface between slag and metal bath
- (ii) Interface between slag and metal droplets
- (iii) Interface between slag and carbonaceous materials.

They estimated the overall rate of reduction to be equal to the rate of addition of ore at stable operation. By determining the overall rate as a function of the amount of slag in both 5-ton and 100-ton furnaces, they calculated the amount of reduction at each site. Katayama et al. (1992) found that for the 5-ton furnace operation, a high proportion (70%) of the reduction occurred at the bulk metal slag interface. The proportions of reduction at locations 2 and 3 were found to increase with increasing experimental scale and the amount of slag. For the 100-ton furnace containing a large amount of carbonaceous material, the amount of reduction at each site was almost equal (34% for site 1, 33% for sites 2 and 3).

Ibaraki et al. (1990) reported that the reduction reaction took place in the slag bulk as well as in the condensed iron zone around the static slag/metal interface. They also reported that the reduction kinetics decreased as the oxygen jet penetrated the iron bath and concluded that the oxygen jet in the slag not only interfered with the reduction reaction, but also reduced the amount of post-combustion and increased the ferrous dust content in the off-gas. They recommended that the blown oxygen should not reach the condensed iron zone, located in the lower one-third of the slag. Katayama et al. (1993a) reported that the temperature of the lower 75% of the slag layer was almost equal to that of the metal bath, while the upper 25% could have large fluctuations in the temperature caused by the interaction with the gas phase in the upper portion of the furnace where temperatures may be 200–300°C higher than in the metal bath.

As mentioned previously, the modeling of the slag behavior is an area that requires further development. Ogawa et al. (1993) modeled the physical behavior of foaming slags by a mechanistic model that considered the effects of the physical properties of the slag and metal on the foam height. The model demonstrated that not only do the surface tension and viscosity of the slag affect the foam height, but the slag/metal interfacial tension and the surface tension of the metal affect the foam height as well. Gou et al. (1994) applied a one-dimensional, fluid mechanic model for gas and liquid two-phase flow to calculate the foam height and void fraction variation with gas velocity. The model requires an experimentally determined parameter of the ratio of the drag coefficient to the effective bubble diameter. The model was able to predict the slag level of those experiments that were used in determination of the above stated parameter. The model does not directly account for the raw materials.

2.5 Future of Smelting Reduction of Iron Ore

Table 6 provides areas of smelting reduction that require further research. The economics of the current smelting reduction processes under development need to be more accurately determined as the development stages become larger. One estimation of the economics of smelting reduction and a comparison between blast furnace, direct reduction, and smelting reduction was provided by Steffen (1989). As seen from Table 3, the development of smelting reduction processes is occurring worldwide. Ibaraki et al. (1995a, 1995b) summarized research performed in Japan between 1988 to 1991 using a 100 metric ton smelter, indicating the highest production rate achieved was 36.4 metric tons of iron/hour. Fine et al. (1989) estimated that based on research and development efforts in Japan, the USA, and Europe, the implementation of a smelting reduction process to produce steel is possible by the year 2000.

Table 6. Areas of Smelting Reduction Requiring Further Research (Fine et al., 1989; Oeters, 1989)

- | |
|-------------------------------------------------------------------------------------------------------------------------------------------------------------------------------------------------------------------------------------------------------------------------------------------------------------------------------------------------------------------------------------------------------------------------------------------------------------------------------------------------------------------------------------------------------------------------------------------------------------------------------------------------------------------------------------------------------------------------------------------------------------------------------------------------------------------------------------------------------------------------------------------------------------------------------------------------------------------------------------------------------------------------|
| <ul style="list-style-type: none"> · Melting and reduction mechanisms of pre-reduced ore in iron oxide containing slag and in carbon containing iron · Sticking behavior of ore fines · Kinetics of high temperature oxidation of liquid iron · Mechanism of carbon monoxide formation under the conditions of smelting reduction · Flow processes in thoroughly mixed metal-slag-gas systems · Mass and heat transfer during post-combustion in thoroughly mixed metal-slag-gas systems · Reactions of FeO-bearing melts with refractory materials · Optimization of reactor geometry in terms of charging and removal of materials · Optimization of slag height and metal bath agitation · Alternative heat sources such as electrical energy · Use of increased amounts of scrap metal and lower grades of iron ore · Removal of sulfur and other trace elements from the off-gas and liquid iron |
|-------------------------------------------------------------------------------------------------------------------------------------------------------------------------------------------------------------------------------------------------------------------------------------------------------------------------------------------------------------------------------------------------------------------------------------------------------------------------------------------------------------------------------------------------------------------------------------------------------------------------------------------------------------------------------------------------------------------------------------------------------------------------------------------------------------------------------------------------------------------------------------------------------------------------------------------------------------------------------------------------------------------------|

3.0 PAPER PROCESSING

3.1 Introduction

The pulp and paper industry is characterized by many operations that are performed under multiphase flow conditions. Typical examples of the major processes that involve multiphase phenomena are the cooking of wood chips in a chemical solution to remove unwanted cross-linking components (lignin) leaving behind a fibrous wood pulp; bleaching of pulp in three-phase mixtures of pulp slurry and bleaching gas (chlorine, chlorine dioxide, oxygen, or ozone); and de-inking of recycled paper in flotation-type devices. Each of these processes and the nature of their three-phase behavior will be discussed in this section. The operational characteristics of these processes may differ somewhat from traditional three-phase fluidized beds, nevertheless, the processes still consist of three-phase mixtures that require intimate contacting of the phases. Since the pulp and paper mills of the future may only consist of improving on existing technologies (Rickard, 1994; Meadows, 1995), a further understanding of the three-phase nature of these processes will assist in attaining these necessary process improvements.

Three-phase mixtures in pulp and paper are unique because of the complex behavior of the solid phase. The solid phase (wood chips or paper pulp) in the pulp and paper industry is a low-density fibrous material (primary cellulose) of varying size, shape, and thickness. The nature of the solid phase is complicated because of the ability of the pulp fibers to absorb water and swell to several times the original volume of the oven dried (O. D.) pulp. This absorbed water becomes part of the fibers, and is not considered part of the suspending medium (Stenuf and Unbehend, 1986). This type of solid phase is in contrast to the high density, primary spherical solid phase seen previously in the smelting operation and the catalyst material used in chemical or hydrocarbon processing. While two-phase pulp slurry pipe flow has been extensively studied (Stenuf and Unbehend, 1986), highlighted by the demonstration of the non-Newtonian and drag reduction characteristics, the three-phase flow behavior requires further study (Lindsay et al., 1995; Reese et al., 1996).

3.2 Chemical Pulping of Wood Chips

Pulping of wood chips refers to the process by which the wood chips are degraded into fibers by removal of the lignin from the cellulose and hemicelluloses. The lignin is a highly polymerized substance that holds the cellulose fibers together. The two primary methods of pulping are chemical and mechanical. Chemical pulping consists of cooking the wood chips with the appropriate chemicals in an aqueous solution at elevated temperature and pressure. The chemicals used in chemical pulping can be either alkaline (kraft process) or acidic (sulfite process). The alkaline kraft process has become the chemical pulping method of choice because of advantages in chemical recovery and pulp strength. However, the formation of organic sulfides in the kraft process has caused environmental concern due to their escape as malodorous gases. A brief overview of the kraft process will be given here. Details on mechanical pulping and the sulfite process can be found in Smook (1992).

In the kraft process, an aqueous mixture of sodium hydroxide (NaOH) and sodium sulfide (Na_2S) is used to break the lignin away from the cellulose fibers. The chemical reactions that occur are complex and not completely understood. The alkaline attack essentially breaks down the lignin molecules into smaller fragments whose sodium salts are soluble in the solution. The cooking of the wood chips is completed when the *kappa number*, a measure of the residual lignin content in the pulp, of the pulp has achieved a desirable level. The primary objective in the cooking of wood chips is to consistently obtain the desired kappa number with a minimal amount of cellulose degradation and a minimal level of unusable (reject) material, producing a pulp of uniform quality while working with unavoidable variations in the wood feedstock. The two factors that drive the kraft pulping reactions are alkali concentration and temperature. The rate of removal of the lignin (delignification) more than doubles over the range of normal cooking temperatures (155–175°C) with every 10°C increase in temperature (Smook, 1992). One drawback to the kraft process (and chemical pulping in general) is that while the method is able to remove a large portion of the lignin, a certain amount of degradation of the cellulose will also occur. Typical yields from kraft processes are between 40% and 50% of the original wood substance compared with 85% to 95% from mechanical pulping. Various factors that affect the chemical cooking of wood chips via the kraft process are listed in Table 7.

Table 7. Factors Affecting Kraft Cooking (After Smook, 1992)

- | |
|------------------------------------------------------------------------------------------------------------------------------------------------------------------------------------------------------------------------------------------------------------------------------------------------------------------------------------------------------------------------------------------------------------------------------------------------------|
| <ul style="list-style-type: none">· Type of wood (hardwood or softwood)· Wood chip quality (size and thickness uniformity)· Wood chip moisture content· Sulfidity of cooking liquor· Strength of chemical application· Liquor-to-wood ratio· Temperature cycle· Cooking time/Reaction rate· Extent of delignification (kappa number)· Residual alkali |
|------------------------------------------------------------------------------------------------------------------------------------------------------------------------------------------------------------------------------------------------------------------------------------------------------------------------------------------------------------------------------------------------------------------------------------------------------|

The kraft process can be carried out in a reacting scheme that is batch or continuous. Advantages of batch and continuous schemes are delineated in Table 8. The vessel in which the cooking takes place is commonly referred to as a digester. The three-phase behavior in the digester is characterized by the wood chips immersed in the aqueous solution, with the gas phase being steam injected for heating purposes and/or volatile organic gases produced as the reaction proceeds. Cooking in a batch digester generally takes 2–4 hours at a maximum temperature around 170°C, see Table 9. The maximum temperature is typically reached in 1.0 to 1.5 hours, allowing the cooking chemicals to penetrate the wood chips. The cooking reactions then proceed for up to 2 hours at the maximum temperature. The heating of the cooking mixture is conducted through direct steam injection or by forced circulation of the cooking chemicals through an external heat exchanger. Batch digesters are fabricated from carbon steel with a size range of 200 to 265 m³ and are capable of producing up to 19 tons of pulp per batch (Smook, 1992).

Table 8. Advantages of Batch and Continuous Digester Schemes (After Smook, 1992)

Batch Digester Advantages	Continuous Digester Advantages
<ul style="list-style-type: none"> · More reliable operation · Greater operating flexibility · Ability to change type of pulp produced · Ability to cook softwood and hardwood concurrently · Ease of start-up and shut-down 	<ul style="list-style-type: none"> · Lower steam requirement (less energy) · More constant steam demand · More compact; less space requirement · Lower capacity requirement of auxiliary components due to constant loading · Adaptable for digestion of all types of wood

Table 9. Cooking Conditions for the Kraft Chemical Pulping Process

Raw Material:	Wood Chips
Chemicals:	NaOH, Na ₂ S anthraquinone, polysulfide (extended)
Cooking Time:	2-4 hours
Cooking Liquor pH:	≈ 13
Cooking Temperature:	170-180 °C
Yield:	40-50%

The increasing demands on the pulp and paper industry to reduce emissions from bleaching operations has lead to modifications of the cooking process to provide a pulp that requires a decreased amount of bleaching. This is accomplished by decreasing the amount of residual

lignin content in the unbleached pulp by extended delignification in the cooking process. The most widely researched method to achieve extended delignification is the addition of additives, such as surfactants, anthraquinone, or polysulfide, to the cooking process. The additives work by either accelerating the delignification or enhancing the penetration and diffusion of the cooking chemicals into the wood chips (Chen, 1994). An example of a mechanism for improved penetration and diffusion through the addition of a surfactant was provided by Chen (1994). The surfactant, Chen (1994) stated, assisted in the removal of hydrophobic extractables that block the cooking chemicals from penetrating the chips. The uniformity of the pulp was also increased under these conditions. A desirable feature of extended delignification is the minimal capital cost requirement for digester modification or retrofitting (McDonough, 1995).

A requirement that has received attention in the literature is a provision for improved removal of the pulp from the digester at the completion of cooking. Traditionally, the pulp has been removed from the digester by blowing the contents under full digester pressure into an adjacent blow tank. This type of removal subjects the pulp to complex two- or three-phase flows with high velocities; the pulp experiences severe temperature and pressure drops and high velocity impacts with the blow tank walls. Therefore, pulp sampled from the digester at the end of cooking but before blowing demonstrated greater strength than pulp tested after the blowing process. Cyr et al. (1989) modified the discharge arrangement on a batch digester by adding dilution liquor and pumping out the contents of a cooled and depressurized digester at a low and controlled flow velocity. With this discharge arrangement, the strength levels of the discharged pulp approached those of the unblown material in the digester at the end of cooking.

Another area where a major research effort has been undertaken is in the automated control of batch digesters. Improved controlling devices for batch digesters are implemented to improve the uniformity of the pulp, reduce production costs, and save energy (Dumont, 1986). The control of batch digesters is complicated because of the inability to measure the kappa number of the pulp in the digester on-line (Lee and Datta, 1994). During a batch cook, the extent of delignification must, therefore, be conducted by secondary measurements. Recall that the kappa number is a measure of the residual lignin content in the pulp and a batch cook

generally targets a set kappa number to reach at the end of the cook. The targeted kappa number depends on the time, temperature, and type of wood chips (hardwood or softwood) in the digester among other factors. The attainment of the targeted kappa number in the digester is critical in decreasing the chemical load in the bleaching of the pulp and, hence, reducing the environmental impact.

The secondary measurements on the extent of delignification focus on determining liquid properties (Paulonis and Krishnagopalan, 1988; Lee and Datta, 1994), such as liquid temperature, lignin concentration, solid concentration, and effective alkali, or also by estimating the extent of carbohydrate degradation during cooking (Alen et al., 1991). Lee and Datta (1994) provided a review of the various empirical models, based on secondary measurements, used to assist in the control of a pulp digester. The empirical nature of the models leads to difficulties in handling major changes in the process. Examples of control techniques include a nonlinear approach using liquid analysis (Lee and Datta, 1994), the use of neural networks (Dayal et al., 1994; Yeager, 1995) and continuous process improvement techniques (Saraiva and Stephanopoulos, 1992). Other procedures to improve and optimize pulp digester operation lie in the improvement of scheduling a set of batch digesters (Hvala et al., 1993; Rihar, 1994) and improvements in the heat economy of the digesters from batch to batch (Tikka et al., 1988; Petrov...i... et al., 1995). While a review on all the various types of control techniques is beyond the scope of this section, the highlighted control procedures/techniques are the most commonly encountered in the literature.

3.3 Pulp Bleaching and Flotation De-inking

The objective of bleaching the pulp is to continue the delignification process started in cooking, thereby removing materials which contribute to the pulp color and leaving behind cellulose and hemicellulose which are inherently white. The bleaching process consists of a sequence of process stages, applying different chemicals in each stage. The most common chemicals used in bleaching stages are listed in Table 10. Based on the bleaching chemicals (i.e., chlorine, oxygen, ozone), the bleaching of pulp occurs in a three-phase mixture. The use of elemental chlorine (Cl_2) has decreased in recent years because of environmental concerns about the

linkage of chlorine bleaching and dioxin in the effluent from the bleaching plant. Elemental chlorine-free (ECF) bleaching sequences, which substitute chlorine dioxide (ClO_2) for elemental chlorine, are the primary choice presently in the paper and pulp industry. Environmental pressures to completely eliminate chlorine based products from bleaching sequences has lead the industry to explore new chemicals and processes to achieve totally chlorine-free bleaching (TCF) in the near future. The high oxidizing potential of ozone has put ozone bleaching technology at the forefront of TCF bleaching. The barriers to overcome in the application of ozone to TCF bleaching are the poor selectivity of ozone (ozone oxidizes cellulose as well as lignin), nonuniform bleaching with ozone that can adversely affect the pulp, and the high cost associated with the production of ozone (Nutt et al., 1993).

Table 10. Common Chemicals used in Bleaching of Paper Pulps

Chemical	Conditions
Chlorine	Acidic medium
Chlorine Dioxide	Acidic medium
Caustic	Alkaline extraction
Oxygen	Alkaline medium
Sodium Hypochlorite	Alkaline medium
Hydrogen Peroxide	Alkaline medium
Ozone	Acidic medium

The bleaching reaction is traditionally conducted in vertical towers approximately ten meters in height with the pulp slurry mixed with the bleaching gas at the inlet and pumped continuously through the tower. The three-phase reacting mixture travels through the column, via upflow or downflow, as a moving bed or plug flow type system. The mixing of the gas and pulp slurry at the inlet, therefore, becomes critical in providing a

uniformly bleached pulp. Coalescence of bubbles can lead to a decreased reaction rate because of a decrease in the surface area of the bubbles in contact with the pulp slurry and an increase in channeling of the gas phase through the reactor, which decreases the residence time of the gas phase in the reactor.

These bleaching reactions can be carried out under a wide range of weight percent of pulp or consistency (based on the oven dry weight of the pulp in the slurry) of the pulp phase. The choice of the percentage of pulp or pulp consistency at which the bleaching will take place is important due to several factors. The first is that the bleaching reaction occurs quickly once the bleaching chemical comes into contact with the pulp phase, especially in the case of ozone. This means that the bleaching reaction is mass transfer limited. The greatest resistance to mass transfer in a well mixed system occurs in the liquid phase that separates the gas bubble from the pulp fibers; i.e., in the mass transfer from the bulk gas phase to the surface of the fiber, see Fig. 4. Therefore, a reduction in the amount of liquid present (an increase in pulp consistency) decreases the resistance to mass transfer (White et al., 1993). Increasing the pulp consistency, however, renders the pulp less amenable to mixing in traditional mixers and more complicated designs for high consistency (25% to 28%) bleaching, in some cases, are required. An example of this, shown in Fig. 5, is the high consistency ozone bleaching paddle conveyor reactor developed by Union Camp Corporation, which is a horizontal, tubular reactor with shaft-mounted paddle-type internals (White et al., 1993). High and medium (10–14%) consistency bleaching reduces the volume of pulp slurry to be pumped and the amount of effluent to be treated at the cost of increased mixing requirements and, possibly, more complicated reactor design. Hurst (1993) demonstrated that the effectiveness of ozone as a bleaching chemical increased with increasing pulp consistency under similar reaction conditions (mixing intensity, reaction time). The downside of high consistency ozone bleaching is a loss in the viscosity of the pulp (cellulose); however, Kappel et al. (1994) reported that the strength properties were not significantly affected. Hurst (1993) also stated that increasing the reaction time for low consistency (3–9%) pulps provided results similar to the high consistency case.

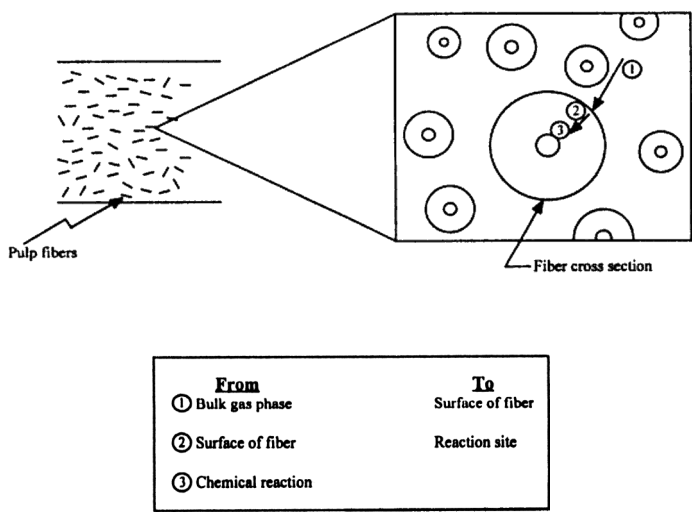


Figure 4. Mass transfer mechanism in pulp bleaching applications. (From White *et al.*, 1993.)

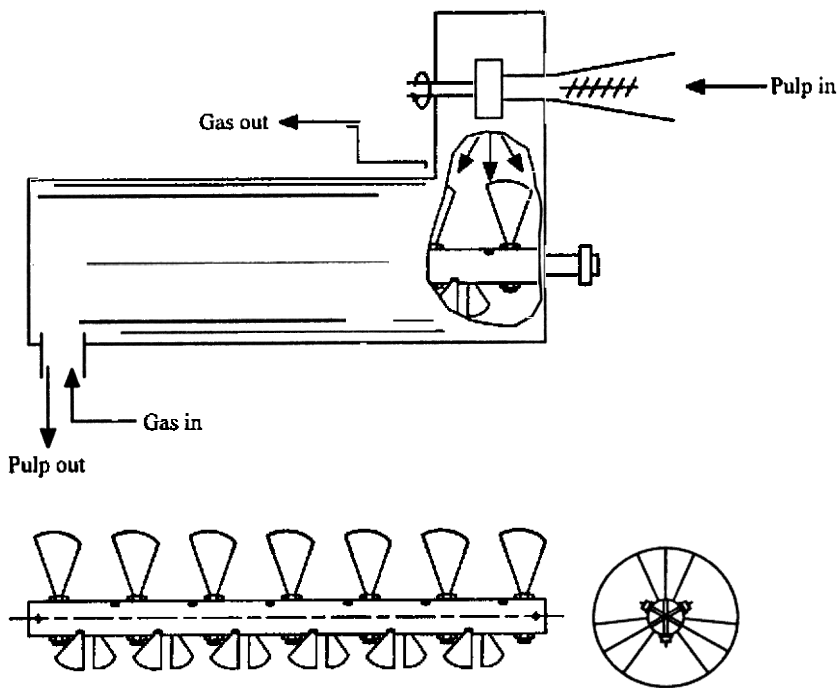


Figure 5. Union Camp Corporation's high consistency ozone bleaching paddle conveyor reactor. (From White *et al.*, 1993.)

Flotation de-inking is becoming an important process in recycling of paper fibers as the demand of recycled fiber grows based on environmental and social concerns. In flotation de-inking, gas bubbles and flotation chemicals are introduced with a slurry of recycled paper into a flotation cell where the objective is for the ink particles to detach from the fibers and adhere to the gas bubbles, then, for the ink-laden bubbles to rise to the upper portion of the cell to be removed as a foam layer. The recycling of fibers by using flotation cells is typically conducted in a series of 6 to 10 cells for efficient ink removal, which is usually in the 50–70% range. Flotation cells for de-inking evolved from mineral flotation with the notable difference that flotation de-inking occurs at much higher Reynolds numbers than mineral flotation (Lindsay et al., 1995). Several designs of flotation cells are available (see Smook, 1992), with the primary performance improvement through the years of development being a decrease in power consumption (McKinney, 1995).

The hydrodynamic behavior of the flotation cell is of paramount importance in achieving efficient operation. The basis for flotation de-inking is the hydrophobic nature of the ink particles and their ability, with the assistance of added chemicals, to adhere to the bubbles. Therefore, high bubble surface areas and the opportunity for bubble-ink particle collisions are required for efficient removal of the ink particles. Typical ink particles removed in flotation de-inking are in the size range of 20 to 200 μm . High volumes of air injected into the cell provides the required surface area for increased probabilities of bubble-ink particle collisions; however, excess turbulence can be detrimental to the overall performance because of remixing or detachment of the ink particles from the bubble (Seifert, 1994). Optimal circulation of the three-phase mixture is also required so that the bubbles carrying the ink particles reach the upper surface and are removed, not re-entrained into the cell. Pulp consistencies in flotation cells, with a range usually around 0.8–1.2%, are lower than those encountered in bleaching operations. The pulp slurry residence time in the cell is 5–20 minutes. Other factors affecting the efficiency of the flotation cell are the temperature and pH, which need to be optimized based on the chemicals and even the type of material to be recycled.

The chemicals added to the flotation cell assist in separating the ink from the fiber and enhance the ability of the ink particles to adhere to the bubble surface. A common chemical added to the cell is sodium hydroxide (NaOH) which causes the fiber to swell, thus releasing the ink particle

(Turvey, 1995). The addition of NaOH has the advantage of increasing the strength of the fibers, but the optimal pH of the cell may be significantly influenced by the addition. Other additives to the flotation cell are surfactants. The surfactants act by reducing the surface tension of the liquid, thus decreasing the bubble size to provide the high surface area and optimal bubble size for ink particle capture. The addition of any chemicals leads to consideration of their effects downstream from the flotation cell. The selection of chemicals, therefore, has to be performed carefully so that minimal adverse effects, both in the use of the recycled fibers and in the environmental impact of the effluent, are considered. Another consideration in the recycling of fibers is the effect of recycling on the quality of the pulp fibers. A review of this complicated topic is beyond the scope of this chapter, however, a recent review by Howard (1995) is recommended for the interested reader.

4.0 CHEMICAL PROCESSING

4.1 Introduction

This section covers recent advances in the application of three-phase fluidization systems in the petroleum and chemical process industries. These areas encompass many of the important commercial applications of three-phase fluidized beds. The technology for such applications as petroleum resid processing and Fischer-Tropsch synthesis have been successfully demonstrated in plants throughout the world. Overviews and operational considerations for recent improvements in the hydrotreating of petroleum resids, applications in the hydrotreating of light gas-oil, and improvements and new applications in hydrocarbon synthesis will be discussed.

4.2 Hydrotreating/Hydrocracking Petroleum Intermediates

The hydrotreating and conversion of petroleum resids into viable diesel and other lighter fuels has become important due to the large reserves of heavy crudes. *Petroleum resids* are the residual portion of the initial atmospheric crude oil distillation containing the higher molecular weight organics and many organic-metallic complexes. With stricter air pollution control and increasing mandates for the burning of cleaner fuels, hydrotreating becomes essential in the removal of the heavy metals,

including sulfur, to produce a cleaner burning fuel. Three-phase ebullated or fluidized beds are becoming the reactor of choice for processing of petroleum resids. A three-phase ebullated bed reactor used for hydrotreating consists of a liquid phase containing the petroleum reactants, an inlet gas phase of hydrogen with an outlet gas phase that contains the clean, lower molecular weight organic products, and the solid phase catalysts. In the ebullated bed reactor, the bed of catalysts is expanded by the upflow of feed hydrogen and oil and internal recycle of liquid products. The internal recycling establishes a complete mixing of the liquid phase in the reactor. The solid phase is also in a completely mixed state because of the bubbling action of the gas phase. In general, the petroleum resids from the atmospheric distillation are vacuumed distilled to produce a vacuum gas oil and a vacuum residual. It is these streams that are then hydrotreated in ebullated beds to produce cleaner fuels and/or feed streams that respond better to the fluid catalytic cracking (FCC) to produce the final fuel products.

The main objective in hydrotreating is product upgrading of heavy feedstocks through the removal of heteroatoms and metals. Because of the complex nature of the chemical processes involved, hydrotreating processes include several types of catalytic reactions that compete for the available hydrogen. These reactions include hydrodesulfurization, hydrodemetallization, hydrodenitrogenation, hydrodeoxygenation, and hydrocracking. Typically, hydrotreating catalysts consist of Mo on γ - Al_2O_3 with Co or Ni promoters. The specific surface area of hydrotreating catalysts ranges from 100 to over 300 m^2/g , and pore sizes regularly show a distribution between 40 and 200 Å. A thorough discussion of the reactions and catalysts has been provided by Fan (1989) and will not be repeated here.

Commercially demonstrated examples of ebullated bed technology for hydrotreating include Texaco's H-Oil¹ and T-STAR^{1,2} technologies and the LC-Fining process. Typically, hydrotreating of heavy crudes is conducted at temperatures between 300 and 425°C and at pressures between 5.5 and 21 MPa. Typical resid conversion is 60 ~ 65%; however higher conversions have been reported with recycle improvements (Boening et al., 1987). The applications for ebullated bed technology has expanded

¹The H-Oil and T-STAR processes are jointly licensed by Texaco and HRI, Inc.

²Acronym for Texaco Strategic Total Activity Retention.

beyond the treatment of heavy residuals to include, as mentioned previously, the pretreatment of light gas oils before entering the FCC unit. The T-STAR process has been demonstrated for vacuum distillate (light gas oil) hydrotreating/hydrocracking and can be used separately or in series with the H-Oil process, which treats the vacuum residuum (Clausen et al., 1992).

The ebullated bed reactors are operated with hydrogen and liquid feed flowing upward to expand the catalyst bed and distribute gas, liquid, and catalyst evenly across the reactor cross section. The catalyst particles are maintained in a well-mixed state, and fresh catalyst is added and withdrawn periodically to achieve uniform catalyst activity and constant product quality. The process of treating heavy crudes has been discussed in detail previously (Fan, 1989); here the process will only be discussed when combined with a process such as the T-STAR technology in a combination refinery process. The T-STAR process can be designed and operated as a separate mild hydrotreater/hydrocracker or, as mentioned, can be combined as an in-line reactor with an H-Oil reactor (Clausen et al., 1992). The inherent advantages of the use of three-phase technology, including constant catalyst activity, isothermal processing, low pressure drop, and a continuous, well-mixed reactor system, has also led to the development of the ebullated bed as a viable process to pretreat the feed to the FCC unit.

The products from the T-STAR process vary somewhat depending on the application and inlet feedstocks but generally consist of a low sulfur gasoline capable of direct inclusion in the gasoline pool, a diesel fuel capable of direct inclusion to the diesel pool, and a hydrotreated vacuum gas oil which has a FCC cracking response better than virgin gas oil. The T-STAR process can be adjusted to effectively change the reactor from a hydrotreater to a hydrocracker to increase production of either gasoline or diesel by adjusting the severity of the system. A T-STAR process in the H-Oil/T-STAR complex is used to enhance the quality of conventional H-Oil distillate products and produce a hydrotreated gas oil, which provides an excellent FCC feed (Clausen et al., 1992; Johns et al., 1993).

The T-STAR ebullated bed is shown schematically in Fig. 6. The figure demonstrates that a uniform catalyst distribution is maintained throughout the reaction chamber via the upward flow of the hydrogen, feed oil, and recycle oil. The internal recycle allows for increased conversion and assists in maintaining a uniform temperature throughout the reactor. Careful monitoring of the temperature in an ebullated bed

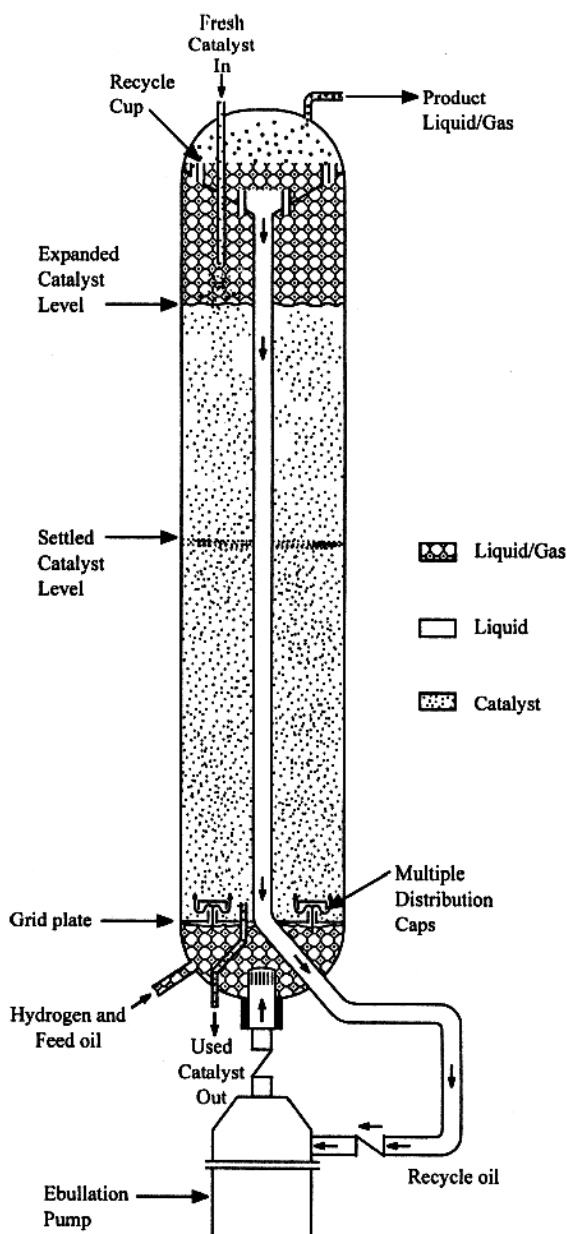


Figure 6. T-STAR three-phase ebullated bed for hydrotreating petroleum intermediates. (From Clausen et al., 1992.)

reactor is essential to prevent temperature runaway because of formation of stagnant regions or maldistribution of gas and liquid flows. The ease of on-stream catalyst replacement is also demonstrated. Since the presence of internals in an ebullated bed reactor lead to catalyst expansion in the annular region of the fluidized bed, the operation can be more precisely termed *annular three-phase fluidization*. In an air-water system at atmospheric conditions, the behavior of annular three-phase fluidized beds is different from the behavior of a “conventional” (no internals) three-phase fluidized bed with equal cross-sectional area. This altered behavior is due to the imposed physical constraints on the bed hydrodynamics, which are absent in a conventional fluidized bed of equal cross-sectional area (Fan et al., 1987a). Note, however, that a commercial ebullated bed reactor is designed with a small inner column to outer column diameter ratio and that hydrogen-hydrocarbon systems at industrial hydrotreating conditions have extremely high gas holdup with small dispersed bubbles; consequently, the physical constraints on the hydrodynamics caused by the presence of the inner column under these conditions can be negligibly small (Fan, 1989). Gas holdup (volume %) in the ebullated bed reactor can be as high as 0.50 (Tarmy et al., 1984) while the bubble size may be as small as 0.68 mm.

As described, ebullated or three-phase reactor technology has considerable flexibility in processing various feedstocks and in providing a range of products in the hydrotreating/hydrocracking of petroleum intermediates. In hydrotreating light cycle gas oil, ebullated bed technology was found to have several advantages over fixed bed hydrotreating including: smaller reactor requirement, lower hydrogen consumption, lower pressure operation, and a lower utility cost (Johns et al., 1993). The ability to continuously replace catalyst, remove large amounts of heat, and operate continuously without any quenching steps allows the ebullated bed to produce a diesel fuel that meets the EPA mandated restrictions on sulfur content. A pilot scale reactor system developed by Texaco implemented the ebullated bed technology for a six month period with constant catalyst activity maintained, and no operational problems were reported (Johns et al., 1993).

In normal operation of ebullated bed reactors, the reactor feed temperature is the control variable. The desired reactor feed temperature depends on both the feed rate and feed composition. The feed temperature is chosen such that the overall heat generation in the reactor is used to elevate the low temperature feed material to the bed temperature during

the adiabatic operation of the reactor. Additional temperature control can also be provided by immediately shutting off the hydrogen supply. Ideally the ebullated bed reactor operates without any internal nonuniformities; however, in practice such nonuniformities may occur. Adequate pressure drop across the distributor plate is needed to provide uniform gas and liquid distribution in the reactor. During steady state operation, the superficial gas velocity decreases axially because of hydrogen consumption, yet, for a given axial location, the velocity is nearly uniform with respect to radial and angular position. Other factors affecting the normal operation of ebullated bed reactors include process parameters associated with the internal recycle stream variabilities, such as liquid velocity, gas velocity, recycle cup design, and gas bubble and catalyst entrainment.

4.3 Fischer-Tropsch Synthesis

One of the most important, and perhaps the best studied, applications of three-phase fluidization is for the hydrogenation of carbon monoxide by the Fischer-Tropsch (F-T) process in the liquid phase. In this process, synthesis gas of relatively low hydrogen to carbon monoxide ratio (0.6 ~ 0.7) is bubbled through a slurry of precipitated catalyst suspended in a heavy oil medium. The F-T synthesis forms saturated and unsaturated hydrocarbon compounds ranging from methane to high-melting paraffin waxes (MW > 20,000) via the following two-step reaction:



The overall reaction of the desired hydrocarbon synthesis is thus



Selectivity to desired products including light hydrocarbons, gasoline, or diesel fuel depends upon the catalyst employed, the reactor temperature, and the type of process employed. Products of the F-T synthesis are suitable for further chemical processing because of their predominantly straight chain structure and the position of the double bond at the end of the chain. By-products formed on a lesser scale include alcohols, ketones, acids, esters, and aromatics.

The catalysts used in the F-T synthesis are produced from iron precipitation and are typically less than 50 μm in size. With the small size of the catalyst particles, the three-phase reacting system is commonly referred to as a *slurry bubble column*. The highly exothermic nature of the desired synthesis is the cause of two of the main technical problems associated with the F-T synthesis: that of removal of the heat of reaction, amounting to about 25% of the heat of combustion; and avoidance of local overheating of the catalyst, which favors methane formation and catalyst deactivation (Kolbel and Ralek, 1980). The use of a slurry bubble column reactor effectively eliminates these problems by virtue of its excellent heat transfer characteristics and temperature uniformity. Other advantages offered by the slurry bubble column over fixed beds or moving beds in the absence of liquid media include high catalyst efficiency; favorable catalyst regeneration conditions; flexibility in establishing operating conditions, which allows economical control of the synthesis; ease of addition or removal of catalyst; and simplicity of construction and, therefore, lower capital costs. One disadvantage of the slurry bubble column in this case is the degree of backmixing of the liquid and, to a lesser extent, the gas phase, which limits the conversion and specific product selectivity attainable. The backmixing problems, however, can be reduced by using baffles.

Transport properties and reaction engineering aspects of F-T synthesis have been the subject of comprehensive reviews, e.g., Kolbel and Ralek (1980), Anderson (1984), and Saxena et al. (1986). Readers are referred to these references for details on the F-T synthesis and the extensive literature listings contained in them.

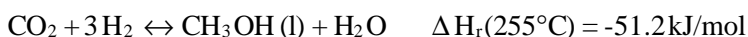
One recent development in low-temperature F-T synthesis that requires mentioning is the development by Sasol of a commercial scale *Slurry Phase Distillate process*, which produces high quality fuels, solvents, paraffins, and waxes from hydrogen and carbon monoxide. The process is located in a plant in Sasolburg, South Africa and consists of a 4.8 m diameter slurry bed reactor capable of producing environmentally friendly diesel from natural gas, providing the opportunity to convert remote natural gas reserves into low aromatic content, sulfur-free diesel fuel that burns cleanly with low particulate emissions. Sasol believes the reactor technology and operational mode provides the capability for performing exothermic reactions in slurry phase catalytic systems beyond F-T synthesis (Inga, J. R., personal communication, 1994).

Another current development in the use of F-T chemistry in a three-phase slurry reactor is Exxon's Advanced Gas Conversion or AGC-21 technology (Eidt et al., 1994; Everett et al., 1995). The slurry reactor is the second stage of a three-step process to convert natural gas into a highly paraffinic water-clear hydrocarbon liquid. The AGC-21 technology, as in the Sasol process, is being developed to utilize the large reserves of natural gas that are too remote for economical transportation via pipelines. The converted liquid from the three-step process, which is free of sulfur, nitrogen, nickel, vanadium, asphaltenes, polycyclic aromatics, and salt, can be shipped in conventional oil tankers and utilized by most refineries or petrochemical facilities.

The three-step process for the AGC-21 technology is shown in Fig. 7. The three-phase slurry reactor contains an internal heat transfer coil to provide effective heat removal from the exothermic reaction. The feed to the hydrocarbon (F-T) synthesis step is a hydrogen/carbon monoxide synthesis gas (syngas) with 2/1 H₂/CO ratio. The product from the slurry reactor is a high wax content material, which undergoes further upgrading in the third step. The catalyst is multimetallic, cobalt-based solid particles optimized for operation in a slurry environment (Eidt et al., 1994). Separations are required to recover the product from the catalyst containing slurry. Demonstration of the process has been conducted at Exxon Research and Development Laboratories in Baton Rouge, Louisiana (Everett et al., 1995) with a slurry reactor which was 1.2 m in diameter and approximately 21 m in height. The design and development target for the AGC-21 process are facilities capable of producing 8–16 km³/day of liquid hydrocarbon (Eidt et al., 1994).

4.4 Methanol Synthesis

Synthesis gas can be reacted or reformed to make methanol through highly exothermic reactions:



The first reaction produces methanol with a low hydrogen consumption, but evolves significantly greater amounts of heat. The second reaction evolves less heat, but consumes more hydrogen and produces the by-product steam. Thermodynamically, low temperatures and high pressures favor methanol formation. The reactions are carried out with copper-containing catalysts with typical reactor conditions of 260°C and 5 MPa (Probstein and Hicks, 1982).

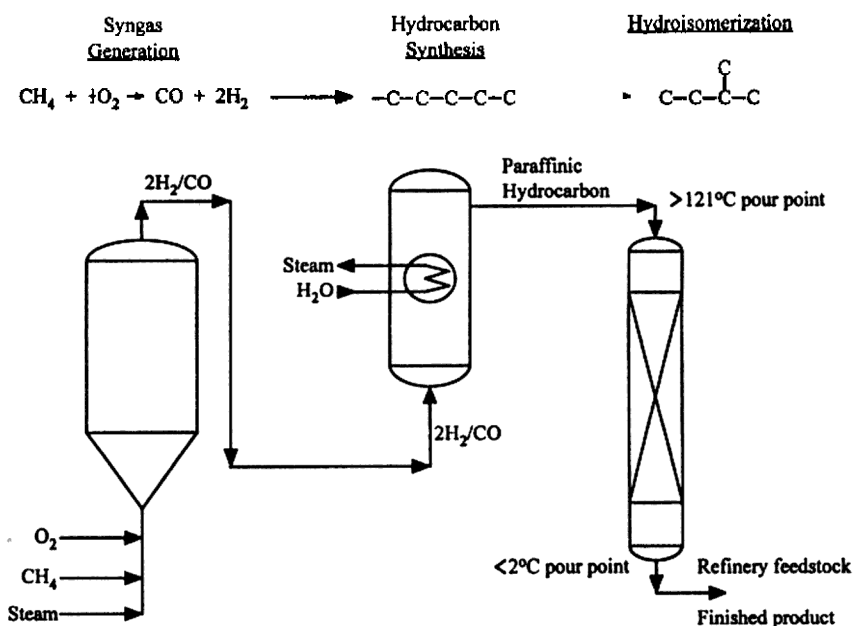


Figure 7. Exxon's AGC-21 process for conversion of natural gas into liquid hydrocarbons. (From Eidt *et al.*, 1994.)

Three-phase reactor systems are ideally suited for methanol production because of the ability to provide intimate contact between the gaseous phase reactants and the solid phase catalysts and to remove the large amounts of heat created by the high heats of reaction. In the three-phase system, an inert liquid phase circulates between the reactor and an external

heat exchanger providing the necessary heat removal. The inherent temperature uniformity of three-phase systems increases catalyst life, insures optimum selectivity and reaction rate, and reduces NO_x formation. The three-phase systems can be operated in a fluidized bed mode with catalyst particles between 3 and 6 mm in size or in a slurry bubble column mode with catalyst particles about 50 μm in size. Research efforts in catalyst activation procedures, choice of liquid medium, reactor hydrodynamics, and reactor modeling are currently being pursued for improving the process efficiency, design, and evaluations (e.g., Toseland et al., 1995).

Part II: Three-Phase Biofluidization

5.0 BIOLOGICAL APPLICATIONS OF THREE-PHASE FLUIDIZATION

5.1 Introduction

The many positive features of three-phase fluidization are readily apparent to biochemical engineers. Improved mass transfer, improved solid and liquid mixing, elimination of clogging, and other advantages of the technique as compared to packed bed and suspended cell bioreactors, detailed in Table 11, have been confirmed for a wide spectrum of biological processes, such as wastewater treatment, antibiotic production, and animal cell culture. By immobilizing cells on or in particles, washout of biomass is prevented even at relatively high flow rates, unlike the situation in continuous suspended cell reactors. Several limitations to the technique, listed in Table 12 exist; however, the favorable aspects of three-phase biofluidization often outweigh the negatives and have encouraged development of many applications, especially in wastewater treatment. Numerous examples of full-scale three-phase fluidized wastewater treatment facilities exist (Fan, 1989). Industrial fermentation and cell culture applications have been somewhat slower to develop, but are becoming more and more common.

Table 11. Advantages and Positive Features of Three-Phase Fluidized Bed Bioreactors

Advantages and Positive Features		References
immobilized cells	<ul style="list-style-type: none">• higher cell density results in higher productivity• no washout at high flow rates• may eliminate need for cell recycle	Andrews and Przechdzicki, 1986; Kargi and Toprak, 1994
greater stability	<ul style="list-style-type: none">• tolerates periods of down-time• less affected by shocks of toxic material (no washout, adsorbent particles)	Livingston and Chase, 1991; Yongming et al., 1993
degree of axial liquid mixing can be varied	<ul style="list-style-type: none">• can tailor mixing to biokinetics	Andrews and Przechdzicki, 1986; Fan, 1989
freely fluidized particles	<ul style="list-style-type: none">• no clogging and easy dispersal of gas evolved during fermentation• possibility to add/remove fourth phase for product removal• can use smaller particles than packed beds, resulting in improved intraparticle mass transfer• low pressure drop	Andrews and Przechdzicki, 1986; Qureshi and Maddox, 1988; Davison and Scott, 1992; Lazarova et al., 1994
operational flexibility	<ul style="list-style-type: none">• can treat high strength wastewaters at low rate or dilute wastewater at high rate	Borja and Banks, 1994
mechanical simplicity	<ul style="list-style-type: none">• simple construction• sterility• more easily maintained• relatively low capital cost	Siegel and Robinson, 1992; Kargi and Toprak, 1994; Merchuk et al., 1994

Table 12. Limitations of Three-Phase Fluidized Bed Bioreactors

Disadvantages		References
insufficient data and/or models available	<ul style="list-style-type: none"> • scale up difficult • sparse data from actual fermentations data 	Davison, 1989; Schügerl, 1989; Siegel and Robinson, 1992
potential for undesired particle stratification	<ul style="list-style-type: none"> • affects substrate concentration to which biomass is exposed 	Andrews and Przedziecki, 1986; Lele and Joshi, 1992
aeration rate affects agitation	<ul style="list-style-type: none"> • recycle rate can be varied to affect both 	Merchuk et al., 1994
potentially lower cell density than in packed beds	<ul style="list-style-type: none"> • lower potential volumetric productivity 	Shu and Yang, 1996

Though the various biological applications of three-phase fluidization are at somewhat different stages of development, these areas share similar process considerations that are not relevant to three-phase fluidized chemical processes, primarily as the result of the complex interaction between the biological systems and the reactor hydrodynamics, mixing characteristics, and transport phenomena. This interaction is schematically depicted in Fig. 8. The biological reaction is the goal of the process, thus the effect of the reactor characteristics on the biokinetics and vice versa are critical to the design and operation of a three-phase fluidized bed bioreactor.

This section of the current chapter goes beyond a simple listing of current three-phase biofluidization applications to consider the differences in conventional three-phase fluidization and biofluidization from the aspect of reactor design and operation. Past research into three-phase biofluidization has been summarized in several excellent reviews (Andrews, 1988; Fan, 1989; Heijnen et al., 1989; Schügerl, 1989; Siegel and Robinson, 1992), and this chapter will concentrate on the main research themes and advances of the last few years. Though gas continuous three-phase fluidized bioreactors exist (Fan, 1989), we consider here only those bioreactors in which the liquid phase is the continuous phase.

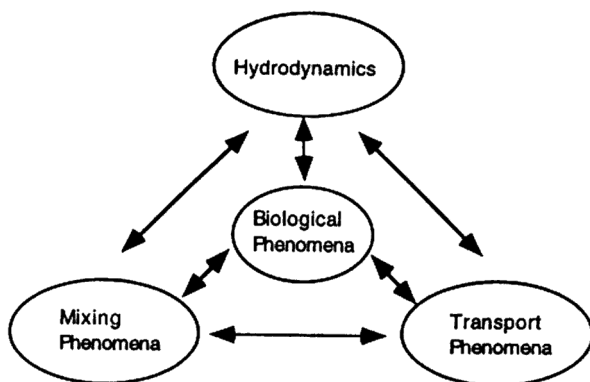


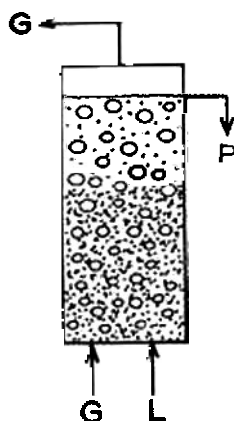
Figure 8. The relationship between biological, hydrodynamic, mixing, and transport phenomena in three-phase fluidized bed bioreactors.

The definition of phases in a three-phase fluidized bioreactor is not always as clear as in traditional three-phase fluidization applications. The solid phase is made up of bacterial, fungal, plant, or animal cells, immobilized on or in some type of support or self-immobilized in the form of flocs or pellets. If a support particle is not present, the reactor is considered to be a three-phase bioreactor if the bioflocs or cell aggregates are greater than $10\text{ }\mu\text{m}$, at which scale they can be considered heterogeneous to the liquid phase in terms of fluid dynamics (Fan, 1989). The liquid phase constitutes the medium for cell growth. The gas phase may be supplied to the reactor through a distribution plate, as is typical for other three-phase fluidization applications, or the gas phase may be generated within the reactor as part of the biochemical reactions taking place, or both. Depending on whether the fermentation is aerobic or anaerobic, the gas phase may be air, oxygen, or an inert gas. If evolved during the fermentation, the gas phase may be, for example, carbon dioxide, methane, or hydrogen.

There are a wide variety of three-phase fluidized bioreactor designs possible. The conventional reactor, shown in Fig. 9, is fluidized by both gas and liquid entering at the bottom of the reactor and leaving at the top and is the most common type of three-phase fluidized bed bioreactor. This reactor may be configured to operate with little axial liquid mixing or in a well-mixed mode by adding a recycle stream. The airlift reactor or draft tube fluidized bed reactor, Fig. 10, is also frequently used. In this reactor, gas is injected at the bottom of a draft tube placed in the center of the

column, and a cyclic flow of liquid, particles, and, sometimes, gas results. The draft tube fluidized bed bioreactor is well-mixed and has excellent mass transfer characteristics (Kang et al., 1991).

It is well understood in bioprocessing that process parameters, such as temperature, substrate concentration, and pH, affect bioreactor performance (Nagamune et al., 1988), but certain parameters not typically considered in bioreactor design, such as particle size or concentration and biofilm thickness and morphology, can dramatically affect the stability of a three-phase fluidized bed bioreactor (Oh et al., 1988). Table 13 lists many of the parameters that must be considered by the biochemical engineer in order to successfully design and operate such a bioreactor. Many of the system parameters are discussed in detail by Fan (1989) and will not be discussed further here. A comprehensive discussion of the biological parameters is beyond the scope of this chapter, and the reader is referred to the abundant literature in this field; however, this section of the current chapter attempts to provide an overview of the key biological considerations for the design and operation of three-phase fluidized bed bioreactors.



- | | |
|-------------------|------------------------------|
| L: Liquid Stream | • Immobilized Cell Particles |
| G: Gas Stream | ○ Gas Bubbles |
| P: Product Stream | |

Figure 9. Conventional three-phase fluidized bed bioreactor.



L: Liquid Stream
G: Gas Stream
P: Product Stream

• Immobilized Cell Particles
○ Gas Bubbles

Figure 10. Airlift or draft-tube three-phase fluidized bed bioreactor.

Table 13. System and Biological Parameters that Affect Three-Phase Fluidized Bed Bioreactor Performance

System Parameters	Biological Parameters
Reactor geometry and distributor design	Growth rate
Process configuration	Production rate
Gas and liquid velocities	Biomass concentration
Recycle rate	Intraparticle biomass growth
Immobilization method	Diffusivity in biofilm and bioparticle
Particle properties (density, size, porosity, shape, wettability, size distribution)	Biofilm properties (density, thickness, active fraction)
Inlet and outlet substrate concentrations	Biofilm erosion rate
Liquid properties	Biogas production rate
Temperature	

5.2 Applications

The most widespread biological application of three-phase fluidization at a commercial scale is in wastewater treatment. Several large scale applications exist for fermentation processes, as well, and, recently, applications in cell culture have been developed. Each of these areas have particular features that make three-phase fluidization particularly well-suited for them.

Wastewater Treatment. As can be seen in Tables 14a to 14d, numerous examples of the application of three-phase fluidization to wastewater treatment exist. Laboratory studies in the 1970's were followed by large scale commercial units in the early 1980's, with aerobic applications preceding anaerobic systems (Heijnen et al., 1989). The technique is well accepted as a viable tool for wastewater treatment for municipal sewage, food process waste streams, and other industrial effluents. Though pure cultures known to degrade a particular waste component are occasionally used (Sreekrishnan et al., 1991; Austermann-Haun et al., 1994; Lazarova et al., 1994), most applications use a mixed culture enriched from a similar waste stream or treatment facility or no inoculation at all (Sanz and Fdez-Polanco, 1990).

Table 14a. Recent Three-Phase Biofluidization Research on Treatment of Municipal Wastewater

Waste Stream	Inoculum	Carrier	Comments	References
municipal sewage	raw sewage	biofloc	effluent quality remained high through decrease in temperature from 20° to 5°C	Sanz and Fdz-Polanco, 1990
	mixed culture	AC	FBR was less affected by low temperatures than conventional reactor	Tseng and Lin, 1994
nitrate-containing wastewater	garden soil leachate	AC	AC biocarriers provide uniform biomass distribution and rapid restart ability	Coelhoso et al., 1992
	mixed culture	sand	rate-limiting step (reaction rate vs. diffusion rate) varied with reactor height	Green et al., 1995
nitrogen and phosphorus-containing gray water	activated sludge	biofloc	draft tube reactor; aerobic draft tube and anaerobic annular region allow two zones of microbial action	Hano et al., 1992
synthetic wastewater of glucose with or without sulfate	municipal sewage	biofloc	kinetics of organic substance decomposition in presence of sulfate reduction elucidated	Matsui et al., 1993

AC = activated carbon

Table 14b. Recent Three-Phase Biofluidization Research on Treatment of Toxic Wastewater

Waste Stream	Organism	Carrier Bead	Comments	References
phenol	Mixed culture	sand	draft tube improved fluidization; staged reactors gave excellent degradation	Etzensperger et al., 1989
		activated carbon	draft tube fluidized bed	Tzeng, 1991
			draft tube controlled biofilm thickness	Fan et al., 1987b
			FBR was less affected than conventional systems by low temperature	Tseng and Lin, 1994
		anthracite coal	oscillations of phenol concentration in effluent in response to inlet change	Worden and Donaldson, 1987
chlorophenols	sewage from coal conversion plant	activated carbon	biokinetic parameters and phenol diffusivity in biofilm estimated	Tang and Fan, 1987
	<i>Pseudomonas</i> sp.	PVA-alginate beads	counter-current fluidized bed reactor with aeration	Wu and Wisecarver, 1989
	nonacclimated activated sludge	Celite™, a silica-based support	low excess biomass production	Mäkinen et al., 1993
		sand; Celite R-633™; volcanicite; pumice	high rate bioremediation at low temperatures (4-10 °C) demonstrated	Järvinen et al., 1994
		unspecified	<i>Pseudomonas</i> spp. dominate biofilm after two years maintenance in continuous aerobic fluidized bed reactor	Puhakka et al., 1995
dichloroaniline	commercial starter culture	diatomaceous earth	biomass capable of degrading recalcitrant compound was slow growing and required special start-up procedure - packed bed biofilm development	Livingston, 1991
polluted soil	mixed soil organisms	sand	tapered column allows stratification of fine and coarse particles; independently adjustable retention times	van der Jagt et al., 1993
nitrate and selenium	<i>Thauera selenatis</i>	sand	2-stage system of recycled sludge-blanket reactor followed by fluidized bed reactor	Macy et al., 1993

Table 14c. Recent Three-Phase Biofluidization Research on Treatment of Food Plant Wastewater

Waste Stream	Organism	Carrier Bead	Comments	References
sugar-containing wastes	<i>Z. mobilis</i>	sintered glass	stable hydrolysis of waste starch, even in presence of lactic acid	Weuster et al., 1989
high salt-content, pigmented wastewater	Mesophilic sludge	Cristobalite™	addition of trace elements improved treatment of high salt and pigmented wastewater	Tanemura et al., 1994a
food-manufacturing wastewater	Mesophilic sludge	Cristobalite™	higher efficiency than that of upflow anaerobic sludge blanket	Tanemura et al., 1994b
synthetic glucose-yeast hydrolysate substrate	Mixed culture from anaerobic waste treatment reactor	sand	study of biofilm effects on oxygen transfer	Ryhiner et al., 1988
molasses and whey substrates	Sludge from an anaerobic digester	sand	at high loadings, FBR performance was better than packed bed reactor, which clogged	Denac and Dunn, 1988
ice-cream wastewater	Active municipal sludge	saponite (Magnesium silicate)	anaerobic fluidized bed tolerated shock loading; effluent quality degraded temporarily	Borja and Banks, 1995
fruit processing wastewater	Brewery wastewater sludge	saponite	various retention times (2.5 to 12.5 days) removed >97% of COD	Borja and Banks, 1994
low-sulfate lactate medium	Methanogenic consortium	porous glass	reactor response to shock loads determined by population distribution in consortium	Zellner et al., 1994
propionate-containing synthetic wastewater	Co-culture of propionate degraders	sand	during startup, bacterial population distribution in effluent not the same as in biofilm	Heppner et al., 1992
almond seed extract	activated sludge or soil slurry inocula	sand	aerobic degradation of low cyanide/high COD wastewaters demonstrated	Petrozzi and Dunn, 1994

Table 14d. Recent Three-Phase Biofluidization Research on Treatment of Industrial Wastewater

Waste Stream	Inoculum	Carrier Bead	Comments	References
monosodium glutamate fermentation wastewater	Mixed culture	activated carbon	FBR was less affected by low temperature than conventional systems	Tseng and Lin, 1994
pickling and plating wastewater from steelworks	<i>Thiobacillus ferrooxidans</i>	biofloc	hybrid circulating airlift/activated sludge reactor	Fujii et al., 1988
nitrate and selenium-contaminated wastewater	<i>Thauera selenatis</i>	sand	2-stage system of recycled sludge-blanket reactor followed by fluidized bed reactor	Macy et al., 1993
regeneration of ferrous sulphate solution	<i>Thiobacillus ferrooxidans</i>	sand	sand found to be inappropriate carrier for <i>Thiobacillus ferrooxidans</i> in FBR	Halfmeier et al., 1993

The advantages of three-phase fluidization are especially suited to wastewater treatment. For instance, the high biomass retention inherent in immobilized cell reactors allows high pollutant loading, and the ability of the reactor to handle suspended solids without clogging is ideal for many sewage streams (Andrews, 1988; Weuster et al., 1989). Three-phase fluidized bed bioreactors allow for flexible operations; flow rate and pollutant loading can be varied over a wide range, a requirement in many sewage treatment systems (Tzeng, 1991). The high productivity of three-phase fluidized bed bioreactors results in relatively compact units. This is of particular value when a given substrate can not be degraded by the wastewater treatment bioreactor that treats general plant effluents; a three-phase fluidized bed bioreactor with an inoculum tailored to the recalcitrant substrate can easily be placed at the point of generation of that substrate, treating it before the waste streams are commingled.

Current work in this area is focusing on improved carrier materials, tailoring the reactor/inoculum system to a specific waste stream, improving reactor start-up, and determining optimum operating conditions. Low temperature treatment has been shown to be feasible (Sanz and Fdez-Polanco, 1990), and responses to shock loading of organics have been elucidated in several cases (Zellner et al., 1994; Borja and Banks, 1995). Adsorption and desorption of degradable substrates by the support particle can be effective in preventing toxic shock caused by sudden increases in the substrate concentration and can prevent excess amounts of the substrate in the reactor effluent. The ability of the support particle to desorb the substrate is critical in allowing regeneration of the particles (Mol et al., 1993; Petrozzi et al., 1993). Automatic control of pH has also been studied as a method of protecting the reactor from toxic surges in effluent pollutant concentrations, improving reactor stability and effluent quality, and reducing costs for alkali to treat reactor imbalances (Denac et al., 1990; Ehlinger et al., 1994).

Conditions during start-up can have a dramatic impact on time required to reach reasonable performance levels and on the ultimate reactor performance. Dilution rate, loading rate as measured by chemical oxygen demand (COD), carrier choice, inoculum amount, inoculum strategy, and inoculum species distribution are critical parameters (Sreekrishnan et al., 1991; Araki and Harada, 1994; Austermann-Haun et al., 1994; Yongming et al., 1993). Pore characteristics have a strong influence on time required for start-up and on the ultimate biomass density in the

reactor; high porosity, adequate pore size, and large surface area all contribute to rapid reactor start-up and high cell density, though no single one of these parameters by itself is an adequate predictor of optimal cell retention for successful reactor start-up and operation (Yee et al., 1992). Control of reactor pH by controlling the feed rate has been shown to result in more rapid reactor start-up than without pH control (Hsu and Shieh, 1993).

During start-up, the microbial population distribution in the biofilm varies with time. Initial colonization of the particle may be by one or more species that alter the surface favorably for colonization by other species. For instance, in the operation of a butyrate-degrading fluidized bed bioreactor, methanogens attached to the sand particles early in the start-up process and produced a primary matrix of heteropolysaccharides that allowed attachment of other bacterial species (Sreekrishnan et al., 1991; Zellner et al., 1991; Yongming et al., 1993). This is contrary to findings in an acetate-propionate-butyrate degrading reactor, in which facultative anaerobes were found to be the initial colonizers (Lauwers et al., 1990).

The COD loading profiles used for start-up may be based on maximum efficiency or maximum loading. In the former, COD loading is gradually increased and residence time is gradually decreased as the biofilm develops; high COD removal percentages are achieved early in the reactor lifetime, but initial loading is low. The maximum loading profile starts with a short residence time and high COD loading, resulting in initially low COD removal efficiencies; the initially high substrate concentrations have been suggested to increase the rate of reactor start-up (Hsu and Shieh, 1993; Yongming et al., 1993).

One of the problems associated with waste treatment is the presence of recalcitrant or nonbiodegradable compounds in the waste stream (Keller, G., personal communication, Nov. 3, 1995). If the bioreactor cannot degrade toxic compounds that the law requires to be removed, either an alternative chemical or physical process must be completely substituted for the bioprocess or a supplemental process must be added to the treatment system. The combination of biodegradation with physical adsorption in a fluidized bed reactor has been successfully demonstrated for the treatment of cyanide-containing, phenolic wastewaters (Pfeffer and Suidan, 1989); the biofilm was immobilized on granulated activated carbon which acted as a sink for both the degradable substrate and toxic, nondegradable compounds. Fresh carbon was periodically added to the reactor, replacing exhausted carbon, so that the toxic nonbiodegradable compounds did not

build up in the bulk reactor fluid. Because much of the degradable substrate was consumed by the biofilm, carbon requirements were reduced from what they would be if no biodegradation took place (Pfeffer and Suidan, 1989).

Fermentations. Recent years have seen many investigations of fermentations to produce high-value products, such as pharmaceuticals and recombinant proteins, in fluidized bed bioreactors. Continuous production of these products in three-phase fluidized bed bioreactors is especially attractive, because the simplicity of construction of these bioreactors reduces the opportunities for contaminating organisms to gain entry to the reactor during long-term production. The advantages of three-phase fluidized bed bioreactors have also been applied to more traditional bacterial fermentations, such as lactic acid or solvent production. For fermentations such as these that exhibit product inhibition, the potential to integrate product removal with the fermentation by adding adsorbent particles as part of the solid phase of the fluidized bed is a unique advantage currently being explored by several researchers (van der Wielen et al., 1990; Davison and Scott, 1992; Kaufman et al., 1995). Though several commercial scale three-phase fluidized bed bioprocess operations exist (Fan, 1989), much of the work in applying three-phase fluidization to fermentation is still at a laboratory scale. A partial survey of this burgeoning research is given in Table 15.

Fermentation applications in three-phase fluidization have lagged those of wastewater treatment, because the goal, biosynthesis of useful chemicals, is more constrained than that of simple biodegradation of waste. Sterilization, pure culture preparation, separation of intermediate or product inhibitors, bioreactor control, specialized techniques of microbial immobilization, and product recovery must be considered. Oxygen demands are generally higher for aerobic fermentations than they are for aerobic wastewater treatment applications, because the higher substrate concentrations in a fermentation feedstock result in higher metabolic requirements for oxygen (Andrews, 1988).

Several areas are receiving much of the research attention. Approaches that integrate product recovery with the fermentation in a three-phase fluidized bed bioreactor reflect general research trends in biochemical engineering (Yabannavar and Wang, 1991; Davison and Thompson, 1992). The successful use of three-phase biofluidization has also been demonstrated for recombinant protein systems, where it may have some benefit in improving plasmid stability (Shu and Yang, 1996).

Table 15. Recent Applications of Three-Phase Biofluidization to Fermentation Processes

Product	Organism	Carrier Material	Comments	References
ABE fermentation	<i>Clostridium acetobutylicum</i>	bonechar	packed bed clogged; fluidized bed was stable	Qureshi and Maddox, 1988
		alginate beads	gas-sparging strips solvents from broth, reducing toxicity	Mollah and Stuckey, 1993
		oxygen-reducing membrane fragments in κ -carrageenan beads	membrane fragments used to provide oxygen-free microenvironment for <i>C. acetobutylicum</i>	Godia et al., 1990
ethanol	<i>Saccharomyces cerevisiae</i>	porous microcarriers - Celite R-63™	long term operation demonstrated (226 days)	Nguyen and Shieh, 1992
		calcium alginate beads	nonsterile feed and bead re-use successful	Bravo and Gonzalez, 1991
	<i>Saccharomyces carlsbergensis</i>	calcium alginate	CO ₂ bubbles enhanced mixing; productivity in multistage greater than in single stage FBR	Tzeng et al., 1991
	<i>Zymomonas mobilis</i>	porous sintered glass beads	stable, even for nonsterile feed; productivity 2X that of packed bed	Weuster et al., 1989
lactic acid	<i>Lactobacillus delbreuckii</i>	calcium alginate beads	biparticle fluidized bed for product extraction	Davison and Thompson, 1992
	<i>Lactobacillus bulgaricus</i>	agarose beads	product inhibition effects	Bassi et al., 1991
acetic acid	<i>Acetobacter aceti</i>	calcium alginate beads	demonstrated dependence of $k_p a$ on solid holdup and particle diameter	Sun and Furusaka, 1990
penicillin	<i>Penicillium chrysogenum</i>	expanded polystyrene beads	inverse fluidized bed; biofilm eroder in inner draft tube	Ramsey et al., 1991
		urethane foam	long term production (> 2 months)	Kobayashi et al., 1990
patulin	<i>Penicillium urticae</i>	κ -carrageenan beads	comparison of FBR modes	Berk et al., 1984
recombinant GM-CSF	<i>S. cerevisiae</i>	sintered glass beads	plasmid stability increased with solids concentration	Shu and Yang, 1996
ferrous iron oxidation	<i>Thiobacillus ferrooxidans</i>	styrofoam	inverse fluidized bed	Nikolov and Karamanev, 1987
atropine	<i>Atropa belladonna</i>	biofloc	segmented bubble column	Kwok and Doran, 1995
xylitol	<i>Candida tropicalis</i>	porous glass beads	low pH allows use of nonsterile feed	da Silva and Afshar, 1994
hydrocortisone biotransformation	<i>Arthrobacter simplex</i>	polyacrylamide-hydrazide beads	integrated product recovery; included cosolvent for better substrate solubility	Silbiger and Freeman, 1991
lactic acid starter culture	<i>Lactobacillus plantarum</i>	biofloc	biofloc size is reduced over that in CSTR, therefore higher productivity	Barreiro et al., 1989
glucomylase	<i>Aureobasidium pullulans</i>	calcium alginate beads	repeated batch use of immobilized cells successful for FBR	Federici et al., 1990

Cell Culture Applications. Animal cell immobilization on microcarriers is a widely used technique in animal cell culture (Kratje et al., 1994) and is as easily applied to biofluidization as to the stirred tank applications for which it was initially developed. Cell culture applications, which frequently require long culture times, benefit from the mechanical simplicity of the three-phase fluidized reactor because of the reduced likelihood of contamination. Avoidance of high intensity shear caused by agitation (Venkat et al., 1996) is another advantage of the use of

three-phase fluidized bed bioreactors for cell culture, especially for bioreactors of the airlift or draft tube type (Siegel and Robinson, 1992). Table 16 lists a number of recent cell culture applications for three-phase fluidization. These include production of monoclonal antibodies and therapeutic proteins, such as erythropoietin. Plant cells have also been cultured in airlift reactors (Scragg, 1992).

The combination of three-phase fluidization and cell culture may represent an ideal union of new technology and immediate application; because the high-value products of mammalian cell culture require relatively small production scales (on the order of 100 liters rather than 100,000 liters), it is possible to investigate the usefulness of three-phase fluidization in what would otherwise be considered a pilot scale set up without having to build an expensive, large scale unit.

Table 16. Recent Applications of Three-Phase Biofluidization to Cell Culture

Product	Cell line	Carrier	Comments	References
monoclonal antibodies	fusion of peripheral blood mononuclear cells with CBF7 cells	macroporous polyethylene beads	superior to CSTR	Reiter et al., 1994
	hybridoma cells	calcium alginate beads	FBR showed higher viability than suspension culture	Shen et al., 1994
	murine hybridoma cells	collagen beads w/ SS beads entrapped in them	SS beads for density modification of particle	Shirai et al., 1994
recombinant antibody	BHK 21 cells	Siran™ porous glass beads	synergistic effects of process variables	Rachet and Griffiths, 1993
recombinant human erythropoietin	mouse fibroblast cell line	macroporous cellulosic support, Cellsnow™	airlift type reactor superior to fluidized bed	Terashima et al., 1994
thrombomodulin	CHO-K1 cells	collagen microspheres	continuous culture with serum-free medium	Ogata et al., 1994
recombinant human interleukin-2	BHK cells	porous glass carriers	evidence of mass transfer limitations	Kratje and Wagner, 1992

BHK = baby hamster kidney cells

SS = stainless steel

CHO = chinese hamster ovary cells

5.3 Bioparticles

The type of bioparticle chosen for three-phase biofluidization often differs from that used in traditional three-phase fluidization. Small, dense particles, similar to those used in traditional catalytic three-phase fluidization applications, were often used in the initial studies of biofluidization, and for some time it was generally assumed that a bioparticle consisted of a biofilm grown on a small, dense particle (Heijnen et al., 1989). There are presently many applications, however, using cells entrapped in low density gel beads or growing within low density porous particles (Fan, 1989). These low density particles (alginate beads, 1.05 g/cm^3 ; biofilm covered sand, 1.07 g/cm^3) cause striking differences in the hydrodynamic characteristics of the biological systems compared to particles traditionally used in three-phase fluidization, such as glass beads (2.5 g/cm^3). Furthermore, the density of the particle often changes with time during the bioreaction because of cell growth, again affecting the hydrodynamics of three-phase fluidized bioreactors.

Immobilization Methods and Particle Selection. Many methods of immobilization have been developed; these and their advantages and disadvantages have been well reviewed (Fan, 1989) and will not be discussed in detail here. Immobilization by the natural formation of a biofilm on a solid support and by the entrapment of cells within a polymer such as calcium alginate are the methods most frequently used in biofluidization research. The growth of animal cells on and in microcarriers, such as macroporous sintered glass spheres, is also a widely studied method of immobilization for three-phase biofluidization. Choice of method and particle material are determined by effects of particle characteristics on reactor performance. Desirable particle qualities include ease of handling and preparation for immobilization, reusability, suitability for steam sterilization, and low cost (Gonçalves et al., 1992). Table 17 lists several examples of particles in use in three-phase biofluidization research.

It must be recalled in selecting a particle that cell immobilization of any means can affect biological processes through various physicochemical effects, such as partitioning and diffusivity, and by directly affecting cell physiology and morphology. For instance, the optimal process pH for immobilized cell systems is likely to differ from the optimal pH for suspended cell culture because of the effects of surface phenomena on local pH values (Gonçalves et al., 1992).

Table 17. Examples of Particle Materials used for Various Three-Phase Fluidized Bioreactor Applications

Wastewater Treatment	Fermentation	Cell Culture
granulated activated carbon	granulated activated carbon	collagen microspheres
sand	bonechar	porous glass microcarriers
anthracite coal	polyurethane foam	gel beads (alginate, carrageenan, etc.)
diatomaceous earth	gel beads (carrageenan, alginate, etc.)	dextran beads
biofloc	biofloc	cellulose beads
porous glass beads	styrofoam	
saponite	porous glass beads	
	polyacrylamide beads	
	polystyrene beads	

The particle materials also affect the ability of various organisms to colonize the particle and form an active biofilm through complicated mechanisms of surface charge, roughness, and porosity (Fan, 1989; Grishin and Tuovinen, 1989; Gonçalves et al., 1992). Cells growing within particle pores may be protected from shear effects (Grishin and Tuovinen, 1989; Livingston and Chase, 1991). Colonization ability has been shown to vary with species as well as with particle material (Lazarova et al., 1994). Even in studies where biomass holdup was constant, the support material affected the biomass activity (Ruggeri et al., 1994). Attrition of particles can also be important; because the attrition rate varies with superficial fluid velocity (Nelson and Skaates, 1988), a candidate material must be tested under the range of conditions anticipated in the fermentation. Colonization is also affected by process conditions such as fluid velocities and even influent composition, underscoring the need for particle screening under the expected process conditions (Gonçalves et al., 1992; Mol et al., 1993).

Biofilm Effects. Particle size and density are especially important in determining the success of biofluidization. Bioparticle size and density are determined by the initial particle properties, the extent of biomass growth, and biofilm density. For a biofilm covered support, the apparent particle density is determined by Eq. (7) (Fan, 1989).

$$\text{Eq. (7)} \quad \mathbf{r}_p = (\mathbf{r}_s - \mathbf{r}_{bw}) \left(\frac{d_o}{d_p} \right)^3 + \mathbf{r}_{bw}$$

Particle sizes used for aerobic waste treatment generally range from 100–1000 μm in size, with most being less than 500 μm in diameter, and reported biofilm thicknesses range from 40–1200 μm , with 100–200 μm being typical (Fan, 1989).

The terminal settling velocity of the particle is determined by the particle size and density as shown in Eq. (8) (Kunii and Levenspiel, 1991):

$$\text{Eq. (8)} \quad u_t = \left[\frac{4 d_p (\mathbf{r}_s - \mathbf{r}_f) g}{3 \mathbf{r}_f C_D} \right]^{0.5}$$

The effect of biofilm volume on the terminal settling velocity can be described by Eq. (9) (Andrews and Przewdziecki, 1986):

$$\text{Eq. (9)} \quad \frac{u_t}{u_{ts}} = \frac{(1 + Bx)^{1/(2-e)}}{(1 + x)^{1/3}}$$

This equation is plotted in Fig. 11, showing that for relatively dense support particles, biofilm growth can reduce the settling velocity if the biofilm density is less than that of the biofilm-free particle. As such bioparticles gain biomass, they will rise to the top of the bed and may even elutriate from the reactor (Sreekrishnan et al., 1991; Myška and Švec, 1994), reducing achievable conversion rates. This situation could be resolved by using lower density particles, such as expanded polystyrene or

polyethylene beads currently used for inverse airlift reactors (Nikolov and Karamanev, 1987; Garnier et al., 1990), for which the settling velocity actually increases as the biofilm grows (Andrews and Przedziecki, 1986).

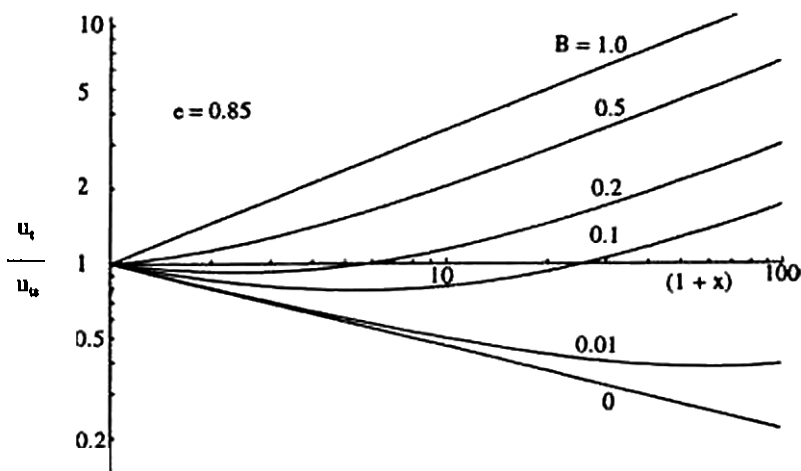


Figure 11. Effect of biofilm growth on terminal settling velocity.

Biofilm thickness and, therefore, bioparticle size, depends on the sum of biofilm growth and biofilm detachment. Detachment of biomass is a function of many parameters, including reactor operating conditions, particle material parameters such as surface roughness, and species specific parameters such as biofilm morphology (Chang et al., 1991). Increased medium concentration and fluid turbulence, as measured by the reactor Reynolds number, increased the rate of biofilm detachment in one study (Chang et al., 1991). This is supported by studies that showed that the removal of biomass could be controlled to a large extent by the gas and liquid velocities; increases in either increased the rate of biofilm removal (Roustan et al., 1993; Trinet et al., 1991). In cases where increasing the gas and liquid velocities is either ineffective in removing the desired

amount of biomass from the particles or is undesirable from an operations standpoint, the addition of a draft tube to the reactor may provide the level of turbulence required (Livingston and Chase, 1991). Alternatively, the optimal biofilm thickness can be maintained by removing particles as the biofilm grows thick and stripping or washing some of the biofilm from the particles (Andrews and Przechdziecki, 1986; Tzeng, 1991).

Modeling studies have shown that when the bed is not monosized and the difference in particle sizes is great enough, it is possible that the large particles will not reach a lower settling velocity than the small particles; hence the large particles will remain in the bottom of the bed (Myška and Švec, 1994). If biofilm thickness control is desired, removal of particles at a location other than the free surface would have to be implemented in this case.

Novel Bioparticle Research. Two major thrusts have been seen in recent particle research—the area of density manipulation so that particle density suits the desired fluidization mode, and the development of magnetic particles for use in magnetically stabilized fluidization. Intraparticle mass transfer is also of interest. Table 18 lists several novel particles developed in recent years to address these and other concerns.

Several methods have been suggested for increasing bioparticle density. Stainless steel mesh has been used as a support framework and density modifier for bioflocs for wastewater treatment. The large void volume available in the mesh, the capability of the relatively denser particles to withstand elutriation at high fluid velocities, thereby allowing higher reactor throughput, and the ability of filamentous organisms to be retained within the mesh were some of the advantages cited (Kargi and Toprak, 1994). Entrapment of stainless steel beads in collagen particles upon which mouse hybridoma cells were immobilized (Shirai et al., 1994) and the inclusion of α -alumina in calcium alginate beads (Paz et al., 1993) have also been demonstrated as methods to increase bead density.

Though most particle density manipulation research has focused on increasing density, one report addresses the possibility of decreasing particle density to allow low aspect bioreactors with low liquid velocities required for fluidization of low density bioparticles. Hollow glass spheres were co-immobilized with yeast cells in calcium alginate beads. The final particle density after cell growth could be varied in proportion to the percentage of hollow glass spheres incorporated (Vorlop et al., 1993).

Table 18. Examples of Recently Devised Novel Bioparticles

Purpose of Novel Particle	Particle material	Organism	Product / Process	References
density modification	alginate beads with α -alumina	<i>Acetobacter</i> sp.	acetic acid production	Paz et al., 1993
	alginate beads with entrapped hollow glass spheres	yeast	ethanol	Vorlop et al., 1993
	collagen beads with entrapped SS balls	murine hybridoma cells	monoclonal antibodies	Shirai et al., 1994
prevent reduction in effectiveness factor with microbial growth	alginate beads with entrapped microporous particles	<i>Zymomonas mobilis</i>	ethanol	Seki et al., 1993
provide oxygen to bacteria via algae	carrageenan beads with immobilized co-culture	<i>Bacillus subtilis</i> and <i>Scenedesmus obliquus</i>	α -amylase	Chevalier and de la Noüe, 1988
provide flexibility in derivatization	magnetic silica support particles	various organisms may be possible	tested for enzyme immobilization	Goetz et al., 1991
allow magnetically stabilized bed	magnetic alginate beads	yeast	ethanol	Weng et al., 1992

Large, light, granular particles that allow biomass growth without alteration of particle physical properties, hence, no change in fluidization characteristics, have been used for wastewater treatment in a three-phase fluidized bed; the particle material was not specified (Roustan et al., 1993). Another approach to avoiding undesired solid stratification is to periodically remove excess biofilm from the particles (Tzeng, 1991; Livingston and Chase, 1991).

Magnetic beads or support particles are used in magnetically stabilized fluidized beds. The advantages of such a bioreactor are discussed in a Sec. 5.10. A method for manufacturing a magnetic pellicular bead by electrostatically depositing alternating layers of silica and polymer onto magnetic core particles, followed by burning of the polymer and sintering of the silica, was developed to allow exploitation of the multiply derivatizable silica for various biological immobilization processes (Goetz et al., 1991). The resulting particle was dense and, thus, had increased settling velocity, allowing increased flexibility in operating conditions for the magnetically stabilized fluidized bed. This particle has been used to immobilize enzymes, but its porosity and material of manufacture suggest that it may also be suitable for microbial immobilization.

Improvement of intraparticle mass transfer is the goal of some particle research efforts. One novel approach that has been recently tested is the co-immobilization of algae with bacteria; the algae produced oxygen and the bacteria produced the desired product (Chevalier and de la Noüe, 1988). Another method used microporous particles entrapped within alginate bead bioparticles to prevent excess biomass growth that could hinder intraparticle mass transfer (Seki et al., 1993).

5.4 Hydrodynamics

Predictions of bioreactor hydrodynamics and individual phase loadings are important to allow the design engineer to specify column dimensions and to size the required pumps and blowers. The hydrodynamics of three-phase fluidized bed reactors have been studied and reviewed (Muroyama and Fan, 1985; Fan, 1989), though additional work is needed to fully understand these complex systems. The necessity for further study is even greater for three-phase fluidized bed bioreactors, the hydrodynamics of which vary greatly from traditional catalytic systems (Davison, 1989; Tang and Fan, 1990; Karamanev et al., 1992; Nore et al., 1992). As described in Sec. 5.3, the low density bioparticles common in three-phase biofluidization have dramatically different hydrodynamic characteristics than do the dense particles traditionally used in three-phase fluidization. Furthermore, the fluid flow rates used in biofluidization are relatively low compared to those found in traditional fluidization, corresponding to relatively slow biological reaction rates and the need to prevent excess erosion of the biofilm or bioparticle (Tang and Fan, 1990).

The hydrodynamic characteristics of a three-phase fluidized bed bioreactor depend on a number of factors, including particle properties, such as size, density, wettability, and roughness; fluid properties, such as flow rates, surface tension, viscosity, presence of surfactants, and electrolyte concentration; and reactor design, including column geometry and gas distributor design. Major differences between the hydrodynamics of low density systems, as typified by many biological processes, and high density systems include the presence of significant axial variation of individual phase holdups in the low density systems that are not apparent in high density particle systems (Tang and Fan, 1989; Tang and Fan, 1990), greater axial dispersion of solids (Bly and Worden, 1990), changes in bubble coalescence characteristics caused by the presence of fermenta-

tion medium components or by compounds produced by the growing cells (Sun and Furusaki, 1988; Bly and Worden, 1990; Béjar et al., 1992), and change in gas holdup because of biological gas production within the bed (Davison, 1989). These and other differences are further discussed in the following sections, with a view towards assisting the biochemical engineer to avoid pitfalls in designing three-phase fluidized bioreactors. Unless otherwise noted, the hydrodynamics discussed are those of conventional three-phase fluidized bed reactors, as shown in Fig. 9.

Fluidization Regime. As for traditional fluidization applications, the fluidization regime—dispersed bubble, coalesced bubble, or slugging—in which a three-phase fluidized bioreactor operates depends strongly on the system parameters and operating conditions. Generally, desirable fluidization is considered to be characterized by stable operation with uniform phase holdups, typical of the dispersed bubble regime. It would be useful to be able to predict what conditions will produce such behavior.

One approach recently suggested is the mapping of satisfactory and unsatisfactory biofluidization regions according to two parameters based on easily measured physical properties of the phases, such as viscosity, density, and surface tension (Béjar et al., 1992). The success of these parameters in predicting satisfactory fluidization has been demonstrated in both a straight, well-mixed, gas-fluidized bed of calcium alginate-immobilized yeast (Béjar et al., 1992; Vorlop et al., 1993) and in a tapered single-pass liquid-fluidized bed of calcium alginate-immobilized bacteria (Davison et al., 1994). Roustan et al. (1993) also applied mapping parameters to high and low density particles to predict fluidization regime with some success; however, separate maps were required for each type of particle because particle density was not included in the parameters. Further research is required to confirm the broad applicability of this approach to the prediction of whether successful fluidization is possible.

Solids Holdup. The active biomass concentration in the three-phase fluidized bed bioreactor is determined by the biofilm characteristics and the solids holdup. Because metabolic rates are moderate relative to chemical catalytic rates, solids holdup in biofluidization applications are generally larger than in chemical applications. Reported overall solids holdups in various three-phase fluidized bioprocesses range from 0.02 to 0.6, with most studies in the range of 0.05 to 0.4 (Sun and Furusaki, 1988; Davison, 1989; Kobayashi et al., 1990; Karamanev et al., 1992; Potthoff and Bohnet, 1993; Roustan et al., 1993; Badot et al., 1994). Solids holdup

below 0.55 has been recommended to prevent particle agglomeration (Andrews, 1988). Depending on bioparticle size and density, the liquid velocity will have to be adjusted to produce suitable bed porosity. Estimation of the solids holdup for expected operating conditions, along with required solids loading, is a requirement for sizing of the reactor.

The Richardson-Zaki correlation (Richardson and Zaki, 1954)

$$\text{Eq. (10)} \quad e = \left(\frac{u_l}{u_i} \right)^{\frac{1}{n}}$$

is well-accepted as a description of bed expansion in liquid-solid systems, and, with some modifications, is applicable to two-phase biofluidization (Myška and Švec, 1994). Bed expansion behavior in three-phase fluidization is more complex. This is illustrated by the observed initial contraction of some beds of small or relatively low density particles (especially pertinent to biofluidization) upon the addition of gas flow (Davison, 1989; Fan, 1989; Tang and Fan, 1989; Roustan et al., 1993). Fan (1989) provides an extensive listing of expansion correlations for three-phase fluidization and describes various approaches to predicting bed expansion in three-phase fluidization. The presence of biofilm, however, may cause these correlations to be in error, and additional work is needed in this area.

Gas Holdup. Determination and prediction of gas holdup is important in biofluidization because it provides an estimate of bed expansion and freeboard requirements and void space in the reactor, which is unavailable for bioreaction (Charles and Wilson, 1994; Bajpai et al., 1990). Estimates of gas holdup and expected bubble size can also assist in predicting oxygen transfer, a critical factor in aerobic bioprocesses, by providing an estimate of interfacial area for gas-liquid mass transport. Reported values for gas holdup range from 0.01 to as high as 0.45; values of 0.02 to 0.20 are typical (Davison, 1989; Tang and Fan, 1989; Bly and Worden, 1990; Tang and Fan, 1990; Potthoff and Bohnet, 1993; Sajc et al., 1995). Phase mixing is also affected by gas holdup, as described in Sec. 5.5.

Many factors affect gas holdup in three-phase fluidized systems, including bead size and density, liquid physical properties, temperature, sparger type, and fluid superficial velocities (Bly and Worden, 1990). System parameters such as reactor and gas distributor design can have

such an impact on the bubble and liquid flow behavior that not only are phase holdups affected, but different bubble flow regimes can be established in two systems operated under the same conditions (Bly and Worden, 1990; Tang and Fan, 1990). Results from different bioreactors must be compared with caution; however, some generalities can be made.

Overall gas holdup increases with gas velocity in the dispersed bubble regime for both low and high density particle systems (Davison, 1989; Tang and Fan, 1989; Bly and Worden, 1990; Nore et al., 1992; Potthoff and Bohnet, 1993). As gas velocity increases and the system enters the coalesced and slugging regimes, the rate of increase in the overall gas holdup decreases (Bly and Worden, 1990).

The type and loading of solid particles can affect gas holdup, though the effect is somewhat unclear, undoubtedly because of system differences. Bly and Worden (1990) found that the addition of low density particles to two-phase systems generally increased gas holdups, while the addition of high density particles decreased gas holdups. This concurs with the observation of Davison (1989) that gas holdup decreased at the top of a three-phase low density particle system in the region where it became a two-phase system (above the top of the bed). Tang and Fan (1989, 1990), also working with low density particles, however, found that gas holdups decreased with the addition of the solid phase and that as the terminal velocity of the particles increased from 0.026 m/s to 0.055 m/s, the overall gas holdup decreased further. This was attributed to the higher tendency for bubble coalescence in beds of larger terminal velocity particles. Potthoff and Bohnet (1993) found no significant influence of low density solids loading on gas holdup. Karamanev et al. (1992), working with low density polyurethane particles, found that addition of solids decreased gas holdup and that the effect was greater in a draft tube fluidized bed bioreactor.

In a study of the effect of electrolyte concentration on gas holdup, Bly and Worden (1990) found a strong effect. A salt solution resulted in twice the gas holdup that distilled water did under otherwise identical operating conditions, because the salt solution suppressed bubble coalescence. Investigation of this phenomenon is important in biofluidization, because biological media commonly have high electrolyte concentrations.

Axial variation of gas holdup depends on operating conditions and the particular bioprocess occurring in the reactor. For a gas-producing fermentation, gas holdup increased from 0.0 to almost 0.5 with axial

position as gas was produced until a point near the top of the bed, where the coalesced gas freely escaped as it rose into the solid-free region (Davison, 1989). In a study of three-phase fluidization of low density particles without gas-generating biomass, Tang and Fan (1989) found that the axial gas holdup variation could be regarded as negligible.

5.5 Phase Mixing in a Three-Phase Reactor

The degree of mixing of the phases within a three-phase fluidized bed bioreactor is important to reactor performance. Depending on the degree of mixing, individual bioparticles may experience different substrate and product concentrations, thereby influencing the overall reactor kinetics. In mixed culture systems, such as are used in wastewater treatment, the degree of mixing may affect the population dynamics and species selection within the reactor (Gommers et al., 1986; Yang, 1987).

Liquid Mixing. It has generally been found that liquid mixing in a three-phase fluidized bed of low density particles is similar to that of beds of high density particles (Gommers et al., 1986) and is strongly dependent on the regime in which the fluidized bed is operating (Fan, 1989). Axial dispersion models are generally used to describe the degree of liquid mixing, and the presence of a gas phase has been found to have a strong effect. A near absence of axial liquid mixing (dispersed bubble regime), near complete mixing, or a mixing state somewhere between these two may occur, depending on reactor conditions (Fan, 1989). Reactor diameter has an influence on mixing, with increased influence of the gas phase on liquid mixing as the diameter increased (Gommers et al., 1986).

Of interest to biofluidization is the effect of low gas flow rates, such as those found in gas-producing bioprocesses, on liquid mixing. Davison (1989) estimated the axial dispersion in both inert and fermenting three-phase fluidized bed bioreactors and found that gas flow rates comparable to that produced by the fermenting organisms increased axial dispersion. Gommers et al. (1986) obtained similar results previously, though it was noted in this study that very small (1–2 mm) bubbles produced in some bioprocesses may not have as great an effect on hydrodynamics as do larger, sparged bubbles, though flow rates may be comparable. Schoutens et al. (1986a, 1986b, 1986c) found similarly small bubbles with little effect on liquid mixing in their study of a fermenting three-phase fluidized bed bioreactor. In the design of a three-phase fluidized bed bioreactor, the extent of biogas production and whether the small biogas bubbles coalesce into larger bubbles should be considered for their effect on phase mixing.

Solids Mixing and Stratification. Bioparticle size and density has been demonstrated to strongly influence solids mixing in three-phase fluidized bed bioreactors (Bly and Worden, 1990). Small, light particles were more readily drawn into bubble wakes than were large, heavy particles and are, therefore, subject to greater mixing (Tsuchiya et al., 1992). Increased gas velocity has been shown to increase axial solids dispersion; increased liquid circulation velocity, as when the static liquid to static solid bed height ratio is reduced, decreased axial solids dispersion (Tang and Fan, 1989). Fluidization regime is also important, with the larger bubbles of the coalesced and slugging regimes producing increased solids dispersion.

The above is true for nonbiological fluidization as well as for biofluidization. An important difference is the changing nature of solids mixing and stratification in biofluidization as a result of biofilm formation, as was discussed in Sec. 5.3.

5.6 Mass Transfer

Mass transfer considerations are critical in any bioprocess. In typical, aerobic, suspended cell fermentations, the major concern is the oxygen transfer rate, determined by the overall mass transfer coefficient, k_1a , and the driving force. In three-phase biofluidization, in which the cells are immobilized as a biofilm or within carrier particles, the situation is further complicated by possible intraparticle diffusion limitations. Numerous recent studies have addressed these issues.

Gas-Liquid Mass Transfer. Gas-liquid mass transfer within the three-phase fluidized bed bioreactor is dependent on the interfacial area available for mass transfer, a ; the gas-liquid mass transfer coefficient, k_1 ; and the driving force that results from the concentration difference between the bulk liquid and the bulk gas. The latter can be easily controlled by varying the inlet gas concentration. Because estimations of the interfacial area available for mass transfer depends on somewhat challenging measurements of bubble size and bubble size distribution, much of the research on increasing mass transfer rates has concentrated on increasing the overall mass transfer coefficient, k_1a , though several studies look at the influence of various process conditions on the individual parameters. Typical values of k_1a reported in the literature are listed in Table 19.

Table 19. Typical Values of k_1a as Reported in the Literature

System	Particle	k_1a , min ⁻¹	References
conventional 3PFB	glass, $\rho = 2.5$ g/cm ³ , $d_p = 0.38$ mm	0.15-2.2	Roustan et al., 1993
	unspecified, $\rho = 1$ -1.6 g/cm ³ , $d_p = 2.7$ -4.0 mm	0.5-3.0	
	polystyrene, $\rho = 1.05$ g/cm ³ , $d_p = 2.0$ mm	0.7-3.2	Tang and Fan, 1990
	acrylic, $\rho = 1.18$ g/cm ³ , $d_p = 1.5$ mm	0.56-1.5	
	acetate, $\rho = 1.3$ g/cm ³ , $d_p = 1.0$ mm	0.80-2.2	Kang et al., 1991
	glass, $\rho = 2.5$ g/cm ³ , $d_p = 1.0$ mm	0.12-2.1	
	glass, $\rho = 2.5$ g/cm ³ , $d_p = 3.0$ mm	0.3-4.8	
DTFB	polyurethane, $\rho = 1.03$ g/cm ³ , $d_p = 3.0$ mm	0.60-2.5	Karamanev et al., 1992
	polyurethane, $\rho = 1.03$ g/cm ³ , $d_p = 3.0$ mm	0.75-5.8	Karamanev et al., 1992

Fluid velocities can have a significant effect on k_1a . Increased gas velocity within the dispersed bubble regime has been found by many investigators to substantially increase k_1a (Tang and Fan, 1990; Karamanev et al., 1992; Nore et al., 1992; Roustan et al., 1993). Increased liquid velocity also appears to increase k_1a (Kang et al., 1991); Tang and Fan (1990) determined that the increase in k_1a was due to an increase in k_1 .

Particle properties and solids loading have also been shown to have a significant effect on k_1a . Decreased particle density has been found to increase k_1a (Nore et al., 1992; Tang and Fan, 1990), and increased particle size also increased k_1a (Kang et al., 1991); the latter appears to be caused by an effect on k_1 , because bubble size and, therefore, interfacial area, was not affected (Sun and Furusaki, 1988).

The addition of high density particles, such as those used in traditional three-phase fluidization applications, decreased k_1a (Kang et al., 1991; Roustan et al., 1993); increased bubble coalescence was suggested as the cause. Adding large, low density particles, of the type often used in three-phase biofluidization, was found in one study to increase k_1a at low solids loadings (Karamanev et al., 1992), but to decrease k_1a as solids holdup increased. Other investigators report a continuous decrease in k_1a with increased solids concentration (Sun and Furusaki, 1988; Tang and Fan, 1990); however, Roustan et al. (1993) reported little effect of low density solids holdup on k_1a . Contrary to studies of three-phase fluidized

bed reactors containing rigid solids, the loading of the soft solids (polyurethane) in a draft tube three-phase fluidized bed bioreactor or in a conventional three-phase fluidized bed bioreactor did not strongly affect the volumetric mass transfer coefficient (Karamanev et al., 1992). Another study suggested that the presence of low density particles (polyurethane) promoted bubble coalescence, thereby decreased interfacial area and, hence, the volumetric mass transfer coefficient (Kobayashi et al., 1990).

Draft tube fluidized bed bioreactors have been very successful at increasing mass transfer rates, with increases in k_1a on the order of 1.5 to 3 times higher than fluidized beds without draft tubes (Karamanev et al., 1992). It has been suggested that the addition of the draft tube increases the bubble rise velocity through the increased liquid velocity within the draft tube, thereby decreasing the likelihood of bubble coalescence at the base of the reactor. The decrease in time for mass transfer appears to be offset by the larger available interfacial area for mass transfer; furthermore, many of the resulting small bubbles are entrained in the annular flow, providing additional retention time for mass transfer (Karamanev et al., 1992).

The use of floating bubble breakers has been used to increase the volumetric mass transfer coefficient in a three-phase fluidized bed of glass beads (Kang et al., 1991); perhaps a similar strategy would prove effective for a bed of low density beads. Static mixers have been shown to increase k_1a for otherwise constant process conditions by increasing the gas holdup and, therefore, the interfacial area (Potthoff and Bohnet, 1993).

Paz et al., (1993) have modified the density of calcium alginate beads by adding α -alumina to the gel in an attempt to produce beads that were more effective at breaking up bubbles in a three-phase fluidized bed bioreactor than were normal density calcium alginate beads, thereby causing an increase in interfacial area. Production of acetic acid by alginate plus alumina entrapped *Acetobacter* sp. cells was more than 2.5 times that of cells trapped only in alginate; the measured volumetric mass transfer coefficient was over three times greater.

Understanding the effect of reactor diameter on the volumetric mass transfer coefficient is critical to successful scale up. In studies of a three-phase fluidized bed bioreactor using soft polyurethane particles, Karamanev et al. (1992) found that for a classical fluidized bed bioreactor, k_1a could either increase or decrease with a change in reactor diameter, depending on solids holdup, but for a draft tube fluidized bed bioreactor, k_1a always increased with increased reactor diameter.

Tang and Fan (1990) recommended basing volumetric mass transfer coefficient determinations on the entire axial concentration profile, thereby avoiding errors caused by end effects. Kang et al. (1991) further demonstrated the applicability of this method, successfully adopting the axial dispersion model for determination of the volumetric oxygen transfer coefficient in a three-phase fluidized bed of glass beads plus floating bubble breakers. Perhaps some of the discrepancies and contradictions seen in the various studies cited above could be explained by applying this approach to the various experimental systems.

Intraparticle Mass Transfer. One way biofilm growth alters bioreactor performance is by changing the effectiveness factor, defined as the actual substrate conversion divided by the maximum possible conversion in the volume occupied by the particle without mass transfer limitation. An optimal biofilm thickness exists for a given particle, above or below which the particle effectiveness factor and reactor productivity decrease. As the particle size increases, the maximum effectiveness factor possible decreases (Andrews and Przedziecki, 1986). If sufficient kinetic and physical data are available, the optimal biofilm thickness for optimal effectiveness can be determined through various models for a given particle size (Andrews, 1988; Ruggeri et al., 1994), and biofilm erosion can be controlled to maintain this thickness. The determination of the effectiveness factor for various sized particles with changing biofilm thickness is well-described in the literature (Fan, 1989; Andrews, 1988)

Use of bioflocs rather than supported film particles will maximize the effectiveness factor for a given particle, but uneven growth of flocs can cause severe stratification in the bed. If stratification can be overcome by methods such as the use of a tapered bed to control porosity; the removal, breaking up, and recycle of biomass at the bottom of the bed; or, ideally, the use of microbial strains or species that will stop growing at a desirable floc size, such as a *Zymomonas mobilis* strain that stops growing at one millimeter in diameter (Scott, 1983), the use of bioflocs rather than support particles can improve reactor productivity.

5.7 Modeling

The complexity of the three-phase fluidized bed bioreactor is gradually coming under control as more sophisticated models become available. The chief need is for a model that integrates the microbial kinetics with the

reactor hydrodynamics in a dynamic fashion; both present challenging problems, and combining the two requires even greater insight.

Table 20 presents the features of several models presented in the literature in recent years. It is not an exhaustive list, but demonstrates some of the advances made in modeling in recent years. These advances are expected to overcome industrial resistance to the use of these complex systems.

Table 20. Recently Developed Three-Phase Biofluidization Models

	Dynamic model	Intraparticle diffusion	Liquid-solid mass transfer	Gas-liquid mass transfer	Predict reactor performance	Inhibition kinetics	Maintenance energy	suspended cells	Biofilm growth and/or sloughing	Steady state multiplicity	Low density bioparticles	Gas holdup	Solids holdup	Liquid holdup	Bubble wake	Axial liquid mixing	In situ gas production	Reactor geometry	Nonconventional reactor	Process
Hano et al., 1992		X		X	X							X							ω	m
Tang et al., 1987	X	X	X		X	X			X										3	C
Tang and Fan, 1987		X	X		X	X				X									3	C
Tong and Fan, 1988		X	X	X	X	X				X	X								3	C
Livingston and Chase, 1989		X	X		X	X													3	C
Oureshi and Maddox, 1990		X			X	X														B
Livingston, 1991		X	X		X	X													3	D
Weuster-Botz, 1993		X			X	X	X	X												A
Schoutens et al., 1986a, 1986b					X	X					X	X	X	X		X			1	B
Tang and Fan, 1989											X		X		X					G
Lele and Joshi, 1992			X	X									X					X	2	G
Chang and Rittmann, 1994												X	X	X				X		G
Farag et al., 1989	X				X	X						X	X	X	X	X		X		A
Worden and Donaldson, 1987	X	X		X	X	X			X				X	X					4	C
Wisecarver and Fan, 1989		X	X	X	X	X			X	X		X	X	X		X				C
Petersen and Davison, 1995		X			X	X					X	X	X	X		X	X	X		A

1 = airlift

2 = inverse airlift

3 = draft tube fluidized bed

4 = fluidized bed + stirred tank

A = ethanol production

B = solvent fermentation

C = phenol degradation

D = 3,4 dichloroaniline degradation

E = denitrification

As can be seen in Table 20, only a few models have incorporated both bioreactor hydrodynamics and microbial kinetics into their scheme (Worden and Donaldson, 1987; Farag et al., 1989; Wisecarver and Fan, 1989; Petersen and Davison, 1995). Of these, only a few include experi-

mental validation of their simulation results, and all of these modeled the phenol degradation process (Worden and Donaldson, 1987; Wisecarver and Fan, 1989). Development of integrated models for other biofluidization applications would be beneficial to future industrial developments.

Few models include the effects of *in situ* gas formation on the fluidization properties of the reactors; this improvement, along with improvements in other areas, such as inclusion of improved structured models of microbial kinetics or inclusion of maintenance energy requirements or the effects of suspended cells on the reaction rate, might produce more accurate models, though it is unclear at this point whether the increased complexity would be justified.

5.8 Scale Up

As mentioned previously, the design of a three-phase fluidized bed bioreactor is complex, even more so than the design of a nonbiological three-phase fluidized bed reactor. Scale-up to commercial size is relatively common for wastewater treatment, but because of the increased constraints in biosynthetic processes, fewer examples exist for these. Several are listed in Table 21. As process development techniques continue to improve as a result of advances in the understanding of engineering fundamentals, computing power, and analytical methods, the daunting task of designing a commercial scale three-phase fluidized bed bioreactor becomes less intimidating and is expected to be undertaken more frequently in the future. The traditional, linear scale-up approach, proceeding from kinetic studies at lab scale, determining pilot plant specific correlations in small pilot plants, building a large demonstration unit based on pilot plant experiments then developing a model specific to the large demonstration unit, and, finally, building the commercial reactor and only then tuning the correlations for the final plant, is being replaced by a more interactive approach, in which a unified model that considers kinetics, thermodynamics, hydrodynamics, and hardware is reconciled to data at all scales. Not only does this allow more confidence in the final design, it also results in a better understanding of the process (Tarmy and Coulaloglou, 1992).

An example of the application of a unified model to the design of a three-phase, fluidized bed bioreactor is the scale down, scale up procedure. A model of the full scale reactor is developed, then is used to design

a scaled-down laboratory reactor. The laboratory reactor is built and used for a series of experiments, the data from which are used to validate the model. If the model is validated, it can then be used as the basis for a full scale design. Schoutens et al. (1986a, 1986b, 1986c) used this approach to show that a fluidized bed reactor was the preferred design for the production of butanol and isopropanol by *Clostridium spp.* immobilized in calcium alginate beads (Schoutens et al., 1986a). The model, developed for a 50–65 m³ reactor, was shown to be accurate in predicting the results in 10–15 dm³ reactors, thereby confirming its reliability for large scale design, according to the authors (Schoutens et al., 1986c).

Table 21. Examples of Pilot and Large Scale Applications of Three-Phase Biofluidization to Fermentation Processes

Product	Organism; carrier	Reactor type and size	Comments	References
yeast biomass	<i>S. cerevisiae</i> ; biofloc	airlift tower loop reactor; 4000 L	gas holdup greater in pilot plant than at lab scale	Fröhlich et al., 1991a; 1991b
xanthan gum	<i>Xanthomonas campestris</i> ; biofloc	airlift; 1200 L	oxygen depletion in downcomer	Suh et al., 1992
		bubble column; 50 L	improved performance compared to airlift reactor	Suh et al., 1992
ethanol	<i>Z. mobilis</i> ; porous glass carriers	continuous FBR; 55 L	nonsterile hydrolyzed B-starch successful feed	Weuster-Botz et al., 1993
	<i>Z. mobilis</i> ; κ-carrageenan beads	FBR; 40L	hydrodynamics improved compared to lab scale; no slugging	Webb et al., 1995

Another, more traditional, approach to scale-up is application of similarity through dimensional analysis. One comparison of several such design criteria (biological, dynamic, and geometric) for biological fluidized bed reactors found that of the parameters tested, the sludge retention time (STR), the Peclet number, and the particle Reynolds number were most suitable for scale-up (Ozturk et al., 1994). Because of constraints on particle size and material, and fluid viscosity, it is difficult to maintain similarity in all relevant dynamic similarity criteria simultaneously. Conservative measures, such as using low estimates of such values as the overall mass transfer coefficient (Ryhiner et al., 1988), are suggested, in any case.

Time constants for the process can provide relevant information for scale up. A comparison of the conversion time constant to the time constant for mixing allows determination of whether mixing will affect the process (Gommers et al., 1986; Schoutens et al., 1986a, 1986b, 1986c). If mixing is incomplete or the time constant for mixing is much larger than the time constant for conversion, conditions will differ at different heights in the reactor and biological stratification, which may or may not be desirable, may occur (Gommers et al., 1986).

Few other design examples exist in the literature. Schneeberg (1994) provides one in which a fluidized bed upgrade is added to an existing paper mill wastewater treatment plant. Badot et al. (1994) also gave a brief example of design for both a pilot scale and industrial scale reactor for various wastewater treatment applications. Andrews (1988) provided another example of aerobic wastewater treatment focusing on bioparticle optimization.

5.9 Process Strategy

Before the details of a particular reactor are specified, the biochemical engineer must develop a process strategy that suits the biokinetic requirements of the particular organisms in use and that integrates the bioreactor into the entire process. Reactor costs, raw material costs, downstream processing requirements, and the need for auxiliary equipment will all influence the final process design. A complete discussion of this topic is beyond the scope of this chapter, but a few comments on reactor choice for particular bioprocesses is appropriate.

For those bioprocesses that follow Monod kinetics without substrate inhibition, a reactor configuration approaching plug flow behavior will give the highest rates of conversion. In three-phase fluidization, this means a high height to diameter ratio, within power consumption limits. The use of multiple stages is one possibility for overcoming the power consumption limitation on reactor height and would have additional benefits for bioprocesses in which separation of biomass growth and product generation is desirable (Fan, 1989).

If substrate inhibition exists, a well-mixed bioreactor is desirable. Mixing in three-phase fluidized bed bioreactors can be increased by adding an external recycle loop, by inserting a draft tube in the reactor, or by decreasing the height to diameter ratio.

Conversely, product inhibition suggests the use of a reactor that emulates plug flow, as for the Monod kinetics without substrate inhibition discussed above. Alternatively, in situ product removal may alleviate product inhibition and improve productivity (Yabannavar and Wang, 1991). A bioparticle reactor for simultaneous fermentation/adsorption of fermentation or enzyme reaction products has been suggested and demonstrated by several workers (van der Wielen et al., 1990; Davison and Scott, 1992; Kaufman et al., 1995). Such a reactor makes use of the particle stratification observed in fluidized bed reactors, according to particle size and density. This allows a denser adsorbent particle to be added at the top of the reactor, from which it falls through the fluidized bed of biocatalysts, absorbing product as it passes. The dense beads are removed from the base of the bed and may be regenerated by product recovery for further use. By removing the product, which may inhibit the biological reactions taking place in the reactor, productivity is improved.

When mixed cultures are involved, the reaction kinetics may be complicated by interspecies relationships. For example, in the treatment of various waste waters, a Monod-type kinetics relating removal rate to organic loading rate has been verified (Converti et al., 1993). As expected, when the loading rate was increased or the residence time was decreased, either of which increase the substrate concentration, removal rate increased (Converti et al., 1993); however, this increased removal rate came at the cost of decreased removal efficiency. The initial biodegradative reaction (acidogenic) increased in rate faster than did the final reaction (methanogenic), resulting in a deleterious accumulation of organic acids. This had to be monitored and ameliorated through the addition of base to the reactor to protect the methanogenic stage (Converti et al., 1993).

For situations, such as the example above, where mixed cultures of degradative organisms have different optimal growth conditions, multiple stages would be desirable (Converti et al., 1993). This approach has been successfully demonstrated and, with the addition of a recycle stream from the second stage to the first, has been shown to have the additional cost-saving benefit of reducing operating costs by decreasing the amount of caustic required for pH control, the major operational cost for full-scale anaerobic treatment plants (Romli et al., 1994). Another approach to multiple environmental optima for various species is the stratified bed suggested by Yang (1987), shown in Fig. 12. Use of support beads of various terminal velocities and a tapered bed can result in little or no axial

solid mixing; organisms would then be allowed to colonize the particular reactor region in which environmental conditions were optimal for each species involved.

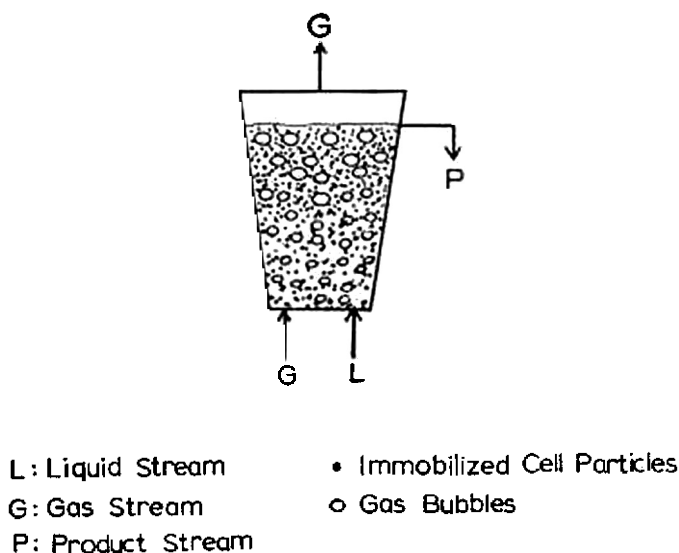


Figure 12. Tapered-bed three-phase fluidized bed bioreactor.

5.10 Novel Reactors

Magnetically stabilized fluidized beds, in which a magnetic field is applied to the fluidized bed of magnetic particles, stabilizing the bed, have been suggested for several different bioprocesses (Hu and Wu, 1987; Siegel, 1987; Bramble et al., 1990; Terranova and Burns, 1991; Weng et al., 1992). Among the advantages cited for such a bioreactor include low pressure drops and ease of solids handling as expected in fluidization, yet somewhat ordered bed structure with little or no solids mixing, depending on flow regime, as expected in a packed bed, so that particle residence time can be tightly controlled. The stabilized bed allows higher flow rates without particle elutriation than could be used in conventional fluidization. Possible fluidization regimes described in the literature include particulate fluidization under weak magnetic fields, chain fluidization under increased magnetic fields, and, finally, magnetically condensed, in

which the bed is no longer fluidized. For the particulate and chain regimes, bed height has been shown to decrease as the field strength is increased. Gas holdup was affected by magnetic field strength, as well, increasing with increasing field strength (Hu and Wu, 1987), probably because magnetically stabilized particles had a greater tendency to break bubbles apart (Weng et al., 1992), and smaller bubbles have a slower rise velocity, resulting in greater gas holdup. Gas-liquid mass transfer was increased for the same reason (Weng et al., 1992). Radial distribution of gas and liquid flows tended to flatten with increased magnetic field (Hu and Wu, 1987; Weng et al., 1992).

Several applications of magnetically stabilized fluidized beds for bioprocessing have been demonstrated. Continuous cell suspension processing has been demonstrated in a magnetically stabilized fluidized bed that acted like a moving depth filter from which the solid matrix could be continuously removed to avoid clogging (Terranova and Burns, 1991); though this was demonstrated in a two-phase system, similar three-phase applications could be envisioned. Continuous ethanol fermentation has been performed in a three-phase magnetic fluidized bed (Weng et al., 1992). Production of caffeine and theobromine by plant cells in alginate magnetized with magnetite (Fe_3O_4) has also been demonstrated (Bramble et al., 1990). Other applications are likely to be demonstrated in the future.

Several improvements in the conventional airlift reactor have been suggested. Inverse fluidized bed bioreactors, based on airlift bioreactor principles and shown in Fig. 13, have been developed by several workers (Garnier et al., 1990; Nikolov and Karamanev, 1987, 1990). Low density, biofilm-covered particles are floated in the annular region of the airlift reactor; as the biofilm thickness increases, the particle density also increases and the particle bed expands downward. When the density is sufficiently high so that the particles reach the bottom of the bed, the particles are swept into the airlift sparged section in the reactor center where hydrodynamic forces strip some of the biofilm from the particles which then travel to the top of the reactor and return to the annular region. This cyclic mixing pattern has been shown to maintain a uniform biofilm thickness (Garnier et al., 1990). By adding a contained fluidized bed of coarser, denser particles in the airlift section, Nikolov and Karamanev (1987), improved attrition of biofilm from the particles. This reactor was superior to a conventional airlift reactor that used suspended cells for aerobic wastewater treatment by a mixed bacterial culture and for ferrous iron oxidation by *Thiobacillus ferrooxidans*.

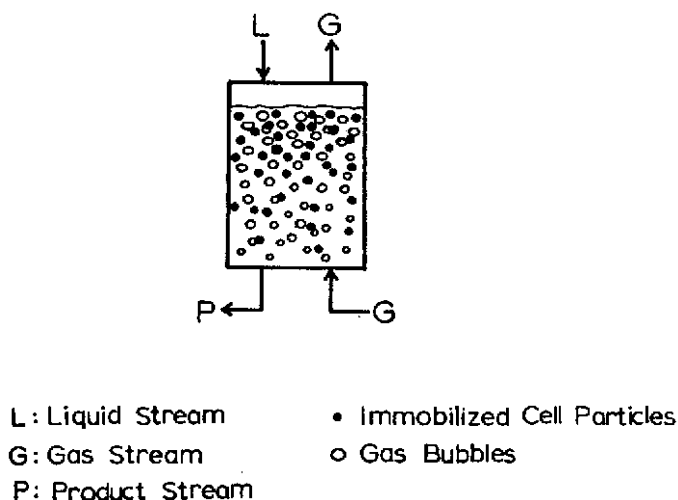


Figure 13. Inverse three-phase fluidized bed bioreactor.

In order to increase radial mixing in airlift reactors, Merchuk et al. (1993) placed helical flow promoters (helical baffles) into the upper annular region, causing secondary flows that not only increased radial mixing, thereby improving light (for plant cell culture), heat, and mass transfer, but also enhanced the fluidization of solid particles in the reactor by generating swirling flow at the base of the reactor.

The *dually injected turbulent separation* (DITS) three-phase fluidized bed bioreactor described by van der Jagt et al. (1993) separated large and small soil particles for optimal simultaneous bioremediation. Air and recycled liquid were simultaneously injected into the reactor base, fluidizing coarse, heavy soil particles in the lower region of the reactor and suspending fine particles in the upper region. Because the small particles in a contaminated soil carry a disproportionate amount of the pollutant, they require greater time for efficient biodegradation of the contaminant. By exploiting the stratification caused by fluidization, this reactor design allows large particles to be drawn off separately from the small particles, which are recycled to the bottom of the reactor and thus receive the longer treatment they require. Reactor size and cost is kept at a minimum, because each portion is treated only as long as absolutely required.

A continuous centrifugal bioreactor, in which cells are fluidized in balance with centrifugal forces, has been designed to allow high density cell cultivation and superior aeration without elutriation of the suspended cells (van Wie et al., 1991). Reactor performance was hampered by elutriation of biomass by evolved gas in an anaerobic fermentation, indicating that it may not be suitable in its present state for three-phase fermentations. Immobilization of the cells on denser particles may overcome this problem.

In order to simultaneously achieve the advantages of plug flow operation (controlled residence time, reduced product inhibition) along with the advantages of intense mixing in each consecutive stage (good transport properties), the Blenke-Cascade reactor has been designed at the University of Hohenheim (Kottke et al., 1991). This reactor is a heavily baffled tower divided into many chambers by the baffles. Each chamber is well-mixed by fluidizing gas passing up the tower; the solid particles (biocatalysts) and liquid may flow co- or countercurrently.

Several researchers have suggested contained fluidized bed for bioprocesses; such a reactor is depicted in Fig. 14. Kalogerakis and Behie (1995) have designed a three-phase/two region bioreactor for vaccine production. The bioparticles (microcarriers for animal cell culture) are contained in one region of the reactor and are kept in suspension by gentle mechanical agitation. An overall liquid flow is imposed on the whole reactor by the action of sparging in a separate central region, resulting in something of a hybrid of an airlift reactor and agitated reactor. Because the sparged section provides excellent aeration, the outer cell-containing region requires only mild agitation.

Naouri et al. (1991) described another contained fluidized bed, the so-called *high compacting multiphasic reactor (HCMR)*, which they used for malic and lactic acid fermentations for wine improvement. Bioparticles were contained within a tapered region and liquid was rapidly recycled through this region by pumping; improved liquid/solid contact was cited as the advantage of this reactor.

Gas logging, the adherence of small bubbles to particles, causing them to rise to the surface in the reactor and form an inefficient packed bed with poor mass transfer properties, can be a problem in various fermentations and in wastewater treatment. A double entry fluidized bed reactor has been developed with simultaneous top (inverse) and bottom (conventional) inlets to overcome this problem (Gilson and Thomas, 1993).

Effluent is drawn off from a side port. Under conditions in which a conventional three-phase fluidized bed bioreactor operated in an unstable manner because of gas logging, the new bioreactor converted glucose to ethanol at a 27% higher rate. *Saccharomyces cerevisiae* was grown in alginate beads for this reaction.

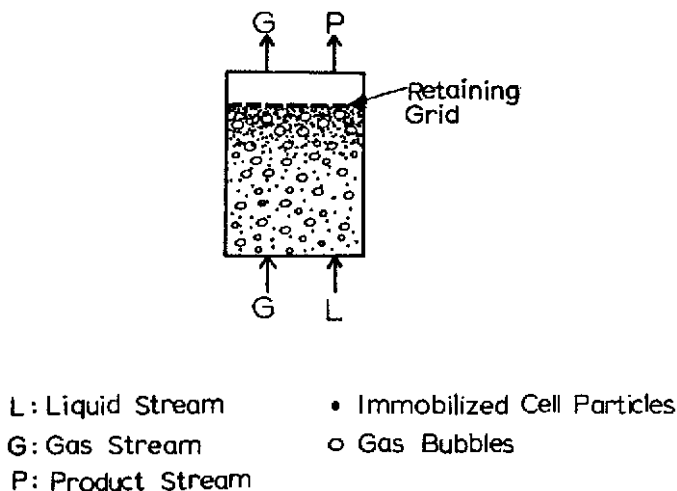


Figure 14. Contained three-phase fluidized bed bioreactor.

5.11 Economics

The economics of ethanol fermentations have been examined by several researchers (Busche and Allen, 1989; Busche et al., 1992; Harshbarger et al., 1995). Though the economic feasibility of the ethanol fermentation is dependent on the price of competitive petrochemical routes (and is currently unfavorable), the application of three-phase fluidized bed bioreactor technology improves the economics over those for conventional reactors by reducing operating costs through improved conversion and yield, by lowering utilities costs, and by reducing capital costs. Similar improvements were found when three-phase fluidized bed bioreactor technology was applied to the acetone-butanol-ethanol fermentation, with the addition of a membrane process to remove product and

prevent product inhibition (Qureshi and Maddox, 1992). Another ABE fermentation scheme that included product removal by the inclusion of a fourth, extractive phase, showed outstanding improvements in process economics, reducing projected product costs by more than half (Busche and Allen, 1989); this improvement was not sufficient to beat the price for petrochemically derived butanol, but is an indication that as petroleum prices rise, three-phase biofluidization has a definite place in bioprocess design. These improvements in process economics are likely to be applicable to other fermentation processes.

For waste treatment rather than fermentation for product formation, again few examples of process economics exist in the literature. Those that do, favor fluidization. Badot et al. (1994) described an industrial prototype fluidized bed reactor that competed favorably on an economical basis with activated sludge processes for treating carbon pollution and was estimated to be economically comparable to fixed bed processes for denitrification. Schneeberg (1994) described the successful and economically-sound implementation of fluidization as an upgrade to an existing wastewater treatment plant. The restricted space available for extension of the wastewater plant made fluidization particularly advantageous in this case.

5.12 Summary

The complexity of the interaction of reactor hydrodynamics and performance with the biological metabolic processes is the major deterrent to widespread use of three-phase fluidization in biological processes. Most commercial applications of three-phase fluidization have thus far been in the area of wastewater treatment. Commercial fermentation and animal cell culture applications exist, but much of the work in this area remains at laboratory scale. In fermentation or cell culture systems, the solid phase is typically much lower in density than that found in traditional three-phase fluidized systems, and reactor hydrodynamics and transport properties can vary dramatically from those well-studied systems. As a greater understanding of reactor fundamentals for the new applications is obtained, more successful commercial applications of three-phase biofluidization for fermentations and cell culture are likely. Fortunately, the last few years have seen great strides in understanding the complex relationships of biofluidization, allowing increased confidence in design of large scale systems based on laboratory data.

ACKNOWLEDGMENT

The authors would like to express their appreciation to researchers at BHP in Australia for providing information on the recent developments in smelting reduction of iron ore.

NOTATIONS

a	=	Gas-liquid interfacial area
B	=	Ratio of buoyant density of the biofilm to the buoyant density of the support
C_D	=	Drag coefficient
d_o	=	Diameter of biofilm-free particle
d_p	=	Diameter of a particle
e	=	Exponent on Reynolds number coefficient correlation
F_r	=	Radiation heat flux in the r direction
F_z	=	Radiation heat flux in the z direction
g	=	Gravitational acceleration
DH_r	=	Heat of reaction
k_a	=	Absorption coefficient
k_l	=	Gas-liquid mass transfer coefficient
n	=	Richardson-Zaki index
r	=	Radial coordinate
S_H	=	Source term for enthalpy equation
T	=	Temperature
u_i	=	Extrapolated liquid velocity as $e \rightarrow 1$ for liquid-solid fluidized bed
u_l	=	Superficial liquid velocity
u_t	=	Terminal settling velocity of a single particle
u_{ts}	=	Terminal settling velocity of a biofilm-free particle
x	=	Ratio of film volume to support volume
z	=	Axial coordinate

Greek Symbols

e	=	Void fraction
r_{bw}	=	Wet density of biofilm

r_f	=	Density of fluid
r_p	=	Apparent density of bioparticle
r_s	=	Density of nonporous particle or effective density of nearly nonporous particle
s	=	Stefan-Boltzmann constant

REFERENCES

- Alen, R., Hentunen, P., Sjoestroem, E., Paavilainen, L., and Sundstrom, O., "New Approach for Process Control of Kraft Pulping," *J. Pulp Paper Sci.*, 17(1):J6 (1991)
- Anderson, R. B., *The Fischer-Tropsch Synthesis*, Academic Press (1984)
- Andrews, G., "Fluidized-Bed Bioreactors," *Biotechnol. Gen. Eng. Rev.*, 6:151 (1988)
- Andrews, G. F., and Przezdziecki, J., "Design of Fluidized-Bed Fermentors," *Biotechnol. Bioeng.*, 28:802 (1986)
- Araki, N., and Harada, H., "Population Dynamics of Methanogenic Biofilm Consortium during a Start-Up Period of Anaerobic Fluidized Bed Reactor," *Wat. Sci. Tech.*, 29(10-11):361 (1994)
- Aukrust, E., and Dowling, K. B., "The AISI Direct Steelmaking Program," *AIME Ironmaking Conf. Proc.*, p. 659 (1991)
- Aukrust, E., "Planning for the 400,000 tons/year AISI Ironmaking Demonstration Plant," *AIME Ironmaking Conf. Proc.*, p. 341 (1993)
- Austermann-Haun, U., Seyfried, C. F., Zellner, G., and Diekmann, H., "Start-Up of Anaerobic Fixed Film Reactors: Technical Aspects," *Wat. Sci. Tech.*, 29(10-11):297 (1994)
- Badot, R., Coulom, T., de Longeaux, N., Badard, M., and Sibony, J., "A Fluidized-Bed Reactor: The Biolift Process," *Wat. Sci. Tech.*, 29(10-11):329 (1994)
- Bajpai, R., Thompson, J. E., and Davison, B. H., "Gas Holdup in Three-Phase Immobilized-Cell Bioreactors," *Appl. Biochem. Biotechnol.*, 24/25:485 (1990)
- Barreto, M. T. O., Melo, E. P., and Carrondo, M. J. T., "Starter Culture Production in Fluidized Bed Reactor with a Flocculent Strain of *L. plantarum*," *Biotechnol. Lett.*, 11:337 (1989)
- Bassi, A. S., Rohani, S., and MacDonald, D. G., "Fermentation of Cheese Whey in an Immobilized-Cell Fluidized-Bed Reactor," *Chem. Eng. Comm.*, 103:119 (1991)

- Béjar, P., Casas, C., Gòdia, F., and Solà, C., "The Influence of Physical Properties on the Operation of a Three Phase Fluidized-Bed Fermenter with Yeast Cells Immobilized in Ca-Alginate," *App. Biochem. Biotechnol.*, 34/35 (1992)
- Berk, D., Behie, L. A., Jones, A., Lesser, B. H., and Gaucher, G. M., "The Production of the Antibiotic Patulin in a Three Phase Fluidized Bed Reactor: I. Effect of Medium Composition," *Can. J. Chem. Eng.*, 62:112 (1984)
- Birch, J. R., Boraston, R., and Wood, L., "Bulk Production of Monoclonal Antibodies in Fermenters," *Trends in Biotech.*, 3(7):1 (1985)
- Bly, M. J., and Worden, R. M., "Gas Holdup in a Three-Phase Fluidized-Bed Bioreactor," *Appl. Biochem. Biotechnol.*, 24/25:553, (1990)
- Boening, R. E., McDaniel, N. K., Petersen, R. D., and Van Driesen, R. P., "Recent Data on Resid Hydrocracker," *Hydrocarbon Proc.*, 66:59 (1987)
- Borja, R., and Banks, C. J., "Kinetics of an Anaerobic Fluidized Bed System Used for the Purification of Fruit Processing Waste-Water," *Chem. Eng. J.*, 54:B25 (1994)
- Borja, R., and Banks, C. J., "Response of an Anaerobic Fluidized Bed Reactor Treating Ice-Cream Wastewater to Organic, Hydraulic, Temperature and pH Shocks," *J. Biotechnol.*, 39:251 (1995)
- Bramble, J. L., Graves, D. J., and Brodelius, P., "Plant Cell Culture Using a Novel Bioreactor: The Magnetically Stabilized Fluidized Bed," *Biotechnol. Prog.*, 6:452 (1990)
- Bravo, P., and Gonzalez, G., "Continuous Ethanol Fermentation by Immobilized Yeast Cells in a Fluidized-Bed Reactor," *J. Chem. Tech. Biotechnol.*, 52:127 (1991)
- Brotzmann, K., "Smelting Reduction in Iron Baths," *Steel Res.*, 60:110 (1989)
- Busche, R. M., and Allen, B. R., "Technoeconomics of Butanol Extractive Fermentation in a Multiphase Fluidized Bed Bioreactor," *Appl. Biochem. Biotechnol.*, 20/21:357 (1989)
- Busche, R. M., Scott, C. D., Davison, B. H., and Lynd, L. R., "Ethanol, the Ultimate Feedstock," *Appl. Biochem. Biotechnol.*, 34/35:395 (1992)
- Chang, H. T., Rittmann, B. E., Amar, D., Heim, R., Ehlinger, O., and Lesty, Y., "Biofilm Detachment Mechanisms in a Liquid-Fluidized Bed," *Biotechnol. Bioeng.*, 38:499 (1991)
- Chang, H. T., and Rittmann, B. E., "Predicting Bed Dynamics in Three-Phase, Fluidized-Bed Biofilm Reactors," *Wat. Sci. Tech.*, 29(10-11):231 (1994)
- Charles, M., and Wilson, J., "Fermentor Design," *Bioprocess Engineering: Systems, Equipment, and Facilities*, (B. J. Lydersen, N. A. D'Elia, and K. L. Nelson, eds.), p. 3, John Wiley & Sons, New York (1994)

666 *Fluidization, Solids Handling, and Processing*

- Chen, G. C., "Application of a Surfactant as a Kraft Pulping Additive," *Tappi J.*, 77(2):125 (1994)
- Chevalier, P., and de la Noüe, J., "Behavior of Algae and Bacteria Co-Immobilized in Carrageenan, in a Fluidized Bed," *Enzyme Microb. Technol.*, 10:19 (1988)
- Clausen, G., Chan, T., Nongbri, G., and Kaufman, H., "Texaco Processes for a Bottomless Hydrogen Refinery," paper presented at the Japan Petroleum Institute Conference on Refining Technologies, Tokyo (1992)
- Coelhoso, I., Boaventura, R., and Rodrigues, A., "Biofilm Reactors: An Experimental and Modeling Study of Wastewater Denitrification in Fluidized-Bed Reactors of Activated Carbon Particles," *Biotechnol. Bioeng.*, 40:625 (1992)
- Converti, A., Del Borghi, M., and Ferraiolo, G., "Influence of Organic Loading Rate on the Anaerobic Treatment of High Strength Semisynthetic Waste Waters in a Biological Fluidized Bed," *Chem. Eng. J.*, 52:B21 (1993)
- Cyr, M. E., Embley, D. F., and MacLeod, J. M., "Stronger Kraft Softwood Pulp - Achieved!," *Tappi J.*, 72(10):157 (1989)
- da Silva, S. S., and Afschar, A. S., "Microbial Production of Xylitol from D-Xylose using *Candida Tropicalis*," *Bioproc. Eng.*, 11:129 (1994)
- Davison, B. H., "Dispersion and Holdup in a Three-Phase Fluidized-Bed Bioreactor," *Appl. Biochem. Biotechnol.*, 20/21:449 (1989)
- Davison, B. H., and Scott, C. D., "A Proposed Bioparticle Fluidized-Bed for Lactic Acid Fermentation and Simultaneous Adsorption," *Biotechnol. Bioeng.*, 39:365 (1992)
- Davison, B. H., and Thompson, J. E., "Simultaneous Fermentation and Separation of Lactic Acid in a Bioparticle Fluidized-Bed Bioreactor," *Appl. Biochem. Biotechnol.*, 34/35:431 (1992)
- Davison, B. H., Knopp, S. A., Godia, F., and Solá, C., "Stability Characterization and Comparison of Two Fluidized-Bed Bioreactors," *Bioproc. Eng.*, 10:1 (1994)
- Dayal, B. S., MacGregor, J. F., Taylor, P. A., Kildaw, R., and Marcikio, S., "Application of Feedforward Neural Networks and Partial Least Squares Regression for Modelling Kappa Number in a Continuous Kamyrdigester," *Pulp & Paper Can.*, 95(1):26 (1994)
- Deckwer, W. D., *Bubble Column Reactors*, John Wiley & Sons, Chichester, England (1992)
- Denac, M., and Dunn, I. J., "Packed- and Fluidized-Bed Biofilm Reactor Performance for Anaerobic Wastewater Treatment," *Biotechnol. Bioeng.*, 32:159 (1988)

- Denac, M., Lee, P. L., Newell, R. B., and Greenfield, P. F., "Automatic Control of Effluent Quality from a High-Rate Anaerobic Treatment System," *Wat. Res.*, 24:583 (1990)
- Donath, E. E., "Hydrogenation of Coal and Tar," *Chem. of Coal Utilization* (H. H. Lowry, ed.), Supplementary Volume, p. 1041, John Wiley (1963)
- Dumont, G. A., "Application of Advanced Control Methods in the Pulp and Paper Industry - A Survey," *Automatica*, 22:143 (1986)
- Ehlinger, F., Escoffier, Y., Couderc, J. P., Leyris, J. P., and Moletta, R., "Development of an Automatic Control System for Monitoring an Anaerobic Fluidized-Bed," *Wat. Sci. Tech.*, 29(10-11):289 (1994)
- Eidt, Jr., C. M., Bauman, R. F., Eisenberg, B., Hochman, J. M., and Lahn, G. C., "Current Developments in Natural Gas Conversion Technology," *Proc. of the 14th World Petroleum Cong.*, p. 249, John Wiley & Sons (1994)
- Endo, I., Nagamune, T., Kato, N., Kobayashi, T., and Nishimura, M., paper 25c presented at the AIChE Annual Meeting, Miami Beach (1986)
- Etzensperger, M., Thoma, S., Petrozzi, S., and Dunn, I. J., "Phenol Degradation in a Three-Phase Biofilm Fluidized Sand Bed Reactor," *Bioproc. Eng.*, 4:175 (1989)
- Everett, B. M., Eisenberg, B., and Baumann, R. F., "Advanced Gas Conversion Technology: A New Option for Natural Gas Development," presented at the First Doha Conference on Natural Gas, Doha, Qatar (1995)
- Fan, L. S., Kitano, K., and Kreischer, B. E., "Hydrodynamics of Gas-Liquid-Solid Annular Fluidization," *AIChE J.*, 33:225 (1987a)
- Fan, L. S., Fujie, K., Long, T. R., and Tang, W. T., "Characteristics of Draft Tube Gas-Liquid-Solid Fluidized-Bed Bioreactor with Immobilized Living Cells for Phenol Degradation," *Biotechnol. Bioeng.*, 30:498 (1987b)
- Fan, L. S., *Gas-Liquid-Solid Fluidization Eng.*, Butterworth, Boston (1989)
- Farag, I. H., Ettouney, H. M., and Raj, C. B. C., "Modeling of Ethanol Bioproduction in Three-Phase Fluidized Bed Reactors," *Chem. Eng. Comm.*, 79:47 (1989)
- Farrand, B. L., Wood, J. E., and Goetz, F. J., "Post Combustion Trials at Dofasco's KOBM Furnace," *AIME Steelmaking Conf. Proc.*, p. 173 (1992)
- Federici, F., Petruccioli, M., and Miller, M. W., "Enhancement and Stabilization of the Production of Glucoamylase by Immobilized Cells of *Aureobasidium pullulans* in a Fluidized-Bed Reactor," *Appl. Microbiol. Biotechnol.*, 33:407 (1990)
- Fine, H. A., Fruehan, R. J., Janke, D., and Steffen, R., "Conclusions on the Development of Smelting Reduction," *Steel Res.*, 60:188 (1989)
- Flickenschild, J., "Results from the Corex-Plant Operation at ISCOR, Pretoria," *Techno Meeting*, IISI, Stockholm (1991)

- Fröhlich, S., Lotz, M., Korte, T., Lübbert, A., Schügerl, K., Seekamp, M., "Characterization of a Pilot Plant Airlift Tower Loop Bioreactor: II. Evaluation of Global Mixing Properties of the Gas Phase During Yeast Cultivation," *Biotechnol. Bioeng.*, 37:910 (1991a)
- Fröhlich, S., Lotz, M., Larson, B., Lübbert, A., Schügerl, K., Seekamp, M., "Characterization of a Pilot Plant Airlift Tower Loop Bioreactor: III. Evaluation of Local Properties of the Dispersed Gas Phase During Yeast Cultivation and in a Model Media," *Biotechnol. Bioeng.*, 38:56 (1991b)
- Fruehan, R. J., Ito, K., and Ozturk, B., "Analysis of Bath Smelting Processes for Producing Iron," *Steel Res.*, 60:129 (1989)
- Fujii, M., Matayoshi, Y., Umeda, T., Matsubara, S., Fukunaga, K., and Nomura, Y., "Research on Treatment by *Thiobacillus ferrooxidans* of Pickling and Plating Waste Waters at Steelworks," *Nippon Steel Technical Report*, 37:59 (1988)
- Garnier, A., Chavarie, C., Andre, G., and Klvana, D., "The Inverse Fluidization Airlift Bioreactor, Part I: Hydrodynamic Studies," *Chem. Eng. Comm.*, 98:31 (1990)
- Gaskell, D. R., "Research Needs; Slag Properties and Chemistry," *Steel Res.*, 60:182 (1989)
- Germain, A., L'Homme, G. A., and Lefebvre, A., *Chem. Eng. of Gas-Liquid-Solid Catalyst Reactions* (G. A. L'Homme, ed.), p. 265, CEBEDOC, Liege (1979)
- Gilson, C. D., and Thomas, A., "A Novel Fluidised Bed Bioreactor for Fermentation of Glucose to Ethanol Using Alginate Immobilised Yeast," *Biotechnol. Tech.*, 7:397 (1993)
- Godia, F., Adler, H. I., Scott, C. D., and Davison, B. H., "Use of Immobilized Microbial Membrane Fragments to Remove Oxygen and Favor the Acetone-Butanol Fermentation," *Biotechnol. Prog.*, 6:210 (1990)
- Goetz, V., Remaud, M., and Graves, D. J., "A Novel Magnetic Silica Support for Use in Chromatographic and Enzymatic Bioprocessing," *Biotechnol. Bioeng.*, 37:614 (1991)
- Gommers, P. J. F., Christoffels, L. P., Kuenen, J. G., and Luyben, K. C. A. M., "Gas-Phase Influence on the Mixing in a Fluidized Bed Bio-Reactor," *Appl. Microbiol. Biotechnol.*, 25:1 (1986)
- Gonçalves, L. M. D., Barreto, M. T. O., Xavier, A. M. B. R., Carrondo, M. J. T., and Klein, J., "Inert Supports for Lactic Acid Fermentation - A Technological Assessment," *Appl. Microbiol. Biotechnol.*, 38:305 (1992)
- Gou, H., Irons, G. A., and Lu, W. K., "Mathematical Modeling of Postcombustion in a KOBM Converter," *Metallurgical Transactions B*, 24B:179 (1993)

- Gou, H., Irons, G. A., and Lu, W. K., "A Mathematical Model for the Fluid Dynamics of Slag Foaming in Smelting-Reduction," *Turkdogan Symp. Proc.*, p. 83 (1994)
- Green, M., Schnitzer, M., and Tarre, S., "Kinetics of a Fluidized-Bed Reactor for Ground-Water Denitrification," *Appl. Microbiol. Biotechnol.*, 43:188 (1995)
- Grishin, S. I., and Tuovinen, O. H., "Scanning Electron Microscopic Examination of *Thiobacillus ferrooxidans* on Different Support Matrix Materials in Packed Bed and Fluidized Bed Bioreactors," *Appl. Microbiol. Biotechnol.*, 31:505 (1989)
- Gudenau, H. W., Wu, K., Nys, S., and Rosenbaum, H., "Formation and Effects of Slag Foaming in Smelting Reduction," *Steel Res.*, 63:521 (1992)
- Gudenau, H. W., Yang, T., Germershausen, T., Rosenbaum, H., and Wu, K., "Heat Transfer in an Iron Bath of a Two-Stage Smelting Reduction Process," *Steel Res.*, 64:372 (1993)
- Halfmeier, H., Schäfer-Treffenfeldt, W., and Reuss, M., "Potential of *Thiobacillus ferrooxidans* for Waste Gas Purification. Part 2. Increase in Continuous Ferrous Iron Oxidation Kinetics Using Immobilized Cells," *Appl. Microbiol. Biotechnol.*, 40:582 (1993)
- Hano, T., Matsumoto, M., Kuribayashi, K., and Hatate, Y., "Biological Nitrogen Removal in a Bubble Column with a Draught Tube," *Chem. Eng. Sci.*, 47:3737 (1992)
- Hara, S., and Ogino, K., "Slag-Foaming Phenomena in Pyrometallurgical Processes," *ISIJ Int.*, 32:81 (1992)
- Hardie, G. J., Cross, M., Batterham, R. J., Davis, M. P., and Schwarz, M. P., "The Role of Mathematical Modelling in the Development of the Hismelt Process," *10th Process Technol. Conf. Proc.*, p. 102, Toronto, (1992)
- Hardie, G. J., Wright, J. K., and Batterham, R. J., "Pulverised Coal Based Direct Smelting: The Hismelt Process," *VDEh Blast Furnace Committee Meeting*, "Use of Coal for Hot Metal Production," Duesseldorf, March (1993)
- Harshbarger, D., Bautz, M., Davison, B. H., Scott, T. C., and Scott, C. D., "Economic Assessment of Ethanol Production Comparing Traditional and Fluidized-Bed Bioreactors," *Appl. Biochem. Biotechnol.*, 51/52:593 (1995)
- Heijnen, J. J., Mulder, A., Enger, W., and Hoeks, F., "Review on the Application of Anaerobic Fluidized Bed Reactors in Waste-Water Treatment," *Chem. Eng. J.*, 41:B37 (1989)
- Heppner, B., Zellner, G., and Diekmann, H., "Start-Up and Operation of a Propionate-Degrading Fluidized-Bed Bioreactor," *Appl. Microbiol. Biotechnol.*, 36:810 (1992)
- Hirai, M., Tsujino, R., Mukai, T., Harada, T., and Omori, M., "Mechanism of Post Combustion in the Converter," *Trans. ISIJ*, 27:805 (1987)

670 *Fluidization, Solids Handling, and Processing*

- Hirata, T., Ishikawa, M., Mori, T., and Anezaki, S., "Improvement of In-Bath Smelting Reduction Process Through Side and Bottom Blowing," *AIME Ironmaking Conf. Proc.*, p. 761 (1991)
- Hirata, T., Ishikawa, M., and Anezaki, S., "Stirring Effect in Bath-Smelting Furnace with Combined Blowing of Top and Side Blown Oxygen and Bottom Blown Nitrogen," *ISIJ Int.*, 32:182 (1992)
- Hoffman, J. P., "A Look at the Problems Facing the Developer of Smelting Reduction using the Liquid Bath Approach," *Steel Res.*, 62:331 (1991)
- Howard, R. C., "The Effects of Recycling on Pulp Quality," *Technol. of Paper Recycling* (R. W. J. McKinney, ed.), p. 180, Blackie Academic & Professional, London (1995)
- Hsu, Y., and Shieh, W. K., "Startup of Anaerobic Fluidized Bed Reactors with Acetic Acid as the Substrate," *Biotechnol. Bioeng.*, 41:347 (1993)
- Hu, T. T., and Wu, J. Y., "Study on the Characteristics of a Biological Fluidized Bed in a Magnetic Field," *Chem. Eng. Res. Des.*, 65:238 (1987)
- Hurst, M. M., "Effects of Pulp Consistency and Mixing Intensity on Ozone Bleaching," *Tappi J.*, 76(4):156 (1993)
- Hvala, N., Strm. .nik, S., and, erneti. ., J., "Scheduling of Batch Digesters According to Different Control Targets and Servicing Limitations," *Computers Chem. Eng.*, 17:739 (1993)
- Ibaraki, T., Kanemoto, M., Ogata, S., Katayama, H., and Ishikawa, H., "Development of Smelting Reduction of Iron Ore - An Approach to Commercial Ironmaking," *Iron & Steelmaker*, 17(12):30 (1990)
- Ibaraki, T., "Fundamentals of the Bath Smelting Reduction and Functions of the Slag on the Iron Bath," in *Turkdogan Symp. Proc.*, p. 73 (1994)
- Ibaraki, T., Yamauchi, M., Sakamoto, Y., Hirata, H., and Kanemoto, M., "Experimental Operation of Smelting Reduction With a 100 mt Smelter - I. Operation and the Slag in the Smelter," *Iron & Steelmaker*, 22(3):83 (1995a)
- Ibaraki, T., Yamauchi, M., Matsuo, M., and Katayama, H., "Experimental Operation of Smelting Reduction With a 100 mt Smelter - II. Post-Combustion and Dust," *Iron & Steelmaker*, 22(3):91 (1995b)
- Inatani, T., "The Current Status of JISF Research on the Direct Iron Ore Smelting Reduction Process (DIOS Project)," in *AIME Ironmaking Conf. Proc.*, p. 651 (1991)
- Japan Metal Bull.*, (as quoted by Steffen, 1989) p. 31 (1988)
- Järvinen, K. T., Melin, E. S., and Puhakka, J. A., "High-Rate Bioremediation of Chlorophenol-Contaminated Groundwater at Low Temperatures," *Environ. Sci. Technol.*, 28:2387 (1994)
- Johanson, E. S., "Gas-Liquid Contacting Process," U. S. Patent 2,987,465 (1961)

- Johns, W. F., Clausen, G., Nongbri, G., and Kaufman, H., "Texaco T-STAR Process for Ebullated Bed Hydrotreating/Hydrocracking," paper presented at the 1993 National Petroleum Refiners Association Annual Meeting, San Antonio, TX (1993)
- Kalogerakis, N., and Behie, L. A., "Oxygenation Capabilities of New Generation Three Phase - Two Region Bioreactors for Microcarrier Cultures of Animal Cells," *Fluidization VIII*, (C. Laguerie, and J. F. Large, eds.), p. 441, Engineering Foundation, Tours, France (1995)
- Kang, Y., Fan, L. T., Min, B. T., and Kim, S. D., "Promotion of Oxygen Transfer in Three-Phase Fluidized-Bed Bioreactors by Floating Bubble Breakers," *Biotechnol. Bioeng.*, 37:580 (1991)
- Kappel, J., Bräuer, P., and Kittel, F. P., "High-Consistency Ozone Bleaching Technology," *Tappi J.*, 77(6):109 (1994)
- Karamanev, D. G., Nagamune, T., and Endo, I., "Hydrodynamic and Mass Transfer Study of a Gas-Liquid-Solid Draft Tube Spouted Bed Bioreactor," *Chem. Eng. Sci.*, 47:3581 (1992)
- Kargi, F., and Toprak, H., "Rational Design of Metal Mesh Particles for Biological Fluidized Bed Reactors," *J. Chem. Tech. Biotechnol.*, 59:201 (1994)
- Katayama, H., Ohno, T., Yamauchi, M., Matsuo, M., Kawamura, T., and Ibaraki, T., "Mechanism of Iron Oxide Reduction and Heat Transfer in the Smelting Reduction Process with a Thick Layer of Slag," *ISIJ Int.*, 32:95 (1992)
- Katayama, H., Ibaraki, T., Ohno, T., Yamauchi, M., Hirata, H., and Inomoto, T., "The Characteristics and the Function of a Thick Slag Layer in the Smelting Reduction Process," *ISIJ Int.*, 33:124 (1993a)
- Katayama, H., Ohno, T., Yamauchi, M., Kawamura, T., Hirata, H., and Matsuo, M., "Raw Material Feeding and Its Influence on Operation Performance of Smelting Reduction Process with a Large Amount of Slag," *ISIJ Int.*, 33:376 (1993b)
- Kaufman, E. N., Cooper, S. P., Clement, S. L., and Little, M. H., "Use of a Biparticle Fluidized-Bed Bioreactor for the Continuous and Simultaneous Fermentation and Purification of Lactic Acid," *Appl. Biochem. Biotechnol.*, 51/52:605 (1995)
- Keogh, J. V., Hardie, G. J., Philp, D. K., and Burke, P. D., "Hismelt Process Advances to 100,000 t/y Plant," *AIME Ironmaking Conf. Proc.*, p. 635 (1991)
- Kobayashi, T., Tachi, K., Nagamune, T., and Endo, I., "Production of Penicillin in a Fluidized-Bed Bioreactor Using Urethane Foams as Carriers," *J. Chem. Eng. Jpn.*, 23:408 (1990)
- Kobayashi, T., Suda, T., Nagamune, T., and Endo, I., "Continuous Production of Penicillin in a Fluidized-Bed Bioreactor," *J. Chem. Eng. Jpn.*, 23:505 (1990)

672 *Fluidization, Solids Handling, and Processing*

- Kolbel, H., and Ralek, M., "The Fischer-Tropsch Synthesis in the Liquid Phase," *Catal. Rev. - Sci. Eng.*, 21(2):225 (1980)
- Kottke, V., Hartmeier, W., and Blenke, H., "The Blenke-Cascade: A New Type of Apparatus for Fluid Systems," *Universität Hohenheim Report for Biotechnica '91*, International Trade Fair for Biotechnology, Hannover (1991)
- Kratje, R. B., and Wagner, R., "Evaluation of Production of Recombinant Human Interleukin-2 in Fluidized Bed Bioreactor," *Biotechnol. Bioeng.*, 39:233 (1992)
- Kratje, R. B., Reimann, A., Hammer, J., and Wagner, R., "Cultivation of Recombinant Baby Hamster Kidney Cells in a Fluidized Bed Bioreactor System with Porous Borosilicate Glass," *Biotechnol. Prog.*, 10:410 (1994)
- Kunii, D., and Levenspiel, O., *Fluidization Eng.*, Butterworth-Heinemann, Stoneham, MA, (1991)
- Kwok, K. H., and Doran, P. M., "Kinetic and Stoichiometric Analysis of Hairy Roots in a Segmented Bubble Column Reactor," *Biotechnol. Prog.*, 11:429 (1995)
- Lauwers, A. M., Heinen, W., Gorris, L. G. M., and van der Drift, C., "Early Stages in Biofilm Development in Methanogenic Fluidized-Bed Reactors," *App. Microbiol. Biotechnol.*, 33:352 (1990)
- Lazarova, V., Capdeville, B., and Nikolov, L., "Influence of Seeding Conditions on Nitrite Accumulation in a Denitrifying Fluidized Bed Reactor," *Wat. Res.*, 28:1189 (1994)
- Lee, J. H., and Datta, A. K., "Nonlinear Inferential Control of Pulp Digesters," *AIChE J.*, 40:50 (1994)
- Lele, S. S., and Joshi, J. B., "Modelling of Air-Lift Fluidized Bed: Optimization of Mass Transfer with Respect to Design and Operational Parameters," *Chem Eng. J.*, 49:89 (1992)
- Liang, W., Yu, Z., Jin, Y., Wang, Z., and Wu, Q., "The Phase Holdups in a Gas-Liquid-Solid Circulating Fluidized Bed," *Chem. Eng. J.*, 58:259 (1995)
- Lindsay, J. D., Ghiaasiaan, S. M., and Abdel-Khalik, S. I., "Macroscopic Flow Structures in a Bubbling Paper Pulp-Water Slurry," *Ind. Eng. Chem. Res.*, 34:3342 (1995)
- Livingston, A. G., and Chase, H. A., "Modeling Phenol Degradation in a Fluidized-Bed Bioreactor," *AIChE J.*, 35:1980 (1989)
- Livingston, A. G., "Biodegradation of 3,4-Dichloroaniline in a Fluidized Bed Bioreactor and a Steady-State Biofilm Kinetic Model," *Biotechnol. Bioeng.*, 38:260 (1991)
- Livingston, A. G., and Chase, H. A., "Development of a Phenol Degrading Fluidized Bed Bioreactor for Constant Biomass Holdup," *Chem. Eng. J.*, 45:B35 (1991)

- Macy, J. M., Lawson, S., and DeMoll-Decker, H., "Bioremediation of Selenium Oxyanions in San Joaquin Drainage Water Using *Thauera selenatis* in a Biological Reactor System," *Appl. Microbiol. Biotechnol.*, 40:588 (1993)
- Mäkinen, P. M., Theno, T. J., Ferguson, J. F., Ongerth, J. E., and Puhakka, J. A., "Chlorophenol Toxicity Removal and Monitoring in Aerobic Treatment: Recovery from Process Upsets," *Environ. Sci. Technol.* 27:1434 (1993)
- Matsui, S., Yamamoto, R. I., Tsuchiya, Y., and Inanc, B., "The Kinetics of Glucose Decomposition with Sulfate Reduction in the Anaerobic Fluidized Bed Reactor," *Wat. Sci. Tech.*, 28(2):135 (1993)
- McDonough, T. J., "Recent Advances in Bleached Chemical Pulp Manufacturing Technology, Part 1: Extended Delignification, Oxygen Delignification, Enzyme Applications, and ECF and TCF Bleaching," *Tappi J.*, 78(3):55 (1995)
- McKinney, R. W. J., "Wastepaper Preparation and Contamination Removal," *Technol. of Paper Recycling*, (R. W. J. McKinney, ed.), p. 48, Blackie Academic & Professional, London (1995)
- Meadows, D. G., "The Pulp Mill of the Future: 2005 and Beyond," *Tappi J.*, 78(10):55 (1995)
- Merchuk, J. C., Ladwa, N., and Bulmer, M., "Improving the Airlift Reactor: The Helical Flow Promoter," *3rd Int. Conf. on Bioreactor and Bioprocess Fluid Dynamics*, (A. W. Nienow, ed.), p. 61, Information Press, Ltd., Oxford (1993)
- Merchuk, J. C., Ben-Zvi (Yona), S., and Niranjana, K., "Why Use Bubble-Column Bioreactors?," *Trends Biotechnol.*, 12:501 (1994)
- Mol, N., Kut, O. M., and Dunn, I. J., "Adsorption of Toxic Shocks on Carriers in Anaerobic Biofilm Fluidized Bed Reactors," *Wat. Sci. Tech.*, 28(2):55 (1993)
- Mollah, A. H., and Stuckey, D. C., "Maximizing the Production of Acetone-Butanol in an Alginate Bead Fluidized Bed Reactor Using *Clostridium acetobutylicum*," *J. Chem. Tech. Biotechnol.*, 56:83 (1993)
- Muroyama, K., and Fan, L. -S., "Fundamentals of Gas-Liquid-Solid Fluidization," *AIChE J.*, 31:1 (1985)
- Myška, J., and Švec, J., "The Distributive Properties of a Fluidized Bed with Biomass," *Wat. Res.*, 28:1653 (1994)
- Nagamune, T., Endo, I., Kato, N., Nishimura, M., and Kobayashi, T., "The Effect of Cultivation Conditions on the Penicillin Production Using a Urethane Foam-Supported *Penicillium chrysogenum*," *Bioproc. Eng.*, 3:173 (1988)
- Naouri, P., Bernet, N., Chagnaud, P., Arnaud, A., and Galzy, P., "Bioconversion of L-Malic Acid into L-Lactic Acid Using a High Compacting Multiphasic Reactor (HCMR)," *J. Chem. Tech. Biotechnol.*, 51:81 (1991)

674 *Fluidization, Solids Handling, and Processing*

- Nelson, T. B., and Skaates, J. M., "Attrition in a Liquid Fluidized Bed Bioreactor," *Ind. Eng. Chem. Res.*, 27:1502 (1988)
- Nguyen, V. T., and Shieh, W. K., "Continuous Ethanol Fermentation Using Immobilized Yeast in a Fluidized Bed Reactor," *J. Chem. Tech. Biotechnol.*, 55:339 (1992)
- Nikolov, L. N., and Karamanev, D., "Experimental Study of the Inverse Fluidized Bed Biofilm Reactor," *Can. J. Chem. Eng.*, 65:214 (1987)
- Nikolov, L., and Karamanev, D. G., "The Inverse Fluidized Bed Biofilm Reactor: A New Laboratory Scale Apparatus for Biofilm Research," *J. Ferm. Bioeng.* 69:265 (1990)
- Nore, O., Briens, C., Margaritis, A., and Wild, G., "Hydrodynamics, Gas-Liquid Mass Transfer and Particle-Liquid Heat and Mass Transfer in a Three-Phase Fluidized Bed for Biochemical Process Applications," *Chem. Eng. Sci.*, 47:3573 (1992)
- Nutt, W. E., Griggs, B. F., Eachus, S. W., and Pikulin, M. A., "Developing an Ozone Bleaching Process," *Tappi J.*, 76(3):115 (1993)
- Oeters, F., "Mixing with Heat and Mass Transfer in Metallurgical Systems," *Steel Res.*, 60:185 (1989)
- Oeters, F., Zhang, L., and Steffen, R., "Considerations on Process Technologies of Smelting Reduction Including Scrap Melting," *Turkdogan Symp. Proc.*, p. 23 (1994)
- Oeters, F., and Xie, H., "A Contribution to the Theoretical Description of Metal-Slag Reaction Kinetics," *Steel Res.*, 66:409 (1995)
- Ogata, M., Marumoto, Y., Oh-I, K., Shimizu, S., and Katoh, S., "Continuous Culture of CHO-K1 Cells Producing Thrombomodulin and Estimation of Culture Conditions," *J. Ferm. Bioeng.*, 77:46 (1994)
- Ogawa, Y., Katayama, H., Hirata, H., Tokumitsu, N., and Yamauchi, M., "Slag Foaming in Smelting Reduction and Its Control with Carbonaceous Materials," *ISIJ Int.*, 32:87 (1992)
- Ogawa, Y., Huin, D., Gaye, H., and Tokumitsu, N., "Physical Model of Slag Foaming," *ISIJ Int.*, 33:224 (1993)
- Oh, D. K., Hyun, C. K., Kim, J. H., and Park, Y. H., "Production of Penicillin in a Fluidized-Bed Bioreactor: Control of Cell Growth and Penicillin Production by Phosphate Limitation," *Biotechnol. Bioeng.*, 32:569 (1988)
- Ozturk, I., Turan, M., and Idris, A. H., "Scale-Up and Biomass Hold-Up Characteristics of Biological Fluidized Bed Reactors," *Wat. Sci. Tech.*, 29(10-11):353 (1994)
- Paulonis, M. A., and Krishnagopalan, A., "Kappa Number and Overall Yield Calculation Based on Digester Liquor Analysis," *Tappi J.*, 71(11):185 (1988)

- Paz, E. D. D., Santana, M. H. A., and Eguchi, S. Y., "Enhancement of the Oxygen Transfer in a Circulating Three-Phase Fluidized Bed Bioreactor," *Appl. Biochem. Biotechnol.*, 39/40:455 (1993)
- Petersen, J. N., and Davison, B. H., "Development of a Predictive Description of an Immobilized-Cell, Three-Phase, Fluidized-Bed Bioreactor," *Biotechnol. Bioeng.*, 46:139 (1995)
- Petrov...i..., J., Hvala, N., Bitenc, A., and Strm...nik, S., "Low-Cost Steam Consumption Control System for Batch Pulp Cooking," *Control Eng. Practice*, 3(3):357 (1995)
- Petrozzi, S., Kut, O. M., and Dunn, I. J., "Protection of Biofilms Against Toxic Shocks by the Adsorption and Desorption Capacity of Carriers in Anaerobic Fluidized Bed Reactors," *Bioproc. Eng.*, 9:47 (1993)
- Petrozzi, S., and Dunn, I. J., "Biological Cyanide Degradation in Aerobic Fluidized Bed Reactors: Treatment of Almond Seed Wastewater," *Bioproc. Eng.*, 11:29 (1994)
- Pfeffer, J. T., and Suidan, M. T., "Continuous Processing of Toxic Organics in a Fluidized-Bed GAC Reactor Employing Carbon Replacement," *Biotechnol. Bioeng.*, 33:139 (1989)
- Pothhoff, M., and Bohnet, M., "Influence of Solids Concentration and Static Mixers on Fluid Dynamics in Three-Phase Fluidized Bed Bioreactors," *Chem. Eng. Technol.*, 16:147 (1993)
- Probstein, R. F., and Hicks, R. E., *Synthetic Fuels*, McGraw-Hill, New York, (1982)
- Puhakka, J. A., Herwig, R. P., Koro, P. M., Wolfe, G. V., and Ferguson, J. F., "Biodegradation of Chlorophenols by Mixed and Pure Cultures from a Fluidized-Bed Reactor," *Appl., Microbiol. Biotechnol.*, 42:951 (1995)
- Qureshi, N., and Maddox, I. S., "Reactor Design for the ABE Fermentation Using Cells of *Clostridium acetobutylicum* Immobilized by Adsorption onto Bonechar," *Bioproc. Eng.*, 3:69 (1988)
- Qureshi, N., and Maddox, I. S., "A Mathematical Model of a Fluidized Bed Reactor for the Continuous Production of Solvents by Immobilized *Clostridium acetobutylicum*," *J. Chem. Tech. Biotechnol.*, 48:369 (1990)
- Qureshi, N., and Maddox, I. S., "Application of Novel Technology to the ABE Fermentation Process: An Economic Analysis," *Appl. Biochem. Biotechnol.*, 34/35:441 (1992)
- Racher, A. J., and Griffiths, J. B., "Investigation of Parameters Affecting a Fixed Bed Bioreactor Process for Recombinant Cell Lines," *Cytotechnol.*, 13:125 (1993)
- Ramsay, B. A., Wang, D., Chavarie, C., Rouleau, D., and Ramsay, J. A., "Penicillin Production in an Inverse Fluidized Bed Bioreactor," *J. Ferm. Bioeng.*, 72:495 (1991)

676 *Fluidization, Solids Handling, and Processing*

- Reese, J., Jiang, P., and Fan, L. S., "Bubble Characteristics in Three-Phase Systems used for Pulp and Paper Processing," *Chem. Eng. Sci.*, 51:2501 (1996)
- Reiter, M., Buchacher, A., Blüml, G., Zach, N., Steinfeldner, W., Schmatz, C., Gaida, T., Assadian, A., and Katinger, H., "Production of the HIV-1 Neutralising Human Monoclonal Antibody 2F5: Stirred Tank Versus Fluidized Bed Culture," *Animal Cell Technology*, (R. E. Spier, J. B. Griffith, and W. Berthold, eds.), p. 333, Butterworth-Heinemann, Oxford (1994)
- Richardson, J. F., and Zaki, W. N., "Sedimentation and Fluidization Part I," *Trans. Inst. Chem. Engrs.*, 32:35 (1954)
- Rickard, J. C., "The 2020 Mill-Utility Requirements for Market Kraft Pulp," *AIChE Symp. Series: Advances in Forest Products Environmental and Process Eng., The 1993 Forest Products Symp.*, (C. L. Verrill, ed.), 90(302):167, AIChE, New York (1994)
- Rihar, M., "The Software Simulator as an Effective Tool for Testing Control Algorithms," *Simulation*, 63(1):6 (1994)
- Romenets, V. A., "Process of Liquid Phase Reduction of Iron: Development and Implementation," *Steel in the USSR*, 20:366 (1990)
- Romli, M., Greenfield, P. F., and Lee, P. L., "Effect of Recycle on a Two-Phase High-Rate Anaerobic Wastewater Treatment System," *Wat. Res.*, 28:475 (1994)
- Roustan, M., Capdeville, B., and Bastoul, D., "Influence of the Hydrodynamic Behaviour of a Three-Phase Fluidised Bed Used for Effluent Treatment," *3rd Int. Conf. on Bioreactor and Bioprocess Fluid Dynamics*, (A. W. Nienow, ed.), p. 323, Information Press, Ltd., Oxford (1993)
- Ruggeri, B., Caire, G., Specchia, V., Sassi, G., Bosco, F., and Gianetto, A., "Determination of Optimal Biofilm Activity in a Biological Fluidized Bed (BFB) Reactor," *Wat. Sci. Tech.*, 29(10-11):347 (1994)
- Ryhiner, G., Petrozzi, S., and Dunn, I. J., "Operation of a Three-Phase Biofilm Fluidized Sand Bed Reactor for Aerobic Wastewater Treatment," *Biotechnol. Bioeng.*, 32:677 (1988)
- Sajc, L., Obradovic, B., Vukovic, D., Bugarski, B., Grubisic, D., and Vunjak-Novakovic, G., "Hydrodynamics and Mass Transfer in a Four-Phase External Loop Air Lift Bioreactor," *Biotechnol. Prog.*, 11:420 (1995)
- Samejima, H., Nagashima, M., Azuma, M., Noguchi, S., and Inuzuka, K., "Semicommercial Production of Ethanol using Immobilized Microbial Cells," *Annals New York Academy of Sciences*, 434:394 (1984)
- Sanz, I., and Fdz-Polanco, F., "Low Temperature Treatment of Municipal Sewage in Anaerobic Fluidized Bed Reactors," *Wat. Res.*, 24:463 (1990)

- Saraiva, P. M., and Stephanopoulos, G., "Continuous Process Improvement through Inductive and Analogical Learning," *AIChE J.*, 38:161 (1992)
- Saxena, S. C., Rosen, M., Smith, D. N., and Ruether, J. A., "Mathematical Modeling of Fischer-Tropsch Slurry Bubble Column Reactors," *Chem. Eng. Comm.*, 40:97 (1986)
- Schneeberg, E., "Increase of Efficiency of an Activated Sludge Plant in Paper Manufacturing Industry by Application of a Fluidized Bed System," *Wat. Sci. Tech.*, 29(12):177 (1994)
- Schoutens, G. H., Guit, R. P., Zieleman, G. J., Luyben, K. C. A. M., and Kossen, N. W. F., "A Comparative Study of a Fluidised Bed Reactor and a Gas Lift Loop Reactor for the IBE Process: Part I. Reactor Design and Scale Down Approach," *J. Chem. Tech. Biotechnol.*, 36:335 (1986a)
- Schoutens, G. H., Guit, R. P., Zieleman, G. J., Luyben, K. C. A. M., and Kossen, N. W. F., "A Comparative Study of a Fluidised Bed Reactor and a Gas Lift Loop Reactor for the IBE Process: Part II. Hydrodynamics and Reactor Modelling," *J. Chem. Tech. Biotechnol.*, 36:415 (1986b)
- Schoutens, G. H., Guit, R. P., Zieleman, G. J., Luyben, K. C. A. M., and Kossen, N. W. F., "A Comparative Study of a Fluidised Bed Reactor and a Gas Lift Loop Reactor for the IBE Process: Part III. Reactor Performances and Scale Up," *J. Chem. Tech. Biotechnol.*, 36:565 (1986c)
- Schügerl, K., "Biofluidization: Application of the Fluidization Technique in Biotechnology," *Can. J. Chem. Eng.*, 67:178 (1989)
- Scott, C. D., "Ethanol Production in a Fluidized-Bed Bioreactor Utilizing Flocculating *Zymomonas Mobilis* with Biomass Recycle," *Biotechnol. Bioeng. Symp. Ser.*, 13:287 (1983)
- Scragg, A. H., "Bioreactors for the Mass Culture of Plant Cells," *Plant Biotechnology: Comprehensive Biotechnol.*, (M. W. Fowler, and G. S. Warren, eds.), p. 45, Second Supplement, Pergamon Press, Oxford (1992)
- Seifert, P., "Recent Innovation in Paper Recycling," *Tappi J.*, 77(2):149 (1994)
- Seki, M., Naito, K. I., and Furusaki, S., "Effect of Co-Immobilization of Microporous Particles on the Overall Reaction Rate of Immobilized Cell Biocatalysts," *J. Chem. Eng. Jpn.*, 26:662 (1993)
- Shah, Y. T., *Gas-Liquid-Solid Reactor Design*, McGraw-Hill, New York, (1979)
- Shen, B., Greenfield, P., and Reid, S., "Calcium Alginate Immobilized Hybridomas Grown Using a Fluidized-Bed Perfusion System with a Protein-Free Medium," *Cytotechnol.*, 14:109 (1994)
- Shinotake, A., and Takamoto, Y., "Combustion and Heat Transfer Mechanism in Iron Bath Smelting Reduction Furnace," *La Revue de Metallurgie - CIT*, p. 965 (1993)

678 *Fluidization, Solids Handling, and Processing*

- Shirai, Y., Yamaguchi, M., Kobayashi, A., Nishi, A., Nakamura, H., and Murakami, H., "Change in Growth Kinetics of Hybridoma Cells Entrapped in Collagen Gel Affected by Alkaline Supply," *Cytotechnol.*, 14:129 (1994)
- Shu, C. H., and Yang, S. T., "Effect of Particle Loading on GM-CSF Production by *Saccharomyces cerevisiae* in a Three-Phase Fluidized Bed Bioreactor," *Biotechnol. Bioeng.*, 51:229 (1996)
- Siegel, M. H., and Robinson, C. W., "Applications of Airlift Gas-Liquid-Solid Reactors in Biotechnology," *Chem. Eng. Sci.*, 47:3215 (1992)
- Siegell, J. H., "Liquid-Fluidized Magnetically Stabilized Beds," *Powder Tech.*, 52:139 (1987)
- Silbiger, E., and Freeman, A., "Continuous Δ^1 -Hydrocortisone Dehydrogenation with in Situ Product Recovery," *Enzyme Microb. Technol.*, 13:869 (1991)
- Smook, G. A., *Handbook for Pulp & Paper Technologists*, 2nd ed., Angus Wilde Publications, Vancouver (1992)
- Sreekrishnan, T. R., Ramachandran, K. B., and Ghosh, P., "Effect of Operating Variables on Biofilm Formation and Performance of an Anaerobic Fluidized-Bed Bioreactor," *Biotechnol. Bioeng.*, 37:557 (1991)
- Steffen, R., "Direct Reduction and Smelting Reduction - An Overview," *Steel Res.*, 60:96 (1989)
- Stenuf, T. J., and Unbehend, J. E., "Hydrodynamics of Fiber Suspensions," *Encyclopedia of Fluid Mechanics, Slurry Flow Technol.*, (N. Cheremisinoff, ed.), 5:291, Gulf Publishing Co., Houston (1986)
- Suh, I. S., Schumpe, A., Deckwer, W. -D., "Xanthan Production in Bubble Column and Air-Lift Reactors," *Biotechnol. Bioeng.*, 39:85 (1992)
- Sun, Y., and Furusaki, S., "Mean Bubble Diameter and Oxygen Transfer Coefficient in a Three-Phase Fluidized Bed Bioreactor," *J. Chem. Eng. Jpn.*, 21:20 (1988)
- Sun, Y., and Furusaki, S., "Continuous Production of Acetic Acid Using Immobilized *Acetobacter aceti* in a Three-Phase Fluidized Bed Bioreactor," *J. Ferm. Bioeng.*, 69:102 (1990)
- Takahashi, K., Muroya, M., Kondo, K., Hasegawa, T., Kikuchi, I., and Kawakami, M., "Post Combustion Behavior in In-Bath Type Smelting Reduction Furnace," *ISIJ Int.*, 32:102 (1992)
- Takashiba, N., Nira, M., Kojima, S., Take, H., and Yoshikawa, F., "Development of the Post Combustion Technique in Combined Blowing Converter," *Tetsu to Hagane*, 75:89 (1989)
- Tanabe, H., Takahashi, K., Ariyama, Y., Kitagawa, T., Ozeki, A., and Yamaga, M., "The Primary Stage of the Development of Smelting Reduction Process in NKK," *AIME Ironmaking Conf. Proc.*, p. 89 (1989)

- Tanaka, H., Enoki, N., Kaneki, N., Sakai, H., Shimada, K., and Hara, H., "A Three-Phase Fluidized Bed Fuel Cell," *J. Electrochem. Soc.*, 137:2798 (1990)
- Tanemura, K., Kida, K., Ikbai, Matsumoto, J., and Sonoda, Y., "Anaerobic Treatment of Wastewater with High Salt Content from a Pickled-Plum Manufacturing Process," *J. Ferm. Bioeng.* 77:188 (1994a)
- Tanemura, K., Kida, K., Teshima, M., and Sonoda, Y., "Anaerobic Treatment of Wastewater from a Food-Manufacturing Plant with a Low Concentration of Organic Matter and Regeneration of Usable Pure Water," *J. Ferm. Bioeng.*, 77:307 (1994b)
- Tang, W. T., and Fan, L. -S., "Steady State Phenol Degradation in a Draft-Tube, Gas-Liquid-Solid Fluidized-Bed Bioreactor," *AIChE J.*, 33:239 (1987)
- Tang, W. T., Wisecarver, K., and Fan, L. S., "Dynamics of a Draft Tube Gas-Liquid-Solid Fluidized Bed Bioreactor for Phenol Degradation," *Chem. Eng. Sci.*, 42:2123 (1987)
- Tang, W. T., and Fan, L. -S., "Hydrodynamics of a Three-Phase Fluidized Bed Containing Low-Density Particles," *AIChE J.*, 35:355 (1989)
- Tang, W. -T., and Fan, L. -S., "Gas-Liquid Mass Transfer in a Three-Phase Fluidized Bed Containing Low Density Particles," *Ind. Eng. Chem. Res.*, 29:128 (1990)
- Tarmy, B. L., Chang, M., Coulaloglou, C. A., and Ponzi, P. R., "The Three-Phase Hydrodynamic Characteristics of the EDS Liquefaction Reactors: Their Development and use in Reactor Scaleup," *Proc. 8th Int. Symp. Chem. Reaction Eng.*, 30:239 (1984)
- Tarmy, B. L., and Coulaloglou, C. A., "Alpha-Omega and Beyond - Industrial View of Gas/Liquid/Solid Reactor Development," *Chem. Eng. Sci.*, 47:3231 (1992)
- Terashima, S., Kamihira, M., Ogawa, T., Ohno, M., Iijima, S., and Kobayashi, T., "Continuous Production of Human Erythropoietin by Immobilized Recombinant L-929 Cells," *J. Ferm. Bioeng.*, 77:52 (1994)
- Terranova, B. E., and Burns, M. A., "Continuous Cell Suspension Processing Using Magnetically Stabilized Fluidized Beds," *Biotechnol. Bioeng.*, 37:110 (1991)
- Tikka, P. O., Virkola, N. E., Pursiainen, S. A., and Haemaelae, I. T., "Process Chemistry and Control of Rapid-Displacement Heating," *Tappi J.*, 71(2):51 (1988)
- Tong, C. C., and Fan, L. S., "Concentration Multiplicity in a Draft Tube Fluidized-Bed Bioreactor Involving Two Limiting Substrates," *Biotechnol. Bioeng.*, 31:24 (1988)

680 *Fluidization, Solids Handling, and Processing*

- Toseland, B. A., Brown, D. M., Zou, B. S., and Dudukovi., M., "Flow Patterns in a Slurry-Bubble-Column Reactor Conditions," *Trans. Inst. Chem. Engrs.*, 73:297 (1995)
- Trinet, F., Heim, R., Amar, D., Chang, H. T., and Rittmann, B. E., "Study of Biofilm and Fluidization of Bioparticles in a Three-Phase Liquid-Fluidized-Bed Reactor," *Wat. Sci. Tech.*, 23:1347 (1991)
- Tseng, S. -K., and Lin, M. -R., "Treatment of Organic Wastewater by Anaerobic Biological Fluidized Bed Reactor," *Wat. Sci. Tech.*, 29(12):157 (1994)
- Tsuchiya, K., Song, G. H., Tang, W. T., and Fan, L. S., "Particle Drift Induced by a Bubble in a Liquid-Solid Fluidized Bed with Low Density Particles," *AIChE J.*, 38:1847 (1992)
- Tsujino, R., Mukai, T., Hirai, M., Nakamura, K., and Harada, T., "Investigation of the Effect on Post Combustion in LD Converter (Study of Post Combustion in LD Converter-III)," *Trans. ISIJ*, 25:B-294 (1985)
- Turvey, R. W., "Chemical use in Recycling," *Technol. of Paper Recycling*, (R. W. J. McKinney, ed.), p. 130, Blackie Academic & Professional, London (1995)
- Tzeng, J. W., *Study of Fluidized Bed Reactors - Fluid Dynamics and Bioreactor Appl.*, Doctoral Dissertation, The Ohio State University (1991)
- Tzeng, J. W., Fan, L. S., Gan, Y. R., and Hu, T. T., "Ethanol Fermentation Using Immobilized Cells in a Multistage Fluidized Bed Bioreactor," *Biotechnol. Bioeng.*, 38:1253 (1991)
- Utigard, T. A., and Zamalloa, M., "Foam Behaviour in Liquid FeO-CaO-SiO₂ Slags," *Scand. J. Metallurgy*, 22:83 (1993)
- van Wie, B. J., Brouns, T. M., Elliott, M. L., and Davis, W. C., "A Novel Continuous Centrifugal Bioreactor for High-Density Cultivation of Mammalian and Microbial Cells," *Biotechnol. Bioeng.* 38:1190 (1991)
- van der Jagt, M. H., Kleijntjens, R. H., van der Lans, R. G. J. M., and Luyben, K. C. A. M., "A Continuous Three Phase Suspension Reactor for the Microbial Decontamination of Excavated Polluted Soils," *3rd Int. Conf. on Bioreactor and Bioprocess Fluid Dynamics*, (A. W. Nienow, ed.), p. 335, Information Press, Ltd., Oxford (1993)
- van der Wielen, L. A. M., Potters, J. J. M., Straathof, A. J. J., and Luyben, K. C. A. M., "Integration of Bioconversion and Continuous Product Separation by Means of Countercurrent Adsorption," *Chem. Eng. Sci.*, 45:2397 (1990)
- Venkat, R. V., Stock, L. R., and Chalmers, J. J., "Study of Hydrodynamics in Microcarrier Culture Spinner Vessels: A Particle Tracking Velocimetry Approach," *Biotechnol. Bioeng.*, 49:456 (1996)
- Vorlop, K. D., Estape, D., and Gòdia, F., "Design of Ca-Alginate Immobilized Yeast Cell Beads with Controlled Low Density to Enhance Their Fluidization Behaviour in Bioreactors," *Biotechnol. Tech.*, 7:287 (1993)

- Webb, O. F., Davison, B. H., Scott, T. C., and Scott, C. D., "Design and Demonstration of an Immobilized-Cell Fluidized-Bed Reactor for the Efficient Production of Ethanol," *Appl. Biochem. Biotechnol.*, 51/52:559 (1995)
- Weng, D., Cheng, L., Han, Y., Zhu, W., Xu, S., and Ouyang, F., "Continuous Ethanol Fermentation in a Three-Phase Magnetic Fluidized Bed Bioreactor," *AIChE Symp. Series*, 88(289):107, AIChE, New York (1992)
- Weuster, D., Aivasidis, A., and Wandrey, C., "Ethanolfermentation of Sugar Containing Wastes with *Zymomonas mobilis* in a Fluidized Bed Reactor," *DECHEMA Biotechnol. Conf.*, 3:507 (1989)
- Weuster-Botz, D., "Continuous Ethanol Production by *Zymomonas mobilis* in a Fluidized Bed Reactor. Part I. Kinetic Studies of Immobilization in Macroporous Glass Beads," *Appl. Microbiol. Biotechnol.*, 39:679 (1993)
- Weuster-Botz, D., Aivasidis, A., and Wandrey, C., "Continuous Ethanol Production by *Zymomonas mobilis* in a Fluidized Bed Reactor. Part II. Process Development for the Fermentation of Hydrolysed B-Starch without Sterilization," *Appl. Microbiol. Biotechnol.*, 39:685 (1993)
- White, D. E., Gandek, T. P., Pikulin, M. A., and Friend, W. H., "Importance of Reactor Design in High-Consistency Ozone Bleaching," *Pulp & Paper Can.*, 94(9):16 (1993)
- Wisecarver, K. D., and Fan, L. S., "Biological Phenol Degradation in a Gas-Liquid-Solid Fluidized Bed Reactor," *Biotechnol. Bioeng.*, 33:1029 (1989)
- Worden, R. M., and Donaldson, T. L., "Dynamics of a Biological Fixed Film for Phenol Degradation in a Fluidized-Bed Bioreactor," *Biotechnol. Bioeng.*, 30:398 (1987)
- Wu, K. Y. A., and Wisecarver, K. D., "Biological Phenol Degradation in a Countercurrent Three-Phase Fluidized Bed Using a Novel Cell Immobilization Technique," *AIChE Symp. Series*, 86(276):113 (1989)
- Yabannavar, V. M., and Wang, D. I. C., "Extractive Fermentation for Lactic Acid Production," *Biotechnol. Bioeng.*, 37:1095 (1991)
- Yang, S. T., "A Novel Gradient Particle Bed Bioreactor for Mixed Culture Fermentation," presented at the AIChE Annual Meeting, New York (1987)
- Yeager, R., "New Profits from Advanced Control," *PIMA Magazine* (Paper Industry Management Association), 77(1):6 (1995)
- Yee, C. J., Hsu, Y., and Shieh, W. K., "Effects of Microcarrier Pore Characteristics on Methanogenic Fluidized Bed Performance," *Wat. Res.* 26:1119 (1992)
- Yongming, L., Yi, Q., and Jicui, H., "Research on the Characteristics of Start Up and Operation of Treating Brewery Wastewater with an AFB Reactor at Ambient Temperatures," *Wat. Sci. Tech.*, 28(7):187 (1993)

- Zellner, G., Geveke, M., de Macario, E. C., and Diekmann, H., "Population Dynamics of Biofilm Development During Start-Up of a Butyrate-Degrading Fluidized-Bed Reactor," *Appl. Microbiol. Biotechnol.*, 36:404 (1991)
- Zellner, G., Neudörfer, F., and Diekmann, H., "Degradation of Lactate by an Anaerobic Mixed Culture in a Fluidized-Bed Reactor," *Wat. Res.*, 28:1337 (1994)
- Zhang, L., and Oeters, F., "A Model of Post-Combustion in Iron-Bath Reactors, Part 1: Theoretical Basis," *Steel Res.*, 62:95 (1991a)
- Zhang, L., and Oeters, F., "A Model of Post-Combustion in Iron-Bath Reactors, Part 2: Results for Combustion with Oxygen," *Steel Res.*, 62:107 (1991b)
- Zhang, L., and Oeters, F., "A Model of Post-Combustion in Iron-Bath Reactors, Part 3: Theoretical Basis for Post-Combustion with Preheated Air," *Steel Res.*, 64:542 (1993a)
- Zhang, L., and Oeters, F., "A Model of Post-Combustion in Iron-Bath Reactors, Part 4: Results for Post-Combustion with Preheated Air," *Steel Res.*, 64:588 (1993b)

Dense Phase Conveying

George E. Klinzing

1.0 INTRODUCTION

The term *dense phase* became popular in the conveying business in the mid 1970's when a particular pneumatic conveying vendor coined the phrase to mean the pulsed piston type of flow that is often encountered in the handling of plastic pellets. Before that date, *dense phase* usually meant a high concentration of solids moving with a heavy concentrated layer at the bottom of the pipe. Thus one is faced with a dilemma of the exact meaning of *dense phase conveying*. Presently, one must use the words *dense phase* with other descriptors attached so as not to confuse and mislead people of the exact condition of flow explored. Figures 1 and 2 were prepared by Dhodapkar (1991) and present a comprehensive grouping of terms that could all generically be called *dense phase conveying*. Figure 3 shows some specific terms that have been used by particular vendors in their search to be different and to have a better and unique system. A comprehensive review of *dense phase transport* has been prepared by Konrad (1986) and can be referred to for further details.

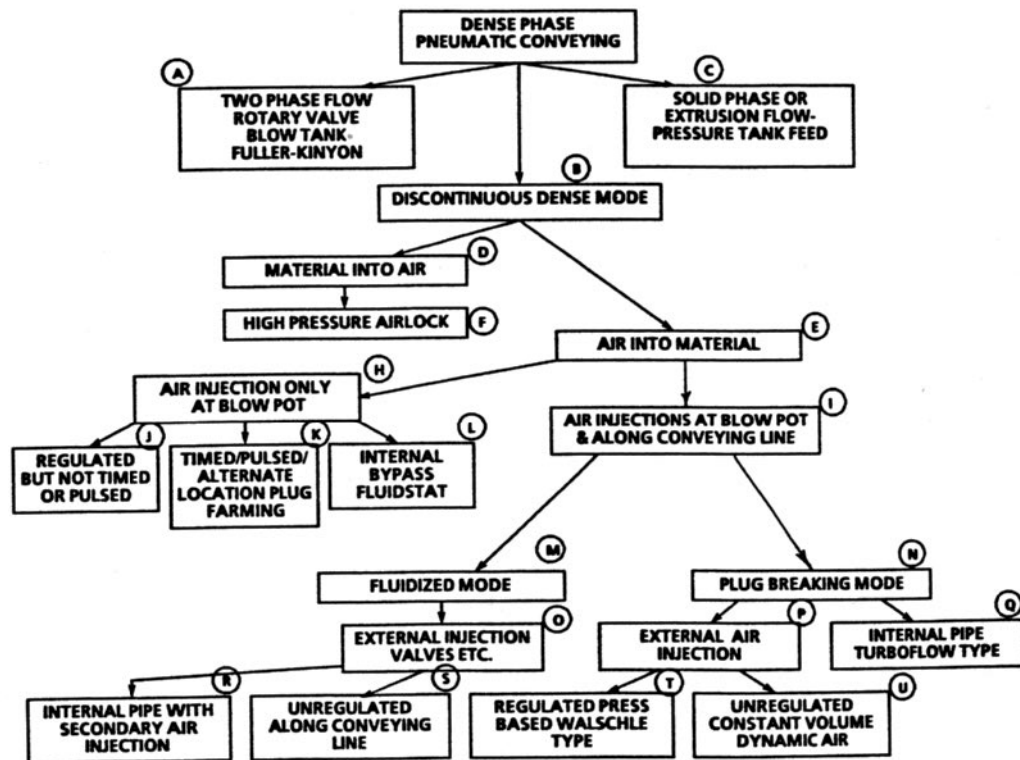


Figure 1. Breakdown of dense phase pneumatic conveying systems.

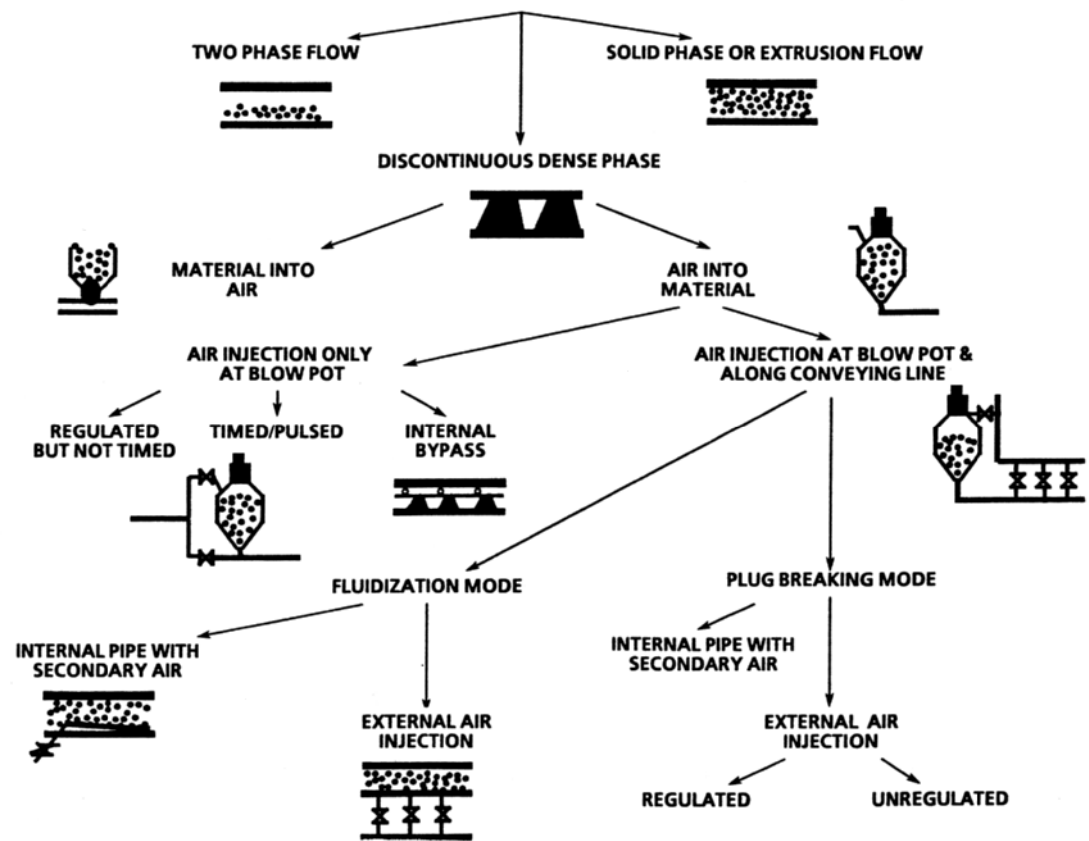


Figure 2. Sketches of dense phase pneumatic conveying systems.

High Pressure Airlock - Waeschle, Fuller, Allied Flotronics
Fuller Kinyon Pump - Fuller
Plug Forming Systems - Warren Spring Labs, Takt-Shub (Buhler), Sturtevat
External Air Injection - Dynamic Air (Booster type system), Gericke (sonic nozzles)
Internal Air By-pass - Fluidstat (Buhler), Turbuflow
External Air Injection - Pneumosplit, Dynamic Air, Fluidschub (Buhler), Gericke
Internal By-pass - Fluidstat (Buhler), Turbuflow

Figure 3. Classification of dense phase systems by vendors.

One can construct a number of different systems that would convey material in the dense phase condition. Figures 4–16 is a compilation of these systems indicating their unique characteristics.

The *Gatty system* has air injected from a sub-pipe mounted inside the main conveying line. Since this system is without controls, it performs better for well-behaved plastic pellet systems. It is difficult to maintain a low velocity conveying condition with this system, Marcus et al. (1990).

The *Buhler Fluidstat system* was first developed by Munschelk-nautz using a series of bypass pipes every half meter or so. Solids having good air retention properties are handled nicely with this system. A variation of this technique is the *Moller Turbuflow system*. The designers of this system claim that turbulence is regenerated in the conveying line.

A *trace air system* uses a series of boosters employing a pressure regulator and a check valve. The Semco systems is depicted in Fig. 6. Dynamic Air incorporates a similar concept controlling the air volume rather than the pressure.

Warren Springs Laboratories has developed a *pulsed conveying system* consisting of a flow vessel and an air knife downstream from the discharge valve as shown in Fig. 8. The plug lengths are controlled by the air knife operation time. An intermittent solids feed system shown in Fig. 9 can also control the size of the plug from both the air injection time and the discharge valve timing.

Buhler has also developed a *Takt-Schub system* which incorporates a double pulse system. The blow vessel has two gas inlet valves whose timing can be controlled. The system is operated in an alternating pulsing manner.

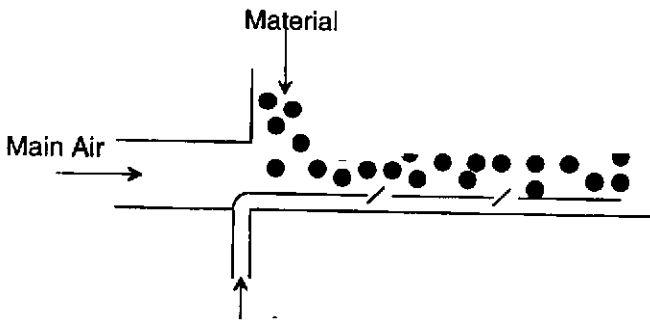


Figure 4. Gatty's dense phase system.

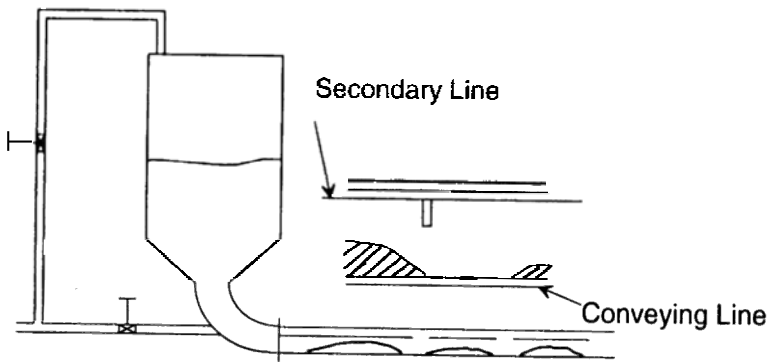


Figure 5. Turbuflow dense phase system.

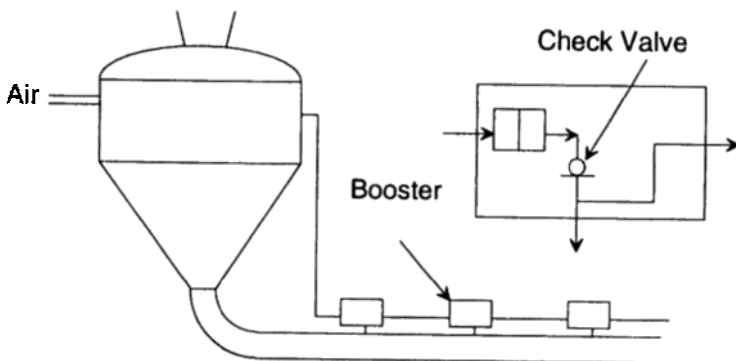


Figure 6. Trace air dense phase system (Semco).

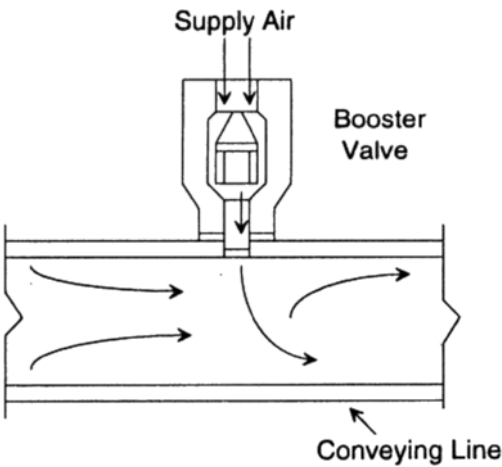


Figure 7. Dynamic Air dense phase system.

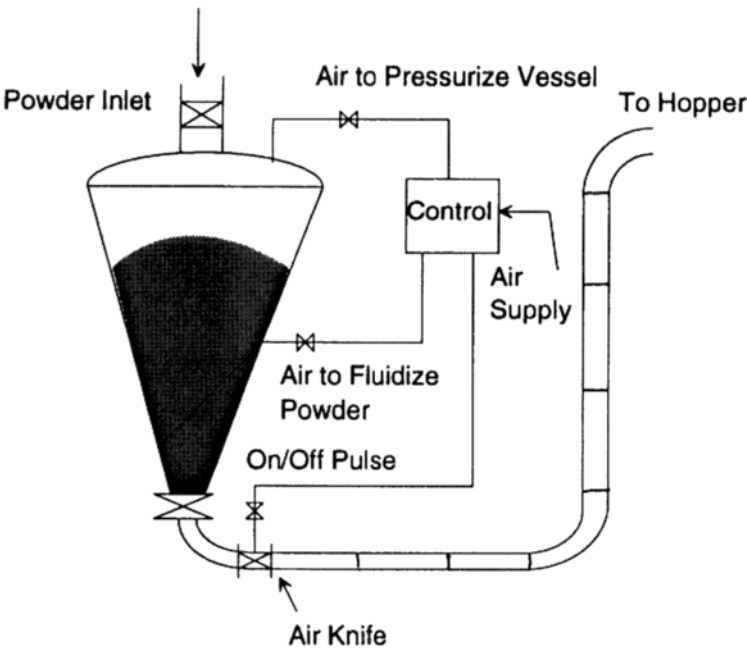


Figure 8. A pulse phase system arrangement.

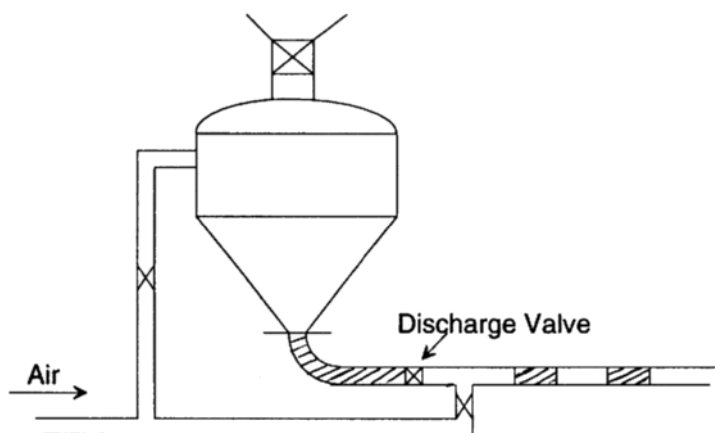


Figure 9. Intermittent solids feed system.

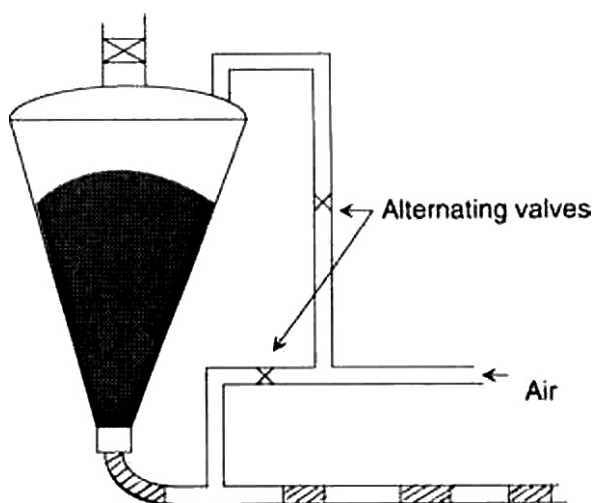


Figure 10. Takt-Schub system by Buhler.

Another system is the *plug pulse system* seen in Fig. 11. The discharge valve is alternatively activated with a gas pulse. This system works well for free flowing materials. The *minipot* is a variation of the plug pulse system. The operation of the minipot is depicted in Fig. 12.

Waeschle (Fig. 13) has developed a pressure sensing plug system. The boosters in this system are actuated by pressure rises in the line. The *Fluid-Schub system* of Buhler, Fig. 14, uses valves to inject air from an auxiliary air line. A system that produces extruded flow of long plugs can also be devised as shown in Fig. 15.

A new low velocity conveying system has been devised by Molerus and Siebenhaar (1990) and is shown in Fig. 16. This system relies on vibrations being put into the system by an unbalanced motor. These vibrations cause the materials to move with a low velocity throughout the system. This system is particularly useful for fragile materials.

In viewing all these systems one is faced with the over riding question on how to analyze, predict and scale such operation. For some designs, unfortunately, the only solution is to build a unit and test it. Others have some basic physics that can be reviewed. Assumptions for analysis can be made which often result in idealized systems rather than the real thing. This condition is not all bad because now one has a limit or a bound that can bracket the design and scale operations.

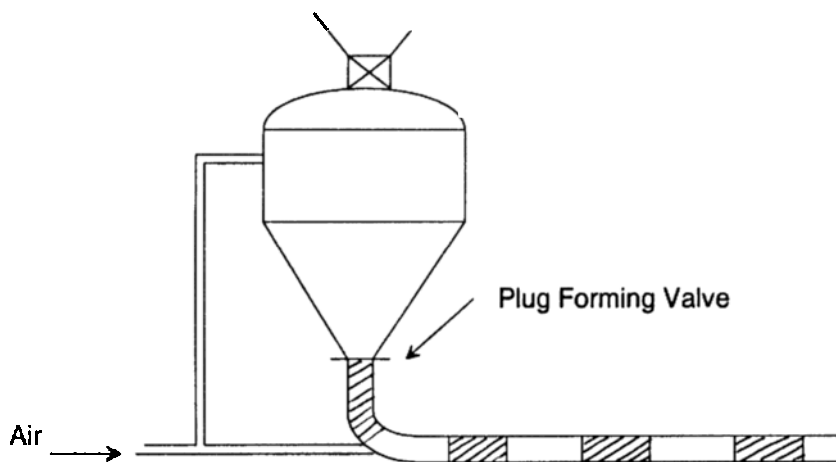
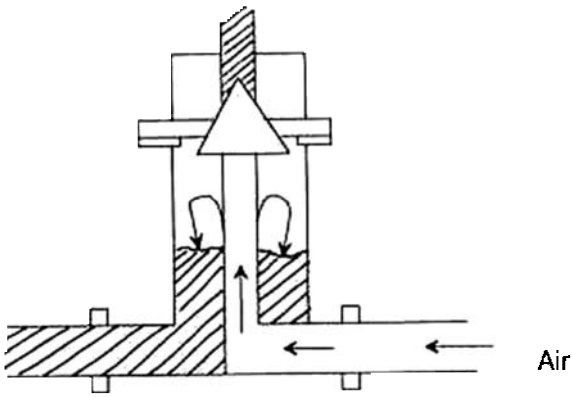
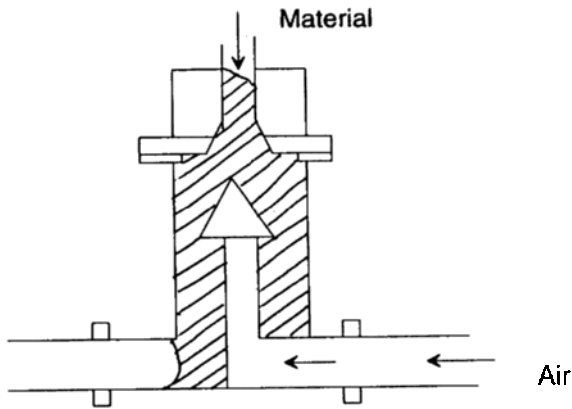


Figure 11. Plug pulse conveying system.



Conveying



Filling

Figure 12. Minipot conveying system.

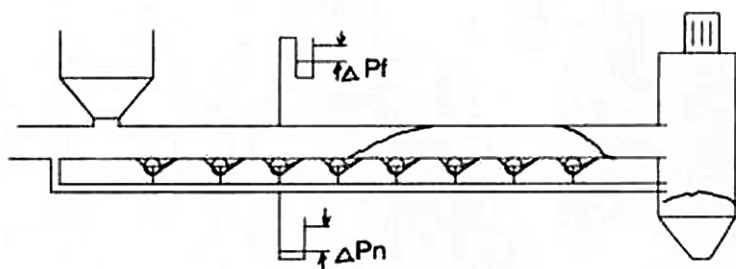


Figure 13. Pneumosplit (*Waeschle*).

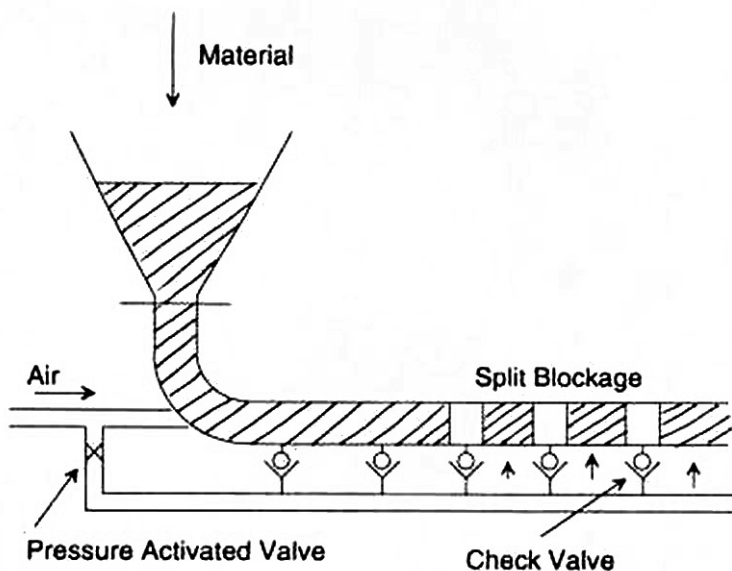


Figure 14. Fluid-schub system (*Buhler*).

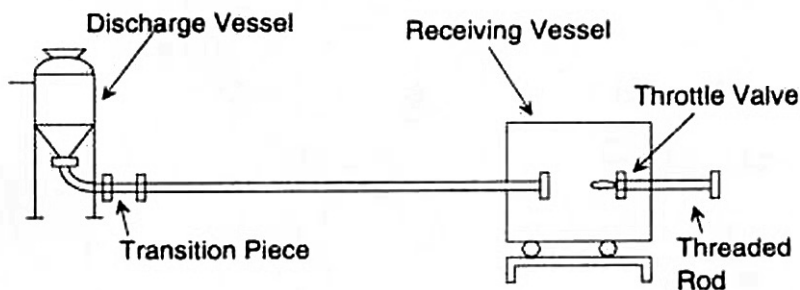


Figure 15. Extruded flow system.

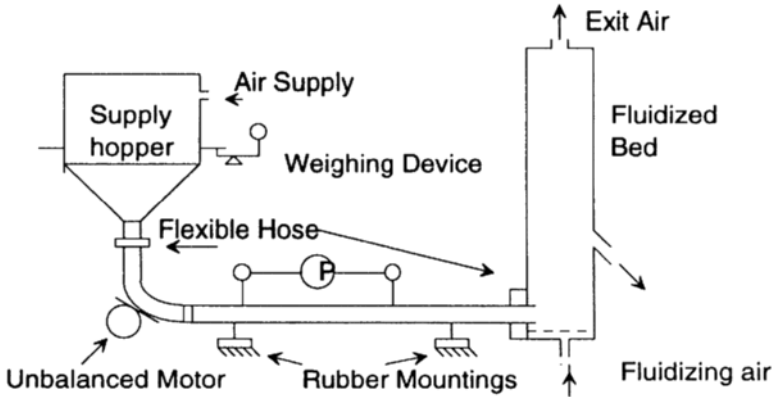


Figure 16. Molerus dense phase transport system.

2.0 ADVANTAGES OF DENSE PHASE CONVEYING

There have been a number of advantages that have been listed for dense phase conveying by Paul (1990). These are quoted as

- (i) Decreased energy usage due to significantly reduced volumes of air.
- (ii) Reduced material breakage or degradation due to slower conveying velocities.
- (iii) Reduced pipeline wear due to lower conveying velocities.
- (iv) Smaller conveying pipeline sizes due to heavier line loading capabilities.
- (v) Smaller dust collection requirements at the material destination due to lower conveying air volumes.

In addition Paul has prepared a chart listing the characteristics of the dense phase conveying in comparison to dilute and medium dense phase systems as shown in Fig. 17.

Vendors have used certain types of dense phase conveying operations. In the trade, these vendors and their unique modes of transport have been classified in Fig. 3.

Characteristic	Dilute Phase	Medium Dense Phase	Dense Phase
Required air velocity at pick-up point	greater than 3,000 ft/min	1,500 to 2,500 ft/min	less than 1,200 ft/min
Typical pick-up velocity	4,000 ft/min	1,800 ft/min	900 ft/min
Material velocity at convey line termination	greater than 5,000 ft/min	3,000 to 5,000 ft/min	less than 3,000 ft/min
Typical terminal velocity	6,000 ft/min	4,000 ft/min	2,500 ft/min
Conveying pressure range	less than 12 psig	15 to 30 psig	greater than 40 psig
Typical conveying pressure	10 psig	25 psig	60 psig
Material to air ratio (#:#)	less than 10:1	20:1 to 30:1	more than 50:1
Typical material to air ratio (#:#)	5:1	22:1	90:1
Material flow characteristics	particles suspended in the airstream	saltated flow	plug flow
Energy usage	highest	depends on the application	lowest
Typical application	nuisance dust collection, non-abrasive materials	multiple source/multiple destination systems	abrasive or fragile materials
Advantages	continuous material flow	best for vacuum/pressure systems	high capacity or long distance conveying

Figure 17. Pneumatic conveying system classification (by Paul, 1991).

3.0 BASIC PHYSICS

A starting model can be selected depending on the type of dense phase transport. Modeling a homogeneous dense phase would use the same approach as dilute phase with a new frictional term. This approach would have two contributions due to the gas alone and the linear combination with the solids contribution.

$$\text{Eq. (1)} \quad \Delta P = \Delta P_{gas} + \Delta P_{solids}$$

Mathur and Klinzing (1981) have developed a frictional term to account for the solids pressure drop which is meant for high loading systems ($m_L = 10$ to 50). Their expression for f_s is

$$\text{Eq. (2)} \quad f_s = 55.5 D^{1.1} / (U_g^{0.64} d_p^{0.26} r_p^{0.91})$$

where the pressure drop for the solid contribution is

$$\text{Eq. (3)} \quad (\Delta P / L)_{solids} = f_s (1 - e) r_p U_f^2 / D$$

A work by Stegmaier (1978) has also developed a friction factor associated with the solids flow. This expression is

$$\text{Eq. (4)} \quad f_s = (2.1 / 4) m_L^{-0.3} Fr^{-1} Fr^{*0.25} (d_p / D)^{-0.1}$$

where

$$\text{Eq. (5)} \quad (\Delta P / L)_{solids} = m_L f_s r U_f^2 / D$$

and

$$\text{Eq. (6)} \quad Fr = U_f^2 / gD$$

$$\text{Eq. (7)} \quad Fr^* = U_t^2 / gD$$

696 Fluidization, Solids Handling, and Processing

Weber (1973) has developed a simple expression for dense phase which can be written as

$$\text{Eq. (8)} \quad -dP/P = \mathbf{b}g\mathbf{m}_L dl / (RTV_p/V_f)$$

This equation can be integrated to yield

$$\text{Eq. (9)} \quad P_1 = P_2 \exp(\mathbf{b}g\mathbf{m}_L l / [R'TV_p/V_f])$$

where $\mathbf{b} = \sin \mathbf{a} + \mathbf{m}_k \cos \mathbf{a}$
 \mathbf{m}_k = coefficient of sliding friction

Wen and Simon (1959) have recommended an overall expression that lumps the air and solids pressure contributions together.

$$\text{Eq. (10)} \quad \Delta P/L = 3.79W(144 * V_g^{0.55})(d_p/D)^{0.25}$$

where W - lb/ft²s
 V_g - ft/s

The Wen and Simon expression has often been used to calculate the pressure loss in systems where one has a high concentration material at the bottom of the pipeline. This type of flow is often called *two-phase flow*. Wirth and Molerus (1986) have termed this two-phase flow as *strand flow* and have developed a technique to predict the pressure loss in such flows. Using Figs. 18 and 19 one can follow the procedure:

(i) Calculate the friction number Fri from

$$\text{Eq. (11)} \quad Fri^2 = V_g^2 \frac{\mathbf{r}_p}{[\mathbf{r}(1 - \mathbf{r}/\mathbf{r}_p)(1 - \mathbf{e})Dgfr]}$$

where \mathbf{e} = voidage of strand (0.4)
 fr = coefficient of sliding friction = 0.6

(ii) The loading μ_1 is set and $\mathbf{r}\mu/[\mathbf{r}_p(1 - \epsilon)]$ is calculated.

(iii) These values locate a point on the Fig. 18 and from the ordinate the reduced pressure drop can be found.

With a simulation technique Peng et al. (1994) have studied the particle-particle collisions with rotational and floating mechanisms of coarse particles in horizontal flow for higher concentrations of particles. Figure 20 gives the distribution of particles across the pipe cross-section. One notes that higher concentrations are seen at the bottom of the pipe.

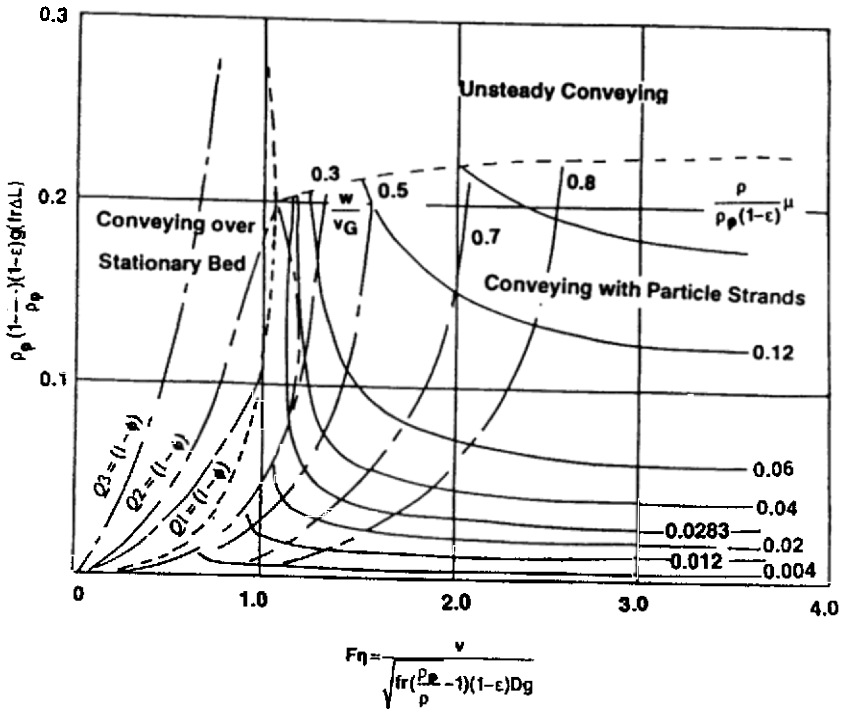


Figure 18. Additional pressure drop and state diagram for stable conveying particle with sliding strands ($e = 0.4$). (Wirth and Molerus, 1986.)

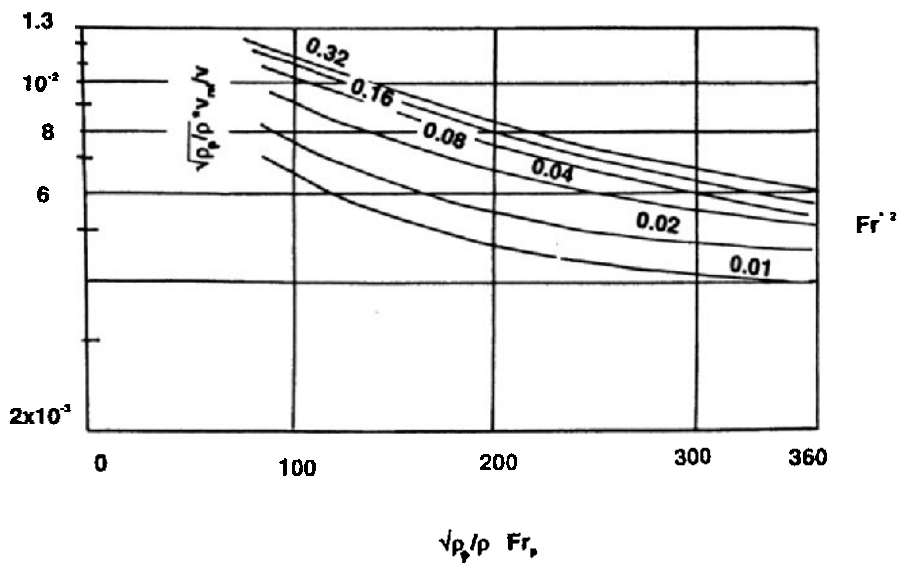


Figure 19. State diagram for suspended flow conveying in horizontal pipes. (Wirth and Molerus, 1986.)

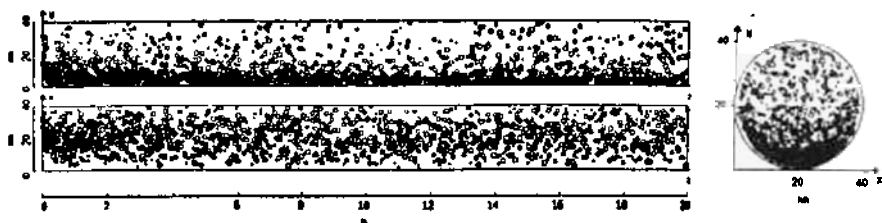


Figure 20. Dense phase simulation by Peng, Tomita and Tashiro (1991)..

4.0 PULSED PISTON FLOWS

Welschof (1962) carried out tests on dense phase plugs having a low velocity of 1 m/s. Later Lippert (1965) did an systematic analysis of the plug flow behavior. Following these researchers in the plug field were Weber (1973), Konrad et al. (1980) and Legel and Schwedes (1984). In

these analyses, a moving packed bed model was proposed using the theory of soil mechanics. An experimental study by Dickson et al. (1978) showed how a plug moved by mechanical means requires a force that increases exponentially with plug length. A simple force balance for a cohesive powder inclined in a plug at an angle of α can be given as

$$\text{Eq. (12)} \quad \frac{dP}{dZ} = \frac{d\mathbf{s}_{Ax}}{dZ} + \frac{4t_w}{D} + g \sin \alpha$$

Konrad was the first to address the issue of pulsed piston transport using the properties of the solids as they slide through the pipe in a plug-like motion. The friction generated in such systems often can be likened to bin and hopper flow and design, requiring shear stress measurements such as carried out by the Jenike shear stress unit. The final expression using the Konrad approach can be written for horizontal flow as

$$\text{Eq. (13)}$$

$$\frac{\Delta P}{L_p} = \frac{4m_w K_w F'}{D} + \frac{4m_w (K_w + 1) c' \cos f \cos(w - f_w)}{D} + 2r_b g \tan f_w + 4C_w / D$$

The stress terms F' at the front of the plug and B' at the back of the plug, dependent on the pressure drop and powder properties, can be developed from a momentum balance but often times they are set equal to each other. Using the momentum balance

$$\text{Eq. (14)} \quad F' = r_b \frac{dV_p^2}{1 - d}$$

where

$$\text{Eq. (15)} \quad d = \frac{1}{1 + c' / 0.542 (gD)^{1/2}}$$

The term c' is zero for cohesionless powders such as plastic pellets. As one sees, there are several parameters that need to be measured specifically

for the particular material conveying. This type of data is difficult to generalize which makes pulse piston modeling particularly difficult. Other investigators have studied the pulse piston flow operation (Legel and Swedes, Lippert, Aziz and Klinzing, 1988). Pulse piston operations are often demonstrated at trade shows where plastic pellets are used to demonstrate the concept. Plastic pellets are unique materials in that they can actually form their own pulsed pistons without special feeding devices. Cohesive materials require special feeder arrangements as has been seen in the specific examples shown above.

Weber (1973) has put forth a rather simple approach to pulsed piston modeling which couples the gas and solid behavior. The expression that Weber suggested is given in Eq. (9). One notes that this expression has an exponential decay of the pressure as the plug length decreases. This behavior has often been seen in industrial operations.

A series of studies were performed by Borzone and Klinzing (1987), Gu and Klinzing (1989) and Aziz and Klinzing (1990) on plug flow of coal. In order to transport plugs of fine materials, especially in the vertical case, it is necessary to have a sudden application of pressure so that the transport gas does not leak through the plug. It is very apparent that there exists a minimum plug length for material transport in this mode or else there will be a breakthrough of the gas leaving a mound of material on the bottom of the pipe. Their modeling was confined to modifying the work of Konrad for cohesive flow, as well as that of Weber. Good agreement was seen between the experiment and model as shown in Fig. 21. When increased pipe diameters were studied in vertical flow, the minimum plug length did not vary significantly with pipe diameter while the maximum plug lengths decreased with pipe diameter to maintain stable plugs. The vertical plugs were dominated by the gravitational force. The concept of plug length and optimum operation is one that often is of concern. Aziz, in his study of fine coal, found that there is a minimum plug length that will form in order to convey in the piston model. This minimum condition is of interest in the design of any pulse piston operation. Unfortunately, the ability to predict such a minimum length is lacking. Known powder properties are essential to predict the minimum plug lengths. Figure 22 shows the various modes of collapse of the horizontal plugs when the plug length is below the minimum value. It has also been observed by Aziz that a layer of material can be deposited on the bottom of the pipe and a plug-like flow will move with this as its base, thus transporting in a half-plug mode. The pressure drop across a plug can be represented by a straight line behavior as predicted by the

Konrad model for relatively short plug. Longer plugs (3 meters +) show an exponential pressure drop across the plug. Figure 23 indicates this behavior observed by Aziz. This nonlinear increase in pressure across a long plug can be observed in a simple experiment developed by Arnold (1992). A plug of solids supported by a loose fitting disk attached by a wire over a pulley shows that as the plug length increases the force necessary to move the plug increases exponentially. Addition of a small amount of lubrication or fluidization air shows a marked decrease in the force to move the plug for the apparatus shown in Fig. 24.

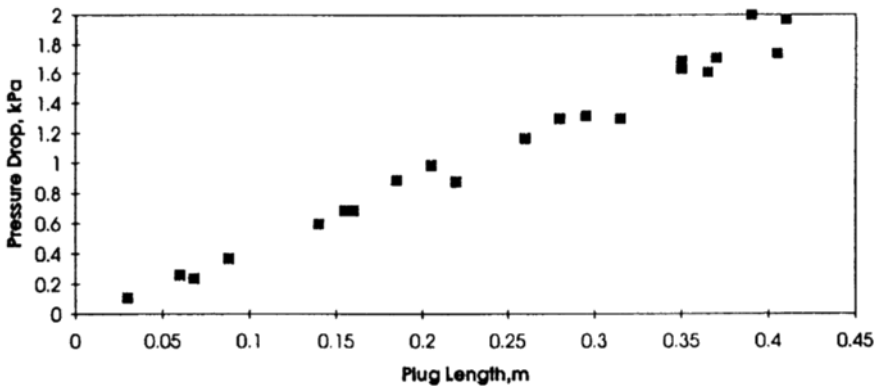


Figure 21. Pressure drop versus plug length. (Aziz and Klinzing, 1990.)

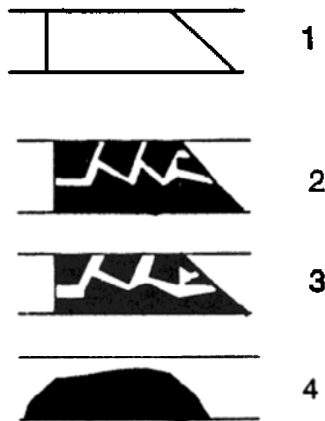


Figure 22. Hypothesis of plug collapse (increasing gas leakage with position).

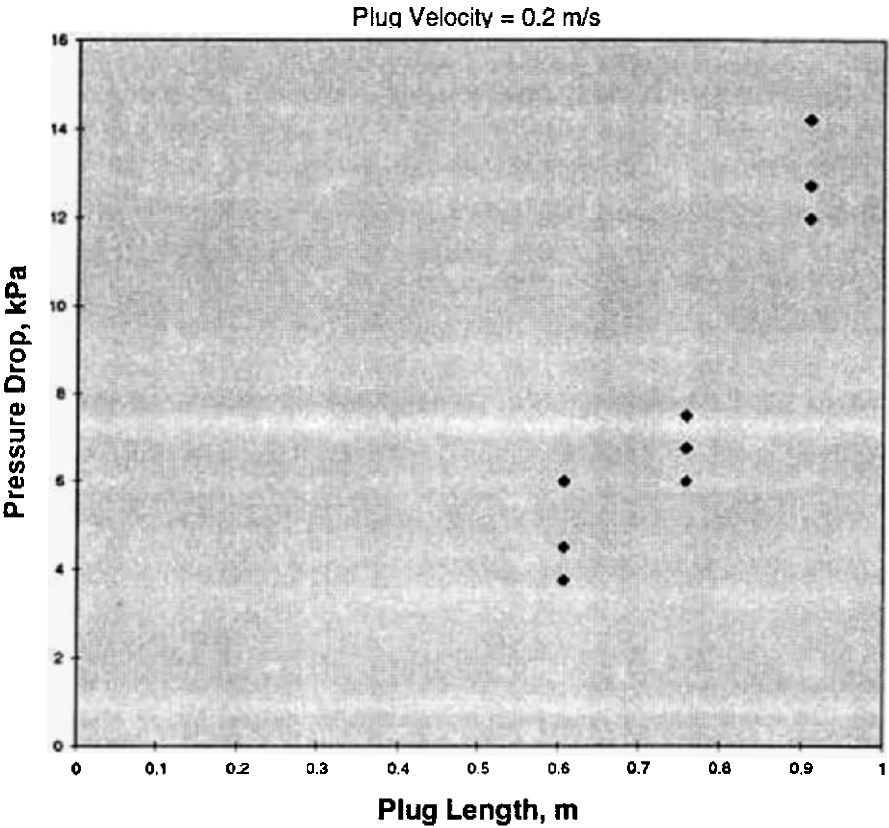


Figure 23. Pressure drop for Pittsburgh coal for a discrete plug flow.

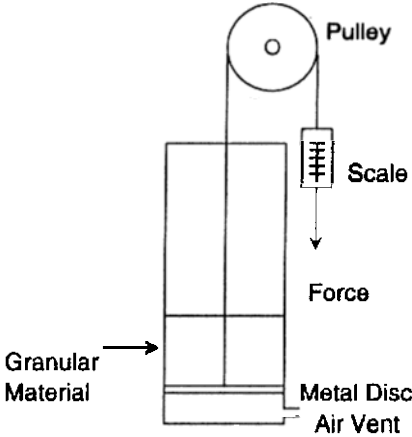


Figure 24. Arnold's plug flow device.

Recently, Destoop (1994) has addressed a system consisting of a piston being conveyed in a pulse piston fashion. Likewise Plasynski et al. (1994) have also addressed this type of flow giving an expression for modeling and predicting the minimum plug length. The minimum plug length can be found by solution of a force balance shown in Fig. 25 and represented as

$$\text{Eq. (16)} \quad A_T dP = s_{Az} A_T + t_w A_{cl} + t A_i$$

where A_T = transverse cross sectional area at failure

$$= (1/8)D^2(q - \sin q)$$

A_{cl} = circumferential area at failure

$$\begin{aligned} A_i &= \text{interfacial powder area at failure} \\ &= D \sin(q/2) L_{sp} \end{aligned}$$

In addition, for the system one sees as the line length increases the length of the gas plugs will expand. Figure 26 shows an example of this condition for a specific example.

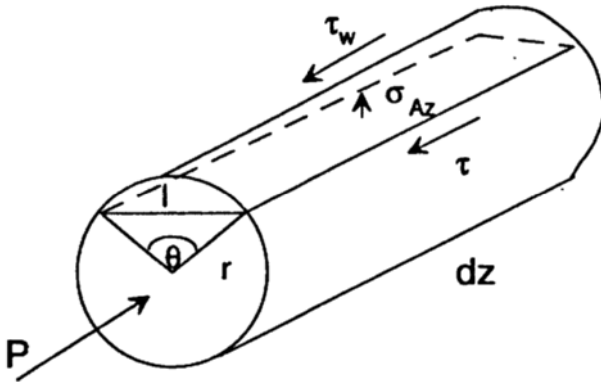


Figure 25. Plug flow shear mechanism.

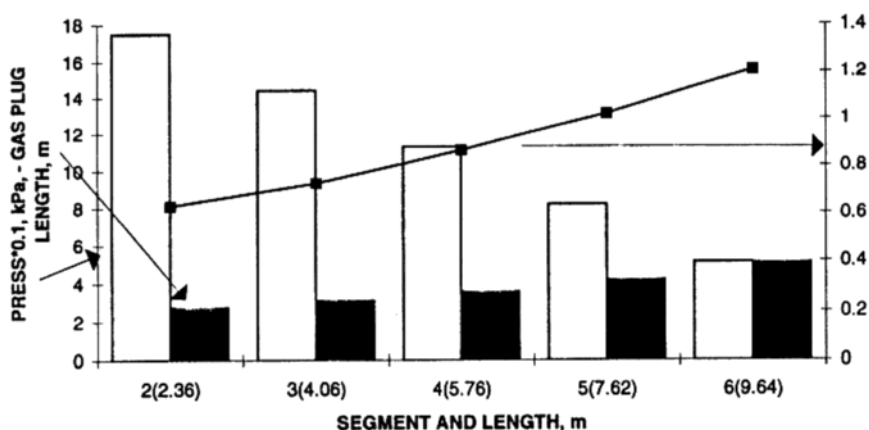


Figure 26. Plug and air gap flow behavior with distance.

Recently Min (1994) under the direction of Wypych has experimentally studied the conveying of plastic particles and wheat over a sizable distance in the pulsed piston operation. The results that they obtained experimentally agree qualitatively with the model suggested by Plasynski et al. and Destoop. Figure 27 exhibits this length of the air gap as a function of air or solids flow rates at constant air or solids mass flow. There is design strategy for this type of flow that can be suggested.

Tsuji et al. (1990) have modeled the flow of plastic pellets in the plug mode with discrete dynamics following the behavior of each particle. The use of a dash pot/spring arrangement to account for the friction was employed. Their results show remarkable agreement with the actual behavior of real systems. Figure 28 shows these flow patterns. Using models to account for turbulent gas-solid mixtures, Sinclair (1994) has developed a technique that could have promise for the dense phase transport.

Further analysis of plug flow has been given by Destoop and Russell (1995) with a simulated computer model for catalyst and polymer materials. The model was developed based on piston-like flow of plugs separated by plugs of gas. The model has been employed taking into account the product grade, temperature, flow rates and line configuration.

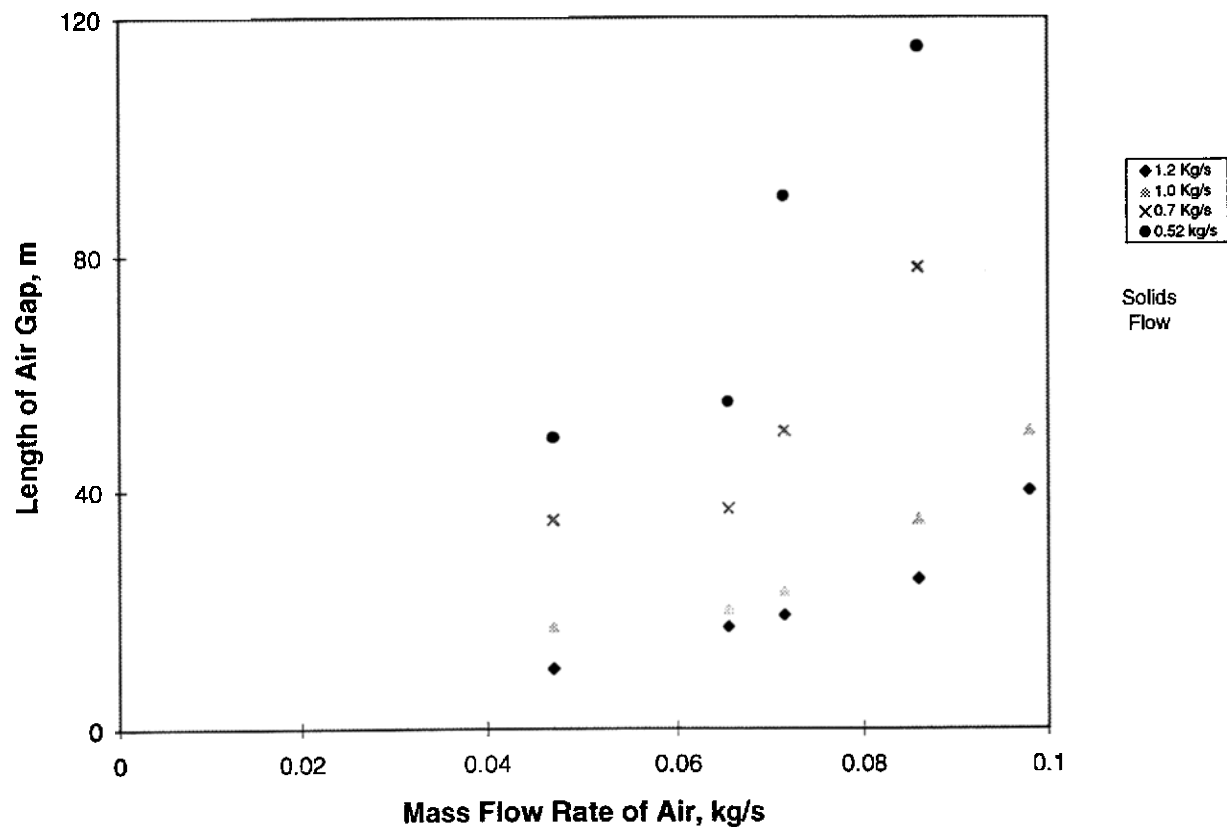


Figure 27. Air flow gap length versus mass flow rate of air for plastic pellets. (Min, 1994.)

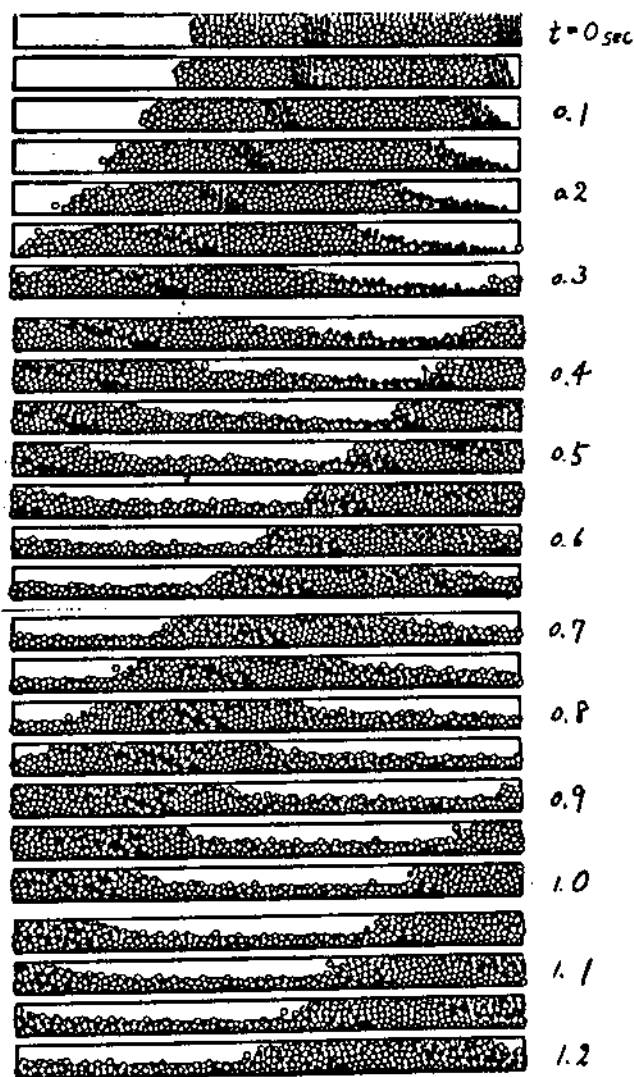


Figure 28. Plug flow simulation. (By Tsuji *et al.*, 1990.)

5.0 VERTICAL FLOW SYSTEMS

The use of recirculating fluid beds has caused considerable interest in dense phase vertical conveying. These units are indeed dense phase transport systems with a significant amount of recirculation taking place.

There are several researchers who have addressed this operation. Of particular note is the modeling of Yang (1988) and the analysis of Knowlton (1994) for particularly large diameter units. Yang presented a model that describes the dynamics of a circulating fast fluidized bed. The dilute phase region was correlated with a set of equations he previously developed for this type of flow. The pressure drop in the dense phase with an annular region is given as

$$\text{Eq. (17)} \qquad \Delta P = r_p (1 - e_{ave}) L$$

with the solids inventory in this region as

$$\text{Eq. (18)} \qquad I = r_p (1 - e_{ave}) A_r L$$

The height of the dense phase L is obtained by a pressure balance around the complete circulating fluidized bed loop. Good agreement is seen with this model and the existing data in the field.

Knowlton has cautioned on the difference between small diameter and large diameter systems for pressure losses. The difference between these systems is especially apparent for dense phase flow where recirculation occurs and wall friction differs considerably. Li and Kwauk (1989, 1989) have also studied the dense phase vertical transport in their analysis and approach to recirculating fluid beds. Li and Kwauk's analysis included the dynamics of a vertical pneumatic moving bed upward transport using the basic solid mechanics formulation. Some noncircular geometries were treated including experimental verification. The flows have been characterized into packed and transition flows. Accurate prediction of the discharge rates from these systems has been obtained.

Vertical pneumatic moving bed transport was also explored with a theoretical and experimental study by Li and Kwauk (1989). A criterion was put forth for stable operations which include absence of bubbles, slugs and voidage pockets, and having a constant mean particle velocity. There should be a means of suppressing fluidization and bubbling and sufficient hydrodynamic drag to permit lower-layer particles to be lifted to the upper layers. With a pressure drop of 1.5 times that to overcome gravity, the critical pneumatic moving-bed transport can occur.

Li (1994) has also studied the mechanics of arching in moving-bed standpipe flow. He was able, for this downflow situation, to obtain the critical arching span which agrees with reported data. The critical or minimum radius R_c for no arching is given as

$$\text{Eq. (19)} \quad R_c = \frac{f_c \sin 2\bar{b}'}{[1 - k \frac{(1 + \sin d)}{(1 + \cos 2b \sin d)} \frac{\sin 2\bar{b}'}{2 \tan d}]} \frac{1}{[r_b g + \Delta P / \Delta h]}$$

6.0 BOOSTERS

The topic of boosters is often seen as either the salvation or demon of dense phase transport. The design of the appropriate placement of booster is still evasive. Often too many boosters are utilized such that the overall gas usage turns out to have a dilute phase system. The Waeschle Company has designed a unique booster system that has individual controls. This design can handle most situations; for example, if a long plug forms by the union of two plugs or other flow hindrances, the system responds by injecting air to assist in the transport. This action breaks the plug into more manageable plug lengths. Overall care must be taken in using the boosters. Boosters can help in the conveying of a variety of difficult materials. When the flow causes stresses to be built up at bends and other stress points, the proper application of a booster can provide the added air to permit trouble-free conveyance. One needs to remember that a particular booster application that worked for one material will probably not work for another.

Secondary air injection for the transport of solids has seen little analysis in the literature despite the prevalence of this technology in industry. One exception is the recent work of Dhodapkar et al. (1995). This analysis employs the use of a sizable pilot unit for developing operational guidelines for Geldart type B and D, free flowing, plastic pellets and granular polymers. Booster air was shown to lower the average velocity, permit higher operating pressures, and reduce the unstable operation of the system. Pressure fluctuations were significantly reduced for the Geldart type B material when using boosters. They also found that flow can be initiated successfully in a full line at lower conveying pressures with booster air injection.

NOTATIONS

A	- Area
C	- Internal cohesion coefficient
c'	- Cohesion coefficient
c_w	- Wall cohesion coefficient
D	- Diameter of pipe
d_p	- Particle diameter
F	- Stress at the front of the plug
f_s	- Solids friction factor
Fr	- Froude Number
g	- Gravity constant
K	- Coefficient of internal friction $(1-\sin^2 f)/(1+\sin^2 f)$
K_w	- Coefficient of internal friction at the wall
l	- Length of sector at failure
L	- Length of plug or transport distance
n	- Number of plugs in the pipeline
P	- Pressure
R	- Gas law constant
T	- Temperature
U_g	- Superficial velocity
U_f	- Fluid velocity
V	- Volume
W	- Solids flux
z	- Distance

Greek

α	- Angle of inclination
ϵ	- Voidage
f	- Angle of internal friction
f_w	- Angle of wall friction
q	- Sector angle at failure
ρ	- Gas density
ρ_b	- Bulk density
ρ_p	- Particle density
σ	- Normal stress
τ	- Shear stress
τ_w	- Wall shear stress
m_L	- Solids loading
$\sin w \sim \sin f_w / \sin f$	

Subscripts

- C1 - section at failure
- i - integer, interfacial
- sp - plug
- T - total
- w - wall
- z - distance

REFERENCES

- Arnold, P., Personal communication (1992)
- Aziz, Z. B., and Klinzing, G. E., "Plug Flow Transport of Cohesive Coal: Horizontal and Inclined Flows," *Powder Tech.*, 55:97-105 (1988)
- Aziz, Z. B., and Klinzing, G. E., "Dense Phase Plug Flow Transfer: The 1-inch Horizontal Flow," *Powder Tech.*, 62:41-49 (1990)
- Borzzone, L. A., and Klinzing, G. E., "Dense Phase Transport: Vertical Plug Flow," *Powder Tech.*, 53:273 (1987)
- Destoop, T., "Mathematical of Dense Phase Conveying Systems - A Revolutionary Move Towards 'Smart' System Control," *Proc. of 1994 Bulk Solids Handling Conf.*, Rosemont, IL (1994)
- Destoop, T., and Russell, B., *Proceedings of the Fluidization and Particle Systems Sessions of AIChE Annual Meeting*, pp. 351-355, Miami, FL (1995)
- Dhodapkar, S. V., Jacob, K., and Merrick, D., *Proc. of the Fluidization and Particle Systems Sessions of AIChE Annual Meeting*, Miami, FL (1995)
- Dhodapkar, S. V., Personal communications (1991)
- Gu, H., and Klinzing, G. E., "Vertical Plug Flow of Cohesive Coal in 2- and 4-Inch Pipes," *Powder Tech.*, 57:59-67 (1989)
- Knowlton, T., "The Effect of the System Pressure/Pipe-Diameter/Mass Flux Interaction on Pressure Drop in Dilute Phase Pneumatic Conveying," *Proc. of Pneumatic Conveying Workshop, Powder Technol. Forum*, AIChE, Denver (1994)
- Konrad, K., "Dense Phase Pneumatic Conveying: A Review," *Powder Tech.*, 49:1 (1986)
- Konrad, K., Harrison, D., Nedderman, R. M., and Davidson, J. F., *Proc. of Pneumotransport 5*, Paper E1, BHRA, p. 225, Cranfield, Bedford, UK (1980)

- Legel, D., and Swedes, J., "Investigation of Pneumatic Conveying of Plugs of Cohesionless Bulk Solids in Horizontal Pipes," *Bulk Solids Handling*, 4(2):53–59 (1984)
- Li, H., "Mechanics of Arching in a Moving-Bed Standpipe with Interstitial Gas Flow," *Powder Tech.*, 78:179–18 (1994)
- Li, H., and Kwauk, M., "Vertical Pneumatic Moving-Bed Transport - I. Analysis of Flow Dynamics," *Chem. Engr. Sci.*, 44:249–259 (1989)
- Li, H., and Kwauk, M., "Vertical Pneumatic Moving-Bed Transport - II. Experimental Findings," *Chem. Engr. Sci.*, 44:261–271 (1989)
- Lippert, A. "Die Staub-Luft-Forderung Pulvern und Schuttgutern mit hohen Konzentrationen im Gasstrom-ein neuer Fordergang," Dissertation TH. Univ. of Karlsruhe (1965)
- Marcus, R. D., Rizk, F., Klinzing, G. E., and Leung, M., "Pneumatic Conveying of Solids," Chapman Hall (1990)
- Mathur, M. P., and Klinzing, G. E., "The Dense and Extrusion Flow Regime in Gas-Solid Transport," *Can. J. of Chem. Engr.*, 59:590–594 (1981)
- Molerus, O., and Siebenhaar, W., "Vibration Induced Pneumatic Conveying," *Pneumatech IV*, p. 213, Glasgow, Scotland (1990)
- Min, B., "Ph.D. Dissertation, University of Wollongong, Australia (1994)
- Paul, K. D., "Dense Phase Pneumatic Conveying Improving Efficiency," *Powder and Bulk Engr.*, p. 41 (1991)
- Peng, X., Tomita, Y., and Tashiro, H., "Effect of Particle-Particle Collision and Particle Rotation upon Floating Mechanism of Coarse Particles in Horizontal Pneumatic Pipe," *JSME Intl. J., Series B*, 37(3):485–490 (1994)
- Plasynski, S. I., Dhodapkar, S. V., and Klinzing, G. E., *Powder Tech.*, 81:3–7 (1994)
- Sinclair, J., *Proc. of Pneumatic Conveying Workshop*, Powder Technology Forum, AIChE., Denver (1994)
- Stegmaier, W., *Fordern und Heben*, 28:363 (1978)
- Tsuji, Y., Tanaka, T., and Ishida, T., "Graphic Simulation of Plug Conveying," *Proc. of Pneumatech*, 4:39–50 (1990)
- Weber, M., "Stromungs-Foerdertechnik," *Krausskopf Verlag*, Mainz (1973)
- Welschof, G., "Pneumatische Forderung bei Grossen Fordergutkonzentrationen," *VDI-Forschungsscheff*, p. 492, VDI Verlag, Dusseldorf (1962)
- Wen, C. Y., and Simons, H. P., *AIChE J.*, 6:263–8 (1959)
- Wirth, K. E., and Molerus, O., "Critical Velocity and Pressure Drop for Horizontal Flow," 9:156–166 (1986)
- Yang, W. C., "A Model for the Dynamics of a Circulating Fluidized Bed Loop," *Second Int. Conf. on Circulating Fluidized Bed*, Compiègne, France (1988)

11

Design Considerations of Long-Distance Pneumatic Transport and Pipe Branching

Peter W. Wypych

1.0 INTRODUCTION

The pneumatic transportation of bulk solids through pipelines has been in existence for over one hundred years. Some of the earlier applications included the vacuum unloading of grain from ships and the extraction of sawdust from timber mills.

This method of conveying now is being selected for an increasing number of industrial applications and products and hence, is playing a more vital and integral role in numerous bulk handling operations and processes. Some of the major reasons are listed below.

- Enclosed, safe and environmentally attractive method of transport suitable to a wide variety of products, including those with bacteria-prone, toxic or explosive properties.

- Simple systems requiring a prime mover, a feeding device, a conveying pipeline and a cleaning or disengaging device (Marcus et al., 1990).
- Flexibility in pipeline layout.
- Ability to distribute product to a number of different areas within a plant and/or pick up material from several different locations.
- Low maintenance and manpower costs.
- Multiple use—a single pipeline can be used for a variety of products.
- Ease of automation and control.

Unfortunately, many new and old systems have not been designed properly and are being operated inefficiently. Some of the major consequences include high energy consumption, excessive system erosion, inadequate conveying capacity, unexpected pipeline blockages, excessive product damage and hence, poor quality control and/or increased maintenance. These problems have resulted mainly from

- A lack of appreciation of product properties and/or characteristics
- Inadequate and/or inaccurate design procedures
- Selecting unsuitable hardware and/or mode of transport (Wypych, 1995a)
- Improper commissioning and/or operation of the plant

A significant number of developments have occurred over the past decade to address these important issues of pneumatic conveying (Wypych, 1995a). This chapter summarizes some of the major design considerations that have resulted from this work in relation to long-distance and pipe branching applications.

2.0 LONG-DISTANCE PNEUMATIC CONVEYING

With the advent of high-pressure feeders after World War II (e.g., blow tanks, screw pumps), many designers and users began to apply pneumatic conveying to much greater distances and/or capacities (e.g.,

714 *Fluidization, Solids Handling, and Processing*

$L \geq 1$ km and/or $m_s \geq 100$ th^{-1}). However, in many cases, this resulted in various problems, such as

- higher than expected pressures and energy consumption,
- excessive transport velocities, system erosion (e.g., pipes, bends) and product damage,
- low system reliability (mainly due to premature failure of valves and instrumentation),
- inadequate conveying capacity, and/or
- unexpected material buildup and/or blockages along the pipeline.

These problems in turn were hampering the successful design and/or operation of long-distance pneumatic conveying systems and hence, the future potential of this method of transport to a wide variety of industries.

To overcome these problems, a number of interesting developments in research and technology have occurred over recent years and these have resulted in the following important design considerations.

- Characterization and classification of the material(s) to be conveyed.
- Improved blow tank design to ensure an efficient and controlled discharge rate of material.
- New test-design procedures for the accurate prediction of pipeline pressure drop, including the effects due to horizontal/vertical flow and bends.
- Stepped-diameter pipelines to minimize pressure drop, velocity, wear and power consumption.
- Reliable valves for blow tank filling, venting and discharge.
- Manual or automatic back-pressure unblocking of conveying pipelines.

2.1 **Product Characterization and Classification**

The characterization and classification of bulk solids is becoming an increasingly important design requirement to assess the suitability of

pneumatically conveying a material over long distances. The current trends and experiences indicate that the major influential parameters include

- Particle size *and* distribution
- Particle density, bulk density and particle shape
- Cohesive, wet, sticky and/or electrostatic properties (if applicable)
- Temperature of product and carrier gas
- Permeability (or fluidization) and deaeration characteristics of the material (Mainwaring and Reed, 1987; Jones and Mills, 1989), which depend strongly on the above parameters

Possibly, the most difficult aspect of determining particle size is selecting initially the correct or relevant definition and then calculating a mean or average diameter to represent the complete bulk solid. To some extent, this will depend on the following.

- The measuring apparatus and its principle of operation
- The final application or requirements (e.g., determination of free-settling velocity v_{∞} , minimum fluidization velocity V_{mf} , minimum transport velocity V_{fmin} , and/or pipeline air pressure drop Δp_l)
- The basis of definition used in a theoretical or empirical relationship (e.g., sieve or volume measurement)

In some cases, especially for very fine powders, researchers have looked at other properties to explain or classify product behavior. For example, Geldart et al. (1984) have found that the ratio of “tapped” to “aerated” bulk density provides a good indication of the likely fluidization characteristics of fine and cohesive powders.

However, this section pursues particle size measurement and evaluates its importance (as well as density) for the purpose of classifying the suitability of powders for long-distance pneumatic conveying applications. Initially, an appreciation of the fundamentals and the existing powder classification techniques is required.

Physical Properties. To determine or calculate particle size, it is important to be aware of the following different definitions and related properties (Geldart and Abrahamsen, 1981; Allen, 1975).

716 *Fluidization, Solids Handling, and Processing*

d_p = Arithmetic mean of adjacent sieve sizes.

d_{pm} = Mean particle size from a standard sieve analysis,

$$= \text{Eq. (1)} \quad \frac{\Sigma(\Delta M)}{\Sigma\left(\frac{\Delta M}{d_p}\right)}$$

where ΔM is the mass percent of product between adjacent sieves.

d_{pwm} = Weighted mean diameter (Allen, 1975) based on sieve analysis,

$$= \text{Eq. (2)} \quad \frac{\Sigma(\Delta M d_p)}{\Sigma(\Delta M)}$$

d_{sv} = Diameter of a sphere with the same surface area to volume ratio as the particle.

d_{svm} = Mean surface volume diameter,

$$= \text{Eq. (3)} \quad \frac{\Sigma(\Delta M)}{\Sigma\left(\frac{\Delta M}{d_{sv}}\right)}$$

d_v = Diameter of a sphere with the same volume as the particle.

d_{vm} = Mean (equivalent) volume diameter,

$$= \text{Eq. (4)} \quad \frac{\Sigma(\Delta M)}{\Sigma\left(\frac{\Delta M}{d_v}\right)}$$

d_{vwm} = Volume weighted mean diameter (Allen, 1975),

$$= \text{Eq. (5)} \quad \frac{\Sigma(\Delta M d_v)}{\Sigma(\Delta M)}$$

$$\begin{aligned}
 d_{50} &= \text{Median particle diameter (Allen, 1975).} \\
 d_{v50} &= d_{v50} \text{ for a volume diameter distribution.} \\
 d_{v50} &= d_{v50} \text{ for a sieve size distribution.} \\
 \Psi &= \text{Particle sphericity (Geldart and Abrahamsen, 1981).} \\
 &= \text{Eq. (6)} \quad \frac{d_{sv}}{d_v}
 \end{aligned}$$

Assuming the following results of Geldart and Abrahamsen (1981) and knowing (or assuming) appropriate values of sphericity, the various diameters d_{svm} , d_{v50} , d_{p50} , and d_{vm} may be determined for any given material. This information is particularly useful when it becomes necessary to compare the classification of different bulk solids, whose size distributions were determined on different machines or using different techniques (e.g., sieve analysis, volume-based measurement).

$$1.1 < \frac{d_v}{d_p} < 1.2, \quad \text{Average } \frac{d_v}{d_p} \approx 1.127$$

Some typical values of sphericity are listed below.

Pulverized coal	$\psi \approx 0.56$ (angular)
Cement	$\psi \approx 0.59$ (angular)
PVC powder	$\psi \approx 0.81$ (irregular spheroids)
Calcined alumina	$\psi \approx 0.84$ (coarse spheroids)
Hydrated alumina	$\psi \approx 0.86$ (rough spheroids)
Fly ash	$\psi \approx 0.90$ (approximate spheres)

After determining the relevant physical properties (i.e., particle size, solids particle density and bulk density), the next step is to evaluate some of the existing techniques of powder classification.

Powder Classification Techniques. The Geldart (1973) fluidization, and Dixon (1981) slugging classifications have been found useful in explaining:

- some of the feeding problems that can occur in blow tank feeders (Wypych and Arnold, 1986a),
- the differences that can occur in flow performance and minimum transport behavior (Wypych and Arnold, 1984).

Modifications to the Geldart (1973) fluidization diagram have been proposed by Molerus (1982) and Zenz (1984), but are not considered here as they require some knowledge or measurement of particle adhesion forces and bulk surface tension, respectively. That is, detailed investigations into evaluating and/or developing such fluidization diagrams are beyond the present scope of work.

Another useful classification technique that makes use of two different bench-type experiments (i.e., permeability and deaeration) has been presented by Mainwaring and Reed (1987). The above three classifications are described in the following sections.

Geldart (1973) Fluidization Classification. An “ideal” fluidization curve is presented in Fig. 1, which also shows schematically a typical fluidization test chamber (with the relevant variables Δh , Δp and V_f). Also, the method of determining V_{mf} (i.e., using the “Air-Decrease Test”) is demonstrated in Fig. 1. However, due to varying material properties (e.g., cohesion, wide size distribution), the “actual” variation of pressure in a fluidized bed may be quite different to that shown in Fig. 1 (Anon., 1983). Such information can be useful in providing further insight into a material’s behavior with air, which is important for pneumatic conveying, especially when long distances are involved.

Using fluidization data obtained from several researchers, Geldart (1973) characterized powders into four groups (i.e., A, B, C and D), according to their fluidization behavior and developed a classification diagram, as shown in Fig. 2. Note that r_f is the “operating” air density. The interested reader is directed to the Geldart (1973) paper for detailed descriptions of the various groups (including a numerical technique to distinguish between each one), and the Geldart et al. (1984) paper for more recent investigations into the fluidization of cohesive powders.

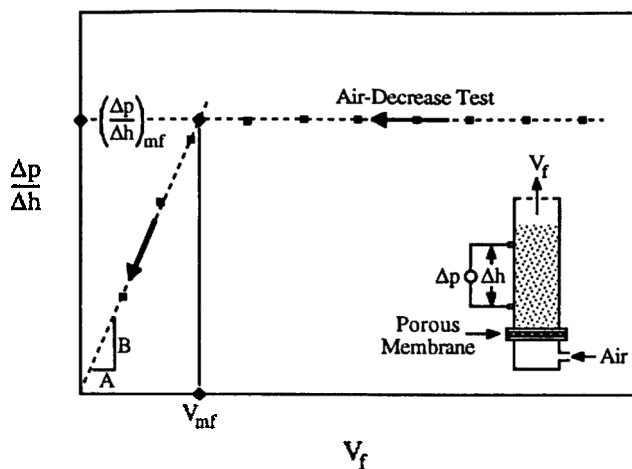


Figure 1. “Ideal” fluidization curve, showing typical test chamber and relevant parameters Δh , Δp , V_f and V_{mf} .

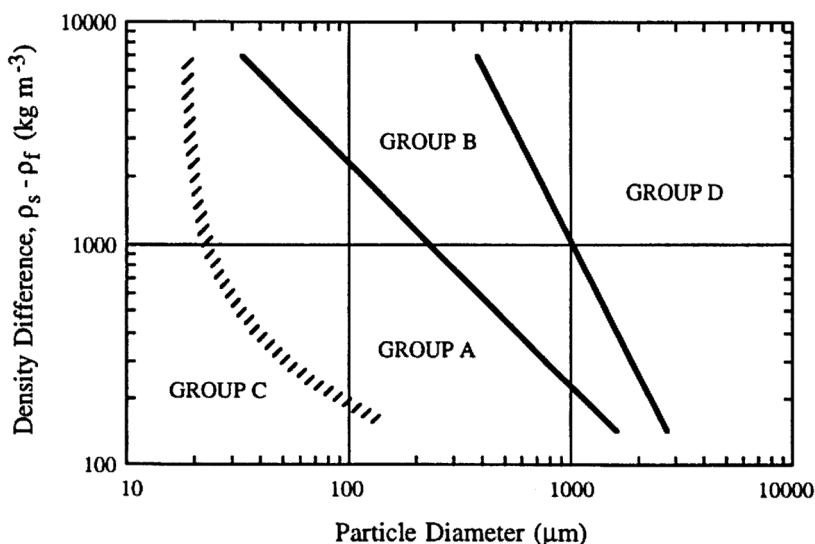


Figure 2. Fluidization Classification Diagram. (Geldart, 1973.)

The classification diagram of Geldart (1973) was never intended to predict pneumatic conveying behavior. However, it has been accepted by many researchers that the aeration and fluidization characteristics of bulk solids are important parameters in determining dense-phase suitability, such as fluidized dense-phase and low-velocity slug-flow (Wypych, 1995a). Based on experience and as explained later, this information is useful also in evaluating qualitatively a material's performance over long distances. Hence, it is important to appreciate the differences between the following four categories, as proposed by Geldart (1973).

Group A powders show a limited tendency to form bubbles and generally exhibit considerable bed expansion between the minimum fluidization velocity V_{mf} , and the minimum bubbling velocity V_{mb} . These powders also retain aeration and the fluidized bed collapses very slowly when the gas is turned off.

Group B materials fluidize readily and tend to form bubbles, which grow rapidly by coalescence. However, bed expansion is small. That is, the minimum bubbling velocity, V_{mb} , usually is approximately equal to (or only slightly greater than) the minimum fluidizing velocity V_{mf} . The fluidized bed does not retain its aeration and collapses quickly when the gas supply is removed.

Group C powders are of small particle size, cohesive by nature and hence, difficult to fluidize. Either the fluidized bed lifts as a solid plug of material or forms stable channels of air flow, which allows the fluidizing gas to escape. The latter phenomenon is referred to simply as "channelling". It may be possible to fluidize such powders by mechanical agitation (e.g., stirring, vibration).

Group D products generally are of large particle size and/or very high solids particle density. In some respects, fluidization behavior is similar to Group B, although higher gas velocities are required for fluidization.

Note the "mean diameter" used by Geldart (1973) is actually a *surface volume mean diameter* d_{svm} , based on Eq. (3). However, comparing the fluidization curves of several materials with the Geldart (1973) diagram (e.g., fly ash, pulverized coal, coarse ash, PVC powder and screened coke), Wypych (1989b) found the following:

- The reciprocal form of particle size definition, i.e., Eqs. (1), (3) and (4), tends to “overemphasize” the influence of the finer particles (i.e., in terms of the Geldart [1973] classification descriptions),
- The weighted or product type of definition, i.e., Eqs (2) and (5), tends to “under-emphasize” the influence of the finer particles (or overemphasize the coarse end of the size distribution),
- The relatively wide particle size distributions of the pulverized coal and fly ash (e.g., 1 μm to 200 μm) seem to be the major contributing factor to the effects described above (i.e., the materials tested by Geldart [1973] had fairly narrow size distributions),
- The discrepancies described above are not so apparent for PVC powder, which had a relatively narrow size distribution (i.e., with respect to fly ash and pulverized coal),
- The median particle diameter, d_{v50} , seems to provide a better indication of fluidization performance, as described by Geldart (1973).

Therefore, based on the results of Wypych (1989b), the Geldart (1973) classification diagram does seem to provide a reasonable technique for predicting fluidization behavior (i.e., using d_{v50} instead of d_{svm} , especially for products having a wide particle size distribution). However, it should be noted that when Geldart proposed his classification diagram, he suggested a shaded boundary region between Groups A and C. This indicates that some degree of overlap may exist between the two categories (i.e., some typical Group C powders could display Group A performance, or vice-versa). However, for the following reasons, it is believed that ultimately the actual product(s) should be tested in a large-scale fluidization test rig (e.g., similar to the one shown in Fig. 1), so that actual characteristics and behavior may be established and confirmed.

- Perhaps the greatest difficulty in predicting fluidization performance via the Geldart (1973) classification is deciding on a single diameter to represent the *complete* material, especially if the product possesses a wide particle size distribution. This is supported to some extent by the more recent bulk density approach proposed by Geldart et al. (1984).

- There is some doubt over the location of the boundary separating Groups A and C. The particle size versus density relationship proposed by Geldart (1973) may not be sufficient to define these regions. For example, refer to Geldart et al. (1984).
- Products lying close to a particular boundary may exhibit fluidization behavior from either one of the adjoining categories (e.g., a product which is in close proximity of the A-B boundary may exhibit characteristics from either Group A or B). It is difficult to estimate the “error” or “tolerance” associated with each boundary (e.g., between Groups A and B, or B and D).

Appreciating the possible limitations of the Geldart (1973) classification diagram, this technique still provides a good *initial* indication of what to expect when a given product is fluidized or mixed with air. Even though fluidization may be confirmed by experiment and used subsequently in the design of feeders (e.g., to establish possible rat-holing problems inside a blow tank, Wypych and Arnold, 1986a), the application of such information to predicting pneumatic conveying performance is a different matter and in fact, has been found to be inadequate (Wypych and Arnold, 1986b; Lohrmann and Marcus, 1984).

Dixon (1981) Slugging Classification. In an attempt to describe the natural behavior of different solids in dense-phase, Dixon (1979) developed theoretical slugging diagrams for different pipe diameter systems on the basis of the Geldart (1973) fluidization classification diagram (i.e., Groups A, B, C and D). Although Dixon’s diagrams were based on slugging criteria (Yang, 1976) for vertical transport, he indicated that they also generally support the observed behavior of materials in horizontal pipes. However, Dixon (1981) stated that there is some doubt over the location of the boundary between Groups A and C, and he subsequently reproduced this Geldart boundary directly onto the slugging diagrams. Refer to Figs. 3 and 4 for examples of slugging diagrams for 50 and 100 μm NB pipe diameter systems. For detailed descriptions of the various slugging classifications and the mathematical formulae to distinguish between each category, the reader is referred to the papers (Dixon, 1979; Dixon, 1981).

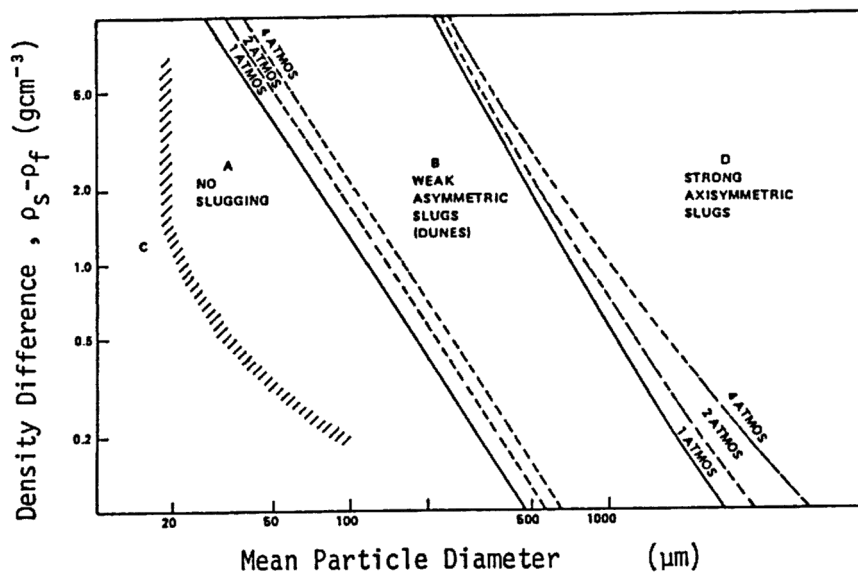


Figure 3. Slugging diagram for 50 mm pipe diameter system. (Dixon, 1981.)

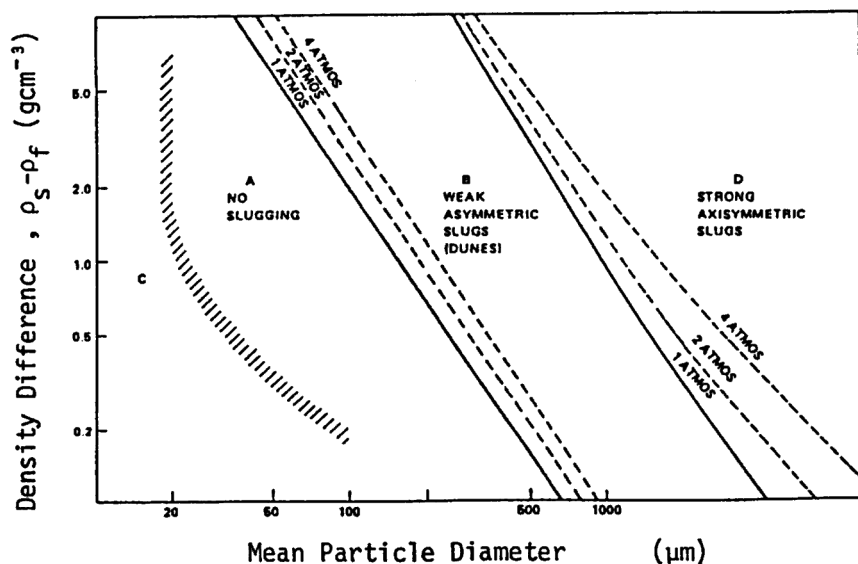


Figure 4. Slugging diagram for 100 mm pipe diameter system. (Dixon, 1981.)

A brief description of each of the four “slugging” categories, as suggested by Dixon (1979) is listed below.

Group A powders are the best candidates for dense-phase conveying and can achieve high solids/gas loadings. Note the “dense-phase” referred to here actually is “fluidized dense-phase” (Wypych, 1995a).

Group B powders can be troublesome (e.g., severe pipe vibrations) if high solids/gas loadings are contemplated.

Group C products arguably are the worst candidates for (fluidized) dense-phase conveying. This can be attributed to their poor fluidization characteristics. If these can be overcome, and it is possible that *not* all Geldart (1973) Group C powders possess poor fluidizing characteristics, then they should show the good performances attributable to Group A powders.

Group D materials are also good candidates for dense-phase conveying. Although they have relatively low solids/gas ratios (i.e., compared with Group A powders), they probably can be conveyed at higher loadings than Group B materials. Note the “dense-phase” referred to here actually is “low-velocity slug-flow” (Wypych, 1995a).

The following comments are based on the findings of Wypych (1989b) who compared the actual conveying characteristics of several materials with the slugging classifications of Dixon (1979) and Dixon (1981).

- For a product that is well contained “inside” a particular group (i.e., A, B, C or D), the Dixon (1981) slugging diagram and classifications generally provide a good *initial* indication of what to expect when the product is conveyed in the dense-phase mode.
- It is believed that the one main factor that will “upset” the suggestions of Dixon (1979, 1981) is particle size distribution. Note that a similar problem was described earlier for the Geldart (1973) diagram. Also, it is quite possible that differences in “particle shape” could contribute to this effect. For example, Dixon (1979, 1981) based most of his suggestions and observations on plastic powders and granules (i.e., relatively smooth particles with narrow size ranges).

- Materials that lie close to or are on a classification boundary may exhibit slugging behavior from either one of the adjoining categories. This could be explained further by the “particle size distribution” problem or limitation described above.
- The “particle to pipe diameter” ratio may be an influential parameter in predicting dense-phase performance. For example, this diameter effect was noticed recently when the good dense-phase (low-velocity slug-flow) performance of a granulated sugar in a 105 mm diameter pipeline could not be repeated in a 155 mm diameter pipeline. The shift to the “right” of the Group B-D boundary (i.e., as seen in Figs 3 and 4) with increasing pipe diameter would explain this difference in performance.
- The change in slugging characteristics of a given material due to increasing or decreasing operating pressure is difficult to confirm.

To emphasize some of the above comments and suggestions (as well as some of those presented earlier in relation to the Geldart [1973] diagram), the PVC powder results (Wypych, 1989b) are summarized below.

- PVC powder: $d_{v50} \approx 152 \mu\text{m}$, $r_s = 1400 \text{ kg m}^3$, $r_{bl} = 575 \text{ kg m}^{-3}$
- According to the fluidization diagram presented in Fig. 2, PVC powder was found to be classified as Geldart (1973) Group A (although close to the A-B boundary). Testing the product in a fluidization rig (Wypych, 1989b) confirmed the good fluidization characteristics suggested by Geldart (1973). This result was supported by the material’s excellent air-gravity conveying performance (Wypych and Arnold, 1985a). Based on these results, it would be reasonable to assume that this material would be suited to fluidized dense-phase.
- However, the PVC powder was tested in a 52 mm internal diameter pipeline, 71 m in length, and found to exhibit unstable plugging in the vicinity of saltation or minimum pressure (i.e., prior to the fluidized dense-phase region). That is, dilute-phase transport was *only* possible on this test rig. Also, solids/gas loadings were quite low (e.g., max $m^* \approx 20$). Note that the unstable plugging was accompanied by sudden increases in pressure and severe pipe vibrations.

- These unexpected results were confirmed by the Group B classification of Dixon (1979, 1981), (i.e., could be troublesome in dense-phase and produce severe pipe vibrations).

The above results demonstrate the danger of predicting the suitability of dense-phase based on only fluidization characteristics. Similar limitations have been observed by Lohrmann and Marcus (1984) with three Geldart (1973) Group A materials. In contrast, the Group B suggestions of Dixon (1979, 1981) not only confirm the observed minimum transport behavior (e.g., pipe vibrations, require high velocities), but also seem to explain the observed (Wypych, 1989b) flow behavior (i.e., dunes growing to fill the pipe causing the high velocity slugs of air to force their way through the material).

The apparent anomaly between poor dense-phase performance and good fluidization characteristics (as suggested by the PVC powder results) seems to be explained by the property of deaeration. That is, although this material displayed good fluidization characteristics and is classified as Geldart (1973) Group A, it was found to deaerate quickly. For example, on several occasions the expanded bubbling bed was seen (Wypych, 1989b) to lose its height in less than one second (i.e., after the fluidizing air was removed). On the other hand, “good” dense-phase materials, such as pulverized coal and fly ash, usually display excellent fluidization characteristics *but* also retain their aeration for considerable lengths of time (e.g., 10 to 30 minutes).

Mainwaring & Reed (1987) Classification Diagrams. The empirical classification technique proposed by Mainwaring and Reed, 1987, emphasizes the importance of permeability (obtained from a fluidization test) and deaeration. Jones and Mills, 1989 came to a similar conclusion and suggested further that the ratio of tapped to poured bulk density provides a good indication of the air retentive properties of a given material. Also, Geldart et al., 1984 proposed a similar ratio to distinguish between Group A and Group C powders.

The classification technique (Mainwaring and Reed, 1987) basically consists of two empirically-based diagrams, as shown in Figs. 5 and 6. To use these graphs, the following factors need to be determined.

- Pressure drop per unit length of bed, $\Delta p/\Delta h$, see Fig. 1.
- Value of $\Delta p/\Delta h$ at minimum fluidization, $(\Delta p/\Delta h)_{mf}$, see Fig. 1.
- Permeability factor, $k_p = A/B = V_f/(\Delta p/\Delta h)$, Fig. 1.

- $V_{mf} = k_p (\Delta p / \Delta h)_{mf}$.
- Deaeration factor, $k_d = t(\Delta p / \Delta h)$, where t = time taken for a deaerating bed to reach a pressure drop per unit length of $\Delta p / \Delta h$.
- Factor, $X = (k_d / r_s) / (\Delta p / \Delta h)$.

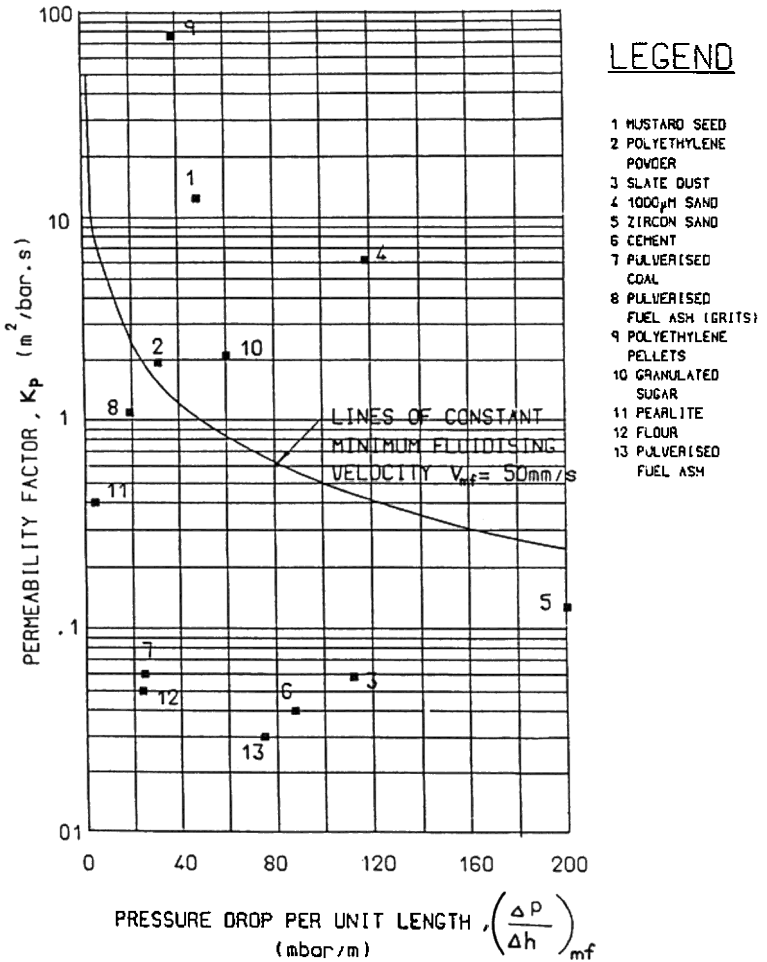


Figure 5. Pressure drop per unit length versus permeability factor. (Mainwaring and Reed, 1987.)

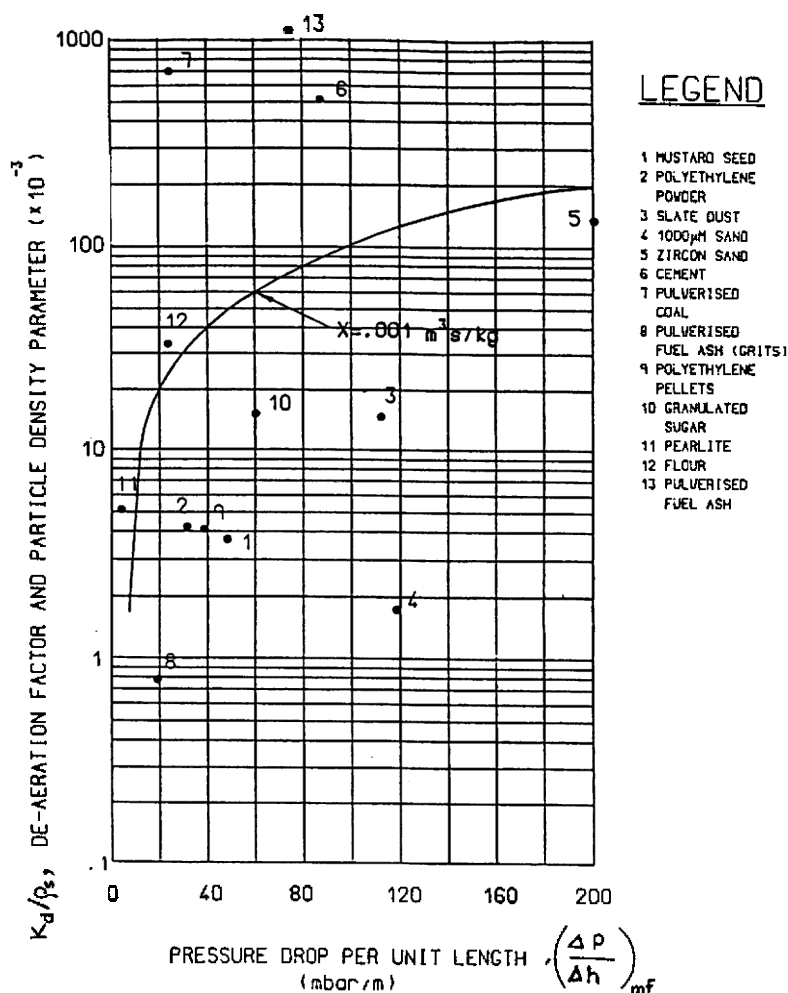


Figure 6. Pressure drop per unit length versus deaeration and particle density factor (Mainwaring and Reed, 1987).

Figure 5 is a plot of permeability factor k_p versus $(\Delta p/\Delta h)_{mf}$ and contains the boundary $V_{mf} = 50 \text{ mm s}^{-1}$. Figure 6 is a plot of k_d/r_s versus $(\Delta p/\Delta h)_{mf}$ and contains the boundary $X = 0.001 \text{ m}^3 \text{ s kg}^{-1}$. By using both Figs. 5 and 6, it is possible to propose the following three criteria relating to the potential modes of pneumatic conveying in conventional pipelines.

- If for a given material, $V_{mf} > 50 \text{ mm s}^{-1}$ (i.e., *above* the boundary shown in Fig. 5) and $X < 0.001 \text{ m}^3 \text{ s kg}^{-1}$ (i.e., *below* the boundary shown in Fig. 6), then dense-phase low-velocity slug-flow (Wypych, 1995a) is possible (e.g., mustard seed, polyethylene powder, 1000 μm sand, polyethylene pellets and granulated sugar). Note that dilute-phase also is possible.
- If $V_{mf} < 50 \text{ mm s}^{-1}$ and $X > 0.001 \text{ m}^3 \text{ s kg}^{-1}$, then fluidized dense-phase (Wypych, 1995a) is possible (e.g., cement, pulverized coal, flour, fly ash). Note that dilute-phase also is possible.
- If $V_{mf} < 50 \text{ mm s}^{-1}$ and $X < 0.001 \text{ m}^3 \text{ s kg}^{-1}$, then “fluidized” dense-phase or low-velocity slugging flow is not possible in a conventional pipeline (e.g., slate dust, zircon sand, fly ash grits). That is, *single-slug conveying* (Wypych, 1995a), *bypass conveying* (Wypych, 1995a) or dilute-phase may have to be considered for these materials.

Application to Long-Distance Pneumatic Conveying. From the above three classifications, there is sufficient evidence to suggest that powder classification (i.e., to select ultimately the most suitable mode of conveying for a given product and its behavioral properties) depends on the following properties:

- Particle size distribution and density.
- Particle shape or sphericity (as indicated by the definitions of diameter).
- Deaeration and permeability.
- The ratio of tapped to poured (or perhaps fluidized) bulk density.
- Diameter of conveying pipeline or particle to pipe diameter ratio.

Also, it seems that most of these properties are interdependent. For example, deaeration and permeability (Mainwaring and Reed, 1987) and perhaps the bulk density ratio (Jones and Mills, 1989) seem to provide an adequate mechanism to detect changes in material performance due to different particle size distribution, density and/or shape. However, possibly the greatest disadvantage or limitation of these empirical techniques is the need to standardize the experimental apparatus and techniques. For exam-

ple, the measured values of deaeration rate depend on the size of the plenum chamber and to some extent the type of gas distributor. Also, different devices and techniques are available to determine vibrated or tapped bulk density. Standardization is necessary so that the results will be applicable on an international level and can be used/compared by other researchers.

Based on the previous classifications and discussions, as well as the author's own experiences, it is suggested that the following design procedure and considerations be adopted to provide an initial indication of dense-phase suitability, which as described below also has been found useful in assessing conveying performance over long distances.

- For a given bulk solid, determine particle size distribution, median particle diameter d_{v50} (e.g., using a Coulter Counter or a Malvern Laser Diffraction Analyser) and r_s .
- Classify the bulk solid according to the Geldart (1973) fluidization diagram. This information is useful in estimating say, potential rat-holing problems inside blow tanks. If the material is relatively close to a classification boundary, then expect fluidization behavior from either one of the adjoining groups.
- Test the bulk solid in a fluidization chamber to confirm both the Geldart (1973) classification and the material's air retention properties (i.e., by undertaking deaeration experiments).
- Classify the bulk solid according to the Dixon (1979, 1981) slugging diagram that matches the existing or proposed diameter of pipeline. Based on the research and consulting experience of the author, the following possibilities are proposed in relation to the Dixon (1979) classifications.
 - Typical Group A materials (e.g., cement, baghouse fly ash, pulverized coal, carbon fines) are the best candidates for "fluidized" dense-phase (Wypych, 1995a) and long-distance pneumatic conveying. It is possible to achieve high values of solids/gas loading (e.g., $m^* = 150$ over 200 m; $m^* = 25$ over 1 km). These materials retain their aeration for considerable lengths of time.

- Typical Group B materials (e.g., alumina, PVC powder, fine sand, castor sugar) may cause serious problems in fluidized dense-phase (e.g., unstable plugging, severe pipe vibrations, high pressures) and hence, may need to be transported in dilute-phase over long distances (i.e., using conventional pipelines). It still may be possible to convey these materials in “dense-phase” using low-velocity slug-flow or bypass pipelines (Wypych, 1995a). Also, for the coarser Group B materials (e.g., fine sand, castor sugar), it may be possible to consider the alternative of single-slug dense-phase conveying (Wypych, 1995a). Of these three options, bypass conveying is preferred when long distances are involved, especially when $L > 500$ m.
- Typical Group C materials (e.g., precipitator fly ash, lead fume, zinc dust) may behave like Group A powders (i.e., good fluidized dense-phase or long-distance performance). However, these materials can be quite cohesive and it is important to ensure buildup problems do not occur inside the blow tank feeder or along the pipeline. For example, precipitator fly ash with $d_{v50} \approx 10 \mu\text{m}$ has been conveyed successfully and efficiently over long distances, whereas lead fume with $d_{v50} \approx 5 \mu\text{m}$ has been found to cause buildup and eventual blockage problems inside the pipeline. Flexible hoses or “collapsible” pipelines may be used to prevent this buildup of material. Another option is to consider low-velocity plugging using either an air-knife at the beginning of the pipeline or a bypass conveying pipeline. In some cases, the plugs tend to be “self-cleaning”. However, these options do not become practical over long distances and must be considered carefully in terms of capital and maintenance costs.
- Many typical Group D products (e.g., wheat, rice, sugar, plastic pellets, cereals, barley, malt, agglomerated milk powder) have relatively narrow

size distributions, high permeability and display natural slugging ability (Wypych and Hauser, 1990) and good low-velocity slug-flow (Wypych, 1995a). However, this mode of flow usually is limited to conveying distances of $L < 500$ m. The Group D materials that possess wide size distributions (especially a considerable amount of fines) and/or unusual particle shape (e.g., crushed coal, petroleum coke, crushed bath, rice hulls) usually are not suited to low-velocity conveying. In these cases, the options are dilute-phase or single-slug dense-phase (i.e., these materials usually are too coarse for bypass conveying). However, when long distances are involved, dilute-phase may be the only practical option.

- If any material is in the vicinity of a classification boundary (i.e., Group A-B or Group B-D boundary), then due to particle size distribution it is possible that the material may exhibit flow behavior or performance from either one of the adjoining categories.

Case Study. The above approach was applied recently to investigations into blockage problems occurring on a long-distance pneumatic conveying system handling baghouse fly ash at a coal-fired power station. It was reported by the operator that the blockages

- occurred mainly at the beginning of the pipeline,
- were accompanied by severe pipe vibrations,
- eventually cleared themselves after a period of time.

During a site inspection it was found that in between baghouse cleaning cycles, each blow tank was allowed to be filled with the coarser particles falling through the dust collection hopper. A sample of material was collected directly from a blockage inside the pipeline and also from the receiving silo which contained the conveyed product. The physical properties of the “successful” (fine) material were found to be $d_{v50} \approx 15 \mu\text{m}$, $r_s \approx 2200 \text{ kg m}^{-3}$ and $r_{bl} \approx 900 \text{ kg m}^{-3}$, and for the “troublesome” (coarse) material $d_{v50} \approx 100 \mu\text{m}$, $r_s \approx 1900 \text{ kg m}^{-3}$ and $r_{bl} \approx 800 \text{ kg m}^{-3}$. Note a considerable amount of unburnt particles was observed in the latter sample

and this explained the somewhat lower value of r_s . As a result of applying the powder classification techniques (Geldart, 1973; Dixon, 1981) and the other suggestions made in this chapter, it was found that

- the fine ash was classified as a Group C powder—this material was conveyed successfully in fluidized dense-phase over long distances,
- the coarse ash was classified as a Geldart (1973) Group A material—subsequent fluidization tests confirmed good fluidization characteristics *but* poor air retention properties (i.e., the material deaerated quickly as soon as the fluidizing air was removed),
- the coarse ash according to Dixon (1981) was classified as Group B in a 50 mm NB pipe system and was located on the Group A-B boundary in a 100 mm NB pipe system (i.e., refer to Figs. 3 and 4).

Based on these findings as well as the nature of the blockages, the coarse ash was considered as a typical Dixon (1981) Group B material (i.e., troublesome in fluidized dense-phase causing severe pipe vibrations). It was recommended to the power station that the baghouse operating sequence be changed in such a way to ensure the blow tanks were filled only during the cleaning cycle. This change was made easily via the control system and the plant has been operating successfully since this time.

2.2 Blow Tank Design

Some typical “conventional” blow tank designs are illustrated in Fig. 7. This type of feeder has been used successfully in industry to handle a wide range of products over relatively short distances (e.g., $L = 100$ to 200 m). However, the application of this type of blow tank to greater distances and/or capacities (usually in conjunction with a second blow tank unit in series or parallel to ensure an essentially continuous mode of flow) resulted in a number of problems.

- Incomplete and/or inefficient discharge of material from each blow tank mainly due to rat-holing or funnel-flow effects promoted by
 - low pressure drop across the bed of material (under steady-state conditions),

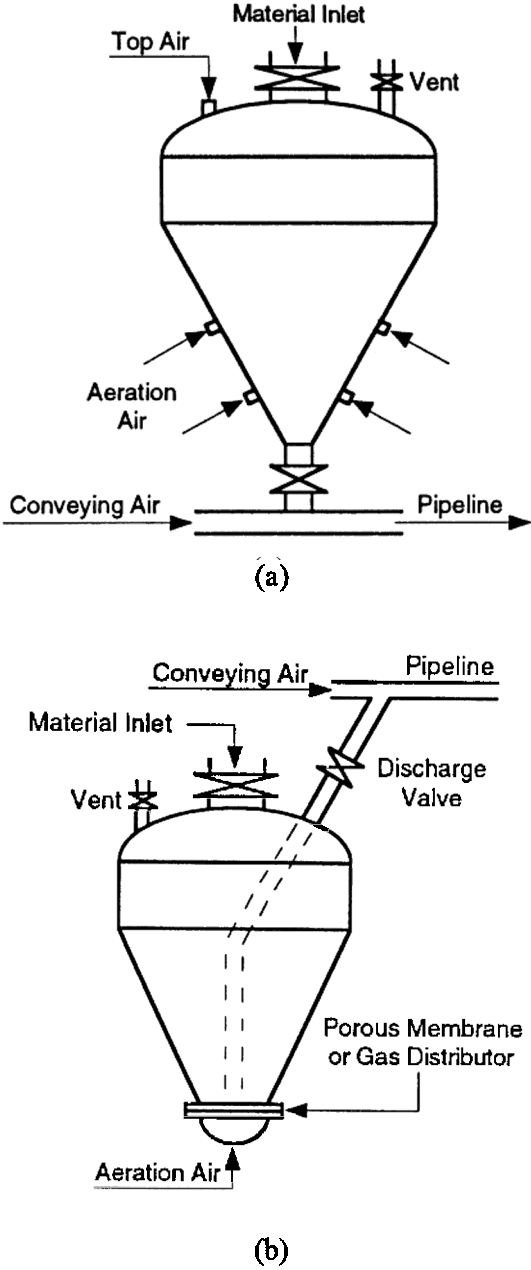


Figure 7. “Conventional” blow tank feeders: (a) bottom-discharge arrangement; (b) top-discharge arrangement.

- cohesive properties of the bulk solid, and/or
- inappropriate method of blow tank air injection (e.g., single-point injection, excessive top-air promoting material compaction),
- Flow instabilities or even pipeline blockage during start-up procedures due to surge effects caused by the initial high pressure drop across the blow tank (and hence high instantaneous flow rate of material),
- Pipeline blockage during shutdown procedures due to surge effects caused by the sudden venting of high pressure air down the pipeline (and hence, acceleration of product towards the end of the pipeline).

To avoid these problems, a number of significant developments have occurred in the area of blow tank design, such as:

- Method of air injection (Kennedy, et al., 1987), in particular the fluidizing-discharge-cone (Wypych, 1995a).
- Cone-dosing valve (Cürten, 1982) to control and meter the product into the pipeline. This is achieved by the movement of a double cone in the vicinity of the blow tank outlet. The cone moves continuously up and down inside the vessel but the stroke is adjusted by a proportional-integral (PI) controller based on a conveying line back-pressure measuring signal and set-point. The higher the conveying or operating pressure, the lower the cone set point inside the vessel thus restricting the flow of solids into the conveying pipeline (until a satisfactory conveying pressure is restored). Furthermore, the cone dosing system provides an additional and useful feature of mechanical agitation (and hence, flow assistance) of materials possessing cohesive and/or poor flow properties, such as manganese oxide (Wypych, 1989a).

These developments have resulted in a much more reliable and efficient blow tank feeding system, especially for long-distance applications, as shown in Fig. 8. Such systems now have been used successfully in many installations throughout Australia to meet the increasingly demanding requirements of conveying capacity and distance.

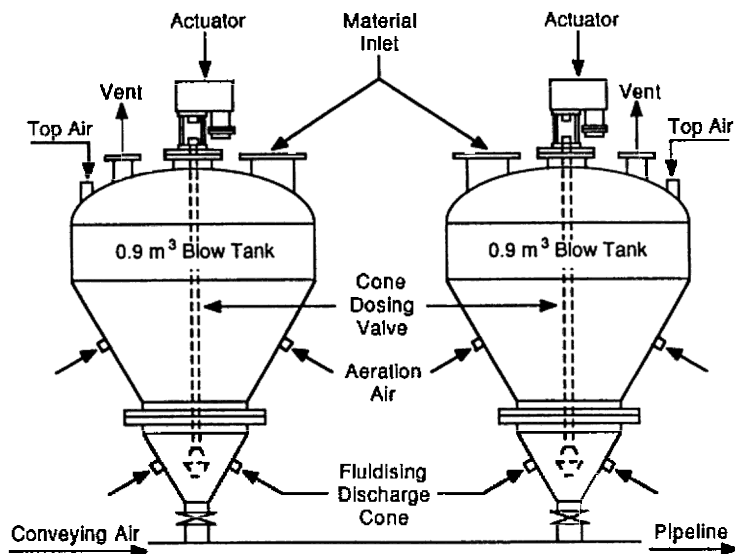


Figure 8. Preferred tandem blow tank feeding system for long-distance pneumatic conveying.

Note, other options to control the discharge of material from the blow tank feeder include a rotary valve and an oscillating or modulating valve (Marcus, et al., 1980), as shown in Figs. 9 and 10, respectively. However, the former option requires special start-up and shutdown procedures (e.g., minimizing pressure drop across the valve) and is limited to low-temperature and low-abrasive applications. Also, the valve needs to be designed to handle high static pressures and will add to the capital and maintenance cost of the system. The latter option of using a modulating valve will increase maintenance costs, especially if the same valve is used for blow tank isolation.

It should be realized also that either option shown in Fig. 9 or 10 will produce a non-symmetrical flow pattern inside the blow tank (i.e., due to preferential feeding at the blow tank outlet) and hence, promote the possibility of arching, rat holing and/or formation of dead regions. For these reasons, the combined fluidizing-discharge-cone and cone-dosing valve system shown in Fig. 8 is preferred.

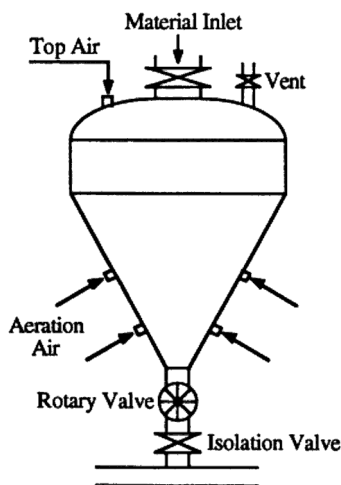


Figure 9. Rotary valve feed rate controller.

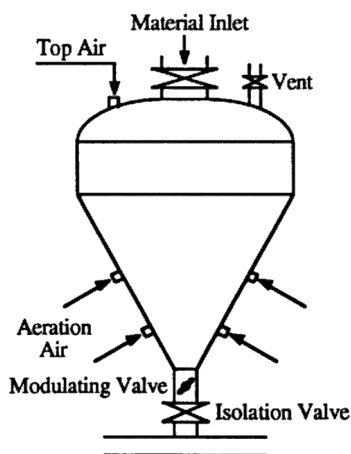


Figure 10. Modulating valve controller.

Case Study. As a part of the initial design of two 350 MW units for a coal-fired power station, it was required to:

- collect all the ash from the electrostatic precipitators and economizers,

- transfer this material at $m_s \approx 100 \text{ t h}^{-1}$ over a total distance of $L \approx 1.5 \text{ km}$ to a final storage silo, and
- provide a fly ash resale facility outside the boundaries of the power station (i.e., to enable easy access for the contractors to pick up and deliver the ash to various cement plants).

Tandem 7 m³ bottom-discharge cone-dosing blow tanks, similar to those shown in Fig. 8, were employed for this purpose and also to regulate the feed of material into the pipeline and alleviate the occurrence of imminent blockages (Wypych, 1995b).

2.3 Conveying Characteristics

When it is necessary to design or evaluate a proposed pneumatic conveying system, it is recommended strongly that the designer obtain as much information as possible on the actual material(s). Armed with the knowledge of steady-state conveying characteristics, it is quite a simple task to determine the minimum conveying velocity, optimal operating conditions for the product, and the pipeline diameter and compressor/blower rating to suit a given m_s and L .

Alternatively, conveying characteristics may be used to investigate operational problems that an existing plant may be experiencing (e.g., frequent blockages, reduced conveying rates). Problems of excessive product degradation and/or system wear also may be minimized by using such information to establish a safe minimum value of m_f for a given m_s . That is, conveying characteristics will determine whether an existing plant is operating at an optimal condition. If not, they will reveal what modifications would be necessary to achieve the desired result.

Conveying characteristics also will provide useful information when an existing plant needs to be upgraded to achieve say, a higher conveying rate of solids. For example, it will be possible to determine whether the system *and* the material will be able to cope with the increased pressure and/or air flow requirements (i.e., whether the combination of pipe size and blower/compressor rating will be sufficient).

The determination of steady-state conveying characteristics for a given product and test rig has been the subject of a number of earlier investigations such as Mason et al. (1980) and Mills et al. (1982). A standardized test procedure also has been developed and presented by

Wypych and Arnold (1985b) and hence, only a brief description is presented here. The test procedure basically consists of three different types of experiments which are applied to the material until sufficient data have been collected for the determination of conveying characteristics. The steady-state parameters generated specifically for this purpose are

- m_f = Supplied mass flow rate of air (kg s^{-1}),
- Δp_t = Total pipeline air pressure drop (kPa),
- m_s = Mass flow rate of solids or conveying rate (kg s^{-1} or t h^{-1}).

Some typical examples of pneumatic conveying characteristics for three different fly ash samples conveyed on the same long-distance test rig are presented in Figs 11, 12 and 13. Some important information regarding these materials and results is summarized below.

- Fly Ash A1 (Fig. 11): $d_{v50} = 5 \mu\text{m}$, $r_s = 2540 \text{ kg m}^{-3}$, $r_{bl} = 670 \text{ kg m}^{-3}$, Geldart (1973) and Dixon (1981) Group C material.
- Fly Ash A2 (Fig. 12): $d_{v50} = 75 \mu\text{m}$, $r_s = 2500 \text{ kg m}^{-3}$ and $r_{bl} = 1175 \text{ kg m}^{-3}$, Geldart (1973) Group A material but Dixon (1981) Group B material. The latter was confirmed by the nature of the blockages obtained on the test rig (e.g., severe pipe vibrations), as well as the rapid observed deaeration rate of the material.
- A company was intending to transport Fly Ash A2 through a long-distance conveying system that was designed to handle 45 t h^{-1} of Fly Ash A1. From Figs 11 and 12, it can be seen quickly that A2 would have required almost twice as much air than A1 and hence, a significant increase in running costs and possibly wear.
- Fly Ash B (Fig. 13): $d_{v50} = 12 \mu\text{m}$, $r_s = 2215 \text{ kg m}^{-3}$ and $r_{bl} = 955 \text{ kg m}^{-3}$, Geldart (1973) and Dixon (1981) Group C material. It is interesting to see how much lower the pressures are for this material compared with Fly Ash A1.

The above three conveying characteristics demonstrate the wide range of performances that can occur for fly ash and hence, the importance of employing such information in the design and optimization of long-distance systems.

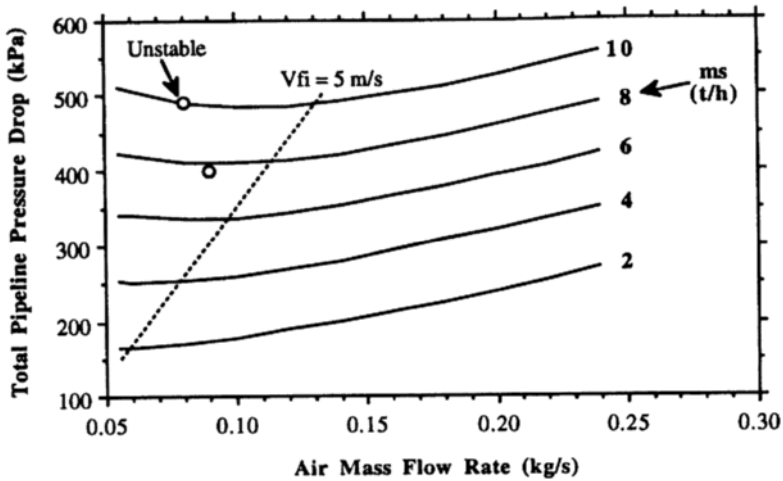


Figure 11. Test rig conveying characteristics of fly ash A1, $L = 945 \text{ m}$, $D = 69/81 \text{ mm}$ and $r = 1 \text{ m}$.

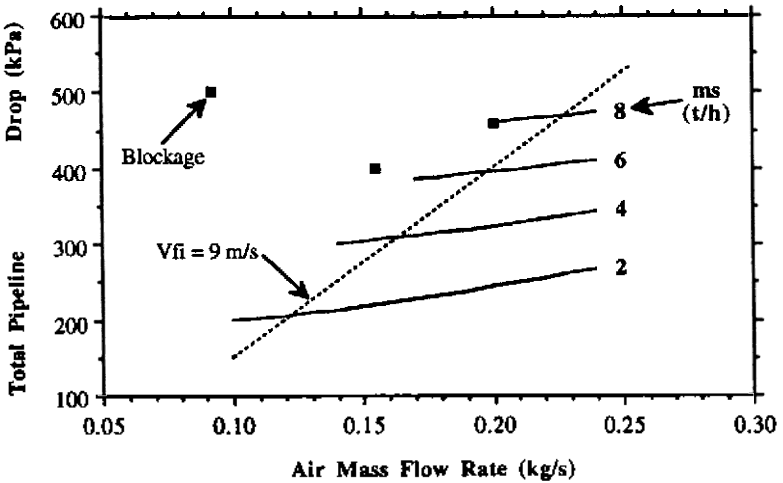


Figure 12. Test rig conveying characteristics of fly ash A2, $L = 945 \text{ m}$, $D = 69/81 \text{ mm}$ and $r = 1 \text{ m}$.

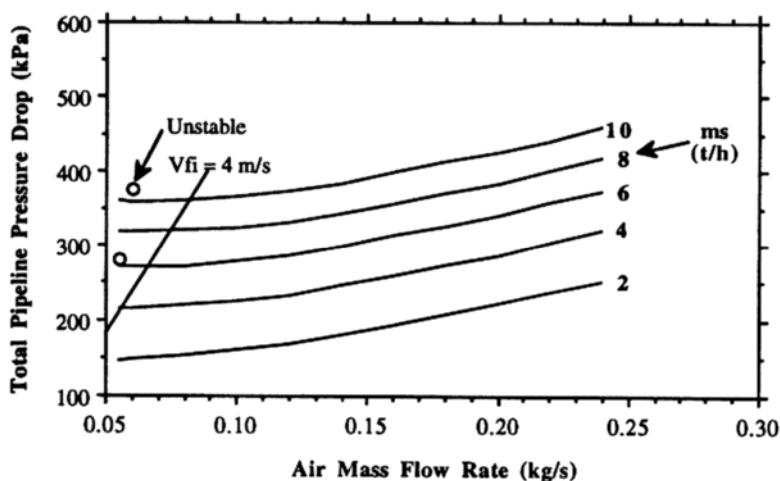


Figure 13. Test rig conveying characteristics of fly ash B, $L = 945$ m, $D = 69/81$ mm and $r = 1$ m.

2.4 Pressure Drop Prediction

For long-distance and/or large-throughput applications, it is essential to predict accurately the total pipeline air pressure drop, Δp_t . For example, even with a “good” existing model predicting say, $\Delta p_t = 500$ kPa $\pm 30\%$, the resulting uncertainty still would be too great (i.e., 350 to 650 kPa) and could lead to serious operating problems (e.g., inadequate capacity, pipeline blockage). Also, various major deficiencies exist with current models, such as the following:

- Existing correlations usually are based on low values of air density, whereas r_f can have a significant effect on Δp_t
- Products that are suited to long-distance transportation usually have a wide range of particle size (e.g., fly ash, $d = 1$ to 300 μm), and it is difficult to represent adequately such materials by the single diameter required by most models
- Most existing models are suited only to “pure” dilute-phase or dense-phase (high m^*) applications, whereas the possible modes of flow over long distances occur between these two extremes (e.g., dune-flow, sliding beds, irregular slugging, etc.—usually at moderate m^*).

For these reasons and other complex influences (e.g., large-diameter pipelines, particle-wall friction, particle shape, bends, etc.), it has been accepted that if high accuracy is needed, then some form of empiricism must be adopted. The preferred test-design procedure is listed below.

- Firstly, as described previously, characterize the bulk solid to be conveyed by undertaking particle size, particle density, loose-poured bulk density, fluidization and deaeration tests. Then classify the material using both the Geldart (1973) and Dixon (1981) diagrams to establish possible feeding problems and dense-phase suitability, which provides an indication of long-distance performance. For example, based on experience, Dixon (1981) Group A (and some Group C) powders display good fluidized dense-phase (Wypych, 1995a), as well as long-distance performance (e.g., high m^*).
- Using a standardized test procedure (Wypych and Arnold, 1985b), determine test rig conveying characteristics, similar to those shown previously in Figs. 11–13.
- Where the required conveying lengths and/or diameters cannot be tested, appropriate scale-up procedures (Pan and Wypych, 1992a) are employed. By monitoring the pressures along the straight sections of a test rig pipeline and also monitoring bend effects, determine exponents x_1, \dots, x_4 and y_1, \dots, y_4 in the following pressure drop equations.

$$\text{Eq. (7)} \quad \Delta p_s = \Delta p_{sf} + \Delta p_{ss}$$

where Δp_{sf} can be determined from Wypych and Pan (1991) and

$$\text{Eq. (8)} \quad \Delta p_{ss} = I_{ss} m^* \frac{r_{fm} V_{fm}^2}{2D} \Delta L_s$$

$$\text{Eq. (9)} \quad I_{ss} = x_1 m^{*x_2} Fr_m^{x_3} r_{fm}^{x_4}$$

$$\text{Eq. (10)} \quad \Delta p_b = \Delta p_{bf} + \Delta p_{bs}$$

where Δp_{bf} can be determined from Wypych and Pan (1991) and

Eq. (11)
$$\Delta p_{bs} = I_{bs} m^* \frac{\mathbf{r}_{fo} V_{fo}^2}{2}$$

Eq. (12)
$$I_{bs} = y_1 m^{*y_2} Fr_o^{y_3} \mathbf{r}_{fo}^{y_4}$$

Note that the exponents x_1, \dots, x_4 and y_1, \dots, y_4 are valid only for the test material and bend geometry, respectively.

To demonstrate the scale-up accuracy of the above design equations, thirty-eight experiments were carried out (Pan and Wypych, 1992a) with a particular fly ash over a very wide range of conveying conditions (i.e., from dilute- to fluidized dense-phase) on the test rig Pipeline I shown in Fig. 14.

In each experiment, it was believed that all the transducers along the pipeline (Tb-Te) were installed beyond any bend effects. Based on the data obtained from these experiments, the exponents in Eqs. (9) and (12) were determined by minimizing the sum of the squared errors of pressure at points Te2, Tc1, Tc2, Tc3 and Tc4, starting from point Te1. The determined values of exponent are listed in Table 1.

Additional experiments then were carried out on Pipelines II and III, which are shown in Figs 15 and 16 respectively and detailed in Table 2.

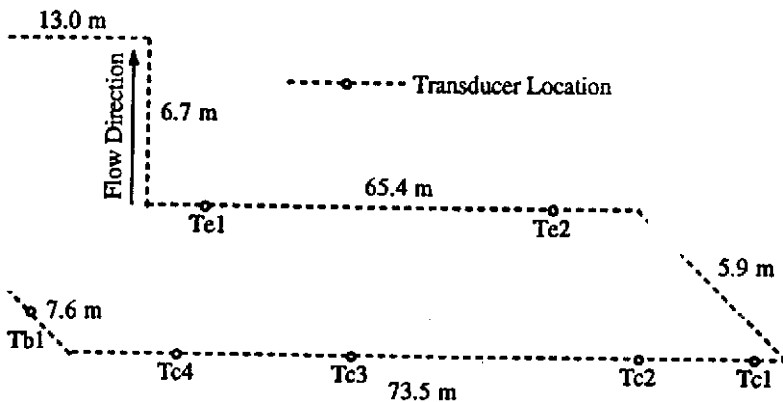


Figure 14. Schematic layout of Pipeline I, $L = 172$ m, $D = 69$ mm, $r = 1$ m.

Table 1. Values of Exponent Based on Data Obtained from Pipeline I, $L = 172\text{ m}$, $D = 69\text{ mm}$ and $r = 1\text{ m}$

Exponent	Value of Exponent
x_1	5.306
x_2	-0.436
x_3	-1.934
x_4	-0.117
y_1	0.052
y_2	0.658
y_3	0.673
y_4	-1.495

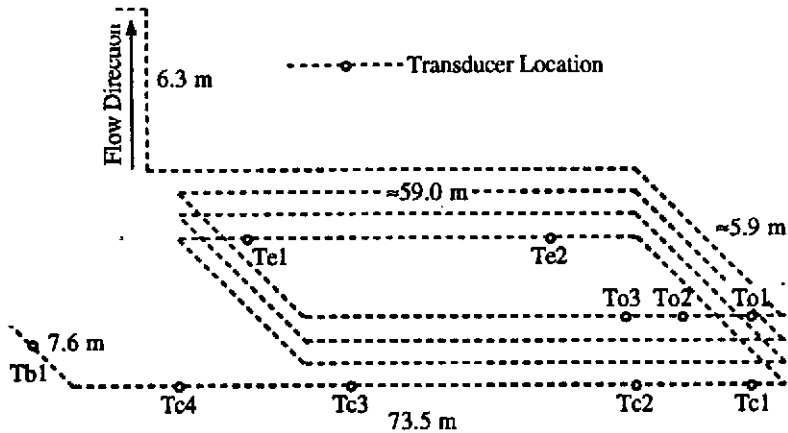


Figure 15. Schematic layout of Pipeline II, $L = 554\text{ m}$, $D = 69\text{ mm}$ and $r = 1\text{ m}$.

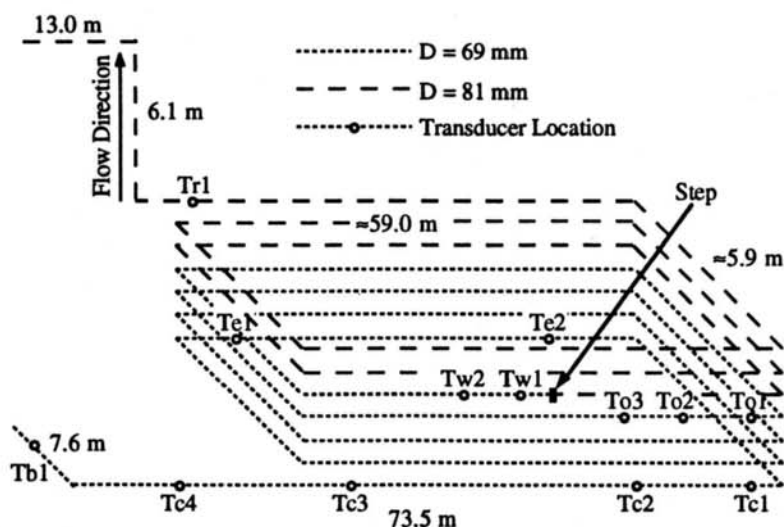


Figure 16. Schematic layout of Pipeline III, $L = 945$ m, $D = 69/81$ mm and $r = 1$ m.

Table 2. Configuration of Test Rig Pipelines

Pipeline	D (mm)	L (m)	No. of Bends	No. of Straights	No. of Exp Data	Range of m^* Values
I	69	172	5	6	38	3 - 76
II	69	554	17	18	14	3 - 22
III	69/81	564/381	17/12	13/18	8	2 - 12

Using the above exponents and pressure drop equations, the total pipeline air pressure drop and selected pressures were predicted for each Pipeline I, II and III, starting from the end of pipeline or points along the pipeline. Some of the predictions are presented in Fig. 17, from which it can be seen that the agreement between predicted and experimental values is quite good.

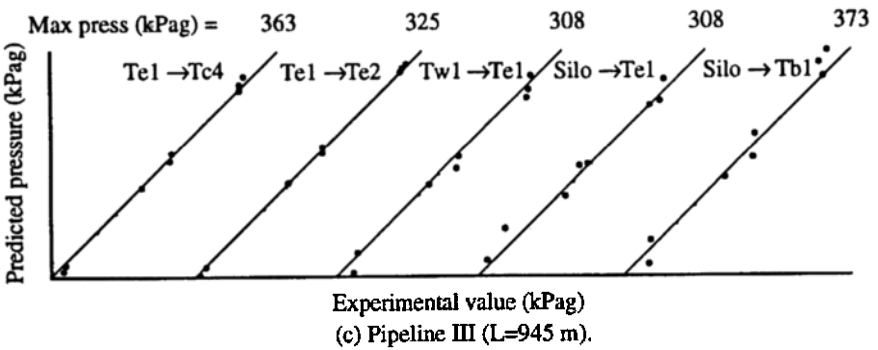
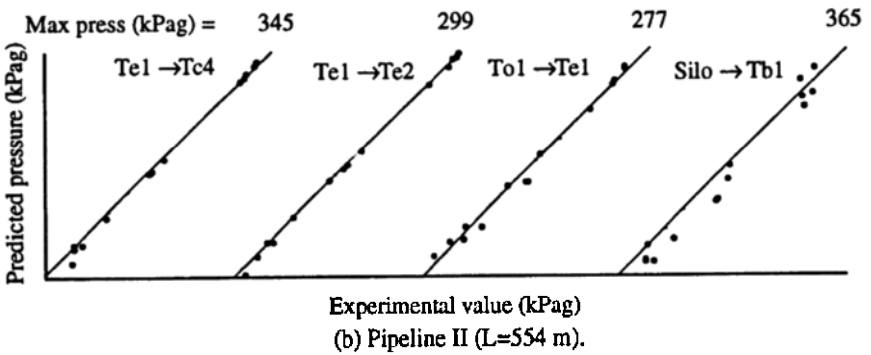
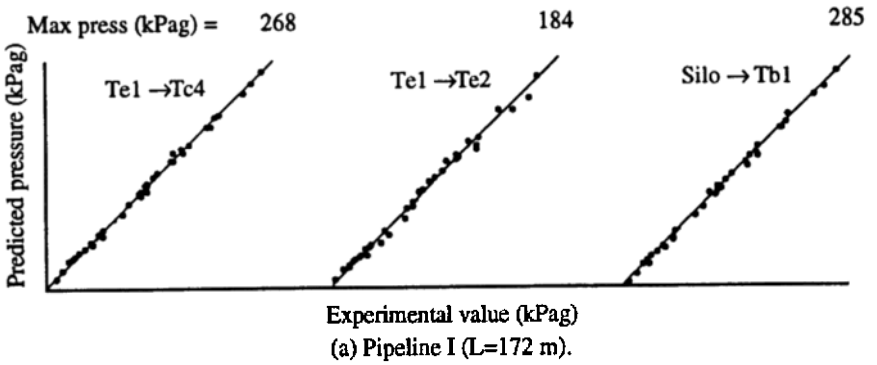


Figure 17. Predicted pressure vs experimental value, based on data from pipeline I. (Note: Te1 → Tc4 means the predicted pressure at Tc4, starting from Te1).

The above test-design and scale-up procedures have been applied to numerous long-distance systems (e.g., fly ash, pulverized coal) and have been found to provide good accuracy and reliability. Some examples of these results have been presented by Pan and Wypych (1992a) and Pan and Wypych (1994). The interested reader is referred to these papers for further details. The above procedures also have been used successfully to

- Predict conveying characteristics for a wide range of pipeline configurations (Pan and Wypych, 1994)
- Investigate the effect of bend number and radius on conveying performance (Wypych and Pan, 1993)
- Compare the pressure drop caused by horizontal and vertical sections of pipe (Wypych and Pan, 1993)
- Predict the pressure drop of large-throughput cement pneumatic conveying systems (Wypych, 1992)

2.5 Stepped-Diameter Pipelines

It is recognized commonly that

$$\text{Eq. (13)} \quad \text{Erosion} \propto \text{Velocity}^n$$

where the power index, n , ranges from 2 for ductile materials to 6 for brittle materials (Marcus et al., 1990). Hence, one direct way of reducing pipeline wear (e.g., pipe, bends) is to limit the “natural” increase in velocity in the direction of flow (i.e., due to the expansion of the carrier gas). This can be achieved by increasing the bore of the conveying pipeline in the direction of flow. Other advantages of stepped-diameter pipelines include the minimization of pressure loss, air flow and hence, power consumption, which are particularly important when considering long-distance and/or large-throughput applications. By selecting accurate stepping pipe criteria and models to predict pressure drop (Wypych and Reed, 1990), it is possible to optimize the design of these pipelines and obtain more efficient transportation over longer conveying distances (e.g., up to $L = 3$ or 4 km).

Some examples of long-distance stepped-diameter pipeline systems include 100 t hr⁻¹ of fly ash over 1.5 km (Wypych, 1995b) and 24 t hr⁻¹ of pulverized coal over 1.8 km (Wypych et al., 1990). Some of the different pipeline configurations considered for the latter are repeated in Table 3 below. Note:

- The relationship “ $Fr_{min} = 6 = \text{constant}$ ” was found to represent adequately the reliable *transport limit* of this material and hence, was employed as the *pipe stepping criterion* (i.e., to the optimize L_n and minimize m_f),
- An accurate I_s correlation based on experimental data was employed to predict the values of Δp_f .

From Table 3 it can be seen that by optimizing the configuration of pipeline, it is possible to reduce pressure loss, air flow, transport velocity, and hence, pipe/bend wear. Depending on hardware requirements and reliability, which would to some extent govern the maximum operating pressure of the system (e.g., say, 400 or 500 kPag), Pipeline Nos. 5 or 6 could be selected for this long-distance application. However, if diverter valves are required at the end of the pipeline, it may be more convenient to select Pipeline No 5 (i.e., $D_1 = 154$ mm instead of 203 mm).

Table 3. Pipeline Configurations and Predicted Operating Conditions for 24 t hr⁻¹ of Pulverised Coal over 1.8 km (*Wytych, et al., 1990*)

Pipe No	D_n (mm)	L_n (m)	m_f (kg/s)	m^* (-)	$\Delta p t$ (kPa)	Fri (-)	V_{fi} (m/s)	V_{fe} (m/s)	P (kWh/t/km)	% Diff wrt No 6
1	203	1800	1.22	5.5	272	6	8.5	31.3	6.1	97%
2	154	1800	0.87	7.7	430	6	7.4	38.8	5.5	77%
3	127	1800	0.7	9.6	595	6	6.7	46.1	5.2	68%
4	203	853	0.7	9.6	327	6	8.5	18	3.9	26%
	154	947				6	7.4	14.7		
5	154	1117	0.56	12	453	6	7.4	25	3.6	16%
	127	683				6	6.7	10.8		
6	203	436	0.51	13.2	401	6	8.5	13	3.1	0%
	154	733				6	7.4	14.7		
	127	631				6	6.7	10.8		

2.6 Valves

Blow tank technology was introduced extensively after World War II to not only improve plant efficiency but also to extend the future potential of pneumatic conveying (e.g., long-distance and/or large-throughput

applications). However, the resulting higher operating pressures, together with other factors such as product abrasion and/or high temperatures, resulted in the premature failure of crucial valves (e.g., blow tank inlet, blow tank discharge). A wide range of different “off-the-shelf” valves for gas, hydraulic and/or slurry service then were tested (e.g., ball, butterfly, plug and air-on-sleeve pinch valves). Unfortunately, most of these were found unsuitable, achieving service lives from only a few hours to a few days.

Consequently, more elaborate designs had to be tested and/or developed for this application of pneumatic conveying. The following two valves have been found useful in particular areas. Note that in each case it is imperative to ensure fast actuation time (e.g., 1 second for a 100 mm nominal bore NB valve and a few seconds for a 300 mm NB valve, if possible). Large-bore solenoid valves and quick-exhaust valves usually are required for this purpose. Also, note that each one of the following valves provides a full cross-sectional area of flow in the open position and a 100% seal in the closed position. One of the major problems of air-on-sleeve pinch valves is that they do not provide these important features for pneumatic conveying applications (e.g., a small hole in a closed sleeve quickly erodes due to the subsequent high velocities of air and solids).

The high-pressure pinch valve shown in Fig. 18 has been applied successfully to several abrasive pneumatic conveying applications, mainly for blow tank discharge. For example, this pinch valve has been quite successful in handling abrasive and coarse materials, such as crushed bauxite, zircon and sub 20 mm crushed brick (Wypych, 1995b), as well as high throughputs, such as 100 t h⁻¹ of cement (Wypych, 1995b). Also, by replacing existing chrome-plated butterfly valves with high-pressure pinch valves in cement plants, it has been possible to extend the service life of blow tank discharge valves from ≈ 2 weeks to over 8 months (Timms, 1992). However, it is important to select a valve which has the actuating rods “tagged” or connected to the sleeve. This will ensure a full-bore flow area when the valve is opened. Note that this type of valve is not suitable for high-temperature applications (e.g., ≥ 200 °C), where the sleeve will work-harden and fail prematurely.

The rotating-disc valve shown in Fig. 19 is gaining popularity for blow tank inlet and discharge applications. As the disc is spring-loaded and “self-lapping,” the valve automatically adjusts for wear. Also, as no packing, seals or o-rings are used (i.e., the disc and seating surfaces are metallic),

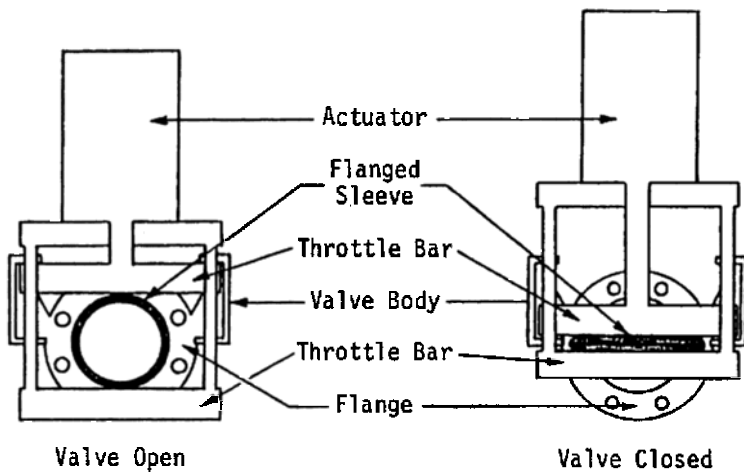


Figure 18. High-pressure pinch valve (Larox Pty Ltd).

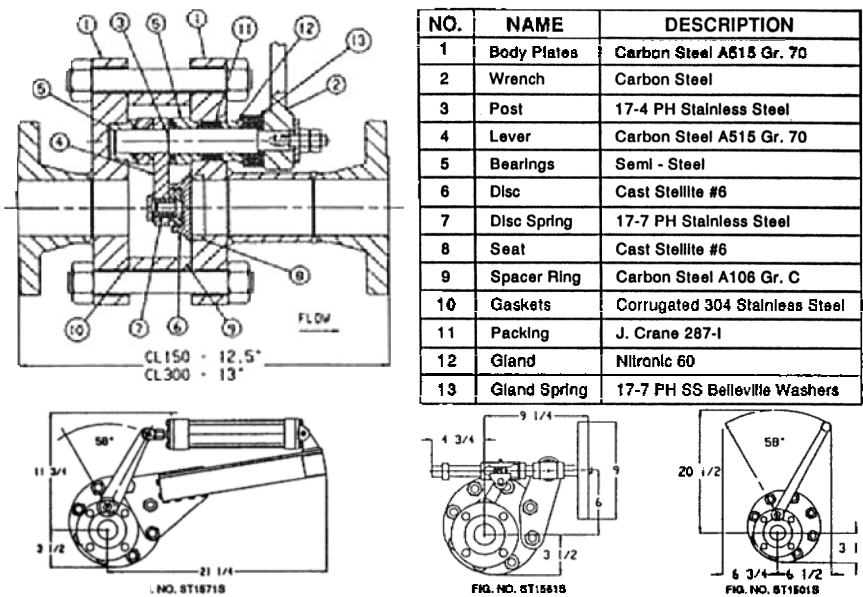


Figure 19. Rotating-disc valve (Everlasting Valve Co.).

high temperatures and pressures are possible (e.g., up to 900°C and 69000 kPag). The rotating-disc valve has been used successfully (Wypych, 1995b) as a discharge valve for 7 m³ blow tanks transporting hot and abrasive ash from a power station precipitator at a rate of 100 t h⁻¹ over a total distance of 1.5 km. These discharge valves have operated continuously on a 24-hour basis and achieved a service life of at least 12 months (i.e., without any form of maintenance). However, to ensure that the valve body does not fill up with ash, purge-air has been used during actuation of the valve.

2.7 Pipeline Unblocking Techniques

Following numerous blockages on the test facilities at the University of Wollongong (attempting to determine the minimum conveying velocity of various materials over long distances), a pipeline unblocking system was developed and installed at the end of the pipeline. Refer to Fig. 20 for a typical arrangement.

The system incorporates only one component in the pipeline, allowing the pipeline to be back-pressurized from the silo to the blockage with air at a slightly higher pressure than the conveying pressure. The back-pressure then is released in a controlled manner such that the blockage is drawn through the conveying line. These systems have been incorporated successfully in the control circuits of plants handling difficult-to-convey materials and also have been used on conveying pipelines up to 1.5 km in length (Wypych, 1995b).

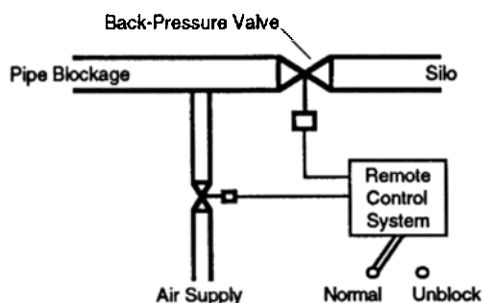


Figure 20. Schematic layout of pipeline unblocking system.

2.8 General Considerations

The following comments and recommendations are based on the research findings presented and cited in this paper, as well as the consulting experiences of the author.

For the general purpose of minimizing air flow, transport velocity, wear and power, the fluidized dense-phase mode of flow is preferred for long-distance applications. Efficient blow tank feeders, rotary-screw compressors, refrigerated dryers and stepped-diameter pipelines also are recommended. For products that are not suited to fluidized dense-phase, the possible modes of flow include dilute-phase (suspension flow) or bypass conveying (Wypych, 1995a).

It is believed that the air velocities in a large-diameter dilute-phase system can be 50 to 100% higher than an equivalent well-designed dense-phase system. Hence, much greater wear problems are expected in the dilute-phase system, although significant advances have been made in the technology of wear-resistant materials and bends (Wypych and Arnold, 1993). Other features involved with dilute-phase transport systems include:

- Limited operating pressures (e.g., 80 to 100 kPag for Roots-type blowers)
- Large-diameter pipelines
- Greater conveying velocities and system erosion (i.e., due to the larger pipe diameters)
- Larger dust collectors to cope with the greater volumes of conveying air

Note, the velocities required in large-diameter dilute-phase systems must be high to ensure suspension flow, avoid product deposition, and facilitate good clean-out. This comment is based on personal experiences involved with large-diameter pipeline systems used to unload ships (e.g., 350 mm NB pipelines 25% full of deposited cement) and provide fuel to boilers (e.g., deposition of pulverized coal even at high velocities such as 30 m s⁻¹). Note, blow tank feeders (i.e., instead of rotary valve feeders) can be used effectively to assist in the cleaning/purging of pipelines (e.g., clean-blow cycle). However, with a Roots-type prime mover and a large-diameter (large-volume) pipeline, the effectiveness of the purge or clean-blow cycle will be reduced significantly (i.e., due to the pressure limit of 100 kPag).

In contrast, a well-designed dense-phase system will operate at significantly less velocities and wear, as well as provide more efficient cleaning/purging operations (i.e., due to having smaller pipe diameters and greater pressures, if needed). One other interesting issue is that a blow tank dense-phase system is inherently more “self-cleaning” than a dilute-phase system (i.e., due to the natural variations in pressure and increased material concentration/turbulence). Quite often dense-phase systems have been installed in Australia to overcome buildup problems displayed by dilute-phase systems, where the air can flow easily over deposited material.

When evaluating a material for the purpose of establishing dense-phase and long-distance suitability, it is important to undertake all the necessary tests (e.g., particle sizing, particle and bulk densities, fluidization and deaeration). Also, if possible, it is useful to compare such results with those obtained on previously conveyed similar materials (e.g., fly ash). However, it should be noted that such an evaluation only is a qualitative one and it is not possible to predict say, minimum air flows or pipeline pressure drop based on such data (i.e., pilot-scale tests normally are required to confirm minimum velocities, friction factors, etc., especially over long distances and for large-diameter pipes).

Many designers and researchers in the past have placed a great deal of emphasis on the importance of solids loading or the solids-to-air mass flow rate ratio, m^* . However, it should be realized that this parameter is dependent on particle and loose-poured bulk densities; conveying distance and pressure available; frictional properties and minimum transport conditions of material (which will affect the maximum values of m^*). Hence, it is difficult and misleading to apply “general” values of m^* to different systems and materials. The objective always should be to achieve a well-designed long-distance transport system operating at optimal conditions— m^* only should be considered as a consequence of achieving this result.

3.0 PIPE BRANCHING

The branching of pipes/ducts in pneumatic conveying has the following two main applications in industry.

- Extraction of dust via a network of branched ducts, where the particulates are transported under vacuum conditions. Some common examples include the control of dust in materials

handling operations, including conveyor transfers, screening, filling bins, ship loading, etc.

- The simultaneous splitting and distribution of solids-gas mixtures for applications requiring multipoint injection, where the mixtures are transported usually under positive-pressure conditions. Some common examples include tuyere injection for blast furnaces, large burner nozzles for pulverized coal-fired boilers, small coal-fired plasma torches providing start-up and support energy for boilers, injection of pulverized fuel into calciners, etc.

Some of the important issues that should be considered when designing, improving or operating any such pipe branching applications are described in the following sections.

3.1 Dust Extraction

Most practical dust extraction systems involve multiple hoods linked to a duct network serving a central gas cleaning unit and prime mover. This is very similar to an air conditioning system where the air is supplied from an air handling unit through the duct network to diffusers serving the occupied spaces. In fact, most duct sizing methods are based on air conditioning principles and/or techniques, such as the Total Pressure Method (ASHRAE, 1985), the Velocity Pressure Method (ACGIH, 1992) and the Constant Pressure Gradient Sizing Method (DASCG and AIRAH, 1987). Also, some “air-conditioning” computer programs, such as DON-KEY (DASCG and AIRAH, 1988), may be employed to assist in the design of the ductwork (i.e., based on one or two of these sizing methods).

The objective of the design/analysis process is to ensure (as far as possible) that the correct quantity of air flows through each hood. As different air quantities, hood types/sizes and/or duct lengths usually are involved, this is not always a simple task. The correct air flows may be achieved by performing:

- A “rough” duct design and then making adjustments during commissioning using blast gates or dampers to control air flow
- A more involved design where the system is inherently balanced.

The latter method is preferred for the following reasons:

- Dampers may increase maintenance costs
- Dampers may be tampered with during the life of the plant
- Damper control may be prohibited when handling dangerous or explosive materials
- The “rough” duct design method may result in premature dust deposition or excessive system erosion (due to incorrect duct sizes and velocities)

Hence, even if the “rough” duct design technique is selected, some form of balancing still should be performed so that the final duct sizes are close to optimal (in terms of pressure and velocity).

The correct application of either sizing technique will result in a duct network that works well on *air*. It is equally important to ensure that each air flow is adequate to transfer all the *particulates* from the hood/enclosure to the collection and/or cleaning device. Unfortunately, many dust control systems have been designed and/or are being operated with little or no regard for what actually has to go through the hood-duct network. This can result in:

- Particulate deposition and buildup inside the duct(s)
- Eventual choking of duct branch(es)
- Inefficient performance of the *overall* dust control system.

Case Study. Such a situation was found to occur in the duct network shown in Fig. 21 and installed to extract iron oxide dust at various points along a cold strip processing line. The stated problems were insufficient suction at the hoods, buildup of contaminant in the hoods and along the processing line (causing cleanup problems due to eventual mixing with hydraulic fluid, lubricant, water, etc.). Analysis of the system found the following:

- Branch II-V contained more bends and was over three times longer than branch I-V
- Branches I-V and II-V were sized to provide an approximate 35%–65% split-up in air flow, respectively (i.e., using pressure-balancing techniques)
- The system would have worked initially on air, however, the lower section of branch II-V was completely blocked with contaminant

- Velocities in excess of 60 m s^{-1} were occurring in branch I-V causing excessive pressure loss and wear. Note the potential seriousness of wear in ductwork (especially bends/elbows) has been emphasized previously by Eq. (13). For example, assuming $n = 3$, which without other data is used to represent most industrial situations, a velocity increase of only 20% will result in a 73% increase in wear. Hence, it is important to ensure that the transport velocities are not only adequate to avoid deposition problems but also minimized for wear reasons.

The solution to the above problem is to re-size the entire network, in particular branches I-V and II-V, with the aim of ensuring a suitable minimum transport velocity along each section of duct.

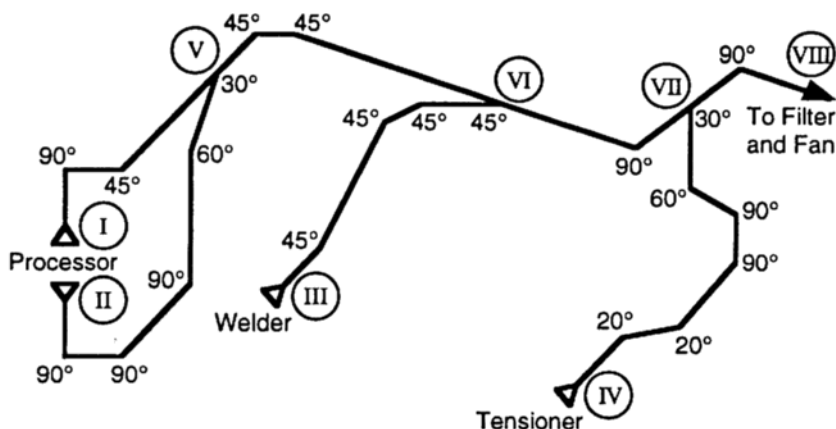


Figure 21. Duct network for extraction of iron oxide dust.

Minimum Duct Velocity. Once the types and locations of hoods, enclosures and booths have been established and the exhaust rates determined, it is necessary to design the ductwork to transfer the contaminated gas to the collection or cleaning device. An essential parameter required for this purpose is the minimum duct or conveying velocity, V_{fmin} , which is required to:

- Avoid the gradual buildup of a particular contaminant with time
- Know whether any toxic or bacteria-prone particles are being left inside the ductwork (e.g., for servicing or maintenance purposes)
- Establish whether any appreciable buildup will affect dust extraction efficiency

Unfortunately, the current selection of V_{fmin} is based on a general list, such as that given in Table 4, where:

- The list of contaminants is very general and open to interpretation
- The suggested velocities can vary considerably between say, 15 and 20 m s⁻¹ (even for the same application area)
- No consideration is given to the influence of particle properties and/or duct diameter

Table 4 Minimum Conveying Velocities (*ACGIH, 1992*)

Nature of Contaminant	Industrial Examples	V_{fmin}	
		(ft min ⁻¹)	(m s ⁻¹)
Vapours, gases, smoke	All vapours, gases and smoke	1000-2000	5-10
Fumes	Welding	2000-2500	10-12
Very light fine dust	Cotton lint, wood flour	2500-3000	12-15
Dry dusts and powders	Fine rubber dust, bakelite moulding powder dust, cotton dust, light shavings, soap dust, leather shavings	3000-4000	15-20
Average industrial dust	Grinding dust, dry buffing lint, coffee beans, granite dust, silica flour, general materials handling, brick cutting, clay dust, foundry, limestone dust, asbestos dust	3500-4000	18-20
Heavy dusts	Heavy/wet sawdust, metal turnings, foundry tumbling barrels and shake-out, sand blast dust, wood blocks, brass turnings, cast iron boring dust, lead dust	4000-4500	20-23
Heavy or moist	Lead dust with small chips, moist cement dust, asbestos chunks from machines, sticky buffing lint	> 4500	> 23

For example, for the iron oxide dust considered in the previous case study, Table 2 suggested $V_{fmin} = 18$ to 20 m s^{-1} (i.e., assuming an “average industrial dust”). On analysis of the sample, it was found $d_{p50} \approx 80 \text{ }\mu\text{m}$, which appeared to support this classification. However, upon further examination of the actual distribution of size, a significant proportion of the material was found $> 1000 \text{ }\mu\text{m}$ (e.g., large flakes). A minimum conveying velocity of at least $V_{fmin} \approx 25 \text{ m s}^{-1}$ was estimated for this “dust.” This explains why the iron oxide material built up and eventually blocked branch II-IV, which was sized/balanced mainly for air distribution purposes and produced transport velocities $< V_{fmin}$.

As a result of some recent investigations into the deposition (saltation) of small particles in large diameter ducts (Cable, 1994; Miletich, 1994) and analogous work in pneumatic conveying (Wypych and Reed, 1990; Zenz, 1964; Cabrejos and Klinzing, 1994), some other interesting characteristics of V_{fmin} are listed below.

- V_{fmin} appears to increase with duct diameter, D . This trend has been recognized in many “traditional” pneumatic conveyors (Wypych and Reed, 1990; Zenz, 1964; Cabrejos and Klinzing, 1994), but also appears to be relevant for dust extraction (Cable, 1994; Miletich, 1994), which can be considered as a form of low-concentration pneumatic conveying (e.g., $V_f = 10 \text{ m s}^{-1}$ may be suitable for a particular contaminant in a duct size of $D = 100 \text{ mm}$ but may cause deposition in $D = 300 \text{ mm}$). Further evidence of this can be seen in the work of Zenz, 1964, who found that single-particle saltation, which is analogous to the deposition of low-concentration particulate suspensions in dust extraction, increases with duct diameter according to the following relationship.

$$\text{Eq. (14)} \quad V_{fso} \propto D^k$$

where $k = 0.4$ to 0.6 . However, based on experience, Eq. (14) appears to provide conservative values of V_{fso} , especially in large-diameter ducts. This has been confirmed by Cable (1994) and Miletich (1994) who both employed 200, 300 and 480 mm diameter steel ducts, and Cabrejos and Klinzing (1994) who used a 50 mm diameter copper tube.

- V_{fmin} appears initially to decrease with decreasing particle size and then increase for very fine particles (due to cohesive and interparticle forces). This trend is predicted (Wypych, 1993) by three different saltation velocity models and also can be found in many industrial applications. For example, in an article describing the installation of a dust extraction system for very fine clay dust in a brick manufacturing plant (Anon, 1995), it was stated that a high velocity of 24 m s^{-1} was needed to maintain dust suspension—this velocity is approximately equal to the 25 m s^{-1} estimated for the (coarser and heavier) iron oxide dust described above. Note, this example also provides further support to the inadequacy of Table 4, which nominates a velocity of $18\text{--}20 \text{ m s}^{-1}$ for “clay dust.” It should be noted that these unusually high velocities may be indicative of what would be needed to ensure “clean” ductwork (i.e., without any form of deposition), whereas in practice a small amount of deposited material is considered normal. Nevertheless, it is essential to ensure that such a buildup does not increase gradually with time. Also, in some applications, especially those handling dangerous and/or bacteria prone contaminants, it may be necessary to maintain “clean” ductwork (i.e., for safety, hygienic and/or maintenance reasons).
- The velocity needed to *re-entrain* deposited particulates (V_{fup}) may need to be determined for particular applications. The velocity V_{fup} is being found (Zenz, 1964; Cabrejos and Klinzing, 1994) to be much greater than V_{fmin} (i.e., the *saltation* or *deposition velocity*) and again increase with duct diameter (Cabrejos and Klinzing, 1994). Also, similar to V_{fmin} , V_{fup} appears to increase with *decreasing* particle size, where very fine contaminants are more difficult to re-entrain (i.e., due to interparticle forces).

The further development of accurate models to predict the above parameters (including the effects of particle properties and duct diameter) is being pursued currently, and considerable effort still is required before such models can be applied solely in design practice (i.e., without the need for experience or comparative data).

At this stage, operators of dust control systems should at least be aware of these various issues and their relative importance, which will vary from problem to problem. Hence, it is essential that the engineer or consultant responsible adopts a systematic approach to the solution of the problem in which all the relevant issues are considered and dealt with in the appropriate order.

If accurate design/analysis data are necessary (e.g., V_{fmin} , V_{fup}), it is possible to obtain the information needed by undertaking the appropriate bench-type tests and large-scale test-design procedures, similar to the approaches employed for pneumatic conveying (Pan and Wypych, 1992a; Arnold et al., 1994).

3.2 Flow Splitting

The layout of a typical flow-splitting system is depicted in Fig. 22. For an even split-up and distribution of material, it is essential that each pipe branch offers the same resistance to flow. This can be achieved easily by ensuring that each pipe branch has the same length, type and location of bends, as depicted in Fig. 23. This preferred approach is more feasible when small diameters of pipeline are involved. However, the installation of identical pipe branches is not always possible. In such situations, the traditional approach has been to install additional pipes/bends in the lower resistance branches, such as branch Nos. 1 and 4 shown in Fig. 22. The problem with this approach is that bend pressure drop depends not only on conventional parameters, such as m_p , m_s , material properties, wall material, temperature, bend geometry, etc., but also on bend location (Wypych and Pan, 1993; Pan and Wypych, 1992b). Hence, simply ensuring each pipe branch comprises the same length of pipe and number of bends still can cause inaccuracies in flow splitting efficiency.

By employing accurate test-design procedures (Pan and Wypych, 1992a), it is possible to model and design each pipe branch separately so that the system ultimately is well balanced. However, such a system may not be reliable over time due to uneven wear in the pipes/bends, changes in material property and/or on-site conditions.

Splitters. The following common splitters have been introduced to improve the efficiency of flow splitting.

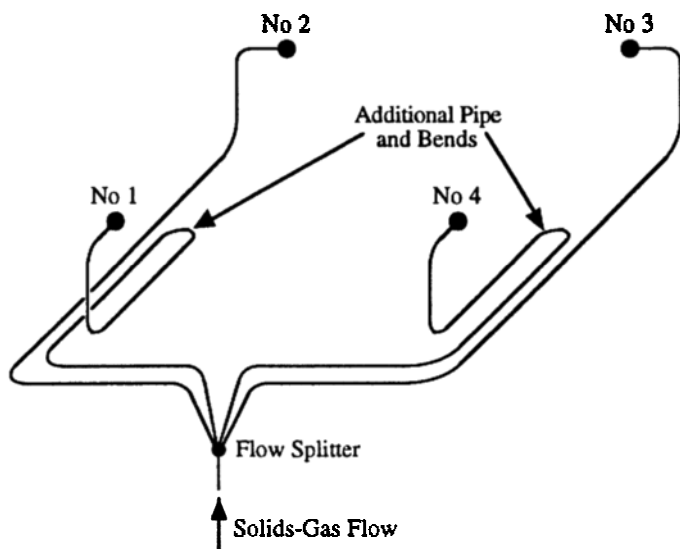


Figure 22. Traditional method of pipe branch layout for injection systems.

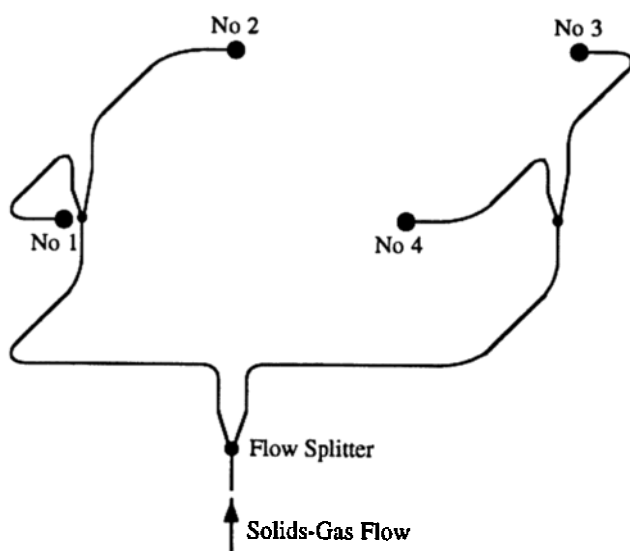


Figure 23. Preferred method of pipe branch layout for injection systems.

- Conventional riffle box, as shown in Fig. 24, used normally for 2-way splitting in coal-fired furnace and boiler applications. The riffles plates will be subjected to wear and over time could affect flow splitting efficiency.
- Cone splitter, as shown in Fig. 25, used in general injection applications for up to 8-way splitting and claimed (Hilbert, 1982) to achieve $\pm 10\%$ accuracy in splitting. It should be noted that such figures depend more on the design of the pipe branches downstream of the splitter, rather than the splitter itself.
- Rotary splitter (Selves and Barnes, 1993), which can be used to provide up to 36-way splitting. Due to its intermittent operation, the pulsing flow in the branches downstream of the splitter would not be suitable for applications requiring a smooth and regular injection of material.

The above devices are flow intrusive, subjected to wear and the splitter itself cannot control changing downstream conditions. A potentially more direct and efficient approach is to monitor the change in flow conditions downstream of a splitter (Barnes and Murnane, 1995) and employ active splitters (Selves et al., 1995) to control the split ratio of air and hence, material. Some of the active splitters being investigated and developed by Selves et al., 1995 include:

- Modified riffle box, as shown in Fig. 26, which uses air injection to control the split ratio.
- Induced swirl, as shown in Fig. 27, which imparts to the solids-gas flow a swirling action and also controls the rate and direction of rotation of swirl via tangential nozzles. However, the residual swirl that would occur in the downstream pipe branches may cause problems if several swirl inducers follow one another (Selves et al., 1995). This problem could be eliminated by introducing the dropout box splitter shown in Fig. 28.

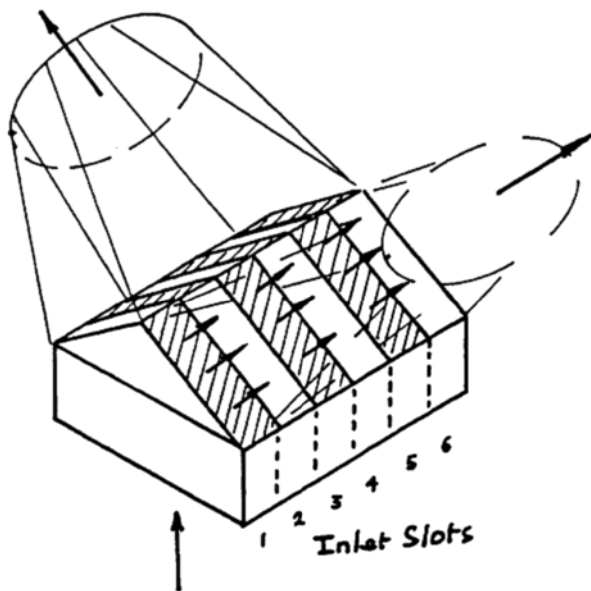


Figure 24. Conventional riffle box. (Selves et al., 1995.)

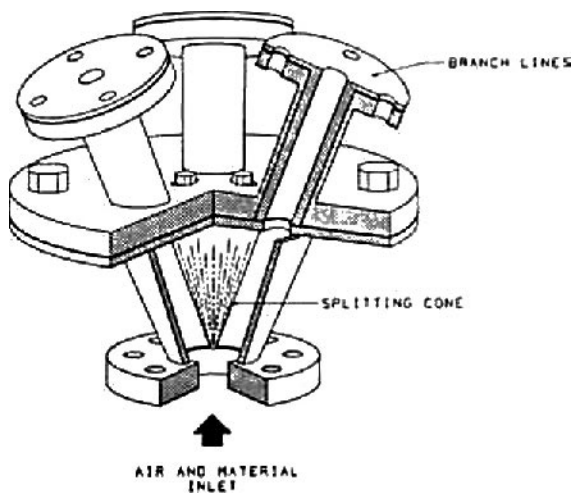


Figure 25. Cone splitter. (Hilbert, 1982.)

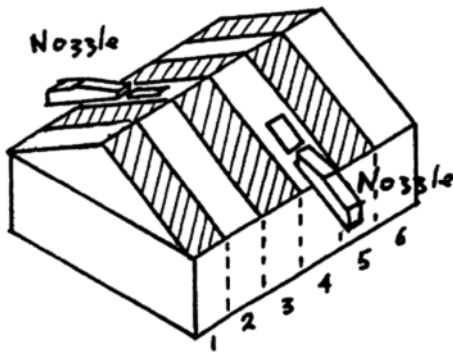


Figure 26. Modified riffle box (*Selves et al.*, 1995).

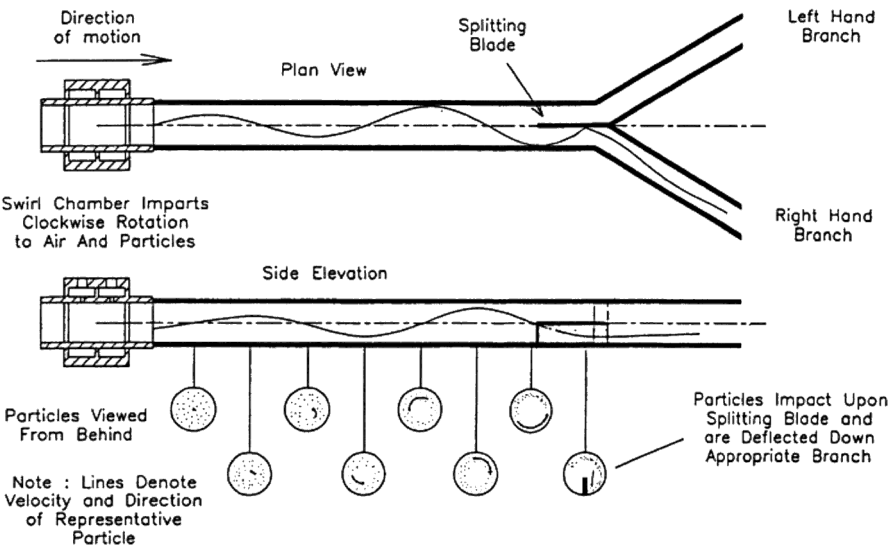


Figure 27. Control of split ratio using induced swirl and a Y splitter. (*Selves et al.*, 1995.)

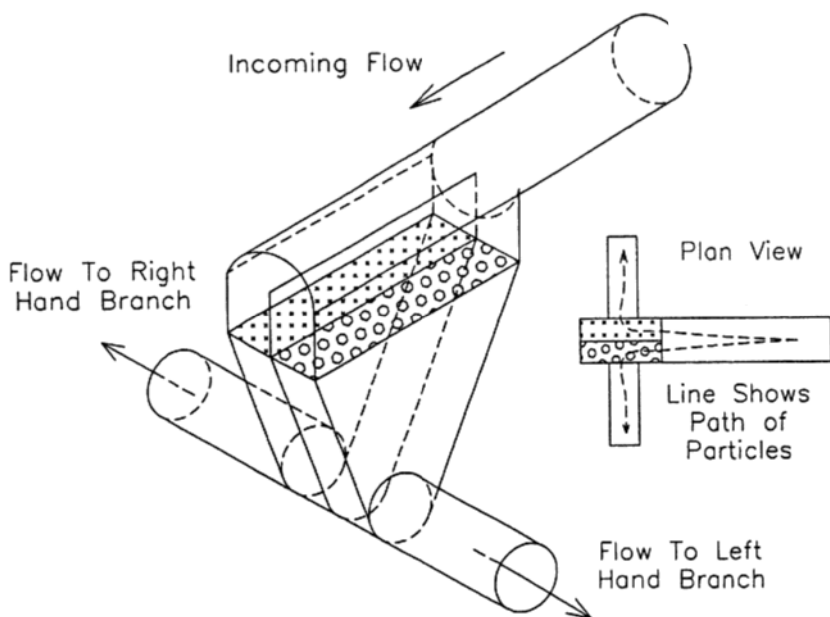


Figure 28. Improved dropout box splitter (*Selves et al., 1995*).

General Considerations. Some other important considerations that should be made when designing a flow splitting system are listed below.

- The splitter should provide a symmetrical split in all planes and preferably should be installed in the vertical plane (if possible).
- The solids-gas flow upstream of the splitter should be uniform and regular.
- Sufficient upstream pipe should be used to eliminate any flow separation effects caused by in-line components, such as bends and diverters (e.g., “roping” in dilute-phase).
- Special care should be taken when selecting the mode of solids-gas flow. For example, flow separation and roping could occur even in very dilute-phase conveying systems (e.g., $m^* \leq 1$ for coal-fired boilers). Fluidized dense-phase also is possible for some systems and can offer many

advantages (e.g., reduced air flow, velocity, wear, power). However, this mode of flow can be more irregular than dilute-phase (e.g., increased pressure fluctuations) and hence, produce flow splitting problems, even with active splitters. The objective here should be to achieve the minimum air flow that is needed to ensure smooth and consistent flow under all operating conditions.

3.3 Pressure Loss

For dust extraction systems, the concentration of solids usually is quite low. For this reason, the methods employed to calculate pressure loss are based on air-only conditions. Comprehensive information is available (ASHRAE, 1985; ACGIH, 1992) to assist the designer in estimating the pressure loss caused by pipe branches, ducts, elbows, etc.

In contrast, the amount of material being conveyed inside each pipe branch of a flow splitting application is very high and hence, design cannot be based on air-only analyses alone. For example, Low et al., 1987 have proposed the following empirical relationship to determine the head loss of a pipe branch.

$$\text{Eq. (15)} \quad K = K_f(1 + C m_f^a)$$

where K is the branch head loss for solids-gas flow, K_f is the branch head loss for air-only conditions and can be calculated theoretically from (Low et al., 1987), $C = 0.22$ and $a = 1.27$ appear to represent satisfactorily both 90°- and 45°-branches with different branch diameters and products (Low et al., 1987). Further examples of empirically based pressure loss equations for Y-splitters of various angles and subjected to plastic pellets under different solids loadings have been presented and cited by Marcus et al., 1990.

Good flow splitting design is dependent on the accurate prediction of the pressure drop caused by the various bends, branches and straight sections of pipe. This can be achieved by employing the above branch model(s), proven for the particular material and application, coupled with the accurate “pipeline” test-design procedure described in Sec. 2.4 of this chapter.

NOTATIONS

a	Power index
C	Constant
d	Particle diameter, m
d_{50}	Median particle diameter, m
d_p	Arithmetic mean of adjacent sieve sizes, m
d_{p50}	Value of d_{50} based on a sieve size distribution, m
d_{pm}	Mean particle size from a standard sieve analysis, Eq (1), m
d_{pwm}	Weighted mean diameter based on a sieve analysis, Eq (2), m
d_{sv}	Diameter of a sphere with the same surface area to volume ratio as the particle, m
d_{svm}	Mean surface volume diameter, Eq (3), m
d_v	Diameter of a sphere with the same volume as the particle, m
d_{v50}	Value of d_{50} based on a volume diameter distribution, m
d_{vm}	Mean equivalent volume diameter, Eq (4), m
d_{vwm}	Volume weighted mean diameter, Eq (5), m
D	Internal diameter of pipe, m
Fr	Froude No, $Fr = V_f (gD)^{-0.5}$
g	Acceleration due to gravity, m s ⁻²
k	Power index
K	Pipe branch head loss for solids-gas flow
K_f	Pipe branch head loss for air-only conditions
L	Total effective length of pipe or section of pipeline, m
L_h	Total effective length of horizontal pipe, m
L_v	Total effective length of vertical pipe, m
m_f	Air mass flow rate, kg s ⁻¹
m_s	Solids mass flow rate, kg s ⁻¹
m^*	Solids to air mass flow rate ratio, $m^* = m_s m_f^{-1}$
n	Power index
NB	Nominal bore
P	Specific power, W h t ⁻¹ m ⁻¹
r	Centreline bend radius, m
t	Time, s
V_f	Superficial air velocity, m s ⁻¹
V_{fso}	Single-particle saltation velocity, m s ⁻¹
V_{fup}	Re-entrainment velocity, m s ⁻¹
V_{mb}	Minimum bubbling velocity, m s ⁻¹

768 *Fluidization, Solids Handling, and Processing*

V_{mf}	Minimum fluidization velocity, m s^{-1}
x_1, \dots, x_4	Exponents
X	Factor (Mainwaring and Reed, 1987)
y_1, \dots, y_4	Exponents
Δh	Difference in height, m
ΔL_s	Length of straight section of pipe, m
ΔM	Mass percent of material contained in a given size range, %
ΔM_i	Value of ΔM for size range i , %
Δp	Pressure drop, Pa
Δp_b	Pressure drop caused by bend, Pa
Δp_s	Pressure drop caused by straight section of pipe, Pa
Δp_t	Total pipeline air pressure drop, Pa
k_d	Deaeration factor (Mainwaring and Reed, 1987)
k_p	Permeability factor (Mainwaring and Reed, 1987)
I_b	Particle-wall friction factor in bend
I_s	Particle-wall friction factor in straight pipe
r_{bl}	Loose-poured bulk density, kg m^{-3}
r_f	Air density, kg m^{-3}
r_s	Particle density, kg m^{-3}
ψ	Particle sphericity

Subscripts

i	Initial value (at beginning of pipe)
e	Final or exit value (at end of pipe)
f	Fluid (gas)
m	Mean value (based on average air density)
min	Minimum value
n	Value relating to pipe section n (starting from end of pipeline)
o	Value relating to bend outlet
s	Solids

REFERENCES

- ACGIH, *Industrial Ventilation: A Manual of Recommended Practice*, 21st Ed, American Conf. of Governmental Industrial Hygienists, Inc., Cincinnati, USA (1992)
- Allen, T., *Particle Size Measurement*, Chapman and Hall Ltd, London, 2nd Ed (1975)
- Anon, "Dynamics of Gas/Solids Systems," *Pneumatic Handling of Bulk Mat., Part A: Fundamentals*, Bulk Solids Handling Unit, Thames Polytechnic, London (1983)
- Anon, "Dust Suspended from Workplace," *PACE, Process and Control Eng.*, p. 56 (1995)
- Arnold, P. C., Wypych, P. W., and Reed, A. R., "Advances in the Design of Pneumatic Transport Systems," *Powder Handling & Processing*, 6(1):9–21 (1994)
- ASHRAE, *ASHRAE Fundamentals Handbook*, American Society of Heating, Refrigerating and Air Conditioning Engineers, Inc, Atlanta (1985)
- Barnes, R. N., and Murnane, S. N., "The Sensing of Unbalanced Pulverised Coal Feed Rates at the Exit of Riffle Boxes in Coal-Fired Power Station Fuel Distribution Systems," *5th Int. Conf. on Bulk Mat. Storage, Handling and Transportation*, Newcastle, IEAust, Proc., 1:273–281 (1995)
- Cable, P. M., *Design Requirements of Ind. Dust and Fume Extraction Systems*, BE Thesis, Dept. of Mech. Eng., Univ. of Wollongong (1994)
- Cabrejos, F. J., and Klinzing, G. E., "Minimum Conveying Velocity in Horizontal Pneumatic Transport and the Pickup and Saltation Mechanisms of Solid Particles," *Bulk Solids Handling*, 14(3):541–550 (1994)
- Cürten, H. J., "Concepts and Results of Pneumatic Conveying of Support Materials in German Underground Mining," *Pneumatech 1, Int. Conf. on Pneumatic Conveying Technol.*, Stratford-Upon-Avon, UK (1982)
- DASCG, and AIRAH, *Mechanical Engineering Services Design Aids No. DA3, Air Conditioning Duct Design Manual*, (F. Wickham, ed.), Dept Administrative Services Construction Group and AIRAH, Aust Govt Publishing Service, Canberra, Aust (1987)
- DASCG, and AIRAH, *Mech. Eng. Services Design Aids No DA4, User Guide for the Computer Program DONKEY*, (F. Wickham, ed.), Dept Administrative Services Construction Group and AIRAH, Aust Govt Publishing Service, Canberra, Aust (1988)
- Dixon, G., "How do Different Powders Behave?," *Bulk-Storage Movement Control*, 5(5):81–88 (1979)

770 *Fluidization, Solids Handling, and Processing*

- Dixon, G., "Pneumatic Conveying," *Plastics Pneumatic Conveying and Bulk Storage*, Applied Science Publishers, London (1981)
- Geldart, D., "Types of Gas Fluidization," *Powder Technol.*, 7:285–292 (1973)
- Geldart, D., and Abrahamsen, A. R., ("Fluidization of Fine Porous Powders, Recent Advances in Fluidization and Fluid-Particle Systems," *AIChE Symp. Series*, AIChE, 77(205):160–165, New York (1981)
- Geldart, D., Harnby, N., and Wong, A. C., "Fluidization of Cohesive Powders," *Powder Technol.*, 37:25–37 (1984)
- Hilbert, J. D., "Multiple In-Line Splitting of Pneumatic Conveying Pipelines," *J. Pipelines*, 3:161–172 (1982)
- Jones, M. G., and Mills, D., "Low-Velocity Pneumatic Conveying: Product Characteristics," *Interbulk 89, Seminar on Pneumatic Conveying: Potentials and Capabilities*, Birmingham, Organised by Glasgow College, Glasgow, Scotland and Thames Polytechnic, London, England (1989)
- Kennedy, O. C., Wypych, P. W., and Arnold, P. C., "The Effect of Blow Tank Air Injection on Pneumatic Conveying Performance," *Pneumatech 3, Int. Conf. on Pneumatic Conveying Technol.*, Jersey, Channel Islands, UK (1987)
- Lohrmann, P. C., and Marcus, R. D., "The Performance of a Bottom-Discharge Blow Vessel Pneumatically Conveying Three Group A Materials," *Bulk Solids Handling*, 4(2):409–412 (1984)
- Low, H. T., Winoto, S. H., and Kar, S., "Pressure Losses at the Branches of a Pneumatic Conveying System," *Bulk Solids Handling*, 7(6):865–867 (1987)
- Mainwaring, N. J., and Reed, A. R., "Permeability and Air Retention Characteristics of Bulk Solid Materials in relation to Modes of Dense-Phase Pneumatic Conveying," *Bulk Solids Handling*, 7(3):415–425 (1987)
- Marcus, R. D., Leung, L. S., Klinzing, G. E., and Rizk, F., *Pneumatic Conveying of Solids*, Chapman and Hall Ltd, London (1990)
- Mason, J. S., Mills, D., Reed, A. R., and Woodcock, C. R., "The Use of Product Conveying Characteristics in the Design of Pneumatic Conveying Systems," *Powder Europa. 80*, Seminar D, pp. 58–80 (1980)
- Miletich, D., *Atomisation and Pneumatic Conveying of Coarse Aluminium Powder*, BE Thesis, Dept of Mech Eng, Univ. of Wollongong (1994)
- Mills, D., Mason, J. S., and Stacey, R. B., "A Design Study for the Pneumatic Conveying of a Fine Particulate Material," *Solidex 82*, pp. C1–C75 Harrogate, UK (1982)
- Molerus, O., "Interpretation of Geldart's Type A, B, C and D Powders by Taking into Account Interparticle Cohesion Forces," *Powder Technol.*, 33:81–87 (1982)
- Pan, R., and Wypych, P. W., "Scale-Up Procedures for Pneumatic Conveying Design," *Powder Handling & Processing*, 4(2):167–172 (1992a)

- Pan, R., and Wypych, P. W., "Bend Pressure Drop in Pneumatic Conveying of Fly Ash," *Powder & Bulk Solids Conf.*, Reed Exhibition Companies, USA, Proc, pp. 349–360, Rosemont, Illinois, USA (1992b)
- Pan, R., and Wypych, P. W., "Design of Economic Pneumatic Conveying Systems," *MECH'94, Int. Mech. Eng. Congress & Exhibition*, IEAust, Proc, 2:137–141, Perth, WA (1994)
- Selves, T. P., and Barnes, R. N., "A Review of In-Line Splitting Techniques used in Pneumatic Conveying," *4th Int. Conf. on Bulk Materials Storage, Handling and Transportation*, 2:353–358, IEAust. Proc, Wollongong (1993)
- Selves, T. P., Barnes, R. N., and Reed, A. R., "The Use of Flow Diverting Air Injection to Actively Control the Split Ratio of Pneumatically Conveyed Particulate Materials," *5th Int. Conf. on Bulk Materials Storage, Handling and Transportation*, IEAust. Proc, 1:263–271, Newcastle (1995)
- Timms, G., "Pneumatic Conveying - a New Application for Larox Pinch Valves," *Larox News*, 14:8–11 (1992)
- Wypych, P. W., *Pneumatic Conveying of Manganese Oxide*, ITC Bulk Materials Handling Report for BHP Engineering, North Sydney, NSW (1989b)
- Wypych, P. W., *Pneumatic Conveying of Bulk Solids*, PhD Thesis, Department of Mechanical Engineering, Univ. of Wollongong (1989b)
- Wypych, P. W., "Pressure Drop in Cement Pneumatic Conveying Systems," *Powder & Bulk Solids Conf.*, Reed Exhibition Companies, pp. 467–471, Rosemont, Illinois, USA (1992)
- Wypych, P. W., "Optimising & Upgrading Pneumatic Transport Systems," *Nat. Conf on Bulk Materials Handling*, Yeppoon, Qld., IEAust. Proc., pp. 197–203 (1993)
- Wypych, P. W., "Latest Developments in the Pneumatic Pipeline Transport of Bulk Solids," *5th Int. Conf. on Bulk Materials Storage, Handling and Transportation*, Newcastle, IEAust, Proc, 1:47–56 (1995a)
- Wypych, P. W., "Engineering Design in the Pneumatic Pipeline Transport of Bulk Solids," *Mech. Eng. Trans.*, IEAust, ME20(4):293–298 (1995b)
- Wypych, P. W., and Arnold, P. C., "The Use of Powder and Pipe Properties in the Prediction of Dense-Phase Pneumatic Transport Behavior," *Pneumatech 2*, Canterbury, England, Organised by the Powder Advisory Centre, London (1984)
- Wypych, P. W., and Arnold, P. C., "Predicting and Improving Flow Performance in Dense-Phase Pneumatic Transportation," *Int. Symp. on the Reliable Flow of Particulate Solids*, Organised by the Chr Michelsen Institute, Bergen, Norway (1985a)
- Wypych, P. W., and Arnold, P. C., "A Standardised-Test Procedure for Pneumatic Conveying Design," *Bulk Solids Handling*, 5(4):755–763 (1986b)

- Wypych, P. W., and Arnold, P. C., "Pneumatic Transportation and Fluidization Performance of Power Station Fly Ash," *Bulk Solids Handling*, 6(1):93-97 (1986a)
- Wypych, P. W., and Arnold, P. C., "Feasibility and Efficiency of Dense-Phase Pneumatic Transportation," *Mech. Eng. Trans.*, IEAust, ME11(1):1-5 (1986b)
- Wypych, P. W., and Arnold, P. C., "Minimising Wear & Particle Damage in Pneumatic Conveying Systems," *Powder Handling & Processing*, 5(2):129-134 (1993)
- Wypych, P. W., and Hauser, G., "Design Considerations for Low-Velocity Conveying Systems & Pipelines," *Pneumatech 4, Int. Conf. on Pneumatic Conveying Technology*, pp. 241-260, Glasgow, Scotland, Powder Advisory Centre, UK (1990)
- Wypych, P. W., Kennedy, O. C., and Arnold, P. C., "The Future Potential of Pneumatically Conveying Coal through Pipelines," *Bulk Solids Handling*, 10(4):421-427 (1990)
- Wypych, P. W., and Pan, R., "Determination of Air-Only Pressure Drop in Pneumatic Conveying Systems," *Powder Handling & Processing*, 3(4):303-309 (1991)
- Wypych, P. W., and Pan, R., "Pressure Drop due to Solids-Air Flow in Straight Pipes and Bends," *Freight Pipelines*, (G. F. Round, ed.), pp. 49-67, Elsevier Science Publishers BV, Amsterdam, Netherlands (1993)
- Wypych, P. W., and Reed, A. R., "The Advantages of Stepping Pipelines for the Pneumatic Transport of Bulk Solids," *Powder Handling and Processing*, Vol 2(3):217-221 (1990)
- Yang, W. -C., "A Criterion for Fast Fluidization," *Pneumotransport 3*, Paper E5, Univ. of Bath, England (1976)
- Zenz, F. A., "Conveyability of Materials of Mixed Particle Size," *Ind. Eng. Chem. - Fund*, 3(1):65-75 (1964)
- Zenz, F. A., "Pneumatic Conveying from Grains to Powders," *Pneumatech 2*, Univ. of Kent, Canterbury, England, Organised by the Powder Advisory Centre, London (1984)

Cyclone Design

Frederick A. Zenz

1.0 INTRODUCTION

A cyclone represents the simplest and most easily fabricated piece of processing equipment. In principle it operates as a fluid driven centrifuge in which dispersed matter is condensed into its bulk state against the internal walls of a cylindrical vessel by an accelerated settling rate induced under an enormously higher gravitational field. The phenomenon is identical (Zenz, 1989, Ch. 1) to the condensation of molecular matter from a dispersed vapor state. Because of its simple mechanical structure and, in the past, its lack of criticality to acceptable plant operation, its design approaches have suffered. The literature varies from highly theoretical analyses of the forces governing aerodynamic particle trajectories to the observed performances of diametrically opposed empirical innovations for collecting, for example, shredded paper.

The early design approach (Rosin et al., 1932) remains to date as the only complete and logical basis for a dimensioning procedure yielding consistently verifiable results, but only when concomitant with strict attention paid to inlet and outlet peripherals. Industrial consortia (AIMS, 1989 to date) are engaged in continual experimental investigations of such

peripherals and their effects on destroying or enhancing the levels of performance predicted for the basic designs. Since several readily available references (Zenz, 1975; Zenz, 1989, Ch. 7), replete with worked examples, detail the basic dimensioning procedure, this chapter will be devoted primarily to emphasizing the precautions, essentials and peripherals within the design steps necessary to achieve a desired performance. Though discussed here in terms of a separation of solid particles from a gas, the relationships apply equally well to the separation of particles from a liquid, liquid droplets from a gas, and gas bubbles from a liquid.

2.0 REQUIRED DESIGN DATA

It should be incumbent on any designer, regardless of the procedure adopted, to document all of the following input data in order to substantiate the derivation of any anticipated or verifiable subsequent performance:

- (i) The viscosity, density and flow rate of the carrier gas entering the cyclone
- (ii) The particle size distribution of every species of feed particles in terms of the diameter of their aerodynamically equivalent spheres
- (iii) The apparent densities of the feed particles
- (iv) Any non-uniformity in the particle concentration gradient in the inlet stream
- (v) The rate of feed of the particles, as for example, lbs/unit volume of gas or as lbs/ unit time
- (vi) The required, or desired, particle collection efficiency
- (vii) The maximum available or permissible pressure drop
- (viii) Any known limits on particle impact velocity, surface characteristics, or bulk flow ability which would lead to any intolerable particle attrition, or equipment erosion
- (ix) Any space limitations on overall equipment height or width and the means of removal of the collected solids as for example through a dipleg pipe to a fluidized bed, through a rotary valve or ejector to a bin or conveying line, or intermittently to a sealed container

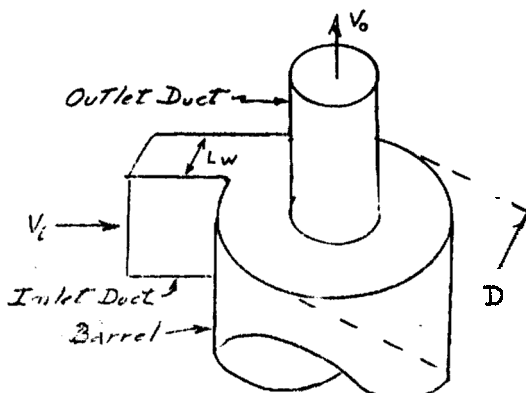
- (x) Any pressure or piping limitations dictating the shape of the cyclone inlet or of the transition ducting between cyclones in series.

3.0 CORRELATING FRACTIONAL COLLECTION EFFICIENCY

The traditional (Rosin, et al., 1932) mechanistic approach equates the time necessary for a particle to settle at a Stokes' law velocity across the width of a cyclone's inlet duct, to the available residence time of the carrier gas stream in its number of spiral traverses within the barrel. With reference to Fig. 1, this permits solving for the smallest particle size able to cross the entire width and reach the wall in the available time.

$$\frac{L_w}{V_t} = \frac{\pi D N_s}{V_i}$$

$$V_t = \frac{V_i^2 D_{th}^2 (\rho_p - \rho_g)}{(D/2) 18 \mu_g}$$

$$D_{th} = \sqrt{\frac{9 L_w \mu_g}{\pi N_s V_i (\rho_p - \rho_g)}}$$


The diagram shows a cross-section of a cyclone separator. It consists of an inlet duct on the left, a central barrel, and an outlet duct on the right. The inlet duct has a width labeled L_w and an arrow indicating an inlet velocity V_i . The barrel is a cylinder with a diameter labeled D . An arrow points to the barrel with the label 'Barrel'. The outlet duct is at the top, with an arrow indicating an outlet velocity V_o and the label 'Outlet Duct'. A dashed line shows a spiral path from the inlet duct towards the wall of the barrel. The distance from the centerline to the wall is indicated as $(D/2)$.

Figure 1. Derivation of D_{th} .

On the inherent assumptions that: (a) all entering particles are uniformly dispersed over the area of the inlet duct, (b) the barrel is a perfect cylinder with a straight inlet duct entering tangentially, (c) the trajectory of the incoming particles will not result in any impingement on the gas outlet duct, (d) that the velocity of the downwardly spiraling gas

remains constant, (e) the cyclone is long enough to exceed the depth to which the downward spiraling gas aspires before reversing its net direction through an inner upward spiral toward the gas outlet, (f) the number of spiral traverses is a function of either the gas inlet velocity or outlet velocity whichever is the greater and (g) the inlet dust concentration is no greater than 1 grain/cu.ft. of gas in order that particle travel to the barrel wall rests solely on the aerodynamics of individual particles, it is possible by trial and error to derive generalized correlations of cyclone performance from experimental data, but only when obtained with equipment and conditions all in conformance with the traditional mechanistic approach and with full recognition of the "required design data."

Unfortunately the literature is rampant with data obtained from cyclones of so wide a variety of deviating dimensional ratios and ill defined particle properties, sizes and loadings, that full agreement between designers, theorists and practitioners has not yet been achieved. However, in practice, the enormous number of cyclones installed in identical industrial process applications in the petroleum and petrochemical industries (Zenz, A.P.I., 1975) throughout the world and spurred by a common interest in economics and environmental regulations, has led to the correlations shown as the solid curves in Figs. 2 and 3.

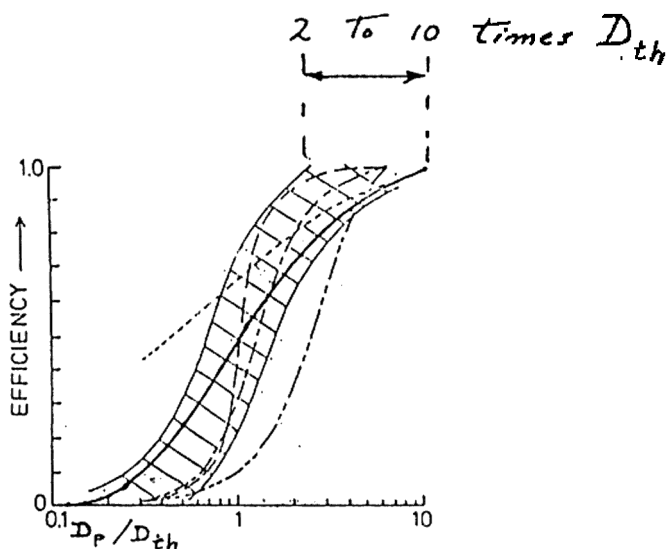


Figure 2. Fractional efficiency curves.

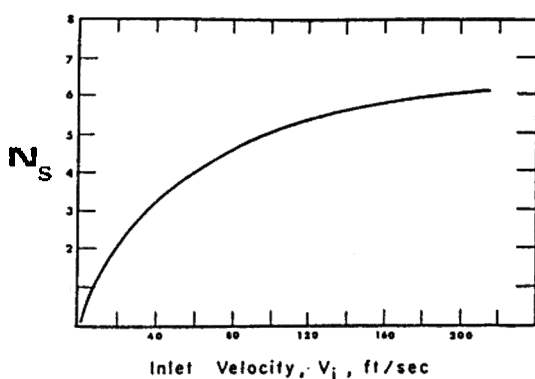


Figure 3. Correlation of barrel traverses.

The broad spectrum of derived fractional efficiency curves in Fig. 2 simply reflects the effects of cyclone designs deviating from consistence with the basic premises and from ill defined particle characteristics.

The most common source of apparent discrepancies between actual cyclone performance and the predictions based on Fig. 2 lies in the definition of feed particle size and density. Coulter Counter, laser, screen, etc., analyses of size simply reflect a dimension which may not cavalierly be taken as the diameter of aerodynamically equivalent spheres even if the apparent particle density is absolutely known and even if microscopic examination were to confirm perfect sphericity, unless the particle surface were also perfectly smooth. "Shape factors," intended to correct such measured dimensions to those of aerodynamically equivalent spheres, incorporate surface texture as well as overall irregularities in shape. The apparent aerodynamically intended Bahco or Sedigraph procedures inherently incorporate an assumed apparent particle density which must be independently determined in order to define the diameters of the aerodynamically equivalent spheres. Sorting out the results of measurements of fixed bed pressure drop, incipient fluidization velocity, bulk density, blow out velocities, settling rates, microscopic examination, free fall velocities, etc., (Zenz, 1996) through established correlations can result in consistent design data well worth the effort not only in increasing the credibility of the design procedure, but in avoiding subsequent litigations.

4.0 EFFECT OF SOLIDS LOADING

At solids inlet loadings greater than 1 grain/cu.ft. of gas, the frictional resistance to settling diminishes and the “plowing” effect of larger particles on the smaller particles, all drifting to the barrel wall, contribute in increasing degree to cyclone overall collection efficiency. The best (Hoffmann, et al., 1992) available empirically correlated effect of loading published to date is shown in Fig. 4.

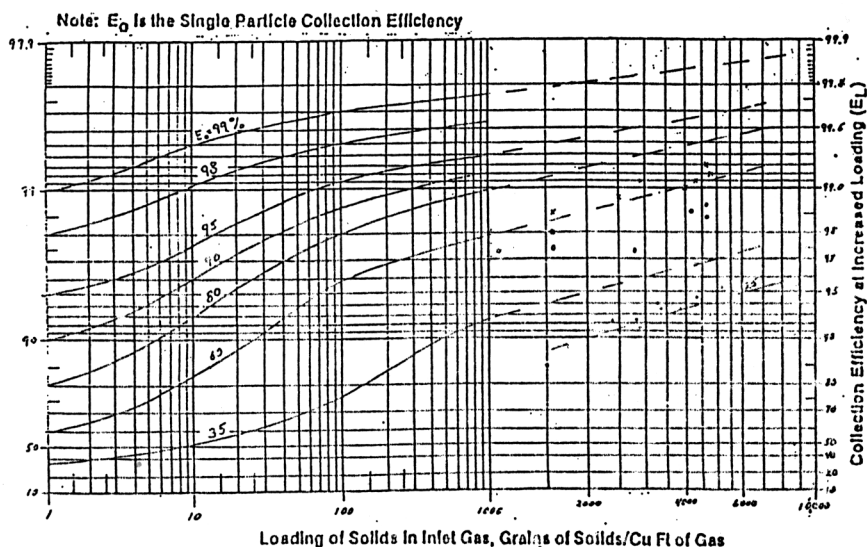


Figure 4. Effect of loading on efficiency.

5.0 CYCLONE LENGTH

As illustrated in Fig. 5, the outer downwardly spiralling gas velocity decays as gas “peels off” into the inner upwardly spiralling exiting vortex. The length of this inner vortex, the *natural vortex length*, L , (Alexander, 1949) then represents the distance below the edge of the gas outlet tube below which no feed gas remains to peel off into the inner vortex. If the

distribution of the feed gas inflow along the length L is considered proportionately constant in all cases, then it is found (Zenz, 1989, Ch. 7) that the average inflow velocity, V , over the surface area of the exiting vortex falls in a narrow range between 4 and 5 ft/sec.

Based on the average *peel off velocity* of 4–5 ft/sec, reducing the gas outlet tube diameter lengthens the natural vortex length, L . If L is extended to the point where it would touch the cyclone cone, its centrifugal force will, in effect, “grind” the downwardly spiralling stream of collected solids more forcefully against the cone wall causing erosion in the area of contact. In low loaded cyclones, such contact will also lead to some degree of reentrainment and hence to reduction in collection efficiency. If the gas outlet tube diameter is reduced in order to increase outlet gas velocity to a value greater than the inlet velocity, and thereby decrease D_{th} to increase collection efficiency at lower overall pressure drop, then the cyclone must also be lengthened to “contain” L . A conservative design clearance between the periphery of the natural vortex length and the cone wall is suggested as 2" as shown in Fig. 5.

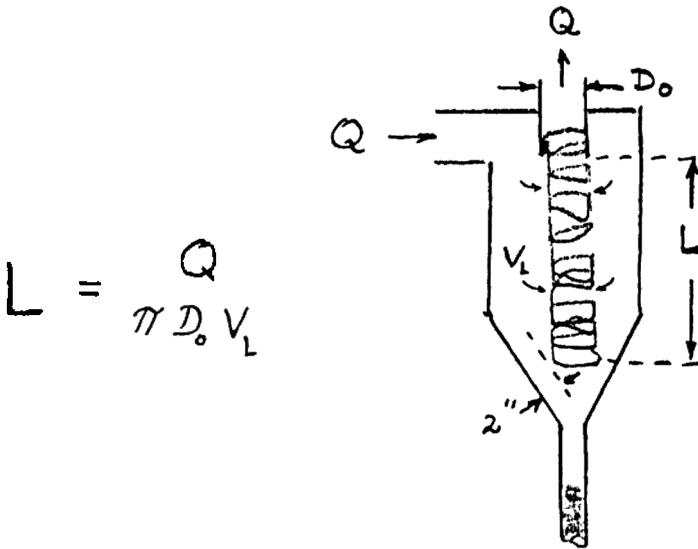


Figure 5. Natural vortex length.

6.0 CONES, DUST HOPPERS AND EROSION

Cones are attached to cyclone barrels simply as a transition to the diameter of the so-called dipleg pipe necessary to allow exit of the stream of collected solids (Zenz, 1975). The cone is irrelevant to the cyclone's performance; many installations in specific applications, as well as smaller units operating in parallel in multi-clones, are seldom provided with cones. Ideally, a conventional cone should be tapered to the angle of repose of the bulk collected solids under the centrifugal acceleration field within the cyclone. Such sophistication is generally disregarded and the cones sloped at 60 to 80 degrees from horizontal. The steeper this slope, the less the possibility of erosion within the upper end of the dipleg at the point where the stream of collected solids cascades from the edge of the cone's apex and impacts the dipleg wall.

Three patents (MacLean, et al., 1982) assigned to Texaco filed in the latter half of 1980 resulted from an in-house review of all observed instances of erosion of cyclones in Texaco's FCC units. The patents specify that to minimize erosion and maximize collection efficiency, the length of the cyclone relative to its barrel diameter is to conform to the relationship:

$$H/D = 4.49 - 1.09 (A_o/A_i)$$

However, the eroded regions which led to this relationship were all located in the so-called dust hoppers and not in the cyclone cones. Texaco's personnel failed to realize that the erosion in the dust hoppers is due to impingement by the stream leaving the edge of the cone's apex. The simple solution to such erosion is to eliminate the dust hoppers. There are numerous cyclones without dust hoppers operating in the process industries, including FCC installations, which are free of erosion in their cones and dipleg pipes provided that they "contain" the natural vortex length free of touching the cone wall. It is, however, imperative that in fabrication a cyclone cone always be rolled as opposed to being formed on a brake. As illustrated in plan and isometric views in Fig. 6, the condensed stream of collected solids spiralling down on the surface of the cone impinges the metal past any bend (resulting from fabrication on a brake) at an angle of attack steeper than 0 degrees. This has been evidenced in numerous instances as a spiral pattern of eroded holes and parallels the

mechanism which leads to dust hopper erosion patterns. Poor quality interior finish in the form of seam weld burrs or lining irregularities induce similar points of severe erosion.

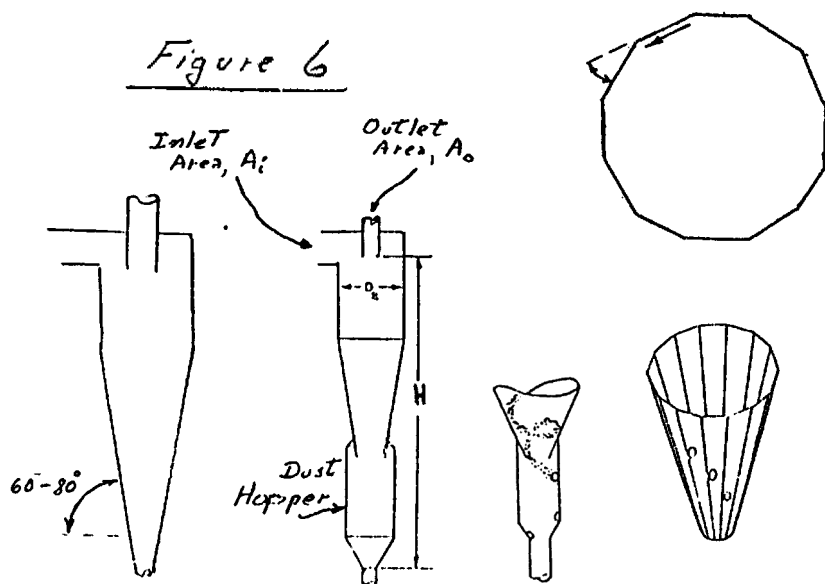


Figure 6. Cones, dust hoppers and erosion.

7.0 CYCLONE INLET AND OUTLET CONFIGURATIONS

Cyclone inlets should always be rectangular in shape rather than round. A round pipe entering a cylindrical barrel affords only one point of tangency, whereas a rectangular duct is tangent along an entire side providing proximity to the barrel wall to a greater number of entering particles.

When a high velocity gas stream bearing particulates or liquid droplets enters tangentially into a vertical pipe, the particles or droplets will collect into two streams, one spiralling downwardly and the other

spiralling upwardly; the latter eventually reaches a limiting height whereupon gravity causes it to head back down as depicted in Fig. 7. Any domed head (designed to withstand high internal pressure) on a cyclone, therefore, permits such an upward spiral to follow an inward path directly to the top of the gas discharge tube, as in Fig. 8, on which it may then spiral down and be sucked into the exiting gas vortex when it reaches the bottom edge of the gas discharge tube. Inserting a false roof into such an existing design will result in substantial improvement in performance. This situation is equally acute in instances where under high temperature operations a protruding internal gas outlet tube would fail structurally. In such instance, external cooling by forced or natural convection can be provided via a folded annulus as illustrated in Fig. 9.

Ideally, the gas outlet tube should protrude below the cyclone roof a distance equal to the height of the inlet duct to minimize bypassing of a portion of the inlet flow directly into the gas outlet. The effect on collection efficiency of shortening the gas discharge tube has been treated in the literature (TerLinden, 1949). The argument that lengthening the tube beyond the inlet duct height will afford a greater gas residence time (greater number of spiral traverses) has never been demonstrated. Since the natural vortex length is measured from the bottom edge of the gas outlet tube, its lengthening must be accompanied with a commensurate increase in overall cyclone length.



Figure 7. Natural split in particle paths.

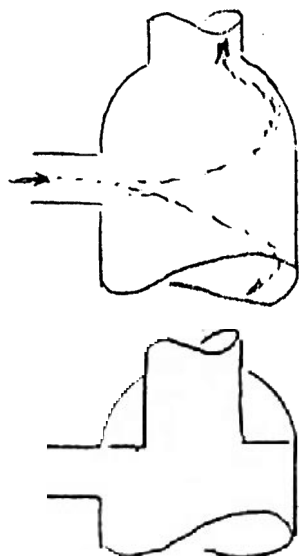


Figure 8. Cyclone roof design.

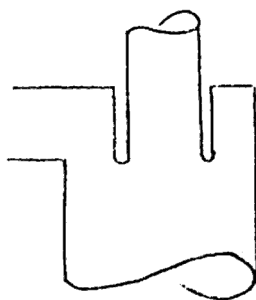


Figure 9. Dimpled outlet tube.

All cyclone design procedures bear the inherent condition that the solids enter uniformly dispersed over the cyclone's inlet area. This is generally the case where a cyclone is hung inside a vessel above a

contained fluidized bed or where the cyclone is external but close-coupled to the wall of a large vessel as in the case of fluidized bed combustors. If the entering stream is not uniformly dispersed, as induced in Fig. 10 by a preceding elbow, collection efficiency will be poorest in arrangement Fig. 10(a) and exhibit a decrease in efficiency with increase in either loading or inlet velocity. This is attributable to the more densely concentrated stream of solids entering adjacent to the gas discharge tube. The effect is more pronounced with a preceding downflow elbow, as in Fig. 10(a), than with an upflow elbow as in Fig. 10(b), presumably because in Fig. 10(b) there is an outlet tube length over which some particles may have a greater chance to reach the barrel wall rather than all hug the gas discharge tube and escape under its bottom edge drawn in with the exiting gas spiral.

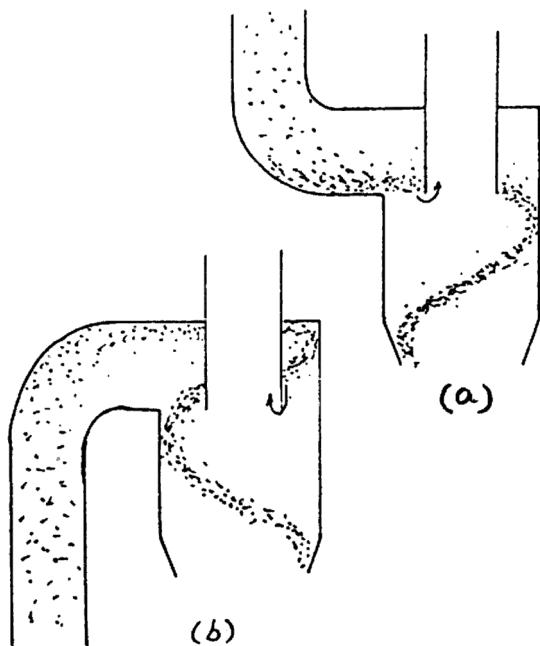


Figure 10. Effect of preceding elbows.

Three generic forms of cyclone can be characterized by their inlet configurations as illustrated in Fig. 11. At equal gas inlet or gas outlet velocities, the tangential generally yields the highest collection efficiency. At very high inlet particle loadings, differences between the three forms

may be minimal and the volute the better choice. For example, in a 3-stage series arrangement one could expect to find either of the three as the first stage, possibly a volute for the second stage, but certainly never any other than a tangential for the third stage handling the lowest inlet loading and smallest particle sizes. In general, the greater the extent to which the volute or scroll encircles the barrel, as in Fig. 11(b), the greater the loss in performance. This has been attributed to a disturbance of the spiralling flow paths due to the ledge of the volute inside the barrel (particularly in instances where the ledge has been seen to accumulate a layer of particles impinged upon by succeeding inflowing particles). The generally poorer efficiency of the axial or radial vane inlet of Fig. 11(c) has been correlated as simply reflected in a halving of the effective number of traverses of the barrel in the calculation of its characteristic centrifuged diameter D_{th} .

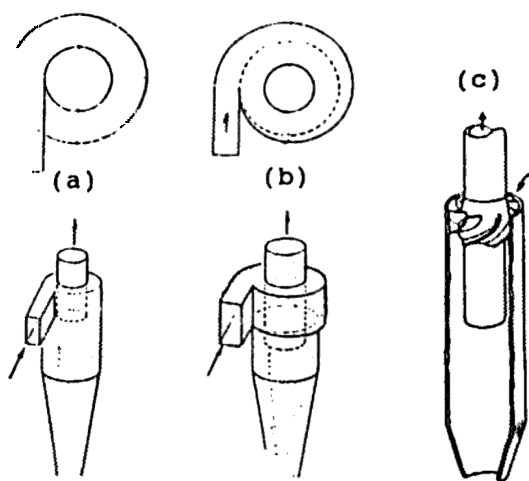


Figure 11. Generic cyclone forms.

8.0 THE COUPLING EFFECT

In a single stage installation, overall collection efficiency is not influenced by the external terminus of the gas discharge tube, whether a round elbow, Fig. 12(a), a mitered elbow, Fig. 12(b), or a volute housing,

Fig. 12(c). However, in a multistage installation where the gas and uncollected solids from a prior stage immediately enter a close-coupled subsequent stage, the overall 2-stage efficiency can exceed that based on the combined efficiencies calculated for each individual cyclone, if the terminus of the gas discharge tube of the preceding stage is designed to maintain the centrifugal discharge flow. Because of the spin in the exiting gas's natural vortex, which spin continues in its passage up through the gas discharge tube, there can be an appreciable concentration of particles near (if not directly contacting) the inner wall of the gas discharge tube (Silverman, 1950). If the terminus of the gas discharge tube preserves this centrifugal spiralling flow, via a tangential coupling to the subsequent stage, as illustrated in Fig. 12(d), then in effect the gas discharge tube acts as an axial flow pre-separator or low efficiency, single traverse, intermediate cyclone. The particles entering the subsequent stage are then not uniformly dispersed in the entering gas, as is assumed in applying conventional cyclone design procedures and, therefore, these procedures predict a lower efficiency than actually obtainable in practice. The added efficiency, induced by the ducting arrangement in Fig. 12(d), is referred to as giving rise to the *coupling effect*.

Figure 12

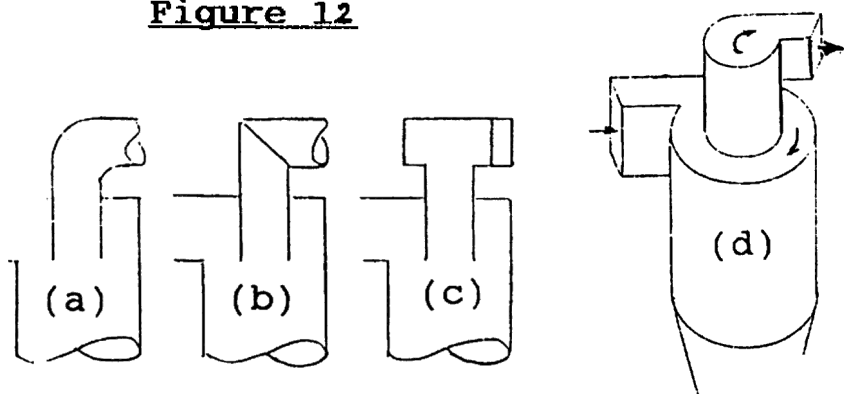


Figure 12. Gas outlet tube design.

9.0 PRESSURE DROP

The addition of small amounts of solids (Yuu, et al., 1978; Kane, et al., 1973; Kang, et al., 1989; Knowlton, et al., 1977; Baskakov, et al., 1980) in the gas entering a cyclone at first reduces the pressure drop until, at higher loadings, it increases the pressure drop. The former is attributed to the reduction of viscous drag at the walls (or the “lubrication” by the “rolling” of the particles) while the latter is attributed to increasing pressure drop required to accelerate the greater masses.

The equations given in various references (Zenz, A.P.I., 1975; Zenz, 1989, Ch. 7) apply to conditions where the solids loadings exceed that at which any reduction in loading would cause pressure drop to be greater than that given by those equations. The oft-quoted (Stairmand, 1951) equation for cyclone pressure drop applies solely to gas alone bearing no solids. The data shown in Fig. 13 taken from a recent paper (Dry, et al., 1993) are typical of the effect of low loading where the pressure drop at zero solids loading decreases gradually to about 0.4 times this pressure drop, before beginning to increase again by virtue of further increase in loading.

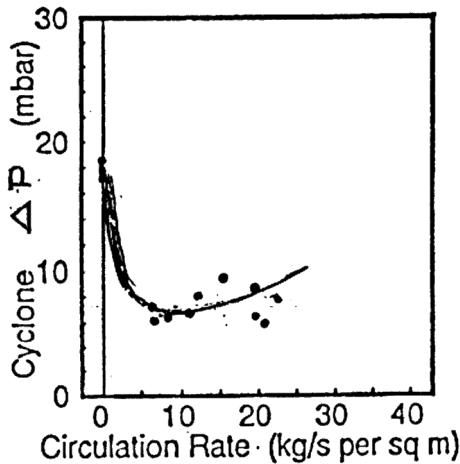


Figure 13. Pressure drop and loading.

10.0 SPECIAL CASES

There are instances in specific industries, or in unusual applications, which would appear to exhibit major deviations from all the foregoing "best design practice." This is most frequently associated with unconventional characteristics of the solids being handled. Figure 14 illustrates a particular case in point. This unit has: (a) essentially no barrel beyond the inlet height, (b) a gas discharge tube with half of its perimeter cut away over about half its length (this portion covered with a coarse screen), (c) a relatively high ratio of inlet height to inlet width ($80''/18'' = 4.44$ as compared to the conventional ~ 2.2 – 2.7), and (d) a relatively high outlet to inlet area ratio of 3.14 (compared to 0.4 to 1.5).

This unit operates with air under a positive inlet pressure and discharges to ambient. It is fed shredded paper ranging in size from $1/2'' \times 1/2''$ to $1/2'' \times 6''$. It constitutes essentially a single traverse cyclone, which is sufficient for such large "particles." The screen on the gas discharge tube allows escape of the air on the inside radius of the first turn and thus "shrinks" the usual natural vortex length to zero. The 24" I.D. cone apex is open to an unsealed collection or baling bin and hence some amount of gas underflow augments discharge, rather than reentrainment or hang-up. The so-called "tangentials" offered for example by American Air Filter Corp. illustrated in Fig. 15 constitutes, in effect, a horizontally oriented version of Fig. 14.

The European patent office recently granted two applications to the A. Ahlstrom Corp. (Hyppanen, et al., 1991) relating to what is described in the text, and in the apparatus and method claims, as a centrifugal separator of "square cross-section." The patent applications make no mention, nor give any examples, of what separation efficiencies can be anticipated. The suggested advantages lie in the fabrication convenience and economy afforded by the flat, as opposed to conventionally curved, water walls. The efficacy of Ahlstrom's separator lies in the solids, at high loadings, piling up in the corners so that the effective inside diameter approaches the contours of a cylinder. This follows the principle of using TEEs or mitered elbows in pneumatic conveying lines as introduced over 50 years ago and as employed in the separator developed for their TRC process jointly by Stone & Webster Engineering Corp. (Gartside, 1985) and Gulf Oil (now Chevron). That separator, illustrated in Fig. 16, was essentially a square section box, all dimensional design ratios of which were optimized in a modeling program at PEMM-Corp studying 32

variations. The optimum configuration yielded 95% collection efficiency of a high fines content FCC catalyst. The arrangement in Fig. 16 represents a half-turn cyclone with restricted drawoff maintaining thereby a dense phase layer of collected solids as a contoured erosion shield.

Figure 17 illustrates another form of a "less than one turn" cyclone in which the rectangular box of Fig. 16 is now an open channel allowing even more rapid separation of gas and solids. This arrangement has achieved a factor of three reduction in catalyst losses in several operating FCC regenerators. FCC catalyst separation in the developer's (Zenz, 1988) laboratory tests yielded collection efficiencies greater than 99%. The important aspect of the curving channels in Fig. 17 is that they maintain the collected solids as a dense phase stream at all times as they terminate tangential with a collection vessel's wall.

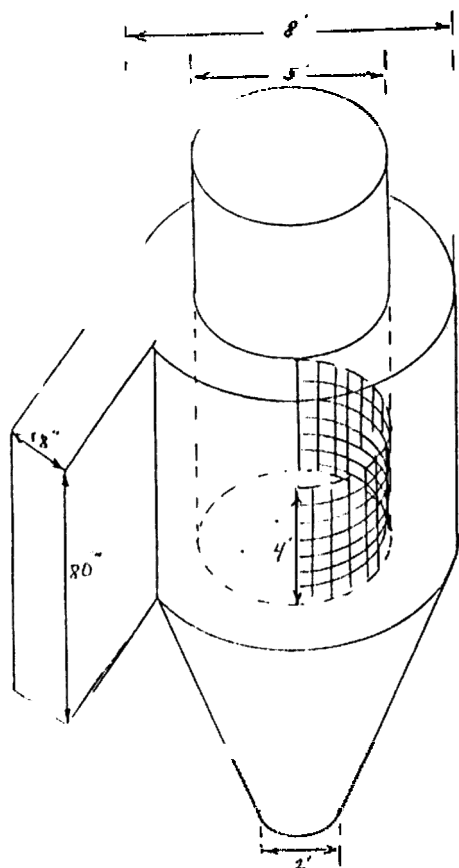


Figure 14. Shredded paper collector.

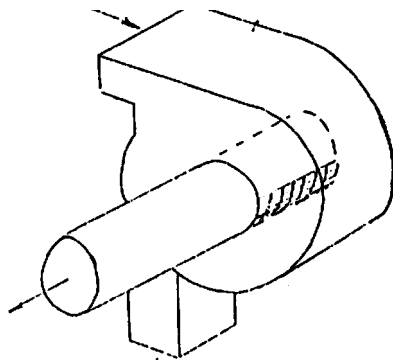


Figure 15. Tangential single turn cyclones.

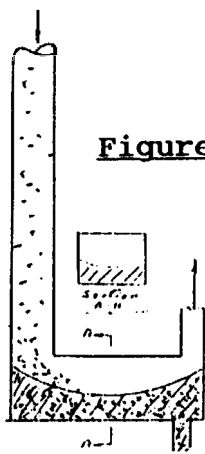


Figure 16. Rectangular mitered elbow cyclone.

Cyclones are still simply gravity settling chambers in which a particle's settling velocity is increased by making the particle heavier (through a centrifugal field greater than 32.2 ft/sec/sec and in which sufficient residence time is provided via an induced number of barrel traverses to achieve settling over a distance Lw with the predictability of performance dependent on attention to all design peripherals.

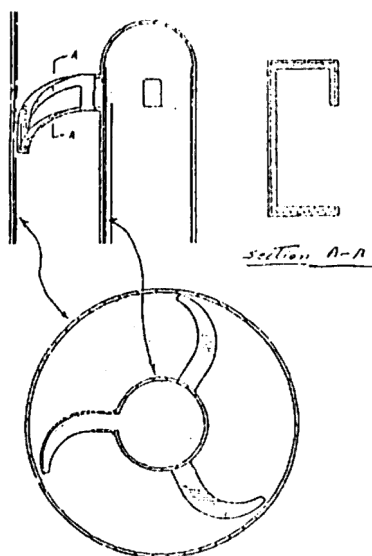


Figure 17. Curved “ARM” collector.

11.0 BED PARTICLE SIZE DISTRIBUTION AND CYCLONE DESIGN

In a fluidized bed reactor, entrained particles leaving in a dilute phase stream are conventionally and desirably either partially or wholly condensed into a bulk stream and returned to the bed via a centrifugally driven cyclone system. At equilibrium, or when steady state operation is attained, any particle loss rate from the cyclones, as well as the remaining bed particle size distribution, are functions of (a) the rate of any particle attrition within the system and (b) the smallest particle size that the cyclone system was designed to completely collect (i.e., with 100% efficiency), or conversely the largest size which the system cannot recover. These two functions result in an interdependency between loss rate and bed particle size distribution, eventually leading to an equilibrium state (Zenz & Smith, 1972; Zenz, 1981; Zenz & Kelleher, 1980).

Case A. To illustrate, consider a situation in which a reactor is charged with a catalyst having a size distribution ranging from 1 to 150

microns. Suppose that the cyclone system was designed to retain all particles 10 microns or larger in size and that the particles are so “strong” that there will be no attrition. As time progresses after start-up, the bed will approach a size distribution from 10 to 150 microns. All particles smaller than 10 microns will have been lost, only the fluidizing off gases will leave through the cyclone system. No additional catalyst will need to be charged to make up for the loss from the cyclone system because no further particle loss occurs once the 0 to 10 micron fraction of the charge has left the system. The mean particle size of the equilibrium bed will be larger than that of the original catalyst charge, since the weight percent of all sizes smaller than the largest will have decreased in proportion to the lost weight fraction of the 0 to 10 micron particles in the original charge.

Case B. Suppose, more realistically, that the catalyst undergoes a known, experimentally determined, rate of attrition as a function of particle size (Zenz, 1971; Zenz & Kelleher, 1980). The particle loss rate from the cyclone system will now approach and finally equal the rate of production of 0 to 10 micron particles by attrition from all the larger sizes. To maintain reactor inventory, this loss rate will be replaced, at an equal rate, with fresh catalyst. Since the rate of attrition of any size particle depends on its concentration in the stream subjected to the attrition (as finer particles effectively “cushion” the coarser), and since the loss is replaced with fresh catalyst (containing the coarsest), the bed size distribution will reach a steady state between 10 and 150 microns in which the mean size, as well as all sizes smaller than the largest, will now be decreased from what would have prevailed under conditions of zero attrition.

Case C. Now suppose that in order to maintain conversion in the reactor the equilibrium bed must be further increased in catalytic surface area, or in other words must maintain a greater “fines” content under steady state operation. This would require the cyclone system to now retain all particles smaller than say 5 microns in diameter. Since the existing system design could not retain particles smaller than 10 microns, the cyclone system must be modified to meet the new and more stringent specification. This can be accomplished either by replacing the final collection stage with a larger number of smaller cyclones in parallel, still operating at the same inlet and outlet velocities, or by modifying the existing cyclone system’s final stage to operate at higher inlet and outlet

velocities. Both changes are designed in principle to reduce the time required for particles to reach and “condense” on the barrel walls. Replacing the final stage with a multiplicity of smaller units is likely the more costly modification, but would advantageously not increase the catalyst attrition rate. The less costly expedient of simply modifying the internal dimensions of the inlets and outlets of the existing cyclones would simultaneously increase the catalyst attrition rate, so that when the new steady state is reached, the bed would have a size distribution from 5 to 150 microns, a mean particle size smaller than in all previous cases, a greater weight fraction of all sizes smaller than the largest, and a loss rate of 0 to 5 micron particles likely greater than the weight rate of loss of 0 to 10 micron particles in case B. This will require more fresh catalyst makeup to maintain reactor inventory. The time required to reach the new steady state equilibrium will be principally a function of the entrainment rate and the reactor catalyst inventory. There are cases illustrated in the literature in which this could take as long as a year (Zenz & Smith, 1972).

The choice of cyclone modification, from an operating point of view, becomes a balance of incremental profit from increased conversion, versus catalyst makeup charges, and from a capital cost point of view, the price of either of the cyclone modifications, which must be depreciated. In many instances, there is an additional background time element, involving ongoing development of more attrition resistant and/or active catalyst.

12.0 CENTRIFUGAL VERSUS CENTRIPETAL CUT POINT PARTICLE SIZE

Though the efficiency of a cyclone is relatable to the smallest particle size it will collect with 100% efficiency (or conversely the largest particle that appears in its loss), it must be borne in mind that any such evaluation, or comparison among designs, must be conducted under identical conditions of loading and feed particle size distribution as well as gas density, viscosity and inlet velocity. In operation a cyclone, losing a substantial amount of fine particles when fed a high concentration of fines is not necessarily to be regarded as an inherently poor design. It should principally be evaluated in terms of the largest particle that it loses (i.e., is unable to collect). In a similar situation in which such a cyclone acted as a second stage where its preceding unit recovered a reasonable amount of

small particles or where it was preceded with less attrition, the loading to this now second stage would have a lower percentage content of small particles and hence would show a higher total efficiency. This higher efficiency simply reflects a feed containing less losable material; the maximum size lost would still be the same as when fed material with a greater concentration of the unrecoverable particle sizes, where it had then been considered a poorer efficiency cyclone. The differentiation between collection efficiency and maximum unrecoverable or lost size has never been clearly established.

Maximum unrecoverable particle size is overshadowed at high loadings where bypassing to the outlet tube can cause larger particles to be lost though the overall efficiency may be high. Fundamentally the cut point diameter or maximum size lost is observable only at low loadings less than about 50 grains/cu.ft. and reasonably predictable by equating the centrifugal force of the exiting vortex (impeding particle loss) to the net or average radial inflow (centripetal force) to the exiting vortex. The low loading (exiting) cut point diameter differs in its derivation and hence its significance from the higher loading ("inlet catch") D_{th} of Figs. 1 and 2. A lack of appreciation between these two distinct, albeit seemingly interrelated, performance criteria is likely one of the causes of the 5-fold variance in the intercepts of experimental fractional efficiency curves, at 100% collection, illustrated in Fig. 2.

13.0 CYCLONE DESIGN EXAMPLES

With consideration to the domestic industrial practitioner, the following illustrative examples utilize conventionally recognizable units as viscosity in centipoise, density in lbs/ft³, velocity in ft/sec, vessel dimensions in inches, and particle diameter in microns.

Example A. Suppose it was desired to design a cyclone to collect all particles larger than 97 microns and release no more than 60 lbs/hr from a 6328 ACFM gas stream bearing 80 grains of solids per cubic foot of gas. The particle size distribution and density of the solids is given in Fig. 18; the gas has a density of 0.1 lbs/ft³ and a viscosity of 0.02 centipoise. The pressure drop across the cyclone is not to exceed 10" H₂O. Note from Fig. 1 of the text that 100% collection efficiency of 97 micron particles would require a D_{th} of 9.7 microns which would be collected at an average 50%

efficiency. From considerations of cost, capacity, size and inlet pressure drop, the optimum ratio of height-to-width of a rectangular inlet lies between 2 and 3 (avg. = 2.5) so that cyclone capacity can be expressed as:

$$\text{Eq. (1)} \quad \frac{\text{ACFM}}{60} = 2.5 L_w^2 V_1 n$$

Solving for L_w and substituting in the definition of D_{th} given in Fig. 1 of the text:

$$\frac{9.7}{12 \times 25,400} = \sqrt{\frac{9 \times 0.02 \times 0.000672}{3.14 N_s V_1 (85 - 0.1)}} \sqrt{\frac{6,328}{n 150 V_1}}$$

which for the case of a single unit (i.e., $n = 1$) reduces to

$$\text{Eq. (2)} \quad N_s V_1^{1.5} = 2908$$

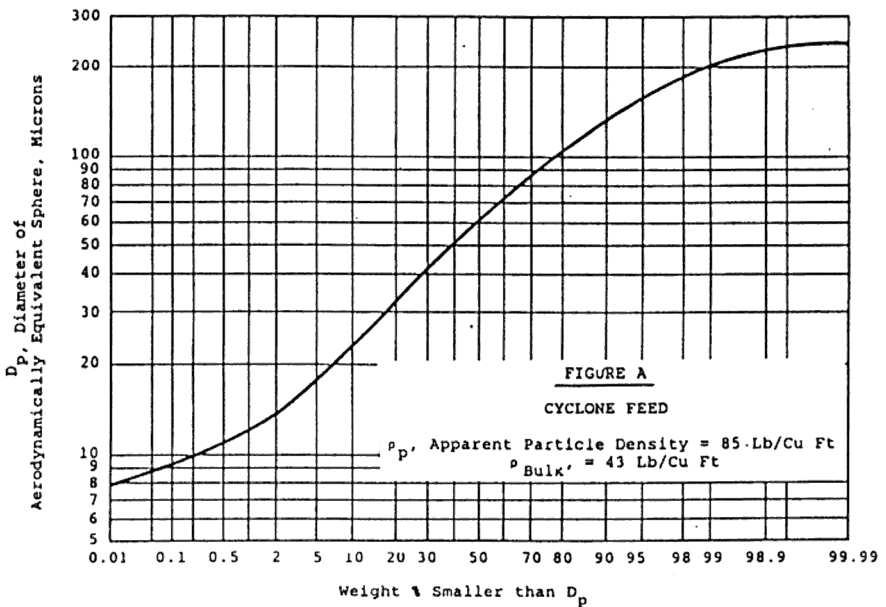


Figure 18. Particle size analysis of cyclone feed.

796 *Fluidization, Solids Handling, and Processing*

From Fig. 3 of the text, a velocity of 75 ft/sec and its corresponding N_s of 4.5 would satisfy (2), in which case, from Eq. (1):

$$L_w = 12 \sqrt{\frac{6328}{2.5 \times 75 \times 60}} = 9 \text{ inches}$$

therefore, inlet height = 22.5", and from Fig. 19, gas outlet tube I.D. = $9 \times 2 = 18$ "; assuming 1/4" wall thickness, gas outlet tube O.D. = 18.5". Therefore, barrel I.D. = $2(9) + 18.5 = 36.5$ " and from Fig. 19, $L_{min} = 54$ ". Minimum dipleg I.D., d , conservatively assuming 100% collection efficiency and 20% safety factor is calculable from the dimensionless gravity flow equation:

$$\frac{6328 \times 80 \times 4 \times 144}{60 \times 7000 d^2 3.14} = 1.2 \times 43 d^{1/2}$$

from which $d = 1.8$ " or a design minimum of $1.2 \times 1.8 = 2.2$ " which from Fig. 19 calls for a 4" industrial minimum, and thus in summary, a cyclone having the dimensions shown in Fig. 20.

The overall collection efficiency shown in Table 1 is determined from Fig. 2 of the text for the feed distribution given in Fig. 18. From Fig. 4 of the text at 80 grains/cu.ft., $E_L = 98.7\%$, therefore:

$$\text{Loss Rate} = \frac{6328 \times 60 \times 80 (1 - 0.987)}{7000} = 56.4 \text{ lbs/hr}$$

which meets specifications on performance (i.e., less than 60 lbs/hr loss rate).

The anticipated pressure drop is calculable from the relationships in Fig. 21. Assuming the cyclone is located within, or attached externally to, the shell of an 8' diameter fluidized bed reactor operating at a superficial gas velocity of 2 ft/sec, then:

$$\text{Area ratio} = \frac{(22.5 \times 9) 4}{144 (8)^2 3.14} = 0.028; \text{ hence } K = 0.5$$

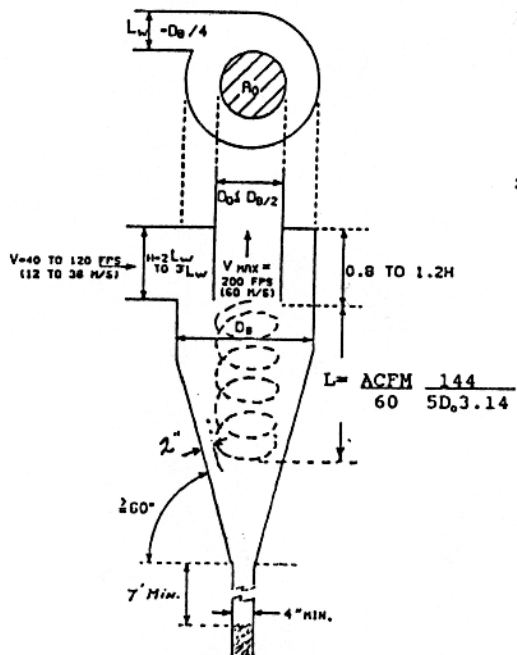


Figure 19. Bases for sizing cyclone in Example A.

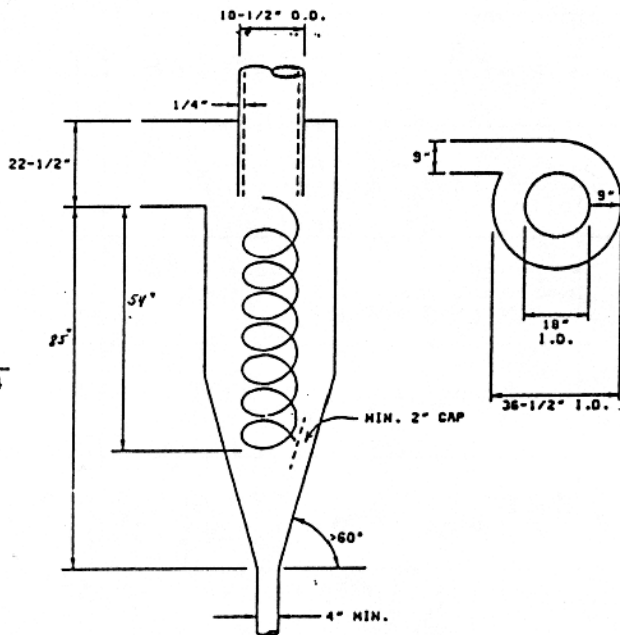


Figure 20. Cyclone design for Example A.

Table 1. Prediction of Cyclone Collection Efficiency

From Fig. 18		From Fig. 2		① X ④
① Weight Fraction	② D_{pmn} Microns	③ $D_p/9.7$	④ E_o	
0.02	12	1.237	57	1.14
0.03	16	1.649	67	2.01
0.05	20.5	2.113	74	3.70
0.10	28	2.887	81	8.10
0.10	38	3.918	86	8.60
0.10	47	4.845	89	8.90
0.10	56	5.773	92.1	9.21
0.10	67	6.907	95	9.50
0.10	79	8.144	97.3	9.73
0.10	95	9.794	99.7	9.97
0.10	116	>1.0	100	10.0
0.05	144	>1.0	100	5.0
0.03	170	>1.0	100	3.0
0.02	205	>1.0	100	2.0
1.00			$\Sigma = 90.86\% = E_o$	

Inlet contraction loss:

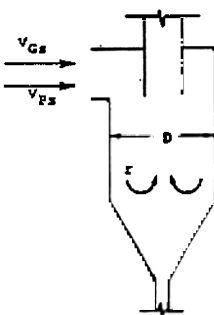
$$\begin{aligned}\Delta P_{(s-i)G} &= 0.00298(0.1)[1.5(75)^2-(2)^2] \\ &= 2.513'' \text{ H}_2\text{O}\end{aligned}$$

Solids acceleration loss:

$$\begin{aligned}\Delta P_{(s-i)G} &= 80(75)^2/7000(167) \\ &= 0.385'' \text{ H}_2\text{O}\end{aligned}$$

Barrel loss:

$$d_{hi} = 4(22.5 \times 9)/2(22.5 + 9) = 12.857''$$

Nomenclature

ΔP = Pressure Drop, In. H₂O
 L = Loading Lb Solids/Ft² of Gas
 V = Velocity, Ft/Sec.
 ρ_G = Gas Density, Lb/Ft³
 μ_G = Gas Viscosity, Lb/Ft Sec.
 D = Diameter

Subscripts

G = Gas
 P = Particle
 i = Inlet
 s = Superficial
 B = Barrel
 e = Exit
 r = Reversal

(Cyclone Exit + Cyclone Barrel)
 or (Cyclone Inlet + Vessel)

Area Ratios	-K
0	0.50
0.1	0.47
0.2	0.43
0.3	0.395
0.4	0.35

1. Inlet Contraction:

$$\Delta P_{(s-i)G} = 0.00298 \rho_G (V_{Gi}^2 - V_{Gs}^2 + K V_{Gi}^2); K = f \left(\frac{\text{Area at } i}{\text{Area at } s} \right)$$

2. Particle Acceleration:

$$\Delta P_{(s-i)p} = L V_{Gi} (V_{pi} - V_{ps}) / 167$$

For small particles having a low terminal velocity, V_{ps} is usually taken as V_{Gs} and V_{pi} taken as V_{Gi} .

3. Barrel Friction:

$$d_{hi} = 4 (\text{Inlet Area}) / (\text{Inlet Perimeter})$$

so that:

$$\Delta P_B = f D_B \rho_G N_s V_{Gi}^2 / 26.2 d_{hi}$$

where f is the friction factor obtained from a conventional Fanning friction chart giving f as a function of Reynolds number R_e

$$R_e = (d_{hi} V_{Gi} \rho_G) / (\mu_G \times 12)$$

D_B and d_{hi} are to be expressed in inches; f is generally of the order of 0.003 to 0.008.

4. Gas Flow Reversal:

$$\Delta P_r = \rho_G V_{Gi}^2 / 335$$

5. Exit Contraction:

$$\Delta P_e = 0.00298 \rho_G (V_{e}^2 - V_{s}^2 + K V_{e}^2)$$

where K is obtained from the table corresponding to the area ratio given as $(D_e/D_B)^2$.

$$\Delta P_{Calc.} = [1 + 2 + 3 + 4 + 5]$$

True ΔP is Obtained from Graph Below

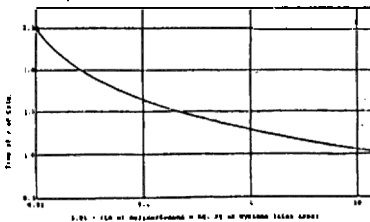


Figure 21. Pressure drop relationships.

800 *Fluidization, Solids Handling, and Processing*

$$Re = \frac{12.857 \times 75 \times 0.1}{12 \times 0.02 \times 0.000672} = 597,888$$

from any Fanning friction factor chart for smooth drawn tubing, $f \sim 0.0033$

$$\begin{aligned}\Delta P_B &= 0.0033(36.5)(0.1)(4.5)(75)^2/26.2(12.857) \\ &= 0.905" \text{ H}_2\text{O}\end{aligned}$$

Reversal loss:

$$\begin{aligned}\Delta P_r &= 0.1 (75)^2/335 \\ &= 1.679 " \text{ H}_2\text{O}\end{aligned}$$

Exit contraction loss:

$$\begin{aligned}V_e &= 6328(4)(144)/3.14(60)(18)^2 = 59.68 \text{ ft/sec} \\ V_B &= 6328(4)(144)/3.14(60)36.5^2 = 14.5 \text{ ft/sec} \\ \text{Area ratio} &= (18/36.5)^2 = 0.243; \text{ hence } K = 0.415 \\ \Delta P_e &= 0.00298(0.1)[1.415(59.68)^2 - (14.5)^2] \\ &= 1.439" \text{ H}_2\text{O}\end{aligned}$$

Total calculated ΔP across cyclone

$$= 2.513 + 0.385 + 0.905 + 1.679 + 1.439 = 6.921" \text{ H}_2\text{O}$$

if specific solids inlet loading were $>10 \text{ lbs/sec} \times \text{ft}^2$.

$$\text{Specific loading} = \frac{6328 \times 80 \times 144}{60 \times 7000 \times 22.5 \times 9} = 0.857 \text{ lbs/sec} \times \text{ft}^2$$

From Fig. 21 at an abscissa of $0.01 + 0.857 = 0.867$, the ordinate equals 1.32; therefore:

$$\text{True cyclone } \Delta P = 1.32 \times 6.921$$

$$= 9.136" \text{ H}_2\text{O, meeting specifications}$$

Example B. Suppose in the previous example that the loss rate had been specified as not to exceed 40 lbs/hr. To minimize the increase in pressure drop accompanying any increase in inlet velocity necessary to reduce D_{th} to a value which would bring performance up to the desired level, it might be more expedient to instead increase the gas discharge velocity.

To find E_L required to meet 40 lbs/hr loss rate set:

$$40 = (1 - E_L)6328(60)(80)/7000; \text{ from which } E_L = 99\%.$$

From text Fig. 4 at 80 grains/ft³, required $E_O = 94\%$. The correspondingly required D_{th} is estimated by ratio from Example A:

$$\frac{D_{th}}{9.7} \sim \frac{1 - 0.94}{1 - 0.9086}$$

from which $D_{th} = 6.3$ microns (estimated) and now checked against the correlation in Fig. 2 of the text for the feed distribution in Fig. 18 (see Table 2)

The 95.41% is slightly better than the required 94% so that the foregoing could be repeated with a new estimate of D_{th} slightly greater than 6.3 microns. However, since the difference between 94% and 95.41% is probably within the accuracy of any practical means of measurement, the value of 6.3 microns will be accepted as the design criterion, in which case, from Fig. 4, $E_L \sim 99.14\%$ leading to a predicted loss rate of:

$$(1 - 0.9914)6328(60)(80)/7000 = 37.3 \text{ lbs/hr}$$

which meets the specified 40 lbs/hr limit.

From the definition of D_{th} in Fig. 1 of the text:

$$\frac{6.3}{12(25,400)} = \frac{9(0.02)0.000672(9)}{3.14N_s V(85 - 0.1)12}$$

or

$$N_S V_e = 796.15$$

which from Fig. 3 suggests $V_e = 140$ ft/sec and $N_S = 5.7$, so that $D_O \sim 11.75''$ and from Fig. 19, $L = 82''$, which results in a unit dimensioned as shown in Fig. 22.

Table 2. Prediction of Collection Efficiency for Cyclone in Example B

From Fig. 18		From Fig. 2		① x ④
① Weight Fraction	② $D_{p\ mean}$ Microns	③ $D_p/6.3$	④ E_o	
0.02	12	1.90	71	1.42
0.03	16	2.54	78	2.34
0.05	20.5	3.25	83	4.15
0.10	28	4.44	88	8.8
0.10	38	6.03	93	9.3
0.10	47	7.46	96	9.6
0.10	56	8.88	98.2	9.8
0.10	67	>10	100	10
0.10	79	>10	100	10
0.10	95	>10	100	10
0.10	116	>10	100	10
0.05	144	>10	100	5
0.03	170	>10	100	3
0.02	205	>10	100	2
1.00			$\Sigma = E_o = 95.41\%$	

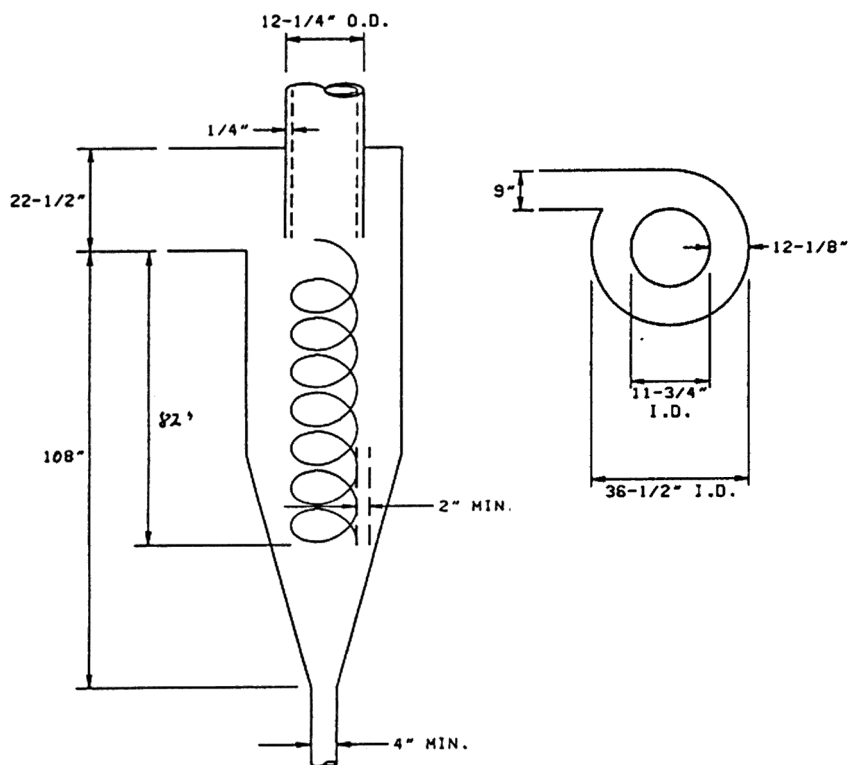


Figure 22. Cyclone design dimensions for Example B.

The cyclone in Fig. 22 will have a greater contraction loss than that in Fig. 20:

$$\text{Area ratio} = (11.75/36.5)^2 = 0.1036; \text{ hence } K \sim 0.47$$

$$\Delta P_e = 0.00298(0.1)[1.47(140)^2 - (14.5)^2]$$

$$= 8.52'' \text{ H}_2\text{O}$$

$$\Delta P (\text{calc'd}) = 2.513 + 0.385 + 0.905 + 1.679 + 8.52$$

$$= 14'' \text{ H}_2\text{O}$$

804 Fluidization, Solids Handling, and Processing

From Fig. 21, at a solids inlet rate of 0.857 lbs/sec·ft², the true $\Delta P/14 = 1.32$, so true $\Delta P = 18.48''$ H₂O which exceeds the specified maximum of 10'' H₂O.

14.0 ALTERNATE APPROACH TO SOLVING EXAMPLE B

If, as an alternative, the D_{th} of 6.3 were to be achieved by increasing the inlet velocity, then Eq. (2) of Example A becomes

$$N_s(V_i)^{1.5} = 6895$$

which from Fig. 3 suggests $V_i = 117.7$ ft/sec and $N_s = 5.4$,

then:
$$L_w = 12 \sqrt{\frac{\text{ACFM}}{150 V_i}} = 7^{3/16}''$$

therefore: inlet height = $2.5(7^{3/16}) = 18''$; $D_o = 14^{3/8}''$; $D_B = 29.25''$ and $L = 67''$ which results in a cyclone dimensioned as shown in Fig. 23.

Pressure drop through the cyclone in Fig. 23 is again calculated from the relationships in Fig. 21. As in Example A,

$$\text{Area ratio} = \frac{18 \times 7.1895 \times 4}{3.14(8)^2 144} = 0.0179; K = 0.5$$

Inlet contraction loss:

$$\begin{aligned}\Delta P_{(s-i)G} &= 0.00298(0.1)[1.5(117.4)^2 - (2)^2] \\ &= 6.160'' \text{ H}_2\text{O}\end{aligned}$$

Solids acceleration loss:

$$\begin{aligned}\Delta P_{(s-i)P} &= 80(117.4)^2/7000 \times 167 \\ &= 0.943'' \text{ H}_2\text{O}\end{aligned}$$

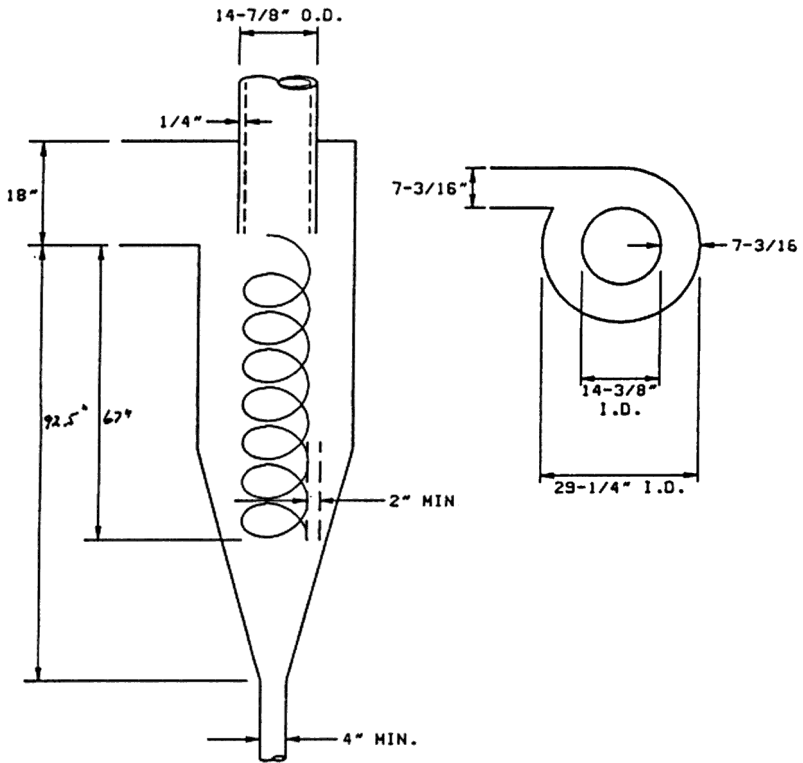


Figure 23. Alternative cyclone design for Example B.

Barrel loss:

$$d_{hi} = 4(18 \times 7.1875)/2(18 + 7.1875) = 10.27"$$

$$Re = \frac{10.27 \times 117.4 \times 0.1}{12 \times 0.02 \times 0.000672} = 747,796; f = 0.00314$$

$$\begin{aligned} \Delta P_B &= 0.00314(29.25)(0.1)(5.4)(117.4)^2/26.2(10.27) \\ &= 2.54" \text{ H}_2\text{O} \end{aligned}$$

806 *Fluidization, Solids Handling, and Processing*

Reversal loss:

$$\Delta P_r = 0.1(117.4)^2/335$$

$$= 4.114 \text{ " H}_2\text{O}$$

Exit contraction loss:

$$V_e = 6328(4)144/60(3.14)(14.375)^2 = 93.58 \text{ ft/sec}$$

$$V_B = 6328(4)144/60(3.14)(29.25)^2 = 22.60 \text{ ft/sec}$$

$$\text{Area ratio} = (14.375/29.25)^2 = 0.2415; K = 0.415$$

$$\Delta P_e = 0.00298(0.1)[1.415(93.58)^2 - (22.6)^2] = 3.54 \text{ " H}_2\text{O}$$

$$\Delta P \text{ (calc'd)} = 6.16 + 0.943 + 2.54 + 4.114 + 3.54$$

$$= 17.3 \text{ " H}_2\text{O}$$

$$\text{Inlet ldg.} = 6328(80)144/60(7000)18(7.1875)$$

$$= 1.342 \text{ lbs/sec}\cdot\text{ft}^2$$

Therefore from Fig. 21

$$\text{True } \Delta P = 1.26 \times 17.3 = 21.8 \text{ " H}_2\text{O}$$

This again exceeds the specified 10" H₂O maximum to a greater degree than the cyclone in Fig. 22, although it represents also a substantially smaller unit.

Since neither design in Figs. 22 or 23 will satisfy the specified pressure drop limitation, the only alternative lies in reducing inlet width without increasing inlet velocity, which requires multiple cyclones operating in parallel as illustrated in the design of Example C.

Example C. Suppose, in the previous Example B, performance must be achieved at a pressure loss less than 10" H₂O requiring therefore multiple cyclones in parallel.

At $D_{th} = 6.3$, Eq. (2) of Example A now reduces to

$$N_S (V_i)^{1.5} n^{0.5} = 6895$$

If $n =$ two cyclones in parallel, then $N_S (V_i)^{1.5} = 4876$ which, from Fig. 3 of the text, would be satisfied with $V_i = 97.3$ ft/sec and $N_S = 5.08$ so that

$$L_W = 12(6328/150(97.3)2)^{0.5} = 5-5/8" \text{ (to nearest } 1/16")$$

Therefore at $V_i = 97.3$ ft/sec and inlet height = $13-7/8"$

$$D_O = 11.25"; D_B = 23", \text{ and } L = 43"$$

which results in 2 cyclones each dimensioned as shown in Fig. 24.

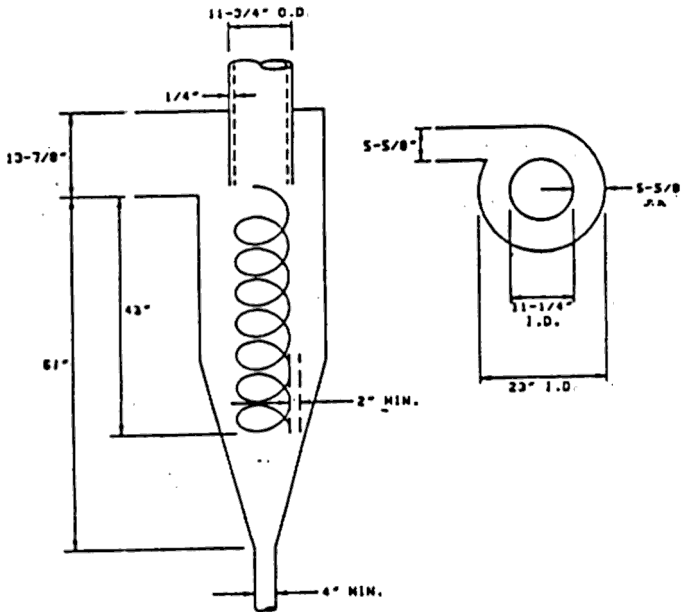


Figure 24. Cyclone design for Example C (one of two parallel units).

808 Fluidization, Solids Handling, and Processing

The pressure drop through 2 parallel units of Fig. 24 at $V_i = 97.3$ ft/sec, $N_s = 5.08$, $V_e = 76.4$ ft/sec, $V_B = 18.28$ ft/sec, with inlet area ratio of 0.0108 so that $K = 0.5$, from Fig. 21:

Inlet contraction loss:

$$\Delta P_{(s-i)G} = 0.00298(0.1)[1.5(97.3)^2 - (2)^2] = 4.23" \text{ H}_2\text{O}$$

Solids acceleration loss:

$$\Delta P_{(s-i)P} = 80(97.3)^2/7000(167) = 0.648" \text{ H}_2\text{O}$$

Barrel loss:

$$d_{hi} = 4(5.625)(13.875)/2(5.625+13.875) = 8"$$

$$Re = 8(97.3)0.1/12(0.02)0.000672 = 482,639; f = 0.00347$$

$$\Delta P_B = 0.00347(23)0.1(5.08)(97.3)^2/8(26.2) = 1.831" \text{ H}_2\text{O}$$

Reversal loss:

$$\Delta P_r = 0.1(97.3)^2/335 = 2.826" \text{ H}_2\text{O}$$

Exit contraction loss:

$$\text{Area ratio} = (11.25/23)^2 = 0.239; K = 0.415$$

$$\Delta P_e = 0.00298(0.1)[1.415(76.4)^2 - (18.28)^2] = 2.362" \text{ H}_2\text{O}$$

$$\Delta P(\text{calc'd}) + 4.23 + 0.648 + 1.831 + 2.826 + 2.362$$

$$= 11.897" \text{ H}_2\text{O}$$

$$\text{Inlet Idg.} = 6328(80)144/2(60)7000(5.625)13.875$$

$$= 1.11 \text{ lbs/sec-ft}^2$$

From graph in Fig. 21:

$$\text{True } \Delta P = 1.29 \times 11.875 = 15.35'' \text{ H}_2\text{O}$$

This still exceeds the design specification of 10'' H₂O and could have been anticipated, since to meet this pressure drop criterion, V_i from Example A must not exceed about 75 ft/sec which would require 6 cyclones in parallel as opposed to the 2 in this Example C.

15.0 ALTERNATE APPROACH TO SOLVING EXAMPLE C

Assume the designer does not desire to use 6 cyclones in parallel, but must still meet all the specifications in Example B (i.e., cannot accept 15.35'' H₂O pressure drop) but is willing to accept 4 cyclones in parallel. Could 4 cyclones suffice (by a reduction in inlet velocity compensated in performance by an increase in exit gas velocity)?

Since true ΔP must be $\leq 10''$ H₂O, then $\Delta P(\text{calc'd})$ must equal or be $< \sim 10/1.3 = 7.7''$ H₂O. In Example C, $\Delta P(\text{calc'd})$ exclusive of exit loss equaled 9.535'' H₂O so that now the following 3 equations would need to be satisfied with $n = 4$:

$$\text{Eq. (3)} \quad 9.535(V_i/97.3)^2 + (V_e/76.4)^2 = < 7.7$$

$$\text{Eq. (4)} \quad L_w = 12[6328/60(2.5)V_i n]^{0.5}$$

$$\begin{aligned} \text{Eq. (5)} \quad & 6.3/12(25400) \\ & = [9(0.02)0.000672L_w/3.14(12)N_s V_e(85-0.01)12]^{0.5} \end{aligned}$$

Equations (3), (4) and (5) reduce to:

$$\text{Eq. (6)} \quad V_i^2 + 0.4018V_e^2 = 7645.3$$

$$\text{Eq. (7)} \quad L_w = 38.97/(V_i)^{0.5}$$

$$\text{Eq. (8)} \quad N_s V_e (V_i)^{0.5} = 3447.3$$

810 Fluidization, Solids Handling, and Processing

Since N_s is a function of V_e , solving Eq. (8) for V_i and substituting in Eq. (6) leads to

$$V_i = (3447.3/N_s V_e)^2$$

which is satisfied with $V_e = 87$ ft/sec at $N_s = 4.81$ so that

$$V_i = 67.86 \text{ ft/sec}$$

$$L_w = 4.75''$$

$$D_o = 7.5''$$

$$D_b = 19.5''$$

$$L = 32''$$

$$\text{inlet height} = 11.75''$$

as summarized in Fig. 25.

Check on performance:

$$\begin{aligned} D_{th} &= 12(25400)[9(0.02)0.000672(4.75)/12(3.14)87(85-0.1)4.81]^{0.5} \\ &= 6.3 \text{ microns (will meet specification)} \end{aligned}$$

Check on pressure drop:

Inlet contraction loss:

$$\Delta P_{(s-i)G} = 0.00298(0.1)[1.5(67.86)^2 - (2)^2] = 2.057'' \text{ H}_2\text{O}$$

Solids acceleration loss:

$$\Delta P_{(s-i)P} = 80(67.86)^2/7000(167) = 0.315'' \text{ H}_2\text{O}$$

Barrel loss:

$$d_{hi} = 4(4.75 \times 11.75)/2(4.75 + 11.75) = 6.77"$$

$$Re = 6.77(67.86)0.1/12(0.02)0.000672 = 284,854; f = 0.0039$$

$$\Delta P_B = 0.0039(19.5)0.1(67.86)^2 4.81/26.2(6.77) = 0.95" \text{ H}_2\text{O}$$

Reversal loss:

$$\Delta P_r = 0.1(67.86)^2/335 = 1.375" \text{ H}_2\text{O}$$

Exit contraction loss:

$$\text{Area ratio} = (7.5/19.5)^2 = 0.148; K = 1.45$$

$$V_B = 6328(4)144/4(3.14)60(19.5)^2 = 12.7 \text{ ft/sec}$$

$$P_e = 0.00298(0.1)[1.45(87)^2 - (12.7)^2] = 3.223" \text{ H}_2\text{O}$$

$$\Delta P(\text{calc'd}) = 2.057 + 0.315 + 0.95 + 1.375 + 3.223$$

$$= 7.92" \text{ H}_2\text{O}$$

$$\text{Inlet ldg.} = 6328(80)144/4(60)7000(4.75)11.75$$

$$= 0.778 \text{ lbs/sec}\cdot\text{ft}^2$$

From the graph in Fig. 21:

$$\text{True } \Delta P = 1.33(7.92) = 10.53" \text{ H}_2\text{O}$$

This barely exceeds the specified 10" H₂O and can be brought to specification by a moderate increase in inlet height to 12" which reduces V_i to 66.6 ft/sec and results in the overall dimensions shown in Fig. 25.

The foregoing examples illustrate the relationships among the variables as they affect performance (collection efficiency) and pressure drop.

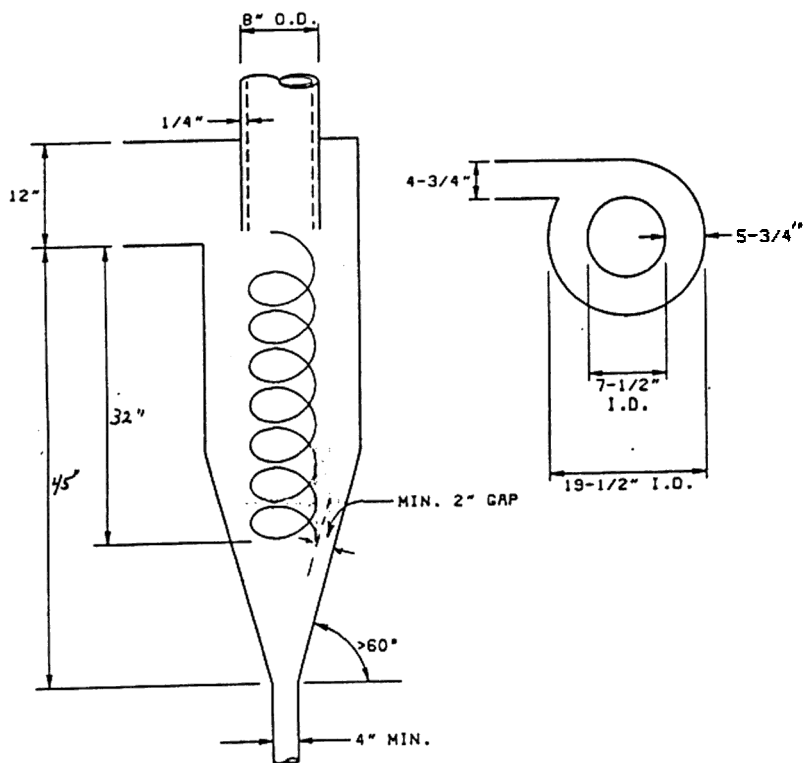


Figure 25. Alternative cyclone design for Example C (one of four parallel units).

16.0 DIPLEG SIZING AND CYCLONE PRESSURE BALANCE

Dipleg Diameter. In the foregoing examples, the minimum 4" I.D. (see Fig. 19) was sufficiently large to pass the collected solids. The basic relationship for sizing diplegs takes the dimensionless form:

$$\frac{4W144}{3.14d^2} = \frac{(gd/12)^{0.5}}{(\tan \alpha)^{0.5}} r_B \sqrt{\frac{r_B - r_G}{r_B}}$$

where: W = lbs of solids collected per second

d = dipleg I.D. inches (minimum)

α = collected solids' angle of internal friction, degrees

ρ_B = collected solids' bulk density, lbs/cu.ft.

ρ_G = density of gas entering cyclone, lbs/cu.ft.

g = gravitational field, ft/sec²

If the fluid stream is a gas, the last term in the above equation is essentially unity. Unless the cyclone itself is rotating or, for example, located on another planet, g can be taken as 32.2. If the bulk solids' angle of internal friction is unknown, then taking an average value of 62 degrees, the equation reduces to:

$$d = (152.8 W / \rho_B)^{0.4}$$

W is generally based conservatively on the assumption of 100% collection efficiency.

Pressure Balance. The extent to which the dipleg of a cyclone is filled with exiting solids depends on the pressure balance around the cyclone and its dipleg. Figure 26 shows a cyclone with pressure P_B (psi) inside its barrel and with its dipleg immersed H_{bed} feet into a fluidized bed of density ρ_{bed} (lbs/ft³). A simple pressure balance treating the dipleg as one leg of a manometer gives the feet of solids in the dipleg (H_{DL}) from:

$$P_B + (H_{DL} \rho_{DL})/144 = P_V = (\rho_{Bed} H_{Bed})/144$$

where ρ_{DL} is the lbs/ft³ bulk density of solids in the dipleg and P_V is the pressure in the vessel in the dilute phase above the bed, psi. ($P_V - P_B$) is determined from the cyclone pressure drop correlations in Fig. 21.

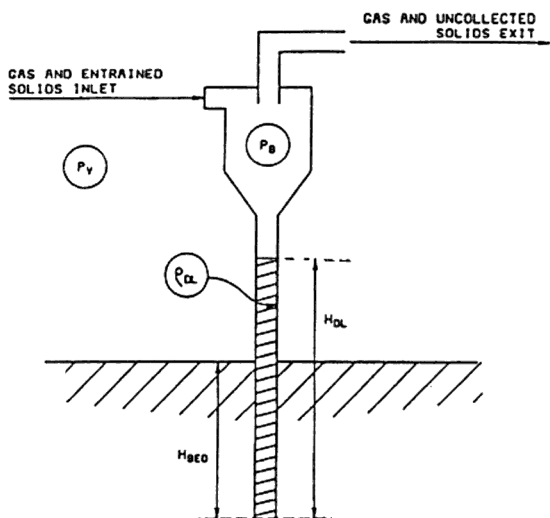


Figure 26. Cyclone pressure balance (no restrictive “valve” on dipleg end).

NOTATIONS

- A_i Gas inlet duct area
- A_o Gas outlet tube area
- D Barrel I.D.
- D_o Gas outlet tube I.D.
- D_p Particle diameter
- D_{th} Smallest particle able to cross width L_w
- E_L Collection efficiency at actual inlet loading
- E_o Collection efficiency at <1 gr/ft³ inlet loading
- H Cyclone height as defined in Fig. 6
- L Natural Vortex Length

L_w	Inlet width
N_s	Number of spiral barrel traverses by particle stream
Q	Volumetric gas flow/unit time
V_i	Gas inlet velocity
V_L	Average net gas "peel off" velocity into exiting vortex
V_o	Gas outlet velocity
V_t	Particle terminal velocity in acceleration field
r_p	Apparent particle density
r_G	Gas density
m_G	Gas viscosity

REFERENCES

- AIMS, Analogies In Matters of Science, P.O. Box 241, Garrison, N.Y. 10524, (1989) to date
- Alexander, R. McK., "Fundamentals of Gas Cyclone Design and Operation," *Proc. Australian Inst. of Min. and Met.*, New Series No's. 152–153, 203 (1949)
- Baskakov, A. P., Dolgov, V. N., and Goldobin, Y. M., *Ural Polytech. Inst.*, Sverdlovsk, USSR (1980)
- Bryant, H. S., Silverman, R. W., and Zenz, F. A., "How Dust in Gas Affects Cyclone Pressure Drop," *Hydrocarbon Processing*, pp. 87–90 (1983)
- Dry, R. J., White, R. B., and Joyce, T., "Correlation of Solids Circulation Rate in Circulating Fluidized Bed Systems," *4th Internat'l. CFB Conf.*, Preprint Vol., pp. 732–737 (1993)
- Gartside, R., and Woebecke, H. N., U.S. Patent No. 4,556,541 (1985)
- Hoffmann, A. C., Van Santen, A., Allen, R. W. K., and Cliff, R., "Effects of Geometry and Solid Loading on the Performance of Gas Cyclones," *Powder Tech.*, 70:83–91 (1992)
- Hyppanen, T., Palonen, J., and Rainio, A., "Pyroflow Compact - Ahlstrom Pyropower's 2nd Generation CFB," *4th Internat'l. CFB Conference*, Preprint Vol., pp. 131–136, (1993); European Patent Applic's. No's. 0 481 438 A2 and 0 481 438 A3, filed (1991)
- Kane, R. S., Weinbaum, S., and Pfeffer, R., *Pneumotransport 2*, (1973)
- Kang, S. K., Kwon, T. W., and Kim, S. D., *Powder Tech.*, 58:211–220 (1989)

816 *Fluidization, Solids Handling, and Processing*

- Knowlton, T. M., and Bachovkin, D. M., *70th Annual A.I.Ch.E. Mtg.*, (1977)
- MacLean, J. P., Cantwell, E., Brown, J. D., and Hoy, H. D., U.S. Patent No. 4,316,729 "Highly Efficient Cyclone Separator" (1982); U.S. Patent No. 4,380,105 "Method for Shaping Forming and Assembling a Highly Efficient Cyclone Separator" (1983); U.S. Patent No. 4,337,068 "Methods for Removing Entrained Solids from Gases" (1982)
- Rosin, P., Rammler, E., and Intelmann, W., "Principles and Limits of Cyclone Dust Removal," *Zeit. Ver. Deutscher Ing.*, 76:433ff (1932)
- Silverman, L., Harvard-AEC Contract AT-30-1, Gen 238, N.Y.O. 1527 (1950)
- Stairmand, C. J., "The Design and Performance of Cyclone Separators," *Trans. Instn. of Chem. Engrs.*, 29:356ff, London (1951)
- TerLinden, A. J., *Proc. Instn. Mech. Engrs.*, 160:233-249, London (1949)
- Yuu, S., Jotaki, T., Tomita, Y., and Yoshida, K., *Chem. Eng. Sci.*, 33:1573-1580 (1978)
- Zenz, F. A., "Find Attrition in Fluid Beds," *Hydrocarbon Processing*, 50:103-105 (1971)
- Zenz, F. A., "Size Cyclone Diplegs Better," *Hydrocarbon Processing*, pp.125-128 (1975)
- Zenz, F. A., "Cyclone Separators," *Manual on Disposal of Refinery Wastes Volume on Atmospheric Emissions*, Ch. 11, Pub. No. 931, American Petroleum Institute, Washington, D.C. (1975)
- Zenz, F. A., *Fluidization and Fluid-Particle Systems*, Vol. II, PEMM-Corp Pub., 1:1-42; 7:253-393; 7:263-264, Chelsea Industrial Park, Wappingers Falls, N.Y. (1989)
- Zenz, F. A., and Kelleher, E. G., "Studies of Attrition Rates in Fluid-Particle Systems Via Free Fall, Grid Jets and Cyclone Impact," *J. Powder and Bulk Solids Tech.*, 4(2/3):12-20 (1980)
- Zenz, F. A., and Othmer, D. F., *Fluidization and Fluid-Particle Systems*, PEMM-Corp Pub., Cold Spring, N.Y. (1960)
- Zenz, F. A., and Smith, R., "When are Fines in Equilibrium," *Hydrocarbon Processing*, 51:104-106 (1972)
- Zenz, J. A., PEMM-Corp, Cold Spring, N.Y., Personal Communications (1988, 1996)

Electrostatics and Dust Explosions in Powder Handling

Thomas B. Jones

1.0 INTRODUCTION

When dissimilar solid materials come into physical contact, complex ionic or electronic interactions almost invariably result in a separation of electric charges. If the materials are then separated, their surfaces retain net electric charge of opposite sign. This charging mechanism, known as *contact electrification* or *triboelectrification*, is almost inevitable during the handling, transport, and processing of granular solids or powders and it is the origin of pronounced and sometimes troublesome or even dangerous electrostatic phenomena. In fluidized and spouted beds, electrostatic effects include particle/wall adhesion, interparticle cohesion, and electrostatic discharges (ESD). Electrostatic adhesion is a significant nuisance; highly charged particles can coat vessel walls making cleanup more difficult in switch loading operations. Charged particles can also interfere with sensor units and other vessel internals. Electrostatic cohesion, the mutual attraction of oppositely charged particles, can seriously affect fluidization conditions, exacerbate bridging phenomena at discharge chutes, and generally make powder handling a more difficult

proposition. Electrostatic discharges can lead to still more serious problems, such as electrical interference which disrupts process instrumentation, physiological shocks to operating personnel, and, under certain conditions, the ignition of flammable dust/air mixtures. The resulting fires or explosions can cause serious damage and injury or loss of life in commercial and manufacturing facilities. A prudent way to think about electrostatic nuisances and hazards in fluidized and spouted beds is to recognize that, quite often, such units form just a small part of a large, complex solids handling system, consisting of hoppers, storage silos, transport containers, scroll feeders, receiver filters, etc., all connected together by pneumatic and vacuum transport lines. Each of these different components is known to contribute to the risk of an electrostatic ignition.

Because particle charging causes significant nuisances that hamper industrial production in fluidized and spouted bed systems and creates genuine hazards that threaten property and human life, it is important for operating personnel and production engineers to become familiar with electrostatic phenomena. In this chapter, we focus on the electrostatic phenomena associated with powder processing and handling and describe certain measures that reduce their adverse effects on productivity and abate fire and explosion hazards. Section 2 is devoted to a review of important aspects of particle charging, including triboelectrification and charge relaxation. In Sec. 3, early investigations of electrostatic effects in fluidized beds are summarized; both phenomenology and quantitative data on particle charging are covered. The rather limited data on charging in fluidized beds are compared to the generally accepted values employed by safety personnel to assess electrostatic hazards in powder handling. Electrostatic ignition hazard fundamentals in powders are the subject of Sec. 4, which summarizes the requirements for ignition and the types of electrostatic discharges. Section 5 focuses on ESD hazards associated with fluidized systems and peripherals, and provides some practical guidelines for their minimization.

2.0 CHARGING OF SOLID PARTICLES

Granular solids and powders charge more readily than any other commercially or industrially important form of material. It is fair to say that, when such materials are handled or processed, particle charging is virtually inevitable. In this section, the important qualitative and quantita-

tive aspects of particle charging relevant to fluidization are examined. The unavoidable tendency in any general treatment of particulate charging is to emphasize polymers, the materials best known for their strong electrostatic activity. There is, however, a clear danger in assuming that only polymers exhibit strong electrostatic behavior. Extremely troublesome particle cohesion and adhesion problems, as well as catastrophic fires and explosions, have occurred with materials to which one might not attribute significant electrostatic activity. For example, powdered aluminum and ordinary granular sugar are just two types of non-plastic materials where serious dust explosions involving loss of life have been experienced and where electrostatic sparks have been implicated as the source of ignition.

2.1 Triboelectrification

Phenomenology. Triboelectrification, also referred to as contact electrification, has been known since the time of the ancient Greeks. Despite the fact that its physics are reasonably well-understood at the fundamental level (Gallo and Lama, 1976; Lowell and Rose-Innes, 1980), triboelectrification remains difficult to predict or to control in the imprecisely defined environments of industry and commerce. The basic phenomenon is depicted in Fig. 1. As a particle of material A approaches the surface of material B, the material with the smaller work function—assumed to be A in the figure—gives up some of its conduction electrons to equalize the Fermi energy levels at the A-B interface. Once this transfer has occurred, an electrostatic equilibrium is achieved. If the materials are now separated (and if at least one of the materials is a good electrical insulator), a portion of the charge separation is locally preserved and thus the two materials now possess net, opposite charge. Materials, powders included, become charged to high levels only if the electrical resistivity is high enough so that the charge is not immediately conducted away. This important point is discussed further in Sec. 2.2.

Triboelectric Series. Prediction of triboelectric behavior in granular solids is hampered by difficult-to-control factors such as particle shape, prior mechanical contacts, material purity, and particle moisture content (which is usually related to airborne humidity). In the absence of any reliable predictive model for powder electrification, the practical requirements of industry necessitate an empirical approach (Taylor and Secker,

1994). A tribo-series provides a simple but effective way to keep track of the sign of charging for two materials that come into contact. Table 1 contains a sample series. According to this series, nylon particles impinging on an aluminum vessel wall will pick up and retain positive (+) charge, while the vessel wall will be left with negative (−) charge, just as depicted in Fig. 1. In principle, one might assume that the further apart two materials are on a tribo-series, the higher will be the charging when they come into contact. Yet, in practice, the many uncontrolled factors involved in the contact electrification process make it difficult or impossible to make any reliable quantitative predictions of solid material charging. Furthermore, comparisons of tribo-series obtained by different investigators reveal at least a few discrepancies in the relative ordering of chargeable materials (Lapple, 1970; Bauser, 1974). These discrepancies may have to do with subtle features such as material purity, moisture content, or surface finish.

In powder and granular solids charging, the predictive value of the tribo-series is still further compromised by the strong influence of particle size. For example, when certain polymer powders are pneumatically transported and dumped into a silo, their fines, remaining in suspension the longest, are often found to possess an electric charge *opposite* that of the larger particles. At present, there is no satisfactory means to predict when such bipolar charging is likely to occur.

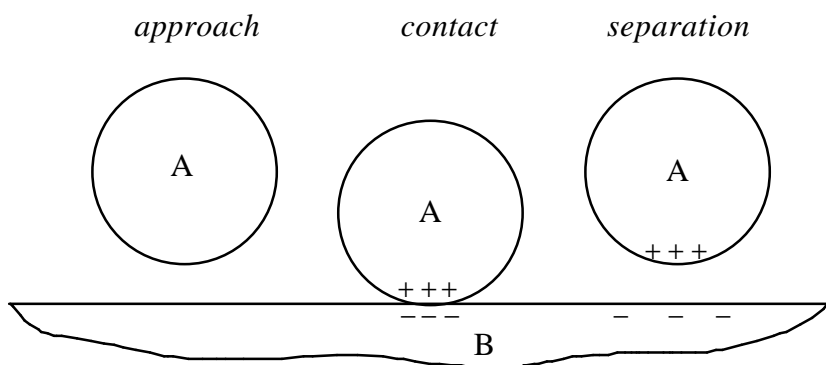


Figure 1. Approach, contact, and separation of two dissimilar solid materials leads to triboelectric charge separation. Here, the particle of material A is assumed to have lower work function and much higher electrical resistivity than the material B.

Table 1. A Sample Triboelectric Series

+ positive end of series →	asbestos
	glass
	nylon
	lead
	silk
	aluminum
	steel
	hard rubber
	nickel & copper
	brass & silver
	synthetic rubber
	saran
	polyethylene
	Teflon
– negative end of series →	silicone rubber

Limits on Particle Charging. The electrical charge carried by a particle resides on the surface. Thus, a fundamental upper limit for particle electrification may be computed by imposing the constraint that the electric field at the surface can not exceed the dielectric strength of dry air, $E_b \approx 30$ kV/cm. According to this hypothesis, the upper limit upon surface charge density becomes

$$\text{Eq. (1)} \quad s_{\max} = e_0 E_b \gg 2.7 \cdot 10^{-5} \text{ C/m}^2$$

where $e_0 = 8.854 \cdot 10^{-12}$ F/m is the permittivity of free space. Harper examined triboelectric charging in certain powders and measured local surface charge densities one full order of magnitude higher than s_{\max} (Harper, 1961). He suggested that such anomalies might be explainable by the very small volume of air that is actually subjected to the high electric field strength. The maximum charge defined in Eq. (1) can be used to define an upper limit on the specific charge q/m (measured in C/kg) of a spherical particle having diameter D (in meters).

Eq. (2) $(q/m)_{max} = 6s_{max}/D r_m$

In Eq. (2), r_m is the mass density of the particle (in kg/m³). The values of specific charge predicted by Eq. (2) are very high, and seldom if ever observed in powders or granular materials. This is because the bulking of powders intensifies the electric field sufficiently so that electrical break-down, most likely taking the form of corona, limits the charge. One source suggests that $s_{max} = 10^{-5}$ C/m² provides a better correlation to powder charging data (Blythe and Reddish, 1979). Table 2 in the next section provides more realistic specific charge estimates for powders.

Charging of Powder. Industrial engineers and safety professionals often resort to an empirical approach to quantify powder charging in processing operations. Refer to Table 2, which tabulates typical specific charge values for moderately resistive powders ($\gamma \approx 10^{12}$ S⁻¹m) observed during some common batch and continuous operations. The large ranges given for the specific charge—as much as three orders of magnitude in some cases—reflect the uncontrollability of certain critical parameters such as particle moisture content and size distribution, as well as the great variability in available industrial process equipment. Empirical data of this sort does provide valuable guidance in estimating charging levels; however, such data can never really supplant the measurements needed each time a new material is introduced or new equipment is installed in an operating line. In particular, the tribocharge level in a powder is strongly influenced by its resistivity. See Sec. 2.2 below.

Table 2. Typical specific charge values (q/m) for moderately insulating powders ($\gamma \approx 10^{12}$ S⁻¹m) in some industrial operations (from Cross, 1987).

Sieving	10^{-5} to 10^{-3} μ C/kg
Pouring	10^{-3} to 10^{-1} μ C/kg
Grinding	10^{-1} to 10^0 μ C/kg
Micronizing	10^{-1} to 10^2 μ C/kg
Pneumatic transport	10^0 to 10^2 μ C/kg

Conspicuous by its absence from Table 2 is charging data for fluidized beds. There are several reasons for this omission. First, fluidization

is less developed as a technology than most other manufacturing processes using powders and granular solids. There simply exists less experience with fluid beds than with, say, pneumatic solids transport systems. Second, triboelectric charging in fluidized beds is complicated by the fact that the principal contacting is between particles within the bed. As a result, the phenomenology of charging in a fluid bed is harder to characterize and to quantify. Particle charging in fluid beds is the subject of Sec. 3.3.

Pneumatic Transport. In modern, large-scale manufacturing facilities where high volumes of granular materials must be handled, pneumatic transport is used very extensively to move product between storage silos, processing vessels, shipping containers and other components. As indicated by Table 2, pneumatic transport creates the highest triboelectric charging levels for dry particulate. It is for this reason that bulking and delivery operations often entail the greatest risk of an electrostatic discharge and dust ignition. Despite the importance of pneumatic conveyance in powder handling and despite its well-known electrostatic charging tendencies, practical investigations of powder charging in such systems has been quite limited. One of the few systematic experimental studies of the phenomenon was conducted using a small-scale rig with a one-meter long test section (Boschung and Glor, 1980). The influence of virtually all the important parameters—flow rate, humidity, powder type, average particle diameter, transport pipe material, and length—were considered. Despite the inevitable scatter in the experimental data, the results confirmed that particle size and material are more important than the wall material and system geometry in determining q/m for powders.

The usual prescription for controlling triboelectrification in pneumatic transport is to limit the flow rate, but this solution conflicts with the tendency to increase plant production levels. One alternate proposal for the control of tribocharging is to exploit the so-called “dense-phase” transport mode (G. Butters, 1985); however, there seems to be some dispute about the efficacy of this scheme (Konrad, 1986).

2.2 Charge Relaxation

All particles, irrespective of resistivity, become charged by triboelectrification, but only highly insulating powders retain high levels of charge. If a powder is not highly insulating and if a conductive path to ground exists, then electrical conduction will dissipate charge too rapidly for the accumulation to occur. For many powders, electric charge decays

naturally according to an exponential relaxation law: $\exp(-t/t)$, where t = time (in seconds), $t = k\epsilon_0 g$ is the relaxation time, k = dielectric constant (dimensionless), and g = resistivity (in $S^{-1}m$). The exponential law is most appropriate when $g \lesssim 10^{13} S^{-1}m$. The electrostatic hazards of powders are sometimes characterized by referring to their measured packed powder resistivity. According to this classification, shown in Table 3, there is little charging when $g \lesssim 10^7 S^{-1}m$ and very strong charging when $g \gtrsim 10^{13} S^{-1}m$. This scheme identifies ranges for safe versus hazardous powders, but leaves a large intermediate range of resistivities where uncertainty reigns. For powders in this range, the circumstances of how the powder is handled determine whether or not an ESD hazard exists.

Table 3. Triboelectrically caused ESD particle charging hazard classification scheme based on powder resistivity γ (Glor, 1988).

Resistivity $g(S^{-1}m)$	Relaxation Time $t(s)$	Specific Charge $q/m(\mu C/kg)$	Level of ESD hazard
$\leq \sim 10^7$	$< 10^{-4}$	10^{-3}	low
$\sim 10^7 \text{ to } 10^{13}$	$10^{-3} \text{ to } 10^2$	$10^{-3} \text{ to } 10^{-1}$	moderate (depends on circumstances)
$\geq \sim 10^{13}$	$> 10^2$	$> 10^{-1}$	high

2.3 Induction Charging of Particles

There is a danger in misinterpreting Table 3 to mean that particulate with high conductivity can never become electrically charged. Consider a conducting particle making contact with either a conducting wall or another particle as shown in Fig. 2. The particle intercepts lines of electric flux and become charged by induction if the contact occurs in the presence of an electric field. The magnitude of this charge may be estimated by considering the problem of a conducting spherical particle of diameter D immersed in a dielectric fluid of dielectric constant k and in contact with a plane conducting wall and a uniform electric field of magnitude E normal to the wall. The result is the so-called *Maxwell charge* (Maxwell, 1891).

$$\text{Eq. (3)} \quad q_{\text{Maxwell}} = p^3 k e_o D^2 E / 6$$

This induction mechanism plays the central role of particle charging in electrosuspensions, that is, beds of highly conductive particles subjected to an externally applied DC electric field (Colver, 1977). Induction also will occur if isolated conductive objects (such as tramp metal debris or hand tools) in a bed of triboelectrically charged, insulating, granular solids make momentary wall contact. The breakdown-imposed limit on particle charge, that is, Eq. (2), is as applicable for induction charging as it is for triboelectrification. It should also be recognized that an externally imposed electric field can influence particle charging via electrolysis and other mechanisms, even when the particle conductivity is too low to support conventional conduction (Loeb, 1963).

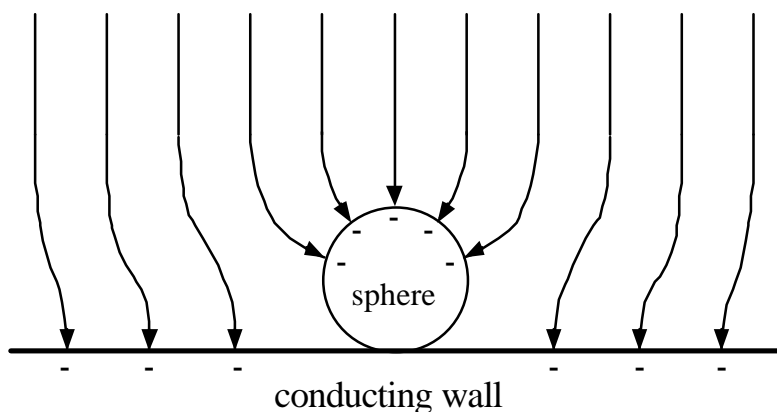


Figure 2. Charging of a conducting particle with diameter D making contact with a conducting wall in the presence of an electric field E .

2.4 Electrostatic Fields and Potentials

Some Basics. The field theory of electrostatics expresses experimentally observable action-at-a-distance phenomena between electrical charges in terms of the vector electric field $\vec{E}(\vec{r}, t)$, which is a function of position \vec{r} and time t . Accordingly, the electric field is often interpreted as force per unit charge. Thus, the force exerted on a test charge q_t by this electric field is $q_t \vec{E}$. The electric field due to a point charge q in a dielectric medium placed at the origin $\vec{r} = 0$ of a spherical coordinate system is

$$\text{Eq. (4)} \quad \bar{E} = \frac{q}{4\pi k \epsilon_0 r^2} \hat{r}$$

where $r = |\bar{r}|$ and \hat{r} is the unit radial vector. Equation (4) is clearly consistent with Coulomb's inverse square law. The electrostatic potential function $\Phi(\bar{r}, t)$, a scalar, is related to the electric field: $\bar{E} = -\nabla\Phi$. For the point charge

$$\text{Eq. (5)} \quad \Phi = \frac{q}{4\pi k \epsilon_0 r}$$

To determine the electrostatic field and potential in a vessel containing charged solids, we must sum the contributions from all the electric charges within the vessel. This is done by invoking the reasonable approximation that the charge may be represented as a continuous distribution and then by performing an appropriate integration over the volume of the charge. Gauss's law expressed in integral form is

$$\text{Eq. (6)} \quad \oint_S \mathbf{k} \epsilon_0 \bar{E} \cdot d\bar{S} = \int_V \mathbf{r} dV$$

where S is the closed surface of integration enclosing the volume V , \mathbf{k} is the dielectric constant of the charged medium, and $\mathbf{r}(\bar{r})$ is a continuous distribution of electric charge per unit volume.

The convenience of Eq. (6) is realizable only in the rather unrealistic situation where the charge distribution exhibits cylindrical or spherical symmetry. For storage silos, blenders, fluidized bed reactors, and other real vessel geometries, integral solutions are usually not possible, necessitating an alternate problem formulation. Poisson's equation serves this need, relating the volume charge distribution to the electrostatic potential.

$$\text{Eq. (7)} \quad \nabla^2 \Phi = -\mathbf{r} / k \epsilon_0$$

To compute electrostatic potential and field distributions in very complex geometries, this equation, or one of its subsidiaries, can be solved numerically subject to a set of boundary conditions (McAllister et al.,

1985). For a grounded metal silo partially filled with charged solids, the solution for the potential is usually displayed as an equipotential plot. One may interpret these plots by an analogy to a geographical contour map; the equipotentials are analogous to lines of constant elevation. Closed equipotential surfaces enclose positive or negative electric charge, just as closed elevation contours enclose a peak or a low point of land. The vector electric field may be envisioned as a set of flux lines, orthogonal to the equipotentials and flowing from higher to lower potential regions (that is, from positive to negative charge). The electric field intensity is greatest where the equipotentials are close together, just as closely spaced elevation contours on a map indicate a steep slope or cliff. Figure 3 shows equipotential lines for the vertical cross-section of a partially filled silo containing a conic heap of uniformly charged powder. Note that the maximum potential occurs on the axis slightly below the powder surface. The strongest electric field occurs in the void space just about the heap near the wall. Electrical discharges along the surface are routinely observed as charged granular material is dumped into large vessels (Maurer, 1979; Britton, 1988), confirming the prediction that the fields are strongest there. This prediction of the electric field distribution—strongest at the wall near the bed surface—can be expected to apply to a fluidized bed.

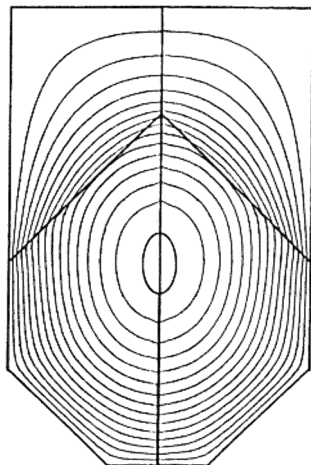


Figure 3. Vertical cross-section showing equipotential contours inside a conductive cylindrical silo containing a symmetric conical heap of uniformly charged solids. The electrostatic potential maximum exists on the center line somewhat below the powder surface, while the maximum electric field intensity occurs near the wall just above the powder.

An Example. Rough estimates for the electric field strength and maximum space potential in a fluidized bed can be obtained from a very simple model, namely, a very long cylinder entirely filled with uniformly charged powder. This model ignores the bed surface, placing the resulting estimate for the potential on the high side, but well within the accuracy requirements of an order-of-magnitude calculation. Assume the grounded cylinder is of diameter D_c and contains a charged powder having dielectric constant k and uniform volume charge density r_0 . Using Eq. (6) and cylindrical symmetry, the vector electric field and scalar electrostatic potential are:

$$\text{Eq. (8)} \quad \bar{E} = \frac{r_0 r_c}{2k\epsilon_0} \hat{r}_c \quad \text{and} \quad \Phi = \frac{r_0 (D_c^2/4 - r_c^2)}{k\epsilon_0}$$

Here, r_c is the radial distance from the axis and \hat{r}_c is the radial unit vector in cylindrical coordinates. These equations correctly predict the maximum field strength to exist at the wall, that is, $r_c = D_c/2$, and the maximum potential to be on the axis at $r_c = 0$. We may use them to estimate the electric field and potential values in a fluidized bed by selecting typical values for the bed parameters:

$q/m = 0.01 \mu\text{C/kg}$ (rather modest triboelectric charging value for polymers)

$e = 50\%$ (nominal value for void fraction in fluidized bed)

$r_m = 2000 \text{ kg/m}^3$ (mass density of solid material)

$k = 2$ (typical dielectric constant for insulating solid in fluidized state)

$D_c = 2 \text{ m}$ (typical fluidized bed diameter)

Using these values in Eq. (8), the electric field at the wall is estimated at 280 kV/m, which is very close to $E_b = 300 \text{ kV/m}$, the breakdown strength of air. The maximum electrostatic potential, measured at the center of the cylindrical vessel, is calculated to be 560 kV. Such high values for electrostatic field and potential guarantee some sort of electrostatic discharge in a vessel. What, in fact, takes place is that a corona discharge (or some other electrical discharge) occurs, probably as the charged material is added. The lesson to be learned from the above calculation is that, even for relatively modest powder charge levels in vessels of moderate size, the

resulting electric field and potential are sufficiently high to produce electrostatic activity when insulating materials are bulked, transported, or fluidized.

Discussion. The triboelectric charging of particulate solids is largely unavoidable during handling. When the electrical conductivity of the material is low, the particles can retain this charge for a long time. The longevity of this charge can be attested to by many processing plant operators and workers, who have experienced powerful electrostatic shocks while attempting to gather samples of polymer granules from grounded tote bins and barrels that have been sitting in place for extended periods. When sufficiently large amounts of charged particles accumulate in a vessel or container, the nuisance value of electrostatic charge transforms into a true hazard. Sparks generated by electric charge from tribocharged powder can ignite suspended dust (or, even more readily, flammable vapors or gases) causing serious fires and explosions. Electrostatic phenomena in fluidized beds are the subject of the next section of this chapter.

3.0 FLUIDIZED BED ELECTRIFICATION

Because of the unavoidable tendency of granular solids to become triboelectrically charged when handled, it is no surprise that electrostatic phenomena are often quite pronounced in fluidized and spouted beds. The vigorous motion of fluidized particles—with constant particle-particle and particle-wall contacts—guarantees that electrical charging will take place. Electrostatic adhesion and cohesion, observed and recorded in the very earliest experimental investigations of fluidization, were immediately identified as experimental nuisances to be overcome. Somewhat later, the hazardous nature of electrostatics came to be appreciated.

3.1 Background

Early Investigations. In the late 1940's and early 50's, research interest in fluidization as a new technological process surged. Almost from the start, experimentalists reported strong electrostatic effects (Wilhelm and Kwauk, 1948; Leva, 1951; Miller and Logwinuk, 1951; Osberg and Charlesworth, 1951). What these and other investigators observed in common included charge-related adhesion of particles to vessel walls and to the glass windows of observation ports and, much more importantly, an

apparent influence of electrostatics on the conditions for minimum fluidization. These effects in their various manifestations were discovered to depend strongly on humidity. Because of the erratic behavior and significant experimental irreproducibility, some workers simply chose to avoid materials found to exhibit strong electrostatic effects while others sought to minimize charging by using humidified air. In these early experiments, it became well established that electrostatics was a nuisance in fluidized bed systems that could not be ignored. At this time, however, safety concerns were not prominently mentioned.

With the better understanding of fluidization achieved during the 1950's came an improved appreciation for the important role played by electrostatics. Katz tested a fluidized bed consisting of two different size cuts of glass beads and observed an elevation-specific size segregation effect, which was exacerbated by static electrification (Katz, 1957). When humidified air was used at a sufficient level to reduce electrostatics, no practical benefit was obtained because high moisture content simply replaced electrostatic with capillary forces. Work that followed established the link between electrostatic interparticle forces and fluidization conditions and, furthermore, demonstrated the importance of particle size in controlling triboelectric charging (Davies and Robinson, 1960).

The first systematic investigation to focus on electrostatic phenomena in fluidized beds was published by Ciborowski and Wlodarski (1962). They monitored electrostatic activity in air-fluidized beds of sand and various polymers by lowering a spherical electrode into the bed and then measuring the static voltage it attained when connected to a high-impedance voltmeter. By varying the position of the electrode, they mapped the distribution of the potential within the bed, finding maximum values just under the surface of the bed exceeding 15 kV. They verified the strong dependence of electrostatic effects on the relative humidity and also noticed that particle charging disrupted good fluidization by promoting the formation of flow channels. Finally, they pointed out the possibility that electrostatic forces might be exploited in new applications for fluidization. Another investigation using a suspended ball electrode to measure electrostatic activity in polymer resins, hydroquinone, and ammonium sulfate provided direct verification that charge accumulation is related to particle resistivity (Kisel'nikov et al., 1967).

Boland and Geldart reported experiments with glass ballotini in a specially designed two-dimensional bed (Boland and Geldart, 1971). To

avoid the influence of suspended or protruding electrodes on fluidization, they used an electrostatic probe mounted flush with the wall. The principal objective of their investigation was to investigate the effectiveness of various measures, including humidification, particle surface treatments, and air ionization in suppressing triboactivity. They found that relative humidities in the 60 to 70% range, while not actually reducing the charging, do increase the surface conductivity so that the charge dissipates more rapidly. They also obtained evidence that bubbling might be an important charge separation mechanism in fluidized beds.

Summary and Critique. All these early studies share in common the quantification of fluidized bed electrostatics in terms of voltages or electric fields measured inside a vessel. Such measurements, with suspended electrodes or wall-mounted probes, are only an indirect indication of particle charging. Though the electrostatic distribution of charge within a bed is geometrically related to the electrostatic potential and the field (see Sec. 2.4), inference of the first from measurement of the second or third is quite difficult in the case of highly insulating granular materials. The value of measuring voltage with suspended electrodes must be questioned on several grounds. First, the probe disturbs the flow, changing the very nature of the solids circulation. Second, particle collisions with the probe introduce a triboelectrification mechanism not present in the undisturbed bed. Third, the connection cable to the probe seriously distorts the electrostatic potential within the bed (Fujino et al., 1985). Because of the problems with suspended probes, the knowledge gained about particle charging in early experiments was largely qualitative. The controlling factors in triboelectrification remained imperfectly understood, the distribution of charge within a bed was not known, and the absolute charge levels attained by the granular solids were unmeasured. The motivation of the research performed on the phenomenon was only to minimize a known experimental nuisance.

Wall-mounted probes, which measure field rather than electrostatic potential, may seem a better choice than suspended probes, but they suffer from the serious problem that charged fines often adhere tenaciously to the sensing electrodes and other surfaces of probes. These charged particles will shield the sensing electrode from the field within the bed and interfere with the measurements. Probably for this reason, very few attempts to use wall-mounted probes are found in the literature.

3.2 More Recent Work

About twenty years ago, intriguing new applications for fluidization in air pollution control—including fluidized bed coal combustion and scrubber technologies—were proposed and investigated. These new concepts were intended to exploit the strong coulombic forces of attraction between fluidized bed particles and submicron particulate pollution. As a result, the direct measurement of particle charge began to take on importance (Tardos and Pfeffer, 1980). While the motivation at the time for such measurements might have been an interest in enhancing the performance of fluidized bed air cleaning systems, the data are just as valuable for the assessment of ESD-induced fire and explosion hazards in fluidized beds (Cross, 1987; Glor, 1988; Jones and King, 1991). Ordinarily, the charging of granular materials and powders is quantified by means of the specific charge q/m , that is, charge per unit mass. Representative specific charge data for fluidized bed particle charging are summarized in Table 4 and some key experiments are briefly reviewed below.

Direct Measurement of Particle Charge. In one experiment, small samples of 2 mm diameter porcelain granules were drawn from the middle of an air-fluidized bed into a Faraday cage to perform charge and mass measurement (Tardos and Pfeffer, 1980). The specific charge values ranged from ~ 0.01 to $\sim 0.1 \mu\text{C/kg}$. Fujino and his colleagues fluidized glass beads and certain polymers including PMMA granules, reporting values from ~ 0.1 to $\sim 1.0 \mu\text{C/kg}$ (Fujino et al., 1985). Very recently, similar values were obtained using glass particles in size cuts from 5–40 up to 70–100 μm (Tucholski and Colver, 1993).

Some investigators have reported significantly higher specific charge values than those reviewed above and it remains quite unclear whether such results can be attributed to differences in the particulate media, to the means used to withdraw particles from the bed, or to the different locations from which particles were collected. For example, in one experiment individual glass beads withdrawn from the freeboard region of a fluidized bed of glass beads were found to have a specific charge in excess of $100 \mu\text{C/kg}$ (Fasso et al., 1982). In this investigation, it was found that the absolute charge per particle varies approximately as the 1.4 power of the diameter, that is, $q \propto D^{1.4}$. In a second test, $\sim 1000 \mu\text{m}$ polystyrene particles, withdrawn by a vacuum sample collector and deposited in a Faraday cage, were found to have a charge of $\sim 40 \mu\text{C/kg}$ (Wolny and Opalinski, 1983). Still another experiment, employing a pneumatic gun to eject individual particles from a

bed of ~500 μm polystyrene granules, resulted in specific charge values exceeding 100 $\mu\text{C/kg}$ (Wolny and Kazmierczak, 1989). The pneumatic ejection technique was employed to overcome the natural tendency of these particles to agglomerate, a phenomenon which the investigators found to interfere with other more conventional particle sampling methods in polystyrene.

Table 4. Specific Charge Data for Particles in Fluidized Beds from Various Sources

Particle types	Specific charge ($\mu\text{C/kg}$)	Method	Source
sieved coal (63 to 75 μm)	-30 to +30 (average near zero)	separation tower	Harris (1973)
porcelain (~2 mm)	0.01 to 0.1	small samples drawn from middle of bed into a Faraday cage	Tardos and Pfeffer (1980)
glass beads (30 to 55 μm)	~30 ~	individual particles drawn from freeboard in a Faraday cage	Fasso et al. (1982)
polystyrene beads (1.02 to 1.2 mm)	~40	vacuum withdrawal of small samples into a Faraday cage	Wolny and Opalinski (1983)
glass beads (200 μm), PMMA (540 μm)	0.1 to 1.0	captured samples from bed in a Faraday cage	Fujino et al. (1985)
polystyrene beads (475 μm)	>100 (dominantly negative)	pneumatic ejection of particles into deflection electrodes	Wolny and Kazmierczak (1989)
glass beads (size cuts from ~5 to ~100 μm)	0.1 to ~10 (net charge observed)	samples collected in a Faraday cage	Tucholski and Colver (1993)

Suspended Probe Measurements Revisited. One group has explored the use of suspended probes to gain more useful qualitative electrostatic data in fluidized beds by developing a capacitive circuit model for the bed (Rojo et al., 1986). Open-circuit voltages induced on immersed

electrodes were measured with an electrostatic voltmeter having very high impedance. By using different electrode geometries, bed diameters, and grounded electrode placements, information about scaling laws for electrification was revealed. Unfortunately, no specific charge data were reported.

Summary of Available Data. Table 4 summarizes the results of the specific charge measurement experiments reviewed above. It is interesting to compare these data to the process-based classification scheme of Table 2. In general, one would not expect fluidization to create the high specific charge levels encountered with pneumatic transport. In pneumatic transport, high speed particle-wall contacts dominate inside the pipe, while in a fluidized bed, lower-speed particle-particle contacts are overwhelmingly favored. At the same time, fluidization might be expected to charge particles more strongly than pouring or sieving. Based on these arguments, one might then estimate that in a vigorously fluidized bed

$$\text{Eq. (9)} \quad 0.01 \mu\text{C/kg} > q/m > 1.0 \mu\text{C/kg}$$

In general, the data of Table 4 tend to confirm this estimated range; however, the upper limit of $1.0 \mu\text{C/kg}$ is considerably exceeded in the case of data obtained with individual particles of tribo-active, insulating polymers. Whether or not significant volume separation of positive and negative charges occurs with these polymers is not known. Thus, the validity of the upper limit in Eq. (9) is difficult to judge.

For fluidized beds consisting of two or more particulate constituents (for example, distinct size cuts or different materials), charge separation is virtually inevitable. An example of bipolar charging is provided by crushed coal which, in the narrow size range from 63 to 75 μm , exhibits a bipolar charge distribution ranging from about -30 to $+30 \mu\text{C/kg}$ with the average charge near zero (Harris, 1973). These values depend strongly on sulfur content. The likely reason for this strong bipolar charging is the heterogeneous nature of coal; when crushed, individual particles vary considerably in their mineral makeup. It should be pointed out that particle-particle triboelectrification does not create significant net volume charge \mathbf{r} unless the various particle populations segregate within the bed. As shown in Sec. 2.4, only charge segregation can create strong electrostatic fields and the associated high electrostatic potentials. If strong particle-wall triboelectrification occurs in a bed of homogeneous particles, then segregation is much more likely.

Methods of Charge Reduction. There are a number of methods for reducing electrostatic charging in fluidized beds, including humidification of the fluidizing air, conductive particle coating, reduced gas flow, careful selection of vessel materials, the choice of more conductive particulate, and finally of course the addition of antistatic agents. As already mentioned, the application of humidified air to reduce electrification in fluidized beds dates from some of the earliest investigations (Osberg and Charlesworth, 1951). Many investigators have studied its practical usefulness (Katz, 1957; Davies and Robinson, 1960; Tardos and Pfeffer, 1980; Guardiola et al., 1996). In general, the conclusion is that relative humidities in the 60% to 70% range are required to reduce charge accumulation significantly. Even then, at least one report observed that the electrostatic effects do not correlate very well with measured specific charge values (Wolny and Kazmeirczak, 1989). There is also the problem that high humidities can increase the cohesive properties of some particles. Like humidification, conductive coatings on particles can reduce electrostatic charge by accelerating the rate at which the charge leaks away from the bed to ground (Katz, 1957; Boland and Geldart, 1972). Unfortunately, many coatings are not sufficiently robust to last very long in a vigorously churning, bubbling bed, especially at elevated temperature. The same problem exists with most of the modern antistatic agents, of which there are many types (anon., 1993). These materials, which work by making the particle surface attract and hold moisture, are sufficiently effective to improve flow characteristics of powders but the coatings cannot be expected to stay intact for long in a fluidized bed.

Another method to reduce the effects of charging is to add a small quantity of fines (conductive or nonconductive). For example, graphite, added to beds of glass beads in amounts of ~0.14% by weight, has been found to reduce electrostatic activity (Bafnec and Beña, 1972). In similar tests, finely ground coal, titanium dioxide, pigment particles, and aluminum powder were introduced into beds of tribo-active polystyrene beads (Wolny and Opalinski, 1983; Wolny and Kazmeirczak, 1989). The mechanism by which the fines reduce tribocharging is believed to be that the smaller particles coat the larger particles and reduce the number of intimate contacts. It is also true that, if the fines are oppositely charged, then the coating will simply shield the particle charge and reduce the effective specific charge q/m . In one interesting experiment, it was shown that the addition of alumina fines to a particle bed of the same material reduces charging, apparently via the same mechanism of the fines coating the larger

particles (Singh and Hsieh, 1987). This successful charge reduction method is a good example of size-dependent tribocharging.

Binary mixtures of glass ballotini and steel beads of nearly equal size ($\sim 500\text{ }\mu\text{m}$ and $\sim 275\text{ }\mu\text{m}$, respectively) also exhibit reduced electrostatic activity, as measured by suspended electrodes (Guardiola et al., 1992). The highly conducting steel beads were added to the glass particles in amounts up to approximately 10% by volume.

The obvious measures of lowering superficial gas velocity in the bed and the selection of wall and/or particulate materials certainly exist. But, in a given process, there is often no practical way to implement such solutions. Fluidization conditions are dictated by the application for which the bed is intended; furthermore, the choice of particulate materials can seldom be made on the basis of electrostatic considerations.

3.3 Beneficial Effects of Electric Charge

Though the focus of this chapter is electrostatic nuisances and hazards associated with fluidization, it must be recognized that in some cases particle charging can be exploited with beneficial effect. Applications that have been proposed and investigated include enhanced collection of gas-entrained particulate pollution such as fly ash in fluidized bed combustion gas cleaners. These electrofluidized beds (or EFB's) function essentially as electric field-assisted gas scrubbers, efficiently removing charged particulate pollution from a gas stream (Melcher et al., 1979a,b). Electrofluidization has also been exploited in powder coating processes (Lupinski and Gorowitz, 1979). A second beneficial electrostatic effect is the electroclamping phenomenon. Here, an imposed DC electric field induces interparticle forces strong enough to suppress bubbling and to control the recirculation of particles in fluidized or spouted beds (Johnson and Melcher, 1975; Talbert et al., 1984; Law et al., 1996). Note that electroclamping is related to strong induced dipole-dipole interactions between particles and does not depend on tribocharging.

4.0 ESD DUST IGNITION HAZARDS

The next task in considering the electrostatic hazards associated with a fluidized bed is to consider the specific conditions required for the ignition of suspended dust and powders. It is crucial to cover this subject because

dust explosions occur only under very stringent conditions imposed upon concentration, oxygen content, and ignition source spatial and temporal characteristics.

4.1 Basics of Suspended Solids Ignition

Preliminaries. The combustion of suspended dusts and powders is quite complex and only imperfectly understood. The complexity stems from both fundamental and practical considerations. On the fundamental side, the ignition of suspensions of finely divided solids is influenced by hard-to-quantify factors such as the time-varying concentration of solids, the chemical activity and morphology of the particulate, and the degree of confinement provided by the vessel. On the practical side, industrial conditions are seldom sufficiently well-controlled or characterized to justify application of existing theoretical models. For all the above reasons, this chapter can provide only a very abbreviated coverage of ignition basics. The reader is referred to other sources for in-depth treatment of dust and powder explosions (Bodurtha, 1980; Bartknecht, 1981; Bartknecht, 1987).

Fire Triangle. In the context of industrial fire and explosion safety, the universally recognized means to introduce the necessary conditions for fires and explosions is the *fire triangle*. The fire triangle, shown in Fig. 4, signifies the three essential requirements for a fire or explosion: (i) fuel, (ii) an oxidizing agent, and (iii) an ignition source. The absence of any one of these elements means that no fire or explosion can occur. In dust explosions, the dust is the fuel while the oxidant is almost always atmospheric oxygen. There are certain powder mixtures that can support potentially hazardous exothermic reactions—the thermite reaction in mixtures of cuprous oxide and aluminum powder is one—but these do not fit the conventional model of a dust deflagration and are not of interest here. In addition to electrostatic discharges, many other ignition sources must be acknowledged, including open flames, overheated bearings, and sparks caused by short circuits in electric power equipment. Of all these, ESD is simultaneously the least likely to cause an ignition *and* the most difficult to control, an irony due to the seemingly capricious nature of electrostatics.

The investigation of an industrial fire or explosion invariably starts with an effort to identify each element in the fire triangle. Quite often, the fuel is known and so either the oxidizer or the ignition source becomes the focus of the investigation. For example, in a blender used to mix a

flammable and strongly triboelectrically active powder, measures might have been taken to inert the vessel, that is, to reduce the oxygen level below the concentration where a fire is possible. If a fire occurs anyway, then the focus of the investigation becomes why and how the inerting system failed. If, on the other hand, measures had been taken to dissipate triboelectric charge, for example, by the addition of an antistatic agent, then suspicion might be cast upon the efficacy of the agent or on the possibility that some other ignition mechanism, such as an overheated bearing, might be responsible.

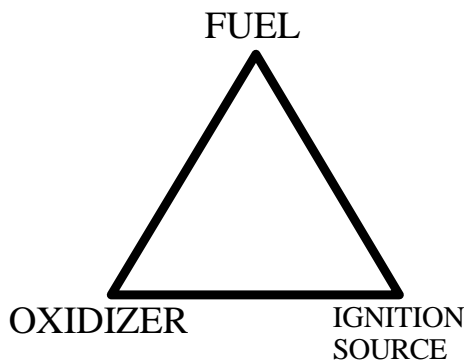


Figure 4. The well-known fire triangle, which depicts the three essential requirements for fires and explosions.

Concentration Conditions for Ignition. The gaseous O_2 and particulate solids concentration conditions required for ignition of dusts and powders suspended in air are far more stringent than those for flammable gases and vapors. It is for just this reason that dust ignition events are in fact relatively rare compared to vapor and gas ignitions. It seems that the probability for simultaneous occurrence of the right concentration values for oxygen and dust, along with a sufficiently energetic ignition source, is low.

For a dust ignition to occur, the suspended solids concentration must lie between lower and upper limits which vary from material to material and are influenced by subtle factors such as particle shape and size distribution. From the standpoint of assessing safety hazards in commercial and industrial operations, the lower explosive limit is the more important one. The rationale of this statement is that, if the possibility of exceeding the lower limit in a powder-handling operation can not be completely ruled out, then a hazard must be recognized and appropriate measures taken. Over the

years, lower explosive limit data have been obtained for the dusts of many important powders and granular solids (National Fire Protection Association, 1986). Table 5, though only representative, shows that most dusts have a minimum explosion concentration in the range from ~30 to ~100 grams per cubic meter. For a cloud of 10 μm diameter polymer particles, this figure translates to ~10 particles per cubic millimeter. A useful rule of thumb helpful in interpreting this result is that a dust cloud in the explosive range will appear optically opaque. If visibility is heavily obscured by a cloud of suspended dust, then it is best to assume that the concentration is right for a dust explosion.

The particulate concentration levels within an operating fluidized bed will exceed the upper explosive limit so that an ignition starting below the surface of the bed is virtually ruled out. The concentration in the freeboard (above the bed) may be in the explosive range; however, the vigorous flow of air or gas through the bed will tend to quench any ignition before it really gets started. In manufacturing processes involving fluidization, the most serious powder explosion risk is probably going to be associated with filling or emptying operations, or when the bed is started up or shut down. In all these situations, there will exist a transient period when the dust concentration in the vessel—probably in the freeboard region—will be in the explosive range. Numerous occurrences of explosions during filling and emptying of storage silos and hoppers have been reported, and there is every reason to anticipate similar hazards in the filling and emptying of fluidized bed systems. Therefore, measures taken to avoid risks in hoppers and silos are appropriate for fluidized beds. These measures are discussed in Secs. 5.1 and 5.2.

Minimum Ignition Energy of Powders. With dust and oxygen concentrations in the correct range, there is still the requirement of a ignition source before a fire or explosion can occur. The more well-known ignition sources—open flames, overheated bearings, and electrical sparks caused by short-circuits—are examples where the available energy is adequate for igniting virtually any suspended dust. On the other hand, electrostatic sparks usually have a limited pool of available energy and, quite often, the electrostatic energy released in an electrostatic discharge is only just comparable to the ignition requirement of the dust. Given the uncertainty of the estimates for the parameters used, the assessment of ESD hazards is quite problematic. Usually, close attention is paid to the *minimum ignition energy* (MIE) of the suspended dust.

Table 5. Representative ignition temperatures, minimum explosion concentration, and minimum ignition energy for selected dusts, from *NFPA Fire Protection Handbook* (National Fire Protection Association, 1986) and other sources.

Types of dust	Ignition temp. of dust cloud, °C	Ignition temp. of dust layer, °C	Min. ignition energy (MIE), <i>J</i>	Min. explosion conc., g/m ³
<u>Agricultural</u>				
corn	400	250	0.04	55.
rice	510	450	0.10	85.
wheat flour	440	440	0.06	50.
wheat starch	430	-	0.025	50.
<u>Carbonaceous</u>				
charcoal, wood	530	180	0.02	140.
KY coal (bit.)	610	180	0.03	50.
PA coal (anth.)	730	—	0.10	65.
CA lignite	450	200	0.03	30.
<u>Drugs</u>				
aspirin	660	—	0.025	50.
vitamin B ₁	360	—	0.06	35.
vitamin C	460	280	0.06	70.
<u>Metals</u>				
aluminum	610	326	0.01	45.
titanium	330	510	0.025	45.
uranium	20	100	0.045	60.
<u>Plastic resins, etc.</u>				
cell. acetate	430	—	0.03	40.
Nylon [®]	500	430	0.02	30.
PMMA	480	—	0.02	30.
polycarbonate	710	—	0.025	25.
PPO	540	—	~0.05	~60.

To measure the MIE of a powder, a sample of the material is placed in a vessel called a *Hartmann cell*, the powder is dispersed by a strong jet of air, and then a capacitive spark of well-characterized energy and time duration is initiated between two electrodes mounted inside the vessel. The spark energy is increased incrementally under ignition occurs. Despite standardized procedures established for these measurements (British Standards Institute, 1991; ISC, 1994), reliable measurement of the minimum ignition energy in dusts is notoriously difficult. There is of course the problem of dispersing the dust reproducibly and uniformly, but there also exists controversy about the nature of the igniting spark. Investigators have found that the wave shape and duration of the current pulse associated with the spark—controlled by the series impedance of the discharge circuit—influence the measured value of the MIE (Eckhoff, 1975; Field, 1982). It is now suspected that the true MIE values of many dusts may be lower by factors from two to five than the accepted data of twenty years ago (Taylor and Secker, 1994). The MIE data in Table 5 must be questioned for this reason. In fact, a much more conservative value of 5 mJ has now been adopted for the MIE of manufactured polymer powders.

Another important discovery is that the measured MIE of powders depends very strongly on particle size. For example, the measured values for polyethylene are 500 mJ and 10 mJ respectively for narrow size cuts centered at 100 μm and 30 μm . This result indicates how strongly fines can influence explosion hazards in powders. In fact, Britton argues that it is the surface-average diameter that provides the best correlation to measured MIE (Britton, 1992). Uncertainties about the accuracy of measured MIE values notwithstanding, the data provided in Table 5 do reveal that the dusts of a wide range of commercial and industrial materials—from agricultural grains to powdered metals and polymer plastics—pose an undeniable explosion or fire hazard when dispersed in air.

4.2 Types of Discharges

An electrostatic dust ignition can occur when the discharge releases sufficient thermal energy within a sufficiently short period of time and small volume to ignite the suspended dust. Electrostatic ignition is complicated by the fact that there are a number of distinct ESD mechanisms important in electrostatic hazards and hazard abatement (Glor, 1988).

Capacitive Discharges. Capacitive discharges are responsible for at least 90% of all dust and vapor ignitions of ESD origin. The

requirements for these most well-known of discharges are two electrically isolated conducting bodies (usually metallic and one of which is usually a grounded pipe or container wall). The metal object can be some ungrounded implement, such as a funnel or scoop shovel, or a metallic pipe or cable that has become ungrounded due to a broken electrical bond. There must exist sufficient potential difference and charge to cause an avalanche breakdown (spark) in the air between the conductors (refer to Fig. 5). The mechanism of charging can be conduction or induction and the charge can be positive or negative. Capacitive sparks readily ignite many flammable dusts.

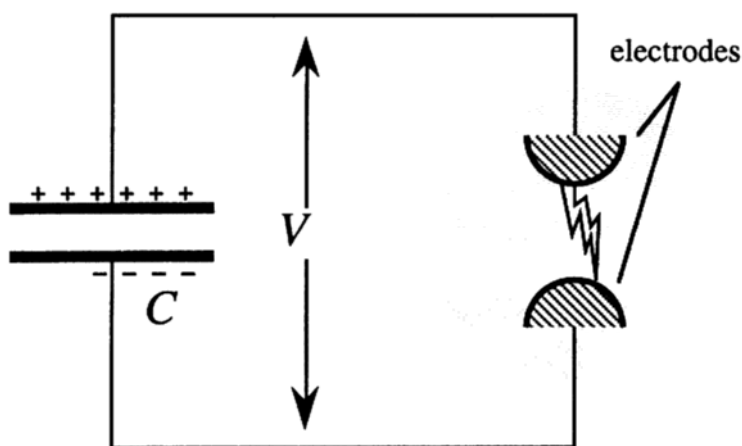


Figure 5. The capacitive discharge. Sometimes series resistance slows the discharge, increasing or decreasing the likelihood of a dust ignition.

Capacitive discharges are characterized by the electrostatic energy U_e converted to thermal energy in the spark. While somewhat difficult to measure accurately, the energy released in a capacitive spark is commonly estimated using the following relationship.

$$\text{Eq. (10)} \quad U_e = \frac{1}{2} C_{\text{object}} V^2 = \frac{Q^2}{2 C_{\text{object}}}$$

Here, C_{object} is the capacitance and V the voltage between the two metal conductors. The capacitance of typical chargeable components depends on their size, shape, and distance from a grounded surface. For purposes of electrostatic hazard assessment, it is usually convenient to rely upon measured data like that in Table 6.

Table 6. Representative Capacitance Values for Typical Components in a Plant or Commercial Facility Handling Powders (*Eichel, 1967*)

Item	Capacitance range (<i>C_{object}</i>)
Small metal implements (funnels, scoops, etc.)	10 to 20 pF
Small metal containers (up to ~50 liters)	10 to 100 pF
Medium sized containers (up to ~200 liters)	50 to 300 pF
Miscellaneous plant components	100 to 1000 pF
Human body (depends on footwear)	200 to 300 pF
Filter receiver components	10 to 100 pF
Typical large transport truck	~1000 pF
Lined cylindrical vessel (4 m diameter)	~100,000 pF

Two distinct conditions must be met in order for a capacitive spark to ignite a flammable dust. First, the voltage difference between the object and ground must be sufficiently high to promote a discharge. The *spark-ing potential* is a complex function of the capacitor's geometry and the length of the gap across which the discharge must jump. At standard atmospheric conditions, the minimum sparking potential is $V_{min} \approx 350$ V and it is achieved at a gap spacing of 6 to 7 μm . According to Paschen's law, the sparking potential is higher for gaps larger *or* smaller than this value (Cobine, 1958). Figure 6 shows the dependence of the sparking potential upon the product of pressure and gap spacing. In general, the following condition on voltage is required for a spark to occur

$$\text{Eq. (11)} \quad V > V_{min}$$

In ordinary practice, the rather conservative value of 100 volts is recommended for V_{min} to provide a margin of safety (Gibson, 1979).

The second condition for an ignition is that the energy released in the spark U_e must exceed the minimum ignition energy (or MIE) of the dust.

$$\text{Eq. (12)} \quad U_e > \text{MIE}$$

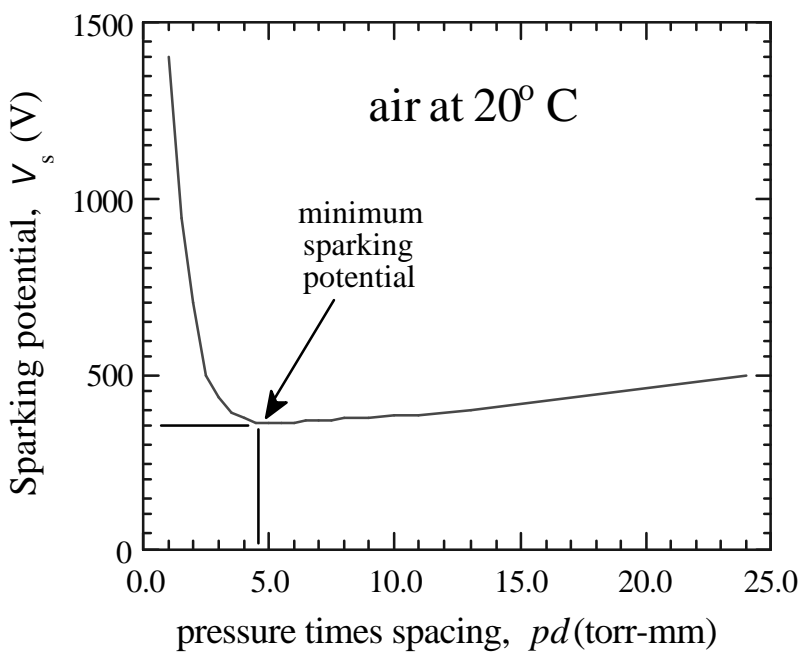


Figure 6. Sparking potential in air as a function of pd , the product of pressure and gap spacing. (Adapted from data of Cobine, 1958.)

Two other useful parameters related to capacitive sparks and dust ignitions are (i) the optimum sparking distance is ~ 10 mm and (ii) the quenching distance is ~ 7 mm. Refer to Sec. 4.1 and Table 5, where MIE is discussed in more detail.

In a specific situation, determination of the voltage V for use in Eqs. (10) and (11) is based on having reliable estimates for charging current and leakage resistance (cf. Sec. II.B of Jones and King, 1991). Figure 7 contains a convenient nomograph for assessment of capacitive discharge ignition risks. With estimates for the capacitance and voltage of an object, the value of U_e is obtained by drawing a straight line between the points on these two scales and then reading the intercept with the middle scale. For convenience, the MIE values of some important powders are indicated on this scale, including the generally accepted value of 5 mJ for polymer powders. Note that, in general, MIE values for vapors are much lower.

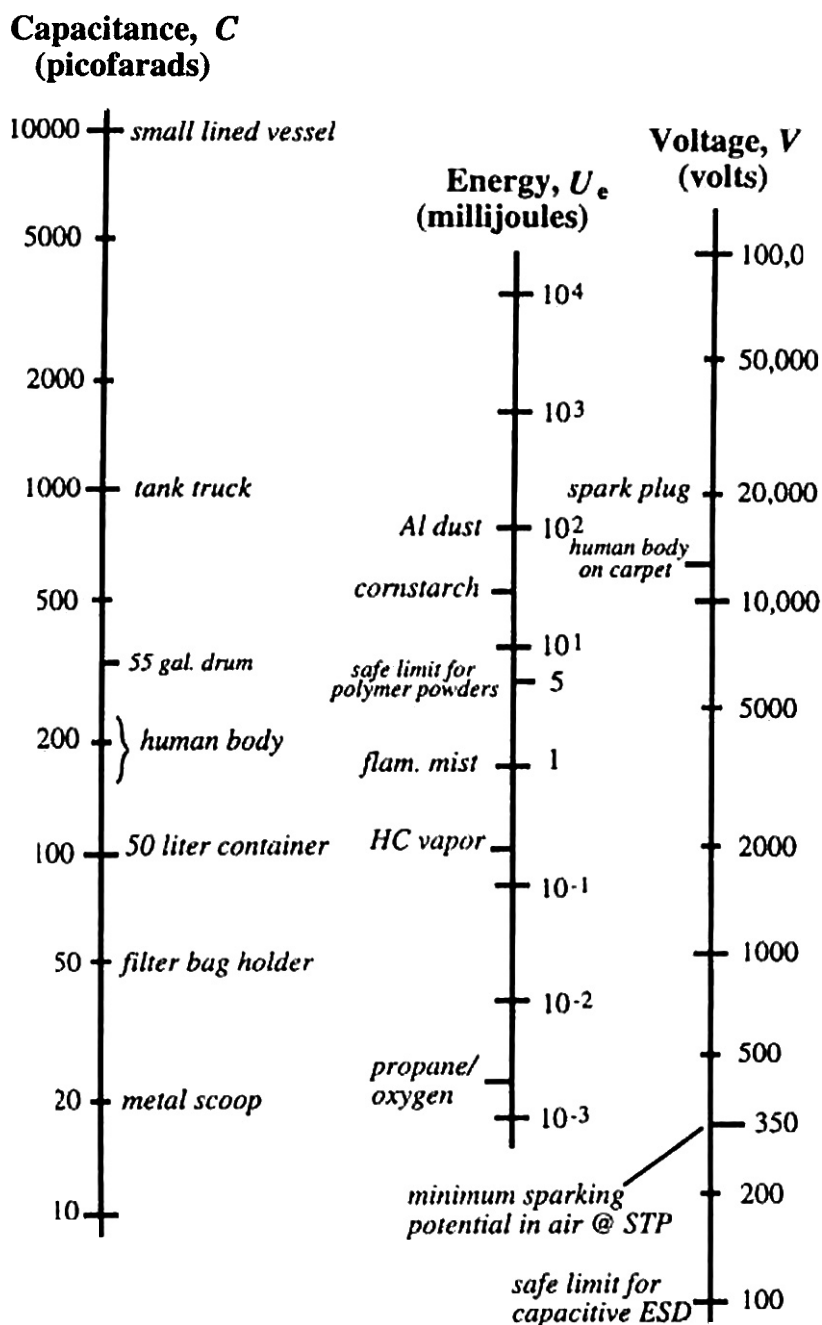


Figure 7. Nomograph for calculation of capacitive electrostatic discharge energies. (Bodurtha, 1980; Jones and King, 1991.)

Brush Discharges. Brush discharges, which have effective energies in the range of ~ 1 to ~ 3 mJ, can occur between a conductor with radius of curvature in the range 5 to 50 mm (0.2" to 2") and either another conductor or a charged insulating surface when the field intensity at the surface of the curved conductor exceeds approximately 5 kV/cm (Maurer, 1979). This type of discharge, which differs from a capacitive spark in that it is more spatially diffuse, is regarded as incapable of igniting any but the most sensitive dusts (though it can ignite many vapors and gases). Brush discharges are favored over capacitive sparks when current flow is limited by the high electrical resistance of the charged insulating surface.

Corona Discharges. Corona discharges, which occur when an electrode or any conductive object with radius of curvature less than ~ 5 mm experiences a strong electric field, are weaker and still more spatially diffuse than brush discharges. They are not sufficiently energetic to ignite even gases or vapors (Glor, 1988), so they present no direct ESD ignition hazard for suspended dusts; however, corona may contribute to accelerated charging of ungrounded metal objects or components within a vessel which may then lead to a capacitive discharge capable of igniting dust.

When the objective is to avoid corona discharges, sharp edges and protrusions, such as threaded bolts, rough welding seams, etc., inside vessels should be eliminated. Corona-induced product degradation, while never documented, may well be a factor to consider in the manufacture of clear or light-colored plastics for products where appearance is important. On the other hand, corona discharges, promoted by internally mounted wires or sharp metal protrusions inside a vessel, have been proposed as a way to promote charge neutralization of powders entering a vessel. Figures 8(a) and (b) show two distinct schemes for discharging powder during filling operations (Blythe and Reddish, 1979; van de Weerd, 1974). While these schemes have been shown to be effective, there has been hesitancy to install them widely, a concern probably due to understandable worries about breakage.

Propagating Brush Discharges. Conditions for a propagating brush discharge occur when a thin insulating layer, backed by a conductor, becomes charged (Glor, 1988). See Fig. 9(a). With spark energies up to ~ 1 J, these are the most energetic of all electrostatic discharges and they are capable of igniting virtually any flammable dust. Many serious ESD ignitions causing personal injuries as well as extensive plant damage have been attributed to propagating brush discharges (Hughes et al., 1975; Lüttgens, 1985). The high available energy for the propagating brush

discharge comes from the thin insulating layer, which acts like a large distributed capacitor. Once a discharge is initiated, electrostatic energy over a considerable area can be converted to heat due to discharges flashing along the charged surface. For this reason, it is best to avoid nonconductive liners on the inside surfaces of vessels, bins, and pipes. Furthermore, it is vitally important not to use pipe, tubing, inserts, or any other components made of plastic in any place exposed to dust. For example, plastic pipe can become conductive on its outside surface due to moisture or contamination, providing the condition for a propagating brush discharge even though the pipe initially does not have a conductive backing (Lüttgens, 1985). Refer to Fig. 9(b) which shows a common and dangerous situation.

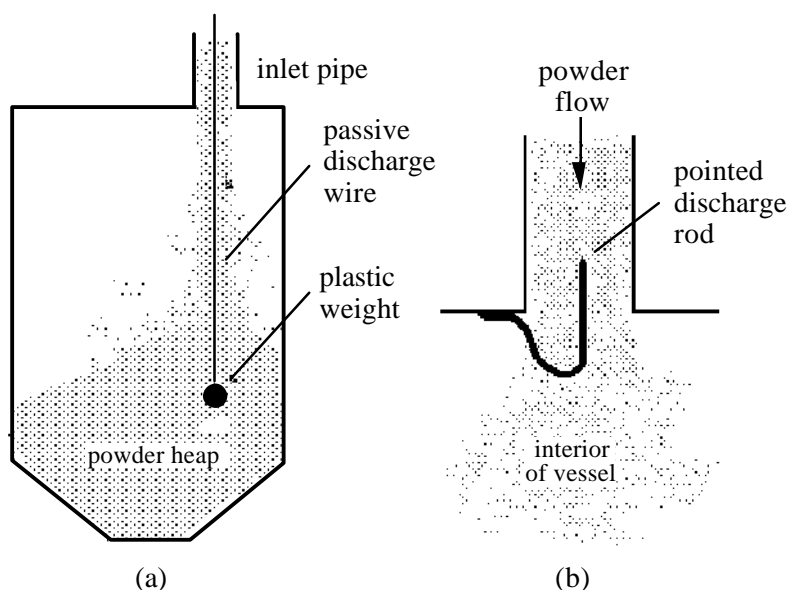


Figure 8. Application of corona to reduce powder charge level in granular solids. (a) Suspended wire for neutralization of charge entering silo (Blythe and Reddish, 1979). (b) Inlet pipe equipped with grounded corona discharge point (van de Weerd, 1974). Corona discharge wires, rods and/or points should have a diameter from 1 to 3 mm and must be securely grounded.

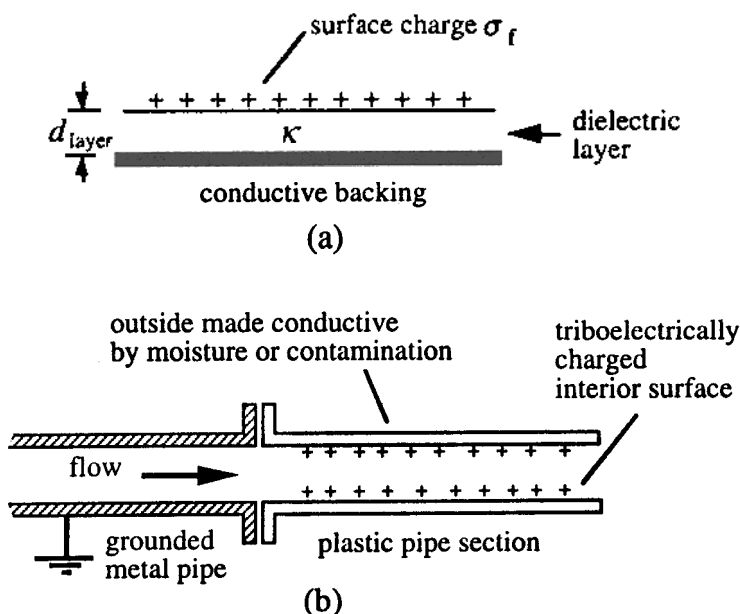


Figure 9. Propagating brush discharges. (a) Insulating dielectric layer of dielectric permittivity ϵ_s , thickness d_{layer} , and surface charge σ_f with conductive backing. (b) Example of improper use of plastic (PVC) pipe where surface charge builds up leading to risk of propagating brush discharge.

The conditions for propagating brush discharges may be quantified in terms of the thickness of the insulating layer d_{layer} and the maximum allowable capacitive energy per unit area u_e (in J/m²) where

$$\text{Eq. (13)} \quad u_e = \frac{1}{2} c_{layer} V_{layer}^2$$

Here, $c_{layer} = \kappa \epsilon_0 / d_{layer}$ is the *capacitance per unit area* (in farads/m²) of the layer. The surface voltage V_{layer} can be related to the accumulated surface charge σ_f (in C/m²) by the following equation:

$$\text{Eq. (14)} \quad V_{layer} = \sigma_f / c_{layer}$$

Incendiary discharges are most likely to occur when the thickness of the insulating layer is in the range $0.1 \text{ mm} \leq d_{layer} \leq 10.0 \text{ mm}$ and when (Tolson, 1989):

$$\text{Eq. (15)} \quad u_e > 1.2 \text{ mJ/cm}^2$$

In applications where an insulating liner is unavoidable, effective criteria for avoiding propagating brush discharges are formulated in terms of the surface charge density S_f and thickness of the insulating layer d_{layer} (Heidelberg, 1970):

- For $S_f \leq 25 \text{ nC/cm}^2$, make insulating layer as thin as possible ($d_{\text{layer}} \ll 1 \text{ mm}$)
- For $S_f > 25 \text{ nC/cm}^2$, make insulating layer as thick as possible ($d_{\text{layer}} \gg 1 \text{ mm}$)

Eq. (15), along with the above conditions upon S_f and d_{layer} , provides the safety engineer with useful quantitative criteria for assessing the likelihood of propagating brush discharges.

Maurer (Cone) Discharges. Maurer or cone discharges, occurring along the conical surface of the powder heap, are driven by the inflow of charged granular material into vessels and silos (Maurer, 1979). They are thought to be a form of brush discharge (refer to Fig. 10). The conditions required for discharges of this type are (i) coarse, insulating, charged particulate material in the size range from ~ 1 to $\sim 10 \text{ mm}$ ($\sim 0.04''$ to $0.4''$), (ii) a specific charge less than $\sim 3 \text{ } \mu\text{C/kg}$, and (iii) continuous rapid inflow of the material into the vessel (Glor, 1988). The flow rate required to initiate the discharge is inversely related to the average particle size: $\sim 2 \times 10^3 \text{ kg/hr}$ for 3 mm particles as opposed to $\sim 25 \times 10^3 \text{ kg/hr}$ for 0.8 mm particles in a 100 m^3 silo (Maurer, 1979). These discharges (with energy $\sim 10 \text{ mJ}$) apparently occur in conjunction with the avalanching of particles down the sides of the conical heap. They probably regulate the dissipation of excess charge accumulating at the surface of the growing heap as the electric field reaches the conditions for brush discharges.

At least one powerful dust explosion is believed to have been ignited by this type of discharge (Maurer et al, 1989). The explosion occurred when a granular product was being transferred into a large vessel ($\sim 20 \text{ m}^3$ or $\sim 700 \text{ cu. ft.}$). The 2 to 3 mm ($\sim 1/8 \text{ in}$) diameter particles became charged during pneumatic conveyance, causing an electrostatic discharge that ignited airborne fines. It is conjectured that these fines were due to either product attrition or residues left over from previous batches stored in the vessel. Since many blended polymers use $\sim 1 \text{ mm}$ diameter polystyrene or polyethylene granules, there is reason to be wary of this potential ESD ignition hazard, because the complete removal of fines can never be

guaranteed. Note that changing to larger sized particles in an operation may actually increase the ESD-induced dust ignition hazards because larger sized particles charge more readily and bulk to greater densities.

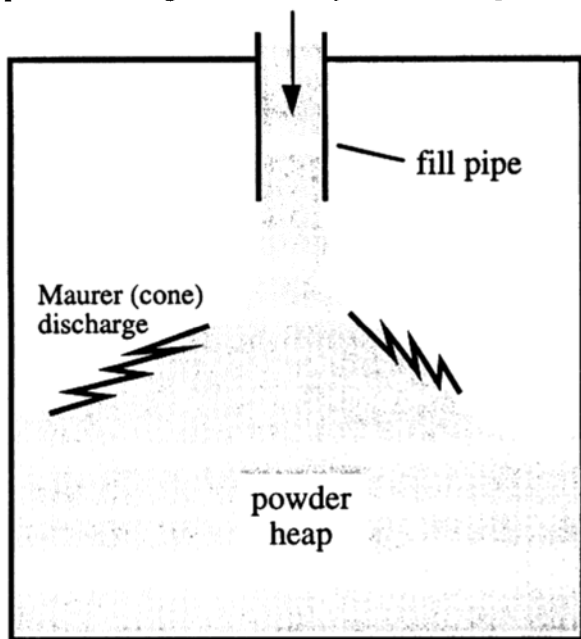


Figure 10. Maurer (cone) discharges manifest themselves as irregular sparks spreading outward toward the wall from the top of the conical powder heap. They are only active when charged material is being added. (*Maurer, 1979.*)

4.3 Charge Dissipation

The diagram shown in Fig. 11 provides a simplified, schematic representation of industrial electrostatic hazards in powder handling. According to this diagram, the sequence of events leading to a fire or explosion is: (i) charge separation, (ii) charge accumulation, (iii) electrostatic discharge, and, finally, (iv) ignition. Competing with the electrostatic discharge are several harmless mechanisms that dissipate electric charge and either limit exposure to or altogether prevent dangerous situations. The principal dissipation mechanisms are electric conduction and corona, though brush discharges, including Maurer discharges, may accomplish the same purpose.

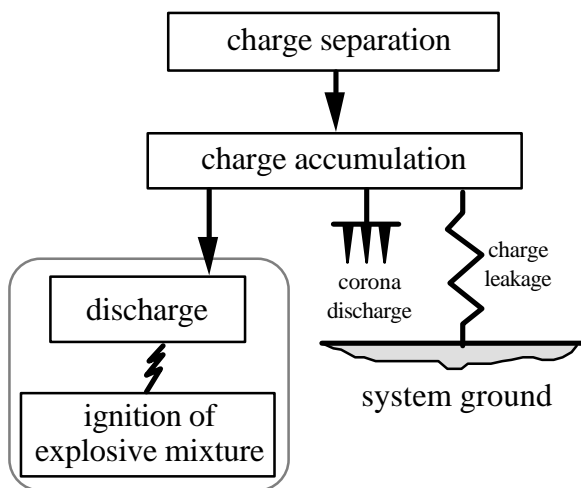


Figure 11. Model for electrostatic hazards associated with the accumulation of charged powders, based on Glor (1988).

Charge Leakage. The resistor shown in Fig. 11 represents the leakage of electric charge to ground. In a typical manufacturing facility, this resistance may represent the flow of charge to ground directly through the charged powder and/or some other (possibly ill-defined) current path. The current may be coming from the charged powder itself or from an ungrounded metallic component. For each such mechanism, there is a time constant which is often exponential in nature. We have already discussed one such time constant, the charge relaxation time $t = ke_0g$ defined in Sec. 2.2. As long as $g \ll 10^7 \text{ S}^{-1}\text{m}$, charge relaxation can prevent hazardous charge buildup in a powder by dissipating tribocharge virtually as rapidly as it accumulates. Even when $g > 10^7 \text{ S}^{-1}\text{m}$, charge relaxation still helps by limiting the period of exposure to ESD hazards in a vessel as charged powder is transported into a silo or other vessel.

In the case when an isolated conductor becomes electrically charged, other leakage paths can help to dissipate hazardous levels of electricity. The charge residence time in such a case is a capacitive circuit time constant: $t_{ckt} = RC$, where R is leakage resistance and C is capacitance. Consider the realistic case of a conventional filter bag holder which has become ungrounded, yet still has leakage resistance to ground of $R \approx 10^6$ ohms. From the nomograph of Fig. 7, the capacitance of a filter bag holder is estimated to be $C \approx 50 \text{ pF}$. Then, $t_{ckt} \approx 5 \cdot 10^{-5} \text{ s}$, indicating that the charge

will dissipate rapidly and present no capacitive spark hazard. A conservative rule of thumb is that, if the leakage resistance of a conductor is less than $\sim 10^6$ ohms, then the electrostatic hazard due to a capacitive spark is low (Jones and King, 1991).

A situation in seeming contradiction to the above statement can arise if an ungrounded, metallic object located inside a vessel itself receives charge from the electrically charged powder via such ordinarily harmless mechanisms as a corona or brush discharge. If the charging occurs rapidly enough, that is, faster than the RC time constant of the conductor, then a capacitive discharge capable of causing an ignition is possible (Britton and Kirby, 1988).

Discharge-Limited Charging. The pointed electrode array in Fig. 11 is intended to represent corona and other low-energy electrostatic discharge mechanisms. In general, these mechanisms are strongly nonlinear, displaying a voltage or, more properly, an electric field threshold which must be exceeded before corona can occur. As mentioned in Sec. 4.2, corona is most likely to occur when metallic objects of small dimensions or surfaces having sharp points are exposed to a strong electrostatic field. At atmospheric conditions for parallel wires, the corona onset condition is (Cobine, 1958)

$$\text{Eq. (16)} \quad E > E_c = 30 \left(1 + \frac{0.3}{\sqrt{D_{\text{wire}}}} \right)$$

where D_{wire} is the wire diameter (in cm) and E_c is the electric field at the surface of the wire (in kV/cm).

In the case of charged powder entering a silo, the Maurer discharge mechanism continuously dissipates charge as shown in Fig. 10. The details of this mechanism—thresholds, inlet flow requirements, etc.—are not as well-documented or understood as they should be.

Charge Control. In the abatement of electrostatic hazards, two distinct strategies for the control of electric charge exist. One strategy, used more extensively in liquids than in granular solids, is to employ conductive additives. These additives, while not really reducing the triboelectric activity, do provide a conductive path through the charged material to ground. In effect, the relaxation time t is reduced by artificially decreasing the material resistivity g . Refer to Table 3, where are categorized the charging tendencies of powders in terms of their effective bulk resistivities.

For powders and granular solids, there are two types of antistatic agents: surface- and volume-active additives. Surface-active agents, which increase the surface conductivity of individual particles, are effective because triboelectric charge is always situated on the surfaces of individual particles. Most if not all surface-active agents are hygroscopic and thus attract a thin film of water to the surface; it is this moisture that is responsible for the increased surface conduction (van Drumpt, 1991). The effective bulk resistivity of the particles g_{eff} may be estimated by assuming that the particles are spherical and of radius R (Jones, 1995).

$$\text{Eq. (17)} \quad g_{eff} = \frac{1}{g^{-1} + 2s_s / R}$$

where s_s is surface conductivity in Siemens. Note that surface treatment will have a significant effect on the resistivity only when $s_s \geq R/2g$. For purposes of static reduction in polymer materials, values of $s_s \approx 10^{-9}$ Siemens are achievable (van Drumpt, 1991). Such surface conductivity values, while sufficient to reduce flow-related problems in powders (Orband and Geldart, 1995), are apparently several orders of magnitude below those needed to eliminate entirely dust ignition hazards. In low humidity environments, the effectiveness of surface agents is reduced. Furthermore, they are susceptible to removal by exposure to solvents and contact with surfaces. Volume-active agents are usually added to a material during its formulation, a step that would be quite impossible for many of the solid materials which one might wish to fluidize. Even for polymers, there is an upper limit on the amount of antistatic agent that can be added before the mixture either becomes thermally unstable or manifests problems during extrusion.

The other method of controlling electrostatic charge is to add ions of the opposite sign to neutralize the excess charge. Corona neutralization, described in Fig. 8, is a passive method which exploits the electric field due to the excess charge itself to generate the opposite-sign charge. Other far more elaborate means also have been developed. One such device uses compressed air driven through a supersonic nozzle equipped with an AC corona needle (Corion, 1989). The positive and negative ions produced by the corona serve as preferential sites for moisture condensing out of the compressed air in the expansion zone downstream from the supersonic transition within the nozzle. The result is an electrically neutral, high-speed jet of charged droplets. Because of their high mass and low effective

mobility, these “heavy ions” can be directed to surfaces and granular solids as much as several meters distant from the nozzle. This type of neutralizer has possible application in neutralization of powders entering blenders and silos from pneumatic transport pipes. It might also be possible to install them within fluidized and spouted beds

5.0 ESD HAZARDS IN FLUIDIZED BED SYSTEMS

A survey of the electrostatic hazards literature reveals very little on the subject of ESD ignitions in fluidized or spouted beds. Apparently, electrostatic ignitions of suspended dust during fluidization are relatively rare. This is the case despite the strong electrostatic charging of particles, which is due to the vigorous churning that takes place in a fluidized bed, and despite other unmistakable signs of electrostatic activity within a bed, namely pronounced particle/wall adhesion. There are several reasons for the lack of fires and explosions. First, triboelectric charging within the bed is sufficiently bipolar so that strong electrostatic fields and high potentials usually have little chance to develop. Second, the particle concentration within a bed proper is too dense for any ignition. Third, gas and solids flows within the freeboard region, where the average dust concentration conditions may be in the correct range, are too vigorous to allow an ignition to propagate and evolve into a fire or explosion.

If these observations and explanations were the complete story, then there would be no motivation to cover electrostatic hazards in a book about fluidization. The need to recognize this subject in fluidization technology stems from the fact that any system designed to process granular materials requires the same peripheral equipment and components found in other powder processing facilities. Such equipment includes pneumatic and/or vacuum transport systems, filter receivers, storage silos, surge hoppers, blenders, grinders, and bulk transport containers. Because ESD-induced explosions or fires have been experienced in all of these components, it may be said that a fluidized bed keeps rather dangerous company.

The purpose of this section is to anticipate and consider risks inherent in fluidization and also to summarize the more thoroughly documented and well-understood risks associated with the kinds of peripheral systems and facilities likely to be found in manufacturing plants using fluidization processes.

5.1 Hazards Associated with Fluidization

Loading and Unloading. Loading granular solids into a fluidizing vessel is indistinguishable from loading any vessel of similar size. Many fires and explosions of electrostatic origin have occurred during vessel loading (or unloading) operations, and for this reason it is prudent to take all the same standard precautionary measures when loading fluidizing equipment. First of all, it is important to recognize that vessel size influences ignition risk and severity, simply because the larger mass of available fuel in a larger vessel will support a more powerful deflagration. A general rule of thumb is that dust explosions are possible only in vessels larger than approximately 1 m^3 in volume, though the more conservative classification scheme of Table 7 is commonly adopted. In any safety assessment, initial effort must be made to measure or obtain a reliable estimate for the specific charge q/m of the incoming granular material. As revealed in Table 2, this quantity depends on the treatment to which the particles have been subjected prior to delivery to the vessel. The table shows that pneumatically transported materials charge the highest and, according to Table 3, should always be presumed to create ESD hazards for moderately or highly insulating particulate matter, that is, $g \geq 10^7 \text{ S}^{-1}\text{m}$.

Table 7. Classification of Factors Involved in Dust Explosion Hazards for the Storage of Flammable Powders (*Glor, 1988*)

Vessel size	Vessel type	MIE $\geq 10 \text{ mJ}$	MIE $\leq 10 \text{ mJ}$
$< 0.2 \text{ m}^3$	unlined & lined	standard measures	standard measures
0.2 m^3 to 2.0 m^3	unlined	standard measures	avoid high-velocity pneumatic transport
	lined	guard against propagating brush discharges	guard against propagating brush discharges
$> 2.0 \text{ m}^3$	unlined	standard measures	special attention required
	lined	special attention required	special attention required

Any rapid dumping of a large volume of dry solids from a loading or surge hopper into a fluidized bed reactor can be quite hazardous for insulating materials. Though other electrostatic discharge mechanisms can occur during such operations, the one most directly linked to vessel loading is the Maurer or cone discharge discussed in Sec. 4.2 and depicted in Fig. 10. This type of discharge is driven by the inflow of charged granular solids and it stops when the inflow stops.

With these observations in mind, the simplest practical measure to reduce electrostatic discharge risks associated with vessel loading is to reduce the rate at which the dry solids are added to the vessel. This approach works because the slower rate of flow provides an opportunity for accumulating charge to relax away by various mechanisms before hazardous conditions become established. Often, the same type of flow limitation is effective in reducing the likelihood of ESD during vessel unloading. In many cases, the maximum safe rate of inflow (or outflow) has to be determined by empirical means.

Hazards During Start-up and Shutdown. It is well-known from in situ measurements that transient field reversals can occur when loading operations are started or stopped (Cross, 1980). Furthermore, electrostatic ignitions are more likely to occur at these times. Fluidized bed start-up and shutdown procedures undoubtedly create transient periods of exposure to electrostatically induced dust ignition conditions. Especially during shutdown, the larger particles will fall quickly, leaving any fines and dust to settle much more slowly and providing some time period where dust concentration conditions in the freeboard are in the ignitable range. To the author's knowledge, the time evolution of dust concentration conditions in a fluidized bed during start-up and shutdown has not been studied and would be a worthy subject for investigation from the standpoint of process safety. With no inflow of powder, Maurer (cone) discharges can be safely ignored; however, capacitive discharges from ungrounded conductors or propagating brush discharges from insulating surfaces are always a threat. The usual precautions of insuring secure grounding and bonding of all plant components (see in Sec. 5.2, "Plant Grounding and Bonding") and avoiding any use of plastic piping or insulating liners where charged granular solids are present (see in Sec. 5.2, "Insulating Liners") are imperative safety measures.

5.2 Hazards in Peripheral Equipment and Processes

Selected aspects of safe practice in solids handling are covered below. For additional information, refer to the rules for plant safety prepared by the Expert Commission for Safety in the Swiss Chemical Industry (ESCIS, 1988). While making no mention of fluidization, this source provides many practical suggestions for the avoidance of electrostatic ignition risks in powder handling operations.

Plant Grounding and Bonding. Most ignitions in manufacturing plants and commercial facilities where flammable dusts are present are due to capacitive sparks, and they can almost always be prevented by bonding together and grounding all conductive components. Therefore, the single most important measure that can be taken to reduce electrostatic risks is to insure that bonds and ground wires are installed in all equipment and that these remain in good repair at all times. Regular inspection and testing programs for bonds and ground connections are absolutely vital in any powder-processing facility. A particularly important inspection issue is to make sure that bonds and grounds are properly used. Far too many preventable accidents have occurred because perfectly adequate ground connections have not been reconnected after maintenance or installation work. The integrity of bonds and ground connections is ordinarily tested by a resistance meter. These measurements should be made at a voltage of 500 V; any lower value may give misleading results. For conductors supposed to be bonded together, the resistance reading should be less than ~10 ohms. Resistances several orders of magnitude higher than this figure, while in fact safe and acceptable, may indicate that corrosion or a damaged cable exists somewhere and that the bond should be checked.

A simple example of the ESD risk associated with failure to bond conductors together is shown in Fig. 12. Here, an ungrounded funnel is being used to dump powder into a mixing vessel. Triboelectrification occurs as the powder slides down the sides of the funnel; both the powder and the funnel become charged. If the funnel collects enough charge to exceed the breakdown condition, a capacitive spark jumps to the grounded vessel, creating the possibility of an ignition of any flammable dust. An ignition in this circumstance is likely to have serious consequences because of direct worker exposure to any explosion or fire that results. The problem is easily avoided by connecting the funnel to the vessel.

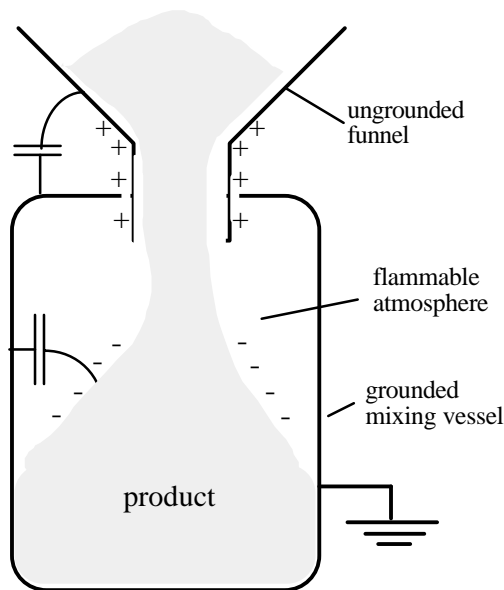


Figure 12. An ungrounded funnel mounted on the top of a grounded mixing vessel. As it falls down, the powder charges the funnel, and if sufficient charge accumulates to exceed breakdown, a spark can jump to the grounded vessel, causing an ignition.

Reports of many actual incidents serve to show how the failure to ground or bond equipment in a plant can cause ignitions via some rather unexpected mechanisms. One such incident occurred in a large hopper used to store polymer granules (Britton and Kirby, 1989). A deflagration occurred as material was being loaded into the hopper from a pneumatic transport line. The granules were too large to ignite and the presence of flammable vapors was ruled out; however, fines were present in the vessel from a previous batch operation. When the loading commenced, the fines resuspended, forming an ignitable cloud. The ignition itself was traced to a braided cable originally installed as a capacitive level meter but no longer in use and disconnected. The cable became charged very rapidly—quite possibly by a Maurer discharge driven by the inflow of powder—and then it capacitively discharged to the tank wall, igniting the dust cloud. Another example involved a metallic flow restrictor held in place by a gasket. Initially, no external bond was provided, because the gasket was itself conductive and provided a good electrical bond. Eventually, the gasket required replacement, but unfortunately the importance of a conductivity

specification for this disposable item was not recognized and an insulating gasket was installed. Thus, the flow restrictor became charged as powder flowed through it and a capacitive spark to ground ignited the powder. These examples serve to make us aware that there are some subtle aspects to bonding and grounding in powder handling equipment. The lesson here is an old one, that seemingly straightforward changes and maintenance procedures can have serious unintended consequences.

Tramp Metal. If a loose metal object, such as a misplaced tool, disconnected electrical cable, or broken blade from a blender falls into a vessel containing charged powder, this “tramp” metal will become electrostatically charged. If the object then comes close to a grounded wall or another metal object, a capacitive discharge may occur. Whether or not the energy of this spark is sufficient to cause an ignition depends on the size of the object and its charge. Table 6 shows that small metal implements generally have capacitance in the 10–20 pF range. Reference to the nomograph in Fig. 7 tells us that, to achieve sufficient energy to ignite polymer powders ($MIE \geq 5 \text{ mJ}$), the object would have to become charged to 20,000 V. For a small object, a brush discharge probably will occur long before such a high potential can be reached. Therefore, electrical discharges from tramp metal objects less than ~5 cm (~2 in.) in size are not ordinarily energetic enough to ignite most dusts. The ESD risk posed by tramp metal when flammable vapors or gases are present in combination with granular solids is much higher (refer to Sec. 5.2, “Available Fuels in Granular Solids Operations”).

Insulating Liners. Plastic film is commonly used as a liner material for paper bags and sacks for packaging many dry products. Such liners, usually electrically insulating, have been reported to create some new electrostatic hazards where none existed before. Refer to Fig. 13 showing the manual operation of dumping the contents of a bag into a mixing hopper. As the contents of the bag slide out, the liner becomes charged and, especially if it partially protrudes into the grounded hopper, a discharge may occur. A number of incidents of this type have been reported, in some cases with injuries to plant operators. The sacks can not be grounded so other methods must be employed to provide worker protection. Serious explosion incidents with larger lined sacks and bags in the past has prompted development of a new class of synthetic cloth materials which have woven semiconducting fibers into the fabric and provided grounding for the fibers (Wurr, 1992). Sacks made from these new fabrics (*flexible intermediate bulk containers* or FIBCs) are useful in dissipating static electric charge while minimizing any capacitive spark hazard.

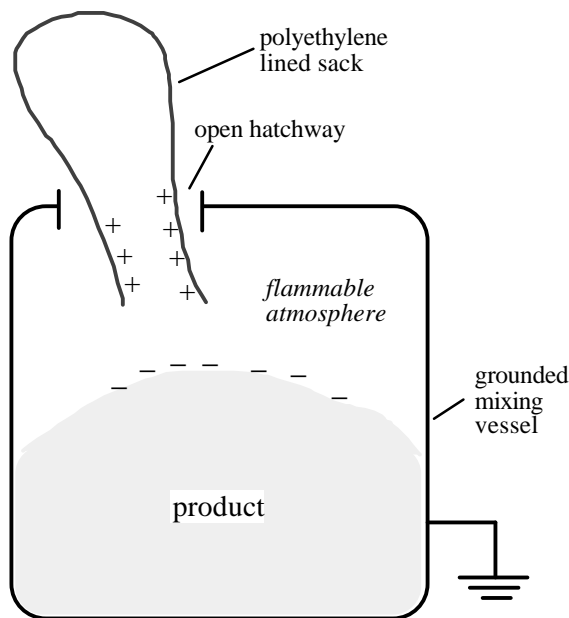


Figure 13. Dumping of dry product from a plastic lined sack into a mixing hopper. The inside of the liner can become charged as the product slides out and a discharge can lead to ignition of a flammable atmosphere under some circumstances.

The use of plastic materials for piping and vessel internals is best avoided whenever possible. Likewise, glass or epoxy liners are not to be used except when absolutely required in a particular manufacturing or processing operation. Plastic, epoxy, and glass can become electrically charged by contact with granular solids. For insulating materials with any kind of conductive backing, such as lined vessels or pipes, very powerful propagating brush discharges, capable of igniting almost any flammable dust, become possible (refer to Sec. 4.2, “Propagating Brush Discharges”). Experience has shown that plastic pipe can become conductive on an exposed surface due to the accumulation of dirt or moisture from rain or snow (Lüttgens, 1985). Once this conductive layer has formed, the conditions are established for a propagating brush discharge.

In the case of lined vessels, one method for avoiding the occurrence of propagating brush discharges is to limit the maximum breakdown voltage of the liner to 4 kV or less (Lüttgens and Glor, 1989). According to this strategy, the liner must be thin enough so that electrical breakdown occurs

through the liner before a propagating brush discharge can happen. Dielectric breakdowns through the liner are much less energetic than a propagating brush discharge and so are less likely to ignite powders. Unfortunately, the 4 kV breakdown restriction imposes an unrealistically low limit on the thickness for most typical liner materials. For example, the glass used in vessel liners, with a breakdown strength of 20 kV/mm, would be restricted to thicknesses less than 200 μm by this rule. Present-day glass-on-metal lining technology is not capable of making chemical-resistant linings with good uniformity less than ~ 1 mm. It is likewise difficult to prepare uniform epoxy liners at these thicknesses. Therefore, elaborate measures such as inerting are often employed when lined vessels are used with triboelectrically active, flammable materials.

Secondary Explosions. The severity of a dust explosion can be greatly magnified if a secondary explosion takes place. Fig. 14 depicts a typical scenario for these destructive events. A localized, possibly quite minor deflagration occurs initially in one part of a plant. The associated air blast disturbs and entrains the dust layer accumulated on the floors and walls of the galleries and passageways connecting different parts of the plant. Then, either the initial thermal blast or the fire from the primary explosion ignites one or more secondary ignitions. These explosions can be very severe, propagating throughout the plant and engulfing an entire facility. Such incidents have been responsible for a number of truly devastating grain elevator explosions causing scores of fatalities. Their severity can be traced to dusty product that has been allowed to accumulate throughout the plant. Secondary explosions are easily prevented by good housekeeping. A useful rule of thumb, permitting quick assessment of the risk of a secondary explosion caused by deposited dust in a plant, is the “paper clip” test. If the deposited dust layer on the floor and other surfaces in a plant exceeds the thickness of a paper clip, about 1 mm (0.04 in), then the risk of a secondary explosion should be considered high. While true that conscientious cleanup practices greatly reduce hazards, a sudden piping or vessel containment failure also can create flammable dust suspensions in the galleries and passageways of any manufacturing facility.

Electrostatics enters into the problem of secondary explosions in several ways. First, an electrostatic spark may be the ignition source of the primary explosion. Second, an electrostatic spark can serve to ignite a dust cloud if particulate spews out at high velocity as a result of a sudden piping or vessel containment failure. Similar containment failures have occurred with insulating liquids and can not be ruled out for powders. For example,

the dust cloud issuing from a break in a pneumatic line is likely to be very highly charged. To guard against ESD ignition in such occurrences, good grounding and bonding practices are important so that the chance of a capacitive discharge is minimized.

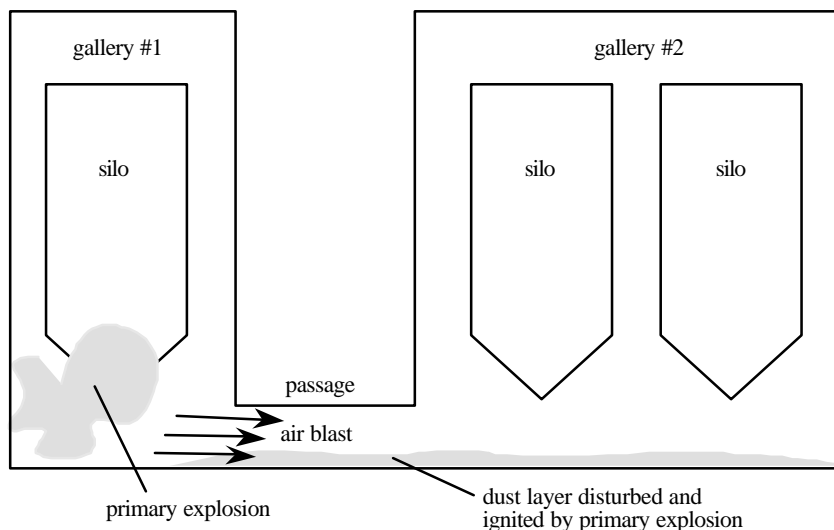


Figure 14. A secondary explosion of the accumulated dust in passage ways and galleries by a minor initial explosion can propagate throughout a plant with devastating results.

Available Fuels in Granular Solids Operations. In powder and granular solids handling operations, dangerous underestimation of the likelihood of ignition results if due consideration is not given to the possibility that “unanticipated” fuel is present. An obvious example involves the form in which polymer solids are commonly packaged for delivery to commercial plastic component manufacturers. There is no possibility that these particles—granules, prills, pellets, tablets, usually sized above ~1 mm—will ignite; however, attrition of these products during handling operations always produces fine particles. These fines settle out slowly and are usually quite flammable. There is also the fairly common situation during switch loading of a vessel that the fines from a previous operation provide the fuel for an ignition caused by the larger granules being loaded into the vessel. Refer back to the switch loading incident described in Sec. 5.2.

Another far more dangerous unanticipated fuel problem exists when a flammable gas or solvent vapor is present with the granular solids. This combination is a serious ESD hazard because it brings together the high charging tendencies of large particles with the low MIE of flammable vapors (Jones and King, 1991). The nomograph of Fig. 7 shows that hydrocarbon vapors can be ignited with an energy of ~ 0.25 mJ, a factor of twenty lower than the conservative MIE value used for polymer powders. When this combination occurs in a vessel larger than approximately 2 m^3 in volume, Table 7 specifies that special precautions are to be taken. This usually means seeking assistance from a qualified safety expert specializing in electrostatic hazards.

5.3 Other Nuisances and Hazards

An ungrounded tote bin containing large granules of certain materials, especially polymers such as polyethylene, can retain triboelectric charge for days or weeks. Many an unsuspecting operator has discovered this lesson the hard way when using a bucket or scoop to collect a sample from a storage bin. If the person receives this shock while standing on a ladder or in any vulnerable position, there is the possibility of dropping a tool or sustaining a fall. Most human subjects can perceive an electrical discharge as low as $1\text{ }\mu\text{C}$ of transferred charge, and strong physiological shocks can cause involuntary muscle contractions. Such discharges are not ordinarily energetic enough to ignite powder (though flammable vapors would present a risk). To avoid unexpected, physiological shocks, tote bins should be grounded. Tote bins made of insulating plastic can be equipped with passive discharge foils, like the one shown Fig. 15, to reduce the risk.

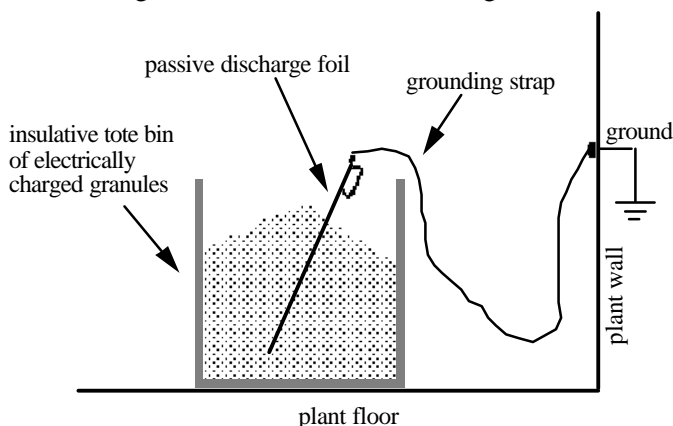


Figure 15. Grounding foil for use in open bins of charged granular material. Foil must remain connected to ground.

The same particle charging that affects fluidization conditions has an adverse effect on powder flow due to increased cohesion. For example, it has been found that electrostatic effects increase pressure drops (Smeltzer, Weaver, and Klinzing, 1982) and also exacerbate choking phenomena (Joseph and Klinzing, 1983) in pneumatic transport lines. Humidification is often not a viable option in reducing these problems. Furthermore, bridging problems at discharge chutes are exacerbated. The conventional solution of using vibration to facilitate powder flow, while effective, is not always practical. There have been incidents where plant operators have encountered flow problems involving hoppers, have opened them up, attempted to unblock the discharge with metal rods or other implements, and have felt or observed strong electrostatic sparks. Besides the obvious ignition hazard involving the powder (or any other flammable material present), there is also the possibility of a worker receiving a shock and sustaining an injury.

6.0 CONCLUSION

The objective of this chapter has been to place in context the electrostatic hazards associated with powder and granular solids handling in facilities where fluidized or spouted bed units are found. The first task undertaken has been to review triboelectrification, the principal charging mechanism associated with powders and granular materials, and charge relaxation, the mechanism by which charge is dissipated. Then, the relationships among charge, electric field, and electrostatic potential were elucidated. Next, certain electrostatic phenomena common in fluidized beds were covered. It is found that bipolar charging during fluidization limits hazards but that the specific charge held by individual particles is high enough to suggest potential risks in the right circumstances. Following this, some general aspects of ESD dust ignition criteria were summarized, including the fire triangle, the MIE (minimum ignition energy) of dusts, and the different types of electrostatic discharges and their relative likelihood of igniting flammable powders. Finally, some of the specific hazards, and steps required to abate them in dry solids handling facilities were discussed. The emphasis has been on known hazards associated with the conventional powder handling apparatus and systems needed in support of a fluidized or spouted bed unit.

A difficulty in convincing the experienced plant engineer or operator of the importance of these issues is that, while electrostatic effects in fluidized beds have been known about for over fifty years, ESD induced fires and explosions within them are apparently quite rare. Skepticism would be the understandable reaction to any statement suggesting that fluidization is inherently dangerous with respect to ESD. Nevertheless, in this chapter, two points are made about ESD hazards and fluidization. First, certain aspects of normal fluidized bed operation (*viz.*, start-up and shutdown) seem to feature all the requisites for a dust explosion caused by an electrostatic spark. After all, a fluidized bed is just a vessel, usually constructed of metal and similar in shape and size to the types of hoppers and reaction vessels that have been blowing up regularly since the beginning of the industrial revolution. Dust explosions, while rare, are not at all unknown and they are a true hazard to be dealt with. Therefore, the same precautions routinely accepted in all other parts of a particulate solids processing facility should without question be taken in fluidized bed units. Second, at least in the fairly typical setting of a manufacturing or powder processing facility, fluidized or spouted bed units are apt to be placed in proximity to rather dangerous company. Pneumatic transport systems and components such as mixing hoppers and storage silos are all well-known to present safety risks (Glor, 1988; Lüttgens and Glor, 1989; Jones and King, 1991). Proper consideration must be given to the hazards associated with any component used in support of a fluidized bed's normal operation.

A listing of general yet practical rules for reducing electrostatic hazards in powder handling seems a good way to conclude this chapter. These rules make no specific mention of fluidization, yet provide excellent guidance in minimizing risks (Jones and King, 1991; Cross, 1987).

- (i) In any plant design, minimize the volume of flammable atmospheres.
- (ii) Reduce electrostatic charging by reducing flow and separation velocities.
- (iii) Ground and bond all metal plant components and accessories. Institute a regular inspection and maintenance program for these grounds.
- (iv) Provide all personnel likely to be exposed to flammable atmospheres with appropriate antistatic footwear.
- (v) Do not use highly insulating flooring materials and do not cover flooring with insulating paints, tapes, or other treatments.

- (vi) Use of plastics such as pipes and funnels in flammable atmospheres should be avoided whenever possible.
- (vii) Electrostatic eliminators, not themselves capable of producing a spark, should be used on sheets and films of insulating materials before they enter hazardous atmospheres.
- (viii) Be especially careful of mixtures of insulating particles and flammable liquids.
- (ix) Specify properly designed explosion suppression or venting or N_2 gas inerting in all vessels containing ignitable powders.
- (x) Exercise good housekeeping practice in powder handling facilities to avoid buildup of dust layers.
- (xi) Exercise special care in all situation where manual operations are performed, providing interlocks, grounding straps, and blast protection.

The relative rarity of dust and powder ignitions makes them a unique sort of industrial safety threat. Because their occurrence is not routine, operating personnel eventually relax their guard, and too often this sort of behavior leads to dangerous incidents. The evidence that dust explosions are almost unknown within fluidized beds is an especially challenging problem for the safety officer, who must encourage vigilance even when no one remembers the last electrostatic incident.

ACKNOWLEDGMENT

The author's understanding of electrostatics and powders has benefited greatly from associations with many individuals who have freely shared their expertise. In particular, he acknowledges close collaborations with J. L. King, formerly of GE Plastics, Parkersburg, West Virginia (USA), and Y. Matsubara of the National Institute of Fire and Disaster in Tokyo, Japan. He gratefully acknowledges past financial support from GE Plastics, Inc., and the Petroleum Research Fund of the American Chemical Society. Over the years, a number of very interesting consulting assignments from Eastman Kodak Company and Xerox Corporation have helped to broaden his perspective of electrostatic hazards. He is also thankful to G. S. P. Castle and G. M. Colver, who brought certain tribocharging data for fluidized beds to his attention.

REFERENCES

- Anon., "Antistatic Agents," *Modern Plastics Encyclopedia*, 70:275–277 (1993)
- Bafrnec, M., and Beña, J., "Quantitative data on the lowering of electrostatic charge in a fluidized bed," *Chem. Engrg. Sci.*, 27:1177–1181 (1972)
- Bartknecht, W., *Explosions*, (translation of German text by H. Burg and T. Almond), Springer-Verlag, New York (1981)
- Bartknecht, W., "Prevention and design measures for protection against dust explosions," in *Industrial Dust Explosions* (K. L. Cashdollar and M. Hertzberg, eds.) ASTM tech. pub. #958, pp. 158–190 (1987)
- Bauser, H. "Static electrification of organic solids," *Dechema Monograph* (Frankfurt: Verlag Chemie) 72:11–29 (1974)
- Blythe, A. R., and Reddish, W., "Charges on powders and bulking effects," *Inst. Phys. Conf.*, Ser. No. 48, pp. 107–114 (1979)
- Bodurtha, F. T., *Industrial Explosion Prevention and Protection*, McGraw-Hill, New York (1980)
- Boland, D., and Geldart, D., "Electrostatic charging in gas fluidized beds," *Powder Technol.*, 5:289–297 (1971/72)
- Boschung, P., and Glor, M., "Methods for investigating the electrostatic behaviour of powders," *J. Electrostatics*, 8:205–219 (1980)
- British Standards Institute, "Control of undesirable static electricity," British Standard #5958, parts 1 and 2, London (UK) (1991)
- Britton, L. B., and Kirby, D. C., "Analysis of a dust deflagration," presented at Flammable Dust Explosion Conf., St. Louis, MO, pp. 375–396 (Nov. 1988)
- Britton, L. G., "Systems for electrostatic evaluation in industrial silos," *Plant/Operations Prog. (AIChE)*, 7:40–50 (1988)
- Britton, L. G., "Using material data in static hazard assessment," *Plant/Operations Prog. (AIChE)*, 11:56–70 (1992).
- Butters, G., "Dust explosion prevention and protection in the plastics industry," *Plastics Rubber Proc. Applic.*, 5:27–33 (1985)
- Ciborowski, J., and Wlodarski, A., "On electrostatic effects in fluidized beds," *Chem. Engrg. Sci.*, 17:23–32 (1962)
- Ciborowski, J., and Zakowski, L., "Dust removal in a fluidized bed; II. Electrostatic effects in a fluidized bed and their effect on dust-removal process efficiency," *Inz. Chem.*, 5:753–762 (1975); English translation in *Int. Chem. Engrg.*, 17:538–548 (1977)
- Cobine, J. D., *Gaseous Conductors*, Dover Press, New York (1958)
- Colver, G. M., "Bubble control in gas-fluidized beds with applied electric fields," *Powder Technol.*, 17:9–18 (1977)

868 *Fluidization, Solids Handling, and Processing*

- Corion Technologies, "Supersonic nozzle electrostatic neutralizer," Corion Technologies, Inc., product literature, Woburn, MA (1989)
- Cross, J. A., "Electrostatic charging and ignition of dusts," *I. Chem. E. Symposium*, Ser. No. 58, pp. 1–10 (1980).
- Cross, J. A., *Electrostatics - Principles, Problems, and Applications*, Adam-Hilger, Bristol (UK) (1987)
- Davies, G., and Robinson, D. B., "A study of aggregative fluidization," *Can. J. Chem. Engrg.*, 38:175–183 (1960)
- Eckhoff, R. K., "Toward a minimum ignition energy for dust clouds," *Comb. and Flame*, 24:53–64 (1975)
- Eichel, F. G., "Electrostatics," *Chem. Engrg.*, 153–167 (Mar. 13, 1967)
- ESCIS (Expert Commission for Safety in the Swiss Chemical Industry), "Static electricity: rules for plant safety," *Plant/Operations Prog.*, 7:1–22 (1988)
- Fasso, L., Chao, B. T., and Soo, S. L., "Measurement of electrostatic charge and concentration of particles in the freeboard of a fluidized bed," *Powder Technol.*, 33:211–221 (1982)
- Field, P., "Dust Explosions," in *Handbook of Powder Technology*, (J. C. Williams and T. Allen, eds.), vol. 4, Elsevier, Amsterdam (1982)
- Fujino, M., Ogata, S., and Shinohara, H., "The electric potential distribution profile in a naturally charged fluidized bed," *Funt. Kog. Kaishi*, 20:280–289 (1983); English translation in *Int. Chem. Engrg.*, 25:149–159 (1985)
- Gallo, C. F., and Lama, W. L., "Some charge exchange phenomena explained by a classical model of the work function," *J. Electrostatics*, 2:145–150 (1976)
- Gibson, N., "Electrostatic hazards in filters," *Filt. and Sep.*, 16:382–386 (1979)
- Glor, M., *Electrostatic Hazards in Powder Handling*, Research Studies Press, London (UK), 1988
- Guardiola, J., Ramos, G., and Romero, A., "Electrostatic behaviour in binary dielectric/conductor fluidized beds," *Powder Technol.*, 73:11–19 (1992)
- Guardiola, J., Rojo, V., and Ramos, G., "Influence of particle size, fluidization velocity, and relative humidity on fluidized bed electrostatics," *J. Electrostatics*, 37:1–20 (1996)
- Harper, W. R., "Electrification following the contact of solids," *Contemporary Phys.*, 2:345–359 (1961)
- Harris, J. O., "Electrostatic beneficiation of eastern Canadian coals using a fluidized bed" M. S. thesis, pp. 74–76, Univ. Western Ontario, London, Ont., Canada (1973)
- Hughes, J. F., Corbett, R. P., Bright, A. W., and Bailey, A. G., "Explosion hazards and diagnostic techniques associated with powder handling in large silos," *Inst. of Physics (UK) Conf.*, Ser. #27, pp. 264–275 (1975)

- International Electrotechnical Commission, Standard IEC, 1241-2-3 (1994).
- Johnson, T. W., and Melcher, J. R., "Electromechanics of electrofluidized beds," *Ind. Eng. Chem. Fundam.*, 14:146–153 (1975)
- Jones, T. B., *Particle Electromechanics*, Cambridge University Press, New York (1995)
- Jones, T. B., and King, J. L., *Powder Handling and Electrostatics*, Lewis Pub., Chelsea, MI (USA) (1991)
- Joseph, S., and Klinzing, G. E., "Vertical gas-solid transition flow with electrostatics," *Powder Technol.*, 36:79–97 (1983).
- Katz, H. M., "Studies of particle size distribution in fluidized beds," U. S. Atomic Energy Commission, Rept. ANL-5725 (May, 1957)
- Katz, H., and Sears, J. T., "Electric field phenomena in fluidized and fixed beds," *Can. J. Chem. Engrg.*, 47:50–53 (1969)
- Kisel'nikov, V. N., Vyalkov, V. V., and Filatov, V. M., "On the problem of electrostatic phenomena in a fluidized bed," *Izv. Vyss. Uch. Zav, Khim. Khim. Tekhn.*, 6:964–969 (1966); English translation in *Int. Chem. Engrg.*, 7:428–431 (1967)
- Konrad, K., "Dense-phase pneumatic conveying - a review," *Powder Technol.*, 49:1–35 (1986)
- Lapple, C. E., "Electrostatic phenomena in particles," *Adv. Chem. Engrg.*, vol. 8, pp. 1–96 (T. B. Drew, G. R. Cokelet, J. W. Hoopes, and T. Vermeulen, eds.), Academic Press, New York (1970)
- Law, S. E., Thompson, S. A., and Balachandran, W., "Electroclamping forces for controlling bulk particulate flow: charge relaxation effects," *J. Electrostatics*, 37:79–94 (1996)
- Leva, M., "Elutriation of fines from fluidized systems," *Chem. Engrg. Prog.*, 47:39–45 (1951)
- Loeb, L. B., "Static Electrification-II," in *Progress in Dielectrics*, vol. 5, pp. 233–289 (J. B. Birks, and J. Hart, eds.) Academic Press, New York (1963)
- Louvar, J. F., Maurer, B., and Boicourt, G. W., "Tame static electricity," *Chem. Engrg. Prog.*, 90:75–81 (1994)
- Lowell, J., and Rose-Innes, A. C., "Contact Electrification," *Adv. Phys.*, 29:947–1023 (1980)
- Lupinski, J. H., and Gorowitz, B., "Powder coating of magnet wire," General Electric Co., Tech. Info. Ser. #79CRD166 (July, 1979)
- Lüttgens, G., "Collection of accidents caused by static electricity," *J. Electrostatics*, 16:247–255 (1985)
- Lüttgens, G., and Glor, M., *Understanding and Controlling Static Electricity*, Expert-Verlag, Ehningen bei Boblingen (Germany) (1989)

870 *Fluidization, Solids Handling, and Processing*

- Maurer, B., "Discharges due to electrostatic charging of particles in large storage silos," *Ger. Chem. Engrg.*, 2:189–195 (1979)
- Maurer, B., Glor, M., Lüttgens, G., and Post, L., "Test rig for reproducible generation of discharges from bulked polymeric granules," *J. Electrostatics*, 23:25–34 (1989)
- Maxwell, J. C., *A Treatise on Electricity and Magnetism* (3rd ed.), Clarendon Press, Cambridge, 1891; republished by Dover Press, New York (1954)
- McAllister, D., Smith, J. R., and Diserens, N. J., *Computer Modeling in Electrostatics*, Research Studies Press, Letchworth, UK (1985)
- Melcher, J. R., Alexander, J. C., and Zahedi, K., "Electrofluidized bed agglomeration and method of agglomerating," US Patent #4,146,371 (27 March 1979a)
- Melcher, J. R., Alexander, J. C., and Zahedi, K., "Fluidized bed particulate collectors," US Patent #4,154,585 (15 May 1979b)
- Miller, C. O., and Logwinuk, A. K., "Fluidization studies of solid particles," *Ind. Engrg. Chem.*, 43:1220–1226 (1951)
- National Fire Protection Association, "Static Electricity," NFPA Standard #77, Quincy, MA, USA (1983)
- National Fire Protection Association, *Fire Protection Handbook* (16th ed.), NFPA, Quincy, MA, USA (1986)
- Orband, J. L. R., and Geldart, D., "The use of an antistatic agent to improve powder flowability," *Part. Part. Syst. Charact.*, 12:204–206 (1995)
- Osberg, G. L., and Charlesworth, D. H., "Elutriation in a fluidized bed," *Chem. Engrg. Prog.*, 47:566–570 (1951)
- Rojo, V., Guardiola, J., and Vian, A., "A capacitor model to interpret the electric behavior of fluidized beds. Influence of apparatus geometry," *Chem. Engrg. Sci.*, 41:2171–2181 (1986)
- Singh, S., and Hsieh, H. P., "Evaluation of the role of electrostatics in the handling of alumina," *Particulate and Multiphase Processes*, (T. Ariman and T. N. Veziroglu, eds.), pp. 299–306, Hemisphere Pub., Washington, DC (1987)
- Smeltzer, E. E., Weaver, M. L., and Klinzing, G. E., "Pressure drop losses due to electrostatic generation in pneumatic transport," *Indust. Engrg. Chem, Proc. Des. Dev.*, 21:390–394 (1982)
- Talbert, C. M., Jones, T. B., and Dietz, P. W., "The electrospouted bed," *IEEE Trans. Ind. Applic.*, IA-20:1220–1223 (1984)
- Tardos, G., and Pfeffer, R., "A method to measure electrostatic charge on a granule in a fluidized bed," *Chem. Eng. Commun.*, 4:665–671 (1980)
- Taylor, D. M., and Secker, P. E., *Industrial Electrostatics: Fundamentals and Measurements*, Research Studies Press, Taunton, UK (1994)
- Tolson, P., "High-energy discharges from plastic surfaces," *J. Electrostatics*, 22:1–10 (1909)

- Tucholski, D. and Colver, G. M., "Triboelectric charging in a circulating fluidized bed," presented at 2nd Int'l. Conf. on Applied Electrostatics, Beijing, China (November, 1993)
- van de Weerd, J. M., "Generation and prevention of electrostatic charges in pneumatic transport of plastic powder," presented at First Int'l Symp. on Loss Prevention and Safety Promotion in the Process Industries, European Federation of Chem. Engrs., pp. 71-74, The Hague, The Netherlands (1974)
- van Drumpt, J. D., "Antistats," *Mod. Plastics Encyclopedia*, 68:150-154 (1991)
- Wilhelm, R. H., and Kwauk, M., "Fluidization of solid particles," *Chem. Engrg. Prog.*, 44:201-217 (1948)
- Wolny, A., and Kazmierczak, W., "Triboelectrification in fluidized bed of polystyrene," *Chem. Engrg. Sci.*, 44:2607-2610 (1989)
- Wolny, A., and Opalinski, I., "Electric charge neutralization by addition of fines to a fluidized bed composed of coarse dielectric particles," *J. Electrostat.*, 14:279-289 (1983)
- Wurr, E., "Electrostatic charge dissipation of FIBCs," *Powder Hand. Proc.*, 4:77-79 (1992)

Index

A

- ABE fermentation 661
- Abrasion 437, 439, 441, 455
- Abrasive materials 749
- Acceleration length 244
- Acceleration of solid particles 243
- Acceleration region 244
- Accommodation constant 197
- Acetic acid 650
- Acetobacter 650
- Acetone-butanol-ethanol
fermentation. *See* ABE fermentation
- Acidogenic 656
- Active splitters 762
- Additives
 - to flotation cell 614
- Adhesion
 - charge-related 829
- Adhesion tension 374, 375, 379
- Advanced Gas Conversion 621
- "Aerated" bulk density 715
- Aeration 251, 252, 720
- Aeration rate 252
- Aeration velocity 254
- Aerobic fermentations 634
- Aerodynamically equivalent spheres 777
- AGC-21 technology 621
- Agglomerates 365, 392
- Agglomeration 333, 334, 418, 423, 645
- Agglomerator 390
- Aggregate clusters 178
- Aggregation 418
- Aggregative fluidization 573
- Aggregative tendency 570
- Agricultural 335
- Agricultural seeds 479
- Air flows 754
- Air handling system 359
- Air injection 735
- Air knife 686
- Air pollution control 832
- Air pressure drop 741, 745
- Air purity 360
- Air tube 289
- Air velocities 752
- Air-Decrease Test 718
- Air-on-sleeve pinch valves 749
- Airlift bioreactor 658
- Airlift reactors 264, 626, 659
- ALFOL process 585
- Alginate 650
- Alginate bead bioparticles 643
- Alkaline kraft process 605
- Aluminum nitride 423
- Amorphous materials 439
- Anaerobic fermentation 583
- Animal cell culture 623, 635
- Annular plenum 361
- Annular three-phase fluidization 618

Annulus thickness 145
 Antibiotic production 623
 Antistatic agents 835, 853
 Applications 263, 295, 319, 334,
 355, 582
 Aqueous solvent processes 359
 Archimedes number 38, 186, 198
 Arching 708
 Aspect ratio 25
 Atomization 339
 Attrition 398, 405, 413, 435, 436,
 437, 439
 in cyclone 469, 473
 cyclone-produced 468
 minimization 475
 of particles 134
 Attrition constant 442
 Attrition extent 446
 Attrition indices 446
 Attrition mechanisms 473
 Attrition modeling 448, 449
 Attrition process 444
 Attrition rate 221, 222, 445, 446,
 450, 638
 Attrition rate distribution model 440
 Attrition resistance 448, 475
 Avalanche breakdown 842
 Avalanching particles 849
 Axial location 182
 Axial positions 181

B

Baffle plates 467
 Baffles 515, 659
 Bag filters 360
 Baghouse 360
 Bahco procedures 777
 Batch digesters
 control 608
 Batch processes 441
 Bauxite 496
 Beads
 magnetic 642
 Bed aspect ratio 25
 Bed collapsing 556
 instrument 569
 three-stage 562

Bed diameter 4, 6, 100, 191
 influence on mixing 20
 smallest 15
 Bed dynamics 4
 Bed expansion 11, 74, 645, 720
 Bed geometry 56
 Bed height 163, 466
 Bed side heat transfer 158
 Bed size 4
 Bed temperature 186
 Bed width 17
 Beds
 three dimensional 16
 two dimensional 16
 Bends 483, 742
 Benzene 585
 Binder 365, 368, 395
 Binder granulation 365
 Binder layer 373
 Binder penetration 380
 Binder viscosity 379, 383
 Binder:powder ratios 372
 Biofilm growth 639
 Biofilms 637, 639, 640
 Bioflocs 626, 641, 651
 Biofluidization 625, 635, 637
 Biological applications 586
 Biological processes 623
 Biological reaction 625
 Biological wastewater treatment 586
 Bioparticles 637
 Bioprocessing 658
 Bioreactor design 627
 Bioreactor hydrodynamics 643
 Bioreactors 586, 632
 centrifugal 660
 inverse 658
 Bioremediation 659
 Biosynthesis 634
 Biot number 504
 Bipolar charging 834, 864
 Birth rates 345
 Bladex 90 DF 405
 Blast furnace operation 588
 Bleaching 609
 pulp 604
 Bleaching operations 607
 Bleaching reaction 610

874 *Fluidization, Solids Handling, and Processing*

Blenke-Cascade reactor 660
Blinded-tee bends 483
Blockage problems 732
Blockages 738, 751
Blow tank design 733, 735
Blow tank discharge valves 749
Blow tank feeder 736
Blowing process 608
Bond Index 447
Bond's Work Index 453
Boosters 708
Bottom spraying 357
Bouduord reaction 555
"Boundary layer"
 of two-phase mixture 196
Brake 780
Branching 754
 pipes/ducts 753
Breakage 405, 439, 441
Breakage function 444
Breakdown strength of air 828
Bridge
 pendular 396
Bridging problems 864
Brush discharges 846, 849, 860
Bubble breakers 650
Bubble breakup 126
Bubble caps 32, 210, 223
Bubble channels 11
Bubble characteristics 13
Bubble coalescence 278, 649
Bubble columns 264
Bubble diameter 16, 49, 275, 388
 calculations 306
Bubble formation 274
Bubble fraction 11
Bubble frequency 276
Bubble phase 236
Bubble properties 65, 66
Bubble region 301
Bubble rise velocity 13, 17, 279
Bubble size 3, 125, 274
Bubble tracks 16, 17
Bubble velocity 15, 77, 388
 calculations 306
Bubble voidage 241
Bubble-cap distributors 476
Bubble-developing region 301

Bubble-induced
 attrition 462, 463, 464, 466, 478
Bubbleless G/S contacting 504, 507,
 556, 569
Bubbles 124, 237, 251
Bubbling 265, 504, 562
Bubbling bed 9, 31, 47, 82
Bubbling bed combustors 3, 84, 90
Bubbling bed models 318
Bubbling bed scaling laws 70
Bubbling dense beds 163
Bubbling dense fluidization 154
Bubbling fluid bed 502
Bubbling fluidization 154
Bubbling fluidized beds 70, 113
Bubbling frequencies 279
Bubbling jets 308
Bubbling velocity 720
Bubbling-slugging transition 80
Bubbling-to-slug flow transition 25
Bubbling-to-turbulent 139
Buhler Fluidstat system 686
Buildup problems 731
Bulk density 715
Bulk solids 714
Buoyancy 526
Buoyancy theory 272
Butenediol 585
Butynediol 585
Butyrate-degrading bioreactor 633
Bypass conveying 729, 731, 752
Bypassing 244, 245, 246, 247, 257
Bypassing characteristics 250, 252

C

CAFM 54
Calcium sulfate 423
Capacitance 848
Capacitive discharge ignition risks 844
Capacitive discharges 841, 842
Capacitive sparks 857
Capillary force 382
Capillary number 382
Capillary state 369
Carbon 633
Carbonaceous material 601
Carbothermal nitridation 423

- Catalyst 446, 564
- Catalyst activation 623
- Catalyst activity 616
- Catalyst attrition 438
- Catalyst attrition rate 793
- Catalyst particles 620
- Catalyst powders 562
- Catalyst replacement 618
- Catalytic cracking 1, 615
- Catalytic processes 475
- Catalytic reactors 435
- Cell aggregates 626
- Cell culture 635, 636
 - applications 623
- Cell suspension 658
- Cellulose 604, 605
- Centrifugal bioreactor 660
- Centrifugal force 794
- Centripetal force 794
- Ceramics 402
- CFB 24
- CFB scaling 91
 - laws 94
- Channelling 567, 720
- Chaotic systems 55
- Characteristic length 526
- Charge control 852
- Charge measurement 832
- Charge neutralization 846
- Charge reduction 835, 836
- Charge-related adhesion 829
- Charge relaxation 851
- Charge relaxation time 851
- Charge residence time 851
- Charge separation 834
- Charged particles 817
- Charging 829
- Chemical industry 335
- Chemical oxygen demand (COD). *See* COD
- Chemical process industry 614
- Chemical reaction 444
- Chlorine bleaching 609
- Chlorine-free bleaching 610
- Choking 96, 864
- Choking condition 259
- "Choking" transition 91
- Choking velocity 142, 145
- Cinnabar 523
- Circulating beds 47, 91
- Circulating fluidization 174
- Circulating fluidized beds 22, 54, 237
- Circulating fluidized model 145
- Circulation model 303
- Circulation times 344, 350
- Classification
 - Mainwaring and Reed 726
 - slugging 722
- Classification diagram
 - fluidization 718
- Classification techniques 718
- Clean-blow cycle 752
- Cluster diameter 49
- Cluster residence time 193
- Cluster Reynolds number 49
- Cluster strands 198
- Cluster velocity 193
- Clustering Annular Flow Model (CAFM) 54
- Clusters 23, 47, 178, 192, 523
 - dense-phase 570
- CMC-Na 397
- CO
 - smelting reduction 592
- CO conversion 6
- Co-immobilization
 - algae with bacteria 643
- Co-MSFB 545
- Coal
 - liquid fuels 583
- Coal ash 423
- Coal combustion 832
- Coal combustion process 476
- Coal gasification 319
- Coal liquefaction 585
- Coalescence 13, 366, 371, 381, 384, 385, 390, 411, 416
- Coalescence rates 15
- Coated particle morphology 355
- Coaters
 - spouted bed 335
- Coating 250, 333
- Coating mass morphology 363
- Coating mass uniformity 344, 354, 363
- Coating models 353
- Coating morphology 344

876 *Fluidization, Solids Handling, and Processing*

- Coating operations 331, 333
- Coating regime 387
- Coating tablets 263
- Coaxial injection 316
- Cocurrent solids flow 541
- COD 633
- Coefficient
 - heat transfer 129, 154
- Coefficient of restitution 31, 381
- Coefficient of sliding friction 31
- Cohesion
 - electrostatic 817
- Cohesive forces 64
- Cohesive powders 718
- Coke 423
- Cold flow studies 318
- Cold models 3, 6, 26, 77, 99
- Collapsing bed 556
- Collection efficiency 779, 780, 782,
784, 794, 811
- Colliding particles 367
- Collisions 441
- Colloidal silica 475
- Colonization 638
- Combustion of suspended dusts 837
- Combustion processes 444
- Combustors 1, 2, 23, 59, 100
- Comminution 435, 445, 463
- Concentration levels
 - for explosions 839
- Concentration profiles 293, 294
- Concentric jets 289
- Conduction 164
- Conductive additives 852
- Conductive coatings 835
- Conductive particles 825
- Cone discharges 849
- Cone-dosing valve 735, 736
- Cone splitter 762
- Cones 780
- Conical distributor plate 244, 247, 252
- Conical grids 211
- Conservation of mass 29
- Contact angle 373, 374, 375
- Contact efficiency 506
- Contact electrification 817, 819
- Contacting
 - particle-fluid 556
- Contained fluidized bed 660
- Containment failures 861
- Continuity 572
- Continuity equations 33
- Continuous cell suspension
 - processing 658
- Continuous coating 354
- Continuous mode 474
- Continuous processes 441, 446
- Continuum model 28, 29
- Contraction of the bed 84
- Control of electric charges 852
- Convection 169, 191
 - two-phase 195
- Convective coefficient 190, 196
 - at the wall 191
- Convective heat transfer 129
- Conversion loss 11
- Conveying 712, 713
- Conveying characteristics 724, 739
- Conveying pipelines 747, 751
- Conveying systems 478, 480, 482
 - pneumatic 738
- Conveying velocity 483, 756
- Cooking
 - wood chips 604, 605
- Copper 493, 519
- “Core-annulus” flow 144
- Correx process 588
- Cork particles 69
- Corona 852
- Corona discharge 828, 846
- Corona needle 853
- Corona neutralization 853
- Couette device 394
- Couette granulator 394
- Coulombic forces 832
- Counter-down 496
- Coupling effect 786
- Cracking 1
- Cracking catalyst 25
- Cracks 398
 - propagation of 398
- Critical specimen size 403
- Critical strain energy release
 - rates 401, 402
- Cultures 635
 - mixed 656
- Cupriferous iron ore 519
- Cushioning effect 472, 480

Cut point diameter 794
 Cycle time distribution 250, 350
 Cyclohexane 585
 Cyclone attrition 478
 Cyclone attrition rate 468, 470, 472
 Cyclone capacity 795
 Cyclone cones 780
 Cyclone design 783
 Cyclone dipleg 316
 Cyclone efficiency 146
 Cyclone inlet velocity 473
 Cyclone inlets 781
 Cyclone roof 782
 Cyclones 174, 360, 467, 468, 773
 low loaded 779
 roof 782

D

Damage 480
 Dampers 755
 DBT 370, 372
 De-aeration 726
 De-aeration factor 727
 De-aeration rate 730
 De-inking 613
 recycled paper 604
 Death rates 345
 Defluidization 118, 421, 423, 556
 Deformation
 granule 392
 Degradation 438, 441, 443
 Degradation behavior 437
 Degradation probability 444
 Delignification 605, 608, 609
 DeMarco-Lockwood flux model 598
 Dense bed 538
 Dense bed expansion 88
 Dense-particle phase 190, 171
 Dense phase 126, 127, 683, 724
 Dense phase convection 191, 192
 Dense phase conveying 480, 683
 advantages 693
 Dense phase suitability 730
 Dense phase system 753
 Dense phase transport 683, 708
 Dense phase transport systems 706
 Density 120, 185
 Density manipulation 641

Density ratio 41, 55, 72, 94, 573
 solid-to-gas 53, 80
 Design decisions 257
 Design procedure 742
 Desulfurization 586
 Deterministic chaotic systems 55
 Devolatilizer 237, 263
 Di-butyl-phthalate. *See* DBT
 Diameter 364
 mean 37
 surface volume mean 720
 Diameter effect 725
 Dicalite 372
 Difficult-to-convey materials 751
 Diffusion coefficients 354
 Digesters 609
 batch 608
 Dilatometer 423
 Dilatometry 418
 Dilute phase conveying 480
 Dilute-phase flow 752
 Dilution liquor 608
 Dimensional analysis 654
 Dimensionless parameters 69, 102
 Dimensionless subsidence time 562, 565
 DIOS process 599
 DIOS smelting 601
 Dioxin 609
 Dipleg pipe 780
 Diplegs 316, 812, 813
 Discharge valves
 blow tank 749
 Discharges 828, 846
 capacitive 841
 electrostatic 850
 Dispersion coefficient 22
 Dissipation mechanisms 850
 Dissolution test 355
 Distribution 533
 Distributor
 bullet-head 516
 Distributor attrition rate 461
 Distributor design 10
 Distributor plates 254, 257, 361
 Distributor zone 537
 Distributors
 gas 476
 DITS 659
 Dividing gas streamline 289

878 *Fluidization, Solids Handling, and Processing*

- Dixon classifications 724
- Dixon slugging classification 722
- Dolomite/limestone 80
- Donor Solvent process 585
- Dose-dumping 354
- Double entry fluidized bed reactor 660
- Downcomer 239, 247, 250
- Downcomer aeration 252
- Downcomer pressure drop 242
- Downflowing layers 24
- Draft tube 237, 238, 239, 240, 247, 250, 335, 356, 362, 364, 650
 - multiple 260
- Draft tube fluidized bed reactor 626
- Drag
 - fluid-particle 51
- Drag coefficient 35, 36, 43, 44, 155
- Drift flux 13
- Drop shatter tests 452
- Droplet size 340
 - distribution 339
- Dry paste 370
- Dual-fluid nozzle 339
- Dually injected turbulent separation (DITS) 659
- Duct design 755
- Duct sizing 754
- Ductwork 756
- Dust 435, 758
- Dust control systems 760
- Dust explosions 837, 861
- Dust extraction 754, 758
- Dust extraction system 759
- Dust extraction systems 766
- Dust hoppers 780
- Dust ignition 836, 838, 841
- Dynacracking process 263
- Dynamic wave 124
- E**
- Ebullated bed 585
- Ebullated bed reactors 615, 616, 618
- Economics 661
- Effective bed emissivity 171
- Effectiveness factor 506, 651
- Efficiency 794
- Elasticity 124
- Electric field strength 828
- Electric field threshold 852
- Electrical discharge 828
- Electrical grounding 857, 865
- Electroclamping 836, 857, 865
- Electrofluidized beds 836
- Electrolyte concentration 646
- Electrostatic discharges 817, 837, 849
- Electrostatic dust ignition 841
- Electrostatic effects 69, 835
- Electrostatic hazards 836, 850, 854
- Electrostatic ignition 818
- Electrostatic measurements 831
- Electrostatic phenomena 829
- Electrostatic potential 828
- Electrostatic risks 857
- Electrostatic sparks 839, 861
- Electrosuspensions 825
- Elemental chlorine-free (ECF)
 - bleaching 610
- Elutriated mass 441, 442, 445
- Elutriated particles 438
- Elutriation of fines 316
- Elutriation of solid particles 315
- Elutriation rate 441, 446, 450, 467
- Emissivity 171
- EMMS model 570
- Emulsion phase 236
- Encapsulation 250
- Energy dissipation 381, 572
- Energy requirement 593
- Energy transfer 153
- Energy-minimized multiscale model 569
- Entrainment 131, 185, 289, 308
 - solids 311
- Entrainment velocity 308
- Equations
 - dimensionless 29
- Equipment
 - fluidization 854
- Equipment efficiency 512
- Equipotentials 827
- Ergun equation 41, 43, 242
- Ergun expression 39
- Ergun relationship 36, 44
- Erosion 223, 747, 780
- ESD 817
- Esters 585
- Ethanol fermentation 658, 661
- Ethanol production 586
- Ethylene polymerization 585

- Euler numbers 169
- Evaporation
 - binder 371
 - of atomized droplets 340
- Evaporation time 343
- Exothermic reactions 837
- Expansion 122
 - dense bed 88
- Expansion effect 483
- Experimental verification 65
- Explosion examples 859
- Explosion incidents 859
- Explosion risk 839
- Explosions 818, 829, 837, 849
 - secondary 861
- Extraction systems
 - dust 754
- F**
- Falling cluster strands 198
- Falling strands 198
- False roof 782
- Fast fluidization 173, 174, 523, 525, 533
- Fast fluidized beds 178, 185
 - hydrodynamics 175
- FCC catalyst 122, 225, 229, 564, 570
- Feed line 289
- Feed temperature 618
- Fermentation 583, 586, 626, 634
- Film coating techniques 332
- Film resistance 165
- Filtration 360
- Fine particles 315
- Fine powder 365
- Fines 315, 435, 440, 835
 - reinjection 315
 - residence time 315, 317
- Fire triangle 837
- Fires 818, 829
- Fischer-Tropsch (F-T) 584, 614, 619
- Fixed bed systems 583
- Fixed beds 169
- Flakes 758
- Flamelike jet 308, 311
- Flammable dust 818
- Flat distributor plate 244
- Flexible intermediate bulk
 - containers 859
- Flocs 651
- Flooding point characteristic 497
- Flotation cells 613
- Flotation de-inking 613
- Flow 115
- Flow aids 392
- Flow behavior 726
- Flow patterns 296
- Flow rates
 - gas 647
- Flow ratio 245, 247
- Flow regime transitions 20
- Flow regimes 154
- Flow splitting 760, 762
- Flow splitting system 765
- Flow system
 - two-phase 572
- Flow through packed beds 154
- Flue gas desulfurization 586
- Fluid bed granulation 366, 372
- Fluid bed granulator 387
- Fluid dynamics model 317
- Fluid flow
 - no net 546
- Fluid mechanics 197
- Fluid penetration rate 377
- Fluid-bed granulator 357
- Fluid-lift solids recirculator 237
- Fluid-particle drag 51
- Fluid-particle interaction 570
- Fluid-particle systems 112
- Fluidization 423, 567, 573, 718
 - classification diagram 718
 - semi- 551
- Fluidization characteristics
 - of particles 556
- Fluidization equipment 854
- Fluidization properties 421
- Fluidization regime 644
- Fluidization regimes 139, 154
- Fluidization systems 583
 - three-phase. *See* Three-phase fluidization systems
- Fluidization
 - velocity 113, 118, 161, 254, 720
- Fluidized bed combustor 59
- Fluidized bed granulation 365
- Fluidized bed process 113, 455
- Fluidized bed tests 449

880 *Fluidization, Solids Handling, and Processing*

- Fluidized
 - beds 1, 22, 100, 435, 445, 585
 - advantages 331
 - with draft tube 356
- Fluidized dense-phase 724, 752
- Fluidizing
 - characteristics 562, 564, 565, 567
- Fluidizing-discharge-cone 735, 736
- Flux model 598
- Fly ash 739
- FMC char 270
- Foaming 600
- Foaming slags 602
- Food industry 335
- Force balance 572, 703
- Force probe 276, 279, 299
- Foscolo and Gibilaro theory 125
- Foster Wheeler circulating bed 100
- Fractional efficiency 777
- Fractional heat recovery 509
- Fracture toughness 399, 400, 402
- Fragmentation 437, 439
- Free fall 506
- Freeboard region 317
- Frequency ratios 69
- Friability 446, 447, 453
- Friability tests 447, 448, 452
- Friction 31
- Friction angle 38, 75
- Friction factor 154, 243, 695, 742
- Froude number 25, 38, 44, 61, 270, 272, 748
- Fuel
 - unanticipated 862, 863
- Funnel-flow effects 733
- Furnace
 - energy efficiency 593
- G**
- G/S contacting 502, 504, 506, 508
 - bubbleless 507
- G/S particle systems 506
- Gas bypassing 244, 245, 247, 250, 252
- Gas conductivity 158
- Gas convection 169
- Gas convective component 87
- Gas density 112, 113, 120
- Gas distributors 209, 455, 476
- Gas filtering 360
- Gas flow 361
- Gas flow rates 647
- Gas handling equipment 357
- Gas holdup 645, 646
- Gas inertia 53
- Gas inlet devices 32
- Gas leakage
 - from bubble 275
- Gas logging 660, 661
- Gas mixing 289
- Gas phase convection 191
- Gas thermal properties 191
- Gas tracer 245
- Gas velocity 10, 173, 422, 441, 464, 480, 482
- Gas viscosity 112, 113, 120, 131
- Gas-solid contacting 4
- Gas-solid two-phase jets 265, 308
- Gas-to-solid density ratio 94, 97
- Gas/solid (G/S) contacting 502. *See also* G/S contacting
- Gasification 263, 319
 - coal 599
- Gasifiers 90, 315
- Gatty system 686
- Gauss's law 826
- Geldart classification 720, 721, 722
- Geldart Group 114, 120
- Geldart Group A powders 119
- Geldart powder categories 75
- Geldart type D 356
- Germination damage 479
- Gill plates 361
- Glass particles 96
- Glucose 585
- Grace-Davison jet-cup attrition test 453
- Grain damage 480
- Grains 398
- Granular particles 642
- Granular solids 817
- Granular surface 382
- Granulation 250, 365, 366, 384, 386, 390, 395, 416
- Granulation operations 331, 333
- Granulation regimes 387
- Granulator 357
- Granulator designs 360

Granule deformation 392
 Granule formation 366
 Granule fracture 405
 Granule growth 368, 373, 380
 Granule size distribution 407, 409, 413
 Granule strengthening 392
 Granules 384, 398
 Gray surface 201
 Green agglomerates 392, 394
 Grid 209
 particle attrition at 135
 Grid design 209, 212
 Grid hole pitch 217
 Grid holes 217
 Grid jet attrition 476
 Grid jet attrition rate 462
 Grid pressure-drop 214
 Grindability 447
 Ground connections 857
 Group A 126, 129, 720, 724,
 730, 733
 Group B 126, 129, 130, 143, 720,
 724, 731, 733
 Group C 720, 724, 731, 733
 Group D 126, 129, 169, 720, 724,
 731, 732
 Growth functions 346
 Growth rate 390
 Gwyn equation 442
 Gwyn-type attrition apparatus 450
 Gwyn-type test 458

H

H-Coal process 585
 H-Oil 615
 H-Oil process 585
 Hamaker's two-flux formulation 172
 Handling operations 862
 Hardgrove Index 447, 453
 Hardness 405
 wall 443
 Hartmann cell 841
 Hazards 829
 electrostatic 818
 Head loss 766
 Heat capacity 191
 Heat exchanger tubes 467
 Heat recovery 509, 523

Heat transfer 87, 129, 130, 131,
 153, 504, 506, 508, 512,
 594, 595, 598, 601
 Heat transfer coefficient 155, 158, 185
 Heat transfer coefficients 179
 at the wall 182
 Heat transfer efficiency (HTE) 593, 595
 Heat transfer parameters 158, 181, 512
 Heat transfer rate 84
 Heat transfer stage 508
 Heat transfer surface 188
 Heating 360
 Heating rate dilatometry 418
 Heavy ions 854
 Helical baffles 659
 Hemicelluloses 605
 Herbs 496
 Heteropolysaccharides 633
 High-pressure feeders 713
 High-pressure pinch valve 749
 HIs melt process 599
 Hole density 217
 Horizontal tube 156
 Hot beds 59, 76, 99
 Hot melt coatings 357
 Humidification 831, 835
 Humidity 443
 Humidity control 359
 Hydraulic nozzles 339
 Hydrocarbon synthesis 4
 Hydrocarbons 6
 "Hydrocol" reaction 6
 Hydrocracking 615, 618
 Hydrodemetallization 615
 Hydrodenitrogenation 615
 Hydrodeoxygenation 615
 Hydrodesulfurization 615
 Hydrodynamic behavior 22
 Hydrodynamic characteristics 295
 Hydrodynamic diameter 25
 Hydrodynamic scaling parameters 69
 Hydrodynamic simulation 88
 Hydrodynamic Theory 124, 125
 Hydrodynamics 4, 6, 13, 35, 124, 178
 bioreactor 643
 Hydrogen consumption 619
 Hydrogenator 263
 Hydrophilic 375

882 *Fluidization, Solids Handling, and Processing*

Hydrophobic 375
Hydrotreating 614, 615, 618
Hysteresis 538

I

Ignition dust and powders 836
Ignition hazard 849
Ignition of suspensions 837
Ignition risks 844
Ignition sources 837, 839
Ignitions 841, 846, 854, 858
Ilmenite ores 423
Immobilization 637, 642
Impact stress 452
Incendive discharges 848
Indentation fracture test 401
Induction charging 824, 825
Industrial applications 582
Inertia 53
Inertial granulation 386
Inertial regime 387
Inerting 861
Inerting system 838
Inhibition 656
Injection
 multipoint 754
Ink particles 613
Ink removal 613
Inlet catch 794
Inlets 781
Inoculum 632
Interaction
 fluid-particle 570
Interfacial energies 373
Internally circulating fluidized bed 237
Internals 6, 467, 478
Interparticle Force Theory 124
Interparticle forces 30, 31
Interparticle friction 38
Intraparticle mass transfer 643
Iron 496
Iron ores 545, 553, 588
Iron oxide dust 755, 758
Iron oxide pellets 588
Iron oxide reduction 599
Iron-bath reactors 588, 590, 593
Isothermal dilatometry 420

J

Jenike shear stress unit 699
Jet
 flamelike 308
Jet attrition 456, 457, 458
Jet attrition test devices 448
Jet flow regimes 265
Jet half-angle 260, 271, 273, 311, 313
Jet momentum flux 272
Jet nozzle 251
Jet penetration 137, 212, 270, 272,
 273, 301
Jet penetration data 138
Jet penetration equation 259
Jet velocity 247, 289, 460
Jet-cup apparatus 453
Jet-cup attrition test 453
Jets
 gas-solid two-phase 265
 upwardly-directed 212
Jetting 265
Jetting fluidized bed 237, 265, 295
Jetting region 264, 301, 457
Jigging 551, 555

K

Kappa number 605, 608
Kernel
 coalescence 411
Kinetic motion of molecules 196
Kinetic wave 124
Kmiec correlation 121
Kolmogorov entropy 55
Kraft process 605
Kramers relation 512

L

Large-diameter pipeline systems 752
Layering 366, 409
LC-Fining process 585, 615
Leaching 492, 496, 502
Leakage
 electric charge 851
Lean gas phase 189
Lean phase gas convection 191
Lean phase heat transfer coefficient 192
Levitation 547, 551

Lignin 604, 605, 608
 Limits
 viscous or inertial 53
 Lined vessels 860
 Liner material 859
 Liquid binder 373
 Liquid bridges 366, 368, 369, 382
 Liquid iron 590
 Liquid mixing 647
 Liquid-solids velocity ratio 496
 Loading and unloading 855
 Local suspension density 186
 Long-distance applications 752
 Long-distance systems 739, 747
 Loss equations 766
 Low-temperature F-T synthesis 620
 Low-velocity slug-flow 724
 "Lubricants" 475
 Lubrication 787
 Lumped coefficients 3

M

Macromixing 583
 Magnesium 423
 Magnetic beads 642
 Magnetic particles 641
 Magnetically stabilized fluidized
 beds 657, 658
 Magnetizing roaster 519
 Mainwaring and Reed classification 726
 Mass coating distributions 351
 Mass distribution 347
 Mass flux 175
 Mass transfer 648, 651
 Mass transfer coefficient 9, 648
 volumetric 650
 Mass uniformity 344
 Materials characterization 398
 Maurer discharges 849
 Maxwell charge 824
 Maxwell's distribution 197
 Mean diameter 720
 Measurement
 particle charge 832
 Mechanistic model
 circulation 303
 Medicinal herbs 496
 Melter-gasifiers 588

Membrane walls 178
 Mercury extraction 523
 Merry's correlation 213, 229
 Metal objects
 tramp 859
 Methanogenic 656
 Methanogens 633
 Methanol 621
 Mickley-Fairbanks model 164
 Microwave heating 360
 MIE 841
 Minimal potential energy 572
 Minimum duct velocity 756
 Minimum fluidization 154
 Minimum ignition energy 839
 Minimum sintering temperature 418
 Minipot 690
 Mixing 6, 20, 413
 of phases 647
 solids 237, 648
 Mixing zone 293
 Mixture density 185
 Modeling 344, 480, 651
 post-combustion 598
 Models 2, 4, 26, 44, 100
 bubbling bed 82
 CFB 91
 design 56, 61
 fluidized bed 26
 gas throughflow 84
 mechanistically based 191
 post-combustion 598
 reactor 653
 simplifications 39
 small scale 39
 Modulating valve 736
 Moller Turbuflow 686
 Momentum balance 598, 699
 Momentum flux 272
 Monoclonal antibodies 586
 Monod kinetics 655, 656
 Morphology of particle coat 354, 355
 Motion equations 28, 29
 Movies 69
 Moving-bed transport 707
 Moving packed bed model 699
 Multi-flux analysis 201
 Multi-orifice plates 361
 Multiphase flow 604

884 *Fluidization, Solids Handling, and Processing*

Multiple draft tubes 362
Multipoint injection 754
Multiscale modelling 571
Multisolids bed 88
Multistage fluid bed 538

N

Natural vortex length 778
Neutralization
 charge 854
NH 514
Nitridation
 carbothermal 423
Non-inertial granulation 386
Non-inertial regime 390, 418
Non-solid granules 392
Nonbubbling system 492
Nondimensionalized values 28
Novel particles 641
Nozzles 339
Nucleation 366, 371, 409
Nuclei size 375
Numerical models 2
Numerical solution techniques 413
Nusselt number 169, 186, 512

O

Off-gas temperatures 594
Olivine sand 77
Ore preheating 519
Organic solvent processes 359
Orifice equation 216
Orifices 461
Oscillating fluid 551
Oscillating valve 736
Oscillation 547, 551
Oscillation generator 555
Outlet tube 782
Oven dried pulp 604
Ozone decomposition 5, 9

P

Packet conductivity 166
Packet model 172
“Pant leg” design 2
Paper
 recycled 604
Paper industry 604

Parametric effects 181, 182
Particle attrition 134, 220, 222
Particle balances 474
Particle characteristics 637
Particle charging 818, 819
 beneficial 836
Particle coating 354
Particle cohesion 418
Particle collision mechanism 314
Particle convection 169
Particle convective heat transfer 131
Particle degradation 435, 441,
 443, 479
Particle density 777
Particle density manipulation 641
Particle diameter 182
Particle drag 95
Particle effectiveness factor 651
Particle electromechanics 869
Particle materials 638
Particle mechanical properties 31
Particle packets 164, 192
Particle sampling methods 833
Particle shape 439, 724
Particle size 2, 3, 62, 113, 114,
 125, 129, 147, 191, 385,
 409, 439, 639, 792, 841
 determining 715
Particle size distribution 11, 380, 436,
 437, 439, 567, 724
Particle size selection 567, 716
Particle sphericity 73, 717
Particle structure 438
Particle terminal velocity 191
Particle trajectories 308
Particle velocity 197, 251, 308, 313
Particle-enhanced convection 196
Particle-fluid behavior 573
Particle-fluid system 571, 572
Particle-gas suspension 201
Particle-particle interactions 31
Particle-to-pipe diameter 725
Particle/gas suspension 185
Particles
 granular 642
 mixed-sizes 158
 novel 641
Particulate fluidization 573
Particulate material 398

- Particulate tendency 570
- Particulate 576
- Paschen's law 843
- Peclet number 654
- Peel off velocity 779
- Pendular bridge 396
- Pendular state 369
- Penetration 212, 377
- Penicillin production 586
- Perforated plates 210
- Permeability factor 726
- Petroleum 335
- Petroleum industry 614
- Petroleum intermediates 618
- Petroleum resid processing 614
- Petroleum resids 614
- pH 614, 633, 637
 - automatic control 632
- Pharmaceutical industry 263, 356
- Pharmaceuticals 335, 479, 634
- Phase mixing 647
- Phosphogypsum 423
- Phthalic anhydride reactor 3
- Physicochemical effects 637
- Pi theorem 26
- Pinch valves 749
- Pipe diameter 725
- Pipeline length 480
- Pipeline unblocking 751
- Pipelines 712, 747
- Pipes/ducts
 - branching 753
- Plant safety 857
- Plastic pipe 860
- Plasticizers 337
- Plates 22
- Plenum 223, 224, 361
- Plowing effect 778
- Plug flow
 - of coal 700
- Plug flow behavior 655, 698
- Plug flow operation 660
- Plug length 700, 703
- Plug pulse system 690
- Pneumatic conveyance 849
- Pneumatic conveying 441, 482, 713, 748
- Pneumatic conveying lines 435, 452, 747
- Pneumatic conveying systems 478, 479, 738
- Pneumatic transport 449, 506, 823, 834
- Pneumatic transport tube 240, 242
- Pneumatic transportation 712
- Poisson's equation 826
- Pollutant loading 632
- Polyethylene particles 100
- Polyethylene plastic 80
- Polymers 402
- Population balance 345, 352, 353, 407, 411, 413, 416
- Pore distribution 380
- Pore size 615
- Porosity 371
- Porous plate distributors 476
- Porous plates 22
- Post-combustion 590
- Post-combustion ratio (PCR) 593, 595
- Potential
 - electrostatic 828
- Potential energy 572
- Powder classification 715, 717, 729
- Powder handling 850
- Powder ignition 836
- Powder processing 857
- Powder systems 332
- Powder-binder systems 369, 372
- Powders 357, 366, 368, 715, 724, 817
 - catalyst 562
 - characterization 562
- Power 572
- Power generation 263
- Pre-reduction 555, 592
- Pre-reduction reactor (PRR) 590
- Predictive tools
 - for scale-up 586
- Preheating
 - ore 519
- Pressure 126, 223, 443
 - elevated 111
- Pressure balance 241, 813
- Pressure drop 243, 707, 726, 741, 811
- Pressure effects 120, 129
- Pressure fluctuations 66, 95, 139, 214
- Pressure loss 696, 766
- Pressurized fluidized bed 76
- Pressurized hot bed 59

886 *Fluidization, Solids Handling, and Processing*

Pretreatment 439
Probabilistic Modeling 352
Probes
 suspended 833
Process conditions 440
Process strategy 655
Process zone 400, 402
Processing time 363
Product inhibition 656
Propagating brush discharge 846
Proportional-integral (PI) controller 735
Proteins 636
 recombinant 634
Pseudo solid-solid reduction 553
Pseudo-layering 409
Pseudo-solid-solid reactions 546
Pulp 604
Pulp digester 609
Pulping 605
Pulse piston modeling 700
Pulse piston operation 700
Pulsed conveying system 686
Pulsed piston transport 699
PVC powder 725
Pyrite 523
Pyrite cinders 496

Q

q/m 834

R

Radial injection 316
Radial position 182, 185
Radiant heat transfer 129
Radiation fluxes 598
Radiation heat transfer 595
Radiative convection 191
Radiative heat transfer 162, 171, 199
Raining 508, 523
Ranz-Marshall relation 512
Rat-holing 730, 733
Rate constant 5
Reactor configuration 655
Reactor diameter 650
Reactor feed temperature 618
Reactor start-up 633
Rebound 368
Recirculating fluid beds 706, 707
Recirculating fluidized bed 237, 257

Recombinant proteins 634
Recycle rate of solids 91
Recycling 613
Reducer
 three-section 555
Reduction
 pseudo solid-solid 553
Reentrainment 759, 779
Refractories 594
Relative humidity 831, 835
Renewal mechanism 164
Reoxidation 594
Resid processing 614
Residence time 15, 197, 217, 497
Residence time distribution 9
Restitution
 coefficient of 31, 381
Return leg 456
Reversals
 transient field 856
Reynolds number 37, 41, 43, 198,
 512, 654
Richardson-Zaki correlation 645
Riffle box 762
Riser density 145
Riser diameters 22
Risers 456
Risks

 startup and shutdown 856
Rittinger's law 463
Roots-type blowers 752
Roping 765
Rotary splitter 762
Rotary valves 455, 736
Rotating-disc valve 749
Rotor granulator 357

S

Saccharomyces cerevisiae 661
Safety 838, 857
Salt solution 646
Saltation 725, 758
Sand 117, 270
Saturated granular surface 367
Saturation 369
Scale models 26, 39, 56, 59, 61
Scale-up 1, 2, 317, 362, 653, 654
 example 363
 jet nozzle 273

- Scaled laboratory models 100
- Scaling 82
 - simplified 44
- Scaling experiments 28
- Scaling laws 54, 94
- Scaling relationships 26, 27, 38, 39
 - verification 65
- Scattering approximation 173
- Scouring action 167
- Screw feeders 455
- Scrubber technology 832
- Scrubbing 585
- Sea sand 565
- Seams 781
- Secondary air injection 708
- Sedigraph 556
- Sedigraph procedures 777
- Seeded coal process 263
- Seeds 496
- Segregation effect 830
- Segregation roasting 519
- Selection-for-breakage 444
- Self preserving 413
- Semco system 686
- Semi-fluidization 551
- Separator 788
- Sewage treatment 632
- SFL. *See* Staged fluidized leaching
- Shallow beds 537
- Shallow fluid beds 541
- Shallow fluidized beds 163
- Shape factors 777
- Shear measuring device 369
- Shear rate 394
- Shear stress 242
- Shocks 863
- Shrouds 219, 230, 289
- Shutdown 260, 735, 736
 - risks 856
- Siderite 270
- Silica 475
- Silo 827
- Simplified scaling 41, 44, 61, 99
- Single plenum 361
- Single traverse cyclone 788
- Single-slug conveying 729
- Sinter-neck growth 420
- Sintering point 422
- Sintering temperature 418, 421
- Sipernat 372
- Size distribution 717, 792
- Slag behavior
 - modeling 602
- Slag foam 599
- Slag layer 589, 590, 594, 599, 600, 601
 - behavior 599
- Slag phenomena 596
- Slip factor 25
- Slip velocity 22, 42, 573
- Slow motion 126
- Sludge retention time 654
- Slug flow 720
- Slug velocity 241
- Slugging 13, 25, 69, 74, 251
- Slugging beds 38
- Slugging characteristics 725
- Slugging classifications 718, 722
- Slugging fluidized bed 73, 240
- Slurry 367
- Slurry bubble column 620
- Slurry bubble column fermentors 586
- Slurry bubble column reactors 585
- Slurry Phase Distillate process 620
- Slurry reactor 621
- Smelting reduction 588, 590
 - economics 603
- Smelting reduction furnace (SRF) 590
- Smelting reduction process
 - two-stage 592
- Snowballing 409
- Sodium carbonate 370, 372
- Sodium hydroxide 613
- Softening point 418
- Solid circulation rate 239
- Solid concentration 179, 185, 190, 191
- Solid flow mass flux 175
- Solid fraction profile 77, 94, 95, 96, 99
- Solid loadings 265
- Solid mass flux 182
- Solid mixing 20
- Solid phase 604
- Solid-solid reduction
 - pseudo 553
- Solid-to-gas density ratio 77, 80
- Solids
 - recycle rate 91

888 *Fluidization, Solids Handling, and Processing*

- Solids circulation 240, 295, 299, 301
- Solids circulation
 - rate 250, 251, 252, 257, 296
- Solids concentration 186, 193
- Solids distribution 518
- Solids distributor 516
- Solids entrainment 311, 313
- Solids feed 32
- Solids flow 695
- Solids flow patterns 296
- Solids flow rates 538
- Solids flow regions 299
- Solids flux 91
- Solids flux profile 24
- Solids holdup 644, 645
- Solids loading 239, 753, 778
- Solids mass flux 473
- Solids mixing 237, 296, 648
- Solids mixing rate 306
- Solids particle velocity 272
- Solids recycle rate 100
- Solids residence time 441
- Solids temperature 514
- Solids transport 251
- Solids-to-air mass flow rate ratio 753
- Solvay process 585
- Solvent Refined Coal process 585
- Solventless coatings 357
- Sorbent material 80
- Sorbitol 585
- Sparger 211
- Sparger grids 218
- Sparking 843
- Sparking potential 843
- Sparks 839, 841, 842
- Specific charge 822, 832, 864
- Spheres
 - aerodynamically equivalent 777
- Sphericity 717
- Spiral pattern 780
- Split plenum 361
- Splitters 760, 765
- Splitting efficiency 762
- Spouted bed coaters 335
- Spouted beds 356
 - multiple 260
- Spouted fluid bed 237
- Spouting beds 38, 74
- Spouting velocity 238
- Spray granules 482
- Spray rate 359, 380
- Spray zone 337, 351, 372
- Spray-dried catalysts 438
- Spray-drying 475
- Stability
 - in fluidized beds 124
- Stability principle 124
- Stabilized bed 657
- Staged fluidized leaching 502
- Stagnant gas stream 341
- Stagnant zones 217
- Stagnation enthalpy 598
- Start-up 259, 260, 735, 736
 - risks 856
- Steel
 - smelting reduction 603
- Steel particles 96
- Stefan-Boltzman equation 171
- Stepped-diameter pipelines 747
- Stickiness 368, 418
- Sticking 366, 381, 384
- Stokes number 383, 384, 385, 386,
387, 392, 394, 416
- Stokes' velocity 775
- STR 654
- Strand flow 696
- Strands 198, 523
- Stratification 648, 651
- Streamline 289, 294
- Strengthening rates 396
- Strengthening time 397
- Stress tensors 30
- Stress tests 452
- Studsvik 96
- Studsvik bed 99
- Submerged heat-transfer tubes 156
- Submerged-jet tests 449
- Subsidence time 562, 565
- Substrate inhibition 655
- Sulfite process 605
- Supercritical fluid 344
- Superficial gas velocity 139, 174
- Superficial velocity 61, 84, 154
- Surface
 - heat transfer 188
- Surface charge density 821

Surface renewal 164
 Surface tension 382
 Surface volume mean diameter 720
 Surface-active agents 853
 Surfactants 337, 379, 608, 614
 Surge effects 735
 Suspended probes 833
 Suspension 201
 Suspension density 182, 185, 190
 Suspension flow 752
 Swarms 523
 Swirl 762
 Switch loading 862
 Synergism number 568
 Synthetic fuel 585
 Synthol CFB reactors 1

T

T-STAR process 585, 615, 616
 Takt-Schub system 686
 Talc 565
 Tangentials 788
 Tapped bulk density 715
 Taylor instability 126, 127
 TCF bleaching 610
 Temperature 223, 443
 elevated 111
 Temperature effects 120
 Temperature range 113
 Temperature run-away 618
 Terminal cross-sectional area 496
 Terminal transport 154
 Terminal velocity 155
 Thermal conductivity 130, 186
 Thermal radiation 190
 Thermal resistance 167, 197
 Thermal shock 443
 Thermal transport 162
 Thermite reaction 837
Thiobacillus ferrooxidans 658
 Three point bend test 401
 Three-phase biofluidization 625
 Three-phase ebullated bed reactor 615
 Three-phase fluidization 582, 583,
 614, 619, 623
 historical development 583
 phases 583
 Three-phase fluidized bed 586
 Three-phase mixtures 604
 Three-phase slurry reactor 621
 Threshold velocity. 452
 Throughflow coefficient 17
 Tidd combustor 77
 Time constant 655
 Time scale factor 362
 Tollmien's Similarity 288
 Tollmien's solution 269
 Torque 370
 Total granulation time 397
 Tote bins 863
 Toxic compounds 633
 Trace air system 686
 Tracer gas 245
 Tracer particles 305
 Tracers 6
 Trajectory calculations 384
 Tramp metal 859
 Transfer coefficient 504
 Transfer factor 506
 Transient conduction equation 164
 Transient field reversals 856
 Transition region 117
 Transition velocity 25, 139
 Transport behavior 726
 Transport disengaging height (TDH) 134
 Tribo-series 819
 Tribocharge 822
 Triboelectric charging 829
 Triboelectrification 817, 818, 819, 823,
 825, 857
 Tube bank 17
 horizontal 16
 Tube circumference 156
 Tube erosion 88
 Tubes 156
 Tumbler tests 453
 Turbulent Bed Contactor 585
 Turbulent convection 199
 Turbulent to fast fluidization 139, 142
 Turndown 214
 Tuyere injection 754
 Tuyere type 477
 Two-flux radiative model 199
 Two-phase convection 195
 Two-phase flow 154, 696
 model 9

890 *Fluidization, Solids Handling, and Processing*

U

Ultrasonic nozzles 339
Unrecoverable particle size 794
Upset conditions 263
Upwardly-directed 212

V

Vaccine production 660
Valves 736, 749
Van der Waals forces 31
Vanadium phosphate catalysts 475
Velocity 155, 254
 effect on attrition 464
 entrainment 308
 particle 197, 251
 relative 387
 vs. temperature 118
Velocity profiles 265, 269
Vena contracta effect 219
Verification of scaling relationships 65
Vertical bed 175
Vertical internals 6
Vertical pneumatic moving bed 707
Vertical tubes 168, 178
Vessel loading 856
Vessel size 855
Viscosity 120, 131
Viscous dominated flow 53
Viscous effects 117
Viscous forces 70, 382
Viscous limit 53, 54, 55
Viscous limit scaling laws 70, 94, 96
Void fraction 165
Voidage 38, 120, 122, 243
 dense-phase 121
 loose packed 75
Voidage distribution 23, 526, 529, 533
Voidage disturbances 124
Voidage in draft tube 364
Volume-active agents 853
Volumetric mass transfer coefficient 650
Volumetric solid loading 252
Volumetric wear rate 403, 405
Volute 785
Vortex 778, 794

W

Wall effects 17, 77
Wall layer 25
Wall-hardness 443
Wall-particle 196
Wall-to-suspension heat transfer 197
Washburn Test 375
Washing 492, 496
Washing column 502
Waste gas 538
Waste treatment 639
Wastewater treatment 586, 623, 632, 641, 642
Wear
 tube 88
Wear problems 752
Wear rate 88, 403, 405
Weepage 209, 223
Weld burrs 781
Wen and Simon expression 696
Wen and Yu correlation 115
Wen and Yu Equation 116
Wet agglomerates 392
Wet scrubbing 585
Wetting 337, 373, 374, 375, 380
Windbox 223
Wood chips 605
 cooking 604
Work Index 447
Wurster Insert 335, 356

Y

Y-splitters 766
Yield number 394
Yield strength 394
Yield stress 400
Young-Dupré equation 373

Z

Ziegler alcohol 585
Zymomonas mobilis 651